LEVEL II (12)

AFWAL-TR-81-4080

AD A108741

PROCEEDINGS OF THE DARPA/AFWAL REVIEW OF PROGRESS IN QUANTITATIVE NDE

ROCKWELL INTERNATIONAL, SCIENCE CENTER
1049 CAMINOS DOS RIOS
THOUSAND OAKS, CALIFORNIA 91360

SEPTEMBER 1981

TECHNICAL REPORT AFWAL-TR-81-4080
Final Report for Period October 1979 — January 1981

DTIC ELECTE DEC 2 2 1981 S D A

DTIC FILE COPY

Approved for public release; distribution unlimited

MATERIALS LABORATORY
AIR FORCE WRIGHT AERONAUTICAL LABORATORIES
AIR FORCE SYSTEMS COMMAND
WRIGHT-PATTERSON AIR FORCE BASE, OHIO 45433

81 12 22 002

NOTICE

When Government drawings, specifications, or other data are used for any purpose other than in connection with a definitely related Government procurement operation, the United States Government thereby incurs no responsibility nor any obligation whatsoever; and the fact that the government may have formulated, furnished, or in any way supplied the said drawings, specifications, or other data, is not to be regarded by implication or otherwise as in any manner licensing the holder or any other person or corporation, or conveying any rights or permission to manufacture, use, or sell any patented invention that may in any way be related thereto.

This report has been reviewed by the Office of Public Affairs (ASD/PA) and is releasable to the National Technical Information Service (NTIS). At NTIS, it will be available to the general public, including foreign nations.

This technical report has been reviewed and is approved for publication.

JOSEPH A. MOYZIS, Jr.
Project Engineer

FOR THE COMMANDER

D. M. FORNEY, Jr., Chief
Nondestructive Evaluation Branch
Metals and Ceramics Division

"if your address has changed, if you wish to be removed from our mailing list, or if the addressee is no longer employed by your organization please notify AFWAL/MLLP, WPAFB, OH 45433 to help us maintain a current mailing list."

Copies of this report should not be returned unless return is required by security considerations, contractual obligations, or notice on a specific document.

AIR FORCE/56780/30 November 1981 — 500

UNCLASSIFIED
SECURITY CLASSIFICATION OF THIS PAGE (When Data Entered)

REPORT DOCUMENTATION PAGE	READ INSTRUCTIONS BEFORE COMPLETING FORM
1. REPORT NUMBER: AFWAL-TR-81-4080	2. GOVT ACCESSION NO. AD-A108 942 / 3. RECIPIENT'S CATALOG NUMBER
4. TITLE (and Subtitle): PROCEEDINGS OF THE DARPA/AFWAL REVIEW OF PROGRESS IN QUANTITATIVE NONDESTRUCTIVE EVALUATION	5. TYPE OF REPORT & PERIOD COVERED: Final Report for period 10/01/79-01/01/81
	6. PERFORMING ORG. REPORT NUMBER: SC5250.22FR
7. AUTHOR(s): R. Bruce Thompson, P.M. Beckham, Program Managers	8. CONTRACT OR GRANT NUMBER(s): F33615-80-C-5004
9. PERFORMING ORGANIZATION NAME AND ADDRESS: Rockwell International, Science Center, 1049 Camino Dos Rios, Thousand Oaks, California 91360 $89949	10. PROGRAM ELEMENT, PROJECT, TASK AREA & WORK UNIT NUMBERS: 2418-06-04
11. CONTROLLING OFFICE NAME AND ADDRESS: Defense Advanced Research Projects Agency, 1400 Wilson Boulevard, Arlington, Virginia 22209	12. REPORT DATE: September 1981
	13. NUMBER OF PAGES: 598
14. MONITORING AGENCY NAME & ADDRESS (if different from Controlling Office): Materials Laboratory, AFWAL/MLLP, Wright Patterson AFB, Ohio 45433	15. SECURITY CLASS. (of this report): UNCLASSIFIED
	15a. DECLASSIFICATION DOWNGRADING SCHEDULE

16. DISTRIBUTION STATEMENT (of this Report)

Approved for Public Release; distribution unlimited.

17. DISTRIBUTION STATEMENT (of the abstract entered in Block 20, if different from Report)

18. SUPPLEMENTARY NOTES

19. KEY WORDS (Continue on reverse side if necessary and identify by block number)

Non destructive evaluation; nondestructive testing; quantitative ultrasonics; eddy currents; signal processing; ultrasonic imaging; acoustic emissions, ceramic NDE; retirement for cause; failure mechanisms; ultrasonic scattering, ultrasonic inversion; electromagnetic techniques.

20. ABSTRACT (Continue on reverse side if necessary and identify by block number)

The edited transcripts of the DARPA/AF Review of Progress in the Interdisciplinary Program for Quantitative Nondestructive Evaluation (NDE) held on July 14-18, 1980, at Scripps Institution of Oceanography, La Jolla, California are presented in this document. Several key topics form the core of these presentations and discussions. They include retirement for cause, quantitative ultrasonics, acoustic emission, electromagnetic techniques, and the reliability of NDE techniques for metals, ceramics, and composites. It is believed that this document provides a reasonable summary of NDE research and development currently underway.

DD FORM 1 JAN 73 1473

$89949

UNCLASSIFIED
SECURITY CLASSIFICATION OF THIS PAGE (When Data Entered)

PREFACE

This report contains the edited transcripts of the Review of Progress in Quantitative Nondestructive Evaluation held at the Scripps Institution of Oceanography, July 14-18, 1980. The review was sponsored by the Defense Advanced Research Projects Agency and the Materials Laboratory of the Air Force Wright Aeronautical Laboratories as a part of the Interdisciplinary Program for Quantitative NDE, Contract No. F33615-80-C-5004. Arrangements for the Review were made by the Science Center, Rockwell International, host organization for the Interdisciplinary Program, and the Scripps Institution of Oceanography, Dr. William A. Nierenberg, Director.

The format selected for this review was the same as that adopted for previous meetings. This included a number of poster sessions in addition to the more traditional technical sessions. It has been found that the poster sessions provide a good way to accommodate the increased activity in this field while maintaining a forum that is highly conducive to technical interchange. As a further means of stimulating this exchange, a number of papers were included which are directly related to the principal technical interests of this program even though they were not directly sponsored by DARPA or the Air Force.

The program emphasized several areas of the progress in quantitative NDE. In addition to the work in quantitative ultrasonics, which has been a main program activity, the latest work in electromagnetic techniques and a proposed strategy for NDE of adhesive bonds was reported. A new concept that has received increasing attention over the past year is the concept of Retirement-For-Cause. Present efforts in this area were reviewed - an area in which advanced NDE techniques can have a very important and quantifiable impact on a major DOD system.

In all these areas, strong emphasis is placed upon the physical interpretation of the quantitative measurements and their evaluation in terms of appropriate failure models. Emphasis is also given in the program to presentations and discussions which address state-of-the-art knowledge related to the development of failure models for both ceramic and metallic materials, and the difference in such models required by the nature of the materials.

Dr. Arden L. Bement, Deputy Under Secretary for Defense Research and Advanced Technology, gave an excellent overview of reliability needs in future DOD systems. In his presentation, which is included in these Proceedings, he provided an overview of current thinking as to the threats facing this country and the future capabilities currently under development. Examined were the role of improved reliability in reducing operating and maintenance costs and increasing military capability, as well as the role of research and development in meeting future reliability requirements. Finally, some of the new policies initiated in the Defense Research and Advanced Technology organizations to develop a more effective R and D program were presented.

The organizers of the Review wish to acknowledge the financial support and encouragement provided by DARPA, the Air Force and the technical participation of members of the Materials Research Council. Special thanks are due to Dr. Bement for his overview. The organizers also wish to thank speakers, session chairmen, authors of poster presentations, and participants who collaborated to provide a stimulating meeting. They wish to acknowledge with thanks the assistance of Mrs. Diane Harris who managed the organizational matters of the meeting and who organized these Proceedings, and Mrs. Sarah Bergmann for her assistance at the meeting. They are also indebted to the management of the Scripps Institution of Oceanography, particularly Dr. William Nierenberg and Mrs. Shirlee Long, UCSD, for their cooperative support in the conduct of the meeting.

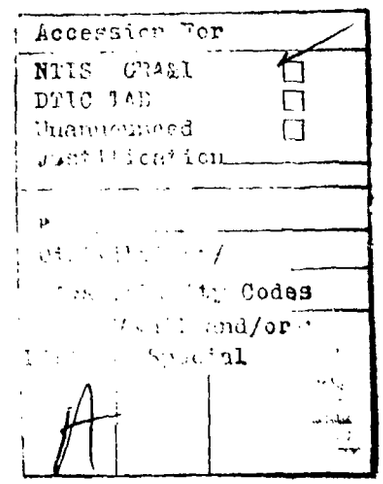

DEFENSE ADVANCED RESEARCH PROJECTS AGENCY/AIR FORCE MATERIALS LABORATORY

REVIEW OF PROGRESS
IN
QUANTITATIVE NDE

July 14 - 18, 1980
Scripps Institution of Oceanography
University of California
La Jolla, California

TABLE OF CONTENTS

SESSION I - INTRODUCTORY — R. Bruce Thompson, Chairman — PAGE

INTRODUCTORY REMARKS
R. Bruce Thompson
Rockwell International Science Center 1

PROGRAM COMMENTS
M. J. Buckley, Defense Advanced Research Projects Agency
J. Moyzis, Air Force Wright Aeronautical Laboratories 4

RELIABILITY NEEDS IN FUTURE DoD SYSTEMS
A. L. Bement, Jr.
Research & Advanced Technology 7

SESSION II - RETIREMENT-FOR-CAUSE — M. J. Buckley, Chairman

ENGINE COMPONENT RETIREMENT-FOR-CAUSE:
A NONDESTRUCTIVE EVALUATION (NDE) AND FRACTURE
MECHANICS BASED MAINTENANCE CONCEPT
C. G. Annis, J. S. Cargill, J. A. Harris, Jr. and M. C. Vanwanderham 12
Materials and Mechanics Technology

INTEGRATION OF NONDESTRUCTIVE EXAMINATION RELIABILITY AND FRACTURE MECHANICS
L. Becker and S. Doctor
Battelle Pacific Northwest Laboratories 21

REMAINING FATIGUE LIFETIME PREDICTION FOR RETIREMENT-FOR-CAUSE IN METALS
W. L. Morris, M. R. James and O. Buck
Rockwell International Science Center 24

SESSION III - COUPLING OF NDE AND FAILURE MODELS — O. Buck, Chairman

ENERGY RELEASE RATES FOR A PLANE CRACK SUBJECTED TO GENERAL LOADING
AND THEIR RELATION TO STRESS-INTENSITY FACTORS
A. Golebiewska Herrmann and George Herrmann
Stanford University 32

ACOUSTIC NONDESTRUCTIVE EVALUATION OF ENERGY RELEASE RATES IN PLANE CRACKED SOLIDS
R. King, G. Herrmann and G. Kino
Stanford University 38

PLANNING ACTIVITY REPORT FOR NDE OF ADHESIVE BONDED STRUCTURES
F. N. Kelley, University of Akron
W. G. Knauss, California Institute of Technology
D. H. Kaelble, Rockwell International Science Center 44

SESSION IV - COMPOSITES, ADHESIVE BONDS, NEW PHENOMENA AND PROBLEMS (Poster)

NDT OF COMPOSITES BY THERMOGRAPHY
P. V. McLaughlin, Jr., E. V. McAssey, Jr. and D. N. Koert, Villanova University
R. C. Deitrich Naval Air Engineering Center 60

PAGE

NONDESTRUCTIVE EVALUATION OF GRAPHITE/EPOXY COMPOSITE DAMAGE
S. W. Schramm, I. M. Daniel and W. G. Hamilton
IIT Research Institute..... 69

NONDESTRUCTIVE EVALUATION OF COMPOSITE MATERIALS WITH BACKSCATTERING MEASUREMENTS
Y. Bar-Cohen, Systems Research Laboratories, Inc.
R. L. Crane, AFWAL/MLLP, WPAFB..... 78

EVALUATION OF THE STRUCTURAL INTEGRITY OF GRANULAR COMPOSITES BY ULTRASONIC TECHNIQUES
H. R. Carleton, W. Burke and W. J. Chen
State University of New York..... 81

X-RAY DIFFRACTION EVALUATION OF ADHESIVE BONDS AND DAMAGE IN COMPOSITES
Charles S. Barrett and Paul Predecki
University of Denver Research Institute..... 87

STUDY PROGRAM FOR ENCAPSULATION MATERIALS INTERFACE FOR LOW-COST SOLAR ARRAY (LSA)
D. H. Kaelble and C. L. Leung, Rockwell International Science Center
J. Moacanin, Jet Propulsion Laboratory..... 93

FRACTURE MECHANICS OF TWO DIMENSIONAL NONCIRCULAR FLAWS
Roger Chang
Rockwell International Science Center..... 100

FLOW DETECTION IN UNDERLYING STRUCTURE - PROBLEMS AND OPPORTUNITIES
J. A. Moyzis, Jr.
Wright-Patterson A.F.B..... 105

NONDESTRUCTIVE EVALUATION (NDE) FOR THERMAL-SPRAY COATINGS
Robert A. Sulit, Naval Surface Force
Vincent D. Schaper and David W. Taylor, Annapolis Laboratory..... 106

IMPROVED IMAGING OF MAGNETIC FLUX LEAKAGE FIELDS
Alfred L. Broz
Army Materials and Mechanics Research Center..... 108

SESSION V - CERAMIC NDE A. G. Evans, Chairman

INTRODUCTION TO CERAMIC NDE
A. G. Evans
University of California..... 109

MICROFOCUS RADIOGRAPHY
W. N. Reynolds
AERE, Harwell, England..... 110

OVERVIEW OF CERAMICS PROJECT
R. Bruce Thompson
Rockwell International Science Center..... 114

ACCEPT-REJECT DECISIONS AND PROBABILISTIC FAILURE PREDICTION
J. M. Richardson and K. W. Fertig, Jr., Rockwell International Science Center
A. G. Evans, University of California, Berkeley..... 119

ACOUSTIC MICROSCOPE OF CERAMICS
L. W. Kessler, D. E. Yuhas and C. L. Vorres
Sonoscan Inc..... 128

NDE FOR BULK DEFECTS IN CERAMICS
B. T. Khuri-Yakub, C. H. Chou, K. Liang and G. S. Kino
Stanford University..... 137

SURFACE ACOUSTIC WAVE MEASUREMENTS OF SURFACE CRACKS IN CERAMICS
J. J. W. Tien, B. T. Khuri-Yakub and G. S. Kino, Stanford University
A. G. Evans and D. Marshall, University of California..... 144

LOW FREQUENCY CHARACTERIZATION OF FLAWS IN CERAMICS
R. K. Elsley, L. A. Ahlberg and J. M. Richardson
Rockwell International Science Center..... 151

PAGE

SESSION VI - ULTRASONIC IMAGING: EUROPEAN EFFORT G. Kino, Chairman

THE APPLICATION OF ULTRASONICS IN NON-DESTRUCTIVE TESTING:
A REVIEW OF SOME OF THE RESEARCH AT UNIVERSITY COLLEGE LONDON
M. D. Ambersley, L. J. Bond, A. L. Downie, W. Duerr, C. W. Pitt,
D. A. Sinclair and I. R. Smith
University College London..... 165

DEFECT CLASSIFICATION AND IMAGING WITH PHASE ARRAY TECHNIQUES
V. Schmitz, W. Gebhardt, F. Bonitz
Fraunhofer Institute fur zerstorungsfreie Prufverfahren..... 179

SCANNED IMAGING TECHNIQUES FOR SURFACE NDE
S. Ameri, E. A. Ash, C. R. Petts and H. K. Wickramasinghe
University College London..... 186

SESSION VII - ULTRASONIC IMAGING AND MICROSCOPE (Poster)

A REAL-TIME SYNTHETIC APERTURE DIGITAL ACOUSTIC IMAGAING SYSTEM
S. Bennett, D. K. Peterson, D. Corl and G. S. Kino
Stanford University..... 194

ADVANCES IN COMPUTER RECONSTRUCTION OF ACOUSTICAL HOLOGRAPHY
V. Schmitz, R. Kiefer, G. Schafer
Fraunhofer Institute fur zerstorungsfreie Prufverfahren..... 203

ACOUSTIC IMAGING BY WAVEFRONT RECONSTRUCTION
K. M. Lakin, W. R. Sheppard and K. Tam
University of Southern California..... 208

IMAGE PROCESSING FOR NONDESTRUCTIVE EVALUATION
M. H. Jacoby
Lockheed Missiles & Space Co..... 212

COLOR GRAPHICS: AN AID TO DATE INTERPRETATION
C. C. Ruokangas and J. F. Martin
Rockwell International Science Center..... 216

RECENT PROGRESS IN MATERIALS STUDIES WITH ACOUSTIC MICROSCOPY
R. C. Bray and C. F. Quate
Stanford University..... 223

ACOUSTIC MICROSCOPY OF CURVED SURFACES
R. D. Weglein
Hughes Aircraft Company..... 231

PHOTOACOUSTIC MICROSCOPY
L. D. Favro, L. I. Inglehart, P. K. Kuo, J. J. Pouch and R. L. Thomas
Wayne State University..... 236

SESSION VIII - ACOUSTIC EMISSION AND MATERIAL PROPERTY MEASUREMENTS W. Pardee, Chairman

THEORY OF ACOUSTIC EMISSION
John A. Simmons and Roger B. Clough
National Bureau of Standards..... 239

REPRODUCIBLE ACOUSTIC EMISSION SIGNATURES BY INDENTATION IN STEELS
Roger B. Clough and John A. Simmons
National Bureau of Standards..... 241

IN-FLIGHT ACOUSTIC EMISSION RESEARCH
John M. Carlyle
Naval Air Development..... 243

SCATTERING OF SURFACE ACOUSTIC WAVES FROM AN ELASTIC PLATE ATTACHED
TO A HALF-SPACE WITH A VISCOUS COUPLANT
D. B. Bogy and Y. Angel
University of California, Berkeley..... 248

PAGE

THE INFLUENCE OF THIN BONDING LAYERS ON THE LEAKY WAVES AT LQUID-SOLID INTERFACES
A. H. Nayfeh
Systems Research Laboratories 254

NON-DESTRUCTIVE ACOUSTIC DETERMINATION OF RESIDUAL STRESSES IN
HYDROSTATICALLY EXTRUDED ALUMINUM RODS
M. P. Scott and D. M. Barnett
Stanford University 263

THE DETERMINATION OF TENSILE STRESSES USING THE TEMPERATURE DEPENDENCE
OF ULTRASONIC VELOCITY
K. Salama, A. L. W. Collins and Jen-Jo Wang
University of Houston. 265

EFFECT OF GRAIN SIZE AND PREFERRED CRYSTAL TEXTURE
ON ACOUSTIC PROPERTIES OF 304 STAINLESS STEEL
N. Grayeli, F. Stanke, G. S. Kino and J. C. Shyne
Stanford University 269

SESSION IX - ULTRASONIC SCATTERING FROM IRREGULAR FLAWS B. Thompson, Chairman

ELASTIC WAVE SCATTERING FROM MULTIPLE AND ODD SHAPED FLAWS
V. V. Varadan, V. K. Varaden and D. J. N. Wall
The Ohio State University 276

APPLICATION OF MOOT TO SCATTERING OF ELASTIC WAVES FROM COMPOUND INCLUSIONS
William M. Visscher
University of California 287

CALCULATIONS OF ELASTIC WAVE SCATTERING FROM VOIDS AND
CRACK-LIKE DEFECTS BY THE METHOD OF OPTIMAL TRUNCATION
J. L. Opsal
Lawrence Livermore Laboratory 292

ELASTIC WAVE SCATTERING CALCULATIONS AND THE MATRIX VARIATIONAL PADE APPROXIMANT METHOD
J. E. Gubernatis
University of California 300

SCATTERING OF ELASTIC WAVES BY COMPLEX DEFECTS; MULTIPLE SCATTERING FORMALISM
Eytan Domany, Weizmann Institute of Science
Leah Mizrachi, International Centre for Theoretical Physics 305

MEASUREMENTS OF SCATTERING FROM BULK DEFECTS
B. R. Tittmann and L. Ahlberg
Rockwell International Science Center 311

SESSION X - ULTRASONIC SCATTERING FROM CRACKS B. Tittmann, Chairman

ULTRASONIC CHARACTERIZATION OF ROUGH CRACKS
M. de Billy, F. Cohen-Tenoudji and Gerard Quentin, Universite Paris 7
Kent Lewis, University of Tennessee
Laszlo Adler, Universite Paris 7 and University of Tennessee 320

ELASTIC WAVES SCATTERING FROM CORRUGATED METAL INTERFACES
A. Jungman and G. Quentin, Universite Paris 7
Laszlo Adler, Universite Paris 7 and University of Tennessee 330

SCATTERING BY SURFACE-BREAKING AND SUB-SURFACE CRACKS
J. D. Achenbach, R. J. Brind and A. Norris
The Technological Institute Northwestern University 340

RESONANCES AND CRACK ROUGHNESS EFFECTS IN SURFACE BREAKING CRACKS
S. Ayter and B. A. Auld
Stanford University 348

PAGE

ELASTIC WAVE SCATTERING FROM GRIFFITH CRACKS
Kent Lewis, Dale Fitting and Laszlo Adler
Ohio State University..... 355

SESSION XI - ULTRASONIC INVERSION: SHORT WAVELENGTH TECHNIQUES J. Achenbach, Chairman

ABOUT THE EFFICIENCY OF USING "EXTENDED" FOURIER TRANSFORMS FOR SURFACE CHARACTERIZATION BY THE DECONVOLUTION TECHNIQUE
F. Cohen-Tenoudji and G. Quentin
Universite Paris 7..... 359

EXACT INVERSE SCATTERING THEORY
Norbert N. Bojarski
Newport Beach, California..... 366

AN EXACT THEORY FOR COHERENT NONDESTRUCTIVE EVALUATION: THE APPLICATION OF THE BOJARSKI EXACT INVERSE SCATTERING THEORY TO THE REMOTE PROBING OF INHOMOGENEOUS MEDIA
W. Ross Stone
IRT Corporation..... 370

DIRECT INVERSION IN COMPLEX GEOMETRIES
Jack K. Cohen and Norman Bleistein
Denver Applied Analytics..... 376

SESSION XII - ULTRASONIC INVERSION: INTERMEDIATE AND LONG WAVELENGTH TECHNIQUES J. A. Krumhansl, Chairman

TIME DOMAIN BORN APPROXIMATION
J. H. Rose, Iowa State University
J. M. Richardson, Rockwell International Science Center..... 382

DEPENDENCE OF THE ACCURACY OF THE BORN INVERSION ON NOISE AND BANDWIDTH
R. K. Elsey and R. C. Addison
Rockwell International Science Center..... 389

RAMP WAVE PROCESSING OF LONG WAVELENGTH ULTRASONIC SCATTERING INFORMATION
Bill D. Cook, Shelford Wilson and Ronald L. McKinney
University of Houston..... 396

ULTRASONIC FLAW CHARACTERIZATION IN THE RESONANCE REGION BY THE BOUNDARY INTEGRAL EQUATION METHOD
L. W. Schmerr, Jr., C. Sieck
Iowa State University..... 398

APPLICATION OF ADAPTIVE LEARNING NETWORKS TO QUANTITATIVE FLAW DEFINITION
M. F. Whalen, P. M. Garafola, L. J. O'Brien and A. N. Mucciardi
Adaptronics, Inc..... 405

SENSITIVITY OF FAILURE PREDICTION TO FLAW GEOMETRY
J. M. Richardson, R. Chang and K. W. Fertig, Jr., Rockwell International Science Center
V. V. Varadan, Ohio State University..... 433

SESSION XIII - ULTRASONIC SIZING OF SURFACE CRACKS L. Bond, Chairman

AN ULTRASONIC TECHNIQUE FOR SIZING SURFACE CRACKS
C. P. Burger, A Singh
Iowa State University and Southwest Research Institute..... 436

DECONVOLUTION PROCEDURE FOR CRACK DEPTH DETERMINATION USING RAYLEIGH WAVES
G. P. Singh and A. Singh
Southwest Research Institute..... 443

CRACK DEPTH MEASUREMENTS WITH THE AID OF SAW NDE
B. Tittmann, L. Ahlberg and O. Buck
Rockwell International Science Center..... 451

PAGE

SESSION XIV - ELECTROMAGNETIC TECHNIQUES J. Martin, Chairman

THE IMPEDANCE OF A LOOP NEAR A CONDUCTING HALF-SPACE
Afroz J. M. Zaman, Stuart A. Long and C. Gerald Gardner
University of Houston..... 457

PROGRESS IN SOLVING THE 3-DIMENSIONAL INVERSION PROBLEM FOR EDDY CURRENT NDE
T. G. Kincaid, K. Fong, M. V. K. Chari
General Electric Company..... 463

DEVELOPMENT OF EDDY-CURRENT PROBES FOR THE EVALUATION OF MAGNETITE IN THE SUPPORT-PLATE CREVICES OF NUCLEAR STEAM GENERATORS
A. Sagar
Westinghouse Nuclear Technology Division..... 469

DETECTION AND CHARACTERIZATION OF DEFECTS BY THE ELECTRIC CURRENT PERTURBATION METHOD
Cicil M. Teller and Gary L. Burkhardt
Southwest Research Institute..... 477

SURFACE FLAW DETECTION WITH FERROMAGNETIC RESONANCE PROBES
B. A. Auld, F. Muennemann, D. K. Winslow
Stanford University..... 485

MEASUREMENT OF SURFACE CRACK OPENING DISPLACEMENTS USING MICROWAVE FREQUENCY EDDY CURRENTS
M. T. Resch, F. Muennemann, B. A. Auld, D. Winslow and J. C. Shyne
Stanford University..... 493

MICROWAVE EDDY-CURRENT TECHNIQUES FOR QUANTITATIVE NDE
A. J. Bahr
SRI International..... 498

SESSION XV - APPLICATIONS (Poster)

FEASIBILITY OF NONDESTRUCTIVELY EVALUATING THE M140 RECOIL PISTON HEAD WELD
Roy L. Buckrop
U. S. Army Armament Command..... 510

WAVEFORM DESIGN FOR MAXIMUM PASS-BAND ENERGY
Steven R. Doctor, Alan G. Gibbs and R. Parks Gribble
Pacific Northwest Laboratories..... 515

APPLICATION OF LASER LIGHT PROBES TO QUANTITATIVE SENSING OF STRESS WAVES
B. Boro Djordjevic
Martin Marietta Laboratories..... 520

A NOVEL DETECTOR ARRAY FOR INDUSTRIAL X-RAY TOMOGRAPHY
P. S. Ong and H. T. Huang
University of Houston..... 526

PULSED ELECTROMAGNETS FOR EMATS
C. M. Fortunko, National Bureau of Standards
D. MacLauchlan, University of New Mexico..... 528

INSPECTION OF WING LAP JOINTS FOR SECOND LAYER CRACKS WITH EMATS
J. F. Martin, P. J. Hodgetts and R. B. Thompson
Rockwell International Science Center..... 535

APPLICATION OF EMATs TO IN-PLACE INSPECTION OF RAILROAD RAILS
H. Maiseri, D. MacLauchlan and G. Alers
Rockwell International Science Center..... 544

INDUSTRIAL PROBLEMS ENCOUNTERED IN THE EDDY CURRENT INSPECTION OF STEEL
G. C. Jeskey, F. P. Vaccaro
The Timken Company..... 548

USING CAPACITIVE PROBES IN ELECTROMAGNETIC NONDESTRUCTIVE TESTING
B. A. Auld and M. Riaziat
Stanford University..... 556

PAGE

ADVANCED ULTRASONIC NDE EQUIPMENT
A. S. Birks, G. J. Posakony
Battelle Northwest Laboratories..... 559

INFLIGHT FATIGUE CRACK MONITORING USING ACOUSTIC EMISSION
P. H. Hutton and J. R. Skorpik
Battelle, Pacific Northwest Laboratory..... 560

THE ANALYTIC SIGNAL MAGNITUDE FOR IMPROVED ULTRASONIC SIGNATURES
Paul M. Gammell
Jet Propulsion Laboratory..... 563

SESSION XVI - TEST BEDS T. Moran, Chairman

FATIGUE CRACK DETECTION AND SIZING IN WELDED STEEL STRUCTURES
I. M. Kilpatrick and J. Cargil
Admiralty Marine Technology Establishment..... 567

TEST BED FOR QUANTITATIVE NDE
R. C. Addison, R. B. Houston, J. R. Martin, R. B. Thompson
Rockwell International Science Center..... 576

GENERALIZED ULTRASONIC SYSTEM FOR MICROCOMPUTER CONTROLLED DATA COLLECTION
Ronald D. Streng
Los Alamos Scientific Laboratory..... 585

ATTENDEES LIST..... 591

INTRODUCTORY REMARKS

R. Bruce Thompson
Rockwell International Science Center
Thousand Oaks, CA 91360

ABSTRACT

This philosophy and directions of the DARPA/AFML Interdisciplinary program for Quantitative NDE are reviewed and the structure of this review meeting is summarized.

Philosophy of Interdisciplinary Program for Quantitative NDE

I would like to make a few, very general, introductory remarks about the philosophy of the Quantitative NDE program and to point out some important features of the meeting this week.

The major reason for developing a quantitative NDE capability is so that strengths or lifetimes can be predicted with as high an accuracy as possible. Figure 1 reviews the steps that are required to predict lifetimes in metals under conditions of cyclic fatigue. The core of the prediction is a failure model, such as fracture mechanics. In order to apply this, one typically needs three types of inputs: environmental considerations, such as stress levels, which are often determined by design; material properties such as toughness, which can be determined from handbooks; and flaw sizes and orientations. Determination of the latter, typically, has been the problem area. That deficiency stimulated the initiation of the Quantitative NDE program several years ago. During this week, the present status of techniques to determine flaw size and orientation, and other input parameters required by specific failure models, will be reviewed.

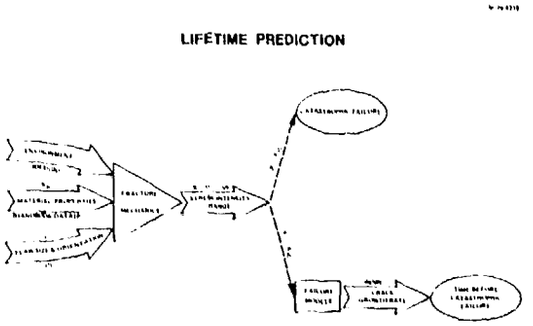

Figure 1. Life prediction.

The meeting, however, does not focus just on the determination of flaw size and orientation, because that does not stand by itself. The results of this determination must be coupled to the failure modeling, and so a number of papers will be included which are concerned with the close interaction between nondestructive measurement and failure modeling in nondestructive prediction of lifetime or strength.

Figure 2 illustrates the latter point a little bit more completely. What the ultimate user of a material system wants is an accept/reject criteria to tell him whether he can accept or reject a part. This can be required during the manufacturing process or after a period of service life. Such a decision must be based on a life prediction. As noted in Figure 1, a deterministic life prediction requires three inputs: environment, material, and flaw descriptors. In Fig. 2, the former two have been combined under the heading failure modeling and the flaw parameters have been highlighted by placing them in a separate box. This is labeled measurement science and consists of inversion techniques whereby flaw parameters are estimated from nondestructively measured data.

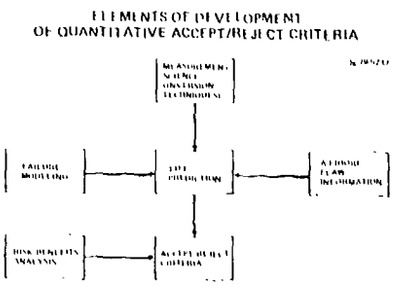

Figure 2. Steps required to establish accept/reject criteria.

In reality, life prediction can never be done in a fully deterministic fashion. Uncertainties

in all of the three inputs imply that only statistical predictions of lives can be made. In the case of flaw sizing, this occurs even with no measurement error, because sufficient information cannot always be obtained to unambiguously determine the necessary parameters. If independent, a priori information about the flaw state can be obtained, this will allow more accurate predictions to be made. The opportunity to use such information is explicitly indicated in the figure. Many measurement techniques do this implicitly. Since one seldom measures enough about a flaw to say unambiguously what it is, one is often injecting some experience or other biassing information while interpreting signals. It would be desirable to formalize and quantify this process.

Once a life prediction is made and the probabilities of various errors are defined, one needs to use some sort of risk/benefits analysis to set the ultimate accept/reject criteria. This is shown at the bottom of Fig. 2. In building a foundation for such capability, the measurement sciences aspects have been emphasized since they have been judged to be the weakest link. Other elements have been introduced insofar as they are needed to complete this scenario.

Figure 3 presents a brief summary of the evolution of a quantitative ultrasonics capability over the last several years. Any new technology should be based on building blocks of fundamental knowledge. These then combine to produce generic long term capabilities. For example, basic theories of energy flaw interactions, verified by experiments, lead to an understanding of this interaction. This understanding, coupled to inversion theories, leads to new techniques to characterize flaws. Finally, if engineering developing is added, prototype, and ultimately on line, systems result.

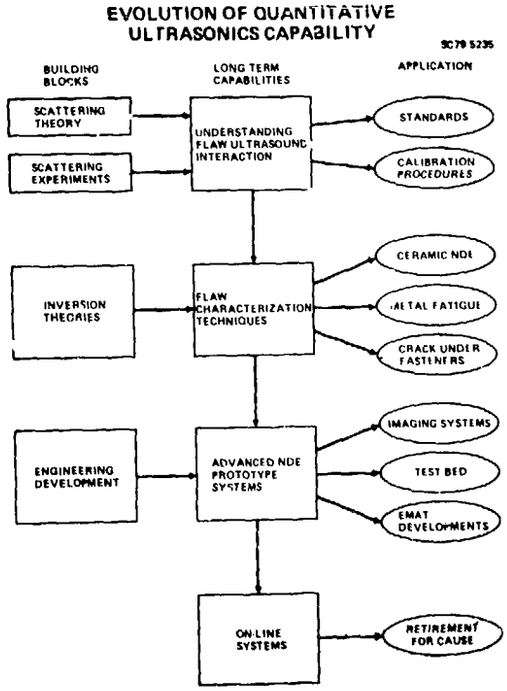

Figure 3. Evolution of quantitative ultrasonics capability.

On the far right of the figure are listed some specific applications that have arisen as a result of this program. Some of these were in the early days of the work, such as development of new standards and calibration procedures. More recently there has been applications of the NDE of ceramics, measurement of metal fatigue, and detection of cracks under fasteners. In the systems area, imaging systems, test beds and some EMAT systems have all been developed. Many of these are ongoing efforts which will be discussed throughout the meeting.

A new concept that has received a high level of attention during the last year is the concept of Retirment-of-Cause. The first session today will discuss the present effort in this area. This is an area in which quantitative techniques can have a very important and very quantifiable impact on a major DOD system.

Structure of the Meeting

Figure 4 presents the program of the meeting. A few remarks about its organization are in order. The first day and a half are concerned with the tight coupling between NDE and fracture mechanics or other failure models. The Retirement-for-Cause session will include three papers. The first will discuss some specific plans, being developed by the Air Force and DARPA, which are directed toward incorporating NDE in a system to inspect in-service turbine disks and return them to service if no flaw likely to produce failure is found. The success of such an approach depends both on the accuracy of the NDE and the failure modeling. The next two papers address these questions. The second discusses evaluations of the reliability of NDE and its coupling to fracture mechanics, and the third discusses the modeling of crack initiation and use of the results in lifetime predictions.

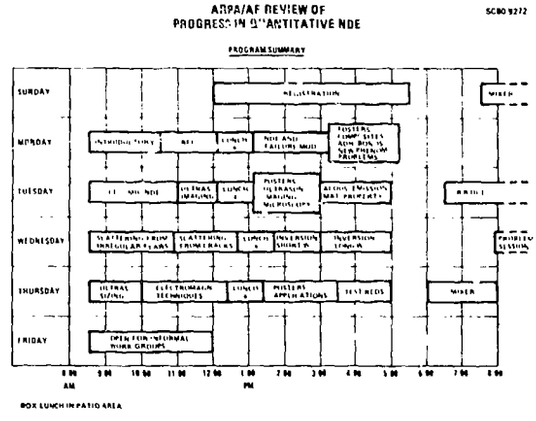

Figure 4. Meeting program.

An important talk in the afternoon session on coupling of NDE and failure modeling will present a proposed strategy for NDE of adhesive bonds. This talk is the result of a planning activity that has been in progress over the last year. Since the subject is an old one that has thus far defied solutions, a significant period has been allowed

for discussion. A broad range of inputs are required to formulate the best possible strategy.

In the ceramics session, we are fortunate to have a paper which was not in the program. Bill Reynolds from the NDE Center at Harwell in England will be with us, and he has consented to give an impromptu report on some of the very interesting microfocus x-ray results that have recently been obtained at that laboratory.

From that point, about two days of technique-oriented papers will be presented: ultrasonic imaging, acoustic emission and material properties, ultrasonic scattering and inversion, and some electromagnetic techniques.

Finally, during the last part of Thursday, application and test bed programs will be discussed. These represent some ongoing programs to transfer quantitative NDE technology into practice.

This meeting has always been characterized by extremely positive technical interchanges between participants from government, industry, and university. This is a very important part of the meeting. Please feel encouraged to exchange thoughts at lunch times, during poster sessions, or any other convenient time.

Closing Comments

It has always been important to receive feedback on the directions of a research program. I would be extremely interested in receiving any comments, particularly from users of this technology, regarding areas that should be emphasized more or should be emphasized less, and regarding directions of research which should be pursued to provide the best scientific foundation for the systems that are being developed for the future.

PROGRAM COMMENTS

M. J. Buckley
Defense Advanced Research Projects Agency
Arlington, Virginia 22205

and

J. Moyzis
Air Force Wright Aeronautical Laboratories
Wright Patterson AFB, Ohio 45433

This is the film which we mentioned last year. It took us a while to get it completed. It is really into management, but it is trying to explain the breadth of work in nondestructive evaluation and its impact. We should have some extra copies of this film available for loan if people are interested in it. We will show the film and make some comments afterwards.

(Film, "Towards a Sound Decision" shown)

I just want to give you a little history because I think we tend to forget where we started from, not that many years ago, in this technology and what led up to the approach which is described in the film. I think this program really had its origins in the Air Force. 1970 to 1972 was a good period, particularly 1970, when you had the crash of the F111 and a major increase in concern about the safety of aircraft structures. A lot of things changed and, basically, what happened was that there was the recognition that nondestructive evaluation or nondestructive inspection had to change from simply the problem of detection to the problem of measurement in order to incorporate fracture mechanics into life prediction. It changed from a zero-defects philosophy to a damage-tolerant philosophy.

At that time there were certainly a large number of techniques available in practice. On the research area you found that almost every program was simply trying to increase the sensitivity of techniques. They were really still pursuing the idea of zero defects. There was no significant university research, at least in any quantity. It was very much people who knew NDE who were working on trying to improve the techniques. There was very limited funding, and this funding was primarily for rather applied problems.

What to do about it led to this program, primarily, and several others to really develop a scientific foundation for understanding the interaction of energy with flaws is the primary initial objective of the program; to develop a new paradigm; that is, a new way of looking at the whole field, a new level of understanding.

There were a series of workshops to identify what were the opportunities, what were the problems, to find people whom we could attract out of other areas to work in this field, and to try to focus basic research. In doing that, for many reasons, we selected ultrasonics as the field in which to work. In this area we had a strong academic base compared to other areas. Its ultimate potential looked behind us, and I think it probably still does for the widest number of things. It is still not a panacea.

I think we found a champion in industry to pull the program together in Don Thompson. This was very important. In fact, it is critical to the whole program of being able to have a core and subcontractors and fit in the pieces in an environment in which the program can be actually managed and not just the money allocated based on need, which has been a problem with a lot of multi-disciplinary programs.

I think the annual open meetings are very important. I think we probably would achieve 50 to 75 percent of the progress if people did not have to get up here and explain their results to their peers. I think having joint support from ARPA and the Air Force has been very important, also. You need the stimulation from the basic side, and you need the pull from the applied side. I think both of those working together have contributed to the success of the program.

But what I really wanted to talk about was how our viewpoint of the field changed. This is sort of the initial model which we had when we started the program. I am speaking simply of the quantitative NDE part. The program had several components, but this was always about two-thirds of the activity. Basically, we said if we are going to get geometrical information about defects, we had to worry about parts, geometry, and transducers. We could either image a defect or go into scattering where we would measure amplitude, phase, and frequency. From the scattering theory we had developed references, we could make comparisons, and then extrapolate or infer what the nature of the defect was.

The program was initially structured something like this. You can see a lot of the people have changed. This is about two-thirds of the program, the basic quantitative NDE, adhesive bonds and composites and strength-related properties; these together were about one-third of the program.

Within about three years, the model had refined itself somewhat, basically realizing that the data inversion was a key item here. Comparison to references was not satisfactory for extracting the data. That changed a lot of the theoretical work. There was still the forward scattering problem being attacked, and the measurement, but increasing emphasis on how do you invert the data. You see much more of that still today. That is a classic problem. At first, I think the theorists were scared by it because it

was not an area in which they had been working, but quickly decided this was a rather exciting problem and one from which they could really get a lot.

About the same time we started to conceptually talk about the problem of coupling this technology into life prediction. At this point, it was simply block diagrams. We were still just working really on the measurement side. We said we had to give this to fracture mechanics somehow and make decisions. People were publishing work on the impact of loss functions, on the decision-making process. But we really had not incorporated it too much into the program.

The program structure had changed a little. Primarily, we shifted over to surface flaws as one of the areas, realizing that surface flaws cause a lot of failures. There was no direct effort in that area in the program which also brought in electromagnetic techniques besides ultrasonics. Advanced materials dealt primarily with ceramics, but also included some additional work on composites and adhesive bonds at this point. Then finally, you get to the model which the film talks about in sort of gross terms, which really comes out as the work in ceramics, where you now have a statistical framework in which to view the whole problem.

I think that the point I wanted to make is that in six years our whole thinking about the area has expanded quite a lot. We have refined it. We have put a mathematical framework around it. I think it is illustrative of how a program like this, although it has basically been one program, evolves continually. The areas change. The basic goal was still there, and that was to ensure the safety, the maximum cost effectiveness of components of structures in service. But the technical approach has evolved in time.

Let me show you what the funding looks like. This dotted line is where the program is currently funded through FY 1980. Do not forget that before this program started in this more or less fundamental work, I do not think you could have found $200,000 within DOD, so it was a major increase at that point. It grew rapidly.

ARPA intentionally reduced their funding in the 1979 time period to try to force the other services to get involved in the program. That is something we have not succeeded in yet, but we are going to make a more conscious effort in the next three to six months. This dotted line is what the level of funding would have been just to correct it for inflation for the next four years. So there has been an erosion in the spending power of this program from that period. That is history.

Some of the things that I think we see for the future are kind of exciting, some of them clearly outside of this program: certainly the general inversion is something that people will search for probably for the next 50 years. It is almost impossible, but we will get there closer and closer for more specific cases, and they will have major impact. If we can do something in radiation to by-pass the bulk of accounting statistics, and allow us to use that technique and avoid all the contact problems for small defects, that will be very powerful. There are some things coming along which clearly help in that area.

I think the fatigue life work, which will be mentioned during this program, is a tremdous potential. If we can ever measure residual stresses and particularly the gradient of stresses in materials, we could have a tremendous increase in our ability to predict remaining life. Artificial intelligence in the NDE system is something we have been talking to people about recently: how to marry the artificial intelligence world into the inspection world and effectively be able to clone the best of the experienced inspector with the physics in a system that most anyone can use. If you understand artificial intelligence or its basic premise, you would understand that. If not, we would have to talk about it some more.

In-service NDE and retirement-for-cause you will hear about this morning. I think it is a very exciting area. It is a case where these technologies do have to come together. There are different levels of sophistication that are possible, but it could be the first case of really applying this whole methodology to real hardware systems and use it to make decisions.

That is really all I have to say. It is nice to be here again and I am glad you could all make it. Thank you.

Dr. Joseph Moyzis from the Air Force Materials Lab would like to say a few words.

Joseph Moyzis (AFWAL): I will talk very briefly here, but I would like to bring up a few points that are of interest to the Air Force in our continuing support for this program. The scientific and technical content of this program is very high, and the Air Force has a continuing interest in such work. However, many of the questions that we get, from our constituency are, of course, a little bit different than the questions you get from a strictly technical, basic research point of view.

There is a continuing Air Force interest indicated by the fact that we are going out right now on a three-year extension of this contract, as Mike's money picture showed. There will be funds out in the future years. But the questions I am asked about a program like this -- and undoubtedly the other services will be asking similar questions if they are asked to put money in -- are "What are we going to get out of this?" "How will what you're doing impact our programs?" and that does not mean back in 1990 or 2000 when we are all done. That means what elements of this program that you have underway now can we transition out today or in the near future? What little bits and pieces of this program will fit in other programs we have going? We have had some successes here. We have had some technical possibilities that have appeared which have attracted funding separate from this program. For example, some of the electromagnetic work, the work being done by Bert Auld et al is being transitioned out into a funding line completely separate from this program to investigate the possibilities of using the ferromagnetic eddy current probe on practical Air Force inspection problems.

We also have some other money for transitioning techniques that are proven out in the test bed program. The objective of this money is the construction of a quantitative ultrasonic inspection module, to try to incorporate some of the techniques that are being developed here, whichever ones are applicable, whichever ones we think can be transitioned at the present time, into an actual module that can be linked to a standard ultrasonic unit so that we can really start to do some flaw sizing. We do not have to have four decimal-place accuracy. In many cases, a rough sorting would help. For example, where you have a real inspection probability curve and you want to reject the flaws that are large and ignore the flaws that are small, it would be nice when you receive the flaw signal if you could just sort into large and small. The better you can do that, the more useful these techniques we are developing will become. That sorting capability alone would be of interest.

In that sense, what we are interested in are transition ideas. I would just like to ask the people here, the people directly involved in the program and the people who are not, that when you see opportunities for such transition possibilities, let us hear about them. We would like to hear what you think your technique could do to fill a gap in the state-of-the-art or handle an inspection problem that exists. We have a lot of problems, and we would certainly like to hear your viewpoint on these transition ideas.

Let me make a suggestion as to how you should communicate your thoughts about the use of the output of your work. There is a prime contractor, there is ARPA, there is the Materials Lab. Hopefully, at a later time, other people. When you have an idea, write it up, Xerox it and send it to everyone involved and let them know what your ideas are. That way I think you are going to get the best consideration from the system for what you are doing.

As far as the future of the program is concerned, we look at this as an evolutionary program, and that has been pointed out by Mike too. Over time the people have changed, the emphasis has changed. We see that going on in the future. No matter how the program goes, we do not see a sharp break either in personnel or in content, in this program. For example, from the point of view of the Materials Lab, we would like to see more in eddy current. We sure would like some good ideas in composites NDE that would attack real, material property problems. And hopefully, we are going to hear about some of that later today. But we look for such emphasis changes to be made rationally.

The last thing I want to say, while we are talking quantitative NDE here, and that is very, very important. There is something the Air Force considers even more important. That is reliability. Quantitative NDE is extremely important to us, and we want to develop that capability, but we absolutely have to get increased reliability. We have to be able to find whatever size flaw we want to find essentially all the time. Pushing a technique to greater and greater sensitivity does not give that capability to us unless we can get at the same time a guarantee that the technique will find what it says it will find essentially all the time. And, so, when you do what you do, it is not only a matter of sizing, it is a matter of getting a technique that will do a consistent job: that will read the same thing consistently time after time on the same kind of defect.

I do want to point out that on Wednesday evening, in this room, I am going to have a session at 8:00 o'clock when we are going to discuss one of the prime inspection problems in the Air Force, cracks in multi-layered structures. You are going to hear about another prime problem, retirement-for-cause this morning. But the cracks in multi-layered structures is still with us. We are looking at various techniques in ultrasonics and electromagnetics and we have money available if anybody comes up with some idea to attack that problem, the detection of flaws around holes in multi-layered structures. I have asked people from the contractors who are presently working on this problem to come in and give a very short discussion of what they are doing, and they will be available for discussion afterward until we all get tired and go home. Thank you.

RELIABILITY NEEDS IN FUTURE DoD SYTEMS

Keynote Address by Arden L. Bement, Jr.
Deputy Under Secretary of Defense for Research and Engineering
Research & Advanced Technology
Pentagon, Washington, D.C.

ABSTRACT

An overview will be presented of the military challenge we are currently facing along with our investment strategy for developing advanced weapons systems. The major role of improved reliability in reducing both the operation and maintenance costs as well as increasing our military combat capability will be examined along with the key role of R&D programs in meeting future reliability requirements. Finally, some of the new policies we have initiated aimed at developing a more effective DoD R&D program will be presented.

Good morning, Ladies and Gentlemen. It is a distinct pleasure for me to join with you in the sixth annual DARPA/AF review of progress in quantitative nondestructive evaluation. The agenda certainly promises a very stimulating and technically exciting meeting.

I would like to provide you with a cursory overview of current OSD thinking as to the threats we are facing, and the future capabilities we are currently developing. The role of improved reliability in both reducing operation and maintenance costs as well as increasing our military capability will be examined and the key role of R&D programs in meeting future reliability requirements will be discussed. Finally, some of the new policies we have initiated to develop a more effective R&D program will be presented.

The Challenge

For years we have acknowledged that the Soviet Union held a quantitative lead in military equipment but believed that our qualitative lead would more than compensate for this. It is time to reexamine that belief and to reject the complacency that went with it. During the decade of the 1970s, the Soviet Union made a major advance in the development and production of defense material, and as a consequence will enter the 1980's in a dramatically different defense posture than they had as they entered the 1970's.

Their objective was to challenge the U.S. lead in defense technology while maintaining their numerical advantage. They have had a remarkable degree of success in achieving that objective by making an enormous investment, and by maintaining an unwavering emphasis on technology. The Soviet Union started the 1970's with an annual defense investment (RDT&E, procurement and military construction) approximately equal to that of the U.S. But they have increased at a steady rate of four percent per year since then, while the U.S. investment decreased in real terms every year until 1975. As a result, the Soviet Union invested over the decade about $240 billion (in FY 1981 dollars) more than the U.S. This differential exceeds the estimated acquisition cost (in 1981 dollars) of 1,000 F-16s, 1,000 F-18s, 10,000 XM-1 tanks, 20 CG-47 guided missile cruisers, 50 SSN attack submarines, 20 TRIDENT submarines (with missiles), the entire M-X program, and an additional $70 billion in R&D.

Generally speaking, they have used this investment increment to produce large quantities of equipment, thus maintaining their numerical advantage. But as they try to match the sophistication of U.S. equipment, the unit cost of Soviet equipment has substantially increased. For example, we estimate that the cost of their MIG-23 approaches that of our F-16.

Another indicator of future plans is the Soviet R&D program. While our estimates of Soviet investment in R&D have significant uncertainties, the evidence is compelling that their program is about twice the size of ours. We can make a fair evaluation of this by observing their test programs, where we can identify about 50 major systems (ships, submarines, aircraft, and missiles) in various stages of test and evaluation. Some of these systems are quite significant. We can also assess some portions of their technology programs. By observing laser test activity, for example, we estimate that their high energy laser program is about four times the size of ours. Overall, during the decade of the 70s, the Soviets invested about $70 billion more than we did in Defense R&D. It is quite clear that their R&D program has had the highest priority access to funds, to trained personnel and to scarce materials, to the extent that they have imposed serious hardships on their non-defense industry. As a result, their non-defense industry is not competitive in world markets.

In summary, we can see the Soviets entering the decade of the 1980s with a commitment to compete in quality with U.S. weapon systems. A major start has already been made in that direction, with the acceptance of the much higher unit cost implied by this commitment. They are accepting this increased unit cost without decreasing their traditional emphasis on quantity, simply by increasing their total investment in weapons production to where it is now 85 percent greater than ours. That they plan to continue this emphasis throughout the 1980s is made clear by the major increases made in the 1970s in production plants and in defense RDT&E.

Our Investment Strategy

The challenge described in the previous section is formidable. We are behind quantitatively in deployed equipment and are falling further behind because of disparities in equipment production

rates. While we are still ahead in defense technology, we are in danger of losing that advantage because of massive Soviet spending in defense R&D. But we also have some distinctive advantages: a superior technological base, a competitive industry with greater productivity, and allies with a substantial industrial capability. In order to meet the formidable challenge we face, our investment strategy must fully exploit these advantages.

Our overriding near term need is to get on with the modernization of our forces. Our technology is of little use to our armed forces when it is not embodied in operational equipment. Most of our ground forces weapon systems now deployed - our main battle tank, our armored personnel carrier, our air defense gun and missile, our attack helicopter - were developed during the fifties and entered production in the sixties. As a consequence they simply do not incorporate current technology, and they provide maintenance and support problems created by their age.

Fortunately, a new generation of weapon systems was developed during the seventies and is now ready for production. This includes: (1) equipment already in production - a new nuclear submarine and missiles, new ships and tactical aircraft; (2) equipment just entering production - a new main battle tank utility helicopter, laser guided projectiles, and the Air Launched Cruise Missile; (3) equipment which will be ready for production in a year or two - a new air defense gun, multiple launch rocket system, air-to-ground missile, and advanced helicopters.

The DoD Science and Technology program provides the technical foundation necessary for the development of new weapons systems and provides us insurance against technological surprise. This technology base permits us to multiply our force effectiveness through improved performance and to develop new technology to address defense costs, acquisition barriers, and readiness. Those requirements that must be addressed by technical solutions include: improved reliability (which is "designed-in" and "manufactured-in" not just "tested-in"); life extension and durability of costly military hardware; conservation, substitution, and recycling technologies for critical materials; increased productivity and reduced manufacturing costs in our defense industrial base.

The Role of Reliability

Many of you are aware of some of the reliability problems we have recently experienced in DoD. The durability and reliability problems associated with the F-100 engine in the F-15 and F-16 aircraft are currently receiving considerable attention.

In the procurement and operation of weapons systems a major objective is to minimize the total life-cycle cost while achieving a given force capability. Weapon system life-cycle analysis must be concerned not only with life-cycle costs but also with the capability of the weapon system. What are you getting for the price you are paying?

This military capability includes a number of areas: availability of the force, particularly in terms of a capability level achieved at some date, the availability of individual systems to conduct combat missions, the sortie success of that weapon system in the conduct of its mission and the mission effectiveness in terms of the design criteria of interest. (In the case of a close-air-support mission, for example, this includes payload capacity, radius, loiter time, maneuverability, delivery accuracy, and survivability.) The design criteria is the component of military capability that is most easily addressed during the development and acquisition of a new weapon system. However, our overall military capability is directly dependent on the availability and reliability of these systems for performing their mission.

In order to illustrate the importance of these issues I have chosen to review with you some of our experiences with the life cycle costs and operational capability of the Air Force A-7D aircraft.

There are obvious problems with examining a specific system. First of all, no one system is really representative. Thus, it is difficult to generalize any lessons which might be learned. Second, the acquisition process is in a constant state of evolution and therefore, it is difficult to discern legitimate similarities between past problems and present procedures. Notwithstanding these difficulties, one way of improving upon our past acquisition performance is to first identify the deficiencies in past programs and second evaluate alternative policies in the "real-world" contexts of those program environments.

Life Cycle Cost of the A-7D

A measure of a weapon's "total cost" is the present value of all previous and forthcoming expenditures directly related to the RDT&E, procurement, and ownership (i.e., operation) of the system. Such a "total cost" is referred to as a life-cycle cost. At the time that a life-cycle cost is calculated, forthcoming expenditures can only be estimated, whereas expenditures to date should be measurable with a fair degree of accuracy. In theory, the life-cycle cost measure is very attractive for indicating the magnitude of the potential tradeoffs of resources among the development, production, and operating phases of a system in order to optimize capability and cost characteristics.

Figure 1 presents an FY 1973 calculated projection of life-cycle cost for the A-7D in terms of FY 1973 dollars. Since the aircraft was still in production during FY 1973, the life-cycle cost is stated in terms of a per aircraft cost rather than a fleet cost. The acquisition cost is based upon the total planned buy (411 aircraft) as of FY 1973. The estimated costs of ownership are based upon the assumption that the FY 1973 observed average per unit operating cost is representative of the ownership costs for the duration of the aircraft's useful life, which is assumed to be 15 years.

With certain assumptions as to discount rate and inflation this viewgraph shows that the cost of ownership is approximately 30 percent higher than the acquisition cost. Since the ownership

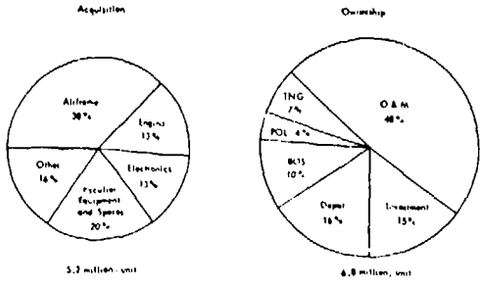

Fig. 1 A-7D 15-year life-cycle cost in 1973 dollars.

costs are so dependent on several unknowns, it is sufficient to conclude that the ownership costs will generally exceed the acquisition costs.

Several of the costs of ownership are not very sensitive to the reliability and maintainability of the weapon system (e.g., training (TNG), petroleum, oils, and lubricants (POL), and base operating support (BOS)). However, the largest portion - the remaining 79 pecent of the ownership costs (e.g., operation and maintenance (O&M), depot, and investment) - are very sensitive to weapon-system reliability and maintainability as well as manning, support, and deployment decisions. The base-level O&M costs alone account for nearly 50 percent of the ownership costs. One of the elements of the O&M cost which is particularly sensitive to the weapon system's reliability and maintainability is the labor cost for unscheduled maintenance at the base.

Therefore, we can potentially avoid major future costs associated with weapon systems by improving the reliability and maintainability of these systems. Clearly we have to address these issues both before, during and after production of weapons systems.

Military Capability of the A-7D

The capability of the weapon system is the other key issue that is impacted by reliability and again I would like to use the A-7D as an example. The tactical mission of the A-7D makes the number of combat sorties that can be generated per day of major importance in determining the military utility of this weapon system.

As shown in Fig. 2, even if no subsystems fail, there is an upper limit to the number of combat sorties that can be launched by the average aircraft in a combat day. For example, for a two hr close air support mission, about 3.3 hours are needed for fueling, gun loading, bomb loading, and preflight and postflight inspections. This means that at most, four and a half sorties can be flown per aircraft in a twenty-four hour combat day.

First, let's focus on the combat readiness assessments for 1968 and 1970. The 1968 assessment is based upon LTV's subsystem reliability estimates which were made midway through the research and development phase. As you can see, the contractor estimated that the A-7D could provide

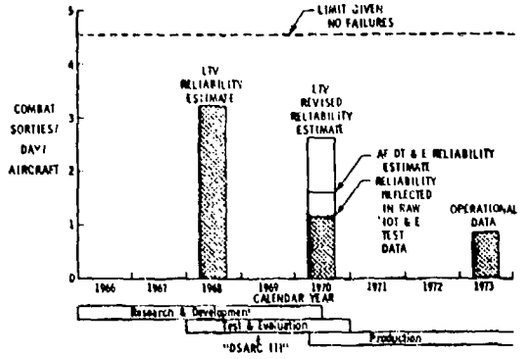

Fig. 2 Combat readiness assessment for the A-7D.

over three combat sorties/day/aircraft. In 1970, towards the end of the test program, the contractor revised its subsystem reliability estimates, and estimated that only 2.5 sorties/day was possible. At about the same point in time, the Air Force made an independent estimate of the subsystem reliability and projected less than a two sortie/day capability. An initial user oriented operational test in 1970 was also conducted and resulted in a sortie rate of slightly over one sortie/day.

Now look at the 1973 operational data in which we obtained a capability of less than 1 sortie/day.

The difference between the limiting number of 4.5 sorties/day and the top of the three bars is totally due to the down-time for unscheduled maintenance which is incurred because of subsystem failures. If no failures occurred, there would be no unscheduled downtime.

Thus far, we have been considering this sortie generation capability on an average aircraft basis. In Fig. 3 we will consider it on a fleet basis. If the aircraft, which were delivered to the Air Force, were as reliable as the contractor's pre-production estimate, then the fleet sortie generation capability would have built up according to the top curve. The 1975 capability would have been about 1400 sorties/day. Of course, the actual buildup followed the bottom curve to a 1975 capability of about 400 sorties/day.

Therefore, we obtained in 1975 only 28% of the military capability that we had planned for in 1968.

Clearly there are many actions that have been taken since we acquired the A-7D to improve the acquisition process. We are continuously striving to develop improved management procedures to obtain the most cost effective weapons system.

However, there is a limit to the reliability improvements we can obtain from management and policy changes alone. We have to develop an engineering capability to "design-in" and "manufacture-in" and not just "test-in" reliability. We are concerned about the entire area of quality and with it the classic problems of accelerated testing and the nondestructive

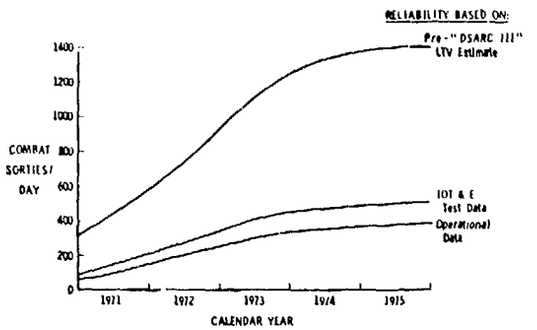

Fig. 3 Estimated combat readiness for the A-7D fleet.

evaluation of the future performance of components. The Department of Defense needs the scientific knowledge which you are involved in developing, and most importantly it needs it reduced to practice in manufacturing and maintenance. In my office we have taken several initiatives to help achieve these objectives.

The sustained growth in the S&T Program over the past three years has made possible a number of beneficial initiatives which were not possible during the "undernourished" years of the early 1970's. We are making substantial progress in closing the interfaces between the Science and Technology (S&T) Program and the Advanced Development Programs to improve the flow of technology toward application. We are strengthening our relationship with universities in order to use the research and development resources of the academic community more effectively. We are able to increase the pace of progress in the research and development cycle through focused investments, critical mass funding, multidisciplinary attack on complex problems, and coupled programs involving university, industrial, and DoD laboratory research teams working in concert to exploit a high-payoff opportunity or meet a military requirement. The program being reviewed at this conference represents one of the best examples of this approach, and I believe the success to date is due, to a large degree, to the strong cooperation between all the participants in this interdisciplinary program. Significant scientific progress in NDE has only recently been achieved and can easily be lost if real growth is not sustained. Continuity in policy and investment is the most important ingredient for building a defense research base which will provide for our future national security.

To maintain this technological lead time, we are applying three basic mechanisms within the S&T Program:

- Real growth in funding our Technology Base;
- Support to enhance and exploit our domestic advantage in commercial technology and our industrial base; and
- Improved cooperation with our Allies.

The funding for the NDE technology base within DoD has increased significantly over the last five years. Since FY 1975 the DoD technology base for NDE has increased from less than 2 million dollars per year to over six million dollars per year. In addition, the Air Force has initiated a major Manufacturing Technology thrust in NDE to reduce this technology to practice that has increased from no investment in FY 1975 to almost $4 million in FY 1980 to a planned expenditure in excess of 18 million dollars over the next three years. The Army is also currently investing several million dollars per year in Manufacturing Technology NDE programs.

We have increased our interaction with our allies in NDE through bilateral agreements, NATO workshops and TTCP activities. For example, the U.S. has proposed that a new panel be established under the TTCP materials subgroup to provide the necessary framework for joint programs and technical exchange between the member countries (US, UK, Canada, Australia and New Zealand).

As you can see from Fig. 4, the increasing investment in NDE is still a very small percentage of the total DoD Science and Technology Program. However, the increasing recognition of the importance of quality in DoD weapon systems, the additional requirements placed on NDE by the desirability of using new materials, design concepts and processing methods to exploit rapid solidification technology, metal matrix and carbon/carbon composites as well as ceramic materials clearly will require increased emphasis for advanced quantitative NDE capabilities to ensure the reliability of future weapons systems.

(Dollars in Millions)	Actual FY 1980	Requested FY 1981
Research		
Services	467	559
Defense Agencies	91	93
Total Research	558	652
Exploratory Development		
Services	1,162	1,405
Defense Agencies	541	667
Total Exploratory Development	1,703	2,072
Advanced Technology Developments	638	612
TOTAL SCIENCE AND TECHNOLOGY PROGRAM	2,899	3,336
Manufacturing Technology (Non-RDT&E)	158	150

Fig. 4 DoD Science and Technology Program

If you will continue the excellent research progress you have been making in this field and focus your research on the critical technical issues required to transition this technology to the user, I will work to ensure that the necessary policy issues are addressed to provide the Department of Defense with the technical capability to field and maintain reliable military systems. We must develop the capability to "design-in" and "manufacture-in" reliability. We can't afford to continue to only "test-in" reliability with future weapons systems.

Don Thompson, Chairman (Ames Laboratory): Thank you very much. We have a few minutes before break for questions and answers.

Doug Ballard (Sandia Laboratories): Could you predict or project what percentage of this downtime for sorties is attributed to electronic gear that we do not test normally by NDE methods? In other words, is the electronics part of the business a major factor rather than structural downtime?

Arden Bement (Deputy Undersecretary of Defense): I can't give you precise numbers on that, but I know for a fact that it is, especially in radar systems, such as the replacement of traveling wave tubes; and it certainly is a very significant contributor in communication systems.

Doug Ballard: Those areas are traditionally neglected by NDE right now. We don't even pay any attention to them.

Arden Bement: Yes, I agree.

Don Thompson, Chairman: Other questions?

Arden Bement: I might say, however, during that era that this aircraft operated, we were still in vacuum-tube technology and are hoping that large-scale integrated circuits will provide improved reliability in some of those systems.

Don Thompson, Chairman: Any other questions? If not, Arden, we thank you very much for your talk and presentation.

ENGINE COMPONENT RETIREMENT-FOR-CAUSE: A NONDESTRUCTIVE EVALUATION (NDE) AND FRACTURE MECHANICS BASED MAINTENANCE CONCEPT

C.G. Annis, J.S. Cargill, J.A. Harris, Jr., M.C. Vanwanderham
Materials and Mechanics Technology
Pratt & Whitney Aircraft Group
Government Products Division
West Palm Beach, Florida 33402

ABSTRACT

Historically, cyclic life limited gas turbine engine components have been retired when they reach an analytically determined life where the first fatigue crack per 1000 parts could be expected. By definition, 99.9% of these components are being retired prematurely as they have considerable useful life remaining. Retirement for Cause is a procedure which would allow safe utilization of the full life capacity of each individual component. Since gas turbine engine rotor components are prime candidates and are among the most costly of engine components, adoption of a RFC maintenance philosophy could result in substantial engine systems life cycle cost savings. Two major technical disciplines must be developed and integrated to realize those cost savings: Fracture Mechanics and Nondestructive Evaluation. This paper discusses the methodology, and development activity required, to integrate these disciplines to provide a viable RFC system for use on military gas turbine engines, and illustrates potential benefits of its application.

INTRODUCTION

Historically, methods used for predicting the life of gas turbine engine rotor components have resulted in conservative estimation of useful life. Most rotor components are limited by low cycle fatigue, generally expressed in terms of mission equivalency cycles. When some predetermined cyclic life limit is reached, components are retired from service.

Total fatigue life of a component consists of a crack initiation phase and a crack propagation phase. Engine rotor component initiation life limits are analytically determined using lower bound LCF characteristics. This is established by a statistical analysis of data indicating the cyclic life at which 1 in 1000 components, such as disks, will have a fatigue induced crack of approximately 0.03 inch length. By definition then, 99.9% of the disks are being retired prematurely. It has been documented that many of the 999 remaining retired disks have considerable useful residual life. Retirement for Cause (RFC) would allow each component to be used to the full extent of its safe total fatigue life, retirement occurring when a quantifiable defect necessitates removal of the component from service. The defect size at which the component is no longer considered safe is determined through nondestructive evaluation (NDE) and fracture mechanics analyses of the disk material and the disk fracture critical locations, the service cycle and the overhaul/inspection period. Realization and implementation of a Retirement for Cause Maintenance Methodology will result in system cost savings of two types: direct cost savings resulting from utilization of parts which would be retired and consequently require replacement by new parts; and indirect cost savings resulting from reduction in use of strategic materials, reduction in energy requirements to process new parts, and mitigation of future inflationary pressure on cost of new parts.

RETIREMENT FOR CAUSE METHODOLOGY

Philosophy - The fatigue process for a typical rotor component such as a disk can be visualized as illustrated in Fig. 1. Total fatigue life consists of a crack initiation phase followed by growth and linkup of microcracks. The resulting macrocrack(s) would then propagate subcritically until the combination of service load (stress) and

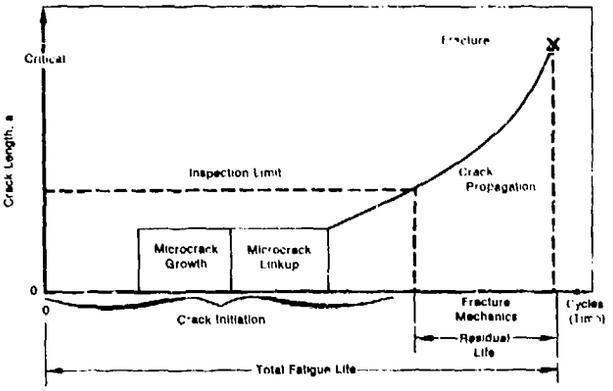

Fig. 1 Total fatigue life segmented into stages of crack development, subcritical growth, and final fracture.

crack size exceeded the material fracture toughness. Catastrophic failure would result had not the component been retired from service. To preclude such cataclysmic disk (and possibly engine) failures, disks are typically retired at the time where 1 in 1000 could be expected to have actually initiated a short (0.03 in.) fatigue crack. By definition 99.9% of the retired disks still have useful life remaining at the time they are removed from service. Under the Retirement-for-Cause

philosophy, each of these disks could be inspected and returned to service. The return-to-service (RTS) interval is determined by a fracture mechanics calculation of remaining propagation life from a crack just small enough to have been missed during inspection. This procedure could be repeated until the disk has incurred measurable damage, at which time it is retired for that reason (cause). Retirement for Cause is a methodology under which an engine component would be retired from service when it had incurred quantifiable damage, rather than because an analytically determined minimum design life had been reached. Its purpose is not to extend the life of a rotor component, but to utilize safely the full life capacity inherent in that component.

Residual Life - For simplicity this paper will consider component life limits which have been determined from the crack initiation characteristics of the specific disk material, and will not address the problem of intrinsic crack-like defects. While damage tolerant concepts are utilized in some instances to establish life limits, the majority of components in current gas turbine engines have life limits set by an initiation criterion.

All fatigue data have inherent scatter. The data base used for design life analyses purposes must be applicable to all disks of a given material, and therefore includes test results from many heats and sources. Data are treated statistically as shown schematically in Fig. 2. The distribution of life, defined as the number of cycles necessary to produce a crack approximately 0.03 in. long, is obtained for a given set of loading conditions (stress/strain, time, temperature). As can be seen, the $\pm 2\sigma$ bounds, which contain 95% of the data, may span two orders of magnitude in fatigue initiation life.

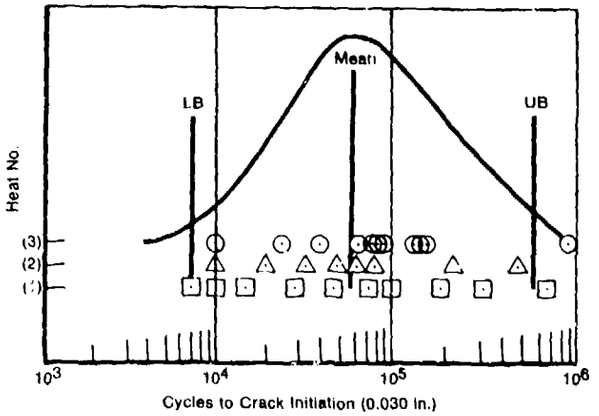

Fig. 2 Material data scatter results in conservative life prediction.

When considered with other uncertainties in any design system (e.g., stress analysis error, field mission definition, fabrication deviations, temperture profile uncertainty) the final disk life prediction is made for disk crack initiation life for an occurrence rate of 1 in 1000 disks. It is at this life that all LCF-limited disks are removed from service. This procedure has been very successful in preventing the occurrence of catastrophic failure of disks in the field. However, in retiring 1000 disks because one may fail, the remaining life of the 999 unfailed disks is not utilized. The amount of usable life remaining can be significant, as shown in Fig. 3, where over 80% of the disks have at least 10 lifetimes remaining.

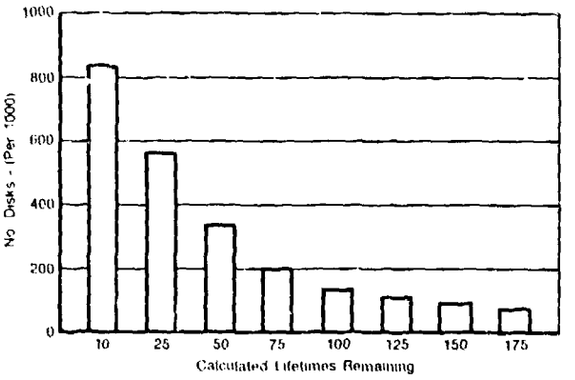

Fig. 3 The majority of disks have useful life after retirement.

The means of extracting the remaining useful life from each disk must be safe to avoid catastrophic failure. This done by determining the disk crack propagation life (N_p) (at every critical location) from a defect barely small enough to be missed during inspection. The Return-to-Service (RTS) interval is then calculated by conducting a Life Cycle Cost (LCC) analysis to determine the most economical safety factor (SF) to apply to N_p (RTS interval = N_p/SF). Cost vs SF is plotted for each individual disk and combined to determine the most economical interval to return a module for inspection. An example is shown in Fig. 4.

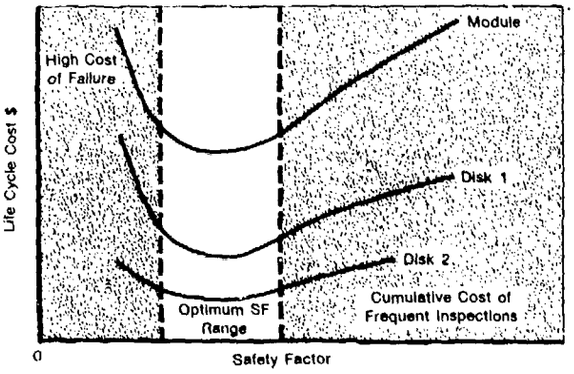

Fig. 4 Safety factor is determined from an economic balance between high cost of failure vs cumulative costs of frequent inspections.

The first required disk inspection is near the end of the analytically determined crack initiation life. Only one disk in 1000 inspected should have a crack and be retired. The other 999 will be returned to service for the calculated RTS interval. This inspection is repeated at the end of each RTS interval with the cracked disks being

retired and all others returned to service. Figure 5 illustrates how the residual life is extracted from each disk after the crack initiation life has been used.

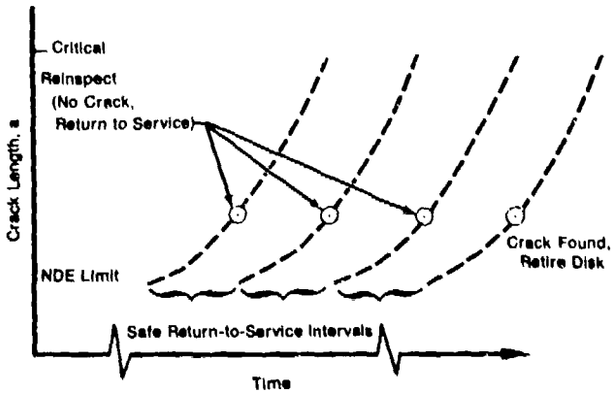

Fig. 5 Base Retirement for Cause concept.

TECHNOLOGY DEVELOPMENT REQUIRED

As Figs. 4 and 5 illustrate, Return-to-Service intervals are based on two broad technologies: Nondestructive Evaluation (NDE) and applied Fracture Mechanics, and evaluated based upon economic factors.

Fracture Mechanics must provide an assessment of the behavior of a cracked part should it pass NDE with a defect just below an inspection limit. To assure safe return to service of a part which may contain a small crack, an accurate crack propagation prediction is imperative. Recent strides in applied elevated temperature fracture mechanics[1-4] have provided the necessary mathematical description (models) of basic propagation, i.e., crack growth under conditions of varying loading frequency (υ), stress ratio (R), and temperature (T). Further work[5,6] has expanded this capability to include loading spectra synergism, i.e., crack growth subjected to (frequent) periodic major load excursions separated by a small number (10-50) of varying subcycles. It is important to note that a typical mission loading spectrum to which gas turbine engines are subjected bears little resemblance to that experienced by air frames, and therefore different predictive tools are required for each.[7]

Referring again to Fig. 5, it is seen that accurate propagation predictions constitute a necessary, but not sufficient, condition for the implementation of Retirement for Cause. The other requisite technology is high reliability nondestructive evaluation (NDE).

NDE must provide the means of screening disks with flaws that could cause component failure within an economically feasible RTS interval. Insufficient NDE reliability has been a major argument against implementation of an RFC maintenance program. NDE capability with acceptable flaw detection resolution has been available for some time,[8,9] but adequate reliability of flaw detection has been lacking.[10] Complementary inspections and improvements in NDE single inspection reliability (by automation), can provide the required reliability for many gas turbine engine components to economically utilize the RFC maintenance concept.

These two requisite technologies are integrated in the component life analysis.

The fracture mechanics approach to estimating component service life is based on the assumption that materials may contain intrinsic flaws, and that fatigue failure may occur as a result of progressive growth of one or more of those flaws into a critically sized crack. Thus, the prediction and monitoring of crack growth as a function of time (or cycles) becomes one of the basic requirements of the analysis system. To utilize such an approach in practice requires quantitative information on component stress, materials characteristics, and nondestructive evaluation (NDE) capabilities. Much of this information cannot be defined as a single value, but must be described by a probability distribution. Two examples are: the probability that a flaw of a given size will exist in virgin material, or the probability of finding a given flaw size with a standard inspection procedure. In order to obtain a deterministic fracture mechanics life prediction (given these distributions), the conventional approach has been to use worst case assumptions for all parameters. Employing all worst case assumptions for all parameters. Employing all worst case assumptions (deterministic) necessarily results in a conservative estimate for the service life of the component.

To circumvent this difficulty, the problem can be treated probabilistically. A closed-form solution, which takes into account all the required probabilities, is far too complex to be practicable. An alternative solution is to employ computer simulation techniques. A probabilistic life analysis[11,12] would use a distribution of flaw sizes. This type of analysis results in failure probability as a function of time, includes NDE reliability, and allows selection of an RTS interval to obtain an acceptable (low) failure probability with realistic NDE reliability.

Both deterministic and probabilistic methods could provide some of the NDE reliability through multiple inspections and/or through higher NDE limits due to shorter RTS intervals. Since many NDE errors are the result of human frailty, multiple inspection and automation can enhance detection reliability. The probabilistic system, however, has the ability to accommodate NDE reliability (probability of detection vs crack length) distributions and assess their effect upon RFC efficiency. Obviously, high reliability NDE is desired to optimize the economic benefits of Retirement for Cause.

The RFC Procedure - The Retirement-for-Cause (RFC) flow chart (Fig. 6) illustrates a simplified view of how this maintenance concept can be utilized. When an engine is returned for maintenance, an economic analysis is performed on the engine component/module identified as a participant of the RFC maintenance program. If the module has already been in service for several inspection intervals, the probability of finding cracked parts may be great enough to make reinspection economically undesirable and specific components of that module are returned without being inspected. This is determined by the economic an-

alysis at decision point one and is one of three possible decisions. An unscheduled engine removal (UER) may bring a module out of service that is more economical to return to service for the remainder of its inspection interval than to inspect and recertify it for a new full interval (the second possible decision at point one). The remaining choice at point one is to tear down the module and inspect the parts. During inspection there again are three possibilities (decision point two). If no crack is found, the part is returned to service. If the disk is found to be unsafe, it is retired. The third choice is to investigate modification or repair of a flawed part. An economically repairable part may be repaired and returned to inspection (decision point three).

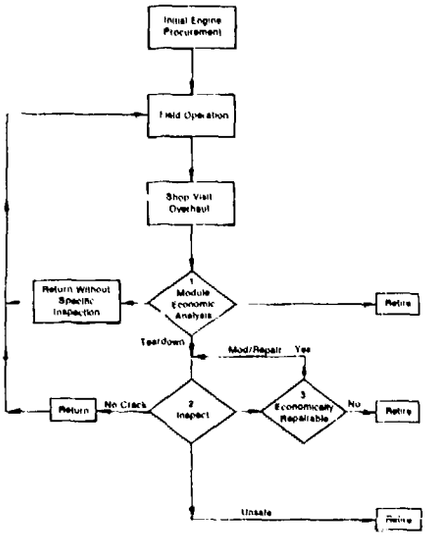

Fig. 6 Retirement for Cause procedure flow chart.

AN APPLICATION OF RETIREMENT FOR CAUSE

The application of a Retirement for Cause maintenance approach to a military gas turbine system has been studied and technology development progams are currently underway. The demonstration engine system is the USAF F100 engine. Under Defense Advanced Research Projects Agency (DARPA) and Air Force Wright Aeronautical Laboratories (AFWAL) sponsorship, a study entitled "Concept Definition: Retirement-for-Cause of F100 Rotor Components" Contract F33615-76-C-5172 (as modified in 1979) was performed. The results of this study are documented in AFWAL-TR-80-....., the final report for that program.

The objective of the program was to determine the feasibility of applying a Retirement-for-Cause (RFC) maintenance approach to the USAF F100 engine. The study was directed primarily toward rotating components of that engine, specifically the various disks and airseals/spaces that comprise the prime rotor structure. The technical effort consisted of five tasks:

- Define an RFC methodology and a means of assessing the ROI for its application
- Evaluate the disks of the F100 engine plus other appropriate engine rotor components for RFC applicability
- Assess nondestructive evaluation (NDE) requirements for implementation
- Establish a ranking of components for development priorities
- Establish development plans leading to implementation.

The methodology has been discussed in the preceding section of this paper. The component evaluations used a deterministic life analysis. Based upon this life analysis and life cycle cost analysis, 21 candidate components were selected, and development priorities established. Nondestructive evaluation requirements were determined for each of the components, and a development plan established, which when followed should enable implementation of RFC for the F100 engine in the 1985 time period.

The development plan is shown schematically in Fig. 7, and addresses the technology development requirements discussed previously. At the present time, many of these areas are the subject of Government contract procurement activities and cannot be discussed in detail. However, to illustrate some of the items which must be addressed, typical NDE requirements can be used as an example.

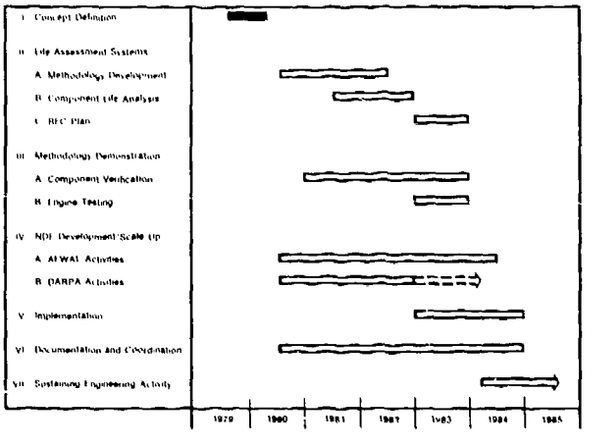

Fig. 7 Development plan engine component Retirement-for-Cause.

A composite sketch of typical gas turbine engine rotor components is shown in Fig. 8. As can be seen, the configuration of these components is complex and will require innovative techniques to enable reliable inspection. Examples of the types of defects which will require detection on these components are shown in Fig. 9. Techniques currently exist, such as eddy current, ultrasound and/or penetrants with the capability to detect these flaws. The major problem to be solved is detecting these flaws in a high volume maintenance environment, and integrating other techniques, such as proof testing, into a system with sufficient reliability to enable Retirement-for-Cause to be economically viable.

Benefits - The assessment of the benefits of a Retirement-for-Cause maintenance approach to a gas

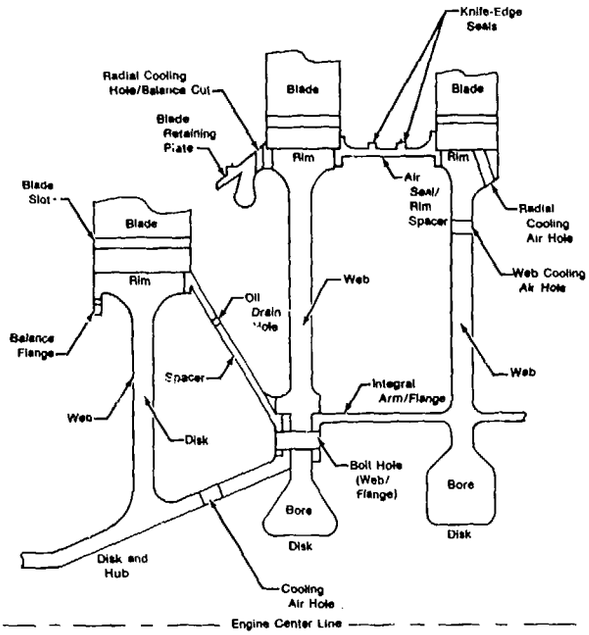

Fig. 8 Composite sketch of typical gas turbine engine rotor components (not all features are on all parts).

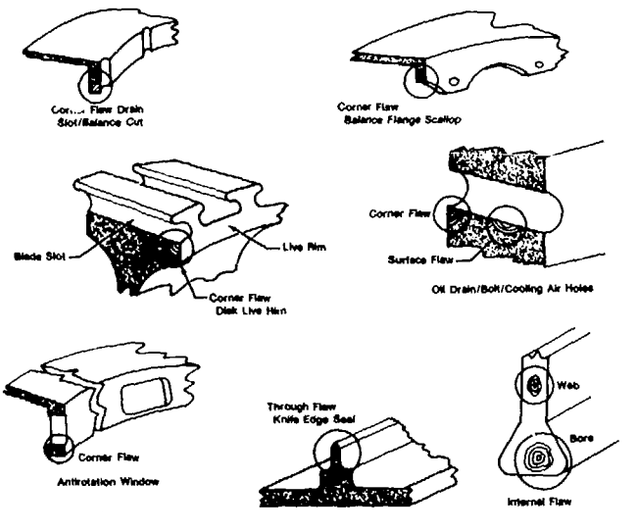

Fig. 9 Sketch of typical gas turbine engine rotor component flaw types.

turbine engine is contingent upon many assumptions. These assumptions include: fleet size, anticipated usage rates, usage life, inspection interval, labor costs, parts cost and many others.

To quantify the benefits of this maintenance concept for the USAF F100 engine, life cycle cost analyses were conducted. These analyses determined the change in life cycle costs of the F100 engine that could accrue based upon implementation of an RFC maintenance procedure in January 1985 as opposed to a continuation of current or baseline maintenance practices.

The life cycle cost benefits amount to an approximate $ .0 million savings over a 15-year period. In comparison to the investment required, the development and implementation of RFC are extremely attractive.

SUMMARY CONCLUSIONS

Realization and implementation of a Retirement-for-Cause Maintenance Methodology will result in system cost savings of two types: direct cost savings resulting from utilization of parts which would be retired and consequently require replacement by new parts; and indirect cost savings resulting from reduction in use of strategic materials, reduction in energy requirements to process new parts, and mitigation of future inflationary pressure on cost of new parts.

The methodology and procedures described herein are applicable to systems other than the F100 engine. A cursory review of other gas turbine engines indicates that the RFC maintenance concept is generic and has direct applicability to rotor components of those engines. In fact, the methodology has broad applicability to other types of engine components, and indeed, to systems other than aircraft gas turbine engines. The decision to apply RFC to other components or systems would be based upon economic factors, predicated upon the remaining anticipated service life of that system, and can be a viable maintenance concept for life limited components of all types.

REFERENCES

1. Annis, C.G., R.M. Wallace, and D.L. Sims, "An Interpolative Model for Elevated Temperature Fatigue Crack Propagation," AFML-TR-76-176, Part I, November 1976, presented at 1977 SESA Spring Meeting, Dallas, TX, May 1977.

2. Wallace, R.M., C.G. Annis, and D.L. Sims, "Application of Fracture Mechanics at Elevated Temperatures," AFML-TR-76-176, Part II, November 1976, presented to Air Force Materials Laboratory, WPAFB, OH, May 1977.

3. Sims, D.L., C.G. Annis, and R.M. Wallace, "Cumulative Damage Fracture Mechanics at Elevated Temperature," AFML-TR-76-176, Part III, November 1976.

4. Sims, D.L., "Evaluation of Crack Growth in Advanced P/M Alloys," AFML-TR-79-4160, September 1979.

5. Larsen, J.M., C.G. Annis, Jr., "Observation of Crack Retardation Resulting from Load Sequencing Characteristic of Military Gas Turbine Operation," presented at ASTM Symposium on Effects of Load Spectrum Variables on Fatigue Crack Initiation and Propagation, San Francisco, CA, May 1979.

6. Larsen, J.M. B.J. Schwartz, C.G. Annis, Jr., "Cumulative Damage Fracture Mechanics Under Engine Spectra," AFML-TR-76-4159, September 1979.

7. Annis, C.G., Jr., "An Engineering Approach to Cumulative Damage Fracture Mechanics in Gas Turbine Disks," presented at ASME Gas Turbine Conference, San Diego, CA, May 1979.

8. Hyzak, J.M., J.E. Allison, W.H. Reimann, "Development of Quantitative NDI for Retirement-for-Cause," AFML-TR-78-198, February 1979.

9. Cargill, J.S. J.K. Malpani, Y.W. Cheng, "Disk Residual Life Studies," AFML-TR-79-123, September 1979.

10. Lewis, W.H., et al, "Reliability of Nondestructive Inspections," SAALC/MME 76-6-38-1, December 1978.

11. Annis, C.G., Jr., F.K. Haake, D.L. Sims, "Probabilistic Fracture Mechanics and Retirement-for-Cause," P&WA internal communication, to be submitted for external publication.

12. Rau, C.A., Jr., "The Impact of Inspection and Analysis Uncertainty on Reliability Prediction and Life Extension Strategy," presented at ARPA/AFML Quantitative Nondestructive Evaluation, San Diego, CA, July 1978.

Bruce Thompson (Rockwell Science Center [now Ames Laboratory]): This community is particularly concerned with techniques that quantify in some detail certain of the flaw parameters. In your estimation of $200 million savings in life-cycle costs, what degree of quantification is assumed in the technique, and how much greater could that be if you had more quantification?

Jack Harris (Pratt/Whitney Aircraft): All right, I will now show you my Achilles heel. In order to conduct these life-cycle cost analyses, we used a 100 percent reliable NDE assumption. We know that's not true. Before you say that 250 million is wrong, we also used an extremely conservative estimate of life. They tend to balance each other. The answer is yes, we can get quantitative; we have defined life from assumed flaw shapes. Quantification of real flaw shapes would give us, I would say, a quantum leap in our accuracy of the predicted lives.

Mike Buckley, Chairman (DARPA): I was curious if Pratt and Whitney had ever looked at this concept in the sense of how it would impact the maintenance requirements, both scheduled and unscheduled and, therefore, the availability of the engine for performing its mission.

Jack Harris: We are in the process right now of an in-depth look at that from the unscheduled engine removal standpoint. We looked at it from the scheduled engine removal standpoint in the previous study, but one of the ground rules that we are operating on is that we are not going to let the forced readiness deteriorate from the levels at which it is currently operating. It is not going to get worse. The question that you're asking me is: Is it going to get better? I hope so, but I'm not sure. But it will not get worse. That's a given.

Mike Buckley, Chairman: You are also fixed by the current maintenance intervals?

Jack Harris: That's right.

Mike Buckley, Chairman: You didn't allow those to float, and I was wondering if in fact you had looked at that question. As the NDE gets better, clearly you can extend the interval safely.

Jack Harris: You can extend the interval safely. Again, we want to cause the least possible change in the current force structural maintenance effort. So we have tailored our Retirement-for-Cause concept to meet those current inspection intervals. There are techniques, for example, proof testing techniques, that would enable you to extend the intervals on certain parts. That's great, but it doesn't do any good on a three-stage fan if we can extend the interval on one part to 5 times but we can't extend it on the other part in the fan module. We have still got to bring the module in at an interval set by the lowest residual life part in the module. Yes, we hope we will be able to extend the intervals as we get further into the program. That remains to be seen. They won't get shorter than the present intervals. By definition, they won't get worse.

Joe Moyzis (AFWAL): When you say worse case, worse case, worse case, you assume a hundred percent reliability in NDE because what else can you do. Talking about realistic P.O.D., you mean a realistic P.O.D. in probabilistic fracture mechanics; is that right?

Jack Harris: Yes. What we hope to be able to do is integrate the entire NDE, life, and economic analysis into one tool that will enable people to make decisions. That is our goal.

John Rodgers (Acoustic Emission Technology Corporation): Taking an engine you essentially developed without Retirement-for-Cause in the conceptual design stages, and you now have an operational system, what do you think would be the economic benefit if you would take a design criteria and apply it to the F-100 today and redesign the engine to take full advantage of quantitative NDE and Retirement-for-Cause analysis? What do you think the resulting factoral economic benefit would be over what you projected in this conservative situation?

Jack Harris: To be honest with you, we can do that today. It is called damage tolerant design, and it is a concept that a lot of people now apply. Unfortunately, it is one of those situations where you can't have your cake and eat it, too. The damage tolerant design concept would enable you to, in effect, design in Retirement-for-Cause from day one. You can do it. There have been some innovative techniques come out our Air Force aero-propulsion lab-sponsored program that say the weight penalties are not going to be near what we thought they were going to be but there would still be weight penalties. Obviously, if the part's going to last - be able to sustain a known flaw for three overhaul increments, the part has to be bigger, it has to be heavier, the stresses have got to be lower so that our weight penalties - I wouldn't even try to make a guess at quantifying that benefit. I think we are premature there. I think within a few years we will have the damage-tolerant design techniques that will enable us to put a very attractive engine, from a weight-performance standpoint, in the field and still get the benefits of Retirement-for-Cause.

We were amazed at the results of this study. We did not design the F-100 engine to operate on a Retirement-for-Cause basis. It was designed to provide the maximum possible performance at

the minimum possible weight. Consequently, we went to very high stresses. We have gotten the performance out of it. We have gotten minimum weight, but we have been astonished to find we can also use Retirement-for-Cause for a significant number of it's parts. Maybe that's serendipity. I don't known, but it sure looks good.

Mike Buckley, Chairman: Have you people worked on the viewgraphs to display to the Air Force some of the disk failures depending on how much maintenance and how many redundant inspections are performed as a function of money? Once you get to a real reliability case, you're going to have to accept a given probability of failure at a given cost, and, of course, we do today, but people don't like to admit it. They still believe it's a perfect system. Has ther been much thought on that yet?

Jack Harris: Yes. I think it would be premature for me to really discuss it, Mike. For the benefit of all of you who are not aware, we will be entering very shortly into a four-year development program to obtain the necessary fracture and life methodologies. We feel we have the firm foundation for that. We have to pull them together and integrate them. That program will start momentarily, I hope, and possibly next year we might be able to discuss that. Yes, we have looked at that. We have made an assessment of how many failures per thousand or per unit might occur and so on.

Mike Buckley, Chairman: That, of course, will be impacted by the quality of the inspection. Procedure to a very large degree and this is where, in many ways, a reliable system is a quantitative system when you get right down to it. There can be other things which destroy that, but -

Jack Harris: Yes, possibly one thing that I may have glossed over. And I certainly didn't do it intentionally. We are looking, as I said, at very uniquely located and oriented flaws in very complex configurations. It would be great if they were just machined, but they're not. They come out of the field; they come into an overhaul system. They have oil on them, they have coke on them in some cases; they're dirty; they may have stains on them; and you're going to have to handle something like 1,000 to 1,200 of those parts a month. It's a pretty large undertaking.

Mike Buckley, Chairman: Last question, Otto,

Otto Buck (Rockwell Science Center [now Ames Laboratory]): Given the detectability of five mils, given a fracture, certain fracture toughness, I guess that the design life is seven years now for the engine?

Jack Harris: The Air Force likes to say the life of the system, just like Arden Bement said, is 15 years.

Otto Buck: What is your estimate at the present time for an inspectable period? How often would you have to inspect? Roughly. Do you have any estimates on those times at the present time?

Jack Harris: Currently, you're dealing with cyclically life-limited parts. The time, in effect, becomes a factor of how many cycles a part accumulates. If you project under the current flight accumulation schedules for the F-15 and F-16, it indicates that you will accumulate a maximum of 12,600 cycles in a 15-year time frame. Beyond that, I would say I would have to do some back-of-the-envelope calculations.

Otto Buck: Two years?

Jack Harris: Figure it out. Divide 15 into 12 and figure how many cycles a year.

Mike Buckley, Chairman: The intervals are established by cycles and they are currently set.

Jack Harris: And equivalent to some service usage. Maybe three years, for example.

Unidentified Speaker: You said 39 tons of cobalt. How many engine disks is that?

Jack Harris: How many engine disks is that? It is anticipated that before the last F-100 engine is retired and melted down, there will be somewhat in the neighborhood of 7- or 8,000 of these engines in the free world, maybe a few of them in the unfree world. But if you look at that, and you just figured how many of these disks, 14- 15,000 nickel-based disks, you're talking about a high percentage volume of cobalt. I can't remember the exact percent, but it's greater than 10 percent by weight in each one of these disks. You work back, and that's how they come up with 39 tons.

The alloys we're looking at are titanium 6246 waspaloy, astroloy and IN-100. The latter three are all cobalt-bearing alloys.

Otto Buck: As far as I know, the materials people right now are trying to make an effort to take the cobalt out of the super alloys, which will help, too.

Jack Harris: There are alloy development programs under way to either go with non-cobalt containing super alloys and develop the processing to get them to equivalent strengths, or to reduce the amount of cobalt used per a given component by new forging techniques. Net shape forging, for example, and a lot of those.

Mike Buckley, Chairman: Thank you very much, Jack.

INTEGRATION OF NONDESTRUCTIVE EXAMINATION RELIABILITY AND FRACTURE MECHANICS

L. Becker and S. Doctor
Battelle Pacific Northwest Laboratories
Richland, Washington

ABSTRACT

In evaluating the integrity of a system using fracture mechanics analysis, it is necessary to know the maximum size of flaws which are likely to be present. The effectiveness in reliability of nondestructive examination techniques are used to establish the probability of detection curves for different types of flaws and for different flaw characteristics, i.e., size, shape, orientation, tightness, roughness and location. This information on flaws must be known in order to ensure the systems integrity. The U.S. Nuclear Regulatory Commission has instituted a research program to establish the effectiveness and reliability of ultrasonic in-service inspections performed on light water reactor primary typing systems. This paper describes the results obtained to date and proposed methods of evaluating inspection reliability. A method has been developed for evaluating inspection reliability based on the measured variability of the inspection process. Estimates of the current level of inspection reliability have been made. Efforts are currently in progress to verify the results of these predictions and the effectiveness of the predictive model.

Bruce Thompson (Rockwell Science Center [now Ames Laboratory]): I have two questions. The first one: it seems to me that the data you showed and what you're going to get out of the round robin is sort of the same thing. Was it the initial experiment you did that helped to structure the round robin the most optimally?

Steven Doctor (Battelle Northwest): That is right. Number one, you have to be able to grow cracks in a known fashion because statistical design says that I want to measure a given size of crack. You don't want cracks scattered all throughout the different sizes because then you don't have a good measure at a particular crack size. There are number of things like that that influence why we did all this preliminary work.

Number two, we wanted to come up with some kind of a beforehand estimate as to the range of variations. So this also impacted the statistical design.

Bruce Thompson: The second question is: it would seem that ultimately, at least as pertains to the crack orientation parameters, roughness, and so forth, you would like to be able to use some sort of a theoretical basis to predict those variations, particularly as you come into new geometries and so forth and so on; and I guess that's one of the things that's being addressed in this program. Do you have any comments, guidance, or whatever in if you think that would be a useful thing? And, if so, how you see things being vectored to reach that purpose?

Steven Doctor: I think it is useful in the sense that right now we're trying to find improved procedures. The better we understand the scattering form for flaws that are not vertical but are off at some misoriented angle, the better we can come up with an improved procedure that has some defense. Right now, the existing code doesn't really have any defense. It is a bunch of work that people have done, but it has not been thorough enough and has not been understood well enough. That is the reason we have an inadequate code section 11 right now.

So, yes, I am all for that; and I think its important. If it can be done in a timely fashion to support this, more power to it. I would like to see that kind of effort integrated in. The sooner it can happen, the better off we're going to be because with this kind of lack of credibility as far as I.S.I. is concerned, the sooner we can turn that around, the better the acceptance of the American public to nuclear reactors. Since we haven't been able to find manykinds of flaws with I.S.I., we can't really justify a program to detect and prevent failures as they're happening, on the basis that we are going in to try to figure out how to detect them.

Dick Berry (Lockheed): Who are the participants going to be on this round robin? Secondly, wasn't there a previous round robin that EPRI sponsored a while back?

Steven Doctor: The question in regard to the previous round robin, I don't know. I know there are some engineering evaluations of advanced techniques that have been going on, but I don't know of an evaluation of ASME code procedure requirements.

Unidentified Speaker: Only RP-605. That was part of the round robin.

Steven Doctor: You're right. That was a plate that originally started out with Babcock and Wilcox. They put in a number of different defects that were welded in place, and this plate was sent around then to a number of researchers within the U.S. and also over in Europe. However, a final report on that effort has not been published.

There are actually seven groups. They are: NES (Nuclear Energy Services), Southwest Research Institute, Peabody, General Electric, Westinghouse, Lambert, McGill, and Thomas. There is one other one.

Otto Buck: (Rockwell Science Center [now Ames Laboratory]): Can you say something if you look at cracks - does mode two - are you balled for difference in crack geometries like mode two cracks, mode one cracks, branched cracks. Did you take those things into consideration in your work?

Steven Doctor: I'm not sure what you mean by mode one and mode two.

Otto Buck: A shear mode kind of crack, crystallogrphic crack, for instance, which is one that is perpendicular to the tri-axis, more roughness and more opening than in a shear mode.

Steven Doctor: Well, in regard to the data base, the bending fatigue cracks are quite smooth and quite open. The thermal fatigue cracks, we don't have as much control over those. They tend not to all lie in a plane, and they tend to be very rough; and sometimes you do get some end effects and discontinuities and things like this, so they are somewhat of a collage, if you will, of all the bad things. They don't tend to splinter up like an IGSCC does, however. They don't give you large amount of branching.

G.J. Posakony (Battelle Northwest): One of the important things to recall on the slides that were shown - we often talk of probability of protection. Steve was talking of probability of recording level. It may well have been detected, but in accordance with the code requirement, it was not reportable. Consequently, the statistic says it's a zero instead of a positive, and it really affects the curves. It affects our ability to get data that we can then translate to other people saying what our reliability of detection is, or reliability of inspection. Very dramatic influence, though, on what the code says we're going to do versus that which is really seen from the instrumentation.

Mike Buckley, Chairman (DARPA): Thanks very much, Steve.

REMAINING FATIGUE LIFETIME PREDICTION FOR RETIREMENT-FOR-CAUSE IN METALS

W. L. MORRIS, M. R. JAMES AND O. BUCK
ROCKWELL INTERNATIONAL SCIENCE CENTER
THOUSAND OAKS, CA 91360

ABSTRACT

A methodology is evaluated to predict the probability of specimen failure with subsequent fatigue, after a short surface crack has been detected in Al 2219-T851 alloy. Cracks are detected and tracked to failure using optical microscopy. Predictions of remaining lifetime distributions are made with a Monte Carlo procedure in conjunction with growth laws which model the effect of grains of differing size, shape and crystallographic orientation in the crack path on propagation rate. Because the surface of the alloy cyclically hardens, the average rate of crack growth is less for cracks formed later during fatigue. The predictive methodology successfully describes this phenomenon, as well as predicts the probability of early failure arising from the statistical nature of the growth process, for failure probabilities substantially smaller than conveniently measureable in the laboratory.

INTRODUCTION

The philosophy of Retirement-For-Cause (RFC) is to derive the optimum use from expensive high performance components by retaining them in service until failure by fatigue is potentially imminent. This is accomplished by inspection of each component at intervals to detect and size cracks which may have developed. A remaining lifetime prediction methodology is then employed to decide how much longer the component may safely be used. Of special concern in developing an RFC strategy is the statistical nature of the crack growth process, which may lead to failures in service substantially earlier than observable in testing small numbers of laboratory specimens.[1,2] Unexpectedly early failures are most likely if the critical crack size is small, so that the growth of short cracks dominates the statistics of failure. In this case small variations in alloy microstructure from component to component can affect growth rates and hence remaining lifetime.[3,5] In low cycle fatigue early failures can also occur for a large critical crack size and arise from linking of multiply initiated cracks, some of which may have gone undetected during inspection.

Recent advances in modeling of the effect of alloy microstructure on the growth of short surface cracks in aluminum alloys makes it practical to consider calculating the probability distribution of remaining lifetime once a short crack has been detected. In this paper we evaluate this procedure by comparing experimentally measured failure probabilities to those predicted from the alloy microstructure. Surface cracks in fatigue specimens are detected and tracked to "failure" using optical microscopy. Crack growth laws which relate the rate of propagation to the size, shape and crystallographic orientation of grains in the crack path are used, in conjunction with a Monte Carlo technique, to obtain predicted probabilities of failure with additional fatigue after detection of a crack of a pre-determined size.[3] Cycles to failure are calculated for failure probabilities as small as 10^{-4} and predicted and experimentally measured failure probabilities are compared for probabilities in the range of 0.03 to 0.5.

The surface of aluminum alloys cyclically hardens during fatigue, which reduces the rate at which short surface cracks propagate across grain boundaries.[6] Consequently isolated cracks, initiated early during high cycle fatigue, propagate more rapidly on an average than cracks initiated later. The hardening is an environmentally enhanced phenomenon which essentially disappears for fatigue in dry as opposed to in humid air. In low cycle fatigue, on the other hand, crack coalescence is more likely for cracks initiated later in lifetime because the density of cracks is larger. Thus, the probability of early fatigue failure for both high and low cyclic stress amplitudes is sensitive to the load history prior to detection of a crack, as well as to the number of cycles applied after a crack has been detected. These phenomena are investigated both experimentally and by computer simulation. Because the detected crack size and post detection loading amplitudes are well known, our predicted probability of early failure defines a lower bound to the scatter in remaining lifetime that would be expected in service for constant amplitude loading.

EXPERIMENTAL PROCEDURE

Flexural fatigue specimens (Fig. 1) of Al 2219-T851, with a yield strength σ_{yield} = 350 MN/m^2, were prepared by machining with progressively decreasing cutting depths (ending with 20 μm) to minimize residual surface stresses. 80 μm of additional material were then removed from each surface using 600 grit emery paper, and a final polishing sequence with Al_2O_3 powder was used to give specimens a mirror like surface finish for ease of crack length measurement. Repeated thickness measurements were made during polishing to maintain flatness and final specimen thickness was 0.1422 cm ± .0003. The resulting residual surface stress, measured by X-ray diffraction, was less than 20 MN/m^2.

Specimens were fatigued in stroke control in laboratory air with fully reversed loading at a frequency of 5Hz. Two maximum stress amplitudes (σ_{max}) were used with $\sigma_{max} = 0.63\ \sigma_{yield}$ or $\sigma_{max} = 0.9\ \sigma_{yield}$. Specimens were transferred at intervals to an optical microscope to measure

FLEXURAL FATIGUE SPECIMEN
GEOMETRY

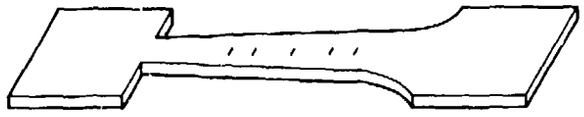

Fig. 1 Flexural fatigue specimen, illustrating location of surface cracks which have been seeded using ink dots.

crack lengths. A bending jig was used to load the specimen surface in tension for improved crack resolution during measurement.

Characterization of early failure requires that lifetime for the growth of large numbers of cracks be determined. At the lower stress amplitude the density of grain sized surface cracks initiated in Al 2219-T851 is extremely small, however. Experimental values are approximately $0.01/cm^2$ after 1.5×10^4 fatigue cycles and $0.2/cm^2$ after $4. \times 10^4$ fatigue cycles. We discovered that a small dot of ink from a felt tip pen placed on the specimen surface during fatigue greatly accelerated the rate of crack initiation, provided that the ink remained liquid during fatigue. The mode of crack initiation was unchanged by this procedure. Cracks could be seeded at any point during fatigue by delaying application of the ink until the specimen had been prefatigued a desired amount. Our procedure was to apply ink dots of approximately 50 μm in diameter along a line with separation between dots of several millimeters. After 5×10^3 fatigue cycles the ink was removed using an acetone solvent and 5×10^3 additional cycles were applied to grow the cracks to grain size. Growth rates after removal of the ink were apparently the same as on un-inked specimens, and we therefore believe that this procedure leaves subsequent growth behavior unaltered.

Using this technique we were able to initiate numerous microcracks within a desired range in fatigue cycles. Our goal was to characterize the growth of cracks of a specific length formed by a specific number of fatigue cycles. What happens in practice, of course, is that most of the early crack growth is arrested by grain boundaries; with the result that a distribution in crack lengths is observed, governed by the distribution in grain sizes. To obtain sufficient data for reasonable statistics, we analyzed the growth of cracks with initial lengths of 80±30 μm. The new length of each crack after each progressive fatigue increment was plotted against its initial length at the

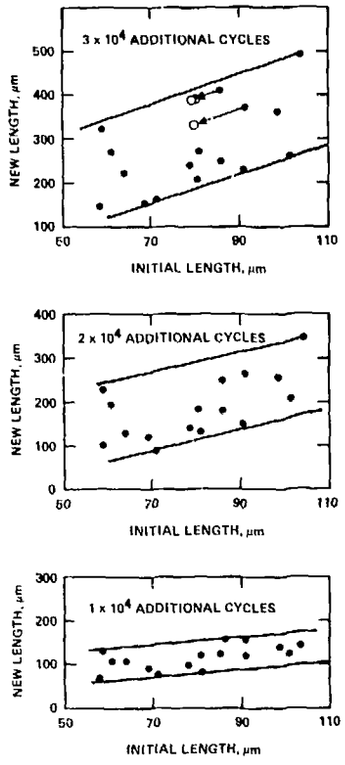

Fig. 2 New lengths (solid dots) of 16 cracks are plotted for 1,2 and 3x10⁴ cycles after detection at 1.0×10^4 cycles, against their initial length. Interpolation procedure illustrated (open circles) in top figure is used to construct an effective distribution in crack lengths corresponding to cracks initially 80μm in length.

first fatigue increment (10^4 cycles) (Fig. 2). A linear interpolation of these data was used to construct an effective distribution in lengths for each fatigue increment that approximates the distribution expected if all the cracks were initially 80 μm in length (Fig. 3). This procedure compensates for the tendency of the average growth rate to increase slightly with a larger initial crack length.

Morris has shown that the growth rate of short surface cracks in aluminum is influenced by non-continuum constraints of the plastic zone size at the surface, caused by the grain boundaries.[7] As crack lengths reach approximately 500 μm, the boundaries can no longer constrain slip and the plastic zone size expands to a size determined by continuum constraints. Thus, the statistical effect of microstructure on growth rate is expected to be of major importance when the cracks are short. Growth to a critical crack size beyond 500 μm adds to the lifetime but does not substantially increase the scatter in remaining lifetime, unless crack coalescence is involved. Additionally, the numbers of cycles to failure after 500 μm is very sensitive to specimen geometry, and for

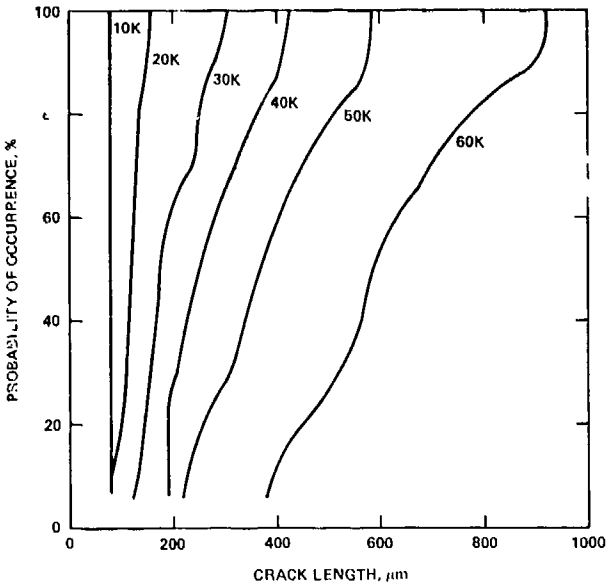

Fig. 3 Probability of occurrence of cracks of length smaller than specified for five increments in fatigue, after detection of cracks 80μm in length after 10×10^3 fatigue cycles.

instance, would be a small fraction of the total lifetime for smooth bar specimens. We, therefore, define "failure" for our experiments to have occurred for a given crack when it reaches 500 μm in length. The cycles required to reach this length for each crack is determined by a linear interpolation between fatigue increments as the length passes 500 μm. Only the faster growing cracks can be characterized with our technique as shadowing of short cracks by neighboring long cracks further suppresses the rate of growth of the shorter cracks. Furthermore, the specimen ultimately fails before all the cracks being tracked can reach 500 μm. The experimental method, therefore, is useful to determine fractional probabilities of failure slightly larger than the reciprocal of the total number of cracks initially seeded.

RESULTS

Remaining specimen fatigue lifetime is frequently determined by growth of the first and largest crack detected. This is not always the case, however, as statistical fluctuations in growth rate can lead to failure from propagation of a crack initiated at a site unrelated to the main detected crack. The probability of occurrence of such initially undetected independent initiations increases with both specimen surface area and with cyclic stress amplitude. Our experimental procedure determines probable remaining lifetime where growth of a detected single crack determines the lifetime. This is a zero surface area limiting case. For comparison, later we calculate the probability of remaining lifetime for a non-zero surface area case, in which cracks unrelated to the main crack may participate in specimen failure.

Probable remaining fatigue lifetime (zero surface area limit) results for the $\sigma_{max} = 0.63\ \sigma_{yield}$ case are shown in Fig. 4. Three cases are illustrated corresponding to 80 μm cracks initiated at 10K, 25K or 40K cycles. The probability of failure is plotted as a function of additional cycles to failure. The data points are experimental whereas the curves are theoretical predictions obtained using growth models discussed later. The trend is for cracks initiated earlier in fatigue lifetime to grow more rapidly on an average. This is entirely the result of a progressive hardening of the surface which makes it more difficult for the short surface cracks to propagate across grain boundaries later in the lifetime.

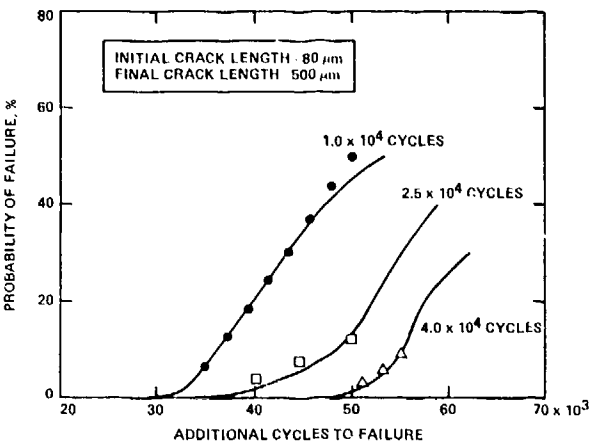

Fig. 4 Additional cycles to "failure" after an 80μm long crack has been detected at 10, 25, or 40×10^3 cycles, for a peak stress amplitude $\sigma_{max} = 0.63\ \sigma_{yield}$. Increased mean in remaining lifetime for later initiated cracks is due to cyclic hardening of the surface. Symbols are experimental data, curves are computer predictions.

Probable remaining fatigue lifetime (zero surface area limit) results for the $\sigma_{max} = 0.9\ \sigma_{yield}$ case are illustrated in Fig. 5. The additional cycles to failure are plotted for cracks initially of 200 μm in length detected at 5K or 10K cycles. Again "failure" is defined to occur as the crack length reaches 500 μm. In this case crack coalescence dominates the growth of cracks initiated at 10K cycles leading to average growth rates faster than cracks formed at 5K cycles.

MODELING AND DISCUSSION

The rate of growth of short surface cracks in Al 2219-T851 is controlled by the size, shape and crystallographic orientation of grains in the path of the crack. As a surface crack tip approaches a grain boundary, slip begins into the next grain. Growth stops at that point on the crack front for a period of incubation during which a mature plastic zone develops in the new grain.[6] The duration of incubation is longer the smaller the grain and the shorter the crack.[4,6] Progressive

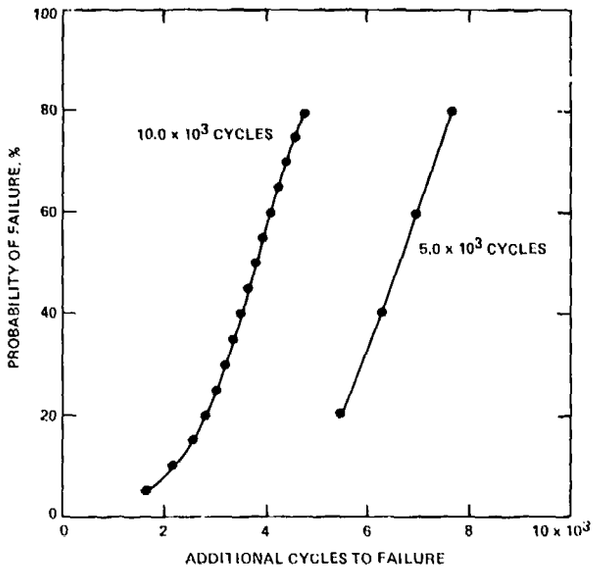

Fig. 5 Probability of failure with additional cycles after a 200μm crack has been detected for high cyclic stress amplitude. Crack coalescence for $\sigma_{max} = 0.90\ \sigma_{yield}$ accelerates average growth rate and is important for later (10×10^3 cycles) initiated cracks, for which the density of surface cracks producing coalescence is larger.

cyclic hardening of the surface reduces the propensity for slip into the new grain, increasing the incubation period for cracks encountering grain boundaries later in the fatigue lifetime.[6] At sufficiently low stress amplitudes the duration of incubation essentially determines the average growth rate. Transgranular propagation into the new grain begins when sufficient deformation has been accumulated to satisfy a critical strain energy density criterion for propagation.[7,8] The rate of subsequent crack growth within the new grain is determined by closure stress developed at the surface crack tip.[4] In the event that the subsequent growth is crystallographic, slip is principally in the plane of the crack, the closure stress is small and the growth rate is comparatively rapid.[4] If subsequent growth is transgranular and non-crystallographic, the closure stress is proportional to the grain size, and hence the rate of crack growth is initially slower into large grains than into small grains. For both growth modes, crack growth rates can be predicted by an effective stress intensity range based growth law for which ΔK_{eff} is calculated from crack length, crack depth, propagation mode and location of the crack tip with respect to the grain boundaries.[4]

Transgranular propagation of short cracks becomes progressively less likely as fatigue progresses, because of the increasing duration of incubation (as the surface hardness during fatigue). A competing intergranular growth mode is observed later in life at low stress amplitude (i.e., when the surface hardening is most pronounced). Growth proceeds by fracture of grain boundaries ahead of but not directly connected to the crack tip, followed by linking of the secondary cracks with the main crack. We have found, by measuring the opening displacement of surface crack tips, that grain boundary cracking ahead of the main crack can occur even if hardening at a surface tip is sufficient to prevent slip from the crack tip into the next grain. In this case, we attribute the grain boundary cracking to an enhancement of the strain amplitude at the boundaries due to the elastic strain field associated with the crack.

Remaining Lifetime Prediction - A computer simulation of the growth process is used to determine the cycles to failure for a series of 80 μm long cracks. For each crack the size, shape and crystallographic orientation of grains in the path of the crack at the surface are selected at random for the growth simulation using distributions in size and shape measured for the alloy, and by assuming that the distribution of crystallographic orientation is random. A simplifying assumption is made in the initial conditions for propagation which makes the calculation substantially easier. We assume that each 80 mm crack is in an 80 μm grain with the surface tips at the grain boundaries. We further assume that the cracks arrived at the boundary at any time during an interval up to 5,000 fatigue cycles before they were detected. This is consistent with experimental observation. More accurate calculation would require modeling and simulation of the crack initiation as well as of the crack growth processes.

The mathematical details of the growth laws, outlined above and used to predict cycles necessary for crack lengths to reach 500 μm, have been discussed elsewhere.[4,6] The predictions shown in Fig. 4 were obtained by simulation of growth for 10^4 cracks for each of the three initial conditions of prefatigue prior to crack detection. The trend for cracks initiated earlier to propagate more rapidly, on an average, is the result of a progressive increase in the duration of the incubation period for transgranular crack propagation across grain boundaries, due to a cyclic hardening of the surface. For the case in Fig. 4, in which 4×10^4 cycles is necessary for initiation, the mode of propagation is predominantly intergranular. Fig. 4 is replotted in Fig. 6 using a log scale to emphasize the very early failure characteristics. Some disagreement exists between prediction and experimental data for 2.5×10^4 cycles to initiation, which we attribute to the simplicity of our assumptions regarding the initial location of each crack with respect to the grain boundaries. In Fig. 7 remaining lifetime predictions for $\sigma_{max} = 0.63\ \sigma_{yield}$ have been extended to probabilities of failure of one chance in ten million by calculating the effect which crack coalescence will have on remaining lifetime. In Fig. 8 we compare calculated remaining lifetime for a zero surface area to a 100 cm^2 surface area case for $\sigma_{max} = 0.63\ \sigma_{yield}$ and 10^4 cycles to initiation. The shorter remaining lifetime for the larger surface area is due to initiation and propagation of cracks other than the main detected crack. Both the coalesence and non-zero surface area calculations were made using experimental values of the average numbers of cracks/cm^2 developed during fatigue.

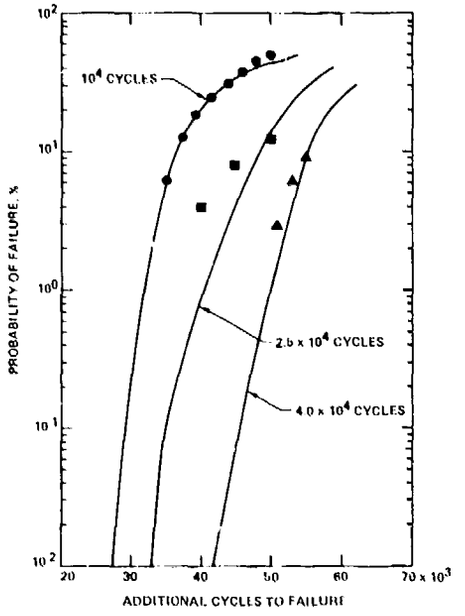

Fig. 6 Results of Fig. 4, shown using a log scale to emphasize the early failure behavior.

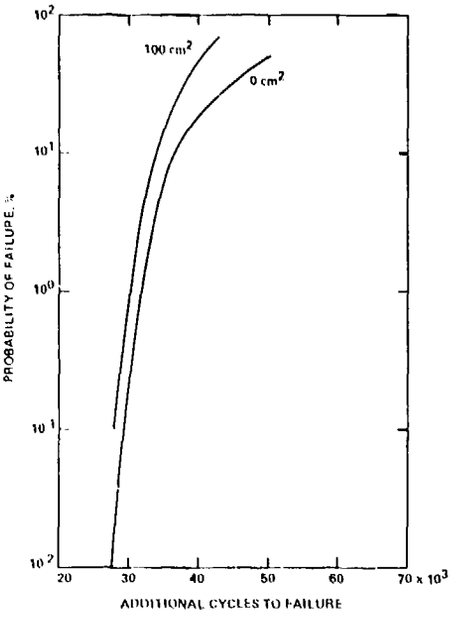

Fig. 8 Probability of failure distribution shifts to smaller numbers of additional cycles for specimens with larger surface area, because of crack initiation and propagation at sites away from the main crack.

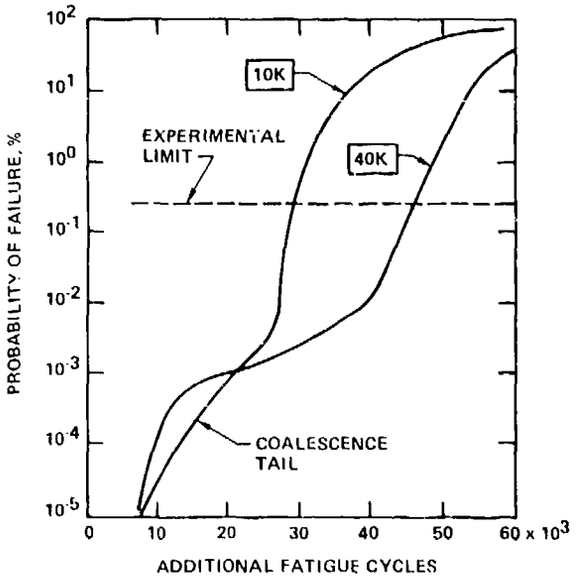

Fig. 7 Probability of failure with additional fatigue cycles for extemely low probabilities of failure is altered by crack coalescence for $\sigma_{max} = 0.63\ \sigma_{yield}$. Coalescence is more important for cracks initiated at 40×10^3 cycles, because the cracking density is higher. Dashed line is approximately the smallest failure probability that can practically be evaluated in the laboratory.

Comments on RFC Strategy - For Al 2219-T851 four separate growth mechanisms govern the statistics of early failure for propagation of short surface cracks. The relative importance of these are a function of the cyclic stress amplitude, of the cycles at which the main crack is formed, and also of the failure probability. For the case of $\sigma_{max} = 0.63\ \sigma_{yield}$ with 10^4 cycles to initiation, specimens with the shortest remaining lifetimes fail by crack coalescence and at longer lifetimes fail by crystallographic crack propagation with growth rates controlled by incubation. Still longer lifetime specimens fail due to transgranular non-crystallographic propagation with rates controlled by crack closure stress and by incubation, and the long-life specimens fail predominantly by intergranular crack propagation. Each separate growth mechanism is sensitive to different features of the alloy microstructure and mechanical properties. Thus, the statistical probability of early failure is governed by different material features depending upon the probability of failure. The probability of very early failure cannot, therefore, be realistically obtained by extrapolation from probability of failure statistics determined in the laboratory and instead must be calculated from a knowledge of the crack growth mechanisms.

SUMMARY

Once a short surface crack of predetermined size has been detected by NDE, statistical variations in the number of cycles to failure, can be substantial. Exceptionally early failures can

occur at a lifetime 1/10 of the mean remaining lifetime determined in the laboratory. These early failures result from rare combinations of the alloy microstructure in the crack path which lead to accelerated rates of crack propagation. Because of their rarity it is unlikely that such failures will be observed during laboratory testing, and even if a single anomolous event is recorded it is likely to be discounted. We have described a method to calculate the probable remaining fatigue lifetime from alloy microstructure, for small probabilities of failure. Such predictions are an essential element in the development of a quantitatively based RFC strategy. A further complexity of the early failure process, which can place additional demands upon NDE of components, is also discussed. For aluminum alloys, remaining fatigue lifetime after crack detection is a function of the prior loading history. If service records on the component are inadequate to extract loading history information an additional requirement is that NDE provide a measure of the accumulated fatigue damage of the surface, as well as detect and size surface cracks, before reliable calculations of probable remaining lifetime calculations can be made.

REFERENCES

1. J. W. Provan: Fracture 1977, Vol. 2, Waterloo, Canada, June 19-24, p. 1170, 1977.

2. L. N. McCartney: Fat. Eng. Mat. and Struct. 2, p. 387, 1980.

3. W. L. Morris, M. R. James and O. Buck: Eng. Fract. Mech. 13, p. 213, 1980.

4. W. L. Morris, M. R. James and O. Buck: "Growth Rate Models for Short Surface Cracks in Al 2219-T851," Met. Trans. A, in press.

5. W. L. Morris, O. Buck and H. L. Marcus: Met. Trans. A., 7, p. 1161, 1976.

6. M. R. James and W. L. Morris: "Quantative Modeling of Fatigue Crack Initiation," accepted by Mat. Sci. and Eng.

7. W. L. Morris: Met. Trans. A. 11, p. 1117, 1980.

8. R. Chang, W. L. Morris and O. Buck: Scripta Met. Vol. 13, p. 191, 1979.

Mike Buckley, Chairman (DARPA): Time for a couple quick questions.

Kamel Salama (University of Houston): Do you have any idea what the mechanism is for the hardening of the surface? Is the formation of a surface oxide important?

Fred Morris (Rockwell Science Center): We know it's environmentally dependent and John Wert has looked at the near dislocation structure at the surface. What we find in the presence of humidity is tangles of dislocations at the surface where there are bands of persistent dry air. I think simply that an oxide forms on the surface in humid air and prevents a certain number of dislocations from escaping through the surface, producing a harder surface.

Ross Stone (IRT Corporation): Don't you notice an effect with the rate of cycling in your fatigue tests?

Fred Morris: We haven't looked very carefully at frequency effects. Our measurements have been done at 10 Hertz. We expect no problem with heating at this frequency, but there must be a frequency dependence of the environmental effect if you go to high enough frequencies.

Ross Stone: Apparently you did ignore residual surface stress in the specimens. Is that because they were negligible?

Fred Morris: They were for our specimens. Each specimen came from the machine shop having approximately 22 ksi residual surface stress. We then took 0.003 of an inch of material off both sides and I polished each one lovingly by hand to an accuracy of 0.00001 of an inch in thickness. We measured until we got down to quite low value of residual surface stress. But we also have a model which predicts the rate at which the residual stresses decay during fatigue. That's one of the things we plan to incorporate into our failure model in the future.

Steve Kellman (Rockwell International): Fred, you mentioned the effect of moisture in the environment. How pervasive are they?

Fred Morris: In aluminum alloys, they show up in the crack initiation rate because it affects the hardening of the surface. They show up in the crack propagation rate both in the hardening of the surface and in surface ductility. And they also show up in the rate at which individual residual surface stresses relax during fatigue. If the air is humid, the surface is harder, there is less relaxation through the surface and the residual stresses stay high. So it's really pervasive, and it's very dependent on alloy type.

Otto Buck (Rockwell Science Center [now Ames Laboratory]): There is a constant in the computer calculations, in the equations that reflect the moisture effect.

Fred Morris: It's all in the models. The results you saw on moisture effect is entirely determined from the computer calculation, and are derived from what we have learned so far about the effects of moisture on growth mechanisms.

Steve Kellman: If you have initial information on the humidity variation with time can you actually calculate life with it?

Fred Morris: Yes, we have done it.

John Rodgers (Acoustic Emission Technology): I'm rather curious, considering the kind of environment that aircraft might be flying in in the European area with what is acknowledged to be acid rain conditions, with pH's ranging down as low as 1.5 or 2 - is this not an important consideration in the moisture effects on the crack initiation and propagation?

Fred Morris: I'm sure it's important. I told you how we started the cracks in those materials. We used felt-tip pen ink to start the crack. So anything you put on that aluminum surface that modifies the near surface ductility can have an enormous effect on the life time.

Chris Burger (Ames Laboratory): What did you consider failure?

Fred Morris: The complete calculations were done to a crack length of 500 microns.

Chris Burger: You were talking then about the surface length of the crack?

Fred Morris: Yes.

Chris Burger: What concerns one from a failure reliability standpoint are the depth of those cracks.

Fred Morris: Of course. And they can be quite shallow, but this is really an exercise in how well our models work. We're also attempting to do the same types of predictions on smooth-bar specimens, carrying it right on up to the critical crack size, but we suffered from some experimental constraints in this measurement, which is the main reason we fixed the maximum length of interest at 500 microns.

Chris Burger: That is surface length?

Fred Morris: That's surface length, and the crack shape factors are typically about 0.1 when the cracks get that long. But if you would take that same crack and put it in a smooth-bar specimen, it would be about 250 microns deep.

Mike Resch (Stanford University): What do you think it is about the felt pen ink that accelerates crack initiation, and what effect might the ink have on the growth kinetics on these very small cracks?

Fred Morris: What we do is use it to start the crack and then take it off.

Mike Resch: How do you take it off? How do you know you don't have ink down in the crack tip that's going to, say, affect the kinetics.

Fred Morris: I wouldn't say it doesn't. We try to get the ink out by ultrasonically cleaning in an acetone bath. However, the growth rates are consistent with uninked specimens. Of course, we have to use that technique, because if we were to rely on naturally started cracks, the chance of finding a natural crack after 10 thousand cycles in that material is one per 10 square centimeters of surface area. And it will take you a week to find it.

Mike Buckley, Chairman: Thank you very much, Fred.

ENERGY RELEASE RATES FOR A PLANE CRACK SUBJECTED TO GENERAL LOADING AND THEIR RELATION TO STRESS-INTENSITY FACTORS

A. Golebiewska Herrmann and George Herrmann
Stanford University
Stanford, California 94305

ABSTRACT

The well-known J integral of elastic fracture mechanics has been related to potential energy-release rate associated with crack extension and has proved to be of great value in fracture testing. In particular, the path-independence of the J integral has been used to an advantage in performing acoustoelastic measurements along a closed contour surrounding a crack tip.[8] In Mode I (opening mode) for example, the J integral depends essentially only on the corresponding stress intensity factor K_I which can thus be determined.

Actually, J is the component of a vector in the plane of the crack and there exists a component of this vector normal to the crack plane, which, however, has not been interpreted properly in the past. It is one aim of this paper to supply a valid interpretation of this path-independent integral and to relate it to still another integral, also path-independent, which has been termed the L integral. It will be further shown explicitly that for a crack under mixed-mode loading this latter integral represents the energy release rate for rotation which can be used to determine both K_I and K_{II} .

INTRODUCTION

For some years now, researchers became interested in path-independent integrals J, L and M. In the context of fracture mechanics the importance of path-independent integrals resides in the fact that they can be related to energy release rates, e.g. to crack extension forces which themselves depend only on stress intensity factors. It was shown by Rice[1] that the J integral is related to the elastic energy-release rate associated with statically extending cracks. Freund[2] has found that in certain special cases the M integral can be related to J, which he has shown to be useful in calculating stress intensity factors without solving the corresponding boundary value problem. The J integral is actually the component J_1 of a vector J_k , (k = 1,2), and since J represents a force, we could expect that J_2 is simply another component of that force. The relation between J_1 and M suggests that there might be a similar relation between J_2 and L , another path-independent integral studied by Knowles and Sternberg[3] and Rice and Budiansky.[4] In order to assign a practical use to J_2 or L (or both), we have to understand the physical meaning of those quantities and to establish possible relations between them (if they exist). This is the aim of this paper.

IS J_2 A PATH-INDEPENDENT INTEGRAL?

We consider a two-dimensional deformation field referred to Cartesian coordinates X_1 , X_2 . The crack of length 2a is placed along the OX_1 axis (see Fig. 1). The J integral is defined as

$$J = \oint_C (W dX_2 - T_i u_{i,1} d\ell) \qquad (1)$$

where C is a contour enclosing the right crack tip, W the strain energy density, T_i the traction, u_i the displacement vector and comma denotes differentiation, e.g. $u_{i,1} = \partial u_i / \partial X_1$. If the crack is subjected to far-field homogeneous applied stresses σ^A_{11} , σ^A_{12} , σ^A_{22} , J equals to (in plane stress)

$$J = (K_I^2 + K_{II}^2)/E \qquad (2)$$

where E is Young's modulus and K_I and K_{II} are stress intensity factors defined as

$$K_I = \sqrt{\pi a}\, \sigma^A_{22} \quad , \quad K_{II} = \sqrt{\pi a}\, \sigma^A_{12} . \qquad (3)$$

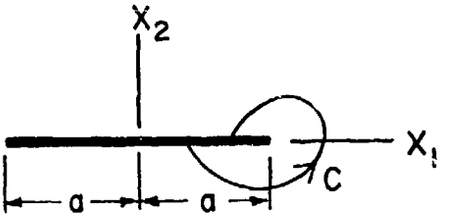

Figure 1

Path C for J Integral

We notice that J given by (2) does not depend on σ^A_{11} and is path-independent: because J can be expressed in terms of quantities which do not depend on the contour.

Actually, J is a component J_1 of a vector

$$J_k = \oint_C (W n_k - T_i u_{i,k}) d\ell \qquad i,k = 1,2 . \qquad (4)$$

The second component of this vector J_2 has been calculated for the infinitesimal contour enclosing the crack tip giving

$$J_2 = -2K_I K_{II}/E \qquad (5)$$

where again K_I , K_{II} are given by (3). Again J_2 does not depend on σ_{11} .

We observe an interesting feature of J_1 and J_2. As given by (4), they seem to be the components of a vector; however, comparing (2) and (5), they do not behave like independent quantities: if $J_1 = 0$, then J_2 is necessarily zero also, by contrast to the basic definition of a vector whose components should be independent from one another. We will return to this point later.

Now we would like to concentrate on the path-independence of J_1 and J_2. The basic practical use of J_1 resides in the fact that it is path-independent, or more precisely: if a contour C encloses the crack tip and starts and ends on the crack face, the value of J_1 does not depend on the particular choice of C . The reason is that along the crack faces, T_i is zero, thus the second term of (1) is identically zero, while the first one vanishes because dX_2 is zero. This argument, however, does not hold for J_2: i.e. the second term (with T_i) vanishes, but not the first one, and J_2 is path-dependent in the same sense as J_1 is path-independent

Exact calculations are given for remote homogeneous fields in Ref. 5. Does this mean that J_2 has no meaning whatsoever? In order to answer this question, we have to establish more precisely what we mean by path-independence: J_1 strictly speaking is not path-independent,either,because if a contour encloses the whole crack, $J_1 = 0$ (see Fig. 2).

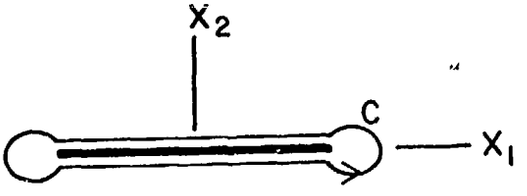

Figure 2

Path C for L Integral

Should a contour enclose a crack tip or the whole crack? Usually we could expect path-independence of some quantity if the contour is taken over all singularities. E.g., Gauss law in electro-statics is

$$\operatorname{div} \vec{E} = 4\pi\rho$$

where $\vec{E}$ denotes the electric field , ρ the charge density. In global form this law is stated as

$$\int_S \vec{E} \cdot d\vec{S} = 4\pi e$$

The surface integral of $\vec{E}$ gives the total charge e inside the volume and is independent on the surface S , as long as all charges are inside S (see Fig. 3).

$$\int_{S_1} \vec{E} \cdot d\vec{S} = \int_{S_2} \vec{E} \cdot d\vec{S} = 4\pi \sum_{i=1}^{n} e_i$$

Thus we have to decide whether a crack or a crack tip is a singularity under consideration. Actually, for J_2 there is no choice; only when the integral is taken around the whole crack does the contribution along the crack vanish and the total value of J_2 is zero (Ref. 5).

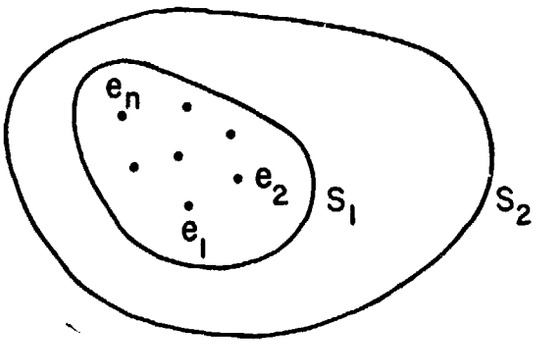

Figure 3

Charges Enclosed by Surfaces S_1 and S_2

RELATIONS BETWEEN M AND J RE-EXAMINED

Freund[2] established a relation between two path-independent integrals M and J . M is given by

$$M = \oint_C (W X_i n_i - T_k u_{k,i} X_i) dS \qquad (6)$$

and J is given by (1). In (6) the contour, however, is taken around the whole crack (see Fig. 2). The relation established by Freund is

$$M = 2aJ \qquad (7)$$

In other words, one quantity connected with the whole crack M is related to another one, namely J , associated with a crack tip only. This was the basis of some of the experimental work reported by R. King, G. Herrmann and G. Kino in a separate paper in these Proceedings.

Before we attempt establishing some relations between J_2 and another path-independent integral, let us re-examine the relation between M and J from the physical point of view. As it is well known, J is related to energy release rates. Let us start with the strain energy of an elastic continuum without defects

$$W = W[\varepsilon_{ij}(X_k)] \tag{8}$$

where $\varepsilon_{ij}(X_k)$ is the strain tensor. The body is in equilibrium, thus

$$\sigma_{ij,j} = 0 \tag{9}$$

where σ_{ij} is the symmetric stress tensor related to W

$$\sigma_{ij} = \frac{\partial W}{\partial \varepsilon_{ij}} . \tag{10}$$

If we differentiate W with respect to X_i, and make use of (10), of the symmetry of stress tensor and of (9) we obtain

$$\frac{\partial W}{\partial X_i} = \frac{\partial W}{\partial \varepsilon_{jk}} \varepsilon_{jk,i} = \sigma_{jk} u_{j,ki} = \sigma_{jk} u_{j,ik}$$
$$= (\sigma_{jk} u_{j,i})_{,k} - \sigma_{jk,k} u_{j,i} = (\sigma_{jk} u_{j,i})_{,k} \tag{11}$$

and finally

$$\frac{\partial}{\partial X_k} (W\delta_{ik} - \sigma_{jk} u_{j,i}) = 0 . \tag{11}$$

If we integrate this expression over any volume inside the body, and then make use of Gauss theorem, we have

$$\int_S (W n_i - T_j u_{j,i}) dS = 0 . \tag{12}$$

For the two-dimensional case S becomes a line and (12) represents a conservation law. Our considerations concerned energy, but (12) is not conservation of energy. Actually, if we define the material momentum tensor b_{ik} as

$$b_{ik} = W\delta_{ik} - \sigma_{jk} u_{j,i} \tag{13}$$

relation (11) can be rewritten as

$$b_{ik,k} = 0 \tag{14}$$

which is very similar to the equation of equilibrium (9), expressing absence of body forces or conservation of linear momentum. In this sense (14) expresses conservation of material momentum in the absence of material forces. To reinforce this suggestion, let us observe that the integral in (12) is identical to that of J_k given by (4); however, the right-hand side of (12) equals zero. If we assume now, in order to distinguish between a continuum without and with defects, that W depends on X_i not only through ε_{ij}, but also explicitly, i.e.,

$$W = W[\varepsilon_{ij}(X_k), X_i]$$

we obtain

$$\frac{\partial W}{\partial X_i} = \frac{\partial W}{\partial \varepsilon_{jk}} \varepsilon_{jk,i} + \left(\frac{\partial W}{\partial X_i}\right)_{exp}$$

which leads to

$$b_{ik,k} = \left(\frac{\partial W}{\partial X_i}\right)_{exp} \tag{15}$$

instead of (14). The right-hand side represents a density of material force, in the same sense as f_i given by

$$f_i = \sigma_{ik,k} \tag{16}$$

represents a body force density; actually if f_i is a gravity force, f_i can be written as

$$f_i = -\frac{\partial U}{\partial x_i}$$

where U is the density of the gravitational potential, to make the formal analogy even stronger.

In classical mechanics, there is a strong relation between admissible transformations and conservation laws: e.g., translational in variance is connected with momentum conservation; presence of forces expresses non-conservation of momentum and in this sense is related to translations. So actually we can "deduce" the forces acting on the object under consideration by inducing a possible translation of that object. In this sense J is precisely a force acting on a crack tip, because to derive it the possible translation of a crack tip, not of a crack, was considered.

Another transformation of interest can be similarity. For a particular case of a crack it can be written as

$$\delta X_1 = \frac{\alpha}{a} X_1 \tag{16}$$

where α is an infinitesimal parameter. This transformation concerns X_1 only if we use the coordinate system of Fig. 1. This transformation leads to the formula (6) for M. The physical meaning of J_1 and M is clear: the translation of both tips by α along X_1, but in opposite directions (Fig. 4a), so $\delta X_1 = \alpha$ at the right tip, and $\delta X_1 = -\alpha$ at the left one, is equivalent to the similarity transformation given by (16) and characterized by the same α (Fig. 4b). In this sense M represents a generalized extension force acting on a crack (Fig. 4).

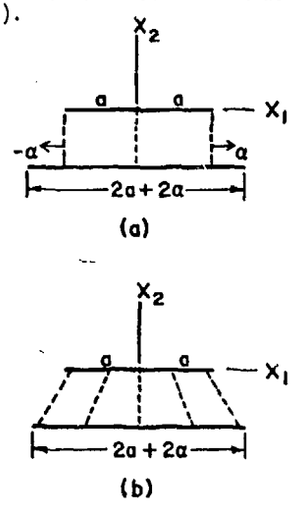

Figure 4
Growth of a crack (a) by translation of crack tips and (b) by similarity transformation

J_2, L AND ENERGY RELEASE RATES

We return to the problem of J_k: does it represent the components of the force acting on a crack, or crack tip, or not? Let us notice that relation (15) is obtained in quite general fashion, for any defect in a continuum, while specific values of J_1 and J_2 given by (2) or (5) were obtained specifically for a plane crack. In this process

the nonequivalence of X_1 and X_2 axes is essential. In other words, as long as all directions are equivalent for a defect, J_1 and J_2 have the same meaning of components of a force; however, the geometry of a crack imposes additional constraints to this interpretation.

Let us consider the simplest example of a rigid bar lying on the plane surface axis X_1 being directed along the bar, X_2 being perpendicular to the plane. The force acting at the end of the bar in the X_1 direction causes translation of the whole body in the X_1 direction. However, a force acting in the X_2 direction causes not a translation in the X_2 direction, but a rotation in the X_1X_2 plane about the other end of the bar. The situation for a crack is similar (though not identical): J_1 and J_2 are situated differently with respect to the crack itself, such that their roles are different. To establish the role of J_2, we will pass now to another path-independent integral, namely the L integral, defined as

$$L = \oint_C e_{3ij}(WX_j n_i - T_i u_j - T_k u_{k,i} X_j)dS. \quad (17)$$

For the configuration given in Fig. 1,

$$L = 2\sigma_{12}^A(\sigma_{22}^A + \sigma_{11}^A)\pi a^2/E \quad (18)$$

or

$$L = -2aJ_2 + 2\sigma_{12}^A(\sigma_{11}^A - \sigma_{22}^A)\pi a^2/E \quad (19)$$

where J_2 is given by (5). The integral L has been found to be the rotational energy release rate (Ref. 5). The relation has the form:

$$L = -\frac{\partial U}{\partial \Phi}$$

where U is the energy of the crack, depending not only on a, but Φ, the angle by which the crack rotates (virtually) in its plane (Fig. 5).

The value of L given by (18) or (19) depends not only on σ_{12}^A and σ_{22}^A but also on σ_{11}^A. From (19) we see that for a certain special stress field L can be expressed in terms of J_2

$$L = -2aJ_2 \quad \text{if} \quad \sigma_{11}^A = \sigma_{22}^A. \quad (20)$$

The relation (20) is similar to (7) except there were no restrictions on the stress field to be satisfied in the case of M and J_1.

The expressions (18) and (20) may be useful in the nondestructive determination of stress intensity factors for cracks subjected to combined loading.

THE CRACK AND GENERALIZED FORCES

The path-dependence of J_2, when taken around one crack tip, indicates that J_2 is not a physically meaningful quantity for measurements concerning properties of materials near a crack. Actually, if we would like to introduce a unified description of the behavior of a crack taking all integrals around the whole crack, we find that

$$J_1 = J_2 = 0$$

and then it is M and L which become physically meaningful. Ascribing to a crack two degrees of freedom, namely extension and rotation, represented by dependence of energy of a crack on a and Φ, we see that L and M are generalized forces associated with those generalized coordinates in the sense of classical mechanics

$$M = -a\frac{\partial U}{\partial a}, \qquad L = -\frac{\partial U}{\partial \alpha}.$$

While tensile forces are concentrated only at the tips, the moments are distributed along cracks, too. These two facts explain why M can be expressed through J_1, while L, in general, can not be expressed through J_2.

The next interesting observation can be made in relation to generalized coordinates: if instead of a, Φ we will use generalized coordinates u, γ, as indicated in Fig. 6, we obtain

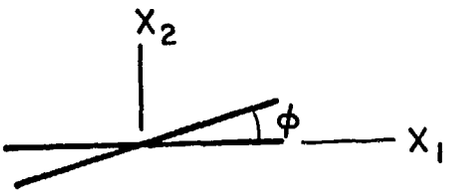

Figure 5
Rotation of Crack

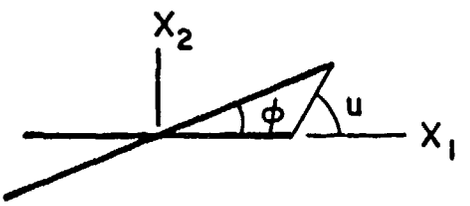

Figure 6
Generalized Coordinates u and Φ

$$\left(\frac{\partial U}{\partial u}\right)_{u-0} = J_1 \cos\gamma - L/a \sin\gamma \,. \qquad (21)$$

The right-hand side represents a generalized force F_u connected with the generalized coordinate u. For the special case $\sigma^A_{11} - \sigma^A_{22}$ it reduces to

$$F_u = J_1 \cos\gamma + J_2 \sin\gamma \,. \qquad (22)$$

In this form (Ref. 6) F_u was ascribed to skewing of a crack rather than to rotation. Without assigning this meaning to expression (22), let us notice that if this is true, in a general case we should use (21) involving L rather than (22) which is only a special case of (21).

Finally, we would like to remark briefly on the sign of L. In the definition given by (17), which repeats the well-known (Refs. 3,4) definition of L, the symbol e_{ijk} is used. Should we interchange the indices j and k, the signs in expressions (18),(19) and consequently in (20),(21), would change. As we realize by now, L represents the moment of material forces. Usually, the moment is given by $e_{ijk} x_j F_k$; it would correspond exactly to the change of sign of L given by (17). Of course, L as given by (17) cannot be represented as a prodict of X_j by another quantity because of the presence of the form $T_j u_j$. A more general treatment of path-independent integrals and their relations to conservation laws will be given in (Ref. 7).

ACKNOWLEDGMENT

This research was supported in part by the Electric Power Research Institute Contract EPRI-609-1 and by the Air Force Office of Scientific Research Grant F49620-79-C-0217 to Stanford University.

REFERENCES

1. Rice, J.R., "A Path Independent Integral and the Approximate Analysis of Strain Concentration by Notches and Cracks", *Journal of Applied Mechanics*, Vol. 35, Trans. ASME, Vol. 90, Series E, June 1968, pp. 379-386.

2. Freund, L.B., "Stress Intensity Factor Calculations Based on a Conservation Integral", *International Journal of Solids and Structures*, Vol. 14, 1978, pp. 241-250.

3. Knowles, J.K. and Sternberg, Eli, "On a Class of Conservation Laws in Linearized and Finite Elastostatics", *Arch. Rat. Mech. Anal.*, 44, 1972, pp. 187-211.

4. Budiansky, B. and Rice, J.R. "Conservation Laws and Energy-Release Rates", *Journal of Applied Mechanics*, Vol. 40, 1973, pp. 201-203.

5. Herrmann, A. Golebiewska and Herrmann, G., "On Energy-Release Rates for a Plane Crack" to be published.

6. Cherepanov, G.P., *Mechanics of Brittle Fracture*, Moscow, Publishing House "Nauka" 1974. English translation to be published by McGraw-Hill.

7. Herrmann, A. Golebiewska, "Material Mementum Tensor and Path-Independent Integrals in Fracture Mechanics" to be published.

8. Herrmann, G. and Kino, G.S., "Ultrasonic Measurements of Inhomogeneous Stress Fields", *Proc. of ARPA-AFML Conference on NDT*, July 1979.

SUMMARY DISCUSSION

Otto Buck, Chairman (Rockwell Science Center [now Ames Laboratory]): Any questions, please?

I have a short question. Let's assume we start out in a mode one and the crack goes over into mode two or something like that. Would you be able to treat that particular situation?

George Herrmann (Stanford University): You mean crack skewing? It's not being treated here.

Otto Buck: What hope do you see for that?

George Herrmann: We see some hope, but completely different considerations will be required here.

Perhaps in answering that question, we might mention that what we see here is for the energy releas for rotation, Sigma 1-1. The applied stress parallel to the crack does play a role, and it is expected that in crack skewing, it most likely will therefore also play a role. But we are not prepared to say at this time just what role that will be

Otto Buck: One more question.

Mike Resch (Stanford University): We talked about these conservative integrals for two-dimensional cracks. What does the J integral mean for a three-dimensional, semi elliptical surface crack?

George Herrmann: It means you have to take an integral, not around a line, but you have to take it around the whole surface. In fact, we have some thoughts along that line - or along that surface, I should say, but we have not proceeded any further than just loosely thinking about it.

Chris Burger (Ames Laboratory): Experiments by Kobyashi and Danielson and a few other people seem to suggest to us that the mode two crack; to talk about mode two crack growth, is really not worth much because the crack turns as quickly as it can and propagates in mode one. How does that relate to your work with J-2.

George Herrmann: There are two points of view. There are those people who say that this crack skewing is completely an irrelevant subject because, as you say, the crack just turns right away, and we are not concerned about the details. There are some other people, however, perhaps including some of us, who think that it might be just interesting to see what is going on in detail before the crack is turning and becomes just a pure mode one crack. What is the mechanism which is taking place? Is there any possible additional material constants which gover at process right at the beginning and so on.

Otto Buck, Chairman: Thank you so much, George.

ACOUSTIC NONDESTRUCTIVE EVALUATION OF ENERGY RELEASE RATES IN PLANE CRACKED SOLIDS

R. King, G. Herrmann and G. Kino
Stanford University
Stanford, California 94305

ABSTRACT

Acoustic measurements, using longitudinal waves in plane specimens, based on the theory of acoustoelasticity, permit the determination of the sum of the principal stresses $(\sigma_1 + \sigma_2)$. By automatic scanning, we are able to make such measurements throughout a region of interest.

In this paper we shall be concerned with the application of this acoustoelastic stress analysis to fracture mechanics. Specifically, the energy release rates for extension and rotation of a crack will be determined experimentally (J integral for extension, L integral for rotation) followed by a numerical adjustment procedure which may be called the *rescaling* technique. If desired the stress intensity factors at a crack tip may also be evaluated. This procedure was applied to three different specimen configurations, and the results compare favorably with purely theoretical predictions.

INTRODUCTION

In this paper a summary is presented of recent efforts at Stanford University on applying acoustoelastic stress analysis using ultrasonics to the evaluation of conservation integrals in fracture mechanics. A brief review is included of the theory of acoustoelasticity and the experimental apparatus and techniques used to make stress measurements with ultrasonics. After discussing the practical importance of nondestructively evaluating three conservation integrals, the so-called J, L, and M integrals, attempts at performing such evaluation using ultrasonic stress measurements are described.

ULTRASONIC STRESS ANALYSIS

The application of acoustoelasticity to stress analysis using ultrasonic measurements has been discussed in detail in the literature,[1-5] including previous work in this field at Stanford. The important features of ultrasonic stress measurements in plane specimens are summarized here.

Due to nonlinear deformation, the velocity of an acoustic wave travelling through a stressed solid is dependent on the state of deformation, and hence through a constitutive law, on the state of stress in the solid. For the case of a longitudinal wave propagated at normal incidence in a plane specimen, the relation between wave speed and stress is

$$\frac{V - V_0}{V_0} \equiv \frac{\Delta V}{V_0} = B(\sigma_1 + \sigma_2) \qquad (1)$$

where V and V_0 are the velocities of the wave in the stressed and unstressed states, respectively, $(\sigma_1 + \sigma_2)$ is the planar first stress invariant, and the proportionally constant B is a material property which depends on the elastic constants of the material, including the third order (Murnaghan) constants. B is calibrated directly for a given material by using a uniaxial tension test. With knowledge of B, relative velocity measurements at many points will enable determination of $(\sigma_1 + \sigma_2)$ throughout a specimen. A diagram of the device we have used for performing such measurements is shown in Fig. 1.

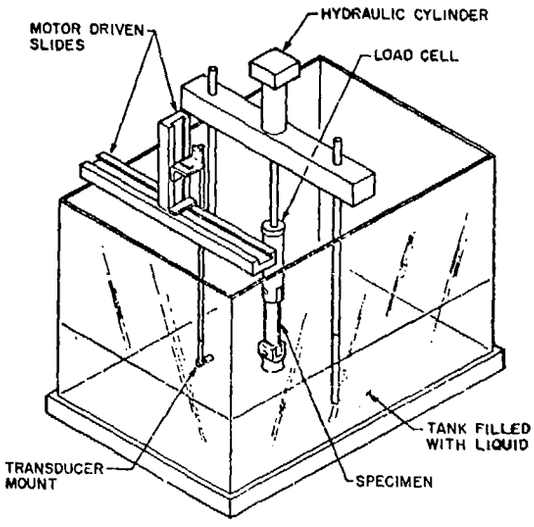

Figure 1. Acoustoelastic scanning device

For the case of shear waves at normal incidence to a plane specimen, the relevant acoustoelasticity relation is

$$\frac{V_1 - V_2}{V_0} = C(\sigma_1 - \sigma_2) \qquad (2)$$

where V_1 and V_2 are the velocities of waves in the stressed medium polarized in the x_1 and x_2 directions, and V_0 is the velocity of the incident wave in the unstressed medium. Thus shear waves permit evaluation of the difference of the in plane principal stresses. In addition, principal directions can readily be found, using shear waves, from a plot of amplitude of received signal versus polarization angle. The constant C in Eq. (2) is also a material property and, as with B, is calibrated using a uniaxial tension test. By simultaneous application of longitudinal and shear wave measurements at many points, all components of the stress tensor can be evaluated throughout a region in plane specimens. A device similar in principle to that shown in Fig. 1 has been constructed for scanning

shear wave measurements, which uses direct contact to couple the waves. Preliminary work is underway in calibrating the constant C using this device, but two-dimensional stress analysis has not yet been successfully performed.

CONSERVATION INTEGRALS

J , L , and M Integrals

The well known J integral is actually one of a series of path-independent conservation integrals which exist in elasticity.[6] Three of these, the so-called J , L , and M integrals, have the potential for practical applicability in fracture mechanics. A theoretical discussion of conservation integrals for plane cracked bodies is made elsewhere in these proceedings,[7] so a brief description of their definition and practical utility will suffice here. The J , L , and M integrals are defined as follows:

$$J = \int_C (Wn_i - T_k U_{k,i})\, ds$$

$$L = \oint_C e_{3ij}(Wx_j n_i - T_i U_j - T_k U_{k,i} x_j)\, ds$$

$$M = \oint_C (Wx_i n_i - T_k U_{k,i} x_i)\, ds$$

where W is the strain energy density, T_k is the traction vector acting on the outer side of C , U_k is the displacement vector, and e_{ijk} is the permutation tensor. For the J integral, C is a contour in the $x_1 - x_2$ plane around the tip of a crack, while for L and M , C completely encloses the crack. These integrals are physically interpreted as energy release rates with respect to translation of the tip of the crack for J and with respect to rotation and self-similar expansion of the entire crack for L and M respectively.

The practical significance of the J integral in fracture mechanics is that comparison of J versus a critical value of J (J_{IC}) provides a useful fracture criterion[8] which remains valid even when general yielding occurs as long as there is no unloading. Thus, if J_{IC} is known for a material, the ability to nondestructively evaluate J will allow assessment of the structural integrity of a cracked element. In situations governed by Linear Elastic Fracture Mechanics (LEFM), the J integral is the same as the crack extension force G_I . Thus

$$J = G_I \sim k_I^2 \qquad (3)$$

In linear elastic cases, use of the J integral has certain advantages over direct evaluation of the stress intensity factor, such as the ability, through path-independence, to obtain knowledge of the near tip stress fields from information along a contour further away from the crack and the smoothing effect of integration on noise in numerical or experimental data.

The M integral is useful because J can be determined from M . For instance, it is easily shown through path-independence arguments that for an interior crack of half length a ,

$$M = 2aJ \qquad (4)$$

It is sometimes more convenient to evaluate M using a closed contour rather than evaluate J along a contour around the tip of a crack, and M can be applied in certain situations involving loading on the crack faces where path-independence of J would no longer hold.

The practical importance of the L integral will arise in mixed mode cases. Since extension of a crack in mixed mode deformation does not occur along its original length but rather at some angle to it, the J integral alone is insufficient to predict onset of crack extension. The L integral may provide the additional information needed in such cases.

Experimental Evaluation of Conservation Integrals

The customary techniques for measuring the J integral involves direct determination of the energy release rate with respect to crack extension using compliance measurements.[8,10] These methods are not suitable for nondestructive evaluation of J in structural elements but rather are designed for laboratory determination of J_{IC} . In contrast, the approach we have used for evaluating J , L , and M is to determine the value of the integrand at points along a contour and then numerically integrate. The difficulty of this approach is evident if the conservation integrals are shown in expanded form. For instance, in plane stress if the material along C is linear elastic, the J integral becomes

$$J = \int_C \frac{1}{2E}(\sigma_{yy}^2 - \sigma_{xx}^2)dy + \frac{\sigma_{xy}}{E}(\sigma_{xx} + \sigma_{yy})dx + \omega_{xy}(\sigma_{xy}dy - \sigma_{yy}dx) \qquad (5)$$

It is seen that evaluation of the integrand requires knowledge of all the components of the stress tensors as well as the rotation ω_{xy} . This is also true for L and M . Three different avenues have been explored for obtaining this information. They are:

1. Use of both shear and longitudinal wave measurements;
2. Use of longitudinal waves and special contours along which the integrand simplifies;
3. Use of longitudinal waves and "rescaling".

Description of each of the methods will follow.

Use of Shear and Longitudinal Waves

As discussed above, simultaneous application of shear and longitudinal wave measurements permits determination of all three components of the plane stress tensor. As seen in Eq. (5), it remains to determine ω_{xy} in order to evaluate J , L , or M . A numerical technique was presented in the 1979 ARPA/AFML Proceedings[11] for evaluating ω_{xy} using the known stress components and forward integration of the compatibility relations. This method has been successfully applied to the evaluation of both

J and M on theoretical data. In addition, since shear wave data were not available, experimental values of σ_{xx}, σ_{yy}, and σ_{xy} were simulated by introducing noise into the theoretical data, and again J and M were successfully evaluated. No further progress has been made on this approach since scanning shear wave data is still not available.

Special Contours

In certain cases, special contours can be found along which the integrand of J, L, or M simplifies considerably. The successful application of this approach on three different specimen configurations has been described in Ref. 12 and will be summarized here. The center-cracked panel specimen shown in Fig. 2 is chosen for illustration purposes because it shows both the utility of the M integral and the simplification along a special contour. The contour used proceeded vertically along the edges of the specimen and horizontally a slight distance from the shoulder as shown. By symmetry it is only necessary to consider one quadrant. Thus

$$M = 4(M_{AB} + M_{BC}) \tag{6}$$

where M_{AB} and M_{BC} are the contributions to M of paths AB and BC, respectively. Note that while the J integral would not be useful along a closed path such as this one (it would vanish identically), the M integral gives a useful result (see Eq. (4)).

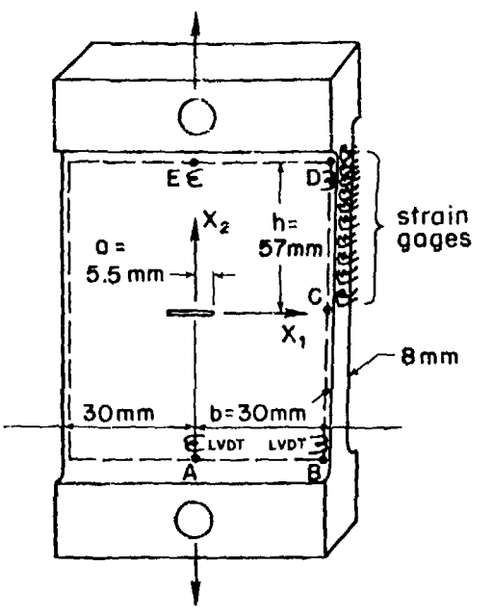

Figure 2. Center-cracked specimen used for M integral experiment.

On the traction-free vertical edge BC, $W = (E/2)\varepsilon_{yy}^2$ and $x_i n_i = b$, so

$$M_{BC} = \frac{bE}{2}\int_0^h \varepsilon_{yy}^2 dy = \frac{b}{2E}\int_0^h \sigma_{yy}^2 dy \tag{7}$$

which can be evaluated using either strain gages or longitudinal wave ultrasonic measurements. Evaluation of M_{AB} is slightly more complicated, but it is shown in Ref. 12 that M_{AB} is approximately given by

$$M_{AB} = \frac{P}{A} - \frac{hbP}{AE} + \frac{4b}{3}[U_y(b,h) - U_y(0,h)] \tag{8}$$

where P is the applied load and A is the cross-sectional area of the specimen. Thus evaluation of M_{AB} requires only two displacement measurements, which is accomplished using linear variable differential transformers (LVDTs). With the specimen loaded in tension to 30000N, the M integral was experimentally found to be 11.52N. The theoretical value for M was found in plane stress using

$$M = 2aJ = 2a\frac{K_I^2}{E} \tag{9}$$

to be 11.23N. (The discrepancy is 3%.) This first experiment used strain gages to evalute M_{BC}. The two other specimens considered were an edge cracked specimen loaded in uniaxial tension and a specimen with free edges and an edge notch into which a wedge was forced. The J integral was evaluated for the former specimen and the M integral for the latter with agreement with expected values within 3% and 12%, respectively. Again the strain gages were employed in these experiments.

Attempts were made to repeat each of these experiments using longitudinal wave measurements with disappointing results. The difficulty is that evaluation of the integrand along paths such as M_{BC} above requires, theoretically, measurements exactly on the edge of the specimen. In practice, measurements are made slightly inside the edge, and the velocity measurements are extrapolated to the edge. The results were erratic and depended to a great extent on the extrapolation scheme used. We feel this is because the theory behind our measurement (Eq. (1)) is not valid near the edge of a specimen, and there are effects such as diffraction which must be accounted for. We concluded that this approach is quite useful in conjunction with strain gage measurements but will not be a fruitful application of ultrasonic measurements unless the difficulties described are overcome.

Longitudinal Wave Measurements and "Rescaling"

A method has been derived for evaluation of conservation integrals solely from knowledge of $(\sigma_{xx} + \sigma_{yy})$ in a region in the vicinity of a crack. This method is based on the following postulate: in the region in which data is taken, it is assumed that the deformation fields in the body vary with position in a geometrically similar manner to the stresses in an analogously loaded infinite plate with an identical crack. This assumption is conceptually similar to that originally made by Theocaris and Gdoutos[13] in photoelastically evaluating K_I, which was also used by Hunter[11] to evaluate K_I from ultrasonic data. One expects this assumption to be a good one as long as the data is taken sufficiently far from the boundaries and close enough to the crack. Mathematically, the assumption is stated as follows: representing stresses in the infinite plate by a superscript "0",

the infinite plate solution can be expressed as

$$\sigma^0_{ij}(x,y) = a_1 f^0_{ij}(x,y) \; ; \; \omega^0_{xy}(x,y) = a_1 g^0_{ij}(x,y) \tag{10}$$

Assume in the region of interest in the finite body containing a crack that

$$\sigma_{ij}(x,y) = a_2 f_{ij}(x,y) \; , \; \omega_{ij}(x,y) = a_2 g_{ij}(x,y) \tag{11}$$

If $(\sigma_{xx} + \sigma_{yy})$ has been measured, then a_2 can be determined:

$$a_2 = \frac{a_1(\sigma_{xx} + \sigma_{yy})}{(\sigma_{xx} + \sigma_{yy})^0} \tag{12}$$

With measured values of $(\sigma_{xx} + \sigma_{yy})$ available at many points, the value of a_2 which will best fit the infinite plate solution to the measured data can be determined. This has been dubbed the "rescaling" method because it involves determination of a multiplicative constant used to "rescale" the infinite plate stresses and rotations. In situations involving more complicated far-field loading, a composite infinite plate solution made up of several superimposed solutions will be needed, and simultaneous adjustment of several multiplicative constants to best fit the composite solution to measured data will be necessary. An example of this is shown below.

This technique has been successfully applied on three different specimen geometries. Each specimen was made of aluminum 6061-T6 for which the B constant in Eq. (1) had previously been calibrated. The experimental procedure in each case was to make a velocity scan in a region of the specimen with no load applied and repeat the scan underload in order to evaluate relative velocity change with stress from which $(\sigma_{xx} + \sigma_{yy})$ could be evaluated using Eq. (1).

The first specimen to be considered was the edge cracked panel shown in Fig. 3 to which uniaxial tension was applied. The ultrasonic scanning was performed in the 15 mm square region shown in the vicinity of the crack, with the specimen unloaded and with a load of 40000N applied. A computer program which makes use of the rescaling method and the elasticity solution for an infinite plate with semi-infinite edge crack under far field tension[14] was run on the experimental data in order to evaluate the J integral. The resulting value of J was 6.35 N/mm , which compares with the theoretical value of J for this specimen and loading (J = 5.83 N/mm) within 9% .

In a second experiment, the J integral was evaluated for the center cracked panel shown in Fig. 4. This is the same specimen used in evaluating the M integral by the "special contour" method discussed above (Fig. 2). With $(\sigma_{xx} + \sigma_{yy})$ evaluated experimentally in the region shown, the rescaling method was used in conjunction with the solution for an infinite center cracked panel under remote tension.[15] The resulting value for J was 1.91 N/mm , which agreed with the theoretical value (J = 1.77 N/mm) within 8% .

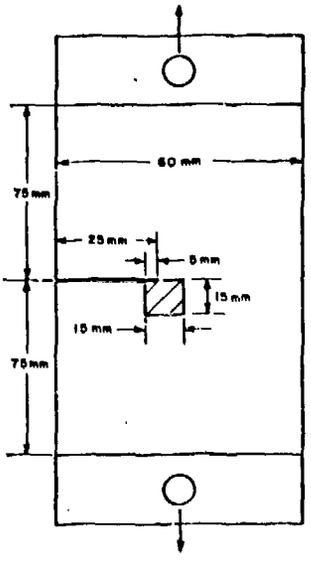

Figure 3. Edge-cracked panel used for acoustic J integral experiment.

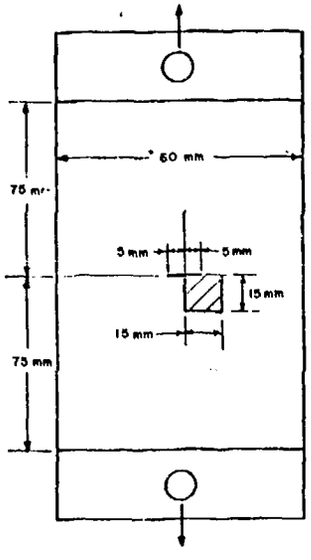

Figure 4. Center-cracked specimen used for acoustic J integral experiment.

Finally, the specimen with slanted central crack shown in Fig. 5 was considered. When this specimen is subject to uniaxial tension, the tractions in a coordinate system normal and tangential to the crack depicted in Fig. 6 result. Thus an infinite plate solution involving far field biaxial tension and shear is needed and obtained by superposition from basic solutions.[14] Simultaneous adjustment of 3 parameters is required to apply rescaling. Both the J integral and the L integral were evaluated in this fashion. The result for J was 3.86 N/mm , which agrees with the theoretical value $(J = (K_I^2 + K_{II}^2)/E =$ 3.63 N/mm) , within 6% . The L integral was experimentally found to be 44.65 N . The theoretical value is found using the relation[8]

$$L = \frac{-2aK_{II}}{E}(K_I + \sigma_{11}\sqrt{\pi a}) \qquad (13)$$

to be 36.3 . The discrepancy between these two values is 22 % . The reason for the larger error in evaluating L has not yet been ascertained.

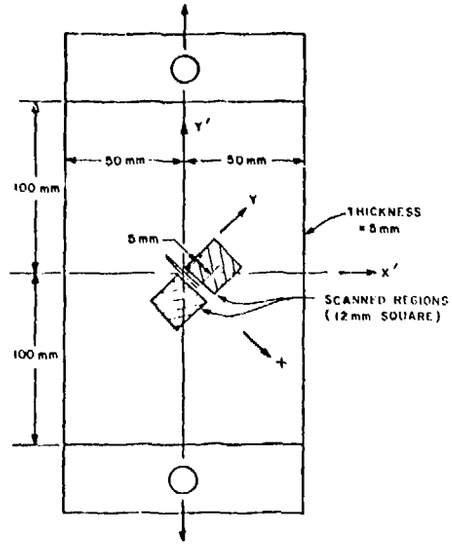

Figure 5. Specimen with slanted central crack used for evaluating J and L .

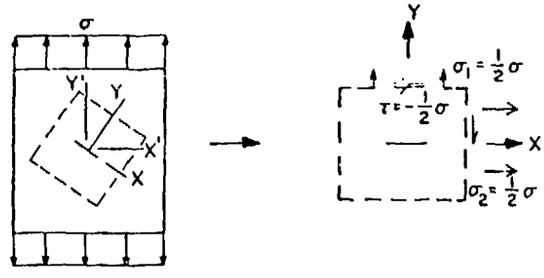

Figure 6. Remote loading of crack in specimen with slanted crack.

CONCLUSIONS

Various approaches have been presented for nondestructive evaluation of conservation integrals in cracked bodies. The most versatile of these appears to be the simultaneous use of shear and longitudinal waves, but this requires the yet-to-be developed capability of shear wave scanning.

The best currently available method appears to be the use of longitudinal waves in conjunction with "rescaling". It was seen that this method worked well on 3 different specimens including one involving complicated mixed mode deformation. With improvement in measurement technology it is hoped this method will be applicable to field as well as laboratory situations.

All the experiments presented were restricted to linear elastic fracture mechanics. A fruitful area for further study should be the application of the techniques presented to situations involving large scale elastic-plastic deformation.

Acknowledgements

This work was supported by the Electric Power Research Institute under Contract No. RP609-1 and by the NSF-MRL program through the Center for Materials Research at Stanford University.

References

1. G.S. Kino, J.B. Hunter, G.C. Johnson, A.R. Selfridge, D.M. Barnett, and C.R. Steele, "Acoustoelastic Imaging of Stress Fields," J. Appl. Phys., vol. 50, no. 4, pp. 2607-2613, April 1979.
2. D.E. Crecraft, "The Measurement of Applied and Residual Stresses in Metals Using Ultrasonic Waves," J. Sound & Vibrations, vol. 5, no. 1, pp. 173-192, 1967.
3. N. Hsu, "Acoustoelastic Birefringence and the Use of Ultrasonic Waves for Experimental Stress Analysis," Exp. Mech. vol. 14, no. 5, pp. 169-176, 1974.
4. G.S. Kino et al., "Acoustic Measurements of Stress Fields and Microstructure," J. NDE, vol. 1, no. 1, 1980.
5. G.S. Kino and G. Herrmann, "Ultrasonic Measurements of Inhomogeneous Stress Fields," Proc. ARPA/AFML Review of Progress in Quantitative NDE, La Jolla, California, July 1978.
6. B. Budiansky and J.R. Rice, "Conservation Laws and Energy Release Rates," J. Appl. Mech., vol. 40, pp. 201-203, 1973.
7. A.G. Herrmann and G. Herrmann, "Energy Release Rates for a Plane Crack Subjected to General Loading and Their Relation to Stress-Intensity Factors," Proc. ARPA/AFML Review of Progress in Quantitative NDE, La Jolla, California, July 1980.
8. J.A. Begley and J.D. Landes, "The J Integral as a Fracture Criterion," Proc. Nat'l Symposium on Fracture Mechanics, vol. ASTM STP-514, 1971.
9. G.H. Lindsey, "Some Observations on Fracture Under Combined Loading," Proc. Nat'l Symposium on Fracture Mechanics, vol. ASTM STP-536, 1972.
10. J.R. Rice, P.C. Paiis, and J.G. Merkle, "Some Further Results of J Integral Analysis and Estimates," Proc. Nat'l Symposium on Fracture Mechanics, vol. ASTM STP-536, 1972.
11. J. Hunter et al., "The Use of Acoustoelastic Measurements to Characterize the Stress States in Cracked Solids," Proc. ARPA/AFML Review of Progress in Quantitative NDE, La Jolla, California, July 1979.
12. R. king and G. Herrmann, "Nondestructive Evaluation of the J and M Integrals," J. Appl. Mech., to be published.
13. P.S. Theocaris and E.E. Gdoutos, "A Photoelastic Determination of K_I Stress Intensity Factors," Eng. Frac. Mech., vol. 7, p. 331, 1975.
14. H. Toda et al., "The Stress Analysis of Cracks Handbook," Del Research Corporation, Hellerton, Pennsylvania, 1973.
15. J. Eftis et al., "Crack Border Stress and Displacement Equations Revisited," Eng. Frac. Mech., vol. 9, p. 189, 1977.

Otto Buck, Chairman (Rockwell Science Center [now Ames Laboratories]): Any questions?

Kamel Salama (University of Houston): In determining the J integral, is this crack 15 millimeters long?

Richard King (Stanford University): The crack is 10 millimeters long.

Kamal Salama: And you have to determine if the stress is 15 millimeters on its side?

Richard King: Yes.

Kamel Salama: How many measurements do you need to take in this square?

Richard King: No systematic study has been made of how few measurements you can get away with. We actually just did it at 1 millimeter point spacing so we took 225 data points; but I'm sure you can get by with much fewer than that.

Neil Paton (Science Center): The theory assumes that you hav an elastically isotropic material, and the material you have is probably not exactly isotropic. Did you measure what the departure from isotropy was and could that explain the discrepancy between the calculated values and measured values?

Richard King: That might be part of it, yes. If you measure that B constant for specimens pulled parallel to the grain and against the grain, you get different values. As a matter of fact, it can differ by as much as 30 percent, I think, and that has not been taken into account. Our specimens are pulled along the rolling direction, and we use that B for the specimens pulled along the rolling direction. And yes, if we do take that anisotropy into account, that might help.

Another thing we're just recently looking into is inhomogeneity in the B constant. We assume it's homogeneous throughout the specimen and we can just get by with one uniaxial tension measurement; and actually we found it does vary a little by maybe 10 percent throughout a nominally nonhomogeneous specimen.

Gary Hawk (Aerospace Corporation): How large a velocity change do you measure?

Richard King: Very small indeed. Relative velocity changes, I think, are down to one part 10 to the fourth.

Chris Fortunko (NBS): (Inaudible)

Richard King: I'm not sure. Well the B constant, and you can work backwards from that. It's of the order of 10 times 10 to the minus six per megapascal.

Roger Chang (Science Center): (Inaudible) Very small cracks, say, 50 microns?

Richard King: I'm not certain. We haven't given any thought to that.

Gordon Kino (Stanford University): We scale it up in frequency, and we look at small samples, yes. It should apply. But the definition in the present system is on the order, at best, of a millimeter and possibly two millimeters.

Otto Buck: I have a short question that goes back to a question after the first one. What would we do experimentally in case of a partial crack? Can you imagine doing thermography; doing it in case of a partial crack?

Gordon Kino: We're trying. Let's put it that way.

Otto Buck: Very good (laughter). Thank you so much.

Richard King: Thank you.

Otto Buck: That's very informative.

PLANNING ACTIVITY REPORT FOR NDE OF ADHESIVE BONDED STRUCTURES

F.N. Kelley
University of Akron

W.G. Knauss
California Institute of Technology

D.H. Kaelble
Rockwell International Science Center

ABSTRACT

Following a workshop held at the Rockwell International Science Center, Thousand Oaks, California in January, 1979, an ad hoc planning activity was undertaken to set forth a program plan to address the needs in NDE for adhesive bonded structures. The objectives of the planning activity were to develop a program rationale and strategy, determine the existence of reasonable approaches, and to propose a detailed plan of action for review at the annual DARPA/AF meeting in September, 1979. The plan encompasses the basic elements of an accept/reject methodology based on fracture mechanics, expected developments of valid flaw growth models, stress analysis, and non-destructive measurement techniques. A central issue is the prospect for determining a valid non-destructive measure of strength for the bonded joint as might be reflected in the tendency for preexistent flaws to propagate under environmental loads.

I. PROGRAM SCOPE AND STRATEGY

This program plan is directed toward methods of establishing the reliability of adhesive bonds as may be employed in primary aircraft structures. Similar approaches may be inferred for fiber-reinforced resin matrix composites in particular instances where matrix-dominated failure modes and delaminations are involved. The central strategy for the plan is based on the concept that the structural design process for bonded joints must be well-established and validated in order that accept/reject decisions might be made from non-destructive measurements information. The plan is presented in the context of a decision methodology, characterized by a systems approach, which is expected to provide a useful framework regardless of the state of development of the various system elements. An essential prerequisite is the knowledge of primary failure initiating defects.

A search of field repair information reveals that a very high percentage of adhesive bond failures experienced on aircraft structures to date have been associated with local damage and intrusion of the environment (usually moisture). While the most experience has been gained on bonded aluminum honeycomb secondary structure, it may be reasonably assumed that damage and environmental intrusion may occur at the edges of bonded panels or more highly loaded primary structural joints. A note of caution which should be added on possible inferences from field experience concerns the more recent developments in pre-bonding surface preparations and their relationship to bond durability. Prior to the PABST[6,7] program, limited information existed on newer surface treatments, such as phosphoric acid anodization, which promises vast improvements in durability. If future bonded joints incorporate these treatments, it is possible that the modes of joint failure may differ from those shown by prior field experience. In any case, flaws are likely to occur from a variety of sources and are likely to grow under operational loads.

Defects, as considered in this plan, are assumed to include a range of geometrical or bounded defects such as cracks and inclusions, as well as boundaryless defects such as uncured or moistured-softened adhesives. The interaction of these "extrinsic" or bounded flaws with the "intrinsic" material state is often a necessary consideration in the use of failure models involving polymeric materials.

One of the more perplexing issues in the evaluation of bonded joint reliability is a determination of the relative importance of the interface between adherend and adhesive and the condition of the adhesive itself. In recent years the designation "interphase" is often employed, since the transition from adherend to adhesive is frequently a material combination of finite thickness, however, ill-defined for analytical purposes. While some program suggestions for the assessment of the structural capability of the interphase in a manufactured joint might be made, it is most likely that measurements and intepretation of failure in this region will continue to be a doubtful undertaking. The structural reliability of the interphase may be enhanced by the careful and complete monitoring of prepared adherend surfaces and adhesives before the joint is formed in the manufacturing process.

An operational definition of strength for adhesive bonds is needed to provide a figure of merit for non-destructive evaluation. At present no single strength characteristic may be uniquely defined. As an operational premise, however, failure will be defined as that condition in which the structure has lost its ability to support the required load. Failures, therefore, may occur due to growth of cracks, and due to geometric instabilities. The growth of a crack (disbond) is presumed to be the principal failure mechanism of concern in adhesive bonded joints, and fracture mechanics should provide material factors most likely to be rated as measures of strength.

As a point of initial departure, the summary statements from the ARPA/AFML workshop held on January 19, 1979, will be used. Six areas of investigation were listed as encompassing the needed, and potentially fruitful, program

activities leading to the goal of reliable adhesive bonded structures. These areas were identified as follows:

1. Flaw growth models (plus nucleation).
2. Stress and fracture analysis.
3. Quality control for bond preparation.
4. Adhesive bulk property measurement correlatable with strength.
5. Cure state monitor.
6. Development and refining of an integrated methodology.

An attempt at providing a methodology as required by item 6 above was made in the form of a logic flow for a structural reliability system as shown in Fig. 1.

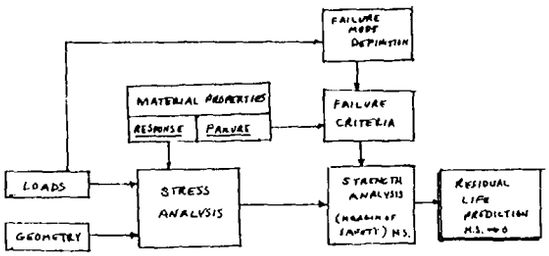

Fig. 1 Elements of a life prediction methodology for structural adhesives.

The diagram shown in Fig. 1 is a simplified schematic system showing the principal elements of the structural design process. Central to the entire methodology is a stress analysis which accepts input in terms of part geometry, environmental loads and a quantitative description of the material properties which encompass those material characteristics necessary to define the distribution of stresses throughout the part. We define this set of material properties by the term response. A second set of properties of equal importance in the strength analysis is referred to simply as failure. A proper definition of a failure "property" would fit the requirement for an operational figure-of-merit for material strength.

The failure criteria as specified in the diagram is an analytical statement of exceedance in which the intrinsic failure limit of a material is compared with the stress and strain requirements generated by the stress analysis. A failure model is implied in which critical stresses and/or strains are incorporated along with relevant material properties.

The output of the strength analysis is presumed to be a structural margin of safety (M.S.) and the life prediction is then based upon the timewise projection of the margin in zero. Life prediction assumes that the mode of failure is known and has been incorporated in the failure criteria. Each structural part subjected to the analysis is expected to demonstrate particular failure modes under the operating loads when the capability of the structure is exceeded. Failure may be the result of an overload or of degraded material properties. Exaggerated loads are sometimes used to fail parts intentionally in order to more clearly define potential failure modes. This procedure is called overtesting.

The methodology outlined in Fig. 1 may be used to examine the non-destructive evaluation process for adhesively bonded structures in terms of needed advances in measurement, anlysis and interpretation of extrinsic and intrinsic flaws. As described thus far the process has not accounted for elements related to the inspection process other than a need for quantifiedd material properties, loads and geometries. It was stated earlier that fracture mechanics holds promise as an approach for providing figures of merit for accept/reject decisions. In the context of the elements shown in Fig. 1, the application of fracture mechanics may lead to a failure criterion based on flaw growth to a critical size. Using for present discussion a viscoelastic analog of the Griffith energy balance relationship, i.e.,

$$\sigma_c = k \sqrt{\frac{E(t)\gamma_c(t)}{a}} \qquad (1)$$

where σ_c is the critical stress required for crack growth, $E(t)$ is a time dependent modulus, $\gamma_c(t)$ is a time dependent cohesive fracture energy, a is a crack length, and k is a geometrical factor, we find that several of the necessary elements for non-destructive evaluation are specified. The material property $E(t)$ representing the response and $\gamma_c(t)$ representing the failure characteristics indicated in Fig. 1 are incorporated in the expression, as well as crack length which could be the object of definition by non-destructive inspection methods. Both $E(t)$ and $\gamma_c(t)$ may be considered material properties which manifest the existence of intrinsic flaws as discussed earlier, as possibly related to poor cure or moisture softening. While Eq. (1) may not be a sufficiently general or correct statement of the conditions necessary for flaw growth, it is illustrative of the kind of relationship needed for this study. Accepting for the moment that non-destructive investigation methods are available to characterize the geometric flaw, the intrinsic property $E(t)$ should be measurable as well since it reflects a small deformation response. Dielectric cure monitors are typical of the measurements which provide information on the intrinsic state of a material, non-destructively. Unfortunately, the determination of $\gamma_c(t)$ requires a series of destructive tests. Since, however, both $E(t)$ and $\gamma_c(t)$ are apparently linked by the same physical mechanisms which determine their time-dependent character, there is some hope that indirect assessments of $\gamma_c(t)$ may be made from a knowledge of $E(t)$.

The discussion to this point has been based entirely on a deterministic approach to failure prediction. In any real case the bonded joint will contain distributed flaws, and both material properties and loads must be interpreted by probabilistic considerations. Accept/reject decisions will be based on measurable conditions of crack size, load history and material state, all viewed against a backdrop concerned with the probability of failure. The generation of a data base on the distribution of naturally occurring flaws forms a part of the program methodology.

II. TECHNICAL DISCUSSION

This brief discussion treats the central aspects of reliability in adhesive bonded structures which are displayed in Fig. 1. In each of these

areas considerable advances in design concepts and property utilization are evident. One issue in any newly proposed program in reliability and life assessment of adhesive bonded structures is how to implement already available analytical tools. This section describes an approach to achieving this important objective.

A. Background

Load transfer between the adherend and adhesive elements of a bonded structure is accomplished by minute differential displacements between these elements.[1,2] Bonded joints cannot be designed on the basis of a uniformly stressed adhesive over the entire bonded area. In regions of high stress, typically at the bond edges and in the immediate vicinity of a damaged area the adhesive may be loaded beyond its elastic yield stress and display high damping and fracture energy due to viscous flow processes. In regions of low stress normally removed some distance from edges and damage zones the adhesive layer is below its yield stress and displays a high elastic modulus and creep resistance with low damping. Figure 2a shows a profile view of a long overlap shear joint with plastic stress of higher magnitude at the bond edges and elastic stresses of lower magnitude in the center region of the bond. Figure 2b shows a short overlap shear joint in which the stresses are essentially uniform due to high adherend stiffness and uniform plastic shear stresses are displayed by the adhesive interlayer over the entire joint. The oversimplified stress profiles of Fig. 2 ignore the cleavage (tension-compression) stress distributions which are highly localized at the bond edges and the stress distributions through the thickness of the adhesive layer which are known to strongly affect fatigue life of an adhesively bonded structure.[3,4]

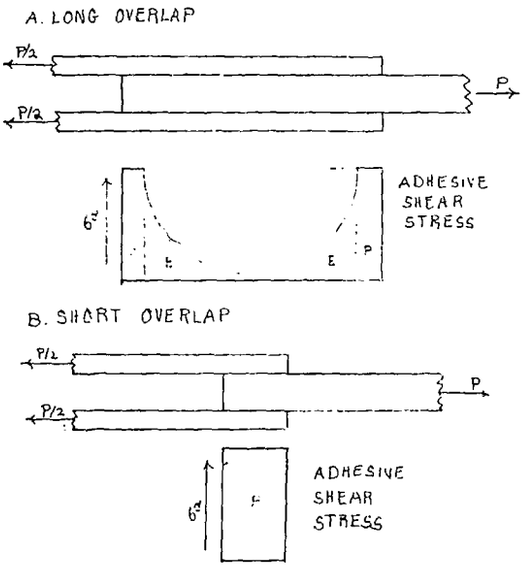

Fig. 2 Influence of lap length on bond stress distribution.

Recent studies of the structural properties of adhesives by Renton[4] provide new recommendations for adhesive test specimens and procedures for defining the engineering structural property of adhesive interlayers using low cost test methods. A thick adherend single-lap shear test, a rectangular butt joint tensile test, and a rectangular scarf joint test were selected and analyzed by Renton.[4] The stress-strain properties of FM73 and FM400 (NARMCO Div., Celenese Corp.) structure adhesives were evaluated using these three test geometries. Based on limited data a promising correlation between adhesive free film properties and thick adherend shear test data was shown.

Studies by Clark and coworkers[5] show that the most prevalent critical bond line defects are crack like voids, circular voids, and porosity, and that these voids can be detected by state-of-the-art NDE (non-destructive evaluation). Defects not detected by state-of-the-art NDE such as weak bonds due to surface contamination, and improper adhesive cure state were excluded from study. These studies show that flaw growth initiates in the regions of high stress concentration near bond edges and flaws and that this growth can be detected by available NDE methodology. Hot-humid environments and low cyclic fatigue rate which lower the adhesive elastic yield stress promote higher flaw growth rates. This study also showed that regions of very thin bond line act to produce adhesive stress concentrations and sites of selective crack initiation and growth.

The Primary Adhesive Bonded Structures Technology Program (PABST) was initiated by the Air Force[6,7] to demonstrate adhesive bonding in highly loaded, primary aircraft structures. In the PABST program the actual stress-strain response of the adhesive was represented by an elastic-plastic idealization of the actual shear stress-strain curve[3,5] as shown in Fig. 3. The idealized stress-strain response (dashed curve, Fig. 3) describes the actual failure stress and strain of the adhesive and the same strain energy to failure which fixes the effective initial elastic modulus, as shown in Fig. 4 different adhesives can show substantially different strength, extensibility and strain energy at room temperature due to differing curve structure and chemistry. At different temperatures, as shown in Fig. 5, a ductile adhesive will display significant changes in stress-strain response as will also occur with changes in moisture content and strain rate. The data summary of Table 1 shows that two to three fold changes in ductile adhesive strength and deformation properties are encountered over the service temperature range encountered in the PABST design and test program.

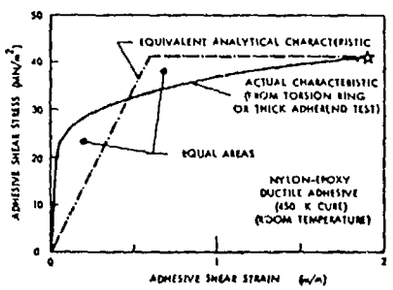

Fig. 3 Elastic-plastic idealization of adhesive shear stress-strain response.

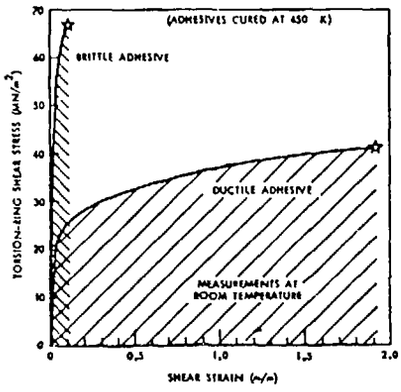

Fig. 4 Comparison between typical shear stress-strain respones of brittle and ductile structural adhesives.

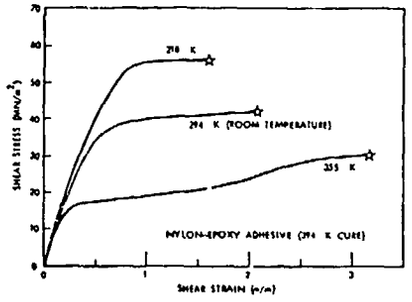

Fig. 5 Typical effects of temperature on ductile adhesive stress-strain response.

Table 1
Typical Adhesive Properties Used in PABST Bonded Joint Analysis[5]

Temperature (°F)	-50	70	140
Effective Shear Modulus (psi)	80,000	70,000	40,000
Shear Strength (psi)	6,000	5,000	2,500
Yield Strain (in/in) = (m/m)	0.075	0.071	0.063
Fracture Strain (in/in) = (m/m)	0.50	1.00	1.50

As mentioned earlier, the failure of ductile adhesives is localized at the regions of high stress at bond edges and near defect regions. Fracture mechanics recognizes and treats three macroscopic modes of crack tip loading as shown in the upper view of Fig. 6. These pure modes of crack tip loading usually appear in combined form in the usual fracture tests used to evaluate adhesive bond strength as shown in the lower view of Fig. 6.

Assuming an idealized fracture mode of loading, the microscopic process by which adhesives undergo failure may be highly heterogeneous as illustrated by the schematic diagram of crazing as shown in the views of Fig. 7. Structural adhe

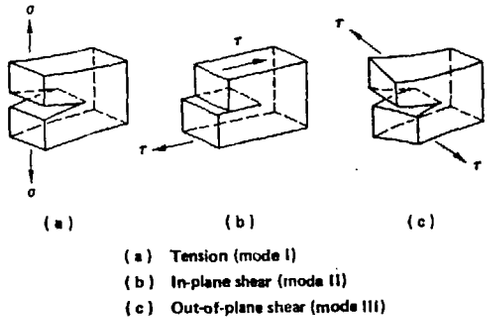

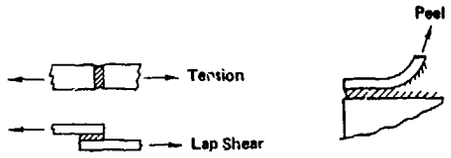

Fig. 6 Schematic diagram of tension, lap shear, and peel tests (lower view) and principal fracture mechanics modes for crack propagation analyses (upper view).

sives are microscopically heterogeneous with even unmodified epoxy networks showing evidence of two phase structure as evidenced by a modular fracture surface. Fracture mechanics analysis is only recently becoming interested in the role of adhesive morphology on fracture energy, fatigue life and structural reliability. The intrinsic scatter in fatigue lifetimes may be dominantly influenced by the samll scale micromorphology of the adhesive phase which is known to dramatically influence fracture energy of adhesive joints.

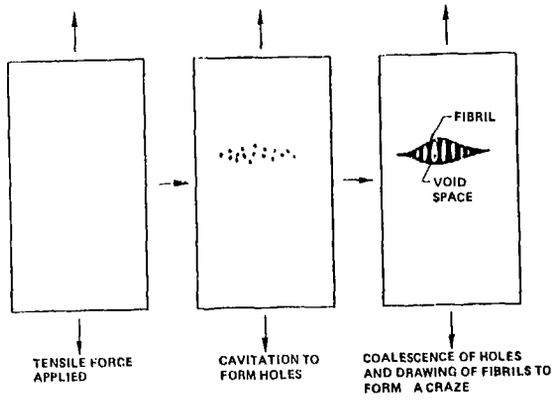

Fig. 7 Schematic diagram of crazing induced by applying tensile force to a polymer. Crazes form at right angles to the direction of stress.

The statistical distribution of adhesive joint strengths (failure load per bonded area) has been shown in a number of studies[8,9] to follow the

standard Weibull distribution function. The Weibull function reflects an extreme value statistic which attributes failure to a single critical defect. When adhesive bonded structures are designed for high structural reliability the average bond strength (Survival Probability = S = 0.50) is much less significant than the achieved strength which correlates with high survival probability $0.99 > S < 1.00$. The important issues of adhesive and joint design for high reliability has recently been reviewed by Kaelble[10,11] as part of a Defense Advanced Projects Agency/Air Force sponsored program. Data presented in this review shows that epoxy structural adhesives display Weibull distributions for cohesive strength in free film form that correlate closely with Weibull distributions of lap shear strengths for epoxy structural adhesives in metal-to-metal joints. The intrinsic structural defects which initiate the cavitation and crazing process shown in Fig. 7 become the subject of materials and process optimization in a generic materials fracture properties study task.

Joint strength and the distribution of joint strengths needs to be directly related to microdefect properties (size, structure, molecular force character, etc.) and the intrinsic distribution of these properties. In other words, the lack of a fundamental materials and process related understanding and control of intrinsic craze zone initiators (see Fig. 7) will continue to lower confidence in high reliability performance of adhesive bonded structures.

B. Approach

1. Materials Characterization

A minimum listing of important subject areas for quantitative materials and process characterization includes:

1. Prepared surface quality assurance.
2. Interphase property measurement.
3. Adhesive chemical and rheological characterization.
4. Bulk properties of adhesive in the joint.
5. Corrosion processes.

Materials selection and process optimization which occurs in preliminary structural design makes extensive use of the above characterizations. This type of quantitative information is only recently being utilized in the nondestructive evaluation (NDE) and life assessment of bonded structures.[10,11] Key detailed materials and process characterization road maps are already developed and available for material and process characterization. Figure 8 presents a detailed flow chart and methodology for quantitative chemical characterization of adhesives, coatings, and composite matrix materials based upon epoxy resin chemistry. In Fig. 9 a detailed flow chart for physical and mechanical response is presented. The flow chart of Fig. 9 includes studies of hydrothermal aging, failure surface analysis (lower section Fig. 9) which is combined with data from manufacturing simulation (upper section Fig. 9). These data are combined in a data analysis (lower box Fig. 9) which draws upon available structure property relations to replace empirical correlations with failure data defined by discrete physical or chemical processes.

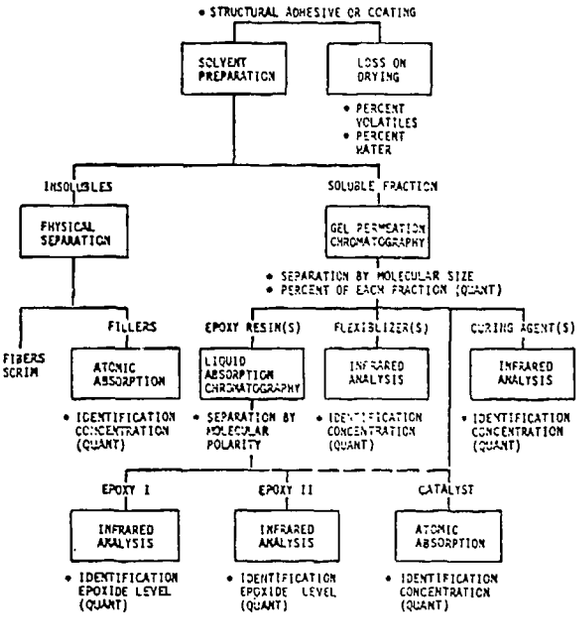

Fig. 8 Chemical analysis.

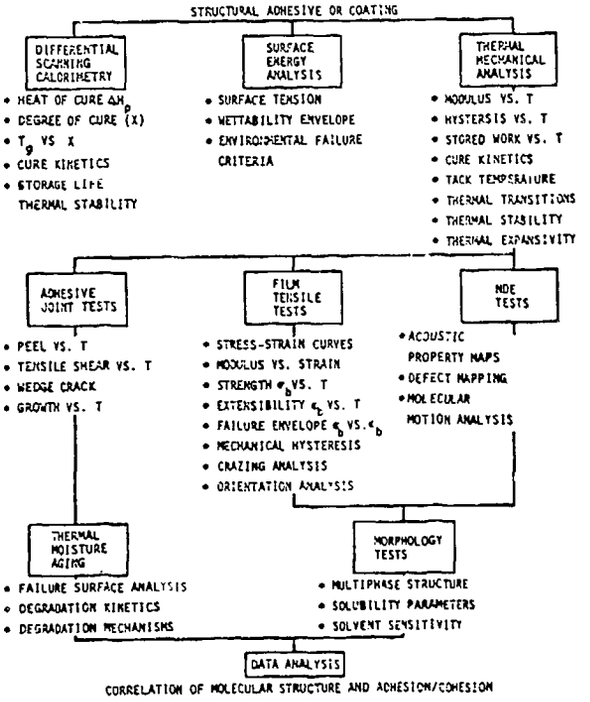

Fig. 9 Physical and mechanical analysis.

2. Loads Definition

During laboratory investigations of a research or development nature it is customary, if not mandatory, to deal with relatively simple loading situations. Before embarking on a research effort such as is before us, it is important, however, to

classify the types of loads and their possible effects on bond (strength) performance.

We distinguish two ingredients in the description of loads or forces acting on bond geometries: a spatial distribution of forces or tractions and their time history. The simplest case arises in situations leading to what one refers to as proportional loading: this type of loading results when the distribution of forces remains invariant in time but the magnitude of the forces or tractions vary. For example, the time-varying pressurization of a fuselage would fall into this category. A special case results when constant loads are applied to a bonded structure. Most laboratory tests fall in this category.

Problems associated with Non-proportional loading are more difficult to deal with, both analytically and experimentally: applied force distributions vary with time and must be reckoned within realistic use environments. An example of this type of loading is given by a (bonded) shaft that is first loaded in axial tension and then subjected to twist.

With regard to loading histories (under proportional or non-proportional loading) one distinguishes monotonic loading (continuously increasing or decreasing loads with time-constant loads as limit cases) and non-monotonic loads. The latter are either of a cyclic or of a purely random nature. Cyclic loads are relatively easily applied in most laboratory environments when they are of the purely sinusoidal type but require less readily available equipment if arbitrarily varying proportional loading histories are required. The latter comprises the cases of random loading which are particularly difficult to deal with whenever one is confronted with history-dependent material behavior such as results with the use of polymeric bonding agents.

If and when our predictive capability of bonded joint behavior progresses to the point where we can predetermine failure behavior for arbitrary load distributions and histories, such distinctions are not necessary. However, in parallel to the failure response of metal structures and monolithic polymer structures, we anticipate that we shall lack this complete capability for more time to come; as a result we shall have to be continuously aware of the possibility of different deformation and failure responses as a result of different load histories.

So far, we have dealt here with applied mechanical forces. It is equally important to consider forces induced in bonded joints during exposure to varying environment. Normal dilation, either as a result of polymer-cure or of normal changes during use; cure-shrinkage; and swelling due to weather or other solvent infusion are factors that give rise to mechanical forces acting on the bond line. To date little more than lip-service has been given to the recognition of these facts, but we think that the time is here when the latter, seemingly less important factors in bond loading, are assessed, particular attention being given to their effect on the long-range performance of bonds.

3. Stress Analysis

As for the performance analysis of any load-bearing structure, a stress and deformation analysis is a necessary ingredient to a life and failure estimate. Today all fracture and deformation failures are based on concepts evaluated within frameworks of solid mechanics analyses of varying degrees of refinement. The degrees of analysis sophistication is often a somewhat debatable issue. Most often it is clear that a simple P-over-A analysis does not form a sufficient criterion and an extremely refined fracture analysis with microstructural material refinements at the crack tip would represent "over-kill." While it has become obvious that a simple P-over-A analysis is insufficient for design purposes, the question as to what constitutes sufficient analysis procedures is yet being debated. No doubt that question will be answered progressively and through trial-and-error procedures in an engineering way.

We distinguish historically two types of analyses: those that deal with stress components averaged over the thickness of the bond, termed for present purposes "thickness-averaged stress analyses," and those in which attention is paid to the detailed distribution that is resolved throughout the bond thickness. It is our opinion that only the latter type of analysis has promise of aiding in the formulation of a framework of predictive failure analysis. That this is so is readily apparent when one inspects newly bonded test samples which have been loaded without inducing gross failure. Fractures are observed readily in regions of stress concentrations which are clearly not identified by a thickness-averaged analysis.

There are several high stress regions that figure prominently in a bonded joint: edges and corners at adherend-to-adhesive interfaces develop high stresses due to material discontinuities. Within the assumptions underlying linearly (visco)-elastic analyses, the stresses may become unbounded at certain points. While the unboundedness is a consequence of the linearity assumption and does not exist in reality, to ignore the location of these excessively high stress regions as the thickness-averaged analysis would do would be folly.

When failure proceeds by the propagation of crack, the stresses at the tip of that crack are again very high and, again within the framework of linearly (visco)-elastic stress analysis, their character depends on whether the crack tip is located at the interface or is embedded in the adhesive. Interface (or interphase) cracks exhibit an oscillatory crack tip stress field that is not supported by physical reasoning and is due to the linearization of the problem. At any rate, the domain in which this anomalous stress-field behavior acts is so small that, from a practical point of view, it is most probably unimportant.

Most practical bonded joints employ adhesive on a carrier or scrim cloth. The adhesive interlayer is thus really a composite and inhomogeneous mateial, and it is not clear at this time under which circumstances this fact can be neglected or must be accounted for.

In connection with cracked bond lines a way of structural failure analysis has developed which we term, for lack of a better term, "thickness-averaged fracture mechanics." We mention this here because of the implication for the requisite stress analysis. In this approach to the bond

failure problem, the adhesive layer and its response is ignored. The attendant stress analysis is thus confined to adherends and the adhesive layer merely serves as a guide for the propagation of the crack.

In opposition to this simplification we must recognize that the stress fields in bonded joints have three-dimensional character. No more is this obvious than when one observes the distinct failure patterns in laboratory specimens which arise from these three-dimensional stress fields. Such facts not withstanding, one is most likely forced to extract maximal information out of two-dimensional analyses, be they of a closed form or other analytical nature or derived from finite element loads.

In most engineering fields drawing on structural or continuum stress analyses, there exists a body of information on characteristics of stress distributions. Stress analysis of bonded joints has been a stepchild of bond strength investigators, primarily because their background did not point up the need for an improved understanding of that aspect in joint failure prediction. As a result we are, at present, short of a body of stress analysis results. It is not that we lack the capability; it is merely that that capability has not been exercised enough. No doubt that deficiency will be removed as time goes on.

It may be illustrative to relate experience in this regard that comes from our early experience with engineering of solid propellant rocket motors. Analysis tools were being developed or were available as they are now. However, we learned that for certain configurations involving high volume constraint, standard notions of stress distributions were rather inadequate (for nearly incompressible solids). Bonded joints place similarly high deformation constraints on the adhesive; the consequences of this are not explored nor understood. Recent results in failure studies simulating long-time endurance failure indicate that such effects are important. In another instance the common notion of what constitutes "rigid" adherends relative to the adhesive has been questioned.

These isolated examples of deviations in stress distribution from an apparently accepted norm make us believe that attention needs to be focused on this area.

A discussion of stress analyses and their application to bonded joint failure prediction would not be complete without calling attention to the need for stress analysis validation. Specifically, one is here concerned with examining in which respect, and by how much, any assumptions underlying currently available analysis codes (linearly elastic, elastic-plastic) violate or corroborate the physical situation. In particular, our visco-elastic stress analysis capability is very limited and assumptions in this regard are even more in need of checking than those already mentioned.

Since stresses cannot be measured directly, any validation procedure must involve the comparison of a displacement field resulting from theory and experiment. Strain gages are, in general, of little usefulness because they are large compared to the thickness of the bond; they may be useful in verifying the surface strain distribution in thin adherends. Other than that, one is bound to rely on displacement measurements. These may be checked at particular points with various displacement gages, or possibly in limited regions, by optical interferometry or speckle interferometry. Verification of deformation in highly stressed domains promises to be very difficult in realistically dimensioned joints because the regions in which they occur are so small.

4. Failure Modelling

We consider two basic types of structural failure: (a) loss of ability of a structure to carry an assigned load and (b) excessive deformation. The latter failure mode is analyzed and predicted completely by a component stress analysis (probably not a linear analysis) and we therefore point out once more the need for advances in our capability to successfully deal with deformation analyses of structural bonds. We shall not concern ourselves with this aspect of failure in this section.

The loss of load carrying ability of a bond is (apart from problems derived from extreme flow of the adhesive) clearly tied to fracture. Therefore an analysis of failure in bonded joints is almost synonymous with the steady fracture progression in a special class of structures.

The problem of bond strength has been investigated for a long time. Most of that effort in the past has been spent on developinng "better adhesives"[12-14] or studying the interface problem.[14-17] Less attention has been directed towards the mechanics of the failure process in the bond-joint geometry.[18-20] Because of its promise as an effective and efficient construction method and because of a basic lack of understanding of joint strength in spite of the extensive chemistry related research, the mechanics aspects of the problem are now being exercised more intensively. In that connection several basic problems have been posed, none of which are resolved in a satisfactory manner though ongoing work is making strides towards practical solutions. Today, the failure of bonded joints is approached largely through the problem of peel testing on the one hand[21] and through what we have referred to as thickness-averaged fracture mechanics on the other. Peel is often associated with soft adhesives and thickness-averaged fracture mechanics with rigid adhesives, although that distinction is not systematically adhered to, since peel tests are also used to evaluate rigid adhesives.

The two approaches differ primarily with respect to the choice of the test geometry. Peel approaches the adhesion problem by specifying relatively thin adherends which undergo large (elastic or elasto-plastic) deformations (see Fig. 10). Test results or analyses are concerned with net forces acting on the adhesive system and the resulting deformations with no or a minimum of attention paid to the detailed process in the adhesive. Thickness-averaged fracture mechanics deals primarily with (two-dimensional) plate or beamlike geometries, two pieces of plate being joined along a line by an adhesive layer (see Fig. 11). Since the adhesive layer is usually thin compared to the thickness of the plates the

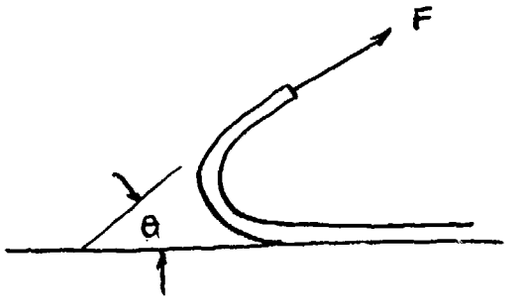

Fig. 10 Peel test geometry

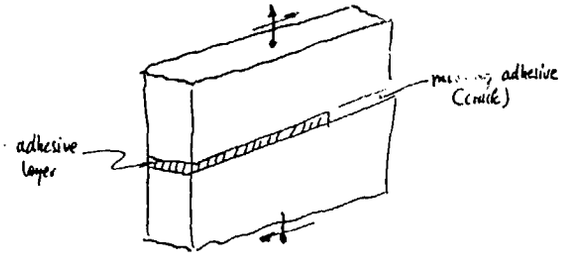

Fig. 11 Standard test geometry used for thickness-averaged fracture mechanics.

thickness of the adhesive layer is deemed negligible, thus reducing the plate problem to the fracture of a homogeneous plate containing a weak internal material plane. The problem is then further analyzed by fracture mechanics concepts developed for homogeneous solids and defining average properties for the adhesive layers. While this appears on first sight a very reasonable approach to a complicated problem, we shall see later that there are pitfalls inherent in this approach. Suffice it to say here that thickness-averaged fracture mechanics makes certain fracture parameters a function of bond thickness whereas in ordinary fracture mechanics such quantities are interpreted as material constants. This limitation poses special difficulties in a technology where bond thickness variations are a fact of life, and where the variations may have to be carefully measured post factor (by ultra sonics?). If time-dependent adhesive properties must be considered, such parameters become rate- or time-dependent quantities which, in the context of thickness-averaged fracture mechanics, would be functions of the bond line thickness also. Both the approaches of peel and of thickness-averaged fracture mechanics to bond fracture have in common that they neglect, by and large, the details of the processes in the adhesive itself. Beyond this similarity there has apparently not been established any quantitative relation between peel and thickness-averaged fracture mechanics. In fact, we are not aware of that question being raised. Instead we experience laboratory tests employing either approach and application of the resulting data to design problems that involve geometries somewhat intermediate to those characteristics of peel and thickness-averaged fracture mechanics. Since the peel mode involves large deformations, in particular much larger than those involved in thickness-averaged fracture mechanics, it is clear that such indiscriminate use of bond strength test results is potentially dangerous. In other words, since bonding is applied to structural adherends of widely varying thicknesses neither the conditions commensurate with peel nor thickness-averaged fracture mechnanics prevail. It appears mandatory therefore to examine the conditions that lead to joint fracture in more detail than either the peel mode or thickness-averaged fracture mechanics can portray.

In order not to mislead the reader, we should mention here that mathematical analyses are being made for layered elastic systems wherein one or more layers contain cracks. Such problems are intended to model the formation and propagation of cracks in adhesive layers and thus the part of the initial process of the adhesion failure. For analytical reasons the geometries are simple and of the type shown in Fig. 12. While these geometries appear reasonable choices, they are not necessarily based on observations preceding joint fracture. What concerns us is not so much the necessary simplicity in the analytical modelling but the prospect that this assumed simplicity prejudices the interpretation of the fracture process which interpretation should be derived from direct observation preceding any modelling and analysis.

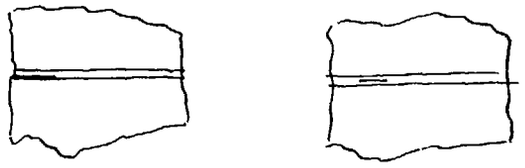

Interface unbond
two-dimensional
or penny-shaped
unbond

Embedded crack
two-dimensional
or penny-shaped
(penny-shaped crack
on bond midplane)

Fig. 12 Two-dimensional bond fracture geometeries.

Connected with this concern is the observation that virtually all information on the fracture process is derived from the post facto appearance of the fractured joint. Reconstruction of the fracture process is thus often made ambiguous because the source of fracture surface features are second-guessed. The need to intensify work on fractographic studies is pointed out later.

There does not exist to date a nearly comprehensive theory of bond fracture. However, once one decides that a quantitative account of the failure process is imperative for a predictive failure theory, one needs to cope with the fact that cracks exist in many shapes and forms and can respond in different ways, depending on the applied loads.

Flaws or cracks may pre-exist in a bond as manufacturing defects or may develop under loading. Cracks located in the interior of a bond area are less detrimental than those located near edges or in stress singularities. Apparently interior flaws have little effect on the strength of a new or intact joint. This is so because by far

most of the load transfer in bond-parallel loading is effected near the bond ends. The severity of flaws in a structural integrity sense depends thus on its location relative to the (current) bond end. If cracks grow from the edge, an interior flaw becomes thus more critical.

In principle the ideas of fracture mechanics are equally applicable to bonded joints as they are to monolithic structures. The differences enter through the materials, in particular polymers, which are not part of a standard engineering repertoire, and through difference in geometries. The latter, especially through the ubiquitous interface boundaries in joint geometries, complicate matters.

Some other features, not normally observed in monolithic fractures, need to be pointed out. In terms of a standard test geometry, a smooth crack front is expected as depicted in Fig. 13. However, it can be shown that in slow model tests a crack may not propagate with a smooth front. Instead the crack front appears (in plain view) as in Fig. 14. It appears thus that present test methods, which are geared to relatively short-term data gathering, could easily (and probably will) misrepresent failure modes encountered under long-time loading. The interaction of the crack tip stress field with the bond interfaces gives rise to changes in the crack path direction, especially when coupled with non-proportional loading. For example, depending on the loading on an adhesive bond, a centrally located crack may grow to the interface. An understanding of whether it stops or grows along the interface requires a fracture criterion that is more general than those developed for cracks propagating along their original axis or in their original plane.

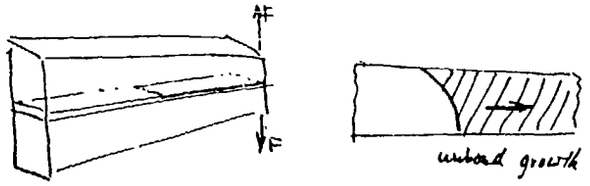

Fig. 13 Crack front in standard tet

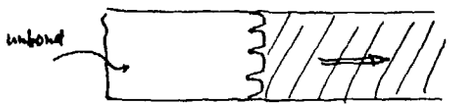

Fig. 14 "Finger" development at front of unbond "Finger" spacing is very regular, shown approximately to scale.

The (two-dimensional) problem of crack extension under loads such that the extension makes some angle with the original crack has been solved for the homogeneous solid. Figure 15 shows the geometry before (a) and after (b) crack extension by a small amount Δc. The criterion for the critical load at which the crack extends as well as the direction is based on an argument of maximal energy release in the crack propagation process. The ratio of difference in the (negative)

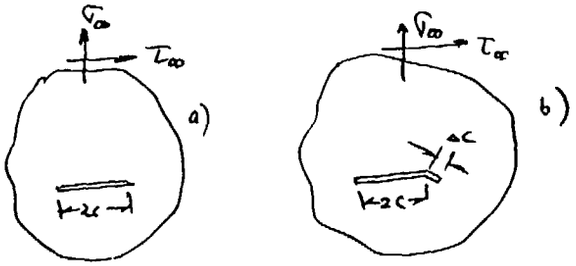

Fig. 15 Non-linear crack growth.

potential energy between the original and crack-extended geometry and the extension Δc is maximized to determine the orientation of the crack extension for a limit $\Delta c \to 0$. The crack is judged to propagate when this maximal energy release rate was just equal to the (constant) intrinsic fracture energy of the material.[22]

The interesting result of such a rather difficult energy analysis is that the much simpler approximate stress criterion gave closely the same result: The stress criterion[23] asserts that fracture occurs along that ray emanating from the crack tip normal to which the tensile stress attains a maximum value with respect to angular orientation of the ray. Crack growth starts when the stress intensity associated with this maximum stress reaches a critical value. As a result of this favorable comparison, an extension of the stress criterion for brittle fracture can be made to crack extension under arbitrary loading. A key development in that extension to fracture development in a three-dimensional context rested heavily on the experimental findings[24] that under a mode III (antiplane shear) loading a crack does not propagate along its original plane but develops crack extensions that spiral from one of the initial crack surfaces around the crack front to the other crack surface in a somewhat helical path (see Fig. 16). The resulting crack-extended geometry is distinctly three-dimensional.

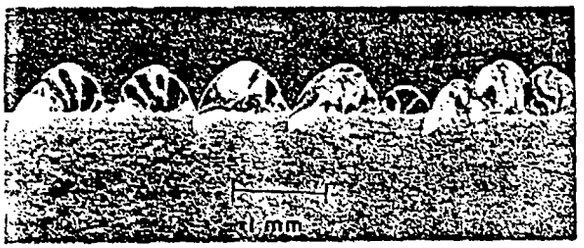

Fig. 16 Cracks generated in antiplane shear.

It follows from the two-dimensional energy analysis results -- which compare well with careful experiments -- and from the just-mentioned findings in mode III failure, that the extension of cracks under general loading should not be analyzed by methods which assume the growth process to occur in the plane of the original crack.

We turn now to a discussion of phenomena in fracture modelling that are concerned with time dependence of the process.

1) Time dependent fracture. The time dependence of the failure process may have several causes. Among these the

a) Viscoelastic properties of the adhesive certainly play a dominant role. While to date "rigid" adhesives are treated (almost?) invariably as time independent, recent tests on typical (supposedly rate-insensitive) adhesives have been shown to exhibit a surprising amount of stress relaxation (on the order to 10 - 20%) within minutes of test start.[25] In the same vein it is known that bonds lose a significant amount of load-carrying ability in a few days' loading; this observation points to significant viscoelastic influence, too. For this reason it is necessary to characterize the viscoelastic behavior of any adhesive.

b) Rate dependence influenced by the geometry. It is a well-documented fact[26] that in peel experiments the path of fracture moves from a intra-adhesive location at high rates of failure propagation (low temperature) to an (apparent?) interface failure at low rates of failure growth (high temperature). Beyond the suggestion that intra-adhesive failure is the result of void formation and coalescence (when uncrosslinked adhesives are used), which void formation does not occur in near-interface failure, this phenomenon is not understood. Gent and Petrich[27] even contend that cavitation may not be responsible for the change in failure mode.

A plausible explanation of this phenomenon in connection with relatively rigid adhesives appears to be related to a combination of non-linear material behavior and the geometry.

The high stresses at the tip of a crack or unbond cause a local mechanical degradation. This irreversible damage occurs in a limited zone, say a typical dimension a. If the crack is embedded in a solid with all geometric dimensions large compared to a we speak of small-scale damage (in metals: small-scale yielding). For small-scale damage fracture characterization can be accomplished in terms of a single parameter, the stress intensity factor, say, without reference to the size of a of the damage zone. This is so because in a characterization test the geometry is taken so that does not enter the considerations. As long as the critical stress intensity factor criterion is applied to geometries in which a is small compared to all other dimensions, this parameter need not be considered.

In this connection we need to mention a phenomenon observed in fatigue failures. When a bond is subjected to "small" cyclic loads (fatigue), fracture occurs along an interface; but when the crack has grown to sufficiently large dimensions so that "catastrophic" failure sets in, then crack propagation occurs through the center of the bond (scrim area). What happens apparently is that during the (low level) fatigue loading, the zone at the crack front is small enough not to play a significant role in the stress distribution. When the load transmitted to the crack-tip in the final stages becomes large as catastrophic fracture approaches, that is no longer the case.

c) Initial propagation and other transient histories of growth. To date, problems in viscoelastic fracture and unbonding have been considered primarily in the context of steady cracking rates. From this viewpoint the rate of crack growth is essentially a function of the instantaneous stress intensity factor. Cracks and unbonds are observed to start propagating with time delay after load application. In some highly crosslinked materials this delay can be interpreted simply as the time required to increase the stress intensity to the point where the flaw growth accelerates to a measurable rate. On the other hand, the deformation and degradation of the material at the crack tip is time dependent so that some of the delay is attributable to deformation without flaw growth. Similar phenomena must occur under (transient) cyclic loading when the flaw grows, on the average, less than the length of the damage zone (long-time fatigue). We thus face a question, the answer to which is important in structural life prediction: Is a substantial portion of the structural life taken up by processes to get the flaw to a growth stage or is the life determined (almost entirely?) by its growth rate? The answer is vitally important in connection with fatigue of polymers. Resolution of that question requires experimental methods that provide high resolution of the deformations at the front of a flaw.

d) Effect of moisture on time-dependent fracture. The observation that cracks can propagate slowly (10^{-7} to 10^{-2} mm/sec) in inorganic (silicate) glasses is often attributed to the influence of moisture. This influence is greatest in the highly stressed region around the tip of the flaw. We would expect that the same is true where polymers are concerned, as long as they are not totally inert to moisture. We know that moisture ingression is a form of plasticization and results in a shortening of the material relaxation times. Due to the highly dilated molecular structure at the crack tip, the diffusion process should be accelerated, and it is just in this critical domain where the creep behavior is accelerated by moisture. One would expect therefore, a dominant effect of moisture on failure rates in some polymers; among these we count the epoxies and polyurethanes, polymers which are used structurally in large quantities.

e) Effect of temperature on fracture and unbonding. For thermorheologically simple elastomers (above the glass transition temperature) it is well established that the rate of failure propagation and temperature are connected by the time-temperature super position scheme. This is true with respect to both cohesive and adhesive failure. While the sensitivity of viscoelastic relaxation to temperature changes decrases notably as a polymer is cooled down through the glass transition temperature, there is every reason to believe that a time-temperature superposition is valid in rigid polymers (below the glass transition temperature). Problems may arise for filled polymers (hard particulate filler, scrim cloth, "toughened" with rubber particles) which are usually not thermorheologically simple.

We consider next in more detail phenomena associated with crack geometries:

2) Load Criterion for Fracture. It follows from the discussion of the influence of temperature on the time history of the fracture process

that temperature changes also induce stresses in a composite structure. Often a temperature increase is used to model the speed-up of the viscoelastic responses (accelerated testing). If this is done it is also necessary to understand the effect of temperature on the mechanical state of stress. For "rigid" polymers this problem leads certainly to dealing with polymer behavior near the glass transition.

The (possibly) thermally induced stresses combine with those due to mechanical loading. We have discussed these already jointly in connection with the stress analysis.

a) Mode interaction.* We shall consider next the response of a crack or cracklike flaw in a bonded joint or composite to mechanical loads. This we do initially without reference to time dependence. We first define some terminology: With reference to Fig. 17, let point A lie on the smooth periphery of a planar crack and establish a Cartesian coordinate system with z tangent to the periphery at point A and x contained in the plane of the crack. With reference to this coordinate system we define the three primary modes of crack deformation, modes I, II and III in standard fracture terminology. These modes describe the relative motion of the upper and lower crack surfaces respectively parallel to the y, x and z directions. We speak of a mode-interaction problem if the loading is such that fracture propagation results in the presence of more than one deformation mode.

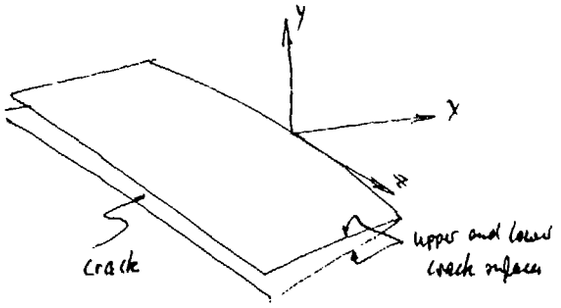

Fig. 17 Local coordinate system at crack front.

In monolithic cracked structures the mode-interaction problem has been considered recently by several authors; a fairly comprehensive review of that problem is documented in Ref. 22. However, in connection with bonded joints the motion of a crack is inhibited by the proximity of the relatively rigid and infrangible adherends. One will therefore have to re-examine the mode-interaction problem for the bond problem. Specific questions arising in this context relate to: the fracture path(s) as a function of the relative magnitude of modes I, II and III; how does this path depend on the relative strength of the interface adhesion and the cohesive strength of the adherend; what is the functional relation between the three modes of deformation at fracture; is such a relation invariant under time-dependent failure processes?

The next question that needs to be considered relates to the fracture path. Fracture in bonded joints is observed to occur along (or near) the interface or in the adhesive. There is no documented criterion that relates the path of fracture to the loads acting on a joint apart from the general criterion that the crack follows a path requiring minimum energy expenditure.

In this connection it is pertinent to discuss the problem of proper test data interpretation for design applications. Suppose an adhesive layer between two relatively rigid adherends is subjected to a general loading up to fracture initiation in a geometry such as is shown in Fig. 18. This type of geometry is a standard way to evaluate the strength of adhesion by thickness-averaged fracture mechanics. Fractures appear (not necessarily visible on the surface) such as indicated in Fig. 18 by solid lines without total failure of the specimen. Upon further loading these cracks may join along the dotted lines in Fig. 18. Generally, cracks open initially so that the newly created fracture surfaces separate. However, as the cracking process continues, a complicated fracture pattern may result.

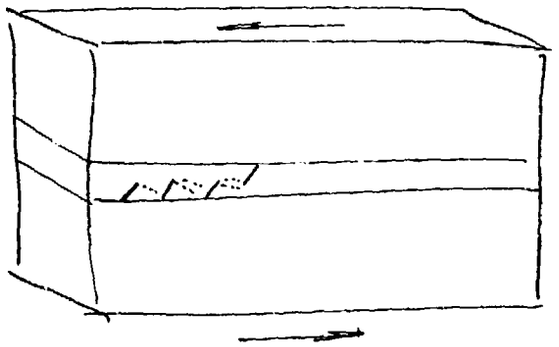

Fig. 18 Fracture path and sequence in shear test.

b) Initiation. Opinions seem to diverge on the importance of initiation in the failure or cracking process. There are those who hold that a "properly designed" bonded joint should never develop a crack and others who claim that cracking cannot be avoided at bond terminations and that bond-life depends on suppression or retardation of continued growth through suitable bonding agents. Apparently observations diverge on this point because we do not understand sufficiently well the interaction of bond geometry, stress field and material properties.

*The definition of the interaction problem is often sloppy. When writers have in mind thickness-averaged fracture mechanics only the deformation of the adherends in the bond-termination region is considered. Therefore, motion of the adherends apart and normal to the bondline is interpreted as a "crack opening" model (mode I). However, if we consider the detailed stress distribution around the front of a disbond between adherend and adhesive, then the deformation under the same loading on the adherends produces both mode I and II motions, the mode II being induced through Poisson coupling from mode I.

Of dominant concern in this regard are the high discontinuity stresses acting almost invariably at the bond termination. Some studies are available that deal with shaping the adherends near to bond termination (tapering) to minimize these stresses. However, the interactions of such geometric variables with bond material characteristics such as nonlinear or "plastic" deformations need to be explored. Standard fracture mechanics principles do not apply for the initiation phase as long as a crack or disbond cannot be identified. Only at the end of this initiation phase can this be done so that time dependent fracture mechanics processes apply. It may be possible, however, to explore the initiation problem through energetics involving appearance of cracks or disbonds of discrete length or size.

5. Fractography. Fracture of homogeneous bodies involves characteristics of the fracture surface features which allow often the reconstruction of the fracture process. These features have been studied completely empirically and constitute an important body of information in fracture analysis.

Similar observations are in progress in the study of bonded joints, most of them presumably as an adjunct in ongoing failure studies. It would be advantageous, however, to structure a program more systematically about fractographic questions, in particular in connection with NDI type investigations. Such a program should comprise NDI of bonded joints subjected to various load histories and (etched) removal of the metal adherends for examination of the fracture feature in the adhesive, probably a painstaking task.

III. PROGRAM PLAN

The program plan is described in the "roadmap" format common to Air Force planning documentation. This format allows the program content to be viewed in context, with interrelationships among the separate work units to be displayed against a time-line. Since there are programs currently underway and in planning by the agencies, it is particularly important to discover those which provide necessary or complementary activity to the main thrust of this plan. These programs will be shown as well with their output contributing at specific time periods in the plan. The most pertinent ongoing effort is indicated on the first block of the roadmap entitled Fatigue Behavior or Adhesive Bonds (Contractor: General Dynamics/Fort Worth). Each block on the roadmap diagram indicates a logical work package with its own objective; however, combinations or further subdivision may be appropriate as the implementation of the plan proceeds. A work package description is included for each block on the roadmap, in which the objective, scope, approach and resource needs are outlined. Finally, a funding summary by fiscal year is provided.

Otto Buck (Rockwell Science Center [now Ames Laboratory]): If I understand you correctly, we now go down the line, having started off with ceramics materials, where we defined different kinds of defects in the ceramics that lead to failure for a given failure strength. The metallic people are now trying to do the same thing, including growth models for the different kinds of defects that have been initiated during fatigue. And so, basically, you are suggesting to follow the same line along adhesives as well as for composite materials. We should identify the defects, get their failure mode, get their growth rates of those modes and come up with a particular fatigue life of the composite or the adhesive bonding.

That's what I see in summarizing your paper and your ideas.

Frank Kelley (University of Akron): I would point out a couple of things which you didn't. I am not sure I have seen in either the ceramics or the metals approach the integration of the nondestructive evaluation process. In the nondestructive inspection process with the design process in which one is really developing accept-reject criteria on the basis of how we designed it. We thought we designed in certain safety. Now I have got a change, a flaw, a change from material; and now I am going to recycle the design process with those new inputs and come out with a change. I have not seen that stated explicitly. It probably is done that way always, but I haven't seen it stated explicitly.

Another way is how do you measure strength? Fracture mechanics has certainly come into the picture in all those cases. In this case, we have material which is, in general, much more dissipated. That character is there.

Paul Gammel (JPL): On the question of being able to assess potential bond strength of a bond rather than just finding a huge defect: if an adhesive bond was a bit on the weak side so it would fail at a high stress or in a long period every time, would you expect there to be any properties, including the spacing of the bond or the accoustic propagation through it, which would show variation at low moderate stresses; stresses you could apply in the field with a simple device of actually stressing the bonds? This is at moderate-to-working loads, would you expect to see anything that would extrapolate, say, that it is going to rip apart?

Frank Kelly: I do not know. I obviously did not make my point very clearly. I do not think you can get an assessment of the strength of the bond from a small deformation property. What I think you can do is tell whether it is getting weaker or stronger. That is, it's something of a relative measurement.

When I talked about the peak in the loss curve, if it really turns out that the peak in the fracture curve is related to the peak in the loss curve - and remember those are both on our master curves so they are on a time and temperature axis so you can take off a particular set of loading conditions which you're interested in and then say this is what my material was when it was made right, and now it is changed. Since I have, like the Mullins data, a linear relationship between fracture and loss, for instance, loss which I measure in a very small deformation perturbation, some sort of a vibration term. If I see the loss has gone down, I can say my fracture energy has gone down, and I then plug that into my flaw growth model and see whether that says the flaw is going to grow at a certain unacceptable rate.

If you accept all of the errors in interpretation which I just gave to a lot of different things; that's the basic idea. I can't tell whether I changed and by how much and whether it made the strength go up or down, but it didn't say I have a way of calculating the intrinsic strength of the bond.

Unidentified Speaker: Just following up your conversation, do you disregard what the nature of the void is, where it is, and in what place?

Frank Kelly: Absolutely not. It becomes a very important part of the overall methodology of the stress analysis which inputs loads, which inputs the local geometry, and which actually resolves the local stress state in which the flaw is imbedded. That then says how the flaw is interacting with the surrounding materials, that is, it's dependent upon its location. But it's dependent in a way that is resolved by the design process, the stress analysis, which you and I can both say is inadequate but at least it requires an analysis.

Roger Chang (Science Center): In very small flaws the microstructure is very important. If there are large flaws, then the fracture mechanics take over, and then you can do this kind of thing. I am wondering at the initiation stage if this method is applicable, say, in really a quantitative way. When you go to a large enough size, it's probably all right.

Frank Kelly: I would think that there is plenty of data on what the manufacturing flaw size might be, and I would say it's large in the context of the discussion which you have just raised; that is, a perfectly formed bond with no flaws is not the case to be treated. We hope to localize the problem based on the experience that the questionable areas are those which are either

highly stressed or those which are in the region of some damage. I would say that there would probably be a valuable contribution to this technology made if one just has a device in which you can go to certain regions of an aircraft and say what is the condition of the bond in the region of this flaw or in the region of this wing root.

John Rodgers (Acoustic Emission Technology Corporation): What primary NDE candidates do you see right now for application to adhesive bonding structures. If you haven't really formulated a firm concept in your mind yet, when in this program do you expect to be making those kinds of decisions?

Frank Kelly: Somewhere in the region of that first diamond on the road map would be a conclusion. Would there be enough data available on the validity of the flaw growth model to say that under the best laboratory conditions in which one does such things as complex Shfar modulus measurements or dielectric measurements or any other measurements that will send energy into the bond and obtain a signal out that one can then transform into something like a loss modulus or a damping factor.

Then the question is: if you can't measure it well enough in the laboratory with the best tools you got, I guess at that stage you say, we just aren't going to ever be able to get to the stage where we can do this in the field. If it looks like there are sensitive-enough parameters, material properties that can be resolved with laboratory devices which essentially put energy in and get a signal out and interpret it in terms of a loss, then the hope might be that you could at least handle a number of the field problems with a device, and it might be an accoustic device of some kind. It could be a dielectric device. That's the stage where you bring in all the brains you can of people who know how to interpret the material and get some information from it. That's when you bring in the adaptive learning networks, too, if you really think you're getting a significant signal.

Boro Djordjevic (Martin Marietta Laboratories): You seem to imply that you have now used extensive analytic approach to defining the problems as well as looking at them in real damages, in real situations. How can you handle the experience which is kind of unique to say that bonded structures, mainly that environment, chemical structures, and usage can influence, really, your different propagation and different instrumentation from just identifiable flaws to a critical defect materials where you can do a fracture analysis and critical stress and the critical size. Is any attention being paid to that?

Frank Kelly: I was with you for a while but I lost the key element of your question.

Boro Djordjevic: In current experience it's very important that chemical and environmental factors behavior either in manfacturing or in service. In a sense you're implying that you will be looking at the real structure such as parts determined as the minor impact or something like that and the theoretical and analytical handling of the critical stress and mechanics are not adequate. You have to consider chemical environment, past history and things like that. When you look into it, how will you handle it?

Frank Kelly: In fact, that's central to the whole plan. Certainly, when one looks at the adhesive layer as a material which is not all that stable. We would like to make it stable, but with the intrusion of moisture with improper cure or with exposure to high heat in the vicinity of an engine or something like that, we expect changes to take place in that material. The changes that are reflected in the material structure on a molecular scale that can be found by certain property measurements.

For instance, the material when it when through cure went from liquid to a rigid solid. One can certainly attempt to make measurements of that transformation, and the degree with which the curing process itself took place. It is just a matter in reverse. If it's been in the field and it has undergone some kind of transformation which has either made it softer or harder, essentially changing its loss properties, that's one of the things I'm talking about. It's changed both the storage modulus and the loss modulus in the complex modulus sense in which I'm talking about material properties. So it's become stiffer and it's changed its loss properties.

If I knew both of those things and they both worked intrinsic to the flaw growth models, then I must input those new values, which I happen to be measuring, with my sensitive little device that looks like the half of a watermelon. Then I'm able to interpret that. I don't mean to leave out, either, those things which also change the stress state such as swelling, the intrusion of moisture which changes the swelling, or change in temperature, or the changes in expansion focus, or the differnce in expansion focus.

All of those factors are important there. But the one thing I am proposing we measure and incorporate into the model is the material properties of the adhesive which are not constant, which might come out of the manufacturing different than they ought to have been, which you ought to be able to assess, or which have changed in the field. I'm not saying that I know it can be measured sensitively enough or which resolution, but I'm saying that's what one would do with the analytic framework.

Boro Djordjevic: You're committing yourself to really trying to pull in many parameters, a difficult task to actually accomplish; then statistically eliminate maybe 5 or 10 which are important to your final decision.

Frank Kelly: I thought we were measuring very few. I was going to measure fracture energy in a laboratory, I was going to correlate it with some important property that probably incorporates stiffness, basic modulus, shear modulus, and loss modulus, something like that. Fracture mechanics attempting to be rather indifferent to stress state, the configuration, testing mode, all that sort of thing, supposed to sweep all those problems under the rug.

Chris Burger (Ames Laboratory): Fracture mechanics is not insenstive to individual stresses. Some of the work that we have done suggests that the residual stresses that arise due to the differential contraction on the cure is higher than the design stress. Do you consider the material visco-elastic enough to relax those out, and do we have any evidence that, in fact, happens?

Frank Kelly: No, we don't and I think that's an excellent point. I think it's probably something that hasn't been treated with the degree of attention it should be treated. I'm sure it came into the discussion, but how one measures residual stress as nondestructive I think is a real valid concern because it then becomes one of the conditions which one inputs to the analysis itself. That is, assuming these residual stresses exist. I don't know.

Dave do you want to add to that anything?

Dave Kaelble (Science Center): No. I think the question and answer are complete. You have to consider these stresses, and they are important, and the added environment stresses, the moisture and swelling, are superimposed on those.

Steve Hart (Naval Research Laboratory): In the new world of better surface preparation, is there experience to show that perhaps the failures are more cohesive than adhesive? Is there any information on that yet?

Frank Kelly: As I said, that's still a debatable point. There is, I believe, at least one workshop that I participated in that concluded that the data said we have been driving the failures into the adhesive layer rather than not. I see Bob Crane raising his hand, so he's probably got some informatikon he wants to add to that.

Otto Buck, Chairman: The Air Force has the word.

Bob Crane (Materials Laboratory, AFWAL/MLLP): We have said, basically, from another report from another program, that the phosphoric acid annodizing surface preparation is certainly much better when done correctly. Unfortunately, what we believed at one time to be a very wide band of tolerance are not quite so wide. So, if you get outside the tolerable band for process variables, it's not quite that good so you're right back into adhesive failures.

Boro Djordjevic: Let me make a comment that Boeing developed one of these processes, but the surface condition which precludes a good bonding has been pretty much identified by extreme magnification using ultramicroscope. The problem comes that if you have a shaded area, even if you do laboratory testing, you're going to maybe have a cohesive failure. But in service a lot of times, those partial (inaudible) go to adhesion failure and actually most of the problem, most of the defect propagation is in an interface, mainly the degradation of oxide. And that is pretty much the case of most of the parts produced now unless there is laboratory simulation.

Frank Kelly: I think there is a lot of data in the (inaudible) program which were unreal parts, and they were sent to be subjected to realistic environments. As was said, if the surface preparation was done correctly, there is a growing body of data saying it's being driven into cohesive failure in the adhesive layer. In fact, it also moves around, as you might expect. A lot of it starts in the scrim and propagates from there, and sometimes will go to one face and then the other.

I guess we are going to be awfully disappointed in our efforts if we conclude that real failures aren't going to take place in adhesives because we just couldn't handle that problem.

Dave Kaelble: I would like to announce that this type of discussion is being continued. The adhesive society has its national meeting in Savannah, Georgia on February 22nd and 25th. We will have a session on NDE methodology as applied to adhesive bonds. This is a call for people who are very interested in having presentations that are occurring here presented again at the adhesion meeting to the open forum to the scientific community in that specialized field and published in the journal. So that's an open invitation. If anybody wants to see me, I can get an announcement. Frank Kelley and I are chairing that session.

Otto Buck, Chairman: I would suggest for time purposes that we are all though the questions - and I think there are a lot more maybe addressed to Professor Kelley or Mr. Dave Kaelble outside, and

there is ample opportunity. Since Dave made a commerical, I have to make a commercial here, too. There is going to be a Session IV this afternoon without a chairman - you're fortunate enough not to have a chairman. That's a poster session on composites, adhesion bonds, new phenomena and problems.

Bruce Thompson (Rockwell Science Center [now Ames Laboratory]): I might say one thing about the problems. One of the philosophies of the meeting is not only to have new solutions but to have some posters describing some problems that various areas of the service have which might be addressed by some of our techniques, so I believe there are three or four posters which are put up in that spirit. We put them up early in the meeting and a little bit out of context so people could go by and look at them and perhaps think about how their technique might pertain to that particular problem.

I know Joe Moyzis has a poster that will relate to the problem workshop that will be held Wednesday evening, so it might be well for people to go by and look at those posters from that point of view.

NDT OF COMPOSITES BY THERMOGRAPHY

P. V. McLaughlin, Jr., E. V. McAssey, Jr., D. N. Koert
Department of Mechanical Engineering
Villanova University
Villanova, PA 19085

and

R. C. Deitrich
Ground Support Equipment Department
Naval Air Engineering Center
Lakehurst, NJ 08733

ABSTRACT

This paper describes ongoing research efforts to evaluate thermographic techniques for locating flaws or damage in structural fiber composite laminates. An infra-red camera with video isotherm readout is used to identify perturbations in uniform or linear thermal fields which may be caused by presence of flaws or damage such as matrix cracks, delaminations, blind side impact damage, and partial through holes. This procedure has potential for rapid qualitative screening of large surface areas. Potential defective areas may then be analyzed by a more accurate (but more time consuming) method .

Two techniques are discussed; externally applied thermal field (EATF) and stress-generated thermal field (SGTF). The EATF technique involves applying heat to a composite structure and observing the resulting transient thermal pattern. The SGTF technique requires stress cycling to create hot spots in regions of high stress concentrations adjacent to flaws or damage sites.

INTRODUCTION

NDE of composite structures in either manufacturing or routine service modes can be an extensive and time-consuming operation by current techniques of ultrasonics, X- or N-rays, etc. Thermographic techniques may have possibilites for rapid screening of large surface areas; suspected small flawed regions may then be quantitatively investigated by a more sophisticated method.

For the past decade or so, many investigators have used various forms of thermography to locate defect or flaws in composite or other structures. The thermographic methods used fall into two categories: Externally applied thermal field (EATF) technique uses a heat source outside the structure (Figs. 1 and 2) to generate transient thermal patterns. Perturbations in the thermal patterns are read by infrared detectors (sensors, cameras, or liquid crystals) and indicate the presence of a flaw or damage (Fig. 2). The stress-generated thermal field (SGTF) technique uses the viscoelastic nature of composite matrix resins to generate heat under cyclic loading. Regions of stress concentration (near flaws or damage) will produce hot spots which can readily be observed by an IR camera (Fig. 3).

The camera used to measure the thermal fields was an AGA Themovision System 680/102 B infrared camera with both black and white and color isotherm video readouts. The black and white screen indicates surface temperature in a continuous shade of gray from black (coldest) to white (hottest). The color isotherm screen is divided into 10 distinct colors representing ten temperatures between black (coldest) to white (hottest). (In the figures of this report they appear as distinct shades of gray.) The sensitivity of the camera can be changed from 1°C (black to white) to 10000C (black to white). Best results were obtained using the 1° through 5°C sensitivities.

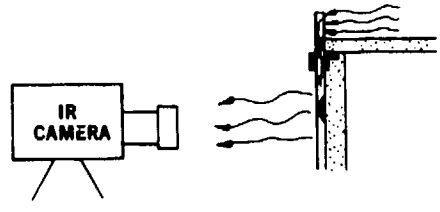

(a) **CONDUCTION**

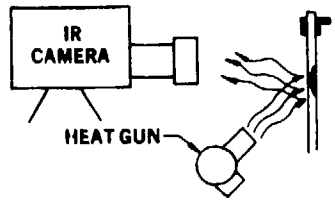

(b) **CONVECTION/RADIATION**

Fig. 1 Schematic diagram of externally applied thermal field (EATF) test setups.

Neither EATF nor SGTF techniques have undergone extensive evaluation for use in detecting flaws or damage in composite structures, although considerable work has been done using thermography to track fatigue crack growth (see refs. 1-3 for example). The purpose of the present program, now ending the first phase of a three phase effort, is as follows:

1. Demonstrate the feasibility of NDE by EATF and SGTF thermographic techniques.
2. Determine the capabilities and limitations of thermography for detecting delaminations, surface cracks, blind-side impact damage in com-

posites - identify ranges of flaw types, sizes, locations, types of materials, etc., for which thermography is effective.
3. Develop methods for EATF heat input and SGTF stress application that best provide for easy flaw identification.
4. Recommend hardware features for large scale usage.

Results obtained to date in the program are presented in this paper by heat application technique and flaw type. Tentative conclusions follow.

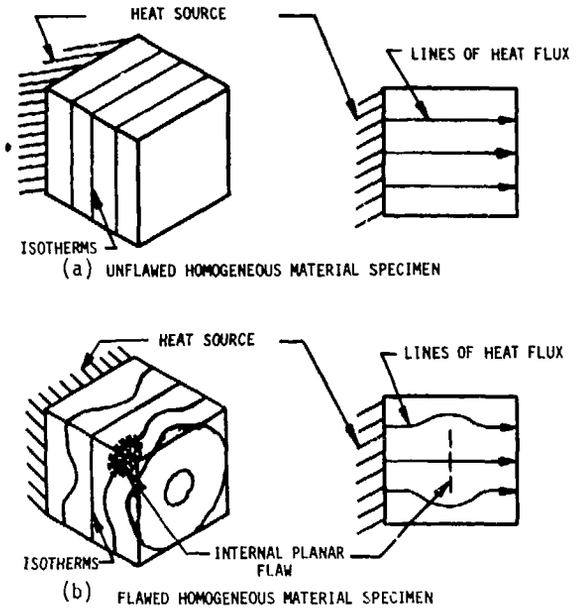

Fig. 2 Temperature fields in flawed and unflawed material with and without internal flaws, EATF.

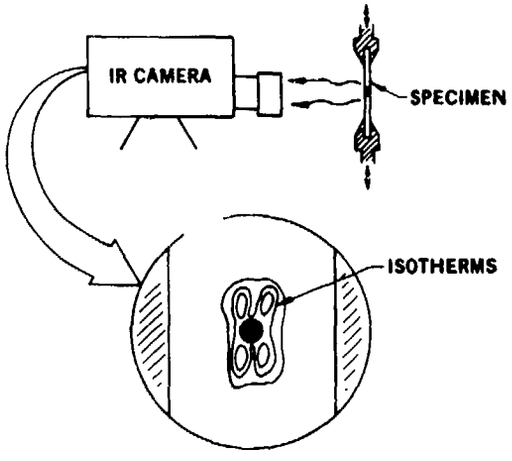

Fig. 3 Stress generated thermal field (SGTF) test setup.

EXTERNALLY APPLIED THERMAL FIELD (EATF)

Two types of EATF heat generation techniques have been studied. The first is application of heat by a strip heater or other source away from the flaw area to be evaluated (Fig. 1a). Heat is conducted in the plane of the material in a direction parallel to the surface, and is called "conduction" method for short. The second is heat application by a convection or radiation source such as a heat gun, space heater, or IR lamp, perpendicular to the surface of the specimen (Fig. 1b). This second method, for convenience, is termed "radiation/convection".

Conduction Method

Four types of flaws were investigated by the conduction method - through holes (to evaluate the effects of material conductivity and anisotropy), partial through holes (simulating blind-side impact damage), delaminations, and surface cracks.

Through holes - Through holes (Fig. 4) obviously do not need any technique other than visual inspection to find. However, 0.64 cm. dia holes were drilled through [0] graphite/epoxy, [0/90] glass/epoxy, and [0] boron/epoxy to evaluate effects of material thermal conductivity and anisotropy. Because conductivity of graphite fibers is high, and epoxy is low, [0] Gr/Ep composites have high fiber direction conductivity and low conductivity transverse to fibers. Isotherm video pictures of the effects of heat conduction parallel to fibers, perpendicular to fibers, and at 45 deg. to fibers respectively, are shown in Fig. 5. Note that large perturbations occur in the parallel and 45 deg. to fiber directions, but small perturbations in the perpendicular to fiber direction. Glass/epoxy is nearly isotropic in thermal conductivity because glass and epoxy conductivities are the same order of magnitude (and it is noted, close to that of transverse graphite/epoxy). The [0/90] glass/epoxy results are similar to [0] graphite/epoxy results in the transverse direction (see bottom left, Fig. 5). Boron conductivity is between that of glass and graphite. Boron/epoxy results are shown bottom middle and right of Fig. 5.

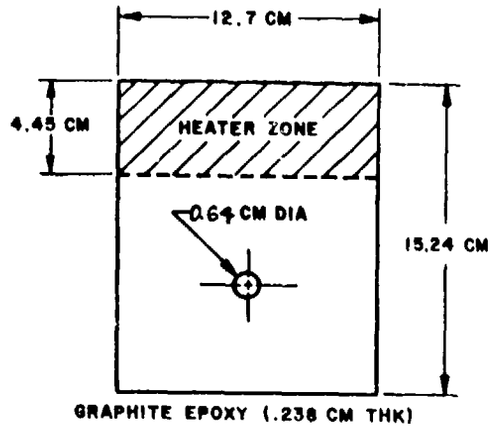

Fig. 4 Graphite/epoxy through-hole specimen.

Partial through holes (simulated impact damage) - Figure 6 shows a graphite/epoxy sample with a flat-bottomed hole drilled about half-way through the back surface, simulating the back-surface shattering of moderate velocity impact damage. Figure 7 shows conduction test results on the [0] Gr/Ep sample. Note that the blind hole causes some identifiable perturbations in the otherwise straight isotherms near the center of the specimen, in spite of the fact that the hole is on the opposite side of the specimen.

Delamination - Two types of delamination were tested by conduction: an induced edge split in [0] Gr/Ep (Fig. 8) and implanted delaminations (mylar-encapsulated glass microspheres) one quarter to one inch square located one to four plies from the surface in [0/±45/90] Gr/Ep (Fig. 9). Note that isotherm perturbations locate the delaminations. Analytical heat transfer calculations (Fig. 10) indicate that a one inch square delamination can be detected in the middle of a 32 ply [0/±45/90] specimen. Glass/epoxy delamination tests are underway, and it is expected that they will more readily be observable in glass/epoxy than graphite/epoxy.

Surface cracks - Heat conducted in a direction perpendicular to surface cracks shows a steep gradient or jump right next to the crack (Fig. 11). On the right, a previously undetected crack from a partial through hole is shown by "kinks" in otherwise smoothly curving isotherms; on the left, the crack at the side of an edge split is highlighted by a 2.5°C jump in temperature.

Radiation/Convection Method

Partial through holes and delaminations in graphite/epoxy were heated by a 350 watt heat gun, and photographs of the resulting infrared camera isotherm pictures were examined.

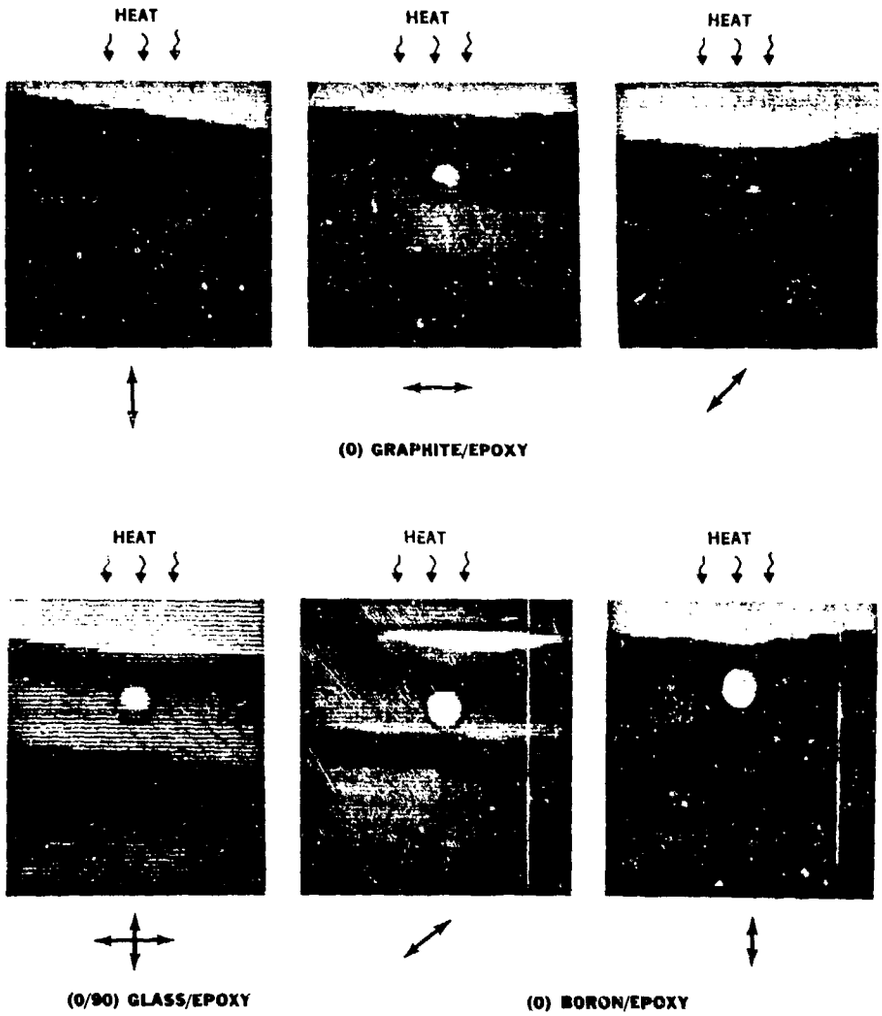

NOTE: Arrows under plates indicate fiber directions. Heat conducted from top of specimens.

Fig. 5 Perturbed isotherm patterns around ¼-inch-diameter (0.63 cm) through-hole in composite plates, EATF.

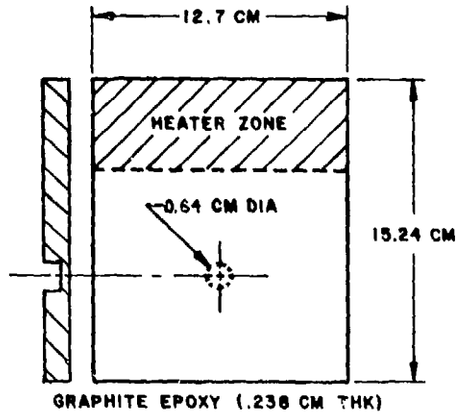

Fig. 6 Specimen with partial through hole in back surface.

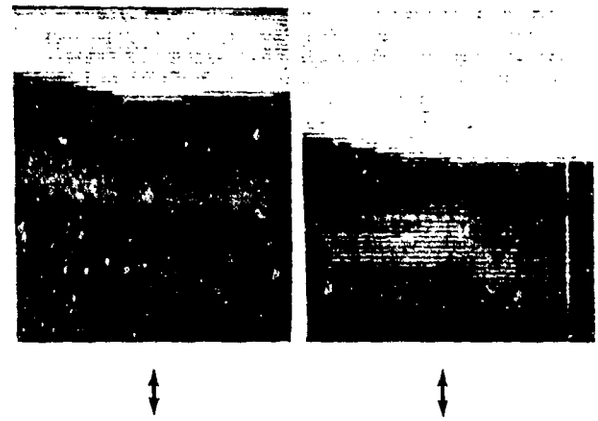

Fig. 7 Graphite/epoxy with partial through hole heat conducted from top edge.

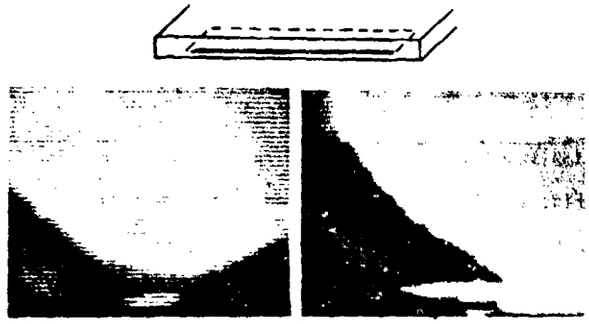

(a) Heated from top (b) Heated from right

Fig. 8 EATF conduction results for edge delamination in [0] Gr/Ep.

Fig. 9 [0/±45/90] Gr/Ep 8 ply sample with ¼" - 1" delams, 1 to 4 plies down from surface.

190.5	190.6	190.7	190.6	190.5
190.6	190.9	191.4	190.9	190.6
190.7	191.4	193.2	191.4	190.7
190.6	190.9	191.4	190.9	190.6
190.5	190.6	190.7	190.6	190.5

1 IN.

Fig 10 Front surface temperature distribution due to delamination 16 plies deep in 32 ply sample of Gr/Ep.

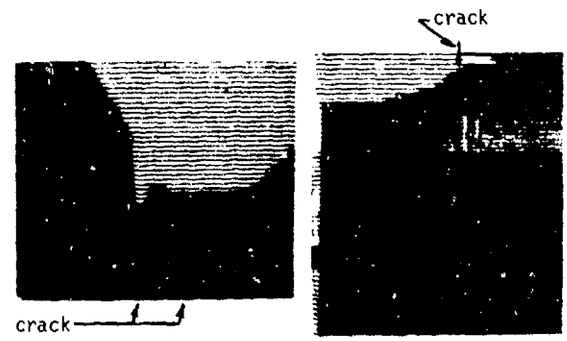

(a) Vertical edge splits (b) Vertical crack

Fig. 11 Surface cracks in Gr/Ep.

Partial through-hole (simulated impact damage) - Figure 12 shows results of heating (left) and cooling (right) the front surface of a [0] Gr/Ep sample with a 0.64 cm dia. back-surface partial through hole. In both cases, a well-defined hot (or cool) spot is produced, giving clear indication of the location and size of the flaw. Note that it is much easier to identify the hot spot from the radiation/convection method than the perturbed isotherms from the conduction method (Fig. 7).

Delaminations - Three different types of delaminations (edge split-Fig. 13, top left, edge delamination-Fig. 13, top right, and implanted mylar-glass microsphere delaminations-Fig. 13, bottom) were tested in Gr/Ep composites. The shapes and locations of the flaws are clearly defined, even in the case of free convection cooling of the surface, Fig. 13, bottom left.

HEATED WITH HEAT GUN COOLED WITH DAMP CLOTH

Fig. 12 Hot and cold spots at partial through-hole on back surface, [0] Gr/Ep.

Effects of Material Conductivity and Applied Heat

In the conduction method, results have shown that high conductivities are required in the direction of intended heat flux. This will insure that a temperature gradient extends along a large enough length of sample to allow detectable perturbed isotherms to form in the flaw vicinity, and will provide a reasonably sized area to be tested. Figure 14 schematically shows that the extent of the thermal gradient will be much larger in aluminum, graphite aluminum, and graphite/epoxy parallel to fiber direction than it will for glass/epoxy (an direction) or graphite/epoxy perpendicular to fiber direction.

The size of applied heat source to achieve significant temperature gradients by conduction in unidirectional graphite/epoxy parallel to fibers is shown in Fig. 15. These analytical calculations agree well with test results, and show that increasing heat input by a factor of ten does not even double the length of composite over which significant temperature gradients are obtained; and in fact indicate an asymptotic limit of about X/L = 0.7. Results of Fig. 14 show that lengths will be considerably less for Gr/Ep perpendicular to fibers and glass/epoxy. Large surface areas will therefore be difficult to examine rapidly by the conduction method. Except for surface crack detection, it appears that radiation/convection is the better method for reasons of both speed and ease of detection.

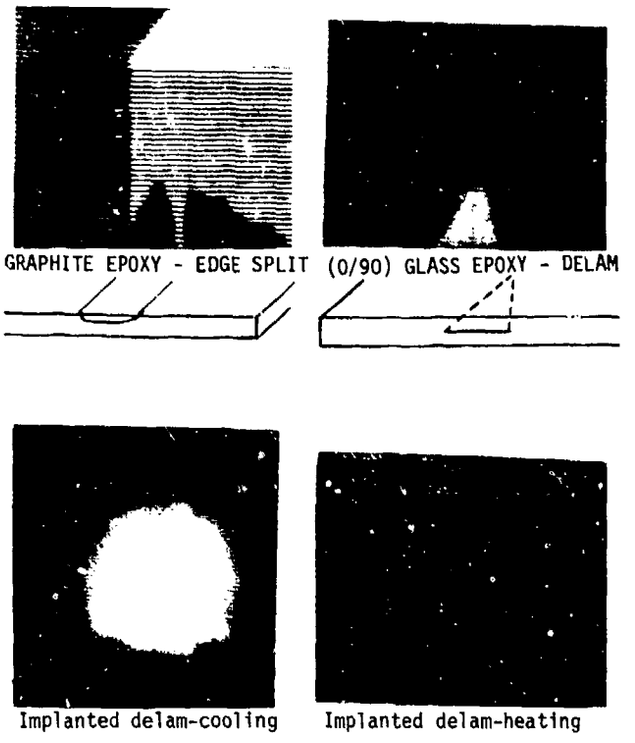

Fig. 13 Radiation/convection EATF detection of delaminations.

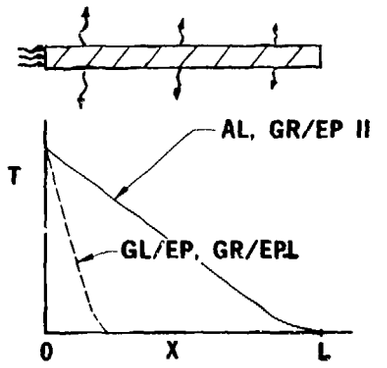

Fig. 14 Temperature (T) vs. Length (X) along wide plate heated at X=0.

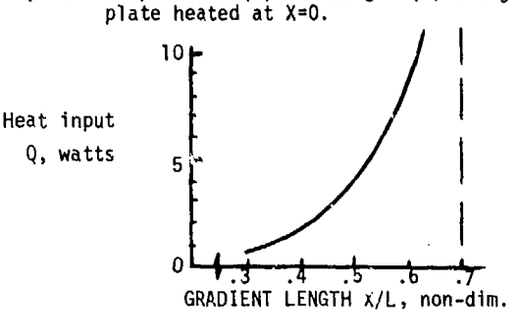

Fig. 15 Heat required to obtain temperature gradient of 0.8°C/cm vs. extent of gradient.

STRESS GENERATED THERMAL FIELD (SGTF)

In using a stress-generated thermal field to locate defects or damage, one must know the load amplitude and the cyclic frequency which will produce desired hot spots and still not damage the structure (a technique for flaw location that reduces either strength or lifetime is hardly nondestructive). Previous research (refs. 1-3) has shown that significant heat can be generated at crack tips or near holes at as low as 0.5 of static ultimate in the 20-50 Hz range of frequency for graphite/epoxy. Henneke et al. (ref. 4) have demonstrated that delaminations can be detected at ultrasonic frequencies with negligible load amplitudes. Figure 16 (upper left) shows that hot spots can be seen near a partial through-hole at as low as 0.1 of static ultimate and one Hz; but that graphite/epoxy (Fig. 16, lower left) exhibits no detectable heat at 0.3 of static ultimate and one Hz. After axial cracks developed in graphite/epoxy samples, however, the rubbing of surfaces generated considerable detectable heat, even at very low load levels (Fig. 16, right).

It is obvious that for flaws other than cracks which produce frictional heat, considerably higher cyclic frequencies than the 50 Hz will be required so that peak loads may be kept below levels which could cause failure. Research is in progress to develop the load-frequency relationship required to provide adequate heat for SGTF thermographic NDE.

SURFACE CHARACTERISTICS

Since thermography relies upon surface infrared radiation detection, reflection from outside energy sources such as sun, lights, or body heat may give undesired signals. Also, soil, abrasions, or different paints may change the emissivity of the surface and cause spurious readings from the IR camera.

Reflectivity

Reflections from body heat and metal objects from unpainted aluminum surfaces are shown in Fig. 17. Reflections from shiny graphite/epoxy samples are similar. To test reflectivity of flat paints, an aluminum sample was painted half flat black, half flat white (Fig. 18a). No reflection of body heat was discernable. When shiny polymeric Naval Aviation paint was tested, however, considerable reflection was obtained from a 60 watt heat source located 1.2 m from the specimen (Fig. 18b). Results show that care must be taken to eliminate sources of

(0/90) GLASS EPOXY
1/4" PARTIAL THROUGH-HOLE

(0) GRAPHITE EPOXY AFTER AXIAL CRACKING FROM 1/4" PARTIAL THROUGH-SLIT

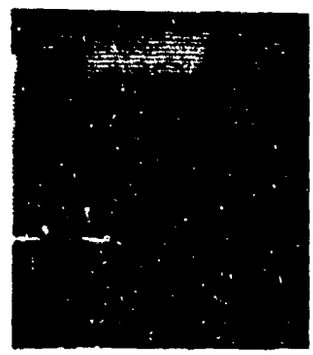

BEFORE AXIAL SPLIT

AFTER AXIAL SPLIT AT 0.3 STATIC ULTIMATE LOAD

(0) GRAPHITE EPOXY WITH 1/4" HOLE

Fig. 16 Stress-generated thermal fields (SGTF)at R = 0.1, 1 Hz.

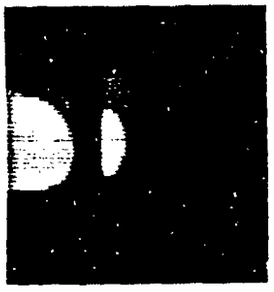

FINGER REFLECTION
WITH ISOTHERMS

FINGER REFLECTION
WITH GRAY SCALE

CAR KEY REFLECTION
WITH ISOTHERMS

CAR KEY REFLECTION
WITH GRAY SCALE

Fig. 17 Heat reflected from unpainted surface of 6061-T6 aluminum specimens.

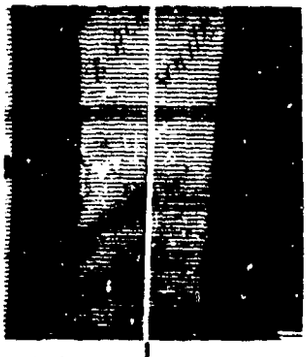

(a) Flat paint (no reflection)

(b) White polymeric Naval Aviation paint (considerable reflection). Similar results with black, orange.

Fig. 18 Attempted IR reflection of heat sources from painted samples.

heat reflection such as lights, sun, etc., in orde to cut down on spurious readings.

Emissivity

Different materials radiate infrared waves at different levels. Emissivity is a measure of a surface's ability to radiate such waves. If a surface has varying emissivity from point-to-point even though it is at constant temperature, it will cause variations in radiation seen by the IR camera that could be taken for flaws by a technician. Figure 19a shows flat black and flat white paints on aluminum where heat is being conducted from the top. Note that there is no difference between the two paint colors, indicating identical emissivity. Naval Aviation paint, on the other hand, exhibits significant differences in emissivity between white and orange (Fig. 19b), and white and black (Fig. 19c). White is on the right in all pictures - samples were heated uniformly. Variations in heat emitted within a given paint sample are discussed below.

Other Surface Phenomena

In Figs. 19b and c, horizontal "streaking" can be seen in the infrared display for supposedly uniform samples of black, orange, and white Naval Aviation paint. Upon investigation, it was found that this nonuniformity is due to variations in paint thickness. The aluminum plates of high conductivity are covered with polymeric paint of low conductivity which acts as an insulator. Paint thickness variations show up as temperature variations on the heated sample's surface. Figure 20 shows this effect on a heated sample with white paint over the entire surface. The only non-uniformities in the sample are the paint thickness variations. At present, it is thought that paint thickness variations will have less effect on materials such as fiber reinforced epoxy composites, because thermal conductivities of paint and structural composites are the same order of magnitude. Samples are being prepared to test this hypothesis.

Abrasions on surfaces can also affect results. Figure 21 shows an infrared black/white photograph of a graphite/epoxy laminated plate whose surface is polished except for four areas which are rough (as if sanded). The picture was taken in complete darkness and the surface was completely uniform in temperature. The rough areas are light and the polished portions of the plate are darker, indicating that abrasions can also give thermographic readings which could be interpreted as flaws or defects.

HARDWARE CONSIDERATIONS

Tests run to date have led to the following conclusions concerning the type of equipment which will be necessary to perform NDE by thermography:

Black, gray, and white isotherm video readout will be as effective in visualizing defects as color isotherms.

Full-scale sensitivity ranges between 1°C and 5°C work best for the flaws and materials tested. Variable positioning of these ranges on the absolute temperature scale is necessary in order to be able to adjust for differing ambient temperatures.

Even for the conduction method of heat application, a radiative heat source has found to be better than strip heaters or thermal blankets for reasons of portability and flexibility.

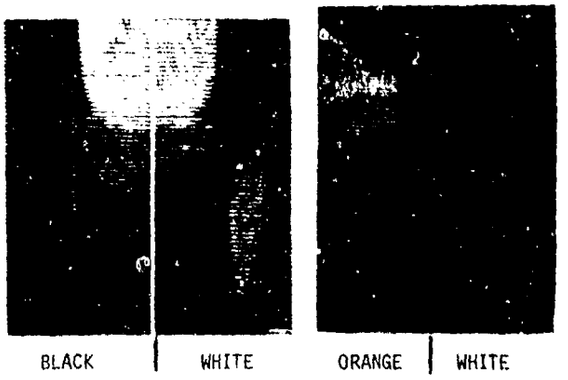

(a) Flat paint (no difference).

(b) Naval Aviation paint (2°C equiv. difference).

(c) Naval Aviation paint (2°C equiv. difference).

Fig. 19 Paint emissivity differences (uniform temp).

Fig. 20 IR radiation difference from uniform temperature aluminum sample painted completely white showing paint thickness variations.

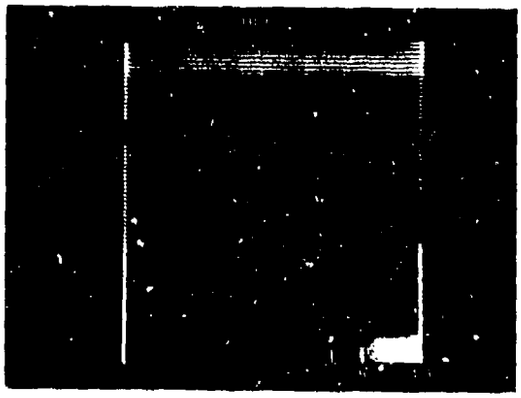

Fig. 21 Rough surface abrasions on polished Gr/Ep surface, constant temp., no reflections.

CONCLUSIONS

The following conclusions have been reached concerning EATF and SGTF thermographic NDE of composites.

The feasibility of locating delaminations, impact damage, and surface cracks in composites by thermography has been demonstrated. It appears that there will be limits on sizes and locations of the various types of flaws which can be detected, and these limits will be dependent upon heat source type and size (EATF), cyclic load level and frequency (SGTF), specimen thickness, and material conductivity. A large radiative heat source capable of causing transient surface thermal conditions will probably be required to obtain optimum flaw detection capability.

Surface characteristics (paint type, emissivity, reflectivity, soil, abrasions) are critical to accuracy of results. Surfaces to be tested must be shielded from background energy inputs such as sun, lights, and engine exhausts.

Additional details of the research performed and some results for aluminum structures can be found in references 5-7.

ACKNOWLEDGEMENTS

This work has been supported by the Naval Air Engineering Center, Lakehurst, NJ, under contracts N68335-78-M-5337 and N68335-79-C-1084. The authors are grateful to Mr. C. Chance of Grumman Aerospace Corp., Dr. W. E. Dance of Vought Corp., Dr. J. F. Kay and Mr. L. R. Nadwodney of Owens/Corning Fiberglas Corp., and Dr. A. J. Hannibal of Lord Corporation for providing composite samples. Thanks are due to Dr. W. R. Scott of the Naval Air Development Center for his advice during this effort.

REFERENCES

1. Reifsnider, K. L., and Stinchcomb, W. W., "New Methods of Mechanical Materials Testing Using Thermography", Proceedings, Infrared Information Exchange, 1976.

2. Whitcomb, J. D., "Thermographic Measurement of Fatigue Damage", NASA Technical Memorandum 78593, May 1978.

3. Charles, J. A., "Liquid Crystals for Flaw Detection in Composites", ASTM Committee D-30 Conference on NDE and Flaw Criticality for Composite Materials, Philadelphia, 10-11 Oct. 1978.

4. Henneke, E. G., II, Reifsnider, K. L., and Stinchcomb, W. W., "NDE of Composites by Vibrothermography", Review of Progress in Quantitative NDE, DARPA/AF, July 14-18, 1980.

5. McLaughlin, P. V., Jr., McAssey, E. V., Jr., and Deitrich, R. C., "Aerostructure Nondestructive Evaluation by Thermal Field Techniques", Report NAEC-92-131, Naval Air Engineering Center, Lakehurst, NJ, November, 1979.

6. McLaughlin, P. V., Jr., McAssey, E. V., Jr., and Deitrich, R. C., "Non-Destructive Examination of Fiber Composite Structures by Thermal Field Techniques", NDT International, Volume 13, April, 1980, pp. 56-62.

7. McAssey, E. V., Jr., McLaughlin, P. V., Jr., Koert, D. N., and Deitrich, R. C., "Thermographic NDT of Composites Using Externally Applied Thermal Fields", Proceedings, 35th Annual Conference, Reinforced Plastics/Composites Institute, S.P.I., February, 1980, pp. 26A 1-8.

NONDESTRUCTIVE EVALUATION OF GRAPHITE/EPOXY COMPOSITE DAMAGE

S. W. Schramm, I. M. Daniel, and W. G. Hamilton
IIT Research Institute
Chicago, Illinois 60616

ABSTRACT

Ultrasonic and acoustic emission techniques were used to monitor and evaluate material damage in a graphite/epoxy laminate containing a machined hole as an initial flaw and subjected to fully reversed spectrum fatigue loading at room temperature. It was found that the flaw growth progressed radially around the initial hole at a uniform rate during cycling at the lower stress levels. At the higher levels, material damage accelerated dramatically, progressing faster in the transverse direction toward the free edges. By close examination of the A-scan and RF spectrum photographs, it was determined that damage modes could be defined as to their extent and relative location within the specimen. These conclusions were supported by photographs of the failed specimen.

EXPERIMENTAL PROCEDURE

Specimen - The specimen was a 16-ply graphite/epoxy (AS3501-5A) coupon of $[(0/\pm45/90)_s]_2$ layup. The specimen gage section was 5.08 cm (2 in.) long and 3.81 cm (1.5 in.) wide. The initial flaw was a 0.795 cm (0.313 in.) diameter hole bored into a previously unflawed/undamaged specimen. The hole was drilled using a diamond tipped coring bit mounted on a variable speed drill press. Figure 1 shows the specimen after the hole was drilled and before fatigue loading was begun. The fiber damage around the hole was caused by the coring bit when it penetrated the back-side of laminate. An ultrasonic C-scan of the specimen, Fig. 2, and corresponding A-scans, showed the damage was superficial. Previous experience indicated that this type of superficial damage does not influence appreciably material damage caused by fatigue loading.

Fig. 1

Test Specimen with Initial Flaw (Hole) Before Fatigue Loading

Loading - The test specimen was preconditioned by oven-drying at 347 deg K (165°F) for five days. The specimen was tested under ambient environmental conditions because the acoustic emission transducers did not work well in humid and/or hot environments.

The specimen was stress-cycled in a five-position chain, with load applied through an electrohydraulic closed-loop system. The load spectrum consisted of 127,500 cycles of tension-compression at various levels of peak stress per life-time. At a cycling frequency of three Hertz, this was accomplished in approximately twelve hours. The

Fig. 2

C-scan of Test Specimen with Initial Flaw (Hole) Before Fatigue Loading

specimen studied was cycled to peak levels of 161 MPa (23 ksi), 223 MPa (32 ksi) and 276 MPa (40 ksi) applied over 510,000, 510,000, and 254,428 cycles, respectively, in an effort to accelerate and extend the material damage.

NONDESTRUCTIVE MONITORING

Acoustic Emission[2] - The acoustic emission system consisted of 0.95 cm (0.38 in.) diameter broadband transducers operational in the 0 to 1 MHz range. A transducer was attached to the specimen using a clip and an acoustic coupling medium to minimize the entrance of extraneous transient noise into the system, Fig. 3. The acoustic signal was fed into a databus after being processed by 180 to 210 KHz filters and then by preamplifiers. The databus operated at a 0.1 sec. sampling rate feeding an eight channel event recorder and chart recorder for hard copies of the data. Acoustic emission records consisted of both instantaneous rate and cumulative counts recorded for the entire fatigue spectrum.

As mentioned earlier, filters were used between the acoustic emission transducer and recorders. The frequency band of these filters was carefully selected to allow only noise generated by the

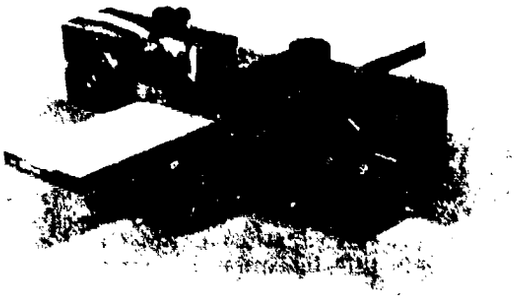

Fig. 3

Specimen with Compression Stabilization Plates and Acoustic Emission Transducer

specimen to be recorded. The filter frequency band was determined by testing until all extraneous noises could be identified and blocked out. Also, to guarantee that no other sound sources existed, the specimen was the only one present in the fatigue chain during testing. The remaining four positions were filled with aluminum "dummy" specimens. Whenever possible the specimen was run at night when the chance of picking up background noise from other electric equipment was at a minimum.

Ultrasonic Monitoring[3] - At intervals corresponding to each half lifetime of loading, the specimens were removed from the fatigue machine and inspected ultrasonically. The ultrasound was transmitted and received with a single 5 MHz focused immersion transducer of 2.54 cm (1.0 in.) diameter and 6.35 cm (2.5 in.) focal length. These dimensions produce a focal spot of approximately 1.27 mm (0.05 in.) in diameter, which is comparable to the thickness of commonly inspected laminates.

The transducer was operated by an ultrasonic analyzer operating in the pulse echo mode. The analyzer provides a time domain output for viewing the received pulse on an oscilloscope (A-scan) and a peak output detector for detecting and recording the local peak within the gated portion of the pulse.

The scanning system that was used to inspect the specimen is capable of automatically scanning and indexing the transducer so specimens up to approximately 38 cm (15 in.) square can be inspected with a single positioning.

The transducer is linked to an X-Y recorder via displacement transducers so that a hard copy of the data can be generated. Figure 4 shows the various types of scans which can be generated by the system at this time. Figure 4a is a C-scan representation of a $[(0/\pm45/90)_S]_2$ graphite/epoxy specimen with an initial flaw in the form of a circular hole. In this mode an alarm circuit with two limits is used which causes the pen to lift from the paper whenever the set limits are exceeded. These limits were determined using a standard specimen.

Figure 4b is an analog scan of the same specimen. In this mode the gated peak voltage of the reflected pulse is recorded as a deflection of the pen normal to the scanning direction. The variations of this voltage are related to the presence of flaws.

Figure 4c is an offset angle analog scan of the same specimen. In this mode a component of the X-axis signal is fed into the Y-axis signal resulting in a perspective view of the specimen. Flaws now appear as troughs and gray tones on a uniformly displaced background.

When a series of C-scans for one specimen are superimposed upon one another a flaw map is generated. In this way the total flaw growth history for a specimen can be presented in one illustration.

The ultrasonic scanning was rigidly controlled with all variable setting controls considered frozen throughout the test. A fixture was used to insure the relative position of the specimen to the scanning transducer for each inspection. Usually the C-scan is the only hard copy representation of a specimen under normal conditions, but this is only a small part of the data available by ultrasonic inspection. In addition to C-scans, such as Fig. 2, the ultrasonic wave was analyzed and recorded on a spot basis by photographing the ultrasonic pulse on the oscilloscope (A-scan) and the frequency spectrum of the pulse.

GENERAL PROCEDURES

To minimize the possibility of generating false or misleading data extreme care was taken during the testing procedure. The testing, including insertion and removal from the fatigue machine, attachment and removal of the acoustic transducer, and ultrasonic scanning, was conducted by one person. Photographs, such as shown in Fig. 1 were taken at regular intervals to supplement the acoustic emission and ultrasonic data. Due to its operation characteristics the ultrasonic scanner may not pick up surface irregularities which can be seen if the specimen is inspected visually.

To avoid damage to the specimen during insertion or removal from the chain a special torquing sequence was developed for the grip bolts. This sequence required the use of a preset torque wrench which would assure satisfactory gripping forces on the tabs of the specimen without causing bending or damage to the specimen. Also, to avoid buckling or bending of the specimen during loading, stabilization plates, visible in Fig. 3, were attached over the center of the specimen gage section. A teflon film was placed on the stabilization plate to minimize friction and extraneous noises.

RESULTS

Acoustic Emission[2] - Figure 5 shows flaw maps of the cumulative damage through 0, 4, 8, and just before 10 lifetimes, respectively. As was seen for other specimens with this initial flaw type,[1] the flawed area increased in a generally radial pattern around the hole at a nearly uniform rate. The damage indicated in Fig. 5a is associated with the fiber breakage caused when the hole was machined. The rapid

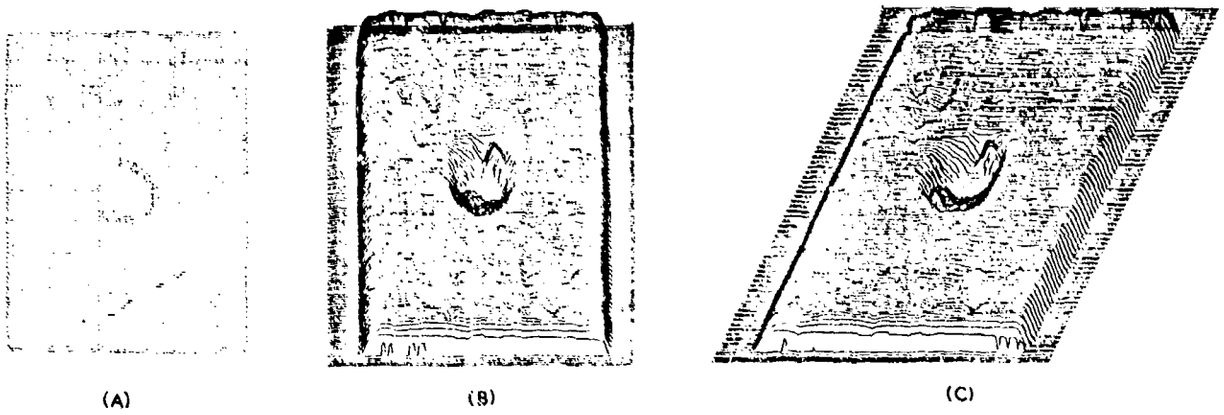

Fig. 4

Ultrasonic C-scans of $[(0/\pm45/90)_s]_2$ Graphite/Epoxy Specimen with a Circular Hole
(a) Pen-Lift Scan, (b) Analog Scan (Normal), (c) Analog Scan (Perspective)

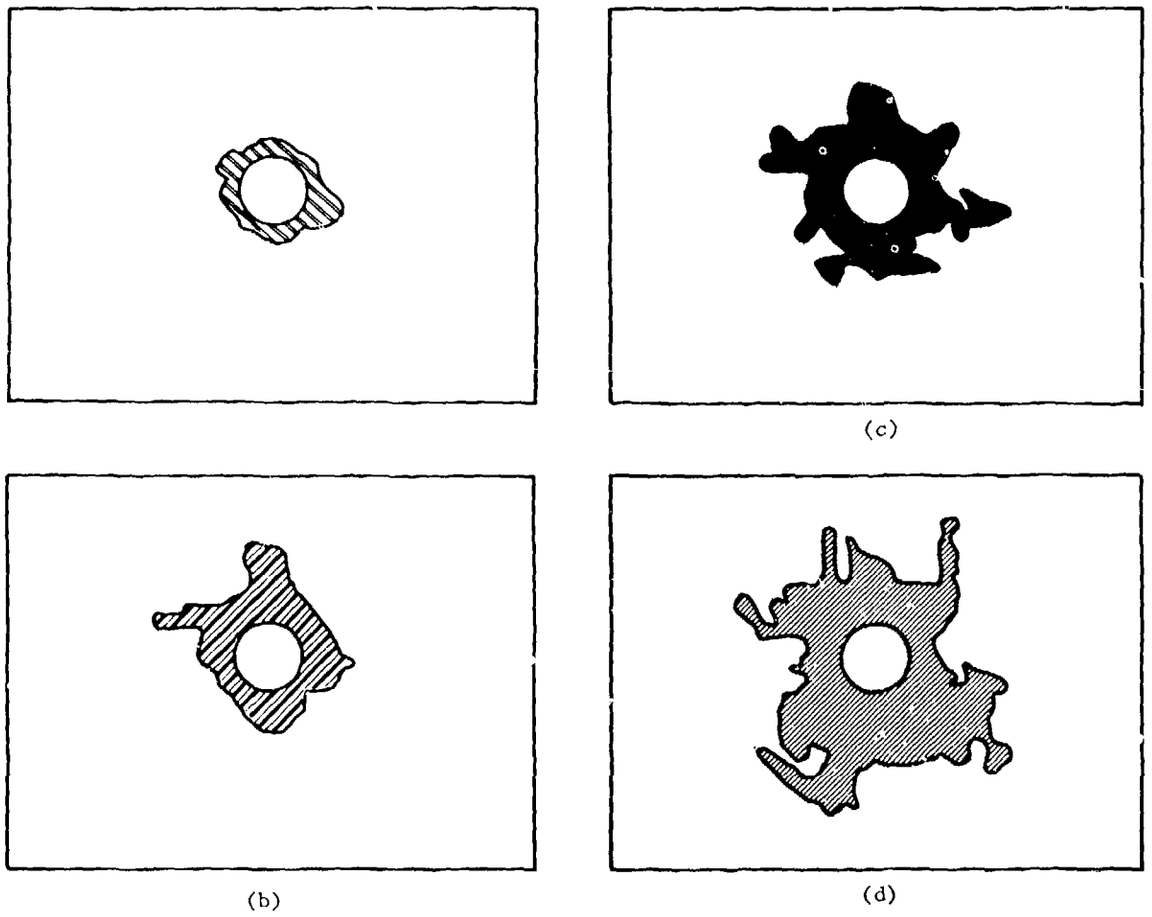

Fig. 5

Cumulative Flaw Growth Under Fatigue Loading in $[(0/\pm45/90)_s]_2$ Graphite/Epoxy Specimen with Circular Hole. (a) Initial Flaws, (b) Four Lifetimes, (c) Eight Lifetimes, and (d) Nearly Ten Lifetimes

acceleration of the flaw damage between Figs. 5c and 5d was expected because the maximum testing stress of 223 MPa (32 ksi) specified in the initial program for this material was exceeded. The maximum peak stress of 276 MPa (40 ksi) was applied at the end of eight lifetimes of testing and maintained until failure, which occured very near the end of the tenth lifetime (1, 274, 428 cycles).

The acoustic emission charts for the first eight lifetimes were definitely in keeping with the relative damage indicated by ultrasonic inspection. Very little acoustic activity was present during this period and it was of a uniform intensity level with the major peaks occuring when high load was applied for short periods. This implies that what little damage did occur during each half-life happened at the higher load levels.

Previous work in monitoring graphite/epoxy laminates under static load indicated that we should not have expected major activity until the 223 MPa (32 ksi) stress limit was surpassed. Figures 6 and 7 show acoustic emission records between 8½ and 10 lifetimes when extensive flow growth was detected ultrasonically.

Figure 6 shows a general increase in the acoustic emission response at peak loads while the response to low load applications decreases during the 9th lifetime. Acoustic emission activity increases generally after 8½ lifetimes up to a point where a large amount of activity is recorded culminating in a massive burst (arrow in Fig. 7). Close examination of the specimen after the 19th half-lifetime showed the presence of a large delamination visible on the boundary of the circular hole. Since no sign of such damage was present before the 19th half-lifetime it has been concluded that the formation of the delamination coincided with the acoustic emission burst. Since the specimen failed before completion of the half lifetime following the one where the massive burst occurred, it is safe to say that the acoustic emission indicated, if not predicted, that failure was imminent.

The specimen failed after 1,274,428 cycles were applied (nearly 10 lifetimes), the load at failure was 22.68 kN (5099 lb) corresponding to a stress level of 276 MPa (40 ksi). Figure 8 shows the failed specimen in the load chain. The specimen failed at the center of the gage section through the circular hole; this indicates that the failure

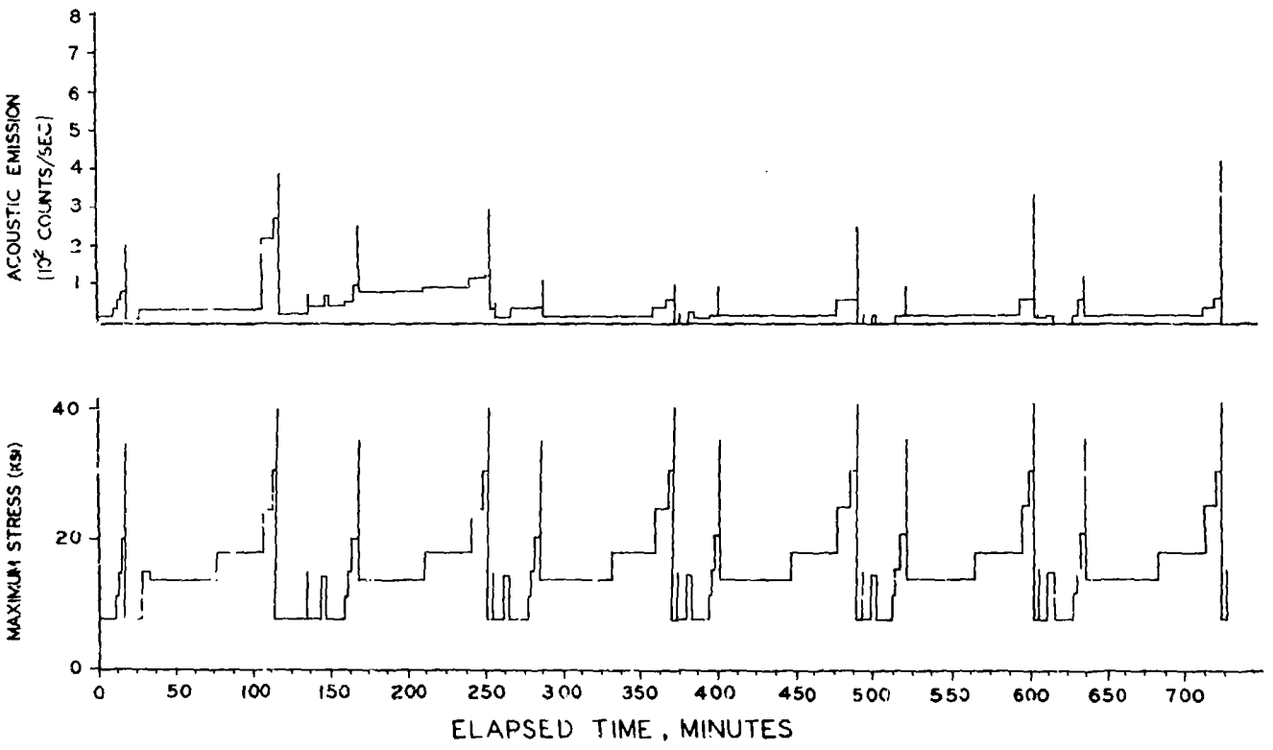

Fig. 6

Acoustic Emission and Corresponding Load Spectrum for $[(0/\pm45/90)_S]_2$ Graphite/Epoxy Specimen with Hole for 8½ and 9 Lifetimes

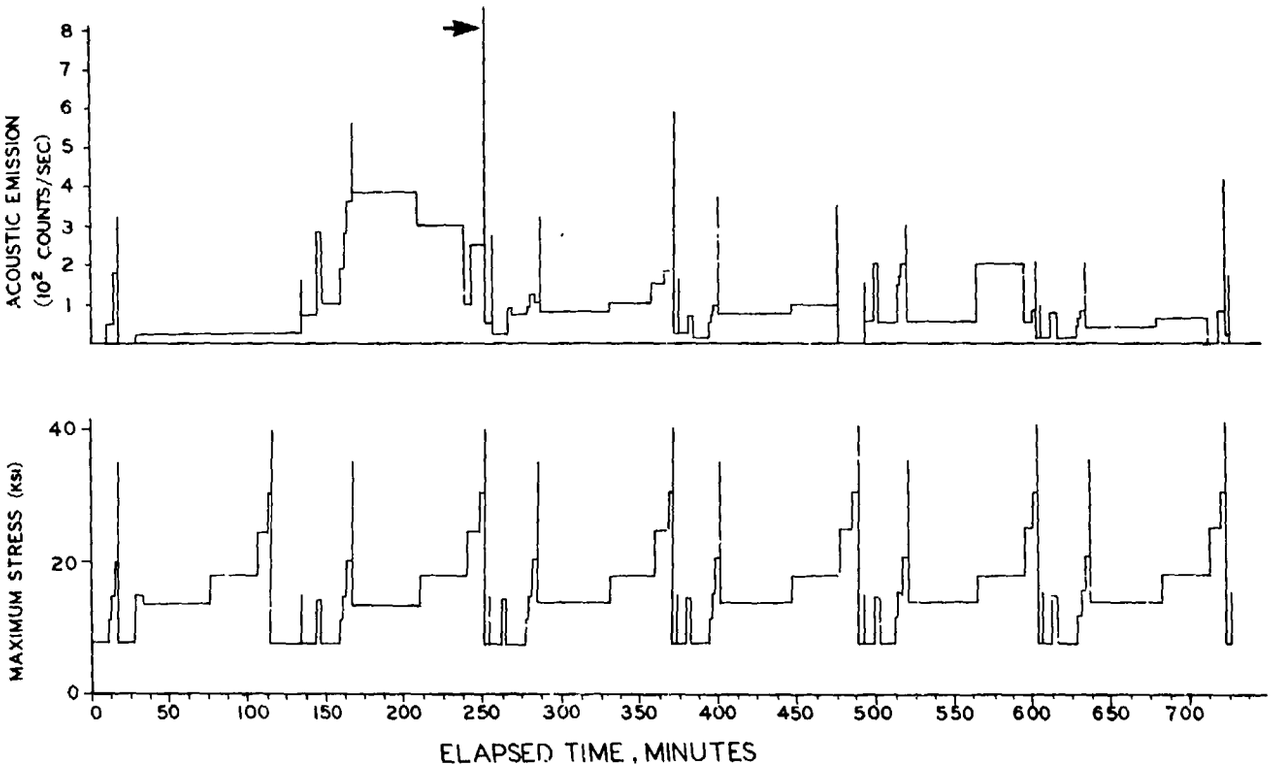

Fig. 7

Acoustic Emission and Corresponding Load Spectrum for $[(0/\pm45/90)_5]_2$ Graphite/Epoxy Specimen with Hole for 9½ and 10 lifetimes

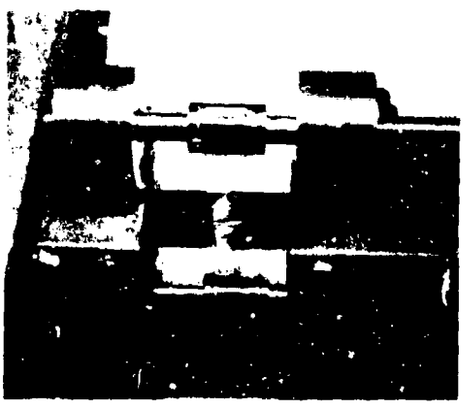

Fig. 8

Failed Specimen in Fatigue Chain

mechanism was material fatigue, not failure, due to bending of the specimen or overtightening of the grips.

Ultrasonic Monitoring - Figures 9, 10, and 11 show representative C-scan, A-scan and RF spectrum data for the test specimen at the indicated inspection times. Figure 9a shows the baseline responses of the A-scan and RF spectrum when no material is seen by the ultrasonic wave. The scatter on the RF spectrum is due to feedback noise from the A-scan oscilloscope. Figure 9b shows the baseline A-scan and RF spectrum responses when the ultrasound passes through an undamaged section of the specimen.

Figure 9c through 11b show how the A-scan and RF spectrum change as fatigue cycles are accumulated. C-scan inspections at 4, 5, and 5½ lifetimes (Figs. 9, 10a, and 10b, respectively) indicate little damage growth in the area of the point of analysis. In contrast, the A-scans and RF spectra have changed appreciably from those in Fig. 9 indicating a definite change in the material integrity near the point of analysis. The characteristic which indicates the material degradation is the back-face reflection of the A-scan wave. The level of ultrasound attenuation, which indicates the presence and severity of an abnormality in the material, is represented by a change in the amplitude of the back-face reflection,

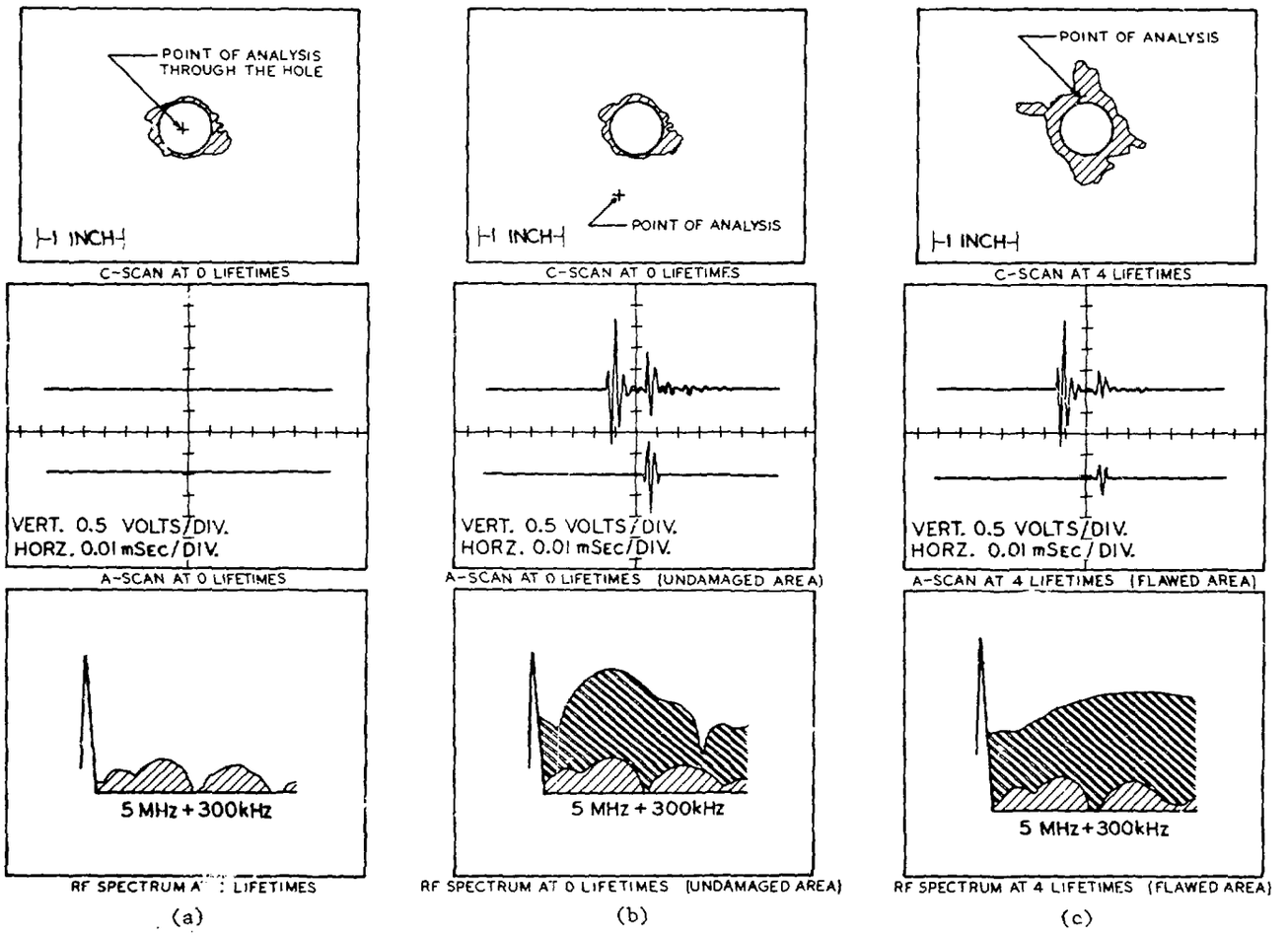

Fig. 9

Ultrasonic Inspection Data at the Indicated Point of Analysis After (a) 0, (b) 0, and (c) 4 Lifetimes of Load Application

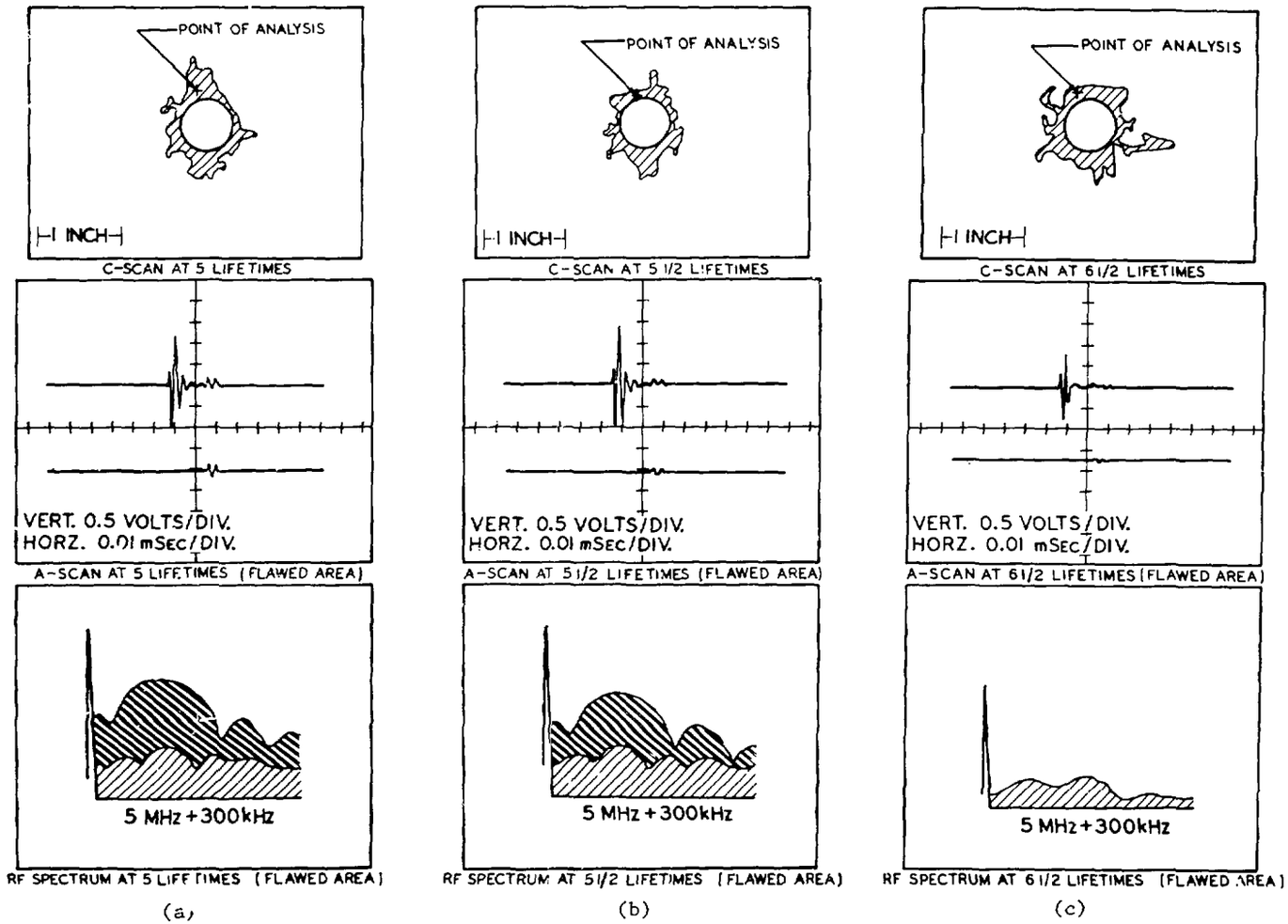

Fig. 10

Ultrasonic Inspection Data at the Indicated Point of Analysis After (a) 5, (b) 5½, and (c) 6½ *Lifetimes of Load Application*

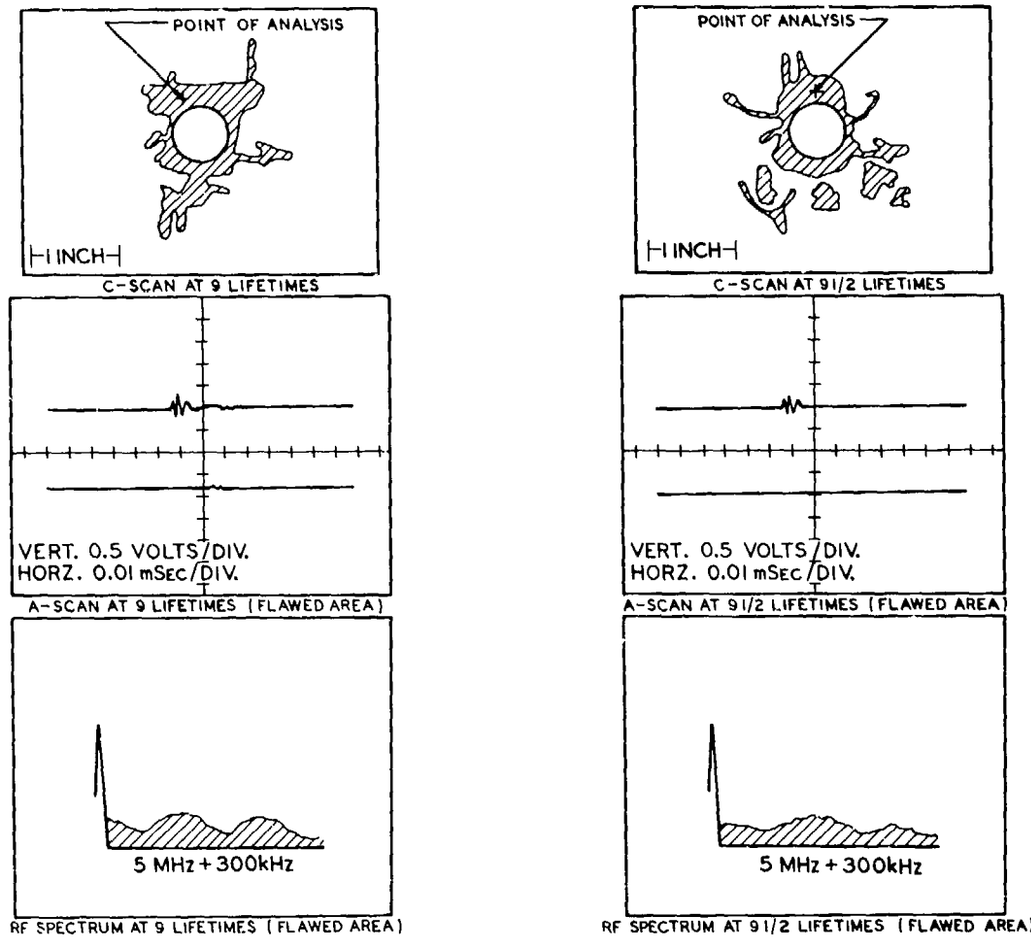

Fig. 11

Ultrasonic Inspection Data at the Indicated Point of Analysis After (a) 9 and (b) 9½ Lifetimes of Load Application

of the ultrasonic wave. For 16-ply graphite/epoxy specimens, the alarm voltage window, indicating no material damage, was 1.5 to 3.5 volts. In Fig. 9b the back-face reflection amplitude is slightly greater than 1.5 volts indicating undamaged material. When the specimen was inspected at the end of 5½ lifetimes, the back-face reflection amplitude had decreased to a value of approximately 0.25 volts. The decrease to 0.25 volts took place in increments of approximately 0.25 volts per inspection. This implies that the severity of the material damage, which was determined to be a delamination in post-failure analysis, increased slowly as the fatigue cycles accumulated. The amplitude of the back-face reflection is of such a magnitude at the 5½ lifetime inspection that the delamination had formed, but was still tight enough to allow passage of the ultrasound between the two adjoining plies.

By the 6½ lifetime inspection, Fig. 10c, and up through the 9 lifetime inspection, Fig. 11a, only a faint back-face reflection amplitude can be seen. During this period it has been determined, using additional data not presented herein, that the delamination began to progress transversely across the specimen from the hole towards the free-edge. This is evidenced by the tendrils of flawed area shown in the C-scan at the completion of 9 lifetimes of cycling, Fig. 11a. When the specimen was inspected after 9½ lifetimes the delamination was severe enough that the ultrasound could not pass across the gap, hence, no back-face reflection was evident. The extent of the area of damage after 9 lifetimes (C-scan Fig. 11a) and the severity of the damage after 9½ lifetimes (A-scan Fig. 11b) given adequate warning of the failure which occurred during the twentieth halflife of cycling. Similar trends are present in other areas of the specimen near the hole, but the volume of data required to show these trends would be extremely high. During the course of the investigation forty-one C-scans, 316 A-scan/RF spectrum photographs, and 120 feet of acoustic emission data was generated for this single specimen.

The photograph (Fig. 12) shows the failed specimen after removal from the fatigue chain. The massive delamination shown on the photo labeled "Failure Surface A-B" was the source of the data presented above. Presently, additional work is being done to correlate C-scan/A-scan/RF spectrum

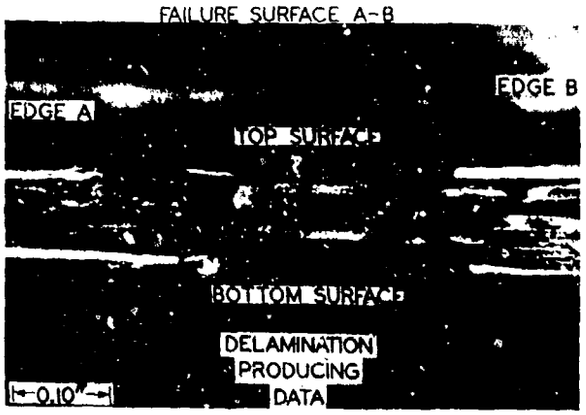

Fig. 12

Failed Specimen After Removal
From Fatigue Chain

data with the photographs of the failed specimen. The goal is to establish a relationship between A-scan/RF spectra signatures, and the type of material damage. In this manner, the criticality of the material damage of a component in-service could be assessed. This ultimately minimizes the need for replacement of good components because they appear to have strength reducing damage.

CONCLUSIONS

1. For the single specimen investigated, there was a clear correlation between acoustic emission activity and material damage.

2. Acoustic emission identified the exact point where major material damage occurred and, in doing so, predicted the failure that followed.

3. Critical flaw sizes must be determined for composites since the formation of noncritical flaws may have a high level of acoustic emission associated with it.

4. Additional work must be conducted to establish a correlation between specific acoustic emission outbursts to the type of material failure which caused the energy release, e.g., fiber breakage or matrix cracking.

5. More sensitive, less environmentally affected, acoustic emission transducers are necessary.

6. Both A-scan and RF spectrum data, when used in conjunction with ultrasonic C-scans, can give an indication of the extent, severity, and location of delaminations within a laminated composite material.

REFERENCES

1. I. M. Daniel, S. W. Schramm, and T. Liber, "Nondestructive Monitoring of Flaw Growth in Graphite/Epoxy Laminates Under Spectrum Fatigue Loading," presented at ARPA/AF Review of Progress in Quantitative NDE, La Jolla, CA, July 3-13, 1979.

2. S. W. Schramm, I. M. Daniel, and W. G. Hamilton, "Nondestructive Characterization of Flaw Growth in Graphite/Epoxy Composites," presented at 35th Annual Technical Conference, 1980 Reinforced Plastics/Composites Institute, The Society of the Plastics Industry, Inc., New Orleans, LA, Feb. 4-8, 1980.

3. T. Liber, I. M. Daniel, and S. W. Schramm, "Ultrasonic Techniques for Inspecting Flat and Cylindrical Composite Specimens," ASTM Conf. on Nondestructive Evaluation and Flaw Criticality for Composite Materials, Philadelphia, PA, Oct. 10-11, 1978.

NONDESTRUCTIVE EVALUATION OF COMPOSITE MATERIALS WITH BACKSCATTERING MEASUREMENTS

by

Y. Bar-Cohen
Systems Research Laboratories, Inc., Dayton, Ohio
and

R. L. Crane
AFWAL/MLLP, WPAFB, Ohio

ABSTRACT

Initial experiments have been performed to characterize the scattering of acoustic waves from glass/epoxy and graphite/epoxy composite panels. Experiments were conducted in the region $0.1 \leq ka \leq 1.0$ on both types of fiber reinforced composites. The data clearly show that a maximum in the backscattering ultrasonic energy occurs for orientations which place the fiber axis perpendicular to the propagation vector.

INTRODUCTION

The propagation of elastic wave through fiber reinforced composite is a very complex process. As it travels through the material, the acoustic wave is dramatically affected by the anisotropic nature of the layered composite. Significant changes also result from the multiple scattering events that occur because of the myriad of stiff fibers in a soft plastic matrix. Only recently have theoretical and experimental studies begun to unravel the subtleties of the acoustic wave/composite interaction.

The objective of this research work has to study the multiple scattering phenomena in fiber reinforced composites, as revealed by backscattering measurements.

RESULTS AND DISCUSSION

An experimental apparatus was built to permit rotating test specimen while maintaining a constant angle of incidence. By varying the fiber diameter and the frequency of the incident wave, tests were conducted in the pseudo-Rayleigh scattering range $0.1 \leq ka \leq 1.0$, where k is the wave number and a is the fiber diameter. The composite materials examined were graphite/epoxy and glass/epoxy. A schematic of the experimental set-up and nomenclature are shown in Fig. 1. Measurements of backscattering were averaged over 32 points on the specimen for a constant incident angle. As expected, the backscattering (scattering detected by the sending transducer) is maximum for orientations that place the fibers in a specific ply perpendicular to the ultrasonic beam, (see Fib. 2). Also shown in Fig. 2 is the effect of surface roughness which contributed about 1 dB to the backscattered energy. This can be nearly eliminated by polishing the specimen surface. In Fig. 3 a schematic diagram is shown as a guide in determining fiber angle in a quazi-isotropic laminate. Using this simple convention then Figs. 4 and 5 demonstrate the ease of using backscattering information to determine ply orientation.

The width of the backscattering peak is affected by both the beam divergence and the uniformity of fiber alignment. If beam divergence is constant, then the peak width may be used to estimate the amount of waviness in an otherwise parallel row of fibers. To demonstrate this, a sample with a 30° misalignment was fabricated. The effect of this misalignment is shown along with perfectly aligned sample in Fig. 6. The increased bandwidth was capable of determining misalignment to an accuracy of $\pm$ 1° of arc. This is shown in Fig. 7, where the actual angle versus the calculated misalignment angles are plotted.

Backscattering is observed whenever a discontinuity is encountered by the acoustic. Defects such as a porosity with spherical symmetry, result in a uniform increase of scattering over wide angles as shown in Fig. 8.

It is concluded that backscattering measurements may be used to determine fibers orientation, misalignment and in some cases the presence of porosity. Further work is underway to quantify the angular dependence and intensity of backscattering in composite materials.

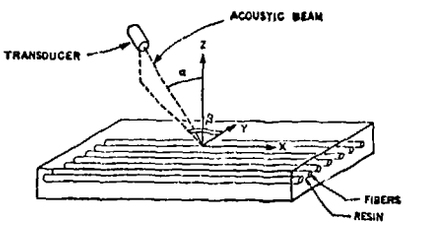

WHERE:

α – ANGLE OF INCIDENCE

β – ANGLE BETWEEN Y-AXIS AND THE TRANSMITTER BEAM TRAJECTORY ON THE LAYER PLANE

Fig. 1. Schematic representation of experimental set-up used to measure backscattering from composite samples.

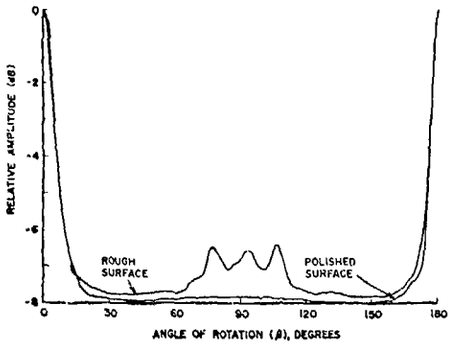

Fig 2 Backscattering from unidirectional ($[0]_8$)Gl/Ep composite for a 30° angle of incidence. The effect of surface roughness is also shown.

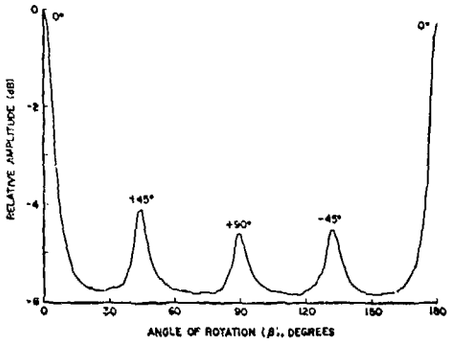

Fig 4 Backscattering from a quazi-isotropic ($[0, \pm 45, 90]_S$) composite for a 30° angle of incidence. Scattering from each ply is apparent (see Figure 3).

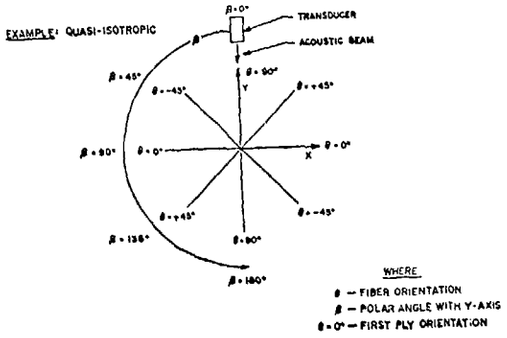

Fig. 3 Angular convention used to determine fiber orientation in backscattering experiments.

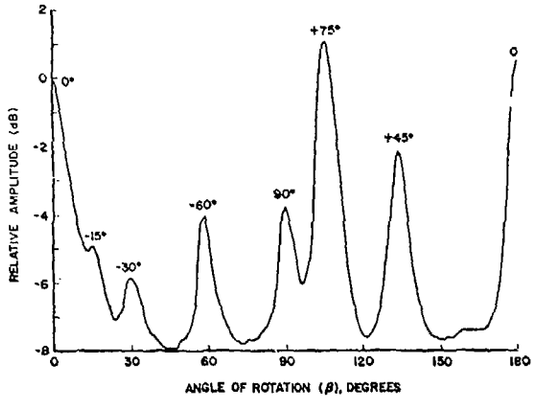

Fig. 5 Backscattering from graphite/epoxy composite $[0^o, -15^o, -30^o, +45^o, -60^o, +75^o, 90^o]_S$. Angle of incidence was 40°.

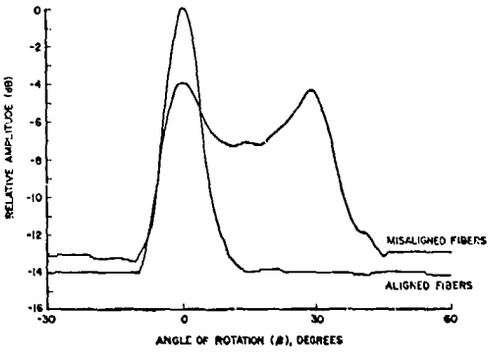

Fig. 6 The effect of misalignment on back-scattering from single-ply glass/epoxy material.

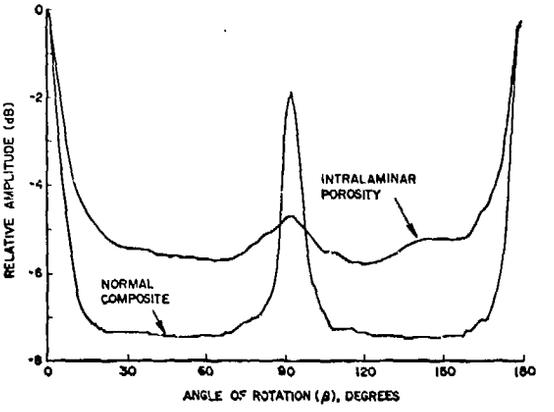

Fig. 8 Backscattering from $[0,90]_{2S}$ glass/epoxy composite both with and without porosity. Glass micro-balloons were used to simulate porosity.

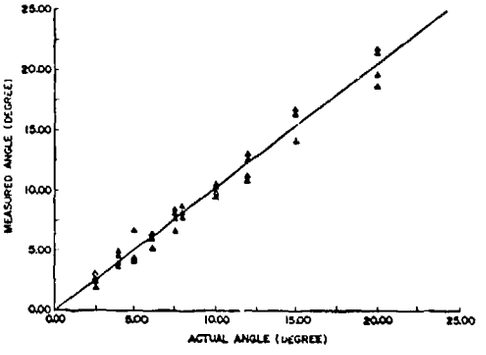

Fig. 7 Comparison of measured and actual fiber misalignment in glass/epoxy composite material.

EVALUATION OF THE STRUCTURAL INTEGRITY OF GRANULAR COMPOSITES BY ULTRASONIC TECHNIQUES

H.R. Carleton, W. Burke, and W.J. Chen
State University of New York at Stony Brook
Stony Brook, N.Y. 11794

ABSTRACT

The development of the mechanical strength of composite materials which are consolidated by cementaceous bonds has been monitored by observation of the ultrasonic properties over the evolution of bond growth. The granular nature and weak bonding of these materials produce high attenuation of the ultrasonic signal and observation is difficult, particularly in larger structures. In order to obtain ultrasonic parameters with high resolution and to overcome the effects of grain scattering, a system based on a minicomputer and array processor has been implemented which provides time and frequency-domain processing and aperture synthesis. This ultrasonic data provides a reliable measure of the structural integrity of these materials.

INTRODUCTION

The quality of composite materials has been traditionally evaluated by the measurement of compressive strength (ASTM-C39). This technique is well established, but is destructive, requires considerable replication, and is of limited value in determining local inhomogeneity and structure. Ultrasonic techniques can provide a non-destructive method of analysis and have been used on larger structures as in the concrete industry[1] to predict the viability of structural materials. A class of composite materials consisting of fly-ash and a form of gypsum ($CaSO_4$) which are bonded into a solid by various cementaceous reactions are currently under study to determine the feasibility of using this process for the ocean disposal of waste from coal-fired power plants[2]. This program involves a five-year study of the integrity of these materials both in the laboratory and on a large scale at a test-site (reef) in the ocean.

Although ultrasonic methods offer promise in providing a method of non-destructive evaluation of these materials, it was found that excessive ultrasonic attenuation due to grain scattering and bond softening may be present and that adequate correlation of ultrasonic properties to the "actual" compressive strengths of the material would have to be developed within the program.

We report here on the first phase of this program in which the materials are characterized ultrasonically by a system which is capable of measuring these properties at three levels. Our results show that the ultrasonic modulus provides a sensitive indication of the compressive strength of these materials (within the statistical limits of the fracture process). Furthermore, the modulus is shown to be a sensitive indicator of the growth of the cementaceous bond and hydration process.

MATERIAL STRUCTURE

Figure 1 is an SEM of the internal structure of a test block of fly-ash and scrubber sludge ($CaSO_4$) mixed in a mass ration of 3 : 1 which has undergone consolidation in sea water for a period of 6 months. The sphericules are fly-ash granules, while the scrubber sludge appears as an amorphous intergranular mass. Two other structural forms are evident and appear only in consolidated materials. The small crystals are believed to be ettringite[3] while the larger crystallites, more evident in Fig. 2, are known to be gypsum ($CaSO_4 \cdot 2H_2O$). These micrographs illustrate the complexity of the material under study. We believe at this time that the increase of modulus of these materials is entirely attributable to the growth of these crystallites in the intergranular voids of the block.

INSTRUMENTATION

The apparatus developed for the detailed evaluation of ultrasonic properties of these materials is shown in Fig. 3. A test tank is provided which mounts a pair of ultrasonic transducers. The receiving transducer is under the control of a mechanical translation device which makes it possible to position the receiving array precisely over a range of 50 cm. The fluid media, in this case water, provides an effective coupling medium and facilitates the rapid interchange of test samples. All work reported here was carried out at 162 kHz which was found to be the best compromise between grain scattering attenuation and resolution.

The ultrasonic system is under control of a PDP 11/34 computer which also provides for storage, processing, and display of the voluminous data. The system can be used as either an intervalometer (time domain) or dispersometer (frequency domain). The mechanical translation system makes it possible to use synthetic aperture analysis to obtain additional resolution and discrimination against multipath effects. After amplification and filtering, the received ultrasonic data can be sent directly to a dedicated 100 kHz A/D converter, or to a high-speed sample-and-hold circuit under control of a synchronizer. The second alternative provides a method of digitizing repetitive ultrasonic signals of much higher bandwidths at the expense of longer acquisition time.

Control software has been developed so that the extensive processing required can be carried out optionally either in software or through use of an array processor (Model MSP-3 manufactured by Computer Design and Applications Inc.). This feature not only makes it possible to retain greater functional control of the process, but provides software backup (at slower speeds) in the event of

limited hardware failure. The logical flow of this process is illustrated in Fig. 4. At each step in the movement of data through the ultrasonic test system, a given process, such as synthetic aperture processing, may or may not be used at the discretion of the operator. If single channel operation were desired, as in low resolution intervalometer work, the data would be passed directly to time domain analysis or storage.

RESULTS

The velocity evolution of two groups of six blocks, with each group having a 1 : 1 (E2C1) or a 3 : 1 (E2C3) fly-ash to sludge concentration is illustrated in Fig. 5. These blocks were aged in laboratory tanks of sea water held at room temperature for more than a year. The blocks were periodically measured for ultrasonic velocity, attenuation, and density. It will be noted that the initial velocities of both compositions were nearly the same, but the growth in velocity for the 1 : 1 material was more rapid and achieved higher values. Since the change in density in this process is small, the increase in velocity is attributable to a growth in the modulus of the composite material, which in turn is due to cementation or crystalline growth in the voids.

This observation is supported by a concurrent study of the density of these materials over the same time period as illustrated in Fig. 6. Our observations indicate that increases in density due to the uptake of water into the pores of these materials is complete in 1 - 2 hours after placement in the tank. The growth in density indicated in Fig. 6 is primarily due to chemical hydration. Hence, crystalline growth is correlated with the evolution of the ultrasonic modulus.

It is highly desirable to use these ultrasonic methods under *in-situ* conditions to predict the structural integrity of composite materials. An evaluation of a large number and variety of blocks was carried out in which the blocks were aged in the laboratory or at sea, measured for ultrasonic velocity, and then tested for compressive strength. These results, after calculating the modulus of each material group from velocity data, are displayed in Fig. 7. The correlation between the compressive strength and the modulus of these materials is indicated by these data. It should be noted that each data point in this figure represents the average of the compressive strength of several blocks. The standard deviation for compressive strength on these materials is high (25 - 50 %) due to the inhomogeneity of the blocks and statistical nature of the fracture process[4].

The results of these studies provide guidelines for the estimation and prediction of the compressive strength of composite materials of this type. Such techniques are not only invaluable for field studies of these and similar engineering materials but also provide a precision method for the controlled study of the cementation process which should be applicable to a wide variety of materials.

ACKNOWLEDGEMENTS

We wish to thank Prof. F.F.Y. Wang and J. Muratore for the compressive strength data and F. Roethal for the scanning-electron microphotographs.

This research is conducted under the auspices of the New York State Energy Research and Development Authority (NYSERDA) with the support of DOE, EPA, PASNY, and EPRI.

REFERENCES

1. Whitehurst, E. A., "Evaluation of Concrete Properties from Sonic Tests", American Concrete Institute Monograph #2 (1966).

2. Carleton, H. R. and Wang, F. F. Y., "Ocean Dumping of Consolidated Coal Wastes - Physical Testing and Lifetime Prediction", Proceedings of the Second International Ocean Dumping Symposium, D. Kester, Ed; Woods Hole, Mass; April (1980).

3. Seligman, J. D. and Duedall, I. W., "Chemical and Physical Behavior of Stabilized Scrubber Sludge", Environment Science and Technology 13, 1082 September (1979).

4. Barrett, C. R. et-al., "The Principles of Engineering Materials", Chap. 6, Prentice-Hall (1973).

Fig. 1 The internal structure of a composite with a fly-ash to scrubber sludge mass ratio of 3 : 1 and 5 % lime which has been aged in sea water for six months. The fly-ash granules are spheroids. Scanning electron micrograph (SEM) at x = 2600.

Fig. 2 Same material as in Fig. 1 in area that emphazises the growth of crystallites in the inter-granular voids. The larger crystal is gypsum while the needle-like structure may be ettringite (see text). (x = 3200).

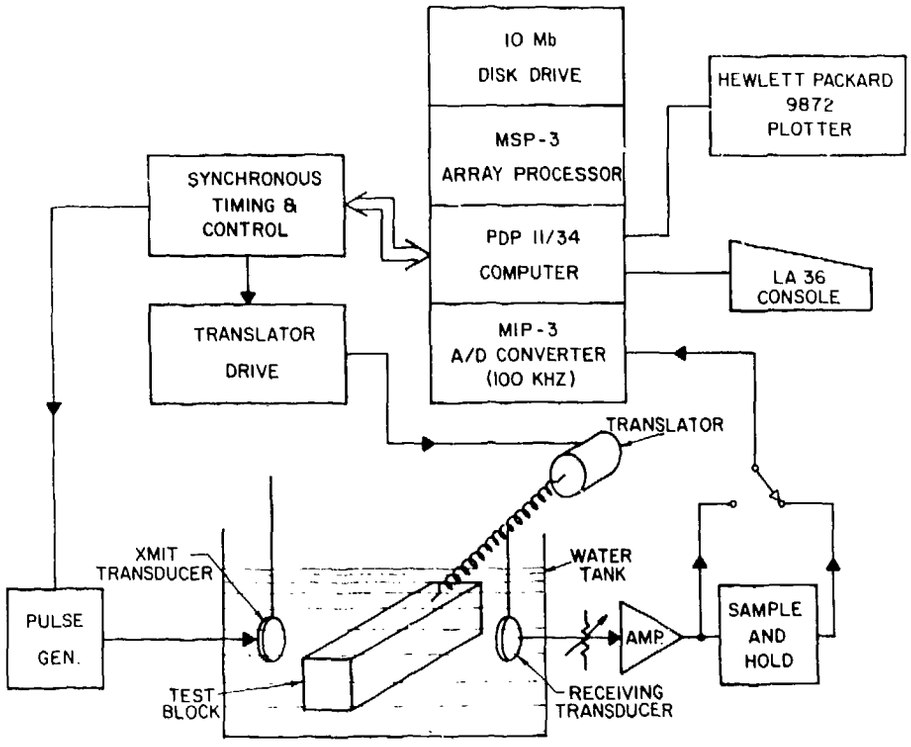

Fig. 3 Laboratory system with dedicated computer facility for the acquisition and processing of ultrasonic data. The sample-and-hold system makes possible the analysis of frequencies to 10 mHz.

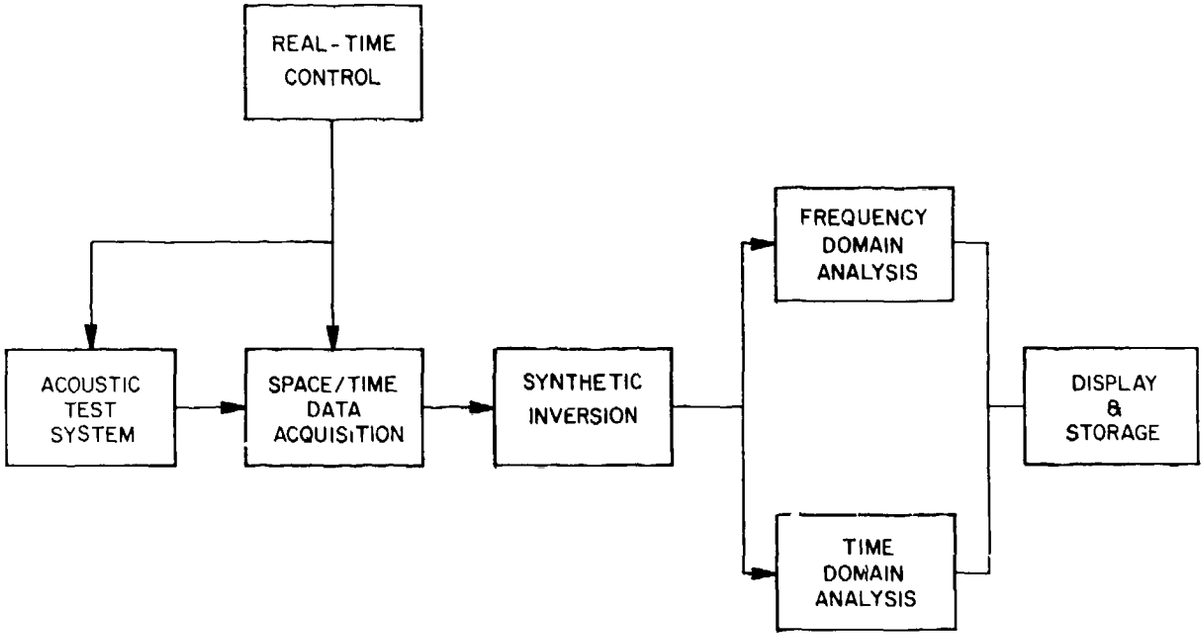

Fig. 4 Conceptual organization of the analysis process. The system may be operated as an intervalometer and dispersometer.

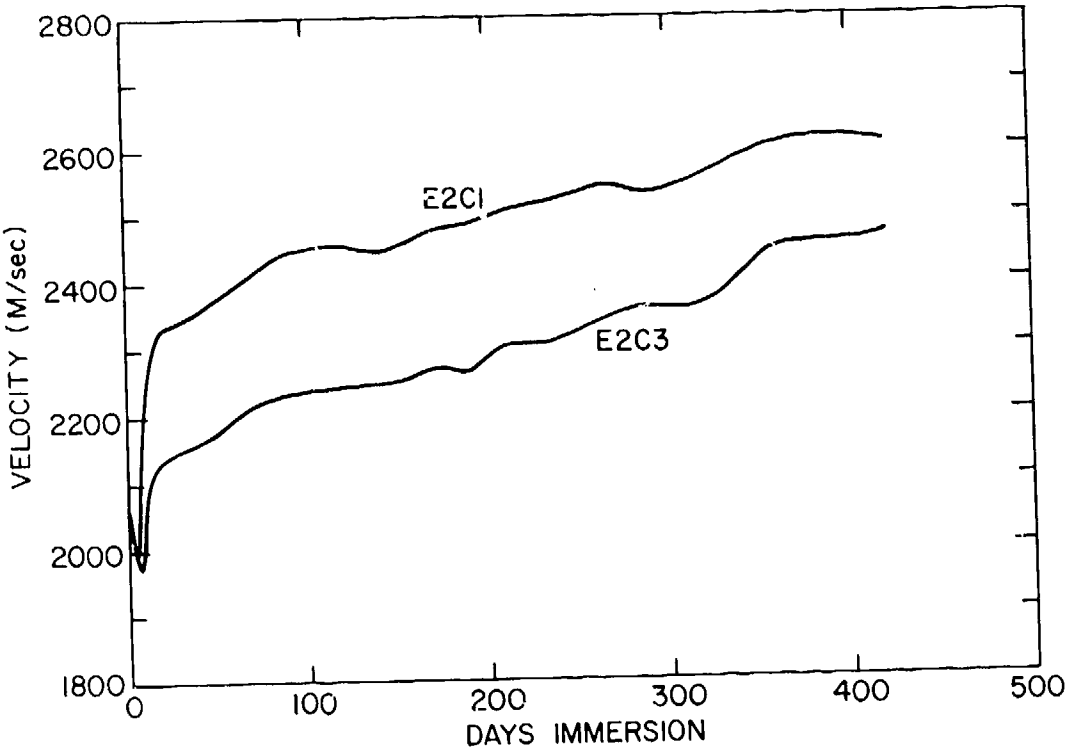

Fig. 5 The velocity evolution of two material compositions aged in laboratory tanks. The more rapid cementation of the 1 : 1 material (E2C1) is clearly indicated by the increase in velocity associated with the increasing elastic modulus of this material.

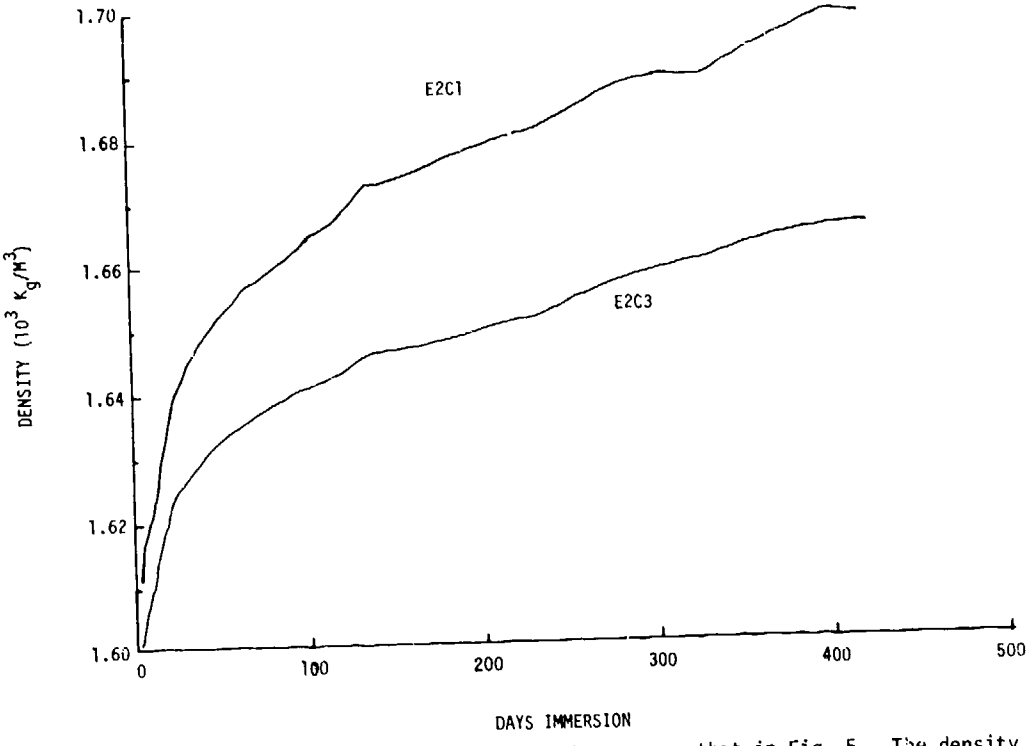

Fig. 6 The density evolution of the same test group as that in Fig. 5. The density increase in the E2C1 group is attributable to crystallite growth through hydration resulting in cementation and increase in elastic modulus.

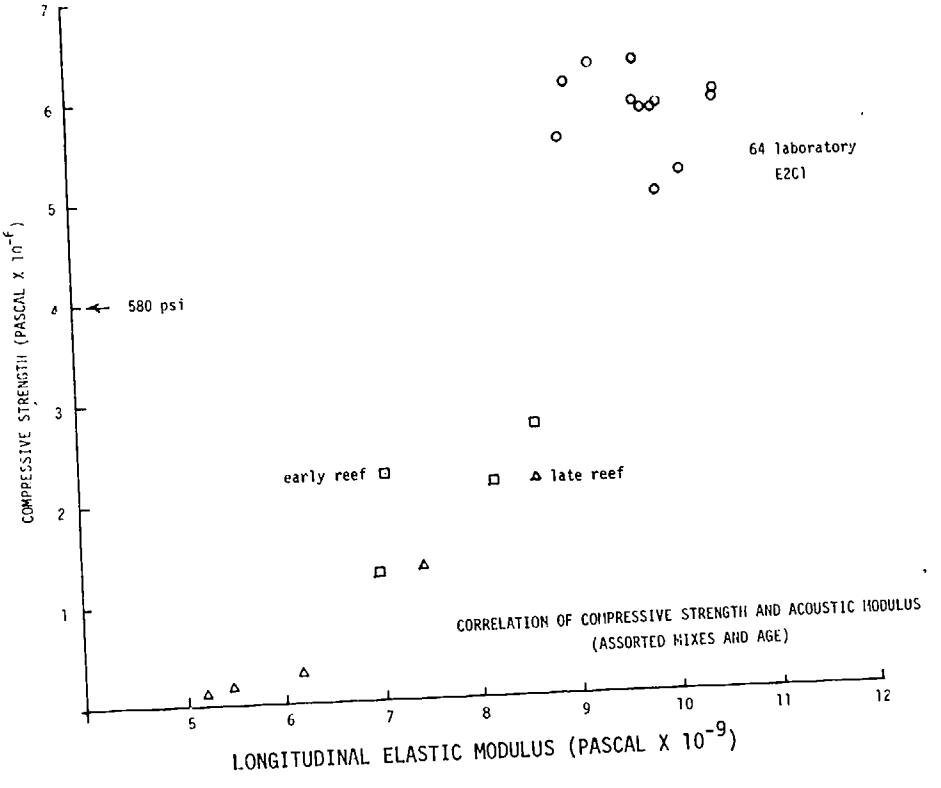

Fig. 7 Correlation of the average compressive strengths of groups of materials (consolidated in sea water for various times) to their elastic moduli as determined by from ultrasonic data at 162 kHz. This correlation forms a basis for the prediction of the integrity of materials of similar composition from ultrasonic velocity data.

X-RAY DIFFRACTION EVALUATION OF ADHESIVE BONDS AND DAMAGE IN COMPOSITES

Charles S. Barrett and Paul Predecki
University of Denver Research Institute
Denver, Colorado 80208

ABSTRACT

Stresses can be measured by X-ray diffraction, not only in metals but also in polymeric composites containing some crystalline filler particles. Diffraction is found effective in disclosing the distribution of stresses over the surface of adhesively bonded joints in aluminum strips when loads well below the yield point are applied. When two 6061-T6 aluminum strips 1/16" or 1/32" thick and 3/4" wide are adhesively bonded in a single lap joint and loaded in tension, maps giving the distribution of the X-ray-measured stresses show clear evidence of the way in which stresses are transferred from one adherend to the other. The maps show the limits of the bonded area with an accuracy about equal to the width (1 mm) of the irradiated area along the specimen. Attendant bending stresses resulting from the loading are also registered. Stress values can be obtained from the observed diffraction angles by calibration with tensile tests of a single unbonded strip. Similar results are obtained for graphite/epoxy laminates adhesively bonded to aluminum when diffraction is from the aluminum, but a much lower accuracy was obtained when diffraction was from the filled composite.

Another X-ray method was developed that appears to be a viable though less accurate method for measuring applied (not pre-existing residual) stresses, and for mapping their distribution around a joint. A thin layer of epoxy paint containing a diffracting filler is applied to a specimen and cured. Diffraction from this paint yields shifts in diffraction angle approximately proportional to the magnitude of applied stresses. A diffracting paint containing, say, aluminum or silver powder can be used on an object that diffracts poorly or in which a filler has not previously been embedded, but the accuracies attainable in stress values are apparently somewhat lower and are being investigated further. When this method is used on the aluminum adherend of a single lap joint and a load is applied, the limits of the bonded area are disclosed by the diffracted beam from the filler in the epoxy paint. This method appears, therefore, to be useful for mapping the areas that are properly bonded and for associated bending stresses, and possibly for non-destructive evaluation of bond defects. Details will be published in Advances in X-Ray Analysis, Vol. 24.

Detection of damage in polymeric composites is possible by X-ray determination of residual stresses. By locally deforming a graphite/epoxy laminate the diffraction from embedded filler powder discloses effects of the deformation not only where damage has occurred but also throughout the immediate neighborhood of the visible damage. Investigation of this method continues with details to be published elsewhere.

INTRODUCTION

X-ray diffraction is widely used for the measurement of residual and applied stresses in metals. A series of experiments has shown that information can also be obtained about residual and applied stresses in polymeric materials, including polymer matrix composites,[1-3] provided suitable diffracting powders are embedded in them before they are cured. Laboratory experiments with an X-ray diffraction method of determining stresses in graphite fiber reinforced epoxy composites have led us to conclude that the method could be extended into one for evaluating adhesive bonded joints. Since the X-ray measurements can reveal the point to point variation in stresses applied to an object, they should serve to map out the areas that are transferring stress from one of the bonded members to another, both with composite and with metallic adherends. A map of an adhesive joint prepared in this way when the joint is loaded should (a) provide evidence of the direct transfer of the applied stress from one adherend to another; (b) serve as a nondestructive method for revealing the outer limits of the bonded area; (c) disclose any unbonded patches within the area that are large enough to significantly alter the stress distribution; and (d) also record any stress components at the surface of an adherend that arise from the bending of adherends as a result of the loading. The method should thus be a direct and quantitative NDE method for comparison with prior discussions of these details in bonded joints,[4,5] including theoretical predictions of the stress distributions.

THE METHOD AND THE SPECIMEN DESIGN

The suggested method as applied to single lap joints reported here, involved measurement of the diffraction angles by two procedures: (1) by fitting a parabola to the diffraction peak in a standard procedure we had previously used;[2] and (2) by a more rapid technique that will be here called a "constant angle" technique. The latter involves measurement of the diffracted beam intensity at a fixed angle on a side of the peak as indicated in Fig. 1, (an angle where the slope is high and the curve is nearly a straight line). Displacement of the peak by stress then is registered as a change in intensity, with the intensity change being approximately proportional to the stress as is seen in calibration runs. A modified version of this technique, (2a), employs measurements at a pair of fixed angles straddling the peak, as indicated in Fig. 1, and taking either the ratio of the two intensities or subtracting one from the other.

Each specimen consisted of a strip cut from 1/16" or 1/32" aluminum sheet (6061-T6) about 19.7 mm wide and bonded to a similar strip or to a 6-ply

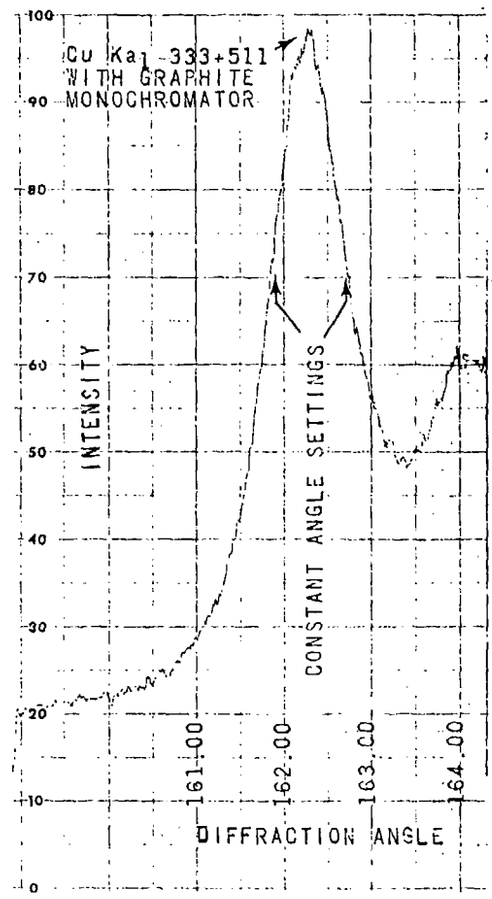

Fig. 1. Profile of diffraction peak used with aluminum. Detector is set at one or both angles indicated, for constant angle method.

unidirectional graphite/epoxy laminate to make a tensile specimen of about 152 mm overall length. Hysol EA9309 epoxy was used at the lap joint and to attach reinforcing tabs at the ends. A teflon film 0.0254 mm thick was inserted at one end of the overlap before curing. The teflon extended across the sample, with its edge perpendicular to the tensile axis, to produce a debond of accurately known position. Tension was applied through clevis grip pins in holes drilled at each end of the sample. A small, manually operated tensile frame held the specimen centered on a Siemens horizontal diffractometer and applied the load used in this and the other similar experiments reported here. An X-ray beam collimated to 0.25° divergence irradiated a spot 1 mm wide on the specimen (or in a few experiments a beam of twice this divergence and width was used). The irradiated spot covered the entire width of the specimen which was 107 mms from the slit and positioned on the diffractometer axis. High angle diffracted rays were passed through a slit 0.610 mm wide at 175 mm from the specimen and into a graphite crystal monochromator and a scintillation counter. The incident $CuK\alpha_1$ radiation diffracted from the (333) and (511) planes in the aluminum adherends produced the peak recorded in Fig. 1. The one or two constant angles chosen were located about 0.40° from the maximum on the peak.

RESULTS WITH LAP JOINTS

Fig. 2 is a plot of results with the constant angle technique (2): counts per second (CPS) with a load of 10 lbs minus CPS for a load of 400 lbs applied to 1/16" (1.588 mm) thick strips of aluminum (6061-T6) and plotted vs. the X-rayed position on the specimen. The adhesively bonded single lap joint had a teflon debond built in. The 10 lb load was used to assure firm seating of the specimen in the grips and firm centering of the specimen on the diffractometer. The plotted intensities thus represent the effect of an increase in load of 390 lbs, which amounts to a change in stress in each single strip of 7.6 ksi (52.4 MPa). Increasing stress at the surface of the aluminum causes a decrease in the 10 lb minus 400 lb CPS, corresponding to an increase in the diffraction angle and a decrease in interplanar spacing of atomic planes parallel to the surface since these planes were the ones reflecting. The incident beam was collimated to 0.25° and was 1 mm wide at the specimen.

The surface stress in the upper adherend of Fig. 2 decreases as the bond is approached, because of the elastic bending which tends to throw the X-rayed surface into compression. This bending stress reaches an abrupt maximum at the edge of the bond as expected[4] and the CPS reaches a very sharp minimum here, showing that this X-ray method can locate the edge of the bond with an accuracy about equal to the width of the X-ray beam. Bending stresses also extend throughout the bonded area as can be seen in a rubber model such as the one reproduced in Fig. 3, and are superimposed on the stresses that would be transferred from one adherend to the other if bending was absent.

Figure 4 records a similar experiment on thinner aluminum strips, with data from each of the adherends. The results of Fig. 1 and the conclusions regarding the stress components arising from bending were confirmed. Again the limits of the bonded area are well marked. In this experiment merely the 400 lb count rate was measured at constant angle. The beam width was 1 mm. Irregularities in the curve within the bonded area are seen which may indicate bond defects, but no other NDE method is yet available to us to check this possibility. The 400 lb load corresponded to double the stress in each adherend that was used for Fig. 2.

The main features shown in Figs. 2 and 4 were also obtained in experiments with the sample of Fig. 2 in which the diffraction peak shifts were determined by technique (1), 5 point parabola fitting. This technique is more laborious than the constant angle technique and fewer data points were obtained, so that evidence regarding irregularities in the bond was inconclusive. However, the minima in count rate at bond limits were clearly present.

Fig. 5 records results with a 1/16" thick aluminum adherend joined to a 6-ply unidirectional graphite/epoxy laminate adherend in which aluminum powder was embedded between the first and second plies nearest the X-rayed surface. Technique (2a) was used, with CPS at 10 lbs minus CPS at 400 lbs load, and with a 1 mm wide beam. The curve of beam intensity (counts in 40 seconds) for the aluminum adherend again shows the minima at bond limits and some unidentified irregularities

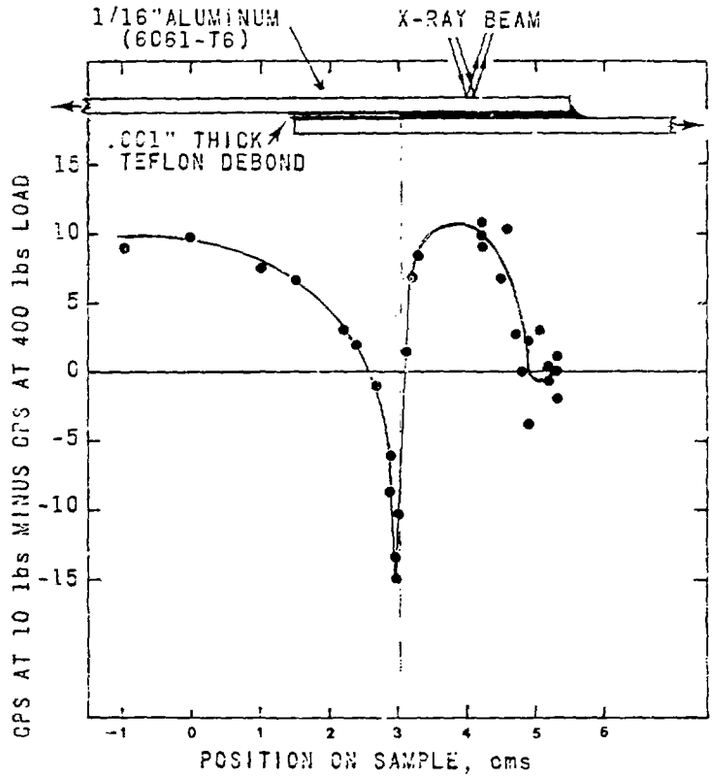

Fig. 2. Counts per second (CPS) vs. position for adhesive joint between aluminum strips 1/16" thick, with teflon debond. Constant angle method, with change in load of 390 lbs (7.6 ksi, 52.4 MPa). Increasing CPS at 10 lbs minus CPS at 400 lbs corresponds to increasing longitudinal tensile stress

Fig. 3. Rubber model of an adhesive joint with load applied, showing bending of the adherends

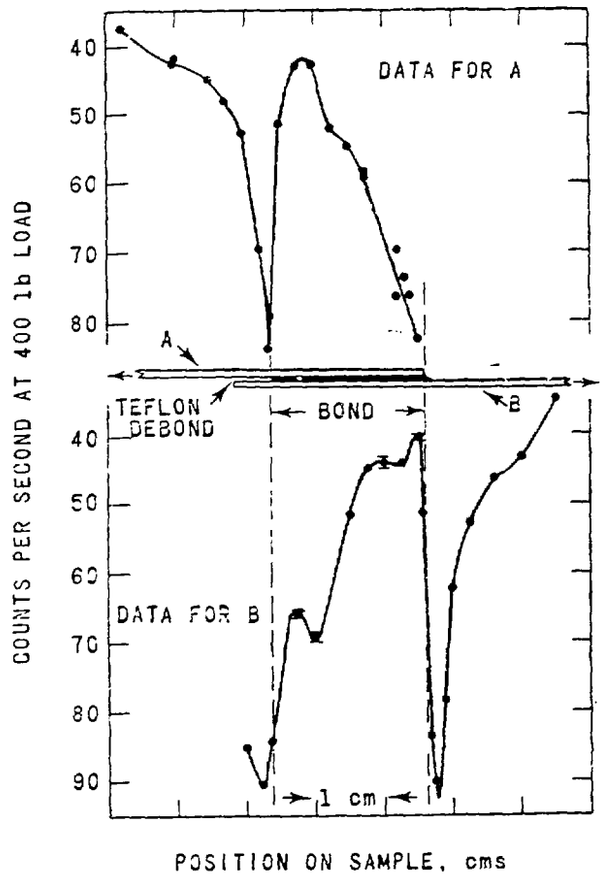

Fig. 4. Diffracted intensities for surfaces A and B of adhesively bonded 1/32" thick aluminum strips. Longidutinal tensile stress increases with decreasing count rate. Constant angle method with 400 lb load.

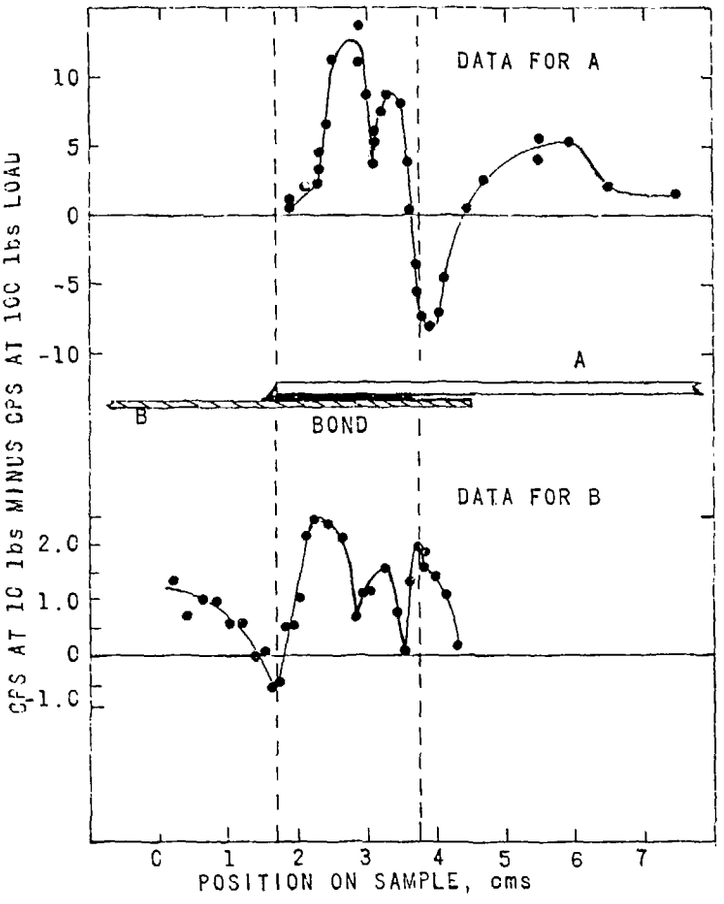

Fig. 5. Diffracted intensities for a 1/16" aluminum strip joined to a 6-ply unidirectional graphite/epoxy composite. Constant angle method.

within the bond. But the data from the aluminum-filled graphite/epoxy are very irregular. Only the minima opposite the end of the aluminum strip and the end of the bond to the composite are prominent.

Fig. 6 shows results from constant angle technique (2) on 1/32" strip bonded to the 6-ply graphite/epoxy laminate and loaded to 400 lbs. The surface stress distribution in the aluminum adherend implied by the upper plot is drawn as a solid line in the lower plot and is compared with a schematic dot-dash curve representing the stress that would be expected in the absence of any bending, if averaged throughout the thickness of the adherend. The displacement of the solid line to lower tensile stress than the dot-dash line corresponds to the stress component from bending, which is longitudinal compressive. The solid line lies above the dot-dash line where bending contributes a longitudinal tensile component. The rubber model of Fig. 3 illustrates these bends in a matched joint; Fig. 6, however, is an unmatched joint with the modulus of the composite much greater than that of the aluminum. The horizontal portion of the dot-dash lines in Fig. 6 represent the CPS obtained from a single aluminum strip, unbonded, subjected to the same load, without bending stresses.

The following paragraphs review briefly some of our research currently underway that is related to the subjects presented here.

STRESS MEASUREMENT WITH DIFFRACTING PAINT

Another X-ray method is being developed that appears to be viable for measuring applied (not pre-existing residual) stresses, and for mapping their distribution around a joint. A thin layer of epoxy paint containing a silver filler was applied to an aluminum specimen and cured. Diffraction from this paint yielded shifts in diffraction angle approximately proportional to the magnitude of applied stresses. A diffracting paint containing a diffracting filler, such as aluminum or silver powder, can be used on an object that diffracts poorly or in which a filler has not previously been embedded. The accuracies attainable in stress values in this way are apparently somewhat lower and are being investigated further. When a diffracting paint was applied to the aluminum adherend of a single lap joint and a load was applied, the limits of the bonded area were disclosed by the shifts in the diffraction angle. The onset of delamination as loads were increased was observed in a tensile

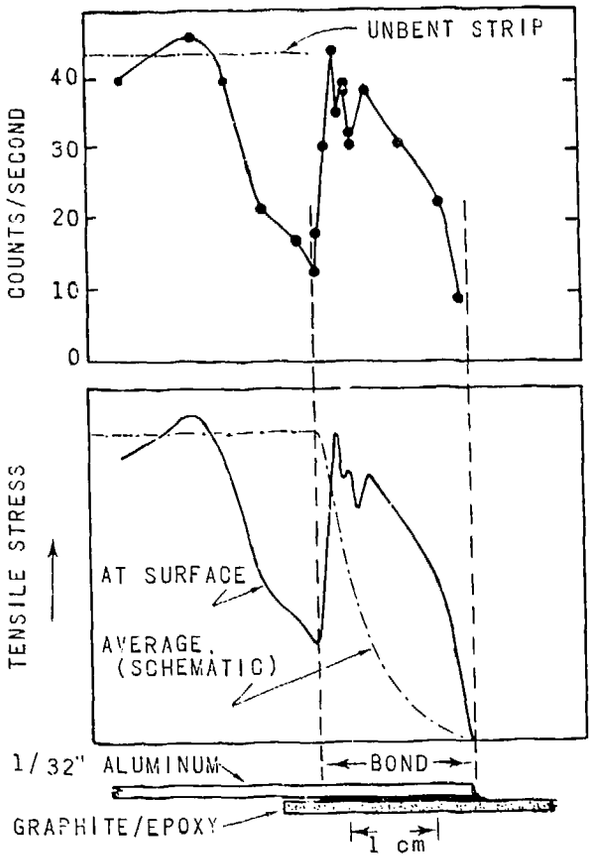

Fig. 6. Adhesive joint between 1/32" aluminum and 6-ply graphite/epoxy unidirectional composite. Upper plot: aluminum diffraction in counts per sec by constant angle method. Lower plot: surface stresses from the diffraction data compared with average stress throughout adherend cross section in the absence of bending (dot-dash line, schematic)

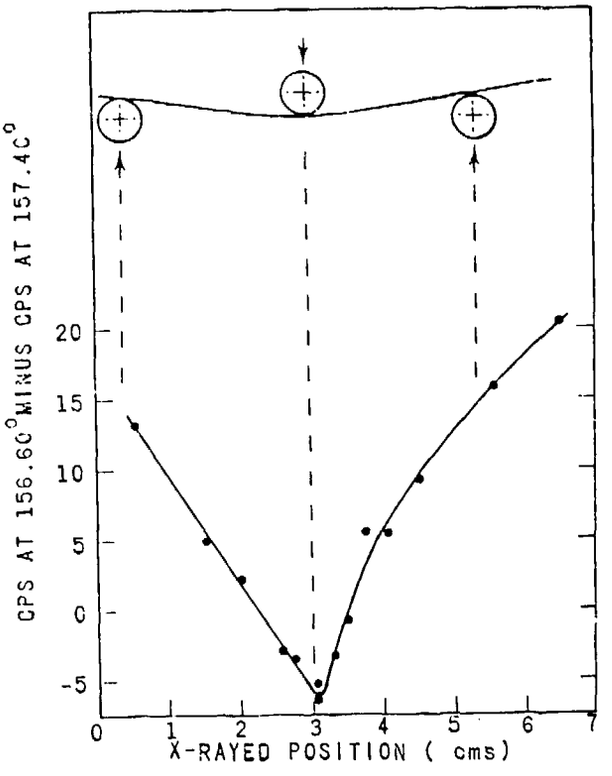

Fig. 7. Diffracted intensities vs. position on 6-ply graphite/epoxy composite after 3-point bending to initial fracture in jig sketched at the top. Constant angles method. Embedded silver powder. X-ray beam 2 mm wide.

experiment on a single composite sample. This method appears, therefore, to be useful for mapping the areas that are properly bonded and associated bending stresses and possibly for non-destructive evaluation of bond defects and of delamination. Further discussion of the method is scheduled for presentation at the 1980 Denver X-ray Conference and inclusion in its proceedings (Advances in X-Ray Analysis, vol. 24).

DETECTION OF DAMAGE IN POLYMERIC COMPOSITES

Our earlier work had suggested that if the filler yield point in a polymer composite was sufficiently low, areas of the composite where applied loads had exceeded the filler yield should be detectable from X-ray measurements of the residual stresses in the filler. A rapid test of this possibility was made by locally deforming a 6-ply unidirectional graphite/epoxy sample in 3 point bending in a jig sketched in Fig. 7. The sample contained Ag filler between the first and second ply on the X-rayed side of the bend. The deflection was increased until the first crack was heard. The sample was immediately removed, and was X-rayed on the compression side 24 hrs later and again 48 hrs later. There was no visual evidence of damage or residual bend anywhere on the compression side, but on the tension side there was a 1.5 cm longitudinal split and a short (2 mm) transverse crack and delamination. The delamination was shallow and not in the plane of the filler particles. The effects on the diffraction angle caused by the deforming were large and clearly showed the region where bending had taken place, with a maximum at the position of the sharpest bend and with effects extending well beyond the crack on the compression side, as shown in Fig. 7. A decrease in CPS in Fig. 7 corresponds to an increase in longitudinal residual tension in the filler.

Since these results show that this method has potential for revealing something of the stress history of composites and for detecting damage, it is being studied further and will be discussed in greater detail elsewhere.

ACKNOWLEDGMENT

This research is supported by the Air Force Office of Scientific Research under grant #77-3284. We are pleased to acknowledge stimulating and helpful discussions with individuals in AFOSR and in Naval Air Systems Command, also J. Toth and Terrell Campbell of Martin-Marietta Denver Division, John Hart-Smith of McDonnell Douglas Corp., and Frank Crossman of Lockheed Research Laboratory.

REFERENCES

1. C. S. Barrett and Paul Predecki, "Stress Measurement in Polymeric Materials by X-Ray Diffraction," Polymer Eng. & Sci., Vol. 16, p. 602, 1976.

2. Paul Predecki and Charles S. Barrett, "Stress Measurement in Graphite/Epoxy Composites by X-Ray Diffraction from Fillers," J. Comp. Mat. 13 61-71, 1979.

3. Charles S. Barrett and Paul Predecki, "Stress Measurement in Graphite/Epoxy Uniaxial Composites by X-rays," Polymer Composites, vol. 1, No. 1, Sept. 1980, in press.

4. L. J. Hart-Smith, "Adhesive-bonded Joints for Composites--Phenomenological Considerations" in Advanced Composites Technology, Technology Conference Associates, P.O. Box 842, El Segundo, Calif. 90245, March 14-16, 1978, pp. 163-173.

5. L. J. Hart-Smith, "Analysis and Design of Advanced Composite Bonded Joints," NACA CR-2218, August, 1974.

STUDY PROGRAM FOR ENCAPSULATION MATERIALS INTERFACE FOR LOW-COST SOLAR ARRAY (LSA)

D. H. Kaelble and C. L. Leung
Rockwell International Science Center

and

J. Moacanin
Jet Propulsion Laboratory

ABSTRACT

The early validation of a 20 year service integrity for the bonded interfaces in low cost solar arrays is an important requirement in the Low Cost Solar Array (LSA) project.

An atmospheric corrosion model has been developed and verified by five months of corrosion rate and climatology data acquired at Mead, Nebraska LSA test site. Atmospheric corrosion monitors (ACMs) installed at the Mead test site showed that protection of the corroding surface by the encapsulant is achieved independent of climatology variations.

A newly designed Mead climatology simulator has been developed in laboratory corrosion studies to clarify corrosion mechanisms displayed by two types of LSA modules at the Mead test site. Controlled experiments with identical moisture and temperature aging cycles showed that UV radiation causes corrosion while UV shielding inhibits LSA corrosion.

The implementation of AC impedance as a NDE monitor of environmental aging in solar cell arrays has also been demonstrated.

MEADCLIMATOLOGY AND CORROSION MONITORS

Two atmospheric corrosion monitors (ACM) were installed at the Mead, Nebraska site. One corrosion sensor is bare so as to represent a corrosion response in the absence of encapsulated protection. The second corrosion cell is covered with 2 mm SYLGARD 184 encapsulant over a reactive primer GE-SS4155. The output of the corrosion monitors is connected into the data acquisition system at Mead. Inspection of Fig. 1 shows that the unprotected ACM corrosion current rises and falls as a direct function of both relative humidity (RH) or moisture supersaturation temperature (T_D-T) during high moisture conditions. Conversely, precipitation produces no special corrosion response not already related to atmospheric moisture saturation level.

The curves of corrosion current ($\log_{10}$ I) versus supersaturation temperature. (T_D-T) shown in Fig. 2 clearly indicate the reversible transition in corrosion rate with level of moisture supersaturation for two cycles of condensation and subsequent surface drying.

A corrosion model has thus been developed, as shown in Fig. 3. The model relates the condensation probability, P_c, to the magnitude of the diffusion controlled corrosion current, I. As shown in Fig. 2, with increasing supersaturation temperatures (T_D-T), the corrosion current displays an upper limiting current I ≈ 15 μA. Referring to Fig. 3, this upper limiting current refers to the condition where condensation probability P_c = 1.0 and the current equals the limiting diffusion current I = I_L.

MEAD CLIMATOLOGY SIMULATOR

The laboratory apparatus constructed to achieve Mead corrosion simulation is shown in Fig. 4(A). This table mounted apparatus consists of two Haake Type K41 thermal regulators (-20°C to 100°C) with liquid circulation. The rear Haake unit circulates thermostatted liquid to the rear copper surface of the corrosion cell, as shown in Fig. 4(B). The liquid temperature of this rear Haake unit and the corrosion cell face is programmed to follow the 3 hour cycles of alternate T_1 = 344K and T_2 = 268K as shown in Fig. 5 by the cam driven West controller affixed to the lower front table surface. The front Haake unit is set at constant elevated temperature T_3 > 307K for conditioning the alternating moist (100% RH) and dry (≈ 0.016 RH) air streams which pass through the corrosion cells. A time selector valve set for six hour intervals switches the air stream from moist to dry air every six hours.

Figure 4(B) shows a close-up view of the corrosion cell. In this view two Solarex cells are thermally attached to the copper back plate of the corrosion cell using thermally conductive thermocote joint compound. The upper Solarex test cell is covered by opaque aluminum foil to prevent direct irradiation by a medium pressure mercury arc lamp.

The different aging effects produced by one month of continuous exposure in the Mead corrosion simulator are shown in Fig. 6. Figure 6(A) shows four encapsulated Solarex solar cells. The upper two Solarex cells were aged in the Mead simulator for one month with the right cell exposed to UV and the left cell shielded from UV. The lower two Solarex cells were cut from a panel aged at Mead for approximately two years. Inspection of Fig. 6(A) shows that the upper right Solarex cell which

was exposed to UV irradiation in the Mead simulator, shows the characteristic staining of the metallized collector as shown by the lower two Solarex cells with two years Mead site exposure. The UV protected Solarex (upper left) retains the metallic luster on all metallized areas indicative of corrosion inhibition by UV protection.

Figure 6(B) shows four Sensor Tech solar cells aged in the Mead simulator for one month. The two left Sensor Tech cells were shielded from UV exposure while the two right cells were exposed to UV. A point source of light focused on the solar cells from near the camera lens shows the higher level of light reflection and loss of efficiency of the anti-reflection coating in the UV exposed right Sensor Tech cells. This loss of anti-reflection efficiency and bleaching of anti-reflection coating of the Sensor Tech cells is a prominent aging characteristic shown for Sensor Tech modules aged naturally at the Mead test site.

The solar cells shown in Fig. 6 were continuously monitored while in the Mead simulator for photovoltaic responses as well as front and back face temperatures. These data were recorded on the multichannel printing recorder shown in the center of Fig. 4(A). Three typical temperature traces recorded by the simulator over a six hour control cycle are shown in Fig. 7. The upper and lower curves of Fig. 7 show the recorded analog signals of short circuit current for the respective UV exposed (upper) and UV shielded (lower) Sensor Tech solar cells. The three temperature curves of Fig. 7 show good heat transfer at the solar cell back surface and maximum thermal gradient through the cell thickness to 10-12°C at the simulation temperature extremes.

AC impedance tests were conducted at various points in the one month Mead exposure experiments. The data summary of Table 1 shows the effects of one month Mead simulation on AC impedance properties. The UV shielded Solarex test cell is unchanged in the AC impedance properties while UV exposure results in a measured increased in shunt resistance. The capacitance of both UV increased by Mead simulation aging while shunt resistance values are only lightly diminished as in lower Table 1. Sensor Tech solar cells are shown in Table 1 to display much higher shunt resistance values than the Solarex solar cells.

CORROSION MECHANISMS AND MATERIAL RECOMMENDATION

Auger electron spectroscopy (AES) has been used to determine the composition of the interfacial region between the encapsulant and the solar cell. To perform the AES analysis, the encapsulant was removed from the support materials, as shown in Fig. 8.

Auger analysis was performed both on the surface as removed and also after sputtering to various depths by argon ion bombardment. An example of the type of spectra obtained is shown in Fig. 9 and 10. Figure 9 is a spectrum taken from the silicon surface of a virgin Sensor Tech cell. The SiO_x anti-reflection coating is observed as well as P, C, Sn and Na. Figure 10 is the spectrum taken after 60 A has been removed by sputtering. Only SiO_x is observed indicating that the contaminating species are only several monolayers thick.

No environmental contaminants were detected on the silicon surface of the Solarex cells which were aged at Mead. Carbon was observed throughout the Ta_2O_5, resulting from the deposition process. However, the metallization of these cells had a layered structure. The upper layer, approximately 50 A in thickness, was a mixture of silver chloride and silver sulfide. Beneath this salt layer there was a 300 A layer rich in silver but also containing moderate amounts of sulfur and chloride. The silver-rich layer as well as the Ta_2O_5 coating contained large amounts of iron. These layers were on top of the Ta_2O_5 anti-reflection coating. Figure 11 shows the Auger spectrum from the surface of the salt layer; Fig 12 is the spectrum after 300 A have been removed by sputtering.

SUMMARY

1. An atmospheric corrosion model has been developed. The model predicts the corrosion rate as controlled by surface condensation and diffusion limited currents.

2. A Mead site climatology simulator has been developed to reproduce Mead climatology at 3 hour cycles with in situ AC impedance and I-V monitoring of single cells.

3. Two independent, materials related corrosion mechanisms have been identified for Sensor Technology and Solarex cells.

ACKNOWLEDGEMENT

This project is performed by the Science Center for the Jet Propulsion Laboratory, California Institute of Technology, under JPL Subcontract 954739. The JPL Low-Cost Silicon Solar Array Project is sponsored by the Department of Energy and forms part of the Solar Photovoltaic Conversion Program.

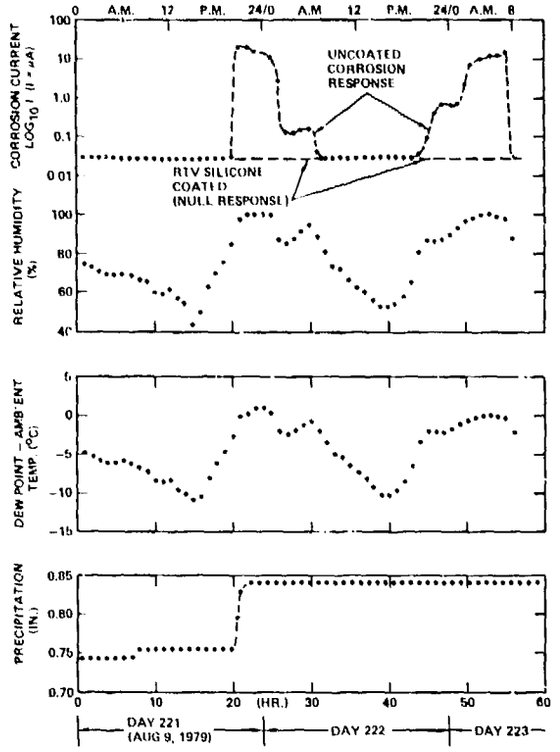

Fig. 1 Mead site moisture and rain climatology.

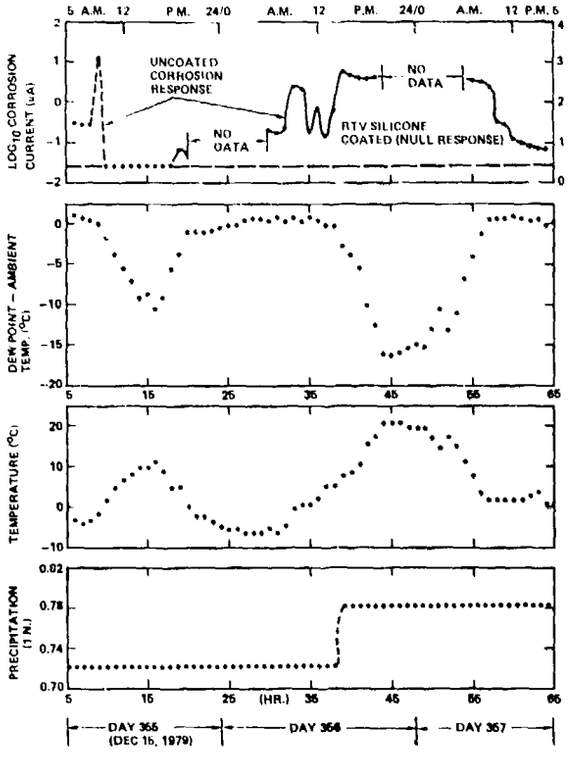

Fig. 2 Mead site freeze-thaw climatology.

(1) CONDENSATION PROBABILITY (P_C):

$$P_C = \frac{I}{I_o} = \exp\left[\frac{-1.756 \cdot 10^{22} \cdot \phi \cdot \nu^2 \cdot \gamma_{LV}^3}{T^3 (\ln P/P_o)^2}\right]$$

WHERE
- ϕ = WETTABILITY PARAMETER
- ν = WATER MOLAR VOLUME
- γ_{LV} = LIQUID-VAPOR SURFACE TENSION
- T = KELVIN TEMPERATURE
- P = LIQUID VAPOR PRESSURE
- P_o = SATURATED LIQUID VAPOR PRESSURE
- I = RATE OF CONDENSATION (DROPS/M^3S)
- I_o = MAXIMUM RATE OF CONDENSATION

Fig. 3 Corrosion model

(2) DIFFUSION CONTROLLED CORROSION:

$$I = P_C \cdot I_L = P_C \cdot \frac{nFDC}{\delta t}$$

WHERE
- I = CURRENT DENSITY (AMPERES/M^2)
- I_L = LIMITING CURRENT DENSITY
- n = NUMBER OF ELECTRONS
- F = FARADAY (96500 COULOMBS/EQUIVALENT)
- D = DIFFUSION COEFFICIENT OF REDUCING ION
- C = CONCENTRATION OF DIFFUSING IONS (MOLES/M^2)
- δ = DIFFUSION LAYER THICKNESS ($\simeq 5 \times 10^{-4}$M IN STATIC SOLUTION)
- t = TRANSFER NUMBER OF ALL IONS IN SOLUTION ($\simeq$ 1.0 IF MANY OTHER IONS PRESENT)

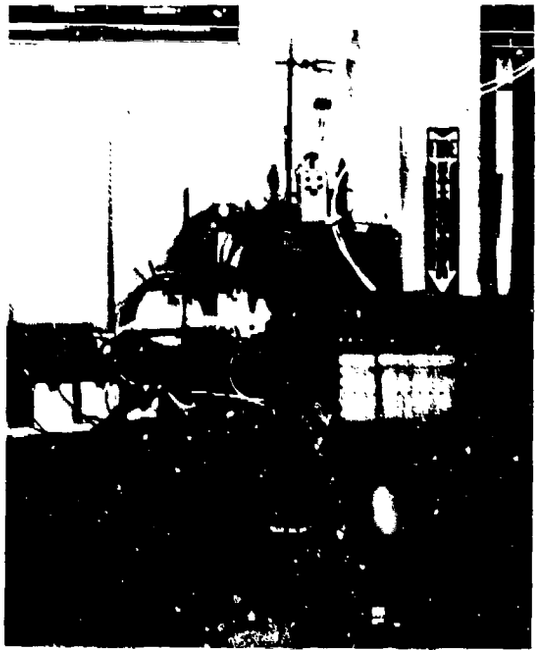

Fig. 4(A) Photoview of Mead corrosion simulator.

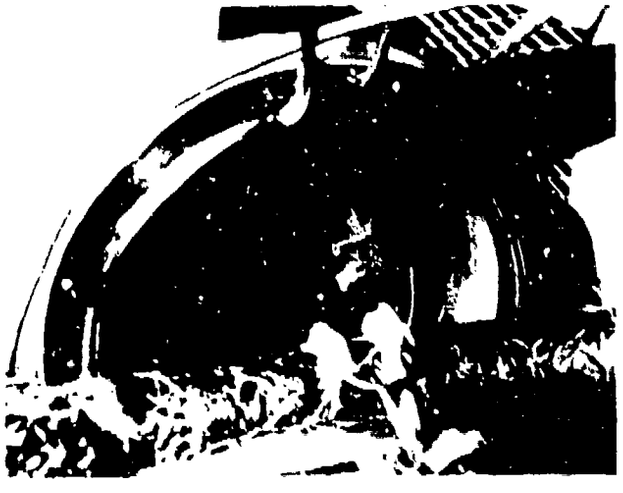

Fig. 4(B) Close view of corrosion cell with UV protected (upper foil covered) and UV exposed Solarex cells.

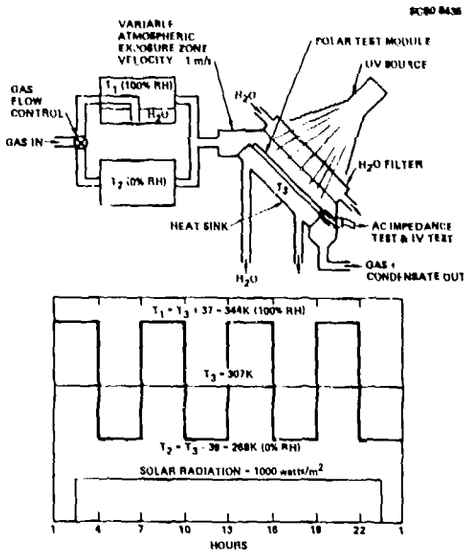

Fig. 5 Environmental solar test cell.

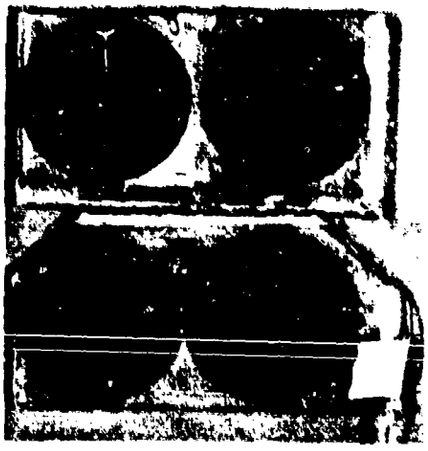

Fig. 6(A) Solarex solar cells subjected to lab simulation aging (top two with left UV protecter and right UV exposed) and Mead aged (lower 2 cells).

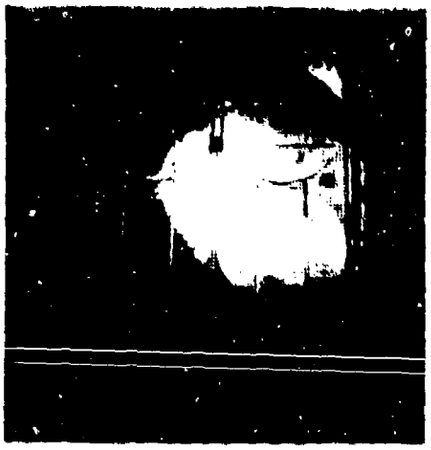

Fig. 6(B) Sensor Tech cells subjected to lab simulation aging with UV protection (left two) and UV exposed (right two).

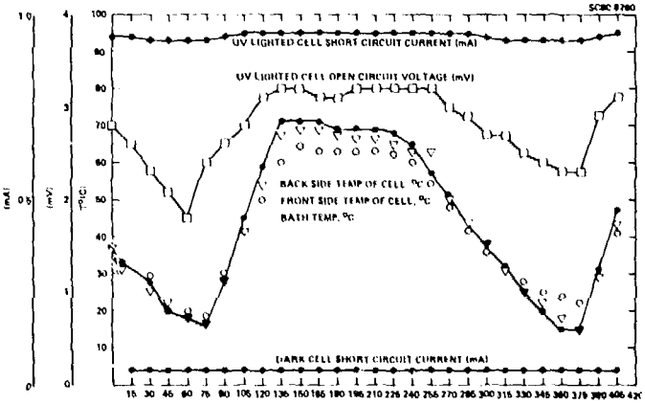

Fig. 7 Monitoring of Sensor Tech 2-cell series response in Mead corrosion simulator for a typical 7.5 hr cycle.

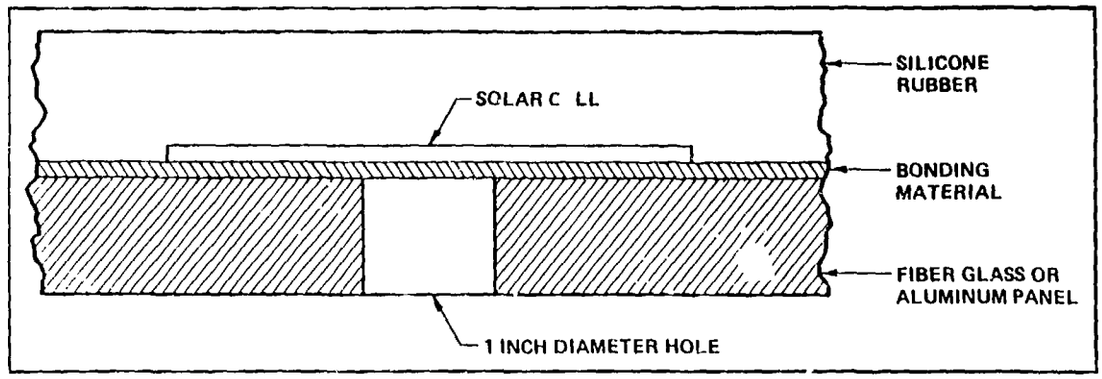

Fig. 8 Removal of silicone rubber for AES.

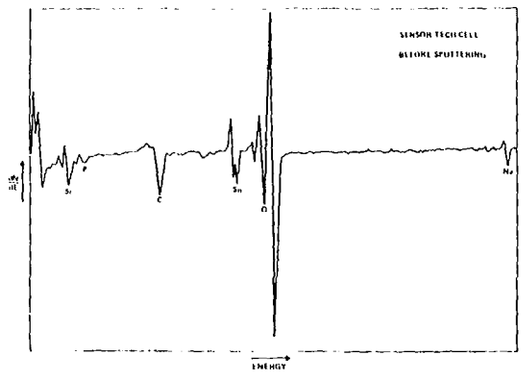

Fig. 9 Auger spectrum of silicon surface of unaged Sensor Tech module No. 5064.

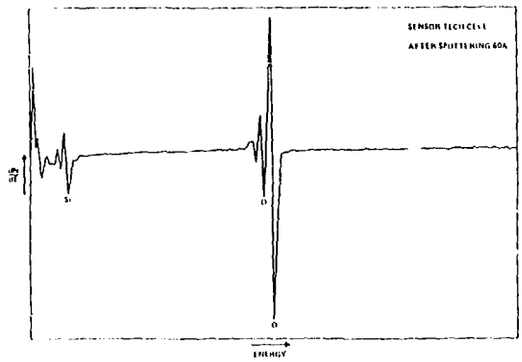

Fig. 10. Auger spectrum of sputtered (60A) silicon surface of unaged Sensor Tech module No. 5064.

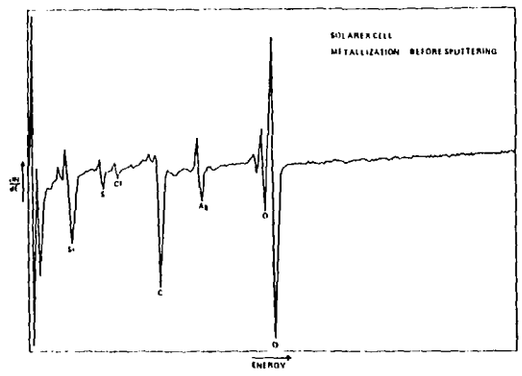

Fig. 11 Auger spectrum of metallization surface of Me:d aged Solarex module No. 0217155.

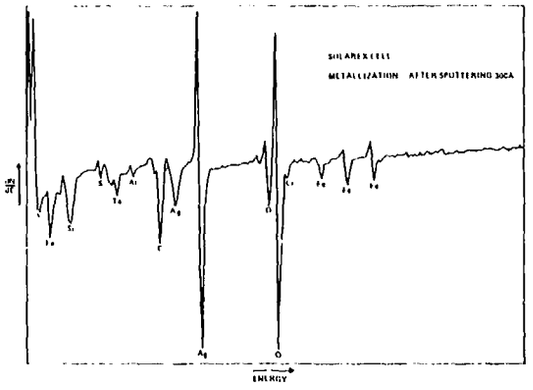

Fig. 12 Auger spectrum of sputtered (300A) metallization of surface of Mead aged Solarex module No. 0217155.

Table I

Mead Simulator Aging Effects on AC Impedance Response
(Tested in Ambient Lab Illumination)

Specimen	R_{sh} (ohm)	R_s (ohm)	C (μF)
Solarex UV shielded (single cell)			
unaged	25.5	1.0	1.48
one month Mead simulator	25.8	1.0	1.47
Solarex UV exposed (single cell)			
unaged	40.8	1.0	1.53
one month Mead simulator	47.2	1.0	1.50
Sensor Tech UV shielded (2 cells in series)			
unaged	368	*	0.21
one month Mead simulator	365	*	0.30
Sensor Tech UV exposed (2 cells in series)			
unaged	540	*	0.21
one month Mead simulator	522	*	0.27

*Small value, below detection capability

FRACTURE MECHANICS OF TWO DIMENSIONAL NONCIRCULAR FLAWS

Roger Chang
Rockwell International Science Center
Thousand Oaks, California 91360

ABSTRACT

The growth of two dimensional noncircular flaws was studied by three independent methods: transfer function analysis, equivalent area approximation, and direct fracture mechanics calculation. All three methods yield results varying within a few percent of one another for the simpler elliptical and rectangular geometries. Results of transfer function and equivalent area methods agree also within a few percent of each other for the more irregularly shaped flaws. The importance of these studies to NDE predictive technology is discussed.

INTRODUCTION

We proposed in previous communications [1,2] empirical transfer functions which convert a two dimensional irregularly shaped flaw in an isotropic elastic medium to a circular flaw of equivalent propagation lifetime. Our further studies suggest that the irregularly shaped two dimensional flaws can also be approximated by circular flaws of equivalent area. If the stress intensity factors at each infinitesimal segment of an irregularly shaped two dimensional flaw are known, direct fracture mechanics calculation of the equivalent circular flaw radius similar to that applied to an elliptical flaw [1,2] should be straightforward. The principle objectives of this investigation are to compare the results of equivalent circular flaw calculations by the three methods: transfer function analysis, equivalent area approximation, and direct fracture mechanics calculation.

REVIEW OF TRANSFER FUNCTION METHODOLOGY [1,2]

For an elliptical flaw with major axis a and minor axis b contained in an infinite isotropic elastic body, analytic expressions for the Mode I stress intensity ranges (uniaxial stress applied perpendicular to the flaw plane) are available [5], i.e.,

$$\Delta K_{Ia} = \frac{\Delta S\sqrt{\pi b}}{E(k)}\sqrt{\frac{b}{a}} \tag{1}$$

$$\Delta K_{Ib} = \frac{\Delta S\sqrt{\pi b}}{E(k)} \tag{2}$$

where ΔS is the applied stress range and $E(k)$ is the complete elliptical integral of the second kind, k being given by $\sqrt{1-b^2/a^2}$. The Mode I stress intensity range for a circular flaw of radius r is,

$$\Delta K_{Ir} = \frac{2}{\pi}\Delta S\sqrt{\pi r} \tag{3}$$

The growth rates at the extremities of the major and minor axes of an embedded elliptical flaw, da/dm and db/dm, proportional to some power of the stress intensity ranges, are, correspondingly,

$$\frac{da}{dm} = A\Delta K_{Ia}^{\alpha} = A\Delta S^{\alpha}\pi^{\alpha/2}\frac{b^{\alpha}}{a^{\alpha/2}E^{\alpha}(k)} \tag{4}$$

$$\frac{db}{dm} = A\Delta K_{Ib}^{\alpha} = A\Delta S^{\alpha}\pi^{\alpha/2}\left(\frac{b^{\alpha/2}}{E^{\alpha}(k)}\right) \tag{5}$$

$$\frac{dr}{dm} = A\Delta K_{Ir}^{\alpha} = A\Delta S^{\alpha}\pi^{\alpha/2}\,(2^{\alpha}r^{\alpha/2}/\pi^{\alpha}) \tag{6}$$

where A and α are environmental dependent material constants and m is the fatigue cycles. In fracture mechanics of engineering materials, α, the Paris exponent, may vary between 2 to 4. The actual value of α will not affect the transfer function methodology approach outlined below.

The growth of a and b are calculated incrementally with Eqs. (4) and (5), until b_f (final dimension of b after f increments) is within a fraction of one percent of a_f (final dimension of a after f increments). The elliptical flaw has now grown into a circular one of radius a_f. Knowing a_f and f, the equivalent initial circular radius r is obtained incrementally in the same time domain according to Eq. (6), starting with $r_f = a_f \cong b_f$. This method is almost exact and becomes increasingly more accurate with finer fatigue increments. Results for r/b versus various a/b ratios (varying between 1 and 11) after 100 increments are shown in Fig. 1 (full curve). After 100 increments, b_f is within 0.1 percent of a_f for all the a/b ratios studied.

The relationship between r/b (equivalent circular flaw of radius r divided by the minor axis of elliptical flaw) and shape of the elliptical flaw is expressed empirically by,

$$\frac{r}{b} = \int_S \sum g_i f_i(R)\, dS \tag{7}$$

where $f_i(R)$ is some arbitrarily chosen mathematical function of the radial distance R from the centroid of the flaw to the infinitesimal circumferential segment dS and g_i is the coefficient of the function f_i. Equation (7) can be approximated by the following summation.

$$\frac{r}{b} = \sum_S \sum_{i=1}^{i=n} g_i f_i\, \Delta S \tag{8}$$

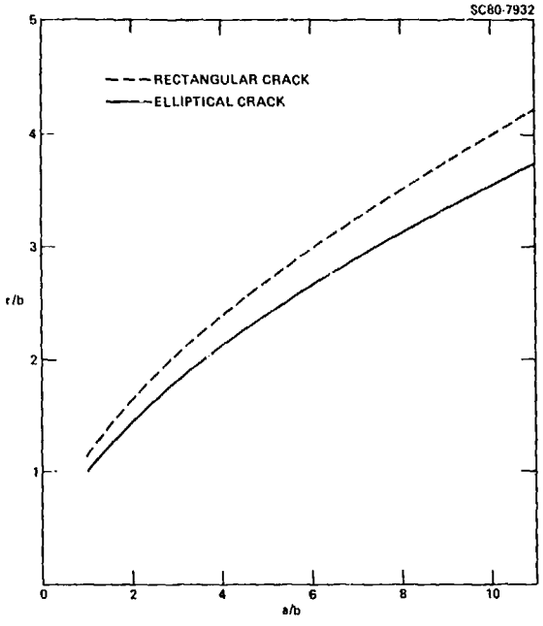

Fig. 1 Transposition plots converting noncircular flaws into equivalent circular flaws (full curve, elliptical flaws of major axis a and minor axis b; dotted curve, rectangular flaws of sides 2a, 2b).

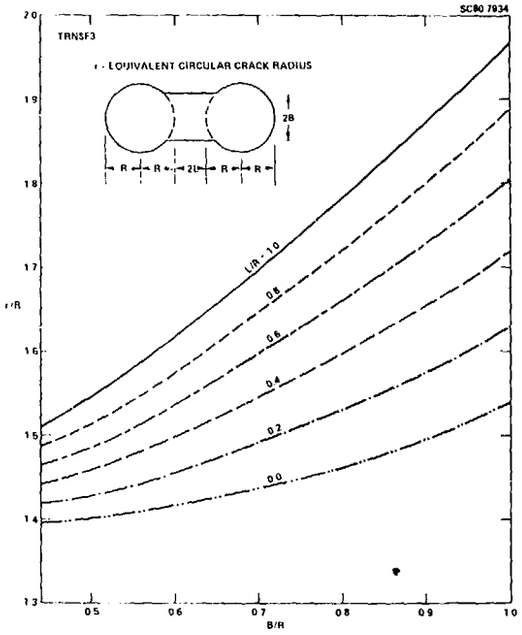

Fig. 2 Same as Fig. 1, symmetric dumbbell flaws of various dimensions.

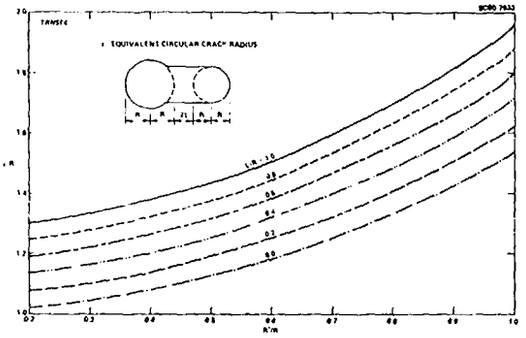

Fig. 3 Same as Fig. 1, asymmetric dumbbell flaws of various dimensions.

where Σ means summation over the circumference of the flaw and n is an integer.

The transfer function given by Eq. (8) for elliptical to circular flaw conversion was applied to nonelliptical flaws. The coefficients g_i were solved by a method similar to Fourier inversion from the fracture mechanics data for elliptical to circular flaw conversion (solid curve of Fig. 1). Equation (8) with these known coefficients was used to estimate the equivalent circular flaw radius of rectangular, symmetric dumbbell and asymmetric dumbbell flaws. The results are summarized in Fig. 1 (rectangular, dotted curve), Fig. 2 (symmetric dumbbell) and Fig. 3 (asymmetric dumbbell), respectively, which are self-explanatory.

THE EQUIVALENT AREA APPROXIMATION

The results of transfer function analysis suggest that the two dimensional irregularly shaped flaws can also be approximated by circular flaws of equivalent area. The equivalent area method is of sufficient importance to NDE predictive technology worthy of more thorough investigation. We hope to do so in the near future. For ellipses of major axis a and minor axis b, the circular flaw radius (having equivalent propagation lifetime) according to the equivalent area approximation is simply $\sqrt{ab}$. We carried out direct fracture mechanics calculations of the normalized equivalent circular radius r/b according to Eqs. (1) to (6) for various aspect ratios of the ellipse (a/b varying from 1 to 11) and various Paris exponents (α = 2.5, 3.0, 3.5 and 4.0). Curves similar to the solid curve of Fig. 1 were obtained but are not reproduced here. These fracture mechanics calculations are compared with those according to the equivalent area approximation. The differences in the equivalent circular flaw radius according to the equivalent area approximation and that from direct fracture mechanics calculation, summarized in Fig. 4, are within 10 percent of each other for all the aspect ratios (a/b =1 to 11) and Paris exponents (α = 2.5 to 4.0) investigated.

NONCIRCULAR FLAWS OTHER THAN ELLIPSES

In a preceding section we used the transfer function method to estimate the equivalent circular flaw radius for noncircular flaws other than ellipses. How accurate are these estimates? To answer the question, direct fracture mechanics calculations for these nonelliptical flaws are necessary. We chose the square flaw in the present study for simplicity. The investigation was carried out in the following way: first we

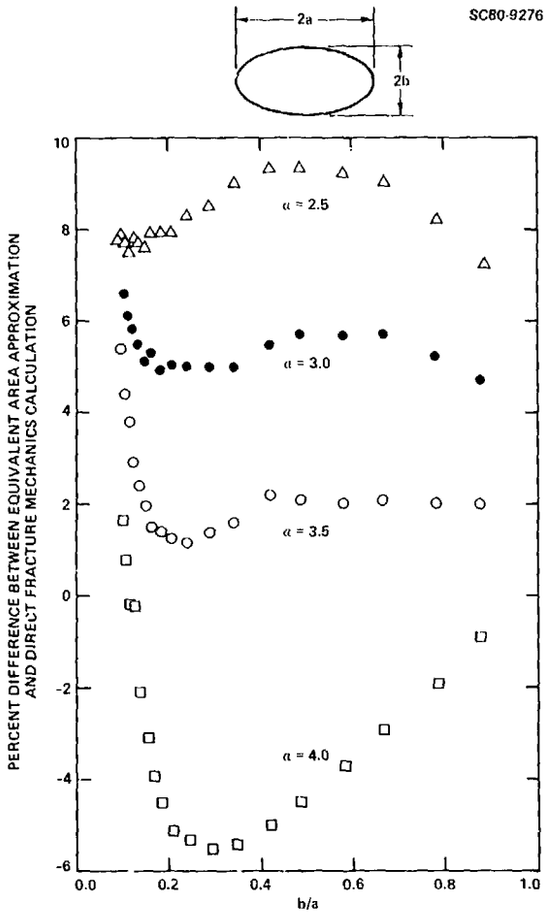

Fig. 4 Comparison of equivalent circular flaw radius results according to the equivalent area approximation and direct fracture mechanics calculations for ellipses with various a/b ratios (1 to 11) and various Paris exponents (2.5 to 4.0).

calculate the Mode I stress intensity factors at the various locations of a square flaw by means of finite element methods. The square flaw is allowed to grow according to the local stress intensity factors via the Paris crack growth equation with $\alpha = 3.5$. A new flaw geometry is generated. Mode I stress intensity factors for the flaw geometry after the first iteration are recalculated and a new flaw geometry is generated in the second iteration. These steps are repeated until the final flaw becomes almost circular. The circular flaw is allowed to shrink according to the Paris equation within the same time domain into a smaller circular one whose radius is the equivalent circular flaw radius.

FINITE ELEMENT METHODS USED TO OBTAIN STRESS INTENSITY FACTORS OF NONCIRCULAR FLAWS

Three methods have been tried. Initially, an axial-symmetric finite element method was used to estimate the ratio of stress intensity factors of square and circular flaws. The full three dimensional stress analysis employing quadratic isoparametric hexahedron elements was then used to calculate the stress intensity factors of noncircular flaws by means of crack opening displacement extrapolation along the flaw front. Both methods yield nearly identical results. Thirdly, the boundary integral equation method [6,7] was applied to our problems. For simple flaw geometries such as circles and squares, no advantage was gained with the boundary integral equation method, however.

In the axial-symmetric method we assume that the stress intensity factor ratios of a square and a circular flaw are equal to the ratios of circumferential stresses (of elements nearest the flaw front) of a cylindral and a spherical void stressed radially along the rotational axis. The stress ratio method used to obtain stress intensity factors has been discussed by the author in a previous investigation [8]. The elements used in one quadrant are shown in Fig. 5 and Fig. 6 for the spherical and cylindrical voids, respectively. Axially symmetric finite element stress analysis employing NASTRAN (NASA Stress Analysis Program) with trapezoidal and triangular ring elements was carried out for these element geometries.

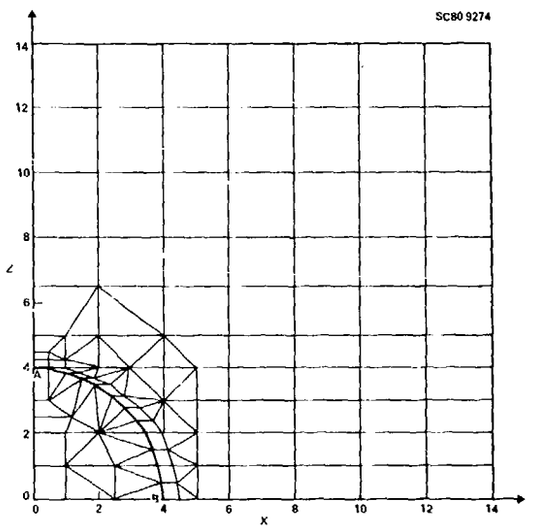

Fig. 5 Schematic nodal structure containing a spherical void for axially symmetric finite element stress analyses (one quadrant is shown, AB is void boundary).

Three dimensional stress analysis employing NASTRAN with quadratic isoparametric hexahedron elements to yield the stress intensity factors is more powerful and rigorous. A schematic of the element structure in one octant for a square flaw is shown in Fig. 7.

Results of the stress intensity factors for the square flaw (normalized against that of a circular flaw) by the two methods are plotted in Fig. 8. Data from an approximate integral equation treatment by Bui [9] are included in Fig. 8 for comparison. Our results agree with Bui's near

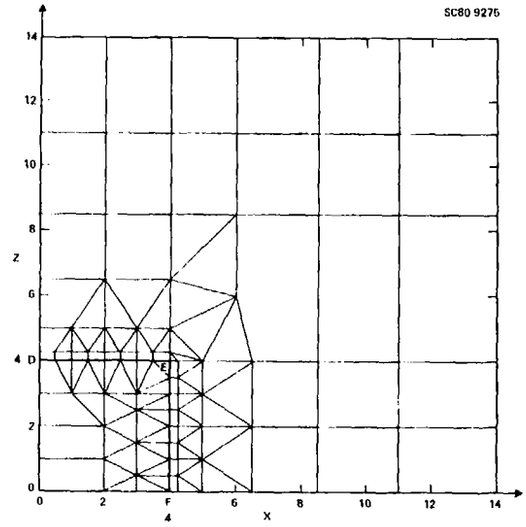

Fig. 6 Same as Fig. 5 for a cylindrical void (DEF is void boundary).

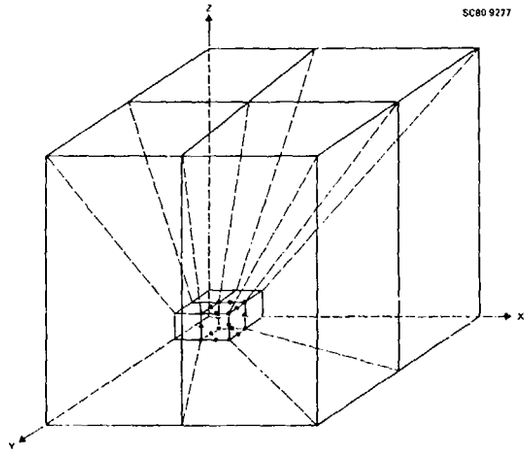

Fig. 7 Schematic nodal structure containing a square or a circular crack for three dimensional finite element stress analyses (one octant is shown; only one isoparametric element is drawn for clarity).

the corner but deviate substantially from his near the edge center of the square flaw.

LIFETIME PREDICTION FOR SQUARE FLAWS BY VARIOUS METHODS

Results of the normalized equivalent circular flaw radius, r/a, for a square flaw of sides 2a calculated fracture mechanically are compared with those estimated by the transfer function and equivalent area methods for the various Paris exponents (α = 2.0 to 4.0) in Table I.

DISCUSSION

The transfer function method and the equivalent area method show promise as convenient mathematical tools for the lifetime prediction of

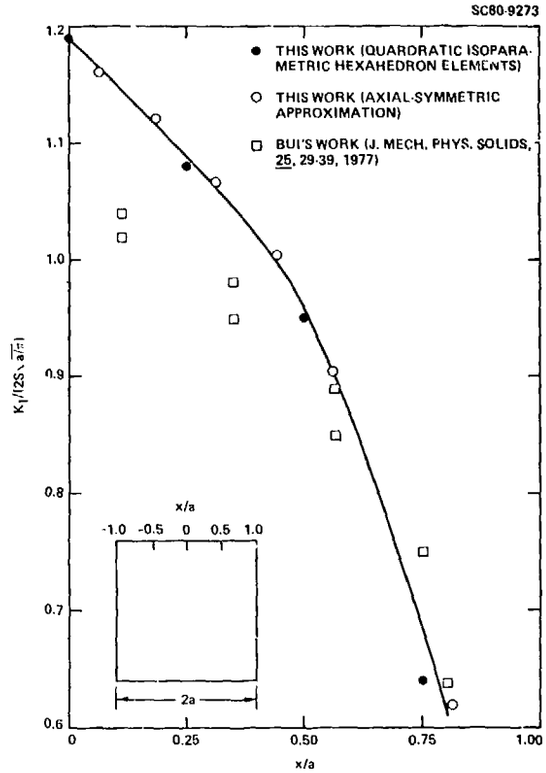

Fig. 8 Comparison of stress intensity factor calculations (rectangular vs circular flaw) by various methods (K_I is Mode I stress intensity for square of side 2a; $2S\sqrt{a/\pi}$ is Mode I stress intensity for circular flaw of radius a; S is applied normal stress).

Table I. Comparison of the Normalized Equivalent Circular Flaw Radius (r/a) by the Three Methods for Square Flaws of Sides 2a

Paris Exponent	Fracture Mechanics Calculation	Transfer Function Analysis	Equivalent Area Approximation*
2.0	1.094	1.112	1.1285
2.5	1.111	1.120	1.1285
3.0	1.126	1.128	1.1285
3.5	1.140	1.136	1.1285
4.0	1.152	1.143	1.1285

*The normalized equivalent circular flaw radius for square flaws of sides 2a according to the equivalent area method is exactly $\sqrt{4/\pi}$ or 1.1285.

irregularly shaped two dimensional flaws. The present investigation deals with simple square flaws. Further comparison of the two methods on other irregularly shaped flaws are in need to substantiate the conclusions reached in this investigation and to define the limits of application of these methods to flaw geometries beyond which they might fail.

For the simpler flaw geometry where lifetime prediction by the transfer function and/or the equivalent area method holds, direct coupling of

these methods to NDE is possible. Such work is currently under study and will be separately reported. For more complicated flaw geometries where lifetime prediction by the transfer function and/or the equivalent area method becomes inaccurate, the more direct fracture mechanics method must be used. The type of crack geometries, where we must use the more rigorous fracture mechanics method of evaluation, has not yet been ascertained. This remains to be an interesting area for future investigation. We made some preliminary comparisons of the equivalent circular flaw radius evaluation by the transfer function method and the equivalent area method for the symmetrical dumbbell flaws shown in Fig. 2. The comparison is summarized in Table II. Direct fracture mechanics evaluation of these irregular shaped flaws has not yet been carried out, however.

Table II. Comparison of Normalized Equivalent Circular Flaw Radius Evaluation by the Transfer Function and Equivalent Area Methods for the Symmetric Dumbbell Flaws (see Fig. 2, B/R = 1.0, L/R = 0.0 to 1.0).

		Normalized Equivalent Circular Flaw Radius (r/R)		
B/R	L/R	Transfer Function Method	Equivalent Area Method	Percent Difference
1.0	1.0	1.96	1.88	4.2
1.0	0.9	1.92	1.85	3.7
1.0	0.8	1.88	1.81	3.8
1.0	0.7	1.85	1.78	3.9
1.0	0.6	1.81	1.74	3.9
1.0	0.5	1.77	1.70	4.0
1.0	0.4	1.72	1.67	2.9
1.0	0.3	1.67	1.63	2.4
1.0	0.2	1.62	1.59	1.9
1.0	0.1	1.58	1.55	1.9
1.0	0	1.53	1.50	2.0

ACKNOWLEDGEMENT

This research was sponsored by the Center for Advanced NDE operated by the Rockwell International Science Center, for the Advanced Research Projects Agency and the Air Force Wright Aeronautical Laboratories under Contract F33615-80-C-5004.

REFERENCES

[1] R. Chang, "Fracture Mechanics Transfer Function for Irregularly-Shaped Two-Dimensional Flaws," Engineering Fracture Mechanics, 13, 223-226, 1980.

[2] R. Chang, "Fracture Mechanics Transfer Function for Two-Dimensional Noncircular Flaws," submitted to Journal Nondestructive Evaluation.

[3] B.R. Tittmann and R.K. Elsley in "Proceedings of the ARPA/AFML Review of Progress in Quantitative NDE," Technical Report AFML-TR-78-55, May 1978, p. 26.

[4] N.E. Paton in "Proceedings of the ARMPA/AFML Review of Progress in Quantitative NDE," Technical Report AFML-TR-75-212, January 1976, p. 89.

[5] G.C. Sih and H. Liebowitz, "Fracture, Volume II, Mathematical Fundamentals," edited by H. Liebowitz, Academic Press, 1968, pp. 68-188.

[6] T.A. Cruse, "Mathematical Foundations of the Boundary Integral Equation Method of Three-Dimensional Stress Analysis," AFOSR-TR-77-1002, Accession Number ADA 043114, July 1977.

[7] C.L. Tan and R.T. Fenner, "Elastic Fracture Mechanics Analysis by the Boundary Integral Equation Method," Proceedings Royal Society London, A369, 243-260 (1979).

[8] R. Chang, "Static Finite Element Stress Intensity Factors for Annular Cracks," Rockwell International Science Center Report SC-PP-80-50.

[9] H.D. Bui, "An Integral Equations Method for Solving the Problems of a Plane Crack of Arbitrary Shape," Journal Mechanics and Physics of Solids, 15, 29-39 (1977).

FLOW DETECTION IN UNDERLYING STRUCTURE - PROBLEMS AND OPPORTUNITIES

J. A. Moyzis, Jr.
Materials Laboratory
Wright-Patterson A.F.B., Ohio

ABSTRACT

Over the last few years a number of R&D programs have been funded by the Materials Laboratory with the object of developing ultrasonic and eddy current techniques for the reliable detection of fatigue cracks in the underlying layers of multi-layer structure. This paper will present a survey of these efforts, discuss the successes achieved and the problems that still remain in this important inspection field.

NONDESTRUCTIVE EVALUATION (NDE) FOR THERMAL-SPRAY COATINGS

Robert A. Sulit, Force Engineering Advisor (N43A)
Naval Surface Force, U.S. Pacific Fleet
San Diego, CA 92155

and

Vincent D. Schaper, Welding Engineer (2803)
David W. Taylor Naval Ship R&D Center
Annapolis Laboratory
Annapolis, MD 21402

THERMAL-SPRAY DEFINITION AND CLASSIFICATION[1]

Thermal spray is the process of depositing metal, alloy, and ceramic coatings on properly prepared substrate materials so that they solidify on and bond mechanically, chemically, and metallurgically to the substrate materials. Thermal-spray coatings are applied to improve surface-wear characteristics, to provide resistance to heat, oxidation, and chemical environments; to restore dimension to the original equipment manufacturer's (OEM) specifications; to reduce erosion wear; and to improve corrosion control.

The authorized use of the thermal-spray processes in the Navy are specified in acquisition and OEM drawings for new equipment; in Technical Repair Standards or TRS's for the naval shipyards.

There are several different thermal-spray processes, they can be conveniently classified by the heat source and the physical form of the material being sprayed. The oxy-fuel or the combustion systems are capable of thermally spraying metal, alloy, and ceramic powders in powder guns; wire in wire guns; and ceramic materials when they are packed into rods or cords and sprayed in wire guns. The electric-arc gun sprays wire materials; and the arc-plasma and the "Union Carbide proprietary" detonation-gun processes sprays powder materials only.

The oxy-fuel temperatures of around 3500°F to the 15K to 30K°F temperatures of the arc-plasma processes gives a full range of thermal sources to melt and atomize all known materials. In addition to the high-temperature capacity, the thermal-spray equipment is designed to propel the atomized spray materials onto the substrate at high velocity. The coating materials must have a plastic range of at least 100 to 150°F.

The impact velocity of the sprayed material on to the substrate is directly related to the coating density, hardness, and bond or tensile strength of the coating to the substrate. The oxy-fuel powder-spray gun has an impact velocity of about 80 to 100 ft/sec and produces the lowest density, hardness, and bond of the thermal-spray processes. The oxy-fuel and electric-arc wire gun have an impact velocity ranging from 1600 to 2000 ft/sec when spraying at atmospheric pressures; about 2200 to 2400 ft/sec, equivalent to the detonation gun, when arc-plasma spraying at partial vacuum of about 50 torr (50 mm of Hg).

Although the heat required for thermal spraying is generally supplied by fuel gas or electricity, one material, a mixture of nickel and aluminum, has been developed to provide additional heat when sprayed. When heated in the gun, nickel and aluminum combine chemically releasing a significant amount of exothermic energy which is added to the heat produced by the gun. The result increases the bond strength as much as ten-fold when used in an oxy-fuel powder-spray gun approaching that obtainable with the arc-plasma spray process.

The wide range of coating materials and thermal-spray processes gives the materials engineer the opportunity to design a coating system to maximize equipment and component service life, restore dimensions, improve the wear, and decrease erosion and corrosion characteristics of hull, mechanical, and electrical (HME) components; these coatings can be applied during original equipment manufacture or during their repair and overhaul. The simpler combustion gun and wire processes are used at intermediate maintenance activities (IMA), i.e., tenders, repair ships and shore IMA's (SIMA's); the arc-plasma system is used at industrial activities as naval shipyards.

SERVICE APPLICATIONS

Wear Coatings and Restoration of Dimensions - Thermal-spray coatings can be applied to buildup worn or mis-machined parts and to improve abrasion resistance. They are not intended to fill gouges or similar localized damage without building up the entire area. Thermal-spray deposits do not restore properties such as tensile strength or resistance to fatigue stresses. However, under compressive loading conditions, they can exceed the original properties. MIL-STD-1687 (SH) approves the following thermal-spray coatings:[2]

"a. Repair of seal (packing) areas of shafts used in oil and fresh water systems to obtain original dimensions and finish.

b. Repair of bearing interference fit areas of shafts to restore original dimensions and finish (except for motors and generators where chrome plating is permissible).

c. Buildup of pump shaft wear ring sleeves to original dimensions.

d. Repair of miscellaneous static fit areas, such as those on electric motor end bells, to restore original dimensions, finish and alignment."

CORROSION CONTROL

The Navy has been using wire sprayed aluminum (WSA) as a high performance marine corrosion-control system for a wide range of shipboard components and spaces on the weather decks and interior spaces. The WSA-preservation system consists of a 0.007 to 0.010 inch of WSA applied over a clean white substrate abrasive blasted with angular grit as aluminum oxide to a 0.002 to 0.003 inch "anchor-tooth" and then sealed with an appropriate organic paint or primer. Large scale use of the WSA-preservation system began with the preservation of steam valves in 1977 and it is now being used routinely in the maintenance and overhaul of many shipboard components and spaces where the conventional paint systems have not been effective. WSA is also being used in new ship construction.

NONDESTRUCTIVE EXAMINATION

We know of no NDE technique suitable for assessing the quality of thermal-spray coatings in the shop and production environment. Current quality assurance procedures being used are:

1. Process control, i.e., spray within the process parameters which have been previously qualified through destructive examination.

2. Coupon analysis, i.e., preparing and spraying a coupon in like manner to that of the production component and conduct destructive tensile, hardness, and/or metallographic examination of the coupon sample.

NDE REQUIREMENTS

Need NDE techniques, equipment, and procedures suitable for intermediate- and depot-level shop repair work and their quality assurance personnel to quantitatively evaluate:

1. Substrate preparation

a. Cleanliness - no contamination as grease/oil, dirt, and oxidation of the substrate.

b. No embedded abrasive blasting material and debris.

c. Anchor-tooth profile in the substrate.

2. Bond or adhesion of the thermal-spray coating to the substrate including areas where bond is below that specified for the coating system.

3. Bond or adhesion between adjacent layers of a multicoat system as nickel-aluminum bond coat topped with an alumina-titania ceramic wear coat.

4. Cracks and "bad volume" under the surface which could result from equipment malfunction, use of bad spray materials, and/or spraying outside the coating parameters.

REFERENCES

1. A PLASMA FLAME SPRAY HANDBOOK, Naval Ordnance Station, Louisville, KY, Report No. MT-043, March 1977.

2. MIL-S-1687(SH), Thermal-Spray Processes for Naval Machinery and Ordnance, 24 Nov. 1980.

IMPROVED IMAGING OF MAGNETIC FLUX LEAKAGE FIELDS

Alfred L. Broz
Army Materials and Mechanics Research Center
Watertown, Maryland

ABSTRACT

The present detection methods for imaging flux leakage are colored particle, fluorescent particle, Hall detectors and coils. These techniques are limited due to the need for the detector to be in close proximity to the material being inspected. Requirements exist in the Army for both remote sensing techniques and techniques which will allow easier analysis of the detected flux leakage.

ARMY PROBLEM

There exists a need for improved imaging of magnetic flux leakage fields.

Ferromagnetic materials can be inspected for surface and subsurface defects by utilizing the magnetic properties of the material. In this method, the test specimen is magnetized by sending an alternating or direct current through the specimen or by placing the specimen in the field produced by a permanent magnet or an electromagnet. Defects are detected by interrogating the test specimen surface with a probe which detects magnetic field inhomogeneities. If the tested material exhibits adequate magnetic retentivity, the specimen can be inspected after magnetization.

Various probes and support instrumentation are used to detect, sense, and image the magnetic field inhomogeneities at the specimen surface. Small ferromagnetic particles, such as iron oxide powder, are the simplest and most common detectors utilized. To improve visibility, the particles are coated with either a colored or a fluorescent substance. These particles are applied dry or dispersed in a liquid to the test item. The particles accumulate at the site of the magnetic leakage field and produce a visible outline of the discontinuity on the surface of the test item when properly viewed. Water and kerosene are the usual liquids the particles are dispersed in, but room temperature curing rubber is also used to provide a replica casting.

The use of small ferromagnetic particles for imaging magnetic flux leakage fields has the following shortcomings.

1. No quantitiative information is provided about the magnetic flux leakage field.
2. The technique is difficult to adapt to automatic inspection procedures.
3. The particles also accumulate at gravity favored sites.
4. Careful handling is required to not disturb the indication.
5. The interior of cylindrical items such as pipe, gun tubes, and projectile components are difficult to inspect using the magnetic particles as the imaging technique.
6. Indications on specimens with a rough surface finish are difficult to interpret.

Hall detectors, induction coils with and without cores, and some semiconductor devices are used as magnetic probes to sense the magnetic leakage field. These magnetic probes are hand-held or attached to a mechanical scanning mechanism. Coil type magnetic probes require rapid relative motion to the magnetic flux leakage field to generate adequate output signals. For crack detection both the magnetizing field and the probe scanning direction must have components normal to the crack orientation.

A significant amount of hardware has been constructed to examine ferromagnetic items with magnetic probes. Automated and semiautomated systems are used to inspect anti-friction bearings, pipe, gun tubes, projectiles, and similar items with cylindrical symmetry.

The use of magnetic probes to inspect items provides a characteristic signature concerning the flux leakage source. From the magnetic signatures obtained, flaw volume, flaw location, flaw depth from surface, flaw orientation, and flaw width can be determined.

The magnetic signatures can be imaged with an oscilloscope, peak and hold detectors to strip chart recorders, oscillographic recorders and scan converters for video display.

The use of magnetic probes to image magnetic flux leakage fields has the following shortcomings:

1. Some magnetic probes require rapid relative motion.
2. Magnetic probes must inspect very close to the specimen's surface (approximately 0.01").
3. Magnetic probes lend themselves to automated inspection but require complex hardware to follow specimen geometry.

With the advent of coherent single frequency light sources, are there other ways of imaging magnetic flux leakage fields? Do there exist any magneto-optical effects which would be useful for imaging magnetic flux leakage? The advantages of such a technique would be:

1. Remote sensing.
2. Quantitative flaw parameterization.
3. Easier automatic inspection.
4. Easier manual and automatic interpretation.

INTRODUCTION TO CERAMIC NDE

A. G. Evans
University of California
Berkeley, California

This morning's session will be devoted to work on ceramics. Ceramics is an area where attempts are under way to try to explicitly predict failure from nondestructive detection and characterization of defects. So we will have a series of talks today, some of which describe the detection and characterization of defects, and others are concerned with the association of those defects to the failure characteristics of the material in an attempt to integrate those two aspects of the failure prediction process.

The first talk will be an overview of the ceramics program to date. This will be presented by Bruce Thompson from the Science Center.

Bruce Thompson (Science Center): Before starting the overview, I would like to conclude my introductory remarks of yesterday with one thing which I neglected to say. If I could have the first slide, please.

On the final day of the program, we have a time period which is indicated as "Open for Informal Working Groups."

Our thinking there was that some people may be able to stay on or even want to stay for the weekend; they might like to use that time to get together and discuss some topics of special interest, and so we have left that time open. More specifically, though, there are a few meeting rooms that are available, and Diane Harris could help you find one if there is a group which would like to continue the discussion of adhesive bonds yesterday or any of the other topics which come up. So please take advantage of that if it suits your interest.

Before going on into my overview, I have another addition to the program. We are fortunate that Bill Reynolds from Harwell has been able to attend the meeting. He was only able to finalize his plans about two weeks ago, so he could not submit a paper. However, they have been doing some very interesting work at Harwell in the area of microfocusradiography. And since the earlier radiographic work was done as a part of this program, and because they have a somewhat more sophisticated instrument that has been able to significantly extend those results, I thought it quite appropriate for him to present a summary of the results that they have obtained.

MICROFOCUS RADIOGRAPHY

W. N. Reynolds
AERE, Harwell, England

Thank you very much.

I should emphasize that what I am going to talk about is really the result of a very brief program which was funded at Harwell by David Godfrey of AMTE, who is probably well-known to ceramic practitioners here. We were very glad to have this contact because it gave us access to the TTCP specimens which were prepared in this country; specimens, in particular, of silicon nitride tiles containing seeded defects, which many of you have studied by various techniques.

My collaborator was Ron Smith in this work. The objective was to compare the sort of ultrasonics that we had with the performance of the radiographic facilities for looking at these very small seeded defects.

Now, I was thinking that my talk would come at the end of this session and, therefore, that you would already be familiar with the types of defects which have been introduced in these tiles and their sizes, but I am afraid I do not really have time in my talk to discuss all that. I imagine that subsequent speakers will be giving you details of that.

The ultrasonics that we used was basically a conventional C-scan using a plane 25-megahertz probe and the usual sort of loss of back-echo technique to see what defects we could find. And naturally, with such a comparatively unsophisticated system, we could see some of the defects, but by no means all of them.

We then went on to the radiography. The particular sort of radiography that we are doing involves the use of a microfocus source. This is now commercial equipment at home, and I am afraid I cannot tell you all the present details of it, but the vital thing about it is that this instrument called the E12 has a 15-micron diameter source of very bright x-rays. This particular manifestation of the instrument operates from 30 to 80 kilovolts. There is another instrument which operates at lower voltage.

Now, when one has this microfocus source, there is great advantage in using a projection system whereby the specimen is quite near the source and the recording plate is a good deal further away, so that one obtains, effectively, a magnification. For reasons which are not obvious, but which can now be justified, there is an improvement in the contrast and resolution in the use of a system of this kind by comparison with what you can get with a contact radiograph.

My colleague, Ron Smith, has recently carried out a Monte Carlo computer calculation showing how scattered radiation in this projection case can be lost entirely to the recording plate; and therefore, the contrast and the resolution of small defects, is improved by comparison, as I say, with the contact radiograph. That paper has been submitted to the British Journal of Nondestructive Testing and should be available at anytime in the next month or two.

What I should just briefly like to do now is show you exactly the numbers that we obtained.

In the first viewgraph (Table 1), for which we must thank our hosts here for producing with their customary generosity and the efficiency we have come to take for granted, at a moment's notice, let me say.

We can see this refers to the material as hot pressed silicon nitride. We have looked up the best available figures that we could find for the density and the acoustic impedance properties, and you can see along the top line there what these numbers work out for each material. From this we then calculated the reflection coefficient and what we thought was possibly of more direct importance, the transmission coefficient, first of all, from the silicon nitride into the defect material and from the defect material back to the silicon nitride, and the final column shows the ultimate transmission through a system of that kind.

We thought, perhaps, either the reflection coefficient or the final products, D1D2 might be the more effective indicator of how likely it was that you could find a given defect by ultrasonics. Of course, the first column, the density, gives a good idea of how likely it is that you will find the same defects by radiography.

The difficulty lies, of course, in the range of silicon carbide, silicon and graphite. We refer to our Chairman up here, I think; his well-known work on the fracture toughness of ceramics strongly suggests that it is materials of this kind which themselves have low fracture toughness and low modulus which may be the most dangerous.

The figures have also been worked out for reaction-bonded silicon nitride (Table 2). And there, again, they may be slightly different, but not substantially. We put in the two cases for carbon. We do not know quite what form the carbon or graphite inclusions might be when they are actually in the ceramic tile. But you can see that when D1D2 approaches unity, it looks pretty unlikely that you would be able to find it by ultrasonics. But when the figure is substantially different from unity, then, of course, there is a very good chance. Of course, the density figures also show some of the impurities will come out as light patches and some of them will come out as dark patches.

Table 1

HPSN: Density and Acoustic Properties of the Inclusion Materials

Material	Density kg m^{-3}	Longitudinal Velocity km/s	Acoustic Impedance kg/m^2s	Reflection Coefficient R	Transmission Coefficient Si_3N_4-to-defect D_1	Transmission Coefficient Defect-to-Si_3N_4 D_2	D_1D_2
HPSN	3.18 10^3	10.5	3.3 10^7	0.00	1.00	1.00	1.00
WC	15.77 10^3	6.6	10.4 10^7	0.52	1.52	0.48	0.73
Fe	7.87 10^3	5.9	4.6 10^7	0.16	1.16	0.84	0.97
BN	2.25 10^3	5.5	1.2 10^7	-0.47	0.53	1.47	0.78
SiC	3.22 10^3	12.0	3.8 10^7	0.08	1.08	0.92	0.99
Si	2.33 10^3	11.9	2.8 10^7	-0.08	0.92	1.08	0.99
C (Graphite) [0001]	2.26 10^3	22.7	5.1 10^7	0.21	1.21	0.79	0.96
C (Graphite) ⊥ [0001]	2.26 10^3	4.56	1.0 10^7	-0.53	0.47	1.53	0.72

Table 2

RBSN - Density and Acoustic Properties of the Inclusion Materials

Material	Density kg m^{-3}	Longitudinal Velocity km/s^{-1}	Acoustic Impedance kg/m^{-2} s^{-1}	Reflection Coefficient R	Transmission Coefficient Si_3N_4-to-defect D_1	Transmission Coefficient Defect-to-Si_3N_4 D_2	D_1D_2
RBSN	2.20 10^3	6.14	1.35 10^7	0.00	1.00	1.00	1.00
WC				0.77	1.77	0.23	0.41
Fe				0.55	1.54	0.45	0.69
BN				-0.06	0.94	1.06	1.00
SiC				0.49	1.49	0.51	0.76
Si				0.35	1.35	0.65	0.88
C (Graphite) [0001]				0.58	0.87	0.42	0.37
C (Graphite) ⊥ [0001]				-0.15	0.85	1.15	0.98

Now, this is our final table of results (Table 3). The defects that we claim to see are as follows:

The column labeled "U" refers to defects which we found by our simple C-scan of the sites and which can be seen on the MUFAX four-level recorder. The X radiograph, the defects found by X-rays, were obtained in many cases by projection radiography. Some of the defects could be found with a magnification factor of about four, but the smallest ones, particularly in the case of boron nitride and silicon we could only see by using a magnification factor of 12. Now it is obviously quite impracticable to completely survey an item with a magnification of 12.

Table 3

Summary of Present Results on Silicon Nitride Tiles

Matrix Material; Defect Type	25 μm	Fine 125 μm	Medium 250 μm	Coarse 510 μm
NC-132 HPSN; Fe	X, U	X, U	X, U	X, U
WC	X	X	X, U	-
Si		X	X	X
SiC				X
BN	X, U	X, U	X, U	X, U
C			X	X, U
NC-320 RBSN; Fe	-	X, U	X, U	X, U
Si	-		X	X, U
SiC	-		X	X, U
Low Density	-			X
C	-	U	X	X
Pores	-	X	X, U	X

Relative effectiveness of detection of seed defect inclusions by ultrasonicsand radiography.

X = radiography
U = ultrasonics

It is a very big microscope job, and to do X-ray microscopy with a large magnification factor is not very practicable. But what we did find is that using our own ultrasonic system and carrying out a B-scan, recording a B-scan along a line in the tile on which we had reason to suppose there were defects, we could identify areas which aroused suspicion, and we would then carry out the projection radiography on those particular areas.

In particular, we were able to find, as we say here, very small defects in the hot pressed silicon nitride. In the reaction bonded silicon nitride, we could not do quite so well, obviously, because there is more background scatter or more noise in the system.

On the whole, we think that these figures are substantially better than others which have been claimed by people elsewhere who have used other systems of radiography. We are therefore suggesting that radiography has an important part to play, in conjunction, you understand, we would suggest, in this important problem of detecting and classifying defects in silicon nitride.

Thank you.

Bruce Thompson (Rockwell Science Center [now Ames Laboratory]): Perhaps we should take a moment or two to entertain any questions on Bill's work before I proceed.

Bill Reynolds (AERE Harwell): I should say I have a copy of the report here. And the people who are interested in the details, I can show you some prints of the radiograph, but I haven't got any slides prepared.

James Aller (NSF): How long was your exposure on the film?

Bill Reynolds: Fairly long. I think of the order of - anything up to two hours.

Unidentified Speaker: Can you describe the microfocus unit a little bit better?

Bill Reynolds: I am afraid I cannot. It has had a long history. Originally the microfocus system depended on a specially developed electrostatic focus, but since then, the whole thing has been taken over by a commercial organization. I do not know exactly what they have done with it. We just use it as a very valuable source of very fine focus x-rays.

Unidentified Speaker: Is it done in vacuum or -

Bill Reynonds: Yes, it's continuously pumped.

P.S. Ong (University of Houston): What spot size, curve, and voltage? Do you have any information about spot size, curving, and voltage of the x-ray tube?

Bill Reynolds: The voltage we used in this particular case was 80 kilovolts; the spot size is 15 micron diameter; and this is continously pumped.

P.S. Ong: Have you ever considered using an image intensifier at all?

Bill Reynonds: We have, in fact, done that. I may say that this is the least important application of the system that we have.

Bruce Thompson: Thank you very much for giving that very interesting but impromptu presentation.

OVERVIEW OF CERAMICS PROJECT

R. Bruce Thompson
Rockwell International Science Center
Thousand Oaks, CA 91360

ABSTRACT

The background and present plans for the ceramics project are reviewed. This provides the framework for the following papers.

Introduction

As was discussed previously, an important element in the development of a quantitative NDE technology is the coupling of nondestructive measurement results, failure modeling, and risk analysis to produce an accept/reject criteria. This basic philosophy was first formulated from first principles in the context of a project to produce a quantitative inspection capability for ceramic materials. In this paper, the history of this project is reviewed and the plans for this year's program, whose results you will hear today, are described

Accept/Reject Criteria

The development of the accept/reject criteria depends on a risk analysis as illustrated in Fig. 1. At the top is an equation for the risk, or cost, associated with the selection of particular accept/reject level. That cost consists of three terms: first term, which is associated with false acceptances, a second term, which is associated with false rejections, and a third, constant term associated with fixed costs. In the equation, w_0 represents the cost of failure (lost in false acceptance), w_1 is the cost of manufacture (lost in false rejection), and b is the fixed costs. The origin of the probability of false acceptance, e_0, and the probability of false rejection, e_1, are illustrated in the graph below. There the probability of a given measurement result, y, is plotted both for parts which will survive and parts which will fail.

$$R = w_0 e_0 + w_1 e_1 + b$$

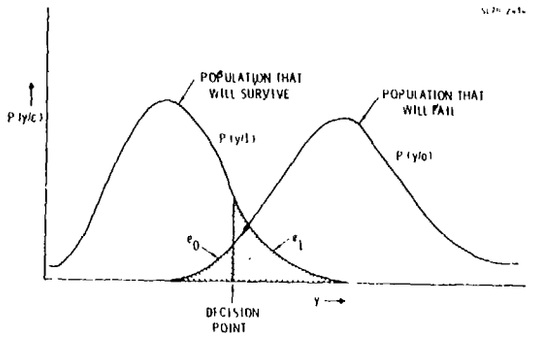

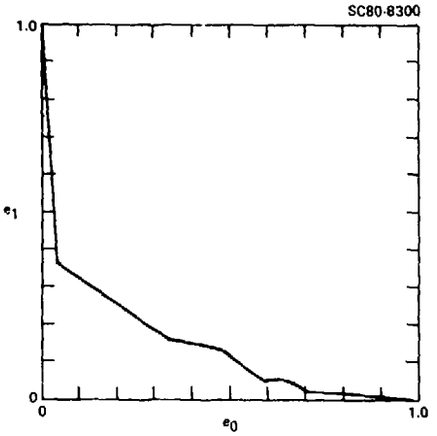

Figure 1. Elements of accept/reject criteria selection (see text for detailed description of figure).

The curve labeled P(y/1) describes the probability that a given measurement result will be obtained on those parts which will survive. Many of these parts will have a very low NDE indication, or even zero indication, as is illustrated by the fact that the curve extends to low values of y. A few, however, may produce a fairly large measurement indication. If this exceeds the decision threshold, false rejections of those parts will occur. The probability of false rejection, e_1, is the cross hatched area under the P(y/1) curve to the right of the decision point.

Similarly, for that population of parts that will fail, there will be a distribution of measurement results, P(y/o). Some of those parts will have measurement results that are lower than the threshold or decision value. Hence, they will be falsely accepted. And, the probability of this is also indicated by a cross hatched area and is equal to e_0.

As indicated in the upper equation, the risk associated with that particular decision point is equal to the sum of the products of the costs of the false acceptances times the probability of the false acceptances plus the cost of the false rejections times that probability plus the constant term. The optimum decision point is then determined by minimizing the total cost. This amounts to a trade-off between the e_0 and e_1, the false accept and false reject probabilities. The relative values of those probabilities vary as one changes the decision point. The next graph is an example worked out for one particular case. One can see that either a very high false accept probability accompanied by a low false reject probability, a very high false reject probability accompanied by a low

false accept probability, or some immediate value can be achieved. The particular point on this curve, and thus the decision threshold, is determined by the condition of minimum cost.

Available Measurement Techniques

In order to minimize the total cost, the false accept versus false reject curve should lie as close to the axes of the last graph in Fig. 1 as possible. Over the past few years, several techniques have been developed with this objective. Limited evaluations have been performed on a set of disk-shaped Si_3N_4 samples containing seeded impurities. This section describes these techniques.

Figure 2 shows a flaw image produced by a scanning laser acoustic microscope (SLAM).[2] From such an image produced in real time, one can make an estimate of the size of the inclusion. This can then be coupled with failure models to produce an estimate of the strength of the part.

Figure 2. SLAM images of Si inclusion in Si_3N_4.

Figure 3 presents results obtained using a high frequency ultrasonic backscattering technique.[3] By analyzing the ultrasonic backscattering in the time domain, one can identify signals corresponding to various ray paths within an inclusion. From these signals, their relative magnitudes and their detailed character in the time domain, one can make estimates of both the size and material of the inclusion. And, as has been shown in failure modeling,[4] a knowledge of the material as well as the size of the flaw is extremely important in determining whether it will or will not lead to failure.

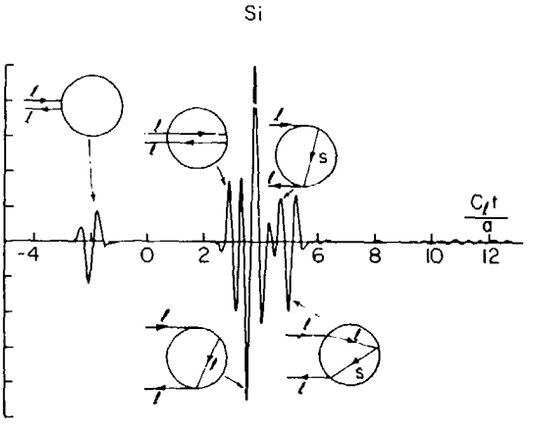

Figure 3. Relative scattering cross-section from Si inclusion in Si_3N_4 as a function of time.

A third specimen is illustrated in Fig. 4. Here, statistical estimation theory approach has been used for sizing flaws.[5] This "unified inversion algorithm" makes use of two particular ultrasonic inputs. One input is associated with very low frequency scattering (long wavelength scattering in the Rayleigh regime), and the other is related to the distance from the flaw center to its front surface. From values of these parameters, estimates of flaw size and material are outlined.

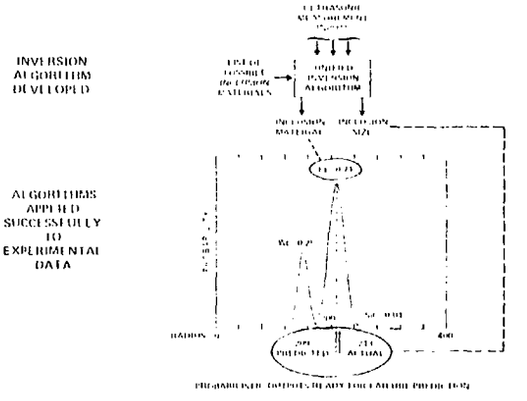

Figure 4. Results of unified inversion algorithm when applied to 200 μm radius Fe inclusion in Si_3N_4.

An important aspect of this approach is that, since it is intrinsically statistical in nature, the output is in the form of a probability distribution. It not only predicts the flaw size and material, but also assigns probabilities and errors to these predictions. In the case shown, there was 71% probability of the detected inclusion being iron, a 25% probability of its being tungsten carbide, and a 4% probability of its being silicon carbide. In fact, it was iron, as was predicted with the highest probability.

Similarly, as shown in the figure, the size predictions are quite accurate. The probabilistic character of the predictions are quite important since, both in the ceramics and metals areas, probabilistic fracture mechanics and life prediction are gaining widespread acceptance. It is going to be very important that NDE techniques also make quantitative probabilistic predictions that can be combined with the probabilistic failure models.

Present Program

The plan for this year, which involves the extension of these ideas to predice st[illegible]gths of components with naturally occurring flaws, is illustrated in Fig. 5. Starting with the samp[illegible] to be discussed below, measurements are being m[illegible]e using the three techniques just discussed. The scanning laser acoustic microscope, high-frequency ultrasonic scattering, and low-frequency ultrasonic scattering. A more generalized inversion algorithm is being developed that will combine all of these inputs to make the best possible estimates of flaw properties. The algorithm will also incorporate inputs from fracture mechanics to make strength prediction. Finally, destructive tests will be made and the predicted strength and the actual or measured strength will be compared.

PROPOSED WORK FLOW DIAGRAM

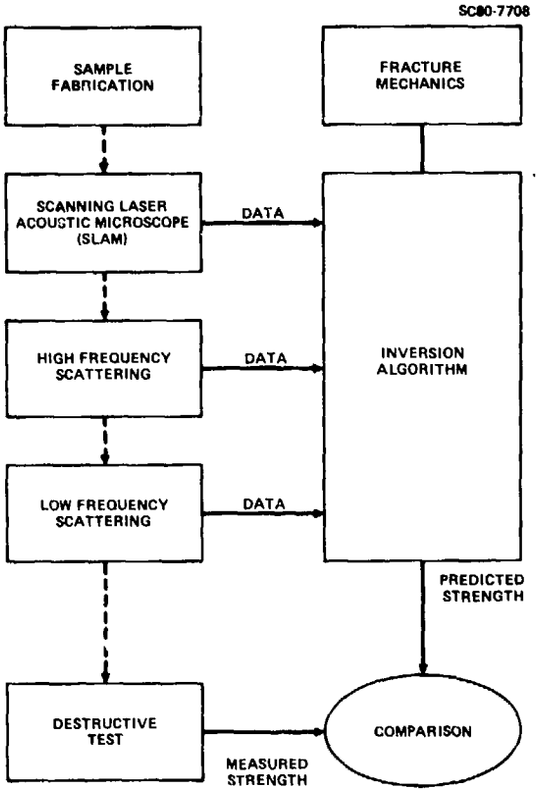

Figure 5. Work flow diagram for ceramics project.

The specimen geometry which has been selected is illustrated in Fig. 6. This is the "button head" specimen which is made from hot pressed silicon nitride. The geometry is particularly suited to destructive tests in a tensile machine.

"BUTTON HEAT" SILICON NITRIDE

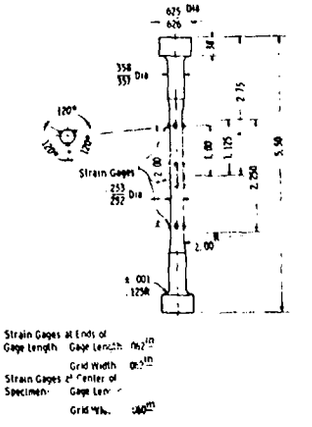

Test specimen dimensions and strain gage locations (1 in. = 25.4 mm, 1 deg = 0.17 rad).

Figure 6. Geometry of "button head" specimen.

The schedule of this effort is illustrated in Fig. 7. Unfortunately, a problem has developed as will be observed by comparing the plan and the actual schedule. Samples were ordered in November and rough billets were received in mid-January, both on schedule. The particular vendor who was doing the final preparation of the botton head specimens promised tham at the end of April. It was planned that the three different measurement investigators would be able to rotate those samples and complete their data collection by the end of September.

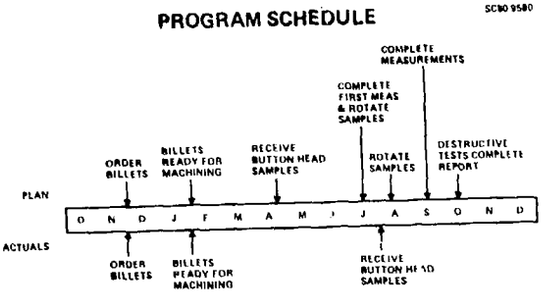

Figure 7. Program schedule.

Unfortunately, the vendor has not yet been able to give us the specimens, and so some of the papers will be less complete than would be desired.

Nevertheless, all the investigators have been developing and refining their techniques. The interim results which are presented give a good indication of what is to come. The results of the final comparison of the destructive tests and the NDE predictions will not be available for a few months.

Questions

Unidentified speaker: What materials are you continuing your work with?

Dr. Thompson: Hot-pressed silicon nitride.

Unidentified speaker: Who is the manufacturer of the ceramics?

Dr. Thompson: The ceramic material came from Norton; however, Norton is not doing the machining.

References

1. R. Bruce Thompson, "Introductory comments", this proceedings.

2. D. E. Yuhas, T. E. McGraw, and L. W. Kessler, "Scanning laser acoustic microscope visualization of solid inclusions in silicon nitride", Proceedings of the DARPA/AFML Review of Progress in Quantitative NDE, AFWAL-TR-80-4078 (Air Force Wright Aeronautical Laboratories, Dayton, Ohio, 1980), p. 683.

3. C. H. Chou, B. T. Khuri-Yakub, K. Liang, and G. S. Kino, "High-frequency bulk wave measurements of structural ceramics", ibid, p. 663.

4. A. G. Evans, M. E. Meyer, K. W. Fertig, B. I. Davis, and H. R. Baumgartner, "Probabilistic models for defect initiated fracture in ceramics", ibid, p. 636.

5. L. A. Ahlberg, R. K. Elsley, L. J. Graham, and J. M. Richardson, "Long wavelength ultrasonic characterization of inclusions in silicon nitride", ibid, p. 656.

Bruce Thompson (Rockwell Science Center [now Ames Laboratory]): So, with that, I think if there are any questions, I would be happy to entertain them; otherwise, we'll go directly into the formal papers.

Unidentified Speaker: What materials are you continuing your work with?

Bruce Thompson: This is a hot-pressed silicon nitride.

Unidentified Speaker: Who is the vendor?

Bruce Thompson: I have debated extensively whether to announce that in public. It was not Norton, from whom we got the billets. We got the billets from Norton, but I suppose I really don't want to pan the vendor in public.

Unidentified Speaker: I was referring to the manufacturer of the cramics.

Bruce Thompson: The ceramic material came from Norton; however, Norton is not doing the machining on it.

Tony Evans, Chairman (University of California Berkeley): We would like to now start the formal series of papers in this morning's session.

ACCEPT-REJECT DECISIONS AND PROBABILISTIC FAILURE PREDICTION*

J.M. Richardson and K.W. Fertig, Jr.
Rockwell International Science Center
Thousand Oaks, California 91360

and

A.G. Evans
University of California
Berkeley, California

ABSTRACT

The purpose of this paper is to discuss recent progress in the development of an NDE decision formalism applied to the case of brittle fracture in ceramics. The on-line input into the formalism is a set of non-destructive (ND) measurements and the on-line output is the probability of failure conditioned on the above measurements. The final accept-reject decision depends only upon the comparison of the above output with a threshold related to the concerns of the user. The formalism involves stochastic physical models of the ND measurement process, the failure process (assuming a given stress environment), and the a priori statistics of defects. The present formalism goes beyond that reported at the previous meeting in several respects: (a) a greater variety of possible defect types are included, (b) a correspondingly grater variety of competing failure processes are considered, and (c) a more diverse set of ND measurements are incorporated. An important general modification of the total formalism has been introduced: namely, the earlier formalism involving a single most significant defect concept has been replaced by a more realistic formalism in which all possible combinations of defects are taken into account. The model of a priori statistics of defects has been accordingly modified with the removal of the extreme value feature. We will present false-rejection false-acceptance probability curves for various sets of synthetic test data and various values of model parameters.

INTRODUCTION

The purpose of this talk is to discuss recent progress in the development of the NDE decision formalism (i.e., the determinatin of the probability of failure conditioned on ND measurements and the associated optimization of accept/reject criteria). Here the application is limited to brittle fracture in ceramics, although the general methodology with suitable modifications is applicable to any mode of failure in any material.

We first discuss the general aspects of probabilistic failure prediction, partly for the purpose of defining notation. We then present a review of past work based upon the dominant-defect approximation. This work involves low-frequency acoustical ND measurements and two alternative failure processes due to voids and subcritical inclusions, respectively. The last part of the talk deals with a more realistic formalism in which explicit consideration is given to all combinations of defects that can occur.

GENERALITIES ON PROBABILISTIC FAILURE PREDICTION

It has been shown[1] that, in the case of single dominant defect, the conditional probability of performance c (c = 1 → survival and c = 0 → failure), is given by

$$P(c|y) = \frac{1}{P(y)} \int dx\, P(y|x)\, P(c|x)\, P(x) \qquad (1)$$

$$P(y) = \int dx\, P(y|x)\, P(x) \qquad (2)$$

where y is an n-dimensional vector representing the results of all nondestructive measurements and x is an m-dimensional state vector representing the characteristics of the single significant defect. The state vector is assumed to have the property

$$P(y, c|x) = P(y|x)\, P(c|x) \qquad (3)$$

at least to a sufficient degree of approximation.

Now, in the case of many defects where the single significant defect assumption is not adequate, the above formalism has to be extended. This will be done in a later section.

With any given loss function, we always obtain an accept-reject decision rule of the game form, namely

$$\begin{aligned} P(o|y) > \lambda &\Rightarrow \text{reject} \\ P(o|y) < \lambda &\Rightarrow \text{accept} \end{aligned} \qquad (4)$$

where the value of the threshold depends on the a priori failure probability and on the various cost components of the loss function. This formalism is depicted in Fig. 1.

It is perhaps desirable to review also the concept of operating characteristic curve, i.e., the plot of the false-reject probability vs the false-accept probability, since this curve will be used frequently as a measure of the effectiveness of the NDE formalism in several cases. The false-accept probability (i.e., the fraction of the failing population that was accepted) is given by

$$e_0 = \int dy\, H[\lambda - P(o|y)]\, P(y|0) \qquad (5)$$

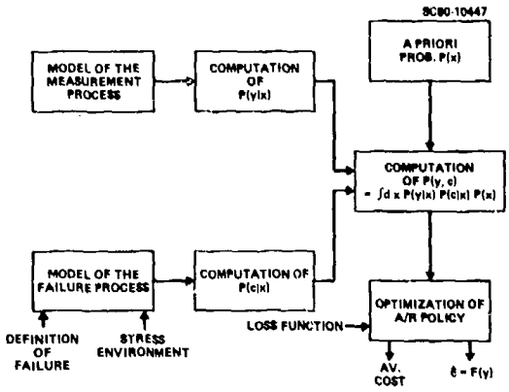

Fig. 1 NDE formalism.

where $H(\cdot)$ is the Heaviside (or unit-step) function defined by

$$H(u) = 0 \quad u < 0$$
$$= 1 \quad u > 0 \qquad (6)$$

where u is a dummy variable. On the other hand, the false-reject (i.e., the fraction of the surviving population that was rejected) is given by

$$e_1 = \int dy\, H[P(o|y) - \lambda]\, P(y|1) \quad . \qquad (7)$$

In (5) and (7) the integrations span the entire n-dimensional measurement vector space. In the case of a single scalar measurement variable the nature of the calculations of e_0 and e_1 are illustrated in Fig. 2. Most of the probabilistic quantities of interest to the user of an NDE system can be derived from e_0, e_1, and $P(0)$.

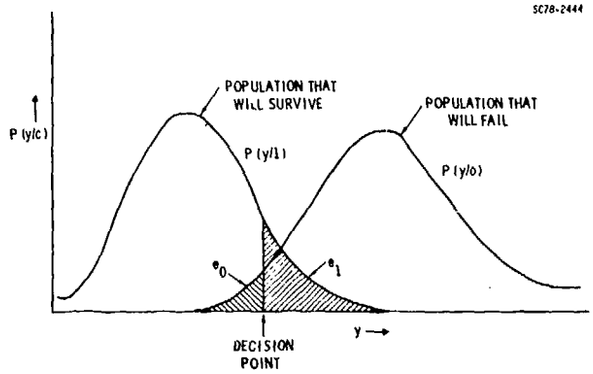

Fig. 2 Calculation of false-accept (e_0) and false-reject (e_1) probabilities.

Eqs. (5 and (7) give e_0 and e_1 as functions of the threshold λ and thus they provide a parametric representation of a curve in (e_0, e_1)-space. This curve is called the NDE operating characteristic. The curve is independent of the loss function (actually, it represents the locus of points representing all possible loss functions) and the a priori failure probability. Thus this curve characterizes the performance of the NDE system in a manner that is independent of external considerations. The nature of e_0 and e_1 is illustrated in

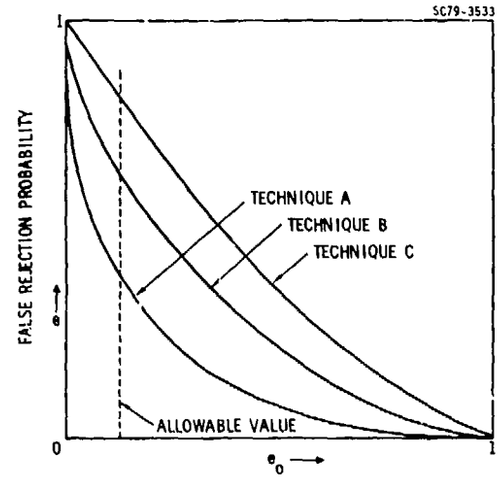

Fig. 3 The operating characteristic as a measure of NDE system effectiveness.

Fig. 3. The closer the operating characteristic curve is to the axes, the better the performance. From Fig. 3, for example, it is seen that technique A is superior to techniques B and C.

REVIEW OF APPLICATIONS

In this section we review previous results in the application of probabilistic failure prediction based on the single dominant defect approximation. In a later section, the many-defect case will be discussed. Here, we consider two failure mechanisms in ceramics: one involving voids with peripheral microcracks and the other involving subcritical inclusions. In the interest of brevity we have omitted as many details as possible; these are discussed in an earlier paper by Richardson, Fertig and Evans.[2] These examples are discussed in the following two subsections. Unfortunately, neither real failure data nor real ND measurement data were available for either example and consequently synthetic theoretical data were used throughout. Various kinds of statistical outputs were computed, but the greatest emphasis was placed upon the so-called NDE operating characteristics.

Failure Due to a Void with Peripheral Microcracks- It is known that voids, which are almost always present in ceramics, are frequent sites for the initiation of crack growth, and hence lead to catastrophic failure under sufficiently large applied stresses. An adequate model of this process involves a random set of microcracks on the periphery of the void. Each crack has a certain probability of propagating to failure depending upon the stress distribution that would exist in the neighborhood of the crack if the crack were not there. We present a treatment of the perhaps over simplified case in which it is assumed that the probability of propagating to failure depends only on the stress at the void surface and that the void is approximately spherical.

Three independent models are involved in the assembly of a decision framework; the estimate of the pertinent defect dimensions from the inspection measurement y given the defect state x; the probability of performance c at a specified ap-

plied stress level $\sigma^{\infty}_{\alpha\beta}$ given the defect state x; and the a priori probability density of the state x of the dominant defect. Each of these models is examined separately and then combined to provide the optimal accept/reject decision rule and associated decision performance measures.

The relevant conditional probability density P(y|x) is implied by the stochastic measurement process

$$y = \eta a^3 + r \tag{8}$$

where y is a possible measured value of $A(\omega)/\omega^2$, i.e., the scattering amplitude for longitudinal-to-longitudinal backscatter divided by the square of the frequency ω, evaluated at a sufficiently small value of ω. The quantity ηa^3 is the theoretical value of the above quantity when the state x = a (the void radius) is assumed to be known. The coefficient η depends only on the known properties of the host material. The additive term r represents measurement error and is assumed to be a Gaussian random variable with zero mean and variance C_r.

We turn to the calculation of P(c|x), the probability of the performance c, given the state x (=a) of the significant defect. In the present model it is assumed, as we have stated, that the only type of defect that is significant in the context of structural failure is a spherical void. As illustrated in Fig. 4 this void has randomly positioned cracks distributed at its surface. With a specified applied stress, each crack has the potential of propagating into a large crack, subsequently causing structural failure. The probability of this happening is a function of the local stress $\sigma_{\alpha\beta}(\vec{r})$ in the neighborhood of the crack (i.e., that $\sigma_{\alpha\beta}$ would exist at $\vec{r}$ if the crack were absent). The cracks are, in this instance, considered to be much smaller than the void diameter, so that the effects of stress gradients into the host can be neglected. The modifications that pertain when this condition is not satisfied has been discussed by Evans, Biswas, and Fulrath.[3]

SC79-3532

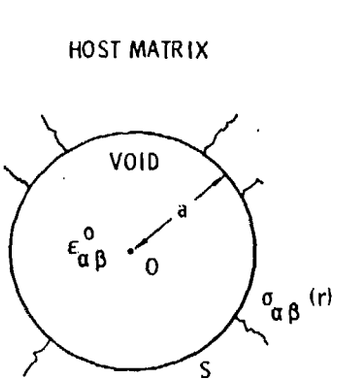

Fig. 4 Void with peripheral microcracks.

Based upon this model the probability of survival, given that the state x = a is specified, is

$$P(1|x) \equiv P(1|a) = 1 - P(0|a)$$

$$= \exp\left(-4\pi n_s a^2 \langle Q\rangle_A\right) \tag{9}$$

where n_s is the average surface density of cracks on the surface of the spherical void and $Q = Q(\sigma_{\alpha\beta}(\vec{r}))$ is the probability that a crack at the position $\vec{r}$ on the surface will propagate to failure. The symbol $\langle Q\rangle_A$ denotes the area average of Q over the surface of the void.

Studies of defect densities in ceramics indicate that the large value extreme, of interest to fracture problems, can frequently be characterized by the cumulative distribution

$$F(a) \equiv \int_0^a p(a)da = 1-\exp\left(-(a/a^0)^k\right) \quad . \tag{10}$$

where a^0 is a critical radius.

Here we combine the last three equations to yield P(y,c) from which we deduce P(y|c) and the classification errors e_0 and e_1.

It is desirable to introduce the dimensionless variables $z = y/C_r^{1/2}$, $\xi = a/a^0$, and an additional dimensionless parameter $\kappa = \eta(a^0)^3/C_r^{1/2}$, which is a signal-to-noise ratio characterizing the observation of elastic waves scattered from a spherical void of radius a^0. Another useful quantity is the dimensionless failure parameter

$$\zeta = 4\pi n_s (a^0)^2 \langle Q\rangle_A \tag{11}$$

whose significance is given by $P(1|x) = P(1|x) - \exp(-\zeta)$ when $a = a^0$ (i.e., the void has the critical radius defined by (10)). We actually compute P(z|c) instead of P(y|c) with a scale factor introduced into the normalization.

In Fig. 5 we present plots of P(x|0) and P(z|1), vs z for k = 3, κ = 10 and ζ = 0.01. These figures show the structure of the c = 0 class (i.e., the normalized population of objects that are going to fail) and c = 1 class (i.e., the normalized complementary population of objects that are going to survive). Moreover, they show the nature of the overlap of the two classes.

In Fig. 6 we also given a plot of e_1 vs e_0 for the same parameter values. This is the so-called "operating characteristic" of the system. It is to be emphasized again that e_0 is the falsely accepted fraction of objects that are actually going to fail. Conversely, e_1 is the falsely rejected fraction of objects that are actually going to survive.

The above results indicate a rather poor NDE performance due, of course, to an excessive overlap of surviving and failing populations. This overlap is due almost entirely to inherent randomness in the failure process remaining even when the state x = a is known with precision. However, one must measure the width of the overlap region relative to the width of the combined populations a situation that is improved by the introduction of stress gradient effects.

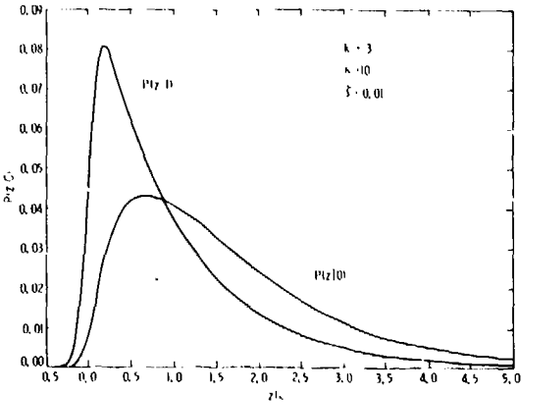

Fig. 5 Failing and surviving population.

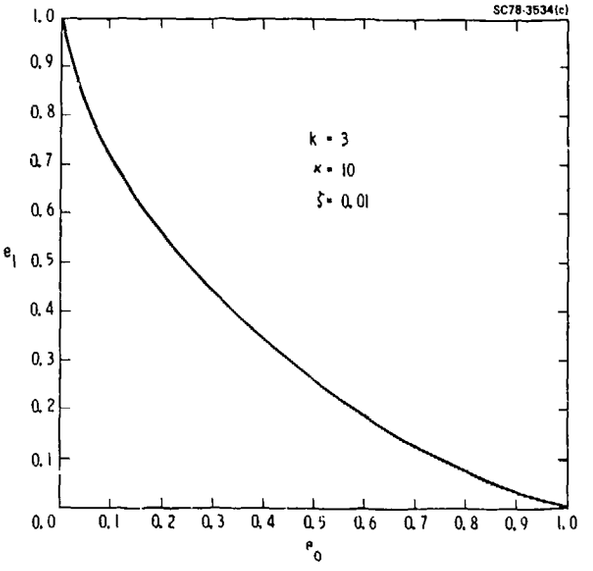

Fig. 6 NDE operating characteristic.

Failure By to Subcritical Inclusion Fracture -The geometrical nature of the model of the defect and its observation by elastic wave scattering is depicted in Fig 7. We assume a semi-infinite specimen with known host material. With the Cartesian coordinate system partially shown, the boundary of the specimen is parallel to the xy-plane and the outward pointing normal lies in the positive z-direction. We assume that the defect is an ellipsoidal inclusion (although the subsequent analysis is limited for the sake of brevity to the oblate spheroidal case) with a known included material. We explicitly show a pulse-echo (i.e., backscatter) measurement with the incident wave pointed in the negative z-direction. However, additional transducer configurations will be considered later.

If the inclusion boundary is assumed to be an oblate spheroid then the state vector x need only be the 4-dimensonal representation of the geometry since the included material is assumed known. We will use of the 4-dimensional state vector given by

SC80-8285

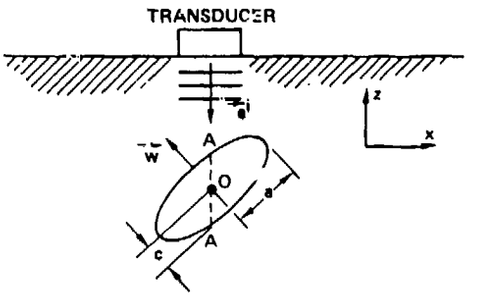

Fig. 7 Subcritical inclusion geometry.

$$x = \begin{pmatrix} a \\ c \\ \theta \\ \gamma_z \end{pmatrix} \tag{12}$$

where θ is the azimuthal angle (in the xy plane) of the symmetry axis defined by the unit vector $\hat{w}$ and where γ_z is the direction cosine of $\hat{w}$ relative to the z-axis. The vector $\hat{w}$ can be expressed in terms of θ and γ_z as follows

$$\hat{w} = (1 - \gamma_z^2)^{1/2} (\hat{e}_x \cos\theta + \hat{e}_y \sin\theta) + \gamma_z \hat{e}_z \tag{13}$$

where $\hat{e}_x$, $\hat{e}_y$ and $\hat{e}_z$ are the unit vectors in the Cartesian coordinate directions. As shown in Fig. 7 a = b is the common length of the two major semi-axes and c is the length of the minor semi-axis.

The measurements are assumed to consist of an arbitrary number of low-frequency longitudinal-to-longitudinal backscatter processes. These are collectively represented by a standard stochastic model of the generic

$$y = f(x) + r \tag{14}$$

where y, f(x) and r are n-dimensional vectors (but considerable attention will be devoted to the case n = 1). In the exact theoretical measurement f(x) the ith component is given by

$$f_i(x) = A_{2,L\to L}(\hat{e}_i, -\hat{e}_i; x) \tag{15}$$

where it is assumed that $\hat{e}_i^s = -\hat{e}_i^i = \hat{e}_i$.

The conditional probability density P(y|x) can be expressed in the form

$$P(y|x) = G(y - f(x), C_r) \tag{16}$$

where G(·, ·) is the n-dimensional Gaussian probability density given by

$$G(u,C) = (2\pi)^{-n/2}(\text{Det } C)^{-1/2}\exp(-\tfrac{1}{2}u^T C^{-1}u) \tag{17}$$

It is assumed that an uniaxial stress σ_∞ is applied in the x-direction. We make the rather crude assumption that at a certain value of σ_∞ this crack forms, as represented by the dashed

line AA in Fig. 7, a plane intersecting the geometrical center of the spheroid and having an orientation perpendicular to the axis of the applied stress, i.e., the x axis. At a sufficiently higher value of the applied stress the crack will propagate from the lower toughness inclusion (i.e., Si) into the higher toughness host material (i.e., Si_2N_4). We assume that the condition for this event can be adequately represented by an empirically recalibrated version of simple fracture mechanics with a Gaussian random additive variable representing inherent variability in the fracture process.

In explicit mathematical terms we assume that the performance variable c is given by

$$c = H(\sigma_f - \sigma_\infty) \tag{18}$$

where $H(\cdot)$ is the Heaviside unit step funtion, σ_∞ is the applied stress, and σ_f is the failure stress. The latter quantity is a random variable given by the random process

$$\sigma_f = \alpha + \beta\sigma_p + s \tag{19}$$

where σ_p is the failure stress predicted according to simple fracture mechanics, α and β are empirical recalibration constants, and s is a Gausian random variable with zero mean and variance C_s. The application of simple fracture mechanics (i.e., the computation of yield stress under the assumption that the ellipsoidal crack is surrounded solely by the host material) gives

$$\sigma_p = \frac{K_{IC}}{Z(\varepsilon'/a')\sqrt{\pi c'}} \tag{20}$$

where K_{IC} is the fracture toughness, a' and c' are the major and minor semi-axis lengths of the fully developed internal crack, and $Z(\cdot)$ is a function defined by

$$Z(u) = \int_0^{\pi/2} d\psi (1-(1-u^2)\sin^2\psi)^{1/2} \quad ^{-1} . \tag{21}$$

As stated earlier, we assume that the fully developed internal crack is represented by the cross-section formed by a plane, perpendicular to the x axis, passing through the center of the spheroid. A straight forward geometrical analysis yields the result

$$a' = a \tag{22}$$

$$c' = (a^{-2} + (c^{-2} - a^{-2})w^2)^{-1/2} \tag{23}$$

where w_1 is the length of the projection of $\hat{w}$ (the unit vector defining the axis of symmetry of the spheroid) onto the crack plane. We obtain

$$w^2 = 1 - (1-\gamma_z^2)\cos^2\theta . \tag{24}$$

Eqs. (16) - (24) thus give σ_p as a function of the state vector x defined by (12).

We turn finally to the calculation of $P(c|x)$. First we observe that, according to the stochastic model (19), the conditional probability density of σ_f is given by

$$P(\sigma_f|x) = G(\sigma_f - \alpha - \beta\sigma_p(x), C_s) \tag{25}$$

where $G(\cdot,\cdot)$ is the Gaussian function defined by (17) which in the present case is specialized to the case of scalar variables, i.e.,

$$G(u,C) = (2\pi C)^{-1/2} \exp(-\tfrac{1}{2} C^{-1}u^2) . \tag{17a}$$

We then obtain

$$P(c = o|x) = \int_{-\infty}^{\sigma_\infty} d\sigma_F P(\sigma_F|x) \tag{26}$$

The a priori probability density $P(x)$, is more complicated because the state vector x is now 4-dimensional in order to characterize fully the spheroidal geometry. We assume that the semi-axis lengths are statistically independent of the angular variables. Furthermore we assume that the latter are distributed with axial symmetry about the z-axis. The detailed analytical representation of these assumptions is given in Ref. (2).

In the numerical computations we have used a Monte Carlo technique in which quantities of the type $\int dx(\cdot)\,P(x)$ are replaced by

$$\sum_{x\in\xi} (\;)/\sum_{x\in\xi} 1 \tag{27}$$

where the samples of the state vector in the set ξ have been drawn at random in accordance with the probability density $P(x)$.

In all computations we will uniformly use the following assumptions and parameter values given in Ref. (2).

In the following paragraphs we present numerical results for three cases to illustrate the separate effects of randomness and completeness in the measurement process and randomness in the failure process.

Case 1 - One Measurement - Random Measurement and Failure Process - In this case we consider a single ND measurement i.e., a pulse-echo, longitudinal-to-longitudinal scattering of elastic waves with the incident propagation in the negative z-direction. Here we assume randomness in both the measurement and failure processes. The particular values for the statistical parameters are given in Ref. (2).

In Fig. 8 we show the computed curves of $P(y|c)$ representing the failing and surviving populations. It is clear that the severe overlap will yield a rather poor NDE performance as indicated by the plot of false-rejection probability e_1 vs false acceptance probability e_0 shown in Fig. 9.

Case 2 - One Measurement - Deterministic Measurement and Failure Processes - Here we consider again a single measurement of the same kind as in the last case. However, for the sake of understanding we eliminate the randomness from the measurement and failure processes by setting the variances $C_r = C_s = 0$. The resultant NDE performance (hypothetical) is given by the e_1 vs e_0 plots in Fig. 10. Although there is a marked improvement in the performance, i.e., the curve has moved

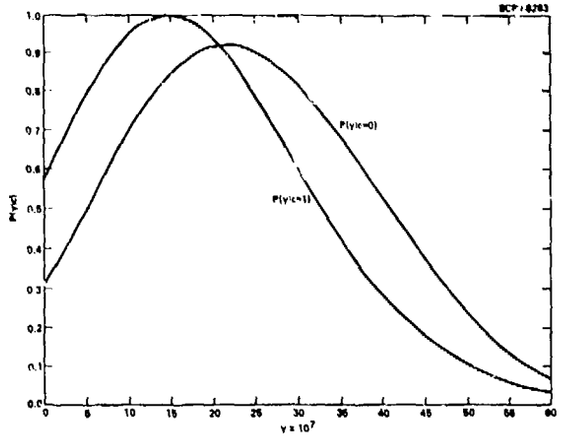

Fig. 8 Failing and surviving populations.

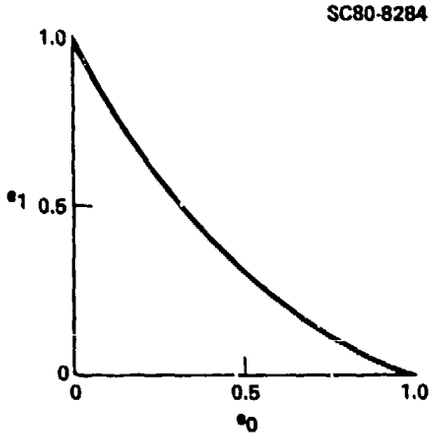

Fig. 9 NDE operating characteristic - one measurement with random measurement and failure process.

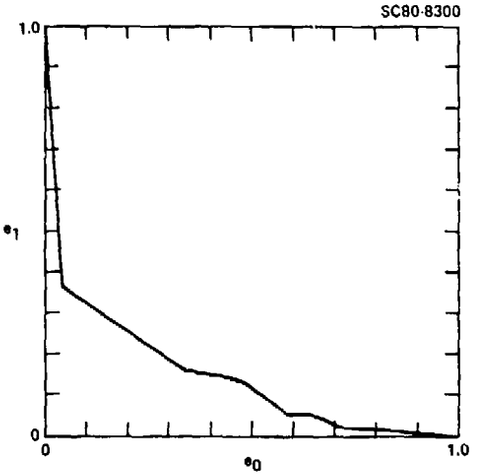

Fig. 10 NDE operating characteristic - one measurement with deterministic measurement and failure processes.

closer to the horizontal and vertical axes, the performance is of debatable merit. This is due to the serious incompleteness of the measurement set. Incidentally, the lack of smoothness of the curve is due to the relatively small fraction of Monte Carlo samples that actually affect the final answer.

Case 3 - Complete Measurement Set - Deterministic Measurement Process but a Random Failure Process -In this case we assume a sufficient diversity of very accurate measurements that the measurement vector y implies a unique estimate of x, namely x(y), with a negligible a posteriori variance (more precisely, a covariance matrix Cov(x|y) whose eigenvalues are sufficiently small in an appropriate sense). However, we assume the same randomness in the failure process as in Case 1. The resultant plot of e_1 vs e_2, the NDE operating characteristic, is presented in Fig. 11. This highly satisfactory result demonstrates clearly that randomness in the present failure process (failure initiated in subcritical inclusions) is not a significant contributor to the degradation of NDE performance.

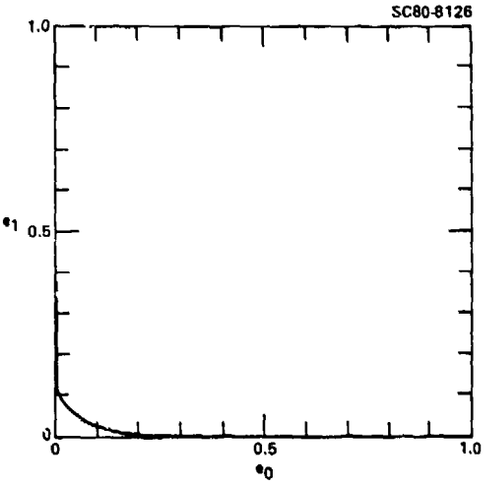

Fig. 11 NDE operating characteristic - complete measurement set.

PROBABILISTIC FAILURE PREDICTION IN MANY-DEFECT SYSTEMS

In the last section on the analysis of accept/reject decisions and the determination of unconditional and conditional probabilities of failure, we explicitly considered a single dominant defect under the assumption that, if there are others, they are insignificant contributors to failure. In the present section we consider explicitly all of the defects that may occur. To be more precise, we consider models of measurement and failure that entail a random number of defects. It is expected that the present treatment will clarify certain obscurities in the use of the dominant defect approximation. Some of these are:

(a) The contribution to failure probability by non-dominant defects.
(b) The contribution to failure probability by unobservable defects.

(c) The approximate nature of the extreme value constraint in the a priori
(d) The clarification of the distinction between detection probability and the a posterior variance of the defect characteristics given that it has been detected.

It is expedient to consider first the case with a random number of defects of a single type. Later, the formalism will be extended to the case involving many types.

The Occupation Number Representation - It is clear that, in order to represent the state of a system containing an arbitrary, random number of defects, the single-defect formalism must be suitably extended. The simplest way to do this is to divide the single-defect state space into small cells and thus represent the state of many defects by the occupation numbers of the cells. To be more explicit, let the domain of definition D of the single-defect state space x be divided into a set of subdomains or cells D_i, i=1,...,p, where, of course,

$$\sum_{i=1}^{p} D_i = D \quad . \tag{28}$$

Let the centroid (or any characteristic position) of D_i be x_i and let its m-dimensional volume be denoted by δx_i. We will denote the number of defects in D_i by the occupation number n_i. To be useful, each δx_i must be so small that the probability that $n_i > 1$ is negligible. The state of the many-defect system is now given by the set of occupation numbers

$$\{n_i\} \equiv (n_1,\ldots,n_p) \quad . \tag{29}$$

If only one defect is present and has a state in D_j, then

$$\{n_i\} = (0,\ldots,n_j = 1,\ldots,0) \quad . \tag{30}$$

The representation of higher numbers of defects is obvious.

It is worth noting that in the above occupation number representation of the state of a many-defect system, there is no need for an arbitrary set of labels for the defects (e. g., defect #1, defect #2, etc.). Furthermore, there is no need for a state vector of variable length as would be obtained if we represented the state of many defects by the concatenation of the states of individual defects.

Using the above occupation number representation, (1) and (2) for the one-defect case are now replaced by the following expressions for the many-defect case:

$$P(c|y) = P(y,c)/P(y) \tag{31}$$

$$P(y,c) = \sum_{\{n_i\}} P(y|\{n_i\})\, P(c|\{n_i\})\, P(\{n_i\}) \tag{32}$$

$$P(y) = \sum_{\{n_i\}} P(y|\{n_i\})\, P(\{n_i\}) \tag{33}$$

It is also of interest to consider the unconditional probability of performance c, namely

$$P(c) = \sum_{\{n_i\}} P(c|\{n_i\})\, P\{n_i\}) \tag{34}$$

In the above expressions the symbol $\sum_{\{n_i\}}$ denotes the summation on all modes of occupancy of the cells D_i, i.e., all combinations of the values $n_i = 0,1$ for $i = 1,\ldots,p$. The interpretations of the probabilities $P(y|\{n_i\})$, $P(c|\{n_i\})$ and $P(\{n_i\})$ are self-evident. However, here it is appropriate to emphasize that the a priori probability $P(\{n_i\})$ does not contain any extreme value (i.e., most significant) constraint as was the case with P(x).

In analogy with (3), the state of the many-defect system in the occupation number representation must satisfy the relation

$$P(y,c|\{n_i\}) = P(y|\{n_i\})\, P(c|\{n_i\}). \tag{35}$$

Special Forms of the Various Probabilities - In this and following sections, we consider special forms of $P(\{n_i\})$, $P(c|\{n_i\})$ and $P(y|\{n_i\})$ when certain statistical independence assumptions are introduced.

Under the assumption that the modes of occupancy of different cells are statistically independent a priori, we can write

$$P(\{n_i\}) = \prod_{i=1}^{p} P_i(n_i) \quad . \tag{36}$$

Since n_i takes only the two values 0 and 1, it follows that

$$P_i(n_i) = (1-n_i)\,(1 - P_i(1)) + n_i\, P_i(1) \tag{36a}$$

The a priori average value of n_i is then

$$\begin{aligned} En_i &= \sum_{n_i} n_i[(1 - n_i)\, P_i(0) + n_i\, P_i(1)] \\ &= \sum_{n_i} n_i\, P_i(1) = P_i(1) \end{aligned} \tag{37}$$

Denoting the a priori average density of defects by $\rho(x)$, we can write

$$En_i = P_i(1) = \rho(x_i)\delta x_i \tag{38}$$

if the variation of $\rho(x)$ over the domain D_i is sufficiently small. We now obtain

$$P(\{n_i\}) = \prod_i [1-n_i + (2n_i - 1)\, \rho(x_i)\delta x_i] \tag{39}$$

We now consider the a priori distribution of the total number of defects in an arbitrary extended region of the single-defect state space x. Let this region be denoted by R and let S be the set of integers i for which D_i is contained in R, i.e.,

$$\sum_{i\in S} D_i = R \quad . \tag{40}$$

The total number of defects in R is then

$$N_R = \sum_{i\in S} n_i \quad . \tag{41}$$

Using conventional arguments we obtain the result that N_R is Poisson-distributed, i.e.

$$P(N_R) = \exp(-\alpha)\ \alpha^{N_R}/(N_R)! \qquad (42)$$

where

$$\alpha = EN_R = \int_R dx\ \rho\ (x) \quad . \qquad (43)$$

This is a direct consequence of the assumption that the modes of occupancy of different cells are statistically independent. This is an acceptable assumption for the a priori statistics of defects but in the case of a posteriori statistics (i.e., conditioned on ND measurements) its validity may sometimes be debatable.

Another topic of interest is the relation between $P(x)$ and $P(\{n_i\})$ if $P(x)$ represents the probability density of the most significant defect in a set of defects. Let the significance of a defect with state x be measured by some function $s(x)$ which may be the volume of the defect, its probability of causing failure, or some related property. In the limit of infinitesimal cells, we obtain

$$P(x) = A\rho(x)\ \exp\Big[-\int_{s(x')\,>\,s(x)} dx'\rho(x')\Big] \qquad (44)$$

The normalization factor A is given by

$$A = [1 - \exp(-EN)]^{-1} \quad , \qquad (45)$$

a quantity that differs negligibly from unity if the average number EN of defects is large.

In the case of spherical voids with peripheral microcracks in a uniform applied stress, the single-defect state vector x reduces to a single scalar quantity, i.e., the sphere radius a. If we assume that a is also the measure of significance, i.e., $s(x) = s(a) = a$, then we obtain

$$P(a) = [1-\exp(-EN)]^{-1}\ \frac{d}{da}\ \exp[-\phi(a)], \qquad (46)$$

where

$$\phi(a) = \int_a^\infty da'\ \rho(a') \quad , \qquad (47)$$

and

$$F(a) = [1-\exp(-EN)]^{-1}\ \{\exp[-\phi(a)] - \exp(-EN)\} \qquad (48)$$

The Failure Probability - In this section we turn to the consideration of the performance probability $P(c|\{n_i\})$ and also the unconditional probability $P(c)$. We will assume that the probability of failure $P(c=0|x)$ due to a single defect with state x is given. In proceeding to the multiple defect case, we will further assume in this case that each defect behaves independently in the failure process and that survival is tantamount to no defect causing failure.

These assumptions imply that

$$P(c=1|\{n_i\}) = \prod_i P(c_i = 1|n_i) \qquad (49)$$

where it is assumed that each factor $P(c=1|n_i)$ is the probability that the cell D_i with n_i defects (n_i=0 or 1) does not cause failure. We assume that $P(c_i=1|n_i)$ is defined by the relations

$$P(c_i = 1|n_i = 0) = 1 \qquad (50)$$

$$P(c_i = 1|n_i = 1) = P(c_i = 1|x_i) \qquad (51)$$

where $P(c_i = 1|x_i)$ is the probability that a single flaw with state x_i does not cause failure. Thus we can write

$$P(c_i = 1|n_i) = 1 - P(c_i = 0|x_i)\ n_i \qquad (52)$$

and

$$P(c = 1|\{n_i\}) = \prod_i [1 - P(c_i = 0|x_i)\ n_i] \quad . \qquad (53)$$

It is understood that $P(c=0|x_i)$ depends implicitly upon the stress environment (random or deterministic) associated with the single-defect state x_i. It is easy to verify that (53) is consistent with the assumptions stated at the beginning of this section.

The calculation of the a priori survival probability involves the consideration of

$$P(c=1) = \sum_{\{n_i\}} P(c=1|\{n_i\})\ P(\{n_i\}) \quad . \qquad (54)$$

from which we obtain

$$P(c = 1) = \prod_i [1 - P(c_i = 0|x_i)\ \rho(x_i)\delta x_i]$$

$$+ \exp[-\int dx\ \rho(x)\ P(c = 0|x)] \qquad (55)$$

in the limit of infinitesimal cells. It is to be understood the $P(c = 0|x)$ is the probability that a single flaw with state x causes failure.

Conditioning on ND Measurements - The problem of conditioning on nondestructive measurements in the case of many-defects systems involves some nontrivial difficulties. Considerable progress has been made in dealing with some of these difficulties using some approaches that commonly used in statistical mechanics. The full discussion of these results will take up far more space than is available here and therefore this discussion will be relegated to a future communication. Here we will describe a rather crude approximation that, besides being easy to describe, has the additional advantage of ready compatibility with the previous work on post-detection processing algorithms.

Let the total domain D of x-space contain a set or regions R_j, $j = 1, \ldots, J$ in which zero or one defect is detected by ND measurements with an acceptable degree of assurance. After subtracting the R_j's from D, one obtains a nonzero domain corresponding to unobservable defects (i.e., those that are too small to be detectable). Let the vector y_j be the measurement vector associated with region R_j. Also, let N_j be the number (0 or 1) of defects observed in R_j. If $N_j = 1$ (i.e., one defect is observed in R_j) the remaining aspects of this ND measurement are represented by the probability density $P(x|y_j)$, $x \in R_j$, where the normalization condition holds:

$$\int_{R_j} dx\ P(x|y_j) = 1 \quad . \qquad (56)$$

If $N_j = 0$ (i.e., no defects are observed in R_j) then no meaningful probability density exists. The function $P(x|y_j)$ is closely analogous to the function $P(x|y)$ introduced in the earlier treatment involving the dominant-defect approximation. However, there is an important difference here; namely, $P(x|y_j)$ is the conditional probability density of the only defect in R_j which $P(x|y)$ is the conditional probability density of the dominant defect in D.

In the case in which the conditional probability of failure is very small (or at least the probability of failure due to each observed defect is very small) we can write the conditional probability of survival of the entire many-defect system in the form

$$P(c = 1|\{y_j\}) = \exp(-\int dx\, \rho(x|\{y_j\})\, P(c = 0|x)) \tag{57}$$

where the conditional mean density is given by

$$\begin{aligned} \rho(x|\{y_j\}) &= \rho(x),\ x \notin R_j,\ j = 1,\ldots, J, \\ &= P(x|y_j),\ x \in R_j,\ N_j = 1 \\ &= 0 \qquad ,\ x \in R_j,\ N_j = 0 \quad . \end{aligned} \tag{58}$$

It is worthy of note that conditional mean density is equal to the conditional probability density in the regions containing one (and only one) defect.

Extensions - In this subsection we discuss certain extensions that could be made in the formalism in order to circumvent the limitations of the simplifying assumptions used up until now.

The first of these assumptions involves the limitation to a single defect type. Here the collective state of an arbitrary number of such defects is given by the occupation numbers associated with cells in the single defect state space x. If all types of defects are described (aside from the type label) in the same state space x, then the extension of the previous formalism to the case of many defect types is accomplished in a very simple manner. One merely makes the substitution

$$x \to \begin{pmatrix} \gamma \\ x \end{pmatrix} \tag{59}$$

where γ is a discrete-valued variable labelling the defect types. In the case of integrations on x, one makes the corresponding substitution

$$\int dx\, (\cdot) \to \sum_{\gamma} \int dx\, (\cdot) \tag{60}$$

Clearly the occupation number n_i associated with cell D_i in x-space must also be subject to the substitution

$$n_i \to n_{\gamma i} \quad . \tag{61}$$

The other modifications are obvious.

However, in most cases it is not appropriate to use the same x-space for all defect types. It is usually necessary to use a distinct version of x-space for each type. For example, in the case of a surface-opening crack it is appropriate to choose x to be a 5-dimensional vector whose components consist of two surface coordinates defining position, an angle variable giving orientation, and two lengths defining the length and depth of the crack. But in the case of an ellipsoidal inclusion (of given material) in the bulk, it is appropriate to choose x to be a 9-dimensional vector giving the position, shape, size, and orientation of the ellipsoidal boundary. There remains an important question concerning the ignorability of position coordinates. In the case of a uniform applied stress, these coordinates can be ignored in the model of the failure process. However, the ignorability in the model of the measurement process requires a careful analysis.

In any case, one must associate with each value of γ a corresponding vector x_γ whose dimensionality and selection of components depend on γ. Thus the substitutions (59) and (60) must now be replaced by

$$x \to \begin{pmatrix} \gamma \\ x_\gamma \end{pmatrix} \quad , \tag{62}$$

and

$$\int dx\, (\cdot) \to \sum_{\gamma} \int dx_\gamma\, (\cdot) \quad . \tag{63}$$

It is useful to give specific examples of the extension of certain mathematical expressions derived in the previous sections. With the appropriate substitutions, (55) is changed to

$$P(c=1) = \exp[- \sum_{\gamma} \int dx_\gamma\, \rho(\gamma,x_\gamma)\, P(c=0|\gamma,x_\gamma)] \tag{64}$$

similarly (57) is changed to

$$P(c=1|y) = \exp[- \sum_{\gamma} \int dx_\gamma\, \rho(\gamma,x_\gamma|y)\, P(c=0|\gamma,x_\gamma)] \tag{65}$$

The remaining modifications are straightforward.

ACKNOWLEDGMENT

This research was sponsored by the Center for Advanced NDE operated by the Rockwell International Science Center for the Defense Advanced Research Projects Agency and the Air Force Wright Aeronautical Laboratories under Contract No. F33615-80-C-5004.

REFERENCES

1. Richardson, J.M. and A.G. Evans, J. Nondestruct. Eval. 1, 37, (1980).
2. Richardson, J.M., K.W. Fertig and A.G. Evans, "Conditional Probability of Failure and Accept/Reject Criteria," Proc. of the DARPA/AF Review of Progress in QNDE, 1979 (ed. by D.O. Thompson and R.B. Thompson), July 1980, pp 229-238.
3. Evans, A.G., D.S. Biswas, and R.M. Fulrath, J. Am. Ceramic Soc. 62, 101, (1979).

ACOUSTIC MICROSCOPY OF CERAMICS*

L. W. Kessler, D. E. Yuhas and C. L. Vorres
Sonoscan Inc.
530 E. Green Street
Bensenville, Illinois

ABSTRACT

The scanning laser acoustic microscope (SLAM) is applied to the problem of nondestructive testing of ceramic materials. The employment of a very high resolution ultrasonic imaging instrument provides capabilities which supplement ultrasonic pulse-echo testing. In addition, by means of showing a picture of the flaw, the SLAM technique provides its own capabilities which alleviate some of the limitations of other techniques. Flaws of various types are documented in this paper.

INTRODUCTION

A desirable performance goal for an ultrasonic inspection method is to be able to confidently and rapidly obtain information on the presence of flaws, on their size, shape and location, and in the case of an inclusion, an identification of the foreign material. With the above information and an a priori knowledge of what constitutes a critical flaw, a decision can be made concerning accepting or rejecting the piece being inspected. With regard to characterizing small flaws (e.g. in ceramic materials) there are obstacles to meeting the above goals by means of "conventional" (pulse echo) ultrasonic testing technique.

In the "pulse-echo" technique the "signal" from the flaw depends upon many factors, for example the flaw characteristics as well as its location within a non-uniform acoustic field produced by the inspection transducer. Since the transducer integrates the acoustic signal over its entire face, a composite signal is generated which depends upon the flaw size relative to the transducer area. The flaw within the material being tested might not be a single-regular-shaped entity such as an idealized spherical inclusion (which would be amenable to mathematical analysis). In fact a typical flaw may be an irregularly shaped inclusion with pores or microcracks alongside. The sample surface might not be flat as well, thus making the scanning operation difficult in searching for flaws.

No single technique can alleviate all the above problems, however, an imaging approach can serve useful functions in these areas: (1) to provide a basis for interpreting conventional ultrasonic signals, (2) to independently provide diagnostic information on flaws, and (3) to rapidly scan large areas for suspicious structures. Though an imaging system generally requires more sophisticated equipment compared to a pulse-echo type flaw detector, often the information obtained (pictorial image) is simpler to interpret.

ACOUSTIC MICROSCOPY

With all imaging techniques the acoustic field is probed on a point-by-point basis instead of being integrated into a composite electrical signal. The scanning can be a slow raster generated by a mechanical apparatus, such as a C-scan system or by more rapid electronic scanning with full grey images. If the images are produced rapidly enough, the potential exists for an on-line quality control inspection.

The results obtained in the paper were obtained on a commercially available Scanning Laser Acoustic Microscope (SLAM) operating at 100 MHz. This instrument, by virtue of the high frequencies employed (viz 30-500 MHz) make it capable of achieving very high resolution, and which, by its novel scanning-laser-ultrasonic detection scheme make it capable of very rapid imagery (30 images per second, typical). The principal of operation of the SLAM is described in the literature and will not be discussed here.

The lower limit on detectable flaw size is set by the wavelength. The resolution, i.e. the smallest defect which can be identified in terms of lateral dimensions is on the order of 25 microns at 100 MHz, which is half an acoustic wavelength. However, the detectability, i.e. the smallest defect which can be found without focusing, is an order of magnitude better. For example, delaminations that have openings of one micron or less, have been detected as long as their spatial extent is on the order of 25 microns. In the case of microporosity, materials which have sub-resolution porosity can be differentiated on the basis of attenuation characteristics of the sample.

There are two types of acoustic micrographs (images) that will be described. The first is a normal amplitude image in which the brightness of the CRT screen relates to corresponding levels of acoustic energy within the field. The second type of image is an interferogram in which the received acoustic signal is electronically mixed with a phase reference signal so that changes in the velocity of sound propagation through various parts of the sample will be displayed on the screen. Interferograms are characterized by vertical fringes whose spacing will be uniform and straight if the velocity of sound is uniform in a flat specimen. Lateral position shifts of the fringes can be used to calculate change in material properties.

The purpose of this paper is to review the use of SLAM for NDE of ceramics. Results obtained on metals have been reported elsewhere.

*Portions of this work were supported by the ARPA/AFML program on Quantitative NDE administered through Rockwell International Science Center, Thousand Oaks, California.

Figure 1 is a disc of hot pressed silicon nitride which is shown in both modes, amplitude (top) and interferogram (bottom). The scale is 3 mm horizontally and there appears to be a fair degree of uniformity in this material. The interferogram, whose fringes are spaced by 85 micrometers, reveals slight deviations in the horizontal direction which are due to 3 micron changes in the sample thickness resulting from surface grinding. The grooves also act as acoustic scatterers which are evident as the diagonal structure on the amplitude micrograph.

In order to maximize the information obtained from an acoustic microscope there are several parameters to consider. One would like the highest resolution possible, but, unfortunately, the higher frequencies are also more highly attenuating by the material and there is less signal to noise ratio. Furthermore, as the frequency is increased (and the wavelength gets shorter) surface roughness becomes more critical; here, sample preparation can play an important role. Therefore, one has to compromise resolution, penetration and sample preparation (if it is allowable).

CHARACTERISTICS OF TYPICAL FLAWS

Several types of flaws such as delaminations, cracks, surface cracks and solid or void type inclusions in materials will be described. Figure 2 shows a ceramic chip capacitor which is an electronic component constructed of many layers of barium titanate ceramic material separated by interlayer metal electrodes. Figure 3 is a magnified optical image of a capacitor that has been destructively cross-sectioned. The thickness of each ceramic layer is approximately 25 microns and each electrode layer is about 2 1/2 microns. This image shows typical defects that are found, for example, delamination at the electrode layer and distributed porosity in the ceramic material. When an acoustic micrograph is produced of this component, the acoustic energy is directed up through the stack rather than parallel to the layers.

Figure 4 is a 30 MHz acoustic interferogram of a typical good ceramic chip capacitor whose size is approximately 6 x 9 mm. The interferogram fringes are fairly straight and uniform indicating uniform density of the ceramic. It is well established that porosity in sintered materials is associated with increased acoustic attenuation and decreased velocity of sound compared with fully dense material. If there are inhomogeneties evident within the field of view of the microscope, fringe deviations and/or dark areas would be evident. If a delamination exists, a corresponding area of reduced acoustic transmission will be evident as seen in Fig. 5. Notice that in a delamination there may still be a slight amount of transmission, but the fringes typically become somewhat scrambled indicating a loss of coherence of the wave. The bright border area, seen in Figs. 4 and 5, is where the acoustic energy is viewed directly, i.e. without passing through the sample. A comparison of the electrical signal levels can be used to ascertain the attenuation characteristics of the sample quantitatively.

Now suppose that the ceramic capacitor is soldered onto an alumina (Al_2O_3) substrate for use in a hybrid microcircuit. Prior to the soldering operation we determined that the layers were all intact and free of delamination. Now we can determine the integrity of the solder joints by observing the transmission level through the Al_2O_3-solder-capacitor structure. In Fig. 6, we observe good acoustic transmission in the areas of the bonds, i.e. at either end of the 2 x 1.5 mm capacitor, and therefore, conclude that the bonds are good.

Suppose that a sample has a surface crack. As shown in Fig. 7 acoustic energy incident upon the crack from below, will partially convert into propogating modes that travel along and parallel to the surface. The discussion here is particularly relevant to cracks that are shallow, that is, perhaps not more than a few wavelengths of sound deep; at 100 MHz, 25-100 microns would be typical. Referring to the diagram, the area to the far right of the crack at the top surface of the sample has acoustic energy from two sources, a surface mode originating from the crack and a transmitted bulk wave from the bottom. The two waves, which are coherent, will interfere and cause a characteristic cone-shaped pattern in the acoustic micrograph. Figure 8 shows an acoustic micrograph of a hot pressed silicon nitride sample which has a ground (not polished) surface and a surface crack (arrow) produced by a Vickers hardness tester instrument. The cone-shaped interference pattern is quite evident and extends well beyond the flaw site. This latter observation is useful for easily locating surface flaws since the pattern, not the crack itself, is all that need be detected. Looking at the surface in the SEM, Fig. 9, one sees the physical indentation due to the Vickers diamond stylus. Beneath the indent there is a half-penny shaped crack which cannot be seen.

If the crack is deep as illustrated in Fig.10, and if the incident waves are at an angle with respect to the surface normal, there will be an acoustic shadow, (low transmission area) because the ultrasound will not jump across the air-filled opening. The measured width of the shadow will permit one to determine the depth of the crack provided the angle of insonification is known.

Figure 11 is an acoustic micrograph of a cracked alumina Al_2O_3 substrate a few millimeters thick. The sharp onset of the shadow defines the location of the crack at the top surface and the shadow width, about 1 mm, indicates that the crack is also 1 mm deep. (The insonification is at 45°.) The grainy structure in the image is caused by the nonuniform microstructure of the alumina itself. Full density alumina, which this is not, has a very clean acoustic transmission characteristic. The nature of the diffraction pattern will depend on the size and shape of the flaw, and also upon whether the flaw is opaque or transmissive to the acoustical wave.

If an inclusion or a void is buried deep beneath the surface of a material and viewed in the SLAM there will be scattered and transmitted energy which will interfere with each other giving rise to a diffraction pattern. This is illustrated in Fig. 12.

Figure 13 is the acoustic micrograph of a 400 micron iron inclusion implanted within a silicon nitride disc. It is located about 3 mm below the surface which is beyond the near field zone of the flaw. There is a characteristic bright diffraction ring in the center and some higher order rings surrounding it. As the flaw gets closer to the surface the image characteristic changes in a well defined manner. A series of acoustic micrographs was generated by sequentially grinding the surface thereby moving it closer towards the flaw. This sequence is shown in Fig. 14. Note that as the flaw gets closer to the image plane (the surface) the diffraction effects are reduced. These effects are an inevitable consequence of any imaging system. In order to determine the flaw size from the image we measure the image of the flaw to the first ring, then the flaw depth by stereometry. With these two data points the flaw size is determined. In the near field of the flaw we don't see diffraction rings and the flaw size is the same as its image.

To complicate life a little more, Fig. 15 indicates a common problem: flaws are not necessarily singular entities. This is a silicon inclusion located in silicon nitride and there is also some concentrated porosity (dark zones) in the same area of the sample. The SLAM image clearly differentiates the two effects. Suppose we were to try conventional high frequency ultrasonic testing. In this particular image, the horizontal field of view is 3 mm. As a side note, typical pulse-echo transducers are about this size or larger. Thus we could expect some difficulty distinguishing the two flaw types from echo signals.

In addition to flat and test samples, the SLAM can be adapted for use on complex geometries. Work has already been performed on turbine blades, tubes and other odd shaped components. In each of these cases, it is up to the investigator to select and optimize an entrance and exit port for the ultrasonic energy. Curved samples will necessarily cause corresponding curvatures to the interference fringes. For example, preliminary experiments have been performed on cylindrical ceramic test bars that are going to be subjected to tensile strength testing. The material is silicon nitride and a photograph of the sample is shown in Fig. 16. An interferogram of a good zone as compared with a suspicious zone is shown in Fig. 17 and it is evident that the differences are clearly distinguishable even though the fringes are curved.

FUTURE WORK

Our approach for further work involves 2 parallel tasks. First, analytical procedures for diffraction phenomenon which have been developed will be brought to bear on SLAM images in order to get as much quantitative information about the flaw as is possible. The second task involves establishing a data flaw library with destructive correlative analysis on naturally occurring flaws. This will guide the analysis work and can be employed to interpret flaw images on actual components which are too complicated for mathematical analysis.

BIBLIOGRAPHY

Kessler, L.W., and Yuhas, D.E., "Acoustic Microscopy 1979", Proc. IEEE, 67, (4) pp. 526-536 (1979).

Kessler, L.W., and Yuhas, D.E., "Principles & Analytical Capabilities of the Scanning Laser Acoustic Microscope", Proc. Scanning Electron Microscopy, 1978; Vol. 1, pp. 555-560, AMF O'Hare, IL. 60666.

Kupperman, D.S., et. al.;"Acoustic Microscopy Techniques for Structural Ceramics", Bulletin of the American Ceramic Society, Vol. 58, No. 8 (1980) pp. 814-841.

Yuhas, D.E. and Kessler, L.W. "Defect Characterization by Means of the Scanning Laser Acoustic Microscope (SLAM)", Proc. Scanning Electron Microscopy 1980, Vol. 1, pp. 385-391, SEM Inc., AMF O'Hare, Chicago, IL . 60666.

Yuhas, D.E. and McGraw, T.E. "Acoustic Microscopy, SEM & Optical Microscopy: Correlative Investigations in Ceramics", Proc. Scanning Electron Microscopy, 1979, 1, SEM Inc., AMF O'Hare, IL. 60666, pp. 103-110.

Kupperman, D.S., et al.: "Evaluation of Ceramic Turbine Blade with an Acoustic Microscope", Proc. First Int'l. Symp. on Ultrasonic Materials Characterization, (June 7-9, 1978, National Bureau of Standards, Gaithersburg, MD.), (In Press) ed. by H. Berger (1980).

Yuhas, D.E., and Kessler, L.W., "Scanning Laser Acoustic Microscope Applied to Failure Analysis", Proc. ATFA - 78 IEEE Inc., New York, N.Y. Catalog No. 78CH1407-6 REG 6., pp. 25-29 (1978).

Yuhas, D.E., and Kessler, L.W., "SLAM the Door on Material Failure from Internal Flaws", Industrial Research & Development, pp. 108-112, July, 1980.

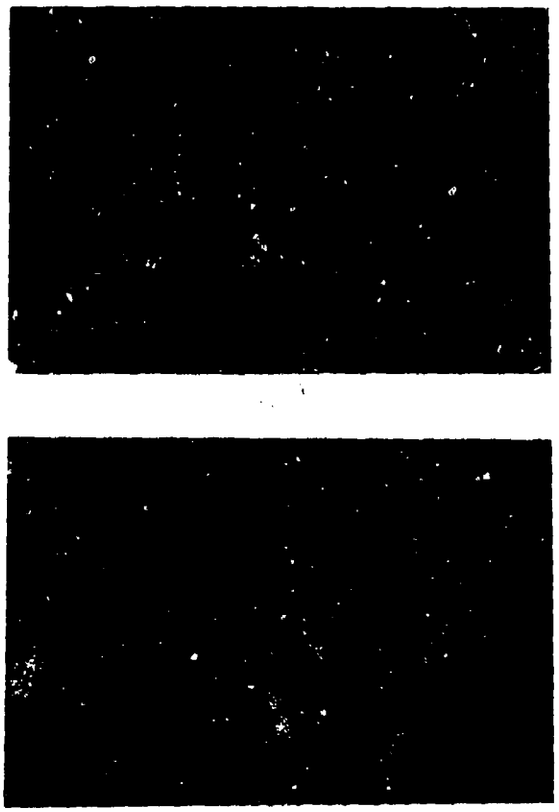

Fig. 1 - Acoustic amplitude micrograph (top) and interferogram (bottom) of a hot pressed silicon nitride disc / mm thick. The ultrasonic frequency is 100 MHz and the field of view is 3 mm horizontally.

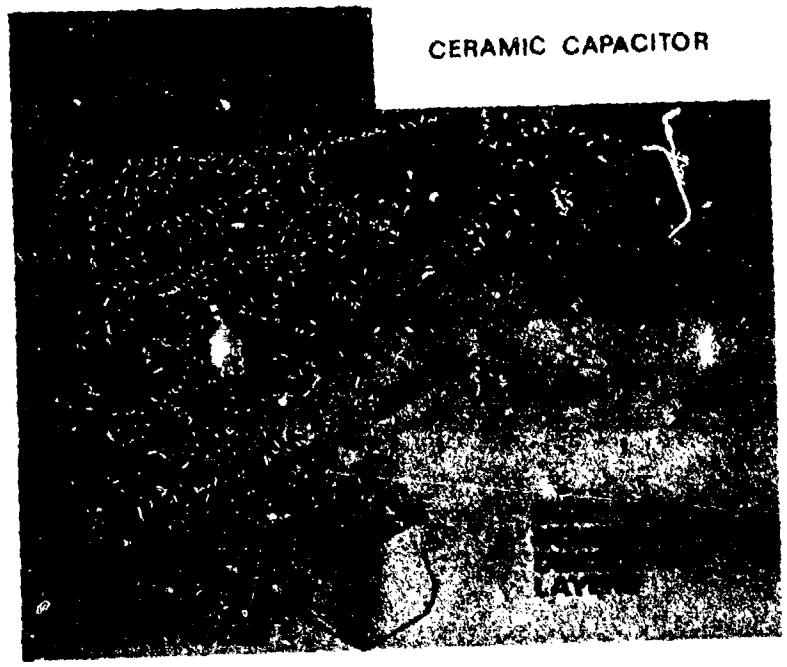

Fig. 2 - Schematic diagram of a ceramic chip capacitor consisting of multilayers of barium titanate.

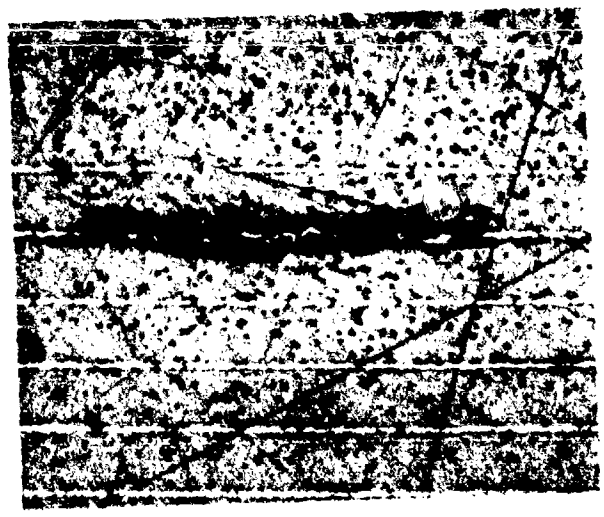

Fig. 3 - Optical view of a cross-sectioned ceramic capacitor revealing delamination at the electrode as well as porosity in the ceramic material.

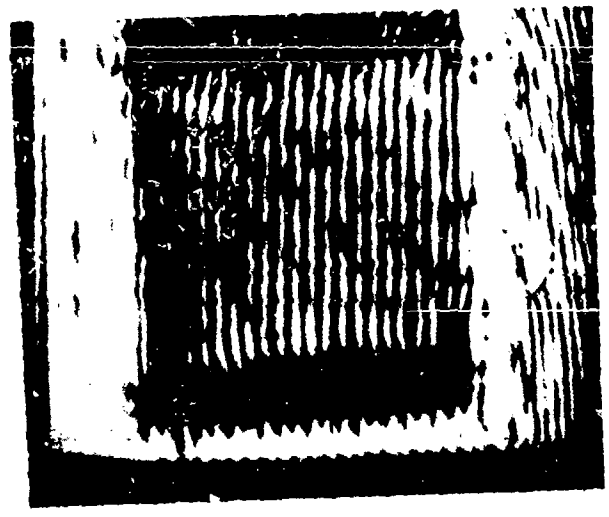

Fig. 4 - Acoustic interferogram of a typical good ceramic capacitor at an acoustic frequency of 30 MHz. The field of view is approximately 10 mm horizontally.

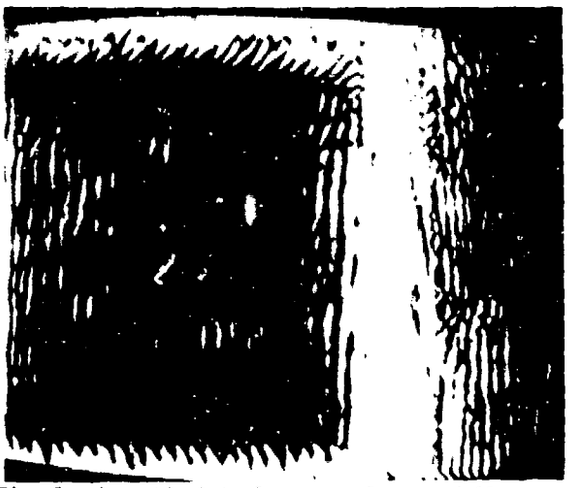

Fig. 5 - Acoustic interferogram of a partially delaminated ceramic chip capacitor.

Fig. 6 - Acoustic micrograph (100 MHz) of a capacitor soldered at either end to an alumina substrate. Acoustic transmission through the ends indicates good bonding.

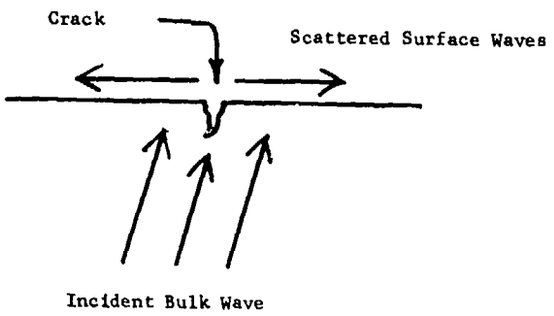

Fig. 7 - Insonification of a sample having a shallow surface crack will result in acoustic energy scattered into modes which propagate along the surface.

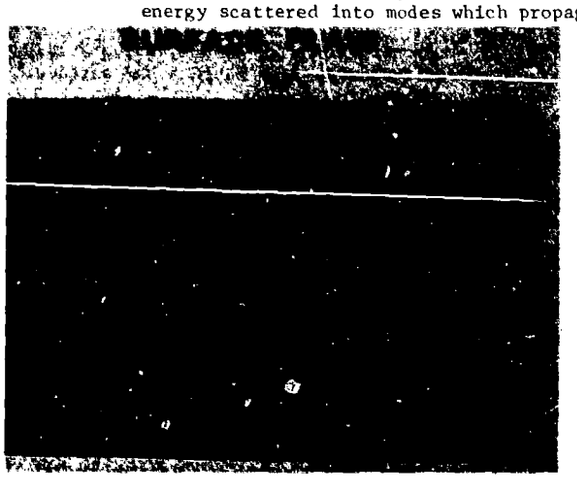

Fig. 8 - Surface flaw in hot pressed silicon nitride. The arrow indicates the site of the crack. The cone shaped interference patter extending away from the crack is caused by the mixing between the surface skimming wave travelling towards the right and the bulk wave according to Fig. 7.

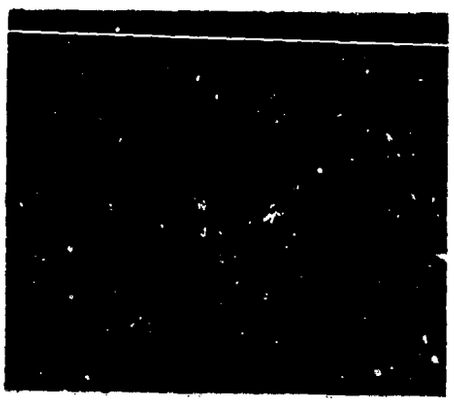

Fig. 9 - Scanning electron microscope view of Vickers indentation which caused the surface flaw on the silicon nitride sample shown in Fig. 8

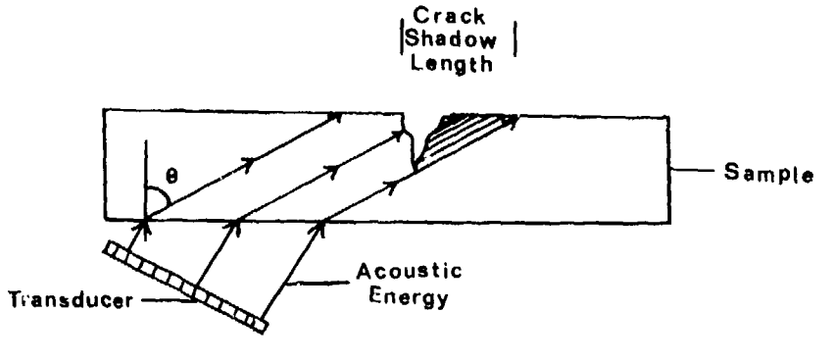

Fig. 10 - Schematic diagram illustrating insonification of a sample having a deep surface crack. A characteristic shadow is produced in the acoustic image whose dimensions are determined by the crack depth and the angle of insonification.

Fig. 11 - Acoustic micrograph of a 1 mm deep crack in an alumina ceramic slab.

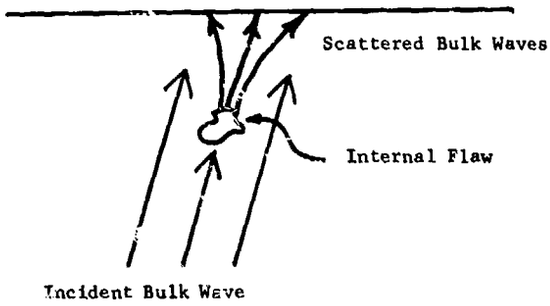

Fig. 12 - Insonification of sample having a void or inclusion deep beneath the surface.

Fig. 13 - An iron inclusion, 400 microns in diameter, is located 3 mm below the surface of a hot pressed silicon nitride sample giving rise to this diffraction pattern.

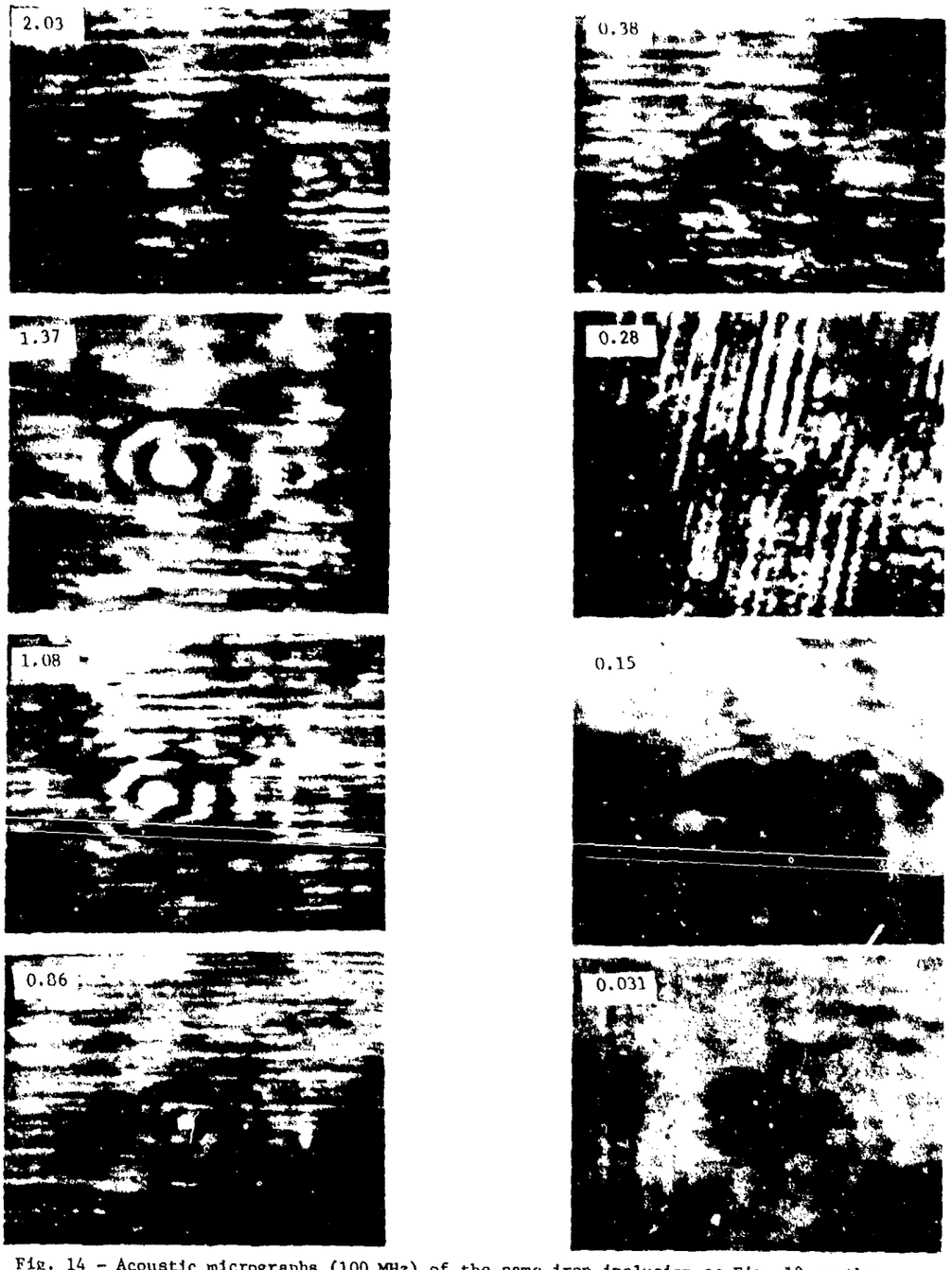

Fig. 14 – Acoustic micrographs (100 MHz) of the same iron inclusion as Fig. 12 as the thickness of the sample was reduced by grinding to bring the flaw closer to the surface. The grooves in each image are due to the rough grinding operation. The depths were measured by a simple stereoscopy technique with the acoustic microscope. The numbers in the flaw location are mi millimeters below surface.

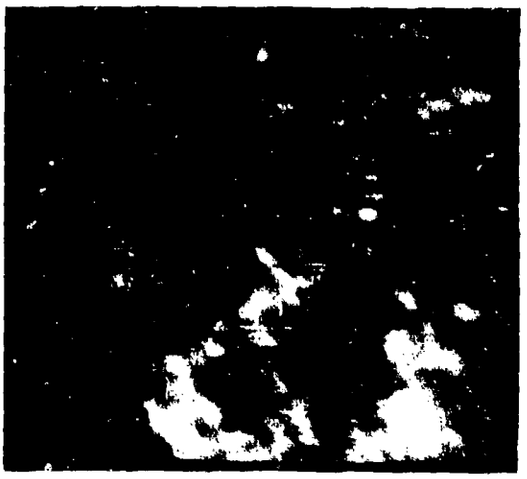

Fig. 15 - Acoustic micrograph of a silicon inclusion and porosity with a silicon nitride sample. The porosity, which is attenuating to the acoustic wave, is located in such a position relative to the inclusion that for certain orientations of the sample one flaw masks the other.

Fig. 16 - Photograph of a cylindrical tensile bar which is made of silicon nitride.

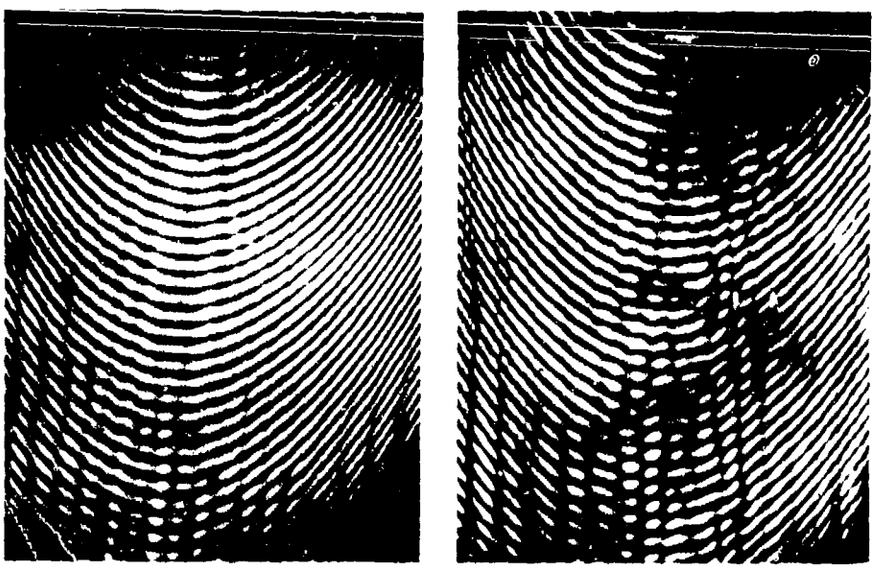

Fig. 17 - Acoustic interferograms of a typical (left) and a suspicously flawed (right) cylindrical tensile test bar shown in Fig. 16.

NDE FOR BULK DEFECTS IN CERAMICS

B. T. Khuri-Yakub, C. H. Chou, K. Liang, and G. S. Kino
Stanford University
Stanford, California 94305

Abstract

A 50 MHz C-scan imaging system is used to find defects in ceramics. The imaging system consists of a microcomputer-controlled scanner for data acquisition and signal conditioning. Synthetic aperture imaging at 50 MHz is carried out to obtain 3-D images of flaws. Image reconstruction is accomplished digitally on a minicomputer. A square synthetic aperture is used to image flaws in flat disc samples and a cylindrical synthetic aperture is used in the cylindrical rod case. We have developed the theory to predict the imaging performance of the two aperture geometries. The respective point spread functions are simulated and agree well with theoretical results. Special attention is given to reconstructing images of specular reflectors. Computer simulations based on theoretical flaw models have been carried out.

Introduction

First, a sample is immersed in a water bath and scanned in C-scan reflection mode to locate the transverse positions and depths of the flaw sites. Then a sampled aperture is synthesized over a relatively small volume of interest around the flaw, as depicted in Figs. 1a and 1b. This operation limits the number of reconstruction points required to a reasonable value. In our imaging system, a single 50 MHz focused transducer, operated in pulse-echo mode, is used. The focal point of the incident beam is located at the water/silicon nitride interface to approximate a point source and also, because of the large velocity mismatch at the interface, to create a wide angle transmitted beam insonifying the interior of the sample. For the flat disc geometry, pulse-echo data is collected over a square 8 x 8 element aperture with a sampling point spacing of two wavelengths. For the cylindrical case, an open-ended sampled cylindrical aperture is used. It consists of a stack of sixteen rings, two wavelengths apart, each ring having 32 evenly-distributed sampling points. Image reconstruction is accomplished by back-projecting the pulse-echo data on a minicomputer. The back projection procedure is illustrated in Figs. 2a and 2b.

We have carried out theoretical analyses and computer simulations to gauge the performance of the two aperture geometries. Much effort was devoted to establishing the respective point spread functions (PSF), the conventional way of specifying the resolving power of an imaging system. Inherent in the PSF concept is the assumption that a finite size reflector is regarded as a collection of point scatterers; thus, every point in the aperture responds to every point in the reflector. This assumption is invalid for strong specular reflectors, as is the case in imaging finite size flaws inside silicon nitride samples. This fact is illustrated in Fig. 3 where we have a two-dimensional fully enclosed aperture imaging a finite size circular defect. Based on the geometric optics argument, a sampling point on the aperture tends to respond only to a point on the defect boundary directly facing it. In reconstructing the image point by back-projection, because of the finite width of the transmitted pulse (typically a few rf cycles), a limited number of sampling points in the vicinity of the actually-excited aperture element will contribute constructively. Outside of this neighborhood, the contributions due to the other sampling points are either negative or random. Hence, 100% coherent summing at an image point is not possible, giving rise to undesirably high sidelobe levels. We concluded that the connection between the PSF and the "resolution" of specular reflector images is not clear.

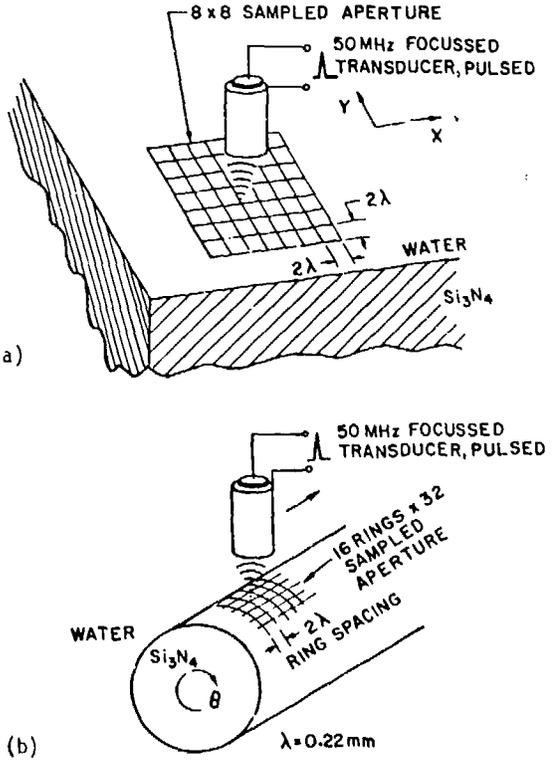

Figure. 1. Imaging flaws inside silicon nitride samples using synthetic aperture techniques: (a) flat disc samples; and (b) cylindrical rod samples.

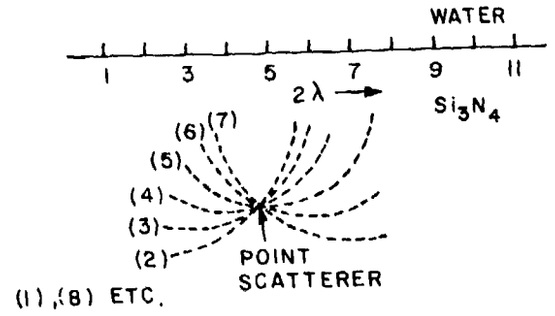

(a) SQUARE APERTURE

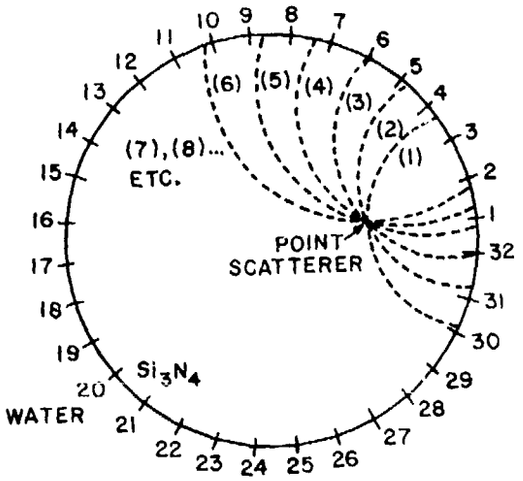

(b) CYLINDRICAL APERTURE

Figure 2. Image reconstruction by back-projection.

For the first time, computer simulated reconstructions based on theoretically-calculated backscattered waveforms for spherical void, iron, and silicon inclusions have been conducted. A typical backscattered waveform from a spherical flaw consists of a front-face echo which demarcates the boundary of the defect, and trailing echoes which are a combination of back-face echoes and mode-converted waves.[1] Different kinds of flaws have distinct backscattered signals. Synthetic focus reconstruction results in an image which shows the defect boundary and the associated "ring" artifact corresponding to later echoes, which is characteristic of the nature of the flaw, as shown in Figs. 4a, 4b, and 4c. However, a significant drawback to these results is that the sidelobe levels are very high. This is a fundamental difficulty with reconstructing images of specular reflectors using the back-projection scheme we have described.

We have developed a new image reconstruction algorithm called "selective back-projection," which

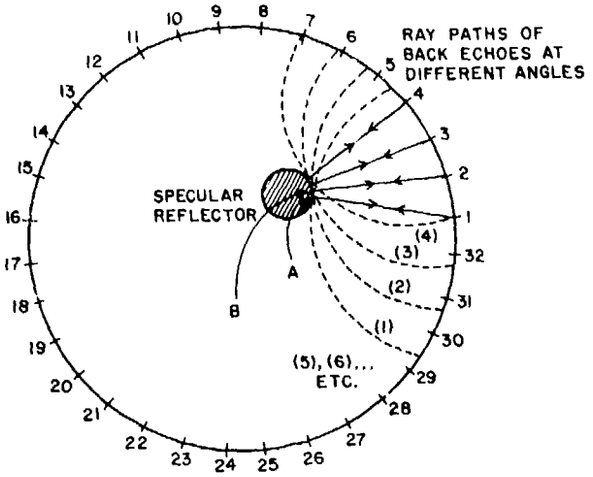

Figure 3. Imaging specular reflector by synthetic focus technique.

to some extent circumvents the difficulties inherent in the conventional back-projection method. In conventional back-projection, the amplitude of an image point is evaluated by summing contributions from all the sampling points in the aperture indiscriminately. This indiscriminate summation in the case of specular reflectors is inconsistent with the fact that an object point on the defect boundary is apparently "visible" to only a localized group of sampling points in the aperture. Thus, the obvious strategy is to only sum over sampling points that contribute constructively, and deliberately leave out sampling points that do not matter. There is also the necessity to distinguish between random and meaningful contributions, which is discussed in detail below. Based on computer simulation results, there is a dramatic improvement in the images generated by selective back-projection over those by conventional back-projection.

HARDWARE DESCRIPTION

The functional blocks of the three-dimensional synthetic focus imaging system are shown in Fig. 5. The scanning mechanism consists of a precision X-Y stage with ±7 μm positional accuracy and a rotator mount accurate to within 1/100 of a degree. A single 50 MHz transducer operated in pulse-echo mode is scanned over the sample of interest to create a synthetic aperture. The pulse-echo data is time-expanded by use of a sampling oscilloscope to facilitate data collection. The scanning and data acquisition operations are coordinated by a microcomputer system which also serves as an off-line data storage unit. Image reconstruction is performed on a minicomputer system in which all the processing algorithms reside. The two computer systems are linked so that data files can readily be retrieved for processing.

THEORY OF OPERATION

Point Spread Function

(1) Square Aperture System. This particular geometry does not lend itself to a complete

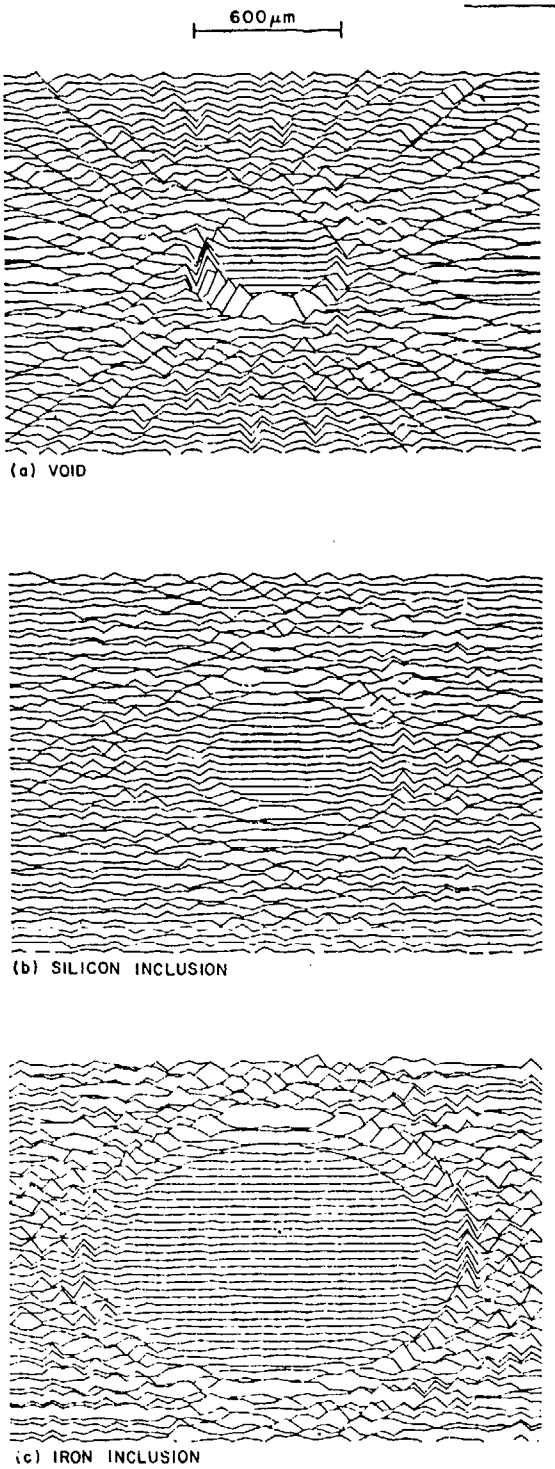

Figure 4. Computer simulation images of different types of circular defects inside silicon nitride: (a) voids; (b) silicon inclusion; and (c) iron inclusion.

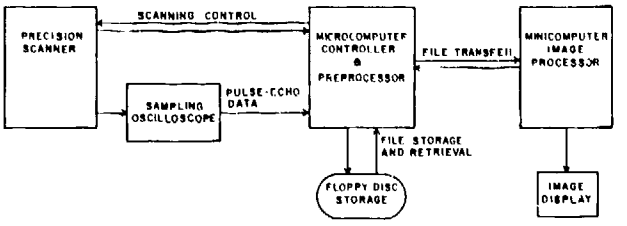

Figure 5. Three-dimensional synthetic focus imaging system.

analytic description because it is basically a wide aperture system and does not admit the paraxial approximation. However, one would not expect the PSF to deviate significantly from the analytical paraxial result.

$$H(x,y) = \frac{\sin\left[\pi \frac{2D}{\lambda z}(x - x_0)\right] \sin\left[\pi \frac{2D}{\lambda z}(y - y_0)\right]}{\sin\left[\pi \frac{2\ell}{\lambda z}(x - x_0)\right] \sin\left[\pi \frac{2\ell}{\lambda z}(y - y_0)\right]} \quad (1)$$

where D is the width of the square aperture, ℓ is the element spacing in x and y, and (x_0, y_0, z) is the location of the point target. The 40 dB lateral single point definition is therefore

$$d_x = d_y = \frac{\lambda z}{2D} \quad (2)$$

Note that the resolution is twice as good as a receiver array focused on a point insonified by a separate source, because in a synthetic aperture system the signal path is twice the distance from an array element to an object point.

Range resolution is primarily determined by the pulse width. The typical impulse response of the transducer used in the imaging system approximates a Gaussian envelope rf pulse four and a half cycles long.

Since the aperture is undersampled by a factor of 4, grating lobes are expected to occur where

$$\Delta x = n(N - 1)\frac{z\lambda}{2D} \quad (3)$$

and

$$\Delta y = m(N - 1)\frac{z\lambda}{2D} \quad (4)$$

$n, m = 1, 2, 3, \ldots$, where $N \times N$ is the number of elements in the sampled square aperture. However, because short pulses are used, there is no longer coherent summing at locations far removed from the point target. Thus, the grating lobe levels are reduced by approximately M/N, where M is the number of rf cycles in the pulse.

(2) Cylindrical Aperture System. Again, we do not attempt to derive the exact expression for the PSF of the system. Rather, we divide the difficult overall problem into two much simpler, mathematically tractable, albeit non-exact, parts. Through this exercise, we can estimate the resolution of the system. The validity of the approximation can easily be checked by computer simulation. We will consider the resolution in the z direction and that in the (r, θ) plane separately.

(a) Definition In z. The resolution of the z direction is assumed to be dependent only on the extent of the aperture in z. Further, we apply the paraxial approximation to obtain the definition in z.

$$H(z)\Big|_{\text{constant } r,\theta} = \frac{\sin\left[\pi \frac{2D_z}{\lambda R}(z - z_0)\right]}{\sin\left[\pi \frac{2\ell_z}{\lambda R}(z - z_0)\right]} \tag{5}$$

where D_z is the width of the aperture in z, ℓ_z is the element spacing in z, and R is the distance of the point target from the aperture. The 4 dB single-point definition in z is therefore

$$d_z = \frac{R\lambda}{2D_z} \tag{6}$$

Also, since the system is undersampled in z by a factor of 4, grating lobes are present. However, the use of short pulses suppresses the grating lobe levels. The aberration in the grating lobes due to the non-paraxial nature of the focusing at the grating lobe locations also serves to reduce their amplitudes.

(b) Definition In The (r,θ) Plane. The PSF in the constant z plane is assumed to depend only on angular (θ) distribution of the aperture. The PSF of a continuous cylindrical aperture at the constant z focal plane is given by

$$H(r,\theta) = \frac{2\pi}{a} K J_0 \left(2^{\prime} \right) \tag{7}$$

The Rayleigh definition d_R is therefore given by

$$d_R = \frac{0.6\,\lambda}{\pi} \approx 0.2\,\lambda \tag{8}$$

Hence, in principle, a remarkable resolution of $0.2\,\lambda$ can be attained. The reasons for this surprisingly good theoretical definition are two-fold. Firstly, a cylindrical system instead of a spherical one is being considered. Therefore, the first zero of the J_0 rather than the J_1 Bessel function dictates the Rayleigh definition. This gives an improvement by a factor of 1.6, but with higher sidelobe levels, and thus a relatively poorer two-point definition. Secondly, because in a synthetic aperture system any ray suffers twice the phase shift that it would in a single lens system, there is a factor of 2 improvement in definition.

IMAGING SPECULAR REFLECTORS

Consider, for instance, a spherical defect of radius b, at the center of an array of radius a, $a \gg b$. Suppose we are trying to obtain an image of a point P on the defect boundary, a distance R from the synthetic aperture array, as shown in Fig. 6. When a transducer is opposite the point P at the point A on the aperture, the response is maximum. Similarly, when the transducer is moved to point B, a point Q on the radial line passing through B and the center Q of the circle have maximum response. If the system is focused on the point P, the signal arriving at B from Q has the wrong time delay. The error in time delay is

$$\Delta T = \frac{2(BP - BQ)}{v} \tag{9}$$

where v is the velocity in the medium. Let angle POQ be θ. Since a or $R \gg b$, it can be shown that

$$\Delta T \approx \frac{4a}{v} \sin^2 \frac{\theta}{2} \tag{10}$$

If we regard the sampling points as essentially continuous, the total contribution to the received signal is

$$\Phi = \int_0^{2\pi} \exp\left[j\omega \frac{4a}{v} \sin^2 \frac{\theta}{2}\, d\theta\right] \tag{11}$$

where we have ignored the amplitude variation due to the change in signal path length. For θ small, Eq. (11) becomes a Fresnel integral. It can be shown that the main contribution to this integral is approximately from the region where

$$4ka \sin^2 \frac{\theta}{2} < \frac{\pi}{2} \tag{12}$$

where $k = \omega/v$. This corresponds to contributions having the same sign. The elements making the main contribution to the image point P are within the angular range.

$$-\frac{1}{2}\sqrt{\frac{\pi}{2ka}} < \sin\frac{\theta}{2} < \frac{1}{2}\sqrt{\frac{\pi}{2ka}} \tag{13}$$

Points outside this range may give in-phase or out-of-phase contributions.

As an example, in silicon nitride, at a frequency of 50 MHz, $\lambda = 220$ μm. A flaw 600 μm in diameter corresponds to $kb = 8.6$. Thus, the angular range 2θ over which all the contributions to received signals are positive, is approximately 50^0. For 32 elements evenly distributed around the aperture, this result implies that only five of them give cumulative contributions to the image of the point P, and

the remaining elements essentially contribute randomly.

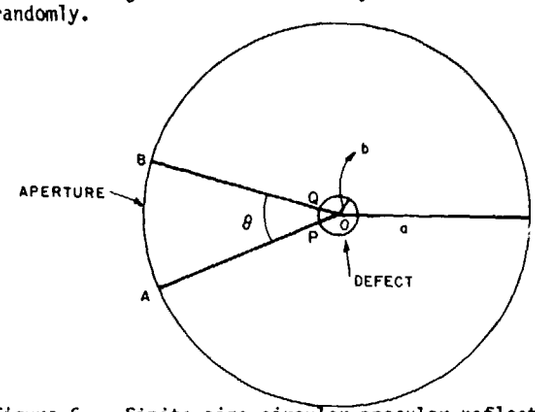

Figure 6. Finite size circular specular reflector using a circular aperture.

SELECTIVE BACK-PROJECTION

Figure 7 diagrams the entire synthetic focus procedure. Without loss of generality, a two-dimensional circular aperture is chosen as a specific example. The aperture synthesis step is mathematically a mapping from the object field $f(x,y)$ into the data field, which is a set of time series. For the purpose of illustration, the time series are ordered in the form of a matrix with each row corresponding to the complete pulse-echo data record at a sampling point. The columns are the progressive time entries of the pulse-echo data records. The synthetic focus step is simply the evaluation of the amplitude of each pixel in the image plane with the aid of a focus map generated independently based on geometric considerations. The focus map maps out a meandering path in the data field matrix, along which the contribution from each sampling point should be picked up for a particular image pixel.

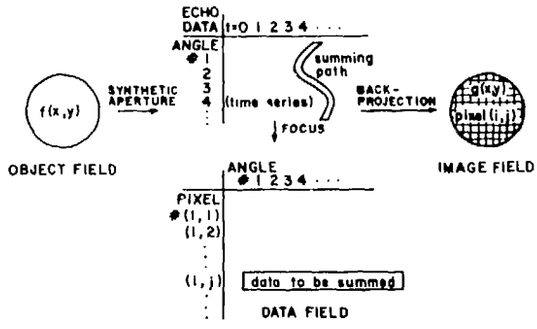

SELECTIVE BACKPROJECTION ALGORITHM:

I. DISCARD ISOLATED VALUES

II. ONLY SUM OVER PACKET OF ANGLES WITH THE SAME SIGN AND MAXIMUM CONTRIBUTION

Figure 7. Selective back-projection algorithm.

As explained before, conventional back-projection indiscriminately sums up all the contributions. The selective back-projection scheme sums up only the subset of contributions from adjacent elements that are of the same sign and give maximum total magnitude. The basis for this strategy is shown in Fig. 3. Although point A on the defect boundary is only physically "visible" to array element 1 in the reconstruction process, the sidelobe due to point B, which physically only excites array element 2, can influence the amplitude at A because of the use of a finite width transmitted pulse. If the sidelobe contribution from B, or equivalently the back-projected contribution from array element 2, is in phase with the main lobe contribution from array element 1, then the main level is boosted. For a smooth specular reflector, constructive contributions should only come from a connected neighborhood of the aperture. Since the data is automatically searched to find the packet of numbers which gives maximum contribution, one does not have to make any a priori assumptions about the orientation and radius of curvature of the surface of the specular reflector.

It is important to point out that even though the main lobe of an image point is boosted by sidelobe contributions from neighboring points, the improvement in overall amplitude is meager because only a small number of array elements are involved. A sidelobe from an image point tends to leave streaks in the image. These streaks come from lone contributions in the selective summing step. Therefore, to reduce the undesirably high sidelobe levels, lone contributions are discarded, and the corresponding pixel amplitudes are set to zero. In other words, one can set up a criterion that an object point has to be "seen" by at least M array elements to discriminate against unwanted sidelobes.

RECONSTRUCTION OF SPECULAR REFLECTORS

Because the selective back-projection algorithm can easily be implemented on a two-dimensional system without excessive computation time, we have, for purposes of illustration, reconstructed images of a void and of silicon and iron inclusions for a two-dimensional system on the computer. 32 evenly-distributed array elements are used. To simulate the pulse-echo data, theoretically derived backscattered waveforms for voids, silicon, and iron inclusions are employed. The calculation is based on the work on Ying and Truell[2,3] on scattering from spherical objects. The pulse-echo data for each array element is generated based on geometric optics considerations. The signal path is assumed to be along the line segment between the array element and the point on the defect boundary directly opposite the element, as shown in Fig. 3. Selective back-projection is then applied to reconstruct the image of the various single defects. The amplitude of each image point is evaluated by inspecting the contributions from all 32 array elements. Only the packet of contribution which gives maximum magnitude is kept. The number of entries in the packet (corresponding to the number of array elements involved) is checked, and if it is more than two, the amplitude of the image point is set to equal the packet sum. Otherwise, the image point value is forced to zero. Note that not all the array elements in the packet contribute equally. The element nearest to the normal of the defect surface at the image point will contribute the most. The neighboring contributions will fall off

approximately cosinusoidally. Thus, the selective back-projection algorithm, when used to image specular reflectors with dimensions greater than one wavelength, is equivalent to a limited angular aperture imaging system with cosinusoidal apodization.

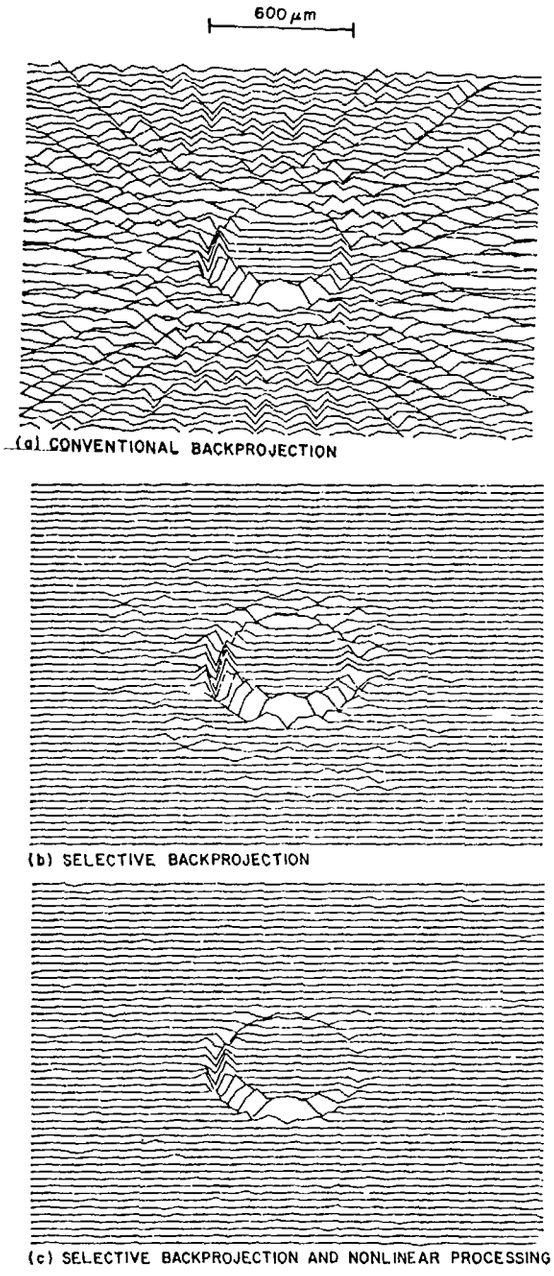

Figure 8. Images of a circular void defect processed by different schemes: (a) conventional back-projection; (b) selective back-projection; and (c) selective back-projection and nonlinear processing.

Figures 8a and 8b show the images of a void 600 μm in diameter obtained by conventional and selective back-projection methods respectively. There is decidedly great improvement in the clarity of the defect boundary in Fig. 8b. The defect boundary amplitude is boosted by 3-4 dB compared to that obtained by conventional back-projection, and the far-out sidelobe is almost completely annihilated by the selective back-projection process.

Similar improvement can readily be observed in Figs. 9 and 10 for the cases of silicon and iron inclusions.

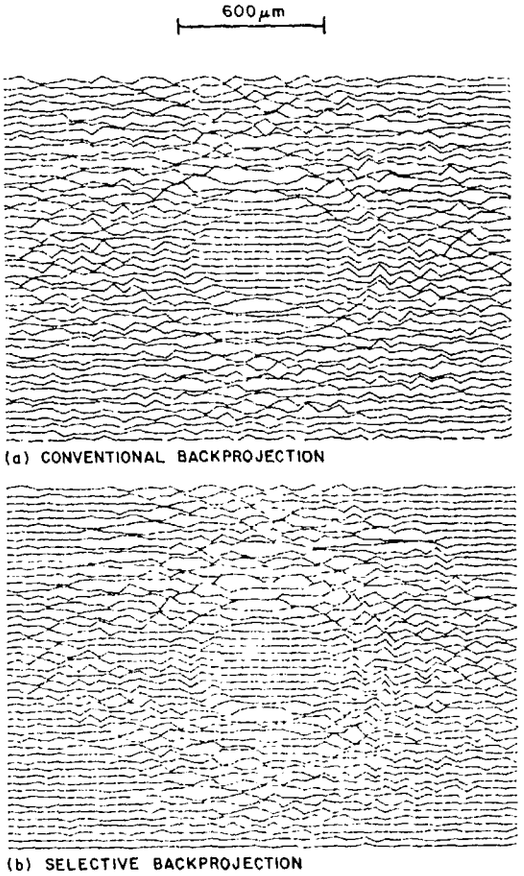

Figure 9. Images of a silicon inclusion defect processed by different schemes: (a) conventional back-projection; and (b) selective back-projection.

Even greater improvement in the image quality can be achieved when selective back-projection is combined with nonlinear processing. This is clearly evident in Fig. 8c for the case of a void.

CONCLUSION

We have developed the theories to characterize the imaging performance of square and cylindrical synthetic apertures. Most of the theoretical predictions are confirmed by computer simulation results. We have established that the three-dimensional synthetic focus technique is capable of extremely good single point resolution in all three directions. The result on the PSF for the cylindrical aperture configuration is of particular importance because of its generality. The theoretical analysis was carried out without

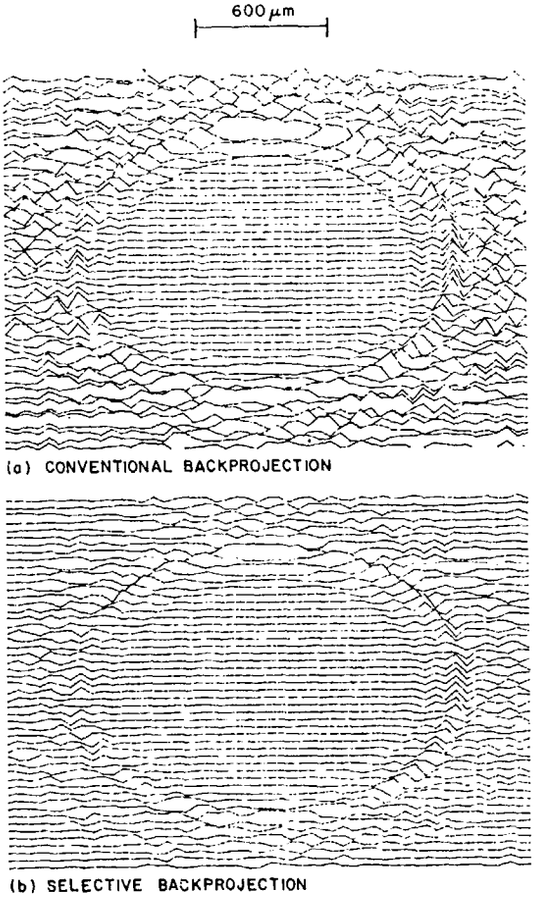

Figure 10. Images of an iron inclusion defect processed by different schemes: (a) conventional back-projection; and (b) selective back-projection.

making any assumption about the position of the image point relative to the aperture. This result may also apply to tomographic systems because of similarity in aperture geometry. In addition, we have analyzed the effect of sampling the aperture. Sampling introduces grating lobes whose positions are nearer to the main lobe than in a rectilinear system, but whose amplitudes are far weaker. Short pulse operation tends to reduce the grating lobe levels.

Specular reflectors present special difficulties for synthetic aperture imaging. Computer simulations show that the conventional back-projection technique is seriously inadequate in reconstructing images of specular reflectors because of the resulting high sidelobe levels. A selective back-projection technique has shown great promise in enhancing the images by suppressing sidelobe amplitudes.

We hope to obtain experimental results on our three-dimensional imaging system in the near future to substantiate the simulation results.

ACKNOWLEDGMENT

This work was supported by the Air Force Office of Scientific Research under Contract F49620-79-C-0217.

REFERENCES

1. C. H. Chou, B. T. Khuri-Yakub, G. S. Kino and A. G. Evans, "Defect Characterization in the Short Wavelength Regime," J. NDE, August, 1980.
2. G. Johnson, and R. Truell, "Numerical Computation of Elastic Scattering Cross-Section, J. Appl. Phys. 36, 3466, 1965.
3. C. F. Ying, and R. Truell, "Scattering of a Plane Longitudinal Wave by a Spherical Obstacle in an Isotropically Elastic Solid," J. Appl. Phys, 27, 1086, 1956.

SURFACE ACOUSTIC WAVE MEASUREMENTS OF SURFACE CRACKS IN CERAMICS

J. J. W. Tien, B. T. Khuri-Yakub, and G. S. Kino
Edward L. Ginzton Laboratory
Stanford University
Stanford, California 94305

and

A. G. Evans and D. Marshall
Materials Sciences
University of California
Berkeley, California 94720

ABSTRACT

We have extended our earlier investigation of scattering from surface cracks. In particular, we have studied the change in the reflection coefficient of a Rayleigh wave incident on a half-penny shaped surface crack along with the corresponding change in the acoustic crack size estimates as the cracked sample is stressed to fracture. We have examined in this manner both cracks in annealed samples and as-indented cracks. We have found that the fracture behavior for cracks in these two types of samples differ quite significantly, with the cracks in the annealed samples exhibiting a partial crack closure characteristic and the cracks in the as-indented samples displaying both crack closure and crack growth effects.

INTRODUCTION

This work is an extension of our earlier study[1] aimed at the establishment of procedures for locating and characterizing surface cracks in structural ceramics. The basic technique we have been using consists of launching a Rayleigh wave on the surface of the ceramic and observing the reflections of the acoustic surface wave from the crack. The particular type of crack we have been studying is a half-penny shaped surface crack introduced at a given orientation into the ceramic surface by a Knoop hardness indentor. In a previous paper,[1] we described a scattering theory valid in the low frequency regime based on the model of an open half-penny shaped crack. This theory related the reflection coefficient measured in the experiment with the crack size and fracture stress of the cracked sample. The theory was shown there to give predictions for the fracture stress which were in good agreement with experimental results. However, predictions for the crack size were observed to be considerably less accurate, with crack size estimates for unstressed samples being smaller by factors of two to three than the actual crack sizes measured after fracture.

Since that time we have extended the theory and correlated our results with what would be expected from fracture mechanics studies of ceramics. A series of experiments on annealed and unannealed samples has demonstrated the power of acoustic techniques for studying cracks in ceramics. The work indicates that cracks in annealed samples tend to be in contact over most of their cross-section and open up with applied stress. At the point of fracture, a very slight growth in crack radius is observed. On the other hand, cracks in unannealed as-indented samples exhibit partial closure at the sample surface. Upon application of stress, crack growth occurs, with crack radii tending to increase on the order of 50% . Upon release of stress, the cracks partially close, with their effective radii decreasing by less than 10% . As stress is further applied, further crack growth is observed, terminating in fracture at lower applied stresses than for equivalent annealed samples. This hysteresis effect has been observed for the first time acoustically. Both the initial crack radius, C_0 , and final radius, C_m , can be measured after fracture. The results obtained can be predicted accurately via acoustic techniques and agree well with the predictions of earlier theories and experiments by Marshall.[2,3,4]

An important result of our work is the demonstration that it is highly desirable to anneal ceramics in which surface cracks are likely to be present. Annealing inhibits further crack growth by relieving the residual stresses that are present. As evidence, we note that when unannealed samples are stressed, the crack radius increases by a factor of approximately two. Annealing, however, causes an increase in the fracture stress observed by a factor of approximately 1.5 .

THEORETICAL REVIEW

A general theory of scattering from flaws developed by Kino and Auld[5,6] forms the basis for our work. The scattering configuration considered is shown in Fig. 1. The reflection coefficient, S_{21} , is defined as the amplitude ratio of the reflected signal from the flaw, A_2 , received by transducer 2 , to the incident signal, A_1 , transmitted by transducer 1 , at the terminals of the transducers. In terms of the input power to the transmitting transducer, P , the Rayleigh wave displacement field when the receiving transducer is used as the transmitter, $u_j^{(2)}$, and the applied stress in the vicinity of the flaw before the flaw is introduced, $\sigma_{ij}^{A(1)}$, S_{21} is given by

$$S_{21} \equiv \frac{A_2}{A_1} = \frac{j\omega}{4P} \int_{S_c} u_j^{(2)} \sigma_{ij}^{A(1)} n_i dS \qquad (1)$$

for the case where the flaw is a void. Here, the integral is taken over the entire surface of the void, S_c .

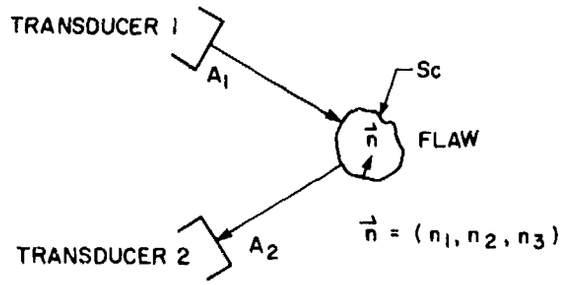

Figure 1 - A schematic of the geometry considered in the derivation of the reflection coefficient, S_{21} , for a flaw. Here, $\vec{n}$ is the inward normal to the flaw surface, S_c .

For the situation of a Rayleigh wave normally incident on a half-penny shaped surface crack of radius a located in the x-y plane (Figs. 2 and 3), the reflection coefficient may be written as

$$S_{11} = \frac{j\omega}{4P} \int_S \Delta u_z \sigma^A_{zz} dS \qquad (2)$$

where Δu_z is the discontinuity in the Rayleigh wave displacement field across the crack and σ^A_{zz} is the applied stress. The integral is now taken over just the semi-circular area, S . The theory we have developed for this configuration is strictly valid only in the low frequency regime (i.e. we require the maximum depth to which the crack extends below the sample surface to be much less than an acoustic wavelength). To take into account the effect of imaging at the surface in increasing the value of the stress intensity factor near the surface, as well as the variation with depth of the Rayleigh wave stress fields, we use the results of Budiansky and O'Connell[7] to write the surface integral in Eq. (2) in terms of a contour integral of the square of the mode I stress intensity factor, K_I , around the crack circumference C (Fig. 3)

$$\int_S \Delta u_z \sigma^A_{zz} dS = \frac{2(1 - \nu^2)}{3E} \int_C a K_I^2(\theta)\, d\ell \qquad (3)$$

Here, ν is Poisson's ratio and E is Young's modulus. The angular dependence of K_I caused by the surface imaging forces may be approximated from the results of Smith, Emery, and Kobayashi.[8] Smith et al. considered the case of a half-penny shaped surface crack in a beam of thickness 2c subject to a bending load. The applied stress then takes the linear form

$$\sigma^A_{zz}(y) = A(1 - y/c) \qquad (4)$$

where A is a constant and y is the distance from the sample surface (Fig. 2). The corresponding stress intensity factor is given by

$$K_I(\theta) = 2\sqrt{a/\pi}\, A[\psi_0(\theta) - (a/c)\psi_1(\theta)] \qquad (5)$$

where the functions $\psi_0(\theta)$ and $\psi_1(\theta)$ were numerically evaluated by Smith et al. (Fig. 4). To make use of these results for our case where the stress is due to the Rayleigh wave and not a bending load, we made a linear approximation to the Rayleigh wave stress field and so evaluated effective values for the constants A and c appearing in Eq. (4). Our result for the normalized reflection coefficient $wk|S_{11}|$, for a semi-circular crack, as a function of the normalized crack depth, $2\pi a/\lambda$, is given by the dashed curve in Fig. 5. Here $k = 2\pi/\lambda$ is the propagation constant of the Rayleigh wave, and w is the width of the acoustic beam at the crack.

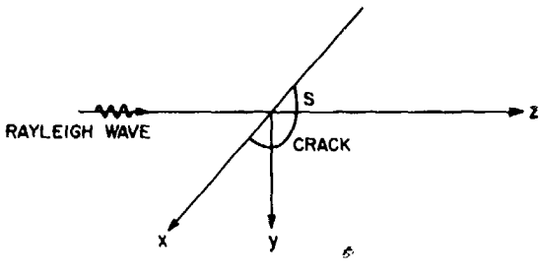

Figure 2 - Scattering geometry for a Rayleigh wave normally incident on a half-penny shaped crack.

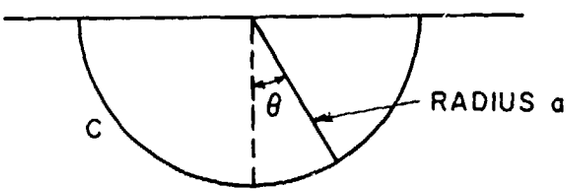

HALF - PENNY SHAPED CRACK

Figure 3 - Schematic of half penny shaped crack geometry.

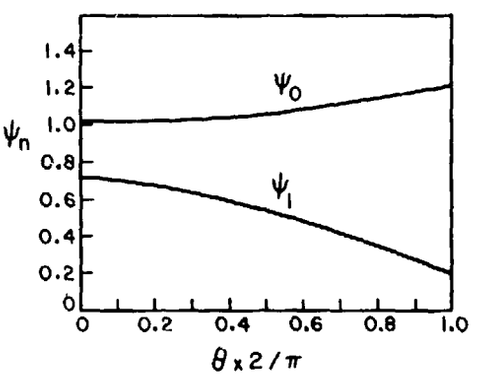

Figure 4 - Angular variation of the functions $\psi_0(\theta)$ and $\psi_1(\theta)$ (after Smith et al.[8]).

EXPERIMENTAL RESULTS

In our experimental studies, we used a commercial hot-pressed silicon nitride (NC-132) ceramic. The samples were in the form of 7.6 cm x 2.6 cm x .64 cm plates with polished surfaces into which cracks had been introduced via a Knoop indentor.

Measurements were made at a frequency of about 8.5 MHz , corresponding to an acoustic wavelength of about 680 μm . Two wedge transducers in the configuration shown in Fig. 6 were used to excite and receive the acoustic signals. The experimental values for the reflection coefficient thus obtained were then corrected for diffraction loss, the surface wave conversion efficiencies of the transducers, and for the effect of the transmitted and reflected acoustic beams each being at an angle α from the crack normal.

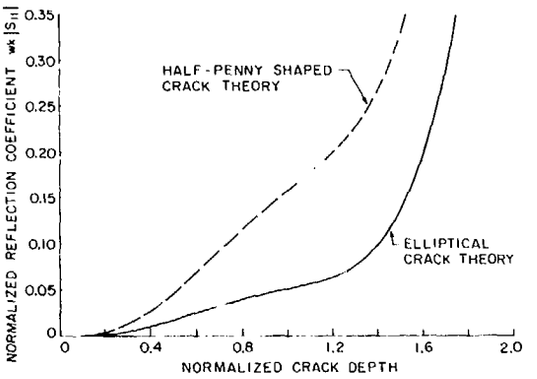

Figure 5 - Comparison of the results for the normalized reflection coefficient, $wk|S_{11}|$, as a function of the normalized crack depth for the half-penny shaped crack theory and the elliptical crack theory. The normalized crack depth is defined for each theory by the quantities $2\pi a/\lambda$ and $2\pi(b + h)/\lambda$, respectively.

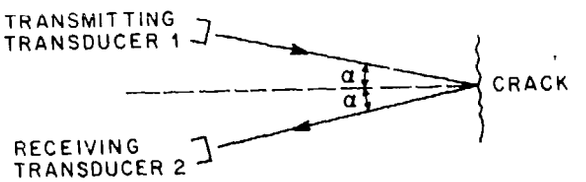

Figure 6 - Experimental scattering configuration used. In our study, $\alpha = 12.5°$.

Measurements were carried out on both annealed and as-indented samples. One sample was annealed in air and another in a vacuum with an annealing period of about six hours at a temperature of 1200°C . An additional three samples were tested in their as-indented state. For all five samples, we monitored the change in the acoustic reflection coefficient while the samples were slowly stressed to fracture in a 3-point bending jig.

Annealed Samples - We found that the cracks in the annealed samples are fairly well modelled by the open half-penny shaped crack theory described in the previous section, subject to the additional observation that in the unstressed state, partial crack closure occurs (Fig. 7). As shown in Figs. 8 and 9, loading the sample from zero stress to fracture produces a steady increase in the acoustic prediction for the crack depth. We additionally observe that if, after a period of loading, the load is reversed until the stress in the vicinity of the crack approaches zero, the crack size estimates tend to return to very near the intial value observed for the unstressed sample (Fig. 9). Application of a load to the cracked sample thus has the effect of causing the crack to open, as indicated by the increase in the acoustic size estimates with increasing load; however, subsequent removal of the load results in a return of the crack to its original partially closed state. Verification of this interpretation is obtained upon inspection of the fracture surface (Fig. 10). Here, only the initial flaw produced by the Knoop indentor is in evidence, as indicated by the single ring near the sample surface. Lastly, we compare the acoustic estimate for the crack depth at fracture with the optically measured crack depth (Table I). For both samples, agreement between these two values is quite good, with the deviation of the acoustically predicted values from the actual values being less than 17% .

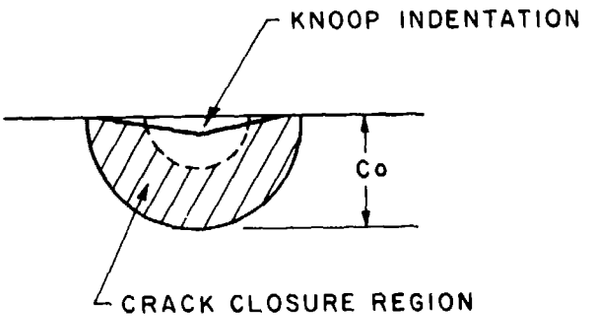

Figure 7 - Fracture model for crack in an annealed sample. C_0 is the depth of the initial flaw produced by the Knoop indentor. In the unstressed state, the crack is partially closed, as indicated.

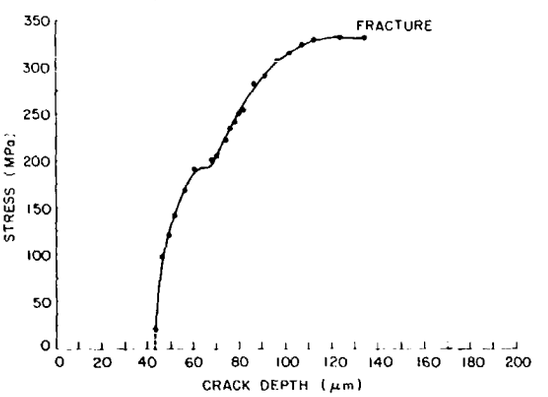

Figure 8 - Stress versus acoustic estimates of the crack depth for the sample annealed in air (sample 1). Crack depth estimates are obtained using the half-penny shaped crack theory (crack depth, C , then equals the half-penny shaped crack radius, a). The kink observed in the curve is believed to be an effect of the severe surface oxidation which occurred during the annealing process.

As-Indented Samples - The fracture model for the cracks in the as-indented samples differs considerably from the model for the cracks in the annealed samples. Firstly, there is crack closure at the sample surface in the vicinity of the Knoop indentation (Fig. 11). This arises because the Knoop indentation technique used to produce the crack creates a plastic deformation

region in the neighborhood of the indentation in which the residual stress fields have not been relieved as in the annealed samples. The second difference is that as the cracked sample is stressed to fracture, the crack grows from an initial depth of C_0 to a final fracture depth of C_m.

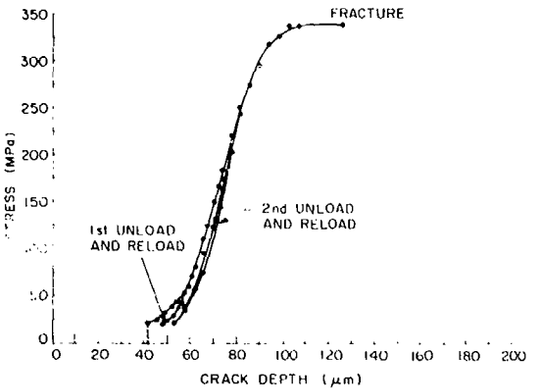

Figure 9 - Stress versus acoustic estimates of the crack depth for the vacuum-annealed sample (sample 2). Two unload-reload cycles were performed on this sample. Crack depth estimates were obtained using the half-penny shaped crack theory (crack depth, C, equals half-penny shaped crack radius, a).

Figure 10 - Typical fracture surface for crack in an annealed sample.

The first problem that we encounter is that our earlier scattering theory based on the model of an open half-penny shaped crack no longer is applicable here. We have not yet developed a theory which accurately models the surface closure characteristic of these as-indented cracks; however, we have worked out a theory based on a very crude approximation for the actual crack configuration which gives surprisingly good crack size predictions. This theory approximates the actual crack by an elliptical crack with semi-major axis a and semi-minor axis b where the surface closure effect is modelled by removing the elliptical crack center to a position a distance h below the sample surface ($b < h$; Fig. 12). We can evaluate the reflection coefficient for a Rayleigh wave normally incident on this type of crack configuration much as we did earlier. Again, the reflection coefficient is given by Eq. (2). Here, however, we must use a generalized form of Eq. (3) to relate the surface integral in Eq. (2) to the contour integral involving the stress intensity factor, K_I, namely

$$\int_S \Delta u_z \sigma^A_{zz} dS = \frac{2(1-\nu^2)}{3E} \int_C \rho(\vec{r}) K_I^2(\theta) d\ell \qquad (6)$$

In Eq. (6), the quantity $\rho(\vec{r})$ is defined for a given point $\vec{r}$ on the crack circumference C as the perpendicular to the tangent line at $\vec{r}$, which passes through the origin of the crack coordinate system. Shah and Kobayashi[9] have evaluated the angular dependence of the stress intensity factor for this type of crack subject to a bending load. The form for the applied stress is again linear

$$\sigma^A_{zz}(y) = C_1 + C_2 \frac{b-y}{b} \qquad (7)$$

where C_1 and C_2 are constants. In terms of C_1 and C_2, and the functions $M_T(\theta)$ and $M_L(\theta)$ numerically evaluated by Shah and Kobayashi, the stress intensity factor may be written in the form

$$K_I(\theta) = \frac{\sqrt{\pi b/a}}{E(k)} (a^2\cos^2\theta + b^2\sin^2\theta)^{1/4} \left\{ C_1 M_T(\theta) + C_2 M_L(\theta) \left[1 - \frac{k^2 E(k) \cos\theta}{(1+k^2)E(k) - (k')^2 K(k)} \right] \right\} \qquad (8)$$

Here, $K(k)$ and $E(k)$ are complete elliptic integrals of the first and second kinds, respectively, and the quantities k and k' are defined by

$$k^2 = 1 - (b/a)^2$$
$$(k')^2 = (b/a)^2 \qquad (9)$$

$M_T(\theta)$ and $M_L(\theta)$ represent the stress intensity magnification factors for the elliptical crack configuration shown in Fig. 12 for the respective cases of a uniform applied stress and a linearly varying applied stress. These functions have been calculated by Shah and Kobayashi for various values of the aspect ratio, b/a, and the depth ratio, b/h. As in the actual crack, the crack width is roughly twice the crack depth, and the region of surface closure is shallow compared to the maximum crack depth. We have chosen to use the Shah and Kobayashi results for $M_T(\theta)$ and $M_L(\theta)$ given for the parameter values $b/a = 0.6$ and $b/h = 0.9$ (Figs. 13 and 14). The result for the normalized reflection coefficient, $wk|S_{11}|$, as a function of the normalized crack depth $2\pi(b+h)/\lambda$, is then given by the solid curve in Fig. 5.

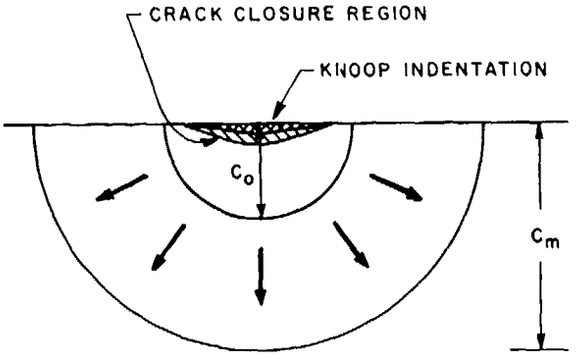

Figure 11 - Fracture model for an as-indented crack. C_0 is the depth of the initial flaw produced by the Knoop indentor; C_m is the depth to which the crack grows before fracturing. Crack closure occurs at the surface in the vicinity of the Knoop indentation.

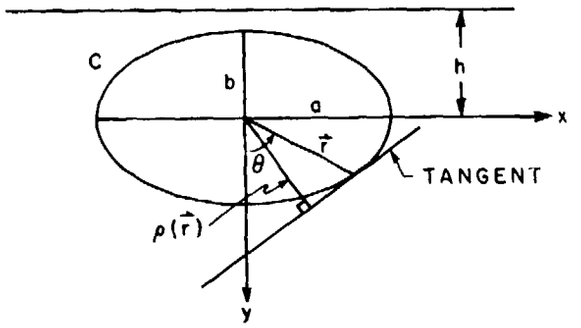

Figure 12 - Schematic of elliptical crack theory geometry.

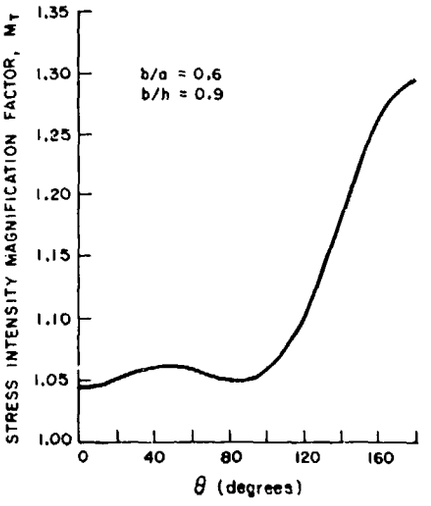

Figure 13 - Stress intensity magnification factor as a function of the angle θ for the elliptical crack configuration of Fig. 12, subject to a uniform applied stress (after Shah and Kobayashi[9]).

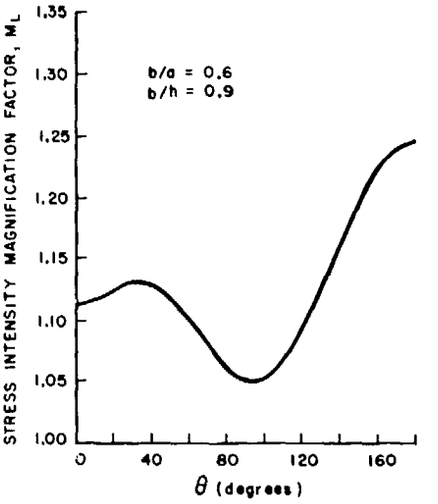

Figure 14 - Stress intensity magnification factor as a function of the angle θ for the elliptical crack configuration of Fig. 12, subject to a linearly varying applied stress (after Shah and Kobayashi[9]).

We used this crude theoretical model to give crack size estimates for the as-indented samples. As with the cracks in the annealed samples, there is a steady increase in the crack depth estimates with increasing load (Figs. 15, 16, and 17). However, with these cracks, crack growth occurs, as indicated by the failure of the cracks to return to their original sizes upon subsequent unloading. In addition, a small decrease in the crack size estimates is observed when the load is relieved, thus indicating a slight tendency of the cracks towards partial closure at the lower boundary upon unloading. Continuous growth of the crack until fracture is evidenced in Fig. 16 where two unload-reload cycles were performed. In each cycle, it is apparent that the crack never fully returns to the size it had previously when the stress is reduced to near zero values.

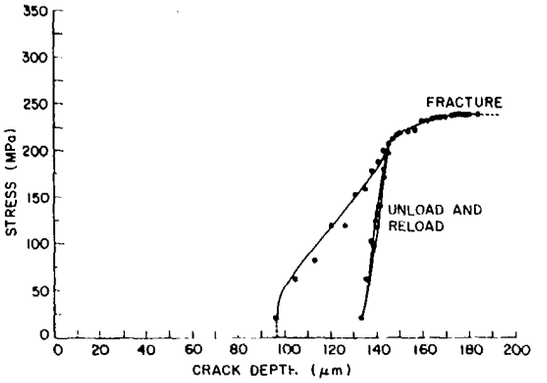

Figure 15 - Stress versus acoustic estimates of the crack depth for as-indented sample 4. One unload-reload cycle was performed. The crack depth, C , equals the quantity b + h (see Fig. 12).

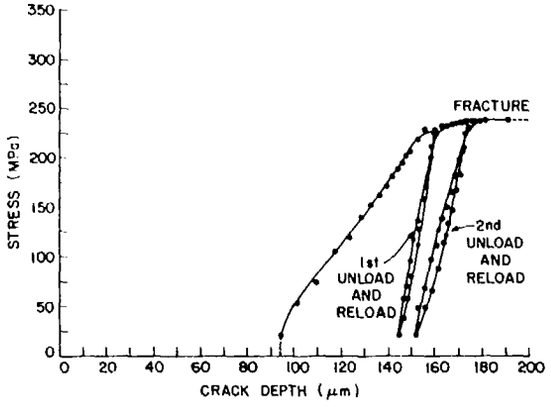

Figure 16 - Stress versus acoustic estimates of the crack depth for as-indented sample 5. Two unload-reload cycles were performed. The crack depth, C , equals the quantity b + h (see Fig. 12).

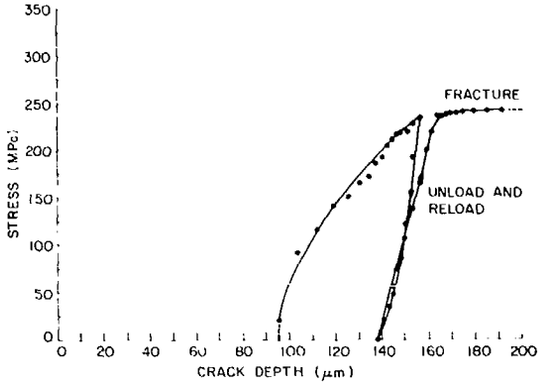

Figure 17 - Stress versus acoustic estimates of the crack depth for as-indented sample 6. One unload-reload cycle, where the sample was fully unloaded, was performed. The crack depth, C , equals the quantity b + h (see Fig. 12).

Examination of a typical fracture surface for these samples reveals the presence of two rings near the sample surface (Fig. 18). The inner ring represents the extent of the initial flaw produced at the time of indentation. The outer ring indicates the extent to which the crack grew before fracture occurred. A comparison of the acoustic estimates for tne initial crack depth, C_0 , and the depth at fracture, C_m , with the corresponding values measured optically is given in Table II. Considering the crudeness of the model used to obtain the acoustic estimates, the agreement between these values is remarkably good.

Lastly, we compare the fracture stresses of the five samples. From Tables I and II, we note that the crack depths at fracture for the annealed samples tend to be much less than those for the as-indented samples. Thus, we expect the annealed samples to fracture at higher stress values than the as-indented samples. In Table III, we show that this is indeed the case.

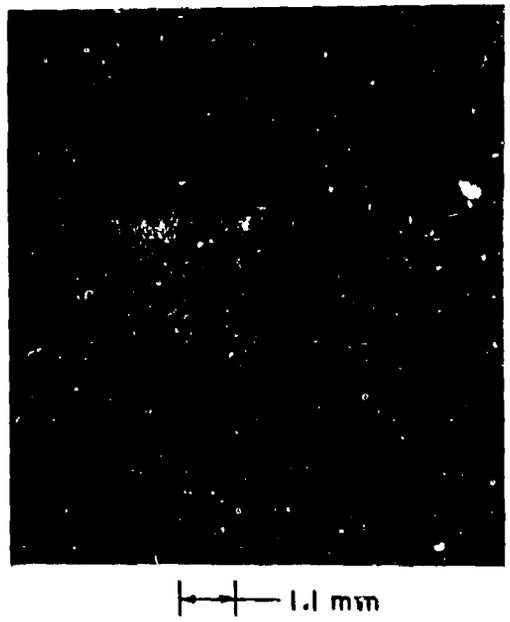

Figure 18 - Typical fracture surface for crack in an as-indented sample.

CONCLUSION

We conclude that the acoustic technique is a powerful method for observing fracture of surface cracks in ceramics. Major differences in the fracture behavior of cracks in annealed and unannealed samples have been documented.

It is apparent that there is a need to improve the acoustic scattering formulae and the estimates of the stress intensity factor for cracks closed at the sample surface. A theory by which to accurately predict how a partially closed annealed crack opens under applied stress would also be of considerable interest. We are currently developing a variational method to deal with the problems encountered in the scattering theory and are considering simple theories to deal with the latter problem.

Acknowledgement

This work was supported by the Office of Naval Research under Contract No. N0Q014-78-C-0283.

TABLE I: Annealed Samples

C_0 = initial crack depth

C_m = crack depth at fracture

$C_0 = C_m$

Sample	Acoustic C_m (μm)	Actual C_m (μm)	Deviation
1	134	115	17%
2	125	115	7%

TABLE II: As-Indented Samples

C_0 = initial crack depth

C_m = crack depth at fracture

$C_0 < C_m$

Sample	Acoustic C_0 (μm)	Actual C_0 (μm)	Deviation
4	97	116	16%
5	94	112	16%
6	96	112	14%

Sample	Acoustic C_m (μm)	Actual C_m (μm)	Deviation
4	184	220	16%
5	191	223	14%
6	185-191	205	7-10%

TABLE III: Fracture Stresses

	Sample	Fracture Stress (MPa)
Annealed:	1	332
	2	340
As-Indented:	4	238
	5	239
	6	242

References

1. J. Tien, B. Khuri-Yakub, and G.S. Kino, "Acoustic Surface Wave Probing of Ceramics," Proc. ARPA/AFML Rev. of Progress in Quantitative NDE, La Jolla, California, July 1979.

2. D.B. Marshall and B.R. Lawn, "Residual Stress Effects in Sharp Contact Cracking: Part 1, Indentation Fracture Mechanics," J. Matls. Science, vol. 14, pp. 2001-2012, 1979.

3. D.B. Marshall, B.R. Lawn, and P. Chantikul, "Residual Stress Effects in Sharp Contact Cracking: Part 2, Strength Degradation," J. Matls. Science, vol. 14, pp. 2225-2235, 1979.

4. B.R. Lawn and D.B. Marshall, "Residual Stress Effects in Failure From Flaws," J. Am. Ceramic Soc., vol. 62, no. 1-2, pp. 106-108, Jan-Feb 1979.

5. G.S. Kino, "The Application of Reciprocity Theory to Scattering of Acoustic Waves by Flaws," J. Appl. Phys., vol. 49, no. 6, pp. 3190-3199, June 1978.

6. B.A. Auld, "General Electromechanical Reciprocity Relations Applied to the Calculation of Elastic Wave Scattering Coefficients," Wave Motion, vol. 1, no. 1, pp. 3-10, January 1979.

7. B. Budiansky and R.J. O'Connell, "Elastic Moduli of a Cracked Solid," Int. J. Solid Structures, vol. 12, pp. 81-97, Pergamon Press, 1976.

8. F.W. Smith, A.F. Emery, and A.S. Kobayashi, "Stress Intensity Factors for Semicircular Cracks: Part 2, Semi-Infinite Solid," J. Appl. Mech., vol. 34, no. 4, pp. 953-959, December 1967.

9. R.C. Shah and A.S. Kobayashi, "On the Surface Flaw Problem," The Surface Crack Physical Problems and Computational Solutions, J.L. Swedlow, ed. pp. 79-124; presented at the Winter Annual Meeting of the ASME, New York, New York, November 1972.

10. G.S. Kino, "Variational Formulae for Scattering of Acoustic Waves by Flaws and for Acoustic Wave Propagation," Ginzton Laboratory Report No. 2634, Stanford University, November 1976.

11. G.S. Kino, "Variational Methods for Calculating J and M Integrals and Acoustic Scattering From Cracks," Materials Research Council Report, July 1980.

LOW FREQUENCY CHARACTERIZATION OF FLAWS IN CERAMICS

R. K. Elsley, L. A. Ahlberg, and J. M. Richardson
Rockwell International Science Center
Thousand Oaks, California 91360

ABSTRACT

There is an increasing need for the characterization of small flaws in ceramic components. This project is concerned with detecting and characterizing flaws in the bulk of ceramic parts. Cylindrical tensile test specimens of hot pressed Si_3N_4 are being prepared and, when available, will be inspected. In preparation for the arrival of the samples, measurement techniques have been developed for inspection of cylindrical shaped samples, signal processing techniques have been developed for obtaining flaw scattering data over a broad range of frequencies and analysis techniques have been developed to automatically extract flaw characteristics from measured data.

INTRODUCTION

Ceramic components are being considered for use in a variety of industrial applications. Their high strength and high temperature capabilities make they excellent candidates for use in jet engines and as high performance ball bearings. In order for ceramic components to qualify for service, it will be necessary to develop NDE techniques which can detect and characterize critical flaws in structural ceramics. Critical flaw sizes in ceramics are smaller than in metals, being typically tens to hundreds of microns.

This requires the use of higher frequency ultrasound and more sophisticated flaw characterization techniques than have previously been employed.

In the previous year of this program [1], samples of hot pressed Si_3N_4 were seeded with small flaws (100 μm to 400 μm diameter). Ultrasonic measurements of these flaws were made and 2 features of the flaw signals were extracted: a radius estimate obtained from the Born Inversion and A_2, the coefficient of scattering at long wavelengths. The features were combined in a probabilistic inversion algorithm which successfully estimated the flaw size and the material of which the flaw is composed.

In this year's program, samples containing only naturally occurring flaws are being examined. The samples are cylindrical tensile test specimens made of hot pressed Si_3N_4 which are scheduled to become available shortly. These samples will be inspected for bulk and surface flaws and then tested to failure. It will be determined whether failure originated at flaws which were detected ultrasonically and if so, how well the failure stress could have been predicted by fracture mechanics from the estimated flaw properties.

This task of the program is concerned with detecting and characterizing bulk flaws in the samples. In order to accomplish this goal, it has been necessary to develop new techniques in 3 areas:

- Inspection through curved surfaces
- Obtaining sufficiently broad bandwidth scattering measurements
- Automating the flaw characterization process.

Inspection through cylindrical surfaces has been performed on aluminum rods with the same dimensions as the ceramic samples will have. Both cylindrically and spherically focussed transducers have been used. Excellent detectability of a simulated 1000 μm flaw was achieved, indicating that significantly smaller flaws should also be detectable.

In order to obtain broad bandwidth ultrasonic scattering data, a technique has been developed to combine, in a statistically optimum manner, ultrasonic measurements from a set of transducers at different frequencies. This technique can provide the broad bandwidth needed to successfully characterize flaws over a significant range of sizes.

Automating of the flaw characterization process has been pursued on several fronts. The extraction of the low frequency features A_2 and τ from measurements has been performed in a statistically optimum manner designed to make the process less sensitive to noise in the measurements. Also, the Born Inversion technique has been developed into a practical form and the accuracy of its results in the presence of noise and limited bandwidth have been measured. Finally, a technique has been developed for determining whether a flaw signal is more likely to be due to a crack or to 2 pores located near one another.

INSPECTION THROUGH CURVED SURFACES

The test specimens to be examined are cylindrical tensile specimens made of hot pressed silicon nitride. Figure 1 shows a sketch of their shape. Failure in the test specimens will likely occur in the central or gage section. This section is a cylinder of 1/4 in. diameter. The goal of this task is to inspect and characterize bulk flaws (voids and inclusions) in the specimens. In order to do this, it is necessary to deal with the severe refraction which occurs when ultrasound enters a high velocity material such as

silicon nitride. Consider a plane wave incident from water onto a cylinder, perpendicular to the axis of the cylinder. The wave will diverge severely once within the cylinder and relatively little energy will impinge on a small bulk flaw.

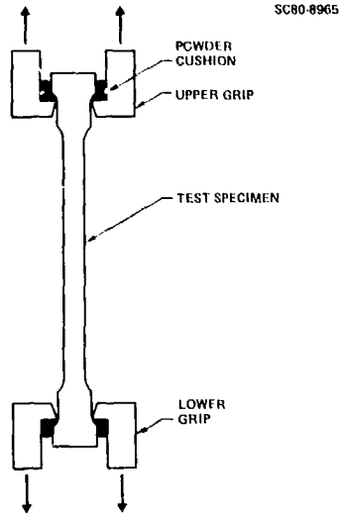

Fig. 1 Cylindrical tensile specimens made of hot pressed Si_3N_4.

In order to overcome this difficulty, one can use instead a focussed incident beam. Figure 2 shows 2 cases of a cylindrically focussed sound beam incident on a cylinder. If the distance of the transducer from the cylinder is such that in the absence of the cylinder the sound beam would have focussed at the location of the center of the cylinder, then the sound beam will focus at the center of the cylinder. This is shown in the left hand sketch of Fig. 2. If the transducer is moved up or down, the focal point will move up or down in the cylinder. The right hand sketch shows the case where the transducer has been moved down far enough that the sound beam is plane within the cylinder. Thus the sound energy can be concentrated at any desired point in the cylinder for obtaining good flaw measurements.

Figure 3 shows experimental measurements made to test this measurement method. In order to simulate the ceramic samples, measurements were made on a 1/4 in. diameter aluminum rod using a 20 MHz 3/8 in. diameter cylindrically focussed transducer with a focal length of 3/8 in. in water. The transducer was set to focus on the center of the rod. The lower curve in Fig. 3 shows the signal measured from a rod with no flaw in it. There is an echo from the front surface of the rod (which heavily saturated the receiving electronics) and an echo from the back surface of the rod. The region in between is seen to be free of unwanted echos which could interface with flaw detections and characterization. The upper curve in Fig. 3 shows the signal received from a rod containing a 1000 μm diameter end-drilled hole. It is seen that there is substantial echo from the hole as well as a second echo caused by the sound pulse traveling 2 round trips between the hole and the front surface. The fact that there is no detectable back surface echo indicates that the focal spot size is smaller than the hole diameter (1000 μm) and that the hole is therefore

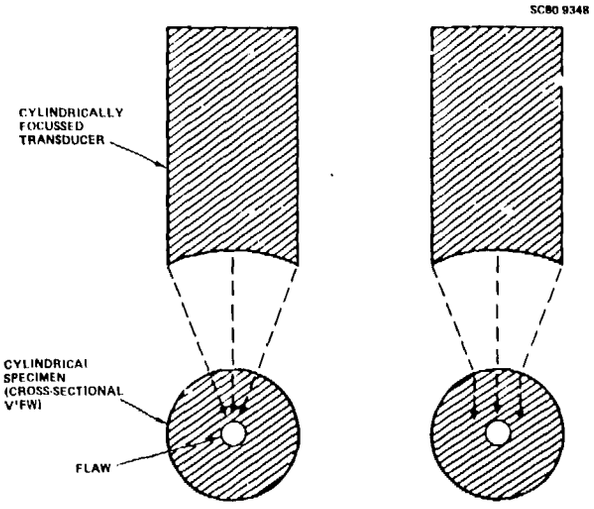

Fig. 2 Cylinderically focussed sound beam incident on cylinder. Varying distance of transducer from cylinder can cause focusing anywhere within or beyond cylinder.

intercepting the entire sound beam. This small focal spot size will allow the concentration of a significant amount of sound energy on the smaller flaws which are of interest in ceramics.

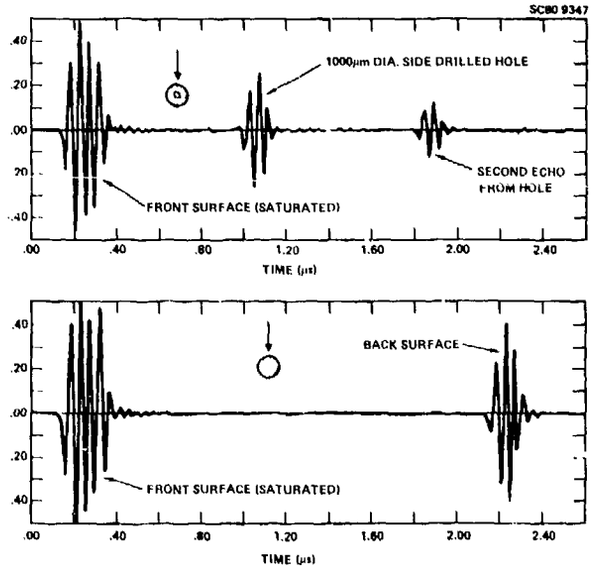

Fig. 3 Measurements with a cylindrically focussed sound beam on a cylindrical specimen. Top: with end-drilled hole to simulate flaw. Bottom: without end-drilled hole.

The focus of the cylindrical transducer is a line focus comparable in length to the diameter of the transducer. Real flaws in ceramics will likely be more sphere-like than the long cylindrical end-drilled hole flaw examined above. Therefore only a portion of the cylindrically focussed beam will impinge on the flaw. An alternative approach which offers some advantages over the cylindrical transducer is the spherically focussed transducer. In this case, the axial extent of the focal spot

in the rod will be much shorter, providing a better concentration of the sound axially. Unfortunately, the sound which enters the part out of the plane perpendicular to the axis of the rod will focus at a different depth than the in-plane sound will. Thus the focal spot will be distorted somewhat in a vertical (radial) direction.

Measurements with a 1/4 in. diameter spherically focussed transducer with a 1 in. focus in water are shown in Fig. 4. The lower curve shows the flaw-free case. As expected, the background noise level is higher than for the cylindrically focussed case. The upper curve shows the echo from the end drilled hole with about a 30 dB signal to noise ratio. Also visible are a second hole echo (1.9 μs), a backsurface echo (2.3 μs) and a creep wave which has travelled around the hole (1.5 μs).

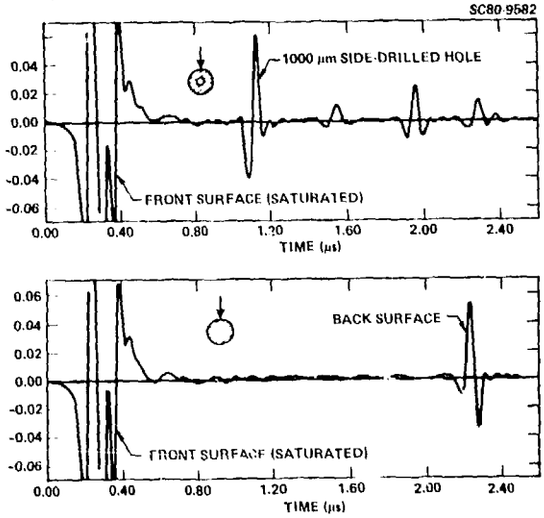

Fig. 4 Measurements with a spherically focused sound beam. Top: with end-drilled hole. Bottom: without end-drilled hole.

For successful flaw characterization it will be necessary to remove the spectrum of the incident pulse from the flaw echos. This will be done by machining a flat surface on one of the ceramic samples parallel to its axis. The echo from this surface will then be used to deconvolve the flaw echos.

BROADBAND SCATTERING MEASUREMENTS

The flaw characterization techniques being developed by the research community make use of the frequency content of the scattering from flaws rather than using only the peak amplitude of the scattered signal, as has traditionally been done. Therefore, it is important to be able to measure the scattering properties of flaws over a broad range of frequencies. Conventional ultrasonic transducers have a limited bandwidth, typically about 2 octaves. A technique has been developed which will combine the data measured by a set of transducers at different frequencies. This combining is performed in an optimum manner with respect to the noise sources which are present in the signals from each transducer. We first present a statistical treatment of the measurement process for a single transducer and then extend the treatment to the multiple transducer case.

For a single ultrasonic transducer operated in pulse-echo mode or for a pair of transducers operated in pitch-catch mode, the received signal from a flaw consists of the impulse response of the flaw convolved with the impulse response of the measurement system, which includes transducer, electronics, cabling, coupling and propagation effects. There will, in addition, be one or more sources of noise (random or systematic) in the signal. The process of removing the properties of the measurement system is therefore one of deconvolution.

When viewed in the frequency domain, the measured signal is the product of the flaw scattering amplitude and the spectral response of the measurement system, plus noise. The algorithms derived in this paper will be concerned with estimating the flaw scattering amplitude A in the frequency domain. An estimate of the impulse response of the flaw (in the time domain) can easily be obtained by performing an inverse Fourier transform on the frequency domain estimate.

Equation 1 is a measurement model which includes 3 noise sources which are commonly encountered.

$$f(\omega) = p(\omega)[A(\omega) + \nu_1(\omega) + \nu_2(\omega)] + \nu_3(\omega) \qquad (1)$$

where

$f(\omega)$ = measured signal
$p(\omega)$ = transducer spectrum
$A(\omega)$ = flaw scattering amplitude
$\nu_1(\omega)$ = coherent clutter
$\nu_2(\omega)$ = grain scattering
$\nu_3(\omega)$ = electronic noise

The three terms ν_1, ν_2 and ν_3 are the three noise sources. Each is described below. An important aspect of each is: what is its frequency dependence? The algorithms developed below must take the frequency dependences of the noise sources into account in order to obtain optimum estimates.

ν_3 is noise in the electronic circuitry used in the measurements. It is expected (and observed) to be white ($\alpha\omega^0$) at the frequencies of interest. It can also include quantization noise of an A/D converter if one is used.

ν_1 and ν_2 are of acoustic origin and have therefore been multiplied (convolved in the time domain) by the transducer and system response $p(\omega)$. ν_1 and ν_2 include a number of noise mechanisms which are grouped into these two categories according to their frequency dependences. These noise sources are not random in the sense of varying with time. Rather they are a coherent part of the measured signal as long as the measurement apparatus is unchanged. However, they are random in the sense that they vary from sample to sample and/or cannot be corrected for in the measurement process. Therefore, they degrade the measurements and must be taken into account when seeking to do optimum flaw characterization.

ν_1 includes signal sources such as reflections from nearby obstacles or surfaces or remnants of earlier arriving but much larger echoes. Their frequency dependence is about the same as that of the incident pulse. Therefore, the frequency

in the rod will be much shorter, providing a better concentration of the sound axially. Unfortunately, the sound which enters the part out of the plane perpendicular to the axis of the rod will focus at a different depth than the in-plane sound will. Thus the focal spot will be distorted somewhat in a vertical (radial) direction.

Measurements with a 1/4 in. diameter spherically focussed transducer with a 1 in. focus in water are shown in Fig. 4. The lower curve shows the flaw-free case. As expected, the background noise level is higher than for the cylindrically focussed case. The upper curve shows the echo from the end drilled hole with about a 30 dB signal to noise ratio. Also visible are a second hole echo (1.9 μs), a backsurface echo (2.3 μs) and a creep wave which has travell d around the hole (1.5 μs).

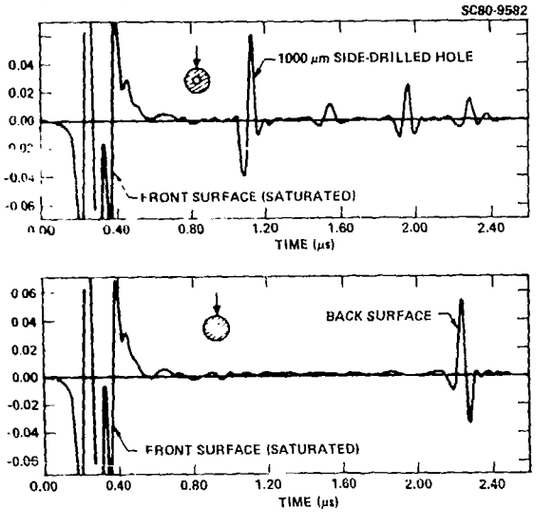

Fig. 4 Measurements with a spherically focused sound beam. Top: with end-drilled hole. Bottom: without end-drilled hole.

For successful flaw characterization it will be necessary to remove the spectrum of the incident pulse from the flaw echos. This will be done by machining a flat surface on one of the ceramic samples parallel to its axis. The echo from this surface will then be used to deconvolve the flaw echos.

BROADBAND SCATTERING MEASUREMENTS

The flaw characterization techniques being developed by the research community make use of the frequency content of the scattering from flaws rather than using only the peak amplitude of the scattered signal, as has traditionally been done. Therefore, it is important to be able to measure the scattering properties of flaws over a broad range of frequencies. Conventional ultrasonic transducers have a limited bandwidth, typically about 2 octaves. A technique has been developed which will combine the data measured by a set of transducers at different frequencies. This combining is performed in an optimum manner with respect to the noise sources which are present in the signals from each transducer. We first present a statistical treatment of the measurement process for a single transducer and then extend the treatment to the multiple transducer case.

For a single ultrasonic transducer operated in pulse-echo mode or for a pair of transducers operated in pitch-catch mode, the received signal from a flaw consists of the impulse respons the flaw convolved with the impulse respo the measurement system, which includes transducer, electronics, cabling, coupling and propagation effects. There will, in addition, be one or more sources of noise (random or systematic) in the signal. The process of removing the properties of the measurement system is therefore one of deconvolution.

When viewed in the frequency domain, the measured signal is the product of the flaw scattering amplitude and the spectral response of the measurement system, plus noise. The algorithms derived in this paper will be concerned with estimating the flaw scattering amplitude A in the frequency domain. An estimate of the impulse response of the flaw (in the time domain) can easily be obtained by performing an inverse Fourier transform on the frequency domain estimate.

Equation 1 is a measurement model which includes 3 noise sources which are commonly encountered.

$$f(\omega) = p(\omega)[A(\omega) + \nu_1(\omega) + \nu_2(\omega)] + \nu_3(\omega) \qquad (1)$$

where

$f(\omega)$ = measured signal
$p(\omega)$ = transducer spectrum
$A(\omega)$ = flaw scattering amplitude
$\nu_1(\omega)$ = coherent clutter
$\nu_2(\omega)$ = grain scattering
$\nu_3(\omega)$ = electronic noise

The three terms ν_1, ν_2 and ν_3 are the three noise sources. Each is described below. An important aspect of each is: what is its frequency dependence? The algorithms developed below must take the frequency dependences of the noise sources into account in order to obtain optimum estimates.

ν_3 is noise in the electronic circuitry used in the measurements. It is expected (and observed) to be white ($\alpha\omega^0$) at the frequencies of interest. It can also include quantization noise of an A/D converter if one is used.

ν_1 and ν_2 are of acoustic origin and have therefore been multiplied (convolved in the time domain) by the transducer and system response $p(\omega)$. ν_1 and ν_2 include a number of noise mechanisms which are grouped into these two categories according to their frequency dependences. These noise sources are not random in the sense of varying with time. Rather they are a coherent part of the measured signal as long as the measurement apparatus is unchanged. However, they are random in the sense that they vary from sample to sample and/or cannot be corrected for in the measurement process. Therefore, they degrade the measurements and must be taken into account when seeking to do optimum flaw characterization.

ν_1 includes signal sources such as reflections from nearby obstacles or surfaces or remnants of earlier arriving but much larger echoes. Their frequency dependence is about the same as that of the incident pulse. Therefore, the frequency

dependence of ν_1 is ω^0. ν_2 is due to grain scattering in the material being tested. It is Rayleigh scattering off of many grains which are smaller than the flaw and its power spectrum is therefore proportional to ω^4.

Which of these noises is dominant depends on the type of material being inspected and on what frequency range is being considered. In fine grained materials, grain scattering noise may be insignificant, although if that is the case one may choose to go to higher frequencies in search of smaller flaws and better resolution. In this case, grain scattering may be the limiting noise at high frequencies. At frequencies low enough that the wavelength is larger than the flaw, the scattering amplitude of the flaw drops off as ω^2 (Rayleigh scattering). In this case, ν_1 becomes dominant. At very low and very high frequencies, where there is little energy in the incident sound pulse, ν_3 will become dominant.

In order to obtain an optimum estimate of the scattering amplitude of a flaw in the presence of noise, we will now derive a series of algorithms for estimation of the flaw scattering amplitude. For a general reference, see [2]. First, we consider the case of a single transducer making pulse-echo measurements or a single pair of transducers making pitch-catch measurements.

Consider a measurement model containing additive noise:

$$f(\omega) = p(\omega) \cdot A(\omega) + \nu(\omega)$$

where

$f(\omega)$ = measured signal
$p(\omega)$ = transducer and other system responses
$A(\omega)$ = flaw scattering amplitude
$\nu(\omega)$ = Gaussian noise.

Let $\nu(\omega)$ have zero mean $E\ \nu(\omega) = 0$ and have a power spectral density:

$$E\ |\nu(\omega)|^2 = C_\nu(\omega)$$

In order to determine the maximum likelihood estimate $\hat{A}$ of A, we wish to maximize $P(A|f)$, the probability of A conditioned on the measurement f, with respect to A. From the measurement model we can write $P(f|A)$, the probability of the measurements f conditioned on the flaw scattering A. The $P(A|f)$ is then determined by

$$P(A|f) = \frac{P(f|A)\ P(A)}{P(f)} \tag{2}$$

The calculations proceed as follows,

$$\text{Log } P(f|A) = -\frac{1}{2} \sum_\omega \frac{|f - pA|^2}{C_\nu(\omega)} \tag{3}$$

$$\text{Log } P(A) = -\frac{1}{2} \sum_\omega \frac{|A|^2}{C_A(\omega)} \tag{4}$$

where

$C_A(\omega)$ = expectation value of $|A|^2$ over the ensemble of possible flaws.

We assume that $C_A(\omega)$ is a constant independent of frequency. We now maximize Log $P(A|f)$ with respect to A^*:

$$\frac{\partial}{\partial A^*} \text{Log } (A|f) = \frac{\partial}{\partial A^*} \text{Log } P(f|A) + \frac{\partial}{\partial A^*} \text{Log } P(A) = 0$$

$$\sum_\omega \frac{-p^*(f - pA)}{C_\nu} + \frac{A}{C_A} = 0$$

Therefore at each frequency

$$\hat{A}(\omega) = \frac{P^*(\omega)\ f(\omega)}{|P(\omega)|^2 + C(\omega)} \tag{5a}$$

where

$$C = C_\nu / C_A$$

Equation (5a) is the desired result. Note that at those frequencies for which the signal-to-noise is good ($C_\nu \ll |P|^2\ C_A$), Eq. (5b) reduces to the expected

$$\hat{A}(\omega) = \frac{f(\omega)}{P(\omega)} \tag{5b}$$

At frequencies where the signal-to-noise is poor ($C_\nu \gg |P|^2\ C_A$), $C(\omega)$ "desensitizes" the estimate, causing

$$\hat{A}(\omega) \to 0$$

in order to avoid a noise dominated result.

The special case of

$$C(\omega) = \text{const}$$

has been used in our lab and elsewhere [3] for a number of years with good success. An example of the application of Eq. (5a) is shown in Figs. 5, 6, and 7. Figure 5 shows a calculation of the magnitude of the pulse-echo scattering amplitude A of a 1200 μm diameter spherical void. The frequencies at which the first few peaks occur are important in sizing such a flaw. Figure 6 shows the magnitude of 5 estimates of this scattering amplitude from experimental data. The data were recorded with a 2.25 MHz transducer whose spectrum is shown as the left-hand curve in Fig. 8. Each curve in Fig. 6 was obtained using Eq. (5a) with a different assumed constant value of $C(\omega)$ (i.e., a different desensitization). The upper curves have too little desensitization and show wild fluctuations below 1 MHz and above 4 MHz. As the desensitization is increased, the noise induced fluctuations decreased while in the region where there is appreciable energy (1.5 MHz to 3.5 MHz), the estimate remains relatively unchanged. Figure 7 shows the optimum estimate of A. (Figure 7 is a replot of the lowest curve Fig. 6). Note that (ignoring an arbitrary scale factor), the estimate of Fig. 7 corresponds well to the theoretical curve (Fig. 5) in the frequency region where there is significant energy and the noise induced fluctuations have been suppressed elsewhere. The first 2 peaks have been accurately located.

Another case of interest is that of noise (of acoustic origin) which has been filtered by the transducer. Consider the measurement model

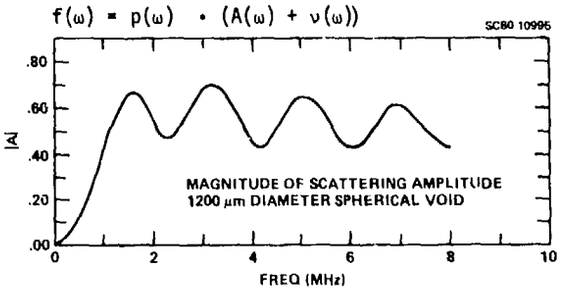

Fig. 5 Calculated scattering amplitude of a 1200 μm diameter spherical void in Ti-6Al-4V.

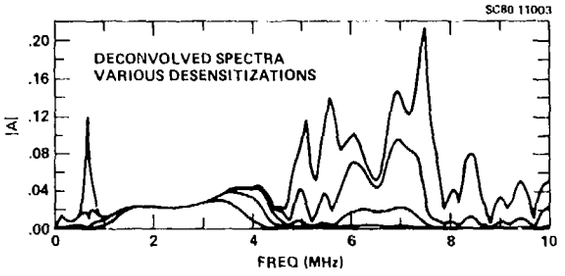

Fig. 6 Deconvolved spectra of a flaw showing noise dominated results at low and high frequencies due to insufficient desensitization.

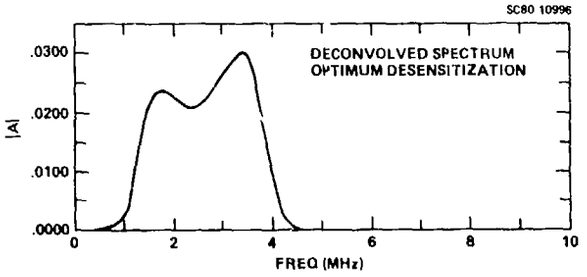

Fig. 7 Deconvolved spectrum with optimum desensitization.

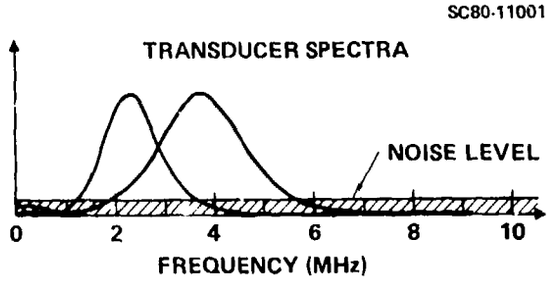

Fig. 8 Magnitude spectra of a 2.25 MHz and a 5 MHz transducer.

where, as before, $\nu(\omega)$ is Gaussian noise with zero mean and power spectral density $C(\omega)$. The derivation of $\hat{A}$ proceeds as above, yielding the result

$$\hat{A}(\omega) = \frac{P^*(\omega)\, f(\omega)}{|P(\omega)|^2\,(1 + C(\omega))} \qquad (5c)$$

Once again, the $\hat{A}$ approaches Eq. (5b) for high signal-to-noise and approaches zero for low signal-to-noise.

Among the advantages of this type of treatment of noisy signals are the following:

1. Any frequency dependence of noise energy can be optimally handled.
2. Systematic as well as random noise sources can be treated. Since $C(\omega)$ serves the purpose of "desensitizing" $\hat{A}$ at those frequencies where Eq. (5b) is not a good estimate, it is not important whether the cause of the misestimate is random noise or systematic signals.
3. Noise which has passed through the transducer (ν_1 and ν_2 in Eq. 1) is treated on an equal footing with noise which has not (ν_3).
4. A final advantage of this technique is that increased bandwidth can be obtained by combining, in an optimum manner, data from several transducers with different center frequencies. A derivation of this result is given in the next section.

Any one piezoelectric transducer has a limited bandwidth, limited by the low and high frequency points at which the signal from the transducer drops into the noise. Figure 8 shows the magnitudes of the spectra of a 2.25 MHz and a 5 MHz transducer. The hatched area is a schematic indication of the noise level that might be present on signals returning from flaws. Each transducer has a comparable percent bandwidth; they overlap in a small region and together cover a broader band than either alone.

Figure 9 shows the measurement situation to be used for combining data from several transducers in order to achieve broader bandwidth data. The figure shows two circular piston transducers of the same diameter at the same distance from the flaw. However, the two transducers have different center frequencies, shown schematically by the different thicknesses of the transducer elements and the different beam widths at the respective center frequencies.

Because the transducers are the same diameter and at the same disance from the flaw, the diffraction patterns from both transducer at any given frequency are the same (assuming that the actual transducers are about equally good approximations to a piston source, which is not always true in practice). Therefore, data from two (or more) transducers can be combined by an algorithm which is a simple extension of the algorithms derived above.

This algorithm will now be derived. Consider the measurement model

$$f_1(\omega) = p_1(\omega)\, A(\omega) + \nu_1(\omega) \qquad (6a)$$

$$f_2(\omega) = p_2(\omega)\, A(\omega) + \nu_2(\omega) \qquad (6b)$$

...

where each equation refers to measurements made with a different transducer having different properties (p_i) and different noise (ν_i). We wish to maximize $P(A|f_1, f_2, \ldots)$, the probability of the

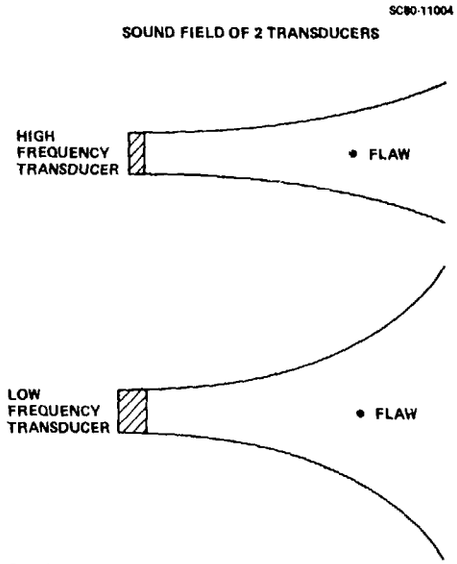

Fig. 9 Measurement of a flaw with two transducers at different frequencies but with same diameter and at same distance.

flaw properties A conditioned jointly on the set of measurements f_i. We make use of

$$P(A|f_1, f_2, \ldots) = \frac{P(f_1, f_2, \ldots|A)\, P(A)}{P(f_1, f_2, \ldots)}$$

and

$$\text{Log } P(f_1, f_2, \ldots|A) = -\frac{1}{2} \sum_i \sum_\omega \frac{|f_i - P_i A|^2}{C_{vi}}$$

The resulting estimate of A is

$$\hat{A} = \frac{\frac{P_1^* f_1}{C_1} + \frac{P_2^* f_2}{C_2} + \ldots}{1 + \frac{|P_1|^2}{C_1} + \frac{|P_2|^2}{C_2} + \ldots} \qquad (7)$$

where

$$C_i = C_{vi}/C_A$$

For a single transducer, this result reduces to Eq. (5a). Note that at frequencies where more than one transducer has appreciable signal-to-noise, the estimate combines the data from all of them. Where one or none of the transducers have sufficient signal-to-noise, Eq. (7) works in the same manner as Eq. (5a).

One more step is needed for Eq. (7) to work. The assumption that the transducers are at equal distances from the flaw implies that the arrival time of the flaw signal at each transducer is the same. If the arrival times differ by more than 5% of a period at the overlap frequency, then the estimate A will be distorted in that region and deconvolutions derived from A will also be distorted.

Experimentally, this requires positioning the transducers with a precision of a fraction of a wavelength or, equivalently, by time-aligning the received signals during postprocessing. In fact, the most accurate method of positioning the transducers is by an ultrasonic arrival time measurement, so that both approaches depend on how accurately the pulse arrival time can be measured.

Because the pulses from the various transducers have different shapes, different measures of pulse arrival time will give different (not necessarily correct) answers. Several measures have been investigated. The first method involves considering the pulse to be of arbitrary shape and measuring the mean arrival time of all frequency components. The arrival time of a particular frequency component of a signal $S(\omega)$ is

$$\tau(\omega) = \frac{d}{d\omega} \arg [S(\omega)]$$

averaging over all frequencies in $S(\omega)$ can be done as follows

$$\hat{\tau} = \frac{\int \tau(\omega)\ |S(\omega)|^2\, d\omega}{\int |S(\omega)|^2\, d\omega}$$

this algorithm is more easily implemented in the time domain, where

$$\hat{\tau} = \frac{\int t\ s^2(t)\ dt}{\int s^2(t)\ dt} \qquad (8)$$

where $s(t)$ is the Fourier transform of $S(\omega)$. Eq. (8) was used successfully to time-align the pulses in the data presented below.

A second (and better) method would be to bandpass the received signals to include only the overlap frequencies, thereby, in effect, eliminating most of the differences in pulse shape. Then by applying Eq. (8) or simply by measuring the difference between the phase curves, a better estimate can be achieved. A potential problem with this method is that if the overlap range of frequencies is too small, then uncertainties of 2π in the phase (one period in the arrival time) can occur. This method could be used for precise time-alignment after the first method had been used for course alignment.

A third (and in principle even better) method of time-alignment would be to make use of our knowledge of the scattering properties of flaws and use the low frequency method of finding the center of a flaw [4]. (Improvements in this method are described under automtic flaw characterization, below) However, it is unlikely in practice that the higher frequency transducers will have sufficient energy at low frequencies for this method to work.

An example of combining data from multiple transducers is shown in Figs. 10 and 11. The two transducers whose spectra are shown in Fig. 8 were used to make measurements of a 1200 μm spherical void flaw in a Titanium-6Al-4V disk. Figure 10 shows the spectra which result from separately estimating A for each transducer using Eq. (5a). Note that each transducer has successfully measured 2 of the peaks in Fig. 5. Figure 11 shows the result of applying the combined algorithm

(Eq. 7). Note that now all of the first three peaks have been successfully measured and that the separate spectra have been smoothly joined in the overlap region. The resulting spectrum is a fairly good reproduction of Fig. 5, except for a gradual increase in |A| with increasing frequency, which is due primarily to the transducer spectra having been measured through a thicker section of titanium than the flaw signals were.

SC80-10999

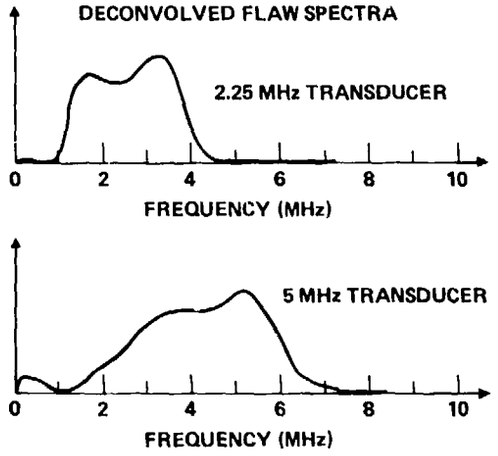

Fig. 10 Deconvolved spectra obtained by each transducer separately. a) 2.25 Mhz b) 5 Mhz.

SC80-11000

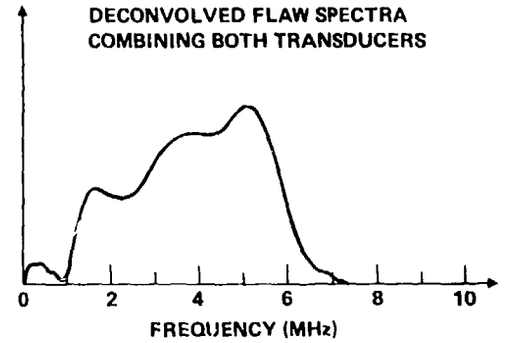

Fig. 11 Combined spectrum obtained from both transducers.

The algorithms developed in this paper (e.g., Eqs. 5 and 7) suggest a matched filtering technique for improved flaw detection. As an intermediate step toward estimating the flaw scattering amplitude, these equations involve terms of the form

$$p^*(\omega)\ f(\omega)$$

that is, the flaw spectrum multiplied by the complex conjugate of the transducer spectrum. Note that $p^*(\omega)$ is the matched filter by which one would multiply $f(\omega)$ in order to optimally detect a flaw whose impulse response was a δ-function. This suggests that because small flaws (especially voids) have relatively short impulse response, detection of flaws could be more successfully done using the Fourier transform of $p^*(\omega)\ f(\omega)$ rather the received signal itself. Computer experiments indicate that flaw signals do not have sufficiently δ-function-like impulse respones to significantly improve detection. However, if it is desired to detect flaws in a particular class, using the Fourier transform of

$$p^*(\omega)\ A_o^*(\omega)\ f(\omega)$$

should improve detection. Here, $A_o(\omega)$ is the scattering amplitude of a typical member of the class of flaws.

AUTOMATIC FLAW CHARACTERIZATION

The new flaw characterization methods which are being developed by the research community often require the extraction of data from ultrasonic measurements by sophisticated techniques. If these methods are to prove useful in field applications, then it will be necessary to fully automate this feature extraction process. If not, then it will be necessary to have highly trained personnel making subtle judgments in routine testing situations. This is not a practical approach in view of personnel availability, labor costs, and required speed and accuracy of inspection. Therefore, full automation of these techniques in the form of robust, noise resistant algorithms is necessary.

In this section, we present 3 results in automated feature extraction and flaw characterization. They are

1. Statistically based algorithms for the extraction of low frequency features A_2 and τ
2. An analysis of the accuracy of the Born inversion when applied to noisy data with limited bandwidth, and
3. An algorithm for deciding if a signal is more likely to be caused by a crack or by 2 voids.

STATISTICAL ALGORITHMS FOR EXTRACTING A_2 AND τ

In recent years the scattering of elastic waves at low frequencies (i.e., in the so-called Rayleigh regime) has received increased attention [5,6,7] particularly in the context of nondestructive evaluation. For example, a relation between low frequency scattering and fracture mechanics has been found [8]. Several investigators [9,10,11] have established that low frequency scattering data is surprisingly rich in information in the elastic wave case compared with the familiar scalar wave case. It has also been found [12,13] that, in the low frequency range extending somewhat beyond the Rayleigh regime, the variation of phase shift with frequency gives information about the location ofthe center of the scatterer.

The inversion technique developed last year for internal flaws in ceramics made use of 2 low frequency features of the scattering of sound from the flaw: A_2 and τ.

A_2 is the lowest order term in an expansion of the scattering amplitude A with respect to frequency:

$$A(\omega) = A_2\omega^2 + O(\omega^4) \quad . \tag{9}$$

The angular dependence of A_2 has been shown [1C,11] to contain size and shape information about the scatterer. τ defines the location of the center of the scatterer with respect to the time origin of the measurements. Thus if a scatterer is displaced by a distance $x = v\tau$ from the center of the measurement coordinate system, where v is the sound velocity in the surrounding medium, then the scattering amplitude will be

$$A'(\omega) = A(\omega)\, e^{i\omega\tau} \tag{10}$$

$$= A_2\omega^2 + i\tau A_2\omega^3 + O(\omega^4) \quad . \tag{11}$$

The two techniques discussed below estimate A_2 and τ from the low frequency portion of measured frequency spectra.

Consider first a noiseless measurement model based on Eq. (11).

$$f(\omega) = p(\omega)\, A(\omega)$$

$$\simeq p(\omega)\, [A_2\omega^2 + i\tau A_2\omega^3]$$

where

$f(\omega)$ = frequency spectrum of measured signal
$p(\omega)$ = spectrum of transducer, electronics, etc.

Estimates $\hat{A}_2$ and $\hat{\tau}$ based on this model would then be

$$\hat{A}_2 = \lim_{\omega\to 0} \frac{1}{2} \frac{d^2 \hat{A}}{d\omega^2}$$

$$\hat{\tau} = \lim_{\omega\to 0} \frac{1}{6i\, A_2} \frac{d^3 \hat{A}}{d\omega^3}$$

where

$$\hat{A}(\omega) = \frac{f(\omega)}{p(\omega)}$$

These estimates were shown [4] to be extremely noise vulnerable, especially because $\hat{A}$ becomes very small as $\omega\to 0$. A noise insensitive algorithm has been developed [4] based on the following measurement model

$$f(\omega) = p(\omega)\, [A_2\omega^2 + i\tau A_2\omega^3 + \nu_2(\omega)$$

$$+ \nu_3(\omega)] + \nu_1(\omega) \tag{12}$$

where

$\nu_1(\omega)$ = electronic noise
$\nu_2(\omega)$ = grain scattering noise
$\nu_3(\omega)$ = "model error" noise.

The electronic noise is taken to be white (independent of frequency) and can include quantitization error of an A/D converter, if used. The grain scattering power spectrum is taken proportional to ω^4.

By "model error", we mean the contribution to the measured signal at higher frequencies due to the fact that the terms of order ω^4 and higher in Eq. (11) become non-negligible. The power spectrum of this "noise" source is therefore taken to be proportional to ω^8.

The estimates $\hat{A}_2$ and $\hat{\tau}$ for this model are

$$\hat{A}_2 = \frac{b_2}{a_4} \tag{13a}$$

$$\hat{\tau} = \frac{b_3\, a_4}{1\, b_2 a_6} \tag{13b}$$

where

$$a_n(\omega) = \sum_\omega \frac{|p(\omega)|^2\, \omega^n}{C(\omega)}$$

$$b_n(\omega) = \sum_\omega \frac{p^*(\omega)\, f(\omega)\, \omega^n}{C(\omega)}$$

$C(\omega)$ is the power spectrum of the 3 noise sources and is of the form

$$C(\omega) = C_0 + |p|^2\, (C_4\omega^4 + C_8\omega^8) \tag{14}$$

where the three terms are the covariance functions (or power spectra) of ν_1, ν_2, and ν_3 respectively.

The algorithm makes use of information from all frequencies in a certain range in making its estimates. This range is determined by $C(\omega)$. Where $C(\omega)$ is large, little contribution is made to the estimate and where $C(\omega)$ is small, a large contribution is made.

Figures 12-15 show the results of testing these estimators on noiseless theoretical data.

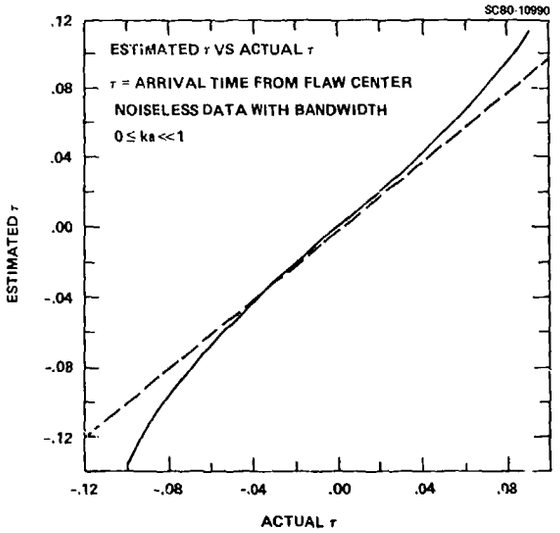

Fig. 12 Estimated τ vs true τ using $0 < ka \ll 1$. Flaw front surface is at $\tau = -0.3$.

In order to see how well they work when there is sufficient low frequency data available that

$$A(\omega) \simeq A_2\, \omega^2 \tag{15}$$

is a good approximation over a usable portion of the spectrum, we used as input

$$f(\omega) = p(\omega)\, A_2\omega^2\, e^{i\omega\tau} \tag{16}$$

In this case, there will be no model errors due to the approximation (15), but if $\omega\tau$ is too large (i.e., the initial choice of coordinate system is

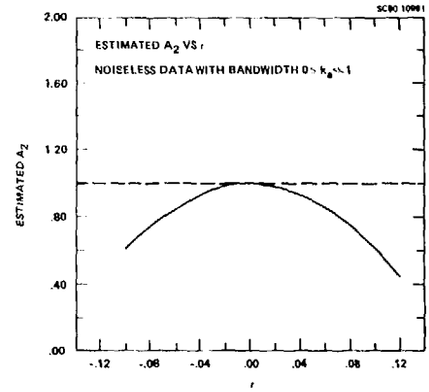

Fig. 13 Estimated A_2 vs true τ using $0 < ka << 1$. Flaw front surface is at $\tau = -0.3$.

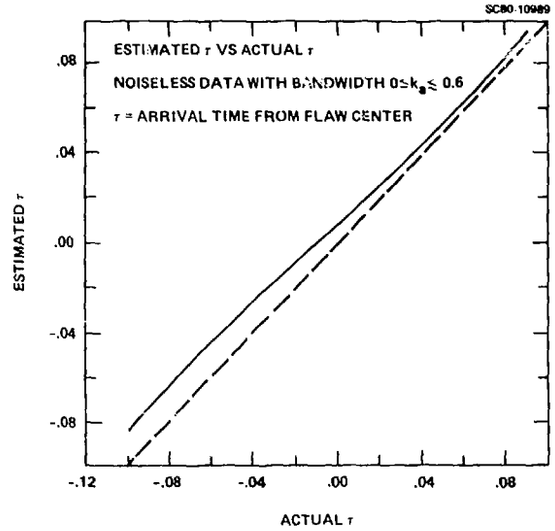

Fig. 14 Estimated τ vs true τ using $0 < ka \leq 0.6$. Flaw front surface is at $\tau = -0.3$.

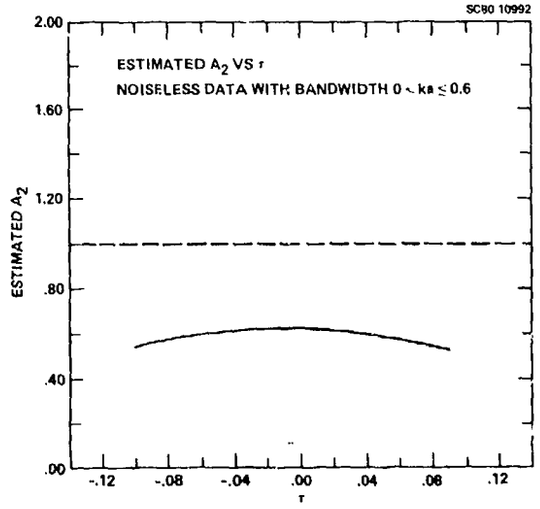

Fig. 15 Estimated A_2 vs true τ using $0 < ka \leq 0.6$. Flaw front surface is at $\tau = -0.3$.

too far from the center of the flaw, then there will be model error due to

$$e^{i\omega\tau} \approx 1 + i\omega\tau \qquad (17)$$

not being a sufficiently accurate approximation and the estimates will lose accuracy.

Figure 12 shows τ, the estimate of τ plotted vs the actual τ used in creating the data (Eq. 16). The dashed line is $\tau = \tau$ for comparison purposes. (In fact, the dashed line was drawn slightly in error and the agreement near $\tau = 0$ is better than indicated.) Note that the estimates are very good near $\tau = 0$ and begin to become less accurate at large τ as Eq. (17) becomes a less good approximation. Note also that an iterative approach could be used to locate the center accurately even if the initial estimate was not good. The time scale used in these graphs is one where the front surface of the flaw occurs at $t = -0.3$.

Figure 13 shows the estimate of A_2 for this case. The correct value is 1.0. Again, the estimate is very good when $\omega\tau$ is sufficiently small.

Figures 14 and 15 show the results when the scattering amplitude of a spherical void is used as input:

$$f(\omega) = p(\omega)\, A(\omega)\, e^{i\omega\tau}$$

In this case, if too wide a range of frequencies is used, model error terms due to Eq. (15) not being a good approximation will cause errors in the estimates. Eq. (15) begins to break down above about $ka = 0.5$. For Figs. 14 and 15, $C(\omega)$ was chosen so that data up to about $ka = 0.6$ contributed. We would therefore expect some error in the estimates. Figure 14 shows estimated τ vs true τ for this case. The estimaes are still good, but there is now a systematic error which would cause one to miss the flaw center by a little. Figure 15 shows the A_2 estimate for this same case. At $\tau = 0$ there is now a systematic error of about 35%. Because flaw size is proportional to $A_2^{1/3}$, this error is not as significant as it may at first appear.

Figures 16 and 17 show the performance of the estimators in the presence of noise. An ensemble of test waveforms of the form

$$f(\omega) = p(\omega)\, A(\omega) e^{i\omega\tau} + \nu(\omega)$$

were tested and the mean and standard deviation of the estimates computed. Figure 16 shows the results for estimating τ. At large signal-to-noise ratios, the standard deviation is small and all estimates are near the mean value. At lower signal-to-noise, the shaded band shows the increasing noise in the estimates. Note that the mean does not change a great deal even when the standard deviation is large.

Figure 17 shows the results for estimating A_2. Again the mean value does not change appreciably even when the standard deviation becomes large. The results are far better than those obtained in [4] for a noiseless treatment.

For a flaw of initially unknown size, we would not know at what frequencies to cut off the calculation because we do not know what frequency corresponds to, say, $ka = 0.5$. Several approximate

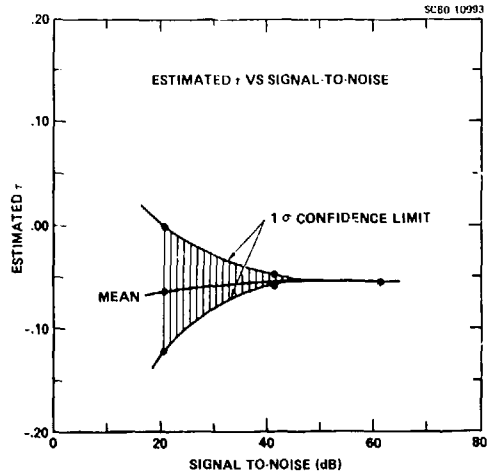

Fig. 16 Estimated τ vs signal-to-noise.

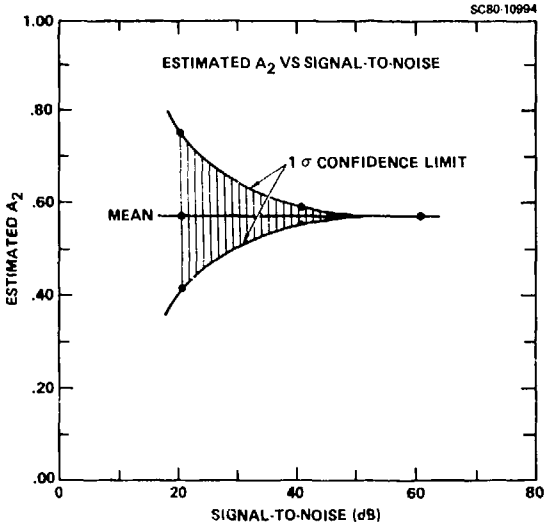

Fig. 17 Estimated A_2 vs signal-to-noise

solutions to this dilema are possible. An initial flaw size estimate can be made from an absolute amplitude measurement or by a higher frequency technique such as the Born inversion. From an initial size estimate, an iterative procedure involving estimating A_2, using that to estimate flaw size and then in turn selecting a new $C(\omega)$ could be used. A more systematic approach is derived in the next section.

In this section we derive an algorithm which avoids the problem of unknown flaw size mentioned in the previous section. It does this by explicitly estimating the model error term C_8 in Eq.(14) and then estimating A_2 and τ using that value for C_8. We assume that in an a priori sense C_0 and C_4 are known, since they can be determined from independent measurements on the post-processing electronics and on other specimens from the same batch. Since C_8 relates to the scatterer of interest whose characteristics are unknown before the measurement of $f(\omega)$, we must assume that C_8 is unknown.

We make the further assumption that the function $p(\omega)$, representing the acoustical system response, has the property

$$|p(\omega)|^2\omega^{10} \to 0 \text{ as } \omega \to \pm\infty \tag{18a}$$

which implies the limit

$$[C(\omega) - C_0]\omega^2 \to 0 \text{ as } \omega \to \pm\infty \ . \tag{18b}$$

These limits certainly hold if, for example, $p(t)$, the time-domain version of $p(\omega)$, is a sinusoid modulated by a Gaussian envelope function. We assume an optimality criterion implying that the optimal estimates are the most probable estimates (given f). We then introduce the further assumption that the a priori probability density of the above parameters is sufficiently flat in an appropriate sense, in which case the most probable estimates become the maximum likelihood estimates.

To provide a simple picture of the estimation procedure, we present the key steps in a somewhat abbreviated symbolic form. The central problem is to maximize the conditional probability density (p.d.) $P(A_2,\tau,C_8|f)$ with respect to A_2, τ, and C_8. In the above expression the symbol f stands for the set of quantities $f(\omega)$, $\omega\varepsilon S$. Using well known relations involving conditional probability densities, we can write

$$P(A_2,\tau,C_8|f) = P(f|A_2,\tau,C_8) \cdot P(A_2,\tau,C_8)/P(f) \tag{19}$$

Without truncating the set $f(\omega)$ in some way, the above conditional and unconditional p.d.'s with respect to f are unnormalizable and therefore must be regarded as relative p.d.'s. However, since Eq. (19) involves only the ratio of such p.d.'s, the lack of normalizability is of secondary importance. Since the divisor P(f) plays the role of normalization factor and can thus be ignored in the maximization problem, the relative conditional p.d. of f can be expressed in the form

$$\log P(f|A_2,\tau,C_8) = -\tfrac{1}{2}\phi - \tfrac{1}{2}\sum_{\omega\varepsilon S}\log\left[C(\omega)C_0^{-1}\right] \tag{20}$$

where the factor C_0, defined by Eq. (18) is introduced into the logarithm to achieve convergence of the sum on ω. The function $\phi = \phi(f|A_2,\tau,C_8)$ is

$$\phi = \sum_{\omega\varepsilon S}[C(\omega)]^{-1}|f(\omega) - p(\omega)\,(1 + i\omega\tau)\,A_2\omega^2|^2 \ . \tag{21}$$

In Eqs. (20) and (21) $C(\omega)$ is assumed to be given by Eq. (14). If the a priori p.d. $P(A_2,\tau,C_8)$ is flat over a region in which $P(f|A_2,\tau,C_8)$ deviates significantly from zero, then this a priori p.d. can also be ignored in the maximization problem.

Thus the maximization problem now involves only $P(f|A_2,\tau,C_8)$ given by Eq. (20) and thus the most probable estimates are then replaced by the maximum likelihood estimates.

In approaching the maximum likelihood problem we note that with C_8 fixed, the maximization of Eq. (20) with respect to A_2 and τ can be done analytically - in fact, this was already done in the earlier paper [4]. We then substitute these best estimates, denoted by A_2 and τ, back into Eq. (20) and then confront the problem of maximizing with respect to C_8, a problem that must be treated computationally. After obtaining the best estimate of C_8, namely C_8, we substitute this value in the analytical expressions for A_2 and τ.

The optimal estimates of A_2 and τ are given in Eq. (13). It is to be noted that a_p is real and positive when p is even, and is zero when it is odd. Also b_p is real when p is even, and imaginary when it is odd. According to the relations (18a) and (18b), a sufficient condition for the existence of a_p is that $p < 8$ and a sufficient condition for the existence of b_p is that $p < 4$ (if $f(\omega)$ is assumed to behave asymptotically like $p(\omega)\omega^4$).

Substitution of the above expressions for A_2 and τ into Eq. (20) yields

$$\log P(f|\hat{A}_2,\hat{\tau},C_8) = -\frac{1}{2}\Psi - \frac{1}{2}\sum_{\omega\in S}\log C(\omega) \tag{22}$$

where

$$\Psi = \phi(f|\hat{A}_2,\hat{\tau},C_8)$$

$$= \sum_{\omega}[C_v(\omega)]^{-1}|f(\omega)|^2 - \left(\frac{b_2^2}{a_4} + \frac{|b_3|^2}{a_6}\right) \tag{23}$$

The non-negativity of Ψ is easily demonstrated. It is also easy to prove that for a noiseless test signal $f(\omega) = p(\omega)(1 + i\omega\tau)A_2\omega^2$, then $\Psi = 0$, whereupon the optimal value of C_8 is given by $C_8 = 0$.

The appropriate computational procedure is first to find the maximum of $P(f|A_2,\tau,C_8)$ with respect to C_8 by a direct numerical maximization procedure thereby yielding the optimal estimate C_8. This estimate depends only on the input signal $f(\omega)$, $\omega\in S$, and various fixed parameters, since Eq. (22) has already been maximized with respect to A_2 and τ. The final step is then to substitute C_8 into $C(\omega)$ entering into the analytical optimal estimates of A_2 and τ given Eq. (13).

ACCURACY OF THE BORN INVERSION

One of the features used in last year's flaw characterization algorithm is d, the estimate of the radius of the flaw given by the one dimensional Born inversion.

This inversion technique makes use of 1 pulse echo waveform and from it derives an estimate of the distance from the center of the scatter to the front face of the scatterer in the direction from which the transducer is viewing the flaw. If this inversion is performed from a number of directions, then the shape of the flaw can be reconstructed.

During this year, we have investigated the robustness of the Born inversion with respect to noise that is present in the measurements and with respect to the limited bandwidth which is available from ultrasonic transducers. This work is described in detail in another paper in this proceedings. The results are summarized below.

The Born inversion was found to require a bandwidth of

$$0.5 < ka < 2$$

in order to give radius estimates accurate to within 20%. If insufficient low frequency data is available, then an underestimate results and if insufficient high frequency data is available, an overestimate results.

Figure 18 shows radius estimates obtained using the calculated scattering amplitude for a spherical void when only limited bandwidth is available. The dashed curve shows the effect of insufficient low ka data. Underestimates of > 20% occurs when $ka_{min} > 0.5$. The solid curve shows the effect of insufficient high ka data. Overestimates of > 20% occur when $ka_{max} < 2$.

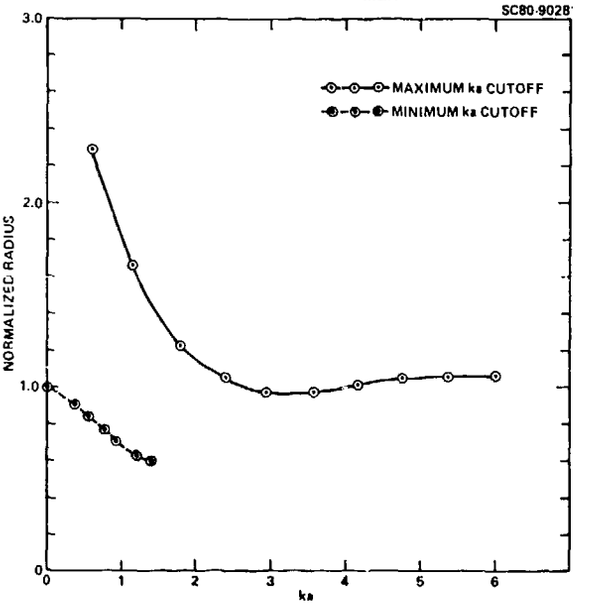

Fig. 18 Effect of limited bandwidth on the accuracy of the Born Inversion.

Figure 19 shows the effect of limiting both low and high frequency bandwidths. The figure shows the estimated radius a divided by the true radius a vs the average wavenumber k of a transducer multiplied by the flaw radius a. Each curve is for a transducer of a different relative bandwidth, expressed in terms of the ratio of the maximum ka of the transducer to the minimum ka.

Note that for the 6:1 transducer, measurements will be accurate to within 20% for a 1.7:1 range of flaw sizes, while for the 10:1 transducer, the range of flaw sizes is about 2.5:1. A good broadband commercial transducer might have a 10:1 range of usable k.

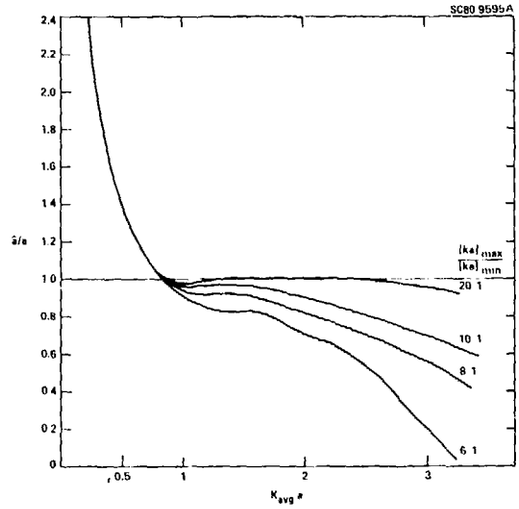

Fig. 19 Accuracy of Born Inversion vs transducer center frequency and bandwidth.

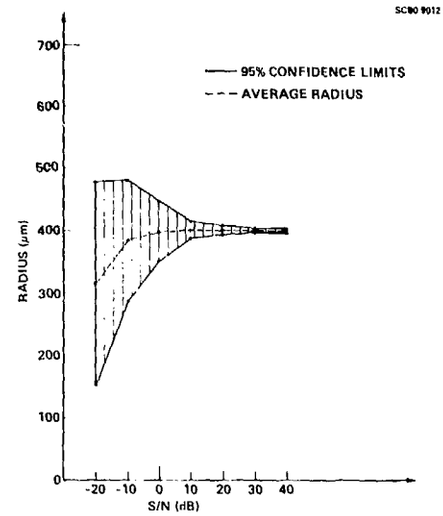

Fig. 20 Radius estimates for ensembles of noisy flaw waveforms vs signal-to-noise ratio.

The sensitivity of the Born inversion to the presence of noise in the data was investigated by adding calculated noise to the calculated scattering amplitude of a spherical void. The noise simulates gain scattering in a metal by having a power spectrum proportional to f^8. A signal-to-noise parameter is defined in terms of the relative energy in the scattering amplitude and in the noise. Figure 20 shows the radius estimtes obtained for ensembles of noisy signals at various signal-to-noise ratios. The flaw has a diameter of 800 μm. For large signal-to-noise, the algorithm correctly estimates the radius to be 400 μm. The dashed curve shows the mean radius estimate for an ensemble of signals at each signal-to-noise ratio. The solid curves show the 95% confidence levels for the ensemble. As the signal-to-noise ratio decreaes, the uncertainty of the estimates increases and the mean of the estimates eventually becomes inaccurate too. However, the 95% confidence level is within 20% of the correct answer down to a signal-to-noise ratio of 0 dB. The upper and lower curves in Figure 21 show flaw signals in the presence of this level of grain noise.

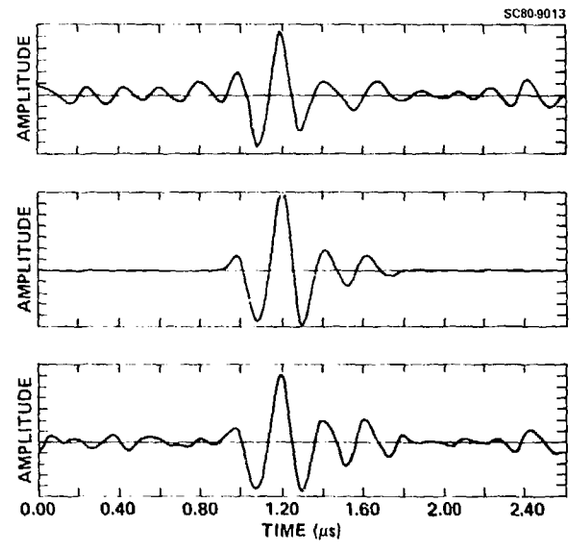

Fig. 21 Experimental and simulated flaw waveforms including grain scattering noise.

DISTINGUISHING A CRACK FROM 2 VOIDS

The effect of a crack on the remaining lifetime of a part will generally be greater than the effect of a region of porosity of comparable size. However, the ultrasonic reflections from a crack and a collection of pores may be similar. There is therefore a need to distinguish between these two types of flaws.

We describe here a simple signal processing technique for distinguishing between the echos from a crack and from a pair of voids separated by a distance equal to the length of the crack. This technique requires only a single pulse-echo waveform.

According to the geometrical theory of diffraction, the backscattered echo from a crack reviewed at an angle other than perpendicular to the plane of the crack consists of echos from 2 "flash points" on the opposite edges of the crack. The time spacing between the two echos is equal to the difference between the travel times to the near and far flash points. Also the two pulses are of opposite polarity. By contast, the echo from a pair of voids spaced a distance equal to the width of the crack will also consist of 2 echos, but they will be of the same polarity. This suggests a technique for distinguishing between the two types of flaws.

The upper curve in Fig. 22 shows a signal measured from one of the spherical "trailer hitch" specimens discussed elsewhere in this report. It consists of 2 pulses. The pulses appear to be of the same polarity, suggesting that the signal is

due to 2 voids. Often, the pulses are not well enough separated or of equal enough shapes for this distinction to be made by the eye. We have therefore developed a more systematic algorithm for this purpose.

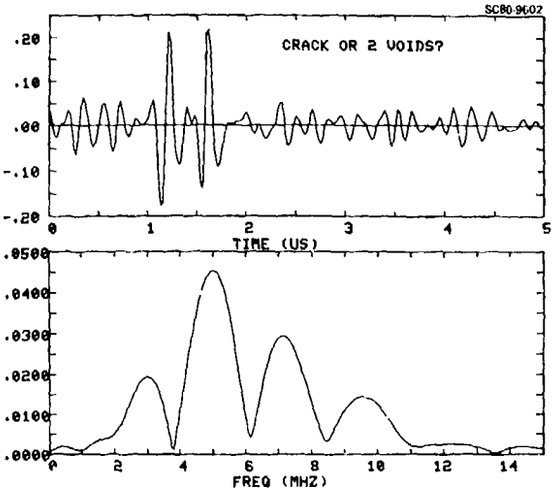

Fig. 22 Measured scattering waveform and corresponding frequency spectrum for a pair of voids.

Consider a signal s(t) which consists of 2 identical pulses $s_0(t)$ separated by a time interval τ and being of either the same or opposite polarities:

$$s(t) = s_0(t) \pm s_0(t) \times \delta(t - \tau)$$

In the frequency domain, this signal has the simpler representation

$$S(\omega) = S_0(\omega)\ (1 \pm e^{i\omega\tau})$$

Here, upper case letters are used for the frequency domain representations of the corresponding time domain quantities. The magnitude of S is

$$|S(\omega)| = |S_0(\omega)| \cdot |1 \pm e^{i\omega\tau}|$$

$$= 2|S_0(\omega)| \cdot \left|\cos \frac{\omega\tau}{2}\right| \text{ same polarity}$$

$$= 2|S_0(\omega)| \cdot \left|\sin \frac{\omega\tau}{2}\right| \text{ opposite polarity}$$

Note that the magnitude of the frequency spectrum of s(t) consists of the spectrum of $s_0(t)$, modulated by either a cosine or a sine function, depending of the polarity relationship of the pulses. The lower curve in Fig. 22 shows $|S(\omega)|$ for the measured signal shown in the upper curve. The modulation is clearly visible and measurement of the peak or valley positions shows it to be a cosine modulation, proving that the signal is from a pair of voids rather than from a crack.

In order to classify the source of the signal automatically and in cases where the data is not as good as that shown in Fig. 22, the following algorithm was developed. The Fourier transform of $|S(\omega)|$ is a type of autocorrelation function of s(t). It consists of a peak at zero lag and smaller peaks at lags equal to multiples of τ. If the negative frequencies of $|S(\omega)|$ are set to zero before Fourier transformation, then there will also be a phase part of the autocorrelation. This phase will equal 0° at a lag of τ if the pulses are of the same polarity and it will equal 180° at τ if the pulses are of opposite polarity. Figure 23 shows the autocorrelation phase measured for 2 "trailer hitch" samples, one containing a crack and the other containing a pair of voids. The autocorrelation phase was measured at a variety of angles of incidence from near normal to the plane of the crack to within the plane of the crack. The phase is near zero at all angles for the 2 voids, as expected. The crack is easily distinguished from the voids at any angle, with its phase being around 130°. The phase is not 180° because the echos from the two flash points are not in practice, quite the same shape. This deviation from 180° may be, in itself, informative about the nature of the flaw.

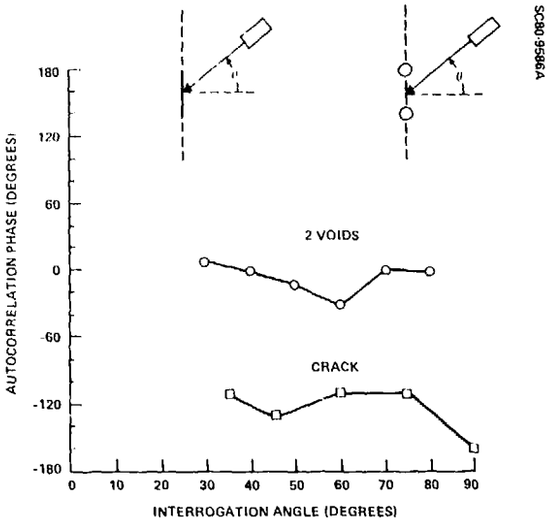

Fig. 23 Auto correlation phase for 2 flaws: a crack and a pair of voids. Flaw type can be identified at any angle $35° < \theta < 90°$.

References

1. L. J. Graham, L. Ahlberg, R. K. Elsley and J. M. Richardson, "Long Wavelength Ultrasonic Characterization of Inclusions in Silicon Nitride," Proceedings of the DARPA/AFML Review of Progress in Quantitative NDE, AFWAL-TR-80-4078, pp. 656-662 (1980).
2. A. D. Whalen, Detection of Signals in Noise Academic Press, New York, 1971, Chapter 11.
3. Y. Murakami, B. T. Khuri-Yakub, G. S. Kino, J. M. Richardson and A. G. Evans, "An Application of Wiener Filtering to Nondestructive Evaluation," Appl. Phys. Lett. 33(8), 15 Oct. 1978, pp. 685-687.
4. J. M. Richardson and R. K. Elsley, "Extraction of Low Frequency Properties from Scattering

Measurements," Proceedings of the 1979 IEEE Ultrasonic Symposium, 79CH1482-9, pp. 336-341.
5. J. E. Gubernatis, J. A. Krumhansl, R. M. Thomson, "Interpretation of Elastic Wave Scattering Theory for Analysis and Design of Flaw Characterization Experiments: I. Long Wavelength Limit," Los Alamos Scientific Laboratory Report, LA-UR-76-2546 (1976).
6. J. M. Richardson, "Direct and Inverse Problems pertaining to the scattering of elastic waves in the Rayleigh (long wavelength) regime," Interdisciplinary Program for Quantitative Flaw Definition, Fourth Annual Report, AFML-TR-78-105, pp. 332-340 (1978).
7. R. K. Elsley, "Flaw Characterization by Low Frequency Scattering Measurements," Interdisciplinary Program for Quantitative Flaw Definition, Fourth Annual Report, AFML-TR-78-205, pp. 400-403 (1978).
8. B. Budiansky and J. R. Rice, "On the Long Wavelength Scattering," Trans. ASME, J. Appl. Mech., Vol. 45, pp. 453-454 (1978).
9. W. Kohn and J. R. Rice, "Scattering of Long Wavelength Elastic Waves from Localized Defects in Solids," submitted to J. Appl. Phys.
10. J. M. Richardson, "The Inverse Problem in Elastic Wave Scattering at Long Wavelengths," Proc. of the 1978 IEEE Ultrasonics Symposium, 78CH1344-1SU, pp. 759-766 (1978).
11. J. M. Richardson, "Scattering of Elastic Waves in the Rayleigh Limit. III. The Probabilistic Inverse Problem," to be published.
12. B. R. Tittmann, R. K. Elsley, N. Nadler, E. R. Cohen, "Experimental Measurements and Interpretation of Ultrasonic Scattering by Flaws," Interdisciplinary Program for Quantitative Flaw Definition, 3rd Annual Report, AFML-TR-78-55, pp. 26-35 (1978).
13. J. M. Richardson, "Scattering of Elastic Waves from Symmetric Inhomogeneities at Low Frequencies," to be published.

THE APPLICATION OF ULTRASONICS IN NON-DESTRUCTIVE TESTING: A REVIEW OF SOME OF THE RESEARCH AT UNIVERSITY COLLEGE LONDON.

M.D. Ambersley, L.J. Bond, A.L. Downie, W. Duerr, C.W. Pitt, D.A. Sinclair & I.R. Smith.
University College London
Department of Electronic and Electrical Engineering
Torrington Place
London WC1E 7JE
Gt. Britain

ABSTRACT

This paper presents a review of some of the research projects at University College London which use ultrasonic waves in non-destructive testing. The projects covered include a low-frequency scanning acoustic microscope, a new dark-field acoustic microscope, an update on finite difference model studies of wave propagation and scattering, developments in mode-conversion techniques for defect characterisation, a new high-resolution acoustic field sampling probe and a resumé of the work on ZnO transducers.

INTRODUCTION

The need for quantitative non-destructive testing, and in particular defect characterisation, has been recognised for many years. It is clear that the achievement of quantatitive NDT must now assume a high priority if the full benefits of the advances in fracture mechanics and related areas of materials science, are to be realised. This has been appreciated for several years in both the USA and the UK and, as a result, there is now considerable interest in this research area in British Universities and industrial laboratories, as well as in their counterparts in the USA.

This paper, together with Ameri et al, (1), (to be presented later), reviews the current work in ultrasonic NDT in the Department of Electronic and Electrical Engineering at University College London. The presentation also extends the work on model studies of wave propagation and scattering given by Bond, (2), at last year's meeting: this work was formerly at The City University, London, and has now moved to join the long-established research in acoustic imaging and microscopy, SAW signal processing and ultrasound-orientated thin film technology, at UCL.

Current studies can be divided into six related groups of projects: (i) use of a laser probe (1,3) to measure material properties such as SAW velocity, elastic constants or crystal orientation, (ii) investigation of the interaction between a propagating wave and a defect using the scattered and mode-converted waves to identify characteristics of the defect by use of the laser probe (3) in an imaging mode to examine cracks or overlay defects, (iii) use of the acoustic microscopy (1) to produce 'acoustic-contrast' images of small structures, (iv) the theoretical investigation of fundamental wave propagation scattering using numerical (finite difference) models (2), together with experimental investigations using short pulse probes, (v) the development of the new family of mode-conversion techniques for defect characterisation, reported at last year's meeting, (2,5), (vi) engineering support for the above activities; typically the development of single crystal and thin film transducers, acoustic lenses and electronic instrumentation.

The following paragraphs consider some specific aspects of these projects - the application of low-frequency (12MHz) scanning acoustic microscope to NDT, a new dark-field acoustic microscope, an update on numerical model studies of wave propagation and scattering (2), developments in mode-conversion techniques for defect characterisation, a new high-resolution acoustic-field sampling probe and a resume of the work on ZnO transducers.

TRANSMISSION SCANNING ACOUSTIC MICROSCOPY FOR DEFECT DETERMINATION IN METALLIC OBJECTS

The Scanning Acoustic Microscope (SAM) has been successfully used to examine a wide range of biological state materials (6). Recent work has tended to concentrate upon the reflection configuration of the instrument which eases alignment constraints in high resolution systems (7), while transmission imaging at lower resolutions has received less attention (8). Both configurations have applications in NDT in the location and detection of flaws and voids within an opaque material. Experimental results from a transmission system will be presented that demonstrate the detection of such defects.* The essential elements of a transmission SAM are shown in Fig. 1.

An acoustic lens produces a diffraction limited focal spot at the object plane. A second lens collimates the energy transmitted through the object. An image is built up by mechanically scanning the object through the focussed beam and using the measured transmissivity at each image point to modulate the intensity of a synchronously scanned display.

The results presented here were obtained using a transmission SAM operating at 12MHz, employing 16mm radius, 25mm aperture fused quartz lenses. The resolution in a steel sample was approximately 650μm.

* Transmission Scanning Acoustic Microscopy for Determination in Thick Objects. D. Sinclair & E.A. Ash (to be published).

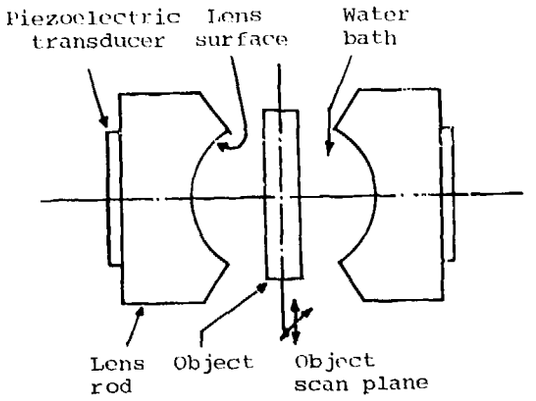

Fig. 1. Transmission SAM Acoustics.

The low path losses (approximately 12dB) in the water bath and the high reflection coefficient at the lens-water interface mean that the system must be pulsed to discriminate between signals passing straight through the system and those that experience multiple reflections. The minimum pulse width used was limited by transducer bandwidth to 1μs, corresponding to 12 acoustic wavelengths. Since the objects examined here are only a few wavelengths in thickness the object's transmissivity closely approaches that of the continuous wave case.

The object is illuminated with a tightly focussed beam and, because the object's transmissivity is a strong function of angle, each of the spatial frequency components making up the beam is subject to a different transmission coefficient. Additionally, there is mode-conversion from the incident and transmitted longitudinal waves to shear, surface and plate modes within the object. Hence, the effective object transmittance is a complex function of both the properties of the sample and the parameters of the acoustic beam.

The resolution achieved within the object is difficult to quantify because of the many modes present within the acoustic beam in the object. The effective lens aperture in the solid will approach 180^0 since the high velocity ratio between the water bath and the sample ensures there will be spatial frequencies extending up to $\pm 90^0$ in the sample. This increase in resolution is offset by the low transmissivity of the object-water interface to high spatial frequencies and the increased spherical aberration associated with these high spatial frequencies. An estimate for the resolution of 1.5 wavelengths in the solid was obtained by examining the edge detail in the images shown below.

The high impedance mismatch at the surface of the sample (approximately 15dB/interface) reduces the overall S/N of the system to 35dB. While these mismatch losses can be tolerated at the low imaging frequencies used here they become a limiting factor in higher resolution systems, since the system path losses rise with frequency squared. By using low frequencies and trading reduced resolution for improved loss in the system this avoids the use of high impedance (and usually poor wetting) fluids such as gallium for the object to lens coupling.

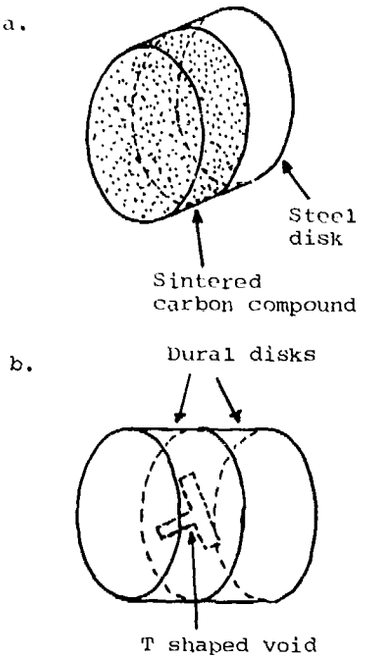

Fig. 2. Geometry of Objects Imaged.

Two types of object have been examined - one containing laminar bonding defects and one containing voids.

All the images shown are of 10 by 10mm fields of view.

In each case the object was embedded in a plate with acoustic properties similar to those of the object. This eliminated standing waves in the scan plane which would otherwise have appeared as strong interference rings in the image.

In the first object type, see Fig. 2(a), a carbon diamond composite 1mm thick was sintered onto a steel base 2.5mm thick and 10mm in diameter. Two samples of this type were examined. In one case the bond between the two materials was thought to be good and in the other it was suspected to be poor. The images obtained are shown in Fig. 3(a) and (b) respectively. In both images the difference in signal level from black to white is about 25dB. It can be seen in the good sample that there is a large area of extremely uniform transmissivity and a smaller area of rather less uniformity where the bond quality may be suspect. However, in the image of the defective sample, it can be seen that there is little large scale uniformity and the variations in transmission are much larger than in the good sample. This indicates the poor overall nature of the carbon steel bond in this sample.

Fig. 3(a) and (b). Images of Good and Poor Carbon-Steel Disks - 10mm square field of view.

The second object type imaged is shown in Fig. 2(b) and was fabricated from two Dural disks clamped together to form a composite disk 12mm in diameter and 4mm thick. A small T shaped depression was machined in the inner surface of one of the disks in which the stem of the T was 2λ and 0.3λ - shown in Fig. 4(a) and 4(b) respectively where λ is the longitudinal wavelength in the Dural. Two small 2λ holes machined in the disk can also be seen in the top portion of Fig. 4(a). An attempt was made to fill the voids within the disks with water before they were clamped together. This was only partially successful since an air bubble can be seen in the cross bar of the T in Fig. 4(a). While the T in Fig. 4(b) is not fully resolved in this image the picture does demonstrate the ability of the SAM to detect, rather than image defects much less than a wavelength in size.

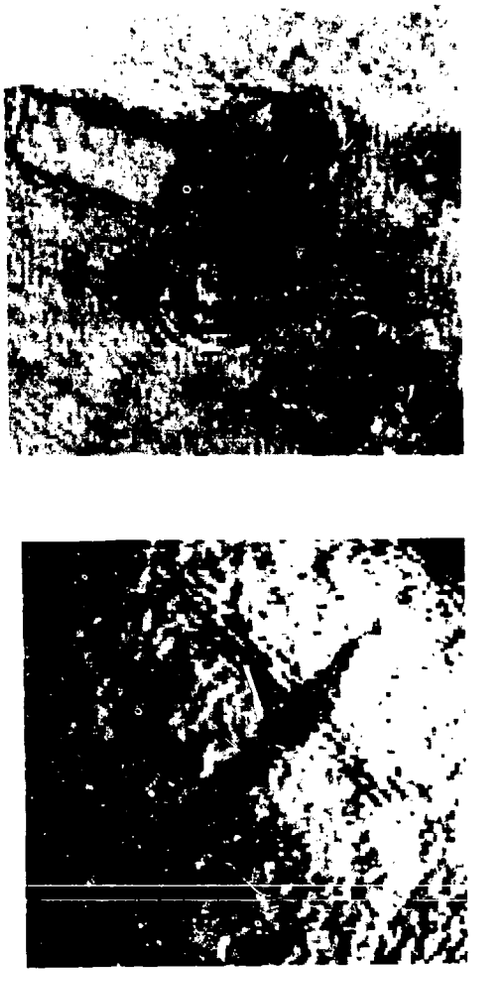

Fig. 4(a) and (b). Images of Dual Disk with 2λ and 0.3λ T Shaped Voids - 10mm square field of view.

DARK FIELD ACOUSTIC MICROSCOPY

Dark field acoustic microscopy has previously been demonstrated (9), and its uses are similar to those in optical microscopy - the examination of highly transmissive, weakly diffractive objects. By excluding the undiffracted energy from the receiver, a more sensitive detector may be used. We have developed a new method for the suppression of this energy (10). Fig. 5 shows the lens arrangement of the dark field microscope. The object plane is illuminated by a normally incident plane wavefront, produced by a suitably spaced piezoelectric transducer. A conventional SAM lens assembly is used to receive the plane wave, and is situated on the source axis. The lens surface is transmissive to zero spatial frequency energy but, because of total internal reflection, the active region of transmission is confined to the centre of the lens. The receiving transducer is only sensitive to normally incident energy, because it is spatially integrating, and so only a small part of the incoming energy is detected. We reduce

this further by the incorporation of an absorbent or reflective stop in the centre of the lens, which obscures the active region. Thus, with no object present no signal is detected, and the system is dark field. A diffracting object produces higher order spatial frequencies, to which the receiving lens is sensitive. Conventional mechanical scanning is used to form an image, which shows the energy diffracted by the object.

The effect of the aperture stop is to narrow the central lobe of the lens focal distribution, with an increase in the sidelobe level. Selection of the stop size must achieve a satisfactory compromise between zero order suppression and the resulting loss in resolution caused by the sidelobes. This on-axis system has two advantages for the applications envisaged. Because the source is unfocussed, alignment of the system is greatly simplified, an important factor with the

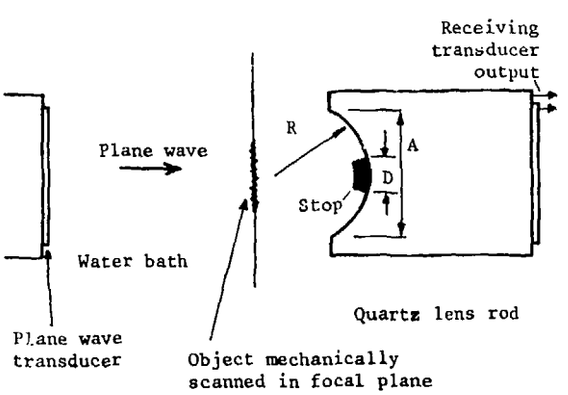

Fig. 5. Dark Field Microscope Lens Configuration

small spot sizes in high frequency acoustic microscopy (>0.3μm). Secondly, because the lens is on the source axis, the spatial frequency response is symmetrical. The lens collects all of the diffracted energy up to the limit imposed by its aperture.

We have built a dark field acoustic microscope operating at 12MHz (wavelength = 150μm). The dimensions of the stop are shown in Fig. 5. Fig. 6 shows a computed model of the focal distribution of the lens, with and without the stop, indicating the increase in sidelobe level, as well as a slightly reduced central lobe width. The stop produced an additional 20dB of zero order suppression. We are experimenting with this system in order to determine its sensitivity for defect detection, and some early experiments have used cracks in solids as diffracting objects. Fig. 7 shows a typical image of a crack in a glass coverslip. The crack, and an associated standing wave pattern in the glass, are clearly shown. Other materials which we are examining include polymer films and human tissue, both of which are highly transmissive to sound waves and may be expected to yield increased contrast with a dark field microscope.

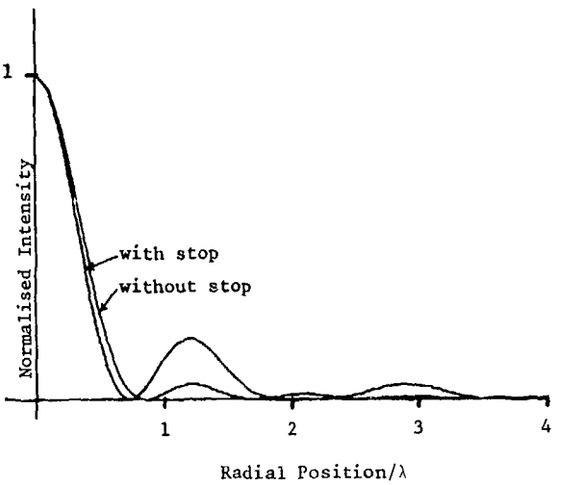

Fig. 6. Computer Lens Focal Distribution (Parameters as in Fig. 5.)

Fig. 7. Dark Field Image of Crack in Glass Coverslip. (< λ/10 wide by 2λ deep).

ELASTIC WAVE PROPAGATION AND SCATTERING

The alternative approach to that of seeking to investigate a feature by producing an image using a technique such as acoustic microscopy, is to study the scattered and mode-converted wavefield by means of measurements which sample the time development of the wavefield at specific points.

The investigation, now at UCL, consists of a mixed numerical model and experimental study of wave propagation and scattering, which is

principally directed toward the characterisation of slots and hence fatigue cracks.

FINITE DIFFERENCE MODELS

The basic techniques used to produce finite difference models of wave propagation and scattering have received extensive coverage in the literature (11) and they were considered at last year's meeting (2). An example of the numerical visualisations, time-snap-shots, for the type of system currently under investigation is shown in Fig. 8. The model is in a cylindrical coordinate system and is using a short pulse of limited width introduced at the inner free surface of a section through an annulus. The main wave fronts are identified.

MODE-CONVERSION TECHNIQUES

In addition to fundamental studies of wave propagation and scattering, the investigations have the aims of providing new and improved methods of ultrasonic testing. The practical studies have concentrated on the development of mode-conversion techniques (2,5).

The basic features of the mode conversion techniques are: the use of short pulse, (broad-band), waves to strike a target, followed by the analysis of the mode-converted waves which are generated; including their frequency content.

COMPRESSIONAL-RAYLEIGH WAVE TECHNIQUE

The conversion of body to surface waves by a surface breaking feature has been reported by several authors including Humphreys and Ash (12) and their possible application to NDT was demonstrated last year (2). This technique has been the subject of further study, the finding of which is now summarised.* The basic experimental configuration is shown in Fig. 9.

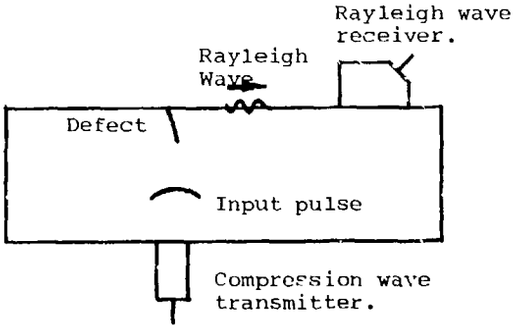

Fig. 9. Basic configuration for the compressional Rayleigh wave mode-conversion technique.

* Ultrasonic mode-conversion techniques of NDT: L.J. Bond (to be published)

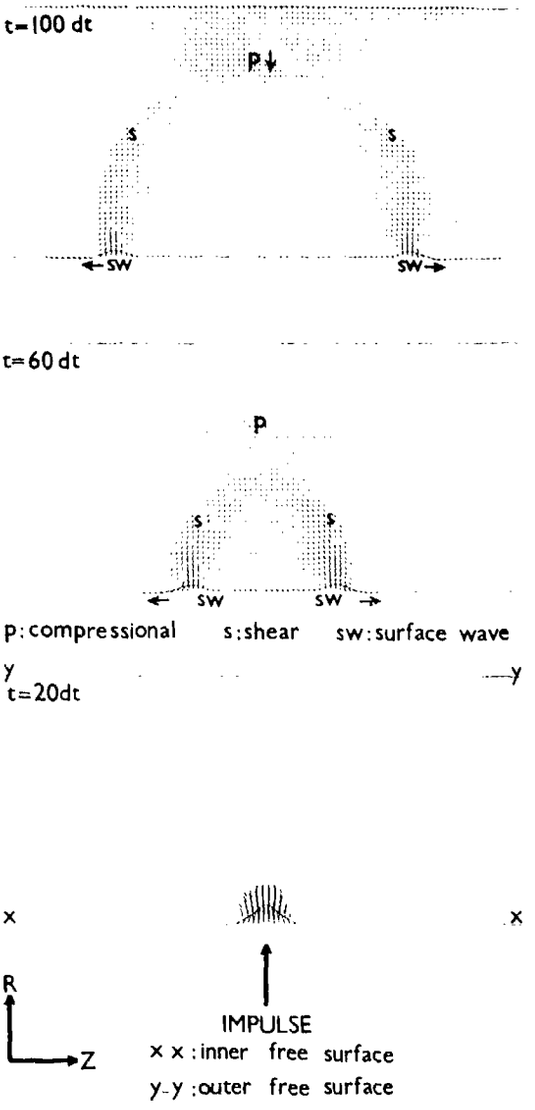

Fig. 8. Compressional Impulse in a Cylindrical System (rz) at Three Time Levels.

For the system shown in Fig. 9 it has been reported that the depth of the slot can be related to the centre frequency of the mode-converted Rayleigh wave pulse by the relationship:

$$\text{Slot depth} \propto 1/f^2 \qquad (1)$$

Further measurements of depth and frequency for both slots in aluminium and steel and fatigue cracks, near normal to the free surface of test blocks have been made, and all data fell in a band near the curve defined by equation 1, passing through the point 1.0mm depth and 1.0MHz, which is shown in Fig. 10. The general form of the relationship (equation 1) was established by experiment. A physically based model is now proposed.

The velocity, (Vr), frequency, (f), and wavelength, (λ), of the mode-converted Rayleigh wave are related in the usual way by:

$$V_r = f\lambda . \qquad (2)$$

The motion of a shallow surface feature struck by an impulse can be expected to be related to the features dimensions i.e., natural frequencies. For the case of a shallow feature where the depth is less than the length of the incident impulse the type of motion shown in Fig. 10a could occur. The motion of the sides of the slot would be such that it would move like a tuning fork, with depth (length) of quarter wavelength.

When the length of slot of quarter wavelength is used as the basic frequency for the Rayleigh wave in equation 1, a relationship between depth of the slot and the frequency of the Rayleigh wave is obtained:

$$f = V_r/4x \qquad (3)$$

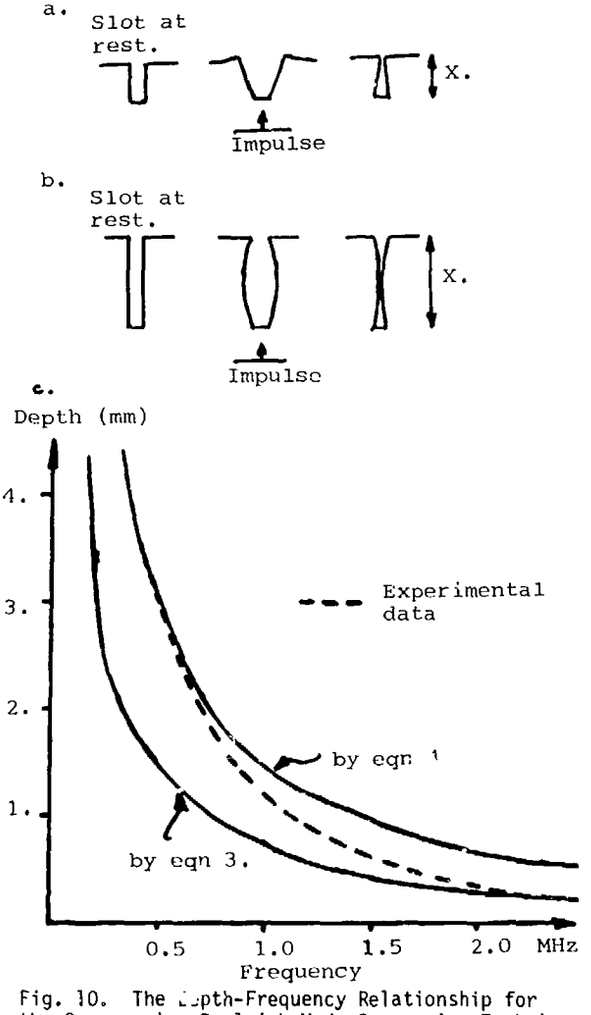

Fig. 10. The Depth-Frequency Relationship for the Compression-Rayleigh Mode-Conversion Technique
(a) Motion of shallow slot
(b) Motion of deep slot
(c) Depth frequency relationship

When equation 3 is plotted with the experimental data the agreement for shallow features is found to be good. However, for deeper features the results do not agree. It is therefore suggested that a different form of motion occurs when the impulse is short compared with feature depth.

For the case of a deeper feature where the incident impulse is short compared with the length of the slot, the sides of the slot can be expected to bow before the top corners move and motion would be as shown in Fig. 10b, where slot length (depth) is half wavelength.

By substitution in equation 2, a relationship between depth and frequency is obtained:

$$f = V_r/2x \qquad (4)$$

which, when plotted with the experimental data (as shown in Fig. 10), is in good agreement for the case when the feature is long compared with the length of the exciting impulse.

The agreement between this simple model and experimental results is seen to be good, as shown in Fig. 10.

A small shift in the position of the curve was found for measurements on steel blocks and this was in agreement with the theory.

USING CONVENTIONAL A-SCAN

The application of the compressional-Rayleigh wave mode-conversion and other similar techniques, require a special short pulse signal generator together with a spectrum analyser.

Investigations have been performed using conventional A-Scan ultrasonic NDT testing equipment, with a range of commercially available probes to apply mode-conversion techniques. This work is illustrated by results obtained by Shear-Rayleigh wave mode-conversion techniques.*

SHEAR-RAYLEIGH WAVE TECHNIQUES

The basic configurations for two shear-Rayleigh wave conversion techniques are shown in Fig. 11a. The mode-conversion which occurs is found to depend on the detailed pulse excitation used and the probe angle, in addition to the relationship between slot depth and frequency of the incident wave. It is found, however, that significant mode-conversion to Rayleigh waves occurs, (20dB above noise), for a wide range of shear wave transducer/defect combinations.

Examples of the type of A-scan obtained are shown in Fig. 11c.

MULTI-PROBE SYSTEMS

The experiments reported so far in this section are two probe methods which relate to the characterisation of slots and cracks normal and near-normal to the surface of blocks in plate configurations. Both the defect geometry and that of the object under test, can be considerably more complex than this.

*Ultrasonic mode-conversion techniques for NDT: L.J. Bond (to be published)

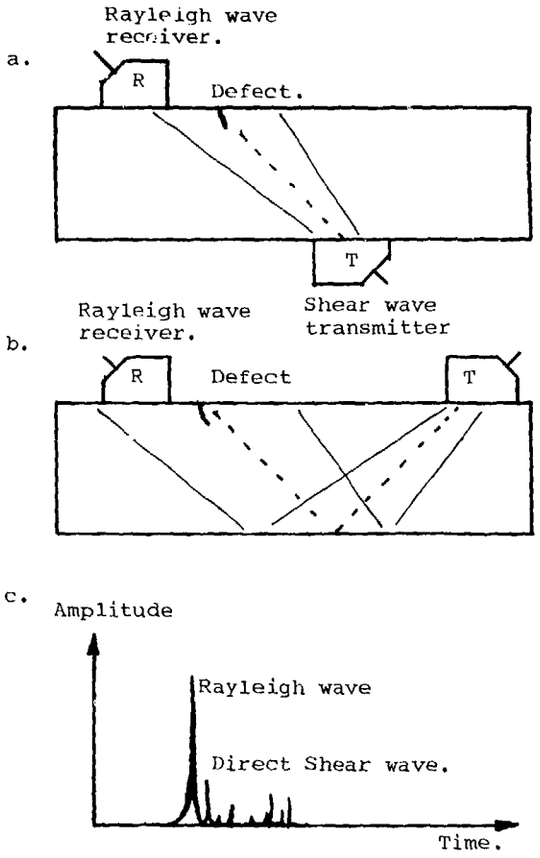

Fig. 11. Shear-Rayleigh wave mode-conversion Techniques:
(a) and (b) Basic configuration
(c) A-scan.

The angular dependance of scattering of compression waves by slots normal to the surface has been investigated both using numerical models and experiments (4). The characterisation of features non-normal to a surface adds further complexity to the experimental results.

An extension of the Compressional-Rayleigh wave system to give both crack length and angle, (depth), is shown in Fig. 12, which uses the relative amplitudes of the spectral content of the signals from the two Rayleigh wave transducers.

For specific types of structure, specific probe combinations can be advantageous and an example for a step section is the system shown in Fig. 13. The use of small computer systems can provide on-line analysis where the interpretation of several signals is complex, for multi-probe systems.

To summarise it has been found that short impulses of elastic waves at ultrasonic frequencies can be used to excite resonance phenomena which can be related to feature dimensions via the frequency content of the mode-converted waves which are produced, and hence, provide a range of techniques for defect detection and characterisations.

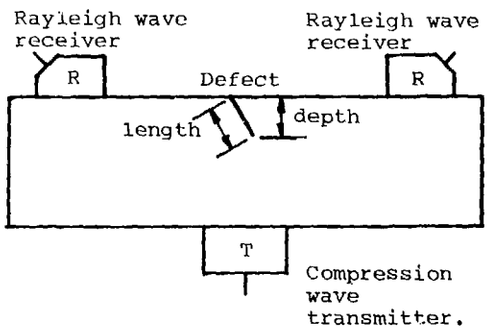

Fig. 12. Three-probe Compressional-Rayleigh mode-conversion.

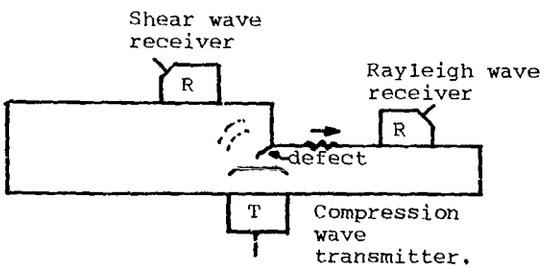

Fig. 13. Three-probe Compressional-Rayleigh Shear System.

HIGH RESOLUTION ACOUSTIC PROBE

The measurement of transducer beam profiles is an important step in the characterisation of a NDT measurement system. Conventional probes use a small piezoelectric chip to provide spatial selectivity. However the dimensions of the chip can be inconveniently small. An alternative approach is shown in Fig. 14.* An aluminium cone is mounted so that the tip of the cone just touches the inner surface of a sheet of mylar film. If an ultrasonic field impinges upon the outer surface of the mylar film, only that portion of the field in the neighbourhood of the cone tip will be coupled into the cone. This energy is collimated by a lens at the base of the cone and detected by a

*High resolution acoustic probe: W. Duerr, D.A. Sinclair, E.A. Ash (to be published)

conventional piezoelectric transducer.

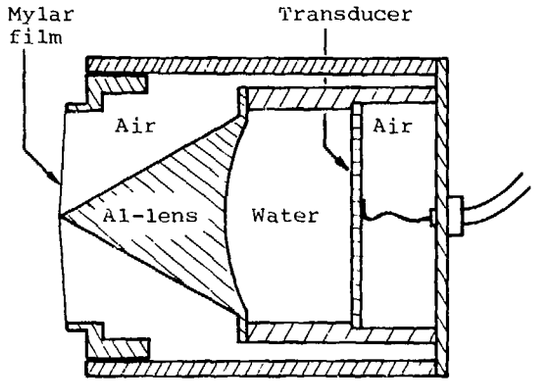

Fig. 14. Components of High Resolution Probe.

The resolution of the probe is determined by the area of contact between the mylar film and the probe tip - a parameter readily controlled in manufacture. Since there is a high velocity ratio between the aluminium and the water coupling the cone to the transducer, a simple spherical lens produces negligible spherical distortion. The air gap between the mylar film and cone sides provides good isolation due to the high impedance mismatch between the air-water and air aluminium interfaces. To provide the best sensitivity, it is essential to reduce the losses within the probe to a minimum. A quarter wave matching layer of 10μm aluminium powder and Araldite epoxy, (1:1 by weight), was used on both the lens and the transducer face. This reduced the insertion loss of the probe by approximately 12dB.

A probe for use at 4.5MHz has been constructed and its resolution determined experimentally. Two probes were placed in a water bath and the first probe used to scan the field produced by the second. The probes were separated by d axially. If the field produced by the first probe in a plane located at the probe tip and orthogonal to the probe axis is $f_1(x,y)$, for unit transducer excitation, then the output of the second probe at scan coordinate (x,y), is given by

$$V(x,y) = \int_{-\infty}^{\infty} f_2(a,b) f_1(x-a,y-b)\,da\,db \qquad (5)$$

where $f_2(x,y)$ is the field distribution $f_1(x,y)$ propagated forward a distance d from the plane of the first probe tip to the plane of the second. Thus it is possible to measure the convolution of the probe spatial sensitivity $f_1(x,y)$ with this same function propagated a distance d.

Fig. 15a shows the result of scanning the two probes in one dimension at a separation of 20μm. Fig. 15b shows the convolution of the probe sensitivities after the effect of the propagation distance between them has been removed. To obtain a single probe's spatial sensitivity, it is necessary to perform a deconvolution on Fig. 15b. In practice it is difficult to perform this since the convolved function in Fig. 15b contains no information about the phases of the spatial frequencies making up $f_1(x,y)$.

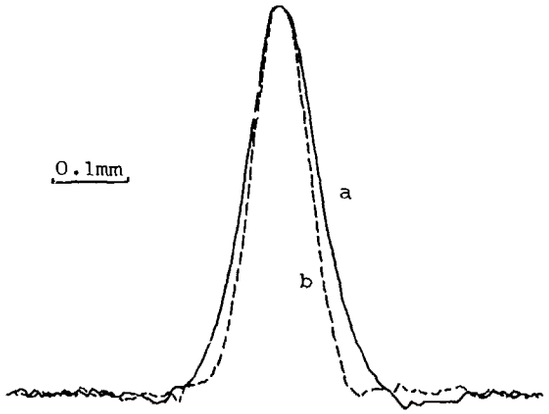

Fig. 15. (a) Result of Two Probe Convolution experiment.
(b) After Accounting for Probe Spacing.

An alternative method of assessing the resolution, is to assume a Gaussian form for the probe spatial sensitivity function. Thus in one dimension:

$$f_1(x) = e^{-x^2/w^2}. \qquad (6)$$

The convolution of a Gaussian with itself is

$$V(x) = \int f(a)f(x-a)\,da = \frac{\sqrt{2\pi}}{w} e^{-x^2/(2w^2)}. \qquad (7)$$

The width of the convolved Gaussian is $\sqrt{2}$ times that of the original Gaussian. Since the 1/e width of the curve in Fig. 15b is 110μm an estimate for the probe resolution is 75μm in water and so it is possible to sample fields with the maximum theoretical resolution. Indeed, in the presence of evanescent fields, sub-half wavelength resolution is possible. There is an almost complete absence of sidelobes in the probe spatial sensitivity. Thus, this system offers improved performance over an arrangement in which a lens alone is used to obtain the spatial sensitivity.

The probe of Fig. 14 has been used to measure the focal plane distribution of a 4MHz fused quartz-water lens, (radius 16mm, aperture 25mm, velocity ratio 3.9), illuminated by an approximately plane wave produced by a transducer glued to the far end of the lens rod. The field obtained is shown in Fig. 16. The measured central lobe half width of 340μm, agrees well with the theoretical value of $\lambda/(2\sin\theta)$ = 312μm, where θ is the half aperture angle of the lens. The lack of symmetry in the beam profile can be attributed to poor bonding of the transducer to the lens rod and consequent non-uniform illumination of the lens aperture. The absence of side lobes in the lens response was due to poor detector sensitivity.

In conclusion, a probe has been demonstrated

which can give at least half wavelength resolution. Manufacturing tolerances should not inhibit the performance of similar probes up to at least 15MHz.

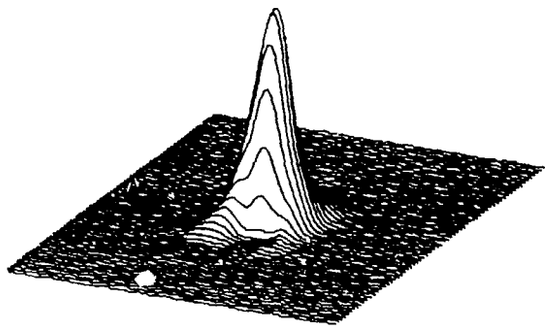

Fig. 16. Focal Plane Distribution of 4MHz Lens (2mm square scan).

ZINC OXIDE TRANSDUCERS

For high frequency (> 100 MHz) attachable SAW and bulkwave transducers for NDT, thin film deposition techniques offer a solution to the problem of fabricating the very thin layers. However, the deposition technique and the material system must be carefully selected; few deposition techniques are capable of depositing single or poly-crystal layers on amorphous substrates, the stoichiometry of the material may be modified by the process and crystallographic orientation, uniformity and thickness control are obviously key requirements.

Zinc oxide deposited by r.f. sputtering appears to be capable of meeting these requirements: certainly groups in Europe (12), Japan (13), the UK (14) and the USA (15), have demonstrated transducers with electro-mechanical coupling coefficients close to bulk material values. The problem is resolved to that of finding the key process parameters which enable the deposition reproducibility to be maintained close to 100%. The latter summarises the objective of the current program at UCL.

The deposition system is similar in many respects to that used by other groups and is illustrated schematically in Fig. 17. The major differences are to be found in the quantity and sophistication of the process monitors built into the plasma chamber; a mass-spectrometer supervises the partial pressure of residual gases and particularly hydrocarbons, (nitrogen and carbon having an adverse effect on the crystallite orientation), while the total plasma pressure, power feed and matching are monitored at several points to maintain process stability (16). The optical film monitor was developed (16) specifically for this application and is of the single beam-path type. The target is 'five-nines' Zinc on a magnetron electrode energised by a 1.5KW r.f. supply. A liquid nitrogen cryo-trap surrounds the plasma, immobilising water vapour and hydrocarbons in this region. A typical deposition starts from a chamber pressure of 10^{-7} T with nitrogen and carbon partial pressures below 10^{-9} T. An oxygen plasma at 10^{-2} T is then initiated with an input power density at the target of $2Wcm^{-2}$. The target-substrate spacing is 4cm and the substrate temperature is held at $400^{o}C$. Under these conditions, the deposition rate is circa 2.5 microns per hour. R.f. bias may be applied to the substrate prior to deposition to effect final cleaning and, during deposition, to alleviate strain in the layer.

Since the need is for a versatile process, ZnO films have been deposited on a wide range of substrates including metallised silica, lattice-matched sapphire, glasses and silicon. The layers have been assessed structurally, (x-ray diffraction, SEM section, electron diffraction), optically, (optical and SEM microscopy for surface topography, and optical waveguiding for gross internal structure), and by SAW and bulk wave delay-line tests. Typical results of the acoustic tests indicate bulk wave transducer double-transit insertion losses ranging from 3dB at 300MHz to 6dB at 650MHz; the evaluations were performed on silica delay lines. The SAW tests to date indicate single transducer loss of 8dB at 170MHz for layers deposited on sapphire with aluminium thin film interdigital electrodes and without a ground plane; the bi-directional loss was discounted.

The correlation of acoustic performance with the desired c-axis orientation, (0002), suggests that the substrate surface is critical in the effect on the growing layer. Also that the process repeatability is clearly related to the stability and reproducibility of the plasma chamber conditions. For example, the substrate influence on the preferred orientation of the ZnO is demonstrated in the x-ray diffraction peak intensity shown in Fig. 18a; this sample was deposited on a glass substrate and, in the same deposition run, a bulk wave transducer was included (gold film on silica). The acoustic wave propagation characteristics of the latter indicated a predominantly (0002) crystallite structure, while the film on glass has a (1010) orientation. In a subsequent run under similar conditions, a thin film of aluminium was pre-deposited onto the glass ..... and the orientation changed to that of (0002) while the (0001) sapphire and Au/silica surface maintained the (0002) structure. In both cases the bulk wave delay lines had similarly low losses of circa 3dB per transit.

The very marked effect of the release of residual gases from the cryo-pump is, we believe, indicative of the need for very precise process control. Fig. 19 shows a SEM micrograph of a cross section of a ZnO film grown on glass. During the deposition process, the liquid nitrogen feed to the cold-spiral was turned off, and the spiral was allowed to warm up. The abrupt change in the mode of growth at this point can be clearly seen. The densely packed layer initially grown under low residual gas pressure conditions gives way to a rather loosely packed structure when the trap released the contaminants. X-ray analysis of this film indicated that the preferred (0002) orientation had been maintained despite the perturbation in the process, but the bulk wave single transit loss had risen slightly to 4dB. The implication in this particular case is that the

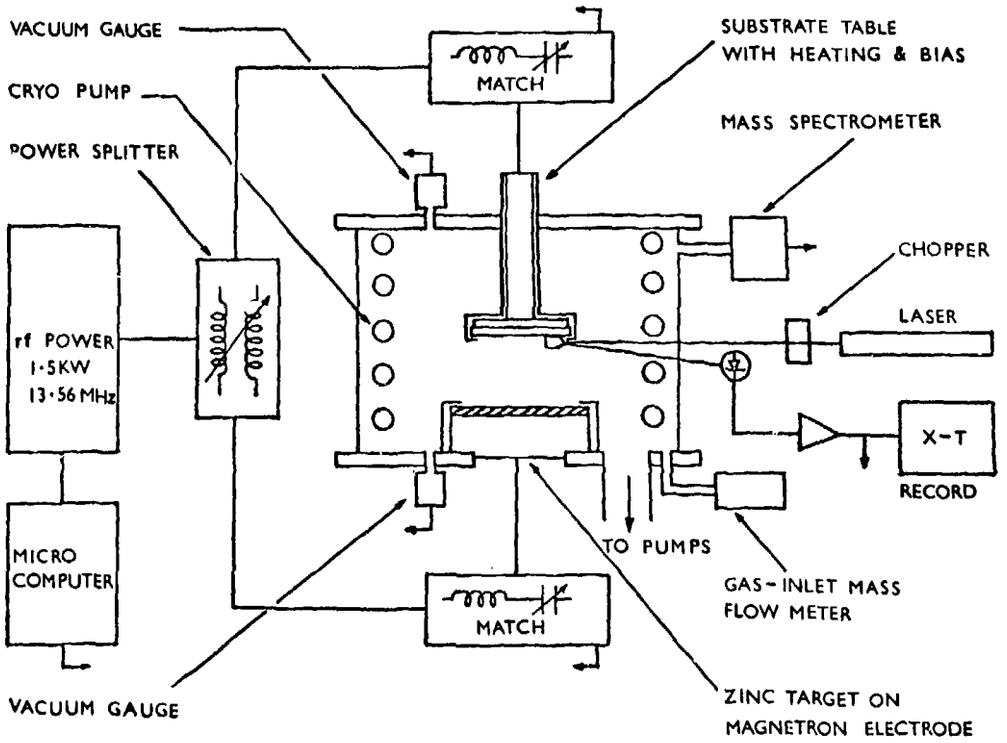

Fig. 17. Schematic of ZnO Deposition System Showing Process Control by Dedicated Microcomputer.

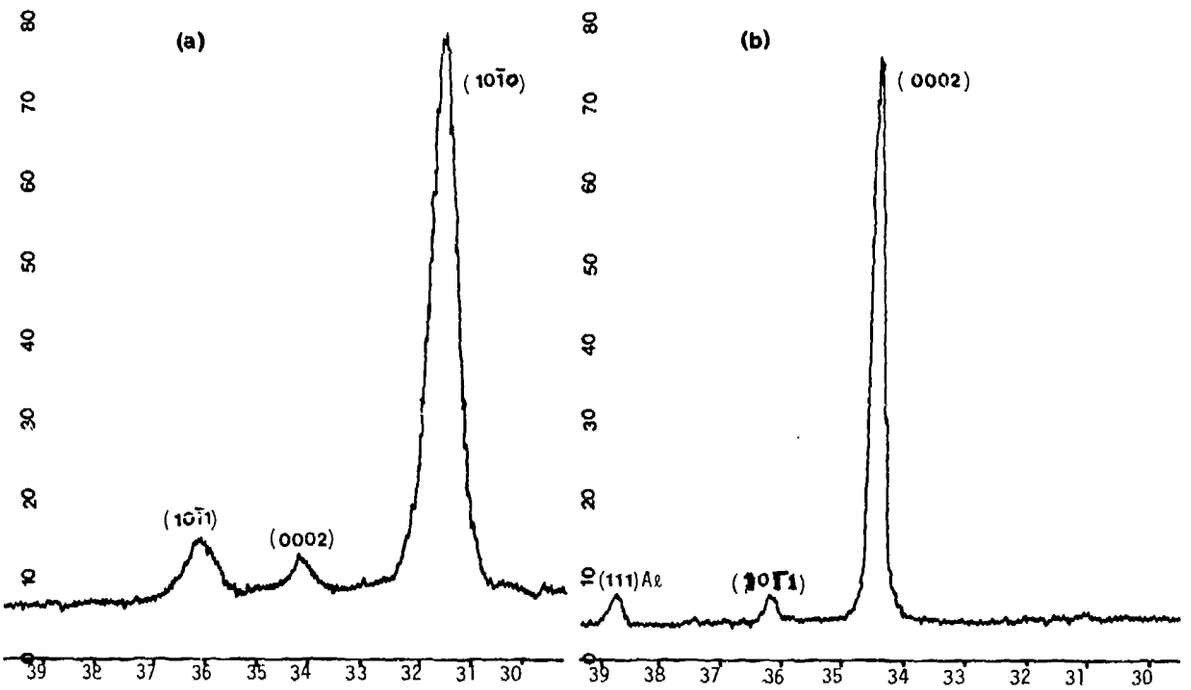

Fig. 18. (a) X-ray Diffraction Peaks for ZnO Layer on Glass, (b) X-Ray Diffraction Peaks for ZnO Layer on Aluminium Film on Glass Deposited under Similar Conditions to (a) Result.

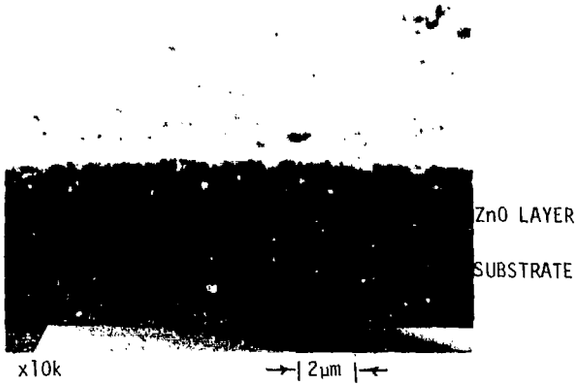

Fig. 19. SEM Section through ZnO Layer Grown on Glass - Note the Change in Density Caused by Sudden Release of Residual During Deposition.

physical structure had been modified without apparently degrading the acoustic performance seriously. It would, however, seem to be unwise to hope that similar failures in the process will always have so little significance, thus our ultimate deposition system will employ a microcomputer to supervise the monitoring during transducer fabrication. An example of the rather dramatic effect of poor process control is shown in Fig. 20 in which the curves labelled (a) are for a bulk wave transducer with mixed orientation in the film, while curve (b) is for a film of the preferred orientation only. The former shows that two types of wave of slightly differing velocities are launched, with the consequence that the desired mode has much higher losses than are acceptable.

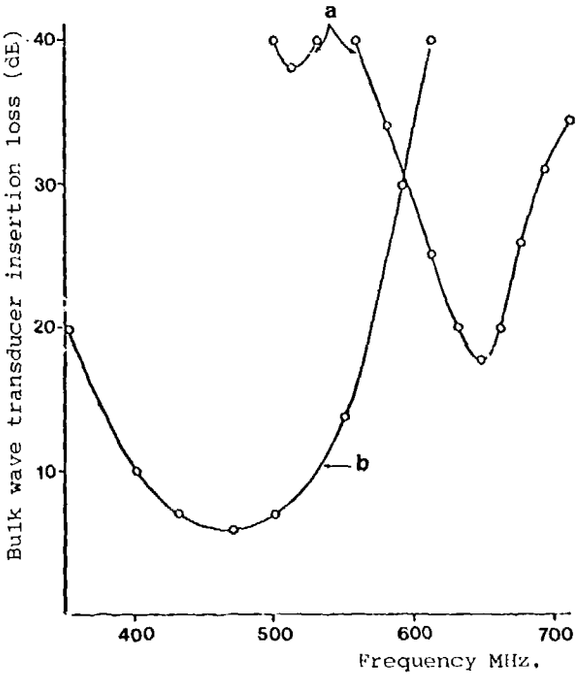

Fig. 20. Transducer Insertion Loss Against Frequency for: (a) Transducer with two crystallite orientations; c-axis normal and parallel, to the major film plane, (b) similar transducer with c-axis predominantly normal to the major film plane.

To summarise, the work is beginning to explain how the acoustic parameters of a transducer relate to the physical properties of the thin film material, and in turn, how these properties can be controlled by modifying the process conditions. A number of important features in this chain of events have been identified and we expect these to lead to a continued improvement in the deposition process.

CONCLUSIONS

A wide range of applications of ultrasonic waves have been demonstrated. In particular the transmission SAM is shown to be a useful tool operating at low frequencies and modest resolutions to give mechanical data and image defects in opaque objects.

The new on-axis dark field system has been demonstrated as a tool for the detection and imaging of weakly diffractive material defects.

The fundamental studies of wave propagation and scattering are continuing to provide descriptions of systems for which no analytical solutions exist, in particular in support of the mode-conversion techniques, which have now proved themselves as practical crack detection and characterisation tools. A high resolution acoustic probe has been demonstrated which offers sub-half-wavelength resolution. Manufacturing tolerances should not be a limiting factor on the probe's performance for frequencies up to 15MHz.

ACKNOWLEDGEMENTS

The authors wish to thank the other members of the group for their contributions to the reported studies, in particular the helpful suggestions and discussions with Professor E.A. Ash and Dr H.K. Wickramasinghe.

W. Duerr, D.A. Sinclair and I.R. Smith are grateful to the Medical Research Council for Research Project support and D.A. Sinclair and I.R. Smith to the Science Research Council for the award of Research Studentships.

M. Ambersley and C.W. Pitt wish to thank the consortium of companies and laboratories supporting the Zinc Oxide program - E.M.I, G.E.C, Philips, Plessey, S.T.L, R.S.R.E and Kings College London.

L.J. Bond and A.L. Downie acknowledge that their work has been performed with the support of the Procurement Executive, Ministry of Defence (U.K.).

All the authors thank the Science Research Council for the Grant to the Microwave Research Unit, and the contribution which this has made to the groups work.

REFERENCES

1. Ameri, S., Ash, E.A., Petts, C.R. and Wickramasinghe, H.K.: (1980) Scanned imaging techniques for surface NDE. Proceedings DARPA/AFML Review of progress in quantitative NDE. La Jolla, USA, July 14-17.

2. Bond, L.J.: (1979) Finite difference methods applied to ultrasonic non-destructive testing problems. Proceedings ARPA/AFML Review of progress in quantitative NDE. La Jolla, USA, July 8-13.

3. Ameri, S., Ash, E.A., Htoo, U., Murray, D. and Wickramasinghe, H.K.: (1979) Laser detection and imaging techniques for surface examination. Proceedings ARPA/AFML Review of progress in quantitative NDE. La Jolla, USA, July 8-13.

4. Ilan, A. and Bond, L.J.: (1980) Interaction of a compressional impulse with a slot normal to the surface of an elastic half space II. Geophysical Journal, Royal Astronomical Society (in press).

5. Bond, L.J.: (1979) Methods of ultrasonic non-destructive testing. Patent application No. 7923729.

6. Quate, C.F., Atalar, A. and Wickramasinghe, H.K.: (1979) Acoustic microscopy with mechanical scanning - A review. Proc. IEEE, 67 (8) 1092-1114.

7. Jipson, V. and Quate, C.F.: (1978) Acoustic Microscopy at optical wavelengths. Appl. Phys. Lett. 32 (12) 789-791.

8. Tai, C.S., Wang, S.K. and Lee, C.C.: (1977) Visualisation of solid material joints using a transmission type scanning acoustic microscope. Appl. Phys. Lett. 31 (5) 317-320.

9. Bond, W.L., Cutler, C.C., Lemons, R.A. and Quate, C.F.: (1975) Dark field and stereo viewing with the acoustic microscope. Appl. Phys. Lett. 27 270-272.

10. Sinclair, D.A. and Smith, I.R.: (1980) Dark field acoustic microscopy. Electronics Letters (in press).

11. Alterman, Z. and Loewenthal, D.: (1972) Computer generated seismograms. Meth. in Comp. Physics, 12 35-164.

12. Lehmann, H.W. and Widmer, R.: (1973) R.f. sputtering of ZnO shear wave transducers. J. Appl. Phys. 44 3868-79.

13. Shiosaki, T.: (1978) High-speed fabrication of high quality sputtered ZnO thin-films for bulk and surface wave applications. IEEE Ultrasonics Symposium Proceedings (IEEE, New York), p.100.

14. Evans, D.R., Lewis, M.F. and Patterson, E.: (1971) Sputtered ZnO surface wave transducers. Electronics Letters 7 557-558.

15. Khuri-Yakub, B.T., Kino, G.S. and Galle, P.: (1975) Studies of the optimum conditions for growth of rf-sputtered ZnO films. J. Appl. Phys. 46 3266-3272.

16. Pitt, C.W., Kirk, I.H. and Stevens, R.J.: (1975) Automatic monitoring of deposition conditions during rf sputtering of dielectric materials. Vacuum 25 265-271.

Gordon Kino, Chairman (Stanford University): I am interested in the focused aluminum conical transducer. Do I understand that to be basically a lens behind - you have got it there (Figure 14), fine. The transducer is out here, and you get a plane wave approaching that lens -

Leonard Bond (University College, London): Yes. You basically get the wave coming in, and it hits the Mylar film. You are just sampling your wave at the tip of the aluminum lens. That then focuses the energy you've captured down through the system, and you're then producing practically plane waves that travel through water to the transducer which is a conventional piezoelectric transducer.

Gordon Kino, Chairman: What is the purpose of the Mylar film?

Leonard Bond: It is basically that the air-aluminum gives better isolation at the cone side rather than having water rest on it.

Gordon Kino, Chairman: Very pretty.

Leonard Bond: It's a very nice little thing, and it seems to work very well.

Mr. Schmitz (Germany): What is the bonding sensitivity of this bond.

Leonard Bond: The sensitivity. At the moment, it is better than 30 db signal to noise in actual experiments. The main problems seem to be with electronics rather than the actual limits on the sensitivity of the probe, so it's something over 30 db signal to noise, and that's the best we have raised so far. It should be a lot better than that.

Bob Bray (Stanford University): I wonder what frequency you use in the probe?

Leonard Bond: At the moment it is being used between 1 and 15 megahertz.

Gordon Kino, Chairman: Is it a broad-band probe or are there several probes?

Leonard Bond: Several, but there has been one particular one that has been working at about 10. It seems to be working okay. It has been demonstrated between 1 and 15. There have been several attempts at that.

Dale Collins (Battelle Northwest): What about the reflection between your water and the lens. It looks like you have reflections bouncing around depending on how sharp a pulse you hit it with.

Leonard Bond: I think its all being used with quite short pulse work.

Larry Kessler (Sonoscan): The zero order stop on your dark field diagram (Figure 5) seemed to be in a funny place. I would expect it to be in the focal zone of the transducer.

Leonard Bond: This is the one like that one shown of my colleagues. I believed him that he was right. If it is not correct, I apologize, and we can check what he actually put in the figure in the paper.

Larry Kessler: The question really is: does that work as well?

Leonard Bond: I understand one of the pictures is that he did say that the stop was different, and this was one of the things that is improving it, and he says it is a new way of actually fabricating a dark field system, and I tended to believe him. I am not an expert on microscopy.

Larry Kessler: Kumar may be able to help.

Kumar Wickramasingne (University College London): It does stop at zero because you go from one side. So the transfer function is a rectangle function. It's a certain function in the system.

Gordon Kino, Chairman: Put another way, Larry, the rays in the center are the ones which correspond to a parallel beam coming back, and you're sorting those out, getting rid of them. You can only receive rays which are coming at an angle.

Larry Kessler: Something doesn't gibe.

Unidentified Speaker: Can you show this view, the previous viewgraph?

Leonard Bond: All three? (Figure 14).

Unidentified Speaker: Yes. In this viewgraph, how do you get rid of all the reflections on the one with the lens, on the interface between the aluminum and the water? Did you mask that somehow, or did you use any damping materials, you know, to avoid any reflections?

Leonard Bond: As Kumar is saying, there is good matching.

Jan Van den Andel (Westinghouse, Canada): How is the whole thing coupled to the material? Is there another water fill or -

Leonard Bond: You then insert it in the water tank.

Jan Van Den Andel: This whole thing goes together in a water tank? Is it possible all these reflections they're talking about in the water that goes back and forth are going beyond the area where you're interested in because there must be reflections.

Leonard Bond: Can you answer that for us, Kumar?

Gordon Kino, Chairman: It it possible that you're getting - perhaps I didn't quite get it either. Maybe you should talk to each other afterwards. Thank you very much.

DEFECT CLASSIFICATION AND IMAGING WITH PHASE ARRAY TECHNIQUES

V. Schmitz, W. Gebhardt, F. Bonitz
Fraunhofer Institut für zerstoerungsfreie Pruefverfahren
Saarbrücken, West Germany

ABSTRACT

The use of arrays and the possibility of electronic beam steering, focusing and side lobe suppression allows a better defect classification and reconstruction of defective areas in work pieces, components and industrial plants. Because of synthesizing a large sector by a narrow ultrasonic beam, the advantage of a narrow beam for good signal/noise ratio is combined with the advantage of a broad beam for good detectability of unfavorable orientations of flaws. A Fortran program has been written for an equidistant or nonequidistant linear array with the arbitrary choice of amplitude and phase of each element. For shear wave excitation, the shear wave point characteristic of a point source is implemented. The phased array technique has been used for distinction between cracks and voluminous flaws and for the destination of flaw inclination and surface curvature. Three evaluation methods can be used: interpretation of the sector display; generation of compound-scan amplitude locus curves, and flaw imaging by superposition of all sector scans on a storage display. The experimental results show that the arrays are a powerful tool in increasing the reliability of nondestructive testing methods.

INTRODUCTION

One of the central points in nondestructive evaluation (NDE) is the flaw analysis, i.e., the determination of shape, size and orientation of defects. Especially, the distinction between cracks and voluminous defects is of great importance. The flaw size is usually estimated by echo height assessment related to the equivalent disc reflector which is oriented perpendicularly to the acoustic axis of the probe. A more far reaching defect characterization is possible by evaluating amplitude locus curves (AOK) which are generated by recording the echo height versus probe position. Classification by such methods has been done until now with only simple model reflectors. Flaws which are large in comparison with the beam diameter can be measured by scanning, however, there is a high probability that the beam is deflected and only flaw edges are recognized. New methods for defect classification and reconstruction arise by using electronically steerable array probes. It is possible to influence the sound field on a large scale by changing the insonification angle, beam diameter, ratio between main lobe and side lobes or to synthesize a large sector by steering a narrow sound beam. The dynamic movement of an image when moving the probe along the surface gives additional information.

To check all these possibilities, a modified medical phased array system has been used. The system operates at 2 MHz and the focus can be varied within the nearfield of a 20 element probe. The effect of the dimensions of the elements of such an array, together with acoustical coupling effects, has been calculated and used for the design of optimized probes.

CALCULATION OF ARRAY BEAM PATTERNS

For the calculation of the beam patterns, the basic Huyghen's principle is used. It is assumed that the single elements of the array are arranged in one line but the distance between two elements can be equidistant or nonequidistant. Each element may be individually excited in amplitude and phase. The program calculates the intensity of one component of particle displacement. For longitudinal waves, it is the normal particle displacement and for shear waves, the tangential displacement in a distance z. The particle displacement can be calculated for up to 500 different points in a constant distance z or in a fixed radius from the array center. Amplitudes, phases and number of elements must be within 100.

With S_{1k} the position of one element, R_{1k} the distance to a field point A(x,y,z), and β_{1k} the corresponding angle to this field point are complex added:

$$u(A(x,y,z)) = \sum_{n}^{L} \sum_{k}^{M} \frac{1}{R_{nk}} e^{i(kR_{nk} - \Phi_n)} u(\beta_{1k}) \quad (1)$$

with

- L = number of array elements
- M = number of division of each element
- k = wave vector
- Φ = phase of each single element
- u = particle velocity of a point source attached to a half space
- R = directivity pattern.

The beam pattern of a point for longitudinal waves has been chosen according to Krautkraemer to $U_N = \cos\theta$ and for shear waves according to Miller/Pursey (Ref. 1).

$$u_T = \frac{\sin 2\theta \sqrt{\mu^2 \sin^2\theta - 1}}{F(\xi)} \quad (2)$$

$$\xi = \mu \sin\theta \quad (3)$$

$$F(\xi) = (2\xi^2 - \mu^2)^2 - 4\xi^2 \sqrt{(\xi^2 - 1)} \cdot \sqrt{\xi^2 - \mu^2} \quad (4)$$

$$\mu^2 = \frac{2(1 - \nu)}{1 - 2\nu} \quad (5)$$

with

ν = Poisson's ratio

The directivity function calculates to:

$$R = u_N \cdot u_N^* \text{ or } = u_T \cdot u_T^* \qquad (6)$$

The program has been written in Fortran, implemented on a PDP 11 and on a VAX. The basic structure is seen in Fig. 1:

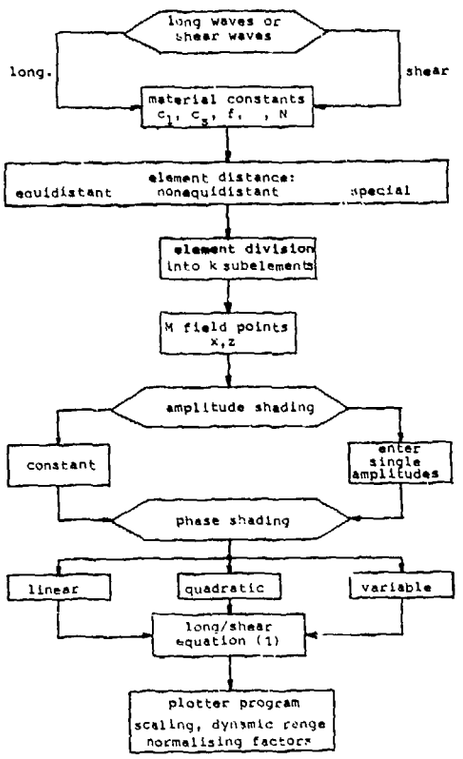

Fig. 1 Program used for the calculation of array beam pattern.

Key elements in array systems are the delay lines, modern equipment use charged coupled delay lines (CCD's). The delay time of these devices is proportional to aninternal clock frequency. The clock frequency is generated by a frequency synthesizer, which is a phase locked loop generator. The time this loop needs to stabilize depends on the accuracy of the frequency needed. The program has been used to calculate the array directivity pattern of an improperly steered array and calculations run for a 20 element array with elements distanced $\lambda/2$ both for longitudinal waves and for shear waves. We have found that instead of a 500 Hz step, a frequency step of 10 kHz is still allowable (Fig. 2(a) and (b).

The use of 100 kHz steps is not recommended because the effect is a second main lobe. Phase errors by use of the 10 kHz steps consist of small shifts in the main lobe of about 3° and a small shift in the distance to the side lobes.

Another application has been to calculate the effect of amplitude shading. Figure 3 shows a 16 element array with elements spaced $\lambda/2$ wave length

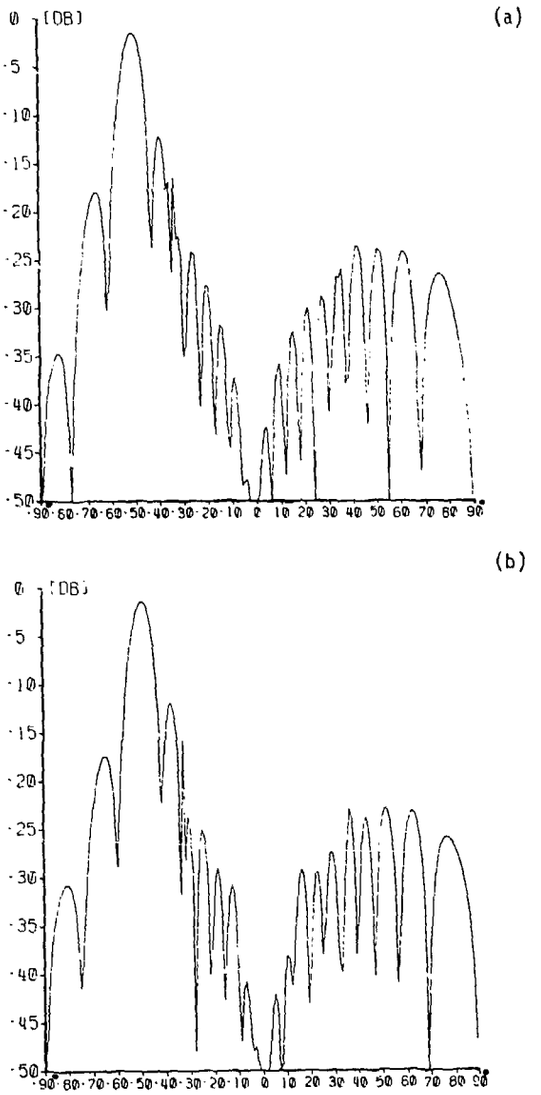

Fig. 2 Directivity pattern of a steered 50°, 20 element array with shear wave excitation. (a) 500 Hz clock frequency; (b) 10 kHz clock frequency.

apart, with and without Hamming weighting. The beam has been steered by 45°. The dotted line corresponds to the nonweighted array. The main lobe/side lobe distance is about 10 dB. The use of the amplitude shading increased this distance to about 25 dB.

A third application is the calculation of directivity patterns for arrays with nonconstant distances of the single elements. One possibility is the sin distribution:

$$s_i = \frac{L}{2N}\left(i + p.\sin\frac{2i\pi}{2N}\right) \qquad (7)$$

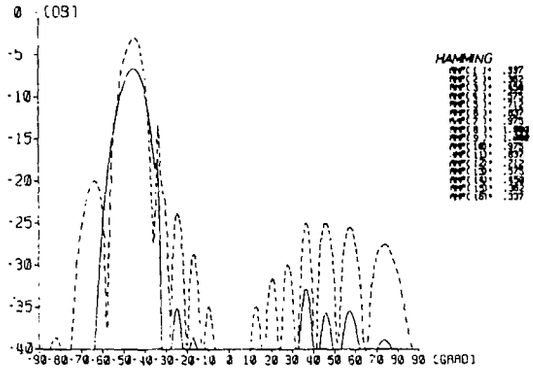

Fig. 3 Array-Shear-Wave-Beam-Pattern, 45° steered, with and without Hamming-weighting.

with S_i = distance of the i-th element to the midth of the array, L = array length, N = number of elements and p = coefficients. The p coefficients cause a narrower element distance in the middle of the array. For a 2 MHz, 11 element array the calculations are performed for an average element distance of 1.5, 0.5 and .75 wavelength. With a 1.5 wavelength element distance, the 11° steering of the array caused a main lobe/side lobe distance of only 4 dB. A weighting by Dolph-Tschebyscheff could increase this distance by only 0.5 dB. An element distance of 1 wavelength allowed a steering of 20° with 6.8 dB side lobe suppression and an improvement by 4 dB. An average element distance of 0.75 wavelength allowed a steering of 30°, with 5.5 dB and together with Dolph-Tschebyscheff shading of 10 dB. The calculations showed in this case, four elements can be saved when steering within 20°.

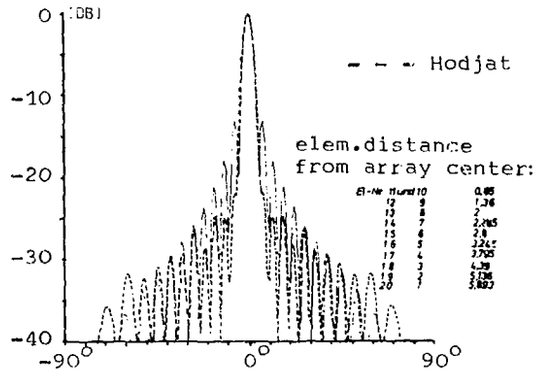

Fig. 4 Directivity pattern with 24 equally spaced elements compared with a 20 element array spaced according to Hodjat (Ref. 2).

DEFECT CLASSIFICATION AND RECONSTRUCTION BY SECTOR-SCANNING

If a scanning array probe is moved across the surface of a metal piece, the angle of maximum echo height changes from probe position to probe position. The position and the movement of an image point in a sector display is proportional to the position and the velocity with which the probe is moved. From the variation of the image, in time, intensity and position, conclusions can be drawn about the flaw parameters like shape, size and orientation. (Ref. 3,4).

First, we will discuss the case of an ideal curved reflector, represented by a cylindrical bore hole.

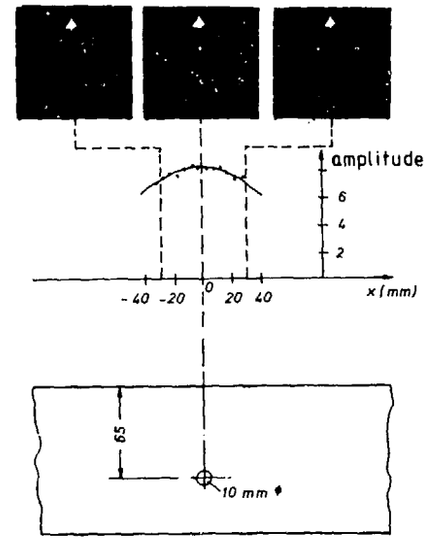

Fig. 5 Sector display and compound-scan-amplitude-locus curve of a curved reflector.

If the scanning probe is moved along the surface of the specimen from left to right, the image point moves across the total sector and finally disappears at the left. Since a curved reflector has no directivity, the intensity variation of the image point is small and is brightest in the middle of the sector equivalent to the smallest time-of-flight. This dynamic behavior allows us to tell this is a curved flaw.

Consider now the case of a planar defect, which is represented in Fig. 6 by a 10 mm flat bottom hole with 30° inclination.

Because a flat reflector has a pronounced directivity, the image point will not move across the whole sector but rather over a short distance. The orientation of the reflector is equal to the orientation of the scan line running through the brightest spot. This is totally different behavior compared to a curved flaw and indicates the inclination of a planar flaw.

DEFECT CLASSIFICATION AND RECONSTRUCTION BY COMPOUND SCAN AMPLITUDE LOCUS CURVE VAOK

A more quantitative description of the flaw parameters is possible by means of a compound scan amplitude locus curve (VAOK) which is generated by recording the maximum echo amplitudes versus the corresponding array probe positions according to Fig. 5 and 6. Because the center of the array

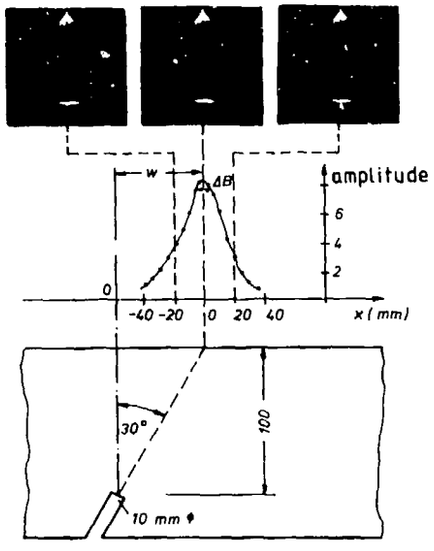

Fig. 6 Sector display and compound-scan-amplitude-locus curve of a planar defect.

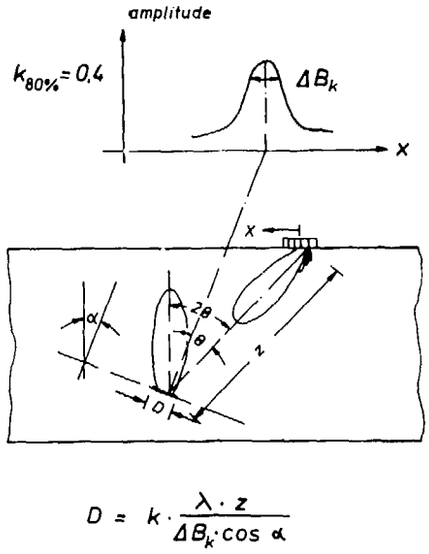

Fig. 7 Relationship between compound-scan-amplitude-locus curve and flaw size D.

beam looks always toward the flaw, the probe characteristic is eliminated automatically. The compound scan amplitude locus curve depicts directly the directivity function of the flaw. In the case of the cylindrical bore hole in Fig. 5, the locus curve reaches a maximum just above the reflector and diminishes slowly to the left or right.

The planar reflector (Fig. 6) maximum amplitude occurs in a position where the ultrasonic beam is incident and perpendicular to the reflector plane. Now the maximum of the locus curve is not just above the reflector but rather shifted by a distance w. The maximum shift which depends upon inclination and flaw depth, besides the shape of the curve, is an important criterion to distinguish between curved and planar defects. From the position of the maximum and the measured flaw depth, the orientation can be determined.

Figure 7 shows the relation between the directivity of a planar reflector and the compound scan amplitude locus curve. Here α is the flaw angle reference to the surface, ΔB the width of the amplitude locus curve, λ the wavelength and z the distance between reflector and probe position. k is a factor depending on the level where the width of the curve is measured. If the width is measured at 80% of its maximum value, k = 0.4.

DEFECT CLASSIFICATION AND RECONSTRUCTION BY COMPOUND SCANNING

The principle of this evaluation method, known for several years in medical diagnostics, is a combination of a sector display and the lateral movement of an array probe. In one probe position, a full sector scan is performed and stored in a storage display or a digital scan converter. Then the probe is moved a distance and the correspondent sector scan is stored but shifted proportional to the array-probe movement. This gives a highly accurate image of an irregular shaped flaw because the probe has a height acceptance angle of about 90°, which is synthesized by steering a focused narrow beam.

In the following, some examples for compound scan imaging are presented. Figure 8 shows the image of a 12 mm side drilled hole in a 150 mm thick specimen at a depth of 100 mm. Surface, back wall, depth of the side drilled hole and its shape are clearly visible. In addition, the figure shows the image of a bottom hole at a 100 mm depth where the cone of 32° and the 20 mm diameter can be read out immedately.

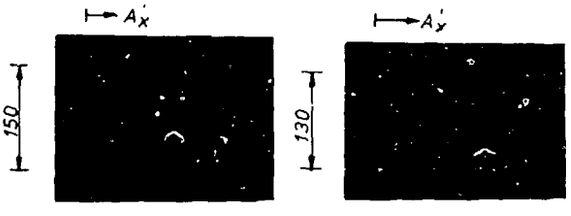

Fig. 8 Compound scan imaging of a cylindrical side drilled hole and a bottom hole with 32° cone.

Figure 9 shows imperfect homogeneous layers in a 300 mm steel specimen. Position and orientation of the layers are evident. Figure 10 shows cross sections of the weld zone in a 1400 x 800 x 200 mm^3 specimen with natural cracks in it. The picture shows front surface, back surface root of the weld, shape and curvature of the cracks. Crack height to 2/3 of the specimen's thickness can be recognized. After destructing the specimen, the true profile could be compared with the measured depth profile. A good agreement was achieved.

The compound scan imaging can be improved to a "roundabout scanning", and in Fig. 11 the flaw

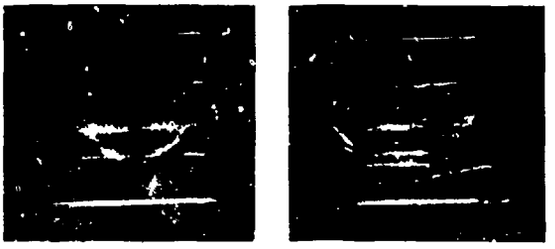

Fig. 9 Compound scan imaging of inhomogeneities in a steel specimen.

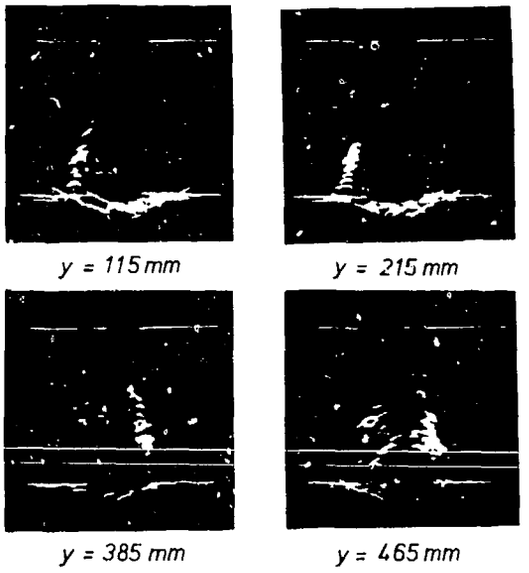

Fig. 10 Compound scan imaging of natural cracks in a weld.

echoes reflected via the backwall are recorded. In this way, not only the upper surface of the defect is reconstructed but also its underside.

CONCLUSIONS

A computer program has been developed which calculates the directivity pattern of a linear array with arbitrarily spaced elements, with free choice of amplitude and phasing of each element. It was shown that the electronic sector and compound scan based upon phased array beam forming techniques is a powerful tool for the flaw analysis. We are convinced that these methods are an important step to distinguish between curved defects and cracks.

ACKNOWLEDGMENTS

This work is supported by the Federal Ministry of Research and Technology within the scope of reactor safety research program.

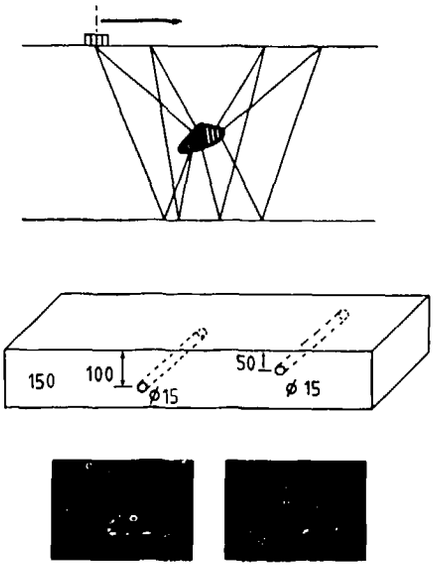

Fig. 11 Compound scan imaging improved to a roundabout scanning.

REFERENCES

1. Miller/Pursey, "The Field and Radiation Impedance of Mechanical Radiators on the Free Surface of a Semi-infinite Isotropic Solid," Proc. Roy. Soc., London, A223, 1954, pp. 521-541.

2. Hodjat, F., Horanessian, S.A., "Nonuniformly Spaced Linear and Planar Array Antennas for Sidelobe Reduction IEEE Transaction on Antennas and Propagation," Vol. AP-26, March, 1978.

3. Gebhardt, W., Bonitz, F., Woll, H., Schmitz, V., "Beam Forming and Defect Characterization by Phased Array Systems," Proc. of Ninth World Conference on NDT, Melbourne, 1979, Paper 4FFD-1.

4. Gebhardt, W., Bonitz, F., Woll, H., Schmitz, V., "Determination of Crack Characteristics Size and Orientation of Defects by Phased Array Technique in NDT," NDE In Nuclear Industry, 11-14.2.80, Salt Lake City, Utah.

Gordon Kino, Chairman (Stanford University): There is time for one or two questions.

Unidentified Speaker: Did you do any samples where the range to the flaw was on the order of magnitude larger than that compared to the flaw size? It looked like the range was about on the order of 10 times the size of the flaw. Did you do any situations where the range was on the order of a hundred times the size of the flaw? Do you have any such samples?

W. Gebhardt (Institute for NDT, Saarbruecken): Some flaw sizes have been two millimeters or three millimeters. The thickness of the specimen is 200 millimeters. I don't understand your question, because the range of the depth of the flaws has been more than 10 times greater than the actual sizes of the flaws.

Unidentified Speaker: The ones you showed were around 10. Were there any that that you did that were around a hundred times?

W. Gebhardt: Not in this sample. But this is the easiest way to do it. It's much more complicated to go below the depths of the flaws.

Unidentified Speaker: So there were other problems when you do that?

W. Gebhardt: You have a divergency of your actual sound beam, so what you lose is a solution probability because it can only focus within the near view length of a pole, and you have enough signal to noise ratio for imaging the complete specimen. What we have here are homogeneous materials. What depths are you thinking about?

Unidentified Speaker: On the order of 50 to a hundred times, and then the inhomogeneity of the medium becomes a greater issue as well as the problems in resolution in the beam itself and the spreading of the beam so that what happens is time doesn't translate into range as easily as you move across this scan, and you don't get that nice -

Gordon Kino, Chairman: Next question.

Bob Addison (Rockwell Science Center): You said that you operated with two megahertz. I wonder that the length of your transient response was of the transducer probe.

Gordon Kino, Chairman: It's about three rf cycles.

Jack Smith: You showed a simulation of a sparse array as an equally spaced element. Did you actually use such an array to make some of the images you showed?

W. Gebhardt: We did not use this array for this image as shown. We have one in our institute but not yet the time for using it on experiments, so perhaps I can give you more details in about a half a year. But it shows to have varied the restrictions if you steer the beam more than 45 degrees.

Gordon Kino, Chairman: So was this the array that was used here; how many elements were used?

W. Gebhardt: Twenty elements equally spaced.

Gordon Kino, Chairman: Equally spaced. And then it was moved along mechanically?

W. Gebhardt: It was gently moved along with the hand-held camera I showed you in the first pictures.

Gordon Kino, Chairman: One more question.

Unidentified Speaker: Did you see any artifacts due to mode conversion?

W. Gebhardt: Yes, we can see this image. No, artifacts I didn't see. But what you can see are mode-converted longitudinal waves and the corresponding images of these mode-converted rays, but because of the different sound velocity and not affected element distance they have another angle in the image and to move velocity into dynamic movement, then the - . So you can't decide if this is an actual defect; longitudal wave or if it is a mode-converted wave which images the same point in space to another image point.

Unidentified Speaker: In the first couple of slides, one or two of the images had a white dot off to the side in various places. Were those mode images, or --

W. Gebhardt: This was a real image. The white dot? Was it the image or the slide?

Unidentified Speaker: I think it was in the second or third slide.

W. Gebhardt: This was the actual image.

Gordon Kino, Chairman: Thank you very much.

SCANNED IMAGING TECHNIQUES FOR SURFACE NDE

S.Ameri, E.A.Ash, C.R.Petts and H.K.Wickramasinghe
University College London
Department of Electronic and Electrical Engineering
Torrington Place
London WC1E 7JE
England

ABSTRACT

A phase sensitive laser probe in which the focussed spot is small, as compared with the acoustic wavelength, is capable of measuring the complex distributions of a SAW field along prescribed scan lines. Using the probe, it is possible, on a defect free sample, to measure the SAW velocity surface with an accuracy of a few parts in 10^5. Such accuracy suggests that the technique is sufficiently sensitive to detect small changes in surface characteristics; the presence of a defect is revealed by perturbations in the relationship between various scans. The scattered radiation patterns from a surface crack irradiated by acoustic surface waves can be utilised to determine the defect size and location with improved accuracy. Results on deliberate and real cracks are presented.

Acoustic microscopy has proved to be a valuable tool for the NDE of complex IC devices. With the advent of VLSI there is a clear need for an acoustic microscope showing sub-optical resolution. We report on the design of a high pressure gas acoustic microscope operating at room temperature which should provide a resolution below 100nm.

Finally, following the demonstration of a photoacoustic microscope at Stanford University, there has been a great deal of interest in the subject of photoacoustic microscopy. We describe the work at University College London which is based on the use of a conventional gas photoacoustic cell together with pulsed laser excitation. A finite difference approach has been used in order to study the effect of an inclusion buried under the surface on the photoacoustic signal. In the case where the thermal properties of the inclusion are known apriori, our one dimensional model indicates that it should be possible to obtain not only the depth of the inclusion beneath the surface but also its thickness.

INTRODUCTION

Detection of surface opening cracks is now quite wide-spread and several techniques capable of estimating the size of such cracks have been reported in the literature (1-6). We have been working on a scheme which is based on the use of a laser probe to record the scattered surface waves from the defect. The scattered field not only provides valuable information about the size and orientation of a surface crack but also enables one accurately to determine its position. Recent results will be presented in the following section.

Acoustic microscopy has proved to be a valuable tool for the NDE of complex IC devices (7). Currently, acoustic microscopes operating at room temperature (using water as the coupling medium) are limited to a resolution which is comparable to that of high quality optical instruments. This limitation stems from the lack of a suitable liquid coupling medium which can offer a performance superior to that in water. We have been investigating an alternative class of fluid which is superior to water, viz gases at elevated pressure. Section 3 will be devoted to discussing the design of a gas acoustic microscope which should provide sub-optical resolution working at rather modest pressures.

Photoacoustic microscopy has attracted considerable interest over the past few years, perhaps mainly as it represents a complementary technique for surface NDE. In section 4 we shall present our initial work in this area.

Finally, section 5 will contain a brief summary of the main points in this paper.

DETECTION AND SIZING OF SURFACE DEFECTS

The technique for obtaining the scattered SAW field from a defect was described in detail at the 1979 DARPA/AFML meeting (8). The heart of the system is a computer controlled laser probe which is capable of recording the complex SAW field with a sensitivity down to 10^{-4} Å in a bandwidth of 1 Hz. Since this system has been considerably modified over the past year, we shall begin with a brief description of the probe.

The basic optical and electronic systems are illustrated in Figs. 1 and 2 respectively. The laser probe is an a.c. interferometer. Coherent light, from a 5mW HeNe laser is directed onto a 25 MHz water Bragg cell which provides a 50 MHz optical carrier.

The use of an optically generated carrier renders the system insensitive to phase variations caused by microphonics in the optical system, as they appear both in the signal as the reference channel. The detected SAW field is finally converted into the in-phase and quadrature components, r and i, using a lock-in-analyser which has an adjustable bandwidth. The three outputs of the detection system, r, i and c are read by the computer, r and i being divided by c in order to eliminate variations due to surface reflectivity.

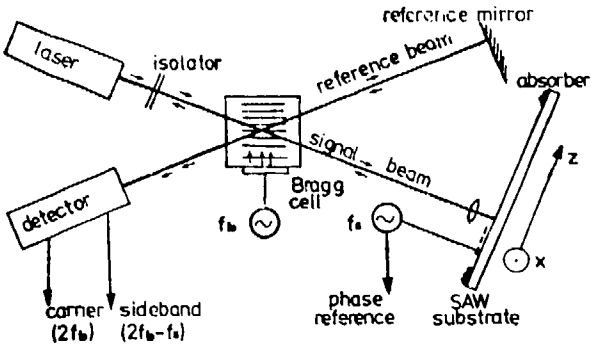

Fig. 1 Schematic Diagram of Phase Sensitive Laser Probe.

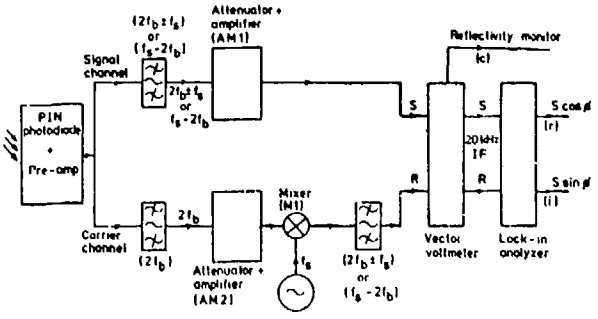

Fig. 2 Block Diagram of Electronics for Recording Amplitude and Phase of SAW Distribution.

The scanning and data logging operations are computerised. The scan positions are programmed and the stepping motors control the positioning with an accuracy of 1 μm. The measured phase accuracy is about ± 3°. Thus, a velocity accuracy of a few parts in 10^5 is readily achieved over 1 cm distance at an operating frequency of 60 MHz (9). Such accuracies achieved in velocity measurements, encourage the use of the device for the evaluation of scattered spectra from measurements on perturbed SAW fields.

We are able to illuminate a surface with a wide SAW beam and then investigate the amplitude of the SAW signal detected along a transverse scan line. In the case of a defect being present, harmonics will be generated in both the transmitted and reflected waves due to the opening and closing of the gap (10). This approach can therefore establish the presence of any defect. This technique has not yet been fully implemented due to the bandwidth limitation imposed by the front end of the detection system.

The other technique for detecting and locating defects is to record the complex field distribution along several scan lines and then use this information to deduce the scattered field. This technique was explained in detail at the previous meeting (8). Very briefly, the SAW field is represented as the sum of an incident (I), reflected (R) and scattered (S) component. By recording the complex fields along three separate scan lines, it is then possible to relate their FT's and thereby obtain I, R and S, (see Fig. 3).

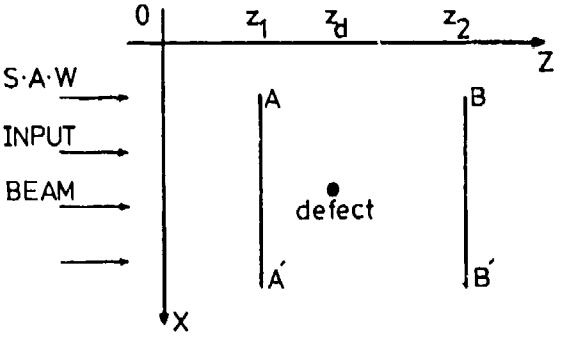

Fig. 3 Recording Configuration for Defect Characterisation.

Several experiments were carried out on real and deliberate cracks. As a test on the information obtained from the processed scattered field, a set of results were obtained for reflection off the edge of a $LiNbO_3$ substrate. The SAW source was an apodizing transducer operating at a synchronous frequency of 44 MHz. The edge was produced deliberately, it was not a cleaved edge. It was at an angle to the incident power flow direction. The reflected spectrum off the edge is shown in Fig. 4a. The reflected spectrum was then repeated by absorbing the incident beam at the edge, Fig. 4b.

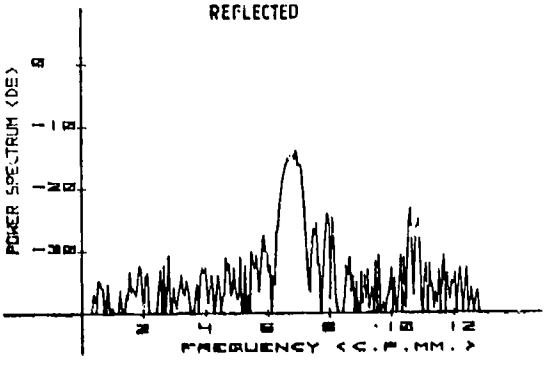

Fig. 4a The Reflected Field for an Exposed Edge.

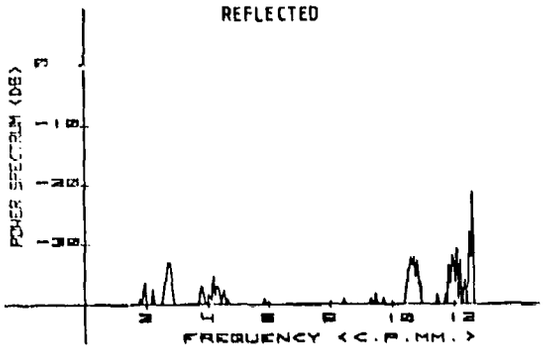

b) The Reflected Field When the Edge is Blocked with a SAW Absorber.

Fig. 4. Determination of R for an Edge.

The most recent results obtained, are a set of measurements achieved on cracks generated on a crystalline quartz substrate. The cracks are generated by rapid cooling of the sample from an elevated temperature. The crack is illuminated by a 100λ aperture uniform interdigital transducer. Fig. 5 represents the results of the incident and reflected spectra evaluated for a multi-cross shape tight crack. Fig. 6 shows the calculated incident and reflected spectra for a triangular crack with irregular sides. In each case, the width of the main lobe relates to the physical dimensions of the crack. However, as shown in Figs. 5 and 6, the recovery of the reflected spectrum is not perfect. The imperfections are attributed to the fact that the subtraction was carried out using a slowness curve which was derived from book values of elastic constants rather than a measured slowness curve for the particular substrate under test. In principle, the reflected spectrum can be used to reconstruct (and hence locate) the defect by backward propagation (11). We have not attempted to do this for this particular data set.

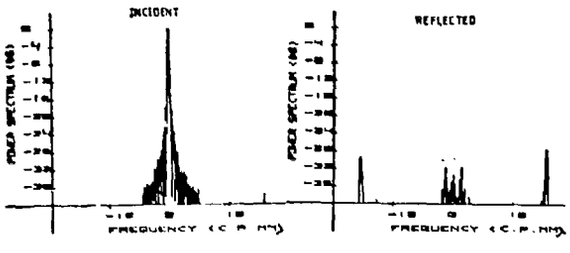

Fig. 5 Determination of I and R for Multi-Cross Tight Crack.

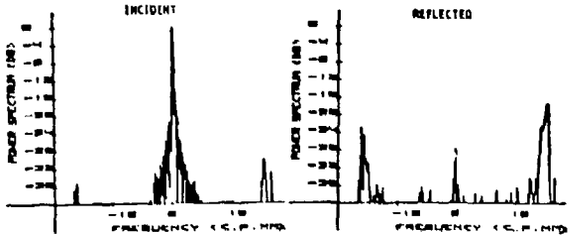

Fig. 6 Determination of I and R for a Triangular Shape Crack.

GAS MEDIUM ACOUSTIC MICROSCOPY

Acoustic microscopy has proved to be a valuable tool for the NDE of complex IC devices (7). By stretching the existing technology to its limits, the reflection SAM has been operated in water at 3 GHz, with a corresponding wavelength of 520 nm (12). With the advent of VLSI, there is a clear need to extend the resolution beyond this point. The major difficulty encountered in improving the resolution of a SAM is the high value of the absorption of sound in water. To obtain a wavelength below 520 nm, one must find a fluid which has a lower velocity, a lower absorption, or, preferably both. One possibility is to use cryogenic liquids such as Argon and Helium (13, 14). However, the use of such liquids involves several instrumental complexities and strict limits on the type of sample which can be studied. For example, the low temperatures involved immediately exclude the study of living biological systems - an application which is ideally suited to acoustic microscopy. It is for this reason that we have begun to investigate an alternative class of fluids - gases at high pressure. It is well known that the velocity of sound in gases is 5 - 10 times lower than that in most liquids. The acoustic absorption on the other hand is typically 100 - 1000 times higher. We have shown that the acoustic absorption - at least in the case of monoatomic gases such as Argon and Xenon - varies inversely with pressure so that it should, in principle, be possible to approach the value in water at elevated pressures (15). The results of our initial work in this area, where we demonstrated a reflection SAM operating in Argon at 30 bar and 45 MHz, with a resolution of 7 μm, appeared in a recent publication (16). This resolution is five times better than what can be achieved in water at the same frequency.

Since the configuration of a gas acoustic microscope is substantially different to a conventional acoustic microscope, we shall briefly describe it here. Fig. 7 shows its basic construction. It consists of a small-volume pressure cell connected to a regulated gas supply. The object is supported on a piezoelectric bimorph, which, when driven at resonance, provides a fast scan out of the plane of the diagram. Both the scanner and acoustic lens are mounted on movable pistons. These pistons are supported by hydraulically reduced micrometer heads

(not shown) such that the slow scan and focussing can be performed externally. A typical result from this apparatus working in Argon at 45 MHz and 30 bar, is shown in Fig. 8.

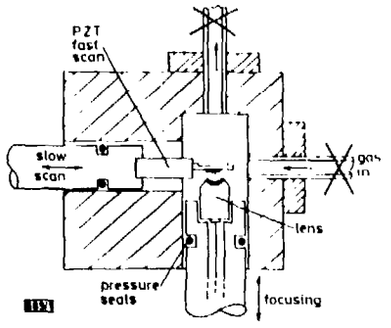

Fig. 7 Configuration of the Gas Acoustic Microscope.

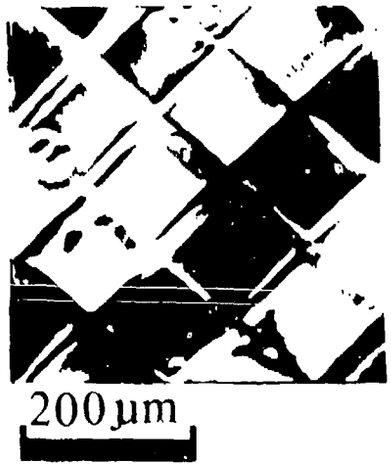

Fig. 8 Reflection Acoustic Micrograph of SEM Finder Grid at 45 MHz.

We can define a new coefficient of merit for a coupling fluid by calculating the minimum wavelength that can be achieved for a fixed loss and transit time within the fluid and relating it to the corresponding value in water.

$$M = \frac{(a/f^2)_w^{\frac{1}{2}}}{(a/f^2)^{\frac{1}{2}}} \left(\frac{C_w}{C}\right)^{\frac{3}{2}}$$

where C is the velocity of sound in the fluid, a/f^2 is its attenuation coefficient normalised with respect of the square of the frequency and the subscript w refers to corresponding quantities in water.

The table below lists the coefficient of merit for several liquids and gases.

Liquid	t(°C)	C/Km/s)	$a/f^2 x10^{17}(S^2/cm)$	M
Water	25°C	1.495	22.0	1.00
Water	37°C	1.523	17.7	1.09
Water	60°C	1.55	10.2	1.39
Carbon disulfide	25°C	1.31	10.1	1.81
Mercury	23.8°C	1.45	5.8	2.04
Argon(40bar)	20°C	0.323	412	2.00
Argon(250bar)	20°C	0.323	83	5.00
Xenon(40bar)	20°C	0.178	953	4.00

From this table, it is clear that gases such as Argon and Xenon under pressure can provide substantial improvements in resolution over water. Specifically, Argon at 40 bar will provide a factor of 2 improvement in resolution over water, while Xenon will provide a factor of 4. The figure of merit varies as $P^{\frac{1}{2}}$, so that, at 250 bar, the value in Argon is 5.

We are currently working on a system which will use Argon at 40 bar as the coupling medium and a 10 µm radius lens as the imaging element. We expect to obtain a resolution of 220nm at 1 GHz. Alternatively, one could use Xenon a 40 bar and obtain a resolution of 170nm at 740 MHz. (17). Although we plan to work with both gases, our initial experiments will be exclusively in Argon, as it is significantly cheaper than Xenon.

One major difficulty encountered with this system is that of matching the acoustic waves into the gas. There is an impedance ratio of $1:10^{-3}$ going from Sapphire to Argon (at 40 bar) so that there will be a two-way loss of 54 dB at this interface. At low frequencies (below 740 MHz) one can use a quarter-wave matching layer of polystyrene to bring this loss down to 7 dB as shown in Fig. 9. At higher frequencies, the losses in polystyrene become too high for it to act as an efficient quarter-wave transformer. In this situation, one could resort to a double matching layer. Fig. 10 shows the computed insertion loss curve for the case of a Fused Quartz lens followed by a quarter wave layer of Tungsten and then a quarter-wave layer of glass transmitting Argon at 100 bar. As we can see, it is possible to achieve an extremely small insertion loss while at the same time preserving enough bandwidth to transmit a 30ns pulse.

Finally, we are in the process of constructing an instrument that would operate at much higher pressures (around 250 bar) with the aim of attaining resolutions well below 100nm.

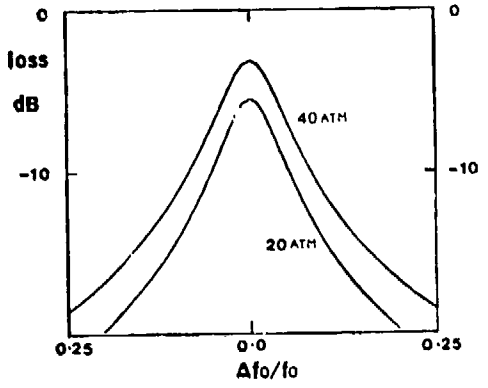

Fig. 9 Insertion Loss Curve for a Polystyrene Matching Layer on Sapphire.

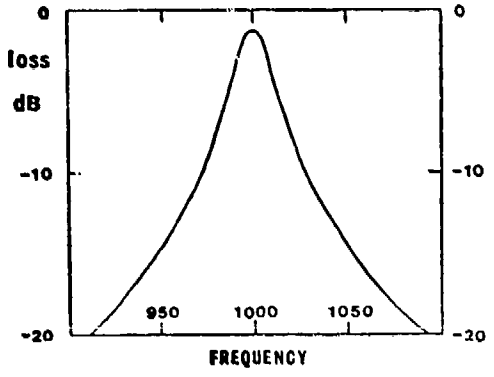

Fig. 10 Insertion Loss Curve for a Tungsten-Glass Matching Layer on Fused Quartz.

PHOTOACOUSTIC MICROSCOPY

Since the first photoacoustic micrograph was published, (18), there has been considerable interest in the subject of photoacoustic microscopy (19,20,21). As the technique can provide information about the thermal properties of the sample being investigated, it represents new tool for surface NDE. For example the presence of a flaw (such as a void) underneath the surface should result in a large change in photoacoustic signal. Indeed recent results on the detection of sub-surface structure are encouraging (20,21,22,23, 24).

The system we are working on is similar in many respects to a system described in the literature (19). A schematic diagram is shown in Fig. 11. It consists of a conventional photoacoustic cell which is mechanically scanned in a raster pattern. Lateral resolution is provided by focussing the laser beam onto the object using a microscope objective. The laser beam is tunable, so that it is possible in principle to record photoacoustic spectra on a microscopic scale.

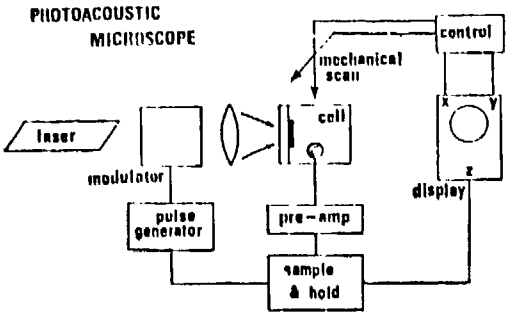

Fig. 11 Schematic Diagram of Photoacoustic Microscope.

Our initial experiments were conducted by modulating the incident laser beam at a few KHz and using a microphone in a phase-locked configuration to detect the photoacoustic signal (19,24). With this system, we have found that the average power level required in order to record images in seconds rather than minutes is around 250 mW and can often result in sample damage. We have therefore resorted to a pulsed system in which we use high peak power, low energy pulses, thereby increasing the signal strength while at the same time limiting the average laser power. Many experiments have not been conducted with this new system, but initial results are encouraging. Fig. 12 shows a photoacoustic signal from an EM grid structure taken using the pulsed system. The average optical power was 100 mW and the pulse width was 10 ms.

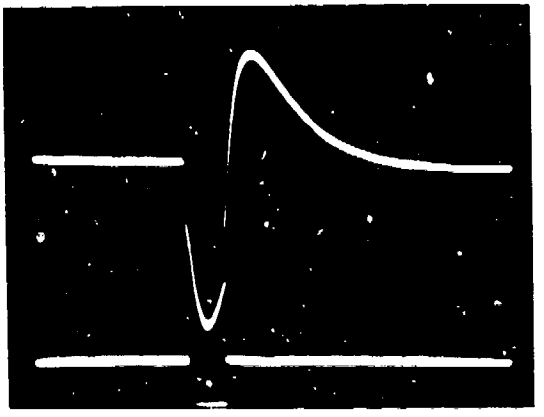

Fig. 12 Photoacoustic signal (top trace) corresponding to input optical pulse (bottom trace).

A finite difference approach has been used to study the effect of pulsing the laser on the photoacoustic signal. We have defined an effective thermal diffusion length for the pulsed case as being the depth below the surface of the material being heated at which the temperature is 1/e of the value at the surface (at the end of the duration of

the pulse). In fact, with this definition, the thermal diffusion length works out to be exactly the same value that would be obtained for the periodic heating case, if the period was taken to be equal to double the pulse width.

We have attempted to model the effect of an inclusion having known thermal properties on the photoacoustic signal (25). Although we have only worked on a one dimensional model (which would apply in practice when the focussed spot is large in comparison to the thermal diffusion length) the results show that it should be possible to obtain both the size (thickness in a one dimensional model) of the inclusion and its depth below the surface. The situation we have modelled is illustrated in Fig. 13. The substrate material is aluminium and there is a nickel inclusion 3 microns thick. Optical absorption takes place in a 1 micron region at the air/aluminium interface. The depth of the nickel inclusion can be varied from 2 μm to 6 μm. We can control the effective diffusion length by varying the pulse width; this can have any value between 0 and 200 ns. Fig. 13 also illustrates the temperature evolution with time. The temperature rises rapidly when the pulse is applied, reaching a maximum at the end of the duration of the pulse, after which the sample cools down slowly to an equilibrium value.

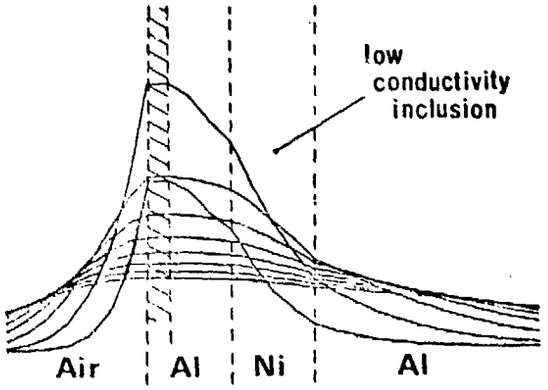

Fig. 13 Configuration Used for Finite Difference Model of Photoacoustic Effect.

With the inclusion at a fixed depth below the surface, we have calculated the maximum surface temperature (KM^2 $Watt^{-1}$) as a function of pulse duration. We have then repeated these results after changing the depth of the inclusion below the surface. Thus we would have one curve of temperature vs pulse width (or temperature vs effective diffusion length in the host material) for each value of the depth of inclusion below the surface. Fig. 14 shows a plot of the maximum surface temperature (normalised with respect to the value obtained with no inclusion) versus the depth below the surface (normalised with respect to the diffusion length in the host material). This plot, in fact, represents many sets of data points obtained for different values of inclusion depth. It is immediately apparent that all these sets in fact lie on one single curve; i.e. the curve is unique for a given thickness of inclusion material. If the inclusion thickness is reduced to 1 μm we obtain a different curve as shown in Fig. 14. In particular, the value corresponding to zero depth below the surface is smaller, and the decay rate with depth below the surface is different. This suggests a technique for getting both the depth below the surface and the thickness of the inclusion. One would simply record the normalised temperature as a function of pulse duration. The next step would be to plot the normalised temperature as a function of X/diffusion length, where X is a constant. One could then vary X until a fit is obtained with one of the curves in the set shown in Fig. 14. The value of X then corresponds to the depth below the surface while the thickness can be deduced by knowing with which curve the best fit was obtained. Although all this is based on a one dimensional model, the results are encouraging, and we are in the process of verifying this technique experimentally.

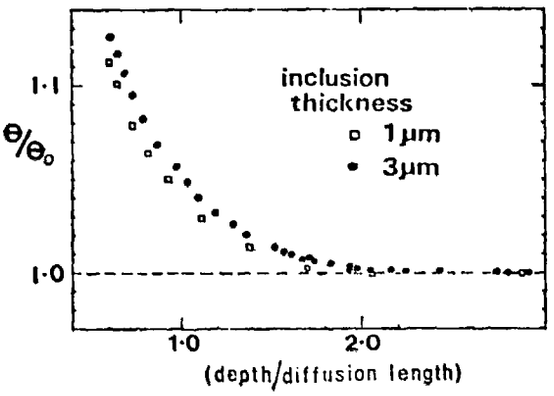

Fig. 14 Plot of Normalised Temperature vs Normalised Depth for Different Inclusion Thicknesses.

SUMMARY

A phase sensitive laser probe has been used to record the complex surface wave field with a sensitivity down to 10^{-4} Å. By recording the complex SAW field along three scan lines, it has been possible to deduce the scattered spectra from real and deliberate cracks. By reconstructing the scattered field, it is possible to locate the defect with an accuracy which is only limited by diffraction.

Recent work on gas acoustic microscopy has been described, and we have indicated that it should be possible to achieve a resolution below 200 nm using gases such as Argon and Xenon at 40 bar. By going to higher pressures (around 250 bar) it should be possible to achieve resolutions well below 100 nm.

Finally we have presented our initial work on photoacoustic microscopy. The system used is a scanned gas photoacoustic cell, together with pulsed laser excitation. A finite difference approach has been used in order to study the effect of an inclusion buried under the surface on the photoacoustic signal. In the case where the thermal properties of the inclusion are known apriori, our one dimensional model indicates that it should be possible to obtain not only the depth

of the inclusion beneath the surface but also its thickness.

REFERENCES

1. Kino, G.S.: "Non-destructive Evaluation", Science, 206, 12 October 1979, pp. 173-180.

2. Tittmann, B.R., Buck, O., Ahlberg, L., Billy, M. de., Cohen-Tenoudji, F., Jungman, A and Quentin, G.: "Surface Wave Scattering from Elliptical Cracks for Failure Prediction", J. Appl. Phys., 51 (1), January 1980, pp. 142-150.

3. Tittmann, B.R., Cohen-Tenoudji, F., Billy, M. de., Jungman, A and Quentin, G.: "A simple Approach to Estimate the Size of Small Surface Cracks with the use of Acoustic Surface Waves", Appl. Phys. Lttrs., 33 (1), 1 July 1978, pp. 6-8.

4. Khuri-Yakub, B.T and Kino, G.S.: "A High Frequency Technique for Surface Flaw Detection in Ceramics", Proc. 1977 Ultrasonics Symp., pp. 53-55.

5. Cuozzo, F.C., Cambiaggio, E.L., Damiano, J.P and Rivier, E.: "Influence of Elastic Properties on Rayleigh Wave Scattering by Normal Discontinuities", IEEE Trans. on Sonics and Ultrasonics, SU-24 (4), July 1977, pp. 280-289.

6. Domarkes, V., Khuri-Yakub, B.T and Kino, G.S.: "Length and Depth Resonances of Surface Cracks and their Use for Crack Size Estimation", Appl. Phys. Ltirs, 33 (7), 1 October 1978, pp. 557-559.

7. Quate, C.F., Atalar, A and Wickramasinghe, H. K.: "Acoustic Microscopy with Mechanical Scanning - A Review", Proc. IEEE, 67 (8), August 1979, pp. 1092-1114.

8. Ameri, S., Ash, E.A., Htoo, U., Murray, D and Wickramasinghe, H.K.: "Laser Detection and Imaging Techniques for Surface Examination", Proc. of ARPA Conference on Review of Progress in Quantitative NDE, July 1979, San Diego, California, (in press).

9. Murray, D.K and Ash, E.A.: "Precision Measurement of SAW Velocities", Proc. 1977 Ultrasonics Symp, pp. 823-826.

10. Buck, O., Morris, W.L and Richardson, J.M.: "Acoustic Harmonic Generation at Unbonded Interfaces and Fatigue Cracks", Appl. Phys. Lttrs, 33 (5), 1 September 1978, pp. 371-373.

11. Wickramasinghe, H.K and Ash, E.A.: "Optical Probing of Acoustic Surface Waves - Application to Device Diagnostics and to Non-Destructive Testing", Proc. of MRI Symp. on Optical and Acoustical Micro-Electronics, Polytechnic Inst. of New York, April 1974, pp. 413-431.

12. Jipson, V and Quate, C.F.: "Acoustic Microscopy at Optical Wavelengths", Appl. Phys. Lttrs, 32, 15 June 1978, pp. 789-791.

13. Rugar, D., Heiserman, J., Minden, S and Quate, C.F.: "Acoustic Micrographs of Human Metaphase Chromosomes", Science (to be published).

14. Heiserman, J.: Private Communication.

15. Wickramasinghe, H.K.: "Improved Scanning Acoustic Microscope", UK Patent Application No. 79 18101.

16. Petts, C.R and Wickramasinghe, H.K.: "Acoustic Microscopy in Gases", Electronics Lttrs, 16 (1), 3 January 1980, pp. 9-11.

17. Wickramasinghe, H.K and Petts, C.R.: "Gas Medium Acoustic Microscopy", to be presented at the International Symposium on 'Scanned Image Microscopy', Royal Society, London.

18. Wickramasinghe, H.K., Bray, R.C., Jipson, V., Quate, C.F and Salcedo, J.R.: "Photoacoustics on a Microscopic Scale", Appl. Phys. Lttrs., 33 (11), 1 December 1978, p. 923.

19. Luukkala, M and Penttinen, A.: "Photoacoustic Microscope", Electronics Lttrs, 15, 1979, pp. 325-326.

20. Busse, G.: "Subsurface Imaging with Photoacoustics", Appl. Phys. Lttrs., 36 (10), 15 May 1980, p. 815.

21. Rosencwaig and Busse, G.: "High-Resolution Photoacoustic Thermal-Wave Microscopy", Appl. Phys. Lett., 36 (9), 1 May 1980, p.725.

22. Busse, G.: "Optoacoustic phase angle measurement by probing a metal", Appl. Phys. Lttrs., 35 (10), 15 November 1979, p. 759.

23. Luukkala, M and Askerov, S.G.: "Detection of Plastic Deformation in Metals with Photoacoustic Microscope", Electronics Lttrs, 16, 3, 31 January 1980, p. 84.

24. Wong, Y.H., Thomas, R.L and Hawkins, G.F.: "Surface and Subsurface Structure of Solids by Laser Photoacoustic Spectroscopy", Appl. Phys. Lttrs., 32 (4), 1 May 1978, p. 538.

25. Petts, C.R and Wickramasinghe, H.K.: To be published.

SUMMARY DISCUSSION

Gordon Kino, Chairman (Stanford University): Time for one or two questions.

Unidentified Speaker: What's your sensitivity for your inclusions?: How small an inclusion?

Kumar Wickramasinghe (University College London): A sensitivity of (inaudible).

Christian Burger (Iowa State University): Do I understand your thermal analysis right? You're hitting the specimen with the laser and then you were measuring the maximum temperature at the spot where you hit it?

Kumar Wickramasinghe: Yes

Christian Burger: How did you measure that?

Kumar Wickramasinghe: The maximum temperature phototransducer signal proportion, not temperature.

Christian Burger: To the maximum temperature.

Gordon Kino, Chairman: If there are no more questions, thank you.

A REAL-TIME SYNTHETIC APERTURE DIGITAL ACOUSTIC IMAGING SYSTEM

S. Bennett, D. K. Peterson, D. Corl, and G. S. Kino
Edward L. Ginzton Laboratory
Stanford University
Stanford, California 94305

ABSTRACT

We report progress with the development of a real-time, 32 element, synthetic aperture acoustic imaging system. Construction and testing of the system hardware is now complete, enabling us to acquire raw acoustic data and focus and display it with a frame rate of 30 Hz .

Performance of the system is currently being assessed. Images of wire targets indicate that the resolution is as predicted by simple theory. The main thrust of our current effort is two-fold: we aim to use the system to examine "real" defects with acoustic surface waves and longitudinal waves, but at the same time improved understanding is needed to interpret the images obtained from more complex object fields. To this end, we are developing both theoretical and computer models for objects such as point targets, plane specular reflectors, and cylindrical inclusions. The results obtained from these models can be compared directly with images generated by the real-time system. It is likely that these results are common to other synthetic aperture systems and to any high frequency inversion process. The effects of nonlinear processing are also examined.

INTRODUCTION

In this paper, we report progress in the development of our real-time synthetic aperture digital acoustic imaging system. Earlier stages of development, which we have described, include an 8-element real-time system,[1,2,3] a 32-element computer-implemented system,[1,2,3,4] and finally a 32-element real-time system.[5] Here we present recent results obtained with the 32-element real-time system.

The operation of the imaging system (see Fig. 1) may be summarized as follows: the device employs a multiplexer to address each element of a piezoelectric transducer array. In turn, a short pulse (typically 2.5 cycles long between 20 dB points), with a center frequency of 3 - 3.5 MHz , is transmitted from the addressed element, and return echoes to the same element are digitized and stored in a 1024 x 8 bit RAM. This process is repeated for each of the 32 elements in the array. A focused image is formed by applying the appropriate delays to each of the digitized time records and then summing the contributions from each element. The delays necessary for focusing the image are stored in a "focus map" also held in the RAM. The focused data is then used to intensity modulate a display tube as the reconstruction takes place. When a complete image has been displayed, the cycle begins again at the data acquisition stage. New data is collected, focused, and displayed at the rate of approximately 30 frames per second.

A software package has also recently been developed which generates simulated echo data for simple objects (point and planar reflectors). This simulated data can be sent to the imaging system, quickly focused (1/30th of a second), then sent back to the computer for further manipulation and display. In this way we can compare images of simulated objects with real images of the same objects.

In the second section, we compare the images derived from simulated data with those obtained from real targets. We have also explored the effects of nonlinear processing on our acoustic images. The second and third sections present comparisons between linearly and nonlinearly processed images. The real-time system has been used to image a number of test objects and specimens with real defects. In the third section, we present images acquired with three different transducers: longitudinal waves in water, surface waves on metal, and longitudinal waves in metal.

IMAGING PERFORMANCE

In this section we compare real-time images with their simulated analogs. Two types of objects are considered here: single point reflectors and two closely spaced point reflectors.

The simulation of point reflectors employs a very simple model. The point reflector is assumed to be a perfect reflector with an omni-directional reflection pattern. Diffraction losses are ignored. In essence, the acoustic pulse received is just a replica of the transmitted acoustic pulse, with a time delay equivalent to the transit time from the transducer element to the point reflector and back.

For the purposes of simulation, the 32-element transducer array is modeled as 32 equally spaced elements (.5 mm center-to-center) with identical cosine-carrier Gaussian-envelope pulses (3.3 MHz center frequency, 2.5 cycles between 20 dB points).

The first test object chosen for comparison was a point reflector, on axis at 80 mm range in water. To obtain experimental data for this object, we used a .25 mm (.5 λ , where λ is the acoustic wavelength of the center frequency of the pulse) diameter wire. The image obtained from the simulated data is shown in Fig. 2. The corresponding image obtained from real data is shown in Fig. 3. The images are presented in four different formats:

(1) a photograph of the display screen. "Tic" marks on all photographs represent 10 mm ;

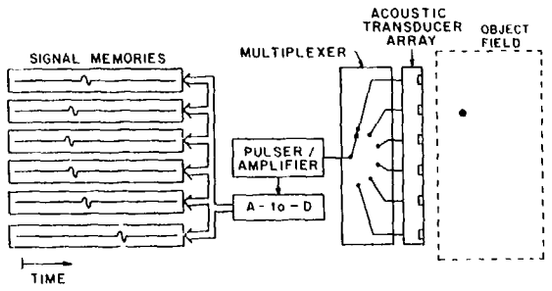

A

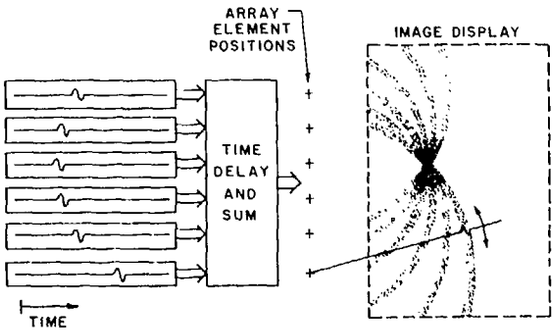

B

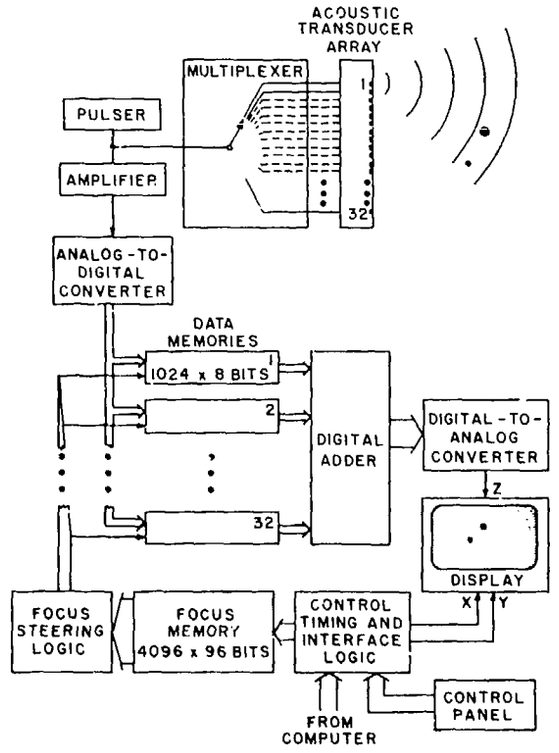

C

Figure 1. System schematic: (a) data collection configuration; (b) image reconstruction process; (c) electronics block diagram.

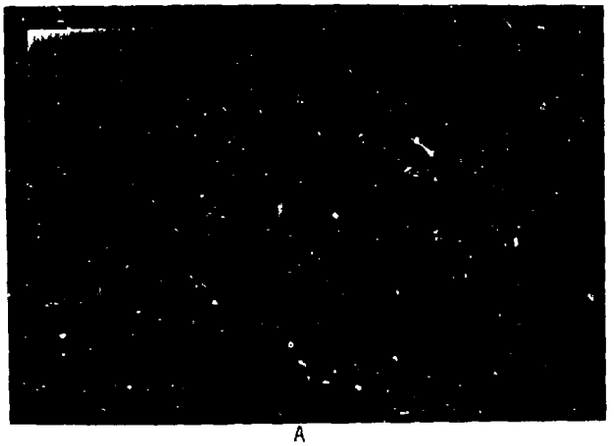

A

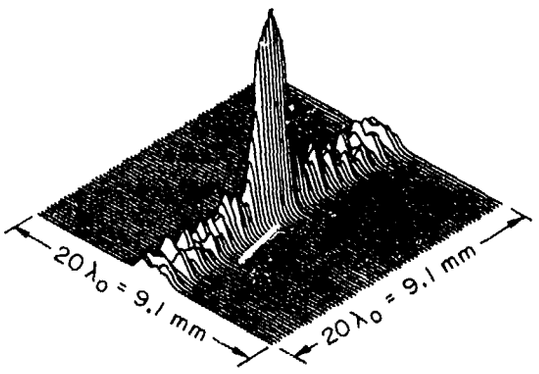

B

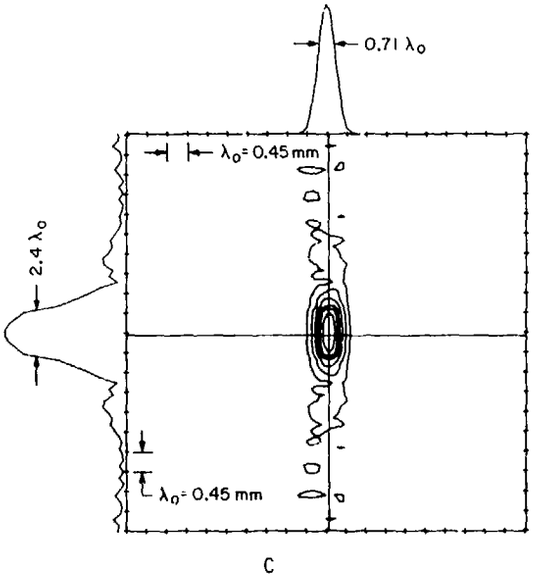

C

Figure 2. Image of point reflector reconstructed from simulated data: (a) photo of video display; (b) three-dimensional plot of 20λ x 20λ area surrounding the reflector; (c) contour diagram and cross-section plots.

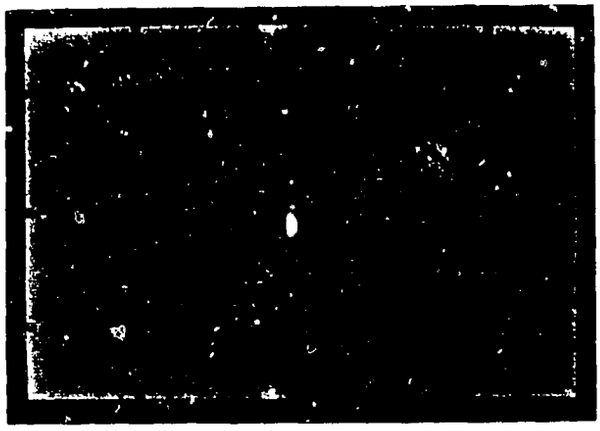

A

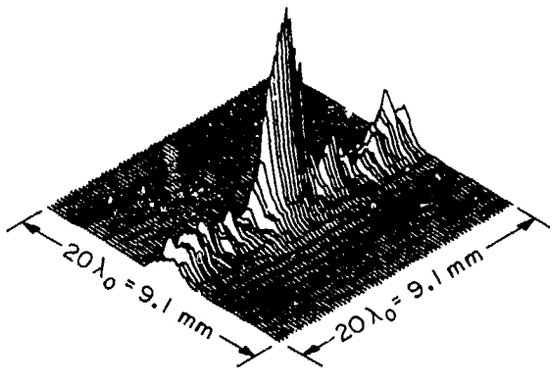

B

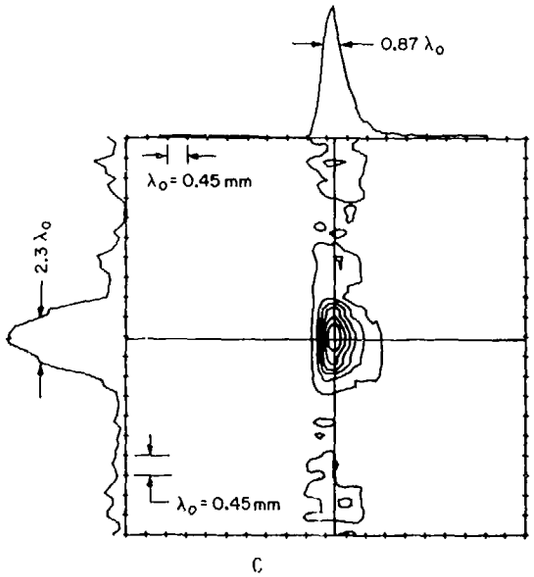

C

Figure 3. Image of thin wire (.25 mm diameter) at 80 mm range: (a) photo; (b) three-dimensional plot of 20λ x 20λ area surrounding the reflector; (c) contour diagram and cross-section plots.

(2) a "3-dimensional" plot of a selected portion of the image, 20 λ x 20 λ (9.1 mm x 9.1 mm);
(3) a contour plot of the same portion shown in the "3-D" plot. "Tic" marks on the axes represent λ = .45 mm . Contour levels are at .85 , .70 , .55 , .40 , .25 , and .10 of the maximum height;
(4) horizontal and vertical cross-sections through the contour plot. The plane of intersection for the horizontal (or vertical) cross-section is indicated by the horizontal (or vertical) line in the contour plot. The corresponding cross-sections are plotted along the horizontal (or vertical) axis.

For ease of comparison, all graphs were normalized before plotting. Image data is envelope detected (absolute value followed by low-pass filter) before displaying.

For this imaging experiment, the range of the target was 80 mm , and the imaging aperture was 16 mm . For conventional optics, this would be an f/5 system. However, since we use round trip delays, instead of one way delays for focusing, we effectively halve the f/number of the imaging system. Thus, the above experiments use an imaging system which has an effective f-number of F/2.5 , where F = f/2 is the effective f/number. To first approximation, the range resolution is determined by the pulse length, and the lateral resolution is determined by the imaging wavelength and f-number . Paraxial, cw optics predicts a lateral resolution of about Fλ . The range resolutions indicated in Figs. 2 and 3 are comparable to λ (~.45 mm) . The lateral resolutions indicated in these same figures are comparable to Fλ (~1.1 mm) . The transducer array used for real data acquisition has two defective elements. These missing elements probably lead to slightly higher sidelobe levels and asymmetrical distribution of sidelobes around the main lobe.[6]

A nonlinear processing scheme has been used to reduce sidelobe levels. The particular nonlinear algorithm we have chosen works as follows:

(1) record the acoustic echo data in real-time;
(2) read this data out to the computer;
(3) "compress" the data by taking the square root of each sample;
(4) write this "compressed" data back into the imaging hardware;
(5) focus the data in real-time (in the usual manner);
(6) read this focused data into the computer; and
(7) "expand" the focused data by squaring each picture element.

We are developing nonlinear amplifiers which will allow us to perform this processing in real-time.

The potential benefits of nonlinear processing have been described elsewhere.[1,2,3] The concept may be illustrated through a simple example. Suppose the return echo from a point target to each of the elements is of amplitude A . After reconstruction, the amplitude of the main lobe will be NA (N = number of elements in the array). The amplitude of the "far-out" sidelobes will be A . Thus, conventional linear processing yields a main lobe to far-out sidelobe ratio of N:1 (30 dB for a perfect 32-element system). With nonlinear processing, the main lobe level is boosted to AN^2

while the far-out sidelobes remain at amplitude A. In this way, nonlinear processing should yield a main lobe to far-out sidelobe ratio of N^2:1 (60 dB for a perfect 32-element imaging system). Nonlinear processing should, for the same reasons, suppress the "near-in" sidelobes (those sidelobes close to the main lobe).

Figure 4 shows the simulated data reconstructed using nonlinear processing (square root compression/square expansion). Figure 5 shows real data reconstructed using the same nonlinear algorithm. The advantage of nonlinear processing is apparent here. For the simulated data, the first sidelobes ("near-in" sidelobes) have dropped from -14 dB for linear processing down to -25 dB for nonlinear processing. A similar, but not quite so dramatic, reduction in sidelobe levels is obtained using real data from the wire target. At present, we sample the echoes at a 10.5 MHz rate. This gives only 3 samples per wavelength. Using a small number of samples per wavelength reduces the amplitude of the main lobe.

The range and lateral resolutions of real images are comparable to those of the simulated images, being approximately λ and $F\lambda$, respectively. Nonlinear processing provides a marked decrease in sidelobe level without any deterioration of the single point resolution. We will show later that nonlinear processing sometimes introduces undesirable artifacts.

Figure 6 shows an image reconstructed from simulation of two point targets at a range of 80 mm, laterally separated by 2 mm. Figure 7 shows an image of two small wires (.25 mm diameter) separated by 2 mm. The two objects are resolvable for both simulated and real echo data. The image of real data has a small bump on axis, behind the two wires. We believe this is due to a mode converted echo which returns later than the front face reflection. Such delayed echoes are also observed for single, thicker (1.25 mm diameter) wire targets. Alternatively, this delayed echo may be due to a scattering interaction between the two wires.

REAL TIME IMAGING APPLICATIONS

In this section we present a series of images demonstrating the performance of the imaging system in a variety of practical situations. Images made with three different types of arrays are shown: longitudinal waves in water,[7,8] surface waves on aluminum using an edge-bonded array,[9] and longitudinal waves in aluminum using a new direct contact array. The latter array represents an important extension to the imaging system for NDE applications, since it is either inconvenient or impractical to provide a water buffer between the transducer and the test specimen. A similar contacting shear wave transducer array is currently being developed.

Figure 8 demonstrates the ability of the system to distinguish small targets close to a large specular reflector. The benefits of nonlinear processing are clear.

The next images (Fig. 9) were obtained using an edge-bonded surface wave array. The surface waves are coupled to the test specimen by means of a polyethylene strip and a thin smear of liquid

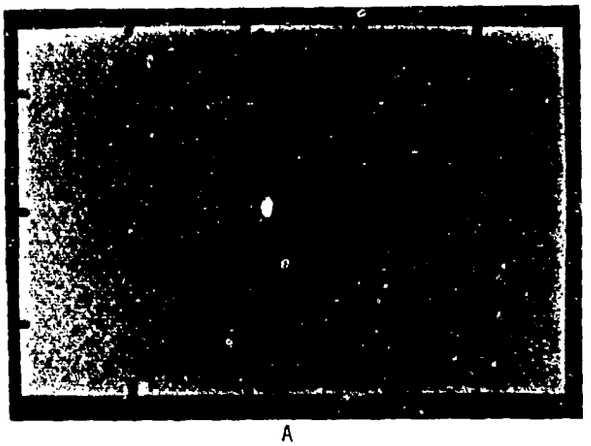

A

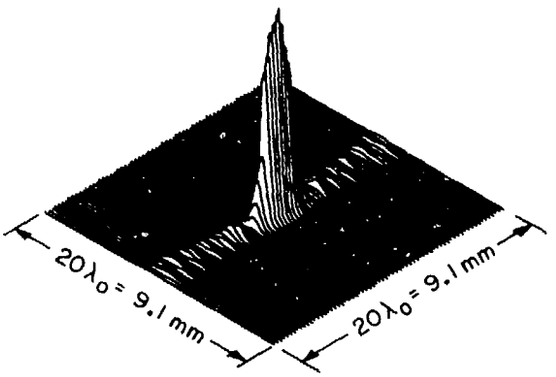

B

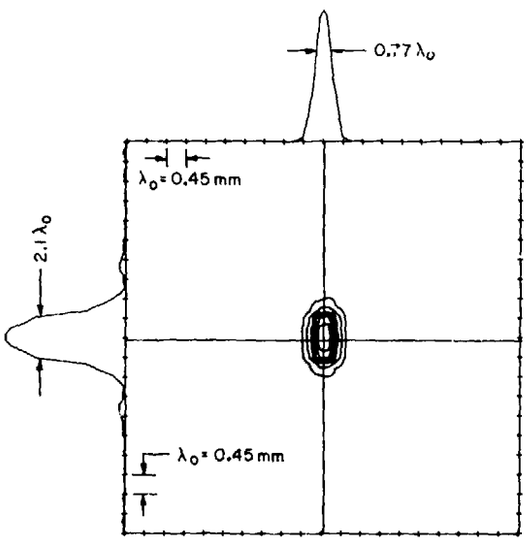

C

Figure 4. Simulated echo data (same as used in Fig. 2) reconstructed using square root/square non-linear processing: (a) photo of display; (b) three-dimensional plot of $20\lambda \times 20\lambda$ area surrounding the reflector; (c) contour diagram and cross-section plots.

A

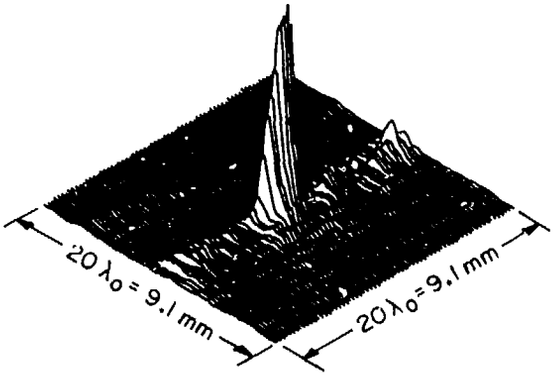

B

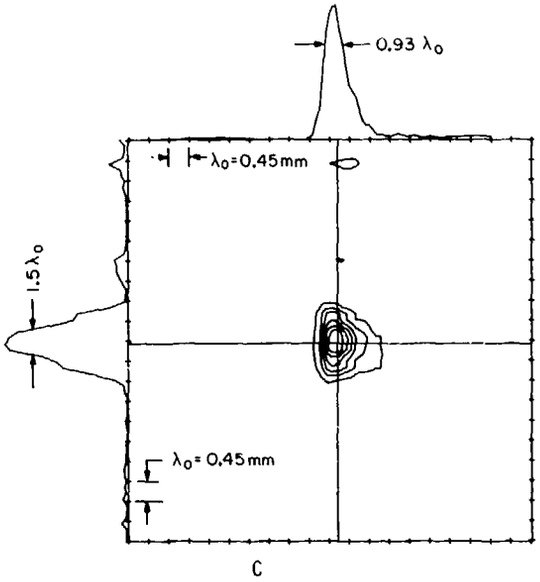

C

Figure 5. Experimental echo data (same as in Fig. 3) reconstructed using square root/square non-linear processing: (a) photo of display; (b) three-dimensional plot of 20λ x 20λ area surrounding the reflector; (c) contour diagram and cross-section plots.

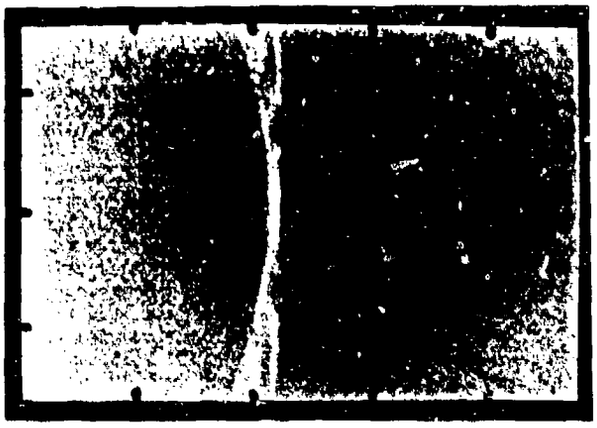

A

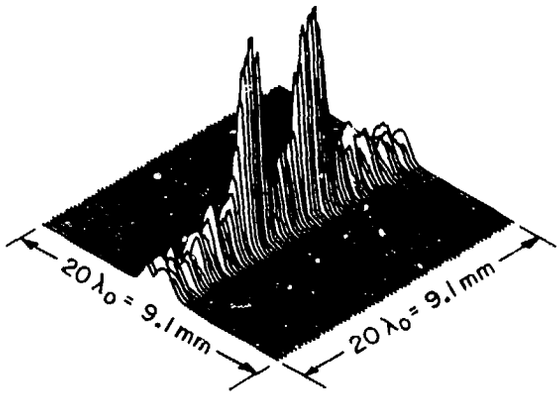

B

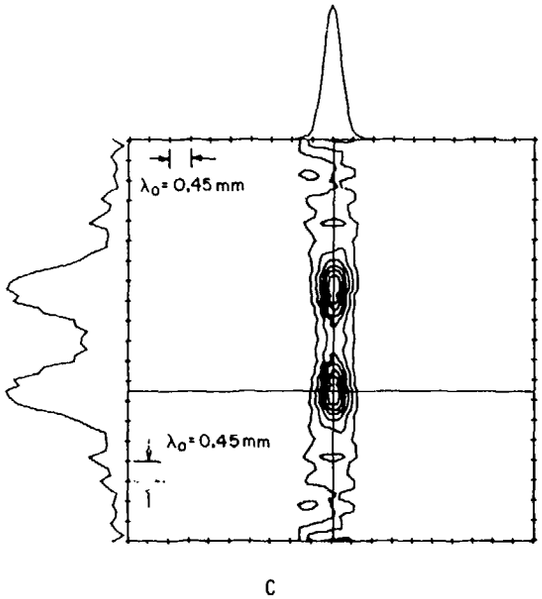

C

Figure 6. Image of two point reflectors separated by 2 mm reconstructed from simulated data: (a) plots of display; (b) three-dimensional plot of 20λ x 20λ area surrounding reflectors; (c) contour diagram and cross-section plots.

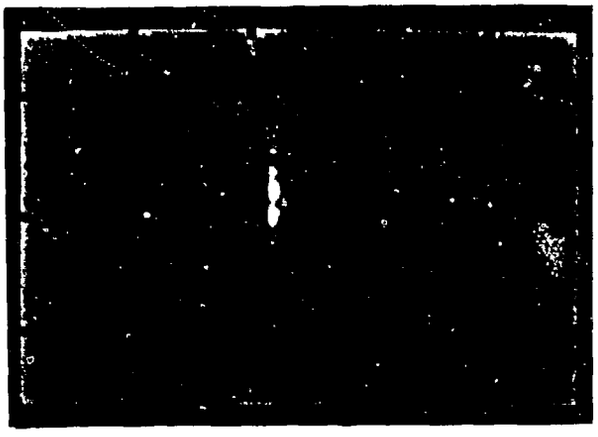

A

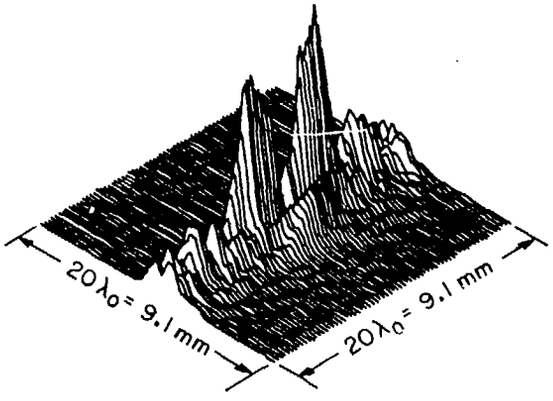

B

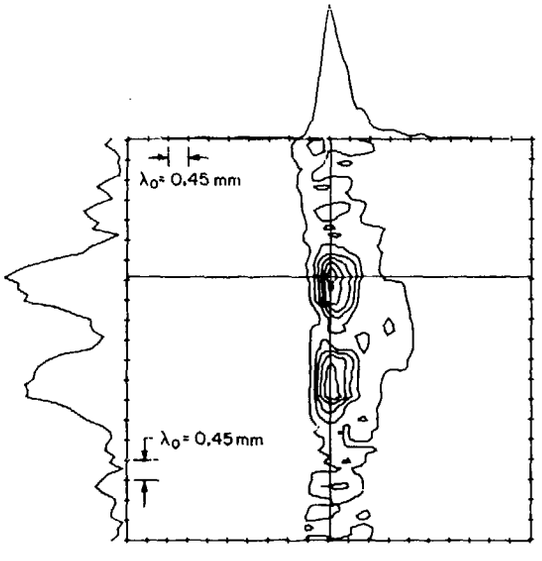

C

Figure 7. Image of two thin wires (.25 mm diameter) laterally separated by 2 mm at 80 mm range: (a) photo of display; (b) three-dimensional plot of 20λ x 20λ area surrounding reflectors; (c) contour diagram and cross-section plots.

couplant (Sonotrac). The acoustic images clearly show the three saw cuts, the corner of the block, and ghost images of the saw cuts reflected in the corner of the block. It is also just possible to discern two short bars, one in the upper left corner and the other along the bottom edge of the image. These correspond to the two edges of the block, indicating that the angular acceptance of the array is at least $\pm 45°$. The value of nonlinear processing in reducing sidelobe levels is apparent in the nonlinear image of Fig. 9.

A further example of surface wave imaging is shown in Fig. 10. Here the test specimen was an aluminum plate with two fatigue cracks, measuring 3 mm and 1 mm wide, with a width to depth ratio of about 2. The cracks are closed at the surface to within a few hundred Angstroms.

The images in Fig. 11 were taken with the new direct contact longitudinal wave array. The test specimen was an aluminum block with $1/16^{th}$ inch holes drilled in it. The placement of the array and the block for the two viewing directions is indicated in Fig. 11. The two linear real-time images are also shown in the figure. It should be emphasized that these images are the first that we have taken using this new type of array and therefore represent only preliminary results.

CONCLUSION

We have demonstrated, by comparison of simulated images with experimental images, that our real-time synthetic aperture acoustic imaging system is capable of diffraction limited performance at a frame rate of 30 Hz. The benefits of nonlinear processing in reducing sidelobe levels have been illustrated for simple objects.

We have imaged several complex objects, including real fatigue cracks. Here, too, the improvement in image quality gained by nonlinear processing is evident. It should be pointed out that the degree of improvement observed with point targets will not be seen for more complex objects. The images of Fig. 10 are a good example of the artifacts to be expected from nonlinear processing. With linear processing, the 3 mm fatigue crack is one continuous line; with nonlinear processing, the same crack might be interpreted as two point scatterers.

Our first images taken with the new direct contacting longitudinal wave array are encouraging. We plan to continue development of this technology. Future effort will also be directed toward a better understanding of the performance of the system in imaging specular reflectors at oblique angles and further exploration of the improvements afforded by nonlinear processing.

Acknowledgements

We wish to acknowledge the work of Alan Selfridge and Pierre Khuri-Yakub in developing the arrays used in this imaging system. This work was supported by the Air Force Office of Scientific Research under Contract No. F49620-79-C-0217.

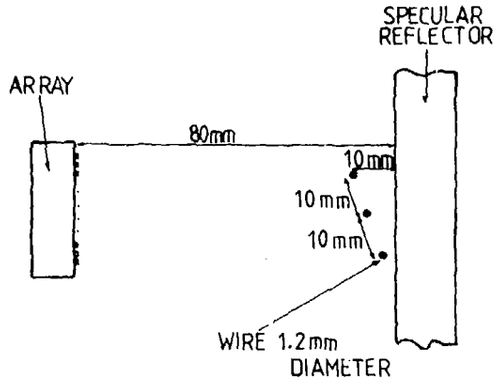

A

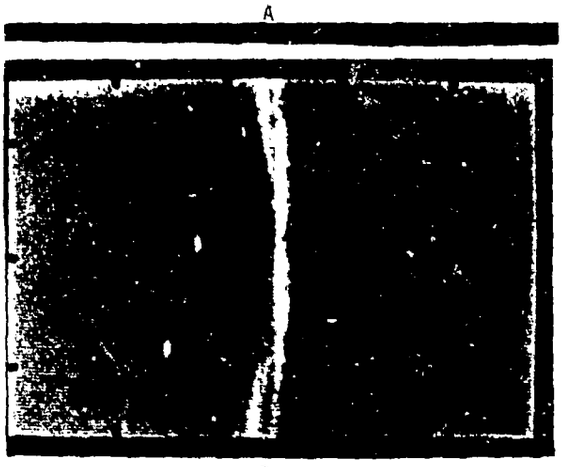

B

C

Figure 8. Image of three wires in front of a specular reflector: (a) schematic of object geometry; (b) real time image with linear processing; (c) image with non-linear processing.

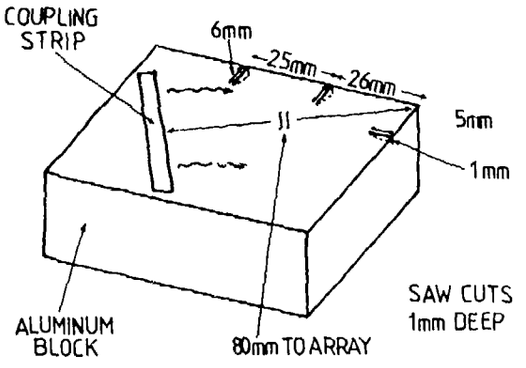

A

B

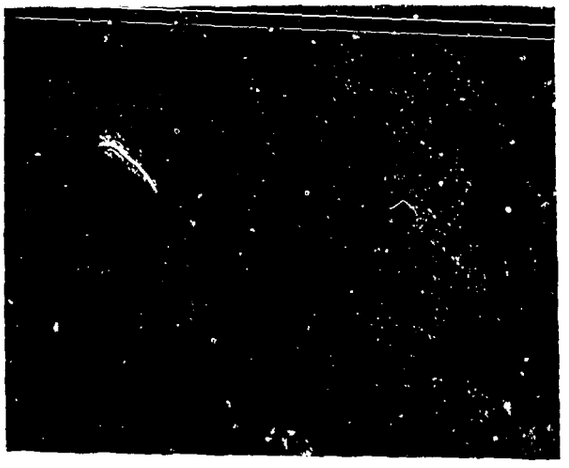

C

Figure 9. Surface acoustic wave images of a test block with three saw cuts along the edges: (a) schematic of object geometry; (b) real time image with linear processing; (c) image with non-linear processing.

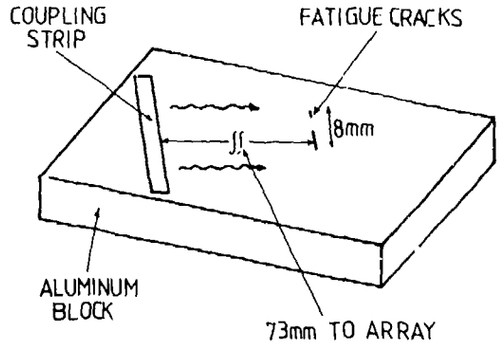

A

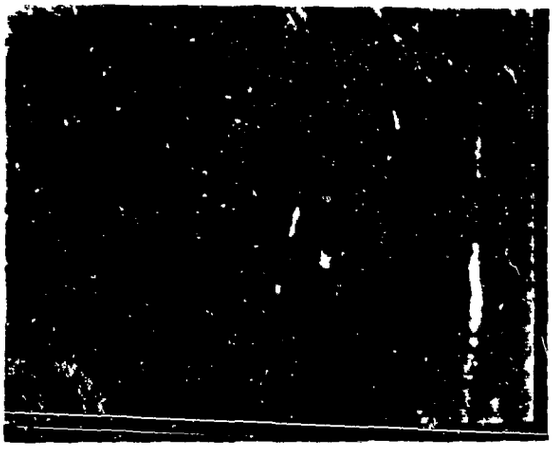

B

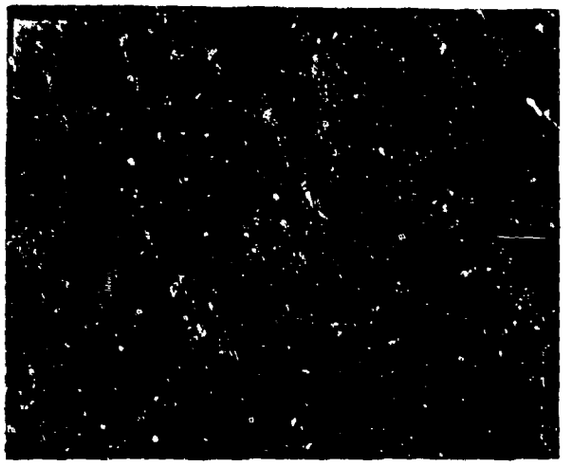

C

Figure 10. Surface acoustic wave images of fatigue cracks in aluminum sample: (a) schematic of object geometry; (b) real-time image with linear processing; (c) image with non-linear processing.

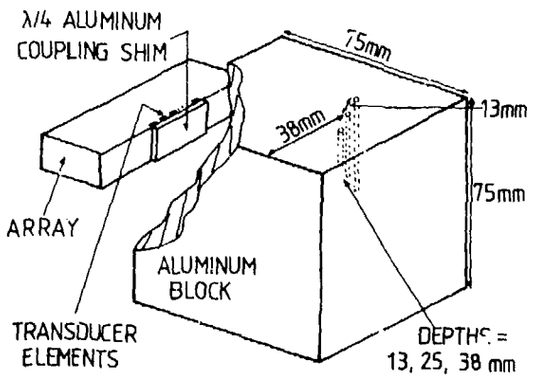

A

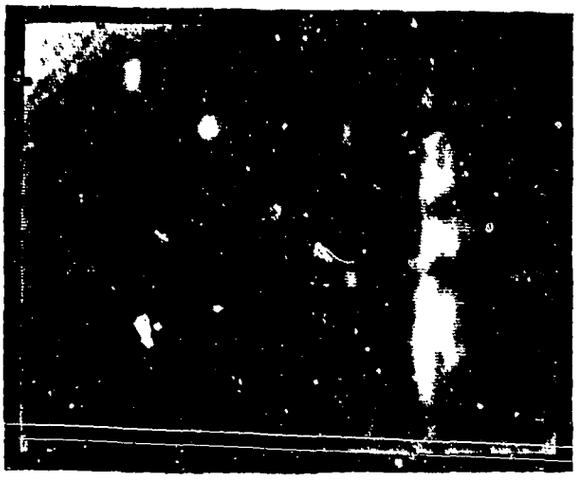

B

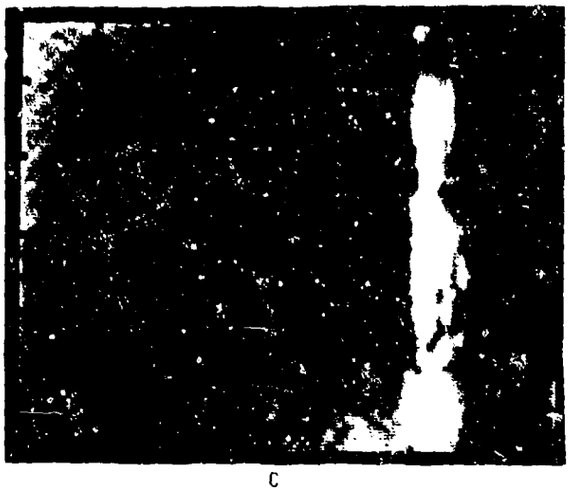

C

Figure 11. Image of three 1/16 inch drill holes in an aluminum block: (a) schematic of object geometry; (b) image with array as shown in (a); (c) image with array rotated 90° from previous position.

References

1. P.D. Corl, G.S. Kino, C.S. DeSilets, and P.M. Grant, "A Digital Synthetic Focus Acoustic Imaging System," Acoustical Holography, vol. 8, A.F. Metherell, ed., Plenum Press, New York, 1980.

2. G.S. Kino, P.M. Grant, P.D. Corl, and C.S. DeSilets, "Digital Synthetic Aperture Acoustic Imaging for NDE," Proc. ARPA/AFML Review of Progress in Quantitative NDE, La Jolla, California, July 1978.

3. P.D. Corl, P.M. Grant, and G.S. Kino, "A Digital Synthetic Focus Acoustic Imaging System for NDE," Proc. Ultrasonics Symposium, Cherry Hill, New Jersey, September 1978.

4. D. Corl, G.S. Kino, D. Behar, H. Olaisen, and P. Titchener, "Digital Synthetic Aperture Acoustic Imaging System," Proc. ARPA/AFML Review of Progress in Quantitative NDE, La Jolla, California, July 1979.

5. P.D. Corl and G.S. Kino, "A Real-Time Synthetic Aperture Imaging System," Acoustical Holography, vol. 9, K. Wang, ed. Plenum Press, New York, 1980.

6. J. Fraser, J. Havlice, G. Kino, W. Leung, H. Shaw, K. Toda, T. Waugh, D. Winslow, and L. Zitelli, "An Electronically Focused Two-Dimensional Acoustic Imaging System," Acoustical Holography, vol. 6, N. Booth, ed., Plenum Press, New York, 1975.

7. G.S. Kino and C.S. DeSilets, "Design of Slotted Transducer Arrays with Matched Backings," Ultrasonic Imaging, vol. 1, pp. 189-209, 1979.

8. G.S. Kino, B.T. Khuri-Yakub, A. Selfridge, and H. Tuan, "Development of Transducers for NDE," Proc. ARPA/AFML Review of Progress in Quantitative NDE, La Jolla, California, July 1979.

9. H.C. Tuan, A.R. Selfridge, J. Bowers, B.T. Khuri-Yakub, and G.S. Kino, "An Edge-Bonded Surface Acoustic Wave Transducer Array," Proc. Ultrasonics Symposium, New Orleans, Louisiana, September 1979.

ADVANCES IN COMPUTER RECONSTRUCTION OF ACOUSTICAL HOLOGRAPHY

V. Schmitz, R. Kiefer, G. Schäfer
Fraunhofer Institute für zerstörungsfreie Prüfverfahren
Saarbrücken, West Germany

ABSTRACT

The article describes the results of two methods: the Fresnel approximation and the convolution method used for the exact Rayleigh-Sommerfeld equation. Curves for the Fresnel approximation are shown as a function of flaw depth and number of sample points. Despite a violation of the fresnel condition, an image can be achieved without visible phase distortion. This and its limits are shown on synthetic and experimental data. By shifting the hologram and not changing the symmetric phase factor, calculation time is saved because the rearrangement in the image space is achieved automatically. The exact method "angular spectrum" has been simplified in three steps. For different insonification angles in shear wave holography, the data set must be multiplied by an aperture function before being Fourier transformed. Examples demonstrate the usefulness of contact technique probes. To improve the recording time, a 140 element array will be multiplexed electronically and moved mechanically.

INTRODUCTION

Image formation in holography can be achieved optically and numerically (Ref. 1). The numerical reconstruction has several advantages versus optical reconstruction: objectivity, reproducibility and free scaling image enhancement. Some shortcomings are: high costs and long reconstruction time with conventional data processing. We will describe here basic developments in performing the calculations on a PDP 11/34 computer, our experiences with the implementation of the Fresnel approximation and the angular spectrum method and show the direction for implementing a fast recording and reconstruction system.

FRESNEL RECONSTRUCTION

A measure for the quality of an acoustic image is the resolution achieved in the image space. In addition, the effect of phase errors introduced by the paraxial approximation or by the expansion of the phase factor have to be carefully investigated. Figure 1 shows a two-dimensional Fresnel reconstruction of flat bottom holes at a depth of 100 mm in steel. The pattern in the center consists of 3 mm holes with edge-to-edge separations down to 1 mm, corresponding to 2.2 wavelengths at 2.66 MHz frequency. A resolution of better than 2 mm at this great depth could easily be achieved. The outer circle demonstrates the sensitivity for the Fresnel reconstruction. The smallest dot corresponds to a 3 mm hole, the largest one to a 10 mm hole.

To investigate the effect of different degrees of violation of the Fresnel conditions I and II (Fig. 2), we used synthetic data and varied the flaw depths z between 60 mm and 200 mm and increased finally the frequency, so that the ultrasonic wavelength decreased from 3 mm to 0.5 mm. Figure 2 shows the phase disturbances when the flaw depth varies. In case No. 1, despite "8" being less than "156", the reconstruction is correct. In cases No. 2 to 6, the error in the square root expansion gets more and more severe and results finally in severe phase distortions. To get a more quantitative description, Fig. 3 shows the Fresnel conditions for three different longitudinal and shear wave wavelengths. If the actual data lie

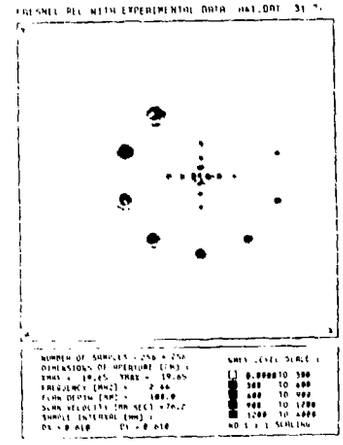

Fig. 1 Fresnel reconstruction, 256 x 256 samples, flaw depth - 100 mm; frequency - 2.6 MHz.

Fresnel-conditions:

I: $z > L_F + L_H$

II: $z^3 > \frac{\pi}{4\cdot\lambda}(L_F+L_H)^4$

$\Delta x_B = \frac{\lambda z}{N \Delta x}$

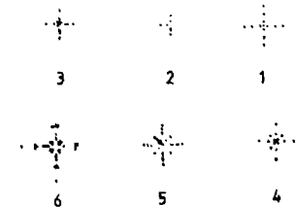

No.	z mm	λ mm	$L_F + L_H$ mm	$z^3 \cdot 10^6$	Right Side II.	I.	II.
1	200	0.5	100	8	156	Yes	No
2	200	3	102	8	28	Yes	No
3	150	3	100	2.2	26	Yes	No
4	120	3	100	1.4	26	Yes	No
5	100	3	97	1.0	23	No	No
6	60	3	101	0.2	27	No	No

Fig. 2 Effect of Violation of the Fresnel conditions.

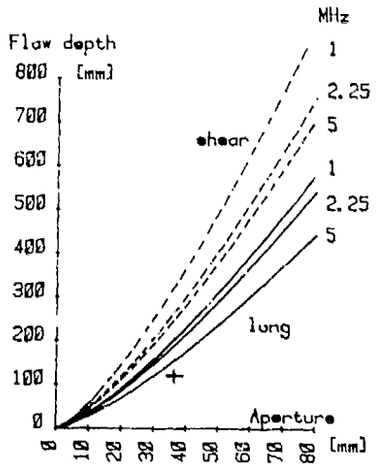

Fig. 3 Validity of Fresnel approximation: region above the curves.

above the curve, the phase distortions can be neglected. If they lie below the curve, there is a large possibility that the result will be correct. This demonstrates clearly that the Fresnel conditions are only a sufficient criterion. Figure 4 shows a correct reconstruction of a Y-shaped flaw in 120 mm depth, where the Fresnel approximation, marked by "+", is slightly violated. The image resolution is about 1.4 mm.

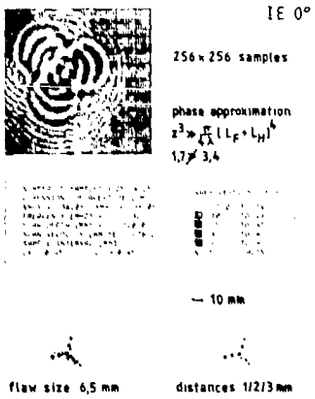

Fig. 4 Fresnel reconstruction with an experimental data set.

In Fresnel reconstruction, the holographic data are multiplied by an exponential function and then Fourier transformed. The integral has to be converted to a discrete Fourier series in order to calculate the FFT in the computer. The substitution, $x' - L_H = x''$, shifts the aperture L_H into the positive domain and the quadratic phase factor is shifted too. To get a nondistorted picture in the image space, we have to exchange the data set $(0, \pi/T)$ with the data set $(\pi T, 2\pi/T)$. This requires additional calculation time. If we shift the hologram by L_H and do not change the symmetric phase factor (Ref. 2), this is done automatically. One additional effect is the shift of the image by the amount of $2\,L_H/\lambda z_{12}$ (Fig. 5).

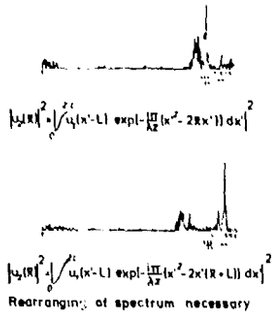

Fig. 5 Fresnel reconstruction with symmetric and asymmetric phase factor.

ANGULAR SPECTRUM METHOD

The interpretation of the Rayleigh-Sommerfeld equation in the form of a convolution leads to an exact solution. But instead of one fast Fourier transformation, we have to perform three FFT's. We will show now that it is possible to use fewer sample points and to decrease the calculation time. The improvement is shown with the aid of a data set of 128 x 128 sample points and longitudinal waves. In the last step, this method , adapted to 45° shear waves.

Figure 6 shows the reconstruction with the angular spectrum method by a computer simulation. At the top, the real part and imaginary part of the exponential function can be seen; in the middle, the real part and the imaginary part of the synthesized holographic data are seen and at the bottom, the intensity distribution in the image space, which reproduces the image of point-like flaws with edge-to-edge separation of 1 mm to 6 mm can be seen.

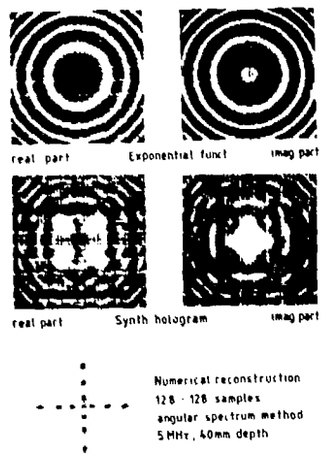

Fig. 6 Angular Spectrum Method with synthetic holographic data set.

For the development of the convolution, we used experimental values of flaws at a depth of 120 mm, with an ultrasonic frequency of 2.32 MHz. The conventional use of the convolution needs a "fill up" by zeros, so if the data set is limited to 128 x 128, only 64 x 64 data can be used for experimental data. This restricts the aperture. Figure 7 shows the data set together with the exponential function and its Fourier transform. Because the exponential function has to be truncated very early, its amplitude has not yet diminished sufficiently. This causes ripples in the Fourier domain and hence phase distortions in the image domain. Nevertheless, the image reconstruction in the figure below agrees very well with the flat bottom holes.

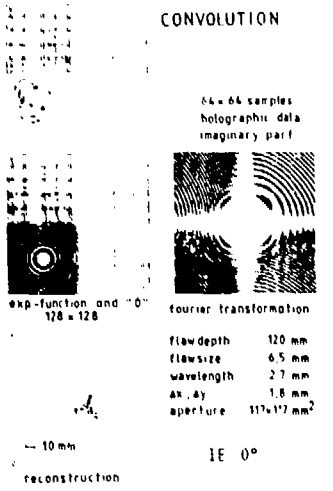

Fig. 7 Angular Spectrum Method filled up by zeroes computer FFT of the exponential function.

This phase error can be avoided by using the Fourier transform of the exponential function taken from -infinity to +infinity. The analytically transformed function extends from $-\infty$ to $+\infty$ too. This function is now shifted in such a manner that the low frequencies lie in the lower left corner. Then this data set is mirrored into the other three quadrants. After multiplication, with the transformed data set, the inverse transform produces the image shown at the bottom of Fig. 8. A comparison in the frequency content of the hologram at the top and the propagation function in the middle shows that only three fringes of the propagation function contribute to the image. Higher frequencies are eliminated by the evanescing hologram transform amplitudes. The sample rate can now be adapted to the highest frequency content of the experimental data and not to the highest frequency of the propagation function in the middle of its aperture. This results in an increase in the investigated material volume, while keeping the computer calculation time and computer memory size constant.

The mirroring of the transformed propagation function into the other three quadrants is the prerequisite for the last step of the development, the use of 128 x 128 experimental values instead of 64 x 64 and adding zeroes to fill up the 128 x 128 data. The software for performing these calculations will run within 40 minutes on a PDP11/50

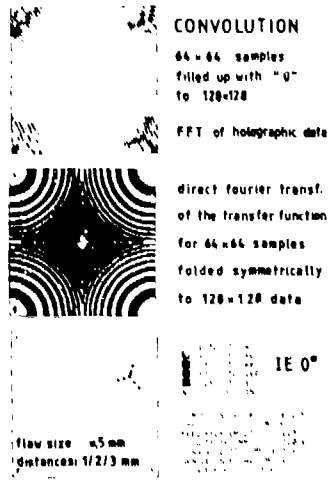

Fig. 8 Angular Spectrum Method, filled up by zeroes, direct calculation of the exponential function and its mirror pictures in the frequency domain.

computer or within five minutes on a VAX. The results are shown in Fig. 9, with two different grey level scales and shows an excellent agreement with the true flaw dimensions.

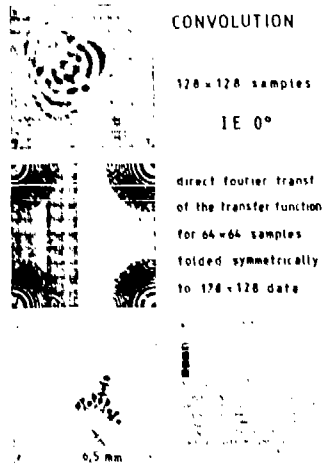

Fig. 9 Angular Spectrum Method; use of the entire field for experimental data, direct calculation of the exponential function and its mirror pictures in the frequency domain.

In the above examples, we used vertical insonification with longitudinal waves. In the case of shear waves, the sound beam modulates the holographic data V(x,y). This means the spectrum is shifted to higher frequencies. By introducing an aperture function, b(x,y), the spectrum can be shifted back. The formalism for pulse echo with longitudinal, or with shear waves under arbitrary angles in x direction, is given by the following equation:

$$|u(x,y)|^2 = |F^{-}\{F^{+}[b(x,y)V(x,y)]\cdot \exp.\ [ikz\sqrt{1-\lambda^2(\xi^2+\eta^2)}]\}|^2 \quad (1)$$

with

$$b(x,y) = \exp.(i\frac{2\pi}{\lambda} x \sin\alpha) \quad (2)$$

In the case of pulse echo 0°, we have $\alpha = 0°$ and $b(x,0) = 1$.

This illumination function, b(x,y), has to be used only in the angular spectrum method. According to the shift theorem, it would only shift the image in the Fresnel approximation formalism. Fig. 10 shows the effect of the illumination function for a 45° shear wave. The information in the frequency domain on the right-hand side is shifted to the lower frequency domain and can now be multiplied by the propagation function to perform the necessary steps for the final Fourier back transformation.

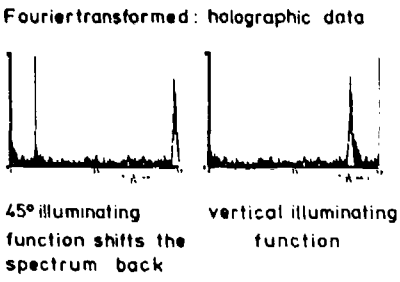

Fig. 10 Effect of the illumination function to correct the modulation by the shear wave insonification.

INSTRUMENTATION

The above formalism has been implemented on a PDP 11/34 computer. To improve the reconstruction time, a MAP 300 array processor will reduce the time between data recording and image presentation to about 60 seconds for a set of 128 x 128 sample points. Until now, a two dimensional scanner moved the probe in a square wave scan pattern. The scan time needed was about 180 seconds. This time can be reduced to about 56 seconds by the application of the electronic scheme shown in Fig. 11. Measurements of the sound field of an 140 element linear 2 MHz array showed amplitude variations of less than 1 dB. These elements will be multiplexed electronically, but eight elements will be switched together to obtain a sufficient signal/noise ratio.

Besides the data recording and reconstructing time, an easy to handle probe and probe holding device are very important. Figure 12 shows a 45°, 2.25 MHz probe in the contact technique with a water gap of about 1/2 mm. The probe is spring loaded against the wall and can follow its curvature. The same technique will be applied to the large 140 mm array or smaller arrays.

CONCLUSIONS

It has been shown that the resolution limit for shear or longitudinal waves is one wavelength

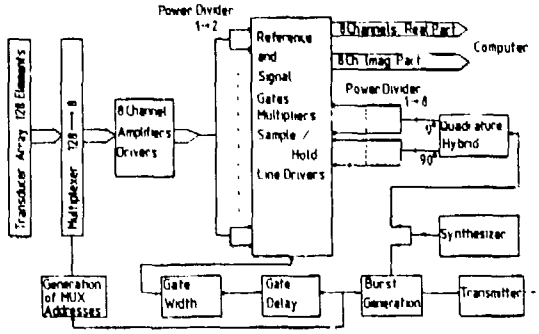

Fig. 11 Quasi-realtime holography.

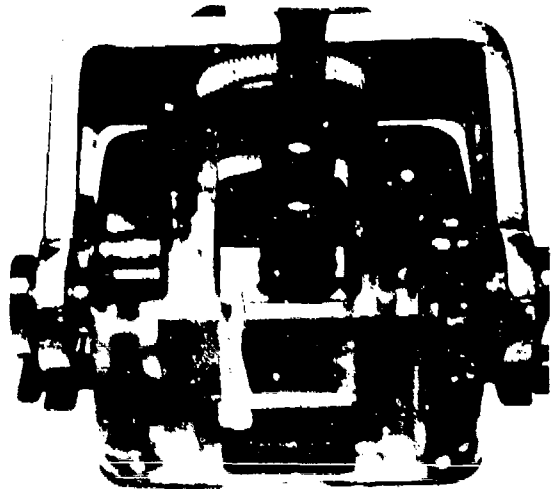

Fig. 12 2.25 Mhz shear wave probe in contact technique for holography.

and it could be achieved by both Fresnel reconstruction, as well as the exact angular spectrum method. Phase errors will cause artifacts if the Fresnel conditions are strongly violated. In most practial cases, as shown by comptuer simulation and corresponding experiments, small violations of the Fesnel condition are tolerable. A technique has been presented where time can be saved in calculating the Fresnel reconstruction because the rearranging in the spectrum is done automatically. Time and computer storage capacity has been saved in the angular spectrum method by calculating a shifted propagation function in the Fourier domain and mirroring it into the remaining three quadrants. In the case of shear waves, the sound beam modulates the holographic data. By multiplying the experimental data by an aperture function, a distortion-free holographic image is calculated. These formalisms have been implemented on a PDP 11/34 computer. Current work is directed towards reducing the data collecting time by multiplying a 140 element linear array.

ACKNOWLEDGMENTS

This work has been supported by the Federal Ministry of Research and Technology within the scope of reactor safety research programs. Many helpful discussions with Priv. Doz. K.J. Langenberg from the University of Saarbrücken are greatly acknowledged.

REFERENCES

1. V. Schmitz, and M. Wosnitza, "Experiences Using Ultrasonic Holography in Laboratory and in the Field with Optical and Numerical Reconstruction", Acoustic Imaging, Vol. 8, Metherell Plenum Publishing Corp., pp. 651-683.

2. K.J. Langenberg, R. Kiefer, M. Wosnitza and V. Schmitz, "Zur Numerischen Rekonstruktion von Ultraschall - Hologrammen," Intern. Symp. "New Methods of Nondestructive Testing of Materials and Their Application Especially in the Nuclear Industry", Saarbrücken, West Germany, September 17-19, 1979.

ACOUSTIC IMAGING BY WAVEFRONT RECONSTRUCTION

K. M. Lakin*, W. R. Sheppard**, and K. Tam**

University of Southern California
Los Angeles, California 90007

ABSTRACT

A reconstruction of the ultrasonic scattered fields in the zone near the scatter constitutes an image of the scatterer or flaw. In a real case the reconstruction zone may contain more than one distinct scatterer and accordingly the entire group form the image. At a remote location the scattered fields form a complicated diffraction pattern which will yield the image if operated on by a suitable set of mathematical operations. The measurement of the remote fields is of major interest as it affects the image quality. Unlike phased array systems, the transducer spacing, hence measurement sampling density, is determined by the spatial frequencies of the diffraction pattern and sampling theory. This paper will describe the implementation of a 64 x 64 2D array and the results obtained in imaging the phase and magnitude of source and scattered fields.

I. INTRODUCTION

Implementation of the coherent wavefront reconstruction imaging system discussed here involved the physical construction of a two dimensional transducer array and associated electronics. Last year we reported on the basic theory and detailed the 64 x 64 transducer array and multiplexer electronics (1). In the interim the receiver circuitry was improved in order to allow coherent phase sensitivity detection with I and Q channel pulse outputs proportional to the real and imaginary parts of the scattered tone burst waveform. Here we will briefly review the important features of the imaging system and then discuss the experimental results that have been obtained to date.

In the most general sense the imaging system is a means of sampling the spatial distribution of waves scattered from an object, Fig. 1. The basic assumption is that the nature of the object is indirectly revealed by the diffraction pattern and directly obtained by a suitable technique which reconstructs fields at the scatterer. The current form of reconstruction requires that the complex form of the scattered fields be measured and processed. Normally this would imply a CW system with a high degree of temporal coherence. However, a CW system would be unusable in a real NDE system because of standing wave effects.

The system being implemented is coherent to the extent that tone burst excitation is employed at frequencies of interest. The length of tone burst must be sufficient to assure complete illumination of the object region so that waves vectorially sum at the measurement plane. Upper bounds on pulse length are determined by stray signal paths and the desire for fast data through-put.

In a time domain echo system two objects might be resolved by using short pulses that require large bandwidths. In a coherent imaging system the spatial bandwidth of the scattered field and sampling system is used to obtain the desired resolution. Since tone burst waveforms are relatively narrow bandwidth, higher signal-to-noise ratios may be obtained using narrow bandwidth amplifiers and coherent detection schemes.

The finite spatial sampling of the scattered fields has some important implications regarding resolution and image quality. Since discrete Fourier transforms are employed in the small angle reconstruction, the image is necessarily periodic in the image plane (1,2), Figs. 1,2. The system resolution is given simply by,

$$\Delta x = \lambda \frac{R}{W}$$

or

$$= \frac{\lambda}{2} \frac{1}{\tan \theta}$$

where λ is the acoustic wavelength and θ the half angle, Fig. 2. Note in particular that the resolution is independent of sampling densities in the measurement plane. However, the image width is given by

$$F = R/\Delta U.$$

Thus coarse sampling gives rise to narrow image fields that may result in aliasing. In general, only the object region should be illuminated if other distortion or ghost effects are to be avoided. These effects may be largely eliminated by simple image processing techniques which increase image width and display resolution.

*Present Address: Ames Laboratory, Iowa State University, Ames, Iowa 50011.
**Present Address: Northrop Corporation, Aircraft Group, 3901 W. Broadway, Hawthorne, CA 90250

II. EXPERIMENTAL RESULTS

The coherent imaging technique has been tested with synthetic aperture data as well as with data taken from the 2D array. In the former case the data has higher signal-to-noise ratio, due to the more efficient transducer used for scanning, and does not have to be normalized. Here we report only on data that has been taken with the 2D array.

In using the 2D array it is necessary to first obtain a calibration matrix which is composed of individual transfer functions of the array elements. The transfer function, as used in this report, is obtained by transtating the array such that a given element is located a fixed distance away from a conventional transducer in a water tank and then recorded the complex wave signal. After each array element has been positioned and measured the transfer function matrix is normalized to the largest signal. A grey scale display of the magnitude and phase of a typical calibration matrix is shown in Figs. 3a,b. Since the 2D array was built as four separate sections the slight lack of parallism is apparent in the phase display. Note that the scan plane itself was not parallel to the transducer plane as indicated by the tilt in the phase characteristics. The slight tilt has no measurable influence on the amplitude of the transfer function.

In the amplitude part of the transfer function matrix it is clear that some array elements or multiplexing chips are inoperative. Isolated zeros in the measured scattered data, due to an inoperative element, do not cause significant errors in the reconstructed image because it appears as a small but uniform amplitude shift after the Fourier transform operation. A small number of zeros in the transfer function may be corrected by a nearest neighbor spatial averaging of the scattered field data assuming a high enough sampling density.

The first case of data measured by the array, and reported here, is the radiated beam from a 0.5" dia (42λdia in water) focused transducer having a 2" focal length. The array was located 16" from the transducer in a water tank environment. Although the measured data is stored in real and imaginary form, the amplitude is shown in Fig. 4 for convenience. Since the computer could handle only part of the 64 x 64 data array, only the even elements are shown. Thus the display density is one half the true sampling density. In Fig. 4 it is clear that useful diffraction data exists well out into the edges of the measurement field. A close up view of the central 32 x 32 measured data is shown in Fig. 5 with the true sampling density.

The 64 x 64 focused transducer data was then reconstructed at several planes; Fig. 6a at the apparent focal point, Fig. 6b slightly closer to the transducer, and Fig. 6c at the plane of the transducer.

The second case considered was the scattering from a through-drilled hole in an aluminum block, Fig. 7. In this case the measured field consisted of the main transducer pattern after reflection minus that part due to the hole in the block. The reconstructed image is shown in Fig. 8. An image more characteristic of the hole would have been obtained by positioning the array out of the main reflected beam.

III. SUMMARY AND CONCLUSION

Implementation of a 2D acoustic transducer array in a coherent imaging system has been carried out using both source and scattered fields. The finite sampling caused by the array and the periodic nature of discrete Fourier transforms places some constraints on the image field and may give rise to aliasing or ghost effects. However, when the data is oversampled image processing techniques may be employed to improve the image display quality.

IV. ACKNOWLEDGEMENTS

This research was sponsored by the Center for Advanced NDE operated by the Science Center, Rockwell International, for the Advanced Research Projects Agency and the Air Force Materials Laboratory under contract F33615-80-C-5004.

V. REFERENCES

1. K. M. Lakin, W. R. Sheppard and K. Tam, "Wavefront Reconstruction Acoustic Imaging Using Two Dimensional Arrays", 1979 Ultrasonics Symposium Proceedings IEEE, Cat. # 79ch1482-9SU.

2. K. Lakin and A. Fedotowsky, IEEE Transactions Sonics and Ultrasonics, SU-23, 317 (1976).

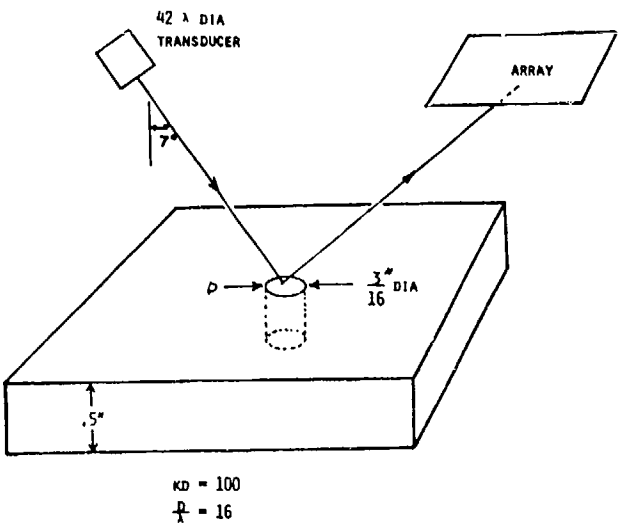

Figure 1. Configuration of Imaging System

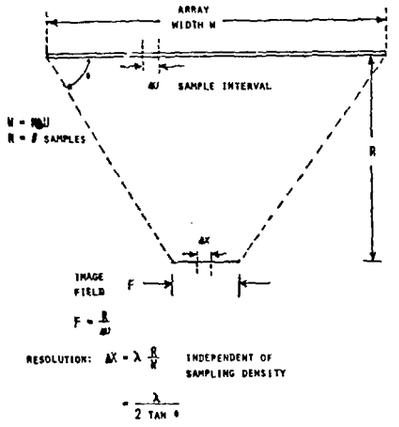

Figure 2. Effect of finite sampling in relation to array and object

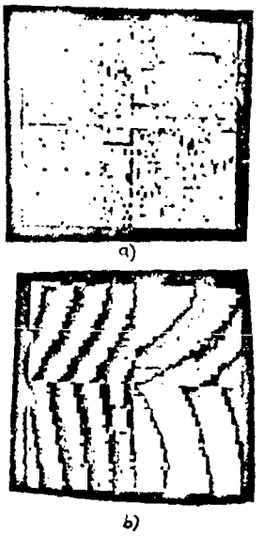

Figure 3. Array transfer function a) amplitude b) phase

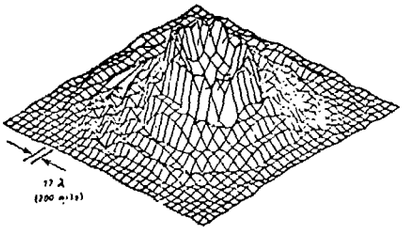

Figure 4. Measured data 0.5" dia focused transducer

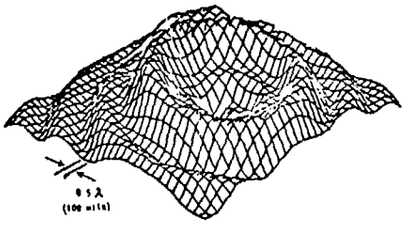

Figure 5. Expanded view of Figure 4 data

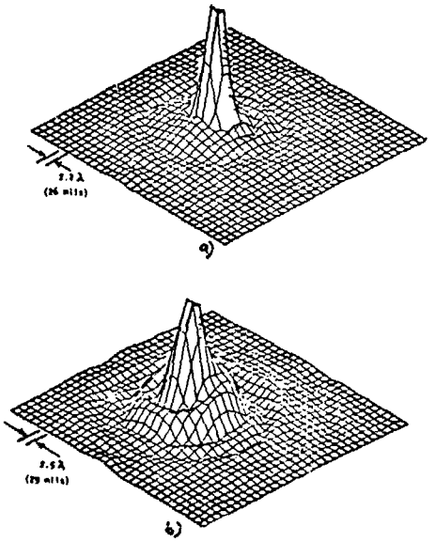

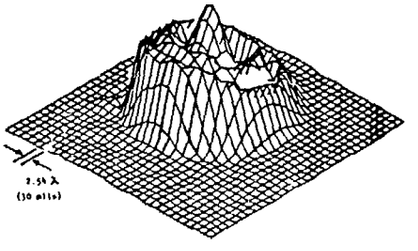

Figure 6. Reconstruction of focused transducer data a) at focal point b) near focal point c) at the transducer

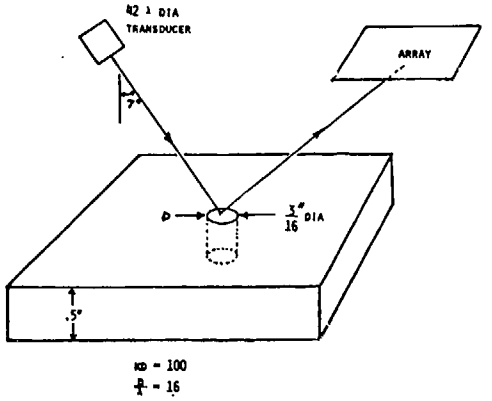

Figure 7. Configuration for scattering data from drilled hole

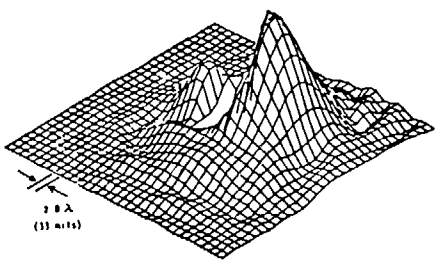

Figure 8. Image of fields at the drilled hole top surfaces

IMAGE PROCESSING FOR NONDESTRUCTIVE EVALUATION

M. H. Jacoby
Lockheed Missiles & Space Co.
Sunnyvale, California 94086

ABSTRACT

Digital image processing techniques can improve the interpretation and evaluation of radiographic and acoustic image data as well as the time domain waveforms produced by ultrasonic, eddy current, and acoustic emission — in two important ways. First, the image or waveform being evaluated can be enhanced to bring out detail not readily apparent to the observer. Second, the properly enhanced image or waveform can be evaluated automatically by computer. The size of defects can be measured, and accept/reject decisions made, without relying on the subjective interpretation of an inspector.

During the past ten years many new and innovative proce es have been developed for image enhancement and restoration. This presentation describes just one: the spatial filtering technique used to put acoustic and radiographic images in a mode suitable for automatic computer evaluation.

INTRODUCTION

The aim of image enhancement is to improve the visual appearance of images or to transform them into a representation suitable for computer analysis.

Review articles by Hunt[1] and Hall[2] give a comprehensive picture of the field and contain a total of almost 100 references and citations. More recently, Harrington and Doctor[3] have extended these techniques to encompass ultrasonic, eddy-current, and acoustic emission testing technology. Pratt[4] has written a textbook that gives mathematical and conceptual background as well as applications.

Pearson and his colleagues at Lockheed have described the use of enhancement methods as a starting point for automatic, computer-based image evaluation (see references 5 through 9).

In this presentation, spatial filtering and its applications to particular radiographic and acoustic images are shown. Other straightforward procedures — contrast stretching, trend removal and smoothing — will be demonstrated as part of the overall spatial filtering process.

SPATIAL FILTERING

Figure 1 reproduces a radiographic image of a glass-wrapped, rubber-insulated, cylindrical pressure vessel. The requirement is to process the image so that cuts in the insulation can be evaluated automatically by computer.

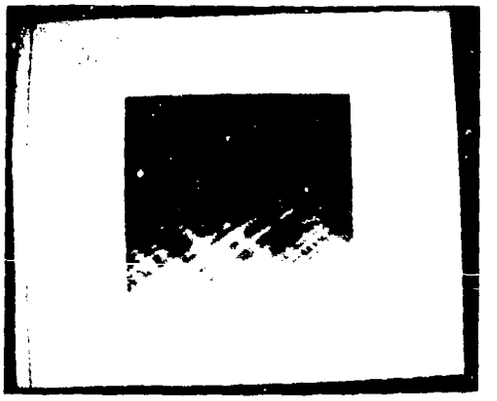

Fig. 1

The radiograph was scanned and digitized with a flying-spot scanner, and the result stored in memory as a two-dimensional 512 x 512 array of picture elements (pixels) with each 50 micron diameter pixel quantized to one of $2^9 = 512$ gray shades. The contrast of the digitized image was stretched to accommodate the full nine-bit range, and global trends in image brightness were removed by curve fitting and subtraction. The result of these manipulations is shown in Fig 2: a cut in the insulation is readily apparent.

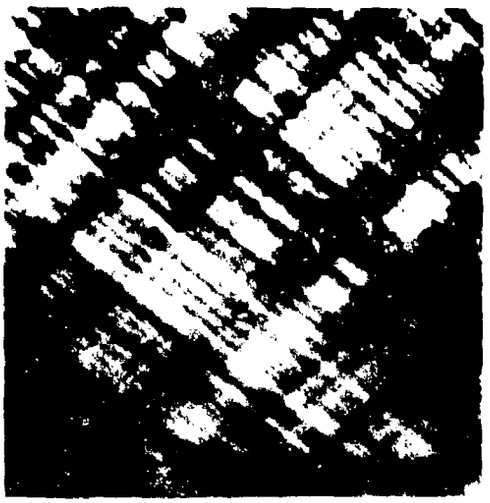

Fig. 2 Contrast enhanced and gradient removed. The long vertical indication on the right hand side is the planned cut in the insulation. The much shorter indication on the left hand side was not planned. A bit to the left of the long indication is a small indication of a high-density inclusion either in the insulation or the glass.

Because of the way the pressure vessel is fabricated, cuts in the insulation can occur only in the vertical or horizontal direction on the radiograph. With this knowledge it is possible to develop a spatial filtering technique that will attenuate the image of the glass case (the cross-hatched lines). The filtered image will then contain only horizontal and vertical components and is thus presented to the computer in a mode highly suitable for automatic evaluation of cuts in the insulation.

In spatial filtering what is done is decompose the two-dimensional matrix of brightness values that represent the image into a linear combination of elementary functions. If Fourier analyses are used for the decomposition, the resulting elementary functions (which are sines and cosines) represent the spatial frequency of the image. The mathematical representation of this decomposition is given by the two-dimensional Fourier integral:

$$f(x, y) = \int_{-\infty}^{\infty}\int F(u, v)\, e^{i2\pi (ux + vy)}\, du\, dv .$$

The complex number F(u, v) is a weighting factor that must be applied to the elementary function $\exp\left[i2\pi (ux + vy)\right]$ in order to synthesize the original f(x,y).

Figure 3 is a representation of the magnitude of the spatial frequency components of the original radiograph. Since F(u,v) is a complex number there is also a spatial phase present. This phase is not shown in the diagram, but it is contained in the values stored in the computer memory.

Fig. 3 Spatial Frequency Spectrum

The two-dimensional Fourier transform of one particular spacing in the image plane is given by the magnitude of the impulse pair in the spatial frequency domain. To remove that particular spacing from the image plane, simply filter out the impulse pair and transform the filtered spectrum back into the image plane. It should be noted that no matter what section of a uniform scene is being considered, the magnitude of the spectrum is always the same and thus the filter function is always the same.

Figure 4 shows the filtered spectrum of the image. All the impulse pairs that make up the cross-hatch indications have been attenuated except one, the pair at u = 0, v = 0. This can be considered as the dc value of the image, and sets the background brightness level of the image.

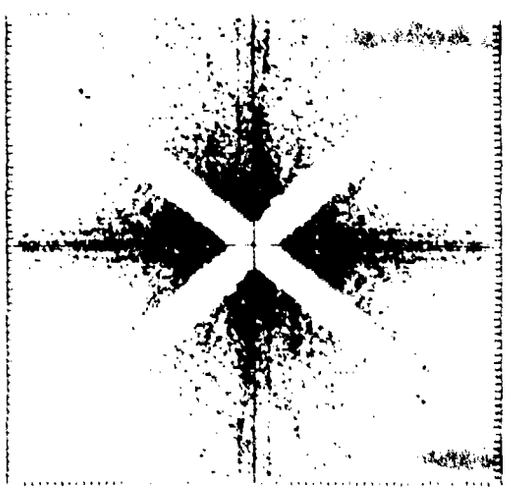

Fig. 4 Filtered Spectrum

Figure 5 shows what happens when the filtered spectrum is transformed back into the image domain. The cross-hatch is indeed attenuated and the cuts in the insulation are quite clear.

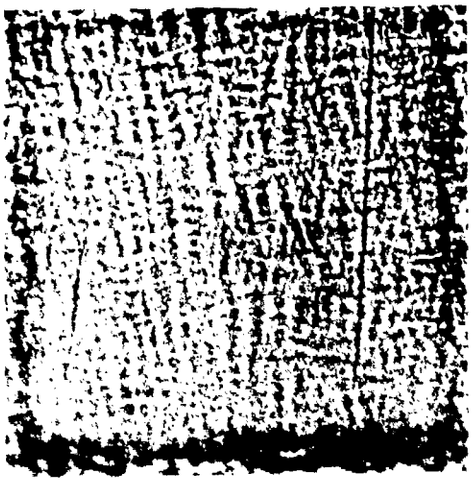

Fig. 5 Result when filtered spectrum is transformed back to image domain.

Figure 6 is a smoothed version of Fig. 5 which somewhat reduces the indications of noise and permits efficient evaluation by computer.

Fig. 6 Smoothed version of above.

It should be noted that the small vertical cut evident on the left hand side of Fig. 6 was not perceived at all on the original radiograph. A high density inclusion is also evident in the filtered image.

Figure 7 is an acoustic image of a graphite-epoxy structure. The filtered image, Fig. 8, is in a mode more suitable for automatic evaluation of the defects.

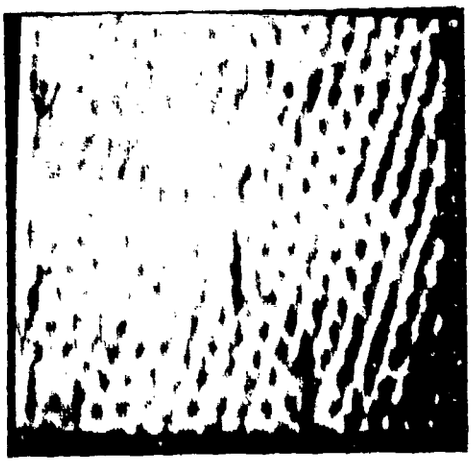

Fig. 7. Acoustic Image

Fig. 8. Filtered Image

REFERENCES

1. Hunt, B. R. "Digital Image Processing." Proc. IEEE 63, 4 April 1975, 693-708.

2. Hall, E. L., et al. "A Survey of Preprocessing and Feature Extraction Techniques for Radiographic Images." IEEE Trans. Computers, C-20 No. 9, Sept. 1971, 1032-1044.

3. Harrington, T. P., and Doctor, P. G. "Data Analysis Methods for Nondestructive Evaluation." Battelle Pacific Northwest Laboratories, Report No. BN-SA-1056, Oct. 1979.

4. Pratt, W. K. Digital Image Processing. New York: John Wiley & Sons Inc., 1978.

5. Pearson, J. J., Fischler, M. A. Firschein, O., and Jacoby, M. H. "Application of Image Processing Techniques to Automatic Radiographic Inspection." Proc. EIA 7th Annual AIPR Symposium, 1977.

6. Pearson, J. J., Fischler, M. A., Firschein, O., Jacoby, M. H., King, J., and Jaffey, S. M. "Automatic Inspection of Artillery Shell Radiographs." 22nd Annual International Technical Symposium, SPIE, San Diego, 1978.

7 Firschein, O., Fischler, M. A. "Associative Algorithms for Digital Imagery." Twelfth Annual Asilomar Conference on Circuits, Systems, and Computers, Nov. 1978.

8. Firschein, O., Eppler, W. G., and Fischler, M. A. "A Fast Defect Measurement Algorithm Suitable for Array Processor Mechanization." IEEE Computer Society Conference on Pattern Recognition and Image Processing, Chicago, 6-8 Aug. 1979.

9. Eppler, W. G., Firschein, O., McCulley, G., King, J., and Pearson, J. J. "Speedup of Radiographic Inspection Algorithms Using an Array Processor." Proc. SPIE, Vol. 207, "Applications of Digital Image Processing III." (1979), 96-103.

COLOR GRAPHICS: AN AID TO DATA INTERPRETATION

C. C. Ruokangas and J. F. Martin
Rockwell International Science Center
Thousand Oaks, California 91360

ABSTRACT

Color displays, because of their high information content, have inherent advantages over monochromatic display terminals. The extra dimensions that color adds to traditional CRT displays can be utilized to provide faster and more accurate pattern recognition for the human eye, as well as a corresponding increase in quantitative and qualitative information. These advantages have been realized in a newly-developed color graphics system for nondestructive evaluation.

INTRODUCTION

The field of color display has gained enormous interest due to recent growth in available graphics hardware and software. The coupling of this new technology with increasingly sophisticated user requirements makes a color graphics system a useful tool for visualizing complex, multidimensional data structures and for displaying results of abstract algorithms. This paper reports selected details of a newly-developed color graphics system (CGS), and its applications, primarily in the field of nondestructive evaluation. The particular hardware will be described as well as the graphics and application software package.

Of necessity, all images reproduced in this publication are in monochrome, and the original information available through the medium of color is therefore compromised. Actual color prints are available on request, although a nominal fee will be charged for requests involving more than one figure.

HARDWARE

The color graphics system (CGS) comprises three separate entities: data sources, a host minicomputer, and a display system. Data sources may be external to the entire system, or may consist of instrumentation attached to the host; in this report the Science Center Test Bed[1] has been primarily used to acquire the data. The host minicomputer utilized is a Data General S/200 Eclipse with tape and disk storage; there is a DMA link between the S/200 and the color display processor. A schematic of this equipment arrangement is shown in Fig. 1.

The display processor, a GENISCO GCT-3000, is linked with a CONRAC 19 in. red-green-blue (RGB) video monitor, a trackball for cursor control, and a keyboard. The processor controls storage of data in 8 parallel internal planes of 512 × 512 RAM memory, which provides the user with 255 (2^8) different integer values that may be assigned to each location in RAM. Each location in RAM corresponds to one spatial location in x and y on the video monitor, called a pixel (picture element). The integer value in the RAM location is interpreted for color intensity level assignment

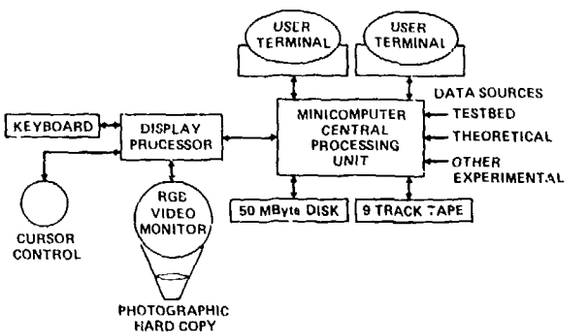

Fig. 1 Schematic diagram of hardware.

by a video look-up table (VLT), described in more detail later, which can be displayed for reference on the monitor. The refresh frame rate is 30 Hz interleaved. A hardware character-vector generator allows enhanced speed for graphics manipulation, and the hardware ZOOM/SCROLL feature provides high speed display enlargements of 1, 2, 4 or 8 times, and horizontal and vertical scrolling of the image. Both of these functions are performed without altering the contents of the RAM memory. A 4 in. × 5 in. view camera is currently being used to generate hardcopy. To avoid flicker, the cathode ray tube in the monitor is of the long persistence phosphor type.

SOFTWARE

Introduction - The goal in the development of this software was to provide highly interactive graphics and image display capabilities in a research environment. To promote simplicity in creating programs to meet new applications, the software was modularized and structured. This was accomplished by the generation of a set of FORTRAN callable subroutines for use by application routines in the host. These subroutines function independently, each having a separate display function, and are merged together to form a comprehensive graphics library in the host, which interfaces with the display processor via an

assembly language driver. The routines in the library generate macro instructions which, when received by the display processor, are executed under the processor's own operating system on the monitor. Several features of the library are noteworthy: it is an independent set of exclusive functions which can be easily accessed in virtually any combination by a user (application) program; the functions allow user control over character and shape generation; the user can easily define new sets of colors (VLT's) to be utilized for a particular application; and the user can interactively control cursor, zoom, and scroll features. Figure 2 indicates the flow of software control, as well as examples of line graphics and imaging. Figure 2a indicates the logical use of the software, including data input from various sources, the development of user interactive routines, and the actual interfacing to the color processor through the set of library functions. Figure 2b exhibits the vector graphics capabilities. Figures 2c and d are examples of images generated from C-scans of an 800 μ flaw; both utilize the hardware zoom capabilities, with 2c set at a zoom factor of 2, and 2d at 8.

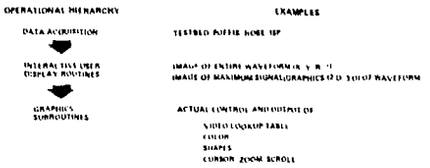

a. Logical use of software.

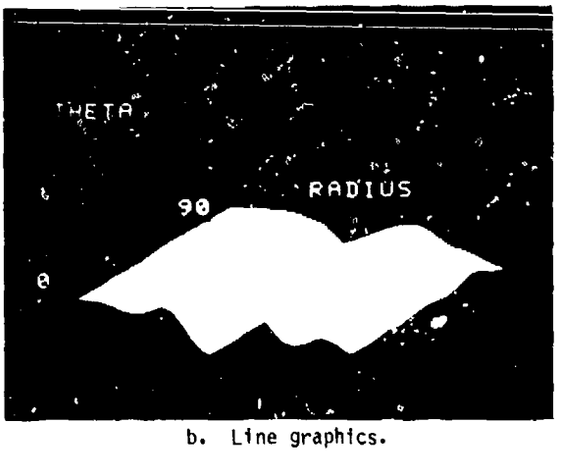

b. Line graphics.

Library Functions -Shape and character generation is provided by routines which construct, in user defined sizes, vectors, filled or unfilled rectangles, three-dimensional boxes, circles generated by separate vectors, and alphanumeric strings in vertical or horizontal directons. Examples of shapes, labels and color control are shown in Fig. 3. Color output can be controlled both by assigning a particular color from the video look-up table (VLT) for succeeding shapes and labels, and by redefining the VLT itself. The VLT is a 256 element array, which is referenced by host programs to assign a particular color to each

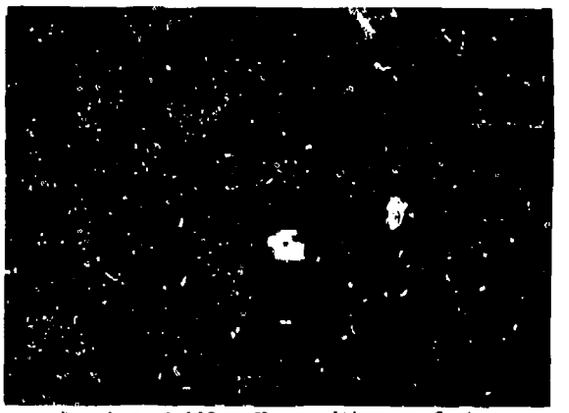

c. Imaging of 800 μ flaw, with zoom factor of 2.

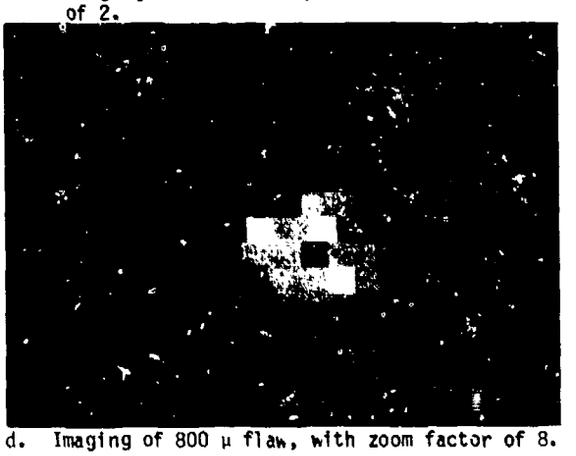

d. Imaging of 800 μ flaw, with zoom factor of 8.

Fig. 2 Logical flow of software plus examples of software to generate line drawings or images.

data value. A simple example of this is the renormalizaton of a parameter such as signal amplitude which may range from 0 to 5 volts into the integer range 1 to 256. The exact value resulting from this mapping of volts to the range 1-256 is then the exact index for the VLT array. If the VLT is a simple linear 16-level gray scale, the resulting image is very easy to interpret: bright areas represent large signal amplitude and dark areas represent small signal amplitude.

Fig. 3 Shape, label, and color control capabilities.

To obtain color images, the VLT values must be tailored to yield a desired pattern. Each element of the VLT consists of 12 bits, 4 each defining red, blue, and green; this allows each of the 256 elements to be defined as one of 4096 (2^{12}) colors, i.e., combinations of various intensities of red, green and blue. It should be noted that changing a VLT, i.e., changing the bit pattern assigned to each of the 256 elements of a VLT, automatically changes the color assignment of the image currently represented on the monitor; therefore, a single image may be displayed with several different VLT's in succession, in an attempt to find the best representation for that image. Figure 4 shows 6 color assignments for a C-scan of a D-shaped titanium sample with 3 flaws. The irregular shape in the upper right hand corner should be ignored. Although reproduced here in monochrome, it is still possible to see that different VLT's can produce quite different results. Unique to this work is the use of graded-intensity four color scales; examples are shown in Figs 4a and 4b. This color structure yields easily quantified contours as well as a large dynamic range. A fifth color is added to indicate signal saturation. Figure 4c shows a more conventional continuous spectrum scale. Figures 4d, 4e and 4f are examples of color scales that identify specific signal ranges by different solid colors; this technique could be valuable for field inspection and recording.

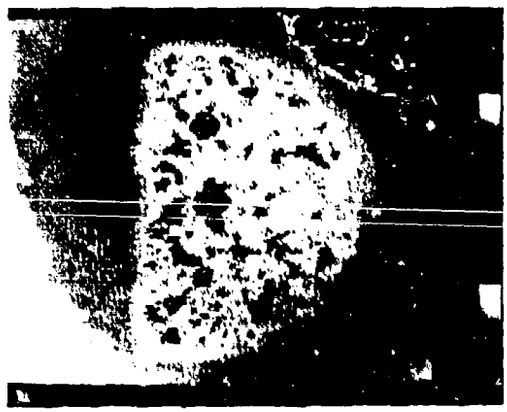

a, b. Two arrangements of the four-color scale: (white, red, green blue) and (red, green, blue, white).

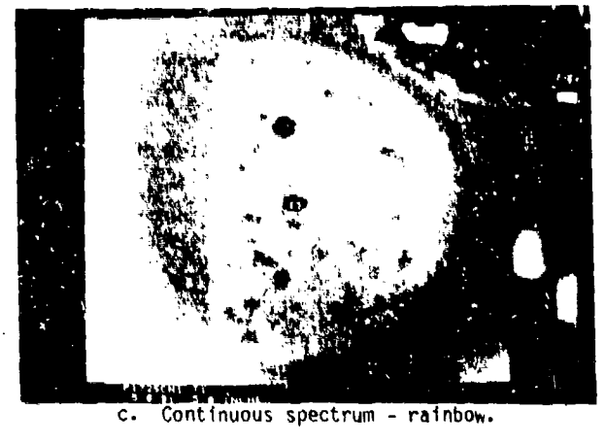

c. Continuous spectrum - rainbow.

d. Two defined ranges.

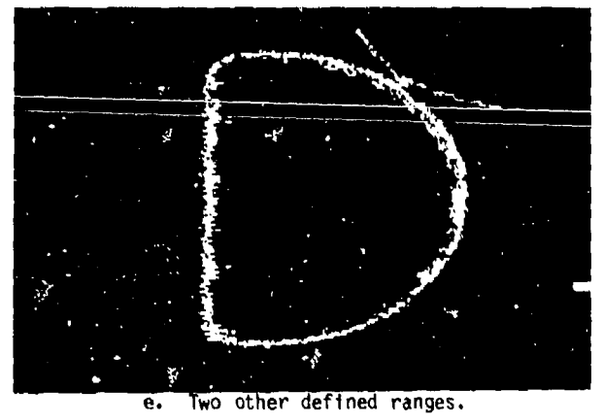

e. Two other defined ranges.

Fig. 4 Six examples of different VLT's

APPLICATIONS

There exists a constant need for improving productivity and reliability, both in general industry and in NDE. To this end, the high content of information and easy interpretation of color displays yields distinct advantages over monochromatic displays. We will briefly describe here various applications of our color graphics system (CGS). Techniques for the acquisition of data vary, but all acquired data require some form of display to be interpreted. In general, there are two basic methods for displaying information: line graphics and imaging. Line graphics include drawing vectors, characters, and points to form

f. Five defined ranges.

Fig. 4 Color assignment by changing VLT's.

ordinary graphs in two dimensions. It also includes perspective drawings of multiple two-dimensional graphs to form three-dimensional graphs. Two and three dimensional graphics are often formed on monochromatic black and white systems; on a CGS, the added dimension of color allows the user to enhance information which may have been obscured in a black and white system. An example of this is shown in Fig. 5 where transducer waveforms for several different settings of the damping parameter have been plotted on the same coordinate axes. Although the various colors reproduce only as various shades of gray in this publication, in the original the color coding allowed easy comparison of all six settings at once.

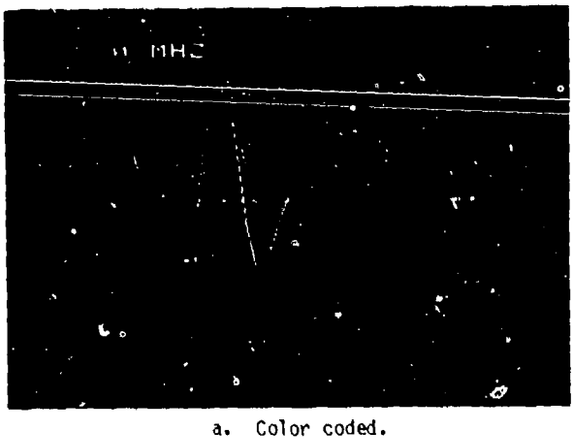

a. Color coded.

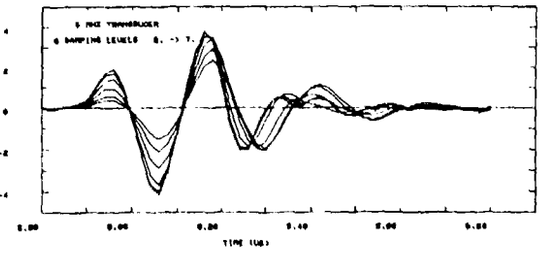

b. Monochromatic.

Fig. 5 Transducer response.

For the purposes of this discussion, the term "imaging" will mean the display of a two dimensional pattern of many tiny rectangles (pixels), each of which displays the value of a parameter by a shade of gray or color value at the relative spatial position it is placed. To interpret any image, a video look-up table or legend must be provided which shows the relationship between the set of color values and the parameter values. Ultrasonic imaging is often done on monochromatic systems that normally yield a reasonable reproduction of the object values; with the use of color, further dynamic range can be gained and specific details of the object enhanced. Figure 6 illustrates both a graphics drawing and an image of the theoretical data describing a 2:1 oblate spherical void.[2] Note the correspondence of the two areas of low level of signal on the image with the valleys shown in the 3-D graphics image. Each representation has certain advantages. The perspective drawing in this case is more immediately recognizable to the untrained eye, but "hides" data values which lie behind large peaks, and is difficult to quantify without painstaking use of a straightedge. The image pattern is more difficult to recognize until the eye is accustomed to the VLT, but it has other advantages:

(a) there is no hidden data;

(b) there is a built-in dynamic range of 1 to 256; and

(c) by using four colors, each shaded from dark to bright, the image is automatically quantified and contoured.

The use of shading in (c) above is, to the knowledge of the authors, unique to the CGS used with the Testbed,[2] but promises to be generally useful in NDE and other imaging applications because of its large dynamic range and natural contouring capability.

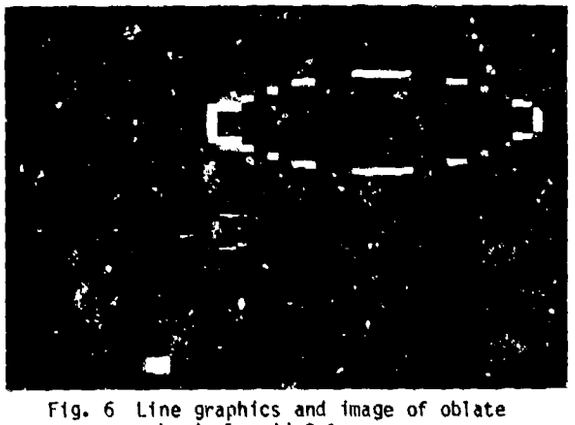

Fig. 6 Line graphics and image of oblate spherical void 2:1.

Most programs developed on this imaging system are for displaying data taken on the Testbed, indicated in Fig. 1 and described in more detail in Reference 1. Data is acquired through an A/D by the S/200 and stored on disk for later analysis and display. The microprocessor is capable of either raster or circular scans, and

the S/200 can acquire either the peak amplitude of a waveform within a time gate, or the full waveform, yielding C- or B-scans. The four resulting combinations are illustrated in Fig. 7. Figure 7a shows a raster C-scan of a 1 in. thick disk of titanium, where the transducer moved back and forth in the x dimension, alternating with small indexing motions in the y dimension. The area scanned is 0.5 by 0.5 in., and the flaw is a seeded 800 micron spherical void. Figure 7b shows a circular C-scan of a similar sample with an oblate void. In this example, the sample was rotated in a full 360° under the transducer before each small index move along the radial dimension. Figure 7c shows a circular B-scan of the same sample used in 7a. The void shows clearly in the center, halfway between the front face echoes and back face echoes. In this display program, one may choose what band of rotation angle will be displayed. In Fig. 7c, the entire 0° to 180° rotation is shown at once. Figure 7d shows a raster B-scan. Nine successive B-scans are shown, one for each of 9 sequential values of the y dimension. Each is a plot of x vs time for a titanium sample with a weld bead on the lower surface. The irregularity in the back face echo at the end of the weld bead shows clearly in the right most image of the middle row.

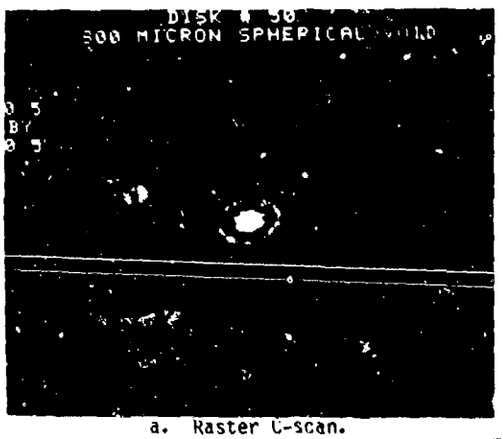

a. Raster C-scan.

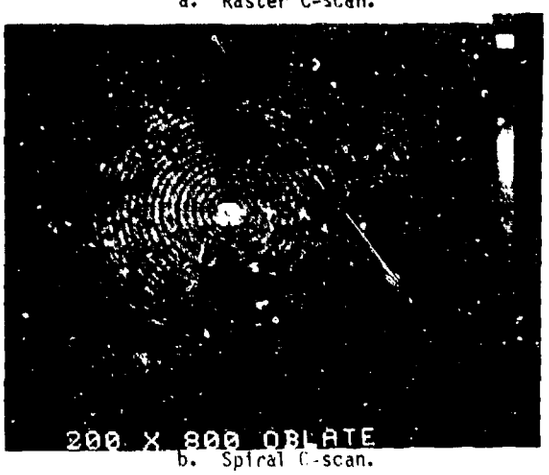

b. Spiral C-scan.

Figure 8 shows a circular C-scan of a 13 in. radius turbine disk. Figures 8b and 8c show two different zooms of that image. Figure 8d shows the output of a diagnostic program designed to read a disk file and show the control data blocks to be sent from the S/200 to the test-bed microprocessor. It also plots the paths the transducer and pivot point will follow with respect to the part itself. This allows rapid checking of a Testbed control block file to make sure the transducer won't hit the part during the scan.

c. Spiral B-scan.

d. Raster B-scan.

Fig. 7 The basic four scan modes.

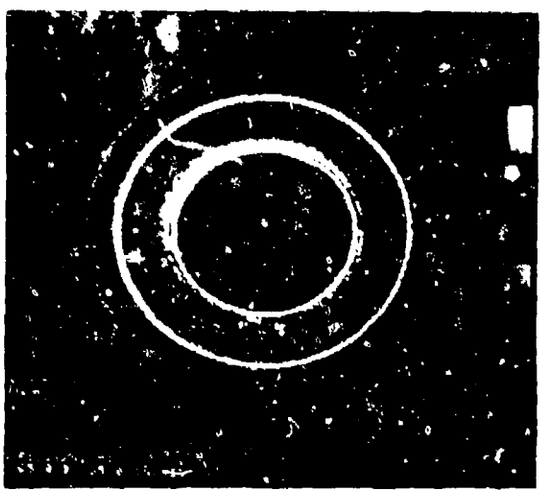

a. Entire image

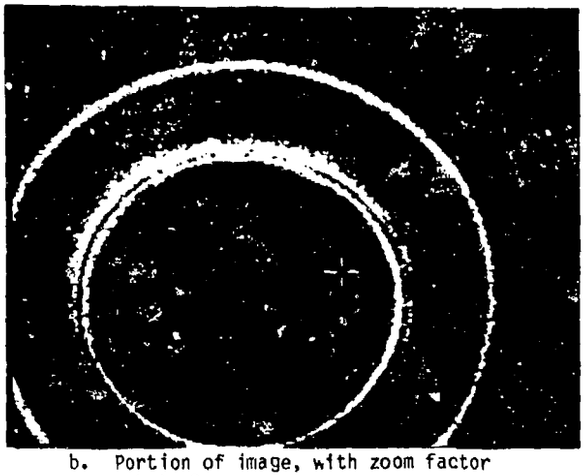

b. Portion of image, with zoom factor set to 8.

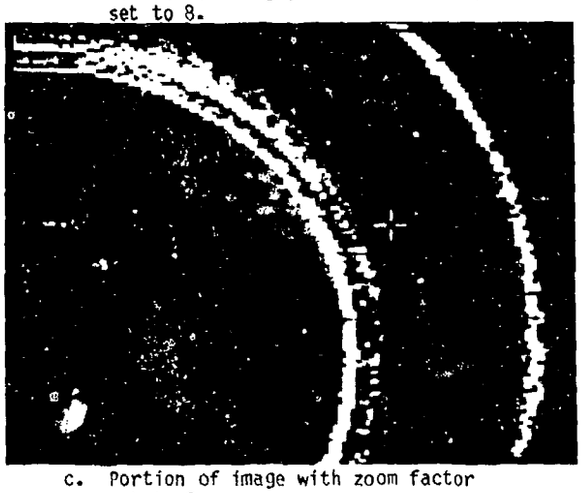

c. Portion of image with zoom factor set to 8.

d. Displays of data blocks and the resulting path of transducer and holder with respect to part.

Fig. 8 Displays used for circular C-scans of a 13 in. radius turbine disk.

Figure 9a shows ultrasonic transmission attenuation C-scans of two pieces of graphite/epoxy composite about 0.100 inches (2.5 mm) thick, imaged in 16-level gray scale. The top piece is held by two pieces of scrap metal and is free of natural defects. It is a calibration piece with an artifical slot and a 0.025 inch (0.64 mm) hole, parallel to the scan plane, which are clearly visible in the otherwise rather uniform pattern. The lower piece is the test piece and has only 5 artificial defects, consisting of drilled through holes: 4 small, 1 larger. The rest of the pattern is caused by poor transmission of ultrasound, probably due to porosity. Figure 9b is the same image with a color VLT. Even in the monochrome rendition of the color image which is presented here, far more detail can be seen and quantified in Fig. 9b than in Fig. 9a.

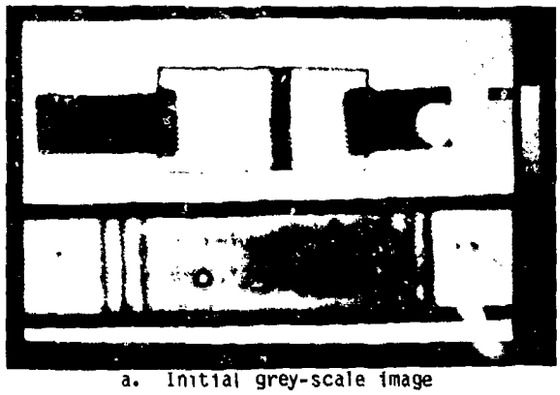

a. Initial grey-scale image

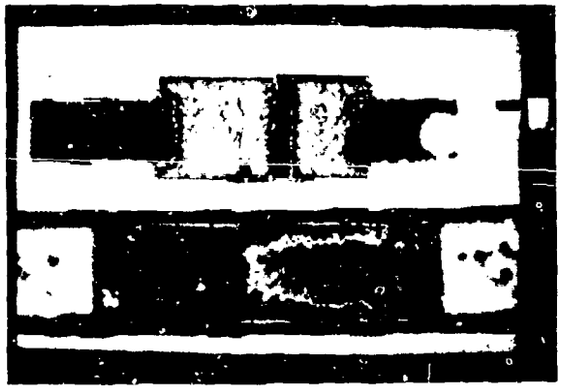

b. Same image with further detail enhanced through color representation.

Fig. 9 C-scans of graphite-epoxy composites.

Other applications have been developed as needs emerged. Figure 10a is an image of 91 POFFIS "waveforms" which resulted from inverting theoretical scattering data representing a quadrant of an 800 micron void.[3] Each waveform is displayed at a different angle, corresponding to the direction in which data was generated.

Figure 10b is a display of data taken with an infrared imaging system of a human face. The data was transferred to the CGS by magnetic tape and translated into a common format.

In summary, the ability of a CGS to display and manipulate a large amount of information, with capabilities not available on monochromatic systems, has been illustrated for a variety of NDE

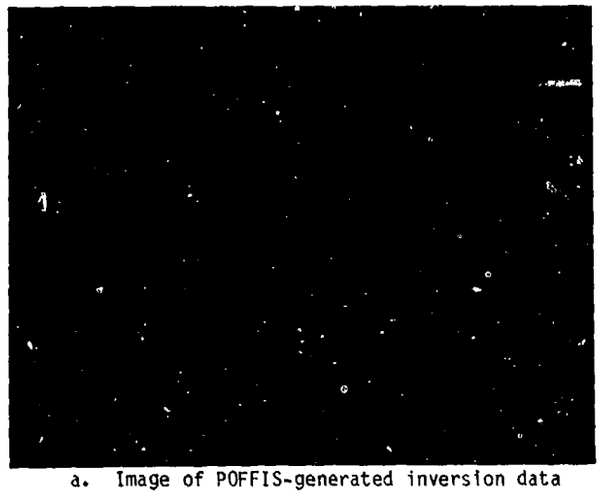

a. Image of POFFIS-generated inversion data

b. Infrared imaging of human face

Fig. 10 Additional applications.

oriented data. It can be expected that more applications will follow. Further software development is now in progress on real time display during scans, and on displaying B-scans obtained from parts with curvilinear profiles. Additional processing of the acquired data, beyond the simple peak amplitude detection shown in this paper, is planned.

ACKNOWLEDGMENTS

The work reported in this paper was supported by the Advanced Research Projects Agency and the Air Force Wright Aeronautical Laboratory under contracts F33615-74-C-5180 and F33615-78-C-5164.

REFERENCE

1. R.C. Addison, R.B. Houston, J.F. Martin, R.B. Thompson, "Test Bed for Quantitative NDE," proceedings of DARPA/AF Review of progress in Quantitative NDE, July 1980.

2. J.H. Rose, R.K. Elsley, B. Tittmann, V.V. Varadan, V.K. Varadan, "Inversion of Ultrasonic Scattering Data," pp. 605-614, "Acoustic, Electromagnetic and Elastic Wave Scattering-Focus on the T. Matrix Approach," V.V. Varadan and V.K. Varadan, eds, Pergammon Press, 1980.

3. N. Bleistein and J.K. Cohen, "Progress on a Mathematical Inversion Technique for Nondestructive Evaluation," Wavemotion 2, pp. 75-81 (1980).

RECENT PROGRESS IN MATERIALS STUDIES WITH ACOUSTIC MICROSCOPY

R.C. Bray and C.F. Quate
Edward L. Ginzton Laboratory
Stanford University
Stanford, California 94305

ABSTRACT

The scanning acoustic microscope operating in water with a frequency of 2.5 GHz (wavelength 6000 Å) has been used to nondestructively characterize materials and devices in a manner inaccessible to optical and electron microscopy.

Adhesion of thin films of Cr on glass (optical masks for photolithography) is shown to be a strong source of acoustic microscope contrast. This offers nondestructive evaluation of film adhesion on a microscopic scale for the first time.

Study of intentionally damaged integrated circuit structures reveals damage features not visible in optical microscopy. Microscopic subsurface imaging of composite structures is presented, as in other recent acoustic microscope imaging of materials. Recent theoretical work in acoustic response of layered materials is reviewed.

The scanning reflection acoustic microscope reveals information complementary to that obtainable by optical and electron microscopy. The acoustic microscope is sensitive to the mechanical properties (stiffness, density, viscosity) of a sample. In some cases information unobtainable by any other nondestructive technique is revealed by acoustic microscopy.

In Fig. 1 a 10 nsec RF pulse applied to the ZnO transducer is converted into an acoustic plane wave pulse propagating in the sapphire towards the hemispherical lens. The lens focuses the sound wave to a diffraction limited spot in the water coupling the lens to the reflecting object, which is mechanically scanned in a raster pattern. The amplitude of the reflected acoustic pulse controls the brightness of a CRT display.

In Fig. 2, we see optical and acoustic micrographs of two samples of chromium on glass masks used for photolithography by a semiconductor manufacturer. In Figs. 2(a) – (c) the 1000 Å Cr film is well adhered to the glass substrate, as determined by the tape test and scratch test for film adhesion. The contrast is uniform across the Cr area of all three pictures. In the acoustic micrographs this indicates uniformity of mechanical properties.

In Figs. 2(d) – (f), micrographs of poorly adhering Cr, the contrast around the edges of the Cr regions indicates different adhesion from the central, presumably better adhered areas. In the optical photo the only evidence of poor adhesion is nicks where the Cr has actually peeled off. The acoustic image can thus show areas of poor film adhesion nondestructively.

In Fig. 3 we see acoustic micrographs at different focal positions of an aluminum line on silicon. The quartz passivation layer on top has been purposely damaged with a diamond indenter. The radial pattern of lines diverging away from the damaged area are mostly not visible in the optical oil immersion micrograph. We believe these are microcracks in the quartz passivation layer and in the silicon substrate. The width of the Aℓ line is 15 μ and the width of the cracks is near the 5000 Å resolution limit of the acoustic microscope at 2.6 GHz.

Figure 4 shows optical and acoustic images of a composite material fabricated by Dupont; hollow glass spheres imbedded in polyethylene. There are several spheres visible in the acoustic images which are completely absent from the optical picture. They are below the surface of the optically opaque polyethylene matrix. Because of the good impedance match between water ($Z = 1.55$ and 10^5 gm/cm^2 sec) polyethyelene ($Z = 1.7 \times 10^5$ gm/cm^2 sec), the polyethylene is transparent to sound and subsurface spheres are easily imaged.

Figures 5 and 6 show polished materials samples in which features are visible in the acoustic micrographs of the polished but unetched samples which are completely invisible in the optical micrographs of the matched sample. Grain boundaries and twin lines visible in acoustic micrographs of the unetched Si sample in Fig. 5 become visible optically only when the sample is etched.

In the case of the polished inconel (Ni/Cr/Fe alloy) sample, there are in fact twin lines within individual grains which are visible in the acoustic images but are not visible even in the optical micrograph of the etched sample. This alloy has similar etch rates for different crystal orientations, so optical images of etched samples mainly reveal the grain boundaries, where the etch rate is higher. The acoustic images reveal a high degree of contrast between different grains, and even within what etching would appear to define as individual grains. We attribute this to the anisotropy of the crystallites and the resultant difference in acoustic reflectance.

We have written the necessary programs to calculate predicted acoustic microscope response for samples consisting of plane solid layers on a solid substrate. The microscope detected power output is plotted versus lens-object spacing Z, as in Fig. 7. In this graph, the curves represent the predicted

microscope $V(Z)$ for three different samples: Glass, 1000 Å Cr well adhered to glass, and 1000 Å of Cr with a vacuum layer between it and glass. The predicted relative contrasts between three such areas in a single acoustic microscope image can be found by noting the three values of $V(Z)$ for a fixed lens - object spacing Z.

The important point about the $V(Z)$ plots at hand is that they successfully predict observed contrast in the acoustic micrographs of well adhered and poorly adhered chromium on glass. They also show that poor adhesion is expected to be directly observable in acoustic micrographs, as we observe from Fig. 2 to be the case. We choose to model a poorly adhering Cr film as a thin layer of vacuum between film and substrate.

In summary we have presented examples of the acoustic microscope's ability to reveal information about materials and structures which is not readily obtainable by any other nondestructive technique.

This work was supported by the Air Force Office of Scientific Research under Contract F49620-78-C-0098.

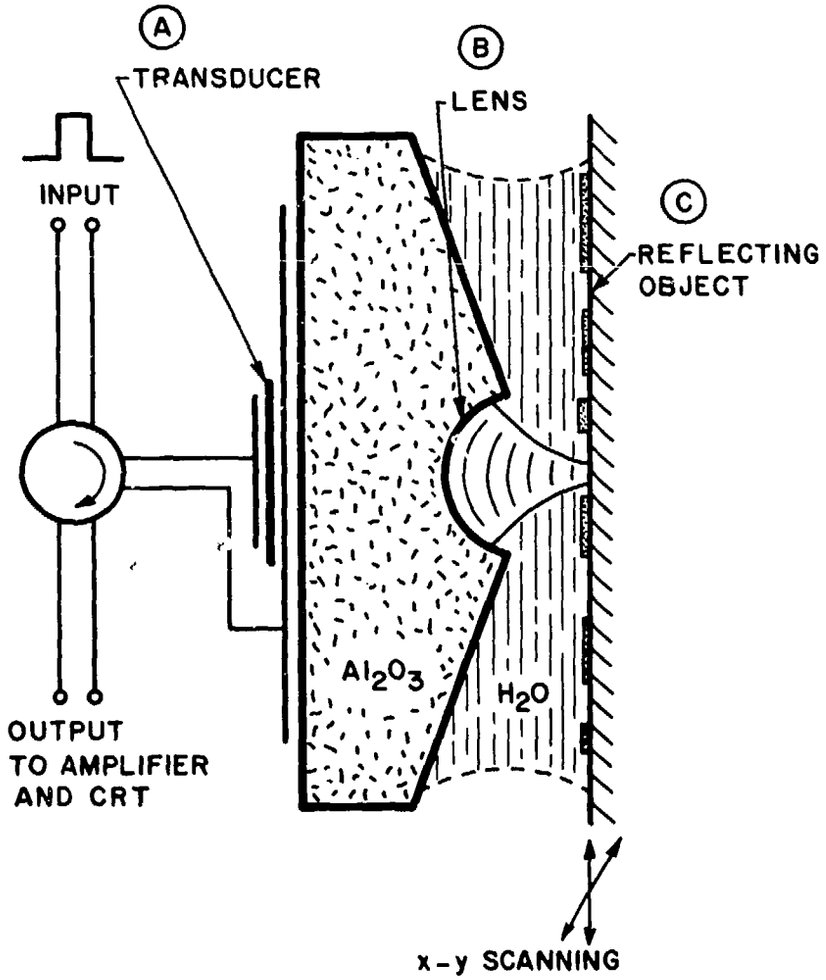

FIG. 1--Acoustic lens.

1000 A Cr ON GLASS (GOOD ADHESION)

30 μ

(a) OPTICAL

(b) ACOUSTIC, FOCUSED ON Cr

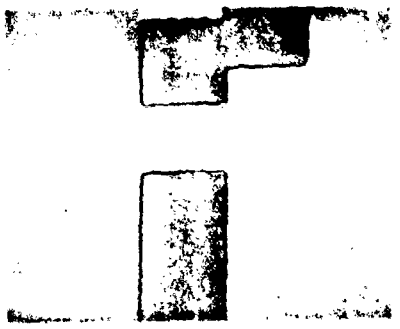

(c) ACOUSTIC, FOCUSED ON GLASS

1000 A Cr ON GLASS (POOR ADHESION)

100 μ

(d) OPTICAL

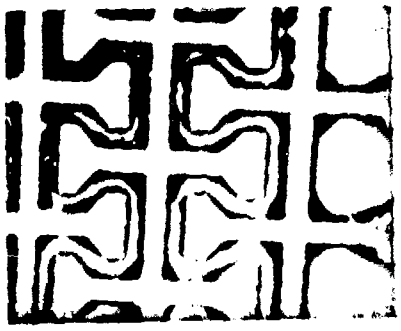

(e) ACOUSTIC Z = -1μ

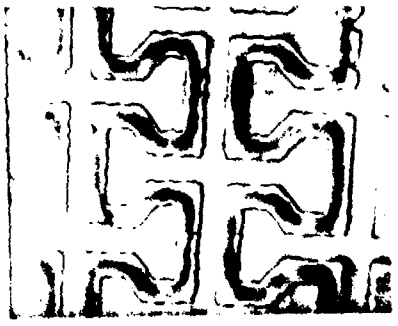

(f) ACOUSTIC Z = -0.5μ

FIGURE 2

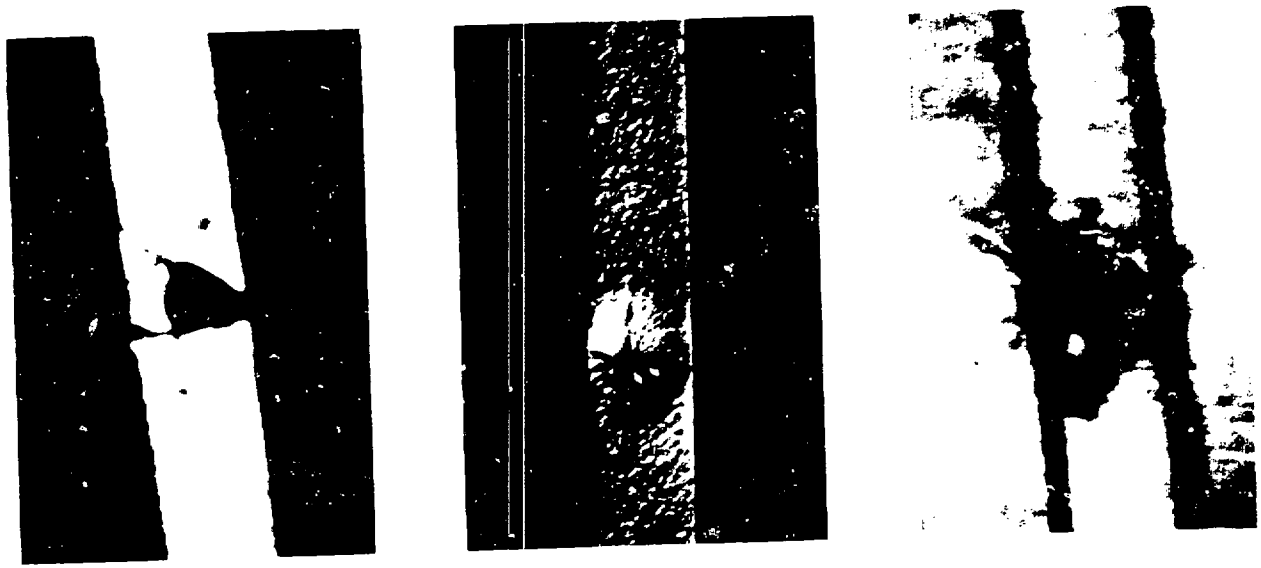

(a) ACOUSTIC
1st FOCUS

(b) OPTICAL

(c) ACOUSTIC
2nd FOCUS

ALUMINUM LINE ON SILICON WITH QUARTZ OVERLAY

FIGURE 3

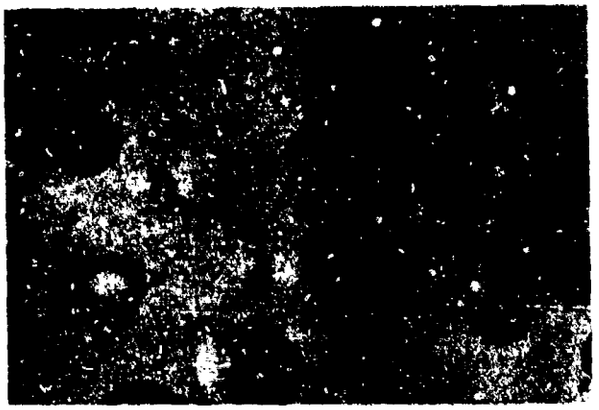

(a) OPTICAL x620

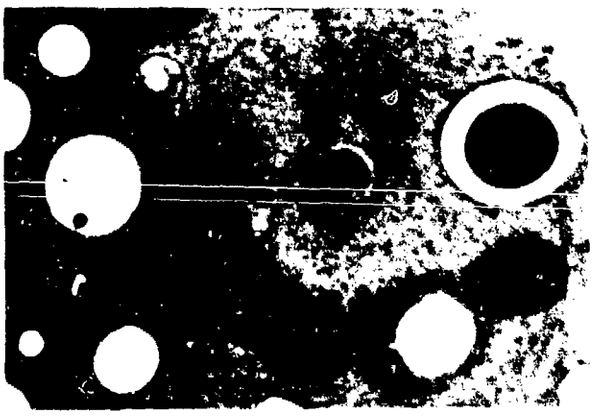

(b) ACOUSTIC (2600 MHz)

POLYETHYLENE TEREPHTHALATE
WITH IMBEDDED GLASS BEADS

FIGURE 4

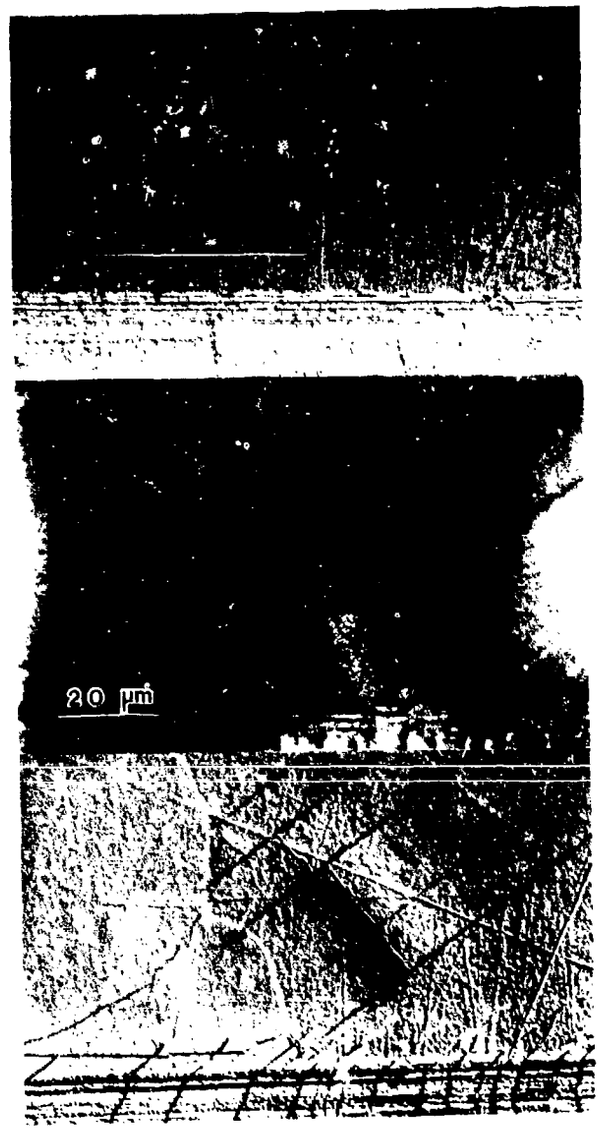

FIG. 5--(Top) Optical micrograph of polished Si sample.
(Center) Acoustic micrograph of same area f = 2.5 GHz.
(Bottom) Optical micrograph of same area after etching.

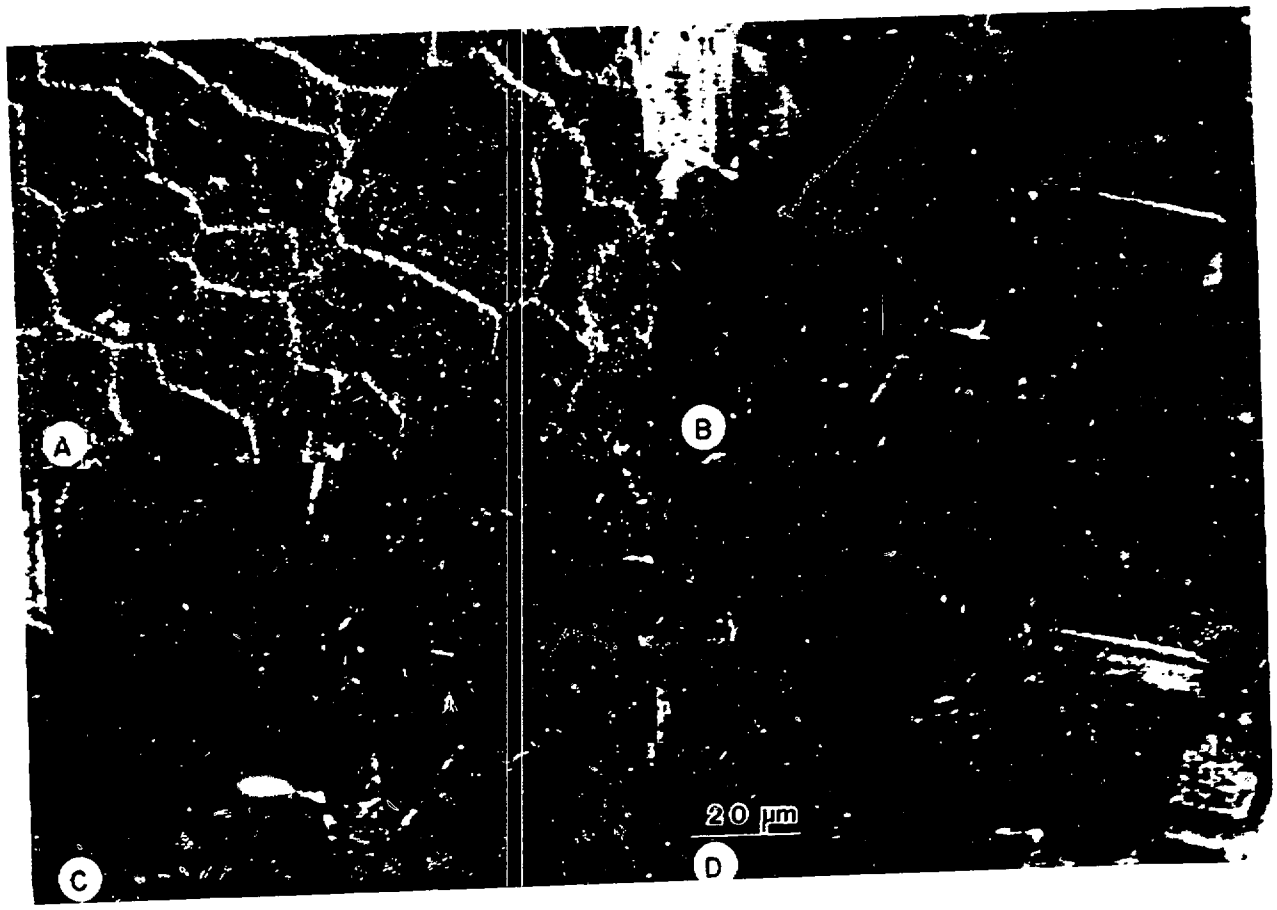

FIG. 6--Inconel alloy. (A) Optical micrograph after etching; (B), (C), (D) 2.5 GHz acoustic micrographs of unetched sample at three different focal positions (z = -1µ, -2µ, -4µ).

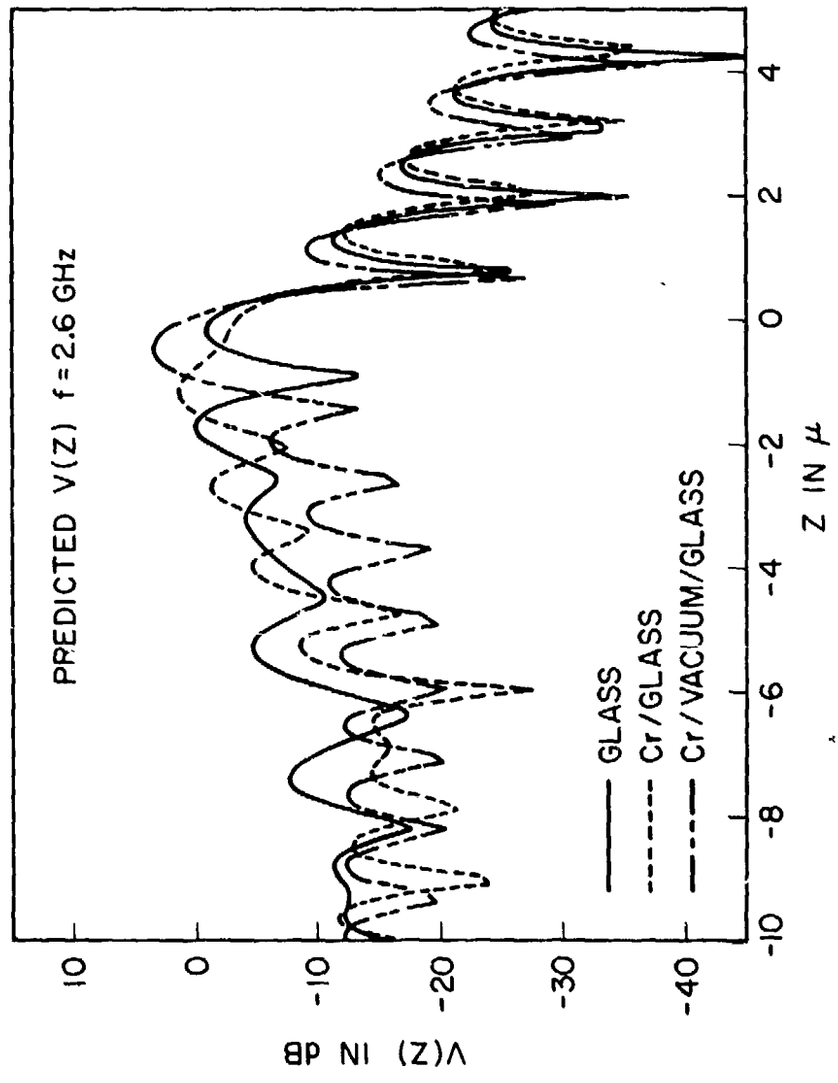
PREDICTED V(Z) f = 2.6 GHz
GLASS
Cr/GLASS
Cr/VACUUM/GLASS
V(Z) IN dB
10
0
-10
-20
-30
-40
-10
-8
-6
-4
-2
0
2
4
Z IN μ

FIGURE 7

ACOUSTIC MICROSCOPY OF CURVED SURFACES

R. D. Weglein
Hughes Aircraft Company
Canoga Park, CA 91304

ABSTRACT

The Metrology and Imaging modes of the acoustic reflection microscope are applied to spherically shaped specimens. Metrology is usually practiced by translating the specimen along the acoustic beam axis. This operation yields a measurement of the local Rayleigh velocity at a single location in the specimen plane. Imaging is accomplished through raster-scanning in the plane transverse to the beam axis.

The two modes are, in effect, simultaneously employed when a nonplanar surface of known curvature is scanned. The resulting image reveals nearly concentric rings with radial, periodic brightness variation, if the surface is spherical in shape. Stainless steel bearing balls of the type used in gyros are used to demonstrate the technique.

It is suggested that the obtained images represent a two-dimensional map of elastic properties applicable to convex (bearing ball) and concave (bearing raceway) surfaces.

THE ESSENTIAL ELEMENTS OF THE REFLECTION ACOUSTIC MICROSCOPE (Figure 1)

Images are obtained by raster scanning (in the X-Y plane) the highly converging sound beam across a planar object using a tiny drop of an "immersion" liquid, usually water. The object is usually situated in the acoustic focal plane and the reflected signals containing acoustic information are displayed on a synchronized cathode-ray tube monitor screen or storage oscilloscope. The focused acoustic beam is formed by a polished hemispherical depression in the sapphire rod shown in the figure. A piezoelectric transducer, consisting of a sputter-deposited layer of zinc oxide, converts the acoustic energy to and from the electrical signals that are imaged on the television screen. The reflection acoustic microscope may be likened to a pulsed radar imaging system in which the target "flies" at constant altitude and speed. In this manner, images of surface as well as subsurface detail are obtained depending on the altitude (at or below the surface) at which the focal plane intersects the object (target). Range-gating (not shown in the diagram) is used to select the desired image pulse from a host of spurious signals generated within the sapphire rod.

BEARING GEOMETRY (Figure 2)

A typical rolling element bearing consists of bearing balls, outer and inner raceways, as is shown in Figure 2. The surface of the bearing ball is convex and spherical. The raceways exhibit both convex and concave surfaces of nearly cylindrical curvatures. Portions of a gyro bearing ball were sectioned and examined in the acoustic microscope, that operates in the pulsed reflection mode in the frequency range near 400 MHz.

THE EXPERIMENT (Figure 3)

Bearing balls were sectioned to provide a comparison of AMS results on both planar and spherical surfaces with different surface finish. The 3/32 inch diameter balls were of 52100 stainless steel. The bearing ball sections were cemented to a fused quartz plate using a low temperature wax.

A scanning electron micrograph of the mounted sections is shown in Figure 3. The ball sections with their planar faces up expose a Hughes-polished 52100 stainless steel surface. The section denoted by the arrow is mounted with the spherical surface pointing up, and, therefore, presents a conventionally lapped bearing ball surface for diagnostic inspection. The arrow points to the apex of the sphere where the measurements were made.

EXPERIMENTAL RESULTS - I (Figure 4)

Acoustic material signatures (AMS) for these two cases are shown in Figure 4. The solid curve represents the measurement on the planar (Hughes-polished) surface, while the dashed curve is for the spherical bearing surface. The AMS curves are the video-detected transducer output power variation with object translation along the lens axis z. The AMS is the result of interference between two component waves that are reflected from the substrate (bearing) into the coupling liquid (deionized water, $v = 1.5$ mm/μs) and are vectorially summed in the piezoelectric transducer. As was shown previously, in the AMS mode Rayleigh waves are launched and detected coherently. From the physical model that was developed to explain the acoustic material signature[1, 2], the AMS period Δz_n is proportional to the square of the mean Rayleigh velocity in the plane of the substrate material. The measured period averaged over all periods in the figure yields the Rayleigh velocity v_R directly as given by Equation 1:

$$v_R = (v_\ell \cdot f \cdot \Delta z_N)^{1/2} = 23.56\,(\Delta z_N)^{1/2} \qquad (1)$$

where the frequency of 370 MHz has been assumed, and v_ℓ is the velocity in water. Measured and derived results from Figure 4 are listed in the table. It can be seen that some difference exists between the two measurements on surfaces that differ both in shape as well as in their preparation.

DISCUSSION (Figure 4 and Table)

1) The local Rayleigh velocity was measured in a 150 μm diameter spot.

2) Amplitude reduction in spherical surface AMS is caused by acoustic beam divergence from curved surface.

3) Rayleigh velocity difference is <u>not</u> caused by curvature.

4) Surface condition is not known but different on bearing surface and planar section.

5) The measured Rayleigh velocity on the bearing surface is 5 percent lower than on planar section. This is consistent with a postulated "softer" bearing layer that results from observed decarburation of the martensitic matrix of 52100 stainless steel, commensurate with precipitation of the harder carbide grains, that occurs during lapping at high temperatures[3].

6) The AMS further yields an upper limit for acoustic absorption a_{max} for 52100 stainless steel on the planar section, a_{max} = 0.12 dB/Rayleigh wavelength at 0.375 GHz.

7) The "skin depth" for Rayleigh waves in this experiment ($\lambda_R/2\pi$) is approximately 1.15 μm.

EXPERIMENTAL RESULTS - II

An acoustic image of the spherical bearing surface, taken with the acoustic microscope, is shown in Figure 5a. This raster-scanned micrograph was taken with the apex of the spherical bearing surface at approximately 40 μm inside the acoustic focal plane (see Figure 5b) at a magnification of 100X. The nominal focal distance of this acoustic lens was previously determined to be 450 μm. The image covers an area approximately 600 μm in diameter, as Figure 5b indicates. The same approximate area, imaged in a scanning electron microscope, is seen in Figure 5c. A number of common surface features, such as surface indentations and debris, are apparent in both acoustic and SEM micrographs.

Superimposed on this surface detail is a series of bright and dark circular regions, visible only in the acoustic micrograph. These nearly concentric rings, denoted by (1), (2), and (3) in Figure 5b, correspond to the similarly numbered peaks of the spherical surface AMS shown previously in Figure 4. The outer ring represents the annular surface approximately in the focal plane, while the inner two bright fields, (2) and (3), represent elastic information at 23 and 40 μm, respectively, in front of the focal plane.

The particular number of rings shown here is quite arbitrary. The number may be increased to a maximum that corresponds to the number of periods shown in Figure 4, merely by further translation of the bearing surface toward the acoustic lens.

DISCUSSION (Figures 5 and 6)

The generation of the concentric set of bright and dark rings in Figure 5a may be related to the corresponding peaks and valleys of the acoustic material signature of Figure 4 with the aid of the construction shown in Figure 6. The spherical surface (Figure 6a) is used as a transfer curve to convert the one-dimensional AMS curve (Figure 6b) into the two-dimensional AMS regional map shown in Figure 6c. The latter is, of course, a qualitative image as approximately inferred from the peaks and valleys of the acoustic material signature. A set of numbers relate spatially the peaks and valleys on the AMS to the corresponding rings of varying degrees of brightness.

Figure 5a, therefore, constitutes a regional map of the acoustic material signature on the bearing ball. Just as the null spacing in the AMS of Figure 4 yields Rayleigh velocity information locally on the surface, so does the radial spacing of the dark rings in Figure 5 yield the Rayleigh velocity in the two-dimensional plane. For example, the radial separation of the dark rings along any radial direction, denoted by Δr in Figure 5, corresponds to the AMS spacing Δz_N and is therefore a measure of the Rayleigh velocity in that direction. Any variation in Δr would therefore reveal a local change in stiffness, density, or a combination of these. In fact, some variation in the width of the dark rings is quite evident in the left side of the imaged region. However, the assignment of a quantitative interpretation must await a full physical characterization (e.g., layer etch and SEM examination) of the surface.

CONCAVE-CYLINDRICAL SURFACES (Figure 7)

The generation of a set of concentric rings of periodically varying brightness was postulated using the convex-spherical surface as a transfer curve. In a similar manner, the raster-scanned acoustic image of a concave-cylindrical surface may be postulated. Such a surface is closely related to the bearing raceway that together with balls constitutes a complete bearing. Figure 7 illustrates the generation of an acoustic image representing the concave raceway surface. The raceway in cross section (Figure 7a) shows a cylindrical surface in the plane of the bearing axis with radius not much larger than that of the bearing ball. The bearing surface is nearly cylindrical since the bearing radius is many times larger than the raceway radius. The predicted qualitative acoustic material signature map is shown in Figure 7c, as a linear bar pattern of alternating brightness but with a variable period dictated by the slope of the circularly cylindrical surface.

SUMMARY AND CONCLUSIONS

- Acoustic microscope was applied to NDE of gyro bearing balls.
- Spherical and planar surface layers of 52100 stainless steel were inspected.
- AMS and imaging modes were used to measure elastic properties.

- Rayleigh velocity and acoustic attenuation values were determined.
- N. D. depth profiling and grain distribution sizing appears possible.
- Concave (race) as well as convex (ball) surfaces may be inspected.
- A. M. is potential low cost NDE technique for Q. C. of bearings.

ACKNOWLEDGEMENT

Supported by DARPA Order No. 3578 under Contract No. F33615-78-C-5196.

REFERENCES

1) Weglein, R. D., "A Model for Predicting Acoustic Material Signatures", Appl. Phys. Lett., Vol. 34, No. 3, pp 179-181, Feb. 1979.

2) Parmon, W. and Bertoni, H. L., "Ray Interpretation of the Material Signature in the Acoustic Microscope", Electronic Letters, Vol. 15, No. 21, pp 684-686, Oct. 1979.

3) Baginski, W. A., "Phase 1 - A New Approach to Advance the State-of-the-Art of Liquid Lubricated Instrument Ball Bearings", Customer Contract No. 04-493431-FS-5, Prime Contract No. F33615-78-C-4196, July 1979. Appendix A to: Gardos, N. M., "Solid Lubricated Rolling Element Bearings - Semiannual Report No. 2", DARPA Order No. 3576, AFML Contract No. F33615-78-C-5196, Hughes Aircraft Company Report No. FR-79-76-1041, 15 August 1979.

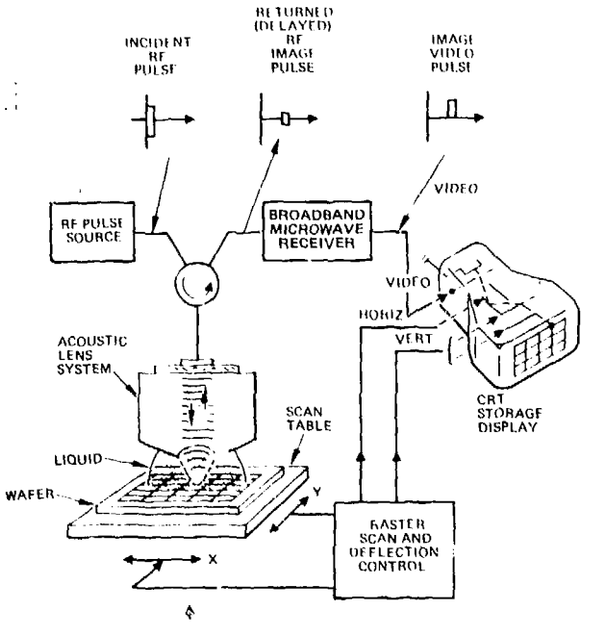

Figure 1. Schematic of Reflection Acoustic Microscope

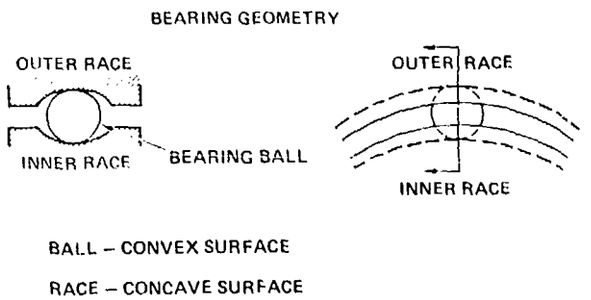

Figure 2. Bearing Geometry showing Convex (Ball) and Concave (Raceway) Surfaces

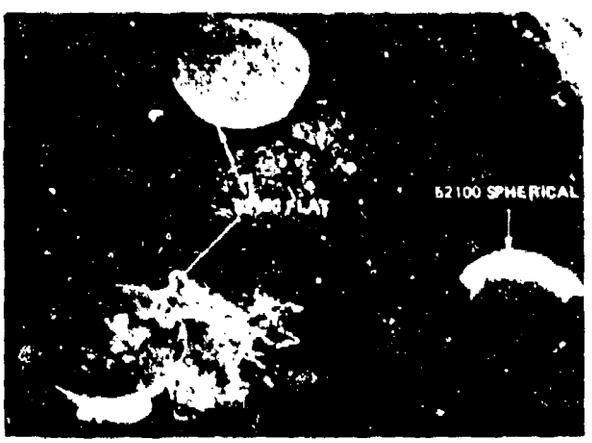

Figure 3. SEM Micrograph of Bearing Ball Sections Mounted for Diagnostic Inspection in Acoustic Microscope

TABLE. MEASURED RAYLEIGH VELOCITIES ON 52100 STAINLESS STEEL GYRO BEARING BALL

SURFACE	TYPE	Δz_N (μM)	v_R MM/μSEC
PLANAR	GROUND AND POLISHED 52100 AT HUGHES	14.6	2.85
SPHERICAL	52100 CONVENTIONAL LAPPING BY BALL MANUF	13.2	2.71
PLANAR	NO. 347 STAINLESS STEEL		2.88*

$^*v_R = \frac{0.87 + 1.12\sigma}{1+\sigma} v_{sh}$; $\sigma_{347} = 0.30$, $v_{sh} = 3.10$ MM/μSEC

Δz_N = AMS PERIOD

v_R = MEAN RAYLEIGH VELOCITY

v_{sh} = SHEAR VELOCITY

σ = POISSON RATIO

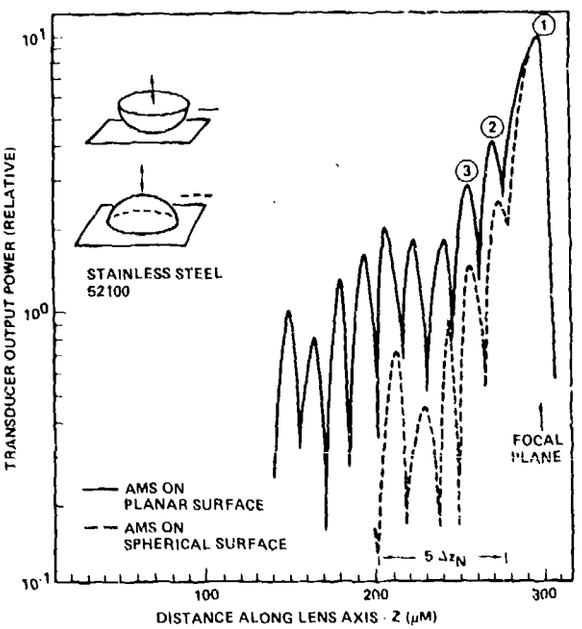

Figure 4. Acoustic Material Signatures on Planar and Spherical Surfaces

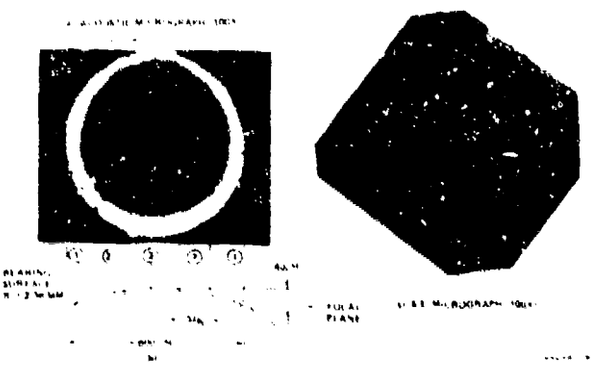

Figure 5. Acoustic and SEM Images of Gyro Bearing Ball Surface

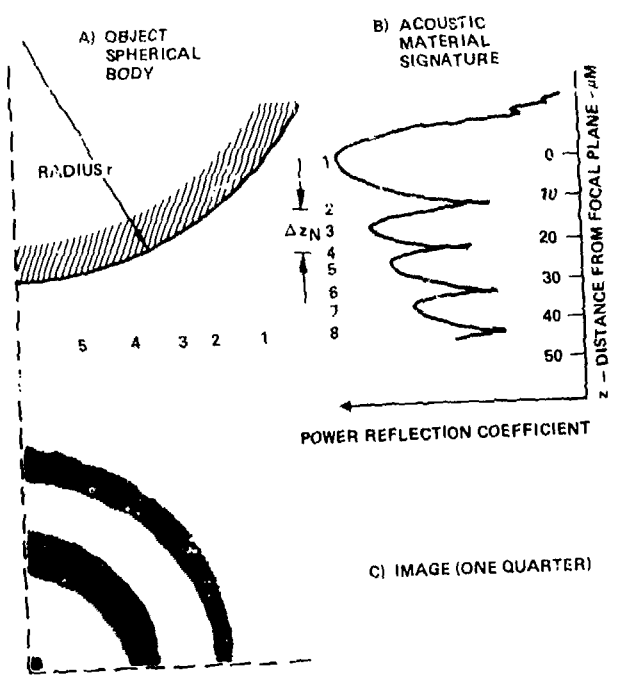

Figure 6. Acoustic Imaging of Convex Surface - Bearing Ball

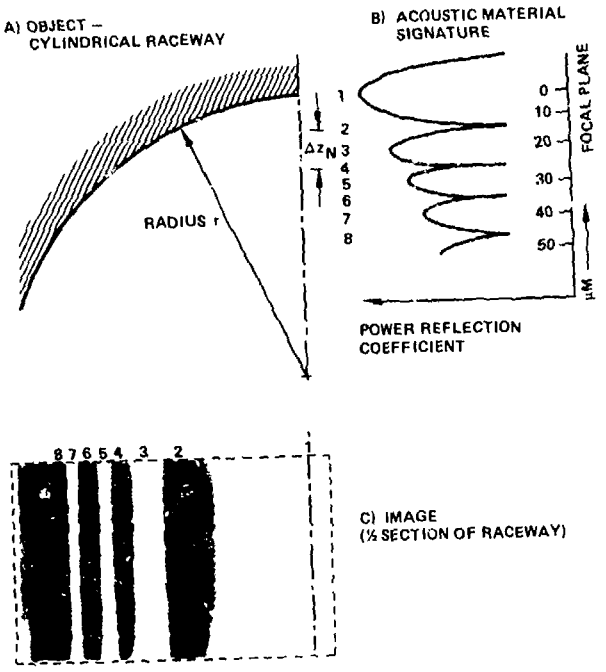

Figure 7. Acoustic Imaging of Concave Surface - Bearing Raceway

PHOTOACOUSTIC MICROSCOPY

L. D. Favro, L. I. Inglehart, P. K. Kuo, J. J. Pouch, and R. L. Thomas
Department of Physics, Wayne State University
Detroit, Michigan 48202

ABSTRACT

Recent advances in scanning photoacoustic microscopy (SPAM) for NDE are described. Conventional and phase-contrast modes are used to detect a well-characterized subsurface flaw in Al, and the results are shown to be in good agreement with calculations based upon a three-dimensional thermal diffusion model. Applications of the technique are given which demonstrate surface and subsurface flaw detection in complex-shaped ceramic turbine parts. Photoacoustic pictures are presented of an integrated circuit semiconductor chip and show 6 μm resolution.

INTRODUCTION

Scanning photoacoustic microscopy[1] (SPAM) is developing into a valuable NDE technique which is particularly applicable for the detection of very small (≳10 μm) surface flaws and somewhat larger flaws located in the near subsurface region (within 1 mm). The technique also has the advantage of being applicable to samples of complex shape. In this paper we first review the essential features of the theory and point out several important parameters by considering the simple case of an opaque solid slab containing a back surface step. We next describe an experimental verification of this theory from measurements of the magnitude and phase of the photoacoustic signal for a rectangular aluminum slab with a variable thickness back surface slot. NDE applications are illustrated by SPAM measurements on ceramics with surface and subsurface flaws (including a turbine stator vane) and on a semiconductor I/C chip.

EXPERIMENTAL TECHNIQUE

A block diagram of the apparatus is given in Fig. 1. The intensity of the laser is chopped at a frequency f_c, and focussed onto the surface of the sample. The resulting ac temperature profile of the surface periodically heats the layer of gas within a thermal diffusion length of the surface, and the resulting pressure variation couples through the gas to the microphone. The output of the microphone is monitored in magnitude and phase by means of a lock-in amplifier which is referenced to the chopping frequency.

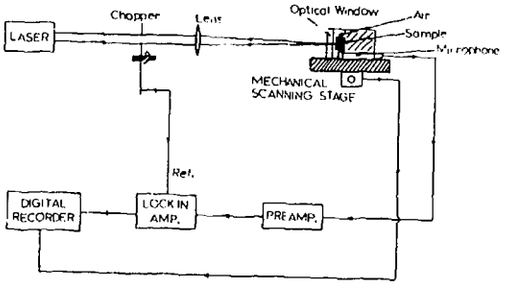

Fig. 1 Block diagram of the apparatus.

THEORY

Consider an opaque solid slab with a back surface step, varying in thickness from $\Delta \gg \mu_s$ to δ, where $\mu_s = (2\alpha/\omega)^{1/2}$, $\omega = 2\pi f_c$, and α is the thermal diffusivity of the sample. We have carried out a Green's function calculation[1] of the resulting ac temperature profile at the surface of the sample and find that the normalized magnitude and phase of the resulting photoacoustic signal is given in Figs. 2 and 3, respectively. Excellent agreement is found with experimental measurements[1] on an aluminum slab containing an 850 μm wide, back surface slot (see Fig. 4). These experiments show that the back surface is detectable in the phase at a depth > 1.82 μ_s, or nearly 1.5 mm for our lowest values of f_c.

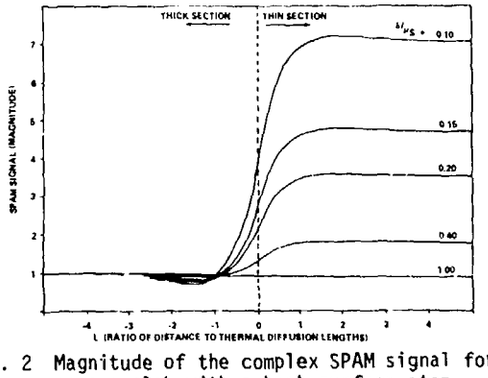

Fig. 2 Magnitude of the complex SPAM signal for an opaque slab with a back surface step.

APPLICATIONS

In order to illustrate the technique for NDE applications, we show a Si_3N_4 ceramic with a 200 μm Fe inclusion and a Knoop indentation[2] (Fig. 5); slip cast Si_3N_4 ceramic stator vanes[3] with surface and subsurface defects (Figs. 6, 7), and a semiconductor IC chip[4] (Fig. 8) with 6 μm resolution.

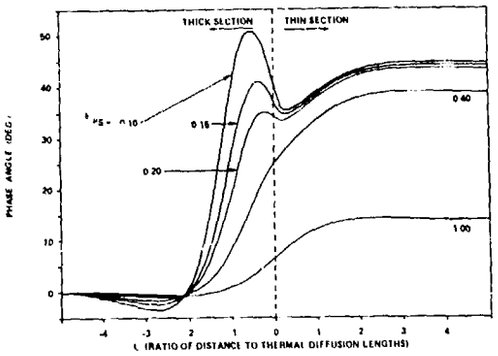

Fig. 3 Phase of the complex SPAM signal for an opaque slab with a back surface slab.

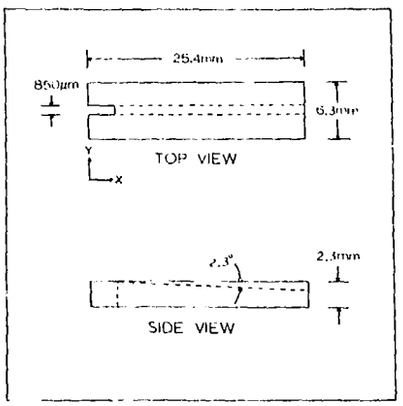

Fig. 4 Aluminum slab with a subsurface rectangular slot.

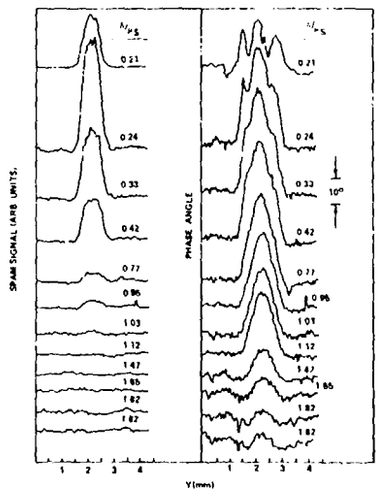

Fig. 5 Magnitude and phase of the observed SPAM signal for the sample described in Fig. 4.

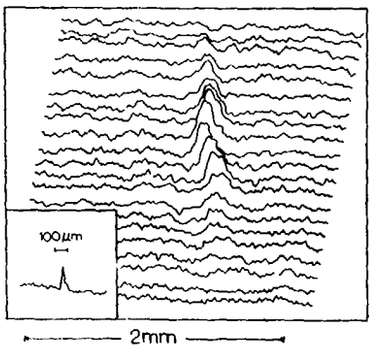

Fig. 5 SPAM signal for a Si_3N_4 ceramic with a 200 μm Fe inclusion. Inset shows the SPAM signal for a Knoop indentation in a Si_3N_4 ceramic.

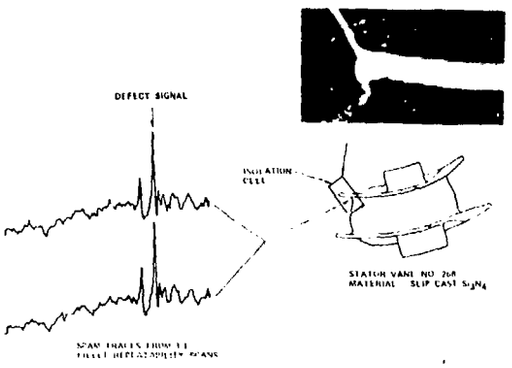

Fig. 6 SPAM traces of the fillet region of the trailing edge of a slip cast Si_3N_4 turbine stator vane.

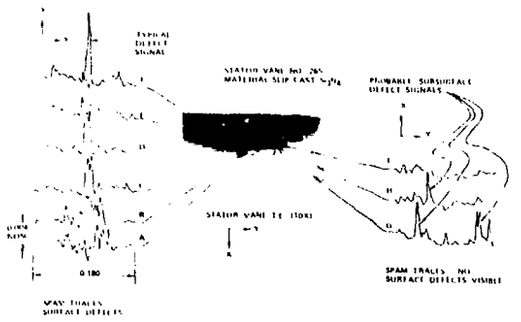

Fig. 7 SPAM traces of a Si_3N_4 stator vane with subsurface defects.

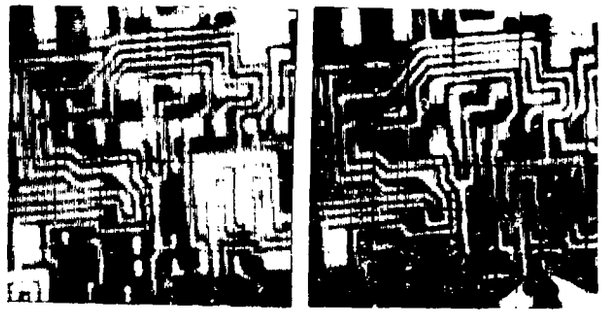

Fig. 8 SPAM micrographs of an I/C circuit. The area scanned is 0.032 inch x 0.032 inch.

ACKNOWLEDGEMENTS

This research was supported by ARO under Contract No. DAAG 29-C-0151, and by AFML/APL under contract No. F33615-77-C-5171, as a subcontract from AiResearch Manufacturing Company of Arizona. The authors wish to acknowledge with thanks the collaboration of J. Schuldies of AiResearch and J. Srinivasan of Carborundum on the ceramic studies, and Y.H. Wong of Bell Labs on many phases of this work.

REFERENCES

1. R. L. Thomas. J. J. Pouch, Y. H. Wong, L. D. Favro, P. K. Kuo, and Allan Rosencwaig, J. Appl. Phys. 51, 1152 (1980).
2. J. J. Pouch, R. L. Thomas, Y. H. Wong, J. Schuldies and J. Srinivasan, J. Opt. Soc. Am. 70, 562 (1980)
3. L. I. Inglehart, R. L. Thomas, and J. Schuldies (submitted for publication.
4. L. D. Favro, P. K. Kuo, J. J. Pouch, and R. L. Thomas, accepted for publication in Appl. Phys. Letters.

THEORY OF ACOUSTIC EMISSION

John A. Simmons and Roger B. Clough
Metallurgy Division
National Bureau of Standards
Washington, D.C. 20234

ABSTRACT

A theory of acoustic emission is presented based on a Green's function type of formalism. Sources are represented by stress drop tensors and conditions derived from which the source can be considered small in terms of wavelength and distance to the transducer. These "pseudopoint" sources are examined over a restricted frequency bandwidth, called the "informative bandwidth". Such a bandlimited system may be described by a transfer function matrix type of formalism, facilitating the analysis and reducing the inverse probelm--where the source is not known a priori--to a deconvolution operation. Due to the tensor nature of the source, multiple transducer measurements (generally six) are necessary to reconstruct the source stress drop. The difficulty of using spectral techniques for data analysis in the presence of multiple sources is discussed. In addition, the strong directionality of the signal with respect to source type and orientation is illustrated by calculating the acoustic emission signals generated by loop expansion of slip and climb (prismatic collapse) type dislocations.

Unidentified Speaker: John, I have a question from the perspective of one who is familiar with a big class of practical acoustic emission proolems. What, if any, fundamental research do you think would be most likely to be useful? What kind of questions would you like to have answers to?

John Simmons (NSF): The first thing we need to know: What are the characteristics of the acoustic emission business so we can discriminate it from the nice patterns you have mentioned. We also need data coming from broadband transducers. We intend, as part of this program, to evaluate the current state-of-the-art, define such a fiberoptic transducers, find out which is more feasible in moving from a laboratory environment into a field environment, and using them to obtain broadband data, as well as regular PZT transducers in the study.

Unidentified Speaker: Can you show the (inaudible)

John Simmons: It is a linear least squares polynominal.

Unidentified Speaker: The two X, (inaudible)

John Simmons: It's just the value of this polynominal. You obtain certain features from your test data, and you assign a weight to each feature. And then you just take the sum of all those weights until you get a number. That's what the y-axis is.

Unidentified Speaker: What are the (inaudible)

John Simmons: In this particular study: There were five features. In the time domain, you were looking at the odd correlation at lag 13 You were looking at the mean of the wave form, the standard deviation of the waveform, and the time domain. Also, you were looking at the total power and the frequency domain.

REPRODUCIBLE ACOUSTIC EMISSION SIGNATURES BY INDENTATION IN STEELS

Roger B. Clough and John A. Simmons
Metallurgy Division
National Bureau of Standards
Washington, D.C. 20234

ABSTRACT

Creating reproducible signals from defects is of great importance for quantitative studies of acoustic emission (AE). A method of doing so is presented here which consists of indentation of hardened steel plates. A survey was made of a variety of steels, including A533B pressure vessel steel with an embrittled weld as well as embrittled W1, O1 and O2 tool steels. Regions in these steels with a Rockwell C hardness greater than about 50 produced detectable AE during indentation. In many cases the signals were reproducible over an appreciable range and appeared to be the same for epicenter measurements as those produced by sudden unloading. However, monitoring on the same surface as the crack in some cases produced sets of two different but reproducible signals which gradually evolved with repeated loading which could be due to crack branching or zigzag motion. Regions in the steels with a hardness less than about 40 on the Rockwell C scale produced no detectable AE, even with appreciable plastic deformation. Examination with scanning electron microscopy indicated that the AE signals were produced by the nucleation and incremental growth of subsurface cracks, generally penny-shaped, 1 to [illegible] millimeter in size. A typical fracture toughness value for such cracks in an embrittled O2 tool steel was calculated to be about $19 MNm^{-3/2}$. AE was also produced in as-received A533B steel by indentation fatigue. The method suggests itself for materials studies of AE as well as a nondestructive method for in situ examination of structures for embrittlement.

William Pardee, Chairman (Rockwell Science Center): I have one quick question. If I were an experimenter with access to the best current hardware electronics, what experiment would you most like to see me do? Which one would be most useful in terms of evolution of the theory? What is the most useful way to take advantage of the theoretical developments?

John Simmons (NBS): Multi-channel source characterization.

William Pardee, Chairman: What frequency range do you think is necessary?

John Simmons: The typical range for that is about between 50 kilohertz and a megahertz.

IN-FLIGHT ACOUSTIC EMISSION RESEARCH

John M. Carlyle
Naval Air Development Center
Warminster, Pennsylvania 18974

ABSTRACT

The detection of crack growth in aircraft structures through the use of acoustic emission techniques has been demonstrated to be feasible in recent years. Numerous problems still remain to be overcome, but a new DARPA program will address the most critical areas and build a flyable acoustic emission monitor demonstrating the new technology. A history of the field and a program overview are given.

INTRODUCTION

Stress waves which result when a material reacts to decrease localized stress concentrations (caused by defects) are termed acoustic emissions. With suitable electronic instrumentation it is possible to locate the source of the emissions and to predict the life expectancy of the part which is emitting. Acoustic emission monitoring is especially attractive for large structural applications (such as nuclear reactor pressure vessels and highway bridges) since minute inch by inch inspection is not necessary in order to locate flaws. Furthermore, the sensitivity of the technique often permits the existence of a flaw to be positively confirmed before it is possible to do so using visual microscopy, ultrasonic, or electromagnetic nondestructive inspection.

Recognizing the potential of acoustic emission monitoring, numerous researchers have devoted effort in recent years toward developing technology that would allow aircraft structures to be monitored with acoustic emission techniques during flight. The rest of this paper will outline tnose projects which resulted in acoustic emission data being gathered during flight, and will discuss how a present DARPA program relates to these projects and how it is designed to further the development of the technology in the field of in-flight acoustic emission monitoring

PREVIOUS IN-FLIGHT AE PROJECTS

C-5A

In-flight acoustic emission research may properly be said to have started with the work of C. D. Bailey at Lockheed-Georgia on a Lockheed C-5A transport from 1973 to 1975. During this period Bailey and his co-workers defined the frequency regime that could be utilized for in-flight acoustic emission monitoring by utilizing a specially designed swept frequency analyzer that monitored 9 locations on the wing, empennage, and landing gear, all fabricated from 7075-T6. This study resulted in the general conclusion that for a 6 dB signal-to-noise ratio the AE monitor should operate at a frequency no lower than 500 kHz for most structural locations [Ref. 1]. They then set about determing if crack AE could be detected during flight. From the results of their noise survey, they concluded that it was feasible to build a monitor that would detect unstable crack growth. Additional studies performed with a commercial linear locating device operating at 750 kHz were inconclusive insofar as detecting stable in-flight cracking was concerned. Bailey has privately stated that he believed this was due to EMI; it could also be due to insufficient power supply filtering and regulation on the laboratory style equipment employed, as well as temperature sensitive components in the preamplifiers that were used (which caused oscillations that were noted in Ref. 1).

KC-135

Building on the experiences of Bailey et al, M.E. Mizell and his colleagues at Tinker Air Force Base designed, in 1976, a custom 32 channel narrow-band acoustic emission system operating at 250 kHz to monitor the lower center wing panels of a Boeing KC-135 tanker. These panels, made from 7178-T6, are brittle and tend to fracture completely under flight loads, producing cracks up to 7 inches long. Taking complete advan- of the fact that only large unstable cracking was required to be detected, Mizell set the triggering parameters of his monitor so that only an AE burst with a frequency content of between 200 to 300 kHz and a duration of at least 576 μS would produce an output [Ref. 2]. Although these settings (and other aspects of the monitor design such as transducer/cable impedance matching transformers and transducer temperature compensators) rejected EMI arising from the operating aircraft and also eliminated benign structural acoustic noise and noise caused by feedback, the sensitivity of

the acoustic emission monitor was compromised to the point that incremental crack growth of less than 5 cm was undetectable. Nevertheless, the monitor fulfilled its objective of sensing complete panel failure during flight, and it is now being installed routinely on Air Force KC-135's.

CF-100

In 1978 S. L. McBride of the Royal Military College of Canada started a program to detect stable crack growth in the forward wing trunnion of the North American CF-100 fighter. Departing from previous work, McBride utilized a single channel system that recorded the acoustic emission waveform via a transient recorder between the frequency limits of 0.1 to 1.0 MHz. The physical situation was advantageous in that the 7075-T6 port wing trunnion contained a 3 mm long crack that was known to grow at an average rate of 5 μm/flying hour. Although it was discovered that amplitude discrimination was not sufficient to separate structural noise from crack noise, McBride was able to successfully use frequency spectral data to distinguish crack AE from other noises. Based on a comparison with laboratory data he reported detecting during flight an acoustic emission signal resulting from a crack advance which generated 1 mm^2 of new fracture surface [Ref. 3]. The disadvantage of this program was that the system design required processing thousands of noise signals for every genuine acoustic emission crack signal and that its sensitivity level for stable crack detection was rather low (a factor of 100 less sensitive than laboratory systems at RMC).

MB 326

The most recent in-flight acoustic emission work was performed by P. H. Hutton and his colleagues at Battelle PNL in 1979 on the wing center section tension member of a Macchi MB 326 trainer operated by the Royal Australian Air Force. This class of aircraft has a well-characterized history of fatigue cracking originating from two specific holes in the 4340 tension member, and periodic inspections (100 flight hour intervals) are made with ultrasonic and/or magnetic rubber nondestructive testing techniques to track the growth of the cracks. Battelle designed a 2 channel coincidence detector which utilized especially fabricated 400 kHz resonant transducers and band-limited preamplifiers along with special power supply filtration and regulation to monitor a specific bolt hole containing several cracks having a total surface length of 7 mm, the longest of which was 2.3 mm. Analysis of the AE data has indicated that the worst type of flight from a cracking stand point (as revealed by AE in this study) is low level flying, followed by acrobatics - presumably this is because of the increased wing flexure and impulsive loading produced by low level flight conditions [Ref. 4]. Crack growth has been found to be linear with the number of acoustic emissions emitted from the bolt hole area (an average of 0.16 μm of surface length/AE event) and benign noise such as EMI and structural vibrations have not proved to be a problem, as evidenced by a drastic reduction in AE counts (from an average of 50/hour to 0/hour) when the accept zone was electronically shifted to an area with no bolt hole [Ref. 5]. The recognized weakness of this program is that there is no protection against accepting fastener noise arising from inside the accept zone of the monitor. Thus it is conceivable that the conclusions described above are fallacious, resulting from the fortuitous behavior of the bolt moving in the hole.

DARPA IN-FLIGHT AE PROGRAM

The conclusions which can be drawn from previous in-flight acoustic emission programs are:

(1) Continuous in-flight acoustic emission monitoring is more desirable than periodic proof-load monitoring for detecting sub-critical crack growth, as evidenced by the acoustic emission data gathered during low level flight conditions and during acrobatic maneuvers with the Macchi MB 326.

(2) Frequency limits for triggering in-flight monitoring systems must be higher than the 100 kHz range generally used in laboratory environments and care must be taken in the system design to guard against EMI and the effects of temperature and altitude on the performance of the monitoring system.

(3) Some form of spatial discrimination must be employed to limit the acceptance of signals to only those arising from a specific area of interest. This allows not only for better noise rejection, but also permits the use of a higher sensitivity to detect smaller crack growth increments.

(4) Techniques need to be developed to positively distinguish between acoustic emissions generated by crack processes and those emissions created near the crack by benign structural phenomena such as fastener fretting.

Recently, a DARPA program has been instituted which will address the technology development need described in (4) above. The program is planned to consist of three phases, the first of which will utilize a selected advanced transducer concept (such as fiber optics, composite piezoelectric, FET, EM/T, PVF, etc) as well as a broad-band conventional PZT transducer to acquire waveform data between the limits of 100 kHz and 2.0 MHz from fatigue cracks and various noise sources (including EMI, fretting bolts, and hydraulic systems) in 2024-T851 and 7075-T651 aluminum undergoing cyclic loading. Following the ideas of Doctor, Harrington and Hutton, features will be extracted from the data set and an algorithm will be developed to classify the waveform as either crack AE or noise [Ref. 6). Figure 1 demonstrates one of the concepts which will be investigated. Phase 2 will consist of fabricating a prototype airborne acoustic emission monitoring system that incorporates these new signal discrimination concepts, as well as techniques proven effective by previous experimenters. The final phase will be composed of a flight test of the new monitor.

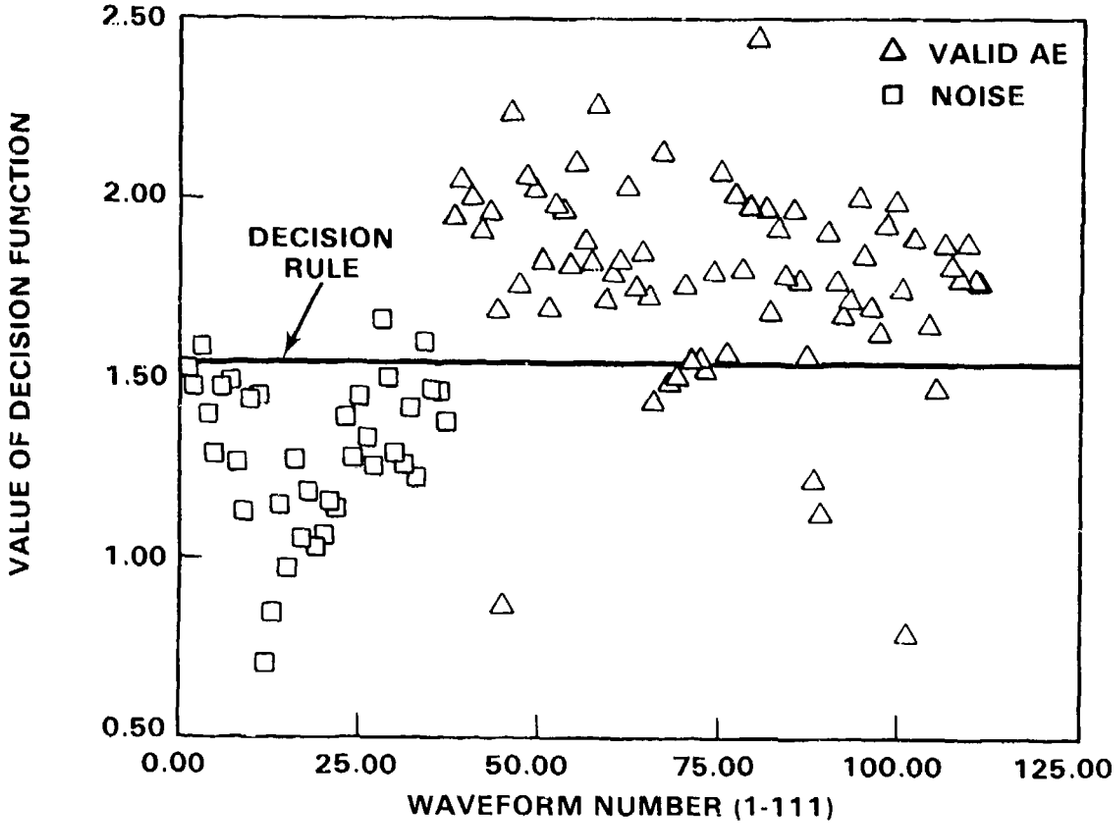

Fig. 1 Result of a pattern recognition study on separating crack AE from noise. Five features were used in a least squares decision rule; the success rate was 89% for the AE and 92% for the noise. (After Doctor, etal, Ref 6)

REFERENCES

1. Lewis, W. H., Jr., Bailey, C. D., and Pless, W. M., "Acoustic Emission Structure-Borne Noise Measurements on Aircraft During Flight", *Technical Report AFML-TR-183*, AF Contract F33(657)-74-C-0588, May 1976

2. Mizell, M. E., and Lundy, M. T., "In-Flight Crack Detection System for the C-135 Lower Center Wing Skin", 25th DOD Conference on NDT, AMMRC, Watertown, MA, 31 Aug - 2 Sep 1976

3. McBride, S. L., "Canadian Forces In-Flight Acoustic Emission Monitoring Program", Technical Report AFML-TR-78-205, Proceedings of the ARPA/AFML Review of Progress in Quantitative NDE, AF Contract F33615-74-C-5180, Pg. 101, Jan 1979

4. Hutton, P. H., and Skorpic, J. R., "Develop the Application of a Digital Memory Acoustic Emission System to Aircraft Flaw Monitoring", Battelle Report PNL-2873, ARPA Order 3476, Code 7DL0, December 1978

5. Hutton, P. H., and Skorpic, J. R., "In-Flight Crack Monitoring Using Acoustic Emission", 26th International Instrumentation Symposium, Seattle, WA, 8 May 1980

6. Doctor, P. G., Harrington, T. P., and Hutton, P. H., "Pattern Recognition Methods for Acoustic Emission Analysis, Battelle Report PNL-3052, July 1979

William Pardee, Chairman (Rockwell Science Center): Are there questions?

John Carlyle (Navel Air Development Center): This is one problem when you're talking about the reproducible sources of acoustic emission (inaudible), but the pictures of the crack you showed were complicated and different.

John Simmons (NSF): That's right.

John Carlyle: How would they generate the same (inaudible)

John Simmons: Simply put: We are not sure. Anyone who has done indentation studies in glass, for example, knows that when you take the indenter out, you get crack propagation in all kinds of directions that are due to the release of the residual stresses. We cannot say during what part of the process these initiative events took place, but we are aware of that fact. We are also aware of the fact that a lot of these cracks are turning. Many of them, however, tend to have what appears to be a rather constant direction. But the answer really is: we don't know; our goal here was to show that, in fact, you could get reproducible acoustic emission events from real materials. As with any expriment, you often times get more unanswered questions than you produce answers. And that's certainly, in our mind, an important unanswered question.

Wolfgang Sachse (Cornell University): How do you know the signals do not come from the indenter?

John Simmons: We tried a number of experiments using different loading apparatuses and different indenters, and you can use materials that don't emit, and it's absolutely silent. So we tried all of what you would call the standard hygienic practices to make sure that the emissions did not come from the indenter. Actually, a much more subtle problem is, in fact, a problem of friction, and this is really very similar to John Carlyle's point. If you lay the plate under the indenter, the fact that the indenter swings down a lever arm puts a slight horizontal component into the force and, remarkably enough, sometimes one block will slip against the place where it's resting. You can get signals that look almost identical with standard acoustic emission signals. And that's, we find, another very disconcerting point. This is easily stopable, once you know it's there, but this ability to distinguish between frictional events and actual emission events is an unanswered question.

Mike Gardos (Hughes): As a lubrication technologist, I am delighted that you have problems where I can help you.

John Simmons: Actually, we use sticky tape to stop it; we don't lubricate.

Mike Gardos: Yes, close enough. Maybe 100 angstroms of mollysulfide that you can spot on the surface would help you. The other thing I would like to mention, I have seen a lot of new indentation studies, and I'm wondering why didn't you use something that's a little more symmetrical like the Brinnel probe, for example. If you load a ball against a glass plate, depending on the load and, of course, the state of the glass, you get the hertzian cone-cracking phenomena, which just happens to be a very nice, symmetrical one. If your loads are higher, then you get not only the circular cracks, but also the radial ones, which are also very symmetrical. So I am quite curious: why wouldn't you use something which is a little more predictable?

John Simmons: Because you need the stress concentration at the indentation tip. In fact, a couple of days before I left, Roger was making up the slide of these 400 reproducible ones. He came into me one evening, and he said, "John, I'm jinxed. I can't get the thing to emit." And we went back and we checked every parameter, and we couldn't find it. And finally, I looked at the indenter and the indentation - and it had just the tiniest, microcrack near the tip of the indenter. And I said, "Roger, I'll bet you because this is very strong steel, you need the tremendous stress concentration at the tip in order to do this. Why don't you put a new indenter in?"

Mike Gardos: You were forced to use the non symmetrical.

John Simmons: You need the stress concentration.

Mike Gardos: But I'm quite serious about the lubricant. If nothing else, spray a little teflon.

Chris Burger (Iowa State University): John, could you just run through your indentation fatigue? How do you do that indentation procedure? You put the load on and take it off? You move the load completely?

John Simmons: Yes. It's not very sensitive to whether you remove the load completely, but in fact we do. If you look at the apparatus, the thing is jacked up at the end. So essentially, we just take the indenter up to where it essentially removes all the load, and then we drop it back in. And we keep doing this. And this almost certainly builds up very strong residual stress

zones. I believe it's from that strong residual stress zone that the cracks tend to be nucleated.

William Pardee, Chairman: Thank you, John

SCATTERING OF SURFACE ACOUSTIC WAVES FROM AN ELASTIC PLATE ATTACHED TO A HALF-SPACE WITH A VISCOUS COUPLANT

D. B. Bogy and Y. Angel
University of California, Berkeley
Berkeley, California 94720

ABSTRACT

The results presented here are part of a study of the interaction between an electro-mechanical transducer plate element and wavelengths in the test structure that are comparable to the plate dimensions. The steady time-harmonic problem is reduced to a system of singular integral equations for determining the tractions generated at the interface between the plate and half-space where a thin viscous couplant is applied. This system is solved numerically for various values of couplant viscosity and incident wavelength. Graphical results for interface tractions and reflected power are presented.

INTRODUCTION

We are interested in the interaction between electro-mechanical transducers and the elastic waves in a test medium in cases when the wavelengths are comparable to the dimensions of the transducer and the propagation vector is not normal to the interface. The ultimate goal of this NSF funded project at Berkeley is to predict what mechanical disturbance is input to the transducer from the electrical output signal. As a first step we will try to predict the electrical output given the mechanical input. Under the conditions of interest the mechanical loading is not spatially uniform over the contact face of the transducer. We will therefore need a plate theory for the piezoelectric element with electroded surfaces which can accommodate the kinds of mechanical and electrical boundary conditions that are appropriate to the transducer design and mounting and the electrical circuitry to which it is connected. Such a plate theory has been derived in Bugdayci and Bogy [1].

The work presented here is also only a preliminary part of this project, but here we focus on the purely mechanical problem of determining the interaction of an elastic plate with a half-space. Specifically, we seek to understand the stresses generated between the half-space and plate when a surface wave impinges on the plate that is attached through a viscous couplant. The dependence of these interface stresses on couplant viscosity and the incident wavelength are the primary concern. We also calculate the power of the reflected and transmitted surface waves as a function of these parameters since these quantities can be compared with experiments. The results summarized here are derived in complete detail in Angel [2] and Angel and Bogy [3].

PROBLEM FORMULATION AND REDUCTION TO INTEGRAL EQUATIONS

Figure 1 depicts the plane strain problem of a surface wave impinging on an elastic plate that is in contact through a viscous couplant with the half-space. All the physical parameters of the problem are shown.

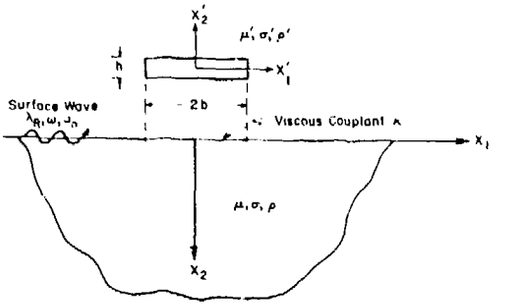

Fig. 1 Geometry, material properties and coordinates for half-space, plate and couplant. Plate and half-space are in contact over $|x_1| < b$, i.e., couplant thickness is neglected.

The problem is easier to formulate when considering the plate as a 3-dimensional continuum. Then, in the reduction to a 2-dimensional plate theory all the required boundary conditions and interior loading will be incorporated. The conditions on the plate are

$$\sigma'_{22}(x'_1, \tfrac{h}{2}, t) = \sigma'_{21}(x'_1, \tfrac{h}{2}, t) = 0, \ |x'_1| < b,$$

$$\sigma'_{11}(b,x'_2,t) = \sigma'_{12}(b,x'_2,t) = \sigma'_{11}(-b,x'_2,t)$$

$$= \sigma'_{12}(-b,x'_2,t) = 0, \ |x'_2| < \tfrac{h}{2}, \qquad (1)$$

$$- \sigma'_{22}(x'_1, -\tfrac{h}{2}, t) = t'_2(x'_1,t),$$

$$- \sigma'_{21}(x'_1, -\tfrac{h}{2}, t) = t'_1(x'_1,t),$$

in which $t'_1(x'_1,t)$ and $t'_2(x'_1,t)$ represent the components of the traction vector applied to the bottom surface of the plate.

The half-space is assumed to be traction free on the boundary outside the contact region. So

the half-space boundary conditions are

$$\sigma_{22}(x_1,0,t) = \begin{cases} 0, & |x_1| > b \\ -t_2(x_1,t), & |x_1| < b \end{cases},$$

$$\sigma_{21}(x_1,0,t) = \begin{cases} 0, & |x_1| > b \\ -t_1(x_1,t), & |x_1| < b \end{cases}. \tag{2}$$

The adhesive bond conditions between the plate and half-space are expressed as

$$u_2(x_1,0,t) = -u_2'(x_1, -\tfrac{h}{2},t),$$

$$\sigma_{21}(x_1,0,t) = \kappa[\dot{u}_1(x_1,0,t)-\dot{u}_1'(x_1, -\tfrac{h}{2},t)],$$

$$t_1(x_1,t) = -t_1'(x_1,t),\ t_2(x_1,t) = t_2'(x_1,t), \tag{3}$$

$$|x_1| < b .$$

We assume an incident Rayleigh wave with $e^{-i\omega t}$ time dependence traveling in the half-space in the x_1-direction is scattered by the plate. Therefore the displacement and stress fields in the half-space are decomposed into their incident and scattered parts as

$$u_\alpha = u_\alpha^{(I)} + u_\alpha^{(S)},\quad \sigma_{\alpha\beta} = \sigma_{\alpha\beta}^{(I)} + \sigma_{\alpha\beta}^{(S)}, \tag{4}$$

in which $u_\alpha^{(I)}$ and $\sigma_{\alpha\beta}^{(I)}$ are prescribed by the incident Rayleigh wave.

The scattered fields in the half-space can be obtained from Lamb's [4] solution. A complete and thorough re-derivation of this solution is carried out in Angel [2] in order to arrive at a form that is suitable for our computations. It is convenient to decompose the problem into its physically symmetric and antisymmetric parts with respect to x_1 and to denote them respectively by superscripts "S" and "A". In time-reduced form the scattered displacements on the boundary of the half-space can be expressed as

$$u_\alpha^{(S)S}(x_1,0) = \int_{-b}^{b} G_{\alpha\beta}(x_1-\xi)t_\beta^S(\xi)\,d\xi$$

$$u_\alpha^{(S)A}(x_1,0) = \int_{-b}^{b} G_{\alpha\beta}(x_1-\xi)t_\beta^A(\xi)\,d\xi \tag{5}$$

in which $G_{\alpha\beta}(x_1-\xi)$ are the surface displacement Green's functions of Lamb's solution.

After reducing the problem in (1) to its corresponding plate theory formulation and decomposing into plate extension and bending, we obtain the solutions in the form

$$u_1'^S(x_1') = \int_0^b G_1'^S(x_1',\xi)t_1'^S(\xi)\,d\xi$$

$$u_2'^S(x_1') = \int_0^b G_{2\beta}'^S(x_1',\xi)t_\beta'^S(\xi)\,d\xi$$

$$u_1'^A(x_1') = \int_0^b G_1'^A(x_1',\xi)t_1'^A(\xi)\,d\xi \tag{6}$$

$$u_2'^A(x_1') = \int_0^b G_{2\beta}'^A(x_1',\xi)t_\beta'^A(\xi)\,d\xi$$

in which $G_1'^S$, $G_1'^A$ are the symmetric and antisymmetric Green's functions for the plate extension and $G_{2\beta}'^S$, $G_{2\beta}'^A$ are those for plate bending.

The integral equations determining the interface tractions result from use of (5), (6) together with the appropriate form for the incident Rayleigh wave in (1)-(4) and they appear in dimensionless form, after appropriate differentiations and integrations, as follows

$$i\alpha\int_{-1}^{x}\tilde{t}_1^L(\xi)d\xi + \int_{-1}^{1} V G_{11}(x,\xi)\tilde{t}_1^L(\xi)d\xi$$

$$+ k^{-1}\int_0^1 V G_1'^L(x,\xi)\tilde{t}_1^L(\xi)d\xi$$

$$+ \int_{-1}^{1} V G_{12}(x,\xi)\tilde{t}_2^L(\xi)d\xi = \tilde{f}_1^L(x)\ ,$$

$$\frac{\varepsilon^2}{2(1-\varepsilon^2)}\ \tilde{t}_1^L(x) \quad - \quad k^{-1}\int_0^1 \Lambda G_{21}'^L(x,\xi)\tilde{t}_1^L(\xi)d\xi$$

$$+ \frac{1}{2\pi(1-\varepsilon^2)}\int_{-1}^{1}\frac{\tilde{t}_2^L(\xi)}{\xi-x}\,d\xi + \int_{-1}^{1} K_{21}(x-\xi)\tilde{t}_1^L(\xi)d\xi$$

$$+ \int_{-1}^{1} \operatorname{sgn}(x-\xi)\bar{K}_{22}(x-\xi)\tilde{t}_2^L(\xi)d\xi$$

$$+ k^{-1}\int_0^1 \Lambda G_{22}'^L(x,\xi)\tilde{t}_2^L(\xi)d\xi = -\tilde{f}_2^L(x),$$

$$\int_{-1}^{1} V G_{21}(1,\xi)\tilde{t}_1^S(\xi)d\xi + \int_{-1}^{1} V G_{22}(1,\xi)\tilde{t}_2^S(\xi)d\xi$$

$$+ k^{-1}\int_0^1 V G_{22}'^S(1,\xi)\tilde{t}_2^S(\xi)d\xi = \tilde{f}_3$$

in which superscript "V" denotes integration from -1 to x, "Λ" denotes differentiation, K_{21} and $\overline{K}_{22}$ are defined by

$$\overset{\Lambda}{G}_{22}(x) = -\frac{1}{2\pi(1-\varepsilon^2)x} + \mathrm{sgn}(x)\overline{K}_{22}(x)$$
$$\overset{\Lambda}{G}_{12}(x) = -\frac{\varepsilon^2}{2(1-\varepsilon^2)}\,\delta(x) + K_{12}(x) \qquad (8)$$

and where

$$\alpha = \mu/\omega\kappa b,\ \varepsilon^2 = (1-2\sigma)/2(1-\sigma),\ k = \mu'/\mu\ . \qquad (9)$$

The symbol $\delta(x)$ in (8) is used to formally denote the Dirac delta function. The functions $\tilde{f}^L(x)$ and $\tilde{f}_3$ stem from the incident Rayleigh wave and are defined by

$$\tilde{f}_1^S(x) = (i\tilde{u}_o/\tilde{s}_R)[\cos(\tilde{s}_R x)-\cos(\tilde{s}_R)],$$
$$\tilde{f}_2^S(x) = -i\tilde{u}_o\tilde{s}_R P(\eta_R)\sin(\tilde{s}_R x)\ ,$$
$$\tilde{f}_1^A(x) = -(\tilde{u}_o/\tilde{s}_R)[\sin(\tilde{s}_R x) + \sin(\tilde{s}_R)], \qquad (10)$$
$$\tilde{f}_2^A(x) = -\tilde{u}_o\tilde{s}_R P(\eta_R)\cos(\tilde{s}_R x).$$
$$\tilde{f}_3 = -2i(\tilde{u}_o/\tilde{s}_R)P(\eta_R)\sin\tilde{s}_R.$$

in which $\tilde{s}_R$ and $\tilde{u}_o$ are the dimensionless Rayleigh slowness and amplitude

$$\tilde{s}_R = 2\pi/\lambda_R = \omega b s_R,\ \tilde{u}_o = u_o/b \qquad (11)$$

and

$$P(\eta_R) = (2\sqrt{(1-\varepsilon^2\eta_R^2)(1-\eta_R^2)} + \eta_R^2-2)/\eta_R^2\sqrt{1-\eta_R^2} \qquad (12)$$

where η_R^2 is the real root in $0 < \eta^2 < 1$ of the Rayleigh equation

$$\eta^6-8\eta^4 + (24-16\varepsilon^2)\eta^2-16(1-\varepsilon^2) = 0\ . \qquad (13)$$

ANALYSIS AND NUMERICAL TREATMENT OF INTEGRAL EQUATIONS

The system of integral equations is singular and of the first or second kind depending on α and ε. The methods of Muskhelishvili [5] are used to determine the types of singularities inherent in the solution. This also depends on the two parameters α and ε, which are defined in (9). Four possibilities arise for the analytical form of the shear and normal interface tractions $\tilde{t}_1^L(x)$ and $\tilde{t}_2^L(x)$. These are summarized below:

Case 1: $0 < \alpha < \infty$, $0 \leq \varepsilon \leq 1/\sqrt{2}$ (viscous coupling)

$\tilde{t}_1^L(x)$ is bounded

$\tilde{t}_2^L(x)$ has a square root singularity at $|x| = 1$.

Case 2: $\alpha \to \infty$, $0 \leq \varepsilon \leq 1/\sqrt{2}$ (smooth contact)

$\tilde{t}_1^L(x) = 0$

$\tilde{t}_2^L(x)$ has a square root singularity at $|x| = 1$.

Case 3: $\alpha = 0$, $\varepsilon = 0$ (welded contact, incompressible half-space)

both $\tilde{t}_1^L(x)$ and $\tilde{t}_2^L(x)$ have square root singularities at $|x| = 1$.

Case 4: $\alpha = 0$, $0 \leq \varepsilon \leq 1/\sqrt{2}$ (welded contact, compressible half-space)

both $\tilde{t}_1^L(x)$ and $\tilde{t}_2^L(x)$ have oscillatory square root singularities at $|x| = 1$.

We are concerned here with Case 1 for which the analysis reveals that the functions $\tilde{t}_1^L(x)$ and $\tilde{t}_2^L(x)$ have the forms

$$\tilde{t}_1^L(x) = \tilde{t}_1^L(1)e^L(x) + (1-x^2)^{1/2}\phi_1^L(x),$$
$$\tilde{t}_2^L(x) = \frac{\phi_2^L(x)}{(1-x^2)^{1/2}}\ ,\ L = S,A \qquad (14)$$

where

$$e^L(x) = \begin{cases} x\ , & \text{if } L = S \\ 1\ , & \text{if } L = A \end{cases}$$

in which $\phi_1^L(x)$ and $\phi_2^L(x)$ are bounded functions.

The numerical methods in Erdogan and Gupta [6] are used to replace the system of integral equations for $\tilde{t}_1^L(x)$, $\tilde{t}_2^L(x)$ by an algebraic system for the bounded functions $\phi_1^L(\zeta_k)$, $\phi_2^L(\eta_k)$ and the value $\tilde{t}_1^L(1)$ in which ζ_k and η_k, $k = 1,2,\ldots,n$ are interpolation points defined as roots of Chebychev polynomials and are given by the expressions

$$\zeta_k = \cos\left(\frac{\pi k}{n+1}\right), \quad \eta_k = \cos\left[\frac{(2k-1)\pi}{2n}\right], \qquad (16)$$

$$1,2, \ldots, n .$$

In order to solve this complex linear system, we decompose all complex functions into real and imaginary parts denoted by superscripts "R" and "I" and obtain a real linear system that is twice as large. The system was solved numerically for the real quantities

$$\phi_1^{LR}(\zeta_k), \ \phi_1^{LI}(\zeta_k), \ \phi_2^{LR}(\eta_k), \ \phi_2^{LI}(\eta_k),$$

$$\tilde{t}_1^{LR}(1), \ \tilde{t}_1^{LI}(1) .$$

for L = S and A, i.e., for the symmetric and anti-symmetric parts of the problem.

NUMERICAL RESULTS AND DISCUSSION

The parameter values for the numerical results are

$$\sigma = 0.25, \ \sigma' = 0.25, \ k = 2, \ \rho'/\rho = 0.5,$$

$$\kappa^* = \kappa/\sqrt{\mu\rho} = (0.01, 0.1, 1, 10). \quad \tilde{h} = h/b = 0.2 ,$$

$$\tilde{u}_o = 1, \ 2/\tilde{\lambda}_R = (0.1 \text{ through } 1.4), \qquad (17)$$

Figures 2 and 3 show $\phi_1^{SR}(x)/\kappa^*$ and $\phi_2^{SR}(x)$ for three values of the dimensionless viscosity parameter κ^*. Similar results were obtained for the other functions.

Since these functions contribute directly to the interface shear and normal stress, we can conclude that the magnitude and functional form of these quantities depend strongly on the viscosity. As would be expected, it also is strongly dependent on the incident wavelength.

We have also calculated the reflected and transmitted power as a function of the incident wavelength for different values of the couplant viscosity. Figure 4 shows the reflected power curves.

The resonance and anti-resonance pattern depends strongly on κ^*. We note that for the low viscosity cases, $\kappa^* = 0.01, 0.1$, resonances occur near $2b/\lambda_R = 0.25, 0.75$ and 1.25 whereas for the high viscosity cases, $\kappa^* = 1, 10$, they occur closer to $2b/\lambda_R = 0.5$ and 1.0.

In an attempt to compare our results with those of Simons [7], who studied the same problem for an extensible membrane welded to a half-space, we took $h/b = 0.01$ and $\kappa^* = 100$. The reflected power curve showed similar resonances and anti-resonances and the actual values were as close as could be expected given the difference in the two models and in the parameters.

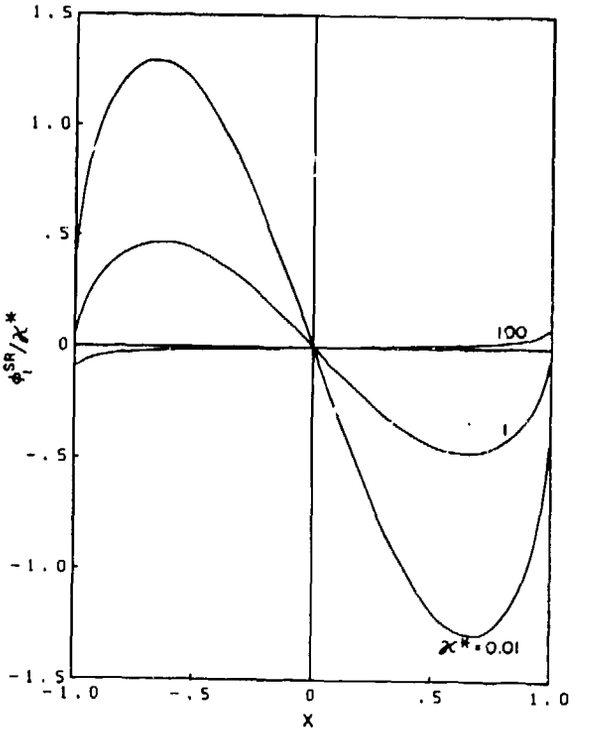

Fig. 2 Symmetric real part of interface shear stress function defined in Eq. (14) for parameter values $\sigma = \sigma' = 0.25$, $\mu'/\mu = 2$, $\rho'/\rho = 0.5$, $h/b = 0.2$, $u_o/b = 1$, $2b/\lambda_R = 0.7$ and $\kappa^* = (0.01, 1, 100)$, $[\tilde{t}_1^{SR}(1)/\kappa^* = -0.02354, -0.3703, -1.537]$.

SUMMARY

We have considered the problem of interaction of elastic surface waves in a half-space with an elastic plate attached through a viscous couplant. The interface tractions transmitted between the plate and half-space are strongly dependent on the couplant viscosity and incident wavelength. The results obtained are preliminary to the prediction of piezoelectric transducer output and its dependence on wavelength (or frequency) and couplant viscosity.

ACKNOWLEDGEMENT

This work was performed under the sponsorship of NSF Grant Eng 77-17150.

REFERENCES

[1] N. Bugdayci and D.B. Bogy, "A two-dimensional theory for piezoelectric layers used in electromechanical transducers," Report No. UCB/AM-80-2, Department of Mechanical Engineering, University of California, Berkeley, March 1980.

[2] Y. Angel, "Scattering of Rayleigh waves by a plate attached to a half-space through a viscous couplant," Ph.D. dissertation, University of California, Berkeley, 1980.

[3] Y. Angel and D.B. Bogy, "Scattering of Rayleigh waves by a plate attached to a half-space through a viscous couplant," in preparation.

[4] H. Lamb, "On the propagation of tremors over the surface of an elastic solid," Philos. Trans. R. Soc. London, Ser. A 203, 1-42, 1904.

[5] N.I. Muskhelishvili, Singular integral equations, Noordhoff Int. Pub., 1977.

[6] F. Erdogan and G.D. Gupta, "On the numerical solution of singular integral equations," Quart. Appl. Math. 30, 525-534, 1972.

[7] D.A. Simons, "Scattering of normally incident Rayleigh waves by thin strips," J. Acoust. Soc. Am. 60, 5, 1100-1107, 1976.

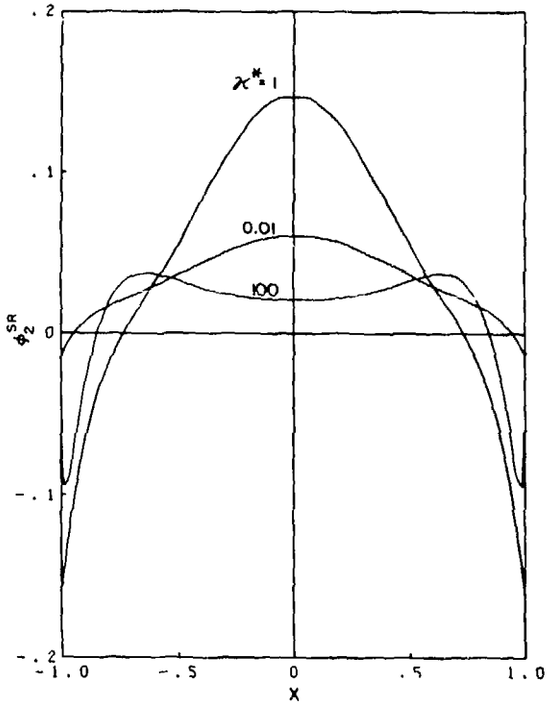

Fig. 3 Symmetric real part of interface normal stress function defined in Eq. (14) for parameter values $\sigma = \sigma' = 0.25$, $\mu'/\mu = 2$, $\rho'/\rho = 0.5$, $h/b = 0.2$, $u_o/b = 1$, $2b/\lambda_R = 0.7$ and $\kappa^* = (0.01, 1, 100)$.

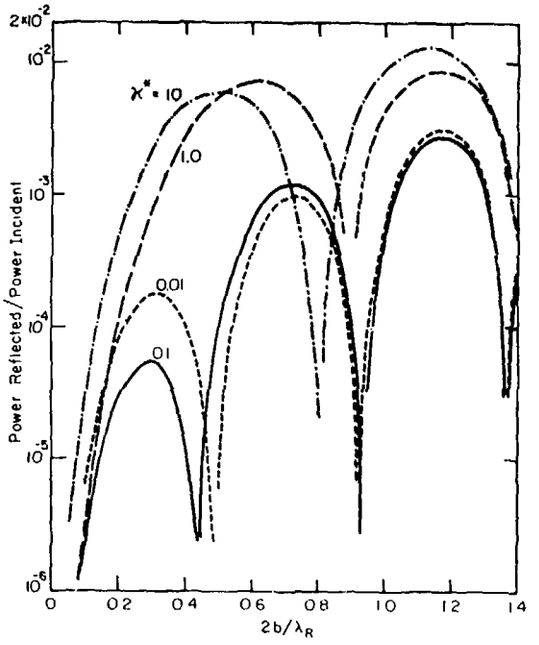

Fig. 4 Power of reflected surface wave versus incident wave number for parameter values $\sigma = \sigma' = 0.25$, $\mu'/\mu = 2$, $\rho'/\rho = 0.5$, $h/b = 0.2$, $u_o/b = 1$ and $\kappa^* = (0.01, 0.1, 1, 10)$.

Mr. Kinsley (Cincinnati): I wonder if you have looked at the dispersive effect of the coupling between the half space and plate. What happens as your B gets very large? What happens to the singularity at the ends of the plate?

David Bogy (University of California, Berkeley): Let me consider the second question first. You can solve the problem. Nothing happens to the singularity. One could surmise the results by looking at this last curve here which is radiated power as a function of 2B over λR. If B gets very large, you approach the results for an infinite plate, which is what this result must be asymtotic to. So I think the width of B really does not matter in the singularity calculation. If B gets large, that means the wavelength is getting relatively small. That means I will have a lot of oscillation under my plate. And that means I have to take a lot more interpolation points in the numerical scheme, and that costs more money. With regards to your first question, I have not considered the dispersion effects of viscosity, I have not looked into that, and I'm not quite sure I understand what dispersion effect you're talking about.

William Pardee, Chairman (Science Center): I think further questions should be reserved for private discussion. Thank you, David.

THE INFLUENCE OF THIN BONDING LAYERS ON THE LEAKY WAVES AT LIQUID-SOLID INTERFACES

by

A. H. Nayfeh
Systems Research Laboratories, Dayton, Ohio 45440

D. E. Chimenti, Laszlo Adler, and R. L. Crane
AFWAL Materials Laboratory, Wright-Patterson AFB, Ohio 45433

ABSTRACT

This paper presents theoretical and experimental results on the problem of bounded acoustic beam reflection at the Rayleigh angle from a fluid-solid interface which is loaded by a thin solid layer. The theoretical development exploits the framework of existing theory to yield a simple, analytic model which is reasonably accurate for thin layers. It is shown that the influence of the layer is contained entirely in the dispersive Rayleigh wavespeed and the thickness-dependent displacement parameter Δ_s. Measurements of the reflected acoustic field amplitude have been performed on several samples of stainless steel loaded with a thin copper layer. We have found reasonably good agreement between the theoretical model calculations and experimental measurements for ratios of the layer thickness to the Rayleigh wavelength as large as 0.3. Beyond this value, some disparity is observed, particularly in the calculation of the thickness-dependent Rayleigh wavespeed.

INTRODUCTION

The energy redistribution that occurs when a bounded acoustic beam is reflected from a fluid-solid interface has been the subject of many analytical and experimental investigations. Following the discovery of analogous effects in optics by Goos and Hänchen [1], Schoch predicted [2]--and later experimentally verified [3]--the beam-displacement effect for an acoustic beam incident on a liquid-solid interface. According to Schoch's predictions, the beam is nonspecularly reflected since it is laterally displaced while retaining, more or less, its original profile. In contrast to these predictions, many experiments [4-7] have revealed that the reflected beam may also suffer severe distortion if it is incident at, or near, the Rayleigh angle. Physically what occurs is the resonant transfer of acoustic energy from a longitudinal wave in the liquid to a pseudo-Rayleigh wave propagating along the liquid-solid interface. As it propagates, the Rayleigh wave re-radiates into the liquid at the Rayleigh angle because of this resonant coupling. The result is a redistribution of the reflected field intensity such that a sizable fraction of the acoustic energy seems linearly displaced along the interface. This energy redistribution includes, in addition to the lateral displacement, a null region and a trailing field which becomes weaker as it extends along the interface away from the incident beam.

Bertoni and Tamir [8] have examined the reflection coefficient for angles close to the Rayleigh angle and constructed a model which explains these distortion phenomena. Specifically, they pointed out that the suitably simplified reflection coefficient has a singularity which leads to solutions corresponding to radiating (leaky) Rayleigh waves. According to their analysis, the distortion is the result of interference between the geometrically reflected field and the field of a leaky Rayleigh wave created by the incident beam at the Rayleigh angle. Breazeale, Adler, and Scott [9] experimentally verified the Bertoni and Tamir model, while Pits, Plona, and Mayer [10] have recently presented theoretical results for the case of a finite beam incident on a solid plate in a liquid. Their results show that distortion of the reflected beam at the Lamb angle can also occur.

This paper investigates theoretically and experimentally, the influence of a thin layer bonded to a solid upon the shift and distortion of the reflected beam. This problem differs from the no-layer case in that the reflection coefficient is not readily available in closed form, and therefore must be derived. The results of this analysis reveal new phenomena that occur in the presence of the layer. Both the Rayleigh wavespeed and the parameter associated with the energy redistribution are frequency dependent in the layer case. These two new effects, in turn, influence the lateral displacement and distortion of the reflected beam.

THEORY

Formulation of the Problem

Consider a thin elastic layer of thickness 2h in welded contact with a solid elastic half-space of different material. Overlying this structure is a fluid (water) half-space as shown in Fig. 1. A coordinate system is chosen with the origin located at the center of the layer and with the positive z-axis pointing downward into the semi-infinite solid. The layer extends from $-h \le z \le h$, with the solid half-space extending from $z = +h$ to ∞ and the fluid extending from $z = -h$ to $-\infty$. In our subsequent analysis we shall identify the field variables and properties of the layer, fluid, and solid substrate with the subscripts o, f, and s, respectively. The fluid medium is subjected to a time-harmonic, bounded acoustic beam incident onto the fluid-solid interface at an angle θ_1 with respect to the surface normal. To reduce the analysis to two dimensions, we assume that no acoustic wave, incident or reflected, has a y-dependence. Alternatively, all particle motion is confined to the x-z plane.

To study the behavior of the reflected beam, one must solve the appropriate field equations in each of the three media (liquid, layer, and substrate), incorporating the appropriate continuity conditions. Formal solutions are obtained by introducing the potential functions ϕ and ψ for each of the media. These functions are related to the particle velocities and stresses by

$$\dot{u} = \frac{\partial \phi}{\partial x} - \frac{\partial \psi}{\partial z} \tag{1}$$

$$\dot{w} = \frac{\partial \phi}{\partial z} + \frac{\partial \psi}{\partial x} \tag{2}$$

$$\sigma_z = (\lambda+2\mu)\frac{\partial^2 \phi}{\partial z^2} + \lambda\frac{\partial^2 \phi}{\partial x^2} + 2\mu\frac{\partial^2 \psi}{\partial x \partial z} \tag{3}$$

$$\sigma_{xz} = \mu\left[2\frac{\partial^2 \phi}{\partial x \partial z} + \frac{\partial^2 \psi}{\partial x^2} - \frac{\partial^2 \psi}{\partial z^2}\right] . \tag{4}$$

where u and w are displacements parallel to the x and z axes, respectively. The terms λ and μ are the familiar Lame' constants and σ_z and σ_{xz} are the normal and shear stresses, respectively. The dot above a variable, such as u, denotes differentiation with respect to time. Since the fluid cannot support a shear wave, the shear potential ψ is identically zero in this medium. In the two solid media ψ has only a single nonvanishing component because particle motion is restricted to the plane of incidence.

The wave potentials ϕ and ψ satisfy separate wave equations for linear, isotropic media, namely

$$\frac{\partial^2 \phi}{\partial x^2} + \frac{\partial^2 \phi}{\partial z^2} = \frac{1}{c_1^2}\frac{\partial^2 \phi}{\partial t^2} , \tag{5a}$$

$$\frac{\partial^2 \psi}{\partial x^2} + \frac{\partial^2 \psi}{\partial z^2} = \frac{1}{c_2^2}\frac{\partial^2 \psi}{\partial t^2} . \tag{5b}$$

The longitudinal and shear wavespeeds for each medium are given respectively by

$$c_1 = \left(\frac{\lambda+2\mu}{\rho}\right)^{1/2} , \quad c_2 = \left(\frac{\mu}{\rho}\right)^{1/2} , \tag{6}$$

where ρ is the density of the medium. The subscripts 1 and 2 denote longitudinal and shear properties, respectively. Solutions of Eqs. (1) - (6) must also satisfy the continuity conditions at the interfaces; in our notation these are

$$u_s = u_o, \; w_s = w_o, \; \sigma_{zs} = \sigma_{zo},$$

$$\sigma_{xzs} = \sigma_{xzo}, \text{ at } z = h \tag{7}$$

$$w_o = w_f, \; \sigma_{zo} = \sigma_{zf}, \; \sigma_{xzo} = 0, \text{ at } z = -h . \tag{8}$$

Reduced Model

In principle, solutions to Eqs. (1) - (5), subject to the continuity conditions of Eqs. (7) and (8), could be formally obtained, but the results would be quite complicated algebraically. Moreover, an attempt to obtain an exact solution could obscure important features of the problem. Therefore, since our principal interest in this problem

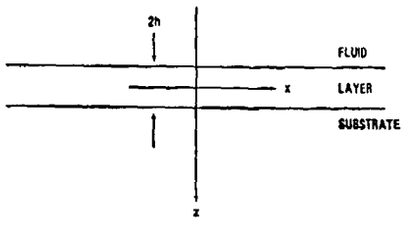

Figure 1 - Coordinate geometry

centers on the case of a thin layer, we include the effect of the layer as a nonzero, homogeneous term in the boundary conditions. To this end we rewrite Eqs. (1) - (5) for the layer in terms of displacements and stresses, average these equations across the layer thickness and satisfy the boundary conditions (7) and (8). We neglect the variations in the displacements u_o and w_o to obtain the substitute fluid interface conditions as a first order approximation in h

$$2h\left[(\lambda_o+2\mu_o)\frac{\partial^2 u_o}{\partial x^2} - \rho_o \ddot{u}_o\right] = -\sigma_{xzs}(0) \tag{9}$$

$$2h\left[\mu_o \frac{\partial^2 w_o}{\partial x^2} - \rho_o \ddot{w}_o\right] = \sigma_{zf}(-0) - \sigma_{zs}(0) . \tag{10}$$

Equations (9) and (10) are significant since they are the only relations that contain the effect of the layer via the modified longitudinal and shear stress boundary conditions. In the absence of the layer (h = 0) they reduce to $\sigma_{zs}(0) = \sigma_{zf}(0)$, $\sigma_{xzf}(0) = 0$, which are the classical liquid-solid stress continuity relations.

Reflection Coefficient and Leaky Wave Dispersion

To determine the reflection coefficient for plane harmonic waves incident from a fluid onto a solid surface, we begin by writing the Fourier transforms of the wave potentials with respect to the x-coordinate and assume exponential solutions in the z-coordinate. These steps lead to formal solutions given by

$$\hat{\phi}(\xi) = \Phi e^{i\zeta_1 z} , \quad \hat{\psi}(\xi) = \Psi e^{i\zeta_2 z} \tag{11a,b}$$

and

$$\hat{\phi}_f(\xi) = \Phi_f e^{i\zeta_f z} + \Phi_f' e^{-i\zeta_f z} , \tag{11c}$$

where the caret indicates a transform, and the prime designates a reflected field. The circular frequency is ω, and the complex amplitudes Φ, Ψ,

Φ_f, and Φ'_f are constants to be determined from the boundary conditions. The wavevector components are given by

$$\zeta_{1,2} = (k^2_{1,2} - \xi^2)^{\frac{1}{2}} , \quad \zeta_f = (k^2_f - \xi^2)^{\frac{1}{2}} \qquad (12)$$

where $\xi \equiv k_f \sin\theta$ with the angle θ measured from the surface normal. The longitudinal and shear wavenumbers are $k_{1,2} = \omega/c_{1,2}$. In the fluid we shorten this notation to $k_f = \omega/c_f$, since there can be no ambiguity. From Eq. (11c) the reflection coefficient, R, is given by

$$R = \Phi'_f/\Phi_f \ . \qquad (13)$$

Inserting the Fourier transformed stresses and displacements into the continuity conditions, Eqs. (7) and (8), yields a system of linear equations that relate the wave potential amplitudes. Using these relations the value of R becomes

$$R = \frac{\zeta_f\ (a_1 b_2 + a_2 b_1) + \rho_f \omega^2 (\xi a_2 - \zeta_{1s} b_2)}{\zeta_f\ (a_1 b_2 + a_2 b_1) - \rho_f \omega^2 (\xi a_2 - \zeta_{1s} b_2)} \qquad (14)$$

where

$$a_1 = \mu_s(2\xi^2 - k^2_{2s}) - 2ih\mu_o \zeta_{1s} \zeta^2_{2o} \qquad (15a)$$

$$b_1 = 2i\xi[i\mu_s \zeta_{2s} - h\mu_o \zeta^2_{2o}] \qquad (15b)$$

$$a_2 = 2i\xi[i\mu_s \zeta_{1s} - h(\lambda_o + 2\mu_o)\zeta^2_{1o}] \qquad (15c)$$

$$b_2 = \mu_s(2\xi^2 - k^2_{2s}) - 2ih\zeta_{2s}(\lambda_o + 2\mu_o)\zeta^2_{1o} \ . \qquad (15d)$$

In the absence of the layer (h = 0) Eq. (14) correctly predicts the reflection coefficient of a liquid-solid interface (see [13] for example). Now we consider the dispersion of the propagating surface waves at the liquid-solid interface. This dispersion is produced by the layer and, therefore, vanishes in its absence.

The expression Eq. (14) for the reflection coefficient contains, as a by-product, the characteristic equation for the propagation of a modified ("leaky") Rayleigh surface wave which propagates along the interface between the fluid and the thin layer bonded to the solid. The vanishing of the denominator in Eq. (14),

$$\zeta_f(a_1 b_2 + a_2 b_1) - \rho_f \omega^2 (\xi a_2 - \zeta_{1s} b_2) = 0 \qquad (16)$$

is the characteristic equation for such waves. If Eq. (15) is substituted into Eq. (16), then for a real frequency ω, Eq. (16) will admit complex solutions of the form

$$\xi = k_r + i\alpha \ . \qquad (17)$$

From Eq. (17) the phase velocity of the Rayleigh wave is given as $c_r = \omega/k_r$, and α is the attenuation coefficient. Note that α vanishes in the absence of the fluid, and hence no attenuation (leaking of energy in the fluid) occurs. In the presence of a fluid these surface waves are called "leaky waves." It will later be shown, as has been done by others [10], that c_r is hardly affected by the presence of the fluid, and therefore, α is very small. However, as shown by Bertoni and Tamir [8], α is important because it is related to the lateral displacement of the reflected beam. Examination of Eq. (16) indicates that in the layer case, the medium is dispersive, and both c_r and α depend on the frequency in a rather complicated fashion. Notice also that Eq. (16) contains the classical characteristic equation for a surface wave, which is obtained by setting h = 0 and ρ_f = 0. Graphical results of c_r as a function of frequency are presented and compared to measurements in Section IV.

Field of the Reflected Beam

In this section we discuss the reflection of a finite-width beam having a Gaussian profile which is incident on the liquid-solid interface at an angle θ_i with the normal. This choice of beam profile or cross-section greatly simplifies the analytic evaluation of the integrals in this and the next subsection. The profile of the beam is characterized by an effective width 2a that is large compared to the wavelength λ in the liquid. Therefore, the acoustic field has significant amplitude only for a distance a on either side of the beam axis. Consider the incident Gaussian beam at z = 0

$$\phi_f(x,0) = \frac{\Gamma_o \exp[-(x/a_o)^2 + ik_i x]}{\sqrt{\pi}\ a \cos\theta_i} \ , \qquad (18)$$

where Γ_o represents the amplitude of the potential in appropriate units; $k_i = k_f \sin\theta_i$ and $a_o = a\sec\theta_i$ is the half-width of the acoustic beam along the x-axis. Since the Fourier transform of (18) is

$$\Phi_f = \Gamma_o \frac{\exp[-(\xi - k_i)^2 (a_o/2)^2]}{\cos\theta_i} \ , \qquad (19)$$

the field of the reflected beam will be given by

$$\phi_f(x,z) = \frac{\Gamma_o}{2\pi} \int_{-\infty}^{\infty} R(\xi) \exp[-(\xi - k_i)^2 \left(\frac{a_o}{2}\right)^2] \times$$

$$\exp[i\xi x - i\zeta_f z] \frac{d\xi}{\cos\theta_i} \ . \qquad (20)$$

Examination of Eq. (20) reveals that it cannot be inverted to give exact analytic results. However, the principal contribution to the integral comes from values of ξ lying in the vicinity of the incident wavenumber k_i. Accordingly, approximate values of $\phi_f(x,z)$ can be obtained by expanding ξ in a Taylor series about k_i. This entails approximations of $R(\xi)$ and $\zeta(\xi)$ for values of ξ close to k_i.

In adopting any form of approximation, care must be used. The straightforward approximation, such as the Taylor-series expansion, is adequate in ranges where $R(\xi)$ is well-behaved, specifically away from the surface-wave pole at $k_r + i\alpha$. If this fact is not taken into consideration, the results of this simple expansion for incident waves near or at the Rayleigh angle are inadequate to

explain the distortion of the reflected beam. By including the influence of the Rayleigh wave pole, Bertoni and Tamir [8] were able to explain these phenomena. In [8] it was also shown that Schoch's results are correct only for very wide beams. Before considering the influence of the Rayleigh wave pole on the reflected beam, we shall apply Schoch's approach to the present problem to obtain an expression for the beam displacement parameter Δ_s. By considering the case of total internal reflection ($\theta_i > \theta_c$), we may write the reflection coefficient in the form

$$R(\xi) = |R(\xi)|e^{iS(\xi)}, \tag{21}$$

where the amplitude $|R(\xi)|$ is very close to unity, and $S(\xi)$ is the phase of $R(\xi)$. Consistent with our previous approximation, the Taylor-series expansion about k_i is used for $S(\xi)$; this result is equivalent to a Fresnel expansion [8]. Then retaining the first term we obtain

$$R(\xi) \simeq R(k_i)\exp[i\{(\xi-k_i)S'(k_i)\}] \tag{22}$$

where $S'(k_i) = S(\xi)/\partial\xi$ evaluated at $\xi = k_i$. Similarly, by retaining three terms in the expansion of ζ_f we obtain

$$\zeta_f = \frac{k_f}{\cos\theta_i} - \xi\tan\theta_i - \frac{(\xi-k_i^2)^2}{2k_f\cos^3\theta_i} \tag{23}$$

Substitution from Eqs. (22) and (23) into Eq. (20) and comparing with Eq. (1a), it can be shown, for angles different from the Rayleigh angle, that the reflected beam profile at any location (x,z) is a modified Gaussian beam. Replacing x with x_r and a_o with a_r in accordance with the relations

$$x_r = x + z\tan\theta_i - S'(k_i) \tag{24}$$

$$a_r^2 = a_o^2 - \frac{2iz}{k_f\cos^3\theta_i} \tag{25}$$

we obtain what amounts to a shifting of the reflected beam along the x-axis by an amount

$$\Delta_s = - S'(k_i) , \tag{26}$$

along with the introduction of an effective complex beam width a_r.

It now remains to derive specific expressions for $S'(k_i)$. This can be done easily by differentiating Eq. (21) with respect to ξ. Noting that since $|R(\xi)|$ is approximately unity, we have

$$S'(k_i) = \frac{R'(k_i)}{iR(k_i)} . \tag{27}$$

Now, by rewriting $R(\xi)$ as

$$R = 1 - \frac{2F}{G + F} , \tag{28}$$

where

$$F = -(\rho_f\omega^2/\zeta_f)(\zeta_{1s}b_2 + \xi a_2) ,$$

$$G = a_1b_2 + a_2b_1 ,$$

we obtain

$$\Delta_s = -S'(k_i) = 2\left[\frac{F'G - G'F}{i(G + F)(G - F)}\right]_{\xi = k_i} \tag{29}$$

Substituting for F and G into Eq. (29), we obtain the lateral displacement of the reflected beam at or near the Rayleigh angle. Since F and G are functions of the frequency ω, Δ_s will also depend on ω in a manner that may be seen from Eq. (29). In the absence of the layer (h = 0), Eq. (53) yields the results that are reported by Schoch [2].

For the special case when the beam is incident at the Rayleigh angle, $\xi = k_r + i\alpha$, one finds that $G(k_r) \sim 0$ and Eq. (29) reduces to the form

$$\Delta_s = - S'(k_r) = - \frac{2iG'(k_r)}{F(k_r)} . \tag{30}$$

Employing the expressions for F and G in the above equation, we obtain, after some algebraic manipulation,

$$\Delta_s = - (\lambda\rho_s/\rho_f)(rs)^{1/2}(T_fD_1/T_1D_2), \tag{31}$$

where

$$s = (c_{2s}/c_r)^2 , \; r = (c_{2s}/c_f)^2 , \; q = (c_{2s}/c_{1s})^2$$

$$s_{1o} = [\rho_o/(\lambda_o+2\mu_o)]^{1/2} = 1/c_{1o},$$

$$s_{2o} = (\rho_o/\mu_o)^{1/2} = 1/c_{2o}$$

$$\bar{\mu}_o = \mu_o/\mu_s , \; \bar{E}_o = (\lambda_o+2\mu_o)/\mu_s$$

$$P_{1o} = s^2 - s_{1o}^2 , \; P_{2o} = s^2 - s_{2o}^2$$

$$T = (s-1)^{1/2} , \; T_1 = (s-q)^{1/2} , \; T_f = (r-s)^{1/2}$$

$$D_1 = 16s - 4s(T/T_1 + T_1/T) - 8TT_1 - 8$$

$$- Q[(2T^2 + P_{1o})\bar{E}_o/T + (2T_1^2 + P_{2o})\mu_o/T_1]$$

$$D_2 = 1 - Q\bar{E}_oP_{1o}(T - s/T_1) ,$$

and

$$Q = 2hk_{2s} = 2h\omega/c_{2s}$$

In the absence of the layer Eq. (31) reduces to

$$\Delta_s \simeq \frac{2\lambda\rho_s}{\pi\rho_f}\left[\frac{r(r-s)}{s(s-1)}\right]^{\frac{1}{2}} \times \left[\frac{1+6s^2(1-q)-2s(3-2q)}{s-q}\right] , \quad (33)$$

which is identical with the results obtained by Schoch (see also [13]).

The dependence of Δ_s/λ on the dimensionless frequency Q for a specific set of elastic constants discussed later is shown in Fig. 2. In addition to the explicit appearance of Q in Eq. (31), c_r contains an implicit dependence on frequency and layer thickness, which also modifies the behavior of Δ_s/λ. The correct value of c_r as a function of Q is obtained from Eq. (16). At Q = 0, corresponding to long wavelength or small layer thickness, the value of Δ_s/λ from Fig. 2 is quite close to the substrate material, as verified in Eq. (33). As the layer thickness or the frequency increases, Δ_s/λ decreases, approaching the value predicted by Eq. (33) for the material properties of the layer. In fact, as expected, the model does not retain validity much beyond Q = 1, considering the approximation implicit in Eqs. (9) and (10). However, the results seem fairly insensitive to the assumption of constant displacement across the layer, although we have determined that the sensitivity can be strongly dependent on the specific combination of properties of the layer and substrate. In any case good agreement with experimental measurements is observed up to Q ≈ 1.5 ($2h/\lambda \simeq 0.25$), as we show in Section IV.

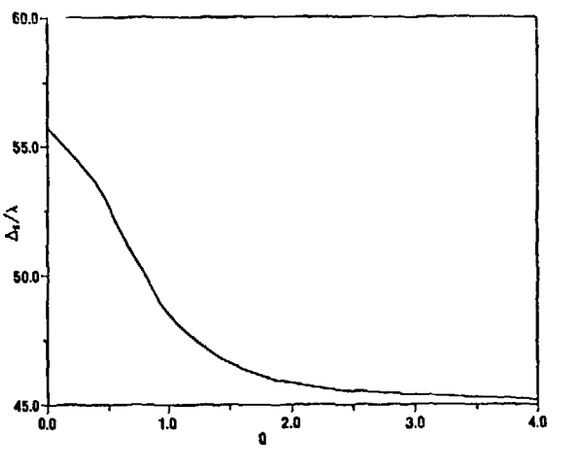

Figure 2 - Displacement parameter over wavelength plotted as a function of the dimensionless frequency-thickness product. Elastic constants are appropriate for a copper layer on stainless steel.

With the above results, the integral of Eq. (20) may now be evaluated. Following the procedure outlined in earlier work [8,14], the reflection coefficient in Eq. (14) is approximated by a truncated Laurent expansion about $\xi = k_r + i\alpha$, keeping only the first term. In this way we consider the influence of only the Rayleigh wave pole on the reflected field, and, correspondingly, the final result will be valid only when θ_i is at or near the Rayleigh angle. Since k_f is constant, the ξ dependence of ζ_f can be explicitly developed by a suitable expansion of terms in Eq. (12). After a change of variable, an application of the convolution theorem, and a contour integration around the upper half-plane, we obtain the final result for the wave potential of the reflected field at the Rayleigh angle

$$\phi_f' = \phi_{sp} + \phi_{lw} ,$$

where the subscripts "sp" and "lw" stand for specular and leaky wave, respectively. These two wave potential components of the reflected field are given explicitly from the above analysis by

$$\phi_{sp}(x,z) = -\frac{\Gamma_o \exp[-x^2/a_r^2]}{\sqrt{\pi}\, a_r \cos\theta_i} \exp[i(\xi x - \zeta_f z)] \quad (34)$$

and

$$\phi_{lw}(x,z) = -2\phi_{sp}(1-\sqrt{\pi}\, a_r \exp[\gamma^2]\, \mathrm{erfc}(\gamma)/\Delta_s) , \quad (35)$$

where

$$\gamma \equiv a_r/\Delta_s - x/a_r , \quad (36)$$

erfc(γ) is the complimentary error function, and a_r is given by Eq. (25) neglecting $S''(k_i)$. It should be noted that apart from a generalization which includes the z dependence, Eqs. (34) and (35) are identical to Bertoni and Tamir's [8] result. This fact indicates that the modification of the reflected field due to the layer is contained entirely in the dispersive Rayleigh wavespeed c_r, the displacement parameter Δ_s, and the dimensionless frequency Q. The model presented here combines the new features that emerge in the layer case with previous results to yield an accurate, yet analytic, expression for the total reflected field.

EXPERIMENTAL PROCEDURE

Experiments in support of the theoretical development of the previous sections were performed to test dependences on important parameters of the model. We varied the layer thickness, ultrasonic frequency, incident angle, and transducer-interface separation distance in the course of many measurements on several samples. For rapid data acquisition and reduction an on-line computer was employed. The specimens used in these measurements are 302 stainless steel electroplated with high-purity copper. Both surfaces of the stainless steel plates (50 x 100 x 10 mm) are machine ground to assure parallelism, then abrasively polished to a mirror finish.

To permit as detailed a comparison with theory as possible, ultrasonic velocity measurements of a representative steel sample have been undertaken. We found the longitudinal wavespeed to be 5.69 ± .02 km/sec, while the transverse wavespeed is 3.13 ± .01 km/sec. These results are within 0.5% of the quoted values for 302 stainless steel [15].

For the copper layer we used literature values [16] of 4.76 km/sec and 2.2 km/sec, where the transverse wavespeed represents a 5% degradation of the value for bulk copper at room temperature. The densities are 8.93 g/cm^3 for copper and 7.9 g/cm^3 for stainless steel.

The transducers used in these experiments are either commercial wideband immersion-type transducers or specially designed "Gaussian beam" transducers. These latter are based on an earlier design [12] and consist of circular quartz plate resonators 2.5 cm in diameter with the water-side electrode completely covering one face, while the opposite face had a strip electrode either 6.4 mm or 3.6 mm in width. This configuration produced a beam whose amplitude distribution in the transducer midplane, perpendicular to the strip electrode accurately described a Gaussian profile, as we have verified in measurements at several frequencies. The Gaussian beam is essential since it corresponds to the incident beam profile assumed in the theoretical model of the previous section. For measurements to determine Rayleigh critical angles the wideband immersion transducers have proven more accurate. Data were acquired by fixing the position of the transmitting transducer with respect to the sample and scanning the receiving transducer across the reflected field, as indicated in Fig. 3. At each point in the discrete scan, the receiver comes to a complete halt, and the data point was read directly into the memory of an on-line computer. Then the receiver position is incremented automatically and the process repeated.

Comparing the measurements with the theoretical model of the previous section requires careful reduction of the data. We corrected the measurements on the basis of a calibration. Since the transducer voltage is proportional to the particle displacement, we obtained the following proportionality between wave potentials in Eqs. (34) and (35) and the transducer signal

$$A_{tr}(x,z) \sim |\phi_{sp} + \phi_{lw}| \ . \qquad (37)$$

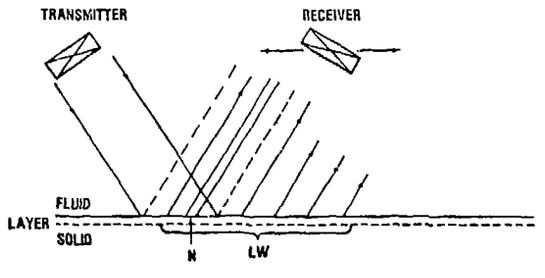

Figure 3 - Schematic of leaky wave experiment. Transmitter is fixed, while receiver scans along x-axis. Dashed lines in reflected field indicate specular reflection. Shaded regions contain most of the acoustic power. Null zone is denoted by N, and leaky wave reflected field by LW.

RESULTS AND DISCUSSION

Measurements of the Rayleigh wave speed in three different samples as a function of Q (= $2h\omega/c_{2s}$) are shown along with the theoretical prediction in Fig. 4. The quantity c_r is inferred by determining the Rayleigh angle with the following procedure. We adjusted transmitter and receiver in Fig. 3 to the same angle, then varied the receiver position and frequency until an absolute minimum in the null region was achieved. Changing angles, the procedure was repeated. From Eq. (31) the beam displacement parameter Δ_s decreases with increasing frequency until the null region become indistinct. Measurements at higher Q values may then be accomplished with a thicker layer. The three samples in Fig. 4 have progressively increasing layer thicknesses, spanning the region from $Q = 0$ to 3. A representative error bar indicates the uncertainty in the data points. Good overlap between the data sets lends confidence to the measurements, but the theoretical curve begins to deviate seriously from the data at about $Q = 1.5$. By $Q = 3$ this disparity has grown to 45% of the range of $c_r(Q)$. The size of this deviation has led us to try to fit other theoretical results in the literature. From this attempt we find that agreement between the approximate model presented here and more complicated exact results is strongly dependent on the specific material parameters of the substrate and layer. In particular as the ratio of substrate-to-layer wavespeeds increases, so does the observed agreement. As mentioned earlier, however, the nature of the assumptions suggests that some deviation beyond $Q = 1$ ($2h/\lambda \approx 0.2$) is not unexpected.

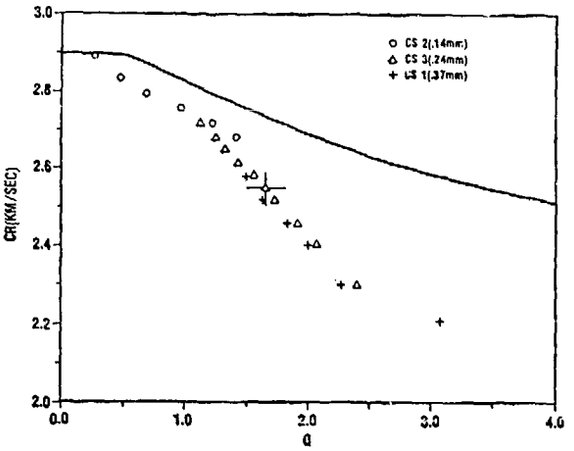

Figure 4 - Surface wave phase velocity plotted versus frequency-thickness product. Solid line is approximate theory, while experimental data points for three samples correspond to symbols indicated on graph. Typical error bars shown for a representative point.

The amplitude distribution curve for sample CS1 at a frequency of 1.5 MHz is shown as a function of receiver position in Fig. 5. These data are recorded by incrementing the x-coordinate of the receiver transducer with the transmitter in a fixed position. The individual points are the experimental data, while the solid curve is the theoretical result from Eqs. (34) - (37). In view of the disagreement between the theoretical value of $c_r(Q)$ and that inferred from Rayleigh angle

measurements, we have inserted the experimentally derived c_r into the expression for Δ_s from Eq. (31) used to derive the theory curve of Fig. 5. Because of signal averaging and system calibration, experimental uncertainty in the signal level is no larger than the plotting symbols in this and subsequent curves.

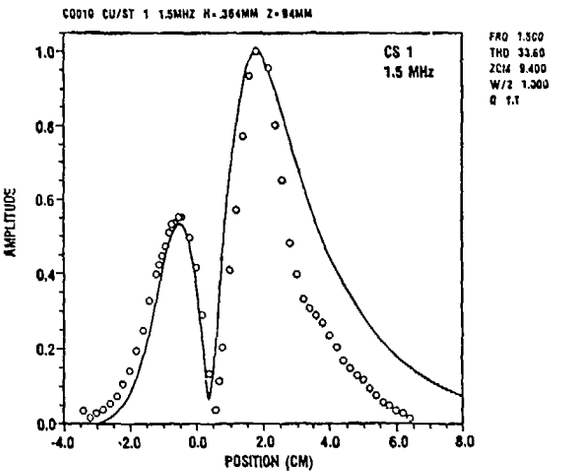

Figure 5 - Reflected acoustic field amplitude plotted versus receiver position for sample CS 1 at 1.5 MHz. Points are experimental data, and solid curve is theory from Eq. (62).

The features of the reflected field indicated schematically in Fig. 3 are apparent in a quantitative sense in Fig. 5. First, near $x \approx -1.0$ cm, a precursor peak appears, due to the coherent sum of ϕ_{sp} and ϕ_{lw} from Eqs. (34) and (35). At higher values of receiver position near $x = 1.5$ cm, a larger displaced reflection is observed, which arises mostly from the leaky-wave term. Between the two peaks is the null region where phase cancellation reduces the signal amplitude to near zero. Similar observations have been made in previous work [8,0]. From $x = -3$ to 3 cm agreement between the data of Fig. 5 and the theoretical prediction is relatively good. The precursor peak height and location of the null are fairly well predicted. Beyond $x \approx 3.5$ cm the experimental trailing field decreases more rapidly than predicted. This occurrence, noticed in several cases, is probably due to the finite y dimension of the Gaussian beam, which is only 20 mm long. When compared to an acoustic path length of 160 mm, the assumption of y-independent incident beam profile appears difficult to fulfill. We have determined the incident acoustic beam halfwidth from measurements at several frequencies with two transducers at varying separations. The wide transducer (6.4 mm) is used for generation, whereas the narrower one (3.6 mm) is the receiver. Inserting this estimate for a/2 into Eq. (25), we examine the theoretical fit, adjusting a/2 by no more than 10% to achieve the best effective width in light of the finite y extent of the transducer. Additional parameters used in the theory are summarized for this and subsequent curves in Table 1.

Figure 6 displays the amplitude distribution for sample CS2 for $Q = .82$. Here theory (solid curve) fits the data points somewhat better than the previous example, although there is still a tendency for the measured field to decrease slightly more rapidly than the model calculation. In addition, we have plotted for comparison the reflected field of the same beam at the same angle of incidence and frequency for a stainless steel sample with no layer present. Although the layer is rather thin ($2h/\lambda \approx .15$), the effect on the reflected field is quite pronounced. The dashed curve, consisting of connected data points, indicates this field in Fig. 6. A small residual beam displacement remains since we are less than 2^o from the appropriate Rayleigh angle for the stainless steel surface (30.8^o). Far from all critical angles, the only contribution to the expression in Eq. (37) is ϕ_{sp}, and the undistorted beam would be centered on $x \approx 0$.

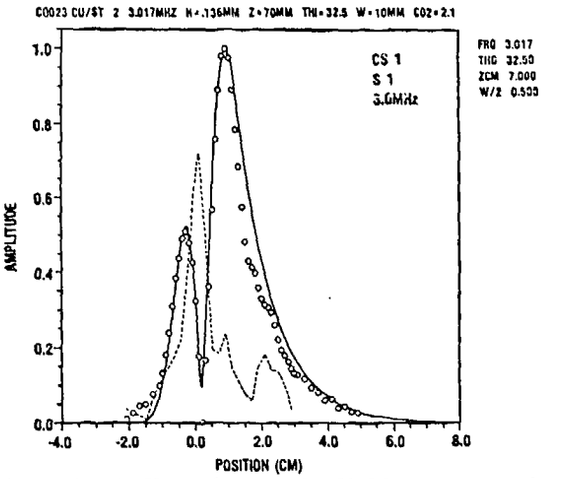

Figure 6 - Reflected acoustic field versus receiver position for sample CS 2 at 3 MHz. Experimental data are plotted discretely, solid curve is theory, and broken curve is experimental data for no-layer case.

As a first-order theory for acoustic reflection at fluid-solid interfaces loaded by a thin layer, the model we present here is qui e adequate, particularly in the region $Q \geq 1$. However, several shortcomings should be pointed out. The calculation of c_r as a function of Q is prohibitively complicated. Expanding Eq. (16) and collecting coefficients of powers of the Rayleigh wavespeed reveals a characteristic equation which is 40^{th} order in c_r. Instead of proceeding in this manner, we have solved Eq. (16) implicitly for c_r by noting that the equation is only second order in Q. The difficulty with this method is that we know an exact complex solution for Eq. (16) at only one value of Q, namely, $Q = 0$. Developing a functional dependence of Q (c_r) for $Q > 0$ requires assumptions concerning the behavior of c_r in the complex plane. Fortunately, we are aided at this point by the fact that $\mathrm{Im}(c_r)/\mathrm{Re}(c_r) \ll 1$, implying that these assumptions do not seriously affect the results. A more general approach, however, would be needed to eliminate this problem and produce a result in better agreement with the data. Additional limitations are the assumption of the Gaussian beam profile and the intrinsic two-dimensionality of the analysis. The first of these could be circumvented by evaluating the reflected field numerically [10], but expanding the analysis to three dimensions would be a very significant complication.

Table 1 - Experimental Parameters

Figure	Sample	2h(mm)	Freq(Mhz)	Q	θ_1(deg)	z(mm)	a/2(mm)
5	CS 1	.37	1.5	1.1	33.6	94.	10.
6	CS 2	.14	3.0	.82	32.5	70.	5.
6	S 1	0.	3.0	0.	32.5	70.	5.

ACKNOWLEDGEMENTS

The authors are pleased to acknowledge helpful discussions with Dr. T. J. Moran. Capable technical assistance was given by D. L. Butler, R. D. Griswold, and K. D. Shimmin.

REFERENCES

1. F. Goos and H. Hañchen, Ann. Phys. (Leipzig) 1, 333 (1947).

2. A. Schoch, Acustica 2, 18 (1952).

3. A. Schoch, Ergeb. Exakten Naturwiss. 23, 127 (1953).

4. W. G. Neubauer, J. Appl. Phys. 44, 48 (1973).

5. W. G. Neubauer and L. R. Dragonette, J. Appl. Phys. 45, 618 (1974).

6. O. I. Diachok and W. G. Mayer, J. Acoust. Soc. Am. 47, 155 (1970).

7. W. G. Neubauer, Physical Acoustics, edited by W. P. Mason and R. N. Thurston (Academic Press, New York, 1973, Vol. X), 104-125.

8. H. L. Bertoni and T. Tamir, Appl. Phys. 2, 157 (1973).

9. M. A. Breazeale, L. Adler, and G. W. Scott, J. Appl. Phys. 48, 530 (1977).

10. L. E. Pitts, T. J. Plona, and W. G. Mayer, IEEE Trans. Sonics and Ultrason. SU-24, 101 (1977); T. D. K. Ngoc and W. G. Mayer, IEEE Trans. Sonics and Ultrason. SU-27, 229 (1980).

11. I. A. Viktorov, Rayleigh and Lamb Waves (Plenum Press, New York, 1967).

12. F. D. Martin and M. A. Breazeale, J. Am. Acoust. Soc. 49, 1668 (1971).

13. L. M. Brekhovskikh, Waves in Layered Media (Academic Press, New York, 1960) pp. 100-122.

14. T. Tamir and H. L. Bertoni, J. Opt. Soc. Am. 61, 1397 (1971).

15. H. E. Boyer, ed., Metals Handbook, Vol. II (American Society for Metals, Metals Park, Ohio, 1976).

16. G. W. C. Kaye and T. H. Laby, Tables of Physical and Chemical Constants (Longman, London, 1973).

17. Mini-manipulator available from Automation Industries, Inc.

William Pardee, Chairman (Rockwell Science Center): Are there any questions?

Unidentified Speaker: Have you included the effect of Lambda?

A.H. Nayfeh (Systems Research Laboratories): Yes, you remember I have included the effect of the layer in the boundary conditions.

Bill Reynolds (AERE, Harwell): I recall seeing some years ago some remarkable illustrations of this displacement on steel specimens which didn't, as far as I know, have a surface layer. Would your work suggest there was perhaps in this steel an atypical surface layer of material which was causing the effect?

A.H. Nayfeh: No. Surfaces without layers do exhibit the Schoch displacement. So what you're saying - Yes, we are saying that the shifting and modulation of the beam is due to the resonant coupling of energy from the beam in the fluid to the pseudo-Rayleigh wave in the surface. And this leads to a displacement and distortion of the reflected beam.

Mike Gardos (Hughes): To answer your question, the answer is yes. When you machine steel, you do have a damage layer on the surface as a matter of fact. You have a very significant subsurface damage layer, and these layers are themselves different from each other. So if you work with real specimens that you machine in a real world, you're going to see the difference in behavior. And if your method is sensitive to that, then you have something.

A.H. Nayfeh: But may I suggest that even smooth surfaces exhibit the displacement and distortion.

Laszlo Adler (Ohio State University): Let me make a point clear. The so-called Schoch displacement, which is a characteristic of the interface, includes the properties of both materials. The Schoch displacement is the parameter which describes the displacement of the reflected field.

A.H. Nayfeh: What you're suggesting could modulate the smooth surfaces. If our analysis is sensitive to this effect, then we might be able to isolate it.

William Pardee, Chairman: This is phenomena not precisely analogous to the effect of surface plasmons or surface plaritons in optics?

A.H. Nayfeh: We mentioned earlier it has been observed in optics.

William Pardee, Chairman: Are there any other questions: Thank you, Mr. Nayfeh.

NON-DESTRUCTIVE ACOUSTIC DETERMINATION OF RESIDUAL STRESSES IN HYDROSTATICALLY EXTRUDED ALUMINUM RODS

M. P. Scott and D. M. Barnett
Department of Materials Science and Engineering
Stanford University
Stanford, California 94305

ABSTRACT

Third order elasticity theory may be used to show that a longitudinal acoustic wave normally incident on a sample in a state of plane deformation experiences a relative velocity shift given by

$$\frac{V - V_o}{V_o} = B(\sigma_1 + \sigma_2)$$

where B is the acoustoelastic constant, σ_1 and σ_2 are the principal stresses normal to the direction of wave propagation, and V_o is the wave velocity in undistorted material. Hence, wave transit time measurements may be used to ascertain the sum $\sigma_1 + \sigma_2$ in the deformed state. We use a double pulse-echo technique to provide an accurate measure of transit time through the thickness of aluminum discs produced by hydrostatic extrusion (25% area reduction). The residual stress state produced during extrusion is axi-symmetric and we are able to separately determine residual radial and hoop stresses by a single longitudinal wave measurement at points on the disc face. The technique is extremely rapid and accurate, and the acoustic results are cross-checked by both x-ray measurements and finite element simulation of the extrusion process.

William Pardee, Chairman (Rockwell Science Center): Bill Moyer.

Bill Moyer (Union Carbide): Would you address the problem of getting zero stress state in the welded position?

Martin Scott (Stanford University): This is a big problem. I think this will require that the theoreticians do more work here. Echo elasticity can be couched in a different way. That is, if we can use an already deformed state, perhaps, as referencing our equation, that would give us a big help. At present, I don't know a better way to do it than simply stress relief. Obviously, if you are talking about a 30-ton pressure vessel, you don't believe that. I don't know what to do about that; this is the best I know how to do it.

Bill Moyer: Is the technique applicable to a weld where the weld nugget is different material so you have a variation in properties as you go across?

Martin Scott: Yes. By calibrating the already deformed state, you can essentially handle those kind of things. However, that has not been done before.

William Pardee, Chairman: How thick were your wafers, and did you have to take any special precautions to avoid introducing additional stresses in moving them out of the rod?

Martin Scott: Yes, to both your questions. They were on the order of anything from 4 millimeters to 6 millimeters in thickness. I used a gassed discharging machine to be very careful, using a very careful polishing technique. Although this technique is not very sensitive, you really don't have to worry about that that much.

John Simmons (NBS): Did you find any differences, in fact?

Martin Scott: There are axial stresses in the rod, and the order of difference is on the order of differences you would expect by adding the elastic solution to the longitudinal stresses; we picked that up.

William Pardee, Chairman: Thank you, Martin.

THE DETERMINATION OF TENSILE STRESSES USING THE TEMPERATURE DEPENDENCE OF ULTRASONIC VELOCITY

K. Salama, A. L. W. Collins and Jen-Jo Wang
Department of Mechanical Engineering
University of Houston
Houston, TX 77004

ABSTRACT

The effects of applied tensile stresses on the temperature dependence of 10 MHz ultrasonic longitudinal velocity have been studied in three types of commercial aluminum alloys, 6064-T4, 2024-T351, and 3003-T251. In all measurements, it is found that the velocity decreases linearly with temperature, and the slope of the linear relationship changes considerably as a function of applied tensile stresses within the elastic limit of the specimen used. Furthermore, the results indicate that the relative changes in the temperature dependence of the velocity due to stress is insensitive to composition and texture, and the data obtained on the different types of aluminum alloys can be represented by a single relationship. The sensitivity of the temperature dependence of the ultrasonic velocity to applied elastic stress is estimated to be ± 8 MN/m^2 which compares favorably with those obtained by other techniques.

INTRODUCTION

There is a general agreement that ultrasonic methods appear to hold the best promise in the nondestructive measurements of bulk stresses in both crystalline and non-crystalline materials[1,2] Calculations have shown that ultrasonic velocity changes are linear functions of applied stress and unknown stresses can be determined when both the velocity in the absence of stress as well as third-order elastic constants are known independently. The measured velocity, however, strongly depends on microstructural features which makes it necessary to develop a calibration between velocity and stress in order to be used in the determination of unknown stresses. In addition, development of preferred orientations (texture) during deformation or fatigue, severely modify the third-order elastic constants. These problems can be solved when the differences between velocities of shear waves polarized perpendicular and parallel to stress directions are used. Due to these differences, a shift in phase will occur, and the out-of-phase components will interfere and cause a change in intensity. This method, however, does not have at present enough sensitivity, and requires an accurate determination of the shear velocity in the absence of stress.

Basically, the temperature dependences of the elastic constants of a solid are due to the anharmonic nature of the crystal lattice. A measure of the temperature dependence of the ultrasonic velocity can, therefore, be used to evaluate bulk stresses. Experiments undertaken on aluminum and copper[3,4] elastically deformed in compression showed that the ultrasonic velocity, in the vicinity of room temperature, changed linearly with temperature, and the slope of the linear relationship changed considerably as the amount of applied stress was varied. In aluminum, the relative changes of the temperature dependence of longitudinal velocity increased by as much as 23% at a stress of approximately 96 MPa. The linear relationship between the temperature dependence of the ultrasonic velocity and the applied stress was then used to determine the change as a function of distance of the tangential component of the stresses developed when an aluminum rod was shrunk fit into a slightly smaller hole drilled into an aluminum disc. Excellent agreement was obtained between the computed stress distribution, and that measured using the temperature dependence method.

In this paper, the effect of tensile elastic stresses on the temperature dependence of the longitudinal ultrasonic velocity has been studied in three aluminum specimens of types 6064-T4, 2024-T351, and 3003-T251. The results obtained on these specimen show that the relative change in the temperature dependence of ultrasonic velocity is a linear function of the amount of elastic tensile stress applied. The results also indicate that the changes in the temperature dependence due to stress is insensitive to composition and texture, and the data obtained on the different types of aluminum alloys can be represented by a single relationship.

EXPERIMENTAL

The ultrasonic velocity was measured on three aluminum specimens of types 6064-T4, 2024-T351, and 3003-T251 at temperatures ranging between 230 and 280K, using the pulse-echo-overlap method. Figure 1 displays the experimental system used in this work, which is capable of measuring changes in the ultrasonic velocity with an accuracy of better than 1 part of 10^5. This system has been described in detail elsewhere[5]. The velocity measurements were made while the specimen was subjected to various amounts of tensile stresses using the arrangements shown in Figure 2. In this arrangement, the specimen is gripped in an Instron machine where a predetermined load is applied and its value is kept constant during the entire velocity measurements.

RESULTS

In all measurements, the velocity was found to decrease linearly with temperature, and the slope of the linear relationship decreased as the amount of applied tensile stress is increased within the elastic limit of the specimen. A typical example of the results obtained on the type 3003-T251 aluminum is shown in Figure 3, where the longitudinal velocity is plotted vs temperature at stress 0, 32.8, 48.6, and 85.1 MPa. The values of the temperature dependence of ultrasonic velocity (dV_ℓ/dT) obtained

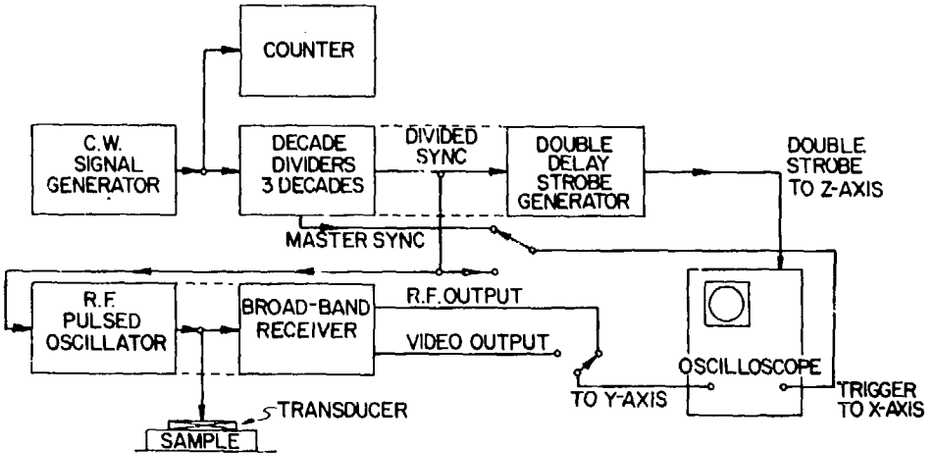

Fig. 1. Pulse-echo-overlap system for measuring ultrasonic velocity.

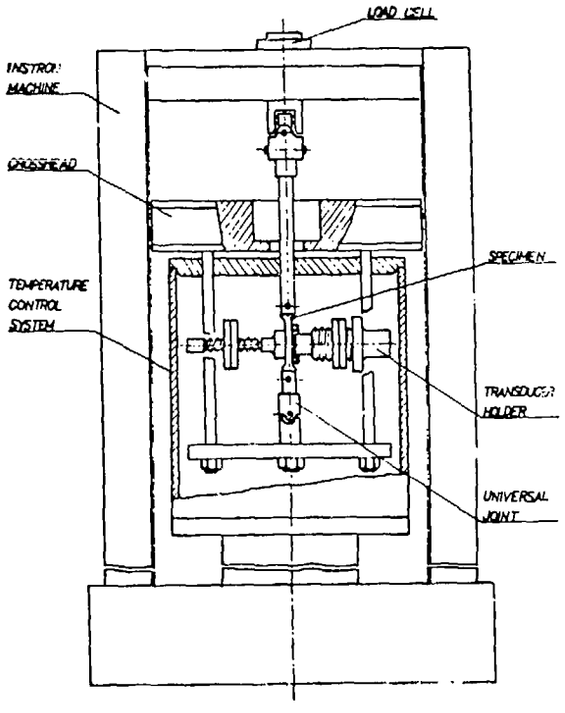

Fig. 2. System used for the application of stress during the ultrasonic measurement.

at various amounts of stress on the three specimens are listed in Table I. Because the values of (dV_0/dT) at zero stress were found to vary from one type of aluminum to the other, the relative change in the temperature dependence, Δ, due to the application of stress was calculated, and its values are listed in Column 4 of the Table.

TABLE 1

Variations of the Temperature Dependence of Longitudinal Ultrasonic Velocity with Applied Tensile Stress in Aluminum

Specimen	Applied Stress (MPa)	-dV/dT (m/s k)	%
6060-T4 #1	0	1.304	0
	36.5	1.205	7.59
	60.8	1.155	11.44
	91.2	1.091	16.33
2024-T351 #2	0	1.187	0
	24.2	1.137	4.2
	73.0	1.073	9.6
3003-T251 #3	0	1.251	0
	32.8	1.167	6.7
	48.6	1.117	10.7
	85.1	1.039	16.9

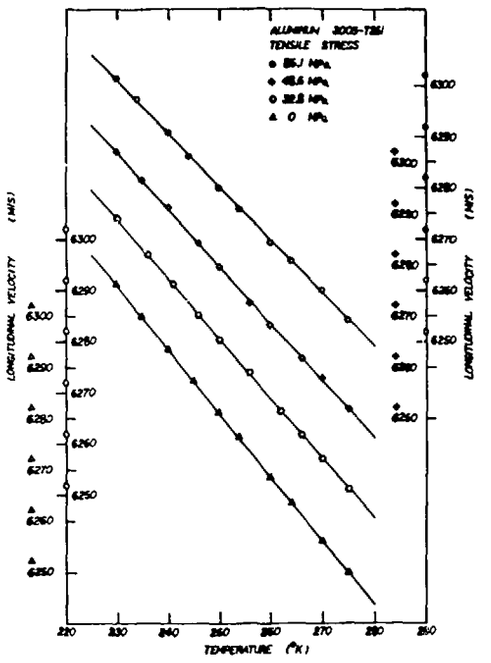

Fig. 3. Effect of applied tensile stress on the temperature dependence of ultrasonic longitudinal velocity in aluminum. Stress is applied in a perpendicular direction to the direction of propagation of the ultrasonic waves.

The relative changes in the temperature dependence $[(dV/dT)_\sigma - (dV/dT)_o]/(dV/dT)_o$ obtained on the three specimens are plotted as a function of applied tensile stress in Figure 4. The figure shows that the data points can be represented by a straight line which passes through the origin. This indicates that, regardless of the type of aluminum used, the relative change in the temperature dependence is a linear function of the applied stress and can be represented by,

$$\frac{(dV/dT)_\sigma - (dV/dT)_o}{(dV/dT)_o} \qquad (1)$$

where K is a constant equals 1.9×10^{-3} per MPa (1.3×10^{-2} per KSI). This value of K is about 20% smaller than that obtained when compressive stresses are used in the measurements.

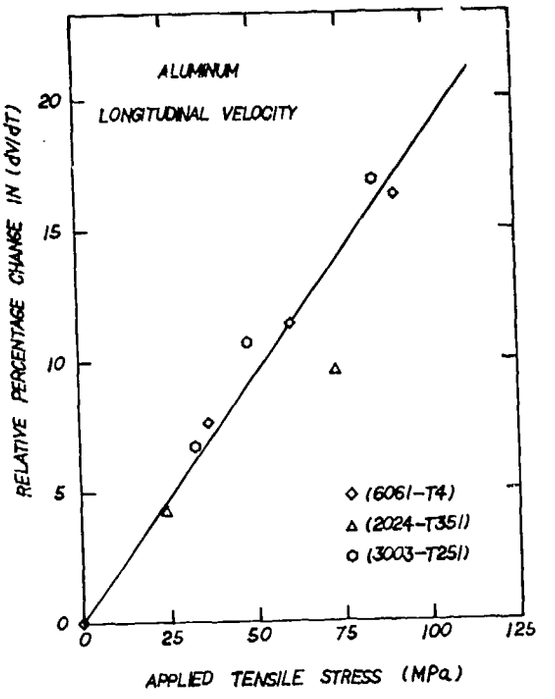

Fig. 4. Percentage of the relative change in the temperature dependence of ultrasonic longitudinal velocity as a function of applied stress in aluminum.

ACKNOWLEDGEMENT

The authors would like to thank the Electric Power Research Institute for the support of this investigation under Grant No. RP823-3.

REFERENCES

1. Proceedings of Workshop on Nondestructive Evaluation of Residual Stress, NTIAC-72-2 (1976).
2. James, M.R. and O. Buck, Critical Reviews in Solid State and Materials Sciences, p. 61 (1980).
3. Salama, K. and C.K. Ling, J. Appl. Phys. 51, 1505, (1980).
4. Salama, K. and C.K. Ling, DARPA/AF annual Review of Progress in Quantitative NDE, July 1979.
5. Salama, K. and R.M. Ippolito, Proceedings of the First International Symposium on Ultrasonic Materials Characterization, NBS Special Publication 596, p. 201 (1980).
6. Salama, K., C.K. Ling and Jen-Jo Wang, Preprint of Technical Papers presented at SESA Fall Meeting, p. 6 (1980).

Martin Scott (Stanford): What was the temperature range in your measurement?

Kamel Salama (University of Houston): We measured from about 280 down to 220K. We are in the process of using higher temperature that goes from 300 degrees to 350 or 360K. Usually, somewhere between 50 and 70 degrees is quite adequate to give you a good determination for the slope of the velocity as a function of temperature.

Christian Burger (Iowa State): You were making your measurements through the thickness, so you were essentially looking at the plane-stress problem?

Kamel Salama: In all cases used in the calibration, the stress applied turned out to be axial. The component of stress which affected the change in the temperature dependence is the axial component. We confirmed this conclusion by having a specimen in an Instron machine where you are applying a pure uniaxial stress and do the velocity temperature measurements, and, as I said, it was about 15 percent smaller than what we got in the previous measurements.

Christian Burger: My difficulty is really with this interference problem you have on the board. How did you get rid of interference?

Kamel Salama: These measurements were done using shear waves. We made three measurements, one longitudinal, which turned out to be constant, where the temperature dependence had no change - or no considerable change as a function of the distance. The second measurement was where the particle velocity was in the tangential direction, the third measurement was where the particle velocity is toward the radius. And these measurements were obtained from the temperature dependence where the particle velocity is perpendicular to that line.

Christian Burger: Thank you.

William Pardee, Chairman (Science Center): I would like to offer Professor Salama my congratulations. We are less than 15 minutes behind, inspite of having one extra talk. There has been some complaint at previous sessions that the stampede towards the door at the end of the session has made it impossible to hear the questions. I would ask you to offer the last Speaker the courtesy of a few brief questions, if necessary.

EFFECT OF GRAIN SIZE AND PREFERRED CRYSTAL TEXTURE ON ACOUSTIC PROPERTIES OF 304 STAINLESS STEEL

N. Grayeli, F. Stanke, G. S. Kino, and J. C. Shyne
Edward L. Ginzton Laboratory
Stanford University
Stanford, California 94305

ABSTRACT

Several acoustic properties have been measured in an annealed round rolled bar of type 304 stainless steel. These properties were observed to depend upon both microstructure and the non-random crystal texture of this single phase, polycrystalline, face-centered cubic alloy. All measurements were made with longitudinal waves propagating parallel to the bar axis. The acoustic velocity was observed to be 0.3% higher near the outer surface than along the center of the bar, consistent with a stronger [111] texture in the outer fibers than at the center. The attenuation coefficient at the center was twice as large as at the outer surface. The measured difference in grain size at the center and surface was consistent with the observed attenuation difference. The acousto-elastic coefficient measured for a uniaxial tension stress applied along a bar diameter was at least 20% higher at the bar center than at its outer surface.

INTRODUCTION

The acoustic properties of solid material depend on their microstructure. This paper describes efforts to correlate several acoustic properties with microstructural variations and preferred crystal texture in 304 stainless steel. Three acoustic properties were measured, longitudinal wave velocity, attenuation coefficient, and acousto-elastic constant.

SPECIMEN MATERIAL

Type 304 stainless steel was chosen as a relatively simple, experimental convenient specimen material. 304 is the most common member of the austenitic, 18 chromium plus 8 nickel, family of stainless steels. The microstructure consists (ideally) of a single phase, face-centered cubic iron containing chromium and nickel in solution. The microstructure is an aggregate of many grains (crystallites). Figure 1 shows the specimen microstructure.

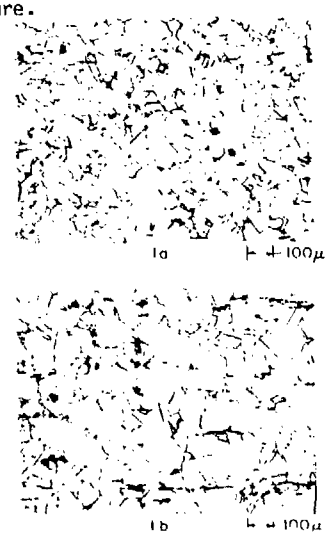

Fig. 1. Photomicrographs of the 304 stainless steel bar grain structure (a) at surface and (b) center radial position.

The specimen material was taken from a 76 mm diameter, rolled bar of 304 stainless steel. Flat acoustic test specimens 1.5 cm thick were cut transverse to and parallel to the bar axis, as shown in Fig. 2.

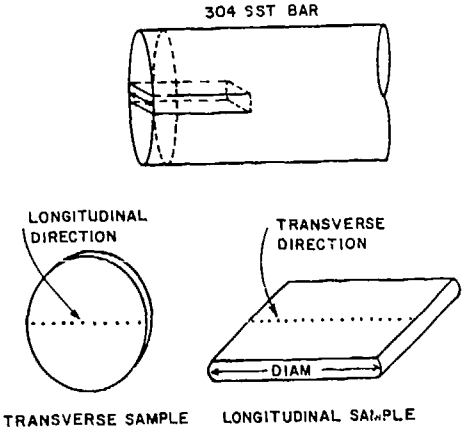

Fig. 2. Sample configuration for velocity and attenuation measurements.

In the as-received condition, the average grain size was about 100 μm, but with a small size gradient from center to surface. The average grain diameter at the center was 120 μm, and it decreased to 90 μm at the surface. Grain size was determined by a mean intercept, lineal analysis. The reported average grain diameters are the true three-dimensional grain size. Average grain diameter is plotted in Fig. 3. The grain structure appeared perfectly equiaxed (no shape anisotropy).

To eliminate any effect of residual stresses possibly resulting from the steel manufacturing process, a transverse specimen of the bar stock was annealed at 1093°C for one hour, then air cooled. This caused a little grain growth. After annealing the center average grain size had increased to 128 μm, while at the surface, no measurable grain growth had occurred. The annealed grain size is plotted in Fig. 3.

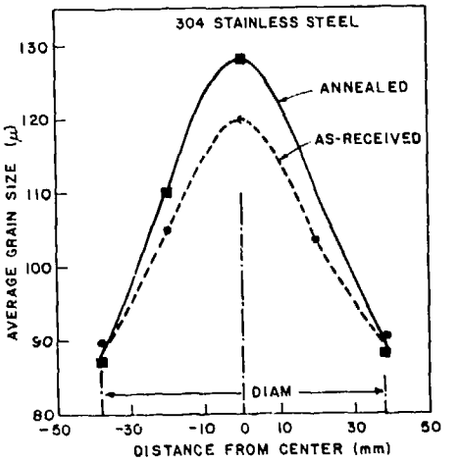

Fig. 3. Average grain diameter vs. radial position in 304 stainless steel as-received and annealed.

Although the grain structure gave no indication of anisotropy (directionality), some degree of preferred crystal orientation must have existed in this wrought 304 stainless steel bar. This is an unavoidable consequence of any plastic forming process. Rolling, wire drawing, extrusion, etc, invariably cause some non-randomness in the crystal orientation of the small grains comprising the polycrystalline microstructure. The degree of nonrandomness or preferred orientation depends on the material and its thermal-mechanical processing history. For face-centered cubic metals such as 304 stainless steel, we must expect some degree of [111], [100], or mixed [111] and [100] fiber texture. That is, a larger than random proportion of grains will be aligned with a [111] (cube diagonal) or a [100] (cube edge) crystal direction oriented close to the longitudinal axis of the bar (parallel to the rolling direction).

Any material property that depends on crystal orientation will be anisotropic in polycrystalline materials with preferred crystal texture. Acoustic velocity, depending directly on elastic constants, is directly affected by a preferred crystal texture, and it will be directionally dependent.

ACOUSTIC VELOCITY

The longitudinal acoustic wave velocity at 5 MHz was measured in the 304 stainless steel using a two-pulse echo system described elsewhere.[1] The accuracy of these measurements was better than ±0.02% , being limited by the acoustic path length measurement (specimen thickness). The velocity was measured at different radial positions along bar diameters in both the transverse and longitudinally cut acoustic specimens. Figure 4 shows how the acoustic velocity, measured parallel to the rolling direction, varied with radial position in the as-received 304 stainless steel. The velocity was about 0.25% higher at the surface of the bar than at its center.

It is apparent that the pattern of velocity variation in the bar is approximately cylindrically symmetrical. Figure 5 shows an acoustical velocity

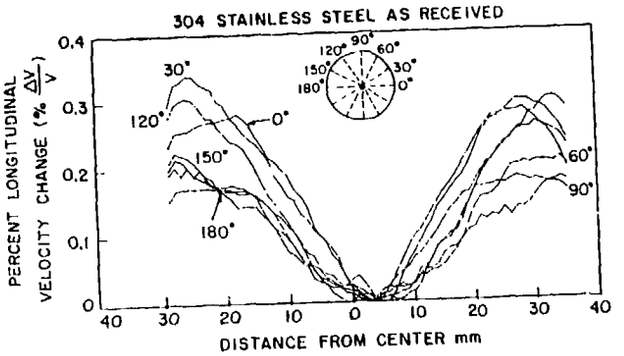

Fig. 4. Acoustic velocity scans along bar diameters in as-received 304 stainless steel. Velocity variation is normalized relative to the center of the bar.

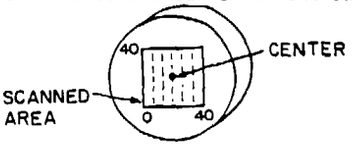

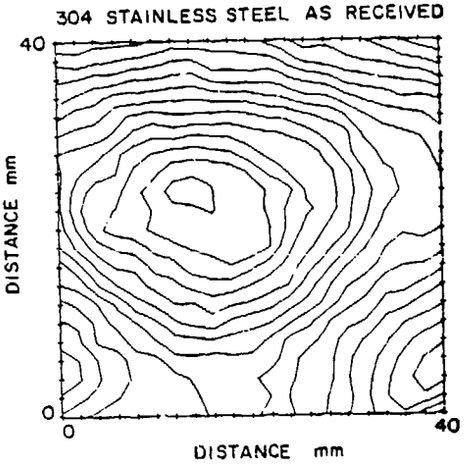

Fig. 5. Isovelocity contours on a cross section of rolled round bar of as-received 304 stainless steel.

scan of the center region of the transverse specimen; the isovelocity contours are roughly, but not perfectly, circular.

The acoustic velocity and its spatial pattern was practically identical in the annealed and as-received transverse specimens. In the longitudinally-cut specimen, the acoustic velocity was nearly indepedent of radial position, and was generally higher than in the transverse specimens. These measured velocities are plotted vs. position in Fig. 6.

In face-centered-cubic crystals, the longitudinal elastic constant is highest in [111] directions and lowest in [100] directions, therefore a [100] fiber texture will reduce the acoustic velocity in the direction of the fiber axis, while a [111] fiber texture will increase the longitudinal acoustic velocity in that direction. Comparison of the measured longitudinal acoustic

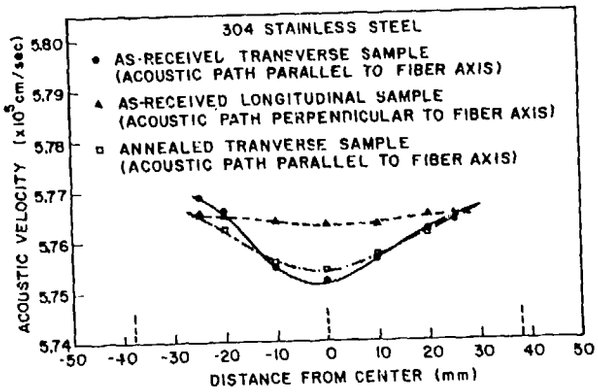

Fig. 6. Acoustic velocity measured at radial position in transverse and longitudinal samples.

velocity changes parallel to and perpendicular to the fiber axis, with the predicted influence on velocity by [100] and [111] fiber textures indicates that the ratio of the amount or strength of [111] fiber texture to [100] fiber texture, $Y_{[111]}/Y_{[100]}$, is largest at the surface and is smallest at the center. This could happen by the [100] texture strength decreasing from center to surface, by the [111] texture strength increasing from center to surface, or both.

CHARACTERIZATION OF TEXTURE BY X-RAY DIFFRACTION

An X-ray diffractometer was used to detect the kind and amount of texture in the 304 stainless steel bar and also to determine the variation of texture from the center to the surface of the round bar. The intensities of diffraction peaks were measured at different locations along the diameter in the as-received bars. The X-ray diffraction line intensities measured on specimens cut longitudinal or transverse to the bar axis are in proportion to the density of crystallites with the corresponding reflecting crystal planes oriented parallel to or transverse to the bar axis. (There is no (100) X-ray peak; the density of (100) planes is proportional to the (200) X-ray peak intensity.)

Comparison of the intensity of the (111) and (200) diffraction peaks at different locations along the diameter of the sample shows that the intensity of the (200) diffraction was stronger at the center and weaker away from the center toward the surface. Also, the intensity of (111) diffraction was stronger at the surface and weaker at the center for the transverse sample. In the longitudinal sample, the (111) peak intensity is uniform along the diameter of the sample, while the (200) peak was slightly stronger at the center than at the surface. A direct comparison of the intensities of the (111) and (200) diffraction peaks between longitudinal and transverse surface orientations would be of doubtful significance, because the differently oriented samples did not include the identical bar diameter. (The acoustic velocity scan suggested some deviation from perfect circular symmetry.) Table I shows the (100) and (200) X-ray diffraction peak intensities, I_{111}, I_{200}, and the ratio of I_{111}/I_{200} along the diameter of the bar.

TABLE I

X-Ray Diffraction Peak Intensities
(arbitrary units)

Longitudinal Sample

Position	I_{200}	I_{111}	I_{111}/I_{200}
surface	2.15	5.5	2.558
half	2.18	5.5	2.523
center	2.25	5.5	2.443

Transverse Sample

Position	I_{200}	I_{111}	I_{111}/I_{200}
surface	1.4	6.5	4.357
half	1.49	5.95	3.993
center	1.6	5.8	3.625

With [111] and [100] fiber textures, variations in the texture strength along the diameter should cause only minimal variation in peak intensities measured in the longitudinal specimen. However, when measured on the transverse specimen, the intensities should sensitively reflect variations in fiber texture strength. The ratio of (111) and (200) peak intensities was almost independent of radial position on the longitudinal sample, but varied considerably in the transverse specimen, as shown in Fig. 7. These X-ray data indicate that there is a duplex [111] + [100] fiber texture with the strength of the [111] component increasing from center to surface while the [100] component decreases from center to surface.

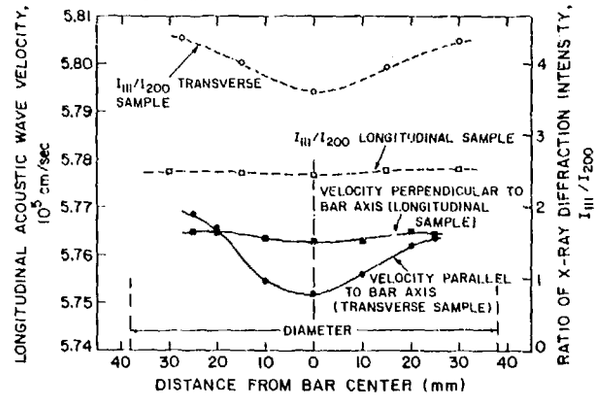

Fig. 7. X-ray line intensity ratio and acoustic velocity measured at varying radial positions in 304 stainless steel bar.

These X-ray data confirm the conclusion drawn from the acoustic velocity measurements that the ratio of [111] to [100] fiber texture increases from the center to the surface.

ATTENUATION MEASUREMENTS

In contrast to acoustic velocity, acoustic attenuation is strongly influenced by microstructure. As an acoustic plane wave passes through a medium, it dissipates energy by a variety of processes, and the wave amplitude decreases

accordingly. Letting U be the wave's displacement amplitude and x the acoustic path length:

$$U(x) = U_0 \exp(-\alpha x) \qquad (1)$$

where U_0 is the amplitude at $x = 0$ and α is the attenuation coefficient, usually expressed in dB per distance.

Attenuation measurements were made on the transverse cut acoustic specimens of the 304 stainless steel bar. Attenuation was measured at different radial positions to study the influence of grain size and preferred orientation. A three pulse-echo method was used with a 10 MHz broadband transducer.[2] The attenuation was measured from 5 to 10 MHz, corrected for diffraction, and plotted as a function of frequency. Figure 8 shows these data for the annealed sample; almost identical attenuation data were obtained from the as-received 304 stainless steel.

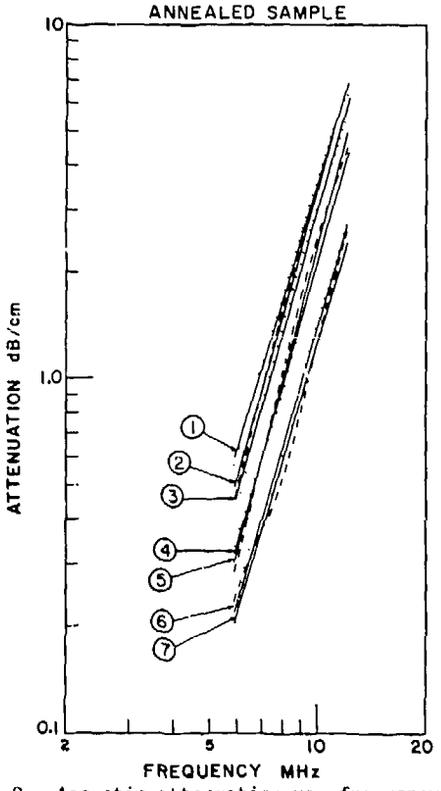

Fig. 8. Acoustic attenuation vs. frequency mesaured at various radial positions, (1) at the center, (2) and (3) 10 mm, (4) and (5) 20 mm, (6) and (7) 25 mm from the center in the annealed 304 stainless steel bar.

In the range of acoustic frequencies used, attenuation occurs predominantly by grain boundary scattering in single phase polycrystalline metals. When the wavelength of the propagating acoustic wave is much larger than the grain diameter, Rayleigh scattering is the predominant attenuation mechanism. In that case, the attenuation is expressed by

$$\alpha_R = S\mu^2\bar{D}^3f^4 \qquad (2)$$

At higher frequencies when the wavelength becomes comparable to the grain diameter, the attenuation is controlled by stochastic scattering, expressed by

$$\alpha_S = S'\mu^2\bar{D}f^2 \qquad (3)$$

In these two relations, μ is the elastic anisotropy factor for each metal crystallite, $\bar{D}$ is the average grain diameter, S and S' contain velocity terms, and f is the acoustic frequency.[3]

The attenuation vs. frequency data of Fig. 8 were fitted to an equation of the form

$$\alpha = Af^n \qquad (4)$$

The frequency exponent, n, decreased from 4.0 at the surface to 3.44 at the center. This indicates that the acoustic attenuation occurred almost entirely by Rayleigh grain scattering. At the bar center, the n value of 3.44, indicating some stochastic scattering, is consistent with the larger grains at the center.

The attenuation was highest at the center position and decreased toward the surface. Figure 9 shows attenuation vs. radial position in the annealed 304 stainless steel as measured at three frequencies. This variation in attenuation with position was caused by the gradient in grain size from center to surface.

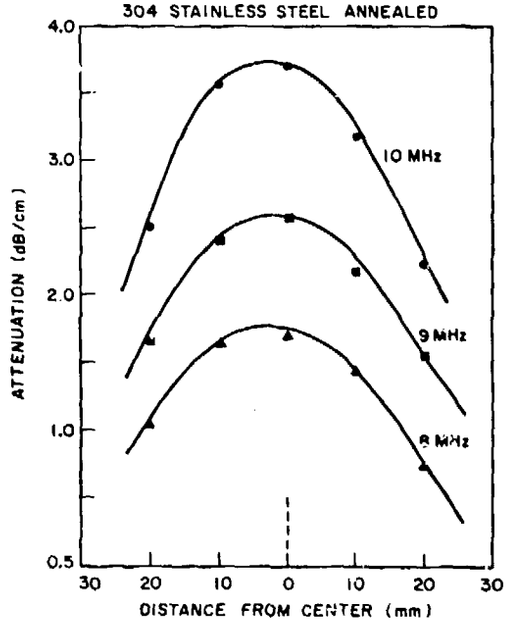

Fig. 9. Acoustic attenuation coefficient vs. radial position in the annealed 304 stainless steel.

ACOUSTOELASTIC EFFECT

Because the elastic constants of materials are not quite independent of the state of elastic stress, acoustic wave velocity depends on the state of static stress of the acoustic medium. This manifestation of nonlinear elasticity, the acousto-elastic effect, provides the basis for acoustic nondestructive stress measurement. For example, in an elastically isotropic solid in a state of plane stress, the longitudinal acoustic velocity perpendicular to the stress plane is linearly proportional to the static stress amplitude:

$$V_\sigma = V_0 + V_0 B(\sigma_x + \sigma_y) \qquad (5)$$

or

$$\frac{\Delta V}{V} = \frac{(V_\sigma - V_0)}{V_0} = B(\sigma_x + \sigma_y) \qquad (6)$$

where V_σ and V_0 are the acoustic velocity in the stressed and unstressed states, σ_x and σ_y are the principal values of the static stress, and B is an acousto-elastic coefficient, an elastic property of the material:

$$B = \frac{\mu\ell - \lambda(m + \lambda + 2\mu)}{\mu(\lambda + 2\mu)(3\lambda + 2\mu)} \qquad (7)$$

where λ and μ are the familiar Lame linear elastic constants, while ℓ and m are two of the three third order Murnaghan nonlinear isotropic elastic constants. Other, similarly constituted, acousto-elastic constants are appropriate for other stress geometries, shear waves, etc. In principle, the relative change in acoustic velocity is linearly proportional to stress, and the acousto-elastic constant of proportionality, such as B, is a simple isotropic property of the material; in reality, it is not.

One difficulty complicating the development of practical acousto-elastic stress measurements is the variability and anisotropy of the acousto-elastic coefficients. An example of variations that occur in the acousto-elastic coefficient B was observed with the 304 stainless steel bar described above.

A piece was removed from the 76 mm diameter round bar, as depicted in Fig. 10. Pin grip end pieces were welded onto the stainless steel sample so that a tensile stress could be applied; the stress axis coincided with a diameter of the original bar stock. After welding, the sample was annealed at 1100^0 C for one hour to remove residual stress. The acoustic velocity of longitudinal acoustic waves was measured along the gauge section of the composite tension test specimen at different values of applied tensile stress. From those data, the acousto-elastic coefficient B was obtained as a function of radial position in the 304 stainless steel bar. Figure 11 shows B as a function of radial position.

The pronounced variation in the acousto-elastic coefficient plotted in Figure 11

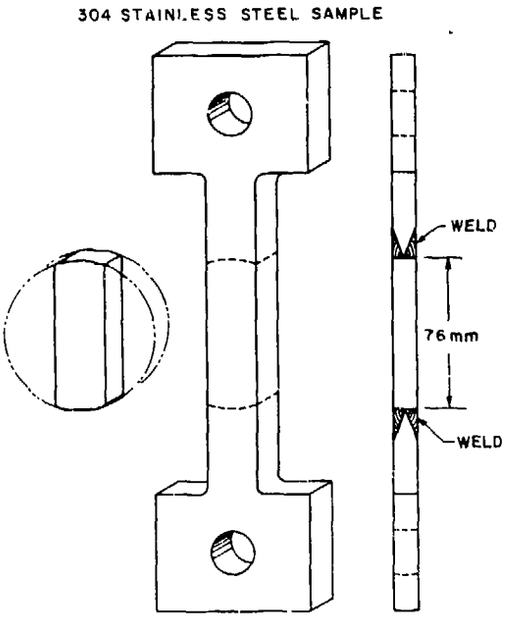

Fig. 10. Tension test specimen constructed from 304 stainless steel bar to measure acoustoelastic coefficient.

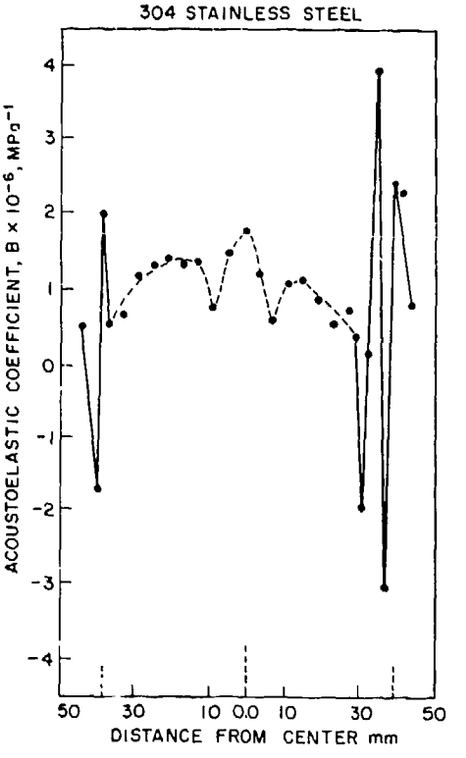

Fig. 11. Acoustoelastic coefficient vs. radial position in 304 stainless steel bar.

can be related to the radially-varying fiber texture discussed in connection with acoustic velocity measurements and to the welds used to construct the specimen. The wild fluctuations in B values measured 30 mm and farther from the

original center line of the round bar occur in the welds (weld material is also 304 stainless steel). Between the welds, the measured B values are highest at the center line and are lower toward the outer surface of the bar. This variation is consistent with the radially-varying fiber texture pattern observed in the bar. The fine scale variation in B near the center of the bar is not understood. Possibly it may reflect fine scale variations in the texture. The acoustic measurements were made using an acoustic beam 1.5 mm in diameter capable of spatially resolving the plotted fine scale B variations.

While explanations for the variability encountered in measuring acousto-elastic coefficients are incomplete and necessarily tentative, it is clear that large variations do occur even from point to point in the same piece of material. Such variations must be better understood if the full potential of acousto-elastic stress measurements is to be achieved.

SUMMARY

The acoustic properties of a bar of 304 stainless steel were observed to depend upon position and orientation in a manner coincident with the variation of grain size and preferred crystal texture in the bar. Acoustic velocity was demonstrated to be a sensitive measure of preferred texture and acoustic attenuation could be correlated with small variations in grain size. The acousto-elastic coefficient exhibited a position dependence apparently related to local variations in preferred texture.

ACKNOWLEDGMENT

The work described in this paper was performed as part of a research program on acoustic nondestructive testing sponsored by the Air Force Office of Scientific Research, Contract No. F49620-79-C-0217.

REFERENCES

1. D. B. Ilic, G. S. Kino, and A. R. Selfridge, Rev. Sci, Inst, 50 (17), 1527-1531 (1979).
2. N. Grayeli, D. B. Ilic, F. Stanke, G. S. Kino, and J. C. Shyne, Proceedings of the DARPA/AFML Review of Progress in Quantitative NDE, 429-434, (1980).
3. I. M. Lifshits and G. D. Parkhomovcskii, Zhur-EKSP-iteoret., Fiz, 20, 175 (1950).

William Pardee, Chairman (Rockwell Science Center): Are there any questions?

Unidentified Speaker: What was the slope of your attenuation, what was the power, and what was the frequency?

Frederick Stanke (Stanford University): The power slope varied between the curves I showed you, between 3.5 and -4. The highest was 3.9. For this sample, the slope of the attenuation was somewhat lower in the center of the sample. That is what we would expect because the grains are larger so the Rayleigh approximation is not as good. At the outside of the sample where the grains are smaller, it approached up to the fourth.

Unidentified Speaker: Can you take into account any sort of damping with dislocation, and would that be affected by an annealing?

Frederick Stanke: Yes. What I have described is simply a measurement system. We have measured the attenuation, and our job now is to interpret what that attenuation comes from, and theory needs to be done. Dislocation attenuation hasn't been something that we have looked into a lot. I was under the impression that the level would be much lower than what we're measuring.

ELASTIC WAVE SCATTERING FROM MULTIPLE AND ODD SHAPED FLAWS

V. V. Varadan, V. K. Varadan and D. J. N. Wall
Wave Propagation Group
Department of Engineering Mechanics
The Ohio State University
Columbus, Ohio 43210

ABSTRACT

Using the T-Matrix or Null Field method elastic wave scattering from the following geometries have been studied (a) Rotationally symmetric configurations consisting of two spheroidal cavities separated by a finite distance and with different eccentricities. Exact calculations are compared with single scattering approximations. The frequency spectra are interpreted for various scattering geometries and compared with experiments. The effect of change in distance between the scatterers is also discussed. (b) Scattering from rotationally symmetric cavities with odd shapes like "Pinnochio", Rockwell Science Center sample #73 and "Micky Mouse", Rockwell Science Center sample #70 was also studied and compared with numerical results using other techniques as well as experiments. Several ways of studying such problems is also discussed. (c) A numerical technique is proposed to study dynamic stress concentrations.

INTRODUCTION

The study of elastic wave scattering from two cavities has important implications from an NDE and fracture mechanics point of view. In many practical applications it is desirable to find out whether the flaw is a single one or two closely spaced ones separated by a small distance. In the latter case, it may be quite likely that the two flaws (cracks) will propagate towards each other according to fracture mechanics principles increasing the possibility of failure. In such cases, dynamic stress concentrations on the surface of each cavity particularly at corners and edges becomes relevant. This report deals with the scattering from two flaws separated by a finite distance (Fig. 1), odd shaped or compound flaws (Fig. 2) and the study of dynamic stress concentrations on the boundary of infinitely long cylindrical samples (2-D problems) with singular corners (Fig. 3). Whenever possible theoretical results are compared with available experimental results.

In a previous report[1], we gave a self-consistent formulation to obtain the T-matrix of two flaws separated by a finite distance. The expression that we obtained was identical to that given earlier by Peterson and Ström[2] for electromagnetic wave scattering from a configuration of two scatterers. Recently Boström[3] has obtained limited numerical results for elastic wave scattering from two cavities. Using the expression for the T-matrix as given in Ref. 1, we have made calculations of the scattering from dissimilar or similar spheroidal cavities for a range of frequencies and a variety of scattering geometries. In all these calculations the configuration is rotationally symmetric about the chosen z-axis. We also give a T-matrix formulation for configurations without rotational symmetry in a subsequent section. This study is still in progress. Numerical results for rotationally symmetric configurations are discussed from an NDE point of view.

Following the discussion of two scatterers, the problem of elastic wave scattering from a compound flaw is presented. As the name suggests, this problem can be viewed as the scattering from a single odd shaped flaw or as a multiple scattering problem of two flaws that are touching each other. Both methods are discussed.

Lastly for a two dimensional example of SH-wave incidence on a cylinder whose cross-section has sharp corners, the dynamic stress concentration around the boundary is studied for several frequencies and angles of incidence. Details of this calculation may be found in a separate report by Wall, Varadan and Varadan[4].

DISCUSSION OF RESULTS FOR ROTATIONALLY SYMMETRIC CONFIGURATIONS OF TWO SCATTERERS

Plane harmonic elastic waves are incident on the configuration shown in Fig. 1. Both flaws that are separated by a distance '2d' are figures of revolution about the common z-axis. Thus, without loss of generality the plane of incidence can be assumed to be the x-z plane. Let $\vec{u}^0$ and $\vec{u}^s$ be the displacement fields due to the incident and scattered waves, given by

$$\vec{u}^0 = \hat{p} e^{i\vec{k}\cdot\vec{r}} = \sum_{\tau=1}^{3} \sum_{nm\sigma} a_{\tau nm\sigma}(\hat{p},\hat{k})\, \mathrm{Re}\, \vec{\psi}_{\tau nm\sigma}(k\vec{r}) \qquad (1)$$

where p is the polarization vector, $k = \vec{k}/|\vec{k}|$ defines the direction of propagation of the incident wave and $|\vec{k}| = \omega/c$, where 'c' is either the velocity of P- (longitudinal) waves or S- (transverse) waves depending on $\hat{p}$. The vector Re $\vec{\psi}$ is the vector spherical function that is regular at the origin. Explicit expressions for these and the associated normalization factors may be found in Ref. 5. The scattered field $\vec{u}^s$ may be represented as

$$\vec{u}^s(\vec{r}) = \sum_{\tau=1}^{3} \sum_{nm\sigma} f_{\tau nm\sigma}\, \vec{\psi}_{\tau nm\sigma}(k\vec{r}). \qquad (2)$$

The expansion coefficients f are unknown and the function $\vec{\psi}$ is the vector spherical function that is outgoing at infinity (see Ref. 5). Our aim is to relate the unknown 'f' to the known 'a' via the T-matrix of the configuration.

In Ref. 1 an expression was obtained for the T-matrix by considering the total field incident on each scatterer and generalizing the definition of the T-matrix. Translation theorems for the spherical basis functions had to be invoked to have a common origin for the coordinate system for the two flaws. The final expression that was obtained can be cast into the form

$$
\begin{aligned}
T(1,2) &= R(\vec{d})T^1\{1 - \sigma(-2\vec{d})T^2\sigma(2\vec{d})T^1\}^{-1} \\
&\{1 + \sigma(-2\vec{d})T^2R(2\vec{d})\}R(-\vec{d}) \\
&+ R(-\vec{d})T^2\{1 - \sigma(2\vec{d})T^1\sigma(-2\vec{d})T^2\}^{-1} \\
&\{1 + \sigma(2\vec{d})T^1R(-2\vec{d})\}R(\vec{d})
\end{aligned}
\tag{3}
$$

where $2\vec{d}$ is the vector joining the centers O_1 and O_2 of the two obstacles, T^1 and T^2 are the T-matrices of the individual obstacles with respect to parallel coordinate systems centered at O_1 and O_2 respectively and $T(1,2)$ is the T-matrix of the configuration. Details of calculating T^1 and T^2 may be found in Ref. 5. The matrices R and σ are translation matrices, convenient expressions for which are given in Ref. 3.

The scattered field coefficients may now be written in vector matrix notation as

$$f = T(1,2)a. \tag{4}$$

For incident P-waves, the coefficients 'a' of Eq. (1) are given as

$$
a_{\tau nm\sigma} = 4\pi\sqrt{\frac{c_p}{c_s}}\ \xi_{nm}\ i^{n-1}\ p_n^m(\cos\alpha)\ \begin{matrix}\cos m\beta;\sigma = 1\\ \sin m\beta;\sigma = 2\end{matrix};
\tag{5}
$$

$$
\xi_{nm} = \sqrt{\frac{\varepsilon_m(2n+1)(n-m)!}{4\pi(n+m)!}}
$$

where (α,β) define the vector k. In all numerical calculations, $\beta = 0$, since the x-z plane is taken as the plane of incidence.

As the distance $2\vec{d}$ between the scatterers becomes large, the expression for $T(1,2)$ as given in Eq. (3) is unsuitable for numerical computations since the matrix elements of $R(2\vec{d})$ become rather large. In this case it is more convenient to use certain analytic properties of the R-matrix when it operates on the plane wave associated with the incident field and the outgoing spherical wave associated with the scattered field at distances far from the scatterer. This was first suggested by Peterson and Ström[2]. Using this idea, the T-matrix simplifies to the following form

$$
\begin{aligned}
T(1,2) \xrightarrow[|\vec{r}|\to\infty]{} &\exp i(k_p d\cos\alpha - k_\tau d\cos\theta)\times \\
&T^1\{1 - \sigma(-2\vec{d})T^2\sigma(2\vec{d})T^1\}^{-1}\times \\
&\{1 + \sigma(-2\vec{d})T^2\exp(2ik_p d\cos\alpha)\} \\
&+ \exp i(k_\tau d\cos\theta - k_p d\cos\alpha)\times \\
&T^2\{1 - \sigma(2\vec{d})T^1\sigma(-2\vec{d})T^2\}^{-1}\times \\
&\{1 + \sigma(2\vec{d})T^1\exp(-2ik_p d\cos\alpha)\}.
\end{aligned}
\tag{6}
$$

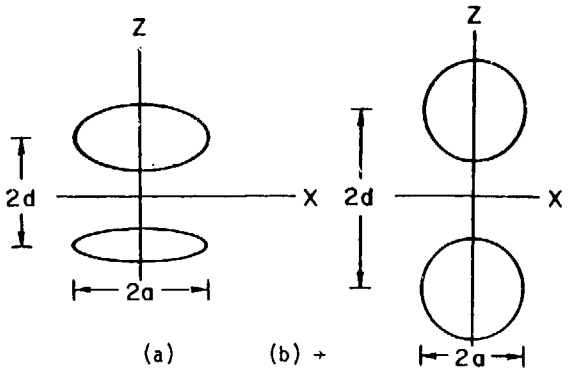

Fig. 1 Rotationally symmetric two scatterer configurations (a) Dissimilar spheroids (b) Identical spheres (c) Dissimilar spheres.

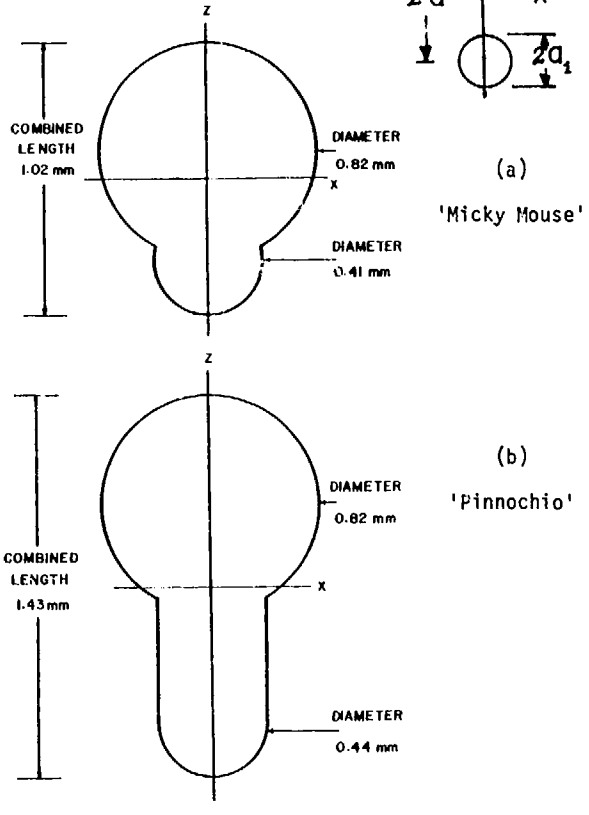

Fig. 2 Rotationally symmetric compound flaws.

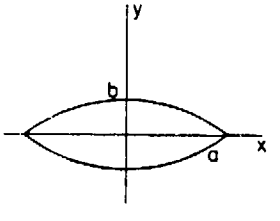

Fig. 3 Cylindrical cavity with sharp corners.

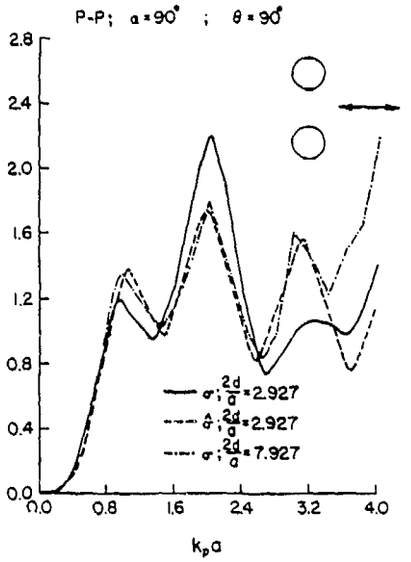

Fig. 4 Back scattering cross section as a function of frequency of identical spheres for incident P-waves.

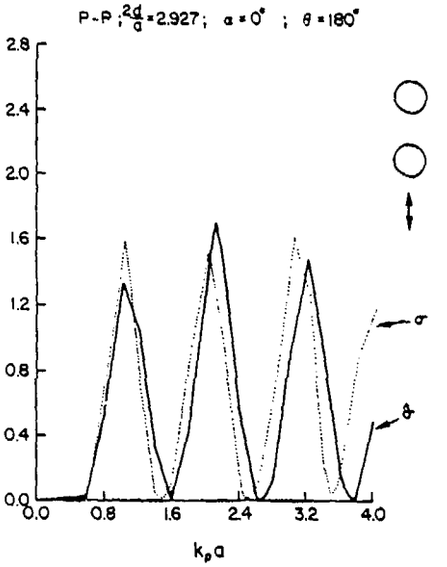

Fig. 5 Back scattering cross section as a function of frequency of identical spheres for incident P-waves.

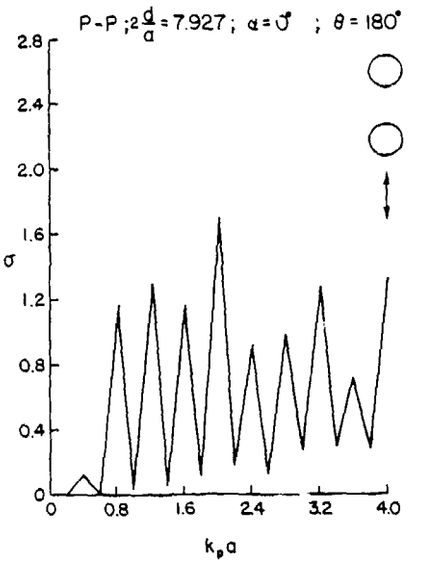

Fig. 6 Back scattering cross section as a function of frequency of identical spheres for incident P-waves.

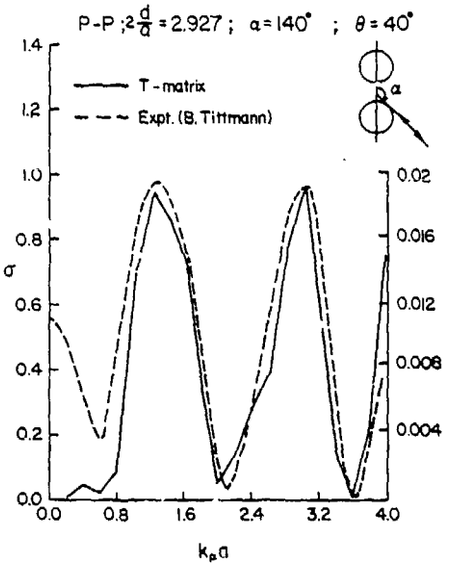

Fig. 7 Back scattering from two identical spheres, comparison of experiment and theory.

In Eq. (6), $k_T = k_p$ or k_s depending on the row index of the appropriate T-matrix element. This expression for the T-matrix is quite well suited for '2d' large. The disadvantage is that it is no longer independent of the scattering geometry. The major computation in Eq. (6) can however be performed independent of scattering geometry.

If the matrix inverses appearing in Eq. (3) are expanded, one can identify the various multiple scattering processes that contribute to the total scattered field. If one wants to include only single scattering, then

$$T(1,2) + R(\vec{d})T^1R(-\vec{d}) + R(-\vec{d})T^2R(\vec{d}) \quad . \qquad (7)$$

The amplitude of the scattered longitudinal field at distances far from the origin is given by

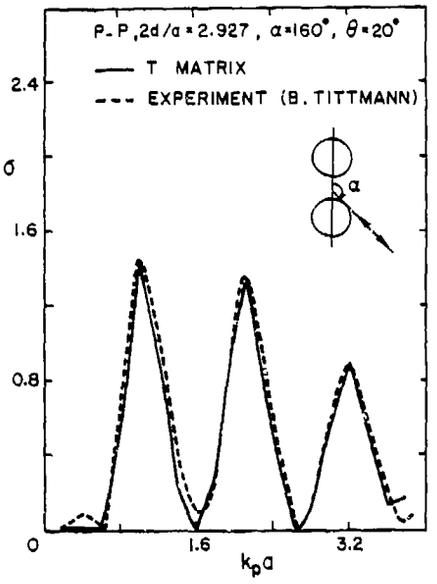

Fig. 8 Back scattering from two identical spheres, comparison of experiment and theory.

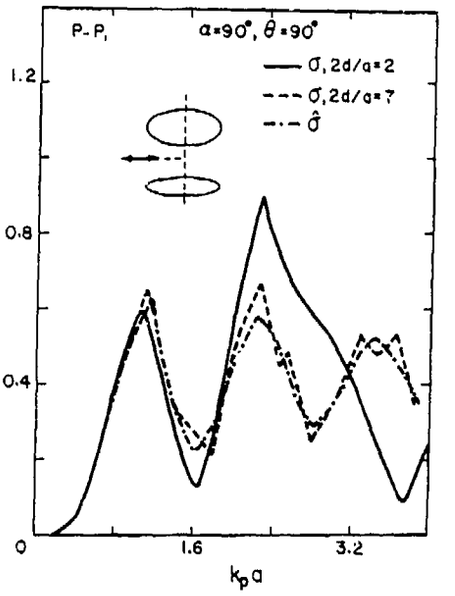

Fig. 9 Back scattering cross section of two spheroids, $b_1/a = 0.5$ and $b_2/a = 0.33$, for incident P-waves.

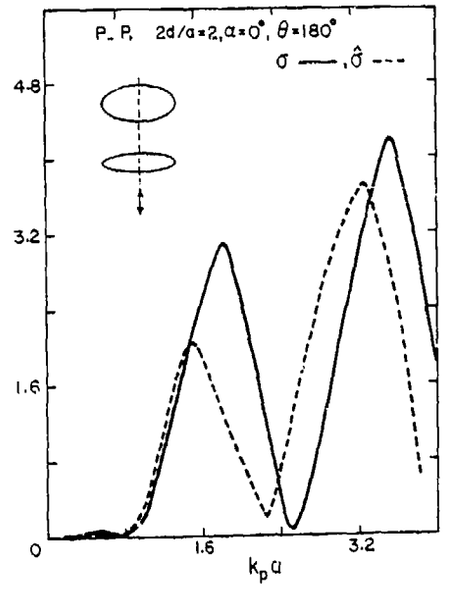

Fig. 10 Back scattering cross section of two spheroids, $b_1/a = 0.5$ and $b_2/a = 0.33$, for incident P-waves.

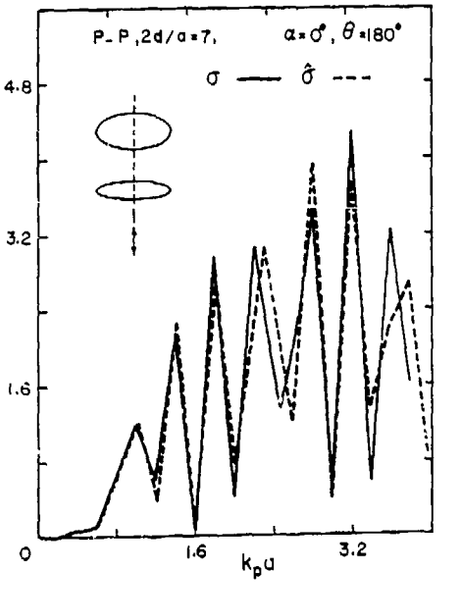

Fig. 11 Back scattering cross section of two spheroids, $b_1/a = 0.5$ and $b_2/a = 0.33$, for incident P-waves.

$$f(\theta,\phi) = \sqrt{\frac{c_s}{c_p}} \sum_{n=0}^{\infty} \sum_{m=0}^{n} \varepsilon_{nm}\, i^{-n}\, p_n^m(\cos\theta) \times \{f_{1nm1} \cos m\phi + f_{1nm2} \sin m\phi\}. \quad (8)$$

The scattered energy or the cross section is given by

$$\sigma(\theta,\phi) = |f(\theta,\phi)|^2/(k_p a)^2 \quad (9)$$

where 'a' is a characteristic dimension of the scatterer. Equations (8) and (9) may be used for both single and multiple scatterer configurations.

In the numerical results that follow, if the single scattering approximation is used for T(1,2) (Eq. 7), the scattering cross section is

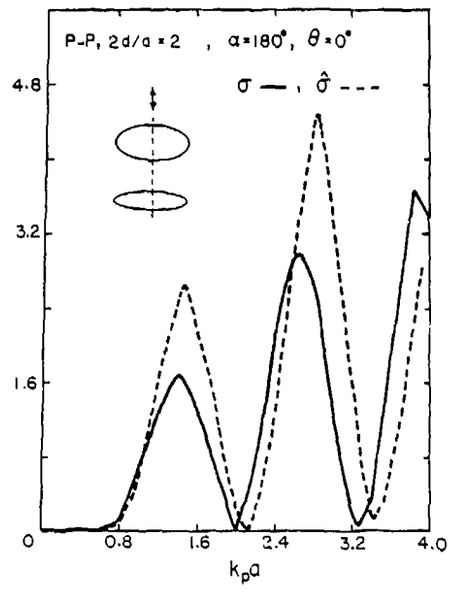

Fig. 12 Back scattering cross section of two spheroids, $b_1/a = 0.5$ and $b_2/a = 0.33$, for incident P-waves.

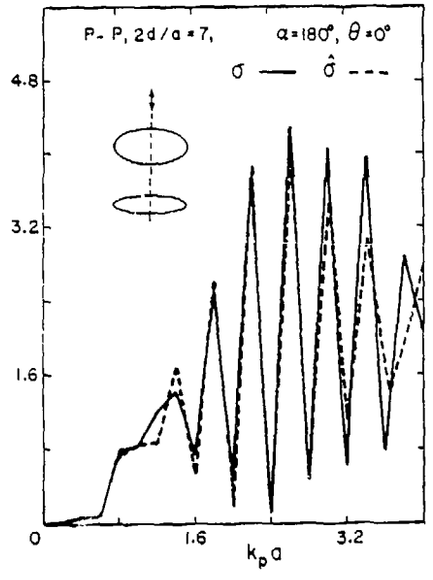

Fig. 13 Back scattering cross section of two spheroids, $b_1/a = 0.5$ and $b_2/a = 0.33$, for incident P-waves.

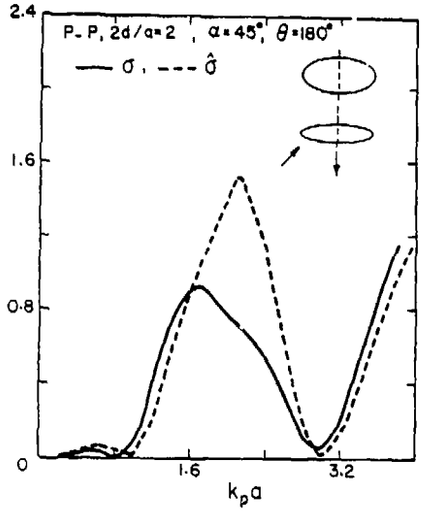

Fig. 14 Bistatic cross section of two spheroids, $b_1/a = 0.5$ and $b_2/a = 0.33$ for incident P-waves.

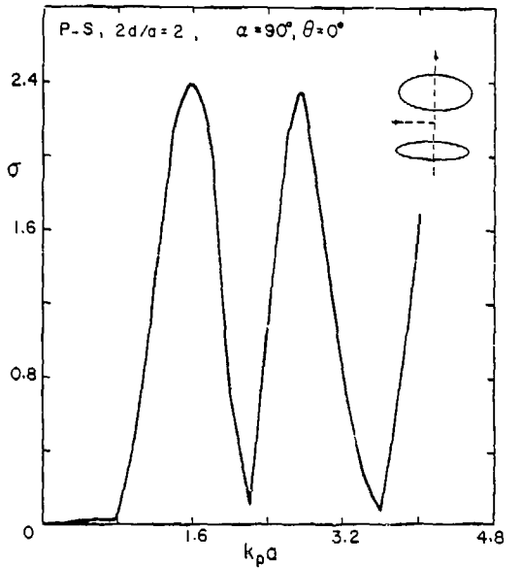

Fig. 15 Mode converted bistatic cross section (P → S) of two spheroids, $b_1/a = 0.5$ and $b_2/a = 0.33$.

distinguished as $\hat{\sigma}$. The two forms σ and $\hat{\sigma}$ are compared for several two scatterer configurations. It must be noted that although $\hat{\sigma}$ may be called a single scattering approximation, it still depends on the distance between the scatterers since the two single scattered complex amplitudes are added together with the proper phase. In the strict sense, a single scattering approximation would just correspond to adding the cross sections of the individual scatterers and all knowledge of the relative phase would be lost. This result is completely independent of the distance between the scatterers and is distinguished as $\sigma_{s,s}$. We also observe that for back scattering at 90° incidence for example, the two single scattered amplitudes are in phase and $\hat{\sigma} = 2\sigma_{s,s}$.

In Fig. 4, the back scattering cross section is plotted as a function of $k_p a$ for P-wave incidence perpendicular to the line joining two identical spheres of radius a. In this case $\hat{\sigma} = 2\sigma_{s,s}$ as discussed above. It is seen that σ approaches $\hat{\sigma}$

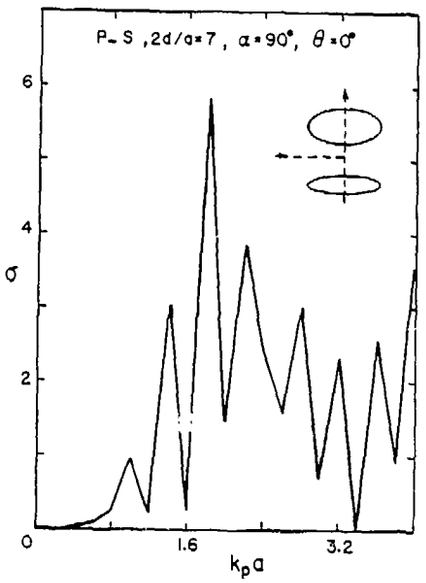

Fig. 16 Mode converted bistatic cross section (P → S) of two spheroids, $b_1/a = 0.5$ and $b_2/a = 0.33$.

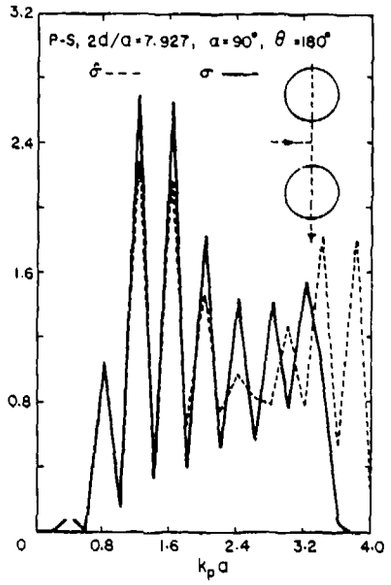

Fig. 18 Mode converted bistatic cross section of two identical spheres.

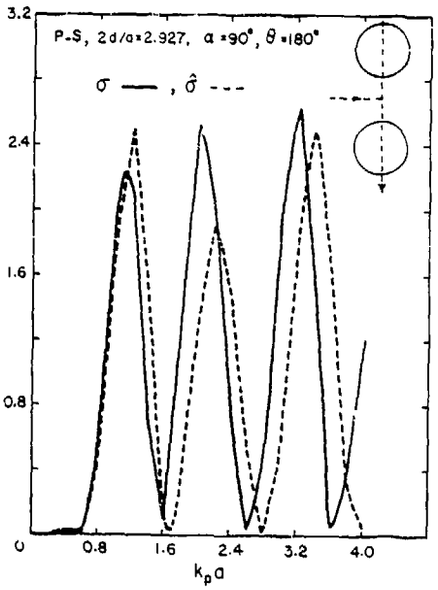

Fig. 17 Mode converted bistatic cross section of two identical spheres.

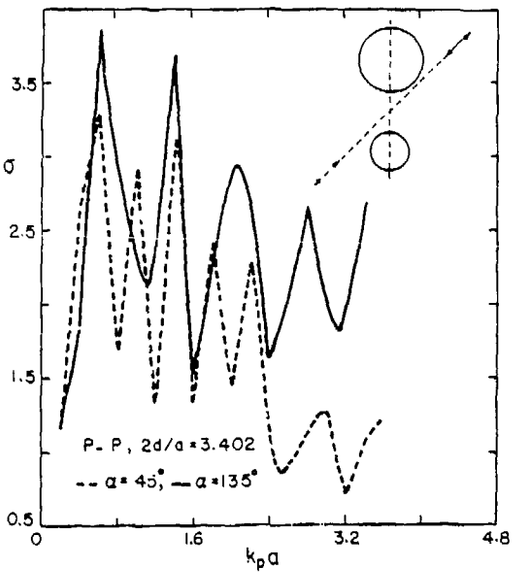

Fig. 19 Back scattering cross section for incident P-waves of two dissimilar spheres, ratio of radii = 3.0, 'a' is the radius of the small sphere.

as the distance between the two spheres increases. In Fig. 5, the back scattering cross section is plotted for P-waves incident along the line joining the two spheres. It is seen that even when the distance between the two spheres is as small as 2.927a, σ and $\hat{\sigma}$ compare very well and display sharp zeroes. The spacings of the zeroes can be correlated to the interference of waves that creep around each of the spheres. The path difference between the two waves is twice the distance between the centers of the spheres and shows up in the spacing of the minima. In Fig. 6 we have the same scattering geometry, but now the distance between the spheres has increased to 7.927a, resulting in very closely spaced minima. In this case σ was almost equal to $\hat{\sigma}$ and hence $\hat{\sigma}$ is not displayed in the graph. In Figs. 7 and 8, for $\alpha = 140°$ and $\alpha = 160°$, the back scattering cross section is compared with experimental results showing excellent agreement. The results were plotted on the same graph by matching just one point, the maximum value of the cross section.

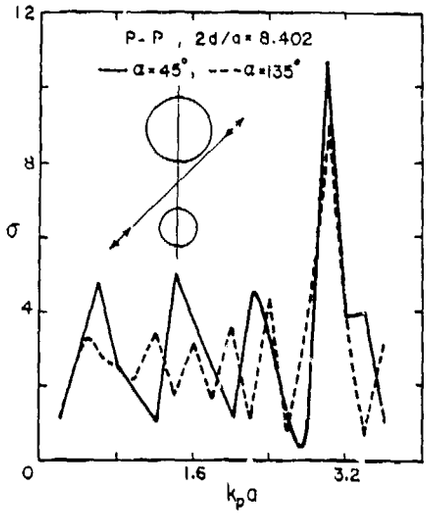

Fig. 20 Back scattering cross section for incident P-waves of two dissimilar spheres, ratio of radii = 3.0, 'a' is the radius of the small sphere.

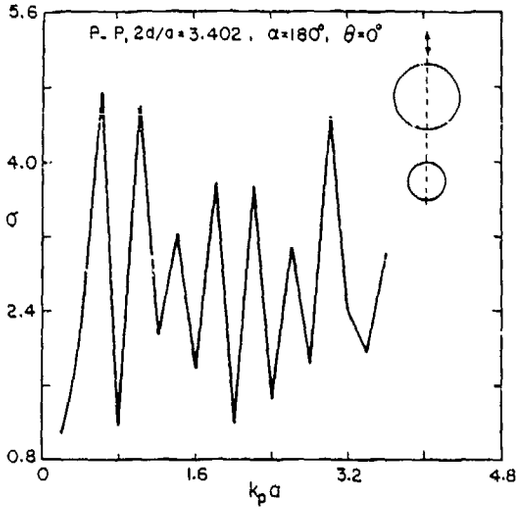

Fig. 21 Back scattering cross section for incident P-waves of two dissimilar spheres, ratio of radii = 3.0, 'a' is the radius of the small sphere.

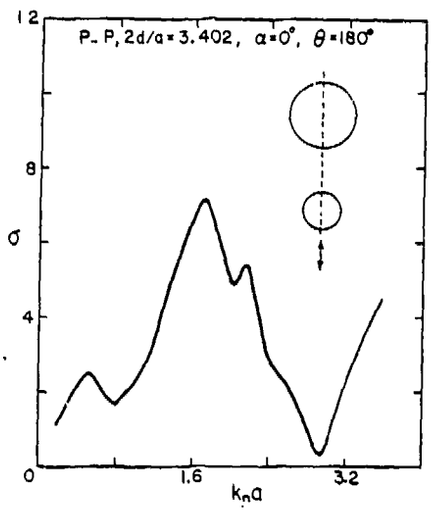

Fig. 22 Back scattering cross section for incident P-waves of two dissimilar spheres, ratio of radii = 3.0, 'a' is the radius of the small sphere.

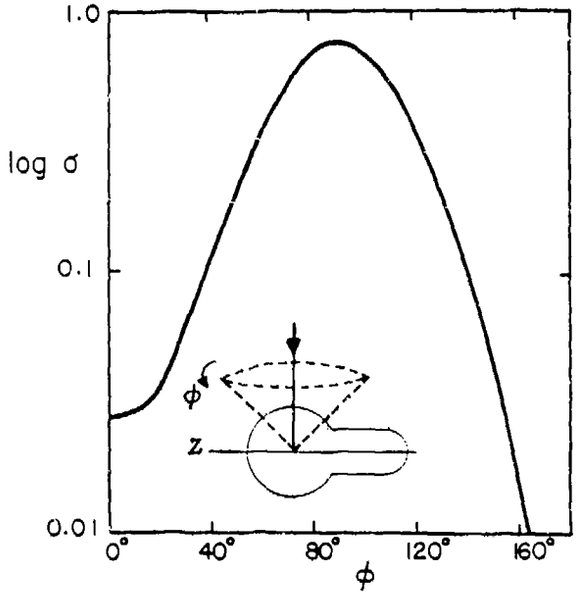

Fig. 23 Angular variation of the bistatic cross section of 'Pinnochio' (Fig. 26) for P-waves incident broadside at $k_p a = 2.0$.

In Figs. 9-14, the back scattering cross section of two dissimilar oblate spheroids, shown in Fig. 1a is considered. The minor to major axis ratios were taken to be 0.5 and 0.33. Although interference of creeping waves does show up in the cross section, specularly reflected waves also contribute to the interference pattern, unlike the case of two identical spheres. In Fig. 15-18, the mode converted cross section is displayed for the geometries in Fig. 1a and 1b.

The next geometry that is considered is the case of two dissimilar spheres of radii a_2 and a_1, with $a_2/a_1 = 2.976$ (see Fig. 1c). In Fig. 19, the back scattering cross section for $\alpha = 45°$ is compared with that for $\alpha = 135°$ when the distance between centers is $3.4a_1$. In Fig. 20, the distance has increased to $8.4a_1$, and cross sections for $\alpha = 45°$ and $\alpha = 135°$ are again compared. It is also interesting to compare Fig. 19 with Figs. 21 and 22. Figure 21 is the back scattering cross section for $\alpha = 180°$, illuminating the big sphere and Fig. 22 is the corresponding result for $\alpha = 0°$ where the

small sphere is illuminated and also a large part of the big sphere. The results for the two cases are strikingly different. In fact, Fig. 21 looks almost like the scattering cross section of the big sphere of radius a_2, if the abscissa is rescaled in terms of $k_p a_2$. The interference pattern is due to the path difference between the specularly reflected wave and a creeping wave.

Samples exist at the Rockwell Science Center for the geometries shown in Figs. 1a and 1c, however experimental results are available only for the case of identical spheres (Fig. 1a).

SCATTERING FROM COMPOUND FLAWS

The compound or odd shaped flaws that have been considered are shown in Figs. 2a and 2b. These are popularly known as "Micky Mouse" and "Pinnochio" respectively. Experimental data is available for both. To date most of the analytical-computational procedures have been confined to idealized scatterers like spheroids, penny shaped cracks or elliptical cracks. All these flaw surfaces can be described by a single equation. The geometries illustrated in Fig. 2 are however compound voids and different equations are needed to describe different portions of the surface. Hence these shapes are quite challenging for numerical computations.

Consider the geometry in Fig. 2a. At the junction, where the two spherical parts intersect, there is a discontinuity in the outward normal. Matrix methods are numerically unstable in the presence of such sharp concavities. Moreover the nature of the stress singularity at a sharp fracture such as this is unknown and remains one of the unsolved static boundary value problems in mechanics. Experimental evidence indicates that these stress singularities do not influence the scattered far field to any great extent. This has also been verified numerically for the two dimensional anti-plane problem. In this case the analytical form of the stress singularity is known.

Two different approaches were used. In one method, the small portion where the two spheres intersect was smoothed out by a straight line segment, in the second method Legendre polynomials were used to fit the contour smoothly. In the latter case there was a still a concavity, but it was not sharp. A third method of calculation is still in progress. This is to consider the void as a compound void with the two parts of the sphere just touching each other, the centers of the parts being separated by a finite distance. The T-matrix of each separate part is computed by closing off the open end by a straight line segment, on which the normal displacement must be prescribed. But the displacement on the straight line segment for the lower sphere will exactly cancel this when the two T-matrices are superposed in Eq. (3) to get the combined T-matrix. Preliminary results indicate that this approach is numerically much more stable and will enable us to consider much higher incident wave frequencies.

In Figs. 23-24, the angular behaviour of the scattering cross section for P-waves which are incident broad side on both samples. The actual scattering geometry is shown in the figures. In Fig. 24, the scattering cross section of a prolate spheroid and a sphere of the same over all

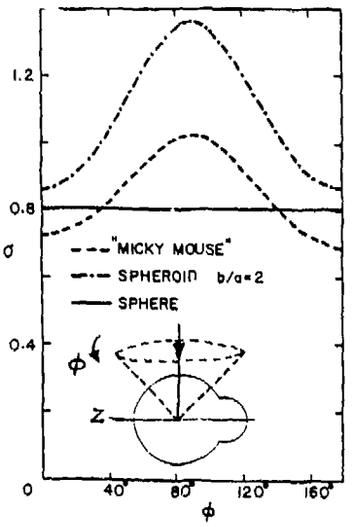

Fig. 24 Angular variation of the bistatic cross section compared for 'Micky Mouse' (Fig. 2a), prolate spheroid and sphere.

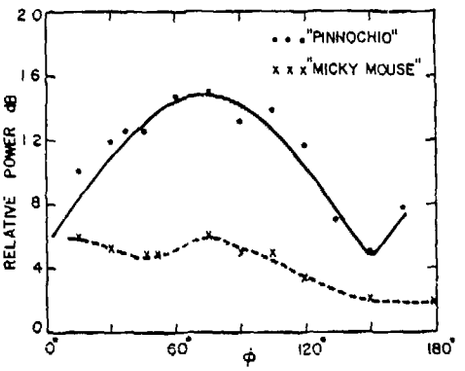

Fig. 25 Experimental results by B. Tittmann corresponding to calculations in Figs. 23 and 24.

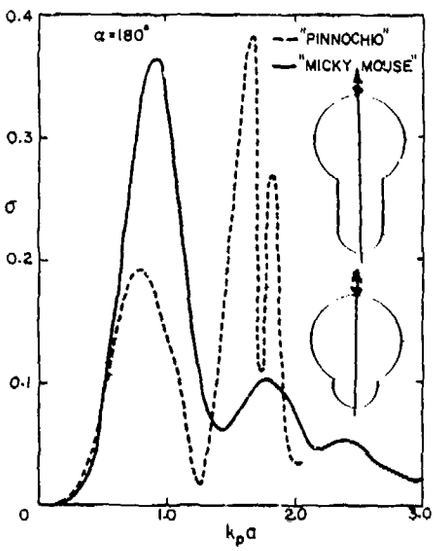

Fig. 26 Back scattering cross section for head on incidence of P-waves.

dimensions as "Micky Mouse" are displayed for purposes of comparison. Both figures indicate a sharp drop in the cross section at $\phi = 0°$ and $\phi = 180°$ corresponding to weak scattering from the two edges. For the case of "Pinnochio", experimental results obtained by B. Tittmann shown on Fig. 25 seems to be in qualitative agreement. Comparison of the numerical results for the spectra with experiments is still in progress, since these became available only recently. In Figs. 26 and 27, the back scattering cross section as a function of frequency is displayed for incidence along the symmetry axes.

DYNAMIC STRESS CONCENTRATIONS

A method is presented for the calculation of dynamic stress concentration factors when a time harmonic SH-wave is incident upon a cylindrical cavity of arbitrary cross section. The stresses in the vicinity of the cavity are markedly different from those that would be present if the cavity were not present. This effect is known as dynamic stress concentration. The study for more general polarizations (in-plane problems) is still in progress. Exact determination of the dynamic stress concentration caused by a cylindrical cavity is only possible for a restricted class of cross sectional shapes, namely those for which the elastic wave differential operator is separable. Pao and Mow[6] give a detailed description of the separation of variables approach for this problem. For more general cross sections, in particular if singular corners are present, a numerical technique is called for. We employ such a technique here.

Our algorithm is based on a method that has been called the null field method by Bates and Wall[7] or the transition matrix (T-matrix) method. It reduces to the solution of a particular integral equation. This method has two major advantages over other methods when applied to the problems discussed here. The solution is unique and solutions of the complimentary problem are decoupled. For cavities, the unknown function is the surface displacement. The evaluation of surface fields is much more difficult than the evaluation of scattered fields. In a sense, with the regular T-matrix approach used in the previous sections, the surface field is in fact calculated. But in the final analysis, due to the particular structure of the formulation (the use of the null field equation), the result is insensitive to an inaccurate determination of the surface field. For the problem at hand since the determination of the surface field is the end result, basis functions used to represent it must be picked with particular care.

When the scatterer has corners it is necessary to ensure that the basis used has the correct edge behaviour. Wedge functions are used for this purpose and they are found from the solution of the canonical problem of scattering from an infinite wedge. The surface of the cavity is divided into several regions and within each region an appropriate basis is used. The null field equations together with the constraint equations necessary to ensure continuity at the nodes are sufficient to solve for the unknown coefficients of the basis. If there are no corners, but just an increase in the stress concentration factor, an appropriate metric function is incorporated into basis representation. Details of the numerical procedure and more extensive results may be found in Ref. 4.

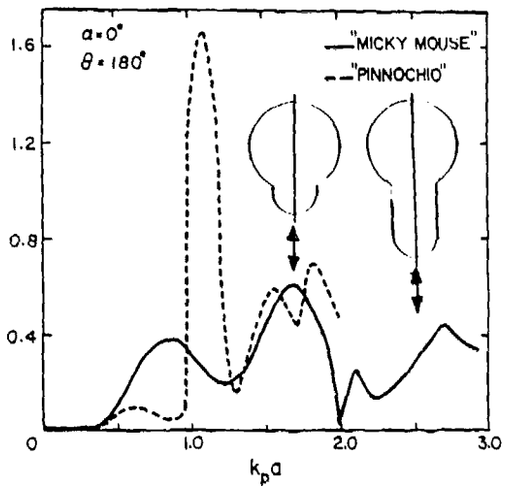

Fig. 27 Back scattering cross section for nose on incidence of P-waves.

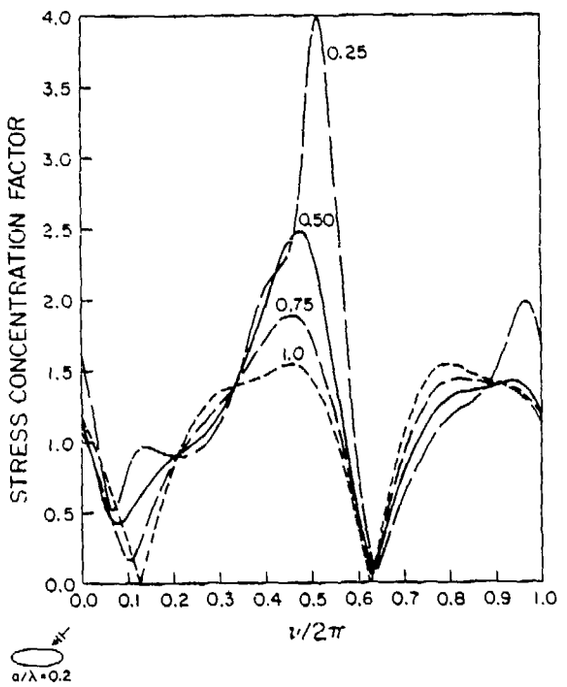

Fig. 28 Dynamic stress concentration on the surface of an elliptical cavity for four different minor to major axis ratios and incident SH-waves.

For the anti-plane problem, the boundary condition at the surface of the cavity may be stated as the vanishing of the normal traction

$$\sigma_{nz} = 0 \text{ on } S$$

where S is the surface of the cavity and $\hat{n}$ is the outward normal in the x-y plane, the z-axis being parallel to the cylinder axis. The only non-zero stress component at the surface is then σ_{tz} where t is taken to be tangent to S in the x-y plane. In Figs. 28 and 29 σ_{nz} is plotted at all points on the boundary. In the abscissa $\nu/2\pi$ is the angular measure as one traverses the contour and it varies from 0 to 1 for a complete revolution. Figure 28 is for an elliptical cavity, the scattering geometry being displayed in the lower left corner. If 'a' is the semimajor axes of the ellipse and 'λ' the incident wavelength a/λ is taken to be 0.2 corresponding to ka 1.4. Four different minor to major axis ratios ranging from 0.25 to 1.0 are considered for this frequency. In Fig. 29, a cavity with corners arising from the sharp intersection of two circles is considered. In this case for 45° incidence, the stress concentration σ_{tz} is plotted for three values of the a/λ ratio 0.02, 0.2 and 0.4.

We conclude this section by observing that the success of this method depends on a good knowledge of the approximate behaviour of the stress in the vicinity of the scatterer. For three dimensional scatterers, many of the canonical problems are unsolved. The choice of appropriate basis functions at corners is crucial. The sharp singularities in the stress manifest themselves as barely discernible discontinuities in plots of the surface displacement, so that the latter must be calculated very accurately.

MULTIPLE SCATTERING CONFIGURATIONS WITH NO ROTATIONAL SYMMETRY

All the cases considered above for both multiple and compound flaws possessed an axis of rotational symmetry. Since vector spherical functions were used to describe the fields, the rotational symmetry renders all matrices diagonal in the azimuthal index. This simplifies the calculation enormously. Without this symmetry matrix sizes will become so large even at small values of $k_p a$ 1.0 to make computations unfeasible. However, the need exists for long wavelength scattering information from non-axes symmetric configurations. It is for this particular application that we propose the following. The formalism that is given below is in principal applicable for the range of frequencies for which the T-matrix of the individual scatterer can be computed, the limitation is in the machine computations.

We consider two coordinate systems centered at 0, x-y-z and x'-y'-z' respectively. Let α, β, γ be the Euler angles of the primed system with respect to the unprimed system (Fig. 30). It is often desirable to calculate the T-matrix of an individual scatterer with respect to a coordinate system that is chosen based on the geometrical symmetries of the scatterer. This will minimize computations. If the scatterer has an axis of rotational symmetry, the T-matrix is diagonal in the azimuthal index. However, it may be necessary to express this T-matrix in a different coordinate system, say the

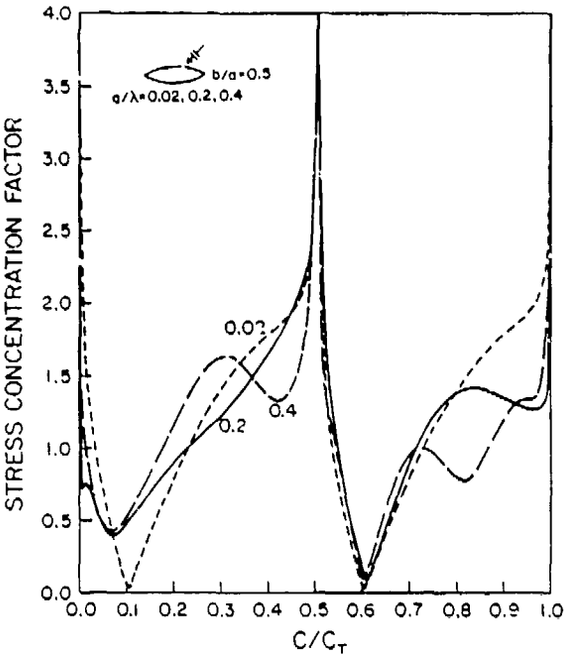

Fig. 29 Dynamic stress concentration on the surface of a cylindrical lens shaped cavity with sharp corners for different incident SH-wave frequencies, c/c_T is the normalized contour length.

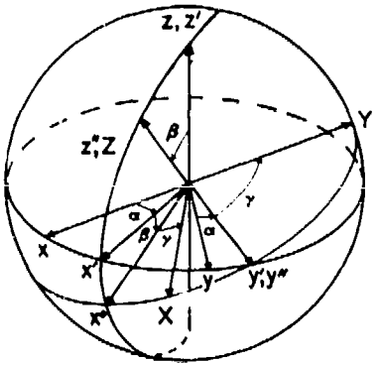

Fig. 30 Euler angles for rotation of coordinate systems.

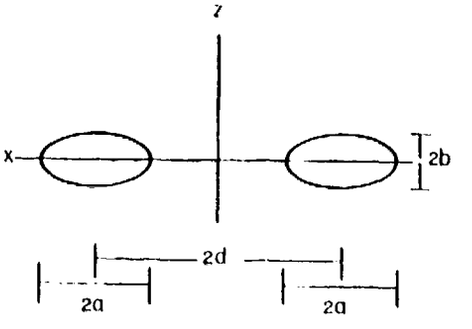

Fig. 31 Spheroidal scatterers with no rotational axis of symmetry.

primed system because the experimental set up may necessitate it or there may be another scatterer with its axis of symmetry aligned with the primed system. For the particular application we have in mind, refer to Fig. 31. Two spheroidal scatterers are considered with their centers separated by a distance '2d', perpendicular to the axis of rotational symmetry. In the previous sections the translation was along the axis of symmetry. The resulting configuration is not rotationally symmetric, hence the total T-matrix loses its block diagonal property. In this case also the expression for T(1,2) given in Eqs. 3 or 6 is applicable if one keeps the general form of the translation matrices. However, it is more convenient to express the T-matrix of the individual spheroids in coordinate system that is rotated by a 90° angle and then perform the translation along this new z-axis.

The transformation of the T-matrix under an Euler rotation may be conveniently expressed by noting that the spherical harmonics used in deriving the T-matrix are the eigenfunctions of the rotation operator[5,8]. Thus if T' is the T-matrix in the primed system, then it is related to the T-matrix of the unprimed system according to

$$T^1 = D^{-1}(\alpha,\beta,\gamma)TD(\alpha,\beta,\gamma) \tag{10}$$

where the rotation matrix D is given by

$$D^n_{m'm}(\alpha,\beta,\gamma) = e^{im'\alpha}d^n_{mm'}(\beta)e^{im\gamma} \tag{11}$$

where

$$d^n_{mm'}(\beta) = \left[\frac{(n+m')!(n-m')!}{(n+m)!(n-m)!}\right]^{\frac{1}{2}}\left(\cos\frac{\beta}{2}\right)^{m'+m} \times \left(\sin\frac{\beta}{2}\right)^{m'-m} P^{(m'-m,m'+m)}_{n-m'}(\cos\beta) \ . \tag{12}$$

In Eq. (12), P^{ij}_n are the Jacobi polynomials which can be expressed in terms of the associated Legendre polynomials. For more details on Eqs. (11) and (12) we refer the reader to Edmonds[9]. If T^1 and T^2 in Eqs. (3) and (6) are replaced by $D^{-1}T^1D$ and $D^{-1}T^2D$, we obtain T(1,2) for the configuration shown in Fig. 31. Numerical computations at wavelengths long comparable to the overall dimensions of the configuration are still in progress.

ACKNOWLEDGEMENTS

This research was supported by the Center for Advanced NDE, operated by the Science Center, Rockwell International for DARPA/AFML under contract #F33615-80-C-5004. The help of Dr. Bo Peterson in some phases of the computation is gratefully acknowledged.

REFERENCES

1. V.V. Varadan and V.K. Varadan, 'Elastic wave scattering by rough flaws and cracks', Interdisciplinary Program for Quantitative Flaw Definition, Special Report fifth year effort, prepared for ARPA/AF by B. Thompson, Center for Advanced NDE, Rockwell International, Thousand Oaks, California 91360 (1979).

2. B. Peterson and S. Ström, 'T-Matrix for electromagnetic scattering from an arbitrary number of scatterers and representations of E(3)', Phys. Rev. D, 8, 3661 (1973).

3. A. Boström, 'Multiple scattering of elastic waves by bounded obstacles', J. Acoust. Soc. Am. 67, 399 (1980).

4. D.J.N. Wall, V.V. Varadan and V.K. Varadan, 'Dynamic stress concentrations of cylindrical cavities with sharp and smooth boundaries I. SH waves', Report submitted to Center for Advanced NDE, Rockwell International (1980), Also submitted for publication.

5. V.V. Varadan, 'Elastic wave scattering', in Acoustic, Electromagnetic and Elastic Wave Scattering - Focus on the T-Matrix Approach edited by V.K. Varadan and V.V. Varadan, Pergamon Press, New York (1980).

6. Y.H. Pao and C.C. Mow, 'Diffraction of elastic waves and dynamic stress concentrations', Crane Russak, New York (1973).

7. R.H.T. Bates and D.J.N. Wall, 'Null field approach to scalar diffraction I. General Method', Phil. Trans. R. Soc. Lond. A287, 45 (1977).

8. V.V. Varadan and V.K. Varadan, 'Multiple scattering of electromagnetic waves by randomly distributed and oriented scatterers', Phys. Rev. D, 19, 2480 (1980).

9. A.R. Edmonds, 'Angular momentum in quantum mechanics', Princeton University Press, Princeton, New Jersey (1957).

APPLICATION OF MOOT TO SCATTERING OF ELASTIC WAVES FROM COMPOUND INCLUSIONS

William M. Visscher
Theoretical Division
Los Alamos Scientific Laboratory
University of California
Los Alamos, New Mexico 87545

ABSTRACT

We show how MOOT (method of optimal truncation, a convergent T-matrix scheme) can be used to calculate elastic wave scattering from compound inclusions; i.e. inclusions which themselves contain flaws - inclusions, voids, or cracks. The general equations are derived, and they are solved for a particular axially-symmetric case - a cracked spherical inclusion immersed in fluid. The crack edge is a circle on the equatorial plane; the crack can extend either inward to the center or outward to the surface of the sphere. Numerical results are given for scattering of acoustic waves from cracked spheres of various materials. Cracked spheres can be fabricated relatively easily, and may be useful in NDE calibrations.

INTRODUCTION

An experimental technique often used in ultrasonic measurements is to immerse an object in a tank of water and study it by scattering acoustic waves from it, the fluid effectively providing a coupling between the transducers and the object. In principle, one can determine all of the structural features of the object in this way. For NDE applications in particular, information is needed about internal flaws such as voids, inclusions, or cracks and about surface cracks and irregularities.

Because the crack is the most common and potentially the most dangerous defect in manufactured items, and the sphere is the simplest shape imaginable, a cracked sphere would seem to be a useful prototype of a compound inclusion. It is relatively easy to fabricate in practice and to compute scattering from, and could serve as a calibration standard, both experimentally and theoretically.

In this paper we will develop a general formalism with which the elastic wave equation can be solved for a system in which a compound inclusion is immersed in a host medium. The host medium may be either a fluid or an elastic solid, the compound inclusion may be complex and the generalization of the theory will be obvious, but we will calculate only included elastic spheres with cracks on their equatorial planes. The crack edges are circular, with the cracks extending either out to the surface or in to the center (see Fig. 1).

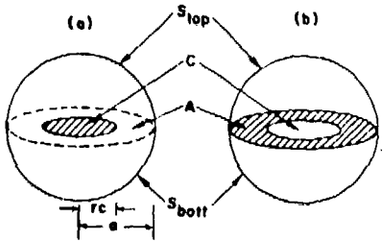

Fig. 1 Cracked spheres. The interior crack (a) has free boundaries; the peripheral crack (b) is fluid-filled. The equatorial plane is divided into a circle (C) and an annulus (A). The top and bottom hemispheres are called S_{top} and S_{bott}.

We will present a brief review of the computational method which we use. It is a straightforward extension of MOOT (method of optimal truncation) which was developed earlier.[1,2,3] We will show how to handle inclusions containing voids as well as internally and peripherally cracked inclusions.

Numerical results for scattering of acoustic waves from cracked spheres immersed in water are given in the final section. Both internal and surface cracks are considered. Results are shown for different crack sizes and are compared with scattering from uncracked spheres. The effects of material properties (acoustic impedances and propagation velocities) on the sensitivity of scattering to internal flaws are very important and probably will be the most stringent limitations on practical applications.

GENERAL DEVELOPMENT

The idea of MOOT will be explained for the simple case of a void within an inclusion, illustrated in Fig. 2. The vector displacement field

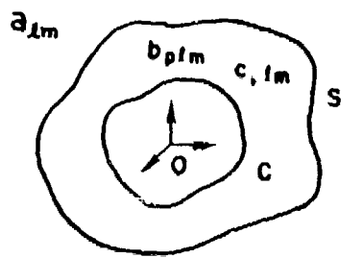

Fig. 2 A void (surface C) within an inclusion (surface S) immersed in a fluid. The displacement outside S consists of a plane wave plus outgoing partial waves (coefficients $a_{\ell m}$); inside S it is expanded in regular (coefficients $b_{p\ell m}$) and irregular (coefficients $c_{p\ell m}$) eigenfunctions of the elastic wave equation. The origin of coordinates is always taken inside C.

in the fluid outside the inclusion is expanded in outgoing eigenvectors of the acoustic wave equation,

$$\vec{S} = \sum d_{\ell m}\vec{S}_{\ell m} + \sum a_{\ell m}\vec{S}^{+}_{\ell m}, \tag{1}$$

where the $\vec{S}_{\ell m}$'s are given by

$$\begin{aligned}\vec{S}_{\ell m} &= k^{-1}\vec{\nabla} j_\ell Y_{\ell m}(\theta,\phi)\\ \vec{S}^{+}_{\ell m} &= k^{-1}\vec{\nabla} h^{+}_\ell Y_{\ell m}(\theta,\phi)\end{aligned} \tag{2}$$

with $k^2 = \rho\omega^2/\lambda$, $d_{\ell m} = 4\pi i^\ell Y_{\ell m}(\theta_0\phi_0)$. $\theta_0\phi_0$ are the spherical angles of the direction of the incident plane wave

$$\vec{S}_{inc}(\vec{r}) = k^{-1}\vec{\nabla} e^{i\vec{k}_0\cdot\vec{r}} = \vec{\nabla}\sum d_{\ell m} j_\ell(r) Y_{\ell m}(\theta,\phi), \tag{3}$$

λ is the fluid bulk modulus, $j_\ell(kr)$ is the regular spherical bessel function, and $h^{+}_\ell = j_\ell + iy_\ell$. The problem is to determine the as yet unknown coefficients $a_{\ell m}$, which we do as follows.

The displacement field inside the inclusion is

$$\vec{S}' = \sum b_{p\ell m}\vec{S}'_{p\ell m} + c_{p\ell m}\vec{S}'_{p\ell m}, \tag{4}$$

where $\vec{S}'_{p\ell m}$ for p = 1 (longitudinal polarization) is as given in (2) but with $k_l = \rho'\omega^2/(\lambda'+2\mu')$, and for p = 2,3 (transverse polarizations) is as given in ref. 2 but with $k_T = \rho'\omega^2/\mu'$, μ' being the shear modulus. $\vec{S}'_{p\ell m}$ is identical to $\vec{S}'_{p\ell m}$ except y_ℓ (spherical bessel function irregular at origin) is substituted for j_ℓ. The extra complexities of (4) are necessitated by the facts that the inclusion, being a general isotropic elastic material, can support shear stresses and therefore transversely polarized waves, and that no radiation condition (outgoing scattered waves at infinity) constrains the interior field, so that both regular and irregular bessel functions are needed.

The stress tensor σ_{ij} is formed by differentiating S_i in the usual way. When it is contracted with the unit normal $\hat{n}$ to a surface, the surface traction $t_i = \Sigma\sigma_{ij}\hat{n}_j$ results:

$$\vec{t} = 2\mu(\hat{n}\cdot\vec{\nabla})\vec{S} + \mu\hat{n}\times(\vec{\nabla}\times\vec{S}) + \lambda\hat{n}\vec{\nabla}\cdot\vec{S}. \tag{5}$$

A surface traction vector $\vec{t}_{p\ell m}$ corresponds to each $\vec{S}_{p\ell m}$. Because $\mu = 0$ in the fluid outside, only p = 1 exists there; all 3 polarizations usually contribute inside the inclusion.

The boundary conditions are expressed in terms of these vectors. On the surface of the void C, the surface traction vector vanishes

$$\vec{t}'(\vec{r}) = 0 \quad \vec{r} \text{ on } C, \tag{6}$$

and on the surface of the inclusion, the normal components of both displacement and surface traction are continuous

$$(\vec{t} - \vec{t}')\cdot\hat{n} = 0 \quad \vec{r} \text{ on } S \tag{7}$$

$$(\vec{S} - \vec{S}')\cdot\hat{n} = 0, \quad \vec{r} \text{ on } S \tag{8}$$

and the parallel components of surface traction on the inclusion vanish;

$$\vec{t}'\times\hat{n} = 0 \quad \vec{r} \text{ on } S. \tag{9}$$

Our task is to choose $a_{\ell m}$, $b_{p\ell m}$, and $c_{p\ell m}$ in such a way that (6), (7), (8), and (9) are satisfied simultaneously. This is obviously an impossible task (unless C and S happen to be concentric spheres, in which case we shall see that the problem is greatly simplified), so we will settle for second best, namely that (6), (7), (8), and (9) be satisfied in a least-squares sense. We form the following positive definite quadratic form

$$\begin{aligned} I = \alpha\int_C d\sigma|(6)|^2 + \beta\int_S d\sigma|(7)|^2 + \gamma\int_S d\sigma|(8)|^2 \\ + \delta\int_S d\sigma|(9)|^2, \end{aligned} \tag{10}$$

where the integrals are over the surfaces C and S, α, β, γ, δ are positive constants, and the integrals are the absolute squares of the left hand sides of the referenced equations. Clearly I = 0 if and only if (6), (7), (8), and (9) hold.

One is always constrained by the realities of computation to truncate the sums in (1) and (4) to $\ell \le \ell_{max}$, where ℓ_{max} is usually quite small (~20 or less). Thus there are a finite number of coefficients $a_{\ell m}$, $b_{p\ell m}$, $c_{p\ell m}$, so that one always has I > 0. Our prescription for the choice of a, b, c is that I be minimized, viz.

$$\left.\begin{aligned} \frac{\partial I}{\partial a^*_{\ell m}} &= 0 \quad m = -\ell,-\ell+1\cdots\ell-1, \ell;\ \ell=0,\cdots\ell_{max}\\ \frac{\partial I}{\partial b^*_{p\ell m}} &= 0\\ \frac{\partial I}{\partial c^*_{p\ell m}} &= 0 \end{aligned}\right\} \quad p = 1,2,3;\ m = -\ell,\cdots\ell-1, \ell;\ \ell = 0,\cdots\ell_{max} \tag{11}$$

There are exactly as many equations in the set (11) as there are unknowns a, b, c, so in the absence of some unforeseen (and as yet unmaterialized) catastrophe (11) forms a set of linear equations which can be solved for the $a_{\ell m}$'s; they, in turn, give scattered amplitudes and cross-sections. Note that the equations (11) are <u>complex</u>, as are the a, b, c,'s; asterisk means complex conjugate. It is easy to see that as one increments ℓ_{max} to $\ell_{max}+1$, then $I(\ell_{max}+1) \le I(\ell_{max})$, so it follows that the approximation scheme results in a monotone convergent sequence with limit 0, if it is assumed that the partial wave series representation of the displacements and stresses converges.

We can write (10) out in vector notation;

$$I = a^+A_{aa}a + a^+A_{ab}b + c.c. + a^+A_{ac}c + c.c.$$
$$+ a^+A_{ad}d + c.c. + b^+A_{bb}b + b^+A_{bc}c + c.c.$$
$$+ b^+A_{bd}d + c.c. + c^+A_{cc}c + c^+A_{cd}d + c.c.$$
$$+ d^+A_{dd}d, \qquad (12)$$

where the A's are matrices whose elements are linear combinations of surface integrals; for example

$$(A_{aa})_{\ell m \ell' m'} = \int_S d\sigma [\beta \hat{n}\cdot\vec{t}^*_{\ell m}\hat{n}\cdot\vec{t}_{\ell' m'} + \gamma \hat{n}\cdot\vec{s}^*_{\ell m}\hat{n}\cdot\vec{s}_{\ell' m'}] \qquad (13)$$

as can be easily verified from (1), (7), (8) and (10). The linear equations (11) are obtained directly,

$$\frac{\partial I}{\partial a^*_{\ell m}} = \left(A_{aa}a + A_{ab}b + A_{ac}c + A_{ad}d\right)_{\ell m}, \qquad (14a)$$

$$\frac{\partial I}{\partial b^*_{p\ell m}} = \left(A_{ba}a + A_{bb}b + A_{bc}c + A_{bd}d\right)_{p\ell m} \qquad (14b)$$

$$\frac{\partial I}{\partial c^*_{p\ell m}} = \left(A_{ca}a + A_{cb}b + A_{cc}c + A_{cd}d\right)_{p\ell m}. \qquad (14c)$$

It might be pointed out that the A matrices in (14a,b,c) are mostly not square; A_{ba}, for example, has about 3 times as many rows as columns because 3 polarizations are usually allowed in the elastic inclusion versus only 1 in the fluid. This causes no problems in the matrix algebra one might do to solve for $a_{\ell m}$; row and column lengths always match properly in matrix multiplications, of course, and matrices which need to be inverted are always square.

The choice of the positive multipliers α, β, γ, δ in (10) is not critical, in fact it is irrelevant as $\ell_{max} \to \infty$. One can make a plausible argument[3] that a reasonable choice is unity for stress integral multipliers (α, β,δ) and minimum of (λ^2k^2,λ^2/a^2) for displacement integral multipliers (γ).

Important simplifications occur in (14) if certain symmetries hold. First, if the scatterer S, C has an axis of symmetry it can be chosen to be the z-axis and all the A matrices are diagonal in m. Then (14) can be solved for each value of $m = 0, 1, \cdots \ell_{max}$ successively, which affords a great simplification and computing economy. If, in addition, the scatterer has complete rotational symmetry, i.e. S and C are concentric spheres, then the A matrices are in addition diagonal in ℓ. In this case (14) degenerates for each (ℓ,m) into a set of 5 simultaneous linear equations for one $a_{\ell m}$, two $b_{p\ell m}$'s, and two $c_{p\ell m}$'s (only p = 1 and p = 3 contribute for $\ell > 0$; if $\ell = 0$ only p = 1 does), so the problem becomes trivial to solve (with a computer) because one needs only to compute coefficients for and solve inhomogeneous linear systems of order 5.

More challenging is the problem we have set out to solve in this note, namely the cracked sphere illustrated in Fig. 1. Again the displacement is expanded outside the sphere as in (1), but now we need separate expansions in the top and bottom hemispheres

$$\vec{s}'_b = \sum b_{p\ell m}\vec{s}'_{p\ell m} \quad \text{(top)} \qquad (15b)$$

$$\vec{s}'_c = \sum c_{p\ell m}\vec{s}'_{p\ell m} \quad \text{(bottom)}, \qquad (15c)$$

where, in contrast to the case of the inclusion Eq. (4), only the regular basis functions are needed. The boundary conditions to be satisfied are that on the top and bottom hemispheres the normal displacements and surface tractions are continuous, and the parallel components of surface traction vanish. In the equatorial plane welded boundary conditions (continuous displacement and surface traction) are imposed on A in Fig. (1a) and on C in Fig. (1c), while free boundary conditions (vanishing surface traction) prevail on C in Fig. (1a) (open crack) and slippery boundary conditions (continuous normal components of displacement and surface traction, zero parallel components of surface traction) hold on A in Fig. (1b). So the interior crack is "clear" and the peripheral crack is "fluid-filled".

A positive definite linear combination of surface residuals like Eq. (10) can now be formed; it will have more terms because there are now more surface segments to consider, and the boundary conditions are different. But the bilinear form in a, b, c, and d is still Eq. (12), and the linear equations (14a,b,c) are unchanged. The matrix elements A will be different; like (13) they can be written down by inspection and evaluated numerically. Then Eqs. (14a,b,c) can be solved straightforwardly on a computer. One can significantly reduce the task of the computer by recognizing that the coefficients $c_{p\ell m}$ are simply related to $b_{p\ell m}$ because of the symmetries of the geometry.[3]

NUMERICAL RESULTS

Elastic properties and densities impose some drastic constraints on the materials which can be studied by ultrasonic immersion. This is illustrated on Fig. 3 which shows backscattering in water from various real and imagined spheres (without cracks). The dot-dash curve is backscattering from a tungsten carbide sphere. Tungsten carbide is so stiff (see Table I) that at these frequencies its scattering is identical, to the resolution of the graph, to that of a rigid sphere of the same density. One could not see the effects of flaws without going to much higher frequencies. A critical parameter here is the acoustic impedance mismatch with that of water, which can from Table I be seen to be extreme; the mismatch is a factor of 65. More hopeful is the case of aluminum, the solid curve of Fig. 3. With the elastic constants tripled one gets the dashed curve, which might marginally be distinguished experimentally from the solid one. The case of lucite, shown in the solid curve of Fig. 4, is much better, by comparison with the dashed curve, which is a fictitious material with the density of lucite and the elastic constants of tungsten carbide. The backscattering

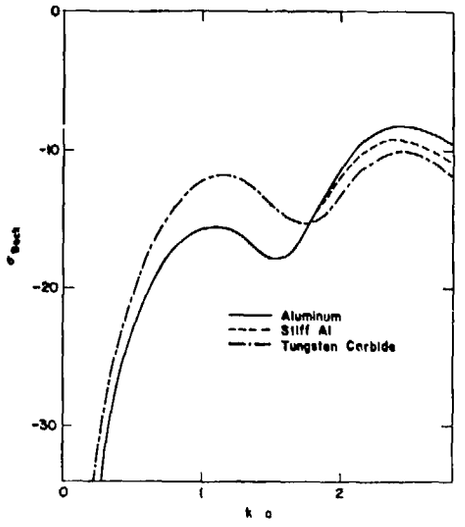

Fig. 3 Backscattering of acoustic waves from spheres in water. To the resolution of the graph, completely rigid tungsten carbide would be the same as the dot-dash curve, and completely rigid aluminum would be the same as the dashed curve.

Material	$\lambda\times10^{-10}$	$\mu\times10^{-10}$	$\rho\times10^{-3}$	v_{long}	ρv_{long} $\times10^{-7}$
Water	.197	0	1.0	1404	.140
Polyethylene	.288	.026	.90	1950	.176
Lucite	.562	.143	1.18	2680	.317
Magnesium	2.56	1.62	1.74	5770	1.00
Pyrex	2.3	2.5	2.32	5640	1.31
Aluminum	6.1	2.5	2.70	6420	1.73
Beryllium	1.6	14.7	1.87	12890	2.41
Titanium	7.8	4.4	4.50	6070	2.73
Tungsten Carbide	17.1	22.0	13.8	6655	9.18

Table I Elastic properties of various materials in MKS units. The final column is the acoustic impedance.

changes by more than a factor of 100 at the ka = 1.6 peak. Effects of this order should be easily measurable.

We have calculated scattering from various cracked lucite spheres. Some of the results are shown in Figs. 5, 6, and 7. Figure 5 pictures the backscattering cross-section $\sigma_{back}(\theta_0=0)$ for incident angle $\theta_0 = 0$ for a lucite sphere with an interior "clear" crack of radius .5a (solid line), and the dashed and dot-dash lines are $\sigma_{back}(\theta_0 = 45)$ and σ_{back} $(\theta_0 = 90)$ respectively. This crack covers 25% of the area of the equatorial plane; its effects on σ_{back} $(\theta_0 = 90)$ are fairly small, as can be seen by comparing with Fig. 4. The deviation of the solid, dot-dash, and dashed lines from each other can be considered the flaw signature; in the absence of the crack they will, of course, condense to one curve, the solid line of Fig. 4.

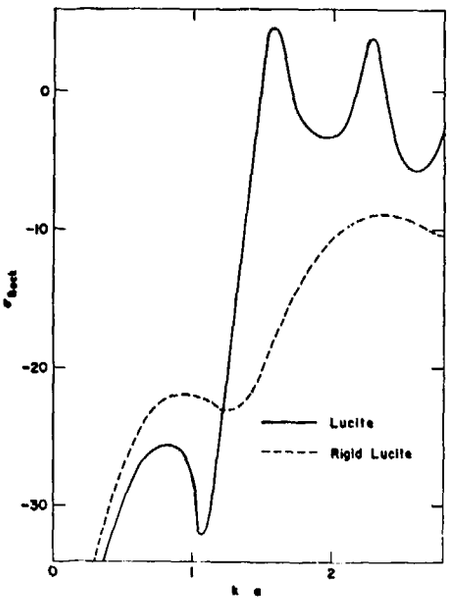

Fig. 4 Backscattering of acoustic waves from lucite sphere in water, and from a fictitious sphere with the density of lucite but with the elastic constants of tungsten carbide.

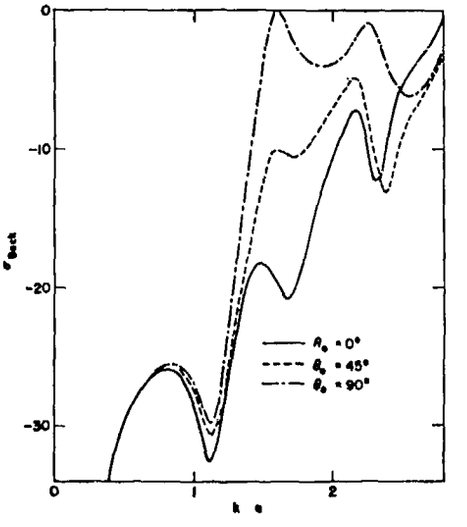

Fig. 5 Backscattering of acoustic waves from a cracked lucite sphere in water. The crack is "clear", circular with half the radius of the sphere. The incident angle θ_0 is the polar angle relative to the axis of symmetry.

Increasing the radius of the crack to .7a so that it covers half the equatorial plane results in the backscattering shown in Fig. 6. Quite similar to the curves of Fig. 5, these cross-sections can be distinguished by the much deeper interference

minima at $k_L a = 2.3$.

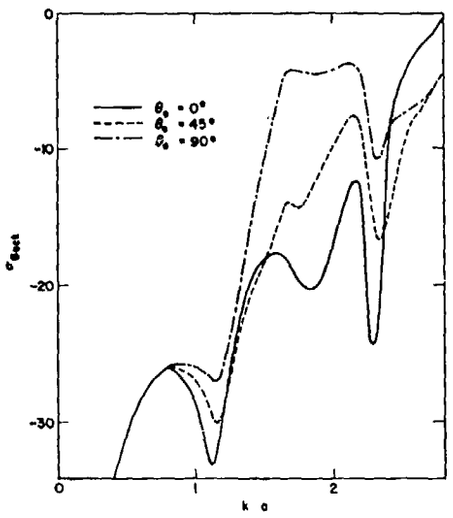

Fig. 6 Like Fig. 5, but the radius of the circle is .7a, so it covers half the area of the equatorial plane.

The result of circumcising the sphere equatorially to a depth of .3a (so the resulting fluid-filled crack has area half that of the equatorial

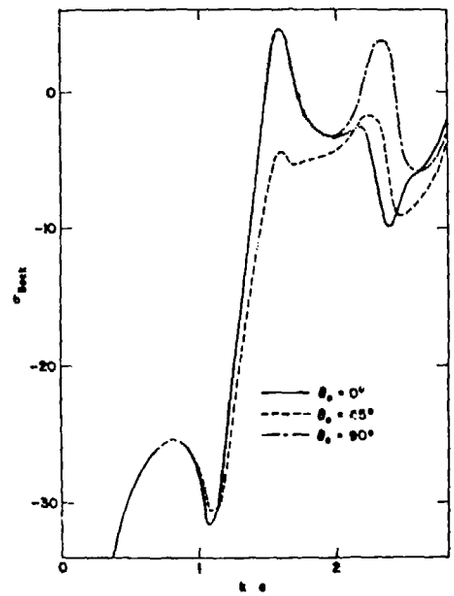

Fig. 7 Backscattering from a lucite sphere with a fluid-filled surface crack of depth .3a around its equator.

plane). The dot-dash curve here ($\sigma_{back}(\theta_0 = 90)$) is nearly identical to the unflawed sphere, and the quantitative changes for $\theta_0 = 0$ and $\theta_0 = 45$ are generally less than for the interior crack. This surface crack is much harder to detect than the interior clear crack of the same area (cf. Fig. 6).

REFERENCES

1. William M. Visscher, J. Appl. Phys. 51, 825 (1980).
2. William M. Visscher, J. Appl. Phys. 51, 835 (1980).
3. William M. Visscher, to be published in Wave Motion.

Support for this research has been provided by the United States Department of Energy.

CALCULATIONS OF ELASTIC WAVE SCATTERING FROM VOIDS AND CRACK-LIKE DEFECTS BY THE METHOD OF OPTIMAL TRUNCATION

Jon L. Opsal
Lawrence Livermore National Laboratory
Livermore, California 94550

ABSTRACT

Visscher's method of optimal truncation for solving elastic wave scattering problems has been applied to voids having surface cracks and sharp edges including some for which experimental data are becoming available. A number of interesting aspects of these results will be discussed and comparisons with existing experimental data presented.

INTRODUCTION

One of the key elements in the development of quantitative ultrasonic NDE is the elastic wave scattering problem. It is essential that practical and reliable methods be found that accurately predict the scattering of elastic waves from flaws of arbitrary size and shape. One method offering some promise in that direction is the method of optimal truncation[1] (MOOT) a least squares boundary residual method originally proposed for electromagnetic scattering[2].

Although the method's utility has been demonstrated for a number of non-spherical scatterers[1,3], there are cases when its convergence to the exact solution becomes difficult, if not impossible, to achieve. In this talk I will first briefly introduce the method and apply it to an example for which experimental data are becoming available. I will then describe a modification that appears to overcome some of the convergence difficulties and illustrate with a specific example. The modified method will then be applied to two examples of practical interest.

THEORY

The basic scattering problem we consider is a void imbedded in a homogeneous isotropic host with material properties λ, μ, and ρ, where λ and μ are the Lame' parameters relating stress to strain and ρ is the density. In terms of these parameters, we seek to solve the elastic wave equation (time dependence, $e^{-i\omega t}$, assumed)

$$(\lambda + 2\mu)\nabla\nabla\cdot u - \mu\nabla\times(\nabla\times u) + \rho\omega^2 u = 0, \qquad (1)$$

for the displacement field, u.

To implement MOOT we first expand the displacement field in some complete set of functions. A suitable set of basis functions for 3-dimensional scattering problems are the solutions to Eq. (1) in spherical coordinates,

$$u_{1\ell m} = \frac{1}{k}\nabla\{Z_\ell(kr)Y_{\ell m}(\theta,\phi)\}, \qquad (2a)$$

$$u_{2\ell m} = i\frac{1}{\sqrt{\ell(\ell+1)}}r \times \nabla\{Z_\ell(Kr)\, Y_{\ell m}(\theta,\phi)\}, \qquad (2b)$$

$$u_{3\ell m} = \frac{1}{K}\nabla \times u_{2\ell m} \qquad (2c)$$

where Z_ℓ are the spherical Hankel (outgoing waves) or Bessel (standing waves) functions and $Y_{\ell m}$ are the spherical harmonics. Also in Eq. (2), k is the longitudinal wave vector, $k = \omega\sqrt{\frac{\rho}{\lambda+2\mu}}$, and K is the transverse wave vector, $K = \omega\sqrt{\frac{\rho}{\mu}}$. The complete solution in terms of these basis functions is given by,

$$u = u_o + \sum_{p\ell m} a_{p\ell m}\, u_{p\ell m} \qquad (3)$$

where u_o denotes the incident wave, presumably known for the scattering problem and the summation contains the unknown coefficient $a_{p\ell m}$ which completely describes the scattered wave. Of the several possibilities which exist for determining the $a_{p\ell m}$, at least in an approximate sense, MOOT selects the most obvious for a demonstrably convergent procedure. When the infinite series in Eq. (3) is truncated, as must be done in practice, an error is encountered in satisfying the boundary conditions. MOOT optimizes the approximate solution by a least squares minimization of that error. The result of that minimization for a void scatterer, is the set of linear equations,

$$\sum_{p'\ell'm'} G_{p\ell m,p'\ell'm'}\, a_{p'\ell'm'} + d_{p\ell m} = 0 \qquad (4)$$

where

$$G_{p\ell m,p'\ell'm'} = \int_{void} dS\; t^*_{p\ell m} \cdot t_{p'\ell'm'}\,, \qquad (5)$$

$$d_{p\ell m} = \int_{void} dS\; t^*_{p\ell m} \cdot t_o\,, \qquad (6)$$

and $t_{p\ell m}$ and t_o are the tractions on the surface of the void derived, respectively, from the displacements $u_{p\ell m}$ and u_o. In this particular case, since the scattered wave is outgoing far from the scatterer, the Hankel functions must be used in Eq. (2).

When considering the convergence of the method, we examine the following quantities: (1) the normalized boundary residual,

$$I/I_o = \int_{void} dS \Big|\sum_{p\ell m} a_{p\ell m}\, t_{p\ell m} + t_o\Big|^2 \Big/ \int_{void} dS\,|t_o|^2 \qquad (7)$$

and

(2) the total normalized cross-section,

$$P = \sum_{\ell m}\{|a_{1\ell m}|^2 + \left(\tfrac{k}{K}\right)^3(|a_{2\ell m} + a_{3\ell m}|^2)\}/\pi(ka)^2 \qquad (8)$$

and (3) the optical theorem

$$P = \mathrm{Im}(F) \quad , \tag{9}$$

where F is the amplitude of the forward scattered wave,

$$F = 4\pi \sum_{\ell m} (-i)^{\ell+1} a_{1\ell m} Y_{\ell m}(\theta_o, \phi_o) \quad . \tag{10}$$

DISCUSSION

For our first example we consider the scatterer shown in Fig. 1. This defect, consisting of a spherical void of radius a with a hemispherical bubble of radius ½a on its surface, is significant since it has been studied earlier both theoretically[4] and experimentally[5]. The previous theoretical calculations[4] based on the DWBA agree very well with the results obtained using MOOT shown in Figs. 2-4 for frequencies corresponding to $ka \lesssim 3$. Such agreement was not unexpected and tends to confirm both methods. Most significantly, there is quite good agreement between both theories and the experimental results[5]. It is also interesting to note that the rather complicated appearing structure of the results shown in Figs. 2-4 can be interpreted in terms of the multiple interferences resulting from the presence of the bubble. For example, the reflection and transmission of the creep wave at the corner where the bubble intersects the sphere explains essentially all of the structure in Fig. 2.

As I mentioned earlier, there are cases when convergent solutions are not obtained with MOOT. These generally occur for large aspect ratios; that is, whenever the largest and smallest dimensions of the scatterer differ by more than about a factor of 2. For such scatterers, the large variation in the Hankel functions (used to represent the scattered field) over the surface of the scatterer makes it extremely difficult to satisfy the boundary conditions. In fact at large enough aspect ratios, the system of equations, (Eq. (4), becomes so ill-conditioned that not even a reasonably good approximation to the exact solution is possible. One way to circumvent this difficulty is to use functions that are well-behaved along the scatterer's boundary to represent the near-field and match those up to the outgoing waves at some other fictitious boundary where the Hankel functions are well-behaved. In Fig. (5), I show how this can be done for the case of an oblate spheroidal void. The spheroid is enclosed by a sphere of radius equal to the major axis of the spheroid. For the near field, between the sphere and the spheroid, the regular Bessel functions are used to expand the displacement and traction fields, with coefficients $b_{p\ell m}$ in the upper half and $c_{p\ell m}$ in the lower half. Outside the sphere, the Hankel functions are used with coefficients $a_{p\ell m}$ as before. One now seeks to satisfy the boundary conditions: (1) zero traction along the surface of the spheroid and (2) continuity of traction and displacement along the spherical boundary. Although this approach has increased the number of unknowns ($a_{p\ell m}$, $b_{p\ell m}$, $c_{p\ell m}$) by a factor of 3, the matrices are now well-conditioned and the convergence properties improved considerably. Before continuing, I want to point out that Bill

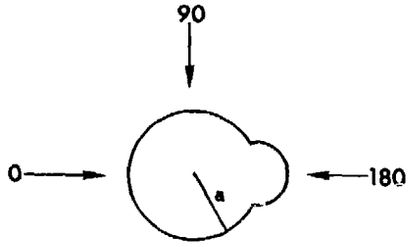

Fig. 1 Spherical void with hemispherical bubble.

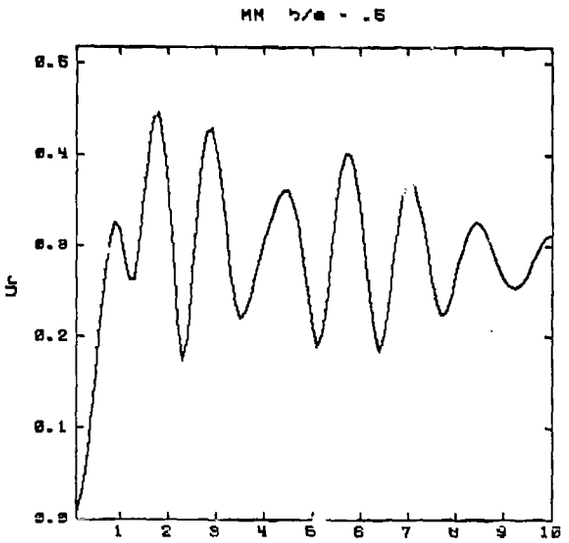

Fig. 2

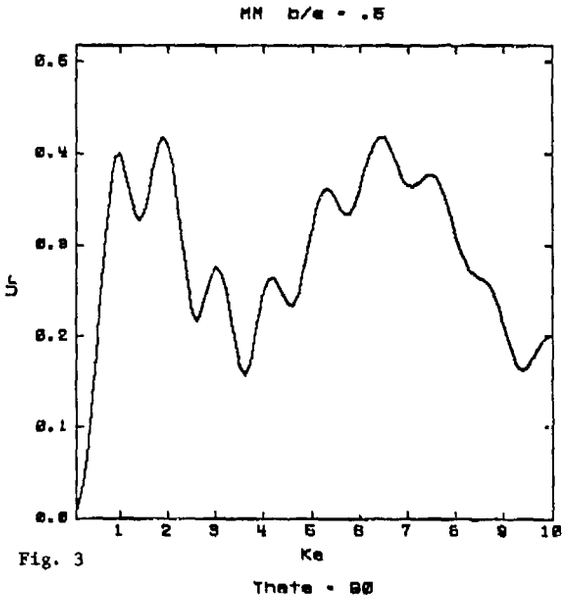

Fig. 3

Figs. 2-3 Backscattered amplitude from void in Fig. 1 for waves incident at 0° and 90°.

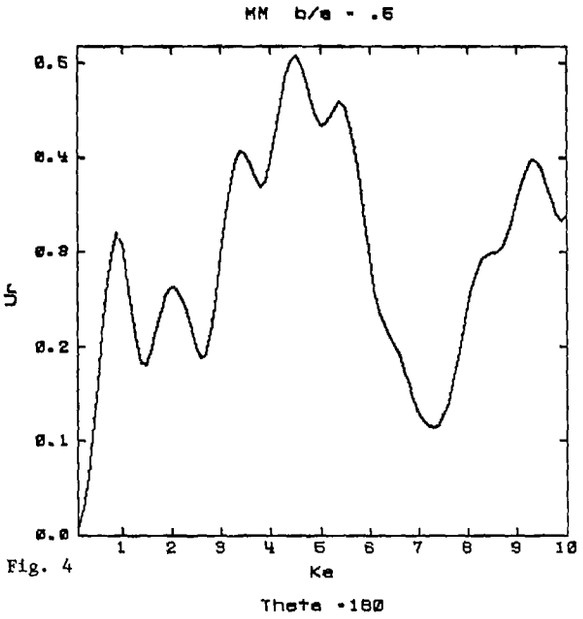

Fig. 4

Fig. 4 Backscattered amplitude from void in Fig. 1 for waves incident at 180°.

Visscher[6] has applied essentially this same approach to circular cracks. For that problem he reasoned that one requires different expansions above and below the crack in order that there be a crack opening displacement, and further that these expansions must be well-behaved at the origin. By collapsing the spheroid in Fig. 5, one obtains the circular crack as modeled by Visscher. To show that this modified version of MOOT has some validity, I show in Figs. (6-8) comparisons with results based on the original version, Eq. (4), for a spheroid with b/a = 0.7.

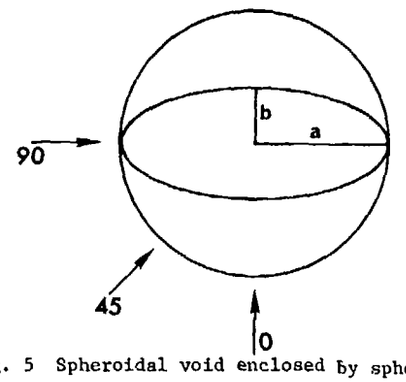

Fig. 5 Spheroidal void enclosed by sphere.

Fig. 6-8 Convergence plots comparing the original (1) and modified (2) versions of MOOT as discussed in the text. Lmax is the highest order Bessel function used in the expansions.

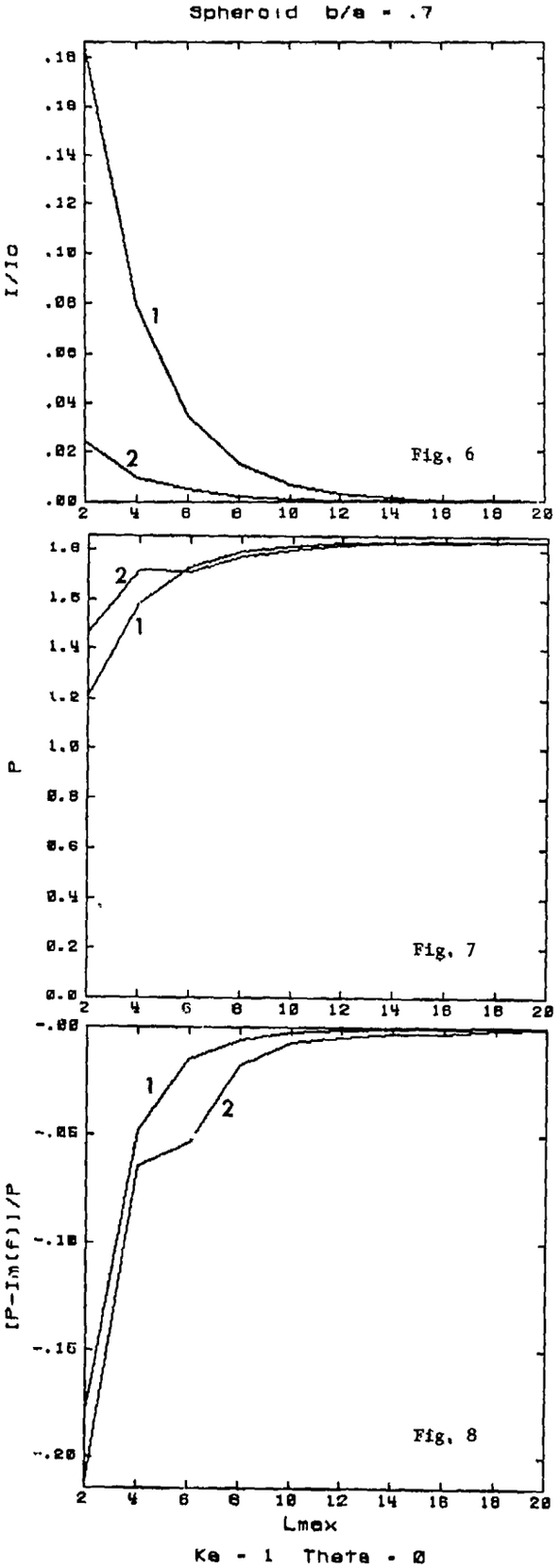

Figs. 6-8 show that the two versions of MOOT give the same results and that for that aspect ratio converge at about the same rate. The modified version,however, has a clear advantage over the original as the spheroid becomes more oblate. This is demonstrated by the comparisons in Fig. 9. Not included are corresponding comparisons for the total cross section and the optical theorem, but the results are essentially the same.

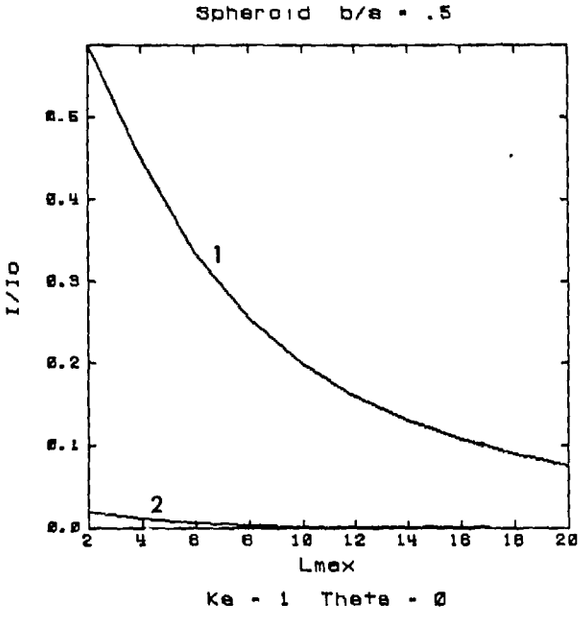

Fig. 9 Plots comparing the convergence of the boundary residual obtained using the original (1) and modified (2) versions of MOOT. Lmax is the highest order Bessel function used in the expansions.

Some results for the 2:1 oblate spheroid are shown in Figs. 10-12.

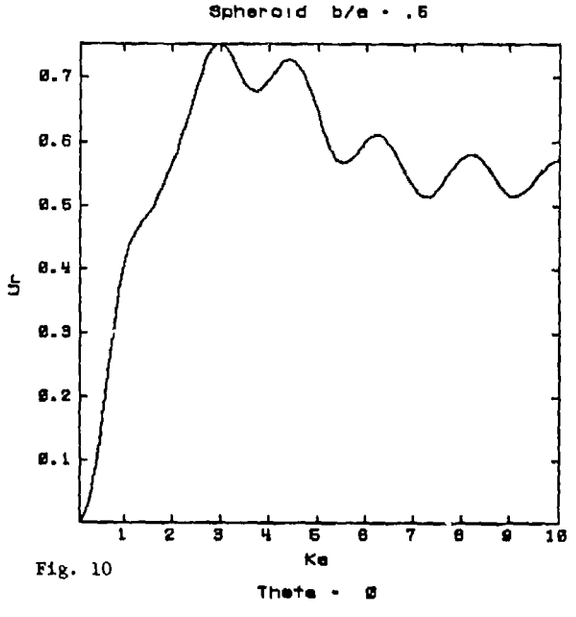

Fig. 10

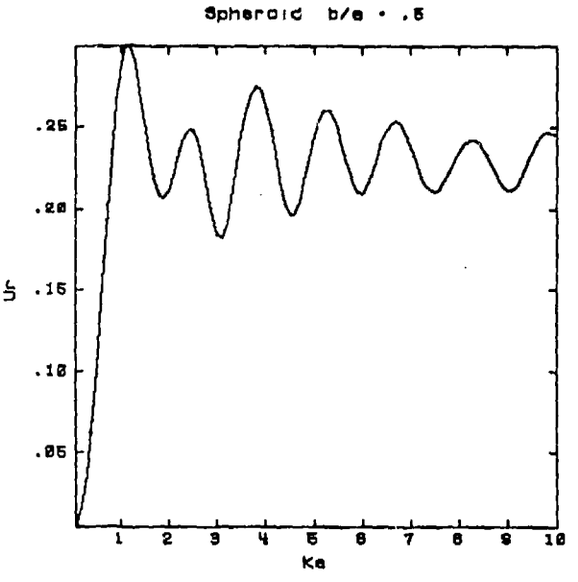

Fig. 11

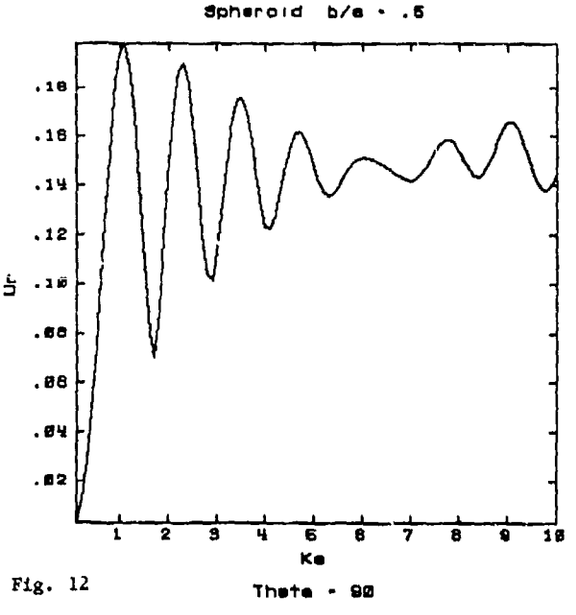

Fig. 12

Figs. 10-12 Backscattered amplitudes from a 2:1 spheroidal void obtained using the modified version of MOOT. Theta is the angle of incidence as indicated in Fig. 5.

By collapsing the spheroid in Fig. 5, one obtains a circular crack. Results for the crack are shown in Figs. 13-15. The results in Fig. 13 for normal incidence are in excellent agreement with the exact results of Mal[7]. For frequencies below ka = 2, the results in Figs. 13-15 are in agreement with Visscher's[6].

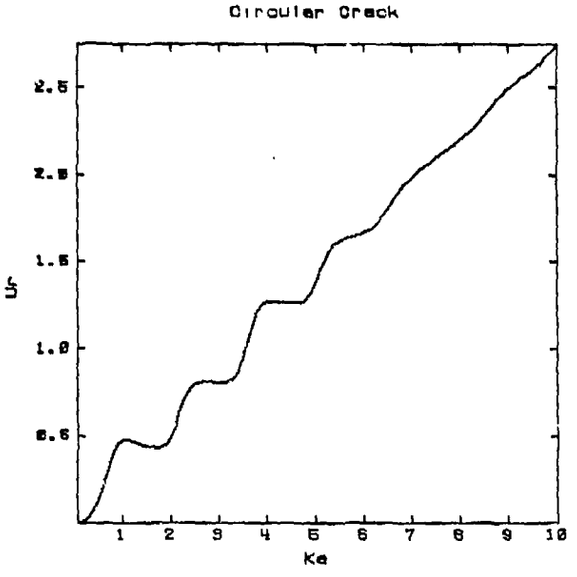

Fig. 13

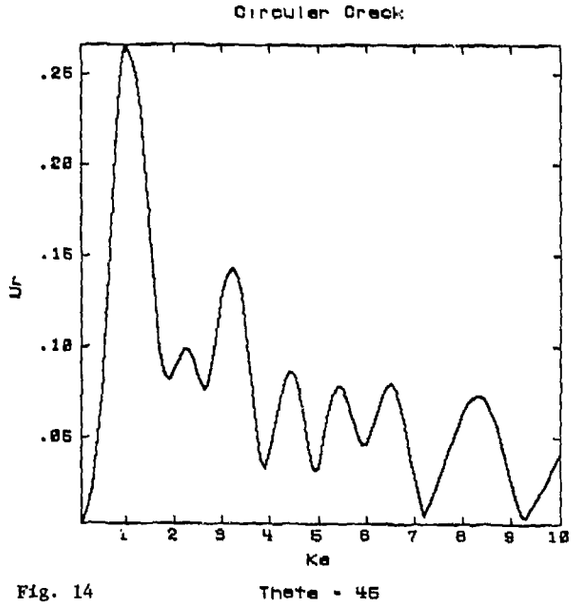

Fig. 14

Figs. 13-15 Backscattered amplitudes from a circular crack obtained using the modified version of MOOT. Theta is the angle of incidence as indicated in Fig. 5.

In conclusion I would like to say that MOOT appears to have a much wider range of applicability than one might have expected, both in terms of the broad frequency range and in the complexity of the scatterers. A final example which really tests the method is the Saturn ring defect shown in Fig. 16. Some initial comparisons with Bernie Tittmann's[8] experimental results are favorable suggesting a certain degree of correctness in the results shown in Fig. 17.

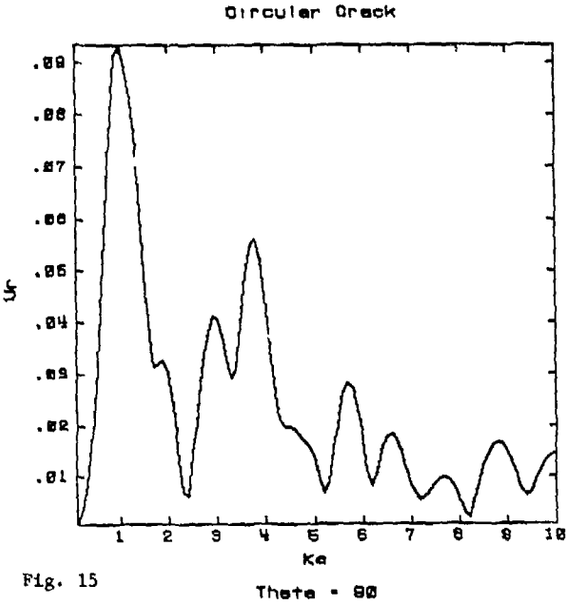

Fig. 15

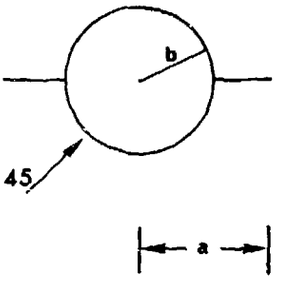

Fig. 16

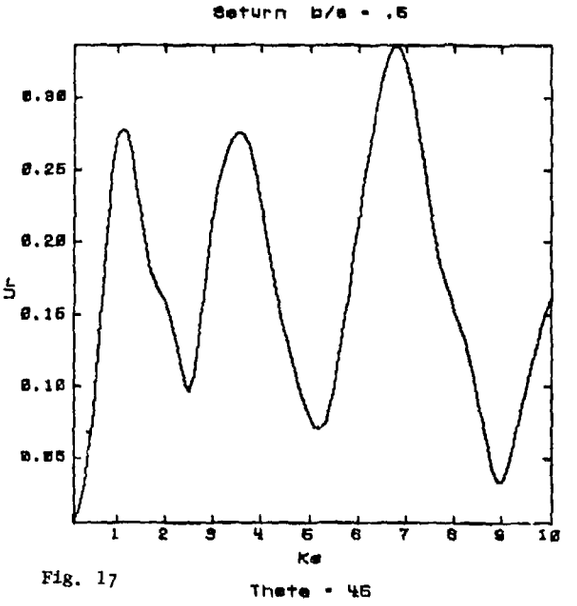

Fig. 17

REFERENCES

1. W. M. Visscher, J. Appl. Phys. 51, 825 (1980), and, J. Appl. Phys. 51, 835 (1980).

2. J. B. Davies, IEEE Trans. Microwave Theory Tech. MTT-21, 99 (1973).

3. J. L. Opsal, Proceedings of the DARPA/AFML Review of Progress in Quantitative NDE, AFWAL-TR-80-4078, p.328. Also in Univ. of Calif. Preprint UCRL-84116, Lawrence Livermore Laboratory.

4. K. E. Newman and E. Domany, Proceedings of the DARPA/AFML Review of Progress in Quantitative NDE, AFWAL-TR-80-4078, p.334.

5. B. R. Tittmann, these proceedings.

6. W. M. Visscher, Wave Motion (to be published), and, these proceedings.

7. A. K. Mal, Internat. J. Eng. Sci. 8, 381 (1970).

8. B. R. Tittmann, these proceedings.

Bruce Thompson, Chairman (Rockwell Science Center [now Ames Laboratory]): We do have a few minutes. Therefore, I suggest we open up questions to any of the first three papers.

Laszlo Adler (Ohio State University): Jon, on the crack nomenclature; the penny-shape crack, I was wondering is that a closed crack or does that have some finite opening?

Jon Opsal (Lawrence Livermore Laboratory): It starts out as a closed crack, and then it opens under load. It's a mathematical crack. I have made real cracks. I have said these things have a little opening to begin with, and you can't tell the differences. I have taken an oblique spheroid that has a very large aspect ratio, and it approaches these results with the crack.

Laszlo Adler: I mean we make these little things that are kind of like pill boxes. They are not really cracks.

Jon Opsal: If you make the aspect ratio large enough, you have a crack.

Laszlo Adler: There is no real opening there?

Jon Opsal: No. A zero volume defect.

Roger Chang (Science Center): On a rectangle, what is plotted in on the last viewgraph?

Vasundara Varadan (Ohio State University): The surface stress.

Roger Chang: Would you show it again, please? The abscissa is the distance along the -

Vasundara Varadan: Along the contour.

Roger Chang: The defect, is it a cube?

Vasundara Varadan: It's a square cylinder. This is a two-dimensional problem. And the wave length was perpendicular to the cylinder. What I have plotted is the surface strength. So CE/CT is equal to one. The maximum is at 0.125. The maxima is at the four corners.

William Pardee (Science Center): I have a question for Vasundara. I had trouble keeping track of various levels of approximation you described. Did you report numerical results more general than the translated T-matrix?

Vasundara Varadan: The quantities that I charted as Sigma were exact results using the full expression for the T-matrix, taking into account all the scattering. I inverted the whole matrix. What I called Sigma hat was allowing the singly spheres. That means I added the amplitudes rather than the cross sections from each one of the spheres or spheroids, so those were the three levels. One was what I called -- which is a full T-matrix. The second one was where you added just two amplitudes to the two singly scattered waves and don't let interfere all but add the two cross sections. It seems like Sigma hat is pretty close to the real Sigma. It's good enough to let them interfere.

Unidentified Speaker: It might be rather useful if these results were taken and put in a time domain with a simple Fourier transform; it offers a little different kind of intuition.

Jon Opsal: I gave my result to Dick Elsley. He has transformed them into the time domain.

Unidentified Speaker: I have a question on the first paper. Were those calculations also for elastic spheres immersed in water?

Vasundara Varadan: No. They were for spherical cavities in elastic solid.

Bruce Thompson, Chairman: I have one question to ask either Bill or Jon. It seems to me, that from the material science point of view a very important problem is a crack that grows from the inclusion, breaks the inclusion and breaks out into the host. You didn't have your host being broken. The Saturn Ring. That's as poor -

Jon Opsal: A cavity with a crack around it.

Bruce Thompson, Chairman: And Bill had a solid medium with a crack on the inside. What are the problems when you try to put that all together and have a crack growing from the inside into the host medium. Is that an order of magnitude or more difficult or just is that simple extrapolation?

Jon Opsal: It's more bookkeeping.

Bruce Thompson, Chairman: A lot more bookkeeping or a little more bookkeeping?

Jon Opsal: No, it's not that much more.

Bruce Thompson, Chairman: One final question.

Chris Burger (Iowa State): Bruce, you were talking about from a theoretical standpoint. I have heard people talking at weld meetings a lot about the significance of porosity. What they observe under the microscope is that the pores are not individual hollow spheres, but the residual stresses - or somewhere in the welding process those pores actually become little spheres with halo-like cracks around them. And when Bill Visscher puts his problem on the board - there is somebody addressing that problem - and then he put the whole thing in a bath of water, and it didn't solve the problem. But could you translate that, essentially, to that kind of problem where you have the hollow sphere with a halo-like crack around -

Bruce Thompson, Chairman: I believe that's what Jon calculated. That is the Saturn Ring defect, I believe.

Jon Opsal: That's just exactly what I was showing.

Bruce Thompson, Chairman: I think Bernie Tittmann will show some experimental results on just that kind of sample.

ELASTIC WAVE SCATTERING CALCULATIONS AND THE MATRIX VARIATIONAL PADÉ APPROXIMANT METHOD

J. E. Gubernatis
University of California
Theoretical Division
Los Alamos Scientific Laboratory
Los Alamos, New Mexico 87545

ABSTRACT

The matrix variational Padé approximant and its generalization to elastic wave scattering are discussed. Predictions of the method for the scattering of a longitudinal plane wave are compared with the exact scattering from spherical voids and inclusions. Its predictions are also compared to those of the first and second Born approximations and to the standard matrix Padé approximant based on these Born approximations.

INTRODUCTION

This is a preliminary report on the application of the Lippmann-Schwinger variational principle to the scattering of elastic waves from voids and inclusions.[1] This particular variational principle has the advantage of being formulated in terms of the scattering matrix and hence directly giving the physical quantities of experimental interest. The trial functions used in this application of the variational principle allow the stationary value of the variational form to be expressed in a compact block-matrix form with the block-matrix elements corresponding to terms in the Born-Neumann series solution to the integral equation of scattering.

Our principal motivation for using the variational approach is to develop a method for treating the scattering of elastic waves from complexly-shaped defects when the wavelength of the incident wave is comparable to the size of the defect and from collections of defects. Present methods, like the eigenfunction expansion methods,[2-5] are for practical reasons limited to axially-symmetric defects and are awkward to apply to a collection of defects.

Below we summarize some exact results from the integral equation approach to scattering theory. Then we discuss four approximations: the first and second Born approximations, the [1/1] matrix Padé approximant, and the variational approach, formally called the variational matrix Padé approximant. The first two approximations are necessary components to our application of the fourth approximation. We include the third method as a way to bridge the variational method and the two perturbation approximations.

EXACT RESULTS

The integral equation describing the scattering of an elastic wave from voids and inclusions is[6]

$$u_i(\vec{r}) = u_i^o(\vec{r}) + \int d\vec{r}' g_{ij}(\vec{r},\vec{r}') v_{jk}(\vec{r}') u_k(\vec{r}') \qquad (1)$$

where $u_i^o(\vec{r})$ is the incident wave. $g_{ij}(\vec{r},\vec{r}')$ is the Green's function, and $v_{jk}(\vec{r})$ describes the void or inclusion. If the void or inclusion is embedded in an unbounded, isotropic medium, then

$$g_{ij}(\vec{r},\vec{r}') = \frac{1}{4\pi\rho\omega^2}\left[\beta^2\delta_{ij}\frac{e^{i\beta R}}{R} + \frac{\partial}{\partial x_i}\frac{\partial}{\partial x_j'}\left(\frac{e^{i\alpha R}}{R} - \frac{e^{i\beta R}}{R}\right)\right] \qquad (2)$$

with

$$R = |\vec{r} - \vec{r}'|$$

and α and β equal to the longitudinal and transverse wavenumbers. We also have that

$$v_{ij}(\vec{r}) = \delta\rho\omega^2\Theta(\vec{r})\delta_{ij} + \delta C_{ikj\ell}\frac{\partial}{\partial x_k}\Theta(\vec{r})\frac{\partial}{\partial x_\ell} \qquad (3)$$

with $\delta\rho$ and $\delta C_{ijk\ell}$ equal to the density and stiffness differences between the flaw and host material and with

$$\Theta(\vec{r}) = \begin{cases} 1, & \text{for } \vec{r} \text{ inside the defect} \\ 0, & \text{otherwise} \end{cases} \qquad (4)$$

The parameter ρ is the density of the host material, and ω is the circular frequency of the incident wave.

In the far-field the solution to (1) has the form

$$u_i \sim u_i^o + A_i\frac{e^{i\alpha R}}{r} + B_i\frac{e^{i\beta r}}{r}$$

with the scattered amplitudes given by

$$A_i = \hat{r}_i\hat{r}_j f_j(\vec{\alpha}) \qquad (5a)$$

$$B_i = (\delta_{ij} - \hat{r}_i\hat{r}_j)f_j(\vec{\beta}) \qquad (5b)$$

and the f-vector defined by

$$f_i(\vec{k}) = \frac{k^2}{4\pi\rho\omega^2}\int d\vec{r}\, e^{-i\vec{k}\cdot\vec{r}} v_{ij}(\vec{r})u_j(\vec{r}) \qquad (6)$$

where $\vec{k} = k\hat{r}$ and $\hat{r}$ is the direction of scattering.

The quantity of experimental interest is the differential cross-section. If the incident wave is a plane wave of the form

$$u_i^o = d_i\, e^{i\vec{k}^o\cdot\vec{r}} \tag{7}$$

then the differential cross-section for the longitudinal component of the scattering is

$$\frac{dP}{d\Omega} = \left|\frac{A}{d}\right|^2 . \tag{8}$$

There is an alternate integral equation approach to the scattering that is formulated in terms of the scattered amplitudes. If both sides of (1) were operated on by $\exp(-i\vec{k}\cdot\vec{r})v_{ij}(\vec{r})$ and then integrated over $\vec{r}$, it follows from (6) that (1) is now equivalent to

$$f_i(\vec{k}) = \frac{k^2}{4\pi\rho\omega^2}\left[\int d\vec{r}\, e^{-i\vec{k}\cdot\vec{r}} v_{ij}(\vec{r}) u_j e^{i\vec{k}^o\cdot\vec{r}} + \int d\vec{r}\int d\vec{r}\,' e^{-i\vec{k}\cdot\vec{r}} v_{ij}(\vec{r}) g_{jk}(\vec{r},\vec{r}\,') v_{jk}(\vec{r}\,') u_k(\vec{r}\,')\right] \tag{9}$$

so with the definitions

$$f_i(\vec{k}) \equiv \frac{k^2}{4\pi\rho\omega^2} T_{ij}(\vec{k},\vec{k}^o) d_j \tag{10}$$

$$V_{ij}(\vec{k},\vec{k}^o) \equiv \int d\vec{r}\, e^{-i\vec{k}\cdot\vec{r}} v_{ij}(\vec{r}) e^{i\vec{k}^o\cdot\vec{r}} \tag{11}$$

and the use of the Fourier transform of (2),

$$G_{ij}(\vec{q}) = \int d\vec{q}\, e^{-i\vec{q}\cdot\vec{r}\,'} g_{ij}(\vec{r} - \vec{r}\,') e^{i\vec{q}\cdot\vec{r}}$$

the equation (9) becomes

$$T_{ij}(\vec{k},\vec{k}^o) = V_{ij}(\vec{k},\vec{k}^o) + \int d\vec{q} V_{ik}(\vec{k},\vec{q}) G_{k\ell}(\vec{q}) T_{\ell j}(\vec{q},\vec{k}^o) . \tag{12}$$

The matrix function $T_{ij}(\vec{k},\vec{k}^o)$ has the following simple relation to the scattered amplitudes

$$A_i = \hat{r}_i\hat{r}_j T_{jk}(\vec{\alpha},\vec{k}^o) d_k/4\pi(\lambda+2\mu) \tag{13a}$$

$$B_i = (\delta_{ij} - \hat{r}_i\hat{r}_j) T_{jk}(\vec{\beta},\vec{k}^o) d_k/4\pi\mu \tag{13b}$$

where λ and μ are the Lamé parameters. The other matrix function $V_{ij}(\vec{k},\vec{k}^o)$ equals

$$V_{ij}(\vec{k},\vec{k}^o) = t_{ij}(\vec{k},\vec{k}^o) S(\vec{k},\vec{k}^o) \tag{14}$$

where

$$t_{ij}(\vec{k},\vec{k}^o) = [\delta_i\rho\omega^2 - \delta\mu(\vec{k}\cdot\vec{k}^o)]\delta_{ij} - \delta\lambda k_i k_j^o - \delta\mu k_i^o k_j \tag{15}$$

and the shape factor

$$S(\vec{k},\vec{k}^o) = \int d\vec{r} D(\vec{r}) e^{i(\vec{k}^o-\vec{k})\cdot\vec{r}} . \tag{16}$$

Several additional definitions and equations will prove useful. First, if we use (9) for incident wave and if we define $U_{ij}(\vec{r})$ by

$$u_i(\vec{r}) = U_{ij}(\vec{r}) d_j \tag{17}$$

then we can rewrite (1) as

$$U_{i\ell}(\vec{r}) = U_{i\ell}^o(\vec{r}) + \int d\vec{r}\, g_{ij}(\vec{r},\vec{r}\,') v_{jk}(\vec{r}\,') U_{k\ell}(\vec{r}\,') \tag{18}$$

where

$$U_{i\ell}^o(\vec{r}) = \delta_{i\ell} e^{i\vec{k}^o\cdot\vec{r}} . \tag{19}$$

Also, we note that the specific formula for the scattering matrix is now

$$T_{ik}(\vec{k},\vec{k}^o) = \int d\vec{r}\, e^{-i\vec{k}\cdot\vec{r}} v_{ij}(\vec{r}) U_{jk}(\vec{r}) . \tag{20}$$

APPROXIMATIONS

The First and Second Born Approximations - A formal solution to the integral equation for the scattering matrix can be obtained , iterating the equation to produce what is often called the Born-Neumann series. If only the first term in this series is used (i.e., no iterations are performed), then the resulting approximation is called the first Born approximation. The first Born approximation to (12) corresponds to[7]

$$T_{ij}(\vec{k},\vec{k}^o) \approx V_{ij}(\vec{k},\vec{k}^o) . \tag{21}$$

If the first two terms of the Born-Neumann series are kept (i.e., one iteration is performed), then the approximation is called the second Born approximation. For (12) the second Born approximation corresponds to

$$T_{ij}(\vec{k},\vec{k}^o) = T_{ij}^{(1)}(\vec{k},\vec{k}^o) + T_{ij}^{(2)}(\vec{k},\vec{k}^o) \tag{22}$$

where

$$T_{ij}^{(1)}(\vec{k},\vec{k}^o) = V_{ij}(\vec{k},\vec{k}^o) \tag{23a}$$

$$T_{ij}^{(2)}(\vec{k},\vec{k}^o) = \int d\vec{q} t_{ik}(\vec{k},\vec{q}) S(\vec{k},\vec{q}) G_{k\ell}(\vec{q}) \cdot S(\vec{q},\vec{k}^o) t_{\ell j}(\vec{q},\vec{k}^o) . \tag{23b}$$

The matrix functions $T_{ij}^{(1)}$ and $T_{ij}^{(2)}$ are called the first and second Born terms.

The evaluation of the second Born term is not a trivial numerical task. Normally, the second Born term is a 6-dimensional integral with a singular integrand. In our particular case, because the defect volume is assumed to be finite, the integral is finite. The way we chose to express the second Born term has reduced the dimensionality of the integration to 3; the integrand is still singular, but the integral is now infinite. A possible advantage to the present approach is the isolation of the shape dependence of problem in the shape factor (16). How second Born term is integrated numerically essentially independent of the flaw shape. The shape factor is just some subroutine, usually a simple one since (16) can often be evaluated analytically or else reduced to a one or two-dimensional numerical integration.

Through the shape factor it is also easy to study multiple defect problems. For example, for N identical defects whose centroids are located by $\vec{R}_i$, the shape factor gets replaced by

$$S(\vec{k},\vec{k}^o)\sum_{i=1}^{N} e^{i\vec{R}_i\cdot(\vec{k}^o-\vec{k})}$$

where $S(\vec{k},\vec{k}^o)$ is the shape factor for one of the defects. The summation in the above is called the structure factor.

The [1/1] Matrix Padé Approximation - If $\underline{F}(x)$ is a matrix function of x and if

$$\underline{F}(x) = \underline{F}^{(0)} + \underline{F}^{(1)}x + \underline{F}^{(2)}x^2 + \cdots$$

then the [M/N] matrix Padé approximation to $\underline{F}(x)$ is defined by[8]

$$\underline{F}^{[M/N]}(x) = \underline{P}_M(x)\underline{Q}_N(x)^{-1} \tag{25a}$$

where

$$\underline{Q}_N(x)\underline{F}(x) - \underline{P}_M(x) = \mathcal{O}(x^{M+N+1}). \tag{25b}$$

(For compactness, we now denote matrices by underlined, capital Roman letters. Below, all matrices representing physical quantities are 3×3.)

Specifically, from (18) and (20),

$$\underline{T}^{[1/1]}(\vec{k},\vec{k}^o) = \underline{T}^{(1)}(\vec{k},\vec{k}^o)[\underline{T}^{(1)}(\vec{k},\vec{k}^o) - \underline{T}^{(2)}(\vec{k},\vec{k}^o)]^{-1}\,\underline{T}^{(1)}(\vec{k},\vec{k}^o). \tag{26}$$

Hence, if the first two terms of the Born series are known, it is a trivial procedure to evaluate the [1/1] matrix Padé approximant. The result may be a better approximation than given by the second Born approximation.

Technically, the definition (21) is of a left-handed matrix Padé approximant. If $\underline{P}_M(x)$ is inverted instead of the $\underline{Q}_N(x)$, then a right-handed matrix Padé approximant is defined. The different definitions can be shown to give equivalent answers.

The Variational Matrix Padé Approximant - First, we identify $\underline{W}(\vec{r})$ as the matrix function satisfying the adjoint equation of (18)

$$\underline{W}(\vec{r}) = \underline{W}^o(\vec{r}) + \int d\vec{r}'\ \underline{g}^*(\vec{r},\vec{r}')\underline{v}(\vec{r}')\underline{W}(\vec{r}) \tag{27a}$$

where

$$\underline{W}^o(\vec{r}) = \underline{I}\, e^{i\vec{k}\cdot\vec{r}}. \tag{27b}$$

Next, we operate on both sides of (18) with $\underline{W}^*(\vec{r})\underline{V}(\vec{r})$, integrate over $\vec{r}$, and subtract (20) from the result to find

$$\underline{T}(\vec{k},\vec{k}^o) = \int d\vec{r} e^{-i\vec{k}\cdot\vec{r}}\underline{v}(\vec{r})\underline{U}(\vec{r}) + \int d\vec{r}\ \underline{W}^*(\vec{r})\underline{v}(\vec{r})e^{i\vec{k}^o\cdot\vec{r}} + \int d\vec{r}\,\underline{W}^*(\vec{r})\underline{v}(\vec{r})\left[e^{i\vec{k}^o\cdot\vec{r}} - \int d\vec{r}'\,\underline{g}(\vec{r},\vec{r}')\underline{v}(\vec{r}')\underline{U}(\vec{r}')\right]. \tag{28}$$

Clearly, if $\underline{W}(\vec{r})$ and $\underline{U}(\vec{r})$ are exact, the above is an exact expression for the scattering matrix. The expression also has the feature that considered as a functional of $\underline{W}(\vec{r})$ and $\underline{U}(\vec{r})$ it is stationary with respect to independent and arbitrary variations of $\underline{W}(\vec{r})$ and $\underline{U}(\vec{r})$ about their exact values. When used as a variational form, the expression is a generalization to elastic wave scattering of the Lippmann-Schwinger variational principle.[9-12]

There are many ways to choose the trial functions $\underline{W}(\vec{r})$ and $\underline{U}(\vec{r})$. We chose

$$\underline{U}(\vec{r}) = \sum_{i=1}^{N}\underline{a}^{(i)}e^{i\vec{k}^{(i)}\cdot\vec{r}}$$
$$\underline{W}(\vec{r}) = \sum_{i=1}^{N}\underline{b}^{(i)}e^{i\vec{k}^{(i)}\cdot\vec{r}}. \tag{29}$$

When (28) is made stationary with respect to these choices,

$$\underline{a}^{(i)} = \underline{b}^{(i)}$$

and (28) can be expressed in the following compact form

$$\underline{T}(\vec{k},\vec{k}^o) = \begin{bmatrix}\underline{T}^{(1)}(\vec{k},\vec{k}^{(1)})\\ \vdots \\ \underline{T}^{(1)}(\vec{k},\vec{k}^{(N)})\end{bmatrix}^T \times \begin{bmatrix}\underline{X}_{11} & \cdots & \underline{X}_{N1}\\ \vdots & & \vdots \\ \underline{X}_{1N} & \cdots & \underline{X}_{NN}\end{bmatrix}^{-1}\begin{bmatrix}\underline{T}^{(1)}(\vec{k}^{(1)},\vec{k}^o)\\ \vdots \\ \underline{T}^{(1)}(\vec{k}^{(1)},\vec{k}^o)\end{bmatrix} \tag{30a}$$

where we have defined

$$\underline{X}_{ij} = \underline{T}^{(1)}(\vec{k}^{(i)},\vec{k}^{(j)}) - \underline{T}^{(2)}(\vec{k}^{(i)},\vec{k}^{(j)}). \tag{30b}$$

Equation (30) is a block-matrix equation: Matrix multiplication is done by the rule of block-matrix multiplication. The transpose operation is on block elements and not on the individual matrices comprising those elements. In (30) the need to calculate the first and second Born approximations is evident. The reader should compare (30) with (26).

RESULTS

For an incident longitudinal plane wave we computed the longitudinal backscattering from spherical defects predicted by each of the four approximations and compared the results to the exact scattering from spherical voids and inclusions.[13] We studied the breakdown of the approximations as ka is increased and as the density and stiffness of an inclusion is incrementally decreased from that of the host material to that of a void. (k is the scattered wave number, and a is the radius of the sphere.)

For the variational part of the calculation

our trial function was

$$\underline{U}(r) = \underline{a}^{(1)} e^{i\vec{k}^0 \cdot \vec{r}} + \underline{a}^{(2)} e^{i\vec{k} \cdot \vec{r}} \qquad (31)$$

not a serious choice. It was, however, an effective and convenient choice to study the internal behavior of our computer program. (If (31) were used to calculate the forward scattering, then the two wave vectors in (31) become equal, and the square matrix in (31) becomes singular and non-invertible. With (31) and the second Born term, only two additional second Born terms are needed for a non-trivial variational calculation.)

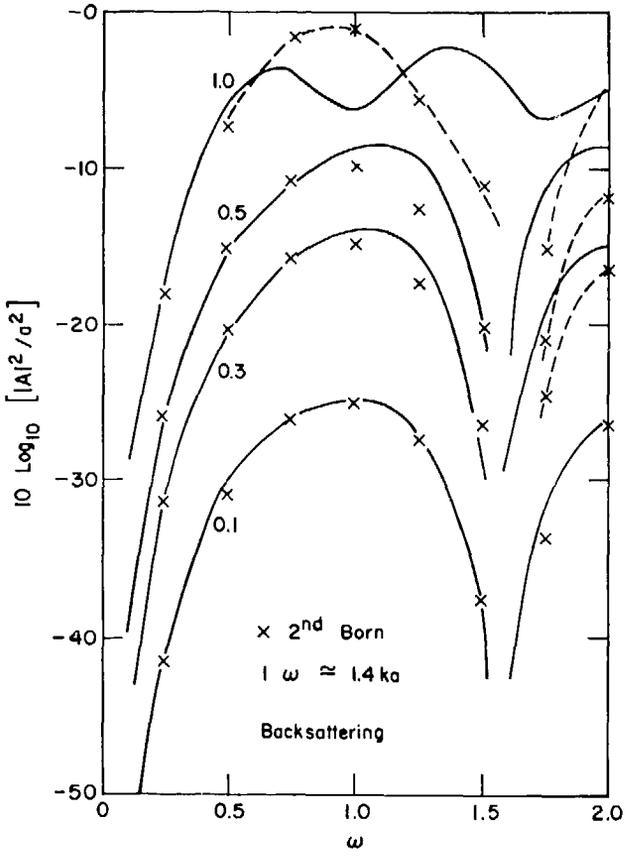

Fig. 1 The longitudinal backscattering from a spherical void and inclusions that is predicted by the second Born approximation plotted as a function of ka. Each line is for an inclusion whose density and Lamé parameters are reduced by a factor of 0.1, 0.3, 0.5, and 1.0 relative to the host medium. The reduction of 1.0 corresponds to a void.

We were uncertain how well the variational calculation would work, but believed that the second Born approximation would have larger ranges of validity than the first Born approximation and that the [1/1] matrix Padé approximant would be at least valid as the second Born approximation. This is what we found. Additionally, we found the variational calculation, when (31) is used, is never better than the first Born approximation. In Fig. 1 we plotted our results only for the second Born approximation. Including the results of the other calculations clutters the figure without revealing more information than what was just said. Presently we are trying to find a more reasonable choice of trial functions. We will report our results elsewhere, accompanied by a more expansive treatment of the theoretical methods.

ACKNOWLEDGEMENTS

This work was supported by the Materials Sciences Division of the Office of Basic Energy Research of the Department of Energy.

We thank G. A. Baker, Jr. for bringing the variational, matrix Padé method to our attention.

REFERENCES

1. B. A. Lippmann and J. Schwinger, Phys. Rev. 79, 569(1950).
2. V. Varatharalulu and Y.-H. Pao, J. Acoust. Soc. Am. 60, 567(1976).
3. P. C. Waterman, J. Acoust. Soc. Am. 60, 567(1976).
4. W. M. Visscher, J. Appl. Phys. 51, 825(1980).
5. W. M. Visscher, J. Appl. Phys. 51, 835(1980).
6. J. E. Gubernatis, E. Domany, and J. A. Krumhansl, J. Appl. Phys. 48, 2804(1977).
7. J. E. Gubernatis, E. Domany, J. A. Krumhansl and M. Huberman, J. Appl. Phys. 48, 2812 (1977).
8. G. A. Baker, Jr., Essentials of Padé Approximants, (Academic Press, New York, 1975), pg. 270.
9. L. P. Bennofy, J. L. Gammel, and P. Mery, Phys. Rev. D 13, 3111(1976).
10. G. Turchetti, Lett. Nuovo Cimento 15, 129(1976).
11. D. Bessis, P. Mery, and G. Turchetti, Phys. Rev. D 15, 2345(1977).
12. P. R. Graves-Morris, Ann. Phys. 114, 296 (1978).
13. C. F. Ying and R. Truell, J. Appl. Phys. 27, 1086(1956).

Bruce Thompson, Chairman (Rockwell Science Center [now Ames Laboratory]): We have, perhaps, time for one question.

Jim Rose (Ames Laboratory): What's included in the scattering? Any double scattering? What have you left in and what have you left out?

Jim Gubernatis (Los Alamos Scientific Laboratory): With respect to variational principle, that's not always a reasonable question. What I am doing can not be described as a perturbation approach. Variational principles in general are non-perturbative. With this particular choice of variational form, it's simply that along with computing the variational results, I also compute the perturbations. I am not identifying something in a small parameter. What I am attempting is to choose a trial wave function which to some extent has an approximate relationship to the physical answer, so what has to be put into the calculation is intuition.

Jim Rose: What's your perturbation to the pade?

Jim Gubernatis: The pade I'm not interested in. I am unclear of the full significance of the word "pade" in the matrix. Variational pade approximant method other than the results are expressible in what is called in the pade literature as the nutall compact form. So the method is really a variational principle. At least I don't see, with respect to pade approximants what it's doing for you other than it does preserve the symmetry (reciprocity) of your matrices. I don't think of the method in terms of perturbations.

Unidentified Speaker: Where is the literature on the method?

Jim Gubernatis: For a start, there were several papers which appeared two years ago in Physical Review. By Bessis and some co-workers.

Bruce Thompson, Chairman: Thank you, Jim. I think perhaps we had better go on.

SCATTERING OF ELASTIC WAVES BY COMPLEX DEFECTS; MULTIPLE SCATTERING FORMALISM

Eytan Domany
Department of Electronics, Weizmann Institute of Science,
Rehovot, Israel

and

Leah Mizrachi
International Centre for Theoretical Physics,
Trieste, Italy

ABSTRACT

Scattering of elastic waves by complex defects is investigated. In previous work the Distorted Wave Born Approximation was developed, in which a general shaped defect is represented as a sphere S and a remainder volume R, the latter being treated in first order perturbation theory. The DWBA was used to study scattering by a sequence of defects representing increasingly larger deviations from spherical; comparisons with experiment and other theories were made. This approach breaks down when scattering by R is of similar magnitude as by S. Such is the case for complex defects such as two spheres, or a sphere and a crack emanating from it. To treat such situations, a multiple scattering formalism was developed.

INTRODUCTION

Development of approximate solutions to the scattering of elastic waves by defects has proved to be most useful for progress in nondestructive evaluation of materials. Applications of such approximate methods include comparisons with experiment, identification of features sensitive to scatterer characteristics of special interest, incorporation in adaptive learning procedures and development of inversion schemes.

Significant progress in this area was achieved during the recent few years. New methods that were developed include the truncated T-matrix approach,[1] variational methods,[2] the Distorted Wave Born Approximation[3] (DWBA) and extensions of geometrical diffraction techniques.[4] Comparison of results obtained using different techniques and also with experiment are most encouraging. However, all techniques have limitations and different regions of validity.

In the DWBA a general shaped defect is represented as a sphere and a remainder volume R which is treated as a perturbation. In some cases this approach gave surprisingly good results even for large volume perturbations. However, in the case of strong scatters (such as cavities), the DWBA will break down when the remainder volume R is large. To investigate the limitations of the DWBA prior to embarking on data inversion based on it, we studied scattering by a sequence of defects with increasing R. The results of this investigation are presented in Section II.

Obviously, the DWBA has quite general limitations. In many practical situations it is not possible to present a defect as a sphere and a small volume perturbation. Two such defects are shown in Fig. 1. The defect of Fig. 1a consists of a sphere with a circular crack emanating from its equator. Since the crack is not a volume perturbation, its contribution to the scattering can not be evaluated by means of the DWBA. Figure 1b presents a compound defect that consists of two closely spaced spheres of slightly differing size. When one sphere is much smaller than the other, the DWBA is expected to yield good results. However, when the sizes are about the same, there is no justification to treat one exactly and the other as a perturbation. This multiple defect is the prototype of situations in bond areas, where one has to deal with an aggregate of equally important volume defects. The aim of our investigation is to develop a method that can provide reasonable approximations to the scattering from defects such as those of Fig. 1a and 1b. The basis of the method is to represent the scatterer as two parts R_1 and R_2, such that the exact or approximate solutions to both problems (R_1 present only, and R_2 only) are known. Then we apply a method of multiple scattering, treating the interaction between the scatterers as perturbation.

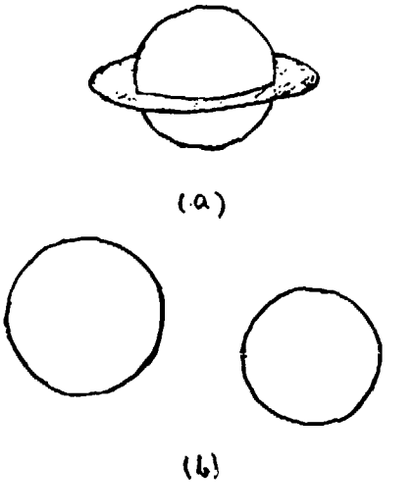

Fig. 1 Two complex defects (a) circular crack emanating from spherical cavity, and (b) two spherical cavities.

This multiple scattering formalism is developed in Section III, and applied for specific geometries in Section IV.

SCATTERING BY NONSPHERICAL DEFECTS - DWBA

The formalism of the Distorted Wave Born Approximation was presented elsewhere;[3] here we only summarize the results. Representing the defect as a sphere S and a remainder volume R, the scattered longitudinal wave in direction r, for an incident longitudinal wave along r_0 is given by

$$\underline{u}_L = \underline{u}_L^S + \hat{r}\alpha^2(D_1 + D_2 + D_3)\exp(i\alpha r)/r$$

where α is the longitudinal wave vector and the coefficients D_j are expressed in terms of the known solutions of the spherical scattering problem, integrated over the volume R. We considered a sequence of defects as shown in Fig. 2. This sequence represents increasing deviations from spherical shape. The defects considered consist of a large spherical cavity (radius 400 μ) and a small hemisphere (of radius 200 μ), connected by a cylindrical "neck" of length 1. We studied the cases 1 = 0, 100, 200, 400 μ. The scattered power was calculated, for illuminations from back, side, and front of the small hemisphere. Both angular distribution of the scattered power at fixed frequencies and the frequency dependence of the backscattered power were calculated. Some of the results of these calculations are shown in Figs. 3, 4, 5. All three figures show the angular dependence of scattered power for $\alpha a = 2$. It should be noted that for $\alpha a = 1$ deviations from the pattern obtained for a sphere (the solid line of Fig. 3, 4) are too small to measure, even for the defect with 1 = 400. Deviation from spherical shape is most noticeable for illumination from the side, i.e., a direction of low symmetry (Fig. 4). This fact is quite important for quantitative defect characterization. Consider now Fig. 5, which compares scattered power for $\alpha a = 2, \theta = 135°$, as a function of the azymuthal angle ϕ, for a sequence of defects. A spherical defect would yield constant scattered power; deviations from spherical shape are, as expected, more pronounced for the higher 1 values. We have also studied backscattered power as a function of frequency, for various directions of incidence and scatterer shapes. However, to our disappointment we found, that backscattered longitudinal power (a relatively simple measurement) is not sensitive enough to the detailed shape of the scatterer. More information can apparently be obtained from analysis of experiments in which angular dependence of the scattered power is measured. Again we observed that deviations from spherical shape are hardly noticeable for $\alpha a < 1.5$.

Detailed comparison of our results with experiment and other methods is given by Tittmann in these proceedings.[8]

MULTIPLE SCATTERING THEORY - GENERAL

In this Section we present a systematic expansion for scattering by two defects. An alternative approach was taken by Varadan et al[9] to the problem of scattering by two spheres. Their work is based on the truncated T matrix approximation. Although limited to problems with

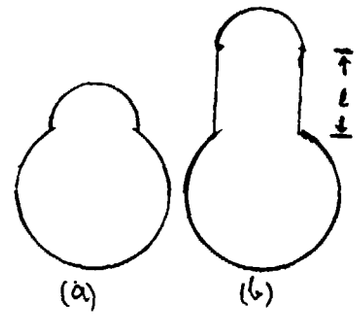

Fig. 2 A sequence of non spherical defects; a small hemispherical cavity is connected to a large spherical one by a "neck" of length 1. As 1 increases from zero, the scatterer deviates more from spherical shape.

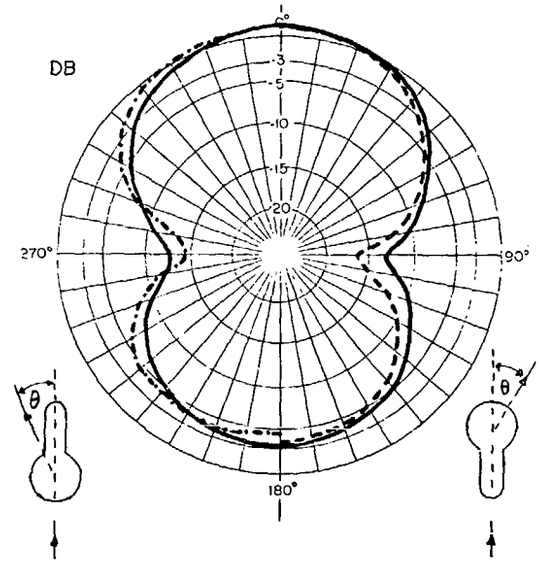

Fig. 3 Scattered power as a function of scattering angle for two directions of incidence, on defect with 1 = 400 μ. The right half corresponds to the situation with the small hemisphere directly illuminated; the left hand side to incidence on the large sphere. $\alpha a = 2$, is the incident wave number and a the large sphere radius, a = 400 μ.

cylindrical symmetry, their method is powerful and can yield approximate solutions of increasing accuracy to the particular problem studied. Our method is easily generalizable for more than two defects and no symmetry requirement is imposed.

Consider an infinite elastic medium characterized by density ρ_0 and elastic tensor C^0_{ijkl}, in which two regions R_1 and R_2 with densities ρ_1, ρ_2 and elastic tensors C^1 and C^2 are embedded. We look for solutions of the wave equation

$$(C_{ijkl}u_{k,l})_{,j} + \rho\omega^2 u_i = 0 \qquad (1)$$

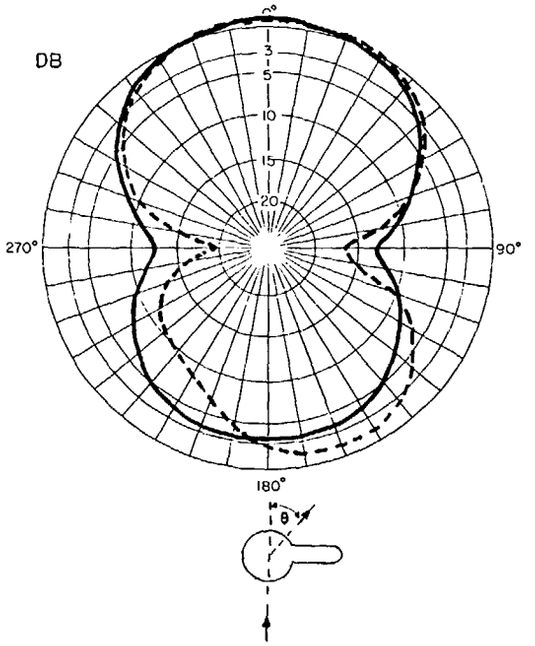

Fig. 4 Angular dependence of scattered power for incidence from the side; a = 2, a = 1 = 400 μ.

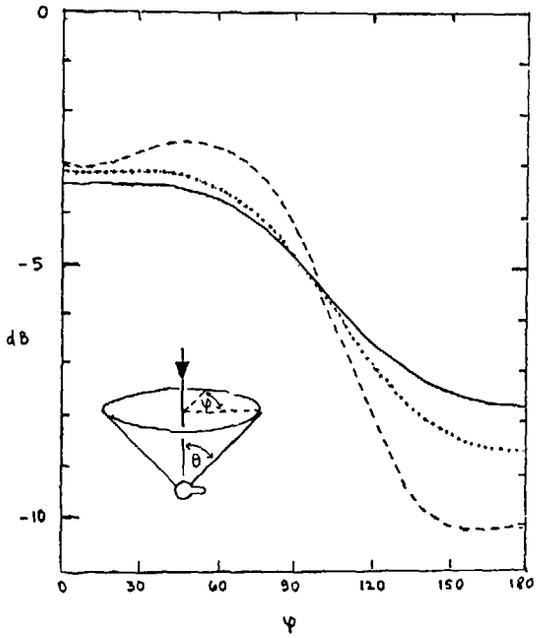

Fig. 5 Power scattered at θ = 135°, as a function of azimuthal angle ρ, for incidence from the side on defects with 1 = 0 (solid line) 1 = 200 μ (dotted line) and 1 = 400 μ (dashed line).

of the form

$$u_i(r) = u_i^o(\underline{r}) + u_i^S(\underline{r}) \quad ,$$

where u^o is a plane wave and u^S an outgoing spherical wave.

Using the formalism developed by Gubernatis et al[5] the solution of (1) can be written as

$$u_i(\underline{r}) = u_i^o(\underline{r}) + \sum_{\alpha=1,2} \int dr' [g^o(\underline{r},\underline{r}') V^{(\alpha)} u(\underline{r}')]_i \quad .)$$

where we used the notation

$$[gV^{(\alpha)}u]_i = [\delta\rho^{(\alpha)}\omega^2 g^o_{im}u_m - \delta C^{(\alpha)}_{jklm} g^o_{ij,k'} u_{l,m'}]\theta_{R_\alpha}(\underline{r}) \quad (3)$$

with

$$\delta_\rho^{(\alpha)} = \rho_\alpha - \rho_o$$
$$\delta C^{(\alpha)} = C^{(\alpha)} - C^o$$

and

$$\theta_{R_\alpha}(\underline{r}) = \begin{cases} 1 & \underline{r} \epsilon R_\alpha \\ 0 & \text{otherwise} \end{cases}$$

and $g^o(\underline{r},\underline{r}')$ is the infinite medium Greens function.

Equation (2) is a generalization of the integral equation for scattering by a single defect. From now on we will suppress all tensorial indices and integrations; thus Eq. (2) is rewritten as

$$u = u^o + g^o V^{(1)} u + g^o V^{(2)} u \quad . \quad (4)$$

It is useful to introduce the solutions to the scattering problems with each defect (i.e., when only α is present);

$$u^{(\alpha)} = u^o + g^o V^{(\alpha)} u^{(\alpha)} = u^o + u^{(\alpha)S}, \alpha = 1,2 \quad (5)$$

and the respective Greens functions that satisfy the equations

$$g^{(\alpha)} = g^o + g^o V^{(\alpha)} g^{(\alpha)} = g^o + g^{(\alpha)S}, \alpha = 1,2 \quad (6)$$

Equations (4)-(6) are integral equations; the (unknown) solution appears on both sides. To express the solution in terms of the incident wave only, one introduces the T matrix. For a single scatterer problem $T^{(\alpha)}$ is defined by

$$u^{(\alpha)} = u^o + g^o T^{(\alpha)} u^o \quad (7)$$

and for the problem with both scatterers present one has

$$u = u^o + g^o T u^o \quad .$$

By generating the infinite Born series using (4) and performing partial summations, one obtains an expansion for T in terms of $T^{(1)}$ and $T^{(2)}$;

$$T=T^{(1)} + T^{(2)} + T^{(1)}g^oT^{(2)} + T^{(2)}g^oT^{(1)} + O(T^{(\alpha)})^3 \tag{8}$$

In the approximation adopted here we neglect all higher than second order terms in the $T^{(\alpha)}$. Physically, our approximation contains the following processes: scattering from R_1 and from R_2 (single scattering processes); scattering from R_1 first and then from R_2 and vice versus (double scattering processes). The first two terms in (8) contribute to the full solution u the coherent sum of the two separate scattering problems; the next two terms constitute the lowest order approximation to the interaction between the scatterers. Using the approximation (8) for the T matrix in Eq. (7), the solution u is expressed as

$$u=u^o + g^{(1)}V^{(2)}u^{(2)} + g^{(2)}V^{(1)}u^{(1)} \quad . \tag{9}$$

Alternatively, this can be rewritten as

$$u=u^o + u^{(1)}S + u^{(2)}S + g^{(1)}SV^{(2)}u^{(2)} + g^{(2)}SV^{(1)}u^{(1)} \tag{10}$$

On these equations are based our approximate solutions for scattering by the defects of Fig. 1. Application to the defect of Fig. 1b with two spherical elastic inclusions is straightforward; the solutions to scattering by a sphere are known,[6] and the spherical Greens functions were expressed in terms of these solutions.[3] As to the defect of Fig. 1a, one needs an approximate solution for scattering by a circular annulus and a generalization of the previous formalism for non-volume defects. Such a generalization is needed for the two sphere defect also, when the two spheres are cavities. This is so since our expression for u involves the exact solution for sphere (1) inside sphere (1) itself, where it is not defined. Therefore in order to use Eq. (9) or (10) for cavities, a formulation of multiple scattering theory on the basis of surface integrals is needed.

Surface Formalism.[7] The starting point is the integral equation for the solution, in terms of integrals over the entire surface of the defect, S.

$$u_m=u^o_m + C^o_{ijkl}\int_S ds'\hat{n}_i[u_j g^o_{mk,l'} - g^o_{mj}u_{k,l'}] \quad . \tag{11}$$

It should be noted that for the case of a cavity (or crack) the normal stress on the surface S vanishes and only the first term in (11) is needed.

This integral equation can be expressed in operator form

$$u_m - u^o_m + \int_S ds' n_i g^o_{mk} V_{ijkl} u_j \tag{12}$$

where

$$V_{ijkl} = C_{ijkl}\overset{\rightarrow}{\partial}_{l'} - C_{ijkl}\overset{\leftarrow}{\partial}_{l'} \quad . \tag{13}$$

The arrow on the partial derivative indicates whether it acts on g^o or u. As above, we will suppress the integration and the tensorial indices to write

$$u = u^o + g^oVu \quad .$$

When the surface of the compound defect is the union of S_1 and S_2, the surfaces of two defects with known solutions, the formalism of part A can be directly applied, again yielding expressions (9) or (10) as the approximate solutions for the compound defect.

APPLICATION TO TWO SPECIFIC DEFECTS

Two Spherical Cavities. The exact solutions for scattering of plane waves by a single spherical cavity are known. We have also been able to express the Green's function associated with a spherical defect in terms of these solutions. The following notation is used: $u^{(\alpha)}$ is the solution associated with sphere α only, and

$$\begin{aligned} \sigma^{(\alpha)}_{ij} &= (u^{(\alpha)}_{i,j} + u^{(\alpha)}_{j,i})/2 \\ \tau^{(\alpha)}_{ij} &= (\hat{n}_i u^{(\alpha)}_j + \hat{n}_j u^{(\alpha)}_i)/2 \end{aligned} \tag{14}$$

We use the convention of Ref. (3), with $u_j(\underline{r},\underline{k},\epsilon)$ denoting the full solution of the scattering problem at point $\underline{r}$, for an incident plane wave with wave vector $\underline{k}$ and polarization ϵ. The displacement field due to two spherical cavities $\alpha = 1,2$ is given by

$$u_m(\underline{r}) = u^o_m(\underline{r},-\gamma(\epsilon_o)\hat{r}_o,\epsilon_o) + \sum_\epsilon \hat{e}^\epsilon\gamma(\epsilon)^2\exp[i\gamma(\epsilon)r]/r[\tilde{D}_2(\epsilon) + \tilde{D}_3(\epsilon)] \tag{15}$$

$\gamma(\epsilon)$ is the wave number for longitudinal ($\hat{e}^\epsilon = \hat{r}$) or shear ($\hat{e}^\epsilon = \hat{\theta}$ or $\hat{\phi}$) waves; the coefficients $\tilde{D}_2$ and $\tilde{D}_3$ are given by

$$\tilde{D}_2 = \frac{\lambda}{4\pi\rho\omega^2}\left[\int_{S_1} ds' n_k u^{(1)}_k(\underline{r}',-\gamma(\epsilon_o)\hat{r}_o,\epsilon_o)u^{(2)}_{l,l'}(\underline{r}',-\gamma(\epsilon)\hat{r},\epsilon)\right.$$
$$\left. + \int_{S_2} ds' n_k u^{(2)}_k(\underline{r}',-\gamma(\epsilon_o)\hat{r}_o,\epsilon_o)u^{(1)}_{l,l'}(\underline{r}',-\gamma(\epsilon)\hat{r},\epsilon)\right] \tag{16}$$

$$\tilde{D}_3 = \frac{2\mu}{4\pi\rho\omega^2}\left[\int_{S_1} ds' \sigma^{(2)}_{ij}(\underline{r}',-\gamma(\epsilon)\hat{r},\epsilon)\tau^{(1)}_{ij}(\underline{r}',-\gamma(\epsilon_o)\hat{r}_o,\epsilon_o)\right.$$
$$\left. + \int_{S_2} ds' \sigma^{(1)}_{ij}(\underline{r}',-\gamma(\epsilon)\hat{r},\epsilon)\tau^{(2)}_{ij}(\underline{r}',-\gamma(\epsilon_o)\hat{r}_o,\epsilon_o)\right] \tag{17}$$

where λ, μ are the Lame parameters and ρ the density of the host medium.

Crack Emanating from Volume Defect. The solution for the scattering problem is again expressed in terms of the solutions for the two separate parts of the defect. In this case, these are a spherical cavity and a circular annulus of vanishing volume, on the surface of which the normal stress

vanishes. For the spherical cavity the exact solution is known; however, this is not so for the annulus. Therefore one needs an estimate for the scattering from the latter defect. We propose the following approximate solution; use a reliable approximation for scattering by a circular crack to obtain the crack opening (i.e., the discontinuity Δu_j on the surface of the crack) and assume that this function represents well the discontinuity for the annulus, even when the central part of the crack is replaced by appropriate boundary conditions on the annulus. Under this assumption one obtains for the scattering from the compound defect the following expression:

$$u_m(\underline{r}) = u_m^0(\underline{r},-\gamma\hat{r}_0,\epsilon_0) + \sum_\epsilon \hat{e}^\epsilon \gamma(\epsilon)^2 \exp[i\gamma(\epsilon)r]/r[D_2'(\epsilon) + D_3'(3)] \quad (18)$$

where $u^{(1)}$ is the solution of the scattering problem from the spherical cavity, $u^{(2)}$ from the circular annulus. This function is expressed as an integral over the discontinuity of the displacement field across a circular crack, $u^{(2)}$, which also enters in the formuli for D_2', D_3':

$$D_2' = \frac{-\lambda}{4\pi\rho\omega^2}\left[\int_{S_1} ds' n_j u_j^{(1)}(\underline{r}',-\gamma(\epsilon_0)\hat{r}_0,\epsilon_0) u_{i,i}^{(2)}(\underline{r}',-\gamma(\epsilon)r,\epsilon) + \int_{S_2} ds' n_j \Delta u_j^{(2)}(\underline{r}',-\gamma(\epsilon_0)\hat{r}_0,\epsilon_0) u_{i,i}^{(1)}(\underline{r}',-\gamma(\epsilon)\hat{r},\epsilon)\right] \quad (19)$$

$$D_3' = \frac{2}{4\pi\rho\omega^2}\left[\int_{S_1} ds' \tau_{ij}^{(1)}(\underline{r}',-\gamma(\epsilon_0)\hat{r}_0,\epsilon_0)\sigma_{ij}^{(2)}(\underline{r}',-\gamma(\epsilon)\hat{r},\epsilon) + \int_{S_2} ds' \sigma_{ij}^{(1)}(\underline{r}',-\gamma(\epsilon)\hat{r},\epsilon)\Delta\tau_{ij}^{(2)}(\underline{r}',-\gamma(\epsilon_0)\hat{r}_0,\epsilon_0)\right] \quad (20)$$

Numerical codes for the approximate solutions based on Eqs. (17)-(20) are currently being developed.

REFERENCES

1. V. Varatharajulu and Y.H. Pao, J.A.S.A. 60, 556 (1976).
2. W.M. Visscher, J. Appl. Phys. (in press). J. Opsal (unpublished).
3. K.E. Newman, S. Teitel and E. Domany, J. Appl. Phys. (in press).
4. J. Achenbach, A.K. Gautesen, J.A.S.A. 61, 413 (1977).
5. J.E. Gubernatis, E. Domany and J.A. Krumhansl, J. Appl. Phys. 48, 2804 (1977).
6. C. F. Ying and R. Truell, J. Phys. 27, 1086 (1956).
7. For a review see J. E. Gubernatis, E. Domany and J. A. Krumhansl, Los Alamos Report No. LA-UR-79 2393, Sept. 1979.
8. B. Tittmann, L. Ahlberg and O. Buck, these proceedings.
9. V.V. Varadan, V.K. Varadan and D.J.N. Wall, these proceedings.

SUMMARY DISCUSSION

Bruce Thompson, Chairman (Rockwell Science Center [now Ames Laboratory]): There is time for one brief question.

Unidentified Speaker: John Simmons (NBS) has just completed a general variational method for dealing with statistical distributions of defects in multiple scattering, and he claims it's the most exact variation.

Eytan Domany (Weizmann Institute of Science): It's a variational method.

Bruce Thompson, Chairman: Thank you, Eytan, we will now move on to the next paper.

MEASUREMENTS OF SCATTERING FROM BULK DEFECTS

B. R. Tittmann, and L. Ahlberg
Rockwell International Science Center
Thousand Oaks, CA 91360

ABSTRACT

This report presents results of measurements of longitudinal wave ultrasonic scattering from complex defects embedded in Ti-alloy by the diffusion bonding process. The defects examined are: circular and elliptical cracks, two overlapping voids consisting of a sphere and a prolate spheroid, two adjacent spherical voids, and a spherical void with an encircling crack. Representative plots are given for the raw waveforms, magnitude (and sometimes the phase) of the deconvolved Fourier transform, and in some cases the time impulse response function. The data are compared to or analyzed in terms of several current theories. While good quantitative agreement was observed over certain ranges, the comparisons point to definite (in some cases not unexpected) limitations in either the pertaining theory or experiment or both. Finally, the results are discussed with an eye toward applications.

OBJECTIVES AND APPROACH

The objective of this task was to carry out experimental studies on metallic components containing defects in its interior with the aid of bulk wave ultrasonic nondestructive evaluation. The investigation had the goals of (1) the design of specimens containing irregular shaped bulk flaws; (2) the characterization of the flaws in experiments which guide and evaluate theoretical scattering models; (3) the testing of inversion algorithms; and (4) the prediction of fatigue lifetime and failure.

The approach was to use diffusion bonded samples as primary test medium. Measurements were made of the angular and frequency or time domain variations of the scattered signals. The results were employed to guide the development of theoretical approaches and to test specific theoretical predictions for the cases of multiple and irregular flaws. As a guide, experimental comparisons of the differences and similarities of the scattering properties of irregularly shaped flaws and ellipsoids were used to identify those aspects of the theory which needed further work and to indicate what physical approximations seem most appropriate. Approximate theories were then checked after development. Similarly the experimental data were used to guide and check inversion algorithms in their attempt to reconstruct the shape, size, and orientation of the flaws. This information was then inserted into fracture mechanics to predict fatigue lifetime and failure, predictions which for selected samples were tested in actual fatigue cycle experiments.

SAMPLE PREPARATION

In close collaboration with the various theoretical groups representing different inversion algorithms, a unique set of diffusion bonded samples were designed and built. These samples containing a variety of irregular and multiple flaws whose scattering characteristics were being obtained in order to guide and evaluate developments of theoretical approaches and to test specific theoretical predictions.

The work was divided according to flaw type. Two flaws were simulated cracks, circular and elliptical in shape, respectively. These flaws were unique in that they possessed zero thickness yet experimentally exhibited a reflection coefficient whose imaginary term was comparable to an air-metal interface. These flaws were investigated in collaboration with Achenbach, who has recently solved the inverse problem on the basis of physical elastodynamics for high frequency far-field elastic waves scattered by a flat crack. One of the flaws was a fatigue crack whose growth history was planned to be monitored in fatigue cycle experiments to test predictions of fatigue life and ultimate failure. Another flaw was a perturbation of the spherical void consisting of a small sphere and a modified prolate spheroid. This work was carried out with close collaboration between experiment and theory with the view of identifying key features suitable for data inversion. Two independent theoretical calculations were available: Domany's Distorted Wave Born Approximation[1] and Opsal's adaption[2] of Vissher's Matrix theory.[3] Another flaw was a simple multiple defect consisting of two slightly separated spherical voids of equal radii. Varadan and Varadan have used matrix theory to solve the problem of scattering from similar defects so that a comparison between theory and experiment was feasible.[4] Finally, the important problem of characterizing cracks growing from weldment voids was investigated with a sample consisting of a spherical void and a simulated (Yttria) crack emanating from the void in the form of a "saturn ring."

RESULTS AND DISCUSSION

A. Samples No. 69 and 72, Simulated (Yttria) Cracks

Achenbach et al[5-8] have developed methods to analyze diffraction of elastic waves by cracks. They showed that good approximations at high frequencies can be obtained on the basis of elastodynamic theory. In the range of frequencies where the wavelengths are of the same order of magnitude as the characteristic length dimension, a, of the crack, the frequency dependence of the scattered amplitude shows oscillatory behavior with a period

that depends on α; alternatively, in the time domain the scattered field manifests itself as two waveforms separated by a time increment which depends on α.

As discussed in detail before,[9] "trailer-hitch" specimens No. 69 and 72 were prepared to simulate circular and elliptical cracks, respectively, by poisoning the bond plane area with yttria powder.[10] The yttria was applied in a liquid suspension which was allowed to dry. Figure 1 shows a schematic of "trailer hitch" No. 69 and a photo of the dried yttria disk just before diffusion bonding. Ultrasonic tests of the bondplane area after diffusion bonding revealed the absence of a disbond anywhere except in the yttria area. Here, observation of complete phase reversal showed that the waves encounter a discontinuity equivalent to a metal-air interface, demonstrating the absence of any transmission through the powder to the opposite face of the simulated crack. The thickness of the yttria layer is estimated to be several yttria grain diameter, or 50 microns.

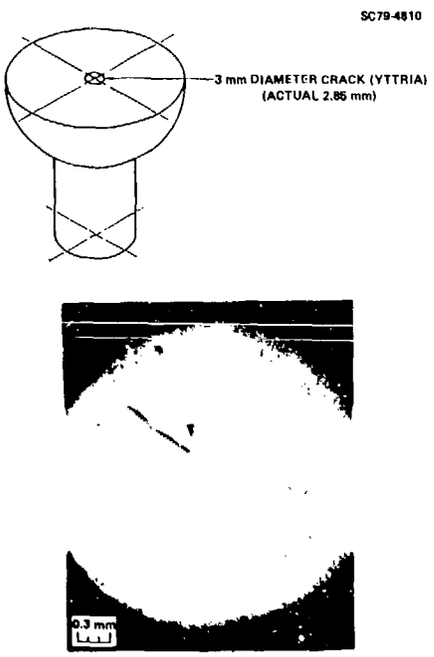

Fig. 1 Sample 69: Circular crack simulated with the aid of yttria powder. Top figure is schematic representation of lower half of "trailer hitch." Lower figure is microphoto of yttria powder dot before diffusion bonding.

Specimens No. 69 and 72 were interrogated in pitch-catch with the transmitting transducer normal to the crack plane while the receiver transducer were placed at 0°, 15°, 30°, 45° and 55° to the crack plane. The transducers were 15 MHz, 6.35 mm diameter broadband Panametrics transducers. Figure 2a shows the pulse echo signal from the crack normal to the crack plane, while 2b, 2c, 3a, 3b, and 3c show the pitch-catch signals at 0°, 15°, 30°, 45° and 55° from the crack plane, respectively. Table 1 is a list of the time signal minima, maxima, and the time between them.

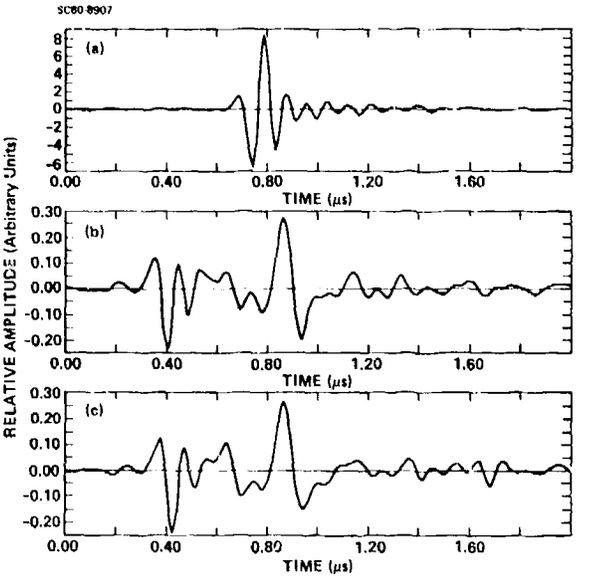

Fig. 2 Time domain waveforms for Sample 69: Circular crack. (a) Pulse-echo signal from crack normal to crack plane. (b) Pitch-catch with transmitter at 90° and receiver at 0° with crack plane. (c) Pitch-catch same as in (b) but receiver at 15°.

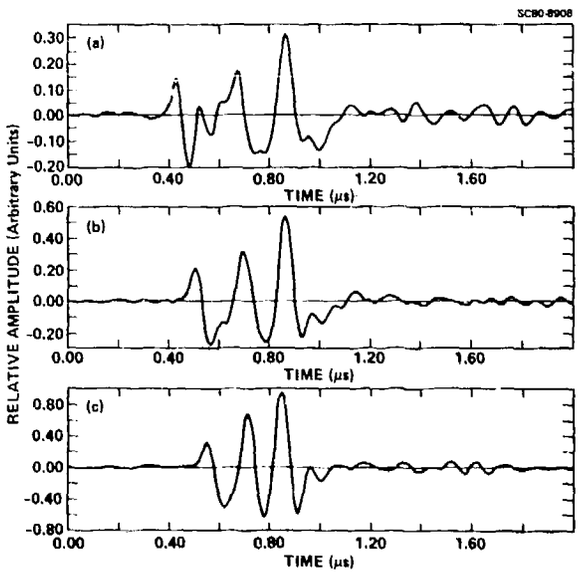

Fig. 3 Pitch-catch time domain waveforms for Sample 69 circular crack. Transmitter normal to crack plane, detector at angles (a) 30°, (b) 45°, and (c) 55° above crack plane. Note coalescence of two "flash-point" signals.

In qualitative agreement with Achenbach et al, the sound field scattered by the crack exhibited two phase inverted waveforms separated by a time interval which decreased as the receiver angle increased. An interesting feature of Table 1 is

Table 1. Time Domain Positions of Waveform Features

Angle from Crack Plane	Time of 1st Minima (μs)	Time of last Maxima (μs)	Δt (μs)
0	0.405	0.868	0.463
15	0.425	0.867	0.442
30	0.480	0.876	0.387
45	0.567	0.866	0.299
55	0.621	0.850	0.229

that the arrival time of the first waveform changes dramatically, whereas the second waveform appears to remain stationary with respect to an arbitrarily chosen reference given by the trigger signal. This result may be a consequence of near-field effects playing a role for the crack edge nearest to the receiving transducer.

Despite this complication, the crack diameter was estimated from the time delays, and Table 2 lists the results in good agreement with the dimensions of the micro photograph of Fig. 1. Figure 4 shows the frequency spectra corresponding to the time domain signals in Fig. 2b and 2c. The spacing between the interference minima gave crack diameter estimates in similarly good agreement.

Table 2. Comparison of Estimated and Actual Crack Dimensions

Angle	Δt (μs)	Crack Dia. (mm)	Manufactured Dia. mm	Error %
0	0.463	2.87	2.85	+ 0.7
15	0.442	2.84	2.85	- 0.3
30	0.387	2.77	2.85	- 2.8
45	0.299	2.62	2.85	- 8.7
55	0.229	2.48	2.85	-16.8

Similar data were obtained on "trailer-hitch" No. 72, a simulated (yttria) crack in the shape of an ellipse. Here, the time delays were obtained systematically as a function of angle around the periphery of the ellipse, with the transducer making a 15° angle with the crack plane. Figure 5 shows a comparison between the estimated shape and the outline of the yttria deposit before diffusion bonding. The systematic overestimate of the dimensions suggests that during the diffusion bonding process the yttria deposit, which may have been too thick, was forced to spread somewhat and caused a somewhat larger disbond area than planned.

B. Sample No. 100, Tensile Fatigue Specimen

Specimen No. 100 was designed to allow the application of the techniques developed in the previous section for failure prediction of a fatigue crack. As shown in Fig. 6, this sample was prepared by introducing a semi-circular slot in each of two blocks which were then diffusion bonded to provide a circular starter notch for crack growth under cyclic tensile fatigue. After diffusion bonding, the block was machined into a "dogbone" geometry with the shape and size shown in Fig. 6.

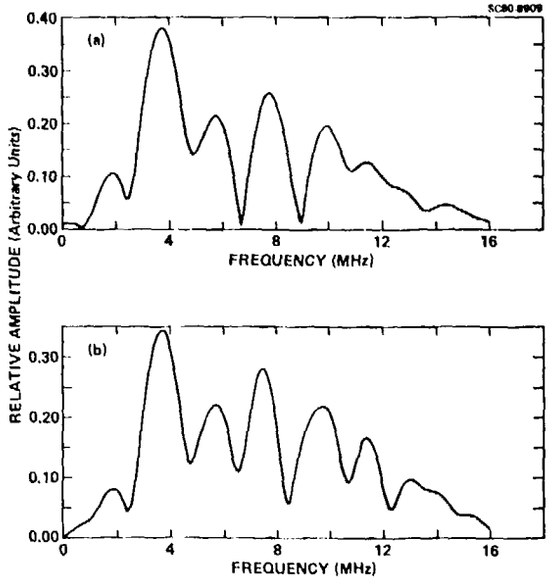

Fig. 4 Frequency spectra obtained by digitizing and Fourier analyzing time-domain signals in Figs. 2b and 2c. The spacing between the interference minima gives crack diameter estimates in good agreement with those obtained from the "flash-point" echo separation.

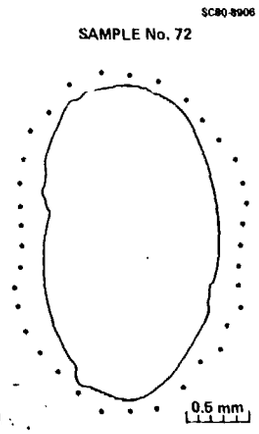

Fig. 5 Sample 72: Elliptical crack simulated with the aid of the yttria powder. The solid line is the outline of the yttria powder region just before diffusion bonding. the data points were obtained from estimates based on pitch-catch scattering data. The discrepancy is thought to be a result of a slight spreading of the yttria powder upon diffusion bonding.

The sample was inspected with ultrasound before and after machining into the "dogbone" shape. This inspection was carried out in order to have good knowledge of the 6.35 mm diameter starter notch slot. Several experiments were performed in the scanning tank, plus standard pulse echo and pitch-catch experiments. Figure 7a

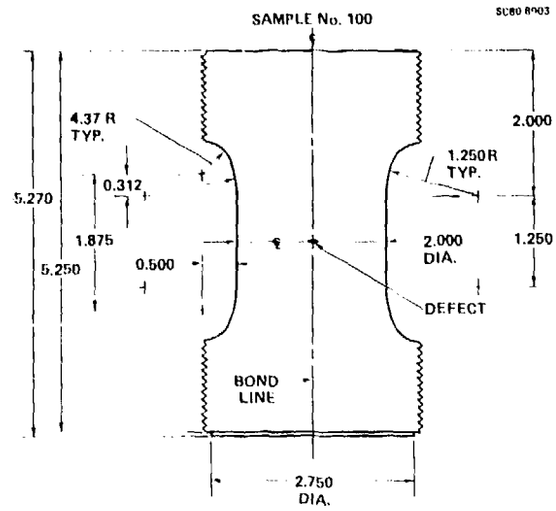

Fig. 6 Sample 100: Tensile specimen with interior fatigue crack starter notch.

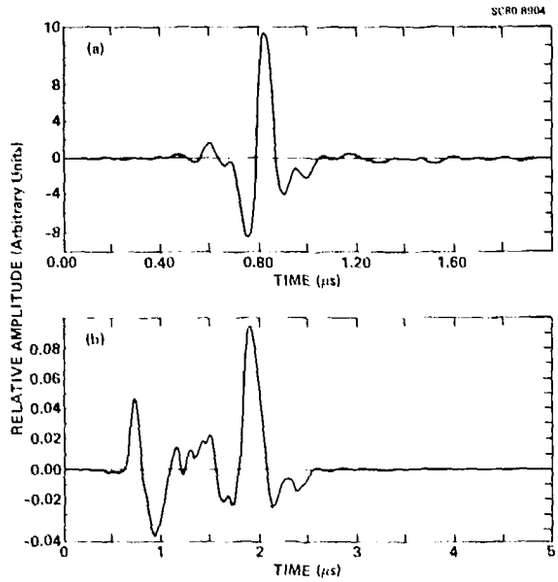

Fig. 7 Time domain waveforms for sample 100. (a) Pulse-echo waveform from transducer normal to the plane of starter notch. (b) Pitch-catch waveform with transmitter normal to starter notch plane and receiver in plane of starter notch.

shows the pulse echo waveform from a transducer oriented normal to the plane of the slot. This interrogation revealed the presence of a small signal originating about 1.25 mm above the main slot, probably due to a small defect in the material. Figure 7b is a pitch-catch waveform received by a transducer which was mounted on an adapter to the cylindrical surface and positioned in the plane of the slot. This waveform is analogous to those obtained with the yttria cracks and gives an indication of the slot diameter. The slot diameter was machined to be 6.35 mm diameter; the diameter estimated from the waveform is 6.11 mm.

The specimen was then fatigue cycled but, unfortunately, the threaded section at the grip developed a crack after only 4470 cycles, so that sample No. 100 failed prematurely and was destroyed. Figure 8 shows a micrograph of a cross section through the starter notch and the crack initiated from it. Closer examination of the starter notch revealed that the two halves intended to be mated in the diffusion bonding process were actually displaced by 10% in the bond plane along the diameter. A small displacement probably also occurred along the thickness of the notch. Calculations to estimate the number of cycles to grow the fatigue crack from the starter notch to its actual size gave $\Delta N = 3270$ cycles which is in reasonable agreement with the actual $\Delta N = 4470$ cycles.[11]

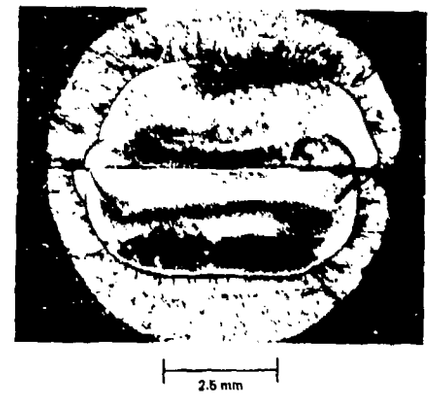

Fig. 8 Micrograph of starter-notch and associated crack.

Unfortunately, the first ultrasonic tests were intended to be performed at 5000 cycles, so that no NDE results are available. Another sample is being readied for new tests. The design has been changed to prevent any future premature failures in the grip section.

C. Sample No. 73, Pinnochio

Previous pitch-catch measurements on the trailer hitches with the goniometer described before[9] have been difficult because of the requirement for strong pressures to be exerted on the goniometer in order to obtain good contact between the "trailer-hitch" sample under test and the end caps which adapt the transducer to the spherical geometry. In order to avoid this problem, the following scheme was devised. First, the transmitting end cap was hard epoxyed to the sample, which resulted in an excellent stationary contact. Second, the goniometer was placed in a water bath, and a focussed transducer was used as a mobile receiver. From the radius of the curvature of the "trailer hitch" and the transducer focal length, the appropriate distance between the sample and transducer could be calculated such that the refracting ultrasonic rays became parallel in the sample. The use of this scheme eliminated lateral forces applied during the rotation of the mobile receiver transducer and still allowed good signals to be obtained without bending or distorting the goniometer.

Figure 9 is a schematic view of the double defect void, nicknamed Pinnochio. Also shown is a

microphotograph of the defect before diffusion bonding.

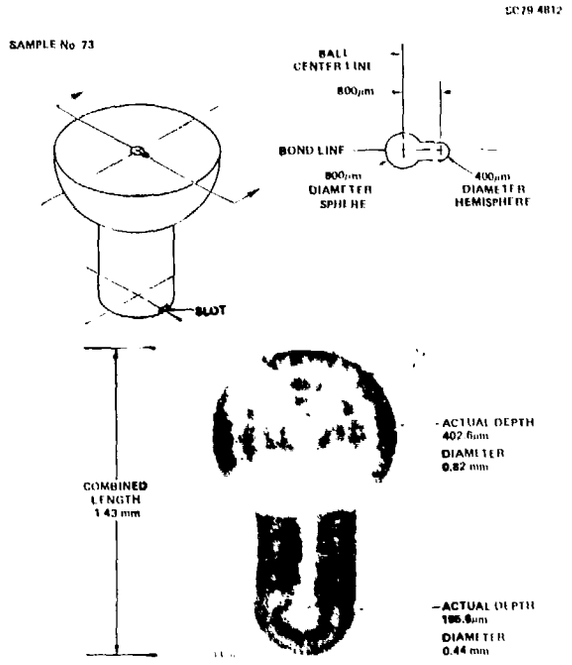

Fig. 9 Sample 73: Pinnochio void. The top view is a schematic presentation of the complex void, while lower figure gives microphoto of one of the defect halves just before diffusion bonding.

Considerable difficulty was encountered in carrying out measurements as a function of angle. In order to demonstrate this problem, the defect was scanned in pulse echo at a 45° polar angle at increments of every 10° in azimuth from 0 to 350°. The results of this experiment are shown in the "waterfall" plot of Fig. 10. The plot shows a succession of time domain waveforms slightly displaced from one another. If the sample had been constructed correctly, the waveforms for azimuthal angles 0° to 180° would have been similar to the waveforms from 360° to 180°. However, in this case there are gross dissimilarities in amplitude, suggesting that the sample was not properly manufactured. Full evaluation of this sample presents yet another challenge to NDE research.

Because of these difficulties, it was decided to carry out our studies in the frequency domain. Figure 11 shows, at the top, a waveform obtained, when the defect was interrogated in pulse-echo from the side, i.e., as a profile of the head and nose. The graph below shows the corresponding deconvolved Fourier spectrum compared with two theories: Domany's Distorted Wave Born Approximation (DWBA)[1] and Vissher's matrix theory.[2-3] The agreement is reasonably good, especially in the frequency range from 1 MHz to 6 MHz. Above 6 MHz as might be expected, DWBA theory becomes less accurate, since ka exceeds the range of applicability of the Born approximation approach. Agreement between matrix theory and experiment is reasonable to as high as 12 MHz.

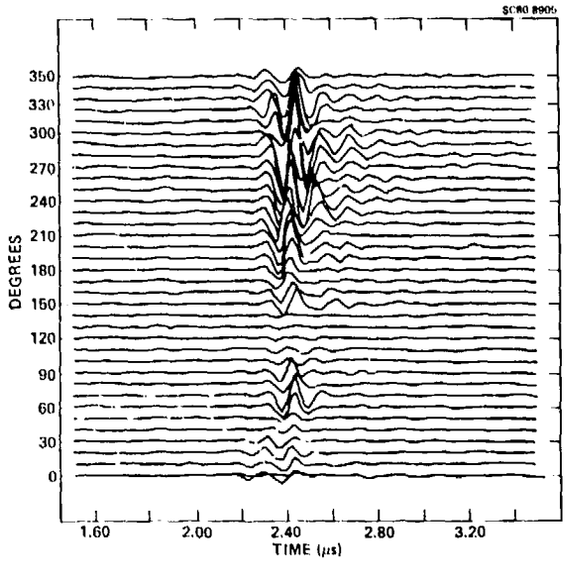

Fig. 10 Sample 73: Pinnochio void. "Waterfall" plot of waveforms obtained by scanning transducer from 0 to 360° in increments of 10°. Note lack of symmetry suggesting a problem in sample preparation.

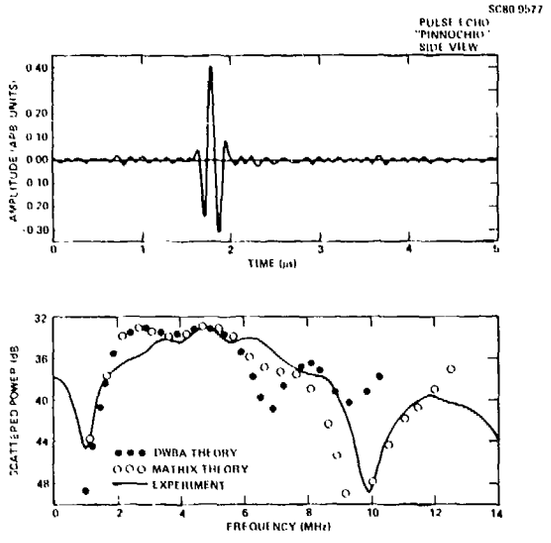

Fig. 11 Comparison between theory and experiment for pulse-echo interogation of side of "Pinnochio" defect.

D. Sample No. 95, Double Void

This defect consists of two 800 μm diameter spherical voids separated center-to-center by 1200 μm. Figure 12 shows the defect schematically and in the form of a microphoto just before diffusion bonding. The defect was studied in pulse-echo in a plane containing the axis through the centers of the two defects and the line normal to the two centers. Figure 13a shows the time-domain waveform for the transducer at 70° from the axis through the void centers. This signal shows two

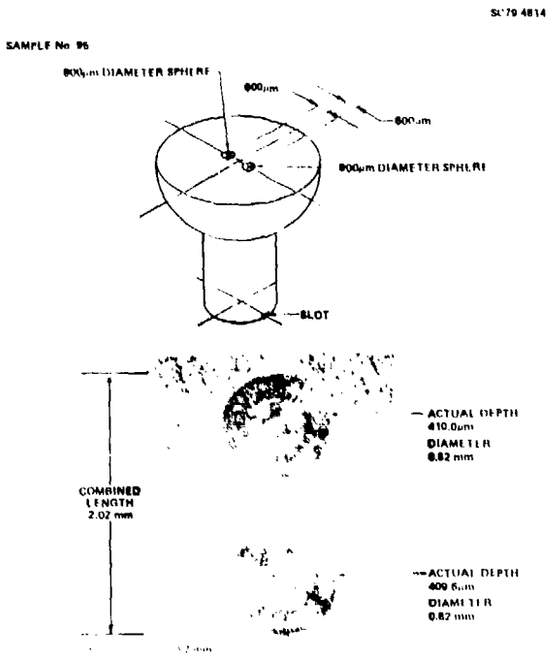

Fig. 12 Sample 95: Double void. Two 800 μm diameter spheres separated center-to-center by 1200 μm. The top shows schematic of the lower half of the trailer hitch, while lower figure shows microphoto just before diffusion bonding.

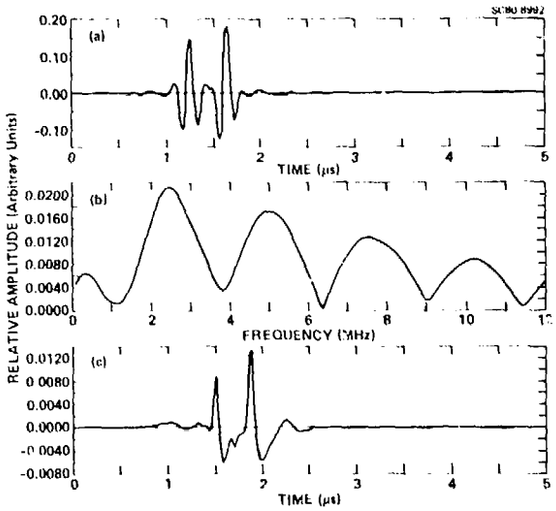

Fig. 13 Sample 95: Double void defect. (a) Pulse echo waveform for 70° from axis through centers of both voids. (b) Deconvolved frequency spectrum of waveform in (a). (c) Fourier transform of spectrum in (b) to obtain impulse response function in time-domain. Note that in (a) the two waveforms do not show phase reversal as did, for example, the double waveforms from the crack.

well-resolved echoes which when Fourier analysed and de-convolved gave well-defined interference minima, as shown in Fig. 13b. Figure 13c is the inverse Fourier transform or the time impulse response function, that is to say, the time-domain waveform of Fig. 13a without the transducer transfer function.

In order to determine the exact phase relationship between these two signals, each signal was windowed, matched according to the waveform centroid and phase compared. Figure 14a is the spectrum of the magnitude ratio and Figure 14b is that of the phase difference. It is interesting to note that the phase difference is approximately zero plus or minus 4 degrees over most of the useful frequency range of the transducer. This result is expected because the signals are reflections from identical sources.

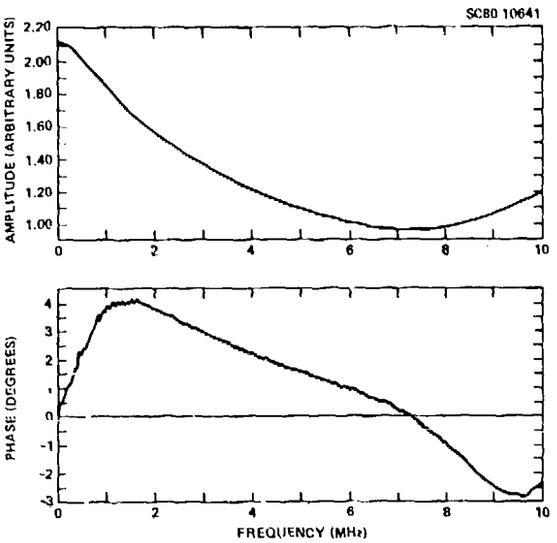

Fig. 14 Amplitude and phase comparisons for the two echoes making up the waveform in Fig. 13a.

Finally, a quantitative comparison was made between the experiment and calculations by Varadan and Varadan.[4] This comparison is shown in Figure 15 which plots the data of Fig. 13b in terms of the scattering cross section versus ka, where a is the radius of the sphere. Nearly quantitative agreement was realized over most of the useful range of the transducer.

E. Sample No. 71, "Saturn Ring"

An extension of the crack problem to important applications is the detection and characterization of cracks emanating from voids. This is a frequently encountered problem in weldments. To simulate this situation a "trailer hitch" sample was fabricated[3] consisting of a spherical void 800 μm in diameter with a yttria powder ring around it having a diameter of 1.51-1.70 mm. Figure 16 shows the bottom half of the trailer-hitch sample with a schematic drawing in the top part of the figure and a photo of the actual defect on the bottom. The microphoto shows one-

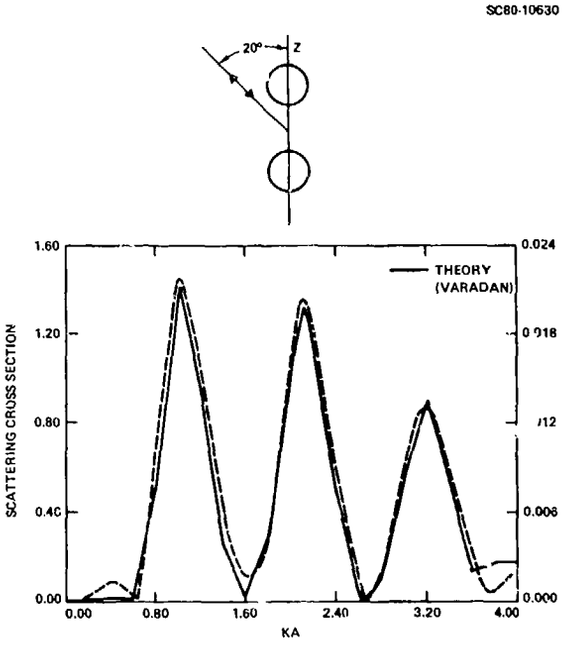

Fig. 15 Comparison between theory and experiment for double-void. The experimental frequency spectrum is fitted to the theory of Varadan at one point.

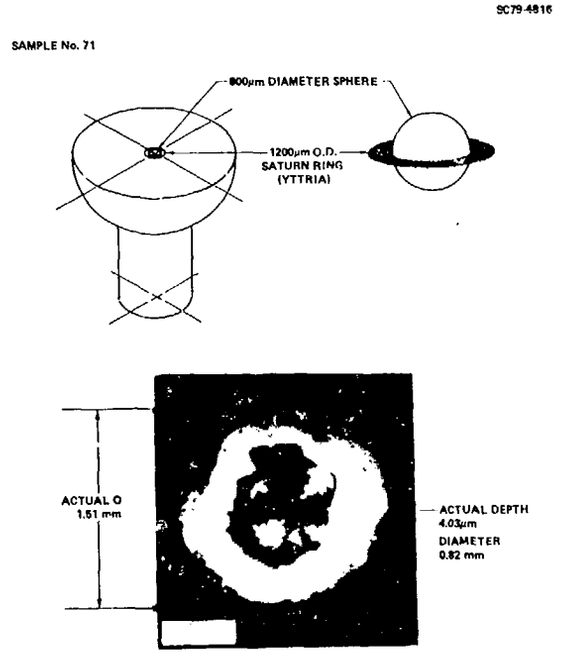

Fig. 16 Simulated crack from weldment void, trailer hitch sample 71: "Saturn Ring." The defect is shown schematically in top part of figure and in a microphoto at the bottom just before diffusion bonding.

half of a sphere and a layer of yttria powder encircling it.

This defect was interrogated with longitudinal waves in pulse-echo and pitch-catch and Figs. 17 and 18 are examples of the pulse echo data. A key feature of the data is the appearance of a double echo as shown in Fig. 17a when the transducer is placed at 45° to the crack plane. As expected, the double echo manifests itself in an interference pattern in the deconvolved frequency spectrum, Fig. 17b and as two impulses in the impulse response function, Fig. 17c. This results is a clear-cut indication of the presence of an additional feature besides the spherical void. The two echoes are about 0.40 μs apart corresponding to a distance of d = 1.7 μm. This value compares favorably with the outer diameter of the yttria ring. Another key feature is illustrated in Fig. 18 which presents a pulse-echo signal normal to the crack plane in Fig. 18a and in the crack plane in Fig. 18b. The main difference between the two signals is the dramatic change in amplitude, a factor of 20. Since a spherical void would give a completely isotropic response, this result shows how much the presence of the crack influences the data.

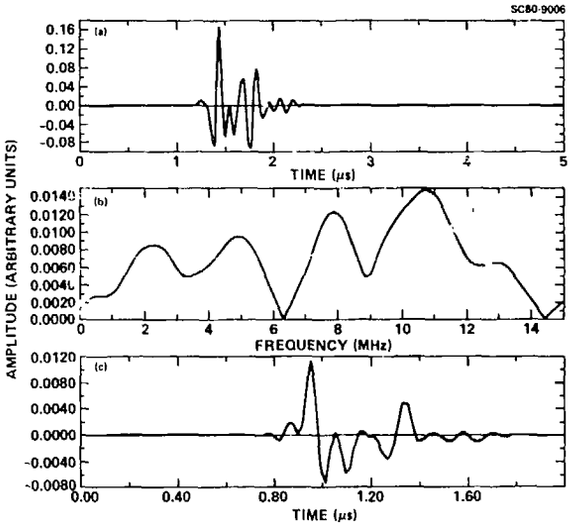

Fig. 17 Saturn Ring defect interrogated in pulse-echo at 45° to plane of crack. (a) Time-domain waveform, (b) deconvolved frequency spectrum, (c) impulse response function. Note the presence of two main echoes rather than just one as would be observed for simple spherical void.

The data of Fig. 17a were examined more critically to achieve a quantitative comparison with theory. Figure 19 shows at the top the received wave form again and at the bottom the deconvolved frequency spectrum. Also shown are points calculated by J. Opsal using Vissher's matrix theory.[3] The theoretical points are fitted to the experimental data at one point. The comparison is in reasonable agreement, especially for the positions of the nulls and peaks in the spectrum. Notice, that the deep null between 6 MHz and 7 MHz makes this spectrum dramatically different from that of a simple spherical void.

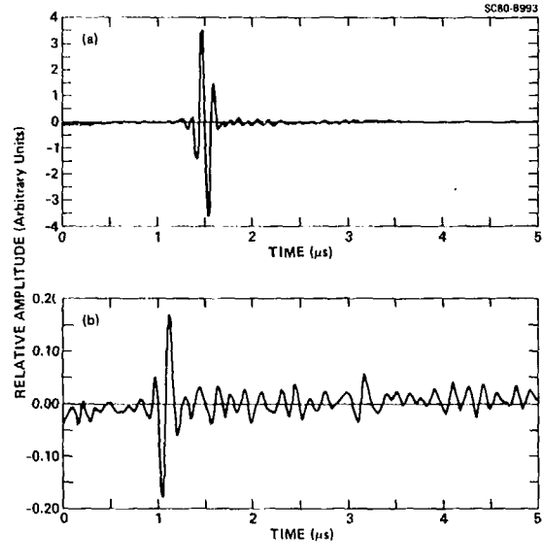

Fig. 18 Saturn Ring defect interrogated in pulse-echo at (a) normal to crack plane (b) in crack plane.

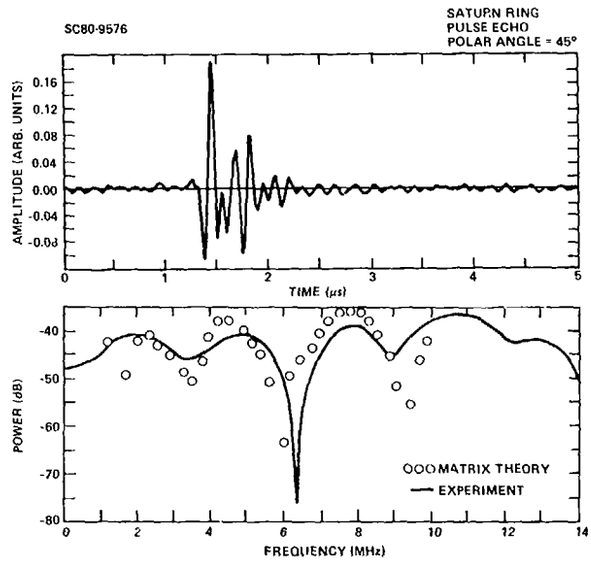

Fig. 19 Frequency spectrum for Saturn Ring interrogated in pulse-echo at 45° to the plane of the crack compared with theoretical calculations.

ACKNOWLEDGEMENT

The authors are grateful to J. Achenbach, V. V. Varadan, V. K. Varadan, J. Opsal, and E. Domany for their calculations allowing the direct comparisons between theory and experiment. They are also indepted to O. Buck for the design and preparation of the fatigue specimen.

This research was sponsored by the Center for Advanced NDE operated by the Science Center, Rockwell International, for the Advanced Research Projects Agency and the Air Force Materials Laboratory under Contract No. F33615-80-C-5004.

REFERENCES

1 E. Domany, K. E. Newman, and S. Teitel "Elastic Wave Scattering by General Shaped Defects: The Distorted Wave Born Approximation," Interdiscipl. Prog. for Quant. Flaw Definition - Special Report Fifth Year Effort, D. O. Thompson, Contract No. F33615-74-C-5180, p. 1 (1980).

2. J. L. Opsal, "Matrix Theory of Elastic Wave Scattering: Application to Scattering of Transverse Waves," Proc. of the DARPA/AFML Review of Progress in Quant. NDE, La Jolla, 1980, in press.

3. W. M. Visscher, "A New Way to Calculate Scattering of Acoustic and Elastic Waves. I. Theory Illustrated for Scalar Waves," J. Appl. Phys. 51 (1980).

4. V. V. and V. K. Varadan, "Elastic Wave Scattering by Rough Flaws and Cracks," Interdiscipl. Prog. for Quant. Flaw Definition - Special Report Fifth Year Effort, D. O. thompson, Contract No. F33615-74-C-5180, p. 13 (1980).

5. J. D. Achenbach, A. K. Gautesen, and H. McMaken, "Diffraction of Elastic Waves by Cracks - Analytical Results," in Elastic Waves and Non-Destructive Testing of Materials AMD - 29, pp. 33-52. The American Society of Mechanical Engineers, New York, 1978.

6. J. D. Achenbach and A. K. Gautesen, "Geometrical Theory of Diffraction for Three-D Elastodynamics," J. Acoust. Soc. Amer., 1978, in press.

7. J. D. Achenbach, A. K. Gautesen, and H. McMaken, "Application of Elastodynamic Ray Theory to Diffraction by Cracks," in Modern Problems in Elastic Wave Propagation, Wiley-Interscience, New York, 1978.

8. J. Achenbach, "Direct and Inverse Methods for Scattering by Cracks at High Frequencies," Interdiscipl. Prog. for Quant. Flaw Definition - Special Report Fifth Year Effort, D. O. thompson, Contract No. F33615-74-C-5180, p. 28 (1980).

9. B. R. Tittmann, "Measurements of Ultrasonic Scattering from Bulk Flaws of Complex Shape," Interdiscipl. Prog. for Quant. Flaw Definition - Special Report Fifth Year Effort, D. O. thompson, Contract No. F33615-74-C-5180, p. 36 (1980).

10. N. E. Paton, "Sample Preparation," in Interdiscipl. Prog. for Quant. Flaw Definition - Special Report Third Year Effort, D. O. Thompson, Contract F33615-74-C-5180, p. 59 (1977).

11. O. Buck, private communication

SUMMARY DISCUSSION

Bruce Thompson, Chairman (Rockwell Science Center [now Ames Laboratory]): I think we have time to entertain one or two questions.

Anmol Singh (Southwest Research Institute): How did you find the response function?

Bernie Tittmann (Science Center): We found the response function in two ways. We cut the trailer hitch in half so we have the flat face at the diffusion bonding plane and then we set the transducer on the top and let it radiate against its metal interface. The other one that we use is a spherical void for which we have the exact calculations, and we can predict what the radiation pattern should look like and then divide out to get the transducer response.

Bruce Thompson, Chairman: Thank you, Bernie. I think the remainder of the questions should be answered at the coffee break. Dr. Tittmann is chairing the next session.

ULTRASONIC CHARACTERIZATION OF ROUGH CRACKS

M. de Billy, F. Cohen-Tenoudji, and Gérard Quentin
Groupe de Physique des Solides, Université Paris 7,
75221 Paris Cedex 07, France

Kent Lewis
Department of Physics, University of Tennessee
Knoxville, TN 37916

Laszlo Adler
Groupe de Physique des Solides, Université Paris 7
75221 Paris Cedex 07, France
and
Department of Physics, University of Tennessee
Knoxville, TN 37916

ABSTRACT

It has been reported before that frequency and angular information from ultrasonic scattering can be used to characterize smooth artificial defects in metals. In this study ultrasonic measurements from fractured and smooth penny-shaped cracks of the same size were carried out. Experimental procedures included the use of broad band and narrow band ultrasonic signals. From angular and frequency dependence of ultrasonic scattering measurements the size, shape, orientation and rms roughness of the fractured surface have been estimated. Ultrasonic measurements of these parameters have been compared to the actual parameters of the defect.

INTRODUCTION

It has been generally accepted that scattering of ultrasonic waves from defects in solids provides a method of quantitative nondestructive evaluation of structural materials. For failure prediction modeling of a structural component, fracture mechanical calculations require such characteristics of an unknown flaw as size, shape, orientation, surface conditions, etc. Recent developments in theoretical and experimental work on ultrasonic scattering from flaws made it possible to calculate and measure the ultrasonic field scattered from cavities when their characteristics were known. The understanding of this so-called direct scattering problem is a necessary preliminary to the inversion problem which is to characterize an unknown flaw from angular and frequency dependence of the scattered field's amplitude and phase. Scattering of ultrasonic waves from crack-like defects with smooth surfaces of circular and elliptical shapes was studied by Adler and Lewis [1] using ultrasonic spectroscopy systems in their experiment and analyzing their results using various modifications [2] of Keller's [3] geometrical theory of diffraction. Achenbach and Gautesen [4] extended geometrical theory of diffraction to three-dimensional diffraction by cracks in solids. Subsequently, Achenbach, Adler, Lewis, and McMaken [5] showed that the measured scattering field from circular defects can be predicted theoretically and suggested an inversion procedure to obtain the size and orientation of circular cracks from features of the amplitude spectra of the scattered ultrasonic wave. The problem was generalized for elliptical cracks by Adler and Achenbach [6]. In the above-mentioned works the artificial cracks had smooth polished surfaces which is not the case for naturally occurring flaws. Now we are addressing the problem of ultrasonic scattering from cracks with random rough surfaces such as the surface of a fractured fatigue sample. For these types of cracks—in addition to geometrical characteristics such as size, shape, orientations—the evaluation of the surface characteristics, cf. rms roughness, correlation length, distribution of roughness, etc., is essential. Methods to study randomly rough large surfaces using ultrasonic scattering have been developed by de Billy, Cohen-Tenoudji, Jungman, and Quentin [7] and will be used here.

THEORY

Geometrical Diffraction Theory. Diffraction of electromagnetic waves using the geometrical theory of optics was introduced by Keller [3] who used the concepts of diffracted rays produced at diffracting edges. These diffracted rays are proportional to the incident ray with a proportionality constant called diffraction coefficients, which are calculated by Keller [3] using a canonical solution which are asymptotic results for diffraction of a plane wave by an edge of a semi-infinite plane for the region $ka \gg 1$ where $k = 2\pi/\lambda$, λ is the wavelength, and a is a dimension of the crack. The basic concept of elastodynamic ray theory was presented by Karal and Keller [8] by introducing longitudinal and transverse rays. Adler et al used Maue's [9] solution as the canonical problem for the elastic wave diffraction from a semi-infinite crack to obtain expressions for the diffracted field from a penny-shaped crack. The three-dimensional ray theory for diffraction by cracks has been discussed in detail by Achenbach et al. [5]. They obtain an expression for a normally incident longitudinal wave diffracted from a penny-shaped crack in solid as

$$U_L = \exp(i\omega S/C_L)(\omega S/C_L)^{-1/2}(1 + S/C)^{-1/2}\, D_L^2(\theta)\, i_L\, U_o \qquad (1)$$

where S is the distance along the diffracted ray from the diffracting edge to the point of observation. C_L is the longitudinal velocity; θ is the angle of diffraction; U_o is the amplitude of the

incident wave and C is the distance to the caustic,

$$C = -a/\cos\theta \qquad (2)$$

where a is the radius of the penny-shaped crack; i_L defines the direction of displacement; D is the diffraction coefficient given in terms of longitudinal transverse and Rayleigh velocities and the diffraction angle (exact expression is given in Ref. 5).

It has been pointed out by Adler and Whaley [10] that the first arriving signal once gated out produces a frequency spectrum which is the result of the interference of the two diffracted rays from the two crack tips. Using this concept Achenbach et al [5] derive an expression by adding the two primary diffracted longitudinal fields from points O_2 and O_1 of the crack edges (Fig. 1)

$$U_L = F(\theta,\theta_o)\exp[i\omega(S/C_L + \bar{S}/C_F) + i\pi/4]\, U_o\, i_F \qquad (3)$$

where

$$F(\theta,\theta_o) = H_1 \exp[-i(\omega a/C_L)(\cos\theta - \sin\theta_o)] + H_2 \exp[i(\omega a/C_L)(\cos\theta - \sin\theta_o)] \qquad (4)$$

and C_F is the sound velocity in the liquid, where H_1 and H_2 are calculated in terms of parameters of the liquid and solid and the diffraction coefficient (for detail see Ref. 5) of particular interest is the absolute magnitude of F

$$|F| = \{(H_1)^2 + (H_2)^2 + 2(H_1)(H_2)\sin[2(\omega a/C_L) + (\cos\theta - \sin\theta_o)]\}^{1/2}. \qquad (5)$$

This result implies that the amplitude of the primary diffracted field is modulated with respect to ω/C_L with period

$$P = \pi/a|\cos\theta - \sin\theta_o|. \qquad (6)$$

Equation (6) is then used to determine the size and orientation of the crack. At two different values of θ, i.e., at two observation points, θ_o and a may be evaluated from the modulation in the frequency domain.

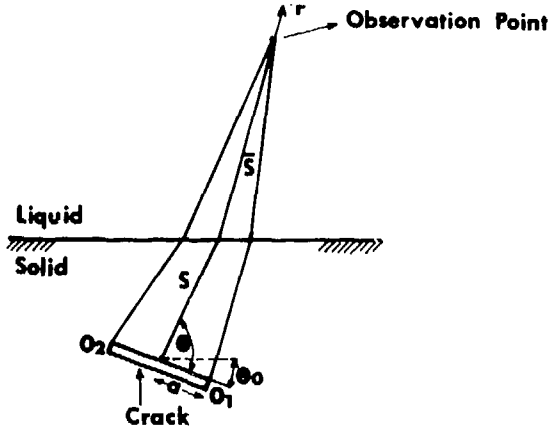

Fig. 1 Diffracted rays from a crack in solid.

Ultrasonic Wave Scattering from Large Randomly Rough Surfaces. The problem of ultrasonic wave scattering from cracks with rough surface has no solution at the present time. The scattering of EM waves from infinitely large random rough surfaces has been treated in detail however by Beckmann and Spizzichino [11], for example. The acoustic wave scattering from large random rough surfaces has also been studied extensively, for example [12]. Consider an incident ultrasonic wave scattered from a random rough surface (Fig. 2).

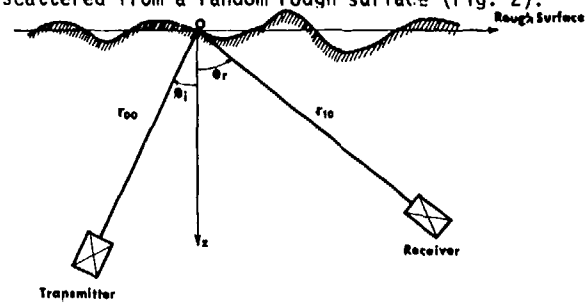

Fig. 2 Geometry of scattering from random rough surfaces.

It is customary to write the total scattered intensity average in two terms: the coherent and the incoherent terms:

$$\langle I\rangle = \langle I\rangle_{coh} + \langle I\rangle_{incoh} \qquad (7)$$

$$\langle I\rangle_{coh} = e^{-g} I_o \qquad (8)$$

$g = k^2h^2(\cos\theta_i + \cos\theta_r)^2$ is the so-called Rayleigh parameter and I_o is the intensity scattered by a perfectly plane surface.

The incoherent part of the scattered intensity is given as

$$\langle I\rangle_{incoh} = \pi A\left(\frac{k}{2\pi\, r_{00}r_{10}}\right)^2 |R(\theta_i,\theta_r)F(\theta_i,\theta_r)|^2\, e^{-g} \times \sum_{m=1}^{\infty}\frac{g^m}{m!}\exp[-k^2b^2L^2/4m] \qquad (9)$$

where

$$A = \frac{\pi\alpha\beta}{4\cdot 3(\log_{10}\ell)}$$ the insonified area

r_{00} is the distance between the source and the origin of the coordinate system, r_{10} is the distance between the receiver and the origin of the coordinate system, $R(\theta_i,\theta_r)$ is the reflection coefficient.

$$F(\theta_i,\theta_r) = \frac{1+\cos(\theta_i+\theta_r)}{\cos\theta_i + \cos\theta_r}$$

L is the correlation length

$$b = \sin\theta_i - \sin\theta_r$$
$$\alpha = r_{00}\tan(\tfrac{\phi}{2})/\cos\theta_i$$
$$\beta = r_{00}\tan(\phi/2)$$

ϕ is the angle of beam spread at 3 dB. Equations (8) and (9) are valid under the following approximations:

1. Only single scattering is considered.
2. Fraunhofer approximation is used. The expression is valid in the far field only.
3. Probability distribution function describing surface roughness is Gaussian in the form:

$$W(\zeta) = \frac{1}{(2\pi h^2)^{1/2}} e^{-\frac{\zeta^2}{2h^2}} .$$

The important parameters describing surface roughness are: the rms roughness h, the correlation length L, and the distribution function W. If the distribution function is a Gaussian, the low frequency approximation of the scattered field will give h while the high frequency approximation can be used to evaluate L.

Ultrasonic Scattering from a Crack with Rough Surface. For a finite rough surface such as a penny-shaped crack in titanium there is no theory available at present and we have used the following approach to evaluate the parameters describing surface conditions.

Calculation of the rms roughness h. By using low frequency approximation at backscattering it can be shown that the dominating term in Eq. (9) is the first term, i.e., all scattering in this case from the surface is coherent [11]. In this case:

$$\langle I \rangle_{total} \simeq e^{-4k^2h^2} \cdot I_o \qquad (10)$$

since $(\cos\theta_i + \cos\theta_r)^2 = 4$ for backscattering, at normal incidence where I_o is the intensity scattered from a smooth surfaced crack of the same size as the surface with rms roughness h. If h is much smaller than the radius of the crack, it may be assumed that the diffraction effect from the crack edge for both rough and smooth surfaced crack of the same size is the same. The low frequency approximation is valid for

$$4k^2h^2 \leq 1 . \qquad (11)$$

If $h \simeq 100\mu$, this condition implies frequencies below 5 MHz.

Calculation of the correlation length L. The correlation length L can be obtained from the total ultrasonic scattered field in the high frequency regime.

The first term in Eq. (7) goes to zero and the total scattered field is due to incoherent scattering only. For normal incidence we obtain:

$$\langle I \rangle \simeq \frac{A}{16\pi r_{00}^4 r_{10}^2} \cdot \frac{L^2}{h^2} \qquad (12)$$

(for backscattering pulse-echo $r_{00} = r_{10}$) using:

$$I_o = \frac{A^2k^2}{\pi^2 r_{00}^2} \qquad (13)$$

we obtain:

$$\frac{\langle I \rangle}{I_o} = \frac{L^2}{16h^2k^2A} \qquad (14)$$

and since the insonified area is the surface of the crack πa^2, we obtain for the correlation length:

$$L = 4hka\sqrt{\frac{\langle I \rangle}{I_o}} . \qquad (15)$$

Determination of the probability density function W. The average ultrasonic amplitude scattered from a rough surface is given as

$$\langle P_S \rangle = P_o \langle e^{-2ik\zeta} \rangle \qquad (16)$$

(see Ref. 11) where P_o is the scattered amplitude from an equivalent smooth surface. $\langle e^{-2ik\zeta} \rangle$ is the mean of the function $e^{-2ik\zeta}$ over the rough surface. Let $W(\zeta)$ be the probability density function of the heights then

$$\langle e^{-2ik\zeta} \rangle = \int_{-\infty}^{+\infty} W(\zeta) e^{-2ik\zeta} \, d\zeta \qquad (17)$$

it appears that $\langle e^{-2ik\zeta} \rangle$ is the Fourier transform of the probability density function $W(\zeta)$ at frequency 2k. The function $\langle e^{-2ik\zeta} \rangle$ is called the characteristic function of the height; when $W(\zeta)$ is Gaussian in the form of

$\frac{1}{(2\pi h^2)^{1/2}} e^{-\frac{\zeta^2}{2h^2}}$ from (12) we obtain:

$$\langle e^{-2ik\zeta} \rangle = e^{-2k^2h^2} . \qquad (18)$$

For any arbitrary probability distribution the characteristic function may be expanded assuming low frequencies to give:

$$\langle e^{-2ik\zeta} \rangle = 1 - 2k^2h^2 + \frac{4}{3} ik^3m_3 + \frac{2}{3} k^4m_4 + \ldots \qquad (19)$$

where

$$m_3 = \int_{-\infty}^{+\infty} \zeta^3 W(\zeta) d\zeta \qquad (20)$$

is the 3rd moment and

$$m_4 = \int_{-\infty}^{+\infty} \zeta^4 W(\zeta) d\zeta$$

is the 4th moment. For a Gaussian distribution $m = 0$ and $m_4 = 3h^4$.

Now let us put $t = \frac{2\zeta}{C}$ for backscattering, then from Eq. (16)

$$\frac{P_S}{P_0} = \langle e^{-2ik\zeta} \rangle = \langle e^{-ik\,t} \rangle = \langle e^{-i\omega t} \rangle \qquad (22)$$

$$\frac{P_S}{P_0} = \frac{C}{2} \int_{-\infty}^{+\infty} W(\tfrac{Ct}{2}) e^{-i\omega t} \, dt = F(\omega) \qquad (23)$$

and the probability density function may be given as

$$W(\tfrac{Ct}{2}) = \frac{2}{C} f(t) = \frac{2}{C} \int_{-\infty}^{+\infty} F(\omega) \, e^{i\omega t} \, d\omega \qquad (24)$$

where f(t) is the inverse Fourier transform of $F(\omega)$, i.e., the probability density function of the surface roughness is proportional to the inverse Fourier transform of the deconvolved (by the equivalent smooth surface) spectrum. In addition to $W(\zeta)$ the following parameters can be calculated also from the time domain deconvolution

$$\langle \zeta \rangle = \int_{-\infty}^{+\infty} \zeta W(\zeta) d\zeta = \text{mean} \qquad (25)$$

$$\langle (\zeta - \bar{\zeta})^2 \rangle = \int_{-\infty}^{+\infty} (\zeta - \bar{\zeta})^2 W(\zeta) d\zeta = h^2 \qquad (26)$$

$$\frac{\langle (\zeta - \bar{\zeta})^3 \rangle}{h^3} = \frac{m_3}{H^3} \quad \text{is the skewness} \qquad (27)$$

$$\frac{\langle (\zeta - \bar{\zeta})^4 \rangle}{h^4} = \frac{m_4}{h^4} \quad \text{is the kurtosis} \qquad (28)$$

higher order moments may also be calculated in the same fashion.

EXPERIMENT

Sample. Penny-shaped crack with smooth surface and radius 1.5 mm has been machined into a Ti-6Al-4V disk of 1.25 cm height and 10.2 cm diameter. The penny-shaped crack with a random rough surface of radius 1.5 mm was formed from a fracture specimen. The specimen has been fatigue tested in room temperature dry air at 20 Hz with a load ratio R of .5. The other half of the fracture specimen is shown on Fig. 3. From the fracture specimen a

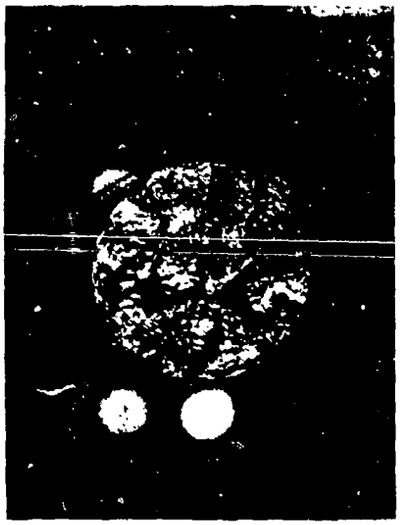

Fig. 3 Photograph of the penny-shaped crack with random rough surface.

cylindrical plug was machined. The end of the plug forms the penny-shape crack with the rough surface. The plug was then driven through the center of 1.25 cm thick and 10.2 cm diameter Ti-6Al-4V disk. The two disks were then diffusion bonded together. On Fig. 4 the two disks are shown before the diffusion process and Fig. 5 shows a photograph of the fracture surface used and Fig. 6 the diffusion bonded sample. A schematic of the defect (one side is smooth and the other side is rough) is shown on Fig. 7.

Experimental Systems for Ultrasonic Scattering. Two basic techniques were used to investigate experimentally the scattering from rough cracks. In both cases the sample is immersed in water and there is a 15 cm water column between the transducers and sample.

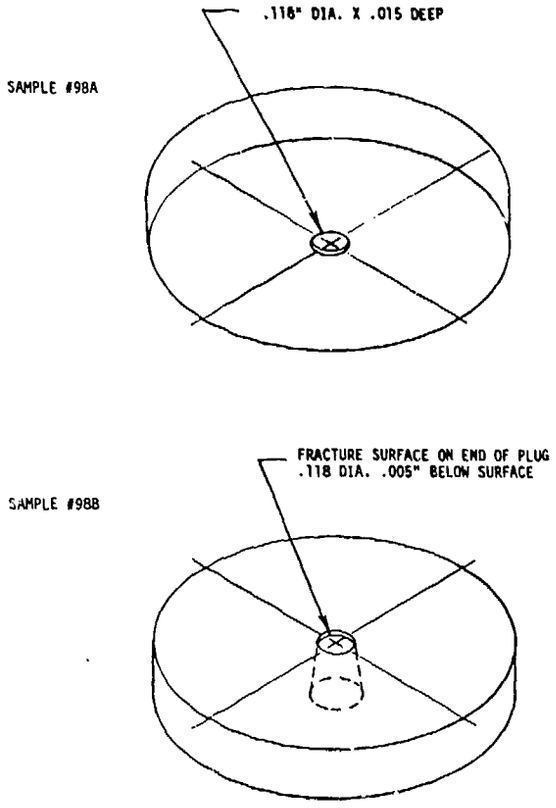

Fig. 4 Schematics of the titanium samples with smooth and rough "cracks" before diffusion bonding.

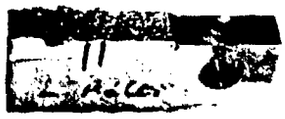

Fig. 5 Photograph of the other half of the fractured specimen which was used for the rough crack.

Fig. 6 Diffusion bonded titanium disk.

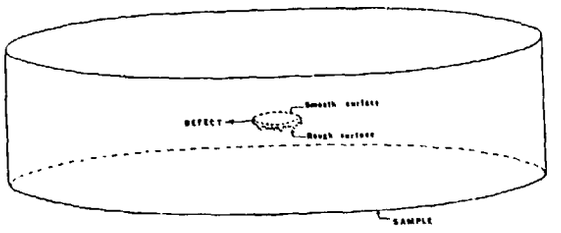

Fig. 7 Schematic of the defect inside the titanium disk.

Ultrasonic spectroscopy. The first experimental setup is a digitized spectrum analysis system described in detail in Ref. 5. It uses a broad band transducer as a source and sites the same or a second identical transducer as a receiver. From the received signal the digitized amplitude and phase spectrum may be obtained. The frequency range of the input signal is from 1 to 16 MHz. This spectrum analysis system is used to determine both geometrical and surface characteristics of the crack.

Narrow band system. The second experimental setup uses a conventional single frequency pulse echo system. The ultrasonic pulse is generated by an Arenberg pulser. The pulses of ultrasound have a 1.5 μsec duration with center frequency ranging from 3 to MHz. The transducers used were commercial narrow band ceramic transducers. The system can be used fully automated (see Ref. 7) with a programmable attenuator and for variable backscattered angles. In this experiment only the normal incidence pulse echo mode was used. From this experiment characteristics of the surface of the crack are obtained.

Direct Measurements of Surface Properties. The parameters describing the surface roughness of the fractured surface (see Fig. 5) were evaluated from the direct measurement of the complementary surface by the use of a conventional profilometer.

Procedure to Determine Size, Shape, and Orientation of Smooth and Rough Cracks. The transmitter launches a longitudinal wave in water for non-normal incidence to the liquid solid surface. Both L and T (longitudinal transverse) waves are produced but only the L wave is used to insonify the crack. At the crack the L wave again produces both L and T waves but these waves are separated due to their separation in time. The receiver is placed in positions to obtain the scattered waves at various polar and azimuthal angles. A specially designed goniometer is used to mount the transmitter and receiver (Fig. 8). The special feature of the goniometer is its flexibility of keeping the polar angle fixed and varying the azimuthal angle. The procedure to obtain amplitude spectra from both smooth and rough cracks were the same. For normal and various angles of incidence both pulse-echo and pitch-catch methods were applied.

RESULTS

Geometrical Parameters. A 45° pulse-echo spectrum of scattered L wave from the smooth crack is shown on Fig. 9 indicating the amplitude modulation predicted by Eq. (6). The modulation frequency remains constant by varying the azimuthal angle for a constant polar angle. This observation indicates the circular symmetry of the crack. Equation (6) is used to obtain for the radius 1.55 mm. The actual radius of the crack is 1.5 mm. The orientation of the crack is also obtained to be $\theta_o = 0$, i.e., the surface of the crack is parallel with the surface of the sample. The spectrum from the rough crack (the crack from the fracture surface) is shown on Fig. 10.

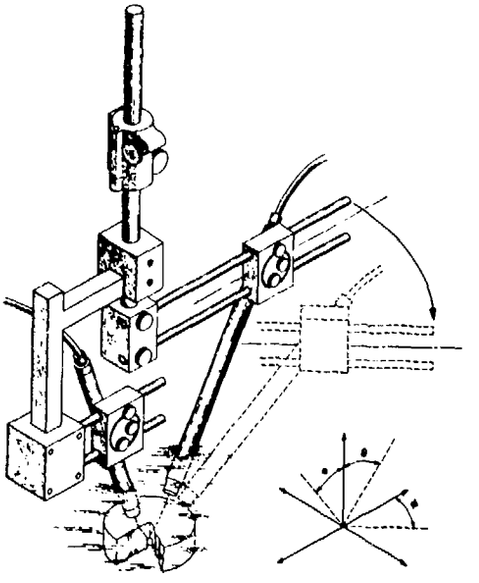

Fig. 8 Goniometer for scattering measurements.

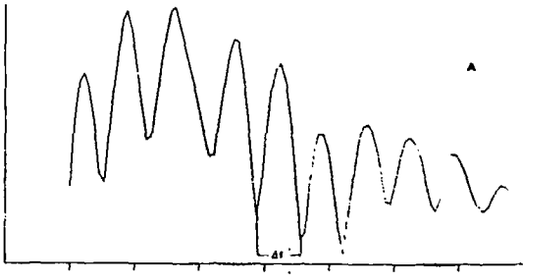

Fig. 9. 45° Pulse-echo spectrum from the smooth crack.

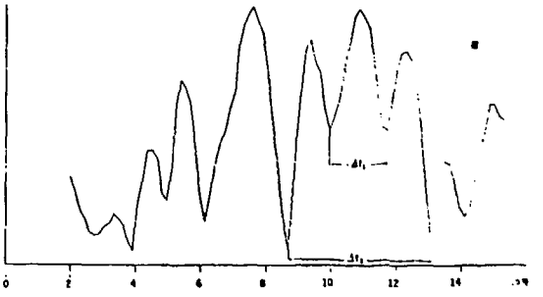

Fig. 10. 55° Pulse-echo spectrum from the rough crack.

Here the 55° (pulse-echo) scattered L wave spectra is shown (Fig. 10). It appears that at least two sets of periodicity of modulation can be identified. From Δf_1 the radius of the rough crack calculated is 1.53 mm using Eq. (6) (actual value is 1.5 mm). The second periodicity Δf_2 may be the result of the nonflat surface.

Identification of the Rough Surface. As was mentioned before, the titanium sample (labelled 98) contains essentially two defects of the same size, shape, and orientation but different surface conditions, one having a mirror-like smooth surface the other one a random rough surface. From ultrasonic scattering data the two surfaces were identified by two independent means.

1. Backscattered pulse-echo spectra are shown on Fig. 11 which were taken at normal incidence from both sides of the defect. As expected, the smooth surface defect would reflect more energy for all frequencies than the rough one. The spectrum with the solid line on Fig. 10 corresponds to the reflected signal from the smooth surface crack.

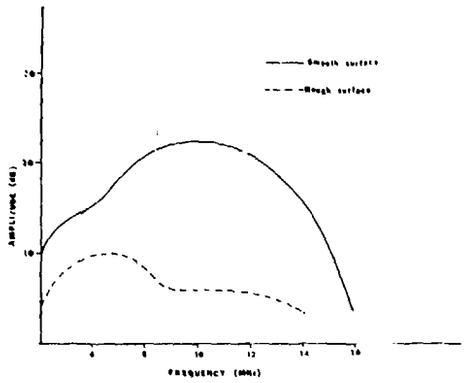

Fig. 11. Backscattered normal incidence spectrum from the smooth and rough crack.

2. The angular dependence of the scattered energy from rough and smooth surface cracks should behave differently. On Fig. 12 the integrated power (for all frequencies) scattered from rough and smooth surfaced defects is compared from 25° to 60°. The variation of the scattered power with angle is much more drastic for the smooth surface (~20 dB) than for the rough surface (~10 dB).

It may be mentioned that the sample on Fig. 6 was mislabeled. The side of rough surface defect was marked as smooth. The ultrasonic experiment results such as Figs. 10 and 11 led us to discover this mistake. Upon re-examination of the sample the surfaces were etched and the error of mislabeling was confirmed. Hence 98A is the rough surface crack and 98B is the smooth surface crack.

Determination of Surface Parameters: rms, Roughness, Correlation Length, Distribution Function.

Direct measurement. A conventional manual profilometer was used to sample the fracture surface of the fatigued specimen (Fig. 5). In the region within the two marked lines (corresponding to the defect's surface) 312 data points were taken at every 20 μm in two perpendicular directions starting in the middle. Result: On Fig. 13, the histogram of the surface is plotted from -230 μm to +230 μm (taking the measurements perpendicular to the surface). N corresponds to the number of points corresponding to the height at (x,y). The solid line is a Gaussian distribution having the same variance as the histogram.

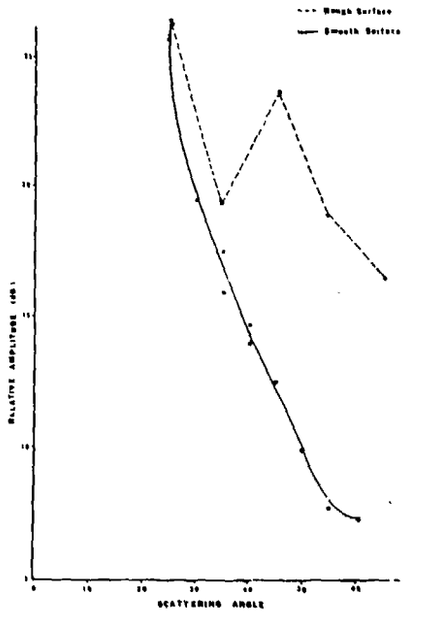

Fig. 12 Angular variation of the integrated power scattered from smooth and rough cracks.

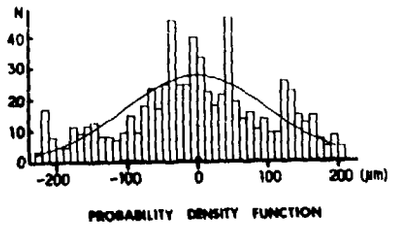

Fig. 13 Histogram of the rough surface.

The rms roughness h is calculated from

$$h = \frac{1}{N-1}\left[\sum_{i=1}^{N}(\zeta_i)^2\right]^{1/2} \qquad (29)$$

where ζ_i is the height at point x,y, and we obtain from Eq. (29) for h = 101 μm. The spatial autocorrelation function is plotted on Fig. 14. The spatial autocorrelation function for N measurement is given as:

$$C_n = \frac{1}{N-n-1}\sum_{i=1}^{N-n}\zeta_i(X)\,\zeta_i(X + m\Delta X) \qquad (30)$$

where n = 0, 1 ... m, m not larger than $\frac{N}{3}$. In this measurement n = 312 and m = 40; X = 20 μm. The two sets of autocorrelation functions (represented by the open circles and by the closed circles) are

results of roughness measurements in two perpendicular directions and indicate anisotropy in the surface roughness. The average value of the spatial correlation function is plotted by the solid line. The autocorrelation length L is defined as the distance measured at the point where the autocorrelation function is 1/e, the value at n = 0 divided by e. The values of the correlation lengths are 450 and 750, respectively, giving an average of 600 m for the autocorrelation length. The skewness and kurtosis are other parameters which characterize the shift and flatness which distinguishes the distribution from a normal Gaussian distribution calculated to give values of -.17 and 2.5, respectively. Recall that for a Gaussian distribution function these values should be 0 and 3, respectively.

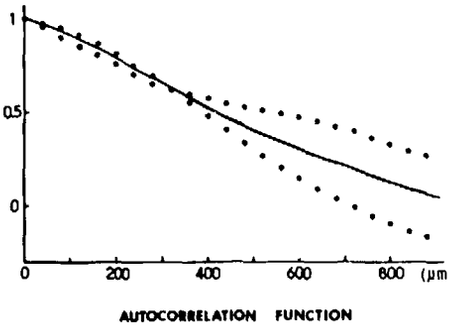

Fig. 14 Spatial autocorrelation function.

Ultrasonic scattering result. The rms roughness h and the autocorrelation length L are calculated from the narrow band experimental result. The probability density function w(ζ), the skewness and kurtosis are obtained from spectroscopy measurements.

1. Result of narrow band measurements. At normal incidence (to the defect surface) the backscattered amplitude differences were measured in dB with a calibrated attenuator. The ratio of the backscattered amplitudes from rough to smooth surface is designated by $\sigma_{r,s}$ and plotted for various frequencies from 3.5 MHz to 18 MHz on Fig. 15. The

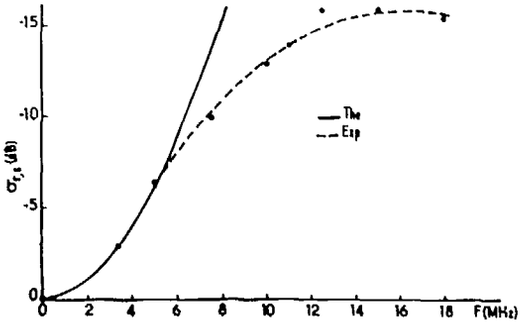

Fig. 15 The variation of the backscattered ultrasonic power (in dB normalized for the equivalent smooth surface) from the rough crack as a function of frequency.

experimental points are connected together with the dashed line. The solid line is a theoretical curve calculated using low frequency approximation (Eq. 10). The theoretical curve fits very well up to 5 MHz (corresponds to kh = .5). The values for h are 117 μm and 121 μm calculated at 3.5 MHz and 5 MHz, respectively. The autocorrelation length L is calculated from the curve at a frequency where the curve levels off to a straight line using Eq. 15 at .2 MHz the correlation length is 650 μm which agrees very well with the value calculated from the autocorrelation function from Fig. 14.

2. Results from ultrasonic spectroscopy. Using a broadband backscattered signal at normal incidence, the RF waveforms and their correspondent spectra are shown on Fig. 16. 98B designates the defect with smooth surface, and 98A designates the defect with rough surface, both time and frequency domain signals are significantly different for 98A and 98B. In the time domain the signal from the rough surface has much lower maximum amplitude than the signal from the smooth surface. In addition there are some details in the front and trail of the signal which is different from the two surfaces. The frequency domain deconvolution is shown in Fig. 17. The normalized intensity spectrum and phase spectrum are shown which were obtained by deconvolving the rough surface data with the smooth surface data. After transforming Fig. 17 to the time domain, the probability density function is obtained versus both time and distance on Fig. 18. The distribution is not quite Gaussian. The deviation from Gaussian is expressed in terms of the higher order movements. From Fig. 18 the following parameters describing the rough surface of the defect 98A were obtained:

h = 131 m
skewness = -0.29
kurtosis = 2.67
5th moment = -1.08
6th moment = 9.64
7th moment = -4.18

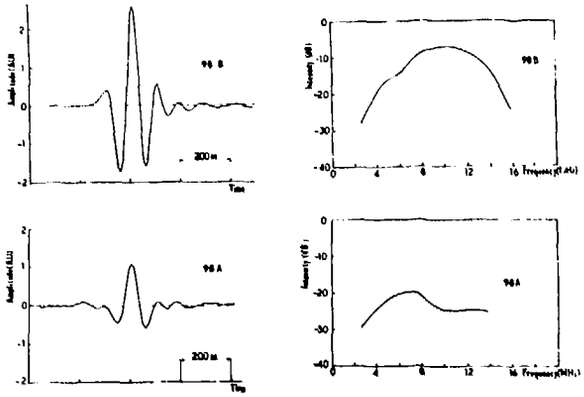

Fig. 16 RF waveforms and their frequency spectra and backscattered waves from smooth and rough cracks.

Using the values of the moments and the low frequency expansion for the characteristic function, the complex amplitude spectrum can be calculated. The result is shown on Fig. 19. The solid line is the experimental amplitude spectrum calculated using moments up to 7th. The dashed line indicates what the spectrum should be if the probability density function of the defect surfaces were a Gaussian. The phase spectra of the experimental

results using the low frequency expansion is given on Fig. 20.

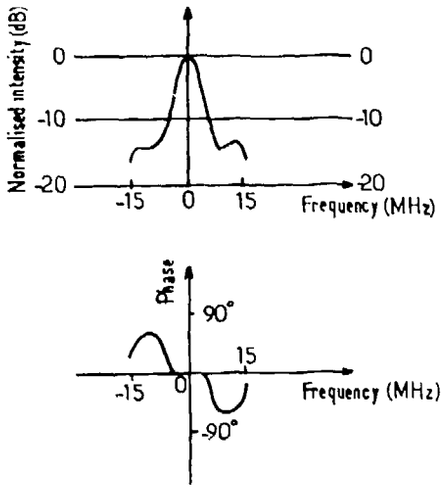

Fig. 17 Frequency domain deconvolution.

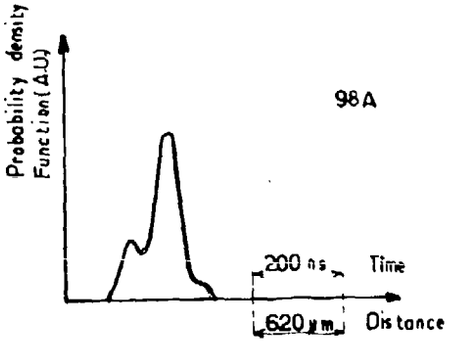

Fig. 18 Time domain deconvolution which gives the probability density function of the surface roughness for the crack.

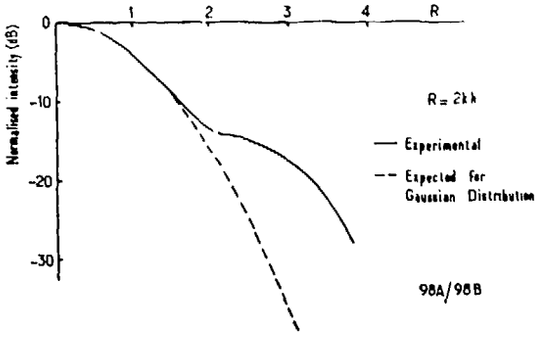

Fig. 19 Calculated theoretical amplitude spectrum for the scattered wave from the rough crack.

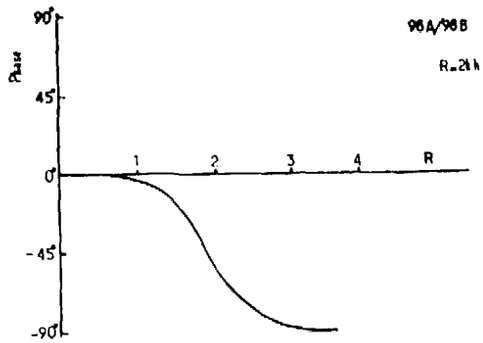

Fig. 20 Calculated theoretical phase spectrum for the scattered wave from the rough crack.

SUMMARY

The problem of characterizing naturally occurring flaws such as a flaw with random rough surface has been considered. The flaw is a penny-shaped crack in diffusion bonded titanium; one side of the crack is polished, the other side is made from a fractured surface. The dimension of the crack is larger than the wave length of the propagating ultrasonic waves, i.e., the region of $ka > 1$ is considered. The rms surface roughness h is smaller than a but k may be smaller or larger than h. In the theoretical analysis an elasto-dynamic diffraction theory, valid only for smooth surfaces, is presented to relate the angular and frequency dependence of the scattered amplitude to the size, shape, and orientation of the crack. On the other hand, the rough surface problem is analyzed based on an electromagnetic scattering theory which is valid for scattering from large surfaces only. By comparing the backscattered amplitude from a rough crack to the backscattered amplitude from a crack with the same area but with smooth surface it is assumed that the diffraction effect (from the edge crack) is separated from the surface roughness effect.

Using ultrasonic scattering measurements based on ultrasonic spectroscopy technique and narrow band technique, the following parameters of the rough crack were determined: size, shape, orientation, rms roughness of the surface, auto-correlation length of the roughness, and the probability density function of the surface roughness. There is good agreement between the experimentally determined parameters of the crack and their actual values. It is hoped that theoretical analysis to treat scattering from rough surface crack using elastodynamics will be developed in the near future to aid real flaw characterization with ultrasonic scattering.

ACKNOWLEDGMENT

This work was supported jointly by the French CNRS and by the Center for Advanced NDE operated by the Science Center, Rockwell International, for ARPA and AFML under contract No. F33615-80-C-5004.

REFERENCES

1. Laszlo Adler and D. Kent Lewis, IEEE Transactions on Sonics and Ultrasonics, SU-23, 5, 351 (1976).

2. D. Kent Lewis, Peter Szilas, Dale Fitting, and Laszlo Adler, J. Acoust. Soc. Am. 63, 575 (1978).

3. J. B. Keller, J. Appl. Phys. 28, 426 (1957).

4. J. D. Achenbach and A. K. Gautesen, J. Acoust. Soc. Am. 61, 413 (1977).

5. J. D. Achenbach, Laszlo Adler, D. Kent Lewis, and H. McMaken, J. Acoust. Soc. Am. 66, 1848 (1979).

6. Laszlo Adler and J. D. Achenbach, accepted for publication in Journal of Nondestructive Evaluation.

7. M. de Billy, F. Cohen-Tenoudji, A. Jungman, and G. J. Quentin, IEEE Transactions on Sonics and Ultrasonics, SU-23, 5, 356 (1976).

8. F. C. Karal and J. B. Keller, J. Acoust. Soc. Am. 31, 644 (1959).

9. A. W. Maue, Z. Ang. Math. and Mech. 33, 1 (1953).

10. Laszlo Adler and H. L. Whaley, J. Acoust. Soc. Am. 51, 881 (1972).

11. P. Beckmann and A. Spizzichino, The Scattering of Electromagnetic Waves from Rough Surfaces, Pergamon Press, 1963.

12. P. F. Welton, J. Acoust. Soc. Am. 54, 66 (1973).

Bernie Tittmann,Chairman (Science Center): I think we have time for one question.

Unidentified Speaker: Laszlo, that theoretical formula is for a single scattering. And being an acoustic representation, it does not include the response of surface waves?

Laszlo Adler (Ohio State University): That is true.

Unidentified Speaker: It seems to me good agreement that neither of the effects are very significant.

Laszlo Adler: I think it is good agreement and definitely there are many areas.

Bernie Tittmann, Chairman: Thank you Laszlo. Would you like to go on to your next paper now?

ELASTIC WAVES SCATTERING FROM CORRUGATED METAL INTERFACES

A. Jungman and G. Quentin
Groupe de Physique des Solides, Université Paris 7
75221 Paris Cedex 05, France

Laszlo Adler
Groupe de Physique des Solides, Université Paris 7
75221 Paris Cedex 05, France
and
Department of Physics, University of Tennessee
Knoxville, TN 37916

ABSTRACT

This is a study of elastic waves diffracted by corrugated metallic surfaces. The corrugations consist of triangular grooves with variable parameters. The results of the narrow band experiments show significant diffraction patterns depending on angle and frequency. In addition, a continuous schlieren system is used to visualize the diffracted orders. Measurements were also carried out using a broadband pulse echo system. The behavior of the received spectra is characteristic of the surface profile. Both front and back surfaces have been investigated.

INTRODUCTION

There is a considerable amount of interest in NDE to study elastic wave interaction with material discontinuities. There are numerous theoretical [1,2,3] and experimental works concentrated on the scattering of elastic waves from single scatterers such as cavities, cracks, etc., in the bulk [4,5] or on the surface [6,7] of materials. The study of elastic wave scattering from multiple structures is not so extensive, however. The scattering of waves from multiple structures, whether they are random or periodic, frequently occurs in materials as the result of grain structure, lamination, fiber reinforcing, multiple defects, surface preparation, etc. The elastic wave diffraction from periodic surfaces has been treated recently by Fokkema and van den Berg [8] but only numerical results are available and only for a few special cases. More extensive results are given for the scattering of electromagnetic waves from periodic and random surfaces by Bechmann and Spizzichino [9].

On the experimental side, ultrasonic wave scattering from periodic surfaces in water has been studied by Jungman et al [10] using ultrasonic spectroscopy. Using an optical model of a diffraction grating, the angular position of the various diffraction orders are related to the grating constant for a given frequency.

In this paper we are addressing the problem of elastic wave scattering from periodically corrugated structures from interfaces and from the bulk of the solid. The following periodic interfaces are considered: (a) solid-air; (b) solid-water; (c) water-solid; and (d) solid-solid. In audition, there are two corrugated structures considered in the bulk of the material: (a) the region of corrugation is much larger than the size of the beam; (b) the region of the corrugation is smaller than the beam size, e.g., a defect with a periodic surface.

DIFFRACTION BY PERIODIC ROUGH SURFACES

Theoretical Considerations. Elastic wave diffraction by a periodic rough surface has been discussed recently by Fokkema and P. M. van den Berg. By using equations of elastodynamics for linear isotropic solids they obtain numerical solutions for the representation integral for the case of sinusoidal periodicity. Incident longitudinal and transverse waves are considered. For a triangular shaped grating surface (which is used in this investigation) the same result is not available although the numerical analysis may be carried out in the same manner. Electromagnetic wave scattering from a triangular shaped grating has been solved using Kirchoff approximations [9]. The intensity of the mth diffracted order is expressed as:

$$I_m = F_2(\theta_i,\theta_d)\,\frac{S\sin(\frac{m\pi}{2}+S)}{(m\frac{\pi}{2})^2 - S^2} \qquad (1)$$

where

$$F_2(\theta_i,\theta_d)\ \sec\theta_i\ \frac{1+\cos(\theta_i+\theta_d)}{\cos(\theta_i+\theta_d)}\ ;$$

$$S = kh(\cos\theta_i + \cos\theta_d)\ ;$$

θ_i is the angle of incidence measured from normal θ_d is the angle of the diffraction of the mth order; h is the depth of the groove; and k is the wave number. The position of the different orders are obtained by the so-called grating equation derived by using phase-delay for the incident and diffracted ray, as

$$(\sin\theta_i + \sin\theta_d) = m\frac{\lambda}{\Lambda} \qquad (2)$$

where λ is the wave length and Λ is the periodicity, m = 0, ±1, ±2 .... m = 0 corresponds to specular reflection. For an incident L wave there may be diffracted L waves, diffracted S waves, and diffracted Rayleigh waves. This mode conversion is not treated by the electromagnetic analysis, and the experimental results (which will follow) can only be qualitatively analyzed.

Experimental Methods. In the study of elastic wave scattering from corrugated structures, three experimental arrangements are used: (1) optical schlieren system for water-solid interfaces; (2) a narrowband pulse-echo and pitch-catch experiment for water-solid and solid-water interfaces; and (3) an ultrasonic spectroscopic system to analyze scattering from all the interfaces. This latter technique is the most relevant to this study.

Optical schlieren system. To visualize the beam pattern of the wave scattered from the corrugated surface a continuous wave schlieren system has been used. The system consists of a light source which is a helium-neon laser and a lens system with two large (30 cm diameter) lenses to obtain a large region to visualize the propagation of the ultrasonic beam. The direct light is blocked out by a small circular dot. For the ultrasonic source a high power CW oscillator excites a quartz transducer operated at resonant frequencies of 2, 4, 6, 10, and 12 MHz. The sample with the corrugated surface is placed in a water tank. Both incident and scattered ultrasonic waves are visualized simultaneously by the visual image which is displayed on a TV camera.

Single frequency experimental system. The experiments with narrowband pulses were carried out using a standard ultrasonic pulse arrangement. A quartz transducer and receiver are mounted on a goniometer (schematic diagram is shown on Fig. 1).

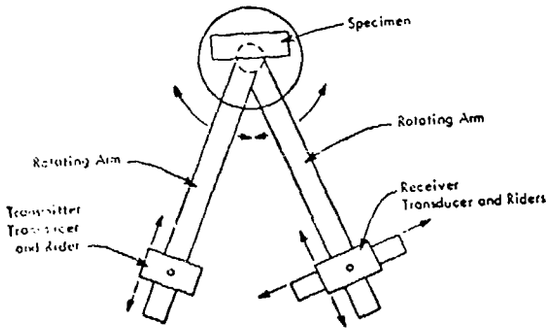

(bf

Fig. 1 Schematic of the goniometer for the scattering experiments.

The system is designed so that the face of the sample forms a vertical plane at the center of a circle formed by rotation of the two arms holding the two transducers. A Vernier scale on each arm permits the angular position of each arm to be read to two minutes of arc. Both arms have transducer holder stages mounted on riders that allowed the transducers to be moved up to 50 cm in a radial direction. In addition, the transducer on the receiver arm can be moved perpendicular to the arm. This way accurate positioning of the center of the scattered beam can be accomplished. The receiver arm can be rotated through almost a complete circle which allows measurement of both backward and forward scattering. The received signal is displayed on an oscilloscope and the amplitude of the received signal is measured off directly.

Ultrasonic spectroscopy. In addition to narrowband experiments, wideband experiments were carried out to study spectral components of the scattered field from corrugated surfaces. A wideband ceramic transducer (bandwidths up to 14 MHz may be obtained) emits a short RF pulse. The scattered signal (from the surface) is received either by the same transducer (pulse-echo) or by another wideband transducer (pitch-catch). The received signal is amplified and gated out in order to select the portion of the signal to be processed. The time domain signal can then be fed either to a conventional spectrum analyzer to obtain the frequency domain information (amplitude or power spectrum) or be sampled and converted to digital information and processed by calculation to obtain the spectrum via a fast Fourier transform. Figure 2 shows a block diagram of the spectroscopy system used.

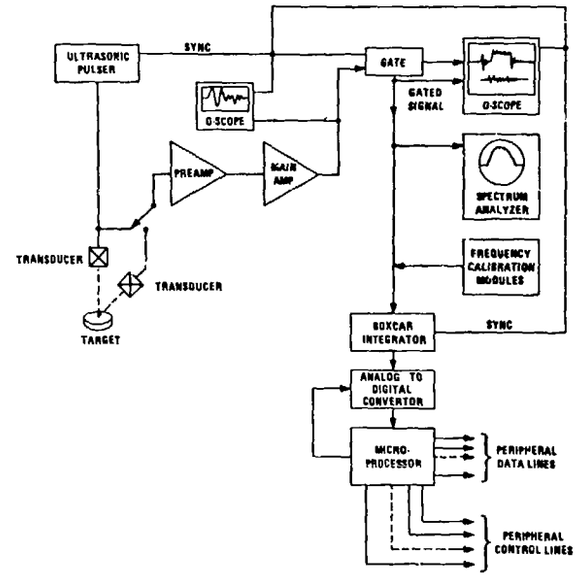

Fig. 2 Experimental system for ultrasonic spectroscopy.

A typical spectrum of a normally reflected signal from a perfectly smooth surface is shown on Fig. 3. This spectrum is used as a reference to that of the scattered spectrum from the periodically rough surface. The spectrum of the scattered wave is deconvolved by the reference spectrum. The samples are placed in a water tank and a goniometer system is used to orient the wideband transducer to the required position to control the direction of the incident and the scattered waves. A typical experimental arrangement is shown on Fig. 4. The transmitter is positioned (with an angle $\theta_i = 0$) relative to the corrugated surface which scatters the waves (reflects, diffracts, etc.) to the receiving transducer positioned at angle θ_d.

SAMPLES

Description of the Corrugated Surfaces. There are several parameters describing a periodic surface such as materials on both sides of the interface, boundary conditions, periodicity, depth and shape of the grating, the area of the grating surface,

etc. A number of different types of samples have been chosen in this experiment to study the effects of these parameters on the scattered field. For all samples a triangular shaped grating was used. The periodicity of the grating varied from 100μ to 1732μ. The depth of grooves varied from 50μ to 500μ (kept constant for each grating surface). The materials used were: stainless steel, brass, duraluminum, polystyrene. Each of the grated surfaces are used under different conditions:

1. The corrugated surface faced the incident beam. This corresponds to water-solid interface.
2. The corrugated surface was on the opposite side as the incident beam which propagated through the solid. This is a solid-water interface.
3. The corrugated surface had an air backing and the beam travelled through the solid. This corresponds to solid-air interface.
4. The grated surface is pressed against a smooth surface in contact with the same solid material. This corresponds to the case of solid-solid interface.

Fig. 3 Power spectrum of the transducer output.

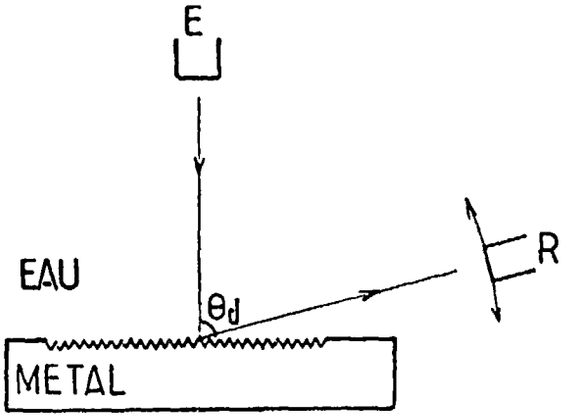

Fig. 4 Schematic of the scattering measurement from a water (eau in French)-metal corrugated interface.

Diffusion Bonded Titanium Samples. In addition there are two special types of corrugated surfaces used. These surfaces are inside the bulk of a titanium alloy. By a diffusion bonding process a corrugated titanium surface is bonded together with a smooth titanium surface. After the bonding the only surface is the corrugated surface. On Fig. 5 machined grooves [total surface 2.126 in (5.4 cm)] are shown on the polished titanium surface of 10.2 cm diameter, before the bonding process. The periodicity of the grating is 1.73 mm and the depth is .5 mm. A titanium disk of the same size with a polished smooth surface is diffusion bonded to produce the sample. Another type of sample is prepared the same way but the corrugated surface was confined in a penny-shaped region of 5 mm, prepared on the end of a titanium plug and driven in through a hole to the large titanium disk. Figure 6 illustrates the surface side view. The corrugation has a periodicity of 300μ. To the corrugated surface which is shown on Fig. 6 is bonded a smooth polished surface titanium disk. In the bulk of the titanium, a so-called penny-shaped crack with a corrugated surface is obtained.

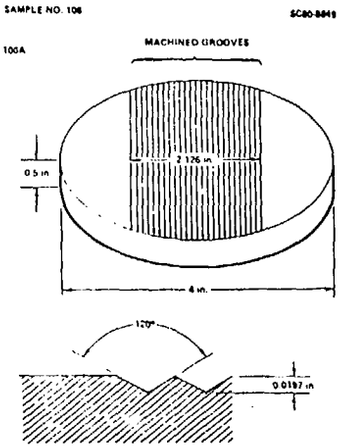

Fig. 5 Corrugated titanium surface before diffusion bonding.

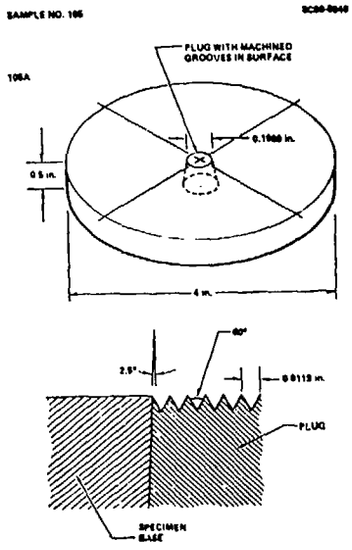

Fig. 6 Photograph of the penny-shaped crack (with periodic surface) in titanium before diffusion bonding.

RESULTS

Schlieren Visualization. Using single frequency quartz transducers for the incident wave, both incident and diffracted waves from the grating are visualized by the schlieren system. On Fig. 7 the transducer and a normally incident 12 MHz wave are shown as diffracted from a water-brass interface. On the surface of the brass is a periodic grating with periodicity of Λ = 200μ. The first two diffraction orders are shown on both sides of the incident beam (the zeroth order coincides with the incident beam for normal incidence). The angular position of the m = -2, -1, 1, 2 can be measured from the photographs as 30°, 30°, 76°, and 82°. The correspondent calculated values using Eq. 2 are 30°, 30°, 90°, 90°. There is some error in the result of the position for the second order, but the positions of the first orders are exactly the same for the experimental results as predicted by the grating equation. On Fig. 8 the diffraction pattern is for a 60° incident 4 MHz wave. The grating is on brass with periodicity of 200μ. On the left the zeroth order is shown (m = 0) which is the specular reflection. The measured position of the diffracted order to the right is 82° and the calculated position for m = -1 is also 82°.

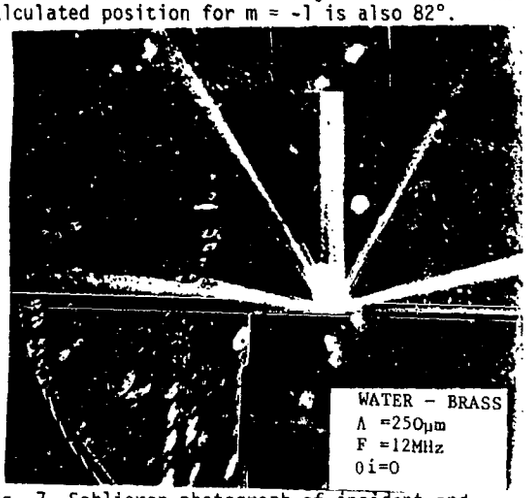

Fig. 7 Schlieren photograph of incident and diffracted ultrasonic waves from a periodic water-brass interface. f = 12 MHz; θ_i = 0°; Λ = 200μ.

Fig. 8 Schlieren photograph of incident and diffracted ultrasonic waves from a periodic water-brass interface. f = 4 MHz; θ_i = 69°; Λ = 200μ.

Single Frequency Results. For a normally incident 5MHz wave the diffraction pattern is shown on Fig. 9 which is measured by a receiver. The brass sample with the periodic surface was facing the incident beam (water-brass interface). The periodicity of the grating is 200μ. The zeroth order and the first diffracted orders are positioned according to the grating equation (Eq. 2). The calculated diffracted angle 49° agrees well with the measured value of 46°. The asymmetry in the diffraction pattern may be due to some discrepancies in the grating. Both forward and backward scattering from the same grating are shown on Fig. 10. The grated surface is opposite to the incident beam. The frequency is 14 MHz and the calculated angle for the first order is 32.7°. The measured angle is 34° for these orders.

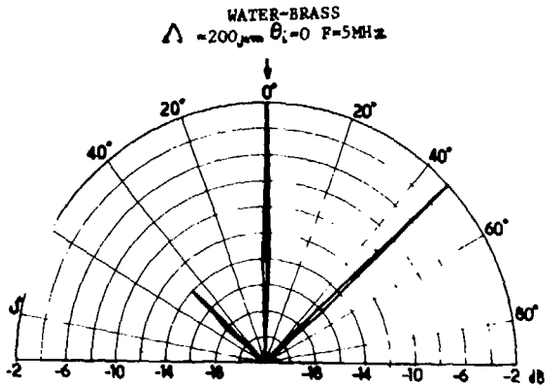

Fig. 9 Polar plot of an ultrasonic wave diffracted from a periodic brass-water interface.

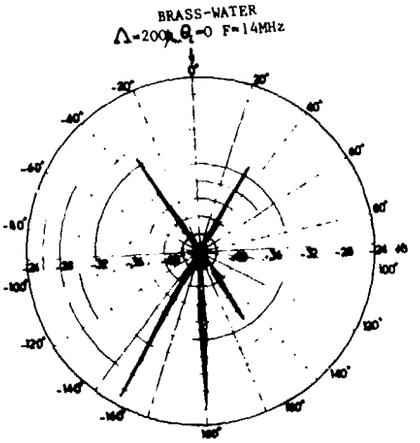

Fig. 10 Polar plot of an ultrasonic wave diffracted from a periodic brass-water interface.

Results of Ultrasonic Spectroscopy. In the narrowband experiments the relationship between the grating periodicity, the applied frequency, and the angles of incidence and diffraction may be found from Eq. 2. The grating equation (Eq. 2) may also be applied to a broadband signal provided the amplitudes of each frequency component are low enough so superposition is valid. Accordingly, at different angles of incidence the various frequencies will diffract to different angular positions as predicted by the grating equation. On the other hand, by placing the receiver in a

fixed position a certain frequency which satisfies Eq. 2 will diffract to that position. A special arrangement was investigated when the incident wave is normal to the grating and the transducer is used both as a transmitter and the receiver. In this case the zeroth diffraction order (specular reflection) is also perpendicular to the grating.

Water-Solid Interface. Observed Anomalies. On Fig. 11 the intensity spectrum of a normally incident reflected signal is shown from a grating with 200μ periodicity on brass. The brass is in water and the water column is about 15 cm to assure far field conditions. The most significant features of these spectra are the two distinct minima occurring at 7.8 MHz and at 10.8 MHz. The energy which is not reflected back at these frequencies to the receiver diffracted to some other position. (This phenomena is similar to the so-called Woods anomalies. Woods has observed missing components from the reflection spectrum of the light from a diffraction grating. This anomaly was treated by Lord Rayleigh [11] where he developed a dynamic theory of grating and found conditions that the missing frequency corresponds to a diffraction order directed along the grating angle (90°). By rewriting Eq. 2 for normal incidence we obtain for the frequency

$$f = \frac{v}{\Lambda \sin \theta_d} \qquad (3)$$

taking $m = 1$ and $\theta_d = 90°$, the calculated values for velocity v from the frequency 7.8 MHz is 1.56×10^5 cm/sec and from the frequency 10.8 MHz is 2.16×10^5 cm/sec. These values correspond to the velocity of sound in water (1.5×10^5 cm/sec) and to the Rayleigh velocity of brass (2.08×10^5 cm/sec). It appears that two waves are coupled along the surface, producing the first diffraction order along the grating at these frequencies: (1) a longitudinal wave in water and (2) a mode converted Rayleigh wave. Using such diffraction gratings as a device to convert longitudinal waves to surface waves has been suggested by Ash [12], and it is a convenient way to observe the spectrum such as shown on Fig. 11. The phenomenon

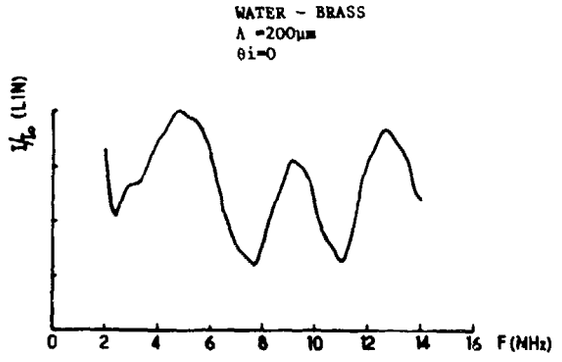

Fig. 11 Ultrasonic pulse-echo spectrum (for normal incidence) from a periodic water-brass interface. The "anomalies" at 7.8 MHz and 11.8 MHz are the diffracted first orders along the interface.

apparently depends on the depth of the grating. On Fig. 12 the pulse-echo spectra are shown from a water-brass interface. For each of the four cases the periodicity is Λ = 250μ, but the depth h has values of 55μ, 66μ, 90μ, and 125μ. The frequency minima which corresponds to first diffraction along the surface with the velocity of sound in water should be 6 MHz and with the Rayleigh velocity should be 8.3 MHz using Eq. 3. For

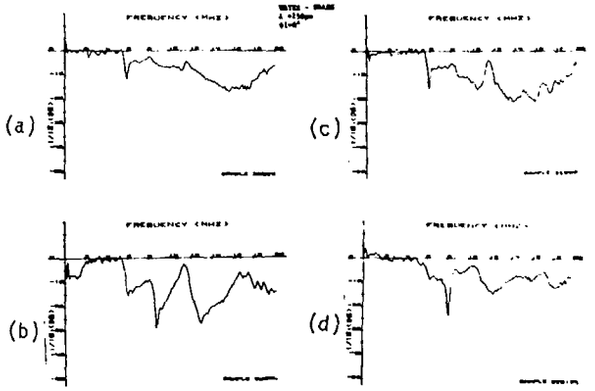

Fig. 12 Pulse-echo spectra (for nonnormal incidence) from a water-brass periodic interface of different h (depth of the groove. (a) h = 55μ; (b) h = 66μ; (c) h = 90μ; (d) h = 125μ.

h = 55μ there is a sharp minimum at 6 MHz and there is no mode conversion to Rayleigh waves. For h = 66μ there are three sharp minima at 6 MHz, at 8.5 MHz, and at 12.8 MHz. The last minimum corresponds to m = 2, the second diffraction order. At h = 90μ again only the 6 MHz minimum is observed and at h = 125μ only the 8 MHz. It appears that there is always some anomaly present. The amplitude of the zeroth order (m = 0) for the components whose first order (m = 1) is along the periodic surface varies with h (may be periodically). Such variation of the amplitude may be seen qualitatively from Eq. 1. By using $\theta_i = \theta_d = 0$ the intensity of the mth diffraction order goes to

$$I \simeq \frac{\sin \frac{4\pi h}{\Lambda}}{\frac{4\pi h}{\Lambda}} . \qquad (4)$$

This relationship, however, is not applicable to the elastic wave case for evaluating the effect quantitatively. Figure 13 shows these periodic behaviors of Eq. 4. There is a sharp minima at h = 66°μ and h = 125°μ.

The phenomena of frequency minima in the pulse-echo spectrum is observed also at other water-solid interfaces. Figure 14 shows the pulse-echo spectrum from water-stainless steel interface for grating of Λ = 1500μ and h = 500μ. The anomalies again show up at three different frequencies: at 1.1 MHz, 2.2 MHz, and 3.3 MHz, corresponding to three diffracted orders along the surface with water velocity and the 2.2 MHz component corresponds to the Rayleigh velocity m = 1 for Rayleigh wave and m = 2 for water (these two effects are separated once the grating has an air backing). The 3.3 MHz is the m = 3 order.

An interesting case is the water-polystyrene interface. Since the velocity of the shear wave in polystyrene is 1.15×10^5 cm/sec, which is less

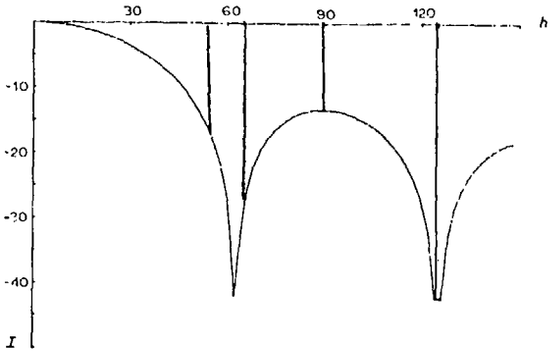

Fig. 13 Calculated variation of the intensity in the zeroth diffracted order from a water-brass interface as a function of grating depth h.

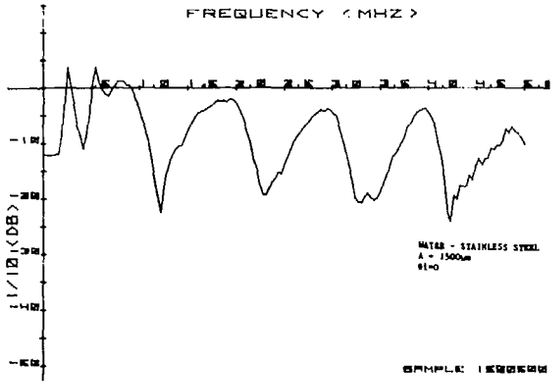

Fig. 14 Pulse-echo normal incidence spectrum from periodic water-stainless steel interface.

than the velocity of sound in water and no real Rayleigh angle exists to generate Rayleigh waves in water by the usual way, i.e., transmitting the beam at oblique incidence. With a grating surface, however, it is possible to generate Rayleigh waves on polystyrene (or on other materials where $v_s < v_{water}$). The backscattered spectrum at normal incidence is shown on Fig. 15 for a periodicity of 1 mm on polystyrene. The first minimum is at 1.05 MHz (the usable range of energy is from .5 MHz), corresponding to the first diffraction order along the surface with Rayleigh velocity, followed by minima corresponding to first order with velocity of sound in water and higher diffraction orders.

To observe the anomalies in the backscattered spectrum at normal incidence may be a convenient way to measure the velocities of various types along the surface. Table 1 summarizes the frequency minima observed in the backscattered spectrum—for different interfaces—together with the velocities of the identified waves and compared to predicted values.

Solid-Water Interface. The anomalies in the frequency spectrum have also been observed for the case when the grated surface was on the opposite side as the transducer. In this case the beam is diffracted at a solid-water interface from the periodic surface. The main feature of the backscattered spectrum at normal incidence is not the same as for the case of water-solid: frequency minimum (anomalies) observed corresponding to the diffracted orders along the surface with the Rayleigh wave of the solid only but no component with velocity of sound in water is observed (see Table 1).

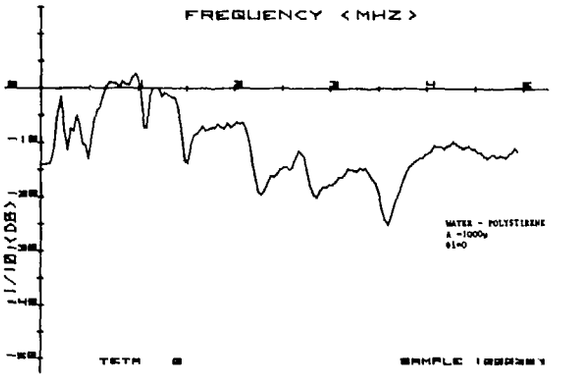

Fig. 15 Pulse-echo normal incidence spectrum from a water-polystyrene interface.

Solid Air Interface. By placing an air backing on the grating (sealing off the grated surface from water) the origin of the frequency minima in the backscattered spectrum is easier to identify. On Fig. 16 the backscattered spectra from the stainless steel-air surface with periodicity of 1500μ is shown. Comparing this to Fig. 14 where the grating is in contact with water, it is apparent that the frequency minimum at 1 MHz on Fig. 14 corresponds to a first diffraction order in water. The 2 MHz frequency minima on Fig. 14 is produced both by m = 2 with sound wave in water and m = 1 with Rayleigh wave at the stainless steel surface. On Fig. 16 in addition to that Rayleigh wave component at 2 MHz there is another minima at 2.8 MHz whose origin is not clear at this point.

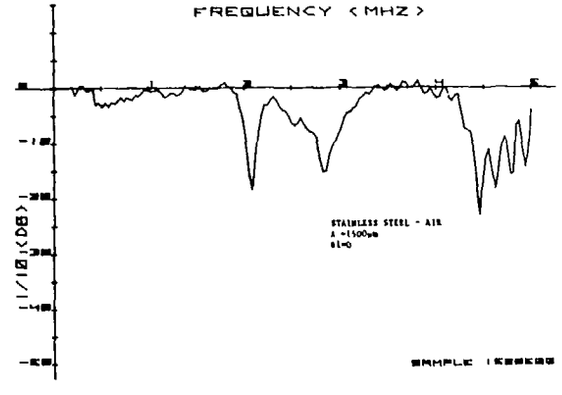

Fig. 16 Pulse-echo normal incidence spectrum from a periodic steel-air interface.

On Fig. 17 the backscattered spectrum from a duraluminum-air surface is shown for a periodicity of 1732μ. The observed minimum at 1.7 MHz corresponds to the Rayleigh wave velocity of the first diffracted order along the interface. By pressing a large smooth duraluminum surface against the grated surface of the one described above we obtained a solid-solid contact. The spectrum,

TABLE 1

ANOMALIES IN THE ULTRASONIC SPECTRUM SCATTERED FROM CORRUGATED INTERFACES

Material	Interface	Sample	Spatial Periodicity Λ (μm)	Peak-to-Valley Height H_{pv} (μm)	Frequency Minima (MHz)	Computed Rayleigh Velocity V_R^C (ms^{-1})	U.S. Estimate Rayleigh Velocity V_R^{US} (ms^{-1})	U.S. Estimate Velocity in Water (ms^{-1})	Other U.S. Measured Velocity (ms^{-1})
BRASS	WATER BRASS	B1	250	55	5.88 (1)	1979		1469	
		B2	250	66	5.99 (1) 8.71 12.78 (2)		2178	1497 1577	
		B3	250	90	5.88 (1) 8.50 10.52 12.16 (2)		2125	1469 1520	2628
		B4	250	125	6.26 (1) 6.09 12.27		2023	1559 1533	
		B5	200	76	7.67 10.95		2190	1534	
		B6	350	50	4.05 (1) 6.00 (1) 8.69 (2) 12.5 (2)		2099 2189	1418 1520	
	Br. Wt.	B4	250	125	8.22		2054		
		B5	200	76	10.50		2103		
	Br. Air	B2	250	66	8.19		2046		
		B5	200	76	10.77		2154		
DURAL	Dural Air	D7	1732	500	0.73 1.73 (1) 2.50 3.63 (2)	2922	2990 3147		1232 4330
	Dural Dural (Contact)	D7	1732	500	1.70 (1) 2.50 3.63 (2)		2946 3147		4330
CARBON STEEL	Water Steel	S8	1500	500	1.08 2.28 3.23 3.43 4.22	2997	3375 3162	1617	4850 5160
	Steel Air	S8	1500	500	2.07 2.82 4.28		3108 (1) 3209 (2)		4235
POLY-STYRENE	Water Polystyrene	P9	1000	288	0.48 1.05 (1) 1.67 2.24 (2) 2.81 3.55 (3)	1074	1050 1120 1184	1470	480 2810
TITANIUM	Diff. Bonding (Ref.)	T10	1732	500	1.39 2.01 3.80 (2) 5.77	2893	3300 3333		2410 3681
	Diff. Bond. (Ref.)	T10	1732	500	0.32 1.91 (1) 3.43 (2)		3303 2968		558
	Diff. Bond. (Crack 5 mm ϕ)	T11	300	260	9.59		2876		

(1) First order of diffraction along the surface.
(2) Second order of diffraction along the surface.

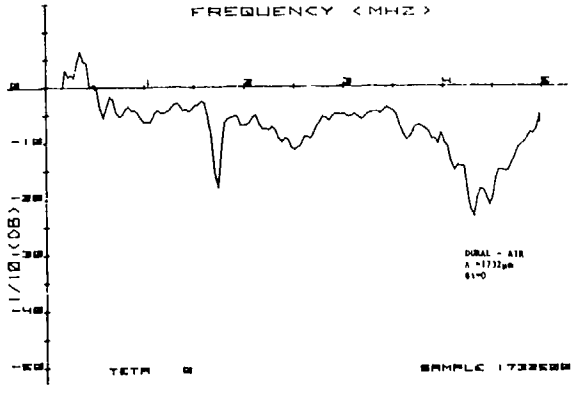

Fig. 17 Pulse-echo normal incidence spectrum from a periodic dural-air interface.

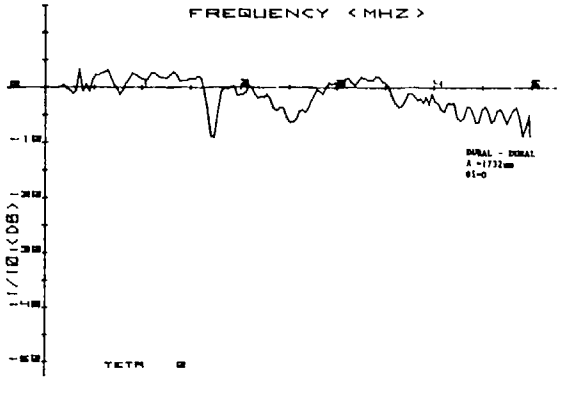

Fig. 18 Pulse-echo normal incidence spectrum from a periodic dural-dural interface.

however, remained approximately the same. The frequency minima on Fig. 18 is at the same position as on Fig. 17.

Diffusion Bonded Titanium. One problem of NDE is to evaluate the quality of bonding between two solid interfaces. The number of contact points between the two surfaces, their distribution, rms roughness, etc. may be important parameters to consider for quantitative evaluation of diffusion bonding. With that in mind, ultrasonic spectroscopy was applied to the diffusion bonded titanium sample with periodic contact. The details of dimensions are given on Fig. 5.

Using a pulse-echo system, the backscattered spectrum from the grated surface at various angles of incidence were recorded. The backscattered spectrum for normal incidence is shown on Fig. 19. There are two distinct minima at 1.5 MHz and at 3.8 MHz. These anomalies are not easily explained. The Rayleigh velocity would produce on a free titanium component which is 1.7 MHz. The deviation may be due to several factors, e.g., nonflatness of the contact, induced stress, etc. The origin of the 3.8 MHz minimum on Fig. 18 is not clear at this point either. The forward scattering (180°) or through transmitted spectrum (obtained by a receiving transducer) shows also two frequency minima on Fig. 20 which we cannot explain. For non-normal incidence, scattering of both incident L waves and mode converted S waves (at the interface of the sample) are studied. On Fig. 21 the back-scattered (pulse-echo) spectrum is shown for a 19° incident wave in water. Since this angle is above the longitudinal critical angle, a 43° shear wave enters into the titanium sample, this 43° shear wave in titanium is diffracted by the grating and different orders of diffraction maxima occur governed by the grating equation (Eq. 2). The diffraction maxima at 1.4 MHz and 2.8 MHz are obtained at 43° incident angle. This information can be used to evaluate the periodicity of contact at the diffusion bonded surface. For example, the measured maxima from Fig. 21 is used to calculate the periodicity as 1.78 mm which is in excellent agreement with the actual value 1.73 mm.

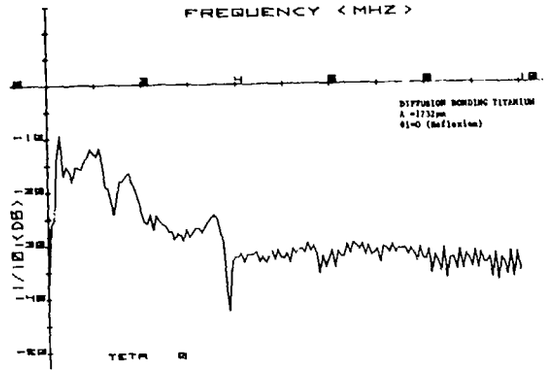

Fig. 19 Pulse-echo normal incidence spectrum from a corrugated diffusion bonded interface in titanium.

Penny-Shaped Crack with Periodically Rough Surface. The effect of the grating surface area on the diffracted field has been considered by scattering from a finite penny-shaped region (a crack) inside diffusion bonded titanium. On Fig. 22 the back-scattered spectrum at normal incidence from the crack is shown photographed together with the reference spectrum. The minimum at 9.69 MHz is the frequency component corresponding exactly to the first diffraction order—produced along the crack (5 mm in diameter) having a periodicity of 300μ—propagating with Rayleigh velocity on titanium. It appears that the anomalies in the frequency spectra are produced by finite periodic surfaces also. It should be interesting to find limiting conditions to obtain this anomaly, both in terms of dimension of the crack and dimension of surface conditions.

At oblique incidence backscattering the spectrum produced is shown on Fig. 23 which is obtained from the crack with a 53°L wave. The maxima at 12 MHz indicate that the periodicity of the surface is 330μ which is in good agreement with the actual value of the periodicity 300μ.

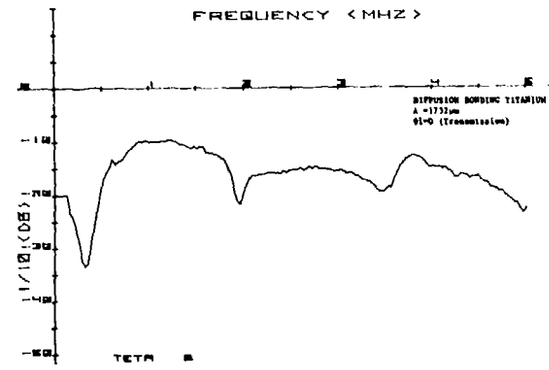

Fig. 20 Through transmission spectrum from a corrugated diffusion bonded interface in titanium.

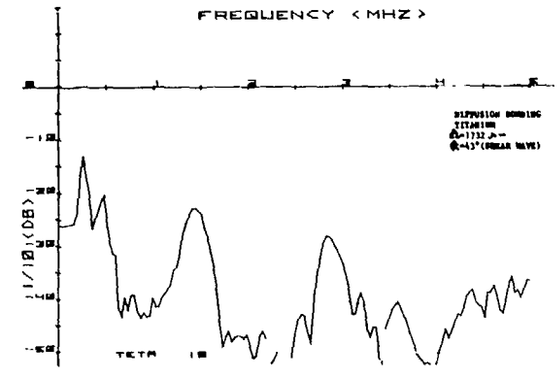

Fig. 21 Diffraction pattern spectrum of an incident 43° shear wave from a corrugated diffusion bonded interface in titanium.

SUMMARY

In order to aid the understanding of the interaction of ultrasonic waves with periodic structures—frequently appearing in various materials—experiments were conducted to study ultrasonic scattering from interfaces with periodic structures. The interfaces between water and various solids such as stainless steel, duraluminum, polystyrene, and brass were studied. The solid-water (water backing on the periodic surface), solid-air, and solid-solid were also considered. In addition, ultrasonic scattering from periodic

surfaces inside diffusion bonded titanium was also studied. Two cases were discussed: (a) the periodic surface is large, and (b) the periodic surface is smaller (finite crack with periodic surface) than the beam. The periodic surface is a triangular shaped grating with periodicity ranging from 100μ to 1730μ.

Both narrowband and broadband experiments were conducted. From the angular and frequency dependence of the scattering the contacts between the two surfaces were accurately determined. A number of anomalies were observed in the backscattering spectrum (at normal incidence) in the form of sharp frequency minima. These missing frequency components (at m = 0, i.e., at the zeroth diffraction order) are first (m = 1) or sometimes higher diffraction orders coupled along the grating surface with velocity of sound in water and/or the Rayleigh velocity in the solid. Although no elastic wave theoretical analysis is available at present to predict these anomalies, electromagnetic and acoustic analogies to this problem have been treated by Lord Rayleigh. It is suggested that spectroscopic studies of scattering from periodic structures should be used as models for non-destructive evaluation of such problems as multiple defects, bonding between two or several layers, and fiber-reinforced composites.

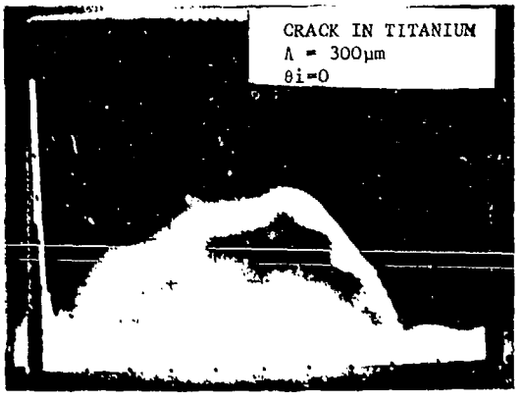

Fig. 22 Pulse-echo normal incidence spectrum from a penny-shaped crack with corrugated surface.

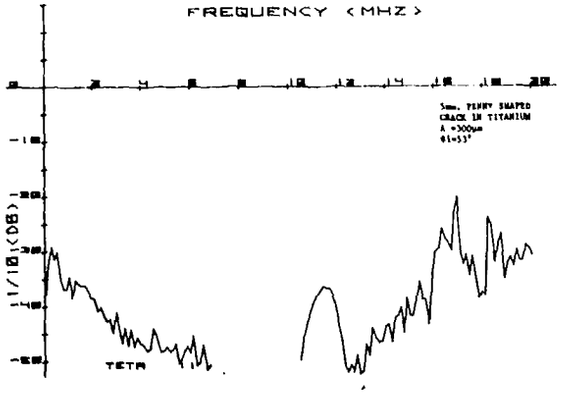

Fig. 23 Diffraction pattern spectrum of a 53° L wave scattered from a penny-shaped crack with corrugated surface.

ACKNOWLEDGMENT

This work was supported jointly by the French CNRS and by the Center for Advanced NDE operated by the Science Center, Rockwell International, for ARPA and AFML under Contract No. F33615-80-C-5004.

REFERENCES

1. J. E. Gubernatis, E. Domany, and J. A. Krumhansl, J. Appl. Phys. 48, 2804 (1977).

2. J. D. Achenbach and A. K. Gautesen, J. Acoust. Soc. Am. 61, 413 (1976).

3. V. Varatharajulu and Y. H. Pao, J. Acoust. Soc. Am. 60, 556 (1976).

4. Laszlo Adler and K. D. Lewis, IEEE Trans. on Sonics and Ultrasonics, S-23 (1976).

5. K. D. Lewis and Laszlo Adler, J. Appl. Phys. 50, 5179 (1979).

6. B. R. Tittman, F. Cohen-Tenoudji, M. de Billy, A. Jungman, and G. Quentin, Appl. Phys. Letters 33, 6 (1978).

7. B. T. Khuri-Yakub and G. S. Kino, Appl. Phys. Letters 32, 513 (1978).

8. F. T. Fokkema and P. M. van den Berg, J. Acoust. Soc. Am. 62, 1095 (1977).

9. P. Beckmann and A. Spizzichino, The Scattering of Electromagnetic Waves from Rough Surfaces, Pergamon Press, 1963.

10. A. Jungman, F. Cohen-Tenoudji, and G. Quentin, Proc. Ultrasonics Int., 385 (1977).

11. Lord Rayleigh, The Theory of Sound (revised), Dover Publications, 1945.

12. E. Ash, Electronic Letters 17, 1 (1968).

Bernie Tittmann, Chairman (Rockwell Science Center): The floor is open for questions.

Ross Stone (IRT Corporation): I apologize if I'm asking an obvious question, but it strikes me that as you scan in frequency and for a fixed angular orientation of your transmitter, scanning your receiver in angle, the signal you build up is exactly proportional to the spatial Fourier transform of whatever the structure is. In other words, if you have a full spectrum of spatial roughness, you will get a full spatial Fourier transform. If one inverted that spatial full Fourier transform, wouldn't you get a picture of the roughness? Have you used that?

Laszlo Adler (Ohio State University): No, we haven't. We would be very interested in a fixed position of the transformer hitting it normally and looking at the back reflection.

Ross Stone: You chose the sample so that you only had one?

Laszlo Adler: It's not easy to have all the angular positions.

Ross Stone: I would suggest you try it. I think it might be successful.

Laszlo Adler: Thank you.

R.D. Weglein (Hughes): I wanted to make a comment that polystyrene is very similar to lucite. I made the same observation using the reflection acoustic microscope where we could measure what I call acoustic material, material based on the surface skimming bulk wave, longitudinal in styrene.

Laszlo Adler: The longitudinal angle, but you do not have a real angle for polystyrene?

R.D. Weglein: It's the angle for the longitudinal wave.

Laszlo Adler: I think the other component is not quite as intense as the general --

R.D. Weglein: That's because the reflection is strong, very strong, so the incident amount of energy that's transmitted and leaks into the surface is very small than it would be for a Rayleigh wave.

Laszlo Adler: I didn't say you cannot have a surface. You cannot have a Rayleigh wave generated on the polystyrene with the usual technique because you don't have a Rayleigh angle, but you can have a surface. I observed that, also.

Bernie Tittmann, Chairman: We will now move on to the next paper.

SCATTERING BY SURFACE-BREAKING AND SUB-SURFACE CRACKS

J.D. Achenbach, R.J. Brind and A. Norris
The Technological Institute
Northwestern University
Evanston, IL. 60201

ABSTRACT

This paper is concerned with exact solutions and approximate solutions in the high-frequency domain for scattering of time-harmonic waves by surface-breaking cracks and cracks which are located near a free surface. Both incident surface waves and incident body waves have been considered. The high-frequency approximate solutions are generally based on elastodynamic ray theory. Some approximate solutions based on the Kirchhoff approximation have been included for comparison.

INTRODUCTION

Elastodynamic ray theory provides a powerful tool for the computation of fields generated by scattering of time-harmonic waves by cracks, when the wavelengths of the incident wave is of the same order of magnitude as characteristic length parameters of the crack. Ray theory has the advantage of simplicity and intuitive appeal. The rules that govern reflection, refraction, and edge diffraction of rays are well established, and it is generally not difficult to trace rays from a source via the scatterer to an observer. Fourier methods can be used to relate pulses in the time domain to spectra in the frequency domain.

Experimental setups generally include instrumentation to gate out the relevant pulses in the scattered field on the basis of arrival times. The application of a Fast Fourier Transform to these pulses subsequently yields frequency spectra. In the frequency domain the raw scattering data can conveniently be corrected for transducer transfer functions and other characteristics of the system, which have been obtained on the basis of appropriate calibrations. The corrected amplitudes and phase functions can then be compared with theoretical results that have been obtained by harmonic analysis. For short pulses the frequency spectra of the diffracted signals are centered in the high-frequency (short wavelength) range. Ray theory gives excellent results at such high frequencies.

High-frequency incident waves give rise to interference phenomena which can often easily be interpreted on the basis of ray tracing, and which can provide the basis for an inversion procedure. Particularly the first arriving signals, which are related to the longitudinal waves in the solid, often give rise to a simple structure in the frequency domain.

Considerable progress has been achieved in recent years in the application of elastodynamic ray theory to scattering by cracks. For cracks in unbounded solids theoretical results have been given by Achenbach et al [1]-[4]. For two-dimensional problems ray theory results have been compared with exact results in Ref.[5], and with experimental results in Ref.[6].

In this paper we consider surface-breaking cracks and cracks in the immediate vicinity of a boundary. We start with a brief discussion of exact solutions. For the surface breaking crack we briefly discuss the application of ray theory. For the sub-surface crack approximations to the scattered field are obtained both by ray theory and by the Kirchhoff approximation. We also discuss some pulse-echo computations for the case that the transducer is near the zone of specular reflection from a surface-breaking crack.

2. SURFACE-BREAKING CRACKS

The surface breaking crack is one of the most harmful crack configurations, and it is thus not surprising that there is a considerable interest in their detection. In this section we review solutions to the direct scattering problem for incident surface waves and incident bulk waves. The geometry is shown in Fig. 1.

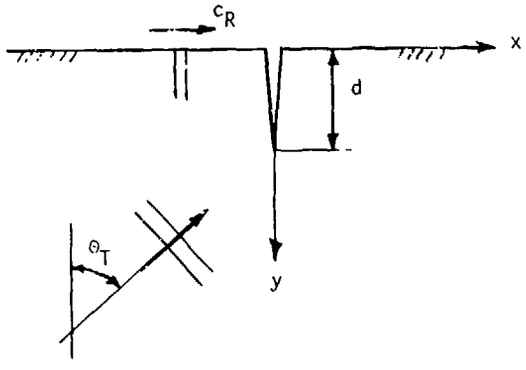

Fig. 1 Surface-breaking crack in an elastic solid.

2.1 Incident waves of anti-plane strain. With reference to the coordinate system shown in Fig. 1, waves of anti-plane strain are defined by displacements in the z-direction which are functions of x and y only. These displacement components, w(x,y) satisfy the reduced wave equation

$$\nabla^2 w + k_T^2 w = 0 . \qquad (2.1)$$

In Eq.(2.1), ∇^2 is the two-dimensional Laplacian and $k_T = \omega/c_T$, where ω is the circular frequency and c_T is the velocity of transverse waves. Here it is implied that the waves are time-harmonic, but the term $\exp(-i\omega t)$ has been omitted, as it will be in the sequel. The boundary conditions are

$$y = 0, \; -\infty < x < \infty: \quad \frac{\partial w}{\partial y} = 0 \qquad (2.2)$$

$$x = 0, \; 0 \le y < d: \quad \frac{\partial w}{\partial x} = 0 . \qquad (2.3)$$

An incident wave of anti-plane strain can be expressed in the form

$$w^i(x,y) = A \exp[ik_T(x\sin\theta_T - y\cos\theta_T)] \qquad (2.4)$$

where $(\sin\theta_T, \cos\theta_T)$ defines the propagation direction. In the absence of the surface breaking crack, the incident wave would give rise to a reflected wave of the form

$$w^r(x,y) = A \exp[ik_T(x\sin\theta_T + y\cos\theta_T)] . \qquad (2.5)$$

It is easily checked that the following condition is satisfied

$$\lim_{y\to 0} \frac{\partial}{\partial y} [w^i(x,y) + w^r(x,y)] = 0 . \qquad (2.6)$$

The total field generated by the interaction of the incident wave (2.4) and the reflected wave (2.5) with the crack, can be expressed by

$$w^t(x,y) = w^i(x,y) + w^r(x,y) + w^s(x,y) \qquad (2.7)$$

where $w^s(x,y)$ is the scattered wave. According to (2.2), $\partial w^t/\partial y$ vanishes at $y = 0$: Equations (2.6) and (2.7) then imply that the boundary condition on the scattered field is

$$\frac{\partial w^s}{\partial y} = 0 , \quad y = 0, \; -\infty < x < \infty . \qquad (2.8)$$

It follows from (2.3)-(2.5) and (2.7) that the scattered field must satisfy the following condition on the crack faces

$$\frac{\partial w^s}{\partial x} = -2iAk_T \sin\theta_T \cos(ik y \cos\theta_T), \quad x = 0^{\pm}, 0 \le y \le d . \qquad (2.9)$$

The problem defined by Eqs.(2.1), (2.8) and (2.9) has been solved as a specific and separate problem by Stone et al [7] and Datta [8]. An easier way to obtain a solution can be based on the observation that for anti-plane strain the solution to the surface-breaking crack can be obtained directly from the solution for a crack of length 2d in full space by symmetry considerations. The geometry for this case is shown in Fig. 2.

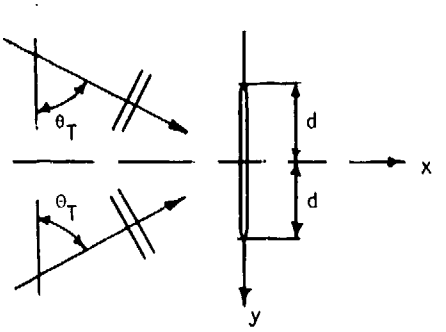

Fig. 2 Crack in unbounded medium with symmetric system of incident waves.

The two incident waves can now be represented by (2.4) and (2.5), and hence (2.6) holds. The scattered field is again defined by (2.7), and the conditions on the crack faces is given by (2.9), except that this condition is now defined over the interior crack of length 2d. Because of the symmetry with respect to y of the right-hand side of (2.9), $w^s(x,y)$ will be symmetric with respect to y, and hence (2.8) will be satisfied automatically.

The high-frequency scattered field for the interior crack can be found in books on acoustics, see, e.g., Ref.[9].

2.2 Incident waves of in-plane strain. Unfortunately, the simple symmetry considerations that hold for the case of anti-plane strain are not valid for the in-plane case. Symmetry considerations do not work because of mode coupling of longitudinal and transverse waves at a traction-free plane. Thus, it is not possible to construct a system of incident waves in an infinite solid with an interior crack, so that the conditions for a surface-breaking crack are automatically satisfied. Hence the problem of scattering by a surface-breaking crack must be considered as a completely separate problem.

Exact solutions for the two-dimensional geometry of a crack of depth d in an elastic half-plane were given in Refs. [10] and [11]. In Ref.[11] the scattered displacement fields due to either a time-harmonic surface wave or a plane time-harmonic longitudinal or transverse body wave incident upon the crack from infinity are investigated. The total field in the half-plane is taken as the superposition of the specified incident field in the uncracked half-plane and the scattered field in the cracked half-plane generated by suitable surface tractions on the crack faces. These tractions are equal and opposite to the tractions generated by the incident wave in the uncracked half-plane when evaluated in the plane of the crack. By decomposing the scattered field into symmetric and anti-symmetric fields with respect to the plane of the crack, a pair of boundary value problems for the quarter-plane is obtained. These two boundary value problems are reduced by integral transform techniques to two uncoupled singular integral equations, which are solved numerically using a collocation scheme. The derivation of the symmetric equation has been presented in Ref.[10], and the derivation of the anti-symmetric integral equation is presented in

Ref.[11]. The crack-opening displacements are then easily calculated from the solutions of the singular integral equations. The exact representations of the diffracted displacement fields are subsequently obtained in the form of finite integrals over the crack length, which are evaluated numerically.

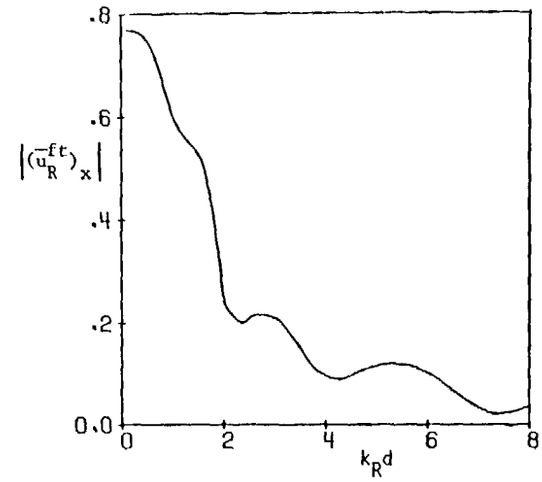

Fig. 3 The total field ahead of the crack (forward-transmitted field)

For an incident Rayleigh wave, Fig. 3 shows the forward-transmitted field, and the back-scattered field is shown in Fig. 4. Apparently, most of the incident wave is backscattered.

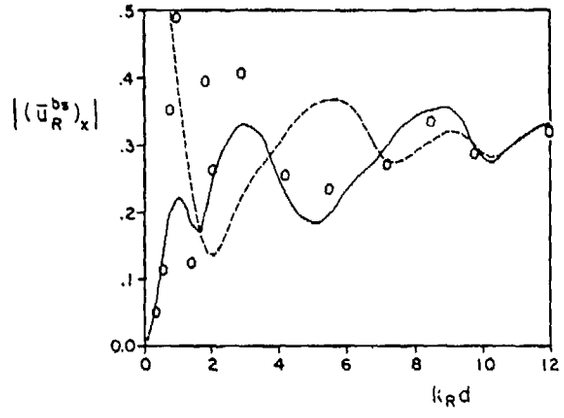

Fig. 4 Comparison of exact and approximate dimensionless x-components of the displacement fields for back-scattered surface waves, where $|(\bar{u}_R^{bs})_x| = |(u_R^{bs})_x| / A(2c_T^2/c_R^2 - 1)$. --- Ray theory of Ref.[12]. O-Exact, see [11]. ——— Asymptotic evaluation of exact integrals of [11].

2.3 Ray Analysis of Surface-Wave Interaction with an Edge Crack In Ref.[12] a simple approximate approach to scattering of Rayleigh surface waves by surface-breaking cracks has been presented, which is valid in the high-frequency range. Solutions are shown to agree well with the results of [11] for $\omega d/c_R > 6$ (see Fig. 4) where ω is the circular frequency, d is the depth of the crack, and c_R is the velocity of Rayleigh surface waves. The method of analysis which is based on elastodynamic ray theory can potentially be extended to scattering by surface-breaking cracks in three-dimensional configurations. The simple concepts of ray tracing that are used suggest simple interpretations of scattering data for the solution of the inverse problem.

An incident Rayleigh wave, propagating in the positive x-direction (see Fig. 1), interacts with the crack. Both the mouth and the edge of the crack act as centers of diffraction, which generate diffracted body waves, and reflected, and transmitted Rayleigh surface waves. The diffracted body waves are neglected but the reflected, transmitted, and diffracted Rayleigh waves are taken into account. The reflections, transmissions, and edge-diffractions are investigated one by one on the basis of elastodynamic ray theory, and the results are then superimposed to yield simple expressions for the back-scattered and forward-scattered Rayleigh surface waves and for the elastodynamic stress-intensity factors, in terms of reflection, transmission, and diffraction coefficients. A simple formula for the inverse problem is presented, which relates the periodicity of the amplitude modulation in the high-frequency range directly to the depth d of the crack.

2.4 Ray analysis of body-wave interaction with an edge crack. Ray theory can conveniently be used to analyze the interaction of in-plane body-waves with a surface-breaking crack. For very short times after the arrival of the first signal, which comes directly from the crack tip, only a few ray-paths need to be considered. Three ray paths are shown in Fig. 5, for an angle of incidence of 60^o, and an angle of observation of 45^o. The incident wave is a longitudinal (L) wave. Since the direction of observation is not near a shadow boundary, or near a boundary of a zone of reflected waves, there are no difficulties with the application of ray theory. In the next section we discuss a case of backscattering for the case that both the angle of incidence and the angle of observation are near 45^o. Then the observation point is near a boundary of a beam of reflected waves, and ray theory cannot be applied in its simplest form.

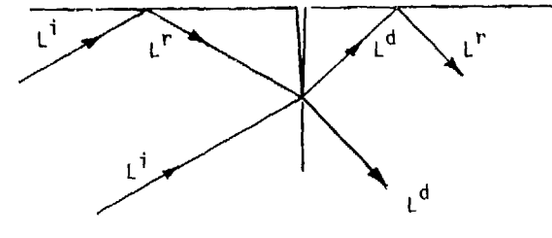

Fig. 5 Three ray paths for incident L-rays

Incident, reflected and diffracted L-rays are denoted by L^i, L^r, and L^d respectively. In Fig.6 we show the following ray paths: L^iL^d, $L^iL^rL^d$, and $L^iL^dL^r$. In the time domain, these ray-paths correspond to the first arrivals. Ray-paths which involve mode conversion (L to T) at the free surface or at the illuminated face of the crack, correspond to later arrivals. In Fig. 6 we have shown the interference of the time-harmonic signals carried by the diffracted L-rays. The figure shows the amplitude modulation for the first two rays (L^iL^d and $L^iL^rL^d$) and for all three rays. The L^iL^d and $L^iL^rL^d$ interference gives rise to a simple pattern in which the crack depth d is related to the spacing of the peaks. The interference of the three rays (L^iL^d, $L^iL^rL^d$ and $L^iL^dL^r$) already produces an amplitude modulation that is not open to immediate interpretation.

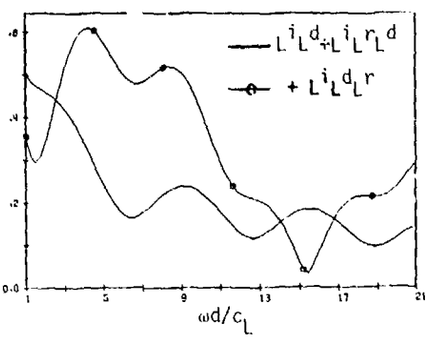

Fig. 6 Amplitudes of diffracted L-rays

2.5 Interference of corner reflection and edge diffraction. When an L-wave transducer is aimed at a surface-breaking crack such that the waves are reflected back from the corner at the crack mouth to the transducer, then under certain circumstances it is observed that the backscattered signal is composed of two distinct parts. These distinct signals in the time domain are thought to be due to reflection from the crack corner and the diffraction from the crack tip. As the transducer is moved slightly, the relative amplitudes of the two signals changes dramatically. In Ref.[13] it has been attempted to estimate the relative amplitudes of the two effects in a high frequency, far field, two dimensional approximation. By high frequency we mean that $k_L\, d >> 1$, by far field that $d/r >> 1$, where r is the distance from transducer to crack-tip. For a two dimensional approximation we assume a line source behavior for the transducer. Implicit in this two dimensional model is that the crack width is much larger than the transducer width.

The geometry, which corresponds to an experimental set-up, is shown in Fig. 7. The surface-breaking crack of length d is normal to the free surface I at a distance b from a vertex of interior angle ϕ, $0 < \phi < \pi/2$. The transducer is free to be shifted along the free surface II. For any

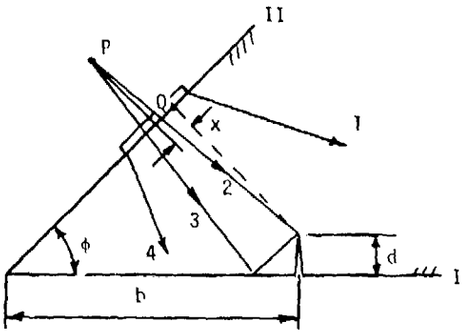

Fig. 7 Surface-breaking crack and location of transducer

positioning of the transducer we define its position as x, where x is the distance of the center of the transducer from Q, the intersection of II and the normal from II to the crack mouth. The distance x is defined as positive in the direction away from the vertex, so for example, in Fig. 7 $x < 0$. The transducer virtual source is at P. A beam of half angle θ_0 emanates from P. Each ray of the beam has an associated angle $\theta \in [-\theta_0, \theta_0]$, where θ is measured clockwise from the central ray.

As the beam proceeds from P, some of its rays will interact with the crack to produce a scattered signal which may be detected by the transducer. In Fig. 7 the rays 1 and 4 do not interact with the crack. Ray 2 is diffracted by the crack tip to produce a cylindrical wave emanating from the tip. The beam between rays 2 and 3 is both reflected from surface I and scattered from the crack surface. The resultant beam is directed back towards the transducer, where it is detected as a signal with a different phase and amplitude than the purely diffracted signal.

The complete analysis of the diffracted and reflected signals is complicated. Since the transducer is located near a boundary of the zone of reflected waves, ray theory cannot be applied directly. A more sophisticated theory, which is called uniform asymptotic theory, and which includes Fresnel corrections, must be used. Details of the application of such a theory to the problem described above, are given in Ref.[13].

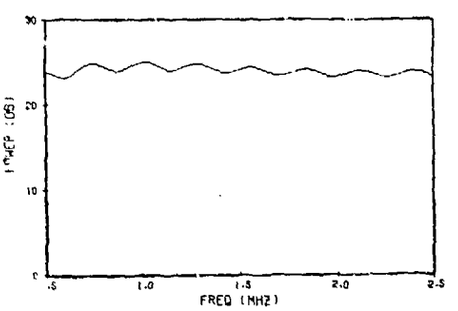

Fig. 8 Power spectrum when the transducer is inside the zone of reflected waves

Figures 8 and 9 show some results. In Fig. 8 the reflected signals from the corner at the crack mouth dominate the diffracted signal from the crack tip. The power spectrum of Fig. 9 is for the case that the reflected and diffracted signals are of the same order of magnitude. This means that the transducer is at the boundary of the zone of reflected waves.

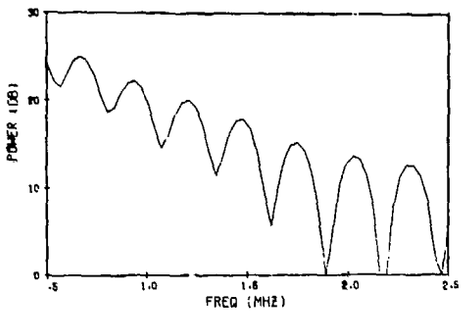

Fig. 9 Power spectrum when the transducer is at the boundary of the zone of reflected waves.

The two curves have been normalized so that they have the same maximum values. Clearly Fig. 9 has a more distinctive character, with a sequency of peaks whose spacing is related to the crack depth d. Figures 8 and 9 show that a slight shift of the transducer transforms the power spectrum from a rather even curve into one with a strong pattern of peaks and valleys, albeit with much smaller actual values of the power.

3. SUB-SURFACE CRACKS

In this Section we summarize some recent results for scattering by a sub-surface crack.

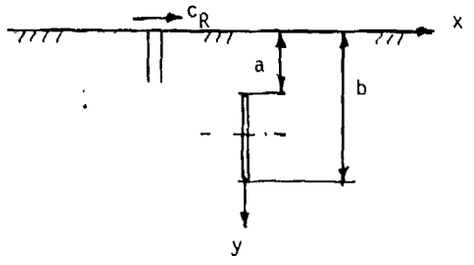

Fig. 10 Geometry for the sub-surface crack

3.1 Scattering of surface waves-exact analysis. In Ref.[14] an exact mathematical analysis has been presented for the scattering of Rayleigh waves by a sub-surface crack. The two-dimensional geometry considered in Ref.[14] is shown in Fig. 10. In Ref.[14] the boundary-value problem for the scattered field is stated, and reduced to an uncoupled system of integral equations, which have been solved numerically. At large distances from the crack the scattered field was shown to consist of outgoing Rayleigh waves and cylindrical body waves.

The integral equations derived in Ref.[14] are of the general form

$$-\sigma^i_{xx} = \frac{\mu}{k_T^2}\int_a^b d_x(y)\, \Gamma_{xx;xx}(0,y;0,y')dy \qquad (3.1)$$

$$-\sigma^i_{xy} = \frac{\mu}{k_T^2}\int_a^b d_y(y)\, \Gamma_{xy;xy}(0,y;0,y')dy \qquad (3.2)$$

together with the side conditions

$$\int_a^b d_i(y)dy = 0\ , \qquad i = x,y\ . \qquad (3.3)$$

$D_i(y) = d_i(y)(b-y)^{\frac{1}{2}}(a-y)^{\frac{1}{2}}$ is continuous in [a,b]. Equations (3.1) and (3.2) must be solved for the density functions $d_i(y)$, i = x,y. In (3.1) and (3.2) σ^i_{xx} and σ^i_{xy} are the stresses due to the incident wave at the location of the crack. The kernels $\Gamma_{xx;xx}$ and $\Gamma_{xy;xy}$ are given by (3.8a,b) of Ref. [14]. Also

$$k_T = \omega/c_T\ ; \quad c_T^2 = \mu/\rho\ . \qquad (3.4\ ,b)$$

The displacement discontinuity across the crack faces may be written as

$$[u_i](y) = \int_a^y d_i(s)ds\ ; \qquad i = x,y\ . \qquad (3.5)$$

Once $[u_i](y)$ has been computed, the radiated elastodynamic field can be computed by the use of an elastodynamic representation integral.

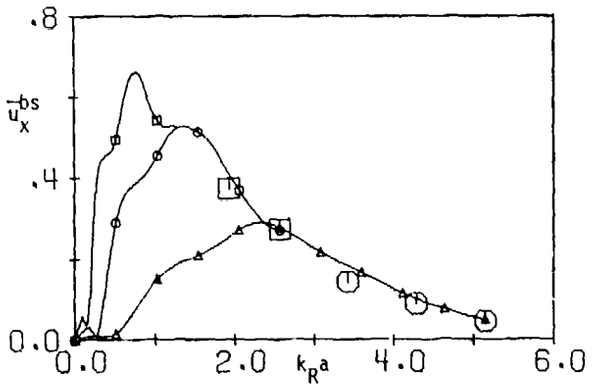

Fig. 11 Horizontal surface displacement in the back-scattered Rayleigh wave vs. $k_R a$,

$\bar{u}_x^{bs} = |\, u_x^{bs} / u_x^{inc}\, |$, -⊖- a/b = .1 , -⊖- a/b = .2, -△- a/b = .4.

For three values of a/b the amplitudes of the horizontal displacement components of the back-scattered and forward-scattered surface waves, are shown in Figs.11 and 12, respectively. The amplitudes are plotted as functions of $k_R a = 2\pi a/\Lambda_R$, where Λ_R is the wavelength of the incident surface wave. It is noted that the amplitudes eventually decrease as $k_R a$ increases, i.e., as the wavelength becomes smaller relative to the distance from the nearest crack tip to the free surface. The reason for the decrease in amplitude is related to the exponential decay of surface waves with depth. A surface wave does not penetrate much deeper into a half-space than approximately one wavelength. Thus as the wavelength decreases the incident wave experiences less scattering by the sub-surface crack. For small enough wavelength the incident wave passes almost unhindered through the gap between the crack tip at y = a and the free surface. Figures 11 and 12 may be contrasted with the corresponding ones for a surface-breaking crack of depth d which have been presented in Ref.[11]. Very short waves are scattered strongly by a surface-breaking crack, and the amplitude spectra for both the forward-scattered and the back-scattered wave show an oscillation about a finite limit as $k_R d$ increases, where the period of the oscillation is directly related to the depth of the crack.

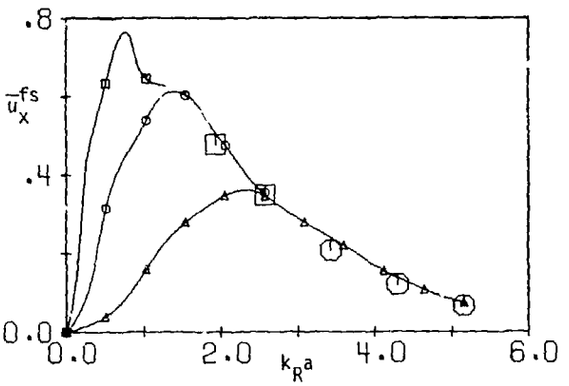

Fig. 12 Horizontal surface displacement in the forward scattered Rayleigh wave vs. $k_R a$, $\bar{u}^{fs} = |u_x^{fs} / u_x^{inc}|$, a/b = .1, a/b = .2, a/b = .4.

The amplitudes of the scattered waves are also small when $k_R(b-a) \ll 1$, i.e., when $\Lambda_R \gg (b-a)$, in the long wavelength limit. It appears that for long wavelengths the scattering by a sub-surface crack and a surface-breaking crack are quite similar. A transition, characterized by a maximum in Figs. 11 and 12 occurs when the wavelength Λ_R is of the order (b-a). Thus, there is an optimum wavelength for a maximum scattering effect, at which the crack can easiest be detected by ultrasonic surface wave methods.

The cost of calculating these results is a function of $k_R(b-a)$ so it has not been possible to obtain the full curves over the whole range. However it is expected that when $k_R b$ is sufficiently large the scattering from the subsurface crack is approximately that due to a semi-infinite slit (i.e., the case when b/a = ∞). The curves are therefore expected to coincide with each other for sufficiently short wavelengths, and to verify this five additional points were obtained and are plotted as the large symbols in Figs. 11-13.

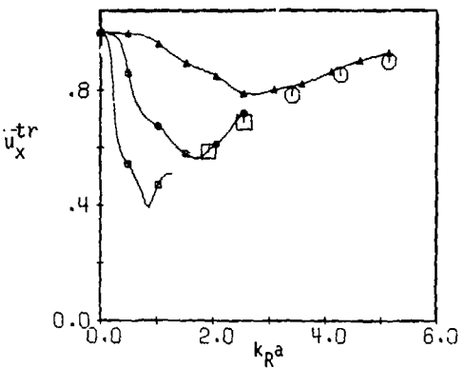

Fig. 13 Horizontal surface displacement in the transmitted Rayleigh wave vs. $k_R a$, $\bar{u}_x^{tr} = |u_x^{tr} / u_x^{inc}|$, a/b = .1, a/b = .2, a/b = .4.

In experiments it is usually attempted to measure the backscattered wave and the forward-transmitted wave, where the latter is the sum of the incident wave and the forward-scattered wave, in the usual way. The amplitude of u_x for the forward transmitted wave is shown in Fig. 13. Consistently with the previous discussion the forward transmitted amplitude first decreases and then increases with increasing $k_R a$, and it approaches the amplitude of the incident wave for sufficiently large $k_R a$.

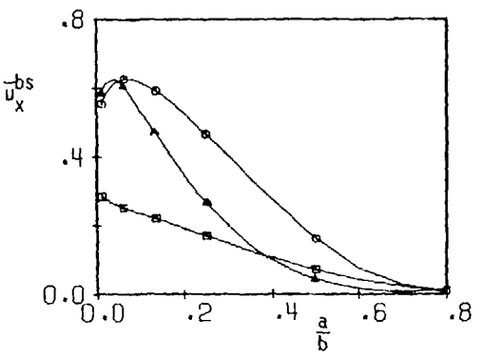

Fig. 14 Horizontal surface displacement in the back-scattered Rayleigh wave vs. a/b, $\bar{u}_x^{bs} = |u_x^{bs}/u_x^{inc}|$, $\frac{\omega b}{c_L} = 1$, $\frac{\omega b}{c_L} = 3$, $\frac{\omega b}{c_L} = 5$.

Figure 14 shows the amplitude of the back-scattered wave as a function of a/b, for specific values of $k_R b$. An increasing value of a/b means in effect a smaller crack, since the crack length is proportional to 1-a/b, and hence a smaller back-scattered wave.

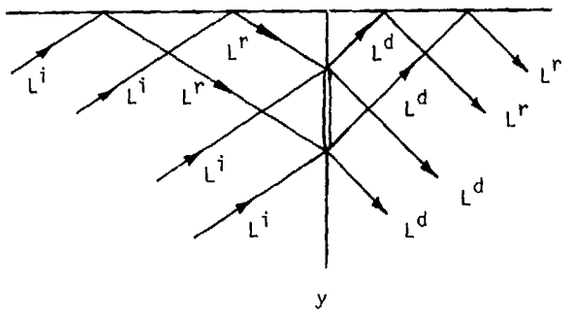

Fig. 15 Ray paths for incident L-rays.

3.2 Ray analysis of body-wave interaction with a sub-surface crack. Three ray paths are shown in Fig. 15. In the terminology of Section 2.4 these ray paths are L^iL^d, $L^iL^rL^d$, and $L^iL^dL^r$. In all three cases the ray paths can be either via the upper or via the lower crack tip. The interference of the time-harmonic signals carried by these ray paths is shown in Fig. 16. The interference of the two L^iL^d paths shows a simple structure of periodic peaks.

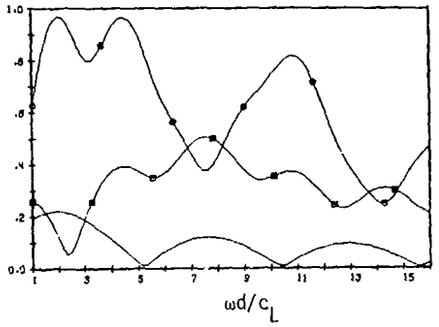

Fig. 16 Amplitudes of diffracted L-waves

—— $L^iL^d + L^iL^d$

—B— $L^iL^d + L^iL^d + L^iL^rL^d + L^iL^rL^d$

—o— $L^iL^d{+}L^iL^d{+}L^iL^rL^d{+}L^iL^rL^d{+}L^iL^dL^r{+}L^iL^dL^r$

ACKNOWLEDGEMENT

This work was carried out in the course of research sponsored by the Center for Advanced NDE operated by the Science Center, Rockwell International for the Advanced Research Project Agency and the Air Force Materials Laboratory under Contract F33615-80-C-5004.

REFERENCES

1. Achenbach,J.D., and Gautesen,A.K., "Geometrical Theory of Diffraction for Three-D Elastodynamics," J. Acoust. Soc. Amer., 61, 1977, pp. 413-421.
2. Achenbach, J.D., Gautesen, A.K., and McMaken,H., "Diffraction of Elastic Waves by Cracks - Analytical Results," in Elastic Waves and Non-Destructive Testing of Materials, edited by Y.H. Pao, AMD-Vol. 29, American Society of Mechanical Engineers, New York, 1978.
3. Achenbach, J.D., Gautesen, A.K. and McMaken,H., "Application of Geometrical Diffraction Theory to QNDE Analysis," ARPA/AFML Review of Progress in Quantitative NDE, edited by D.O. Thompson, Science Center, Rockwell International, Thousand Oaks, Cal., January 1979, pp. 321-330.
4. Achenbach,J.D., Gautesen, A.K. and McMaken,H., "Application of Ray Theory to Diffraction of Elastic Waves by Cracks," in Recent Developments in Classical Wave Scattering: Focus on the T-Matrix Approach, edited by V.K. Varadan and V.V. Varadan, Pergamon Press, 1980.
5. Achenbach,J.D., Gautesen,A.K., and McMaken,H., "Application of Elastodynamic Ray Theory to Diffraction by Cracks," Modern Problems in Elastic Wave Propagation, edited by J. Miklowitz and J. D. Achenbach, Wiley-Interscience, New York, 1978.
6. Achenbach,J.D., Adler, L., Lewis, D. Kent, and McMaken, H., "Diffraction of Ultrasonic Waves by Penny-Shaped Cracks in Metals: Theory and Experiment," J. Acoust. Soc. Am., 66, p. 1848, 1979.
7. Stone,S.F., Ghosh,M.L. and Mal,A.K., "Diffraction of Anti-Plane Shear Waves by an Edge Crack," J.Appl. Mech. 47, pp. 359-362, 1980.
8. Datta,S.K., "Diffraction of SH Waves by an Edge Crack," J. Appl. Mech.46, pp. 101-106, 1979.
9. Bowman,J.J., Senior,T.B.A., and Uslenghi,P.L.E., Electromagnetic and Acoustic Scattering by Simple Shapes, North-Holland, 1969.
10. Achenbach,J.D., Keer, L.M., and Mendelsohn, D.A., "Elastodynamic Analysis of an Edge Crack," J. Applied Mechanics, in press.
11. Mendelsohn,D.A., Achenbach,J.D., and Keer,L.M., "Scattering of Elastic Waves by a Surface-Breaking Crack, WAVE MOTION, in press.
12. Achenbach,J.D., Gautesen,A.K., and Mendelsohn, D.A., "Ray Analysis of Surface-Wave Interaction with an Edge Crack, IEEE Transactions Sonics and Ultrasonics, Vol. SU-27, pp. 124-129, 1980.
13. Achenbach, J.D., and Norris,A., "Interference of Corner-Reflected and Edge-Diffracted Waves for Scattering of Body-Waves by a Surface-Breaking Crack," submitted for publication.
14. Achenbach,J.D. and Brind, R.J., "Scattering of Surface Waves by a Sub-Surface Crack," submitted for publication.

Bernie Tittmann, Chairman (Rockwell Science Center): We have time for two questions.

Don Thompson (Ames Laboratory): Have you looked at the frequency composition of the scattered waves as they travel over the various paths? Presumably the subsurface crack would serve as a filter.

J.D. Achenbach (Northwestern University): The frequency composition? What you are referring to is an experimental pulse and what we are showing here is for a fast Fourier transform of such a pulse. These pictures are for harmonic waves.

Don Thompson: They are that, but would you expect there to be a difference if you started with different pulses?

J.D. Achenbach: You have to work with very short pulses. The higher the frequency content the better results you get.

Don Thompson: The filter characteristics of the various cracks should show up in the comparisons.

J.D. Achenback: Yes. The difference is the form of the amplitude. One being an essentially horizontal ripple, the other being a strongly decaying curve with frequency.

Laszlo Adler (Ohio State University): Have you worked out incident shear waves?

J.D. Achenbach: I'm glad you brought that up, because what we have done here are all first arrival longitudinal waves. Everything can be done equally well for shear waves. But as soon as you start talking about shear waves, you have to include all the preceding longitudinal waves.

Laszlo Adler: There is some indication you may have stronger signals with incident shear waves.

J.D. Achenbach: Definitely, for an incident shear wave, there is an indication that you have stronger signals. Unfortunately, incident shear waves still produces longitudinal waves.

Laszlo Adler: I notice you have a distribution of the input. Do you include finite transducer width?

J.D. Achenbach: Yes. And we integrate over the width of the transducer, quote-unquote transducer, which is just a width here of one inch, I think, or one centimeter.

Laszlo Adler: Not uniform but weighted integration.

J.D. Achenbach: Yes

Bernie Tittmann, Chairman: I just wanted to make a comment that the crack tip when radiated by surface waves radiates bulk waves.

J.D. Achenback: In the present paper we talked about the ray model for back scattering surface waves, and we didn't look into the medium itself, into the bulk waves generated by the surface waves, we can use the ray model for bulk waves as well.

Bernie Tittmann, Chairman: Thank you. We must move on.

RESONANCES AND CRACK ROUGHNESS EFFECTS IN SURFACE BREAKING CRACKS

S. Ayter and B. A. Auld
Edward L. Ginzton Laboratory
Stanford University
Stanford, California 94305

ABSTRACT

This study deals with two different aspects of scattering from the cracks. The first one is the measurement of crack resonances by local probes and the second is the effect of the roughness of the crack forces on the scattering data.

Unlike the scattering measurement reported elsewhere, these measurements of crack resonances are to be performed by local probes. Two different types of probes are described and their problems are discussed.

The effect of crack roughness on the scattering data is investigated via the reciprocity relation. The crack roughness is analyzed using perturbation theory and the equivalent boundary condition concept developed by Brekhovskikh is used to express the fields in the presence of the roughness. The effect of roughness on the scattering data is then discussed in qualitative terms.

INTRODUCTION

In our last year's report [1], we proposed a model to explain the crack resonance phenomena, which regards the resonances as standing waves due to the modes that propagate on crack surfaces along the length and depth directions. For these resonances, we gave the following formulas which agreed well with the available experimental data available at that time [2,3]:

$$f_L \cong \frac{V_L}{2L}\left(M + \frac{1}{2}\right) \qquad (1)$$

$$f_D \cong \frac{V_D}{2D} N \,. \qquad (2)$$

Here, f_L and f_D are length and depth resonance frequencies, V_L and V_D are the velocities of the guided modes along the length and the depth directions, M and N are integers that describe the mode indices. The 1/2 factor in Eq. (1) arises from the boundary conditions of non-zero velocity fields at the crack tips. For large cracks V_L and V_D can be taken as the Rayleigh wave velocities.

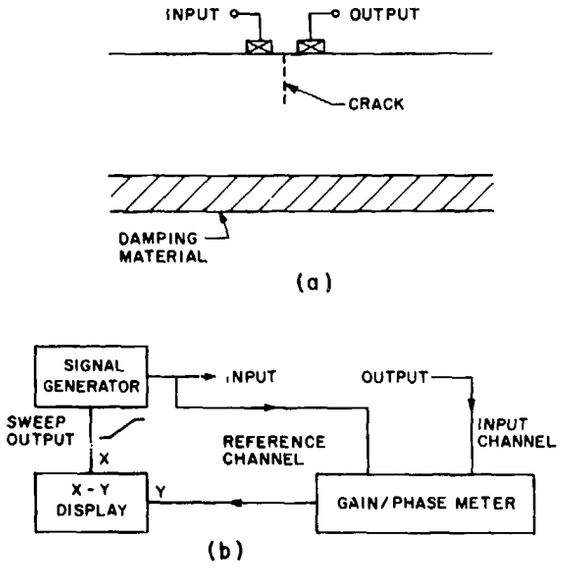

Fig. 1 Measurement scheme of crack resonances

Measurement Scheme — The measurement scheme is outlined in Fig. 1. We place input and output transducers near the crack and we cover the bottom of the plate by a damping material. Within our frequency range of operation (~ 50-1000 kHz) we found that both heavily tungsten loaded epoxy and Duxseal sealing putty work fairly well as dampers. We always repeat the measurements on a control plate (without the crack) to isolate the signature of the crack resonance, with the transducers placed on the same location on both cracked and uncracked plates to eliminate any false signal that might arise due to the lateral plate resonances.

We generally work on cw mode, scanning the frequency and monitoring the output signal through a gain-phase meter (HP 3575A) [Fig. 1(b)].

Transducer Types — We basically worked with large slots, since they are easier to manufacture. Therefore our frequency of operation scaled down accordingly. Typically we worked with slots in the order of tens of millimeters in length and depth and therefore we needed to develop transducers that work in the hundred kilohertz range.

One transducer type is two side electroded length expander bars bonded together [Fig. 2(a)]. One electrode pair acts as the input port to the probe and the other pair is the output port. These transducers have been used successfully to determine the mechanical damping at frequencies of 30 to 200 kHz [4]. To reduce the electromagnetic pickup between the transducers, one of the bars is rotated 90° before bonding. For transducer material, we used Channel 5800 (PZT-8) poled along the direction between the electrodes.

Figure 2(b) shows the response of such transducer with both ends free. The transducer assembly

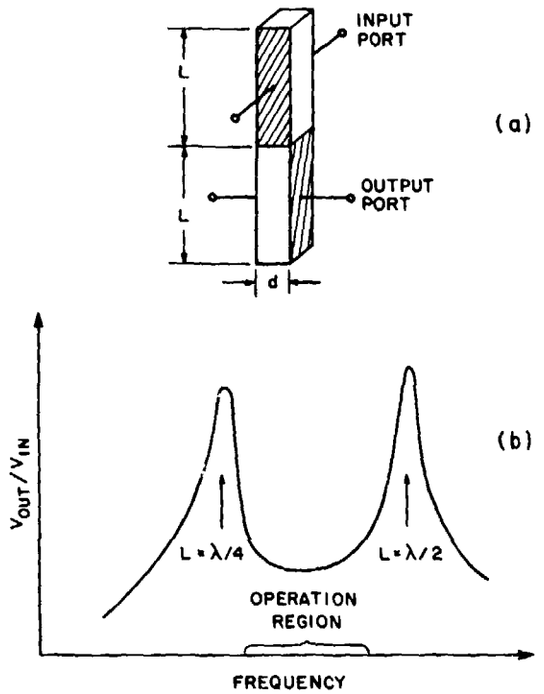

Fig. 2 Length expander transducer. (a) Geometry. (b) Unloaded frequency response.

resonates when $L = \lambda/4$, $\lambda/2$ and $3\lambda/4$. The valley between the first two resonance peaks is found to be the most appropriate region to detect the crack resonances due to its clean and fairly smooth variation. The second valley is not very appropriate, since the transducer is not thin enough for single mode operation in that region. When the transducer thickness satisfies the condition

$$d < 5\lambda \qquad (3)$$

the motion of the bar is basically along the length direction while for thicker transducers higher order modes become more effective [4].

In our frequency range of operation, thickness and practicality considerations limit the transducer thickness to 2-3 mm. Therefore the contact area of the transducer is small and the alignment of the transducer becomes critical. Since our aim was to obtain a removable probe, we avoided permanent bonding of those transducers. Instead, we aligned the transducer by a three point holder and tried water, vacuum grease or medical gels for coupling material. We observed that the coupling depended critically to the coupling material, its amount and the way it was applied. In particular, water was not very useful since it failed to "wet" the contact area properly.

In the experiment we placed the transducer in the vicinity of the crack (about 1 mm near the crack edge) and near the center where the standing wave distribution for the first length resonance is at its peak. In one case we obtained the data given in Fig. 3 with a 27 mm transducer placed near an EDM notch of length 43 mm on aluminum [5]. Theoretical calculations predict a length resonance at f = 52 kHz and there is an "S" type signature on the observed response between 47-58 kHz for the transducer on the cracked plate (Fig. 3). The same kind of signature was obtained from the far field scattering experiments by P. Khuri-Yakub, et al [2] at higher frequencies. Note that the Q for this resonance is around 5.

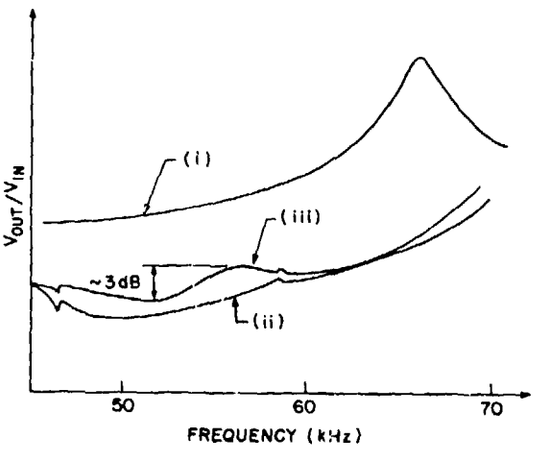

Fig. 3 Experimental results with the length expander transducer. (i) Free transducer. (ii) Transducer on the plate without the crack. (iii) Transducer on the plate with the crack.

As mentioned previously, coupling is the basic drawback of these transducers, leading to poor repeatability of the measurements. The transducer used in obtaining the data given in Fig. 3 was eventually damaged, and we were unable to repeat the results. We will continue to use these transducers in the future, using permanent bonding to eliminate the coupling problem.

The difficulties of the length expander bars led us to look for different transducer type, and we decided to use interdigital transducers with a small number of elements. We used PZT-5H or PZT-8 slabs of thicknesses in the order of 0.3-1 mm and tested several geometries shown in Fig. 4. In Fig. 4(a) we formed the transducer by depositing electrodes on the surface of the slab. Figures 4(b) and 4(c) show counterpoled and unipoled pieces that are bonded to the surface separately. The pieces are epoxy bonded to the surface of the aluminum plate. In all cases we observed that the center frequency is not determined by the separation of fingers, L_S , but rather by the width of each finger L_T . Their efficiencies are surprisingly high, and for the case of a single finger transducer, we obtained an insertion loss as low as 13 dB (including the 6 dB loss due to bidirectionality) between two such transducers. Their bandwidth is narrower than the theoretical expectations. The 15 dB bandwidth is in the order of 35%.

To detect the depth resonances of a 2-D slot, we bonded two single finger transducers on an aluminum plate whose bottom is fully covered with non-uniform grooves of depth ~ 10 mm filled with tungsten epoxy. The total plate thickness is ~ 30 mm, and the

separation between the transducers is 25 mm. We measured the transmission response between the transducers with no slot and then cut the slot, increasing the depth in 0.5 mm increments and measuring the response at each depth (Fig. 5). We

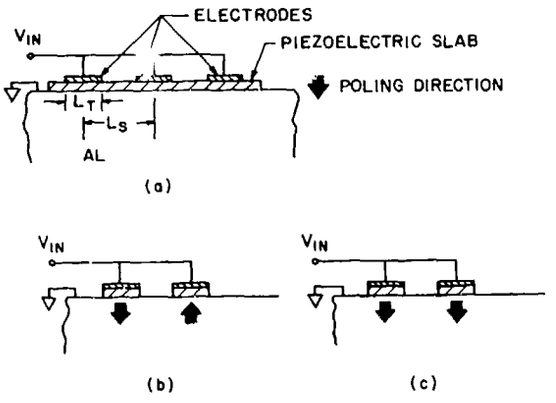

Fig. 4 Bonded interdigital transducers. (a) Single piece transducer. (b) Poled-counterpoled transducer. (c) Unipoled transducer.

were able to see the slot because of its effect on the measurements but were unable to recognize the signature of the depth resonances (if there were any). We have not tried placing transducers closer or further apart, but will do so in the future.

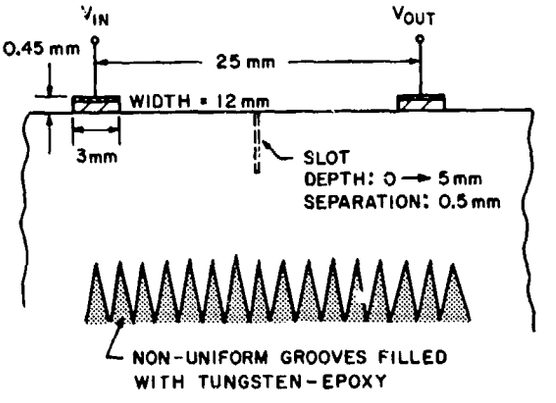

Fig. 5 Crack depth resonance measurements by single element transducer.

ANALYSIS OF ROUGH CRACKS

Consider the scattering geometry given in Fig. 6 where our aim is to calculate the contribution of the surface roughness to the scattering coefficient from transducer 1 to transducer 2. We assume that we can enclose the rough crack with a smooth open crack which is characterized by the surface S_F.

We start with the reciprocity relation [6]

$$\delta\Gamma^{(R)} = \frac{1}{4(P_1P_2)^{1/2}} \int_{S_F} (V_1:T_2 - V_2:T_1)\cdot\hat{n}\, ds \qquad (4)$$

where V_1,T_1 are the solutions in the presence of the smooth crack when power P_1 is applied to the first transducer; V_2,T_2 are the solutions in the presence of the rough crack when power P_2 is applied to the second transducer; $\hat{n}$ is the inward normal (towards the roughness) on the surface S_F; and $\delta\Gamma^{(R)}$ is the contribution of the surface roughness to the scattering coefficient.

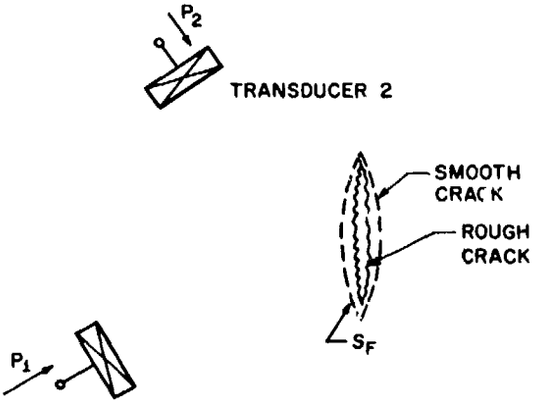

Fig. 6 Reciprocity relation geometry as applied to rough cracks.

Since $T_1 \cdot \hat{n} = 0$ on S_F, Eq. (4) becomes

$$\delta\Gamma^{(R)} = \frac{1}{4(P_1P_2)^{1/2}} \int_{S_F} V_1:T_2 \cdot \hat{n}\, ds \qquad (5)$$

In Eq. (5) V_1 is the velocity field in the presence of the smooth crack, and $T_2\cdot\hat{n}$ is the normal stress in the presence of the rough crack evaluated on the smooth crack surfaces. To evaluate $T_2\cdot\hat{n}$ we follow the analysis of Brekhovskikh [7,8] which has been successfully used to analyze the attenuation of Rayleigh waves on rough surfaces [7,9].

Consider a rough surface, S_R as shown in Fig. 7. We define a flat surface S_F under the roughness, defined by the coordinate variables r_1 and r_2, and denote the normal vectors to the flat and rough surfaces by $\hat{n}$ and $\hat{n}(r_1,r_2)$ respectively. The roughness is then defined as a function of the coordinate variables r_1,r_2,

$$r_n = f_R(r_1,r_2) \qquad (6)$$

where r_n is the coordinate variable in the direction of the normal vector $\hat{n}$. The rough surface can then be expressed by the equation

$$\psi(r_1,r_2,r_n) = r_n - f_R(r_1,r_2) = 0. \qquad (7)$$

Then the normal vector to the rough surface is simply

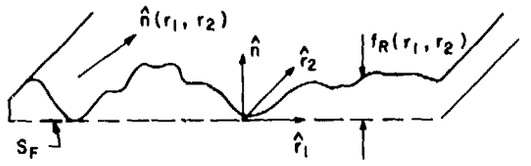

Fig. 7 Surface roughness and associated coordinate variables.

the unit vector in the direction of the gradient of the function defining the rough surface,

$$\hat{n}(r_1,r_2) = \nabla\psi/|\nabla\psi| \tag{8}$$

where

$$\nabla\psi = \hat{n} - \frac{\partial f_R}{\partial r_1}\hat{r}_1 - \frac{\partial f_R}{\partial r_2}\hat{r}_2 \tag{9}$$

and

$$|\nabla\psi| = [1 + (\partial f_R/\partial r_1)^2 + (\partial f_R/\partial r_2)^2]^{1/2}. \tag{10}$$

If

$$(\partial f_R/\partial r_i)^2 \ll 1 \quad i = 1,2 \tag{11}$$

then Eq. (8) can be approximated as

$$\hat{n}(r_1,r_2) = \hat{n} - \sum_{i=1}^{2} (\partial f_R/\partial r_i)\,\hat{r}_i. \tag{12}$$

Since the rough surface is stress free, we have

$$T \cdot \hat{n}(r_1,r_2) = 0 \quad \text{on} \quad S_R \ (r_n = f_R). \tag{13}$$

The stress field can be expressed as the sum of the unperturbed stress field and a first order perturbation, i.e.

$$T = T^{(0)} + T^{(1)} + \ldots \tag{14}$$

where

$$T^{(0)} \cdot \hat{n} = 0 \quad \text{on} \quad S_F \ (r_n = 0). \tag{15}$$

Each term in Eq. (14) is then expanded in power series in r_n. For example,

$$T^{(0)} = T^{(0)}(r_n = 0) + r_n\,\partial T^{(0)}/\partial r_n(r_n = 0) + \ldots \tag{16}$$

Substitution of Eq. (16) into Eq. (14) gives

$$T = T^{(0)}(r_n = 0) + T^{(1)}(r_n = 0) + r_n[\partial T^{(0)}/\partial r_n](r_n = 0) + \ldots \tag{17}$$

Further substitution of Eqs. (17) and (12) into (13), keeping only the first order terms, yields

$$T \cdot \hat{n}(r_1,r_2)\Big|_{S_R} = T^{(1)} \cdot \hat{n}\Big|_{S_F} + f_R[\partial T^{(0)}/\partial r_n] \cdot \hat{n}\Big|_{S_F} - \sum_{i=1}^{2} (\partial f_R/\partial r_i) \cdot T^{(0)} \cdot \hat{r}_i \Big|_{S_F} + \ldots = 0 \tag{18}$$

where we have also used Eq. (15). This leads, within the accuracy of first order perturbation theory, to replacement of the actual boundary condition [Eq. (13)] on the rough surface by an equivalent boundary condition

$$T^{(1)} \cdot \hat{n}\Big|_{S_F} = \{- f_R[\partial T(0) \cdot \hat{n}/\partial r_n] + \sum_{i=1}^{2} (\partial f_R/\partial r_i) T^{(0)} \cdot \hat{r}_i\}\Big|_{S_F} \tag{19}$$

on the flat surface S_F. Note that the left-hand side of Eq. (19) is the quantity required to evaluate the reciprocity integral given in Eq. (5).

One implication of Eq. (19) and Eq. (5) is that the effects of the roughness on different faces of the crack are different. Noting that V_1 in Eq. (5) is the total unperturbed field, the fields on the shadowed face of the crack are less than those on the illuminated face. Since T_2 is related to the roughness function f_R via Eq. (19), the roughness on the illuminated face has more effect on the scattering coefficient than that on the shadowed face.

Example – We chose the simple example of scattering of SH waves from a rough surface (Fig. 8). We assume plane wave incidence at an angle θ and receive the signal at an angle φ, using an infinitely wide transducer.

In free space the SH wave components are

$$V_x = V_0\, e^{-ik_0 \sin\alpha y}\, e^{-ik_0 \cos\alpha z} \tag{20}$$

$$T_{xz} = -\frac{2P_0}{V_0} \cos\alpha\, e^{-ik_0 \sin\alpha y}\, e^{-ik_0 \cos\alpha z} \tag{21}$$

$$T_{xy} = -\frac{2P_0}{V_0} \sin\alpha\, e^{-ik_0 \sin\alpha y}\, e^{-ik_0 \cos\alpha z} \tag{22}$$

where α is the angle of propagation and P_0 is the power per unit length along the angle α.

The unperturbed fields for the problem are the total fields after reflection from the smooth surface S_F, i.e.

$$V_x^{(0)} = 2V_0\, e^{-ik_0 \sin\alpha y} \cos(k_0 \cos\alpha z) \tag{23}$$

$$T_{xz}^{(0)} = i\frac{4P_0}{V_0} \cos\alpha\, e^{-ik_0 \sin\alpha y} \sin(k_0 \cos\alpha z) \tag{24}$$

$$T_{xy}^{(0)} = -\frac{4P_0}{V_0} \sin\alpha\, e^{-ik_0 \sin\alpha y} \cos(k_0 \cos\alpha z) \tag{25}$$

where $\alpha = \theta$ or φ for the two waves shown in the figure. Assuming a one dimensional roughness function $f_R(y)$ and applying Brekhovskikh formula

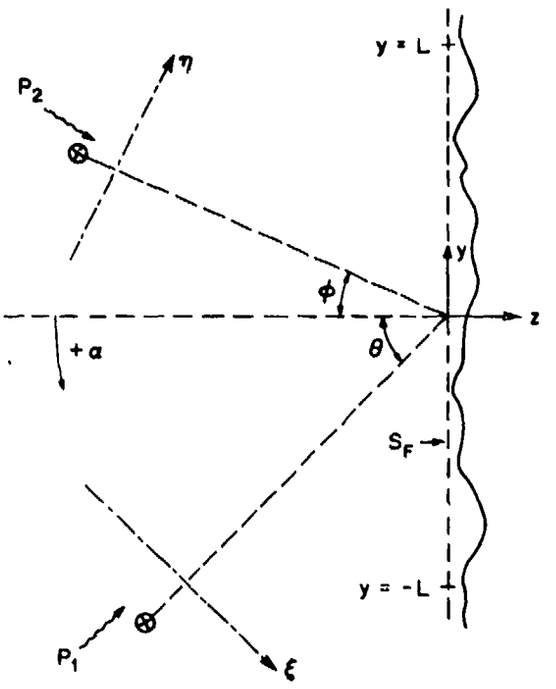

Fig. 8 Scattering of SH waves from rough surfaces.

[Eq. (19)], we find

$$T_{xz}^{(1)}\Big|_{S_F} = \left\{ - f_R(y) \frac{\partial T_{xz}^{(0)}}{\partial z} + \frac{df_R(y)}{dy} T_{xy}^{(0)} \right\}_{z=0}$$

$$= \frac{4P_0}{V_0} e^{-ik_0 \sin\varphi y} \times \left\{ - ik_0 \cos^2\varphi f_R - \frac{df_R}{dy} \sin\varphi \right\}. \quad (26)$$

Substituting Eq. (23) with $\alpha = \theta$ and Eq. (26) into Eq. (5), and assuming periodic boundary conditions along y, we obtain

$$\delta\Gamma^{(R)} = \lim_{L\to\infty} \frac{1}{4(P_1P_2)^{1/2}} \int_{-L}^{L} 8P_0 \times \left\{ - ik_0 \cos^2\varphi f_R - \sin\varphi \frac{df_R}{dy} \right\} \times e^{-ik_0(\sin\theta + \sin\varphi)y} dy. \quad (27)$$

Note that P_1 and P_2 are the acoustic power flow along θ and φ directions respectively (see Fig. 8)

$$P_1 = \int P_0 d\xi \quad \text{and} \quad P_2 = \int P_0 d\eta \quad (28)$$

or

$$P_1 = P_0 \cos\theta \int dy$$

and (29)

$$P_2 = P_0 \cos\varphi \int dy$$

Equation (27) therefore reduces to

$$\delta\Gamma^{(R)} = - \frac{2}{(\cos\theta \cos\varphi)^{1/2}} \lim_{L\to\infty} \frac{1}{2L} \int_{-L}^{L} \times \left\{ ik_0 \cos^2\varphi f_R + \sin\varphi \frac{df_R}{dy} \right\} \times e^{-ik_0(\sin\theta + \sin\varphi)y} dy. \quad (30)$$

In Eq. (30) the limit arises because excitation and reception are with infinitely wide transducers and the roughness of the surface extends to infinity. We identify the exponential term inside the integral as the Fourier transform kernel. Neglecting the difficulties associated with f_R (the total "power" of f_R is infinite), one obtains

$$\delta\Gamma^{(R)} = - 2ik_0 \frac{1 + \sin\theta \sin\varphi}{(\cos\theta \cos\varphi)^{1/2}} \Im\{f_R\} \quad (31)$$

where the Fourier transform variable is

$$k = k_0(\sin\theta + \sin\varphi) \quad (32)$$

and we have used the relation

$$\Im\left\{\frac{df}{dy}\right\} = ik\Im\{f\}. \quad (33)$$

As a check, consider the case when $f_R = f_0$ (constant). This corresponds simply to a shift on coordinate axis z by an amount f_0. Then Eq. (31) says that the scattered field is in the $\varphi = -\theta$ direction, and its value is

$$\delta\Gamma^{(R)} = - i2k_0 f_0 \cos\theta. \quad (34)$$

This is the additional phase shift introduced by the path length difference $2f_0 \cos\theta$ due to the layer of thickness f_0.

If $f_R(y)$ is periodic, i.e.

$$f_R(y) = f_0(1 + \cos k_R y) \quad (35)$$

then in addition to the specular reflection component, there are two other components at angles φ satisfying the relation

$$\sin\varphi = - \sin\theta \pm \frac{k_R}{k_0}. \quad (36)$$

In general, the roughness function $f_R(y)$ is unknown. Therefore it is preferable to take it as a stochastic process and examine the statistics of the scattering coefficient. The first moment (expected

value or mean value) of the scattering coefficient gives simply

$$E\{\delta\Gamma^{(R)}\} = -2k_0 A(\theta,\varphi)\Im\{E\{f_R\}\} \qquad (37)$$

where we have lumped the angle dependence into an angle factor, i.e.

$$A(\theta,\varphi) = \frac{1 + \sin\theta \sin\varphi}{(\cos\theta \cos\varphi)^{1/2}} \cdot \qquad (38)$$

If f_R is an ergodic process (i.e., statistics of the whole ensemble of roughness functions can be determined by examining a single member), then

$$E\{f_R\} = \text{spatial average of } f_R = \bar{z}_0 \qquad (39)$$

and the expected value of $\delta\Gamma^{(R)}$ is simply a phase shift due to the mean value of f_R. For the second moment we have

$$E\{\delta\Gamma^{(R)}\delta\Gamma^{(R)*}\} = 4k_0^2 A^2(\theta,\varphi) S_f \qquad (40)$$

where S_f is the power spectrum (Fourier transform of the autocorrelation function) of the roughness function f_R. The variance of the scattering coefficient is then

$$\text{Var}(\delta\Gamma) = [E\{\delta\Gamma^{(R)}\delta\Gamma^{(R)*}\} - E^2\{\delta\Gamma^{(R)}\}]^{1/2}. \qquad (41)$$

The implications of Eqs. (37) and (41) are the following:

When a scattering measurement is made, the results are obscured by the effect of roughness. If one tests N different rough samples for which the statistics can be determined by examining a single member (ergodicity), the average of the measurements is simply a phase shift due to the mean value of the roughness functions. For any measurement, the measure of the deviation from the ideal value (no roughness case) is related to the variance of the "noise" (contribution of the roughness) which is expressed in Eq. (41). In other words, any measurement value contains an uncertainty for which the measure is the variance.

For instance, if one is making angular scattering measurements in the high k_a regime, one obtains a scattering pattern which can be approximated as [3,10]

$$\Gamma^{(C)} \propto \frac{\sin x}{x}, \quad x = 2\pi \frac{L}{\lambda} \sin\theta$$

and the nulls can be used to determine the length L of the crack. In the presence of the roughness

$$\Gamma = \Gamma^{(0)} + \Gamma^{(R)}$$

and the uncertainty imposed by the roughness will introduce an uncertainty in the position of the nulls.

In the case of resonance measurements, the effect of roughness is attenuating the crack modes that travel along the depth and the length of the crack. Although the resonance frequencies do not change, the Q of the resonances decreases due to the attenuation caused by the roughness. Since these resonances are low Q in nature, the effect of the roughness will either be increasing the uncertainty in determining the center frequency or wiping them off at all.

ACKNOWLEDGEMENTS

The authors wish to thank Dr. P. Khuri-Yakub for his help and suggestions on various parts of this study.

This work was supported by the Center for Advanced NDE operated by the Science Center, Rockwell International, for the Defense Advanced Research Projects Agency and the Air Force Wright Aeronautical Laboratories under Contract No. F33615-80-C-5004.

REFERENCES

[1] S. Ayter and B. A. Auld, "On the Resonances of Surface Breaking Cracks," Presented at the Review of Progress in Quantitative NDE, La Jolla, 1979.

[2] V. Domarkas, B. T. Khuri-Yakub, and G. S. Kino, "Length and Depth Resonances of Surface Cracks and Their Use for Crack Size Estimation," Appl. Phys. Lett. 33, 7, 557-559 (October 1978).

[3] B. R. Tittmann, M. de Billy, F. Cohen-Tenoudji, A. Jungman, and G. Quentin, "Measurement of Angular and Frequency Dependence of Acoustic Surface Wave Scattering From Surface Cracks," Proceedings of the IEEE Ultrasonics Symposium, 78CH 1344-1SU, 379-383 (1978).

[4] W. H. Robinson and A. Edgar, "The Piezoelectric Method of Determining Mechanical Damping at Frequencies of 30 to 200 kHz," IEEE Transactions on Sonics and Ultrasonics SU-21, 98-105 (April 1974).

[5] Aluminum sample – courtesy of B. R. Tittmann, Rockwell Science Center.

[6] B. A. Auld, "General Electromechanical Reciprocity Relations Applied to the Calculation of Elastic Wave Scattering Coefficients," Wave Motion 1, 3-10 (1979).

[7] L. M. Brekhovskikh, "Propagation of Surface Rayleigh Waves Along the Uneven Boundary of an Elastic Body," Soviet Physical Acoustics 5, 288-295 (1959).

[8] B. A. Auld, Acoustic Fields and Waves in Solids, II (New York: Wiley-Interscience, 1973), 309-310.

[9] P. V. H. Sabine, "Rayleigh-Wave Propagation on a Periodically Roughened Surface," Electronic Letters 6, 149-151 (1970).

[10] B. A. Auld, S. Ayter, and M. Tan, "Theory of Scattering of Rayleigh Waves by Surface Breaking Cracks," Proceedings of the IEEE Ultrasonics Symposium, 78CH 1233-1SU, 384-390 (1978).

Bernie Tittmann, Chairman (Rockwell Science Center): We have time for one or two questions.

Gerald Quentin (University of Paris): I think it is quite interesting to work with reciprocity because we can carry out calculations, but there is a problem left with this sphere as it applies only for small slots on the surface. You give the expression that the roughness cannot vary very much with the distance on the surface. And the problem is that you just apply the theory. For example, when we made the experiments with Laszlo Adler on fracture cracks, even at the opening of the crack the slope is quite large.

Sevig Ayter (Stanford University): The theory applies so long as the roughness function - this is the roughness function - so long as the roughness function is small.

Laszlo Adler (Ohio State University): That's what he was saying.

Sevig Ayter: As a perturbation, the roughness function must be small, and also the --

Gerald Quentin: Which is the slope? It almost has to be equal to the angle with the normal.

Sevig Ayter: I don't quite get the implication of your remark.

J.D. Achenbach (Northwestern University): In what you have drawn there, you need a much more gradual slope. Even at this small slope, you would need a small roughness function as well.

Bert Auld (Stanford University): I wanted to make a comment there. I think the approximation there is not the derivative estimate. But the square is small, and I think if you go to second order you can push that up further and you can actually modify the Brekhovskikh theory.

Bernie Tittmann, Chairman: Thank you. We will now have to go on.

ELASTIC WAVE SCATTERING FROM GRIFFITH CRACKS

Kent Lewis
Dale Fitting
Laszlo Adler
Dept. of Welding Engineering
Ohio State University

ABSTRACT

To model elastic wave scattering from fatigue cracks in metals, studies were conducted of wave scattering from artificial cracks using ultrasonic spectroscopy. The cracks are of two dimensional planar strips oriented at various angles and embedded in diffusion bonded titanium alloy. The crack is assumed to behave as a Griffith crack and expressions (derived by Achenbach[1]) to describe diffracted field of elastic waves are used to analyze experimental results.

THEORY

A plane longitudinal wave is incident upon a Griffith crack of length 2d as shown on figure 1.

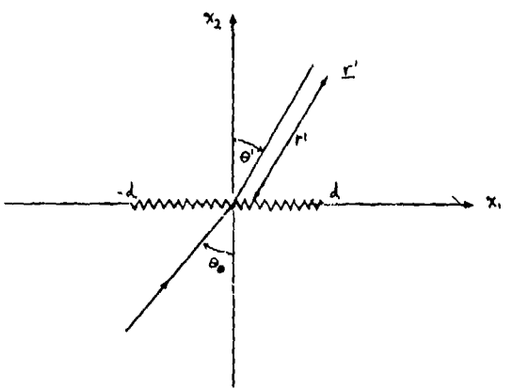

Fig. 1 Coordinate system

The amplitude of the diffracted wave in the far field has been calculated by Achenbach[1] by using an integral representation theorem[2] as

$$u_k^s(r^1) = -\int ds_j(r)\Delta u_i(r)\tau^G_{ij,k}(r^1-r) \qquad (1)$$

where the integration is over the line segment that coincides with the undisturbed crack. In this representation the displacement discontinuity is given as

$$\Delta u_i(r) = u_i(x_1,0^+) - u_i(x_1,0^-) \qquad (2)$$

and $\tau^G_{ij,k}$ are the i,j stress components of the fundamental singular solutions for an unbounded medium. With the assumption that the displacements on the upper half-plane is approximately zero and at the lower half is similar to those corresponding to the reflection of plane waves, the displacement field is obtained. The result has been evaluated for a 500μ length Griffith crack in titanium alloy for an incident 10MHz longitudinal wave and for angle Θ_o=0.

On figure 2, the diffracted amplitude's angular distribution shows a symmetrical diffraction pattern.

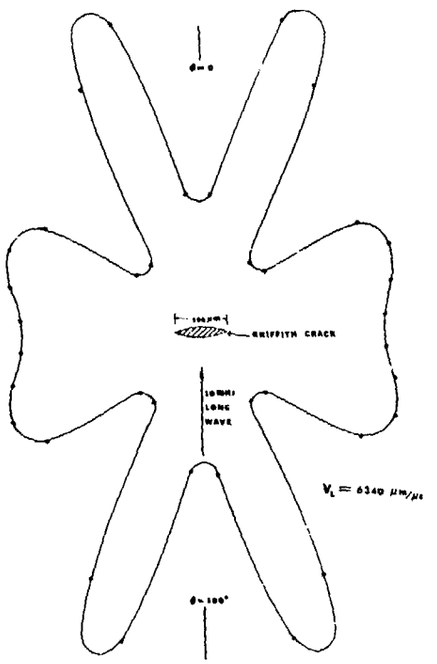

Fig. 2 Diffraction pattern of a 10MHz L-wave by a 500μm Griffith crack in Titanium

EXPERIMENT

Experimental System

The present configuration of the ultrasonic spectroscopy data acquisition and processing is illustrated on figure 3. A fast rise-time pulser produces a high-voltage spike. This wide band electrical pulse excites an untuned highly damped ceramic transducer. The ultrasonic pulse which is

produced contains a broad band of frequencies (figure 4).

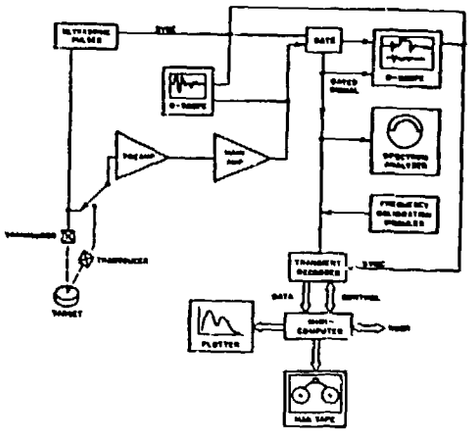

Fig. 3 Experimental system.

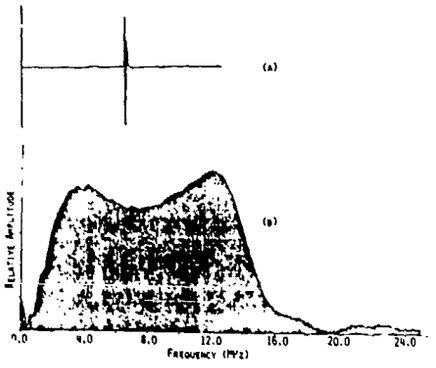

Fig. 4 Transducer output A. Time domain
B. Spectrum.

Ultrasound scattered by the defect is received by either (1) the transmitting transducer (pulse-echo) or (2) a separate receiving transducer (pitch-catch). A goniometer provides precise yet flexible positioning of the transducers for immersion testing. The electrical pulse produced by the receiver is amplified by wide bandwidth gain stage. A stepless gate is used to select a portion of the received signal for further analysis. The receiver output as well as the gated waveform is displayed on an oscilliscope.

The frequency content of the gated waveform is presented on an analog spectrum analyzer. The gated pulse may also be captured and stored through the use of one of two digital data acquisition systems. One system utilizes a high-speed transient recorder to store the signal amplitude at discrete times in its digital memory. A minicomputer controls the acquisition of the ultrasonic pulse and then transfers the digitally represented signal from the recorder to the minicomputer memory. The information may also be permanently stored by recording it onto a magnetic disk. The second data acquisition system is a microcomputer controlled, high resolution, high sample rate, equivalent time device with a 'real-time' spectral display. Sampled signal information is stored on magnetic tape.

Processing of the ultrasonic signal (Fast Fourier Transformation, correlation and deconvolution) is performed on the minicomputer. A graphics terminal provides displays of the spectra and other pertinent information.

SAMPLES

The "Griffith" cracks are fabricated into a diffusion bonded titanium alloy by Rockwell Science Center. The length of the crack is 2388μm. Four cracks were obtained of the same length but with orientations of 0°, 30°, 60°, and 90° relative to the surface of the sample. A schematic of the sample is shown on figure 5.

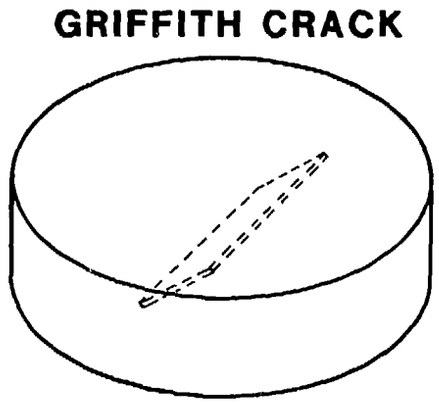

Fig. 5 Griffith crack inside a Titanium disk

RESULTS

Spectra at several scattered angles of a normally incident (to the surface of the sample) L-wave are shown on figure 6.

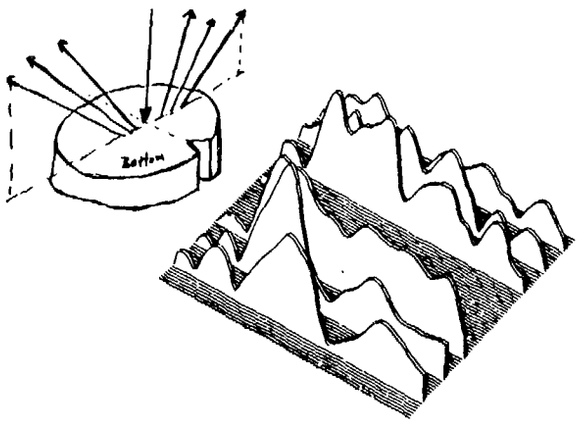

Fig. 6 Experimental amplitude spectra of scattered L-waves at 15° intervals for an incident wave from the bottom.

The Griffith crack is oriented 60° from the surface of the sample. The scattered angles (measured in the titanium alloy) are in 15° intervals. There is an asymmetry in the spectrum because of the tilted cracks. For a crack where the plane is parallel with the sample surface the scattered spectra is symmetrical. Sending the wave from the top surface (rather than from the bottom surface as shown on figure 6) produces the scattered spectra shown on figure 7.

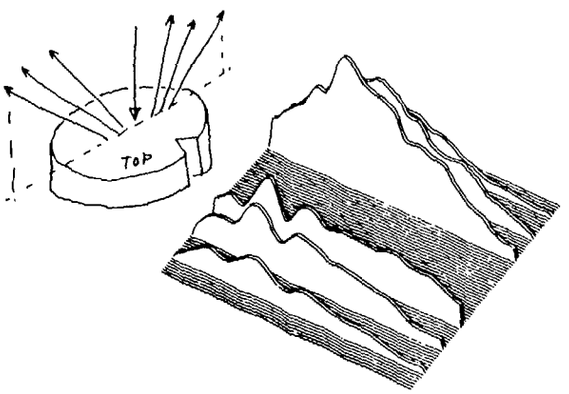

Fig. 7 Experimental amplitude spectra of scattered L-waves at 15° intervals for an incident wave from the top.

The experimentally observed amplitude spectrum is compared to calculate values of the scattered amplitude as a function of frequency. On figure 8A, the orientation of the Griffith crack is shown. The pulse-echo R.F. signal is shown on figure 8B. The experimentally obtained amplitude spectrum (by Fourier analyzing the time domain signal, figure 8B) is compared favorably to the theoretical value of the amplitude spectrum (figure 8C). The comparison between theory and experiment is rather poor for the case when the wave scatters along the surface of the Griffith crack (figure 9). Clearly, the theoretical calculation has to include surface wave generation in this case. The agreement between experiment and theory is reasonably good however, for the angular distribution of the scattered amplitude for a 10 MHz L-wave incident at 150° as shown on figure 10. Due to the geometry of the sample only a limited number of data points were taken.

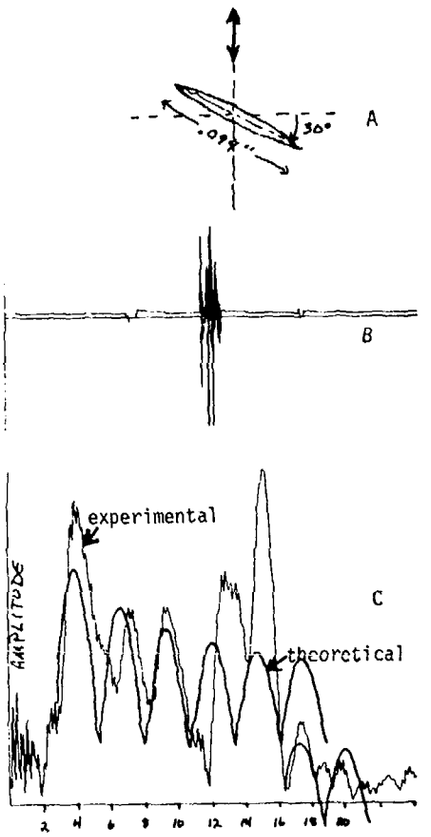

Fig. 8 A. Orientation of the Griffith crack.
B. Scattered time domain signal.
C. Comparison of experimental and theoretical amplitude spectra.

ACKNOWLEDGMENTS

This research paper is sponsored by the Center for Advanced N.D.E., operated by the Science Center, Rockwell International for DARPA and AFML.

REFERENCES

1. Achenbach, F. D. unpublished.

2. Achenbach, F. D. Wave propagation in Elastic Solids. North Holland Publishing Co. Amsterdam, 1973.

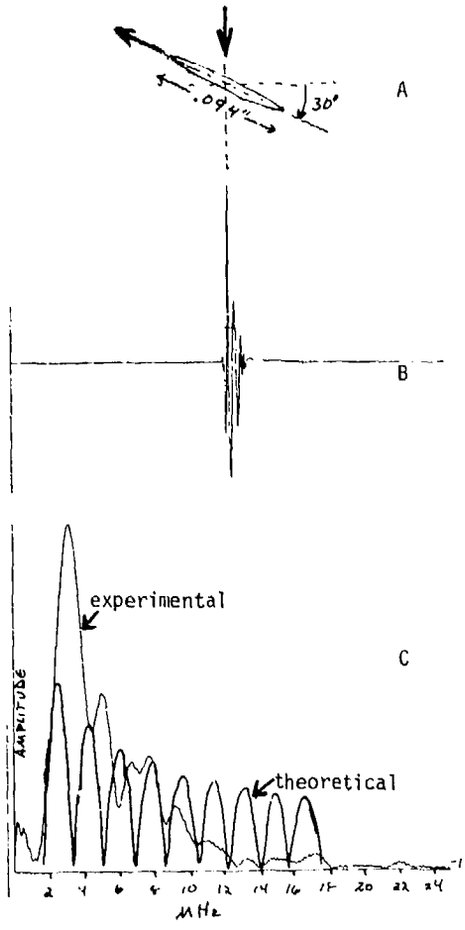

Fig. 9 A. Orientation of the Griffith crack.
B. Scattered time domain signal.
C. Comparison of experimental and theoretical amplitude spectrum.

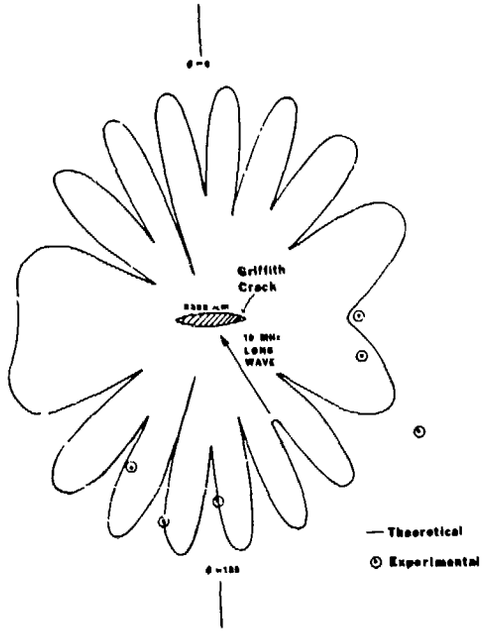

Fig. 10 Comparison between experimental and theoretical angular diffraction patterns.

ABOUT THE EFFICIENCY OF USING "EXTENDED" FOURIER TRANSFORMS FOR SURFACE CHARACTERIZATION BY THE DECONVOLUTION TECHNIQUE

F. Cohen-Tenoudji and G. Quentin
Groups de Physique des Solides, Universite Paris 7,
75221 Paris Cedex 05, France

ABSTRACT

Deconvolution of echoes scattered by a surface tends to give the response function to a Dirac pulse incident on the surface. In some cases, this response function is easily related to the geometry of the scatterer and could be used to characterize it.

In practical, the situation of the Dirac pulse with infinite bandwidth is not realized even by a broad band transducer which acts as a band-pass filter.

We propose here some simple arguments to extend the Fourier spectrum in order to improve the results of deconvolution. Experiments are performed with targets consisting either of small plane surfaces of various shapes or of randomly rough surfaces. Results are in good agreement with those expected using the Kichhoff-Helmholtz integral.

INTRODUCTION

The signal reflected by a surface insonified by a very short ultrasonic pulse contains, in a rather large range of frequencies, information on the scattering properties of the surface. The study of the variation of the scattered signal with frequency can be used to characterize the targets as, for example, defects in metals.[1,2] Indeed, when the dimensions of the target are of the same order of magnitude as the wavelengths of the ultrasonic waves, the scattered signal obeying the diffraction laws is a highly varying function of frequency of which one can infer some dimensions of the scatterer (lengths are estimated within few percent). The targets are generally small and in the far field of the transducers in order that the plane wave approximation can be valid.

The analysis of echoes in the time domain is related to imaging techniques[3] and pulse echo methods are used to get the size of cracks. The methods generally used are high frequency techniques.[4,5] For instance, it was shown by Lloyd[4] who used the Freedman[6] theory on the mechanism of echo formation that one echo signal is generated each time the ultrasonic pulse is incident on a part of the scattering object where a discontinuity appears in the solid angle under which the transducer sees the scattering object. This formulation gives excellent results at high frequencies, when the dimensions of the scattering object are much greater than the ultrasonic wavelength so that the echoes coming from different discontinuities are well separated in the time domain.

Deconvolution of echoes tends to extract information of the whole frequency axis in a given experiment. The method was proposed by Haines and Langston[7] for surface characterization. It tends to recreate the situation where the incident pulse is a Dirac pulse and where the transfer function of the transducers and of the electronic equipment is a constant.

But even broad band transducers delivering band-limiting signals cannot give information on the total frequency axis; it therefore follows that the result of the deconvolution operation can be strongly affected by spurious oscillations. We proposed here to complement the frequency range by extrapolation of the Fourier amplitude toward zero frequency and, moreover, to extend it toward high frequencies by connection of the Fourier complex amplitude of the signal given by a first transducer to that given by a second transducer; the latter working in a higher but connected frequency range than the former.

The technique proposed here is applied to plane targets and to rough surfaces immersed in water.

THEORY

Plane Targets

We first assume that the incident wave can be approximated by a plane wave (experimentally we use a small target placed in the far field of the transducer).

Using the formulation of Neubauer[8] and Johnson[9] of Kirchhoff approximation, the pressure backscattered by a rigid surface A is:

$$p_r(k) = \frac{kB i\alpha}{2\pi} \iint_A R(\theta) \cos\theta \exp(-2ikz)\, da \qquad (1)$$

where α is a phase factor depending on the choice of coordinates, B is a coefficient including the variation of the amplitude spectrum of the incident wave with frequency; da is an elementary area of the scattering surface with z the position of the element da along the axis of propagation of ultrasound Oz; θ is the angle of incidence on the element da; $R(\theta)$ is the reflection coefficient for the angle θ. For a smooth plane target and angle θ is constant and the expression becomes:

$$p_r(k) = \frac{R(\theta) i\alpha kB \cos\theta}{2\pi} \iint_A \exp(-2ikz)\, da \quad . \qquad (2)$$

We can normalize to the value $p_{rO}(k)$ obtained at normal incidence for a calibrated surface A_{cal} placed at the position z_0

$$p_{ro}(k) = \frac{R(0)\,i\alpha k\beta}{2\pi} A_{cal} \exp(-2ikz_o) \qquad (3)$$

it comes:

$$p_r(k)/P_{ro}(k) = \frac{\beta R(\theta)\cos\theta}{A_{cal} R(0)} \iint_A \exp(-2ikz)\, da \quad . \qquad (4)$$

$\beta = \exp(2ikz_o)$ is a pure phase factor depending on the choice of the origin of coordinates.

For a plane surface A tilted by an angle θ with respect to the ultrasonic beam axis, we choose the axis of coordinates Ox' and Oy in the plane of the surface (Fig. 1).

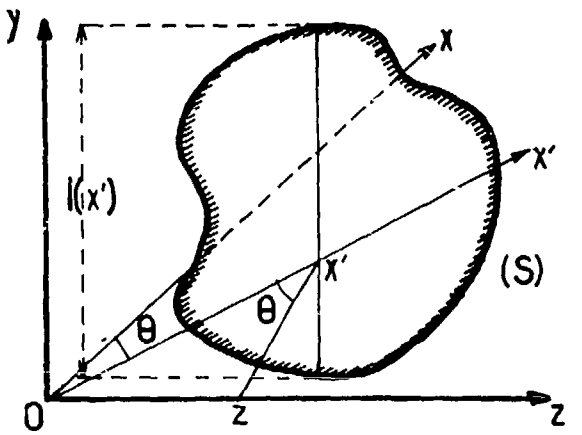

Fig. 1 Scattering geometry.

$x' = z/\sin\theta \qquad da = dx'dy = dy\,dz/\sin\theta$

The integration for the variable y is straightforward and leads to

$$F(k) = \frac{P_r(k)}{P_{ro}(k)} = \frac{\beta R(\theta)}{A_{cal} R(0) tg\theta} \int_{z_1}^{z_2} l(x') \exp(-2ikz)\, dz. \qquad (5)$$

$l(x')$ is the length of the surface at abscissa x' located at position $z = x' \sin\theta$ along the direction of propagation.

Instead of using the space variables, one can use time and frequency[7] by writing $t = 2z/c$; t is the time taken by the wave to make twice the distance between the origin of coordinates and the height z. So that F(k) becomes:

$$F(f) = \frac{c\, R(\theta)\, \beta}{2A_{cal} R(0) tg\theta} \int_{t_1}^{t_2} l\left(\frac{ct}{2}\right) \exp(-2i\pi ft)\, dt. \qquad (6)$$

The complex value of F(f) appears to be proportional to the Fourier transform of the length $l(ct/2)$ of the strip of the surface insonified by the wave at time t/2. It is, in principle, possible to evaluate the shape of the scatterer by obtaining $l(ct/2)$ making an inverse Fourier transform of (f):

$$l\left(\frac{ct}{2}\right) = \frac{2R(0)A_{cal} tg\theta}{c\, R(0)\, \beta} \int_{-\infty}^{+\infty} F(f) \exp(2i\pi ft)\, df. \qquad (7)$$

This inversion supposes that F(f) is known on the total frequency axis; real ultrasonic equipments are band limited so that if one uses instead of F(f) a restriction $F_1(f)$ of F(f) to a band (f_1, f_2), it may appear on the result of the deconvolution spurious oscillations which distort the signal, the period of these oscillations depending on the boundaries f_1 and f_2 (Appendix A). For example, we have simulated on a computer, the effect of the band limitation when the initial signal is a square (duration 830 nanoseconds).

The Fourier transform of this signal is well known to be of the form $(\sin x)/x$. We shall assume the bandwidth of the equipment used to that of a square bandpass filter which cuts off the $(\sin x)/x$ function. Figure 2a shows the result of the inverse Fourier transform for a bandwidth extending from $f_1 = 0.55$ MHz to $f_2 = 3.08$ MHz. The ratio $f_2/f_1 = 5.6$ is approximately that of a commercially available PZT transducer used in the far field region. Two main features can be seen on this graph:

1. The signal has a zero mean value.
2. Spurious oscillations occur.

The zero mean value is a direct consequence that in the frequency domain the value of $F_1(f)$ is zero at zero frequency. The oscillation has a period corresponding to the cutoff frequency f_1 of the filter. We can improve the result by simulating the use of the reunion of the bandwidths of two transducers 0.7 - 3 MHz, 3 - 16.5 MHz. The two edges of the square are more clearly seen owing to the presence of high frequencies in the band, but there is still the slow oscillation due to the low frequncy cutoff (Fig. 2b).

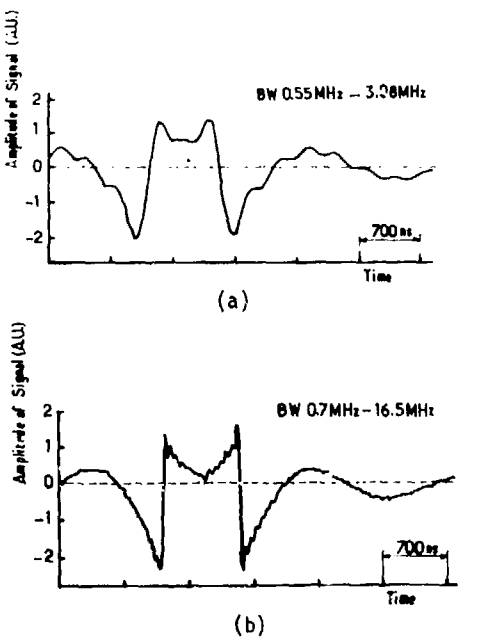

Fig. 2 Computer simulation of the result of band limitation on a reconstruction of a square signal.
a. Bandwidth 0.55 - 3.08 MHz.
b. Bandwidth 0.7 - 16.5 MHz.

Under certain approximations, it is possible to calculate the behavior of the frequency spectrum in the low frequency region. Formula (6) can be written:

$$F(f) = \frac{c\,R(\theta)}{2A_{cal}R(0)tg\theta}\int_{t_1}^{t_2} 1(ct/2)\exp[-2i\pi f(t-t_0)]dt, \quad (8)$$

$t_1/2$ and $t_2/2$ are the times where the wavefront reaches the two extreme edges of the target. The first minimum of the function $|F(f)|$ is generally obtained for a frequency of the order of $f_0 = 1/(t_2-t_1)$. If the lower limit of the band f_1 is less than f_0, for example $f_1 = f_0/2$, the function $F(f)$ will be monotonic for $f < f_1$, and we can use a polynomial expansion of $F(f)$.

Indeed, if we expand in a series the exponential in (8) and if we limit the expansion to the first three terms, when $2\pi f(t-t_0) \ll 1$, it comes:

$$F(f) \simeq D\int_{t_1}^{t_2} 1(ct/2)[1-2i\pi f(t-t_0) -2\pi^2f^2(t-t_0)^2]\,dt$$

$$\simeq D[\int_{t_1}^{t_2} 1(ct/2)dt-2i\pi f\int_{t_1}^{t_2} 1(ct/2)(t-t_0)dt -2\pi^2f^2\int_{t_1}^{t_2} 1(ct/2)(t-t_0)^2dt]+ \ldots \quad (9)$$

with

$$D = \frac{c\,R(\theta)}{2A_{cal}R(0)tg\theta} \quad ;$$

t_0, the time position of the reference surface can be chosen; we will take it so that the second integral in the bracket vanishes; Eq. (9) becomes:

$$F(f) \simeq D[\int_{t_1}^{t_2} 1(ct/2)dt-2\pi^2f^2\int_{t_1}^{t_2} 1(ct/2)(t-t_0)^2dt]. \quad (10)$$

It appears on the last equation that the frequency spectrum is real in the low frequency limit and varies paravolically. We can use this result to reconstruct the low frequency content on a real frequency spectrum. In order to do this we connect the lowest frequency point of the experimental spectrum $F(f_1)$ to the value:

$$F(f = 0) = \frac{R(\theta)\cos\theta\,A}{R(0)A_{cal}}$$

which is known if θ and the area A are known; the area A can be determined by evaluating at normal incidence the ratio of the scattered pressure by surface A to that scattered by the calibration surface A_{cal}. We will connect these two known values by a parabola. The validity of the approximatino depends on the lowest frequency experimentally available and on the length of the surface in the direction of the ultrasonic beam; the following inequality should be verified:

$$2\pi f(t-t_0) \simeq \frac{2\pi Lf\sin\theta}{c} = 2\pi\frac{L}{\lambda}\sin\theta \ll 1$$

where L is the maximum length of the surface along Ox'. The condition being less stringent for a surface with an axis of symmetry along Oy for which the first term ignored proportional to f^3 is zero. This extrapolation toward low frequencies has been made on the spectra corresponding to those of Fig. 2. The results are plotted on Fig. 3a and 3b.

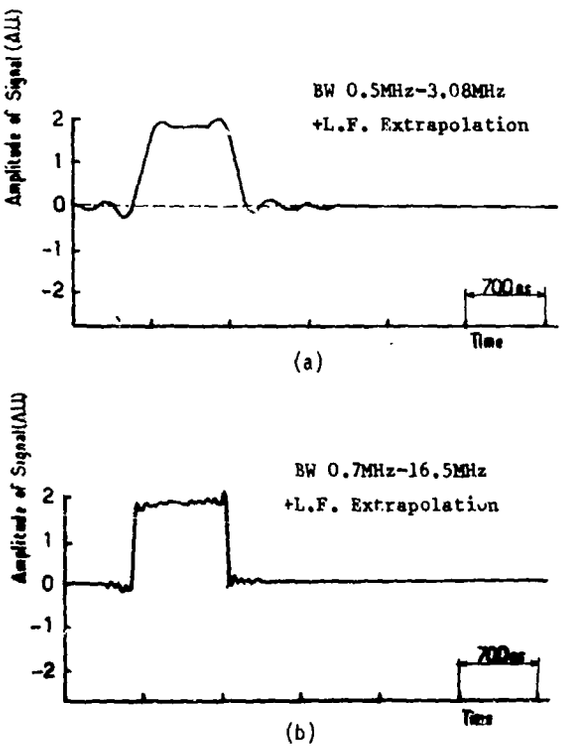

Fig. 3 Improvement of result by low frequency extrapolation.
a. BW 0.5 - 3.08 MHz
b. BW 0.7 - 16.5 MHz

Figure 3a corresponds to the narrower bandwidth of Fig. 2a; the mean value is no longer zero but it is the exact mean value of the signal; the square shape is only distorted by the highest frequency cutoff of the equipment (assumed to be 3 MHz). In Fig. 3b, the square shape of the target is very closely reproduced in the time domain; the only remaining defect is the small spurius oscillation at the highest cutoff frequency (16.5 MHz).

These computer simulations show the usefulness to complement the spectrum for a good restitution of shapes. An important point is to reconstruct a good phase function. Indeed, when one connects the results of two transducers, if the origins of time are not the same in the two experiments, it can appear a phase factor difference between the two Fourier amplitude that could cause, if not corrected, an inadequate final result. Likewise, the phase must be continuous between the low frequency extrapolation and the experimental spectrum. If this last condition is not fulfilled, deformation of the signal may occur (Fig. 4).

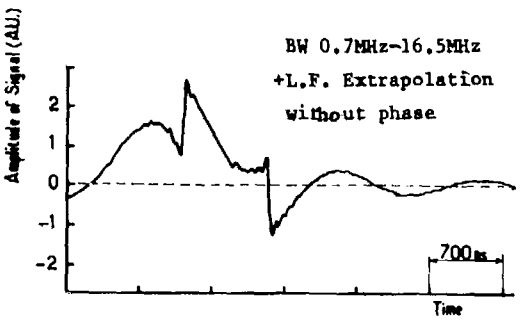

Fig. 4 Effect of a discontinuity in the phase function at the low frequency limit.

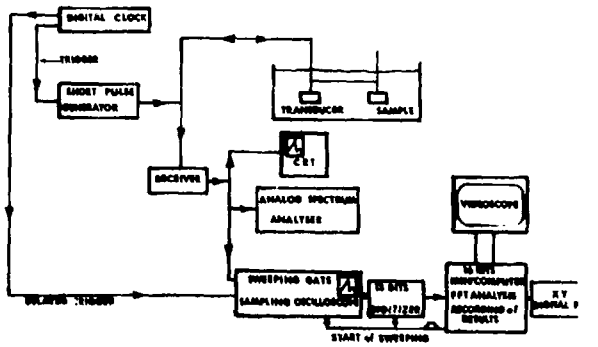

Fig. 5 Experimental equipment.

Rough Surfaces

The method described above can also be applied to the study of randomly rough surfaces. Clay and Medwin[10] have shown that the probability function of heights can be evaluated from backscattered signals at normal incidence. At a given frequency f, the ratio F(f) of the pressure scattered from the rough surface to the pressure reflected by a plane smooth surface is:

$$F(f) = \int_{-\infty}^{+\infty} W(z)\, \exp(-2ikz)\, dz \quad . \qquad (11)$$

W(z) is the probability density function of heights of the rough surface. By the same transformation as in plane targets, $t = 2z/c$, W(z) appears to be proportional to the inverse Fourier transform of the normalized backscattered signal F(f). So in principle, the application of the deconvolution of extended Fourier domain signals described before leads to an evaluation of the function W(z).

EXPERIMENTAL PROCEDURE

A block diagram of the experimental equipment is given in Fig. 5. The transducer is a highly damped PZT ceramic. It is excited by a very short electrical pulse. The echo backscattered from the surface of the sample is in parallel analyzed by a classical spectrum analyzer and fed to a sampling scope. The output signal is then digitized and sent to a minicomputer PDP 11-03 where the final signal processing is achieved. A 1024 points integer FFT algorithm is used for this process. The backscattered signal is first divided by the reference signal (reflected by a small plane located at the same distance of the transducer). The results obtained with two wide-band transducers exhibiting adjacent bandwidth are connected together and the extrapolation towards lower frequencies is performed. Then the inverse Fourier transform of the frequency domain signal obtained is computed and plotted.

In order to realize approximate plane wave situation, the target is placed in the far field region of the transducer, the diameter of the transducer being greater than that of the target. The targets studied were sections of brass rods, parallelepipedic, cylindrical or other.

The built-up spectrum for a square section is plotted in Fig. 6. The spectrum is made of three

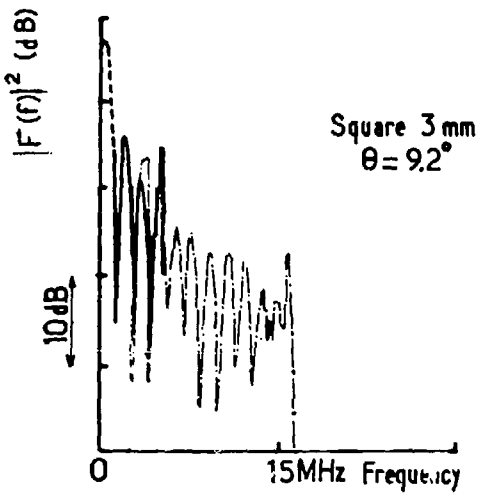

Fig. 6 Reconstructed spectrum for a plane target. —— LF transducer, —·— HF transducer, ---extrapolation.

parts: the continuous line is the result given by a transducer; the part on the right is given by a second transducer and, the part of the left is obtained by the parabolic extrapolation. In Fig. 7 the continuous line is the result of the deconvolution, the dashed line is the theoretical signal.

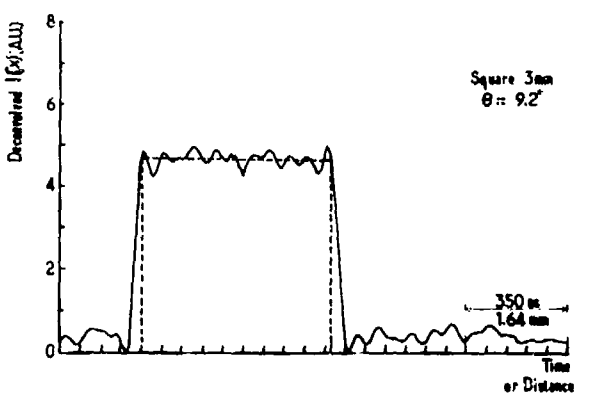

Fig. 7 Deconvolved signal (continuous line) and theoretical signal (dashed line) for a square target.

In Fig. 8, one can see the result of the deconvolution for a rod-section shaped as an M (continuous line); the dashed line is the expected result.

The results obtained for a quasi ellipsoidal section are plotted in Fig. 9. The ratio between the two axis lengths is 2. Figure 9a plots the result when the major axis is horizontal. The amplitude has been adjusted so that the maximum height of the function I(x') is half the width. If one keeps the same vertical scale, and if one conducts the experiment with the major axis vertical, the result of deconvolution should be such that the height is twice the width. This is obtained on the experimental result in Fig. 9b.

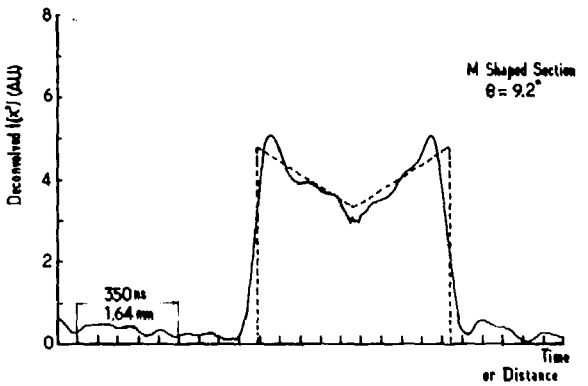

Fig. 8 Deconvolved signal (continuous line) and theoretical signal (dashed line) for an M shaped target.

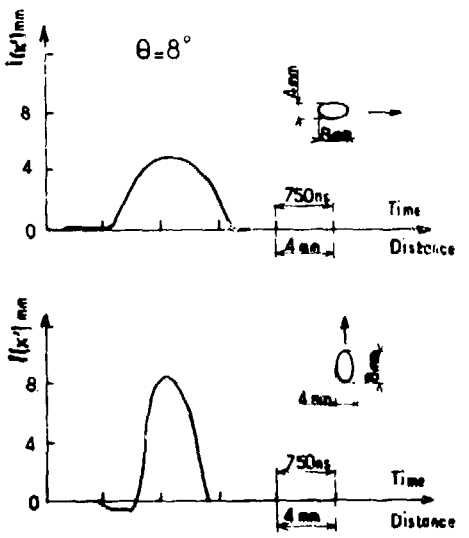

Fig. 9 Deconvolved signal for a quasi-ellipsoidal section. a. Major axis horizontal. b. Major axis vertical.

The results obtained for two samples of the evaluation of the probability density function of the heights are plotted in Figs. 10 and 11. The dotted lines are obtained by mechanical measurements. The continuous lines are the results of the ultrasonic measurements. For that case as for plane targets, the results are satisfactory.

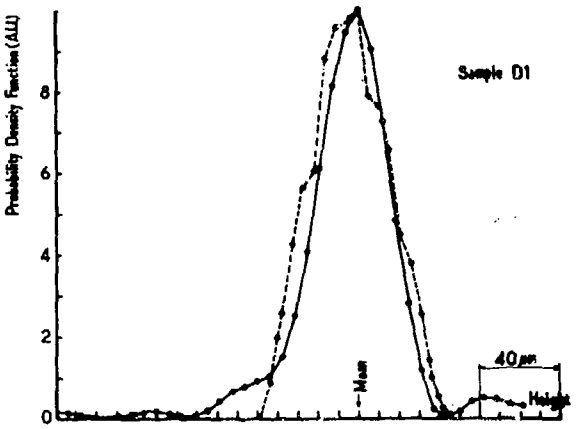

Fig. 10 Probability density function of sample D1. --- Mechanically measured, —— ultrasonic measurement.

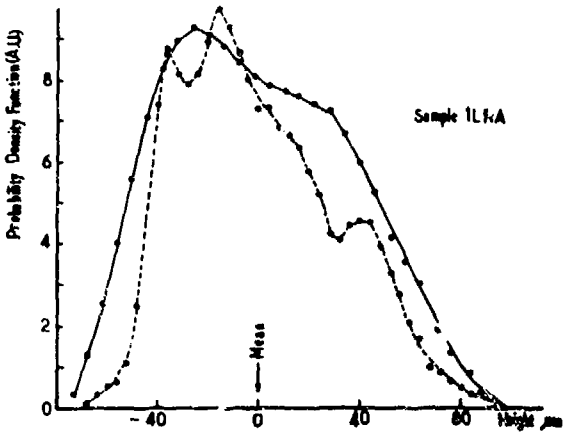

Fig. 11 Probability density function of sample 1LRA. ---- Mechanically measured, —— ultrasonic measurement.

CONCLUSION

We have studied the filtering effect operated by a transducer on the ideal response function of a target to an incident Dirac pulse. The extension of the frequency bandwidth leads to satisfactory results. The method could be useful to complete existing ones for characterization of plane surfaces. This method could be useful for the characterization of plane defect in materials. First results in that direction are promising.

APPENDIX A

Let h(t) be a real function of time and F(f) its Fourier transform:

$$F(f) = \int_{-\infty}^{+\infty} h(t) \exp(-2i\pi ft)\, dt \qquad (12)$$

F(f) is such that $F(-f) = F^{*}(f)$. Let us call $F_1(f)$ the function equal to F(f) between f_1 and f_2 and equal to zero elsewhere. $F_1(f)$ can be written

$$F_1(f) = F(f)[H(f+f_2)-H(f+f_1)+H(f-f_1)-H(f-f_2)] \qquad (13)$$

where

$$H(f) = \begin{cases} 0 \text{ if } f < 0 \\ 1 \text{ if } f > 0 \end{cases} .$$

The inverse Fourier transform of $F_1(f)$ is:

$$h_1(t) = h(t) \oplus \left\{ \frac{\sin 2\pi f_2 t}{\pi t} - \frac{\sin 2\pi f_1 t}{\pi t} \right\} . \qquad (14)$$

That is, if we take the inverse Fourier transform of $F_1(f)$ instead of F(f), the result is the convolution product of h(t) by the functions

$$\frac{\sin 2\pi f_2 t}{\pi t} \text{ and } - \frac{\sin 2\pi f_1 t}{\pi t} .$$

REFERENCES

1. O.R. Gericke, Journal of Metals, 18, (8), pp. 932-937, (1966).
2. J.D. Achenbach, L. Adler and D.K. Lewis, Jour. Acoust. Soc. Am., 66, (4) pp. 1848-1856, (1979).
3. G.S. Kino, Proc. IEEE on Acoustic Imaging, 67, pp. 510-525, (1979).
4. E. Lloyd, Ultrasonics International Conference Proceedings, IPC London, pp. 54-57, (1975).
5. J.K. Cohen, N. Bleistein and R.K. Esley, Proc. of the ARPA-AFML Review, pp. 454-458, Jan. 1979.
6. A. Freedman, Acustica, 12,(1), pp. 10-21, (1962).
7. N.F. Haines and D.B. Langston, J. Acoust. Soc. Am., 67, pp. 1443-1454, (1979).
8. W.G. Neubauer, J. Acoust. Soc. Am., 35, 279, (1963).
9. D.M. Johnson, J. Acoust. Soc. m., 59, 1319, (1976).
10. C.S. Clay and H. Medwin, J. Acoust. Soc. Am., 47, 1412, (1970).

SUMMARY DISCUSSION

J.D. Achenback, Chairman (Northwestern): Let's take time for one question. Is there a quick question? Otherwise, we'll postpone -

Gordon Kino (Stanford): What was the center of the frequency of the two transducers?

Frederick Cohen-Tenoudji (University of Paris): The low frequency transducer was centered at 2.5 megahertz, the high frequency transducer was centered at 8 megahertz. The total bandwidth was approximately from one megahertz to 15 megahertz.

Gordon Kino: Have you worked out the effect of the transverse direction? You're working out shapes from this, so it must depend somehow on how accurately you get the shape, an effect of definition - it's an imaging system.

Federick Cohen-Tenoudju: Yes, I think that the definition will be given by the relation between highest frequency present in the spectrum. We will have the transverse definition given by $\Delta a \approx \lambda_m/(2 \sin \theta)$ where θ is the angle of incidence and λ_m is the minimum wavelength. That's what I usually see. It results in a spread out on the edge typical of the highest frequency present.

J.D. Achenback, Chairman: I'm sure we'll have to cut off the discussion and move to the next two talks.

EXACT INVERSE SCATTERING THEORY

Norbert N. Bojarski
Sixteen Pine Valley Lane
Newport Beach, CA 92660

ABSTRACT

The concepts of reference wave slowness (reciprocal of velocity) and an associated free reference space Green's function slowness spectrum are introduced. A modified Kirchoff surface integral, containing only the imaginary part of this free reference space Green's function slowness spectrum, is formulated, yielding an integral equation for the unknown fields and sources in the interior of a closed surface on which the (remotely sensed) fields are known. A well-posed, analytic closed form solution of this integral equation is obtained.

INTRODUCTION

Presented is a unified approach and solution to the inverse scattering and inverse source problems for the inhomogeneous scalar wave equation

$$\nabla^2\phi + \frac{\omega^2}{c^2}\,\phi = -\rho \quad , \tag{1}$$

subject to the constitutive equation

$$\rho = V\,\phi \quad , \tag{2}$$

and the homogeneous scalar wave equation

$$\nabla^2\phi + \frac{\omega^2}{c^2(\mathbf{x},\omega)}\,\phi = 0 \quad . \tag{3}$$

To this end, the single mixed scalar wave equation

$$\nabla^2\phi + \frac{\omega^2}{c^2(\mathbf{x},\omega)}\,\phi = -\rho \tag{4}$$

is introduced. From an inverse scattering inverse source perspective, Equation 4 reduces to Equation 1 if the medium wave velocity $c(\mathbf{x},\omega)$ is a known constant and the source ρ is the unknown, and Equation 4 reduces to Equation 3 if the sources ρ are known to be zero and the medium wave velocity $c(\mathbf{x},\omega)$ is the unknown.

It is argued that the inverse solution presented is an alternative (to the direct Kirchoff) integration of the wave equation. It is thus appropriate to review some relevant properties of the direct Kirchoff integration

$$\phi = \int_V dv\; G\,\rho + \oint_S d\mathbf{S}\cdot(G\,\nabla\phi - \phi\,\nabla G) \tag{5}$$

of the wave Equation 1. Specifically, the surface integral in Equation 5 is an equivalence statement relating the field at a field point on one side of the closed surface produced by all the sources on the other side of the closed surface, via the fields produced by these sources on this closed surface. The inverse scattering inverse source problem is, however, characterized by both the field point for the unknown fields as well as all the unknown sources being on the same side of the closed surface (on which the remote sensing is accomplished), for which situation the Kirchoff surface integral vanishes, thus rendering this Kirchoff surface integral useless for the inverse scattering inverse source problem. A modified Kirchoff surface integral, which does not suffer from this pathology, is introduced next.

THE INVERSE SCATTERING INTEGRAL EQUATION

Let G be the free reference space Green's function satisfying the inhomcgeneous wave equation

$$\nabla^2 G + \frac{\omega^2}{v^2}\,G = -\delta \tag{6}$$

and the Sommerfeld radiation condition at infinity, where v is any arbitrarily chosen reference velocity.

Next, let an effectal field θ be defined as

$$\theta \equiv \oint_S d\mathbf{S}\cdot(\phi\,\nabla G_i - G_i\,\nabla\phi) \quad , \tag{7}$$

where

$$G_i \equiv Im\; G \quad , \tag{8}$$

which, by Equation 6, satisfies the homogeneous wave equation

$$\nabla^2 G_i + \frac{\omega^2}{v^2}\,G_i = 0 \quad . \tag{9}$$

By Green's theorem, Equation 7 reduces to

$$\theta = \int_V dv\;(\phi\,\nabla^2 G_i - G_i\,\nabla^2\phi) \quad , \tag{10}$$

which, by Equations 4 and 9, reduces to

$$\theta = \int_V dv\;\left[\phi\left(-\frac{\omega^2}{v^2}\,G_i\right) - G_i\left(-\frac{\omega^2}{c^2(\mathbf{r},\omega)}\,\phi - \rho\right)\right] \quad , \tag{11}$$

$$\theta = \int_V dv\; G_i\,\rho + \int_V dv\; G_i\left[\frac{\omega^2}{c^2(\mathbf{x},\omega)} - \frac{\omega^2}{v^2}\right]\phi \quad . \tag{12}$$

[which, for the case of a known constant medium wave velocity c, unknown sources ρ, and a reference velocity chosen as v=c, reduces to the earlier inverse scattering integral equation of this author (Ref 1)].

SOLUTION OF THE INTEGRAL EQUATION

Let a medium reference wave slowness σ be introduced and defined as

$$\sigma \equiv \frac{1}{v} \quad . \tag{13}$$

The inverse scattering integral Equation 12, in terms of this reference slowness, thus is

$$\theta(\mathbf{x},\omega,\sigma) = \int_V G_i(\mathbf{x}|\mathbf{x}',\omega,\sigma)\ \rho(\mathbf{x}',\omega)\ dv'$$

$$+ \int_V G_i(\mathbf{x}|\mathbf{x}',\omega,\sigma) \left[\frac{\omega^2}{c^2(\mathbf{x}',\omega)} - \omega^2\ \sigma^2 \right] \phi(\mathbf{x}',\omega)\ dv' \quad , \tag{14}$$

where in two and three dimensions, the imaginary part of the free reference space Green's functions are

$$G_i(\mathbf{x}|\mathbf{x}',\omega,\sigma) = \tfrac{1}{4}\ J_o(\omega r\sigma) \tag{15}$$

and

$$G_i(\mathbf{x}|\mathbf{x}',\omega,\sigma) = \frac{sin(\omega r\sigma)}{4\pi r} \tag{16}$$

respectively, and where $r \equiv |\mathbf{x}-\mathbf{x}'|$.

Taking the Hilbert transform of Equation 14 with respect to the reference slowness σ yields

$$\frac{1}{\pi}\int_{-\infty}^{\infty} \frac{\theta(\mathbf{x},\omega,\sigma')}{\sigma-\sigma'}\ d\sigma' =$$

$$\int_V \frac{1}{\pi}\int_{-\infty}^{\infty} \frac{G_i(\mathbf{x}|\mathbf{x}',\omega,\sigma')}{\sigma-\sigma'}\ d\sigma'\ \rho(\mathbf{x}',\omega)\ dv'$$

$$+ \int_V \frac{1}{\pi}\int_{-\infty}^{\infty} \frac{G_i(\mathbf{x}|\mathbf{x}',\omega,\sigma')}{\sigma-\sigma'} \left[\frac{\omega^2}{c^2(\mathbf{x}',\omega)} \right.$$

$$\left. - \omega^2\ \sigma'^2 \right] d\sigma'\ \phi(\mathbf{x}',\omega)\ dv' \quad . \tag{17}$$

By Equations 15 and 16, with the aid of References 2 and 3, and twice repeated application of References 4 and 5, it follows that

$$\frac{1}{\pi}\int_{-\infty}^{\infty} \frac{G_i(\mathbf{x}|\mathbf{x}',\omega,\sigma')}{\sigma-\sigma'}\ d\sigma' = sgn(\omega r)\ G_r(\mathbf{x}|\mathbf{x}',\omega,\sigma) \quad ,$$

and (18)

$$\frac{1}{\pi}\int_{-\infty}^{\infty} \frac{\sigma'^2\ G_i(\mathbf{x}|\mathbf{x}',\omega,\sigma')}{\sigma-\sigma'}\ d\sigma' = sgn(\omega r)\ \sigma^2\ G_r(\mathbf{x}|\mathbf{x}',\omega,\sigma) \tag{19}$$

in two and three dimensions, but not in one dimension. In two and three dimensions G_r is the real part of the free reference space Green's function

$$G_r(\mathbf{x}|\mathbf{x}',\omega,\sigma) = \tfrac{1}{4}\ Y_o(\omega r\sigma) \tag{20}$$

and

$$G_r(\mathbf{x}|\mathbf{x}',\omega,\sigma) = \frac{cos(\omega r\sigma)}{4\pi r} \tag{21}$$

respectively.

Thus, with the aid of Equations 18 and 19, Equation 17 becomes

$$\frac{1}{\pi}\int_{-\infty}^{\infty} \frac{\theta(\mathbf{x},\omega,\sigma')}{\sigma-\sigma'}\ d\sigma' =$$

$$\int_V sgn(\omega r)\ G_r(\mathbf{x}|\mathbf{x}',\omega,\sigma)\ \rho(\mathbf{x}',\omega)\ dv'$$

$$+ \int_V sgn(\omega r)\ G_r(\mathbf{x}|\mathbf{x}',\omega,\sigma) \left[\frac{\omega^2}{c^2(\mathbf{x}',\omega)} \right.$$

$$\left. - \omega^2\ \sigma^2 \right] \phi(\mathbf{x}',\omega)\ dv' \quad . \tag{22}$$

Restricting Equation 22 to positive non-zero frequencies ω, permits its rewriting as the principal value integral (i.e., excluding integration over $\mathbf{x}=\mathbf{x}'$)

$$\frac{1}{\pi}\int_{-\infty}^{\infty} \frac{\theta(\mathbf{x},\omega,\sigma')}{\sigma-\sigma'}\ d\sigma' = p\int_V G_r(\mathbf{x}|\mathbf{x}',\omega,\sigma)\ \rho(\mathbf{x}',\omega)\ dv'$$

$$+ p\int_V G_r(\mathbf{x}|\mathbf{x}',\omega,\sigma) \left[\frac{\omega^2}{c^2(\mathbf{x}',\omega)} - \omega^2\ \sigma^2 \right] \phi(\mathbf{x}',\omega)\ dv' \tag{23}$$

Since the imaginary part of the free reference space Green's function is not singular at $\mathbf{x}=\mathbf{x}'$, it follows from the addition of Equations 14 and 23 that for positive non-zero frequencies

$$\frac{1}{\pi}\int_{-\infty}^{\infty} \frac{\theta(\mathbf{x},\omega,\sigma')}{\sigma-\sigma'}\ d\sigma' + i\theta(\mathbf{x},\omega,\sigma) =$$

$$p\int_V G(\mathbf{x}|\mathbf{x}',\omega,\sigma)\ \rho(\mathbf{x}',\omega)\ dv'$$

$$+ p\int_V G(\mathbf{x}|\mathbf{x}',\omega,\sigma) \left[\frac{\omega^2}{c^2(\mathbf{x}',\omega)} - \omega^2\ \sigma^2 \right] \phi(\mathbf{x}',\omega)\ dv' \tag{24}$$

For the inverse scattering inverse source case of a known constant medium velocity c and unknown sources ρ (i.e., wave Equation 1), Equation 24 reduces, after chosing the reference slowness $\sigma = 1/c$, for $\omega>0$, to

$$\frac{1}{\pi}\int_{-\infty}^{\infty} \frac{\theta(\mathbf{x},\omega,\sigma)}{\frac{1}{c}-\sigma}\ d\sigma + i\theta(\mathbf{x},\omega,\tfrac{1}{c}) =$$

$$p\int_V G(\mathbf{x}|\mathbf{x}',\omega,\tfrac{1}{c})\ \rho(\mathbf{x}',\omega)\ dv' \quad . \tag{25}$$

At that reference slowness, the direct Kirchoff integration Equation 5 of the wave Equation 1 can be written as

$$\phi(\mathbf{x},\omega) = p\int_V G(\mathbf{x}|\mathbf{x}',\omega,\tfrac{1}{c})\ \rho(\mathbf{x}',\omega)\ dv' + \phi_i(\mathbf{x},\omega) \quad , \tag{26}$$

since in two and three dimensions the Green's function singularity is weak and removable, and the Kirchoff surface integral represents the incident field. Thus, combining Equations 25 and 26 yields the solution

$$\phi(\mathbf{x},\omega) = \frac{1}{\pi}\int_{-\infty}^{\infty} \frac{\theta(\mathbf{x},\omega,\sigma)}{\frac{1}{c}-\sigma}\, d\sigma + i\theta(\mathbf{x},\omega,\tfrac{1}{c}) + \phi_i(\mathbf{x},\omega) \quad , \quad \omega>0 \quad . \tag{27}$$

For the inverse scattering inverse source case of known zero sources and unknown medium velocity $c(\mathbf{x},\omega)$, i.e., wave Equation 3, Equation 24 reduces, after choosing the reference slowness $\sigma=\frac{1}{c_o}$, for $\omega>0$, to

$$\frac{1}{\pi}\int_{-\infty}^{\infty} \frac{\theta(\mathbf{x},\omega,\sigma)}{\frac{1}{c_o}-\sigma}\, d\sigma + i\theta(\mathbf{x},\omega,\tfrac{1}{c_o}) = p\int_V G(\mathbf{x}|\mathbf{x}',\omega,\tfrac{1}{c_o}) \left[\frac{\omega^2}{c^2(\mathbf{x}',\omega)} - \frac{\omega^2}{c_o^2}\right] \phi(\mathbf{x}',\omega)\, dv' \quad . \tag{28}$$

A digression concerning the wave Equation 3 is now in order. This wave equation can be rewritten as

$$\nabla^2\phi + \frac{\omega^2}{c_o^2}\phi = -\rho_o \quad , \tag{29}$$

where the sources ρ_o are reference sources relative to the arbitrarily chosen reference wave velocity c_o, given by the relative constitutive equation

$$\rho_o = V_o\,\phi \quad , \tag{30}$$

and the potential V_o is a reference potential relative to the arbitrarily chosen reference wave velocity c_o, given by

$$V_o = \frac{\omega^2}{c^2(\mathbf{x},\omega)} - \frac{\omega^2}{c_o^2} \quad . \tag{31}$$

It thus follows that Equation 28 can be written for $\omega>0$ as

$$\frac{1}{\pi}\int_{-\infty}^{\infty} \frac{\theta(\mathbf{x},\omega,\sigma)}{\frac{1}{c_o}-\sigma}\, d\sigma + i\theta(\mathbf{x},\omega,\tfrac{1}{c_o}) = p\int_V G(\mathbf{x}|\mathbf{x}',\omega,\tfrac{1}{c_o})\, \rho_o(\mathbf{x}',\omega,\tfrac{1}{c_o})\, dv' \quad . \tag{32}$$

At this reference slowness $1/c_o$, the direct Kirchoff integration Equation 5 of the wave Equation 29 can be written as

$$\phi(\mathbf{x},\omega) = p\int_V G(\mathbf{x}|\mathbf{x}',\omega,\tfrac{1}{c_o})\, \rho_o(\mathbf{x}',\omega,\tfrac{1}{c_o})\, dv' + \phi_i(\mathbf{x},\omega,\tfrac{1}{c_o}) \tag{33}$$

since in two and three dimensions the Green's function singularity is weak and removable, and the Kirchoff surface integral represents the incident field.

Thus, combining Equations 32 and 33 yields the (same as Equation 27) solution

$$\phi(\mathbf{x},\omega) = \frac{1}{\pi}\int_{-\infty}^{\infty} \frac{\theta(\mathbf{x},\omega,\sigma)}{\frac{1}{c_o}-\sigma}\, d\sigma + i\theta(\mathbf{x},\omega,\tfrac{1}{c_o}) + \phi_i(\mathbf{x},\omega,\tfrac{1}{c_o}) \quad , \quad \omega>0 \quad . \tag{34}$$

The sources, potential, and medium wave velocities can be obtained from knowledge of the fields in a variety of straightforward manners.

One might be tempted to attempt to simplify the solutions (Equations 27 and 34) by applying and executing analytically the Hilbert transform with respect to the reference slowness directly on the surface integral definition (Equation 7) of the effectal field, thus obtaining this definition in terms of the principal value of the real part of the free reference space Green's function, instead of the imaginary part of this free reference space Green's function. The flaw with such an attempt is that on the surface of integration, away from the singular point of the real part of the free reference space Green's function, the principal value and the complete singular real part of the free reference space Green's function are indistinguishable and identical, and the application of Green's theorem as per (Equations 7 and 12) will, by the differentiability and continuity requirement imposed by Green's theorem, fail to generate the principal value of the real part of the free reference space Green's function in the volume interior to the surface of integration, which would have yielded the desired solution, but generate the full singular real part of the free reference space Green's function in this interior, which fails to yield the desired solution, and yield (a slightly modified) version of the integral Equation 12, instead of its solution.

REFERENCES

1. Bojarski, N. N., "Inverse Scattering," Sect. II, October 1973, Third Quarterly Company Report, Naval Air Systems Command Contract N00019-73-C-0312.
2. Bateman, H., "Tables of Integral Transforms," Sect. 15.2, p. 252, (43), McGraw-Hill Book Company, 1954.
3. Op. Cit., Sect. 15.3, p. 254, (11).
4. Op. Cit., Sect. 15.1, p. 243, (5).
5. Gradshteyn, I. S., and Ryzhik, I. M., "Tables of Integrals, Series, and Products," Sect. 3.761, p. 420, (2), Academic Press, 1965.

SUMMARY DISCUSSION

J.D. Achenbach, Chairman (Northwestern University): The paper is open for discussion.

John Richardson (Science Center): The integrals involved in the Weiner-Lee transform, in the case of the factor sigma squared term, are not absolutely convergent; and even though there are ways of getting finite answers out, they are dependent on particular assumptions that you make to achieve convergence and I am rather uneasy about the uniqueness of the answers that you get thereby.

Norbert Bojarski: I share your uneasiness. It's too early. I don't know.

William Pardee (Science Center): I'm skeptical, or at least unconvinced, by your identification of the particular constant by which Weiner-Lee differs from the Hilbert transform with the constant you want to eliminate. In particular, as John alluded to, each integral to the Weiner-Lee transform of the sigma squared term is very singular at the end points. That is where sigma goes to infinity or theta goes to plus or minus PI. In fact, in spite of the sine multiplying the sigma squared sine term the integral diverges as sigma, so they become infinite and oscillate very rapidly. If the transform has the value you desire, then the sum of these coefficients must be zero. And it appears that the terms in the sum are order minus one to the N times something of the order N, which is a delta function-like divergence. In your numerical evaluation, you may well be doing something special at the very small test velocities. That is very large sigma because all of the singularities come from those very small test velocities.

Norbert Bojarski: Let me answer. First of all, I share your uneasiness about it. Let me answer in two parts. First of all, if you look at that expansion of the W.F. of the angle, I think it's relatively clear that the only term that can contribute to the constant to this is the a zero term. I realize I just wanted to belabor that for a moment.

William Pardee: We're talking about constants in sigma. And not constants in theta and they are not the same thing.

Norbert Bojarski: It could very well be what I have done - let me pick the worst possible thing of what I have done. I have picked delta x and delta sigma in such a fashion that I have succeeded in throwing away those parts which retrieve the delta function.

William Pardee: How do you numerically treat those end points of the Fourier?

Norbert Bojarski: I did something very similar in the numerical part. I took sigma. The roster you saw is 128 by 128, so I took 256 points in sigma, centered them at the C, which I know what it is, and went out from there and threw away the one that goes to infinity.

William Pardee: That's the delta function!

Norbert Bojarski: But the point is, I don't care what the rigor is. It could very well be what is lacking here is some rigorous proof of how do you massage this numerical implementation to a formalism to make the delta function go away. It may be that's what's lacking.

William Pardee: It may turn out there is a practical problem related to that lack of rigor in that the results are sensitive to the details of how you treat that.

J.D. Achenback, Chairman: I think further discussion of this will have to take place at the coffee break. Thank you, and let's now proceed to the next talk.

AN EXACT THEORY FOR COHERENT NONDESTRUCTIVE EVALUATION: THE APPLICATION OF THE BOJARSKI EXACT INVERSE SCATTERING THEORY TO THE REMOTE PROBING OF INHOMOGENEOUS MEDIA

W. Ross Stone
IRT Corporation
P.O. Box 80817, San Diego, CA 92138

INTRODUCTION AND SYNOPSIS

In an inverse scattering problem, the fields in the inhomogeneous wave equation are known, and it is desired to solve for the source term. N. N. Bojarski has recently derived an Exact Inverse Scattering Theory for such "inverse source" problems. The problem of determining the generalized refractive index (i.e., the complex permeability and dielectric constant for an electromagnetic problem, or the velocity and absorption for an acoustic problem) distribution of an inhomogeneous medium from measurements of the fields scattered by the medium can be treated using this theory. This solution is applicable to all remote probing problems, and in particular, to nondestructive evaluation (NDE) using coherent radiation.

Although this paper uses scalar notation, all of the results have been shown to apply to the general, full vector field and tensor medium quantities. The equations applicable to the electromagnetic cases are used; however, the theory and results apply equally well to the acoustic equations.

THE BOJARSKI EXACT INVERSE SCATTERING THEORY

To provide the basis for the treatment of the inverse medium problem, this section presents a derivation of N. N. Bojarski's (Refs. 1-4) "Exact Inverse Scattering Theory." Consider a source $\rho(\underline{x})$ in a domain D bounded by a surface S. Then the time harmonic field, $\phi(\underline{x})$, due to $\rho(\underline{x})$ is the solution to the inhomogeneous wave equation

$$\nabla^2\phi(\underline{x}) + k^2\phi(\underline{x}) = -\rho(\underline{x}), \quad \underline{x}\epsilon D \tag{1}$$

where $k = 2\pi/\lambda$. A direct scattering problem is one in which $\rho(\underline{x})$ is known or specified, and a solution for $\phi(\underline{x})$ is sought. The inverse scattering problem is one in which $\phi(\underline{x})$ is known, and $\rho(\underline{x})$ is sought. For the inverse source problem, $\phi(\underline{x})$ is measured over some surface, and the object is to determine $\rho(\underline{x})$. In general, $\rho(\underline{x}) = \rho_m(\underline{x}) + \rho_s(\underline{x})$, where ρ_m is due to interaction with the medium, and ρ_s is due to actual sources. If $n(\underline{x})$ is the complex refractive index of the medium, then

$$\rho_m(\underline{x}) = k^2\left[n^2(\underline{x}) - 1\right]\phi(\underline{x}) \tag{2}$$

In most remote probing problems, $\rho_s(\underline{x})$ is known, and $\rho_m(\underline{x})$ is sought to yield $n(x)$. This is termed the inverse medium problem. If $\phi(\underline{x})$ is specified (as the desired field) and $\rho(\underline{x})$ or $n(\underline{x})$ is sought so as to produce that $\phi(\underline{x})$, the problem is termed an inverse synthesis problem.

Let the following field quantity, $\phi_H(\underline{x})$, be defined:

$$\phi_H(\underline{x}) = \oint \left[g^*(\underline{x}-\underline{x}')\nabla\phi(\underline{x}') - \phi(\underline{x}')\nabla g^*(\underline{x}-\underline{x}')\right] d\underline{S}' \tag{3}$$

where $g(\underline{x})$ is the free space Green's function and the asterisk denotes complex conjugation. g satisfies Equation 1 with $\rho(\underline{x}) = \delta(\underline{x})$. ϕ_H is in the form of the Kirchoff integral with g complex conjugated. Note that if the Kirchoff integral is applied to the field $\phi(\underline{x})$ on S and evaluated at any point $\underline{x}$ inside D, it is identically zero: The Kirchoff integral is nonzero only for points outside D. Conversely, $\phi_H(\underline{x})$ is nonzero only for points inside D. Points outside of D are associated with the direct scattering problem; points inside D are of interest for the inverse scattering problem. This topological difference is the reason why direct scattering solutions are mathematically ill-posed when applied to the inverse scattering problem.

It should also be noted that ϕ_H is the mathematical expression for the reconstruction obtained from a hologram (ϕ in Equation 3) recorded on S. The relationship between holography and inverse scattering, along with an analysis of the consequences for remote probing and coherent imaging applications, has been presented by Stone (Ref. 5). ϕ_H is, in general, known for inverse problems, since ϕ is known over S. ϕ is measured over S for the inverse source and medium problems, or specified over S for the inverse synthesis problem.

Applying Gauss' theorem to Equation 3 converts the surface integral into a volume integral:

$$\phi_H = \int dV\left(g^*\nabla^2\phi - \phi\nabla^2 g^*\right) \tag{4}$$

From Equation 1,

$$\nabla^2\phi = -k^2\phi - \rho \tag{5}$$

and, by complex conjugation of Equation 1 for g,

$$\nabla^2 g^* = -k^2 g^* - \delta \tag{6}$$

Substitution of Equations 5 and 6 into Equation 4 gives

$$\phi_H = \int dV \left[g^*(-k^2\phi - \rho) - \phi(-k^2 g^* - \delta) \right]$$

$$= \int dV \quad (\phi\delta - g^*\rho) \tag{7}$$

and, carrying out the integration over the delta function,

$$\phi_H = \phi - \int dV \; g^*\rho \tag{8}$$

Direct scattering theory gives the result that

$$\phi = \int dV \; g\rho \; + \; \oint dS(g\nabla\phi \; - \phi\nabla g)$$

$$= \int dV \; g\rho \; + \; \phi_i \tag{9}$$

In Equation 8, the first integral is just the superposition integral over the sources. The second term is the Kirchoff integral, and is asssociated with the incident field, ϕ_i. For the inverse scattering problem, ϕ_i can be assumed to be known without loss of generality (e.g., it is the known probing field for the inverse medium case, or the specified incident field in the inverse synthesis case).

Equations 8 and 9 are two independent simultaneous equations in two unknowns, ϕ and ρ. Substitution of Equation 9 into Equation 8 yields

$$\phi_H = \int dV \; g\rho - \int dV \; g^*\rho \; + \phi_i$$

$$= \int dV \; (g - g^*)\rho \; + \; \phi_i \tag{10}$$

or

$$\phi_H(\underline{x}) = 2i \int dV' \; \mathrm{Img}(\underline{x}-\underline{x}') \quad \rho(\underline{x}') + \quad \phi_i(\underline{x}) \tag{11}$$

where Im denotes the imaginary part. Equation 11 is the basic equation of the Exact Inverse Scattering Theory. It is an integral, convolution equation for the single unknown, $\rho(\underline{x})$. It can be solved by standard deconvolution techniques. Quite recently, Bojarski (Ref. 6) has presented a closed-form solution to Equation 11.

UNIQUENESS OF THE SOLUTION

The uniqueness of the solution to Equation 11 was first deduced by Bojarski (Refs. 2,4) and later proven more rigorously be Bleistein and Cohen (Ref. 7). A simpler and more physically understandable proof was presented by Stone (Ref. 8). The result is that the solution to Equation 11 for the source, $\rho(\underline{x})$ is unique if $\rho(\underline{x})$ is identically zero outside some finite domain (i.e., is of bounded support), has finite energy, and does not contain any nonradiating components. A nonradiating source is a source component which produces a field which is identically zero outside a finite region. Although the "nonuniqueness" associated with nonradiating sources has been somewhat troublesome from a mathematical standpoint, it does not affect the uniqueness of results for practical applications (Bojarski Ref. 9). Quite recently, Stone (Ref. 10) has proven that a conjecture by Bleistein and Bojarski (Ref. 4) that nonradiating sources are nonphysical is true.

INCOMPLETE KNOWLEDGE OF $\phi(x)$

Practical inverse scattering problem measurements almost always involve discrete measurements over a limited aperture, as opposed to the continuous measurements over a closed surface used in the above theory. Mager and Bleistein (Ref. 11) have shown that, in the physical optics limit, the spatial bandwidth over which measured data is known is the spatial bandwidth over which the source term can be determined. A similar but more general result follows directly from analysis of the three dimensional spatial Fourier transform of Equations 3 and 11. Let $\underline{\nu}$ be the spatial frequency variable, and let capital letters denote the transformed functions. For the general case, $\Phi_H(\underline{\nu})$ is known over the whole surface S, and thus for all $0 \leq \underline{\nu} \leq \underline{\nu}_0$ (the upper bound is $\underline{\nu}_0$ rather than ∞, since D, and thus S, are of finite size). Since the left side of the transformed version of Equation 11 is known for all $0 \leq \underline{\nu} \leq \underline{\nu}_0$, it follows that $P(\underline{\nu})$ is determined over this range. Now let $\phi(\underline{x})$ be measured at discrete points over a limited aperture. Then $\Phi(\underline{\nu})$ is determined for $\underline{\nu}_1 \leq \underline{\nu} \leq \underline{\nu}_2$, where these spatial bandlimits are determined by the aperture size and sample spacing. It follows from the transform of Equation 3 that $\phi_H(\underline{\nu})$ is similarly bandlimited, and from the transform of Equation 11 that $P(\underline{\nu})$ can be determined over this band of spatial frequencies. It has been shown by Stone (Ref. 12) that, for coherent inverse scattering, the spatial resolution, obtainable with a measurement aperture of given size, may be significantly greater than that predicted by classical incoherent diffraction theory.

THE EFFECTS OF NOISY MEASUREMENTS (REF. 13)

The effects of measurement noise on the reconstructed refractive index can be seen by writing $\phi_H(\underline{x}) = \phi_H(\underline{x}) + \phi_N(\underline{x})$, where $\phi_N(\underline{x})$ contains a contribution due to noise. It follows, using Equation 11, that this is equivalent to a source term $\rho(\underline{x}) + \rho_N(\underline{x})$, where $\rho(\underline{x})$ is the true source and $\rho_N(\underline{x})$ contains the effect of the noise. From this it can be seen that the signal-to-noise ratio of the solution is the signal-to-noise ratio of $\phi_H(\underline{x})$. Since $\phi_H(\underline{x})$ depends on the integral over the measurement surface of the measured field values (Equation 3), the signal-to-noise ratio of $\phi_H(\underline{x})$ [and thus of $\rho(\underline{x})$] is not greater than (and may be less than) the signal-to-noise ratio of the measured data. This has been confirmed by numerical experiments. It should also be mentioned that in addition to being numerically well-posed, the solution can be implemented in an extremely efficient form. This permits addressing problems heretofore impractical because of computational effort or storage limitations.

THE INVERSE MEDIUM PROBLEM

Based on the above theory, the NDE inverse medium problem can be solved by the following steps:

A. Compute $\phi_H(\underline{x})$, using the measured field values in Equation 3 (note that the surface of integration, S, is the measurement surface).

B. Solve Equation 11 for $\rho(\underline{x})$, using $\phi_H(\underline{x})$ from A and the known incident field, $\phi_i(\underline{x})$.

C. Compute the total field, $\phi(\underline{x})$, from the direct scattering result, Equation 9, using $\rho(\underline{x})$ from B.

D. Solve Equation 2 for the desired complex refractive index, $n(\underline{x})$, using $\rho(\underline{x})$ from B and $\phi(\underline{x})$ from C.

Note that for the inverse source problem, only steps A and B are required. However, for the inverse medium problem it is necessary to carry out steps C and D in addition. The solution to the direct scattering problem (step C) is a necessary step in solving the inverse medium problem. It is important to emphasize that the computations involved in steps A through C are all convolution integrals: They can be carried out using fast fourier transform techniques. As a result, computation time and storage requirements are proportional to N $\log_2$N, where N is the number of data points. Step D is an algebraic operation.

THE SYNTHESIS PROBLEM

There is very close relationship between the synthesis problem and the inverse medium problem. In the inverse medium problem a known probing (incident) field is used, and the scattered field is measured. This data is sufficient to obtain a unique solution for $n(\underline{x})$, using the four steps in the previous section. In the synthesis problem, a specified incident field and a desired scattered field are chosen, and the $n(\underline{x})$ required to produce this scattered field is sought. If there are no constraints (other than physical realizability) on the desired $n(\underline{x})$, the same four steps in the previous section will solve the synthesis problem. If there are constraints (e.g., a desired range of values for $n(\underline{x})$, etc.), it is necessary to regularize the solution to these constraints.

A CLOSED-FORM SOLUTION TO THE SYNTHESIS PROBLEM

The author has carried the solution to the synthesis problem one step further. The result is a closed-form, exact solution for the desired refractive index distribution. Let T denote the desired relationship between the incident field, $\phi_i(\underline{x})$, and the scattered field, $\phi_s(\underline{x})$. T can be a function, an operator, or, in the most general case, any desired algorithm. The only requirement is that the operation of T on ϕ_i (denoted $T\phi_i$) result in a field which is a valid solution of the inhomogeneous wave equation. Thus,

$$\phi_s = T\phi_i \tag{12}$$

By definition, the total field, ϕ, is the sum of the incident and scattered fields:

$$\phi = \phi_i + \phi_s \tag{13}$$

Substituting Equation 12 into Equation 13,

$$\phi = (1 + T)\,\phi_i \tag{14}$$

Using convolution notation, Equation 9, the direct scattering result, gives

$$\phi = \rho * g + \phi_i \tag{15}$$

The source term, ρ, is related to ϕ and $n(\underline{x})$ by the constitutive Equation 2. Substituting Equation 2 for ρ and Equation 14 for ϕ into Equation 15 yields

$$(1 + T)\phi_i = \left[k^2(n^2-1)(1+T)\phi_i\right] * g + \phi_i \tag{16}$$

After some algebra, Equation 16 can be solved for n:

$$n^2(\underline{x}) = \left\{k^2\ [1+T]\,\phi_i\right\}^{-1}\left[\mathcal{F}^{-1}\left\{T\tilde{\phi}_i/\tilde{g}\right\}\right] + 1 \tag{17}$$

where the tilde indicates the three dimensional spatial Fourier transform, and $\mathcal{F}^{-1}$ denotes the inverse transform.

Equation 17 is a closed-form solution to the synthesis problem. Furthermore, it is very attractive from the system designer's standpoint. The designer need only specify the desired input field to output field transformation, T, and Equation 17 provides the complex refractive index distribution which will produce that transformation. From the Exact Inverse Scattering Theory it can readily be shown that Equation 17 is numerically stable. Furthermore, it can be evaluated with great efficiency using fast Fourier transform techniques. It is also readily ameanable to regularization for the purpose of incorporating design constraints. Finally, the solution of Equation 17 is unique, and has the same behavior with respect to noise and incomplete measurements as discussed in the sections above.

A CLOSED-FORM SOLUTION TO THE NDE REMOTE PROBING PROBLEM

Let ϕ_i be the known incident field in a remote probing problem, and let ϕ_s be the measured, scattered field. Then the operator T, defined in Equation 12, can be determined, and Equation 17 is a closed-form solution to the remote probing problem.

Unfortunately, this involves a hidden approximation. The field measured is usually the total field, ϕ, – not just the scattered field, ϕ_s – over some surface. Obtaining ϕ_s throughout the volume from ϕ over a surface can be as complex as solving the inverse medium problem. However, under certain conditions, the approximation of ϕ_s throughout the volume by ϕ_H, as determined by Equation 3, may be adequate. Where such an approximation is good, Equation 17 provides a closed-form solution to the remote probing problem. A discussion of the conditions and implications associated with such an approximation

has been given by Stone (Ref. 5). Note that no approximation is involved in the closed-form solution of the above section for the synthesis problem: A designer has the freedom to specify ϕ_s. Indeed, this is usually the desired quantity for specification.

SOME COMMENTS ABOUT "STANDARD" APPROACHES TO THE SYNTHESIS PROBLEM

The synthesis problem is usually approached using direct scattering techniques. As discussed in the second session, this approach is inherently ill-posed. An initial guess at the solution $[n(\underline{x})]$ is made, a direct scattering analysis is carried out to obtain the scattered field, and this sequence is iterated, changing the $n(\underline{x})$ in an attempt to minimize the difference between the computed and desired scattered fields. Ray tracing is the most common direct scattering technique employed. There are many very important reasons for not using such synthesis methods: They are iterative, with no guarantee of the nature or rate of convergence; they are mathematically and numerically ill-posed; they require the designer to specify an optimization criterion which is usually not related to desired design requirements; and (in the case of ray tracing) they are only applicable where the geometrical optics approximation is valid. The previous two sections present two solutions which eliminate all of these objections. However, it is also important to realize that the inverse scattering approaches are many powers of 10 more efficient than standard techniques. One example from optical system synthesis will suffice to demonstrate this. Using the inverse scattering techniques, computation of $n(\underline{x})$ for 200,000 complex values requires of the order of one second using a 10 year old minicomputer with an FFT processing board. A state-of-the-art ray trace design program can, at best, compute 4,000 field values through one element of a guessed $n(\underline{x})$ per iteration in one second, using state-of-the-art, special purpose hardware (faster than a CDC 7600 or an IBM 360/195) – and several thousand iterations are commonly required.

CONCLUSIONS

The following conclusions can be drawn from this work:

A. Inverse scattering problems fall into three classes: Inverse source, inverse medium, and synthesis problems. NDE is an inverse medium problem.

B. The Bojarski Exact Inverse Scattering Theory provides solutions to all three of these problems, and in particular, to the inverse medium and synthesis problems.

C. An exact, closed-form solution to the synthesis problem has been presented in this paper.

D. As shown elsewhere, the solutions of B and C are unique, well-posed, insensitive to noisy measurements, applicable with incomplete data, and computationally efficient.

E. In addition, the closed-form solution to the synthesis problem, presented in this paper, provides a closed-form solution to the NDE remote probing (inverse medium) problem. However, the application to the remote probing problem involves an approximation, the effects of which have been treated in detail elsewhere.

F. The approaches to the synthesis problem presented here are both exact and many powers of 10 more efficient than standard ray tracing techniques.

REFERENCES

1. N. N. Bojarski, "Inverse Scatering," Naval Air Systems Command, third quarterly report to Contract N00019-73-C-0312 (NASC-C2-Q3), October 1973.

2. N. N. Bojarski, "Inverse Scattering," Naval Air Systems Command, final report on Contract N00019-73-C-0312, February 1974.

3. N. N. Bjoarski, "Exact Inverse Scattering," presented at the Annual Meeting of USNC/-URSI, October 20-23, 1975, Boulder, Colorado.

4. N. Bleistein and N. N. Bojarski, "Recently Developed Formulations of the Inverse Problem in Acoustics and Electromagnetics," report MS-R-7501, (AD/A-003 588) Department of Mathematics, Denver Research Institute, University of Denver, Colorado, 1974.

5. W. R. Stone, "Holographic Reconstruction is Usually a Poor Solution to the Inverse Scattering Problem: A Comparison Between the Bojarski Exact Inverse Scattering Theory and Holography as Applied to the Holographic Radio Camera," presented at the 1980 International Optical Computing Conference, April 8-11, 1980, Washington, DC; to appear in SPIE Proceedings, Vol. 231.

6. N. N. Bojarski, "Exact Inverse Scattering," presented at the 1980 DARPA/AF Review of Quantitative NDE, July 14-18, 1980, La Jolla, CA; to appear in conference proceedings.

7. N. Bleistein and J. Cohen, "Nonuniqueness in the Inverse Source Problem in Acoustics and Electromagnetics," Journal of Mathematical Physics, 18: 194-201, 1977.

8. W. R. Stone, "A Uniqueness Proof for the Bojarski Exact Inverse Scattering Theory, and Its Consequences for the Holographic Radio Camera," presented at the URSI National Radio Science Meeting, Boulder, Colorado, January 9-13, 1978.

9. N. N. Bojarski, "A Wave Equation for Radiating Source Distributions," presented at the URSI National Radio Science Meeting, Boulder, Colorado, November 6-9, 1979.

10. W. R. Stone, "The Nonexistence of non-Radiating Sources and the Uniqueness of the Solution to the Inverse Scattering Problem," presented at the North America Radio Science meeting, June 2-6, 1980, Quebec, Canada.

11. R. D. Mager and N. Bleistein, "An Examination of the Limited Aperture Problem of Physical Optics Inverse Scattering," IEEE Trans. Ant. Prop. AP-26: 695-699, 1978.

12. W. R. Stone, "The Resolution of an Aperture for Coherent Imaging," presented at the Optical Society of America Annual Meeting, San Francisco, California, October 23-27, 1978.

13. W. R. Stone, "Numerical Studies of the Effects of Noise and Spatial Bandlimiting on Source Reconstructions Obtained using the Bojarski Exact Inverse Scattering Theory," presented at the URSI spring meeting, College Park, Maryland, May 15-19, 1978.

ACKNOWLEDGEMENT

Many helpful discussions with Dr. N. N. Bojarski concerning the theory are gratefully acknowledged.

Copyrighted © 1980 by W. Ross Stone. All rights reserved. All information contained in or disclosed by this document is considered confidential and proprietary by W. Ross Stone. By accepting this material the recipient agrees that this material is held in confidence and trust and will not be used, reproduced in whole or inpart, nor its contents revealed to others, except to meet the purpose for which it was delivered. It is understood that no right is conveyed to reproduce or have reproduced any item herein disclosed without express written permission from W. Ross Stone. Permission is hereby granted for the 1980 DARPA Quantitative NDE Conference to publish this document as a part of its proceedings.

James Gubernatis (Los Alamos Scientific Laboratory): Where are your calculations?

Ross Stone (IRT Corporation): You're going to see some calculations in the two papers that follow. I don't have any with me here. There are several applications that this has been applied to. The ones I have been most interested in have had to do with inhomogeneous media. In particular, I have several calculations that show the reconstruction of lens-like deformities. I don't have them with me. I will send you a copy.

A. Nayfeh (Systems Research Laboratories): How would you know the shape and make-up of the difference? There is something there, but the make-up -

Ross Stone: The data appears as a surface integral, a Kirchhoff-like integral. In fact, it involves convolution with the conjugate of the Green's function. The defect itself appears exclusively in the source term RHO and you are able to recover that source term by solving the convolution equation. So, no, you do not recover the integral of that source term RHO. You recover RHO and from that you can solve, algebraically, for the defect.

Volker Schmitz (Battelle Northwest): Does the theory you developed still work when the wavelength is comparable to the size of the defects?

Ross Stone: Thank you. The name of this session is "Short Wavelength," and that is a very good point. Yes, it does still work. The effect of wavelength in comparison to the size of the defect is to determine resolution in the reconstruction, but it does not eliminate the possibility of reconstruction. And indeed, you will get useful information out of reconstructions when the wavelength is on the order of the size of the defect.

Gordon Kino (Stanford University): You referred to the fact you could get super resolution, essentially by a definition of phase, which I would agree. But in practice doesn't this really mean that you are back to saying, "I must have a continuous reading over th region of interest." Otherwise, you have a finite sampling, and essentially you're going to get -

Ross Stone: If you know what your sampling interval is, you can remove that effect. First of all, I have recorded and reconstructed three-dimensional images of the ionisphere at radio wavelengths. I noticed in the reconstruction that my resolution was considerably better that what would have been predicted based on a Rayleigh criteria and my sampling. I then went back to the theory and the computer, and I was able to derive analytically and simulate on the computer precisely the result I alluded to there, that the signal-to-noise ratio determines your ability to measure phase. If you can measure phase significantly better than within two PI radians, which likewise implies you have a relatively high signal-to-noise ratio, then you can indeed achieve a resolution significantly better than the Rayleigh resolution in spite of your sampling.

As one example, I plugged in a 15 db signal-to-noise ratio, reconstructed the impulse response on the aperture, where the Rayleigh criterion said the impulse response, for the distance over which I was doing the reconstruction should have been the size of the aperture and, in fact, the response half width was 1/20th of the size of the aperture, exactly as predicted by the theory.

J.D. Achenbach, Chairman: Thank you. We now have to move on to the next talk.

DIRECT INVERSION IN COMPLEX GEOMETRIES

Jack K. Cohen and Norman Bleistein
Denver Applied Analytics
Denver, Colorado 80222

ABSTRACT

Progress on the POFFIS high frequency flow imaging method is described. Both theoretical and experimental advances have occurred during the current year. Some success was achieved at imaging an off-axis trailer hitch flaw. However, the issue of variable speed was not completely resolved and research on this issue will continue.

INTRODUCTION

The objective of our research is to develop a production line technique for imaging flaws in solids. During our first year of support we adapted an appropriate portion of our high frequency inversion theory, originally developed for applications in geophysics, to the situation encountered in nondestructive evaluation. The computer algorithm developed for this purpose produced both an image of the flaw structure and an estimate of its reflection coefficient. The theory for this algorithm was based on reproducing a band-limited version of the characteristic function(s) of the flaw(s) in an otherwise homogeneous body with known external geometry. Below, we refer to this theory by the acronym POFFIS (Physical Optics Far Field Inverse Scattering). We have ascertained that the particular family of observation directions used had a profound influence on the quality of the inversion obtained. Thus, during this first year, we established a suitable (and probably near optimal) family of observation angles given the total number of observations to be made in a given viewing aperture.

Early researches in inversion problems made it clear that while direct estimation of the characteristic function from band-limited high frequency data produces a rather fuzzy image of inhomogeneities, [1 - 6] a derivative of the characteristic function (being more singular) is much more amenable to reproduction by such data. A series of papers by us, our associates and others [3, 7-11] had established the theoretical base for extracting such derivative information from aperture limited, i.e., band-limited and aspect-angle-limited data, in a stable manner. In the final computer implementation, the boundary of a flaw is displayed as the peak of a sinc-like function and the amplitude of this peak is in known proportion to the reflection coefficient.

At the end of our first support year, [12] a series of tests were performed by Richard Elsley at Rockwell. These tests established, to the satisfaction of our sponsors, that our inversion method (as implemented in a FORTRAN code delivered to Rockwell) was extremely stable even in the face of a paucity of viewing angles of observation and lower than desirable frequency range. These tests also indicated, in a preliminary manner, stability and robustness of the method when applied to laboratory data.

The nondestructive testing environment has many features which distinguish it from the geophysical environment and, after our initial success of designing a stable inversion algorithm in the first year, the second and third years have been devoted to improving our inversion method to take account of these features.

In the geophysical case, the layers are more or less horizontal. Consequently, the vertical derivative of the characteristic function provides adequate surface definition for this environment. In the NDE case, however, the orientation of the flaw boundaries is totally unknown. Since a directional derivative involves the cosine of the angle between a surface tangent of the flaw and the observation direction, the indicating peak of the sinc-like function is masked in observation directions which are nearly tangent to the flaw. Although the wide aperture of angles sometimes available to the experimenter would compensate to some extent for this defect of the inversion scheme, it was clearly desirable to extend the theory and implementation to remove this defect, if possible. A major accomplishment of our second year in the program was to do just this. In essence, the idea behind this improvement was to find an algorithm that directly produces the surface of a flaw, rather than its characteristic function. This direct imaging of the surface function (the "singular function" of the surface) obviates the necessity for choosing a fixed derivative direction.[13] This is particularly desirable in the NDE environment, where such a fixed direction has no intrinsic relation to the problem.

An extra benefit of this theoretical advance was that it eliminated the need to compensate for the direction cosine factor in deriving reflection coefficient estimates.

Toward the end of the second support year, we received laboratory data to test the new algorithm. At this time, we discovered several additional features of nondestructive testing data. The most salient of these are the gradual velocity changes from one direction of observation to another and the gradual variations in the geometry of the observation surface.

At the end of the second year, we dealt with these matters by employing measurements made on a

second test object of similar manufacture with a known flaw geometry. This procedure was clearly inaccurate and not generalizable to production line testing. Nonetheless, it sufficed to remove the principal variations in surface geometry and velocity and thus provide a preliminary test of the new "singular function" algorithm. The reproduction of the "unknown" flaw geometry (dimensions on the order of 600 microns) was quite adequate and thus encouraged us to pursue more suitable means of dealing with these variations. [14]

THEORETICAL RESULTS

Clearly, if the surface geometry is unknown to an extent comparable to the flaw sizes we seek to detect, a complete and accurate reproduction of the flaw is impossible. One way to overcome this shortcoming is to use low frequency back face reflections to establish a coordinate system. Another idea is to develop direct methods for measuring the surface geometry of the test object to the necessary accuracy. The program has the issue of surface geometry before it for future research.

During the first quarter of the present support year, we examined the question of estimating the velocity variations. In the experiment of the second year, these variations with direction were observed to be as much as 2% . Since the probing signal travels great distances relative to the diameter of flaws we must resolve, this seemingly small variation can have an effect which is the order of the entire flaw size. It is not clear whether real world objects would have as great a velocity variation as the test objects (which are subjected to great pressure during their manufacture), but nonetheless it seems likely that significant velocity variations will occur. Thus, both we and our sponsors agreed that compensation for velocity variations should be the prime focus of our research.

While the problem of detecting sharp velocity changes such as occur at a flaw boundary of sufficient contrast has been adequately resolved, the general question of detecting gradual large scale changes is more difficult. We have derived an integral equation whose unknown is the desired velocity variation, but its accurate numerical inversion in a three dimensional setting presents both mathematical and technological difficulties not yet resolved. However, the flaw imaging algorithm, as now constituted, requires only the average velocity between the source entry point and the flaw reflection. Thus, detailed, pointwise, velocity determination is not essential to the problem of flaw description.

At present, we have not investigated the possibility of determining the requisite average velocities from the full integral equation. Our first approach has been to attempt to determine a radial velocity in each observation direction. That is, we seek a one-dimensional scheme which will produce corrected average velocities for our three dimensional flaw inversion algorithm. Although not a perfect solution, these corrections should reduce the inaccuracies considerably. Depending on the performance of these one-dimensional corrections, we will later decide whether the question of three-dimensional corrections should be pursued in this problem.

All methods for determining the large scale velocity variations require wide-band data; in particular, low frequency data. During the first half of this year, we considered five possible methods of approximately determining these variations. The first three methods use only a narrow band in the low frequency regime. It is a well developed portion of the Rockwell program, due to Elsley, et al., to measure centroid location and higher moments of the flaw geometry by using low frequency methods. We had hoped that these measurements could be made on the same test object for which we received data and at the same angles as the high frequency data supplied to us. It became apparent, however, that due to the other demands made on the low frequency group at Rockwell, the centroid determinations could not be accomplished in a timely manner. We hope that the Elsley method will be used to determine the centroid location in the near future.

So as not to delay our portion of the program, we developed three methods of a similar type to Elsley's. The first of these is to use the peak obtained by inverse Fourier transforming the observations after applying a low cut digital filter and source signature deconvolution. The idea behind this is that at low frequency the flaw acts like a point located at its centroid. From this measurement and a determination of the elapsed time between signal entry into the medium and signal reflection, an average velocity in each direction is determined.

Our second low frequency approach is to use the same centroid measurement to determine an artificial time origin for each observation which, in effect, places the flaw center (centroid) at the center of an artificial sphere. Thus, this method involves translation of each observation, while the first involves a stretching of each observation.

The third method we developed involves using wide-band measurements to determine a one-dimensional velocity variation profile in each observation direction. An analogous algorithm for the geophysical case had already been developed by us, so it only remained to compute the average variation and construct a computer code.

The fourth method we are considering is the use of the back face reflection. This information is simple to use only for simple geometries such as the "trailer hitch" titanium spheres which are the initial object of our investigations. Nonetheless, at this stage of the research this information is important as a check on the other methods and possibly for providing calibrations.

A final theoretical achievement of the current support year was the development of an algorithm for obtaining flaw descriptions of a body immersed in a fluid bath. This algorithm requires as data the responses from the test object to a family of plane wave probes. It thus has the disadvantage of requiring a large amount of data and subsequent computer manipulation of that data. We hope to find other algorithms for this configuration which make less demand on the experimetns and on the computer.

THE EXPERIMENT

Recently, Dr. James Martin collected an extensive set of data on a trailer-hitch sample containing an oblate ellipsoidal flaw of revolution whose axes are 800 microns and 400 microns (30 mils and 15 mils). To provide a more realistic test of of the POFFIS algorithm, we had requested and Dr. Martin carried out an equipment modification which allowed tilting of the titanium sphere. Since the flow was originally machined with axes respectively normal and parallel to the mounting, this new flexibility allowed for the more realistic case of a flaw orientation whose axes did not coincide with the axes of the observation system.

The inversion scheme is based on a partition of the unit sphere into M latitudes and $2 \cdot M$ longitudes, which are optimally spaced for stability of the scheme. In practice only a subset of the $2 \cdot M^2$ observation will be available and indeed the POFFIS algorithm was successfully tested last year [14] using observations taken only an octant of the surface. In the current set of experiments, we have selected $M = 7$ and thus a full set of observations would total 98. The mounting of the trailer hitch prevents data collection on the southern most latitude so the total feasible number of observations is 84. Since the "limited aperture" aspect of the algorithm is no longer in question, it was decided to collect data at all 84 feasible locations. Dr. Martin took two sets of data at these locations. One was made with a 5MHZ, ¼" transducer ("high" frequency data) while the other was made with a 2¼ MHZ, ½" transducer ("low" frequency data). In order to obtain reflection coefficient estimates, the high frequency data must be deconvolved with respect to the source signature. To obtain this signature, an additional observation was made for each transducer on a hemisphere. Finally, a small number of lines were taken with other transducers.

ANALYSIS

The analysis began with the signature deconvolution of the high frequency data. This provides the primary input data for the inversion algorithm. Since it is known that the internal structure of the test object contains only a single flaw, the deconvolved signals should be constant in magnitude and linear in phase within the frequency band of adequate signal-to-noise ratio. We did, indeed, obtain such a result in the band 1.9 - 11.0 MHZ. The lower value corresponds to a "ka" range of .8 to 1.6 as we move around the ellipsoid. Since the inversion algorithm assumes high frequency data, we applied an additional low cut digital filter and used only the band 4.3 - 11.0 MHZ (ka from 1.8 to 3.6 for the lower value). It was further observed that the amplitude of this deconvolved signal was relatively constant and the phase was nearly linear. See Figure 1.

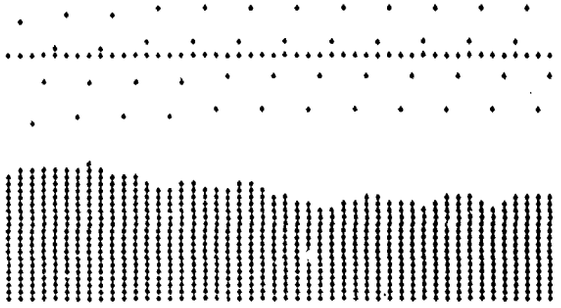

FIGURE 1

MAGNITUDE (LOWER) AND PHASE (UPPER) OF A DECONVOLVED EXPERIMENTAL LINE. THE PHASE IS GIVEN IN THE RANGE $\pm 180^0$. THE FREQUENCY RANGE IS APPROXIMATELY 6-8MHZ IN INCREMENTS OF .5MHZ.

The Fourier inversion of this deconvolved signal produced a band limited pulse, or sinc function. After examining the data, we hypothesized that the observed source line had passed through a caustic on its propagation path. This has the effect of producing a phase shift in the Fourier domain: $+ \pi/2$ for positive frequencies and $- \pi/2$ for negative frequencies. We adjusted for this in the deconvolution and then found that the Fourier transform exhibited the appropriate sinc-like behavior. The question of optimal deconvolution remains before us (especially since the source experiment is not yet completely standardized), but we feel that our current technique provides an adequate result. See Figure 2.

FIGURE 2

INVERSE TRANSFORM OF DECONVOLVED EXPERIMENTAL LINE WITH CAUSTIC CORRECTION.

The next step in the analysis was to deconvalue the low frequency data. This provides the data necessary for the various velocity determination schemes. Here the phase shift problem encountered above did not occur, but a near null in the source frequency spectrum at .4 MHZ (ka from .2 to .4), prevented successful deconvolution in the region necessary for the low band and wide band velocity determination methods. An order of magnitude calculation indicated that a small air gap between the base of the hemisphere and its mounting would cause a frequency null in this range. Dr. Martin was able to separate the hemisphere from its mounting and indeed found such a gap. Furthermore, he has recently informed us that by appropriately altering the mount, he was able to remove the low frequency source null. We look forward to using this new source record in the near future for velocity determinations. While Dr. Martin investigated the source mounting issue, we fell back on the use of back-face reflections to determine a working set of velocities. Since the observation points used are symmetric with respect to the origin, on 70 of the 84 lines we had the opportunity to determine the velocity two times. On several lines, we discovered that there were serious discrepancies in the two velocities determined from opposite directions on the diameter.

Since our inversion method is a three-dimensional synthesis, an incorrect speed determination on a line not only causes a mis-estimate of the flaw size but can also cause a defocussing effect which obscures the indicating sinc-function peaks in the output on that line and nearby lines. Indeed, upon employing the average speed (on the 70 lines where two determinations were possible), we were completely unable to locate peaks at 9 of the 84 output points and peak location was uncertain at several other points. The maximum flaw diameter found was about 600 microns, at approximately the correct orientation, but other geometrical data (axes orientation, volume, etc.) were not computed because of the generally poor results.

In cooperation with Richard Elsley, Dr. Martin has recently discovered a likely cause of the back-face velocity discrepancies we observed. At the lower sampling rate used for the low frequency data, the recording device was found to drop about two data points per record in regions where the recorded signal was of low amplitude.

Given this explanation, it is clear that using the minimum velocity of each pair, rather than the average, probably would have given a more consistent set of velocities. However, since Dr. Martin will soon be able to record a data set which does not have missing points, we do not plan to make further use of the present low frequency data set. However, it is worth noting in passing that each missing data point corresponds to an underestimate of 60 microns in flaw size. Thus, if there were two missing data points on the lines near our reconstructed maximum diameter our flaw size estimate would increase to 840 microns which is in good agreement with the original specification of 800 microns.

Realistically, the effort to reduce the POFFIS inversion method to practice must be regarded as an iterative loop between experiment and theory. Both of these must evolve hand-in-hand for the effort to succeed. It is not surprising that in this first large scale data collection and analysis effort difficulties should emerge both with the experiment and the analysis. These difficulties largely frustrated our efforts to test the velocity estimation techniques described above. However, this data analysis represented only about two months of effort. Furthermore, the rapidity with which these difficulties are being resolved bodes well for future success, both short term and long range.

ACKNOWLEDGEMENTS

The authors wish to express their gratitude to Willene Grady for her fine programming, to J. Martin of Rockwell for his efforts in pursuit of "clean" experiments and to C. Roukangas of Rockwell for her supportive programming efforts.

This research was sponsored by the Center for Advanced NDE operated by the Science Center, Rockwell International, for the Advanced Research Projects Agency and the Air Force Materials Laboratory under contract F33615-74-C-5180.

REFERENCES

1. N.N. Bojarski, "Three dimensional electromagnetic short pulse inverse scattering", Syracuse University Research Corporation, Syracuse, New York, NTIS #AD-845 126 (1967).

2. R.M. Lewis, "Physical optics inverse diffraction", IEEE Transactions on Antennas and Propagation AP-17 (3), 308-314 (1969).

3. N.N. Bojarski, "Inverse Scattering", Company Report # N00019-73-C-0312/F, prepared for Naval Air Systems Command, AD-775 235/5 (1974)

4. W.L. Perry, "On the Bojarski-Lewis inverse scattering method", IEEE Transactions on Antennas and Propagation AP-22 (6), 826-829 (1974).

5. W. Tabarra, "On an inverse scattering method", IEEE Transactions on Antennas and Propagation AP-21, 245-247 (1973).

6. W. Tabarra, "On the feasibility of an inverse scattering method", IEEE Transactions on Antennas and Propagation AP-23, 446-448 (1975)

7. S. Rosenbum-Raz, "On Scatterer reconstruction from far-field data", IEEE Transactions on Antennas and Propagation AP-24, 66-70 (1976).

8. N. Bleistein, "Direct image reconstruction of anomalies in a plane via physical optics far field inverse scattering", J. Acoustical Soc. Amer. 59 (2) 1259-1264 (1976).

9. N. Bleistein, "Physical optics farfield inverse scattering in the time domain", J. Acoustical Soc. Amer. 60 (6) 1249-1255 (1976).

10. R.D. Mager and N. Bleistein, "An examination of the limited aperture problem of physical optics inverse scattering", IEEE Transactions on Antennas and Propagation AP-26 (5) 695-699 (1978).

11. J.A. Armstrong and N. Bleistein, "An analysis of the aperture limited Fourier inversion of characteristic functions", University of Denver Mathematics Department Report, MS-R-7812 (1978).

12. J.K. Cohen, N. Bleistein and R.K. Elsley, "Nondestructive detection of voids by a high frequency inversion technique", Interdisciplinary Program for Quantitative Flaw Definition, Special Report Fourth Year Effort, Program Manager, Donald O. Thompson, prepared at Rockwell International Science Center for ARPA, October, 1978.

13. J.K. Cohen and N. Bleistein, "The singular function of a surface and physical optics inverse scattering", Wave Motion (1), 153-161 (1979).

14. N. Bleistein and J.K. Cohen, "Progress on a mathematical inversion technique for nondestructive evaluation", Wave Motion (2), 75-81 (1980).

J.D. Achenbach, Chairman (Northwestern University): There is five minutes before the next session is supposed to start. Let's have one question.

Gordon Kino (Stanford University): I think I would like to make a comment rather than a question. It seems to me one thing that has got to be done with these numerical techniques - they're very powerful and so on - but somehow you have to get some rough-cut numerical techniques because it is no use doing a measurement where you have to go back six months later and say, "Oh, we didn't have it lined up." You have got to get some technique where you get a quick result on line and then you can massage the hell out of it.

Norm Bleistein (Denver Applied Analytics): We do that by hand and eyeball. I take the input lines that Jim gives me and I have a rough idea what the size and orientation is by doing that. We really can do that kind of thing, so it's really potentially there. And one of the things we are hoping for, for these considerations where we try the data and see what the data is and decide it this way, is that we would formalize those things just because we are repeating the same king of seat-of-the-pants operations over and over again. But I quite agree with you we want to do that as a first step.

TIME DOMAIN BORN APPROXIMATION

J.H. Rose
Ames Laboratory, U.S. DoE
Iowa State University
Ames, Iowa 50011

J.M. Richardson
Rockwell International Science Center
1049 Camino Dos Rios
Thousand Oaks, California 91360

ABSTRACT

The time domain Born approximation for ultrasonic scattering from volume flaws in an elastic medium is described. Results are given both for the direct and the inverse problem. The time domain picture leads to simple intuitive formulas which we illustrate by means of several simple examples. Particular emphasis is given to the front surface echo and its use in reconstructing the properties of the flaw.

INTRODUCTION

Much of the recent development of ultrasonics for quantitative nondestructive engineering (NDE) applications has been due to the close interaction of both theory and experiment. One small difficulty in this situation is as follows. Most of the experiments are performed using a pulsed transducer with a consequent wide band of frequencies. The data is collected as time domain records and may be thought of as the impulse response function of the flaw convolved with the transducer's pulse shape. On the other hand, most of the theory for elastic wave scattering has been calculated in terms of the wavevector $\vec{k}$ of an incident plane wave. The result is a certain mismatch in the comparison of theory with experiment.

The weak scattering limit yields one of the simplest theories of elastic wave scattering. For cases of interest to NDE, this limit was studied systematically by Gubernatis et al,[1] in terms of the Born approximation.[2] Their work was carried out in the wavevector (or frequency) domain and considerable intuitive understanding of the problem resulted. Despite its simplicity, the frequency domain Born approximation has been widely useful in systematizing experimental data. Further, it has led to the development of a rather successful inversion scheme.[3] Recently, the authors have formulated the weak scattering theory in the time domain using the Born approximation.[4] This new formulation is also rich in its own insights and intuitions. The time domain picture gives rise to simple transparent formulas for the scattering problem which allow the solutions of many problems by inspection. The scattering amplitude for more complicated problems can be easily estimated roughly in an intuitive way. Similarly, simple intuitive formulas are obtained for the inverse problem: i.e., determining the shape and the material composition of the flaw from the scattering. It is the purpose of this paper to introduce the NDE community to these new results. Several simple example cases are treated in order to illustrate the straightforward and useful nature of the formulas. The details of the mathematical derivation will be reserved for a forthcoming paper in which we present a time domain integral equation approach. The Born approximation is obtained as the first iteration of this integral equation.

Before proceeding we remind the reader of the practical limitations of the Born approximation for the direct problem. The Born approximation is a weak scattering theory. Good results will be obtained for a finite flaw, in other than the forward scattering direction, if the material parameters of the flaw are sufficiently close to those of the host. However, the approximation is surprisingly robust and useful results have been obtained for a wide class of flaws, including voids. Often in NDE application, the flaws scatter the ultrasound strongly. In such cases, the frequency domain Born approximation yields its best results for lower frequencies and for directly back scattered signals.[1] At high frequencies the Born approximation fails for forward scattering. In the time domain, we expect the back scattered early arriving signal to be best described. Later arriving signals will tend to involve possible multiple reflections which are ignored in the Born approximation.

The Born approximation has been shown to yield an exact inverse method for the shape and material parameters for the weak scattering flaws described above.[5] Further, it has been successful, in several empirical tests, in the determination of the shape and size of strongly scattering flaws such as spheroidal voids.[3,6,7] Recently, the authors have shown that the inverse Born approximation leads to an exact determination of the shape of an ellipsoidal void in an isotropic elastic solid given ideal data for the scattering amplitudes (i.e., precise longitudinal to longitudinal (L+L) pulse-echo data at all frequencies, and for all angles of incidence).[8] These results are most easily elucidated in the time domain and are the subject of a forthcoming paper. The present form of the Born inverse scattering theory has not been tested for crack-like defects or multiple flaws.

The purpose of this paper is to illustrate the use of the time domain Born approximation for the simple case of finite sized volume inclusions with constant material parameters. In keeping with our limited purposes, we consider primarily longitudinal to longitudinal (L+L) scattering. In Section II, we summarize the formulas for the

determination of the impulse response function. Section III illustrates the use of these formulas for two simple flaws. Section IV summarizes the formulas for the inverse scattering problem. Results are discussed both for the determination of the shape and the material parameters of flaws. We also comment on the applicability of these methods for strongly scattering flaws. In Section V we illustrate the use of the inverse scattering method for a spherical flaw. Section VI is a brief conclusion. The appendix gives formulas for the impulse response functions for L → L, L → T, T → L, and T → T scattering from inhomogeneous isotropic flaws with various polarizations of T (transverse) waves.

TIME DOMAIN SCATTERING FORMULAS

Consider an isotropic homogeneous inclusion with material parameter ρ_F, λ_F and μ_F embedded in an isotropic homogeneous host material with constant material parameters ρ_0, λ_0 and μ_0. Here ρ is the density and λ and μ are the Lame parameters. The deviations of the flaws material parameters are defined as $\delta\rho = \rho_F - \rho_0$, $\delta\mu = \mu_F - \mu_0$ and $\delta\lambda = \lambda_F - \lambda_0$. In order to describe the scattering we consider a longitudinally polarized impulse incident upon the flaw which is centered about the origin of coordinates. The incident impulse is described by

$$\vec{U}_I(\vec{r}',t') = U_0\delta(t'-\vec{r}'\cdot\hat{e}_i/c)e_i \qquad (1)$$

Here $\hat{e}_i$ is the direction of incidence, c is the velocity of longitudinal sound in the host, and U_0 determines the magnitude of the impulse. The amplitude of the scattered displacement field far from the flaw is given in the Born approximation[4] by

$$\vec{U}_s(\vec{r}',t') \xrightarrow[r'\to\infty]{} \frac{\hat{e}_0}{r'} f(\hat{e}_i,\hat{e}_0)\frac{1}{c^2}\frac{d^2}{dt'^2}$$

$$\int d^3\vec{r}\,\gamma(\vec{r})\,\delta(t'-\frac{r'}{c}-\frac{\hat{e}_i-\hat{e}_0}{c}\cdot\vec{r}) \quad . \qquad (2)$$

Here $\hat{e}_0$ denotes the direction of scattering. The characteristic function, γ, is one inside the flaw and is zero outside. Hence, it defines the flaw's shape. The function $f(\hat{e}_i,\hat{e}_0)$ depends only on the relative angle between $\hat{e}_i$ and $\hat{e}_0$ and is given by

$$f(\hat{e}_i,\hat{e}_0) = \frac{1}{4\pi}\left[\frac{\delta\rho}{\rho_0}\hat{e}_i\cdot\hat{e}_0 - \frac{\delta\lambda+2\delta\mu(\hat{e}_i\cdot\hat{e}_0)^2}{\lambda_0+2\mu_0}\right] \quad . \qquad (3)$$

Eq. (2) is still somewhat clumsy for describing the displacement field since it depends explicitly on the position and time at which the signal is measured. We obtain an expression which is independent of r' and t' by the transformation

$$\vec{R}(t,\hat{e}_i,\hat{e}_0) = \hat{e}_0\, r'\,\vec{U}_s(\vec{r}',t)/U_0 \quad . \qquad (4a)$$

$$\vec{R}(t,\hat{e}_i,\hat{e}_0) = f(\hat{e}_i,\hat{e}_0)\,\hat{e}_0\,\frac{1}{c^2}\frac{d^2}{dt^2}\int d^3\vec{r}\,\gamma(\vec{r})$$

$$\delta(t-(\hat{e}_i-\hat{e}_0)\cdot\vec{r}/c) \qquad (4b)$$

Here we have set $t = t' - r'/c$. The origin of time is defined by Eq. (1) and corresponds to the unimpeded incident pulse (Eq. 1) crossing the origin of coordinates. Further, we have normalized u_s by r' and u_0 to obtain a quantity, $\vec{R}$, which does not depend either on the intensity of the incident pulse or on the distance at which the asymptotic scattering is measured. $\vec{R}$ is called the impulse response function of the flaw and its expression in Eq. (4) is the basic result of the direct scattering theory. $\vec{R}$ corresponds to the time domain train of signals which would be received by a transducer in the scattering direction e_0 due to an incident delta function displacement pulse in the incident direction e_i.

There are two important observations to be made about $\vec{R}(t,\hat{e}_i,\hat{e}_0)$. First, it is the Fourier transform of the L→L scattering amplitude, $\vec{S}$, in the k-domain.[4] $\vec{S}$ is defined by the asymptotic scattered displacement field

$$\vec{U}_s(|\vec{k}|,\hat{e}_i,\hat{e}_0) \xrightarrow[r\to\infty]{} \vec{S}(|\vec{k}|,\hat{e}_i,\hat{e}_0)e^{ikr}/r \quad . \qquad (5)$$

Then $\vec{R}$ is determined by

$$\vec{R}(t,\hat{e}_i,\hat{e}_0) = \frac{1}{2\pi}\int_{-\infty}^{\infty} d\omega\,\vec{S}(\omega/c,\hat{e}_i,\hat{e}_0)\,e^{-i\omega t} \qquad (6)$$

where we have the relation $\omega = c\,k$.

The second important observation is a simple geometrical interpretation of $\vec{R}$. First we note that f depends only on the angle between the incoming and outgoing wave. The integral in Eq. (4b) corresponds to the cross-sectional area, A(t), of the flaw evaluated on a plane defined by

$$\vec{r}\cdot(\hat{e}_i-\hat{e}_0) = ct \quad . \qquad (7)$$

This plane defines the locus of points in the flaw which have a constant travel time from the initiating transducer to the receiving transducer. The simple planar form of this locus results from the weak scattering assumption that the incident impulse travels at the velocity of the host inside the flaw and that the signal is determined by single scattering events. Figure 1 illustrates the geometrical interpretation of A for a given incident and exit direction. The time dependence of the scattering from quite complicated shapes is now straightforward and a great deal can be learned simply by inspection.

EXAMPLES OF THE DIRECT SCATTERING PROBLEM

The use of the time domain Born approximation to determine the impulse response function is illustrated below for two simple flaws. First, scattering from a cubical flaw is used to illustrate pulse-echo calculations. By altering the incident direction such that the incoming impulse

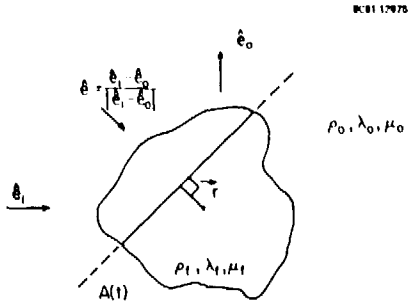

Fig. 1 Shows the geometric interpretation of time domain scattering. The impulse response function is proportional to A"(t). A(t) is defined as the cross-sectional area of the flaw perpendicular to r: and t = $(e_i - e_o) \cdot r/c$.

first contacts on a face, on an edge or on a point, we illustrate several different characteristic forms for $\vec{R}(t,\hat{e}_i,\hat{e}_o)$. Of particular interest, we have included a case in which the front surface echo has no outstanding features and might "disappear" in an experimental measurement. Our second illustration shows the determination of $\vec{R}(t,\hat{e}_i,\hat{e}_o)$ for pitch-catch scattering from a sphere.

The impulse function is conveniently expressed for computational purposes after a change of variable, namely $s = ct/|e_i - e_o|$. Rewriting Eq. (4)

$$\vec{R}(s,\hat{e}_i,\hat{e}_o) = \frac{\hat{e}_o f(\hat{e}_i\cdot\hat{e}_o)c}{|\hat{e}_i - \hat{e}_o|}\frac{d^2}{ds^2}\int d^3\vec{r}\gamma(\vec{r})\,\delta(s-\hat{e}\cdot\vec{r}). \tag{8}$$

Here

$$\hat{e} = (\hat{e}_i - \hat{e}_o)/|\hat{e}_i - \hat{e}_o| \quad .$$

The impulse response function is proportional to the second derivative of the cross-sectional area of the flaw, A(s), projected on a plane perpendicular to e and at a distance s from the center of the coordinate system. For the illustrative cases we choose the origin of coordinates to be the centr of inversion symmetry.

The determination of $\vec{R}$ reduces to finding A"(s). Consider the case when the incident impulse is incident parallel to a cube face. A and A" are shown in Fig. 2. Scattering from a cube face is characteristic of scattering from a flat on a flaw surface which lies parllel to the incident impulse. The front surface echo is the derivative of a delta function. Figure 3 shows the impulse response function when the incident impulse is parallel to a cube edge. The result is a front surface echo consisting of a delta function. Finally, and perhaps most surprisingly, we consider the scattering of the incident impulse which initially contacts the cube on one of its corners (the most common situation for a randomly chosen angle of incidence). The result is shown in Fig. 4. Note that the front surface echo shows no singular behavior. This last result is generally

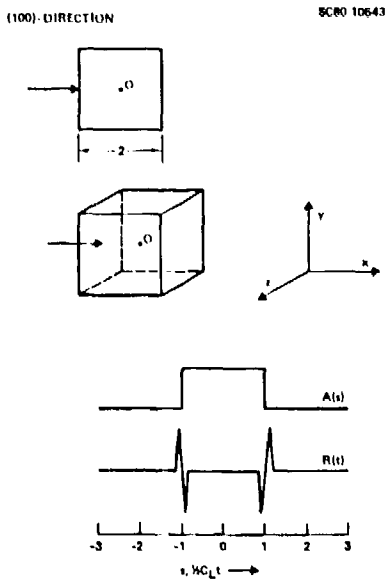

Fig. 2 Pulse-echo scattering from a cube face. The outstanding feature of this result is the appearance of the derivative of a delta function in the front surface echo.

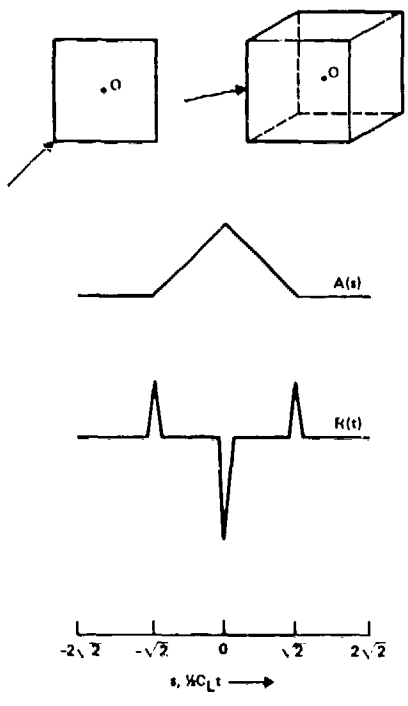

Fig. 3 Impulse response function for pulse-echo scattering from a cube edge. The front surface echo is now a delta function.

true for pulse-echo scattering from the point of a flaw. For these cases the front surface-echo is not notably different from the other parts of the

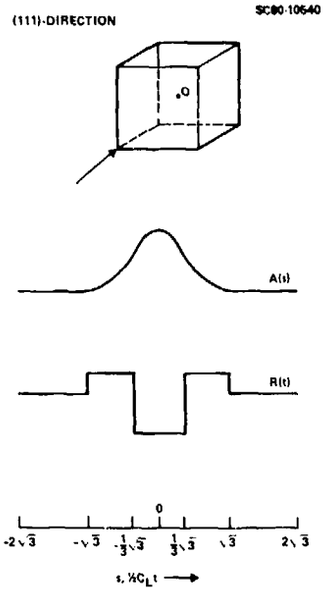

Fig. 4 Impulse response function for pulse-echo scattering from a cube corner. Here there is no singular behavior of the front surface echo.

returning signal. Experimentally, the front surface echo may seem to "disappear." Such a lack of a front surface echo has been observed for star shaped iron flaws in Si_3N_4.[9]

We conclude this section by considering pitch-catch scattering from a spherical flaw. For illustration we have chosen $\hat{e}_i$ such that the angle of incidence is 0° and such that the scattering angle is 120°. The resulting A(s) is on a plane surface perpendicular to the vector $e = (\hat{e}_i - \hat{e}_o)/(|\hat{e}_i - \hat{e}_o|)$. The cross-sectional area of the sphere is given by

$$A(\hat{e},s) = \pi(R^2 - s^2), \ |\vec{s}| < R \quad . \tag{9}$$

Here R is the flaw's radius. A and its first two derivatives with respect to s are shown in Fig. 5. The impulse response function is given by

$$\vec{R}(\hat{e}_i,\hat{e}_o,s) = \frac{\hat{e}_o \, f\,(\hat{e}_i\cdot\hat{e}_o)c}{|\hat{e}_i - \hat{e}_o|^3}(2\pi R)^{-1}[\delta(s+R) + \delta(s-R) - \tfrac{1}{2}R\,\theta(R-|s|)] \quad . \tag{10}$$

The appearance of a delta function in the front surface echo is characteristic of scattering from a flaw which has a finite radius of curvature everywhere. Additionally, we note that the substitution $s = ct/|\hat{e}_i - \hat{e}_o|$ indicates the pulse train will be longest when $\hat{e}_i = -\hat{e}_o$ (backscatter) and will become progressively shorter as $\hat{e}_i \to \hat{e}_o$ (forward scatter). For exactly forward scatter, all of the scattered energy would arrive simultaneously with the incident impulse resulting in the high frequency divergence for forward scatter. These results stem from the Born assumption that the velocity of propagation in the flaw is the same as in the host.

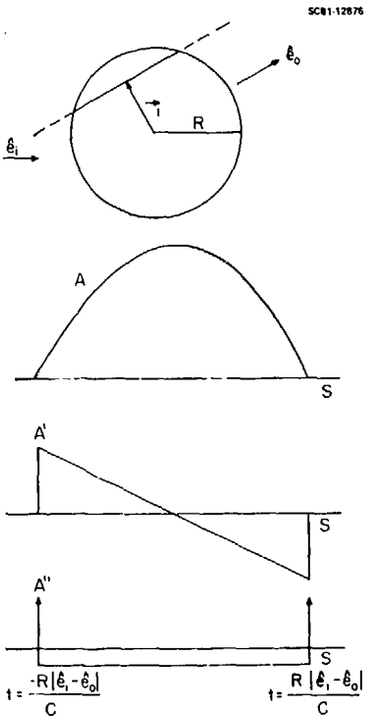

Fig. 5 Pitch-catch scattering from a sphere. Notice that for a flaw with finite radii of curvature the front surface echo is a delta function.

THE INVERSE SCATTERING PROBLEM

For the class of flaws we are considering, the inverse problem consists of two parts. First, the determination of the flaw's characteristic function (i.e., the shape). Second, the determination of the material parameters. Below we give the formula (valid in the weak scattering limit) for exactly reconstructing the shape of the flaw. Then we show how the specular reflection can be used to deduce the material properties of the flaw. We concentrate on the front surface echo (the specular reflection) since we know that the weak scattering assumption is violated for many of the flaws encountered in practice. We expect that the early arriving specular reflection will be given more accurately by the Born approximation than the later arriving signal. Our expectation is based on the fact that by considering only the first arriving signal we avoid multiple reflections within the flaw. Formulas are given for determining $\delta\lambda$ and the difference in the acoustic impedance, δZ, in terms of the front surface echo. We also discuss similar results for $\Delta\rho$ and $\Delta\mu$

which can be obtained from L→T and T→T scattering, respectively.

The shape of a flaw can be determined from L→L pulse-echo data measured for all incident directions, $\hat{e}_i$. The characteristic function is determined from the impulse response[4] and is

$$\gamma(\vec{r}) = \text{const.} \int d^2\hat{e}_i \; R\left(t = \frac{2\hat{e}_i \cdot \vec{r}}{c}, \hat{e}_i, -\hat{e}_i\right) . \quad (11)$$

Geometrically, this is equivalent to adding up the backscattered impulse response functions for all angles of incidence, $\hat{e}_i$, and for those times, $t = 2\hat{e}_i \cdot \vec{r}/c$ which include scattering coming from the point $\vec{r}$. Equation (11) applies to flaws with spatially variable material parameters if we replace the characteristic function, γ, with the acoustic impedance function $\delta z(\vec{r})$. Here $\delta z(\vec{r}) = \rho_f(\vec{r})c_f(\vec{r}) - \rho_0(\vec{r})c_0(\vec{r})$, where $\rho_f(\vec{r})$ and $\rho_0(\vec{r})$ denote the spatially variable densities of the flaw and the host. Similarly $c_f(\vec{r})$ and $c_0(\vec{r})$ indicate the spatially variable longitudinal velocities.

The material properties of the flaw can be extracted from Eq. (4) as follows. The time dependence of the impulse response function is given by the second time derivative of the cross-sectional area function. However, the magnitude of the impulse response function is determined by the angular factor $f(\hat{e}_i \cdot \hat{e}_0)$. By choosing special incident and exit directions we can determine the material properties. Consider the case of direct back scattering in which case $\hat{e}_0 = -\hat{e}_i$. Then

$$f = -\frac{1}{2\pi}\frac{\delta z}{z_0} . \quad (12)$$

Here z_0 is the acoustic impedance ($z_0 = \rho_0 c$) and δz is the difference in the acoustic impedance of the flaw and the host. Thus, if the acoustic impedance of a flaw is greater than that of the host $R(t,\hat{e}_i,-\hat{e}_i)$ will be inverted with respect to the incident pulse. On the other hand, if δz is less than zero, R will be upright.

The Lamé parameter λ can also be determined from L→L scattering. Here choose $\hat{e}_0$ to be perpendicular to $\hat{e}_i$. Then

$$f = \frac{1}{4\pi}\frac{\delta\lambda}{\lambda + 2\mu} . \quad (13)$$

Similarly, $\delta\rho$ can be obtained from L→T scattering and for $\delta\rho$ and $\delta\mu$ from T→T scattering. Thus by considering L→L and T→T pulse-echo scattering alone, we find the material parameters of the flaw. For weak scattering flaws the magnitude of the signal (and front surface echo) determines $\Delta\lambda$, $\Delta\rho$ and $\Delta\mu$ via Eqs. (12) and (13) and their analogs for T→T scattering. For strongly scattering flaws, we do not expect an accurate relation. However, it is possible that by observing the sign of the front surface echo for strongly scattering flaw, we will be able to determine the signs of $\delta\rho$, $\delta\mu$, $\delta\lambda$ and δz. In this connection it is worthy of note that it was shown by one of us[5] that with a sufficient diversity of pitch-catch L→L scattering measurements one can estimate (in principle) the spatial distribution of $\delta\rho$, $\delta\lambda$, and $\delta\mu$.

INVERSE BORN APPROXIMATION FOR THE SHAPE

In order to illustrate the use of the inversion algorithm implied by Eq. (8), we consider the case of a spherically symmetric flaw. Then the time domain inversion algorithm (Eq. 11) reduces to

$$\gamma(|\vec{r}|) = \text{const.} \frac{1}{2r/c} \int_{-2r/c}^{2r/c} R(t,\hat{e}_i, -\hat{e}_i) . \quad (14)$$

Here $\hat{e}_i$ is arbitrary since the flaw has spherical symmetry. The characteristic function is given by a time domain average of the impulse response function about the zero of time. Using the impulse response function for a sphere, which is shown in Fig. 5, we see that the characteristic function, γ, will be a constant for values of r less than the radius. For a value of r equal to the radius, γ will drop discontinuously to zero. Further, γ is zero for r greater than the radius. Thus we have reconstructed the characteristic function of a sphere. The Born inversion algorithm appears to be much more general than its derivation as a weak scattering limit might suggest. Figure 6 shows the reconstruction of the characteristic function for a spherical void in Ti using the exact scattering results of Ying and Truell.[10]

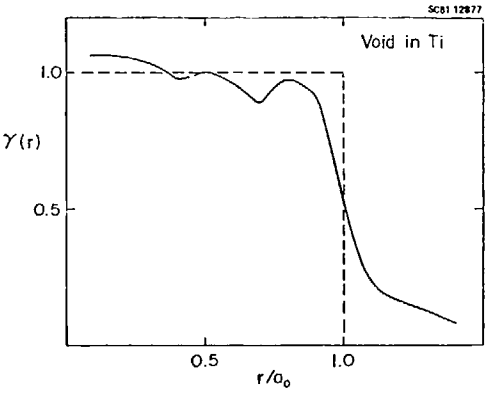

Fig. 6 Calculated characteristic function for a spherical void in T_i using the Inverse Born Approximation.

The inversion algorithm for spherical flaw is significantly simpler to implement than the general form, Eq. (11). It has been found that the simplest form of the inverse Born approximation Eq. (14) can be used to study the shape of ellipsoidal flaws.[3,6,7] In this case, rather than determining the distance from the flaws center to the surface, one determines the distance from the center to the tangent planes to the surface.

In order to implement the inversion formulas, it is necessary to experimentally establish the zero of time, which is defined as the instant the unimpeded impulse would have crossed the center of mass of the flaw. For weakly scattering flaws of arbitrary shape, this zero of time can be determined. For flaws with a center of inversion symmetry, there is a general method for determining the zero of time for arbitrarily strongly scattering flaws. These methods rely upon the low frequency expansion of the scattering amplitude or equivalently the first four moments of the impulse

response function. Details can be found in Refs. 11, 12 and 13. For strongly scattering flaws of general shape (with no center of inversion symmetry), the determination of the zero of time is problematic and the implementation of the inversion algorithm is uncertain.

The time domain Born approximation provides a basis for extending the inversion method suggested by Cook et al.[14] They noted (following Kennaugh and Moffat[15] for the electromagnetic case) that if the time domain pulse-echo scattering response to an incident delta function plane wave is proportional to the second derivative of the cross-sectional area (see Eq. 4b), then the scattering response to a ramp function will yield the cross-sectional area of all sections of the flaw perpendicular to the incident direction. Previously, this inversion method has been justified by the use of the physical optics approximation which is most appropriate for voids and for high frequencies. The time domain Born approximation for the impulse response function indicates the inversion method is also justified for weakly scattering inclusions as pointed out by Cook.[16]

SUMMARY

We have illustrated the use of the time domain Born approximation. Simple examples were chosen to demonstrate the utility of the approximation both for the direct and the inverse scattering problems. Of particular interest is the manner in which the front surface echo depends on the geometry of the scatterer. The front surface echo allows us to determine the sign of δz and $\delta\lambda$ from L→L scattering. L→T scattering allows one to infer $\delta\rho$, while T→T scattering lead to a knowledge of both $\delta\rho$ and $\delta\mu$. The time domain Born approximation provides a convenient intuitive picture for discussing both the direct and inverse scattering problems.

APPENDIX

COMPILATION OF L→L, L→T, T→L AND T→T RESULTS

The direct scattering formulas are listed here for L→L, L→T, T→L, and T→T scattering. Further, the material parameters of the flaw are allowed to vary with position. Since the results are considerably more complicated than the simple case of L→L scattering treated in the main text, we change our notation to a more general form. First, the incident impulse is uniformly chosen to propagate in the +z direction. The asymptotic form of the scattered displacement field is represented

$$r\, U_i^s(\vec{r},t)/U_0 \xrightarrow[r\to\infty]{} A_i(t-r/c_L) + B_i(t-r/c_T) \quad . \tag{A1}$$

Here U_0 is the strength of the incident delta function impulse; c_L and c_T are, respectively, the velocity of longitudinal and transverse sound. Tensor notation is adopted to denote the component of the vectors $\vec{U}$, $\vec{A}$ and $\vec{B}$. $\vec{A}$ represents the longitudinal response due to an arbitrarily polarized impulse. If the impulse itself is longitudinally polarized then $\vec{A}$ is identical to the function $\vec{R}(t,e_i,e_o)$ defined in Section II. $\vec{B}(t)$ is the transverse response to an arbitrarily polarized impulse.

In order to succinctly state the results we define the unit vectors r, θ and ψ, where r is the direction of propagation of the scattered wave.

$$\hat{r} = \hat{x}\sin\theta\cos\psi + \hat{y}\sin\theta\sin\psi + \hat{z}\cos\theta$$

$$\hat{\theta} = \hat{x}\cos\theta\cos\psi + \hat{y}\cos\theta\sin\psi - \hat{z}\sin\theta \tag{A2}$$

$$\hat{\psi} = -\hat{x}\sin\psi + \hat{y}\cos\psi.$$

Here θ and ψ are the polar and azimuthal angles of our spherical coordinate system; and x, y and z are the unit vectors of the rectangular system. Much of the notation in the appendix is taken from the MSC report of Gubernatis et al, which is an excellent account of the frequency space Born approximation.

First, we consider an incident impulse which is longitudinally polarized (Eq. 1). In what follows e_i is always equal to z, the direction of incidence. Nonetheless, we retain e_i for uniformity of notation.

$$A_i(t) = \frac{\hat{r}_i}{4\pi c_L^2}\frac{d^2}{dt^2}\int d^3\vec{r}\,\gamma(\vec{r})\,\frac{\delta\rho(r)\cos\theta}{\rho_0} - \frac{\delta\gamma(r)+2\delta\mu(r)\cos\theta}{\lambda_0+2\mu_0}\,\delta\left(t-\frac{(\hat{e}_i-\hat{e}_0)\cdot\vec{r}}{c_L}\right) \quad . \tag{A3}$$

and

$$B_i(t) = \frac{\hat{\theta}_i}{4\pi c_T^2}\frac{d^2}{dt^2}\int d^3\vec{r}\,\gamma(\vec{r})\,\frac{c_T}{c_L}\frac{\delta\mu(\vec{r})}{\mu_0}\sin(2\theta) - \frac{\delta\rho(r)}{\rho_0}\sin(\theta)\,\delta\left(t-\frac{\hat{e}_i}{c_L}-\frac{\hat{e}_0}{c_T}\right)\cdot\vec{r} \quad . \tag{A4}$$

Now consider an incident impulse transversely polarized in the +x axis. Then

$$A_i(t) = \frac{\hat{r}_i}{4\pi c_L^2}\frac{d^2}{dt^2}\int d^3\vec{r}\,\gamma(\vec{r})\,\frac{\delta\rho(\vec{r})}{\rho_0}\sin\theta\cos\psi - \frac{\delta\mu(\vec{r})}{\lambda_0+2\mu_0}\frac{c_L}{c_T}\sin\theta\cos\psi\;\delta\left(t-\frac{\hat{e}_i}{c_T}-\frac{\hat{e}_0}{c_L}\right)\cdot\vec{r} \quad . \tag{A5}$$

and

$$B_i(t) = \frac{1}{4\pi c_T^2}\frac{d^2}{dt^2}\int d^3\vec{r}\;-\frac{\delta\rho(\vec{r})\sin\psi}{\rho_0} + \frac{\delta\mu(\vec{r})\sin\psi\cos\theta}{\mu_0}\,\hat{\psi}_i + \frac{(\delta\rho(\vec{r})\cos\theta\cos\psi}{\rho_0} - \frac{\delta\mu(\vec{r})\cos 2\theta\cos\psi)}{\mu_0}\,\hat{\theta}_i\,\delta\left(t-\frac{\hat{e}_i-\hat{e}_0}{c_T}\cdot\vec{r}\right) \tag{A6}$$

The third case considered is an incident impulse which is right hand circularly polarized. That is

$$U_{+} = U_o \frac{(\hat{x} + i\hat{y})}{\sqrt{2}} \delta\, t - \frac{\hat{z}\cdot\vec{r}}{c_T} \qquad (A7)$$

we define

$$\hat{x}^{+} = \frac{1}{\sqrt{2}} (\hat{\theta} + i\hat{\psi})$$

$$\hat{x}^{-} = \frac{1}{\sqrt{2}} (\hat{\theta} + i\hat{\psi}) \quad . \qquad (A8)$$

then

$$A_i(t) = \frac{e^{i\psi}\, \hat{r}_i}{4\pi c_L^2} \frac{d^2}{dt^2} \int d^3\vec{r}\gamma(\vec{r}) \frac{\delta\rho(\vec{r})}{\rho_o}$$

$$- \frac{c_L}{c_T} \frac{\delta\mu(\vec{r})}{\lambda_o + 2\mu_o} \sin 2\theta\, \delta\, t \cdot\cdot \frac{\hat{e}_i}{c_L} - \frac{\hat{e}_o}{c_T} \cdot\vec{r} \qquad (A9)$$

Finally

$$B_i(t) = \frac{e^{i\psi}}{4\pi c_T^2} \frac{d^2}{dt^2} \int d^3\vec{r}\gamma(\vec{r})$$

$$\hat{x}_i^{+} \frac{\delta\rho(\vec{r})}{\rho_o} \frac{(1+\cos\theta}{2} - \frac{\delta\mu(\vec{r})}{\mu_o} \frac{\cos\theta + \cos(2\theta)}{2} +$$

$$\hat{x}_i^{-} \frac{\delta\rho(\vec{r})}{\rho_o} \frac{\cos\theta - 1}{2} + \frac{\delta\mu(\vec{r})}{\mu_o} \frac{\cos\theta - \cos 2\theta}{2}$$

$$\delta\, t - \frac{\hat{e}_i - \hat{e}_o}{c_T} \qquad (A10)$$

ACKNOWLEDGMENT

This work was sponsored by the Center for Advanced NDE operated by the Science Center, Rockwell International, for the Advanced Research Projects Agency and the Air Force Materials Laboratory under Contract No. F33615-80-C-5004.

REFERENCES

1. J.E. Gubernatis, E. Domany, J.A. Krumhansl and M. Huberman, Material Science Center, Cornell University, Technical Report 2654 (1975); and J.E. Gubernatis, E. Domany, J.A. Krumhansl: J. Appl. Phys. 48, 2804 (1977).

2. A.K. Mal and L. Knopoff, J. Inst. Math. Applics. 3, 376 (1967).

3. J.H. Rose and J.A. Krumhansl, J. Appl. Phys. 50, 2951 (1979).

4. J.M. Richardson and J.H. Rose, to be published.

5. J.M. Richardson, Proc. of the Ultrasonics Symposium, eds. by J. deKlerk and B.R. McAvoy, 356 (1979).

6. R.K. Elsley and R.C. Addison, Proceedings of the DARPA/AMFL, Review of Progress in Quantitative NDE, 6th Annual Report, in press.

7. J.H. Rose, V.V. Varadan, V.K. Varadan, R.K. Elsley and B.R. Tittmann, Acoustics Electromagnetic and Elastic Wave Scattering-Focused on the T-Matrix Approach, eds. V.K. Varadan and V.V. Varadan, pub. by Pergamon Press, 605 (1980).

8. J. H. Rose and J. M. Richardson, to be published.

9. L. A. Ahlberg, R. K. Elsley, L. J. Graham, and J. M. Richarson, Proc. of the 1979 Ultrasonics Symposium, 79 CH 1482 - 9, pp. 321-326.

10. C. F. Ying and R. Truell, J. Appl. Phys. 27, 1086 (1956).

11. J.M. Richardson, to be published.

12. J.M. Richardson and R.K. Elsley, "Extraction of Low Frequency Properties from Scattering Measurement," Proceedings of the 1979 IEEE Ultrasonic Symposium, 79CH1482-9, pp. 336-341.

13. J.M. Richardson and R.K. Elsley, "Semi-Adaptive Approach to the Extraction of Low-Frequency Properties from Scattering Measurements," Proceedings of the 1980 IEEE Ultrasonic Symposium, 80CH1602-2, pp. 847-851.

14. B.D. Cook, S. Wilson and R.L. McKinney, Proceedings of the DARPA/AMFL Review of Progress in Quantitative NDE, 6th Annual Report, in press.

15. E.N. Kennaugh and D.L. Moffat, Proc. IEEE, 53, 893 (1965).

16. B.D. Cook, private communication.

DEPENDENCE OF THE ACCURACY OF THE BORN INVERSION ON NOISE AND BANDWIDTH

R. K. Elsley and R. C. Addison
Rockwell International Science Center
Thousand Oaks, California 91360

ABSTRACT

The Born Inversions are a set of techniques for reconstructing the shape of a flaw based on the scattering of ultrasound from the flaw. One technique is the one-dimensional Born Inversion, which estimates the radius of a flaw in one direction based on one pulse-echo (i.e., backscattering) measurement in that direction. The robustness of this technique with respect to limitations on the available bandwidth and with respect to the presence of noise in the data have been investigated. The Born Inversion requires a bandwidth sufficient to include at least the range $0.5 < ka < 2$ to give accurate estimates. The estimates continue to be accurate even when the amount of noise energy is comparable to the amount of flaw signal energy in the measurement.

INTRODUCTION

The requirements on the design of structures and machinery are coming more and more to stress maximum performance combined with minimum weight, minimum use of expensive materials and minimum life cycle costs. It therefore becomes more and more important to be able to predict the remaining lifetime of a component. Accurate nondestructive measurements of flaw properties, combined with the discipline of fracture mechanics, can provide these predictions.

Inversion algorithms may be classified in terms of how complete a description of a flaw they attempt to provide. Generally, an algorithm which can provide a detailed description of a flaw will require a large amount of measured data in order for it to work successfully. This data may include measurements from a wide range of angles of inspection about the flaw and/or a wide range of frequencies. Imaging is an example of a technique which requires measurements over a substantial range of angles. Obtaining large amounts of measured data from a flaw will be time-consuming and may require specialized equipment, such as an array transducer or an automated manipulator arm. In some cases, the data may not be available due to geometric limitations on what angles of inspection are possible or limitations on the available range of frequencies due to grain scattering or ultrasonic attenuation. These limitations will restrict the use of such data-intensive inversion algorithms to special inspection problems where the expense is justified by the results which the algorithm provide.

On the other hand, if an inversion algorithm determines only few properties of a flaw, then it may need only a limited amount of data to do so. This will make the algorithm much easier to implement in practical testing situations. Therefore, there is a need for inversion algorithms which:

1. Measure flaw properties that are valuable in predicting the remaining lifetime of a part, and
2. Require only a minimal amount of data to do so.

The properties of a flaw which are important in predicting the remaining lifetime of a part are, in many cases, the overall dimensions of the flaw. For example, the growth of a crack in a metal is largely determined by the cross-sectional dimensions of the crack perpendicular to the direction of the applied stress in the part. It is fortunate that the overall dimensions of the flaw are the properties which are of importance because high frequencies are not required to measure them and high frequencies are the most difficult to generate and propagate through materials. For measuring the overall dimensions of a flaw, the best frequencies are those for which the wavelength of sound is comparable to the dimensions of the flaw.

In ultrasonic nondestructive testing, the minimum amount of data that will be available from a flaw is the reflection of a single ultrasonic pulse from the flaw. This is the data that would be available, for example, if a large part were being scanned by a single transducer operated in the pulse-echo mode. The pulse contains frequency components over, typically, two octaves.

The Born inversion[1,2] is a technique which determines one dimension of a flaw by the use of one pulse-echo waveform reflected from the flaw. The dimension which it measures is the radius of the flaw in the direction of inspection. It does this without making use of the absolute amplitude of the pulse, as is done in conventional ultrasonic testing. Rather, it makes use of the shape of the reflected pulse. Another way of saying this is that it makes use of the relative amplitude and phase of the various frequency components which make up the reflected pulse. This lack of dependence on the absolute amplitude of the pulse makes the technique independent of several factors which disrupt conventional ultrasonic measurements, including coupling, variable attenuation and instrumental variations. This allows the technique to provide an absolute measurement of flaw size, that is, one which does not need a reference sample on which to calibrate.

The Born inversion was first derived for the case of weak scattering flaws. These are flaws whose density and sound velocity differ only a little from those of the host material in which they are located. Cracks, voids and some inclu-

sions do not fall in this class. However, some inclusions, such as Si in Si_3N_4 are weak scatterers.

In this weak scattering limit, the scattering of ultrasound from the flaw can be calculated by an approximate method known as the Born approximation. The scattering from the flaw, expressed as a function of frequency and angle of interrogation, is proportional to the Fourier transform of a quality called the characteristic function of the flaw. The characteristic function is defined as follows:

$$C(\vec{r}) = 1 \quad \text{inside the flaw}$$
$$= 0 \quad \text{outside the flaw}$$

If this function could be calculated, one would then know the location of the boundaries of the flaw, and therefore know its size, shape and orientation. The Born approximation scattering calculation shows that in the weak scattering regime the characteristic function can be obtained by performing a three-dimensional Fourier transform of the scattering amplitude measured as a function of frequency and angle. This procedure is called the three-dimensional Born inversion.

This procedure still requires the measurement and processing of a large amount of data. However, there is a simplification which can be made which produces a one-dimensional Born inversion-algorithm. Consider the case of a spherical scatterer. The scattering amplitude is the same in all directions and the three-dimensional Fourier transform reduces to a one-dimensional Fourier sine transform

$$C(r) = \frac{1}{r} \int_{-\infty}^{\infty} \frac{A(\omega)}{\omega} \sin \omega r \, d\omega \qquad (1)$$

The lower curve in Fig. 1 shows a one-dimensional cross section through the characteristic function of a flaw, as it might be reconstructed from scattering data with limited bandwidth. An estimate of the radius of the flaw can be obtained from the characteristic function by any of several estimators, such as the radius at which the characteristic function drops to 1/2 of its peak value.

In order to understand how the Born inversion works for flaws other than weakly scattering spheres, it is useful to recast Eq. (1) into the time domain. The result is

$$C(r) = C(vT) = \frac{1}{T} \int_{-T}^{T} a(t) \, dt \qquad (2)$$

where v is the sound velocity of the host material, and a(t) is the response of the flaw to an incident δ-function impulse. a(t) is the Fourier transform of the scattering amplitude $A(\omega)$. In what follows, "a" will also be used to indicate the radius of a flaw. Confusion can be avoided by noting that the impulse response will always appear with an argument: a(t), while the radius will appear without an argument. The upper curve in Fig. 1 shows a sketch of the impulse response for a weakly scattering flaw. It consists of (from left to right) a front surface echo, a constant region due scattering from the body of the

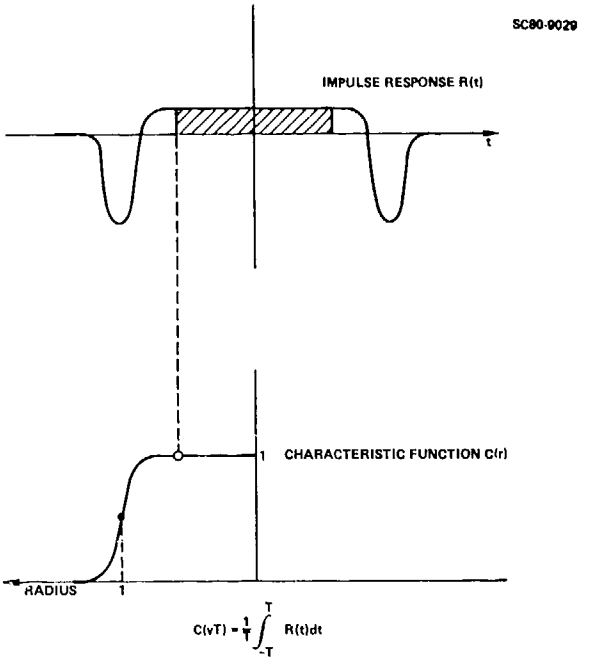

Fig. 1 a) Impulse response of a weak scattering flaw, b) characteristic function derived by Born Inversion.

flaw and a rear surface echo. Equation (2) has a very simple interpretation in terms of this figure. Each point on the characteristic function is calculated by integrating over a central portion of a(t). This portion is shown cross-hatched in Fig. 1. This is called the "expanding window" method of calculating the characteristic function, because the characteristic function can be generated by performing the integration (2) over an ever expanding window of which the hatched area is one example.

Because the impulse response a(t) of a weak scatterer can be calculated by a simple construction based on its shape, it is easy to show that for any ellipsoidal weak scattering flaw, the characteristic function has the same shape as it does for a sphere and gives a measure of the radius of the ellipsoid along the direction of inspection. If a number of these one-dimensional Born inversions are performed from a variety of angles, the shape of the flaw can be traced out.

Thus far, we have considered only weak scatterers. The Born inversion has been shown to work on strong scatterers as well. The reasons why it does can be understood by noting that the Born inversion is essentially measuring the distance from the center of the flaw to the front surface tangent plane in the direction of observation. Note that the rapid fall-off of the characteristic function at r = 1 is primarily due to the sharp front surface echo. Strong scatterers have even more pronounced front surface echoes than do weak scatterers and it is found that their characteristic functions are enough like Fig. 1 to provide good radius estimates.

BANDWIDTH REQUIREMENTS

The Born inversion was found to require a bandwidth of

$0.5 < ka < 2$

in order to give radius estimates accurate to within 20%. If insufficient low frequency data is available, then an underestimate results and if insufficient high frequency data is available, an overestimate results.

Figure 2 shows radius estimates obtained using the calcualted scattering amplitude for a spherical void when only limited bandwidth is available. The dashed curve shows the effect of insufficient low ka data. Underestimates of >20% occurs when $ka_{min} > 0.5$. The solid curve shows the effect of insufficient high ka data. Overestimates of >20% occur when $ka_{max} < 2$.

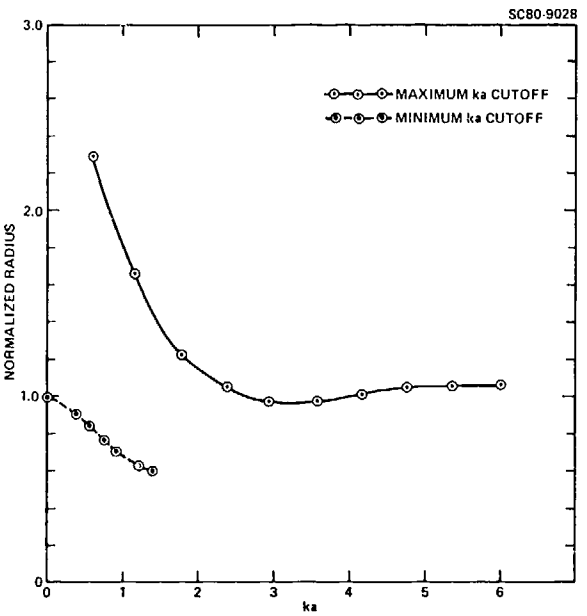

Fig. 2 Effect of limited bandwidth on the accuracy of the Born Inversion.

Figure 3 shows the effect of limiting both low and high frequency bandwidths. The figure shows the estimated radius $\hat{a}$ divided by the true radius a vs the average wavenumber k of a transducer multiplied by the flaw radius a. Each curve is for a transducer of a different relative bandwidth, expressed in terms of the ratio of the maximum ka of the transducer to the minimum ka.

Note that for the 6:1 transducer, measurements will be accurate to within 20% for a 1.7:1 range of flaw sizes, while for the 10:1 transducer, the range of flaw sizes is about 2.5:1. A good broadband commercial transducer might have a 10:1 range of usable k.

SIGNAL TO NOISE REQUIREMENTS

The sensitivity of the Born Inversion to the presence of noise in the data has been investigated by creating simulated experimental waveforms. These waveforms consist of the calculated scattering from a spherical void, with simulated noise added. The noise is selected to model the scattering of ultrasound by grains in the host material. Grain scattering has a power spectrum proportional to f^4 (f = frequency).

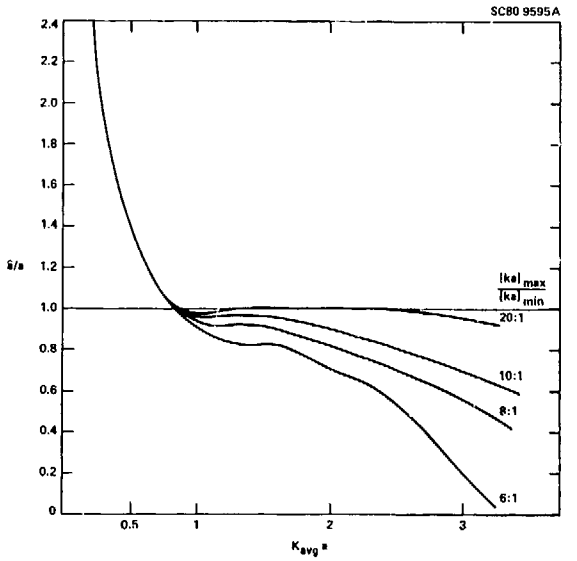

Fig. 3 Accuracy of Born Inversion vs transducer center frequency and bandwidth.

The simulated waveforms are calculated in the frequency domain, then multiplied by the measured spectrum of an ultrasonic transducer and finally put into the time domain.

$$a_X(t) = \mathcal{F}^{-1}\{X(f) \cdot [A(f) + N_g(f)]\}$$

where $a_X(t)$ is the simulated flaw waveform, A(f) is the scattering amplitude of the flaw, $N_g(f)$ is grain scattering noise, X(f) is the transducer spectrum and $\mathcal{F}^{-1}$ refers to a Fourier transform from frequency to time domains. The waveforms are then input to the Born inversion algorithm as experimental signals would be.

The noise waveform has the form

$$N_g(f) = \left(\frac{f}{f_o}\right)^4 N(f)$$

where f_o is a reference frequency and N(f) is a complex valued white Gaussian noise waveform consisting of samples of a Gaussian random variable for which

$$E\ \nu(f)\ \nu(f')^* = \sigma_f^2\ \delta_{ff'}$$

f_o is chosen arbitrarily to be the maximum frequency of the sampled waveform. The mean energy in N_g is therefore

$$U_g = \Delta f \sum_{f=-f_o}^{f_o} \sigma_f^2 \left(\frac{f}{f_o}\right)^4$$

$$= \frac{2}{5} f_o\ \sigma_f^2$$

where Δf is the sample interval of N_g.

The signal to noise ratio of the simulated experimental waveforms is defined to be

$$(S/N)^2 = \frac{\text{energy in flaw signal}}{\text{mean energy in noise signal}}$$

$$= \frac{\Delta f \, \Sigma |A(f)|^2}{U_g}$$

Figure 4 shows simulated and experimental flaw waveforms. The upper curve is an experimental waveform recorded for an 800 μm diameter spherical void. The middle and lower curves are simulated flaw waveforms. The middle curve contains no noise and the lower curve contains enough noise to produce a 0 dB signal to noise ratio. The similarity between the simulated and the measured waveforms is very good.

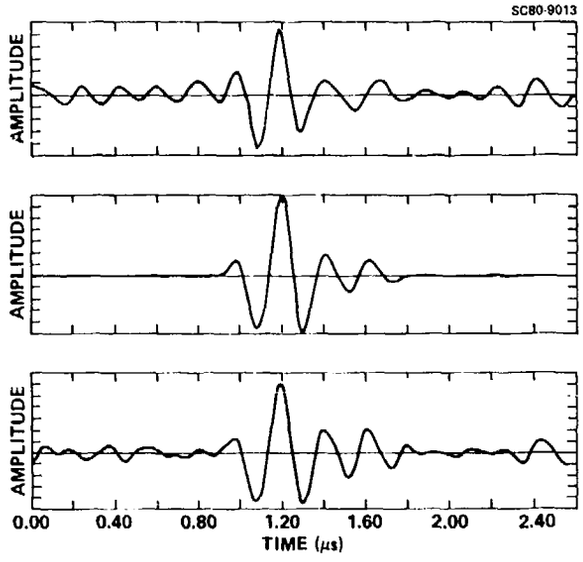

Fig. 4 Experimental and simulated flaw waveforms including grain scattering noise.

Figure 5 shows the radius estimates obtained for ensembles of noised up signals at various signal-to-noise ratios. The flaw has a diameter of 800 μm. For large signal-to-noise, the algorithm correctly estimates the radius to be 400 μm. The dashed curve shows the mean radius estimate for an ensemble of signals at each signal-to-noise ratio. The solid curves show the 95% confidence levels for the ensemble. As the signal-to-noise ratio decreases, the uncertainty of the estimates increases and the mean of the estimates eventually becomes inaccurate too. However, the 95% confidence level is within 20% of the correct answer down to a signal-to-noise ratio of 0 dB. The upper and lower curves in Fig. 4 show flaw signals in the presence of this level of grain noise.

DESCRIPTION OF THE ALGORITHM

An algorithm has been developed to perform the one-dimensional Born Inversion reliably on experimental data. The algorithm is written in Rockwell's ISP signal processing language and is executed on a mini- or a microcomputer. Figure 6 is a block diagram of the algorithm.

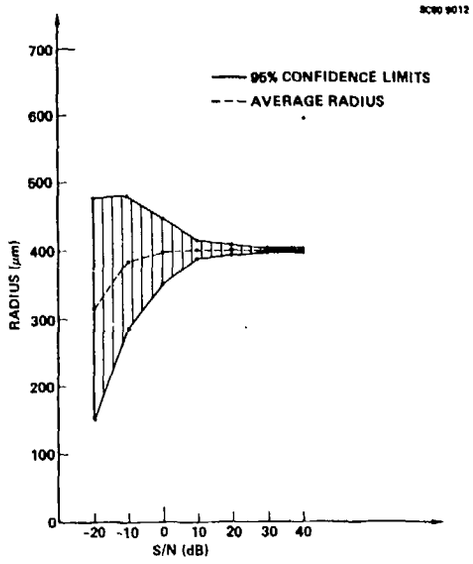

Fig. 5 Radius estimates for ensembles of noisy flaw waveforms vs signal-to-noise ratio.

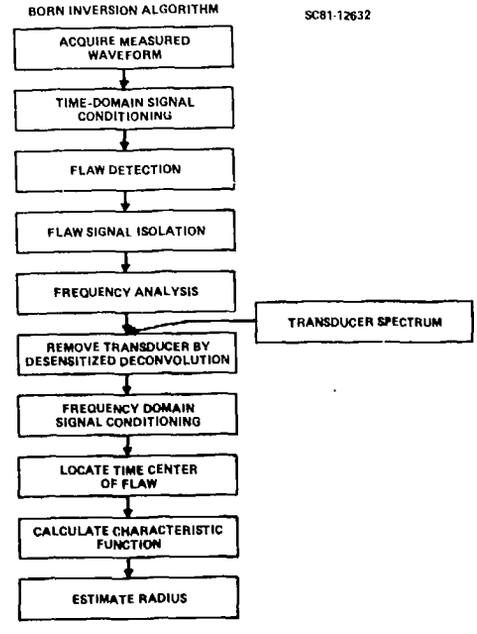

Fig. 6 Block diagram of Born Inversion algorithm.

The implementation of the Born inversion in a working algorithm is most readily done in the frequency domain using Eq. (1). The reason why a frequency domain implementation is better than a time domain implementation is because a measured ultrasonic signal consists of the impulse response of the flaw convolved with the impulse response of

the transducer and other measurement system components (i.e., the incident pulse). This transducer system response must be removed in order to isolate the flaw scattering data for use in the inversion. In particular, the incident pulse has very little energy at low frequencies and at high frequencies. Because there is some noise present in the measurements, a direct time-domain deconvolution of the measurement system response out of the measured signal is vulnerable to instabilities. Instead, it is better to do the signal processing in the frequency domain, where it is possible to make specific corrections in order to desensitize the results to the presence of noise.

After acquisition of the measured waveform, time-domain signal conditioning operations are performed. The primary signal conditioning operation is the subtraction of a measured signal form a flaw free region of the same or a similar part. This subtraction can remove, for example, the tail of a front surface echo or the recovery of the receiver from overload. Due to mechanical and geometrical uncertainties in the measurement process, subtraction usually does more harm than good at high frequencies, so that low passing of the subtractive reference is advisable.

Detection of a flaw signal in the received waveform is usually done simply by noting points at which the signal rises significantly above the background level. Matched filtering of the measured waveform with respect to a prototype flaw signal has been explored. However, because flaws covering a range of sizes and shapes are being searched for and because changes in the size and shape of a flaw cause large changes in the frequency spectrum of the scattering from the flaw, matched filtering did not produce a significant improvement in detectability unless a specific size and shape flaw was being searched for.

For further analysis, the portion of the received waveform containing the flaw signal is now isolated. This is done by multiplying the waveform by a window function of length comparable to the length of the impulse response of the flaw. A shaped window such as a Hanning or Kaiser-Bessel window is often a good choice. However, the convolution of such windows with the spectrum of the flaw signal distorts the important low frequency portion of the spectrum. Therefore a rectangular window is often used.

After frequency analysis, the properties of the transducer and other measurement system components are deconvolved out by division of the flaw spectrum by the spectrum of the measurement system (obtained from the measurement of the reflection from a flat surfaced target). This deconvolution is done in a desensitized manner in order to avoid noise-dominated behavior at high and low frequencies where the transducer has insufficient energy. The algorithm used is the following:

$$\hat{A}(\omega) = \frac{A_x(\omega)/X(\omega)}{1 + C\left|\frac{X_{pk}}{X(\omega)}\right|^2}$$

where $\hat{A}$ is the estimated flaw spectrum, A_x is the spectrum of the measured signal, X is the transducer (and measurement system) spectrum, X_{pk} is the peak value of the transducer spectrum and C is a factor (typical value = 0.01) which determines the degree of desensitization. Note that at any frequency where the transducer has very little energy, $\hat{A}$ is forced to zero to avoid wildly fluctuating results. If additional bandwidth is required, data from several transducers can be simultaneously deconvolved in a noise resistant manner. This technique is described elsewhere in this proceedings.[3]

Next, frequency domain signal conditioning can be performed. In particular, the low frequency portion of the frequency spectrum which was forced to zero by the deconvolution can be fit to f^2 to match the known frequency dependence of the scattering from small flaws.

The location of the center of the flaw in time must now be determined before proceeding with the inversion. This is best done by measuring the phase of the low frequency ($ka < 0.5$) portion of the spectrum. The slope of the phase at low frequencies is a measure of the time location of the center of the flaw with respect to the time coordinate system used. Several methods have been developed for estimating this time center, and are described elsewhere in these proceedings.[4] In some cases, there may be no data available in the measured signal at frequencies below $ka = 0.5$. (Note that the accuracy of the Born Inversion will begin to deteriorate if the minimum ka is much above 0.5). It has been found to be possible in some cases to empirically find the time center even when the low frequency data is not present. One such technique is to select that time center which causes the characteristic function to have zero slope at zero radius. Another is to measure the estimated flaw radius at various assumed flaw center positions τ and select the center position by reference to the radius vs τ curve.

The characteristic function of the flaw is then calcualted by Eq. (1) and the flaw radius is estimated from it. Several estimators of flaw radius were tried. The one which was found to work best is

$$\hat{a} = \frac{\text{area under } C(r)}{\text{peak value of } C(r)}$$

This estimator is insensitive to small errors in the determination of the flaw center and performs remarkably well for inclusions which have very long and complicated characteristic functions due to the internal sound paths within the inclusions.

The results which are presented below were obtained using this algorithm.

EXPERIMENTAL RESULTS

The results of the application of the Born inversion to a variety of flaws is shown in Table I. The first group of flaws are in Ti-6Al-4V and the second group are in hot-pressed silicon nitride. The table lists, in addition to the true and estimated radii of the flaws in the direction of observation, the range of ka (i.e., frequency) available in the experiment and an

RESULTS

Flaws in Ti-6Al-4V

Flaw	S/N (dB)	ka_{min}	ka_{max}	True Radius (μm)	Estimated Radius (μm)	Comments
1. Void Sphere	10	.2	3	400	388	0° Incidence
					389 ± 4	30° Incidence
					402 ± 4	52° Incidence
2. Void Prolate 415 × 806 μm	-10	.5	2.5	415	443	
3. Void Sphere	20	.5	3	400	374	
4. WC Sphere	10	.5	3	400	325	
5. Void Sphere	-13	.6	2.5	400	347	
6. Void Sphere	10	1.2	4.2	600	361	No low ka
7. Void Oblate 390 × 130 μm	-10	.6	1.1	225	330	No high ka

Flaw in Si_3N_4

Flaw	S/N (dB)	ka_{min}	ka_{max}	True Radius (μm)	Estimated Radius (μm)	Comments
1. Fe Sphere	25	.5	4	200	190	
2. Si "Sphere"	10	.5	3	"50"	38	Highly Distorted
3. Void "Sphere"	10	1.0	5.5	250	180	No low ka
4. Void "Sphere"	0	.5	2.8	125	132	

estimate of the signal-to-noise of the measurements.

The comparison between estimated and true radius is seen to be good for most of the flaws and for the others, the reason for the error is evident.

In the titanium samples, flaws 1-5 are estimated to within 20%. Flaw 1 was observed from three different angles of incidence. Flaws 6 and 7 were inspected with insufficient bandwidth for the sizes of flaw being inspected. Flaw 6 was inspected with too little low frequency energy and so the expected underestimate resulted. Similarly, the overestimate of flaw 7 is due the availability of too little high frequency energy.

In the ceramic specimens, flaws 1 and 4 are accurately estimated. Flaw 3 had insufficient low frequency data and was therefore underestimated. Flaw 2 consisted of a diffuse area of mixed chemical makeup and there is therefore no single "true" radius. However, the radius estimate is certainly consistant with the observed size.

ACKNOWLEDGEMENT

This research was sponsored by the Center for Advanced NDE operated by the Rockwell International Science Center for the Defense Advanced Research Projects Agency and the Air Force Wright Aeronautical Laboratories under Contract No. F33615-80-C-5004.

REFERENCES

1. J. H. Rose and J. A. Krumhansl, "Determination of Flaw Characteristics from Ultrasonic Scattering Data," J. Appl. Phys. 54(4), 2951-2952 (April 1979).
2. J. H. Rose, R. K. Elsley, B. R. Tittmann, V. V. Varadan and V. K. Varadan, "Inversion of Ultrasonic Scattering Data," in Acoustic, Electromagnetic and Elastic Wave Scattering-Focus on the T-Matrix Approach, V. V. Varadan and V. K. Varadan, eds., Pergamon Press, pp. 605-614 (1980).
3. R. K. Elsley, L. Ahlberg and J. Richardson, "Low Frequency Characterization of Flaws in Ceramics," these proceedings.

Don Thompson (Ames Laboratory): On your next-to-the-last slide, Dick, what is your reference point of saying - how are you taking KA minimum and KA maximum? Are those zeros?

Dick Elsley (Rockwell Science Center): We know the size of the flaw. And so the frequency band for the transducer gave decent data when converted to K in the numbers that we have used for KA minimum and KA maximum.

Mr. Schmitz (Germany): Let us consider again the problem of sizing to the problem of rattlesnakes, If rattlesnakes are traveling in pairs, could you do it, handle this problem, too? Learning pairs closely related or different in sizes?

Dick Elsley: Both problems would be more difficult. If they are very close together, we get something like a circumscribed flaw, I think. To be able to time gate the two, of course, would be a very convenient way to avoid the problem.

Mr. Schmitz: In terms of wavelengths, two of the wavelengths?

James Krumhansl, Chairman (NSF): If your upper KA is less than the separation K separation instead of KA, something like that, a band width. There is a certain separation, talking about pairs of flaws. Now the critical sort of crossover in data is K times the separation. And if that's much less than one, you don't have a chance of resolution.

Dick Elsley: If the two flaws are the same distance from the transducer and within the beam of the transducer, there will be no way to separate them there. If they're in front of one another and you can time gate, you will be successful.

Norm Bleistein (Denver Applied Analytics): The earlier slide when you were dealing with synthetics, you showed some results from band widths with a ratio of 6 to 1 and 10 to 1. You look at ratios here and they are nowhere near that ratio. I guess it's less than 3 to 1, the kind of ratios we have for KA minimum and KA maximum. What kind of estimates do you have for synthetics? Can you run down things like that?

Dick Elsley: The curve that showed 6 to 1, 10 to 1, 20 to 1, that is where the artificial transducer went out to zero. The artificial transducer is a mathematical formula, and was identical to zero. The 6 to 1 like that would be something smaller, or 5 to 1. Using multiple transducers to get more band width is the way to get around that problem.

Norm Bleistein: What happens when it goes down to 3 to 1?

Dick Elsley: If the center frequency is not around KA equal to one, you will get a series of overestimates.

William Reynolds (Aere Harwell): Could I ask if this technique would be useful in distinguishing in the case of inclusions in silicon nitride between ions, say, and silicon particles of less than 100 microns diameter when they are less than spherical?

Dick Elsley: In the ceramics talk we gave last year, we did essentially that. We combined the Born inversion with the low frequency measurements, measuring the coefficient A2 and got how likely a flaw was to be either iron or something else. In the case of iron and silicon, you might be able to distinguish just by the sign of the selected pulse.

James Krumhansl, Chairman: Thank you, Dick. Let's move on to the next paper.

RAMP WAVE PROCESSING OF LONG WAVELENGTH ULTRASONIC SCATTERING INFORMATION

Bill D. Cook, Shelford Wilson and Ronald L. McKinney
Cullen College of Engineering
University of Houston
Houston, Texas 77004

ABSTRACT

A method of extracting size and orientation of flaws, voids and inclusions, from scattered ultrasonic signals is under investigation. The novel feature of this method is that the time domain ramp function response is used for interpretation. Consider a time domain ramp signal imposing on flaw. The spectral content of this signal decreases inversely with frequency squared. The back-scattered signal from a void, for example increases with the frequency squared. As a consequence, the echo of the ramp function from the flaw is rich in long wavelength information whereas the short wavelength information is de-emphasized. The net result is that the time domain ramp response has a height proportional to cross-sectional area of the flaw and has a length proportional to the flaw depth.

The results of scattering of ramp signals from acoustic targets illustrate the promise of this technique.

James Krumhansl, Chairman (NSF): Was There any particular reason for choosing a ramp function?

Bill Cook (University of Houston): I'll tell you why. The ramp function, as Jim Rose mentioned - he had an answer which was the second derivative of this area you go back to, and the ramp function does two inversions for you.

James Krumhansl, Chairman: Any other questions? Then thank you very much.

ULTRASONIC FLAW CHARACTERIZATION IN THE RESONANCE REGION BY THE BOUNDARY INTEGRAL EQUATION METHOD

L. W. Schmerr, Jr., C. Sieck
Ames Laboratory, DOE
Iowa State University
Ames, Iowa 50011

ABSTRACT

When the wavelength of the ultrasound being used to characterize a flaw is of the same order of magnitude as the flaw size, conventional low and high frequency scattering approximations fail. In this frequency range, called here the resonance region, numerical methods are necessary. Here we show that one such method, the Boundary Integral Equation (BIE) Method, is an effective tool for solving elastic wave scattering problems in the resonance region provided some important modifications are made in the method as used previously by other authors. To illustrate the BIE method, scattering from a cylindrical void in two-dimensions is considered. Comparisons are given with complimentary analytical and experimental results.

INTRODUCTION

With the development of wide band ultrasonic equipment in recent years, much attention has been given to the use of ultrasonic spectroscopy techniques to non-destructively characterize the physical properties of various types of defects in materials. However, little of this data can be used quantitatively until it is coupled with analytical-numerical techniques capable of predicting and classifying flaw scattering properties. In the size-frequency regime where the flaw size and ultrasonic wavelengths are comparable (called here the "resonance" region), low and high frequency approximations fail (1), (2) and one is forced to resort to numerical methods. The only two methods that currently appear viable for solving elastic scattering problems in the resonance region are the Transition Matrix (3), (4) and the Boundary Integral Equation (BIE) Method (5), (6). We will show that the BIE method provides a very effective method of solution for elastic wave scattering problems in this region provided some important modifications are made in the standard BIE formulations.

BIE Formulation - The BIE method consists of writing the solution to a flaw scattering problem in terms of an integral equation over the scattering surface. This integral equation is generated using a fundamental singular solution (Green's Function) for the surrounding media and is solved numerically by subsectioning the surface into patches and choosing simple piecewise representations for the unknown over these patches.

To illustrate the BIE formulation explicitly, consider the scattering of harmonic elastic waves from a flaw in two dimensions (Fig. 1). For this case we have (5)

$$aU_\beta(P)=U_\beta^{INC}(P)+\int_S[t_\alpha^n(Q)U_{\alpha\beta}(Q,P)-\Sigma_{\alpha\beta}^n(Q,P)U_\alpha(Q)]\,dS\,(Q)\quad(\beta=1,2)\qquad(1)$$

where U_β is the displacement of the medium in the X_β-direction due to an incident ultrasonic wave whose displacements are U_β^{INC}. The components of the stress vector are t_β^n on the surface S of a scatterer whose outward normal is $\underline{n}$ (Fig. 1). Point Q is a point of integration on S, and P is a general point that can be either interior to the scatterer, on the scatterer surface S, or exterior to the flaw. In these three cases, the value of "a" in e.g. (1) takes on the value of a=0, a=½, or a=1, respectively. The tensors $U_{\alpha\beta}$ and $\Sigma_{\alpha\beta}^n$ are related to the fundamental solution for an isotropic elastic solid (5), (7).

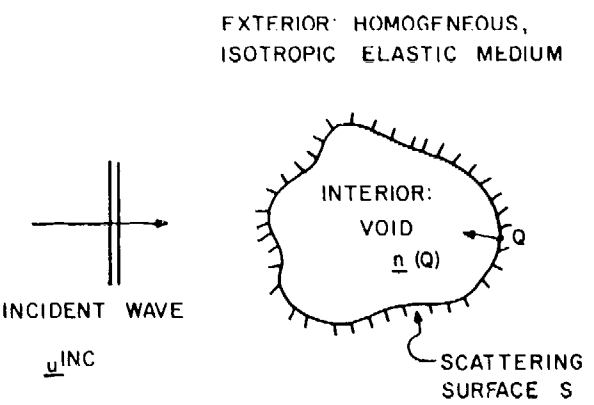

Fig. 1. Scattering geometry

When point P lies on the surface S of the scatterer, Eq. (1) is an integral equation for the unknown stresses and displacements on that surface. That equation can be solved by breaking the surface into straight segments Sn (n=1,2...N) whose centroids are located at points Pn, and assuming the tractions and displacements are constant over these segments. If Eq. (1) (with a=½) is then satisfied at N centroidal points Pm (m=1,2...N) on the surface, we obtain:

$$U_\beta(P_m)/2=U_\beta^{INC}(P_m)+\Sigma_{n=1}^{n} t_\alpha^n(P_n)\int_{S_n} U_{\alpha\beta}(Q,P_m)dS(Q)$$

$$-\Sigma_{n=1}^{n} U_\alpha(P_n)\int_{S_n}\Sigma_{\alpha\beta}^{n}(Q,P_m)dS(Q)\ . \qquad (2)$$

Once the displacements or stresses are specified on the surface, Eq. (2) can be used to obtain a set of simultaneous equations for the remaining unknown surface quantities. These results and Eq. (1) (with a=1) may then be used to obtain the solution at any interior point in the solid. For example, if the flaw is a void, the stresses are zero on S and Eq. (2) becomes

$$\sum_{n=1}^{n}\left[\delta_{\alpha\beta}\delta_{mn}/2+\int_{S_n}\Sigma_{\alpha\beta}^{n}(Q,P_m)dS(Q)\right]U_\alpha(P_m)=$$

$$U_\beta^{INC}(P_m)\ (m=1,2....N). \qquad (3)$$

This is standard BIE formulation which has been used recently by Tan (5), for example, to solve several elastic scattering problems. However, this method has a serious deficiency which was not mentioned in (5). This deficiency is that the approximate numerical solution [Eq. (3)] of Eq. (1) is inaccurate at certain characteristic frequencies. At those frequencies, non-zero fields can exist inside the flaw that do not satisfy Eq. (1), i.e., the left hand side of Eq. (1) is not zero when P is inside the scatterer, as it should be. These non-zero fields inside S cause large errors to occur in the solutions obtained from Eq. (3). To see this we have considered the scattering problem of cylindrical void in an otherwise homogeneous and isotropic elastic solid subjected to a plane incident compressional wave. Using a BIE computer code based on Eqs. (1) and (3), we calculated the far field radial displacement for the scattered waves at a 90° orientation from the incident wave. The magnitude of this radial displacement as a function of frequency is shown in Fig. 2. In that figure we see an overall modulation as a function of frequency together with sharp peaks and dips (marked by arrows in Fig. 2). These rapid variations are not contained in the exact solution to this problem as can be obtained from a separation of variables solution (8). Similar extraneous variations in the frequency domain response also appear in acoustic and electromagnetic BIE formulations (9) and several means to eliminate them have been adopted. One method, which we have used successfully, (9), is to force the solution to zero at a specified number of points inside the scatterer, in order to better satisfy Eq. (1) when point P is inside S. This introduces addition constraints without adding additional unknowns so the system is then overdetermined, becoming:

$$\sum_{n=1}^{n}\left[a_m\delta_{\alpha\beta}\delta_{mn}+\int_{S_n}\Sigma_{\alpha\beta}^{n}(Q,P_m)dS(Q)\right]U_\alpha(P_n)=$$

$$U_\beta^{INC}(P_m)\ (m=1,2,M) \qquad (4)$$

where $a_m=\frac{1}{2}$ when $m\leq N$ and $a_n = 0$ when $m>N$.

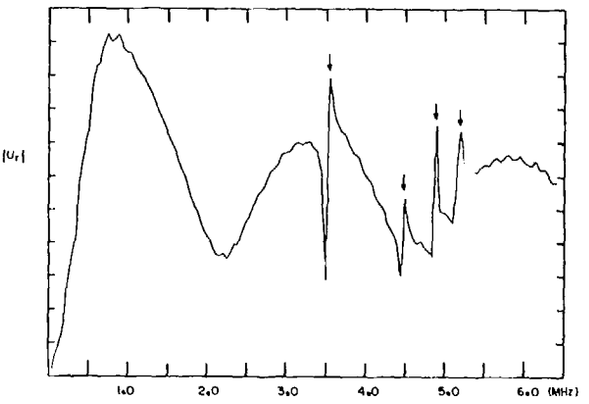

Fig. 2. Radial, far-field displacement at 90° from incident wave, using unmodified BIE formulation.

If Eq. (4) is now solved in the least squares sense, we have found very good results can be obtained at all frequencies with as few as 3 extra equations. Figure 3 shows the same solution as Fig. 2 (solid line) and the solution to an overdetermined set of equations (squares) where Eq. (1) is satisfied at three arbitrary points inside the void. We see the overdetermined solution passes successfully through all the artificial peaks and dips and, in fact, is within several percent of the exact solution. As far as we are aware, this is the first time that this numerical problem with the BIE has been compensated for in this manner for elastic wave scattering problems.

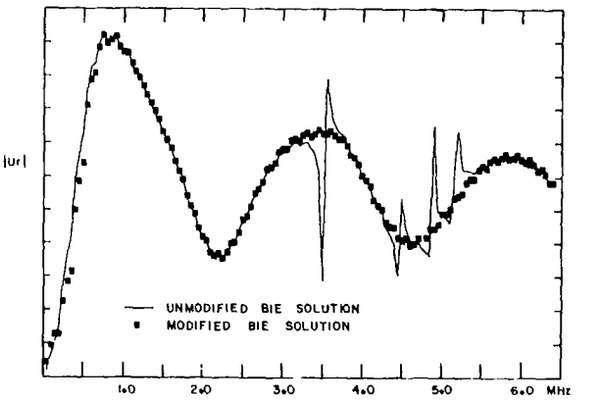

Fig. 3. Radial, far-field displacement at 90° from incident wave. Modified and unmodified BIE formulations.

Experimental Comparisons - After developing an accurate working two-dimensional BIE computer code based on the modifications mentioned above, we have also tested it against complimentary experimental data. For example, as shown in Fig. 4, we machined the faces of an aluminum block at various angles from the top face and placed a through-drilled

1.59mm (1/16") diameter hole in the center of the block. The transmitter was a 10 MHz Panametrics broad-band compressional wave transducer that always remained fixed in location on the top face of the block while a matching receiving transducer was moved onto the various faces. Figure 5 shows the digitized transient response obtained from the receiver at angles of 45°, 90°, and 135° from the transmitter. These responses show two major features: a large front surface reflection (A) and a smaller "creeping wave" contribution (B) which has been found previously by Sachse (10). This creeping wave contribution is basically a grazing incidence wave that wraps around the surface of the cylindrical hole, radiating in all directions. Since the path length and radiation loss grows as the angle between transmitter and receiver becomes smaller, we expect that the creeping wave contribution will become smaller and more separated from the front-surface reflection as the angle decreases, as in fact Fig. 5 demonstrates. The frequency components in the signals of Fig. 5 were computed using the Fast Fourier Transform capabilities of the data acquisition and processing system shown in Fig. 4. and the results are shown in Fig. 6 where we have plotted the magnitude of the Fourier transform of the responses at 45°, 90°, and 135°, respectively. We see a distinct set of modulations in these frequency spectra, together with an overall envelope which is a function of the transmitting and receiving transducer characteristics. Using standard deconvolution techniques (11) to remove these transducer characteristics, we obtained a set of deconvoluted spectra whose magnitudes are plotted on a smaller frequency scale in Fig. 7. Also plotted in Fig. 7 is the magnitude of the radial displacement at the receiving transducer location as computed from the modified BIE formulation described previously. It is seen that within an arbitrary scale factor, both curves show the same overall types of modulation, except in the low frequency region where the deconvolution cannot be expected to be accurate since there is little energy content in the incident pulse.

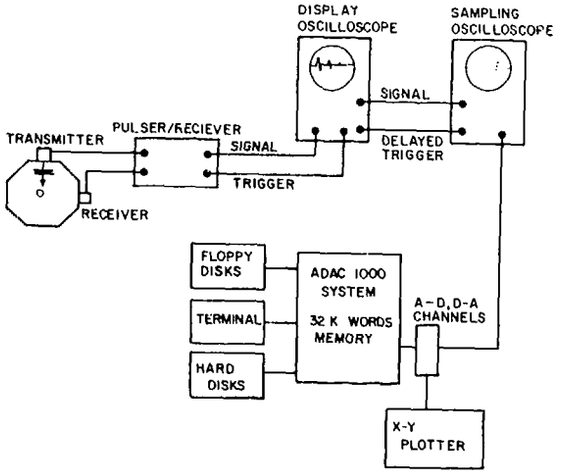

Fig. 4. System configuration.

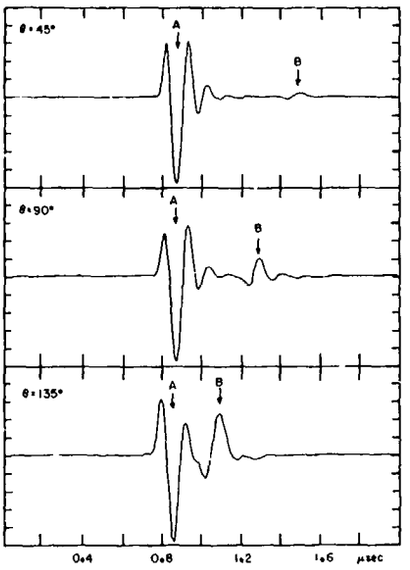

Fig. 5. Front surface and creeping wave contributions at 45°, 90°, and 135° from transmitter.

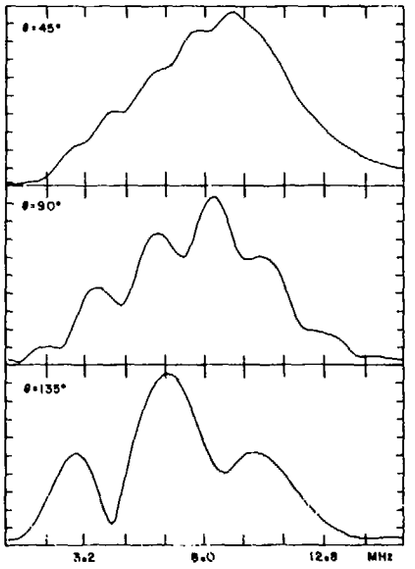

Fig. 6. Magnitude of Fourier transform of the response at 45°, 90°, and 135° from transmitter.

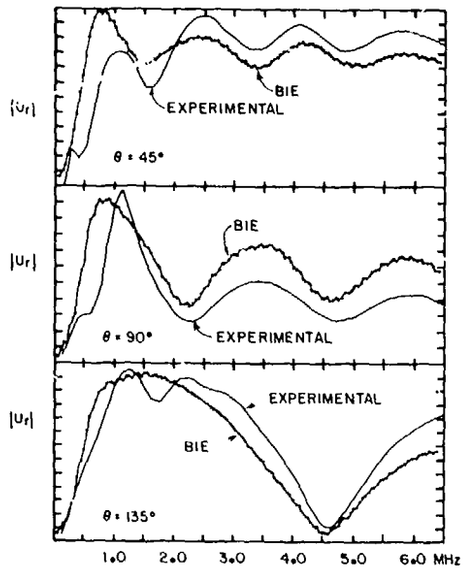

Fig. 7. Comparison of deconvoluted experimental spectral and BIE results.

One aspect of wave scattering experiments in elastic solids which is not found in analogous acoustic or electromagnetic problems is the phenomena of mode conversion between compressional and shear wave disturbances. Thus, when the incident compressional wave from the transducer of Fig. 4 strikes the side-drilled hole, both scattered compressional and shear waves are generated. This mode conversion process, although it makes elastic wave scattering problems more difficult than similar acoustic or electromagnetic cases, also offers the possibility of being used to extract additional information on a flaw's characteristics. These mode converted signals were picked up from the side-drilled hole of Fig. 4 with a 5MHz Parametrics shear wave transducer, producing the transient response shown in Fig. 8 when the receiving shear wave transducer is at 90^0 from the transmitter. The frequency components of this signal were obtained and deconvolved to produce the spectrum shown in Fig. 9. In Fig. 9, the magnitude of the far-field tangential displacement at the receiving transducer location is also plotted from the results of our BIE code. Again, the comparison between the experimental and numerical results is very good to within an arbitrary scale factor.

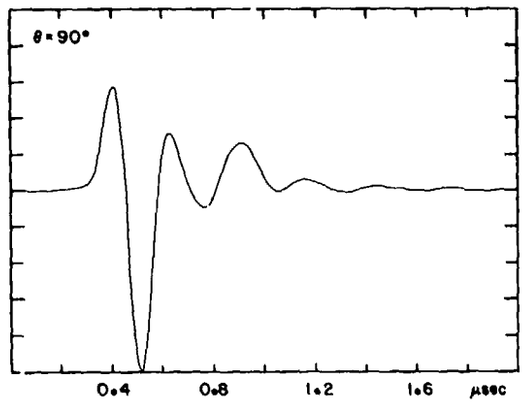

Fig. 8. Scattered shear waves at 90^0 from compressional wave transmitter.

Concluding Remarks - The strength of the BIE approach lies in the fact that it is capable of handling complex flaw geometrics and of working effectively in the resonance region where other methods fail. With some modification, the model presented here can also be applied to three-dimensional voids, inclusions, and cracks and to surface and near-surface flaws as well. Currently, efforts are underway to make these modifications and extensions of the technique. Perhaps the single major disadvantage of the BIE method is that it must obtain a separate solution for each frequency. Thus, over a wide range of frequencies, many solutions are needed. However, BIE solutions are within the capability of many dedicated minicomputer systems currently on the market, so that this limitation can, to some extent, be overcome without incurring excessive computer time costs. In fact, all the results obtained in this paper were computed on the microcomputer based data acquisition and processing system of Fig. 4.

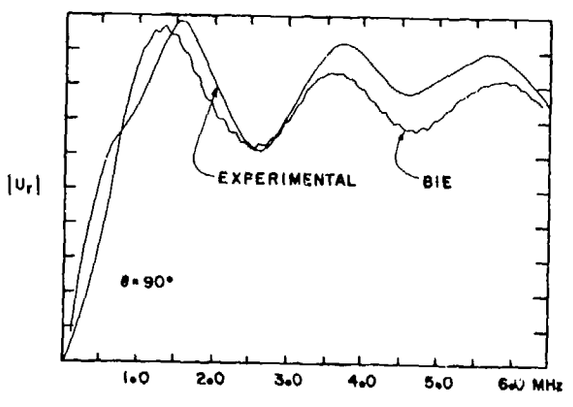

Fig. 9. Comparison of experimental and BIE results for the scattered shear wave.

ACKNOWLEDGEMENTS

This work was supported partially by the National Science Foundation through Grant No. ENG 77-06970 and the Engineering Research Institute of Iowa State University. The U.S. Department of Energy, through Contract No. W-7405-Eng-82, Office of Basic Energy Sciences, Division of Materials Sciences (AK-01-02), provided partial support for the development of the software used in this program.

REFERENCES

1. J. E. Gubernatis, E. Domany, and J. A. Krumhansl, "Elastic wave scattering theory with application to nondestructive evaluation", Los Alamos Scientific Laboratory, LA-UR-79-2393, 1979.

2. J. D. Achenbach, A. K. Gautesen, and H. McMaken, "Application of elastodynamic ray theory to diffraction by cracks" Modern Problems in Elastic Wave Propagation, Ed. by J. Miklowitz and J. D. Achenbach, John Wiley, NY, 219-238, 1978.

3. Y. H. Pao, "The transition matrix for the scattering of acoustic waves and for elastic waves", Modern Problems in Elastic Wave Propagation, Ed. by J. Miklowitz and J. D. Achenbach, John Wiley, NY., 123-144, 1978.

4. P. C. Waterman, "Matrix theory of elastic wave scattering", J. Acoust. Soc. Am. 60, 567-580, 1976.

5. T. H. Tan, "Scattering of elastic waves by elastically transparent obstacles (Integral Equation Method)", Appl. Sci. Res. 31, 29-51, 1975.

6. Y. A. Pao and V. Varatharajulu, "Huygen's Principle, radiation conditions, and integral formulas for the scattering of elastic waves", J. Acoust. Soc. Am. 59, 1361-1371, 1976.

7. A. C. Eringen and E. S. Suhubi, Elastodynamics, Vol. 2, Academic Press, NY, p.435, 1975.

8. Y. H. Pao and C. C. Mow, "Diffraction of elastic waves and dynamic stress concentrations", Crane-Russak, NY, pp.239-253, 1973.

9. H. A. Schenck, "Improved integral formulation for acoustic radiation problems", J. Acoust. Soc. Am. 44, 41-58, 1968.

10. Y. H. Pao and W. Sachse, "Interpretation of time records and power spectra of scattered ultrasonic pulses in solids", J. Acoust. Soc. Am. 56, 1478-1486.

11. E. Nabel and E. Mundry, "Evaluation of echoes in ultrasonic testing by deconvolution", Materials Evaluation 36, 59-77, 1978.

Jim Rose (University of Michigan [now Ames Laboratory]): Essential reduction in the number of terms in your matrix over the T-matrix?

Lester Schmerr (Iowa State): You're asking are the matrices used smaller?

Jim Rose: Can you get as good results resolution as their results with essentially smaller matrices?

Lester Schmerr: I have not done a direct comparison, but I think probably the order of magnitude is pretty much similar. What you need here is about 10 elements per wavelength to do a good job. By a good job I mean within a couple percent of the exact solution. So if you translate that up into whatever ka value that you want, I think the methods come out fairly comparable.

Vasundara Varadan (Ohio State): I wish to make some comments. The first problem that you showed that had the interior resonances in the scattered data was an exact boundary integral solution, but when you introduced an extra point which is in the interior of the scatterer, what you did is exactly the T-matrix method, using the extension thecrum. So what you have really done is the T-matrix calculation using local basis function rather than global functions, which is the method I used when I showed the stress concentration factor results. One might also profit from looking at the electromagnetic literature. They don't call it the boundary method there, but the moment method. They were always plagued by the interior resonances, but they have found ways of getting around that problem. I don't know how complicated they are, but they have found ways of getting around that calculation. But the last calculation you showed is the T-matrix function, using local basis functio.

Lester Schmerr: I mentioned there are other ways of handling that problem of the fictitious resonances. You can modify the integral equation that you start out with, and you get an integral equation which you can show is unique at all frequencies, even the frequencies of the interior problem, the complementary problem - that's been done in the electromagnetic and acoustic cases and worked there, so I don't see any reason why it wouldn't work here.

But you end up dealing with more complicated expressions, so I think it's more convenient to do it this way.

James Krumhansl, Chairman: Opsal.

Jon Opsal (Lawrence Livermore Laboratory): I don't know if I have the right picture of the problem, I feel like I'm missing something. You said that the field inside the void in a solid material and fields inside the void ought to be zero, at least the displacement fields?

Lester Schmerr: Yes.

Jon Opsal: What's the reason for that? There is nothing in the boundary condition that show they vanished, and if I just move inside -

Lester Schmerr: The integral relationships tell you it should be zero.

James Krumhansl, Chairman: The sum of the two terms should be.

Lester Schmerr: You basically cancel off the incident wave.

Jon Opsal: It has to be cancelled by the scattered field. I'm thinking of the scattered field.

Lester Schmerr: The scattered field is the negative of the incidence. As a matter of fact, if you calculate the displacements at an interior point inside the void when you're away from those interior resonances, you get something like 1 percent of 10 percent or less than your incident wave. But as soon as you get near the resonance, it becomes the same order of magnitude.

John Richardson (Science Center): Suppose you have a very tenuous inclusion instead of a void. Suppose you take a limit of the inclusion that essentially becomes increasingly tenuous.

Lester Schmerr: The inclusion will have a real resonance.

John Richardson: Then you let the inclusion become increasingly tenuous until it becomes a vacuum. You end up with a finite displacement field inside.

Lester Schmerr: I have not seen anyone use that limiting process. That might be possible.

James Krumhansl, Chairman: Visscher.

William Visscher (Los Alamos Scientific Laboratory): What do you do about the problem of singularity in fields?

Lester Schmerr: That's a good point. In doing the integrations, you have to evaluate them as principal value integrals, but because you have an explicit expression for the singularity, you can do the principal value integrations exactly.

William Visscher: I can see how that will work if you have certain symmetries, but for generally shaped surfaces?

Lester Schmerr: It doesn't depend on what the symmetry is because you locally have, basically, a flat element and you have the Green's Function for the infinite media.

James Krumhansl, Chairman: The approximation is essentially a flat element. Each one of those elements are treated in that way.

Lester Schmerr: Yes.

Vasundara Varadan: I have one more comment to make regarding computing complex resonances. We have, in fact, used some of these T-matrix ideas and calculated the resonance frequency for an oblate spheroid, elastic one, immersed in water. And these calculations are very, very expensive. We are searching all over for the complex plane for these resonance frequencies. What we found when we looked at complex resonance frequencies reflected in the form function of the scattered field amplitude as a function of frequency was that the resonances that are really deep in the complex plane do not show up in the product of the scattering cross section as a function of frequency. And we found it's only those resonance frequencies that have a real part quite near the real axis that are important. In fact, people at the Naval Research Laboratory, without any justification, have been doing these types of calculations for a long time. They can predict the resonant frequencies of many arbitrary shaped obstacles quite nicely, but what, in fact, they are predicting are only those frequencies. And they can pick those up quite easily from the scattering cross-section as a function of Ka.

Lester Schmerr: Can I make a point here? It is very expensive if you try to do any locating of these resonances in a complex frequency plane. There is a method called Prony's where you can extract those directly from time response, A-scan response. That's much less expensive, if it works.

Unidentified Speaker: We find it's very sensitive to the number of elements you use in Prony's method.

Lester Schmerr: We have tried that in a one-dimensional natural scattering system, and it does work pretty well. You have to be careful when you go from electromagnetic and acoustic to these problems here. Noise levels, for example, are different, especially underwater acoustics, for example. They are terrible. So -

James Krumhansl, Chairman: We'll move on. Very stimulating talk, obviously.

APPLICATION OF ADAPTIVE LEARNING NETWORKS TO QUANTITATIVE FLAW DEFINITION

M. F. Whalen
P. M. Garafola
L. J. O'Brien
A. N. Mucciardi

ADAPTRONICS, INC.
McLean, Virginia 22102

ABSTRACT

Adaptive Learning Networks (ALNs) are algebraic, nonlinear multinomials whose structure and coefficients are learned from empirical data. Over the past several years, their application to quantitative NDE problems has become widespread. The major advantage of the ALN approach is that only a modest data base of experiments is needed, from which the ALN models can be trained. In this work, ALNs are used as a nonlinear, empirical inversion procedure for various defect geometries. Measurements from a sparsely-populated ultrasonic transducer array are input to the ALNs which estimate the defect characteristics. The defects considered are (1) elliptical cracks, (2) irregular-shaped voids, and (3) surface-breaking semielliptical cracks. The models are synthesized from theoretically-generated, forward-scattering data, then evaluated on actual experimental data recorded from titanium and carbon steel samples. The advantage of using theoretical data to train the models is that ultrasonic responses can be generated quickly and inexpensively in a digital computer, thereby avoiding, or greatly minimizing, the expense of calibration sample fabrication. The size and orientation estimates for the experimental evaluation are in excellent agreement with the true defect characteristics.

1. SUMMARY OF RESULTS, CONCLUSIONS, AND RECOMMENDATIONS

RESULTS

During this year's effort, Adaptive Learning Networks (ALNs) were synthesized to estimate the size and orientation of elliptical cracks and to estimate the depth of free-surface cracks. Other objectives were to evaluate the oblate spheroid models developed last year on extrapolative data, and to catalog all important models synthesized to date under the DARPA/AFML program. Table 1.1 summarizes the performance of each of these models on theoretically generated training data.

TABLE 1.1: ALN MODEL PERFORMANCE SUMMARY

Defect Type	Estimated Parameter	Relative Error
Elliptical Crack	Semiminor Axis (A)	22%
Elliptical Crack	Semimajor Axis (B)	13%
Elliptical Crack	Polar Angle (α)	5%
Elliptical Crack	Azimuthal Angle (β)	10%
Elliptical Crack	Rotation (γ)	21%
Free-Surface Crack	Depth	6%
Oblate Spheroid	Minor Radii (A)	9%
Oblate Spheroid	Major Radii (B)	8%
Oblate Spheroid	Polar Angle (α)	5%
Oblate Spheroid	Azimuthal Angle (β)	1%
Crack vs. Void	Defect Type	0%

The error of each of these models, when evaluated on experimentally recorded data, were very similar to the errors based on theoretical data.

It was found that the "ripple frequency" feature of the power spectrum contained considerable information about the size of elliptical and free-surface cracks. The low frequency energy content was found to be indicative of size for the void defects. The spatial distribution of total power was key in estimating the orientation for both crack and void defects. The standard deviation of the power spectrum was an important feature in discriminating cracks from voids.

The oblate spheroid models were evaluated on four defect types, none of which were included in the training data set. These defect types, along with the qualitative estimates of how the models performed in estimating their size and orientation, are summarized in Table 1.2.

TABLE 1.2: SUMMARY OF OBLATE SPHEROID ALN MODEL PERFORMANCE ON EXTRAPOLATION DATA

Defect Type	Estimate Size	Estimate Orientation
Prolate Spheroid	Excellent	Excellent
Grooved Oblate	Good	Good
Sphere with Ring	Fair	Good
Lumpy Sphere	Fair	Poor

The "good" and "excellent" estimates on the prolate and grooved oblate spheroids demonstrate the extrapolative qualities of the ALN solution. The less favorable estimates on the sphere with ring and lumpy sphere indicate the need to develop a generalized solution for complex shapes. Section 5 presents both a graphical and a numerical presentation of the estimated defect sizes and orientations.

CONCLUSIONS AND RECOMMENDATIONS

The inversion of various crack and void defect types, as listed in Table 1.1, can be achieved with a high degree of accuracy via ALN modeling techniques. Additionally, these models perform well when evaluated on defect types unseen during the modeling synthesis. The parameters estimated

for voids (A, B, α, and β) may not have been fully adequate to estimate the more complex defect shapes like the lumpy sphere. It is, therefore, recommended that a more sophisticated parameter set for complex shapes be determined in future efforts.

Both two-dimensional and three-dimensional versions of Achenbach's free-surface forward-scattering theory for semielliptical cracks were investigated in this effort. A favorable match was obtained between theory and experiment for the two-dimensional case only. Consequently, the 2-D theory was used for data base generation. The 3-D theory should be compared against more experimental data as they become available.

The Weiner method for deconvolving the transducer reference from the experimental ultrasonic data is an optimum procedure. This method was employed to deconvolve all of the experimental analyzed data and the process was extremely stable.

The hexagonal array used in this work provided uniform coverage of the spheroid trailer-hitch samples over a wide aperture with a minimum number of elements. This array structure can also be extended to more common part geometries.

Calculation of the "ripple frequency" was accomplished by computing the power spectrum on a power spectrum after subtraction of the spectral envelope. The envelope subtraction was essential to remove the low-quefrency trend in the first spectrum. This method yielded consistently good results for both the theoretical and experimental data.

The forward-scattering theory for the elliptical crack was further verified by comparison to experimental data.

Before further inversions of complex cracks and voids are pursued, a mathematical means for representing these shapes must be defined. Estimation of simple parameters such as A, B, α, and β for complex voids seems to have yielded only marginal results. One recommendation for future work is to estimate the coefficients on a spherical harmonic expansion. There are, however, other ways for representing complex shapes in space, and the method which offers the highest correlation between the scattered ultrasonic field and the defect parameter should be used. Once this mathematical structure is defined, a more ubiquitous ALN inversion model should be derived which performs on both simple and complex shapes and possibly cracks as well as voids.

2. INTRODUCTION

Adaptronics became a contributor to the Interdisciplinary Program for Quantitative Flaw Definition in 1976 after the Second Year Effort. During the first three years, ALNs were successfully applied to the investigation of simple geometries such as spheroidal-shaped voids and elliptical crack defects, both in free space [1, 2, 3]. The ALN models were trained directly from theoretically generated data and evaluated in blind tests on experimentally recorded defect samples.

In the present effort, more realistic defect geometries have been considered. A free-surface crack model has been obtained which measures the depth of surface-connected cracks. Also, last year's oblate spheroid ALN models were evaluated this year with several complex-shaped defects to determine their extrapolative qualities. These defect shapes included: (1) the sphere with ring; (2) lumpy sphere; (3) grooved oblate spheroid; and (4) the prolate spheroid. Additionally, the elliptical-crack ALN models from last year were retrained to include "γ" the third orientation parameter. In last year's effort, this angle was assumed to be zero. A section summarizing all inputs and ALN models synthesized under the DARPA/AFML project is included in this report.

As in the previous three-year effort, the ALN models were trained on theoretically generated forward-scattering data and the inversion algorithms evaluated on both theoretical and experimentally recorded data.

The advantage of training the ALN models with theoretical data is that the scattered field from many defect geometries can be produced quickly and at a fraction of the cost of what is required to fabricate physical defect calibration specimens. The theoretical data have the added advantage of being noise-free. Ultimately, as the theories become more sophisticated, mimicking complicated defect shapes, surface roughness, multiple defects, and flaws in the vicinity of geometrical reflectors, data bases for field and industrial use can be generated entirely in a digital computer. This data base can always be augmented with experimental data from real flaws as it becomes available. The ultimate goal of Adaptronics, with regard to the Interdisciplinary Program, is to develop a generalized ALN model which can be used to invert either simple or complex shapes without the need to retrain the model each time a new defect category is considered. Recent advances in the development of accurate forward-scattering theories allow this goal to be entirely achievable in the very near future.

A block diagram illustrating the overall Adaptronics project philosophy is shown in Figure 2.1. The forward-scattering theories which generated the theoretical training data bases were provided by J. Achenbach, et al., and V. Varadan, for crack-defects and void-defects, respectively. An ALN synthesis program inputted the theoretical data bases to produce the ALN models. These models were evaluated on both theoretical and experimental data. All experimental data were recorded by J. Martin of the Rockwell Science Center. Other contributors were E. Domany, H. McMaken, A. Norris, and B. Tittman.

3. DEVELOPMENT OF ELLIPTICAL CRACK MODELS

DEFECT GEOMETRY

An elliptical-shaped crack oriented at an arbitrary position in space can be represented by two radii (A and B), and three orientation parameters (α, β, and γ).

For the purposes of this study, we assumed these parameters to be defined as follows:

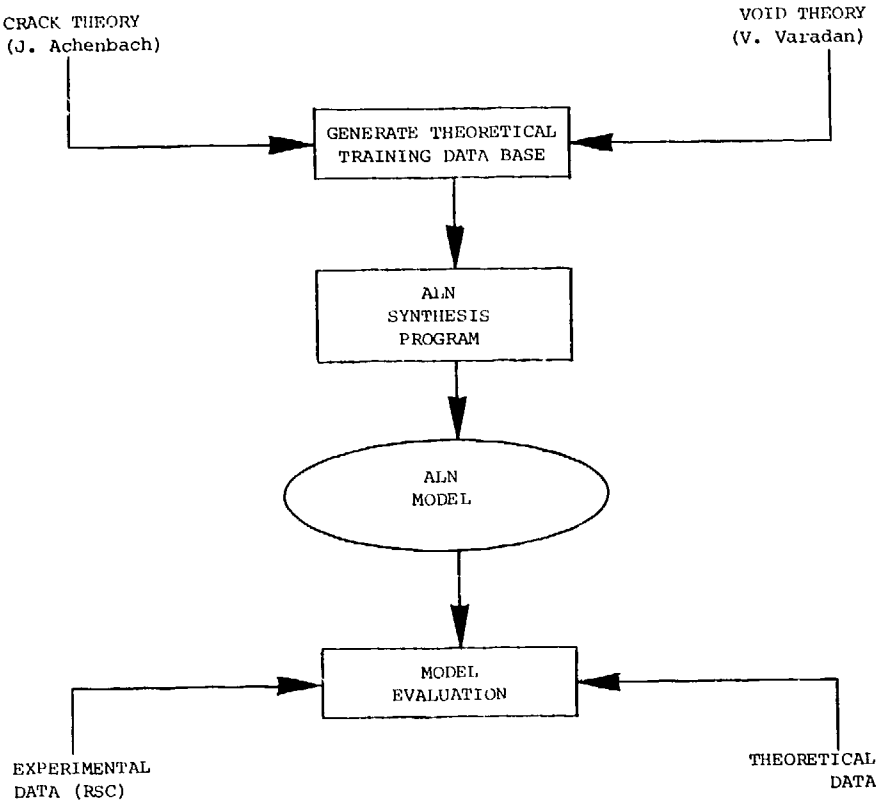

FIGURE 2.1: PROJECT PHILOSOPHY

A - Radius of the minor axis
B - Radius of the major axis
α - First Euler-angle rotation
β - Second Euler-angle rotation
γ - Third Euler-angle rotation

The Euler-angle rotations are defined in Figure 3.1. The first rotation is around the Z-axis; the second rotation is around the new major axis (line of nodes); and the third rotation is around the defect normal.

The Euler rotations are taken to be in the positive counterclockwise direction, and when all three angles are zero, the major axis, B, is assumed to lie along the positive X direction, and the minor axis, A, is assumed to lie along the positive Y direction. This defines a right-handed coordinate system in which the normal to the defect (M in Figure 3.1) lies along the Z-axis. This vertical axis also defines the center position of the receiver.

ARRAY CONFIGURATION

A 19-element hexagonal array was used to measure the scattered field. This array is illustrated in Figure 3.2. The transducer angular positions are defined in Table 3.1. Data were recorded in the pitch-catch mode with the center element acting as the transmitter. All 19 elements served as receivers. Only the L+L mode responses were considered. The mode-converted shear wave response was gated out of the recorded echo transients. The 19 receivers formed a 120° cone-shaped aperture with the transmitter at the cone center.

For the theoretical data, the scattering amplitudes were generated at the 19 positions given in Table 3.1 for each defect specified. This provided 19 different "views" of the elliptical crack over a wide aperture. The defect was assumed to be positioned at the origin. A hexagonally-spaced array is advantageous since all elements are equally spaced. On the surface of a sphere, each element is exactly 30° from its adjacent elements.

THEORETICAL DATA BASE

A computer code representing a far-field approximation to the geometrical theory of diffraction has been developed by Northwestern University for use by Adaptronics in calculating estimates of the power spectrum recorded at a particular location where an input ultrasonic signal is diffracted from a defect of specified geometry. The derivation of this model has been discussed extensively and has been shown to be in favorable agreement with experimental results [4, 5].

TABLE 3.1: RECEIVER ORIENTATION ANGLES

Receiver Number	Polar Angle "θ" (Degrees)	Azimuthal Angle "φ" (Degrees)
1	30	30
2	30	90
3	30	150
4	30	210
5	30	270
6	30	330
7	52	0
8	52	60
9	52	120
10	52	180
11	52	240
12	52	300
13	60	30
14	60	90
15	60	150
16	60	210
17	60	270
18	60	330
* 19	0	0

* Both Transmit and Receive

Theoretical power spectra corresponding to longitudinal mode scattering were generated at each receiver point in the 19-element array using the pitch-catch operating mode with the transmitter located at the center of the array. A total of 22,680 possible experiments were considered and are identified in Table 3.2. To reduce repetition in the data, a random number generator was used to randomly select 7 percent of the 22,680 possible experiments. This resulted in the generation of 1,625 actual cases, broadly distributed across the values listed in Table 3.2. Synthetic spectra were obtained for 14 different defect sizes (A and B), 9 different values of α, 15 different values of β, and 12 different values of γ. The frequency band of interest was from 1.0 to 9.0 MHz with a frequency resolution of 0.20 MHz. The corresponding ka range of the data was from 0.31 to 22.3.

EXPERIMENTAL DATA BASE

The experimental data for training the theoretically trained ALN models were collected at the Rockwell Science Center from a set of known specimens. Defects were machined at the center of titanium hemispheres, which were then diffusion-bonded together to form a sphere. The receiver array shown in Figure 3.2 was placed on the sphere surface. The sample was rotated to simulate various defect orientations. For a comparison of theory and experiment, and for verification of the ability of ALNs to accurately predict sizes and orientations, four experiments were analyzed. The four included three separate orientations of an elliptical yttria disk of dimensions 1.285 millimeters x 0.705 millimeters with a thickness or depth of less than 0.050 millimeters, and one orientation of a cylindrical yttria disk of 1.425 millimeters x 1.425 millimeters, with a depth of less than 0.050 millimeters. The four experiments are summarized in Table 3.3. Figures 3.3 and 3.4 depict the geometry of the two defects.

DECONVOLUTION

Deconvolution of ultrasonic signals is necessary to remove the specific transducer characteristics and to expand the data bandwidth. This is accomplished by dividing the complex spectrum of the data by a complex reference spectrum. The problem with a division is that it often leads to instability in the quotient function near the band limits. A Weiner deconvolution process was used in this work:

$$D(f) = \frac{X(f)R^*(f)}{|R(f)|^2 + |N(f)|^2} \qquad (3.1)$$

where

D(f) = complex deconvolved spectrum
X(f) = complex data spectrum
R(f) = complex reference spectrum
R*(f) = complex conjugate of R
N(f) = noise spectrum

In most applications, the noise spectrum is fairly uniform at all frequencies, hence, $|N(f)|$ can be replaced with a constant factor "c".

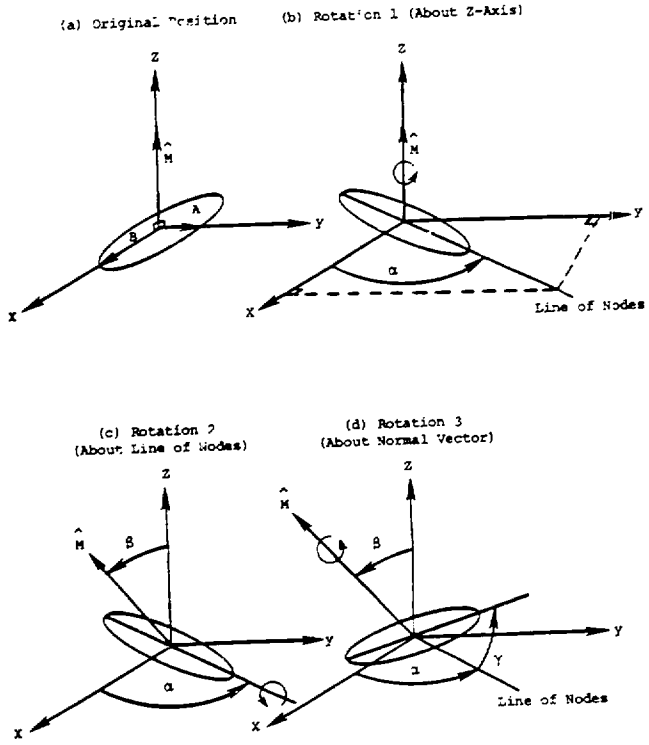

FIGURE 3.1: DEFINITION OF THREE EULER ANGLES TO DESCRIBE ORIENTATION OF ELLIPTICAL CRACK

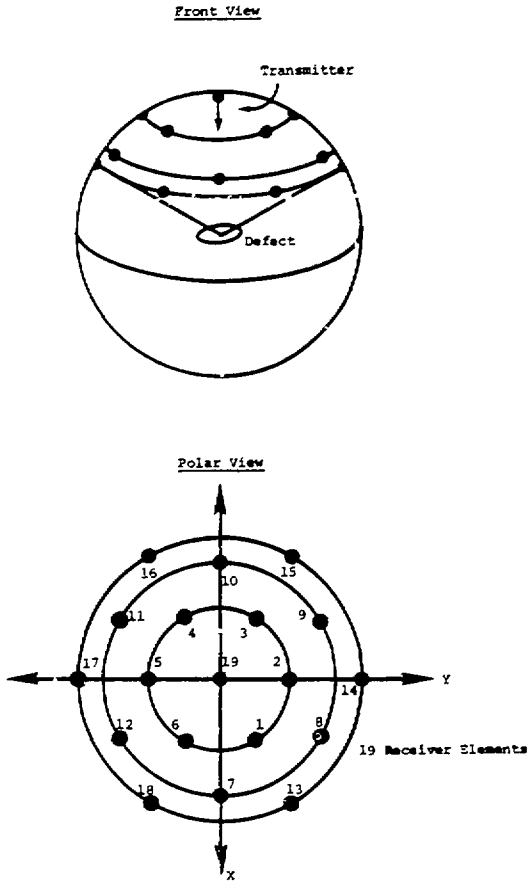

FIGURE 3.2: THE 19-ELEMENT HEXAGONAL ARRAY STRUCTURE

TABLE 3.2: RANGE OF VARIABLE VALUES IN THEORETICAL DATA BASE

Defect Sizes					
No.	Crack Radii A(mm)	B(mm)	No.	Crack Radii A(mm)	B(mm)
1	.312	.312	8	.625	2.500
2	.312	.625	9	1.250	1.250
3	.312	1.250	10	1.250	1.875
4	.312	2.500	11	1.250	2.500
5	.625	.625	12	1.875	1.875
6	.625	1.250	13	1.875	2.500
7	.625	1.875	14	2.500	2.500

Orientation Angles (°)

Alpha (9 cases)

= 1, 10, 20, 30, 40, 50, 60, 70, 80

Beta (15 cases)

= 0, 25, 50, 75, 100, 125, 150, 175, 200, 225, 250, 275, 300, 325, 350

Gamma (12 cases)

= 0, 15, 30, 45, 60, 75, 90, 105, 120, 135, 150, 165

Possible Number of Experiments

14 sizes x 9 Alphas x 15 Betas x 12 Gammas = 22,680

TABLE 3.3: EXPERIMENTAL DEFECTS AND ORIENTATIONS

Experiment Number	Defect Sizes (mm) A	B	C	Orientations (Degrees) α	β	γ
1	1.425	1.425	<50	0	0	0
2	1.285	.705	<50	0	0	0
3	1.285	.705	<50	15	0	0
4	1.285	.705	<50	15	0	90

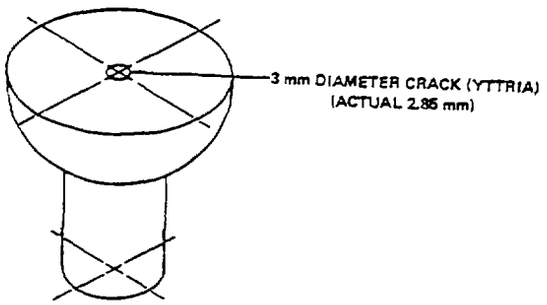

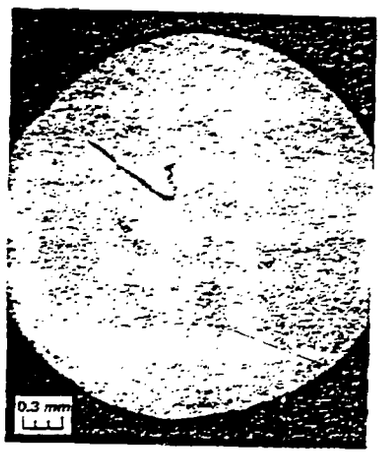

FIGURE 3.3: CRACK GEOMETRY FOR EXPERIMENT 1

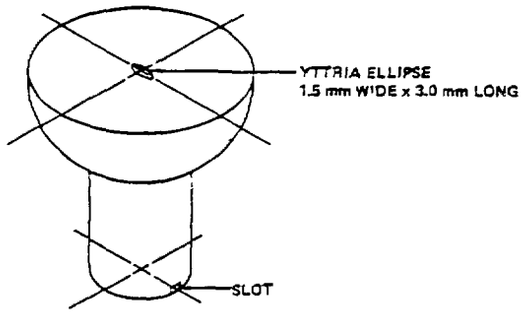

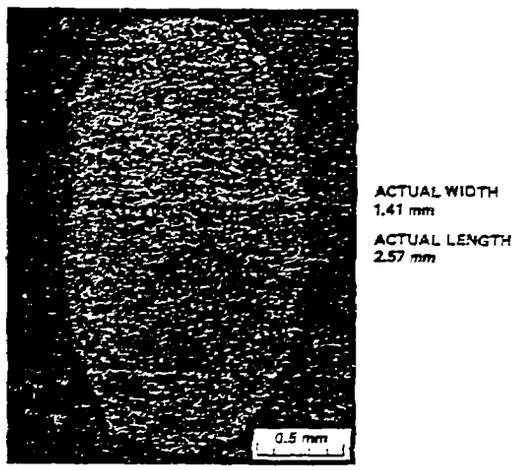

FIGURE 3.4: CRACK GEOMETRY FOR EXPERIMENTS 2, 3, AND 4

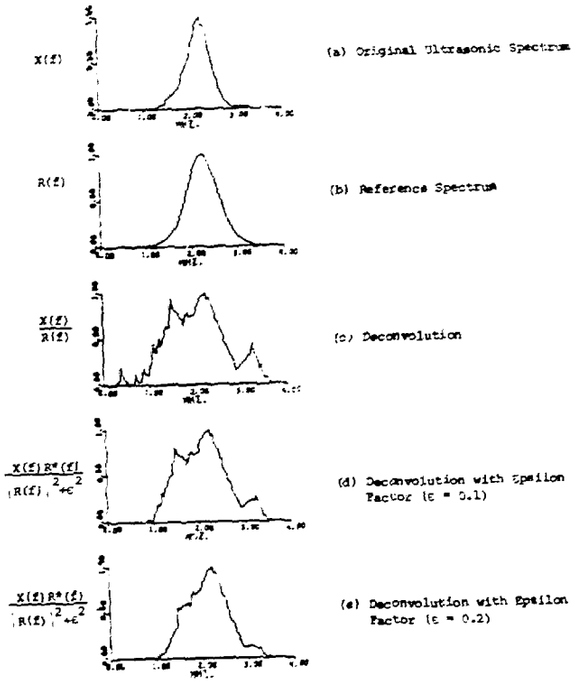

FIGURE 3.5: DEMONSTRATION OF THE WEINER DECONVOLUTION PROCESS

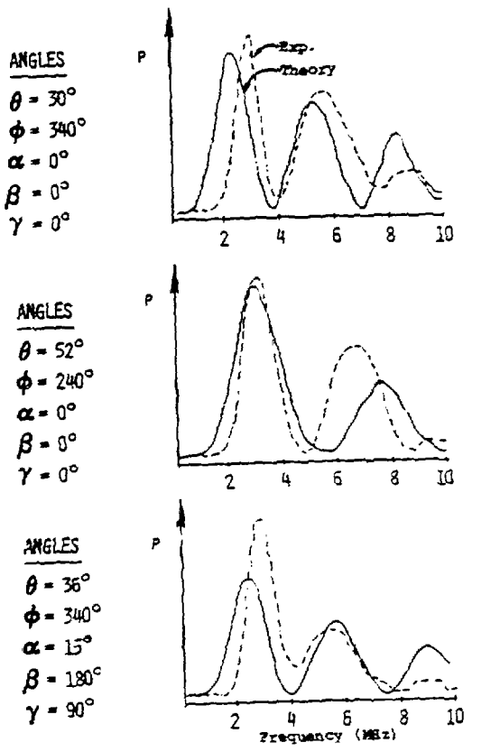

FIGURE 3.6: COMPARISON OF THE THEORETICAL AND EXPERIMENTAL ELLIPTICAL-CRACK POWER SPECTRA (A = .705 mm; B = 1.285 mm)

This method has recently been tested on ultrasonic crack data. The results were quite satisfactory. Figure 3.5 shows the power spectrum of a pulse-echo waveform (a); a reference spectrum (b); and three deconvolved spectra (c, d, and e) where Equation (3.1) was applied for three values of (ε = 0.0, 0.1, and 0.2 times the peak reference power spectrum). When ε = 0, the Weiner method becomes a simple division. Note how stable the deconvolved spectra are for ε = 0.1 and ε = 0.2. Also note the tendency toward instabilities when ε = 0. All experimental data were deconvolved using the Weiner filter.

COMPARISON OF THEORY AND EXPERIMENT

The theoretical elliptical-crack forward-scattering model, provided by Achenbach and McMaken, yielded a far-field physical elastodynamic approximate solution valid in the high ka regime (ka >> 1). Successful comparisons of theory and experiment have been provided in several other works [4, 5]. The most dominant characteristics of the scattered power spectrum is the successive pattern of peaks and troughs occurring at a single rate which shall be called the "ripple frequency." The rippling is caused by interface patterns due to the delayed arrivals of the diffracted waves from the near and far edge of the crack. The ripple frequency was found to be the single most important feature for determining crack size.

In comparing the theoretical spectra to the experimental data collected by Rockwell, several cases were in close agreement with regard to the ripple frequency. This is seen in Figure 3.6 where the parameters of each experiment are listed. The major notable difference between the two spectra types is that the experimental data are attenuated in the higher frequencies. However, no action was taken in the present work to correct this deficiency since the causes of the attenuation are not completely known.

For as many cases which compared favorably, there were at least as many cases which compared poorly. This fact is associated with the difficulty in fabricating controlled defect samples and in collecting noise-free ultrasonic data.

FEATURE EXTRACTION

The ALN synthesis process requires that candidate features be computed from each of the training experiments. In developing the model, the training algorithm determines which features are significant, the weighting coefficients, and the nonlinear multinomial structure. Unimportant features are automatically discarded from consideration.

Two spectral features were computed from each of the 19 receiver power spectra. These were the total power between 1.0 and 9.0 MHz and the ripple frequency. From each spectral feature, a group of 20 spatial features were computed over the 19 receiver locations. A total of 40 candidate features were therefore available for ALN synthesis.

The ripple frequency was determined by taking a power spectrum of the power spectrum and noting the position of the maximum peak. The envelope was subtracted from the first power spectrum to suppress the dominant low-quefrency artifact. This method yielded consistently good ripple frequency estimates for both the theoretical and experimental data; Figure 3.7 illustrates this process. The ripple frequency (τ) has the units of time. This can be converted to a distance measure by multiplying by the longitudinal wave propagation velocity.

The 20 spatial features computed from both the total spectral power and the ripple frequency are defined in Table 3.4. The first nine features are the coefficients of the generalized three-dimensional second-order surface:

$$w_1x^2 + w_2y^2 + w_3z^2 + w_4xy + w_5xz + w_6yz + w_7x + w_8y + w_9z = 1 \qquad (3.2)$$

which best fit through each of the 19 receiver locations. The method of least squares was used to determine the w's. Features #10, 11, and 12 are, respectively, the x, y, and z components of the moment vector of the 19 observations, which is characteristic of the polar orientation of the crack. The four arctangent features (13-16) further characterize the orientation of the defect, and the last four features are the four invariants of the second-order surface, given by the following equations:

$$I_1 = w_1 + w_2 + w_3 \qquad (3.3)$$

$$I_2 = w_1w_2 + w_1w_3 + w_2w_3 - w_4^2 - w_5^2 - w_6^2 \qquad (3.4)$$

$$I_3 = \begin{vmatrix} w_1 & w_4 & w_5 \\ w_4 & w_2 & w_6 \\ w_5 & w_6 & w_7 \end{vmatrix} \qquad (3.5)$$

$$I_4 = \begin{vmatrix} w_1 & w_4 & w_5 & w_7 \\ w_4 & w_2 & w_6 & w_8 \\ w_5 & w_6 & w_3 & w_4 \\ w_7 & w_8 & w_9 & -1 \end{vmatrix} \qquad (3.6)$$

Mathematically, the invariant features are insensitive to rotations of the measured field. Therefore, these features should have been good size estimators. However, the ALN training procedure did not select any of these as informative features.

ALN MODEL RESULTS

Five ALN models were synthesized on the theoretical forward-scattering data to estimate the five defect size and orientation parameters (A, B, α, β, γ). The model structures and coefficients are given in Section 6. Each of the models were evaluated on approximately 1000 theoretical experiments and the four experimentally recorded cases described above. The theoretical results are summarized in Table 3.5.

TABLE 3.5: ELLIPTICAL-CRACK INVERSION RESULTS

(Evaluation on theoretical data)

Parameter	Relative Error
A	21.8%
B	12.6%
α	5.0%
β	9.6%
γ	21.5%

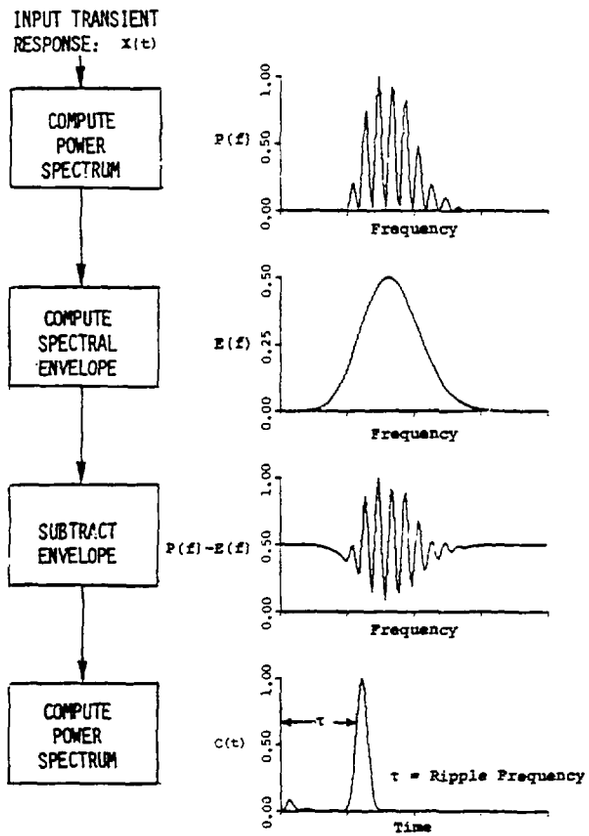

FIGURE 3.7: RIPPLE FREQUENCY CALCULATION

TABLE 3.4: DEFINITION OF THE CANDIDATE SPATIAL FEATURES

Feature Number	Symbol	:	Description
1	w_1	:	x^2 coefficient of the second-order surface
2	w_2	:	y^2 coefficient of the second-order surface
3	w_3	:	z^2 coefficient of the second-order surface
4	w_4	:	xy coefficient of the second-order surface
5	w_5	:	xz coefficient of the second-order surface
6	w_6	:	yz coefficient of the second-order surface
7	w_7	:	x coefficient of the second-order surface
8	w_8	:	y coefficient of the second-order surface
9	w_9	:	z coefficient of the second-order surface
10	$\bar{x}$	:	$\frac{1}{N}\sum_{1}^{19} F_i \sin\theta_i \cos\phi_i$ *
11	$\bar{y}$	:	$\frac{1}{N}\sum_{1}^{19} F_i \sin\theta_i \sin\phi_i$
12	$\bar{z}$	:	$\frac{1}{N}\sum_{1}^{19} F_i \cos\theta_i$
			($\bar{x}$, $\bar{y}$, $\bar{z}$) = Centroid or Moment Vector of F_i
13	ATAN1	:	$\tan^{-1}(\bar{y}/\bar{x})$
14	ATAN2	:	$\tan^{-1}((\bar{x}^2 + \bar{y}^2)/\bar{z}^2)$
15	ATAN3	:	$\tan^{-1}(w_2/w_1)$
16	ATAN4	:	$\tan^{-1}((w_1 + w_2)/w_3)$
17	I_1	:	first invariant of the second-order surface
18	I_2	:	second invariant of the second-order surface
19	I_3	:	third invariant of the second-order surface
20	I_4	:	fourth invariant of the second-order surface

* F_i is the total power or ripple frequency computed at the i^{th} receiver position; θ_i and ϕ_i are the polar and azimuthal angles of the i^{th} receiver position.

The best results were obtained for the orientation parameters α and β. Poorer but still respectable results were obtained for the semi-minor axis, "A", and the orientation angle "γ". The angle, γ, measured the rotation of the defect about its normal. Defects having an aspect ratio close to one produced only subtle changes in the scattered ultrasonic field for varying cases of γ. These subtle changes were difficult to model with the sparsely populated 19-element array. Furthermore, "γ" is not defined for circular defects.

It was noted from the theoretical data analysis that the model error was a function of the defect size. For the ALNs which estimated A and B as the defects became smaller, the size became more difficult to estimate. An explanation of this can be linked to the ripple frequency calculation. Although the power spectrum method of computing the ripple frequency worked well when two or more ripples were present, this technique could not accurately resolve the ripple frequency when fewer than two ripples were present. (This is another way of stating that a wider bandwidth is needed.) Also, power spectra having a fractional number of ripples would be resolved to the nearest integer. For instance, a spectrum with 1.4 ripples would be resolved as having a ripple frequency of 1.0. It is, therefore, understandable that the ALN model to estimate the smaller-size parameter (A) would yield a larger error. It was noted that if the smaller defects ($A \leq 0.625$ mm) were eliminated from the evaluation set, the error for "A" dropped from 21.8 percent to 13.4 percent.

The ALN model results for the four experimental samples are given in Figure 3.8. The true defect size is illustrated to scale along with the estimated defect size. Note that the agreement is quite favorable. The orientation error shown in the last column gives the angle between the true defect normal and the estimated defect normal. Note again that the errors in three of the four cases are very small. The experimental results for estimation of the third angle, γ, were very poor and, consequently, are not shown. It is believed that the subtle changes introduced in the ultrasonic scattering amplitudes by the existence of γ were less than the irreducible error in the ultrasonic measurements. The orientation error in Figure 3.7 was computed only from α and β.

4. DEVELOPMENT OF FREE-SURFACE CRACK MODELS

The majority of the defect characterization work performed in the past few years under this program has been concerned with the development of general inversion procedures which are applicable to flaws occurring in free space. A number of models have been proposed recently which offer the possibility of extending these inversion techniques to cracks attached to a free surface [6, 7]. The purpose of this section is to synthesize ALN models using these new theoretical formulations and to evaluate the resulting networks using experimental observations.

The approach taken in this analysis is shown in block-diagram form in Figure 4.1. The theoretical free-surface crack models can be divided into two separate cases - one representing the two-dimensional problem and the other corresponding to the three-dimensional situation. For the purposes of this study, these two geometrical cases were considered independently. A data base of theoretical approximations was generated for each appropriate model and subjected to various feature extraction operations. These candidate features were then input to ALN models to determine the key parameters as well as the functional relationship between the defect characteristic and these key features. The performance of these models was then assessed by using experimental data collected from a series of fabricated free-surface cracks.

THEORETICAL DATA BASE

The free-surface crack models used in this study represent solutions for a homogeneous, isotropic, linear elastic half-plane which contains a normal edge crack [7, 8]. The geometrical properties of the two cases are illustrated in Figure 4.2. In the two-dimensional situation, the crack is defined to possess a depth, "d", in the half-plane. The crack has a length, "l", and depth, "d", in the three-dimensional model. The models assume that a time-harmonic elastic wave is incident upon the crack and then obtains the total field in the half-plane by means of the linear superposition of the incident fields and the scattered fields. The solutions considered in this study represent far-field approximations corresponding to longitudinal mode scattering.

TWO-DIMENSIONAL FREE-SURFACE CRACK MODELING

A computer code representing the two-dimensional free-surface model was prepared by Northwestern University and used by Adaptronics to generate a number of power spectra corresponding to longitudinal mode pulse-echo recordings over the frequency range from 0.5 to 2.5 MHz. A suite of these spectra obtained for various crack depths is shown in Figure 4.3. For comparison purposes, each of these spectral plots was normalized to a maximum power of unity so that characteristic spectral shapes could be determined visually. It can be seen that the ripple frequency (defined in the previous section) changes quite dramatically from approximately 1.6 MHz at a depth of 2 mm to 1.1 MHz at a 5 mm depth. It is interesting to note that this observation is consistent with the results presented in the previous discussion concerning the ripple period structure of the semielliptical cracks. Other observations which can be made based on the spectra presented in Figure 4.3 concern the distributions of relative power levels in certain frequency bands depending on defect depth. In general, as the defect depth increases, there appears to be an increase in the relative power distributions at the higher frequency levels.

In order to verify that the trends observed in these theoretical spectra are meaningful features for defect inversion exercises, it is necessary to determine how well these theoretically generated quantities conform to experimental observations. To satisfy this requirement, ultrasonic pulse-echo recordings were collected from a series of semi-elliptical free-surface defects fabricated in a carbon steel calibration test block. The experimental setup is shown in Figure 4.4. The transducer used in this collection exercise was characterized by a 1.0 MHz center frequency with 100% bandwidth and was used in the pulse-echo mode.

EXP. NO.	TRUE SIZE (MM)	EST. SIZE (MM)	ORIENT. ERROR (DEGS.)
1	.705 x 1.285	.869 x 1.519	[1] 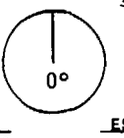 TRUE: α = 0, β = - EST.: α = 0, β = -
2	.705 x 1.285	.645 x 1.117	TRUE: α = 15, β = 180 EST.: α = 12, β = 169
3	.705 x 1.285	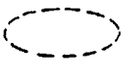 .518 x 1.147	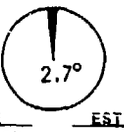 TRUE: α = 15, β = 180 EST.: α = 16, β = 170
4	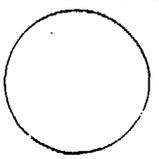 1.425 x 1. 425	.82 x 1.5	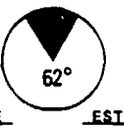 TRUE: α = 0, β = - EST.: α = 62, β = -

[1] ORIENTATION ERROR = $\cos^{-1}\left[x_{true}x_{est} + y_{true}y_{est} + z_{true}z_{est}\right]$

FIGURE 3.8: ELLIPTICAL CRACK INVERSION RESULTS (EXP. DATA)

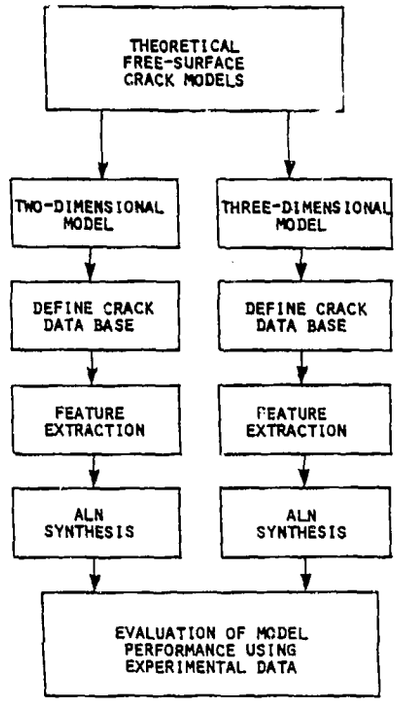

FIGURE 4.1: OVERVIEW OF THE ANALYSIS STEPS INVOLVED IN THE FREE-SURFACE CRACK MODEL STUDY

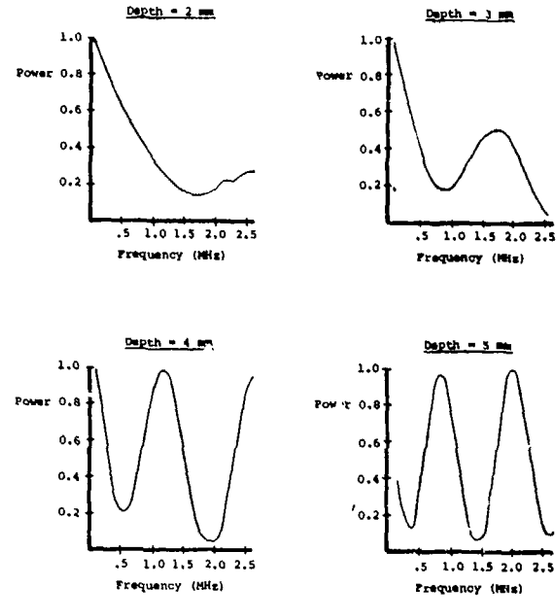

FIGURE 4.3: PULSE-ECHO POWER SPECTRAL L→L BULK WAVE RESPONSES FROM ACHENBACH'S TWO-DIMENSIONAL FREE-SURFACE SEMI-ELLIPTICAL CRACK THEORY (Incident Wave is 45°)

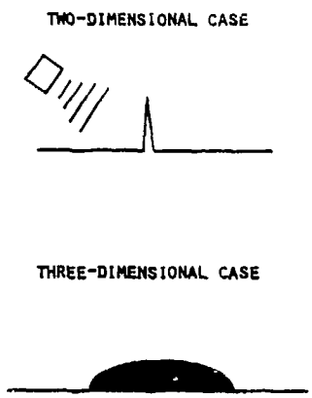

FIGURE 4.2: GEOMETRICAL REPRESENTATIONS OR THE TWO-DIMENSIONAL AND THREE-DIMENSIONAL FREE-SURFACE CRACKS

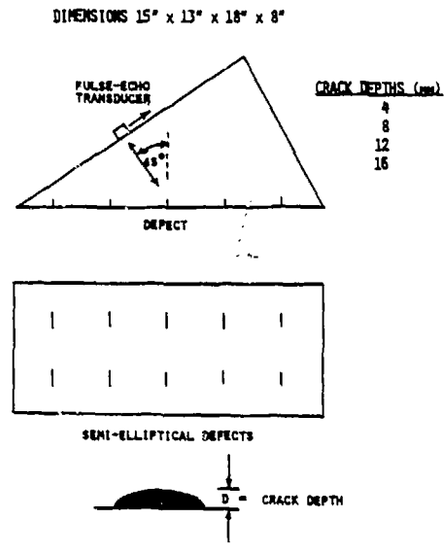

FIGURE 4.4: GEOMETRICAL DESCRIPTION OF THE EXPERIMENTAL DATA COLLECTION EXERCISE

The geometrical configuration of the test specimen enabled a 45° longitudinal wave to be emitted to the test block. A back-wall response was collected and used as a reference signal for deconvolution purposes.

The procedures employed in the data-collection exercises involved manual positioning of the transducer along the 45° edge of the test block to maximize the echo returned from the defect under analysis. Subsequent recordings were then obtained at a spacing of 6 mm in order to simulate a linear array. A total of six individual recordings were made moving up the edge of the calibration block. A comparison of theoretical and experimental power spectra is shown in Figure 4.5 for defect depths of 4, 8, and 12 mm. The transducer location for these spectra corresponds to a position 6 mm away from the direct corner reflection location. The experimental spectra have been deconvolved using the back-wall return as a reference. It can be seen that comparison is quite good for the 8 and 12 mm-deep cracks. Both the ripple periods and power distributions match up well over the frequency band from 0.5 to 2.0 MHz. The comparison presented for the 4 mm case is not as good as that for the larger defects and is probably related to the fact that the theoretical model does not perform well in the small ka region.

A more detailed comparison of the theoretical and experimental spectra obtained at the first four positions in the synthetic array is shown in Figures 4.6 - 4.8 for defect depths of 4, 8, and 12 mm. As noted previously, the comparisons are quite good for the larger defects and are less favorable for the smallest defect depth.

Based upon the close agreement obtained between the theoretical two-dimensional model and the experimental recordings, ALN models were synthesized to estimate the crack depth. The theoretical training data base consisted of ten crack depths and an array of six pulse-echo receivers. The specifics of the training set are described in Table 4.1. These theoretical spectra were then subjected to a number of feature extraction algorithms to determine candidate parameters to input to the ALN depth model. The candidate set consisted of eight individual quantities which are identified in Table 4.2. The features include the ripple period, measurements of power decay across the pulse-echo array, and various ratios of power levels in certain frequency bands.

TABLE 4.1: DATA BASE USED IN TRAINING ADAPTIVE LEARNING NETWORKS (Two-Dimensional Case)

DEFECT DEPTHS (MM)

4, 5, 6, 7, 8, 9, 10, 12, 14, 16

RECEIVERS

6 RECEIVERS OPERATING IN THE PULSE/ECHO MODE SEPARATED BY 6MM (LINEAR ARRAY)

TABLE 4.2: CANDIDATE FEATURES USED IN THE SYNTHESIS OF THE TWO-DIMENSIONAL FREE-SURFACE CRACK MODEL

1 - Ripple Frequency

2 - Decay of Total Power from 0.5 - 2.5 MHz

3 - Decay of Total Power from 0.5 - 1.5 MHz

4 - Decay of Total Power from 1.5 - 2.5 MHz

5 - Decay of Average Power from 0.5 - 2.5 MHz

6 - Ratio of Power in Band from 0.5 - 1.5 MHz to Power in Band from 1.5 - 2.5 MHz

7 - Ratio of Power in Band from 1.5 - 2.5 MHz to Power in Band from 0.5 - 2.5 MHz

8 - Ratio of Power in Band from 0.5 - 1.5 MHz to Power in Band from 0.5 - 2.5 MHz

The resulting ALN model is shown in Figure 4.9 and consists of two input features - the ripple frequency and the slope of the power decay across the six-element array over the frequency band from 0.5 to 1.5 MHz. The average relative error in the defect depth estimate was less than 6%. A scatter plot of the observed and predicted defect depth values is shown in Figure 4.10. The performance of the model was assessed using subsets of the experimental observations discussed previously in this section. The ripple period and power decay parameters were obtained from the observed spectral quantities and input to the ALN model to obtain estimates of crack depth. The results of this analysis are summarized in Table 4.3. The large error for the 4-mm defect has been discussed earlier and is probably a result of extending the theoretical model to small ka regions. The depth estimates for the 8-mm and 12-mm defects are very good with errors of less than 3% being observed.

TABLE 4.3: ALN MODEL PERFORMANCE

TRUE CRACK DEPTH	ALN ESTIMATED CRACK DEPTH
4.00 MM	5.88 MM
8.00 MM	7.81 MM
12.00 MM	12.34 MM

THREE-DIMENSIONAL FREE-SURFACE CRACK MODELING

A computer code representing the three-dimensional free-surface crack model was prepared by Northwestern University and used by Adaptronics to generate a number of power spectra corresponding to longitudinal mode pulse-echo and pitch-catch recordings. An example of spectra obtained from a single pitch-catch arrangement for a series of different crack sizes is shown in Figure 4.11. The source position used in this illustration represents a polar angle of 45° and an azimuthal angle of 0° with reference to the crack. The reciever location is defined with a polar angle of 45° and azimuthal angle of 60°. It can be seen from this figure that, as the defect size increases, the spectral peaks shift to lower frequency levels. The ripple frequency characteristic of the spectrum appears to become greater as the defect size increases.

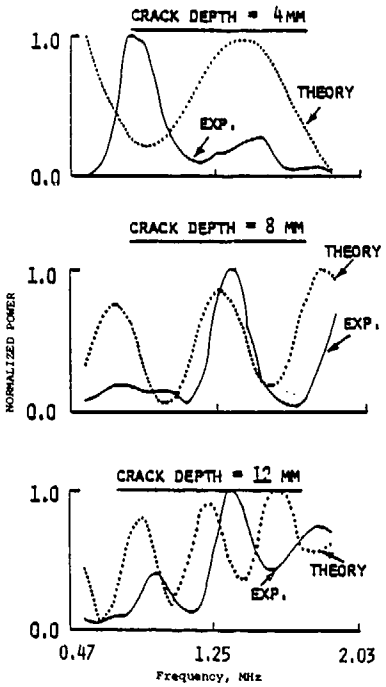

FIGURE 4.5: COMPARISON OF THEORETICAL AND EXPERIMENTAL POWER SPECTRA OBTAINED FOR VARIOUS CRACK DEPTHS

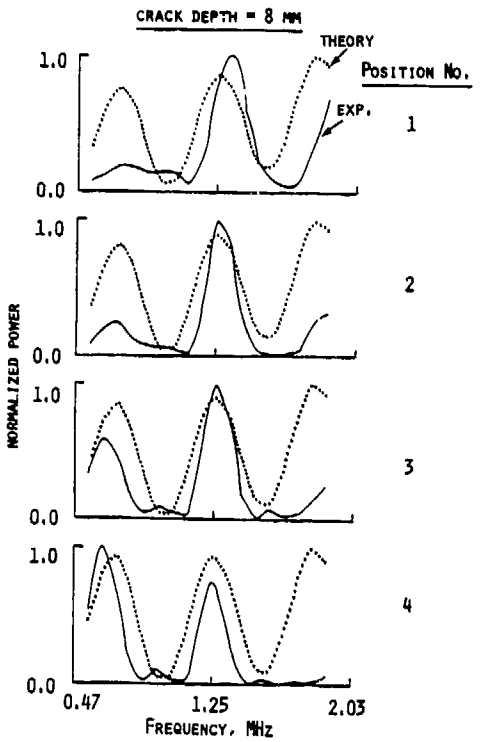

FIGURE 4.7: COMPARISON OF THEORETICAL AND EXPERIMENTAL POWER SPECTRA OBTAINED AT VARIOUS POSITIONS ON THE CALIBRATION BLOCK

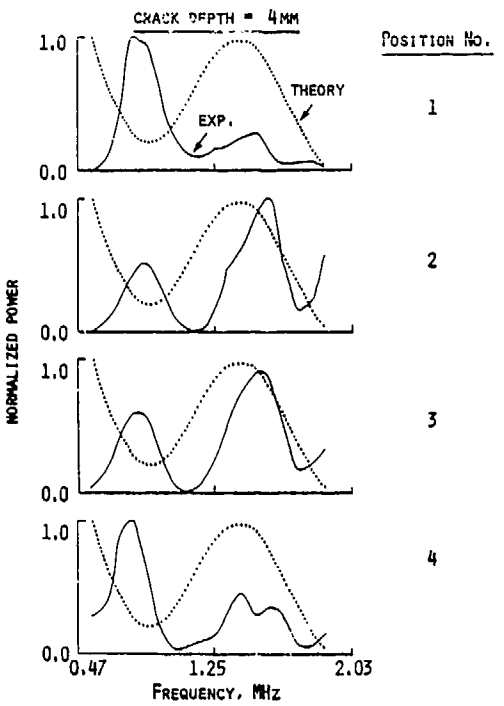

FIGURE 4.6: COMPARISON OF THEORETICAL AND EXPERIMENTAL POWER SPECTRA OBTAINED AT VARIOUS POSITIONS ON THE CALIBRATION BLOCK

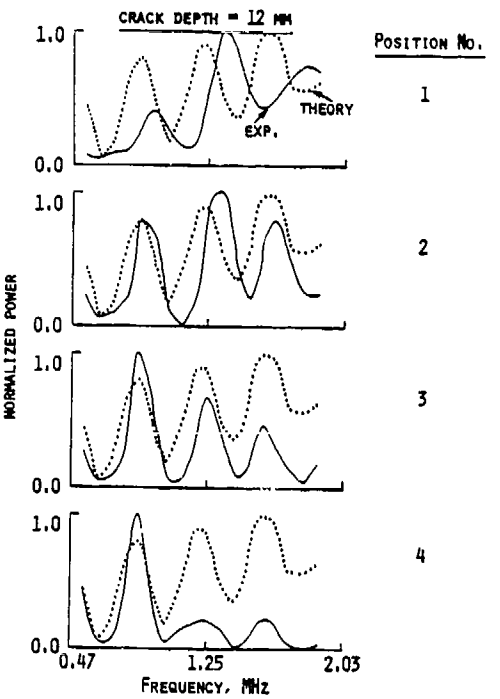

FIGURE 4.8: COMPARISON OF THEORETICAL AND EXPERIMENTAL POWER SPECTRA OBTAINED AT VARIOUS POSITIONS ON THE CALIBRATION BLOCK

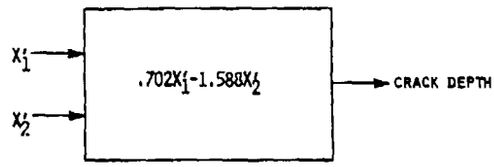

X_1 = SLOPE OF POWER DECAY ACROSS ARRAY IN BAND FROM 0.5 TO 1.5 MHz

X_2 = RIPPLE FREQUENCY

WHERE $X_N' = \frac{X_N - \mu_N}{\sigma_N}$, μ_N = MEAN, σ_N = STANDARD DEVIATION

$\mu_1 = -.1545, \sigma_1 = .01463$

$\mu_2 = .5800, \sigma_2 = .23719$

FIGURE 4.9: ALN MODEL TO PREDICT CRACK DEPTH (Two-Dimensional Case)

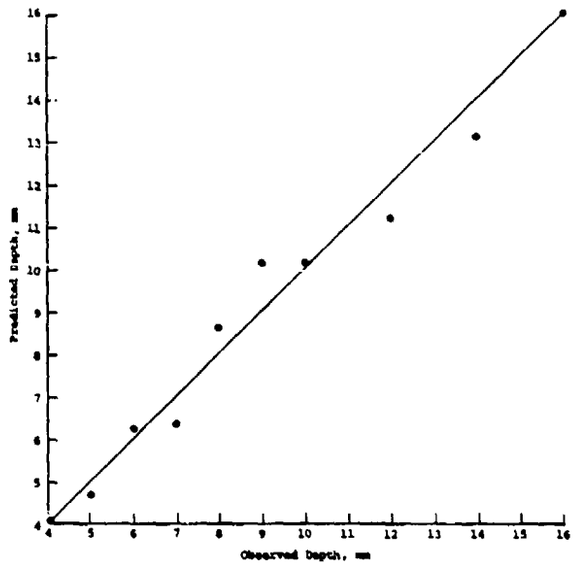

FIGURE 4.10: COMPARISON OF OBSERVED AND PREDICTED DEPTH VALUES FOR THE TWO-DIMENSIONAL MODEL

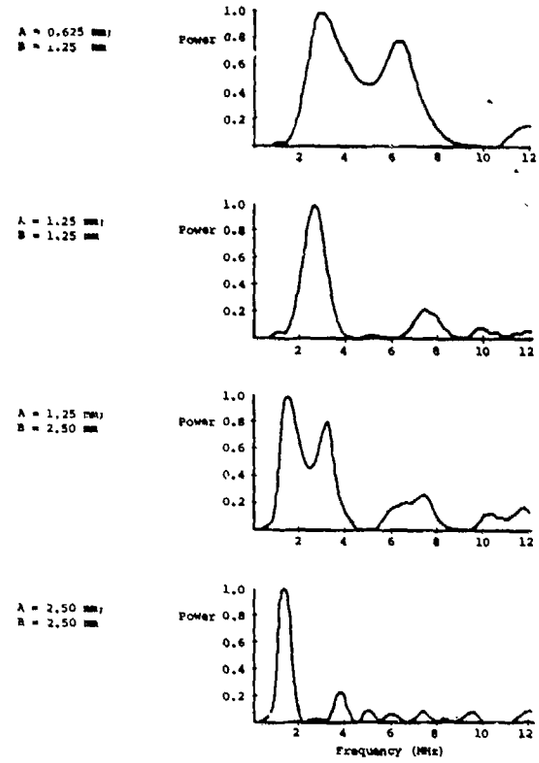

FIGURE 4.11: PITCH-CATCH POWER SPECTRAL L→L BULK WAVE RESPONSES FROM ACHENBACH'S THREE-DIMENSIONAL SEMIELLIPTICAL CRACK THEORY ($\theta_I = 45°$, $\phi_I = 0°$; $\theta_R = 45°$, $\phi_R = 60°$; A = half-length, B = depth.)

Following the procedures outlined in the two-dimensional model discussion, the next step involves a direct comparison of theoretical and experimental data. This requirement is satisfied in Figures 4.12 and 4.13 for a crack of depth 2.4 mm and of length 2.6 mm. The experimental data were collected by the Rockwell Science Center and forwarded to Adaptronics for analysis. The comparison illustrated in Figure 4.12 corresponds to a series of pulse-echo recordings obtained at various locations around the defect origin. In this case, the theoretical spectra were convolved with a back-wall reference recording to enable a quick comparison to be made. Over the frequency range from 5 to 12 MHz, it can be seen that the experimental spectra are characterized by a much higher oscillatory behavior than the theoretical spectra, leading to the conclusion that the ripple frequencies of the two spectra are not very comparable. This same general conclusion can be inferred from a comparison of the pitch-catch spectra shown in Figure 4.13. It is also noted that the actual power distributions are not in very good agreement over various frequency intervals. The reasons for the disagreements reported in this comparison have not been identified with any degree of certainty at this time and could probably be resolved by more comparison studies. Unfortunately, no other experimental observations are available to enable these discrepancies to be identified. Additional uncertainties associated with the true size of the defect used in this single experimental setup further cloud the comparison [9].

Based on these unresolved problems concerning the comparison of the theoretical and experimental three-dimensional crack spectra, the decision was made to defer the ALN analysis of this case until further investigations could be performed.

5. EVALUATION OF COMPOUND VOID MODELS WITH EXTRAPOLATION DATA

SUMMARY

During last year's DARPA/AFML program, Adaptronics developed four ALN inversion models to estimate the size and orientation of oblate spheroid-shaped defects. The details of this work are covered in Reference [3]. In summary, a 19-element pulse-echo hexagonal array, whose receiver location matched those shown in Table 3.1, was used to capture the scattering amplitudes. A theoretical data base was generated from the T-Matrix theory to train the four ALN models. The models estimated the two radii of the spheroid (A and B), and two orientation angles (α and β). These geometrical descriptors are shown in Figure 5.1. The features to train the models were computed from the power spectrum and the characteristic function. Spatial features, similar to those discussed in the above sections, were computed from the spectral features. The model errors, when evaluated on independent theoretical data, were as follows:

Parameter	Relative Error
A	9%
B	8%
α	5%
β	1%

The structures and coefficients of the four ALN models are given in Section 6.

RESULTS

One objective of this year's effort was to evaluate the oblate spheroid ALN models, discussed above, with experimental data of more complex defect shapes. The point of this evaluation was to determine how the ALN models would perform on defects which were not represented in the training data set as a means of qualifying the extrapolative qualities of the models. Four classes of complex defects were evaluated:

(1) Prolate spheroid
(2) Grooved oblate spheroid
(3) Sphere with ring
(4) Lumpy sphere

Experimental pulse-echo waveforms were recorded on each of the four defect categories at several different orientations. These experimental RF transients were recorded at Rockwell Science Center on the trailer-hitch samples and were provided to Adaptronics for further processing. The hexagonal array element spacing was maintained. Fourier transforms and features were computed and the features were processed through the four ALN models. The results are shown both graphically and numerically in Figures 5.2 - 5.5.

The best results were obtained on the prolate spheroids (Figure 5.2). The true prolate size was A = 800 microns and B = 400 microns. This defect was viewed from two different orientations as shown. The true size is indicated by solid lines on the left side of Figure 5.2. The estimated defect size is represented by the broken lines. The two dimensions (A and B) are illustrated as the major and minor axis of an ellipse in the figure. Both the true and estimated sizes are shown numerically in microns. Note that, for both cases, the true and estimated sizes are very close. The true orientations of the two experiments were:

$\alpha = 15, \beta = 90$; and
$\alpha = 30, \beta = 90$.

The estimated orientations were:

$\hat{\alpha} = 21, \hat{\beta} = 94$; and
$\hat{\alpha} = 34, \hat{\beta} = 92$.

Figure 5.2 shows the orientation error which is the angle between the true defect normal and the estimated defect normal. This angle (ψ) was computed as:

$$\psi = \cos^{-1}(X_T X_E + Y_T Y_E + Z_T Z_E) \qquad (5.1)$$

where
$X = \sin\alpha \cos\beta$
$Y = \sin\alpha \sin\beta$
$Z = \cos\alpha$
T = "true"
E = "estimated"

The orientation error is shown as the "blacked-in" portion of the circle on the right side of Figure 5.2. Note that these errors are very small.

The evaluation results for the grooved oblate spheroid are shown in Figure 5.3. The format is the same as that described for Figure 5.2. In this case, three orientations of the same defect were considered. The true defect size was 195

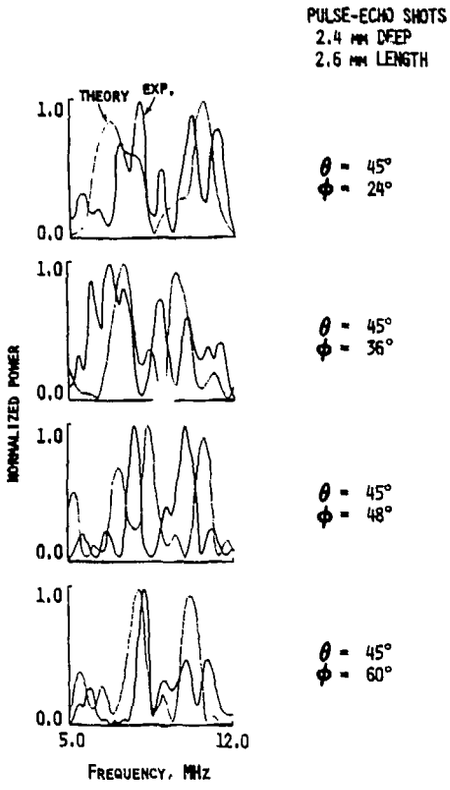

FIGURE 4.12: FREE-SURFACE ELLIPTICAL CRACK SPECTRA (Three-Dimensional Theory)

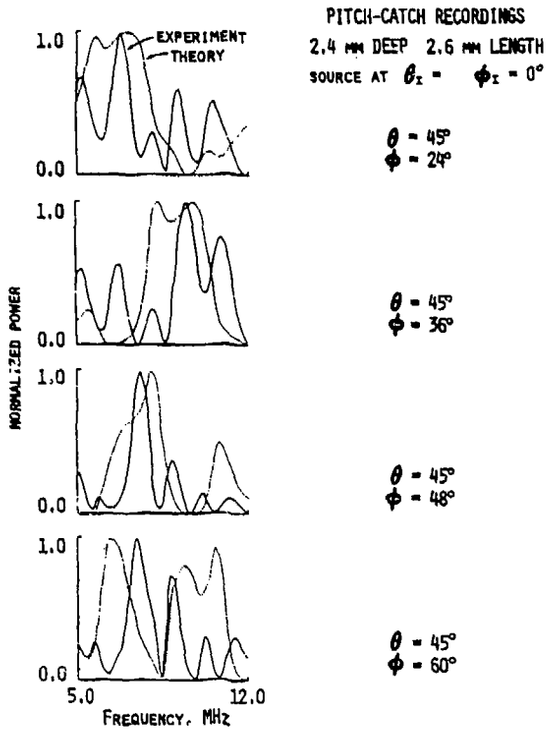

FIGURE 4.13: FREE-SURFACE CRACK SPECTRA (Three-Dimensional Theory)

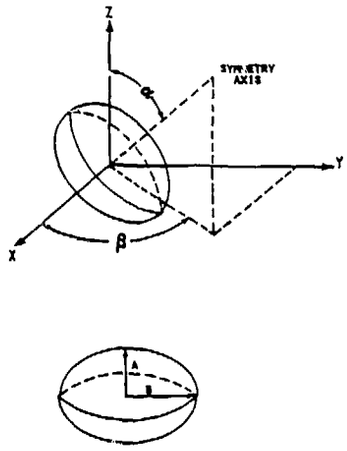

FIGURE 5.1: OBLATE SPHEROID COORDINATE GEOMETRY

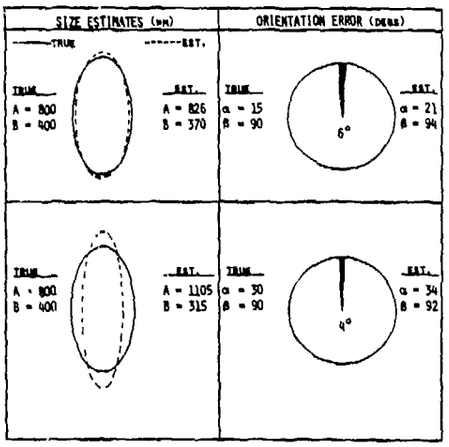

FIGURE 5.2: PROLATE SPHEROID ALN ESTIMATES

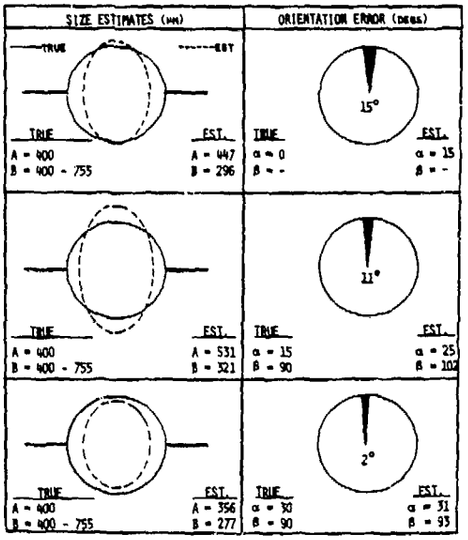

FIGURE 5.4: SPHERE WITH RING ALN ESTIMATES

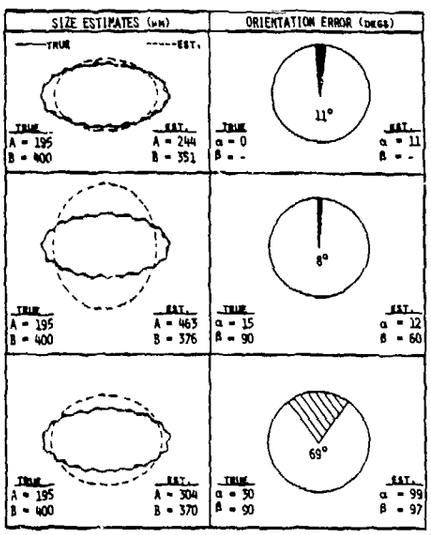

FIGURE 5.3: GROOVED OBLATE SPHEROID ALN ESTIMATES

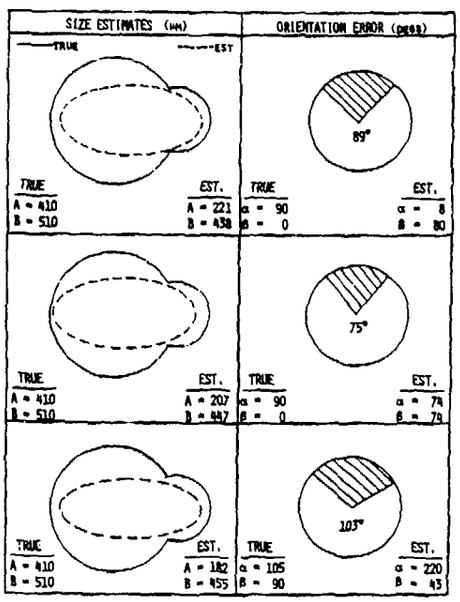

FIGURE 5.5: LUMPY SPHERE ALN ESTIMATES

microns by 400 microns. Small grooves of approximately one micron in depth were machined over the entire surface of the spheroid. The polar orientations (α) of the defect were 0, 15, and 30 degrees. The azimuthal orientations (β) were at 90 degrees for two of the cases, as shown. Estimates for two of the three sizes were very close to the true values. The size estimate for the third defect was very good for the B dimension but about twice the true value for the A dimension, making the overall estimated shape of the defect appear slightly prolate. Two of the three orientation estimates were also quite good as indicated in Figure 5.3.

The next defect tested was the sphere with a ring. This defect was formed by diffusion-bonding the 400-micron hemispheres. An yttria disbonding agent was applied before diffusion to create a 755-micron ring similar to the "Ring of Saturn" but touching the sphere at its equator. The defect simulates a crack in the presence of a void. Data were recorded on three orientations. As indicated in Figure 5.4., each of the size estimates were very close to the actual size of the sphere, but the ring appeared to go undetected. The estimated shapes of all three cases were "egg-shaped." All of the orientation estimates were very close to the true values.

Figure 5.5 presents the true and estimated sizes and orientations for the lumpy sphere. This defect was formed by combining two spheres of unequal size (R_1 = 410 microns, R_2 = 200 Microns) such that the center of the smaller sphere was located at the surface of the larger sphere. The shape of the estimated defect in all three cases was that of an oblate spheroid. The overall estimated defect length was about equal to the true length. In general, the estimated defect size was slightly smaller than that of the lumpy sphere. The orientation errors for all three cases were large. This was probably due to the irregular reflecting surface of the defect, or due to the irreducible error associated with collecting experimental data.

Table 5.1 summarizes the results of this section in a qualitative fashion. The ability of the ALN models, trained only on theoretical oblate spheroid data, to characterize the experimentally-obtained, complex-shaped defects is rated in four categories: excellent, good, fair, and poor.

TABLE 5.1: SUMMARY OF OBLATE SPHEROID ALN MODEL PERFORMANCE ON EXTRAPOLATIVE DATA

Defect Type	Estimate Size	Estimate Orientation
Prolate Spheroid	Excellent	Excellent
Grooved Oblate	Good	Good
Sphere with Ring	Fair	Good
Lumpy Sphere	Fair	Poor

Overall, the ALN models performed quite well when one considers the differences between the training data and the evaluation data:

(1) The training data were theoretically generated, where the evaluated data were experimentally collected.

(2) The training defect types were different from the evaluation defect types.

(3) The training data were noise-free where the evaluation data contained noise.

Additionally, it should be mentioned that all model estimates were the same order of magnitude as the true defect sizes. No "blown-up" outputs resulted.

The results presented in this section demonstrate the extrapolative capabilities of ALN models applied to NDE methods. The fact that some of the defect estimates possessed larger-than-desirable errors can be more directly attributed to the inappropriate type of parameters modeled (A, B, α, β), rather than to the models themselves. Clearly, the models work well for defects of the spheroid type (both oblate and prolate). However, the more complex shapes require a more germane set of parameters to be modeled. A more appropriate set of defect descriptors might be the first several coefficients on a spherical harmonic expansion. Solutions of this type should be considered for future work.

6. ALN NETWORK MODELS

The more significant ALN models developed within the last two years for inverting crack and void defects are covered in this section and are illustrated in Figures 6.2 - 6.12. Each figure shows the element connectivity, the mathematical form of the element, a description of the input features, and the network weighting coefficients. The ALN model is the equation which relates the input feature to the modeled output parameter. In all cases shown below, the output parameter has been chosen to be a specific characteristic of the crack or void defect. One important product of the ALN synthesis procedure is that all insignificant features are eliminated from the final model. The models shown below, therefore, identify which features are significant in performing the inversion.

The network configuration of the ALN model has been adopted since very complicated nonlinear multivariant relationships can be represented in a compact form. For instance, consider the simple hypothetical network shown in Figure 6.1 and assume that each of the elements (boxes) represents the following four-term algebraic relationship of the two input variables:

$$y_1 = a_0 + a_1x_1 + a_2x_2 + a_3x_1x_2 \tag{6.1}$$

$$y_2 = b_0 + b_1x_3 + b_2x_4 + b_3x_3x_4 \tag{6.2}$$

$$y_3 = c_0 + c_1y_1 + c_2y_2 + c_3y_1y_2 \tag{6.3}$$

Substituting Equation (6.1) and (6.2) into (6.3) yields:

$$\begin{aligned} y_3 = {} & c_0 + c_1(a_0 + a_1x_1 + a_2x_2 + a_3x_1x_2) \\ & + c_2(b_0 + b_1x_3 + b_2x_4 + b_2x_3x_4) \\ & + c_3(a_0 + a_1x_1 + a_2x_2 + a_3x_1x_2) \\ & \quad (b_0 + b_1x_3 + b_2x_4 + b_3x_3x_4) \end{aligned} \tag{6.4}$$

Expansion of Equation (6.4) would yield y_3 as a nonlinear function of x_1, x_2, x_3, and x_4 with greater than 60 terms. Therefore, the networks

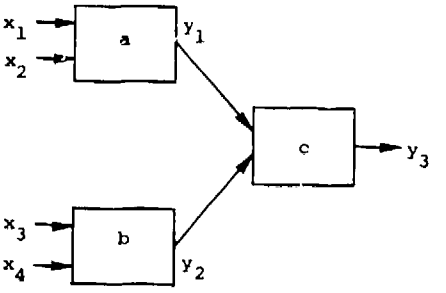

FIGURE 6.1: HYPOTHETICAL NETWORK

ALN STRUCTURE

ERROR ON THEORETICAL DATA = 22%

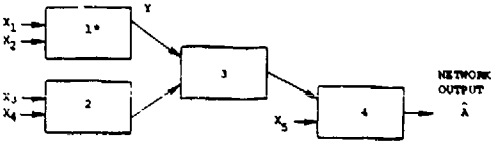

*ELEMENTAL FORM: $Y = w_0 + w_1x_1 + w_2x_2 + w_3x_1x_2 + w_4x_1^2 + w_5x_2^2 + w_6x_1^3 + w_7x_2^3$

		mean ($\bar{x}_i$)	sigma (σ_i)
x_1:	R-Component of the Minor Vector (R) of the total power	.699	.130
x_2:	w_1-Fourbase Coefficient of the Ripple Frequency	-.126	.362
x_3:	w_2-Fourbase Coefficient of the Ripple Frequency	.755	.714
x_4:	R-Component of the Minor Vector (R) of the Ripple Frequency	2.61	1.27
x_5:	Angle of the Ripple Frequency	9.43	5.44

NETWORK WEIGHTING COEFFICIENTS

ELEMENT	w_0	w_1	w_2	w_3	w_4	w_5	w_6	w_7
1	.544	1.240	1.60	.862	0	.150	0	0
2	-.063	.806	.691	.454	.566	0	.282	.040
3	-.172	.878	.704	.454	.168	0	0	0
4	.001	1.012	.034	0	0	0	0	.091

FIGURE 6.2: ADAPTIVE LEARNING NETWORK TO ESTIMATE THE SEMI-MINOR AXIS "$\hat{A}$" FOR ELLIPTICAL CRACK DEFECTS

ALN STRUCTURE

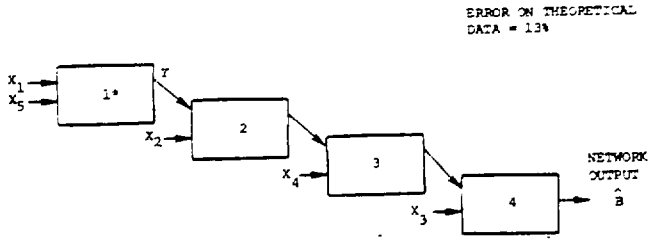

*ELEMENTAL FORM: $Y = w_0 + w_1x_1 + w_2x_2 + w_3x_1x_2 + w_4x_1^2 + w_5x_2^2 + w_6x_1^3 + w_7x_2^3$

FEATURE DESCRIPTION

		Mean ($\bar{X}_i$)	Sigma (σ_i)
X1:	Z-Component of the Moment Vector ($\bar{Z}$) of the Total Power	.699	.130
X2:	w_2-Surface Coefficient of the Ripple Frequency	.027	.070
X3:	X-Component of the Moment Vector ($\bar{Z}$) of the Ripple Frequency	-.017	.347
X4:	Y-Component of the Moment Vector ($\bar{Z}$) of the Ripple Frequency	.036	.364
X5:	Z-Component of the Moment Vector ($\bar{Z}$) of the Ripple Frequency	2.61	1.27

NETWORK WEIGHTING COEFFICIENTS

ELEMENT	w_0	w_1	w_2	w_3	w_4	w_5	w_6	w_7
1	.245	1.045	.962	.102	.485	-.457	-.315	-.117
2	-.015	.943	-.272	0	0	0	0	.008
3	-.107	.956	.052	0	0	.107	0	0
4	-.120	.963	.002	0	0	.120	0	0

FIGURE 6.3: ADAPTIVE LEARNING NETWORK TO ESTIMATE THE SEMI-MAJOR AXIS "$\hat{B}$" FOR ELLIPTICAL CRACK DEFECTS

ALN STRUCTURE

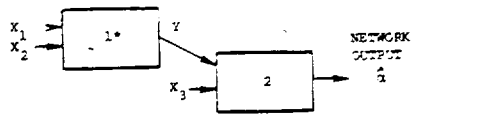

*ELEMENTAL FORM: $Y = w_0 + w_1x_1 + w_2x_2 + w_3x_1x_2 + w_4x_1^2 + w_5x_2^2 + w_6x_1^3 + w_7x_2^3$

FEATURE DESCRIPTION

		Mean ($\bar{X}_i$)	Sigma (σ_i)
X1:	Z-Component of the Moment Vector ($\bar{Z}$) of the Total Power	.710	.131
X2:	ATAN2 of the Total Power	34.1	25.7
X3:	ATAN4 of the Total Power	90.3	25.5

NETWORK WEIGHTING COEFFICIENTS

ELEMENT	w_0	w_1	w_2	w_3	w_4	w_5	w_6	w_7
1	.154	-2.580	-1.752	1.407	1.026	0	.222	0
2	0	1.010	.096	0	0	0	0	0

FIGURE 6.4: ADAPTIVE LEARNING NETWORK TO ESTIMATE THE POLAR ANGLE "$\hat{\alpha}$" FOR ELLIPTICAL CRACK DEFECTS

ALN STRUCTURE

ERROR ON THEORETICAL DATA = 10%

*ELEMENTAL FORM: $Y = w_0 + w_1x_1 + w_2x_2 + w_3x_1x_2 + w_4x_1^2 + w_5x_2^2 + w_6x_1^3 + w_7x_2^3$

FEATURE DESCRIPTION	Mean ($\bar{X}_i$)	Sigma (σ_i)
X1: X-Component of the Moment Vector ($\bar{X}$) of the Total Power	.695	.118
X2: ATAN1 of the Total Power	-9.13	103.
X3: Y-Component of the Moment Vector ($\bar{Y}$) of the Total Power	-.028	.373
X4: w_6-Surface Coefficient of the Total Power	-108.	1934.
X5: X-Component of the Moment Vector ($\bar{X}$) of the Ripple Frequency	-.006	.337

NETWORK WEIGHTING COEFFICIENTS

ELEMENT	w_0	w_1	w_2	w_3	w_4	w_5	w_6	w_7
1	-.975	- .114	.182	0	-.086	.808	0	-.204
2	.279	1.207	-.079	-.466	-.509	0	0	0
3	.031	1.345	-.404	0	-.026	0	-.276	0
4	.032	1.287	-.053	-.357	0	-.407	0	0
5	0	1.102	-.228	0	0	0	0	.033

FIGURE 6.5: ADAPTIVE LEARNING NETWORK TO ESTIMATE THE AZIMUTHAL ANGLE "$\hat{\beta}$" FOR ELLIPTICAL CRACK DEFECTS

ALN STRUCTURE

ERROR ON THEORETICAL DATA = 21%

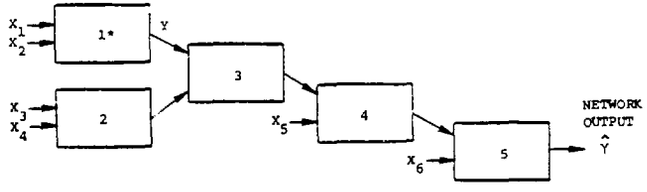

*ELEMENTAL FORM: $Y = w_0 + w_1x_1 + w_2x_2 + w_3x_1^2 + w_4x_1^2 + w_5x_2^2 + w_6x_1^3 + w_7x_2^3$

FEATURE DESCRIPTION	Mean ($\bar{X}_i$)	Sigma (σ_i)
X1: ATAN2 of the Total Power	39.5	9.69
X2: ATAN2 of the Ripple Frequency	10.6	4.83
X3: ATAN1 of the Total Power	-7.70	102.
X4: X-Component of the Moment Vector ($\bar{X}$) of the Ripple Frequency	-.017	.374
X5: ATAN4 of the Total Power	93.2	38.0
X6: ATAN1 of the Ripple Frequency	5.60	103.

NETWORK WEIGHTING COEFFICIENTS

ELEMENT	w_0	w_1	w_2	w_3	w_4	w_5	w_6	w_7
1	.128	- .160	0	0	-.050	.099	.024	.056
2	-.267	.170	- .135	.561	.300	0	0	-.300
3	-.001	1.162	1.045	2.945	0	0	0	0
4	-.117	1.451	.191	0	0	.170	-.520	-.081
5	.071	.939	- .028	.409	0	-.115	0	0

FIGURE 6.6: ADAPTIVE LEARNING NETWORK TO ESTIMATE THE ROTATION ANGLE "$\hat{Y}$" FOR ELLIPTICAL CRACK DEFECTS

ALN STRUCTURE

ERROR ON THEORETICAL DATA = 6%

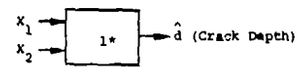

*$\hat{d} = .702X_1 - 1.588X_2$

FEATURE DESCRIPTION

		Mean ($\bar{X}_i$)	Sigma (σ_i)
X1:	Slope of Power Decay Across Array in Band from 0.5 to.1.5 MHz	-.155	.015
X2:	Ripple Frequancy	.580	.237

FIGURE 6.7: ADAPTIVE LEARNING NETWORK TO ESTIMATE THE DEPTH ($\hat{d}$) OF FREE-SURFACE CRACKS

ALN STRUCTURE

ERROR ON THEORETICAL DATA = 9%

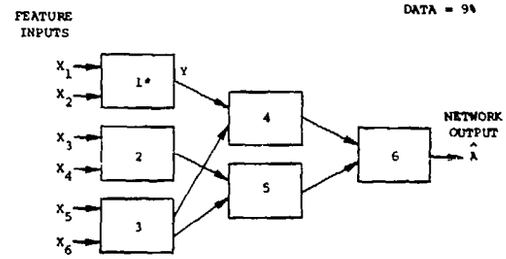

*ELEMENTAL FORM: $Y = w_0 + w_1X_1 + w_2X_2 + w_3X_1X_2 + w_4X_1^2 + w_5X_2^2$

FEATURE DESCRIPTION

X_1: Z-Component of the Moment Vector ($\bar{Z}$) of the First Moment of Power Spectrum

X_2: Z-Component of the Moment Vector ($\bar{Z}$) of Band 1 of Power Spectrum

X_3: X-Component of the Moment Vector ($\bar{X}$) of the First Moment of Characteristic Function

X_4: Z-Component of the Moment Vector ($\bar{Z}$) of the Second Moment of Characteristic Function

X_5: Z-Component of the Moment Vector ($\bar{Z}$) of the Total Power

X_6: ATAN3 of the Total Power

NETWORK WEIGHTING COEFFICIENTS

ELEMENT	w_0	w_1	w_2	w_3	w_4	w_5
1	.233E+05	-.104E+05	-.978E+05	.226E+05	.116E+04	.803E+05
2	.973E+02	-.388E+02	-.701E+01	-.548E+01	.557E+04	.123E+02
3	.678E+02	.641E+02	-.780D+00	-.124E+01	.122E+02	.118E+01
4	.213E+02	.142E+00	.265E+00	-.304E-03	.170E-02	.904E-03
5	-.149E+03	.170E+01	.596E+00	-.550E-03	.195E-02	.747E-03
6	.416E+01	.608E+00	.307E+00	.291E-03	0	0

FIGURE 6.8: ADAPTIVE LEARNING NETWORK TO ESTIMATE SIZE PARAMETER "$\hat{A}$" FOR SPHEROIDAL DEFECTS

ALN STRUCTURE

ERROR ON THEORETICAL DATA = 8%

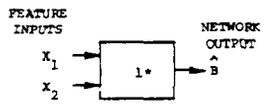

*ELEMENTAL FORM: $\hat{B} = w_0 + w_1x_1 + w_2x_2 + w_3x_1x_2 + w_4x_1^2 + w_5x_2^2$

FEATURE DESCRIPTION

X_1: Z-Component of the Moment Vector ($\bar{Z}$) of the First Moment of Power Spectrum

X_2: Z-Component of the Moment Vector ($\bar{Z}$) of Band 1 of Power Spectrum

NETWORK WEIGHTING COEFFICIENTS

ELEMENT	w_0	w_1	w_2	w_3	w_4	w_5
1	-.162E+04	.793E+03	.400E+04	-.367E+03	-.804E+02	-.346E-04

FIGURE 6.9: ADAPTIVE LEARNING NETWORK TO ESTIMATE SIZE PARAMETER "$\hat{B}$" FOR SPHEROIDAL DEFECTS

ALN STRUCTURE

ERROR ON THEORETICAL DATA = 5%

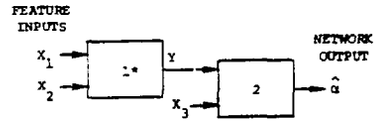

*ELEMENTAL FORM: $Y = w_0 + w_1x_1 + w_2x_2 + w_3x_1x_2 + w_4x_1^2 + w_5x_2^2$

FEATURE DESCRIPTION

X_1: ATAN3 of the Total Power

X_2: ATAN4 of the Total Power

X_3: ATAN2 of the Total Power

NETWORK WEIGHTING COEFFICIENTS

ELEMENT	w_1	w_2	w_3	w_4	w_5	w_6
1	.137E+03	-.151E+01	-.910E+00	.224E-01	-.169E-03	-.507E-02
2	.609E+01	.115E+01	-.445E+00	-.264E-02	-.174E-02	.680E-02

FIGURE 6.10: ADAPTIVE LEARNING NETWORK TO ESTIMATE ORIENTATION PARAMETER "$\hat{\alpha}$" FOR SPHEROIDAL DEFECTS

ALN STRUCTURE

ERROR ON THEORETICAL DATA = 1%

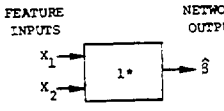

*ELEMENTAL FORM: $\hat{\beta} = w_0 + w_1x_1 + w_2x_2 + w_3x_1x_2 + w_4x_1^2 + w_5x_2^2$

FEATURE DESCRIPTION

X_1: ATAN4 of the First Moment of Characteristic Function

X_2: ATAN1 of the Total Power

NETWORK WEIGHTING COEFFICIENTS

ELEMENT	w_0	w_1	w_2	w_3	w_4	w_5
1	-.576E+00	.402E+0[illegible]	.101E+01	-.124E-03	-.821E-01	-.291E-04

FIGURE 6.11: ADAPTIVE LEARNING NETWORK TO ESTIMATE ORIENTATION PARAMETER "$\hat{\beta}$" FOR SPHEROIDAL DEFECTS

ALN STRUCTURE

ERROR ON THEORETICAL DATA = 0%

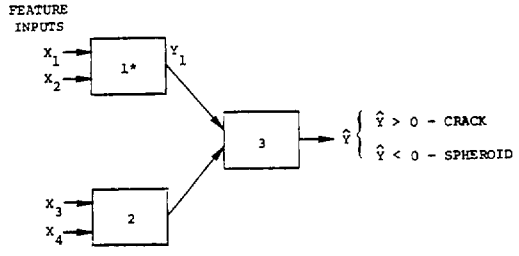

*ELEMENTAL FORM: $Y_1 = w_0 = w_1x_1 + w_2x_2 + w_3x_1x_2 + w_4x_1^2 + w_5x_2^2$

FEATURE DESCRIPTION

X_1: Z-Component of the Moment Vector ($\bar{Z}$) of the Power Spectral First Moment

X_2: Z-Component of the Moment Vector ($\bar{Z}$) of the Low to High Power Ratio

X_3: Y-Component of the Moment Vector ($\bar{Y}$) of the Power Spectral Standard Deviation

X_4: Z-Component of the Moment Vector ($\bar{Z}$) of the Power Spectral Standard Deviation

NETWORK WEIGHTING COEFFICIENTS

ELEMENT	w_0	w_1	w_2	w_3	w_4	w_5
1	-.592E+02	.305E+02	.112E+03	-.309E+02	-.3[illegible]2E+01	-.431E+02
2	.353E+01	.322E+02	-.324E+03	-.238E+05	.238E+05	.513E+04
3	-.303E+00	.613E+00	.463E+00	-.890E-01	.216E+00	.173E+00

FIGURE 6.12: ADAPTIVE LEARNING NETWORK TO DISCRIMINATE TWO-DIMENSIONAL (CRACK-LIKE) DEFECTS FROM THREE-DIMENSIONAL (VOID-LIKE) DEFECTS

shown below can, in some cases, represent many thousands of terms with only a small number of coefficients.

The networks shown in Figures 6.2 - 6.7 are the elliptical and free-surface crack models and have normalized coefficients. All of the input and output variables were scaled by removing the mean ($\bar{x}_i$) and dividing by the standard deviation (σ_i). These scaling values are shown next to each input variable. In order to implement the networks on new data observations, the computed feature values must be scaled by x_i and σ_i in the following manner:

$$x_i' = \frac{x_i - \bar{x}_i}{\sigma_i}$$

where

x_i = the i^{th} spectral feature

$\bar{x}_i$ = mean feature value

σ_i = standard deviation of feature

x_i' = input to network

Figures 6.2 and 6.3 show the ALN models which estimate the semiminor (A) and semimajor (B) axis of the elliptical crack defect. Note that, in each case, four of the five features selected were "ripple frequency" features. The ripple frequency is the single most important feature for determining the defect size. It was, therefore, quite natural for these features to be selected.

Figures 6.4 - 6.6 show the ALN models for estimating the three elliptical crack orientation angles α, β, and γ, respectively. Most of the features selected for these models were total power features. It has been observed that the defect orientation is highly related to the total power spatial distribution. The flat surface of an elliptical crack acts similar to a mirror, reflecting energy in the direction opposite to that of the direction of incidence. The position of this highly directed "specular" reflection yields much information about the angles α and β. The moment vector ($\bar{x}$, $\bar{y}$, $\bar{z}$) attempts to locate the position of maximum energy, hence, locates the specular reflection.

Figure 6.7 illustrates the ALN model to determine the depth of free-surface cracks. The equation is a linear combination of only two features. The ripple frequency feature measures the time delay between the tip diffracted wave and the corner reflection.

Figures 6.8 - 6.11 illustrate the four oblate spheroid models to estimate the defect's size (A and B) and orientation (α and β). The void models were trained on theoretical data of the low ka regime. This means that the defect is small compared to the wavelength of the incident beam. When ka is small (<5), information pertaining to the size of the defect can be found in the low frequency portion of the spectrum. The networks shown in Figures 6.8 and 6.9 support this fact. Most of the features selected measure shifts in the spectral energy, or percent of low frequency energy. The void models to estimate α and β (Figures 6.10 and 6.11) indicate, as for elliptical cracks, that spatial total power distribution is key in estimating the defect's orientation.

Figure 6.12 shows the Adaptive Learning Network to discriminate crack defects from voids. Four spectral features selected as shown. If the network output is positive, the indicated class is of the crack type. A negative model output is indicative of a void.

REFERENCES

1. Mucciardi, A.N., R. Shankar, M.F. Whalen, "Application of Adaptive Learning Networks to NDE Methods", Interdisciplinary Program for Quantitative Flaw Definition, Special Report, Third Year Effort, June 1977, p. 176.

2. Whalen, M.F., A.N. Mucciardi, "Inversion of Physically Recorded Ultrasonic Waveforms Using Adaptive Learning Network Trained On Theoretical Data", Interdisciplinary Program for Quantitative Flaw Definition, Special Report, Fourth Year Effort, June 30, 1978, pp. 55-80.

3. Whalen, M.F., L.J. O'Brien, A.N. Mucciardi, "Application of Adaptive Learning Networks for the Characterization of Two-Dimensional and Three-Dimensional Defects in Solids", Interdisciplinary Program for Quantitative Flaw Definition, Special Report, Fifth Year Effort, submitted Oct. 1979.

4. Adler, L., "Measurement of Scattering from Interior and Surface Cracks", Interdisciplinary Program for Quantitative Flaw Definition, Interim Report, Mar. 31, 1980, pp. 123-137.

5. Adler L., J.D. Achenbach, "Elastic Wave Diffraction by Elliptical Cracks", submitted for publication in Journal of Nondestructive Evaluation.

6. Achenbach, J.D., A.K. Gautesen, D.A. Mendelsohn, "Ray Analysis of Surface-Wave Interaction with an Edge Crack", IEEE Transactions Sonics and Ultrasonics, Vol. SU-27, No. 3.

7. Mendelsohn, D.A., A.D. Achenbach, L.M. Keer, "Scattering of Elastic Waves by a Surface-Breaking Crack", WAVE MOTION, 2, in press.

8. Achenbach, J.D., "Direct and Inverse Methods for Scattering by Cracks at High Frequencies", Interdisciplinary Program for Quantitative Flaw Definition, Interim Report, 1980.

9. Personal communication between J. Martin and M. F. Whalen.

Paul Gammel (J.P.L.): I would like to know if your system depends on deconvolution to move the transducer signature.

Tony Mucciardi (Adaptronics): No. You can either convolve the theoretical resonse with the transducer response, or deconvolve the experimental response from the transducer response to make the experiment resemble the theory. It's more general in the latter case.

Paul Gammell: What was done in your case?

Tony Muccardi: All the results have been presented with the transducer response deconvolved from the experimental data. This approach is quite pleasing because of independence from the transducer. Of course, it's quite possible to go the other way, too.

James Krumhansl, Chairman (NSF): Thank you, we will now proceed to the final paper.

SENSITIVITY OF FAILURE PREDICTION TO FLAW GEOMETRY

J. M. Richardson, R. Chang, and K. W. Fertig, Jr.
Rockwell International Science Center
Thousand Oaks, California 91360

and

V. V. Varadan
Ohio State University
Columbus, Ohio 43210

ABSTRACT

The assumption of ellipsoidal flaw geometry has been widely used in calculations of the probability of structural failure conditioned on nondestructive (ND) measurements. Clearly, in most cases the flaw geometry is not ellipsoidal and in the particular case of cracks the actual geometry may deviate significantly from a degenerate ellipsoid (i.e., a planar crack with an elliptical plan-view shape). We have investigated the sensitivity of a late stage of the evolution of fatigue failure to model errors of the latter type (i.e., deviations from elliptical shape for planar cracks) by considering two different overall theoretical processes. In the first, we start with a non-elliptical crack and calculate its geometry after a given large number of cycles of uniaxial stress applied perpendicular to the crack plane. In the second process, we start with the same crack but perform a simulated set of ND measurements coupled with an inversion procedure based on the assumption of elliptical geometry and then calculate the geometry of this initially elliptical crack after subjection to the above stress history. A measure of sensitivity to model error is then provided by a comparison of the two terminal geometries. Results for several choices of non-elliptical crack shapes and sets of ND measurements will be discussed.

NATURE OF THE PROBLEM

As is well known, the calculation of the probabilities of failure, both unconditional and conditioned on ND measurements, is based on a set of mathematical models, most of which are seriously oversimplified in several respects. The set consists of models of (a) the measurement process, (b) the failure process (including a model of the stress environment), and (c) the a priori statistics of defect properties. It is clear that the modelling of each type of defect underlies all three of the above models and thus the errors in this modelling are a crucial issue.

It is thus obvious that the errors in the defect model affect the interpretation of the ND measurements (in terms of an oversimplified state) and the calculation of conditional probability of failure. The former and latter entail the use of measurement and failure models, respectively, and both entail the use of the a priori statistics model. In any case, we may ask if the effects of the defect model errors in the measurement interpretation and the failure probability calculation tend to compound or compensate for each other. To throw light on this question we have investigated several "theoretical experiments" involving synthetic test data based on defect models that are more complex than the defect model used in the interpretation of ND measurements and the calculation of failure probability.

APPROACH

Here we give more explicit details of the investigation of the "theoretical experiments" alluded to in the last section. A typical "theoretical experiment" is represented schematically in Fig. 1. Here we show the simulation of both the ideal calculation involving no defect model error and a non-ideal calculation involving a certain type of defect model error. We have explicitly considered the example of a planar

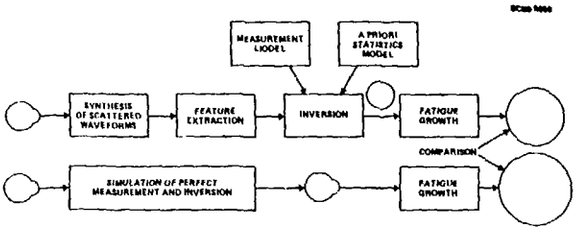

Fig. 1 Schematic representation of "theoretical experiment."

crack in a metal with a non-elliptical plan view which is incorrectly modelled in the non-ideal calculation as having an elliptical plan view with adjustable parameters. The failure process in each calculation is assumed to be a deterministic process under an assumed cyclic stress based on generally accepted concepts of fatigue crack propagation.[1] In the non-ideal calculation, a set of scattered waveforms are calculated by applying scattering theory to the assumed non-elliptical crack. The extraction of features (e.g., the low-frequency scattering amplitude and the distance from the geometrical center to the front-face tangent plane perpendicular to the incident wave direction) for each scattering measurement is straightforward - in fact, the calculations could

be simplified greatly by deducing the features directly from the assumed non-elliptical crack. The inversion process is limited to elliptical cracks and thus it attempts to find the best elliptical crack in terms of fitting the non-elliptical input features. The last stage of the non-ideal calculation is the prediction of fatigue crack growth starting with the best elliptical crack.

The nature of the ideal calculation is readily apparent. In this case, it is assumed that the first three modules of the non-ideal calcualtion are replaced by ideal ones whose final output is exactly the same as the assumed non-elliptical crack. Thus, the prediction of fatigue crack growth starts with the assumed non-elliptical crack.

The initial elliptical and non-elliptical cracks will both grow, after a large number of stress cycles, into much larger planar cracks with nearly circular plan views, each having a characteristic average radius. The comparison of the angular average radii yielded by the ideal and non-ideal calculations will be used as the measure of the sensitivity to model error. An alternative, and perhaps simpler, comparison procedure involves the consideration of equivalent circular cracks. As shown in Fig. 2, a circular crack is equivalent to a planar crack of arbitrary shape if they both evolve asymptotically (under a given cyclic applied stress) into the same large circular crack.

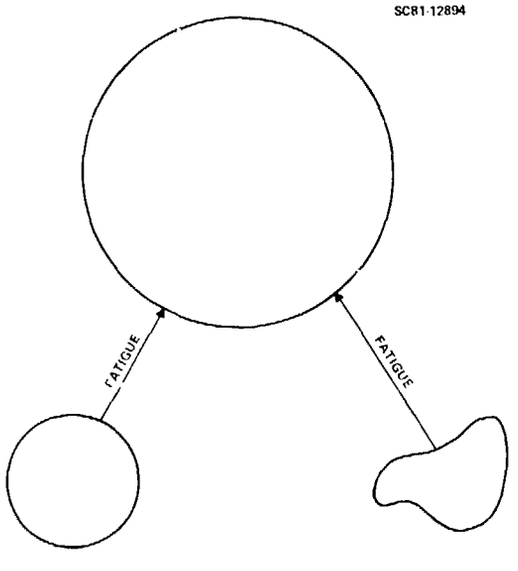

Fig. 2 Equivalent circular crack.

COMPUTATIONAL RESULTS

In this section we present computational results for an extreme form of model error, i.e., we consider the model crack to be circular while the actual (in the sense of the theoretical experiment discussed above) crack consists of two separate co-planar circular cracks. The particular cases considered are depicted in Fig. 3,

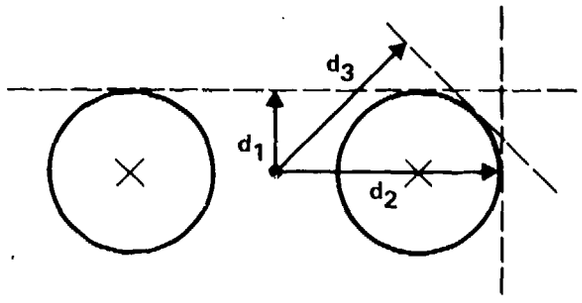

Fig. 3 "Theoretical experiment" using the feature d.

namely (a) two identical circular cracks, both of radius a, with a distance b between centers and (b) two nonidentical cracks, one having radius a and the other having radius a/2, again with a distance b between centers. Less extreme cases are currently under consideration and the results ensuing from these investigations will be presented in a future communication.

We consider mainly two kinds of features, namely A_2 and d for a set of in-plane pulse echo scattering measurements. The quantity $A_2\omega^2$ is the scattering amplitude in the Rayleigh (i.e., long wavelength) regime where ω is the angular frequency. The quantity d is the distance from the geometrical center (assuming that this is defined) to the front-face tangent plane (or tangent line in the crack plane). An alternative geometrical property will also be considered. In our computations the different types of features will be considered individually. A study was made with A_2 and d as simultaneous inputs to a probabilistic inversion[1] algorithm, with varying weights reflecting the assumed standard deviations of the experimental errors ascribed to the two features. The results contained no interesting surprises and will not be reported here.

The first series of theoretical experiments involved the single feature A_2 and a circular crack model. In all cases it was assumed in each case that the equation between the actual cracks was sufficiently large that the quasi-static elastic interactions between the cracks could be neglected in the computation of A_2. With this approximation A_2 consists of the independent contributions of the two circular cracks and hence is independent* of the direction of the incident wave. Efforts to compute the effect of interaction on A_2 ran into computational difficulties and consequently results are not yet available. The fatigue growth of the model and actual cracks was represented in terms of the concept of equivalent circular crack as explained in the last section. In the case of the actual crack the fatigue process was treated both with and without interaction between the separate circular cracks.

*It is to be emphasized that the wavelength is assumed to be large compared with the total complex scatterers composed of both circular cracks.

In Table 1 we present results for the case in which the actual crack consists of two circular cracks with equal radii $a_1 = a_2 = a = 1$ and with various values of the center-to-center distance b. The estimate $\hat{r}$ of the radius of the model circular crack was obtained by observing that A_2 for a circular crack is proportional to the cube of its radius and $\hat{r}$ is the cube root of the sum of the cubes of the radii of the separate circular cracks. The quantity r_{eq} is the radius of the equivalent circular crack. As stated before, it is computed with and without interaction. In Table 2 the radii a_1 and a_2 are different, namely $a_1 = 1$ and $a_2 = 0.5$. The results are of course similar to those with equal radii. Considering the extreme nature of the model error, it is surprising that $\hat{r}$ and r_{eq} are in such close agreement. This means that failure prediction based upon A_2 alone is quite insensitive to model error (at least in the case of fatigue crack growth in metals).

Table 1. Equal Circles (a = 1)

Input Feature: A_2
Model: Circular Crack

b	$\hat{r}$	r_{eq}	
	No Int.	Interact	No Int.
2.5	1.26	1.37	1.31
3	"	1.35	1.27
4.5	"	1.27	1.18
6	"	1.23	1.17

Table 2. Unequal Circles ($a_1 = 1$, $a_2 = 0.5$)

Input Feature: A_2
Model: Circular Crack

b	$\hat{r}$	r_{eq}	
	No Int.	Interact	No Int.
2	1.04	1.11	1.09
3	"	1.09	1.07
4	"	1.07	1.05
5	"	1.07	1.04

A second series of theoretical experiments was conducted with the d's (the distances from the center to the front face tangent planes) as the sole features. There we have considered only the case in which the radii a_1 and a_2 are equal with the common value denoted by a which is set equal to 1. In Table 3, we present results in which it is assumed that the incident directions of pulse-echo elastic waves are chosen to be given by multiples of 45° with representative configurations shown in Fig. 3. The best estimate $\hat{r}$ of the radius of the circular model crack is the average of all of the d's and these estimates are listed in the second column. The values of r_{eq} is the same as those given in Table 1. It will be noted that the agreement between $\hat{r}$ and either of the values of r_{eq} is poor, especially for the larger values of b. This means that failure prediction based upon the d's along is relatively sensitive to model error. In Table 4, we show that a different geometrical feature, the total area of the crack, yields much greater insensitivity to model error.

Table 3. Equal Circles (a = 1)

Input Feature: d's
Model: Circular Crack

b	$\hat{r}$	r_{eq}	
		Interact	No Int.
2.5	1.76	1.37	1.31
3	1.91	1.35	1.27
4.5	2.26	1.27	1.18
6	2.81	1.23	1.17

Table 4. Equal Circles (a = 1)

Input Feature: Total Crack Area
Model: Circular Crack

b	$\hat{r}$	r_{eq}	
		Interact	No Int.
2.5	1.41	1.37	1.31
3	"	1.35	1.27
4.5	"	1.27	1.18
6	"	1.23	1.17

ACKNOWLEDGEMENT

This research was sponsored by the Center for Advanced NDE operated by the Rockwell International Science Center for the Defense Advanced Research Projects Agency and the Air Force Wright Aeronautical Leboratories under Contract No. Fee615-80-C-5004

REFERENCE

1. R. Chang, "On Crack-Crack Interaction and Coalescence in Fatigue," submitted to Engineering Fracture Mechanics.

AN ULTRASONIC TECHNIQUE FOR SIZING SURFACE CRACKS

C. P. Burger[+] A. Singh[++]
[+]Ames Laboratory*, Engineering Research Institute and
Department of Engineering Science and Mechanics,
Iowa State University, Ames, IA 50011
[++]Southwest Research Institute, San Antonio, TX 78230

ABSTRACT

Rayleigh surface waves are proposed as a non-destructive method to find the depth of surface cracks.

The paper describes how dynamic photoelasticity was used to develop an understanding of the subsurface interactions between R-waves and a narrow slot. A frequency analysis of the transmitted wave confirmed that the slot acts as a low pass filter for the high frequency Fourier components of the input wave. It is then shown that the high frequency cut-off in the spectrum of the transmitted wave from broadband ultrasonic surface pulse can be used to determine the depth of surface slots.

INTRODUCTION

During recent years investigators started to recognize the potential value of Rayleigh waves for characterizing surface and near surface defects (1). This wave has its energy confined to a depth of approximately two times its wavelength (2) which makes it eminently suitable for interrogating near surface defects. Reinhardt and Dally (3) used photoelastic visualization to study the interaction of Rayleigh waves with surface flaws. They found the variation of transmission and reflection coefficients for slots with depths up to half of the Rayleigh wavelength. Bond (4) used finite difference modeling to obtain quantitative information on the interaction of Rayleigh waves with boundary and flaw configurations that were analytically intractable. Silk (5) and Hall (6) used timing methods on the Rayleigh w to find the depths of slots and cracks with well defined tips.

Ultrasonic frequency analysis has been used mainly to characterize internal flaws. Adler (7) used this method to determine the shape of buried flaws. Morgan (8) analyzed the reflected signal from a slot milled in aluminum and found certain modulations in the frequency spectrum. These are caused by resonances of the crack faces and as such should contain the necessary information to characterize cracks. Ayter and Auld (9) used analytical methods to relate these resonant frequencies to crack size.

This paper describes an experimental study using the spectral analysis of signals to determine the depth of surface cracks. The technique has much potential for research because there are several different modes of converted and scattered signals that should be investigated to find how they correlate to crack depth. Some theoretical analyses of Rayleigh wave scattering by surface defects has been done by Tittmann(10) and Auld (11), but experimental and numerical studies are needed to fully develop this method to the point where it can provide quantitative information about surface and subsurface defects.

*Operated for the U.S. Department of Energy by Iowa State University under contract No. W-7405-Eng82.

DYNAMIC PHOTOELASTICITY

Dynamic photoelastic visualization (12) of the interaction between Rayleigh waves and slots (13) were obtained on models made from 6.3 mm (1/4 inch) thick sheet of a polyester type material "Homalite-100." R-waves were generated by exploding small lead azide charges on the top edges of the plates. For each slot (width 1 mm) a sequence of 16 dynamic photographs were obtained. These showed the incident Rayleigh wave, its interactions with the slot, and the transmitted and reflected waves after the interaction. Figure 1 shows the photoelastic fringe pattern after the interaction. The following notation was devised to indicate the various waves. A capital letter indicates the type of wave, P for longitudinal wave, S for shear wave, PS for Von-Schmidt wave, and R for Rayleigh wave. A subscript indicates the original wave from which a particular mode converted wave (capital letter) was generated. A superscript identifies the point of origin on the model of reflected or mode converted waves. Another superscript differentiates between a reflected (r) or transmitted (t) component.

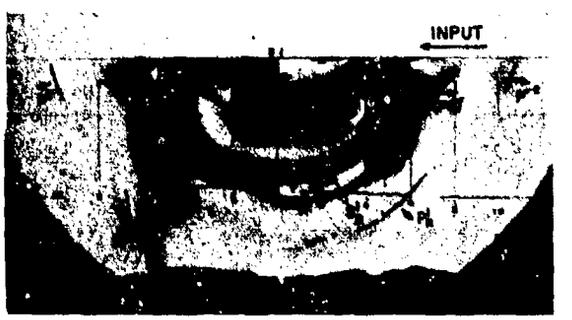

Fig. 1 Photoelastic visualization of R-wave after interaction with a slot.

In this manner the notation S_R^1 indicates a shear wave formed by mode conversion of the original R-wave at the first upper corner of the slot, point 1 on Fig. 1. R^{2r} will be the Rayleigh wave reflected from the original R-wave at the slot tip (point 2). S is an input shear wave which is strong in the interior and reduces to zero at the surface.

The photoelastic results show clearly that the pattern of mode conversions and the intensity of the various waves depend strongly on the depth of the slot.

There are two mode converted longitudinal waves P^2 and P^{1-2}. It is not clear from which wave the two fronts P^2 and P^{1-2} are generated. The source for the former is point 2, and for the latter point 2 and/or the face 1-2. The interaction between the slot and the Rayleigh wave is the most interesting. It is known that the depth of the Rayleigh wave is a function of the wavelength. As the R-wave approaches the slot, it strikes it from the slot opening to the slot tip. The particle motion at the slot opening will contain all the Fourier components, i.e., all the wavelengths of the input wave. The particle motion at the tip will be mainly due to the long wavelength parts of the R-wave.

The interaction of the upper portion of the wave with the slot opening (point 1) generates a reflected R^{1r}-wave. A shear wave, S_R^1, is produced by mode conversion from the R-wave and a transmitted Rayleigh wave turns around the corner and continues down the front face of the slot to the tip. Here a portion of the R-wave mode converts to a shear wave S_R^2, another portion is reflected back up the front face as R^{2r} and the remainder proceeds around the tip and up the face of the slot.

The deeper particle motion of the R-wave will interact with the slot differently. The energy distribution in the Rayleigh wave as it interacts with the slot is sketched approximately in Fig. 2. The figure shows that the deeper particle motion (corresponding to the long wavelengths) goes under the slot and forms another Rayleigh wave, called here an "undercut" R-wave. The deeper particle motion will also form a shear wave at the slot tip which will scatter from the tip. The transmitted signal called R^t is a composite of all the R- and S-waves diffracted from the crack tip. The shear wave is present in the transmitted response at the surface because unlike the input S-wave it does not graze the surface but strikes at an angle.

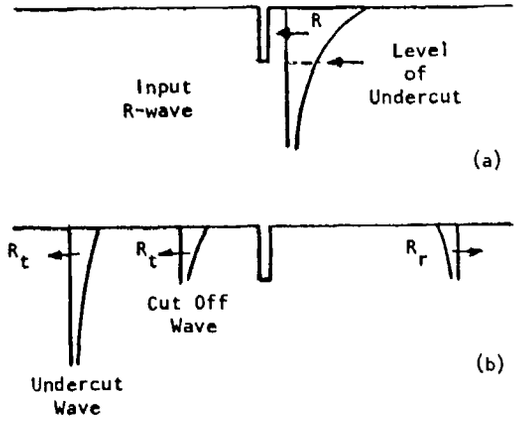

Fig. 2 Formation of the undercut wave.
a) R-wave just before interaction with the slot.
b) Identifiable R-waves after interaction with the slot. Other mode converted waves are not shown.

The fringe order of the transmitted wave at the surface gives the stresses at the surface. Plotting these gives the shape of the wave. When the frequency of the transmitted wave was analyzed, it was clear that the frequency spectrum depends on the depth of the slot. Figure 3 shows the magnitude of the spatial frequency distribution for the transmitted waves from each of the four slots. There are significant differences in the frequency spectrums. As the slot depth is increased from 2.8 to 12.9 mm, the high frequency content drops, while the low frequency content remains strong.

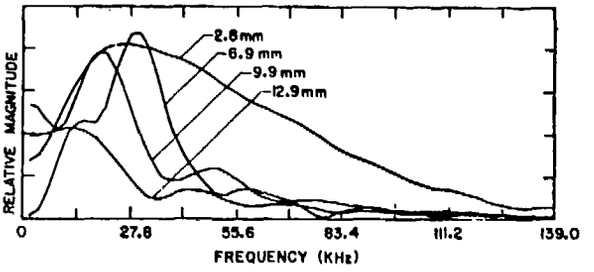

Fig. 3 Frequency magnitude curves for four different slots from transmitted waves in dynamic photoelasticity.

The photoelasticity results suggested that a slot will act as a low pass filter by cutting off the short wavelength (shallow) components while allowing the long wavelength (deep) components of a Rayleigh wave to pass underneath the tip. The frequency spectrum of the deeper portion of the R-wave contain the low frequency (long wavelength) components of the incident wave. It is, therefore, reasonable to suggest that the wavelength at which the frequency of the transmitted wave is "cut off" will be the frequency at which the wavelength relates to the depth of the slot. If this is true, the frequency spectrum of the transmitted wave will give quantitative information on the depth of surface slots.

An ultrasonic test was devised to test this hypothesis. The transducers used were 1-5.5 MHz, broadband, R-wave wedge transducers designed for use on steel. The important specification for them is that the incident wave should have wavelengths that will excite particle motions up to a distance from the surface which is deeper than the slot.

The models were steel blocks, with 0.43 mm wide, machined slots, which were 1, 2, 3, 4, 5, 8, 11, and 14 mm deep. These depths were selected from the consideration that the elliptical particle motion of a R-wave penetrates to a depth of 2λ. Thus, a wavelength in steel of 3 mm corresponds to a frequency of 1 MHz. It will excite particle motion as deep as 6 mm. It was anticipated that the maximum depth to which this analysis would work would be 5 mm. Beyond 6 mm depth there should not be any undercutting.

The test specimens were low carbon steel blocks, 50 x 50 x 180 mm. The slots were machined right across the top faces of the blocks, and the transducers were placed 50 mm on either side of the slots.

The signals received by the transducers for an uncut block and for slot depths of 2, 3, and 5 mm are shown in Fig. 4. The horizontal axes represent time. The sweep rate was 500 nanoseconds per division and the relative sensitivities for the vertical scales are all the same except for the first picture. On the same scale as the others this signal would have been five times larger than shown. Reading from left to right identifies the signals arriving at the "receiver" in sequence. The caption "R" indicates a Rayleigh wave. The first picture represents the "input" signal. This is a pure R-wave.

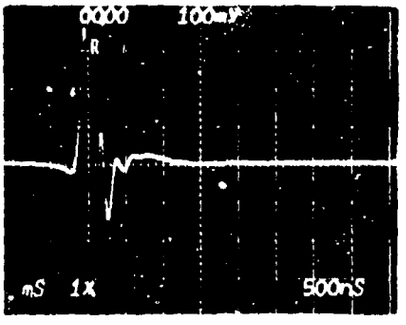

a) Input wave.

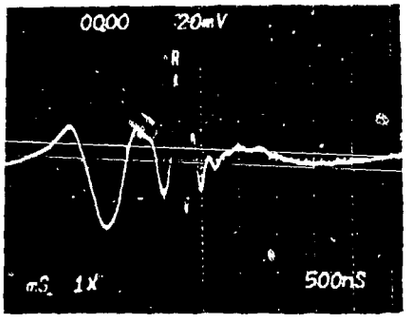

b) 2 mm slot.

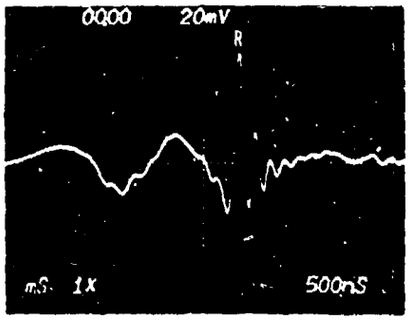

c) 3 mm slot.

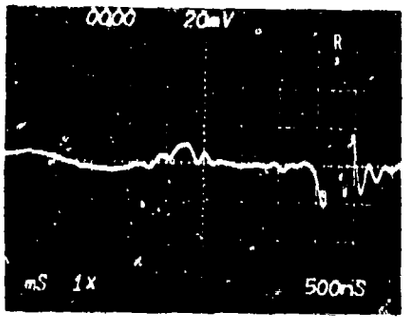

d) 5 mm slot.

Fig. 4 Oscilloscope traces or amplitude vs time 'records' for transmitted waves for different slot depths.

Two characteristics stand out:

1. A sharp signal, captioned R, is observed in all the pictures. The shape of this signal does not change significantly with slot depth. Only its amplitude changes slightly. This signal lags behind all other signals and the lag increases with slot depth. It is the Rayleigh wave which went all around the slot, and is called the "cut off" R-wave.

2. The form of the front signal which leads the cut off R-wave is the same for all the cracks. It has two peaks and a valley. As the slot depth increases from 1 to 5 mm, the signal decreases in amplitude and broadens out. This signal leads the cut off R-wave and could be composed of several interferring waves. These may include: (i) the shear wave that was diffracted by the tip of the slot from the incident shear wave and the deep portion of the R-wave; (ii) the undercut R-wave; (iii) other mode converted waves. Since this signal is a mixture of several waves, it is not perfectly smooth. The various waves present in this signal cannot be identified as they arrive at approximately the same time.

When the slot depth is more than 5 mm, the front signal becomes weak and disappears completely at 11 mm. This is because the depth of the slot becomes greater than the depth of input R-wave. Also the diffracted shear wave from the incident shear wave decreases due to increase in the angle of diffraction.

It is also seen that the cut off R-wave amplitude does not change significantly when the slots are deep. The signal is smaller for the 1 mm slot, and increases 2, 3, and 4 mm. This is because as the slot depth increases from 1 mm onward, a smaller portion of the energy is in the undercut wave. For slots deeper than 5 mm the amplitude of the R-wave changes little with depth. There is no undercutting. The amplitude falls slightly due to more efficient reflection or due to attenuation because the path length from transmitter to receiver is larger with deeper slots.

FREQUENCY ANALYSIS

The schematic of the computer hardware used for the analysis is shown in Fig. 5. The sample is taken from the ultrasonic pulser receiver through a Tektronix sampling oscilloscope. The sampling scope is interfaced to a LSI-11 minicomputer. The software in the system is capable of sampling the signal, finding the FFT, displaying it, and plotting it through a X-Y plotter.

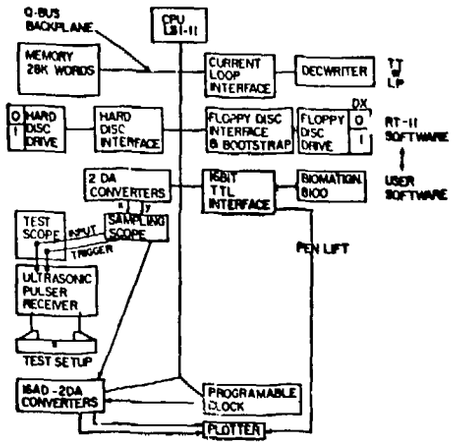

Fig. 5 Schematic of computer hardware.

The transmitted signals were sampled for all the machined slots. Care was taken to include all the transmitted signals in the sample, from the diffracted shear wave to the last signal, which is the cut off R-wave.

The frequency magnitude of all the transmitted signals is plotted in Fig. 6. These resemble very closely those in Fig. 3. The attenuation of frequencies starts from the high frequency end. Careful analysis of the figure reveals that all the curves approach the same plateau at higher frequencies. The plateau is, in fact, the curve corresponding to a slot of 5 mm. After the curves have dropped to the level of the plateau, they follow approximately the 5 mm curve. The curves for 8, 11, and 14 mm deep notches are similar to the one for 5 mm. They are not drawn. The plateau curve corresponds to the frequency spectrum of the cut off R-wave which is the only major signal for slots of 5 mm and longer. Thus, if the cut off R-wave is removed from all the transmitted signals, the plateau will be removed. The last signal, i.e., the cut off R-wave was digitally zeroed and the frequency magnitudes plotted in Fig. 7. The curves obtained were smooth and showed very clearly that the attenuation of frequency components started from the high frequency end and proceeded to lower frequencies as the slot depth increased. These curves correspond to the frequency magnitude of the undercut R-wave, the diffracted S-wave from the incident S- and R-waves, and mode converted waves. The mode converted signals are very small and clearly do not have a significant effect, except in cases where the undercut R-wave and the diffracted S-wave are weak.

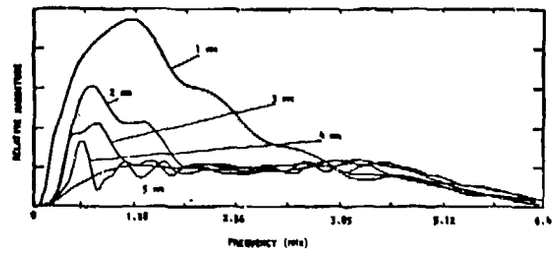

Fig. 6 Frequency magnitude of the transmitted ultrasonic waves.

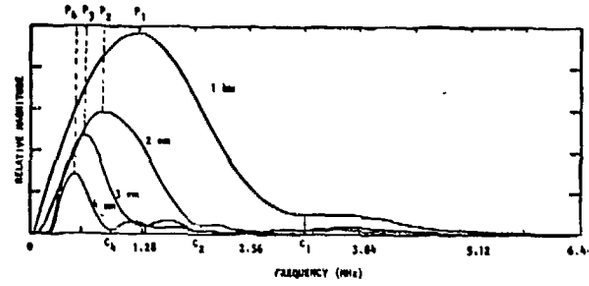

Fig. 7 Frequency magnitude of the undercut R-waves and diffracted shear waves from ultrasonic tests.

Figure 7 confirms what previous figures suggested, namely that the frequency attenuation starts from the higher side and moves to the lower side. To correlate this aspect quantitatively, it is necessary to relate a particular point on the curve to the slot depth. One of the points chosen was where the frequency magnitude first goes to a minimum. It is called the "cut off" point because the frequency components which are higher than the frequency corresponding to this point were "cut off" by the slot. These points on the curves are indicated as C_1, C_2, C_3, and C_4 corresponding to 1 mm, 2 mm, 3 mm, and 4 mm slots. The peak of the curves also relate to the slot depth. These points are called P_1, P_2, P_3, and P_4 as shown in Fig. 7. The "cut off" points and the wavelengths corresponding to the peak and cut off points are tabulated in Table 1 and plotted in Figs. 8 and 9.

Table 1

Slot (mm)	Cut off frequency (MHz)	Cut off wavelength (mm)	Peak frequency (MHz)	Peak wavelength (mm)
1	3.29	0.9	1.25	2.4
2	2.00	1.5	0.85	3.5
3	1.35	2.2	0.64	4.7
4	0.93	3.2	0.52	5.8

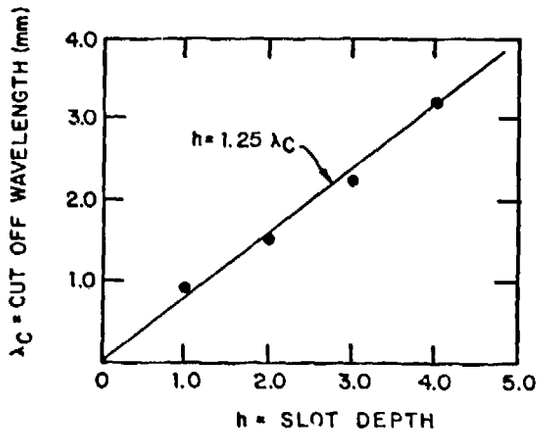

Fig. 8 Relationship between "cut-off" wavelength and depth of surface slots.

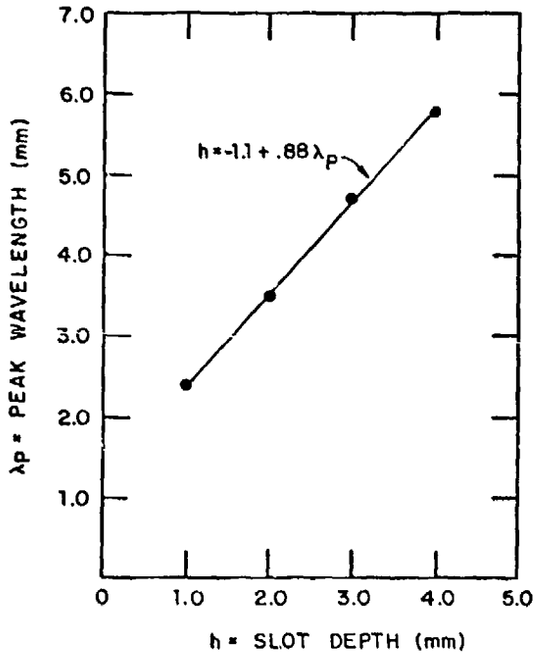

Fig. 9 Relationship between "peak" wavelength and depth of surface slots.

CONCLUSIONS

The property of the Rayleigh wave which relates the wavelength to its depth below the surface has been effectively used to find the depths of slots. Figure 8 shows that the depth of a slot is nearly linearly related to the wavelength. The slope of the line is 0.8. Thus, a slot of 3 mm cuts off all the wavelengths which are less than about 2.4 mm. The theory (2) predicts that the particle motion excited by an R-wave is localized to a depth of 2λ. The results from both photoelastic and ultrasonic tests show that the slot is fairly efficient filter for wavelengths less than 0.8 times the slot depth. The wavelengths in the undercut R-wave and other waves scattered from the slot tip are all longer than 0.8 times the slot depth. Thus:

Slot depth = 1.25 (cut-off wave length).

So in using this technique for inspection purposes the bandwidth of the R-wave should be such that the shortest wavelength (highest frequency) is 0.8 times the shortest crack depth that needs to be inspected. The largest wavelength (lowest frequency) should be longer than 0.8 times the deepest crack that is expected. Increasing the maximum wavelength to one times the crack depth gives a better resolution and should be considered the preferred limit. In doing this the undercut R-wave will be much stronger than the mode converted waves and will thus be affected less by them. Thus, if it is required to size cracks from 1 mm to 10 mm, the wavelengths in the R-wave should be from 0.8 mm to 10 mm.

ACKNOWLEDGMENTS

This research was supported in part by the Director of Energy Research, Office of Basic Energy Sciences, U. S. Department of Energy, WPAS-KC-02-01 and by the National Science Foundation Grant No. ENG77-06970.

REFERENCES

(1) Singh, A., "Crack depth determination by ultrasonic frequency analysis aided by dynamic photoelasticity," M.S. Thesis, Iowa State University, Ames, 1980.

(2) Achenbach, J. D., Wave Propagation in Elastic Solids, Amsterdam: North-Holland Publishing Company, 1973.

(3) Reinhardt, H. W. and Dally, J. W., "Some characteristics of Rayleigh wave interaction with surface flaws," Materials Evaluation, 28, 1970, pp. 213-220.

(4) Bond, L. J., "A computer model of the interaction of acoustic surface waves with discontinuities," Ultrasonics, 17, 1979, pp. 71-77.

(5) Silk, M. G., "Sizing crack like defects by ultrasonic means," Chapter 2 in Research Techniques in Non-Destructive Testing, R. S. Sharpe, Ed. London: Academic Press, 1977.

(6) Hall, K. G., "Crack depth measurement in rail steel by Rayleigh visualization," Non-Destructive Testing, 9, 1976, pp. 121-126.

(7) Adler, L., Cook, K. V. and Simpson, W. A., "Ultrasonic frequency analysis," Chapter 1 in Research Techniques in Ultrasonic Testing, R. S. Sharpe, Ed. London: Academic Press, 1977.

(8) Morgan, L. L., "The spectroscopic determination of surface topography using acoustic surface waves," Acustica, 30, 1974, pp. 222-228.

(9) Ayter, S. and Auld, B. A., "On the resonances of surface breaking cracks," Rockwell International Science Center Preprint, G. L. Report No. 2995, 1979.

(10) Tittmann, B. R., Billy, M. D., Cohen-Tenoudji, Jigman, A. and Quentin, C., "Measurement of the angular and frequency dependence of Acoustic surface wave scattering from surface cracks," IEEE Ultrasonics Symposium Proceedings, Cherryhill, New Jersey, 1978.

(11) Auld, B. A. and Syter, S., "Acoustic wave scattering from surface cracks," Rockwell International Science Center, G. L. Report No. 2927, 1979.

(12) Burger, C. P. and Riley, W. F., "Effect of Impedence mismatch on the strength of waves in layered solids," Experimental Mechanics, 14, 1974, pp. 129-137.

(13) Singh, A., Burger, C. P., Schmerr, L. W. and Zachary, L. W., "Dynamic photoelasticity as an aid to sizing surface crack by frequency analysis," to be presented at the Conference of the Mechanics of Non-Destructive Testing, Blacksburg, Virginia, 1980.

Leonard Bond, Chairman (University College London): As chairman, I will, in fact, make a comment. It's very gratifying to see one's numerical results confirmed by visualization. It's a great relief.

Gordon Kino (Stanford University): We published a paper a year ago on resonances of slots of this kind. I think the basic explanation is that the Rayleigh wave propagates down the slot, so that you get resonance associated with the slot. There is also another resonance associated with the width.

Chris Burger (Ames Laboratory): The resonances are very strongly present. I think we'll talk about those in the next paper which deals with the reflected wave. The transmitted wave does not show strong resonances.

Gordon Kino: You talk about maxima and minima. That's just another word for resonance.

Chris Burger: Maybe. Let us look at the transmitted wave for a slot where we have fairly good separation. We are only looking at the first portion of the wave. Sort of three cross-over points from the slot. This is the kind of characteristic that you can ask a computer to identify. Look at the wave that follows immediately after the third cross-over point. This is the Rayleigh wave which propagated around the slot. The component which we are looking at in the shear that comes from the tip of the slot together with the cut-off Rayleigh wave. I do not think that there are too many resonances in that portion of the wave.

Volker Schmitz (Battelle Northwest): Are the formulas you showed independent of the transducer? If you change the transducer, would it change the frequency spectrum of your transmitted signal? Would it change the formula?

Chris Burger: The answer is probably yes. We do not know. We only did it with one transducer. I'm not proposing that the formula is a unique relationship of how deep the crack is. There is, however, a clear relationship between the characteristic points in the spectrum and the depth of slot. This kind of approach is worth pursuing.

In fact, I don't see much use for a formula for open slots. We need to progress from here to slots where we have residual stresses at the root to see if the technique is sensitive to such stresses. I hope it's not. Then we can move on to open cracks and to closed cracks. At that point we may be interested in devloping more generalized equations that will be of practical value.

Sevig Ayter (Stanford University): In the reduced frequency spectrum, after the first maxima and minima there are a few ripples. Do you try to analyze them?

Chris Burger: Yes, we tried to.

Sevig Ayter: Did you relate it to the resonances?

Chris Burger: Yes, we did get some information, but we were pragmatic at that point. We looked at the main signature, because it contains the most information. We were looking for the strongest indication which relates most diectly and unambiguously with crack depth.

Leonard Bond, Chairman: Thank you very much.

DECONVOLUTION PROCEDURE FOR CRACK DEPTH DETERMINATION USING RAYLEIGH WAVES

G. P. Singh
and
A. Singh
Southwest Research Institute
San Antonio, Texas 78284

ABSTRACT

This paper describes a method for determining the depth of machined slots simulating cracks by the use of Rayleigh waves. Six slots varying in depth from 0.5 mm to 3.0 mm fabricated in medium carbon steel have been sized using a commercially available 1.5 MHz Rayleigh wave transducer. One measurement using the pulse-echo method is made for determining the depth of the crack. Minima in the deconvolved spectra are shown to correspond to various vibration modes of the crack. A fixed-free bar vibration model yields acceptable results. A correlation study between various time-domain features with slot depth is also included.

INTRODUCTION

Surface-breaking cracks have been found in structural components in practically every industry. Historically, such cracks are detected by visual, dye-penetrant, magnetic particle, and ultrasonic techniques. However, these methods either are incapable of yielding crack depth information or have not been used in that mode. One possible solution for detecting and sizing surface-breaking defects is by using ultrasonic Rayleigh waves which have several unique properties for the task. For example, these waves attenuate rapidly towards the inside of the material, and the particles at a depth greater than two wavelengths are practically stationary.

Methods to size surface-breaking cracks using Rayleigh waves in the pulse-echo and through-transmission modes have been reported by several investigators.[1-5] The majority of these techniques were based either on time-of-flight measurement or spectral analysis approaches.[6] Time-of-flight methods to determine the depth of surface cracks have been used by Silk,[1] Silk and Lidington,[2] and Hall.[3] In the pulse-echo mode, the difference between the time-of-arrival of the reflection from the crack opening and from the crack tip were utilized to determine the crack depth. In the through-transmission mode, the total time taken by the Rayleigh waves to go around the crack was shown to be directly related to the depth of the crack provided that the crack was much deeper than the wavelength of the ultrasonic waves.[7] These time-of-flight techniques have limitations when the crack depths are nearly the same magnitude as the wavelength of the propagating wave. In such cases, spectral analysis techniques have been employed.

Burger and Singh's[8] spectroscopic analysis using the through-transmission mode revealed that slots act as low pass filters for the Rayleigh waves. Tittman et al[9,10] related the peak frequency of the reflected Rayleigh wave to the slot depth. They used several angular positions to determine the depth of the cracks. An interference model was proposed to provide information regarding the length of the crack. Similarly, Domarkas et al[11] reported spectral techniques for determining the length and depth of the cracks. Further discussions of their analysis are presented in the next section.

A simple procedure for determining the depth of surface-breaking cracks using one pulse-echo measurement and a conventional Rayleigh wave transducer is described in this paper. It is shown that a fixed-free bar vibration model yields acceptable results. A parametric study of various time-domain features such as pulse duration, rise time, and fall time is presented along with a discussion of the results. The method reported in this paper seems more suitable for field application purposes than presently used approaches.

THEORY

Based on the experimental evidence, the interaction of a Rayleigh wave with a slot can be divided into two regimes: (1) depth of the slot larger than the wavelength and (2) depth of the slot smaller than the wavelength. For cracks with depths much larger than the wavelength, arrival time techniques have been employed.[1,2,3] Obviously, these techniques would be limited to those cracks where crack opening and crack tip signals do not superimpose. In cases where superimposed signals are observed, spectral techniques can be employed to determine the crack depth. Tittman et al[9] used the interference between the wave reflected from the slot opening and the slot tip to determine the depth of electro-discharge machined slots in a plate of commercial aluminum. They found that the interference between the two waves resulted in a peak in the frequency spectrum which is given by

$$f_d = \frac{V_R}{2d} \qquad (1)$$

where V_R is the Rayleigh wave velocity, d is slot depth, and f_d is the peak frequency corresponding to the depth 'd'.

Ayter and Auld[12] presented a theoretical model to explain the resonances observed experimentally in the frequency spectrum of the reflected wave. They addressed the crack as a section of the acoustic waveguide in which resonances are treated as standing waves in the length and depth directions. By taking both faces into consideration, they explained resonances of all orders. The length and depth resonances in the frequency spectrum correspond to

$$f_\ell = \frac{V_R}{2\ell}\left(M + \frac{1}{2}\right) \qquad (2)$$

$$f_d = \frac{V_R}{2d} N \qquad (3)$$

where M and N are the mode indices and f_ℓ is the peak frequency corresponding to a slot of length 'ℓ'.

Domarkas et al[11] have postulated that the incident surface wave excites the crack to vibrate in the length and depth directions. When excited in the depth direction, the crack can be modeled as a fixed-free, laterally vibrating bar. The bar resonates when its length equals $(2N - 1)\lambda/4$ where N is the mode of resonance. Similarly, if the crack tip is assumed to be the fixed end and the crack opening to be a free end, the crack will resonate when its depth equals $(2N - 1)\lambda/4$. This results in absorption of energy and, therefore, sharp minima in the frequency spectrum of the reflected wave corresponding to the resonant frequencies.

The frequency spectra due to such resonances is modulated, and one expects to observe several maxima and minima in the spectrum. Due to the limited bandwidth of the commercial transducers, only few modes are observed. The minima corresponding to the resonant frequency are given by

$$f_N = \frac{V_R}{4d}(2N - 1) \qquad (4)$$

where f_N is the frequency corresponding to a minimum and N is the mode of resonance.

The results due to this fixed-free, laterally vibrating bar model (Equation 4) are compared with the experimental results described in the following section.

EXPERIMENTAL ANALYSIS

An experiment was carried out on an ultrasonic, signal processing test bed system. A KB-Aerotech, UTA-III, was used as an ultrasonic pulser-receiver. The waveform was displayed on a Tektronix scope and was digitized by a Biomation 8100 transient waveform recorder. The digitized waveform was then analyzed using the Data General Nova computer system.

A commercially available 9.5-mm diameter, 1.5 MHz center frequency transducer, mounted on a shoe to yield Rayleigh waves, was used in this experimental set. Data were acquired from a medium carbon steel block with six slots of uniform width (0.4 mm) cut across the entire width of the block. Depths of these slots ranged from 0.5 mm to 3.0 mm. The difference in the depths was taken as 0.5 mm so as to give a data base with a wide range of depths (maximum slot depth = $1.5X\lambda$ center frequency of the input wave).

Figure 1 shows the frequency spectrum of the reflected waveforms from the six slots. The frequency spectra show points of inflexion rather than strong expected modulations (for example Figs. 1c and 1d). These inflexion points correspond to the absorption of energy as outlined previously. To magnify the inflexion points and derive useful information, a deconvolution procedure was applied. It consisted of a complex point-by-point division of a slot spectra with the reference spectra. In this case, the reference was obtained by averaging the six spectra. (Similar results are expected when the reference is taken from a sharp corner on the edge of the block.) Figure 2 shows results of the deconvolved spectra for all of the slots under consideration. Notice that sharp minima are observed corresponding to inflexion points in the frequency spectra (Fig. 1). In almost all cases, several minima are observed. These minima can be shown to correspond to the various modes of resonance. Table 1 shows the calculated frequencies for different modes of resonance from Equation (4) and experimentally observed values. The useful bandwidth of the transducer ranges from 0.7 MHz to 2.75 MHz, and any other frequency is labelled as "out of frequency range."

Table 2 shows the actual depth and the depth calculated using Equation (4). Notice that the average error is 8.2 percent and that most results are within the experimental error bound. The 0.5-mm slot depth yields a rather large error (minima in the spectra and deconvolved signal are not well defined). This is attributed to the slot depth to width ratio which, in this case, is approximately equal to one. The effects due to finite width are expected to reduce when $d/w \gg 1$. (The depth for the 0.5-mm slot is calculated from the first mode, whereas the second mode is used for all other slots.) If data from the 0.5-mm and 1-mm slot are excluded due to an unacceptable d/w ratio, the average error for the rest of the four slots ranging in depth from 1.5 mm to 3 mm is 5.3 percent.

Observations from Fig. 2 also indicate that the minima corresponding to the second mode are the strongest. The minima corresponding to higher order modes are not so well defined, and some of them reduce to points of inflexion. The minima for n = 2 and n = 4 are sharper than those for n = 3. In the case of the 2.5-mm deep slot, the third mode of resonance expected at 1.5 MHz is not observed. The reason for the weaker minima corresponding to n = 3 is not yet clear.

The experimental and theoretical results as shown in Table 1 are in excellent agreement. (Largest error = 10.6 percent and average error = 5.1 percent for four slots 1.5 mm to 3.0 mm.)

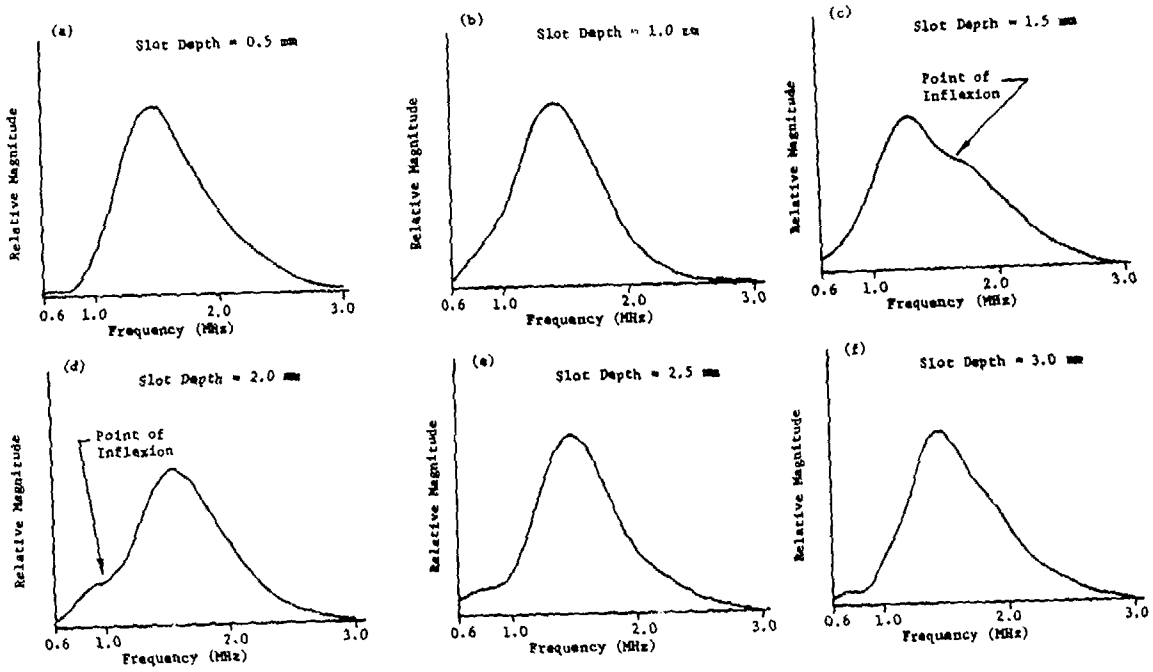

Fig. 1 Frequency Spectra of Various Slots

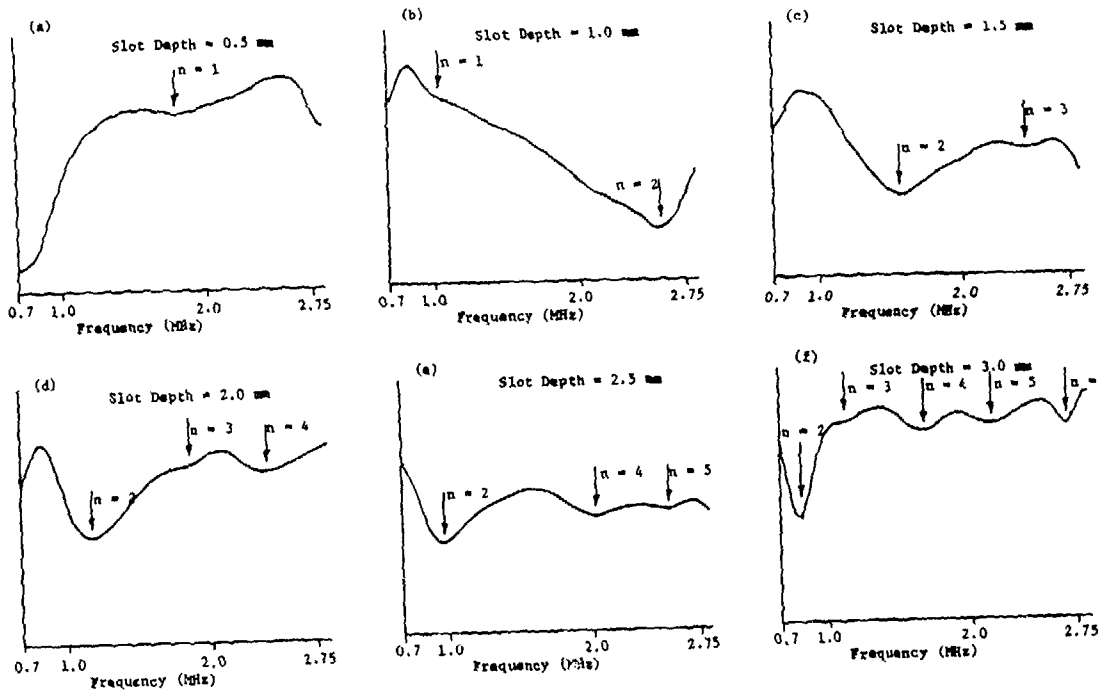

Fig. 2 Deconvolution Results for Various Slots

Table 1 Calculated and Observed Frequency Minima for Various Modes of Resonance

Mode of Resonance / f_N (MHz) / Slot Depth (mm)	N = 1		N = 2		N = 3		N = 4		N = 5		N = 6	
	Calculated	Observed	Calculated	Observed	Calculated	Observed	Calculated	Observed	Calculated	Observed	Calculated	Observed
0.5	1.5	1.77										
1.0	0.75	1.03*	2.25	2.55								
1.5			1.50	1.55	2.50	2.43						
2.0	Out of Frequency Range		1.125	1.16	1.875	1.84*	2.625	2.39				
2.5			0.90	0.96	1.50	N.O.	2.10	2.03	2.70	2.54		
3.0			0.75	0.83	1.25	1.14*	1.75	1.69	2.25	2.15	2.75	2.67

Out of Frequency Range

N.O. - Mode not observed
* - Point of inflexion

Table 2 Measured and Calculated Slot Depths Using $d = V_R/4f_N\ (2N-1)$

Slot Depth Measured (mm)	Resonance Mode	Calculated Slot Depth (mm)	Percentage Error
0.5	1	0.42	16.0
1.0	2	0.88	12.0
1.5	2	1.45	3.3
2.0	2	1.94	2.0
2.5	2	2.34	6.4
3.0	2	2.71	9.7

Average Error 8.2%

The analysis presented could be very simply applied to field situations if the relative magnitude of crack sizes was known a priori. This would not only help select the appropriate frequency transducer, but also help simplify the procedure for determining crack sizes. For example, higher frequency transducers should be employed for the sizing of shallow surface-breaking cracks. For the case of unknown crack depths, a broadband transducer is recommended. This would enable one to observe a number of minima. The difference in frequency between two corresponding minima can be directly related to crack depth using Equation (5).

$$\Delta f = f_{N+1} - f_N = \frac{V_R}{2d}$$

Table 3 shows the slot depth as calculated from Equation (5). The 0.5-mm slot depth could not be calculated since two minima are not observed in the spectrum. The average error using this approach is about 12.3 percent. Interestingly, this approach for crack sizing yields a larger error than the one described previously [Equation (4)].

Various time-domain features have been studied in order to find their correlation with slot depth. A linear correlation, for example, would be very useful in implementing these techniques using existing field instrumentation. Figure 3 shows a correlation between several time-domain features with slot depth. Three features--rise time, fall time, and pulse duration--are plotted. These features are computed from the normalized envelope of the signal. Rise time is defined as the time taken by the signal to reach 90 percent of the peak amplitude from a 10 percent value. Fall time is the converse of rise time. Pulse duration is computed between 10 percent of the peak amplitude points. The results for rise time vs. slot depth are most interesting since they show a piecewise-linear relationship and offer a slight hope for crack sizing using simple measurements and conventional instrumentation.

CONCLUSIONS

A procedure to accurately size crack depths using ultrasonic Rayleigh waves was developed. The feasibility of the technique was demonstrated on slots ranging in depth from 0.5 mm to 3.0 mm. A single pulse-echo measurement to calculate the slot depth makes this technique very practical for field use. A fixed-free, laterally vibrating bar model was found suitable to obtain various minima observed in deconvolved spectra. Excellent agreement between the experiment and the proposed model was shown. Time features were studied in order to correlate them with slot depth. The piecewise-linear nature of the rise time encourages its use for crack sizing using conventional means.

ACKNOWLEDGEMENT

This work was supported by Quality Assurance Systems and Engineering Division of Southwest Research Institute, San Antonio, Texas.

REFERENCES

1. Silk, M. G., "Sizing Cracklike Defects by Ultrasonic Means," Research Techniques in Non-Destructive Testing, Chapter 2, R. S. Sharpe, Ed., London, Academic Press, 1977.

2. Silk, M. G. and Lidington, B. H., "An Evaluation of Single Probe Bulk-Wave Time-Delay Techniques in Sizing Cracks in Steel," NDT International, 10, pp. 129-134, 1977.

3. Hall, K. G., "Crack Depth Measurement in Rail Steel by Rayleigh Visualization," Nondestructive Testing, 9, pp. 121-126, 1976.

4. Reinhardt, H. W. and Dally, J. W., "Some Characteristics of Rayleigh Wave Interaction With Surface Flaws," Materials Evaluation, 28, pp. 213-220, 1970.

5. Bond, L. J., "A Computer Model of the Interaction of Acoustic Surface Waves With Discontinuities," Ultrasonics, 17, pp. 71-77, 1979.

6. Doyle, P. M. and Scala, C. M., "Crack Depth Measurement by Ultrasonics - A Review," Ultrasonics, 16, 1978.

7. Silk, M. G., "The Determination of Crack Penetration Using Ultrasonic Surface Waves," NDT International, 9, pp. 290-297, 1976.

8. Burger, C. P. and Singh, A., "An Ultrasonic Technique for Sizing Surface Cracks." Presented at the DARPA/AFML Review of Quantitative Progress in NDE, La Jolla, July 1980.

9. Tittman, B. R., Buck, O., Ahlberg, L., De Billy, M., Cohen, Tenhoudji, F., Jungman, A., and Quentin, G., "Surface Wave Scattering From Elliptical Cracks for Failure Prediction." Paper received by mail from Tittman, B. R., Rockwell Science Center, Thousand Oaks, California.

10. Tittman, B. R., De Billy, M., Cohen-Tenoudji, F., Jungman, A. and Quentin, G., "Measurements of Angular and Frequency Dependence of Acoustic Surface Wave Scattering From Surface Cracks," Proceedings of the IEEE Ultrasonics Symposium, Cherry Hill, N. J., 1978.

11. Domarkas, V., Khari-Yakub, B. T., and Kino, G. S., "Length and Depth Resonances of Surface Cracks and Their Use of Crack Size Estimation," Applied Physics Letters, 33, 1978.

12. Ayter, S. and Auld, B. A., "On the Resonances of Surface-Breaking Cracks." Presented at the Review of Progress in Quantitative NDE, La Jolla, 1979.

Table 3 Measured and Calculated Average Slot Depths Using $d = V_R/2\Delta f$

Measured Slot Depth (mm)	Calculated Depth (mm)	Percentage Error
0.5	--	--
1.0	1.0	0.0
1.5	1.7	13.3
2.0	2.46	23.0
2.5	2.78	11.2
3.0	3.42	14.0

Average Error 12.3%

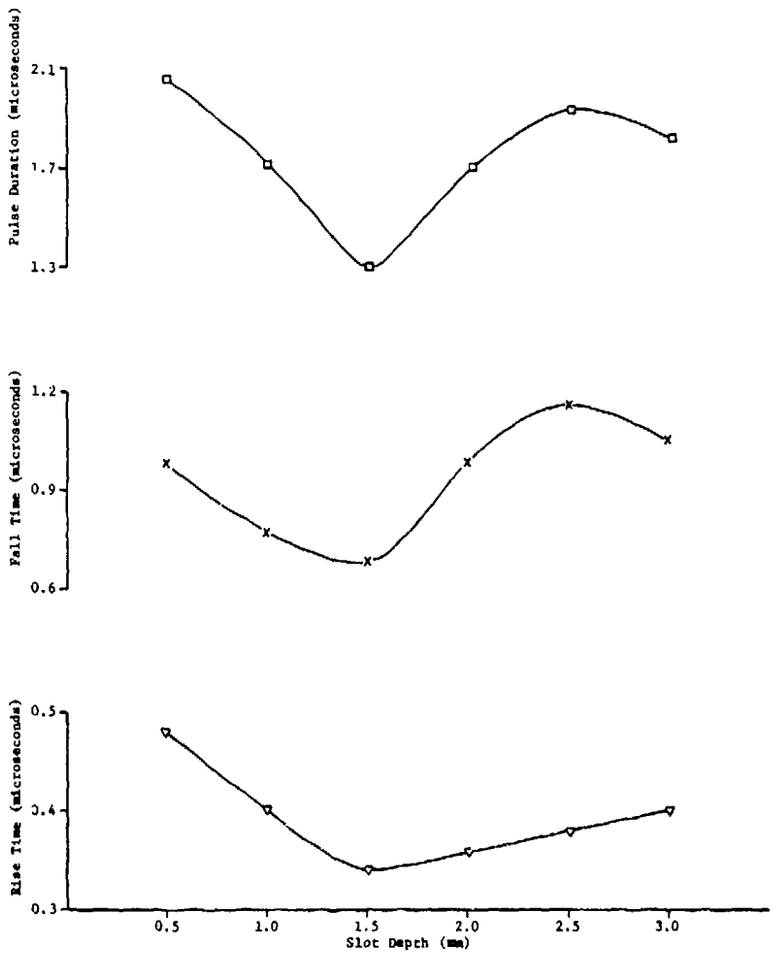

Fig. 3 Time Domain Features Corresponding to Various Slot Depths.

Wolfgang Sachse (Cornell): I wonder, what you described is taking the signal which is transmitted past your slot; had you frequency analyzed that?

Anmol Singh (Southwest Research Institute): This is reflected signal.

Wolfgang Sachse: I wonder if you would also have done the case where you have analyzed the signal which is transmitted past the slot - because I suspect in this case you have observed minima to occur in these frequency spectra. That is the energy absorbed by the slide. Whereas, if you looked in the opposite direction, you would find those frequencies would have peaks in the spectrum. And this is very similar to some work that we described about five years ago at this meeting in the case of inclusions. If you look at the forward scattered signals, it's the peak in the spectrum, because it's radiating energy at those signals. If it's the back scatter signal. It's the mimina that corresponds to the resonance frequencies of your spectrum.

Anmol Singh: During this study at Southwest Research Institute we did not analyze the resonances of the transmitted signal. But since the resonant frequencies for a particular dept correspond to absorption of energy the minimas produced in scattered waves, i.e., the transmitted and reflected components should probably be the same. Thus it is questionable to say that the minimas in the reflected signal will correspond to maximas in the transmitted signal.

While I was at Iowa State University we used dynamic photoelasticity to analyze the transmitted Rayleigh wave signal past a slot. A part of this work was presented by Professor C.P. Burger of Iowa State in the earlier paper. In that study the transmitted signal showed modulations in the frequency spectrum which could not be related to the depth of the slot. This is possible because the transmitted signal is a sum of the undercut and the cut-off Rayleigh waves as described in the earlier paper by Dr. Burger. Thus if we can separate the under-cut and the cut-off waves, and analyze each of them we may be able to relate the modulations in the spectra to the depth of the slot.

James Aller (National Science Foundation): On Table II that you showed, the immediate reaction that I have is that you have a systematic error in your measurements. So my question is: is that possible?

If you just added a fixed calibration number to the calculated depth, you would end up almost on the button.

Anmol Singh: On which column of the figure did you go down?

James Aller: Not the precentage, just the calculated depth column. And if I take the difference between calculated depth and real depth, that looks to be a straight-forward delta of 0.08. And my question is: is that just an artifact of the table, or is it possible you have a systematic error?

Anmol Singh: These is a systematic error in the calculated depth. If it was a random error, the calculated depth would be both greater and less than the actual depth. Here all of them are less than what the actual depth should be.

James Aller: How wide was your slot?

Anmol Singh: It was 0.04 mm. It is possible that the width affects the resonant frequencies which introduce a systematic error in the calculated depths. I believe with deep cracks you may not have this effect, which generates a systematic error. Secondly, to avoid the width effect we are planning to analyze the signal reflected from down steps of different depths. This will also confirm the hypothesis which is based on the resonances of the crack face. We want to study the effect of the reflected wave from these steps. In case of steps, we do not have the width effect as it is a plane face or down step.

Gordon Kino (Stanford University): I have trouble reading the table from here, but as I understood the questioner, there is basically a constant error. It surely is just that these slots are not necessarily a multiple of half wavelength or quarter wavelength. There is an end effect which we talked about last year, and I think this year, too, which has to be taken into account. There is no particular reason to believe it's going to behave like an open circuit. It is something else. So you would expect a constant correction.

Leonard Bond, Chairman (University College London): We have time for one more question.

Sevig Ayter (Stanford University): One comment. You said you only made one measurement. However that assumes that you know the orientation of the slot. If you don't know, you will also have to take some other measurements, since the crack is not infinite. So you have to first determine the orientation and hit the crack with normal incidence.

Anmol Singh: We ought to have a crack, and it should be normal.

Sevig Ayter: So you need more than one measurement to determine first the orientation of the crack, and then depth.

Anmol Singh: In the structural components we know what the direction of the crack is going to be from the direction of the stress.

Sevig Ayter: You mentioned an example in the actual field, so that I have to -

Anmol Singh: That's right. But what I'm saying is if we are inspecting a pipe with cracks, we know the direction in which cracks grow. Also, when the inspection is done, the transducer is moved in different directions. We look at the signal from cracks and obtain the peak response from the cracks. On obtaining the peak signal the transducer is placed normal to the crack.

Leonard Bond, Chairman: I think we better draw discussion on this paper to a close and move on to the next paper.

CRACK DEPTH MEASUREMENTS WITH THE AID OF SAW NDE

B. R. Tittmann, L. Ahlberg, and O. Buck
Rockwell International Science Center
Thousand Oaks, California 91360

ABSTRACT

This report presents results of measurements of crack depth with the aid of acoustic bulk and surface waves. Both simulated and real fatigue cracks were examined. Two techniques were employed, one took advantage of the very efficient mode conversion between acoustic surface waves and shear waves at the crack tip; the other technique used the diffraction of shear waves at the crack tip. Both techniques were used on a number of simulated (spark eroded) and real cracks in Al 2024. In one fatigue specimen which contained an elliptical crack 4.5 mm in length and 1.25 mm in depth, crack closure studies were carried out. The precision of crack depth determination was judged to be better than 10%.

OBJECTIVE

The ultimate objective of this task is to predict the fatigue life of a metallic component with the use of ultrasonic nondestructive evaluation. The work concentrates on predicting the remaining fatigue life for a single fatigue part-through crack above the "threshold" value for macrocrack propagation. Acoustic surface and bulk waves are being used to interrogate the crack during cyclic fatigue. The inversion of the scattering data provides crack size, shape, and orientation as a function of fatigue. With this information and metallurgical data, the remaining fatigue life is obtained from fracture mechanics. The effective stress intensity is studied which should allow inclusion of environmental as well as random loading effects on fatigue life.

INTRODUCTION

During the previous reporting period two techniques were evaluated for measuring the length and depth, respectively, of fatigue cracks with the use of acoustic surface waves.[1,2] Both techniques are specialized to the case in which the wavelength is smaller than both the crack length and depth. The technique for measuring the length is based on the diffraction of surface waves from a crack giving rise to structure in the angular and frequency dependence of the scattered power such that the minima and maxima have positions and spacings which are used to infer the crack length. This technique, developed earlier for spark eroded slots, was also found to give good results for fatigue cracks. The technique for measuring the crack depth is based on multiple conversions of wave energy, starting with a surface wave on the specimen surface, conversion to a guided dispersive wave on the crack face and conversion at the crack tip to a bulk (shear) wave travelling to the opposite wall of the specimen. There, upon reflection, the conversion proceeds in reverse manner so that the transducer used as transmitter may also be used as receiver for this multiply converted return signal. By the use of echo timing techniques based on a good knowledge of the velocities for the various travel paths, the crack depth is determined with good precision.

Auxiliary experiments were conducted to study the effects of crack closure. In Ti-alloy, the closure load was found to depend strongly on crack depth, especially in the near-threshold regime. With the information obtained, the life prediction could be improved considerably. The technique has several disadvantages, such as restrictions on specimen geometry for the proximity of a suitable back wall, sensitivity of the calculations on errors in the shear and Rayleigh wave velocities, and need for refinement in the model describing the interaction between the surface waves and the crack. A fundamental limitation of the technique is its inability to provide information for cracks inclined to the surface.

SUMMARY OF TECHNICAL RESULTS

The work accomplished for the present work period consisted of a continuation of studies started previously with the addition of one new effort.

Continued effort to characterize the interaction of surface and bulk waves with part-through cracks was performed. This work involved close interaction with B. Auld, J. Achenbach, and A. Mal to refine current models for this interaction. The techniques emerging from this effort were tested on the life prediction of an Al fatigue specimen with a single crack whose growth was monitored during the fatigue cycling. This fatigue specimen was constructed from Al 2024-T6 material. Also an apparatus was constructed to impose static tensile stress on the crack for crack closure studies.

In addition, a new approach was developed to determine the crack depth based on diffraction of bulk waves around the tip of the crack. This approach has the major advantage that it would provide the "true" crack depth below the specimen surface, independent of the detailed structure and contour of the crack. The discussion of the detailed experimental results emphasizes this new work.

DETAILED RESULTS

Our recent studies have shown that the use of diffraction of bulk shear waves has led to good success in crack depth measurements on rectangular and elliptical simulated (spark eroded) cracks and real fatigue cracks.

The measurements employed a commercial lucite 45° angle wedge with a 6.35 mm diameter, 10 MHz shear transducer polarized in the vertical direction. Figure 1 shows a schematic of the geometry. The crack depth (d) was obtained from the incident angle of the ultrasonic beam (θ), the shear wave velocity in the sample in the polarization direction (v_s), and the time delay measured between the crack tip and crack mouth reflection signals (t). The depth is then given by $d = v_s t/2\cos\theta$.

SC80-8968

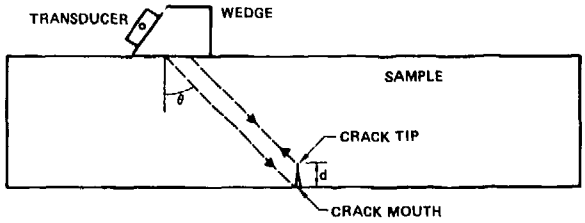

Fig. 1 Schematic diagram showing sample geometry and transducer configuration.

Figure 2 shows the waveforms corresponding to the crack tip and mouth for a 2.54 mm long, 1.27 mm deep rectangular simulated crack. Also shown are a deconvolved frequency spectrum and the impulse response function time domain waveform. Figure 3 shows similar waveforms for a 2.54 mm length, 1 mm depth elliptical simulated crack. Figure 3a shows the "actual" waveform whereas Fig. 3b displays a greatly amplified version. Clearly discernable is the crack tip signal with a good signal-to-noise ratio. It should be noted that the time domain plots show extensive ringing after the crack mouth reflection signals. The reason for this ringing is not clear and remains under study.

In addition to the studies on simulated cracks, measurements were carried out on actual fatigue cracks in Al 2024-T3 tensile specimens. Figures 4a and 4b are the time domain waveforms of two samples, B-1 and C-2 with estimated crack depths of 1.25 and 1.95 mm, respectively. Again in both cases, there is extensive ringing in the signal after the main crack mouth signal. Table 1 summarizes the results of the experiments and compares the estimated with the actual depths.

Table I. Comparison of Measured and Actual Crack Depths

Sample Type	Real Depth mm	Measured Depth mm	Error %
Rect. EDM	1.27	1.34	+5.5
Ell. EDM	1.00	1.05	+5.0
Fatigue B-1	~1.25	1.14	-8.8
Fatigue C-2	~1.95	1.8	-7.7

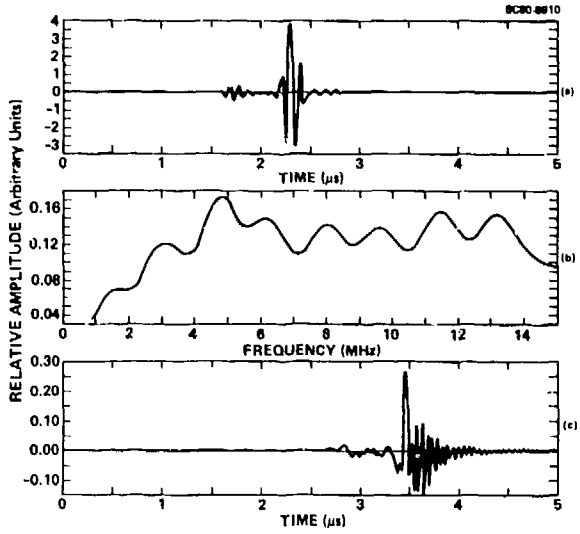

Fig. 2 Shear wave interrogation of 2.54 mm long, 1.27 mm deep rectangular simulated crack prepared by spark erosion. Figure 2a shows the received waveform with two echoes from crack tip and crack mouth, respectively. Figure 2b shows the deconvolved frequency spectrum, showing the interference between the large crack mouth signal and the small crack tip echo. Figure 2c is the result of transforming Fig. 2b back into the time domain to obtain impulse response function.

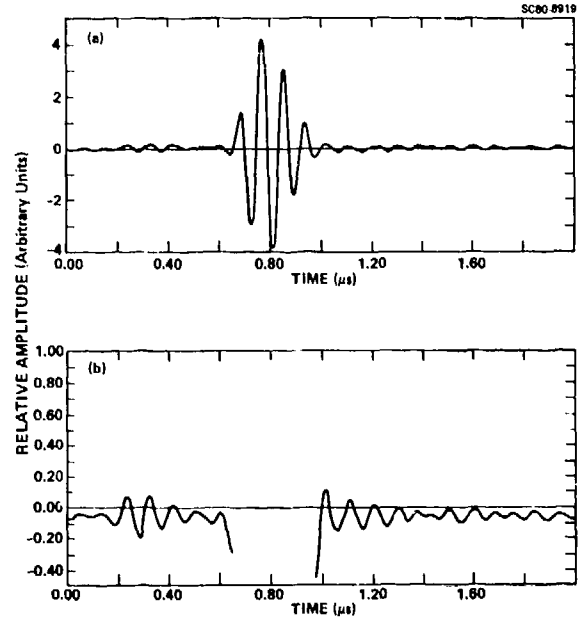

Fig. 3 Same as Fig. 2 for an elliptical slot 2.54 mm long and 1 mm deep. Figure 3a shows the waveform with normal magnification and 3b with x4 magnification. The crack tip echo is clearly discernable. The DC offset probably is an artifact resulting from the overload by the main crack mouth signal.

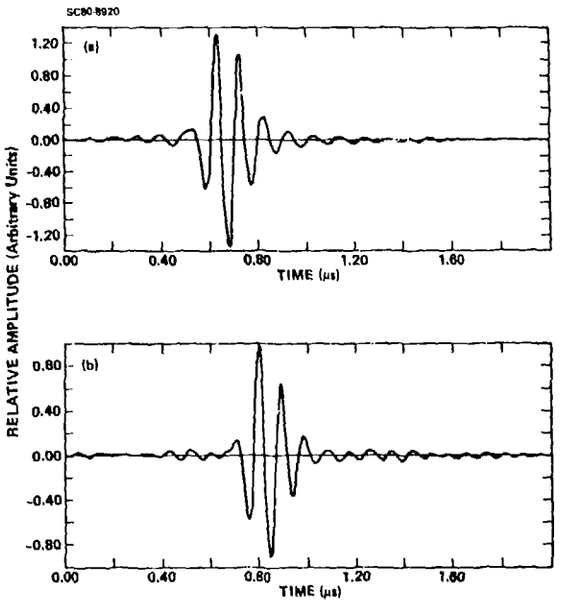

Fig. 4 Shear wave interrogations for two different Al 2024-T3 tensile stress specimens with fatigue cracks whose depth is not known. Figure 4a is for sample B-1 and Fig. 4b is for sample C-2.

As may be seen from Table 1, we found good agreement of real depth and measured depth for the simulated cracks. Noticeable now is the large discrepancy between the estimated crack depth and the measured depth for both fatigue cracks. An obvious cause for this discrepancy is the fact that the cracks are at least closed to the crack tip, so the acoustic signal does not see the true crack depth.[2] Measurements as described above will have to be performed under tensile load (to open the crack fully), which will be the objective of further studies. One interesting feature that these studies will, we hope, reveal is whether the crack depth diminishes monotonically with compressive stress or in whole segments. In terms of the ultrasonic waveforms, in the first case the crack tip echo will be closer and closer to the main echo as the stress increases. In the second case, the crack tip echo will not move but will become smaller at the expense of another crack tip echo growing at a position closer to the main echo.

The tensile fatigue specimen was constructed by using the following procedure. Prior to fatigue, a starter notch was spark eroded (EDM) in the surface of a large dog-bone specimen of 2024-T6 Al. The notch was 2.5 mm long at the surface, 1.25 mm deep and semi-circular in shape. Next the sample was fatigue cycled to initiate a crack and allow the crack growth by about 1.25 mm in radius. Then the initial starter notch was machined off so that the final gauge section was 25.4 mm wide, 9.0 mm thick, and contained an elliptical crack 4.5 mm long at the surface and about 1.25 mm deep.

In the experiments, the crack was illuminated with Rayleigh wave pulses from a direction at right angles to the crack plane. The receiver was situated opposite to the transmitter and across the crack. The data could be collected while the tensile specimen was in a special loading frame. This frame used a manual hydraulic pump that allowed us to achieve stresses in excess of 35 ksi, which was enough to exceed the crack opening stress in this material. Figure 5 shows an example of the received waveforms displaying the primary transmitted signal and then about 4 μs later the signal which, as discussed earlier, is mode-converted to a shear wave at the crack tip and is then reflected from the near surface of the tensile specimen. The waveforms shown in Fig. 5 were obtained at an applied stress of about 30 ksi. Also shown in the figure at the bottom is the frequency spectrum of the primary transmitted signal displaying a center frequency of about 6 MHz. Similarly, the primary reflected signal (crack mouth echo) and the secondary, mode-converted signal (crack tip echo) were observed and Fig. 6 shows the frequency spectra of those signals, respectively. (Note that because of the low signal-to-noise ratio of the secondary, mode-converted signal, the signal processing required extensive smoothing). In contrast, Fig. 7 shows the primary transmitted Rayleigh wave signal and its frequency spectrum at low applied stress. Notice that the time-domain data do not show a secondary signal but exhibit a sizeable pulse immediately following the main signal. (The precursor signal has been identified as a reverberation in the home-made water wedge transducer.) Notice also that the frequency spectrum shows a dramatically lower high-frequency content than the corresponding spectrum at high applied pressure (Fig. 5, bottom). The contrast between these data at low and high applied stress are not completely understood at this time, but are assumed to be associated with crack closure behavior. Figure 8 shows a mosaic of micrographs taken of the fatigue crack at its mouth. The optical estimate for the crack length is approximately 4.5 mm.

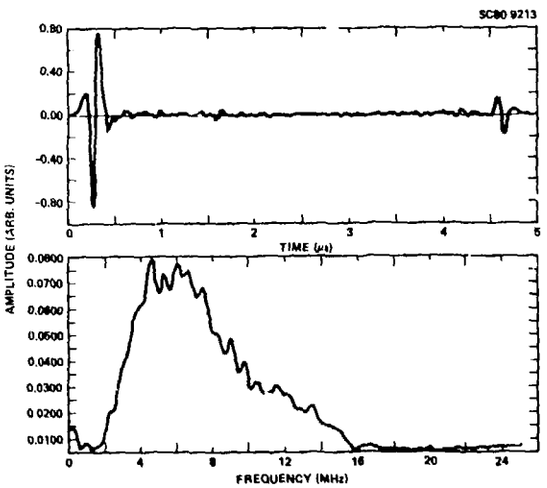

Fig. 5 Time-domain waveforms of primary and secondary Rayleigh wave signals transmitted across the crack (top). Frequency spectrum of primary signal (bottom). Data obtained at 35 ksi.

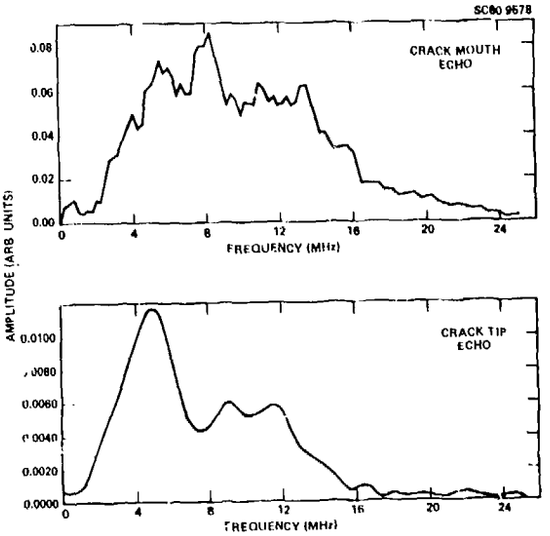

Fig. 6 Frequency spectra of primary (crack mouth echo) and secondary (crack tip echo) Rayleigh wave signals reflected back to the transmitter.

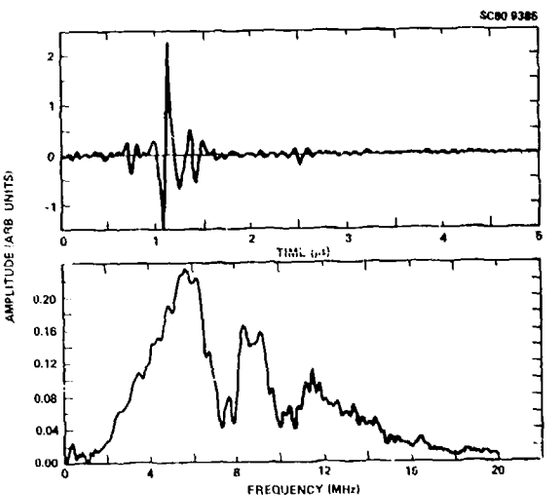

Fig. 7 Data same as that of Fig. 5 but at about 1 ksi.

Next, the peak signal amplitudes were studied as a function of applied stress with the tensile specimen in the loading frame. Figure 9 presents the results of these measurements showing at the top that the primary transmitted signal (labeled "forward scatter") diminishes with increasing applied stress until at some critical stress the amplitude stops changing as the stress is increased further. In contrast, the primary reflected signal (labeled "backscatter") begins at low amplitudes, increases, and then achieves a constant amplitude as the applied stress is increased over the same range of stress values. Thus, the behavior of the reflected and transmitted signals act qualitatively complementary, i.e., the reflected grows at the expense of the transmitted as the crack is opened by the applied stress. Finally,

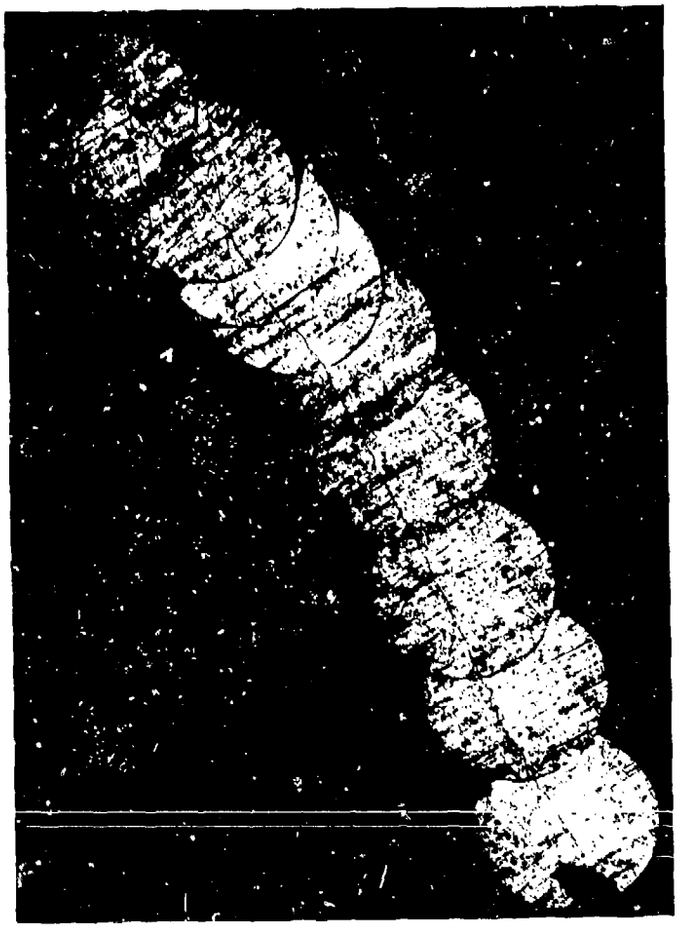

Fig. 8 Mosaic of micrographs obtained for crack in fatigue specimen.

the transmitted, secondary, mode-converted signal (labeled "crack tip") is not visible for low values of applied stress, then appears at about 10 ksi, increases in amplitude with increasing stress, until above about 25 ksi the amplitude remains constant or increases only slightly.

The behavior of the secondary, mode-converted signal was studied in greater detail, as shown in Fig. 10. At the bottom, both the transmitted (labeled "forward scatter") and reflected (labeled "back scattered") signal amplitudes are shown and behave comparably as a function of applied stress. Also shown in the middle plot, is the time delay between the primary and secondary signals. As discussed earlier, the time delay is used to calculate the crack depth which is plotted in the top graph. Also shown are two other sets of data: the solid circles were obtained with use of shear wave diffraction as described earlier for the spark eroded slots. The single data point in the form of an open square is the value obtained from a combined use of optical crack length

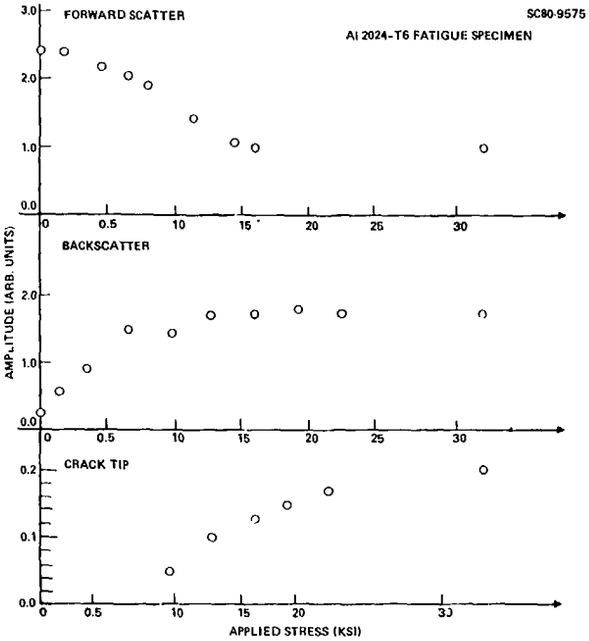

Fig. 9 Rayleigh wave signal wave amplitudes for primary forward scattered pulse (top) primary backscattered pulse (middle) and secondary mode-converted and forward scattered pulse (bottom).

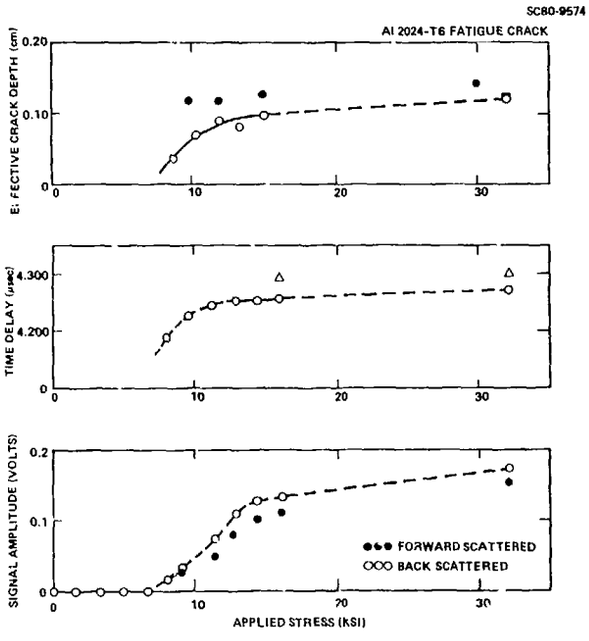

Fig. 10 Effective crack depth as a function of applied stress (top), obtained in part (open circles) from observed time delay between primary and secondary Rayleigh wave signals (middle). Signal amplitudes of secondary signal for both forward and backscattered pulses (bottom).

measurements and crack growth rate data. All three data sets are in reasonable agreement and give an average depth of 1.3 mm ± 0.1 mm at about 30 ksi when the crack fully opens. The increase in effective crack depth at about 10 ksi applied stress and little or no increase beyond 15 ksi is typical of crack closure behavior in this material.

Extensive measurements are planned in the future for the fatigue specimen. The objective is to determine crack length and depth ultrasonically during most of the fatigue life of the specimen. Also, any changes in the behavior under static tensile stress will be monitored. The behavior of the 2024-T6 material will be compared with that in Ti-15A reported on earlier.[2]

ACKNOWLEDGEMENT

The authors are grateful to J. Achenbach, A. Mal and B. Auld for making their theoretical results available prior to publication.

This research was sponsored by the Center for Advanced NDE operated by the Science Center, Rockwell International, for the Advanced Research Projects Agency and the Air Force Materials Laboratory under Contract No. F33615-80-C-5004.

REFERENCES

1. B. R. Tittmann, O. Buck, L. Ahlberg, M. de Billy, F. Cohen-Tenoudji, A. Jungman, and G. Quentin. "Surface Wave Scattering from Elliptical Cracks for Failure Prediction," J. Appl. Phys. 51, 142 (1980).
2. B. R. Tittmann and O. Buck, "Fatigue Lifetime Prediction with the Aid of SAW NDE," J. Nondestr. Eval. 1, 123 (1980).
3. B. R. Tittmann, R. E. Elsley, and N. Paton, "Measurements of Ultrasonic Scattering from Bulk Flaws of Complex Shape," Proc. of DARPA/AF Review of Progress in Quant. NDE, La Jolla, 1979, Report FWOL-TR-80-4078, p. 359.

Leonard Bond, Chairman (University College London): We have time for a few questions. Who would like to start with a question?

Richard Barry (Lockheed Missiles and Space): Would you tell me when you were concerned about the error in some of your measurements from one of the earlier slides, where you measured your actual crack depth, did you measure the average depth or maximum depth?

Bernie Tittmann (Science Center): I measured the actual depth, taking into account the Achenbach flash point concept where it is the extremities that are responsible for generating the sources of the signals.

Unidentified Speaker: On your last slide, if you calculated the depth of the crack from fracture mechanics, what would the shape of that curve look like?

Bernie Tittmann: We didn't do that. That would be an interesting point. You see, fracture mechanics cannot really tell us how well the crack is closed. What fracture mechanics tells us is that after so many cycles, a surface crack assumes a semi-circular shape. Then from an observation of the crack length, we can immediately infer what the crack depth should be if the crack is completely open. Fracture mechanics cannot really tell us how much the crack is closed for a given applied stress. At least we are not that far along.

Would you agree with that, Otto (Otto Buck, Ames Laboratory)? Yes.

Chris Burger (Ames Laboratory): Bernie, in your growth of the cracks where you are opening and closing them, were you running with constant amplitude or constant displacement growth or did you use something like a large overload and then look at the closure phenomena?

Bernie Tittmann: The measurements with large overloads constitute the next phase in our experimentation. All the measurements discussed here were done with a constant stress increment. That's a very interesting question and we hope to shed light on it soon.

Kamel Salama (University of Houston): Do you have any idea how the crack closure stress changed from tensile to compressive? Is that because the residual stress is, for instance, around the crack change direction or change in size?

Bernie Tittmann: You mean in the experiments on Ti-15A? The idea there is that as the crack grows deeper, the plastic zone in front of the crack enlarges and affects the mode of fracture growth, for example, in a transition from Mode I to Mode II. We don't fully understand that yet, but certainly the stress present in the plastic zone affects crack growth dramatically in the titanium.

Leonard Bond, Chairman: One last question.

Fred Vaccaro (The Timkin Company): Bernie. Would you explain the absence of the secondary, mode converted crack tip signal at low applied stresses along the same lines as the lack of high frequency in the signal?

Bernie Tittmann: That's a very interesting point, and I meant to elaborate on it a little bit. If you remember, I showed you a slide of that satellite echo next to the crack mouth. We are speculating that at this point the crack is almost closed. And this process of mode conversion from a surface wave to a shear wave has been modified so that instead of radiating bulk waves, the crack tip reflects the Rayleigh wave very efficiently. But as soon as you open up the crack the source of radiation moves down to the actual crack tip, which radiates bulk wave efficiently into the material.

Leonard Bond, Chairman: I think we better draw the discussion to a close. I would like to thank the speakers for the first session.

THE IMPEDANCE OF A LOOP NEAR A CONDUCTING HALF-SPACE

Afroz J. M. Zaman, Stuart A. Long and C. Gerald Gardner
Department of Electrical Engineering
University of Houston
Houston, Texas 77004

ABSTRACT

The change in complex impedance between an ideal one-turn circular coil located above and parallel to a conducting half-space with respect to a similar isolated coil has been calculated. From this result a series expansion of the integrand allows the solution to be approximated by terms expressed as complete elliptic integrals. Results have been calculated for the change in impedance as a function of the lift-off distance and the conductivity of the half-space for a coil of representative radius.

INTRODUCTION

The eddy current method of nondestructive evaluation entails the induction of eddy currents in a conductive test object by a time-varying field produced by a suitable distribution of impressed currents (via an excitation or primary coil), and the detection of the resultant field, usually by an inductive search coil which may be either a separate secondary coil or the primary coil itself. (See Fig. 1.) The method is ordinarily used at frequencies sufficiently low to neglect effects due to displacement current; hence a theoretical analysis entails calculating either a transfer impedance for a primary coil and secondary coil in the presence of the test object, or the calculation of the self impedance of a primary coil in the presence of the test object. In practice one often needs only the change in impedance produced by the test object or by changes in the nominal properties of the test object (e.g. changes in its geometry or position with respect to the test coil or coils, or distributed or localized changes in the resistivity of the test object). The most general case, allowing arbitrary configurations of primary and secondary coils and arbitrary test objects can be handled only by numerical methods. Certain idealized arrangements can be treated analytically either exactly or in useful approximation. In virtually all cases of practical interest, the analysis eventually reduces to the evaluation of certain integrals which cannot be expressed in closed form in terms of standard transcendental functions.

In this paper we discuss the case of a one-turn circular coil located above and parallel to the surface of a homogeneous conductive half-space. From the standard boundary value problem approach we obtain the general expression for the change in coil impedance, ΔZ, produced by the half space; ΔZ is given in terms of an integral over a separation parameter. A series expansion of one term in the integrand permits the integral to be expressed as a series of terms each of which is expressible in terms of complete elliptic integrals. The leading terms of this series approximate ΔZ asymptotically for sufficiently small values of skin depth of the halfspace.

The problem addressed here has previously been treated by Cheng [1] who evaluated ΔZ by numerical methods for various choices of the relevant parameters. Similarly, Dodd and Deeds [2] have devised a digital computer program capable of handling circular test coils in the presence of layered planar and coaxial cylindrical test objects. Such brute force numerical procedures are valuable for design purposes, but have the disadvantage of somewhat concealing the essentially simple manner in which the final result depends upon the parameters of the problem. The approach taken here, while less universal than the purely numerical approach; results in relatively simple, though approximate and restricted, formulas for ΔZ in terms of the basic parameters of the problem.

For illustrative and comparative purposes, some selected numerical examples are also given.

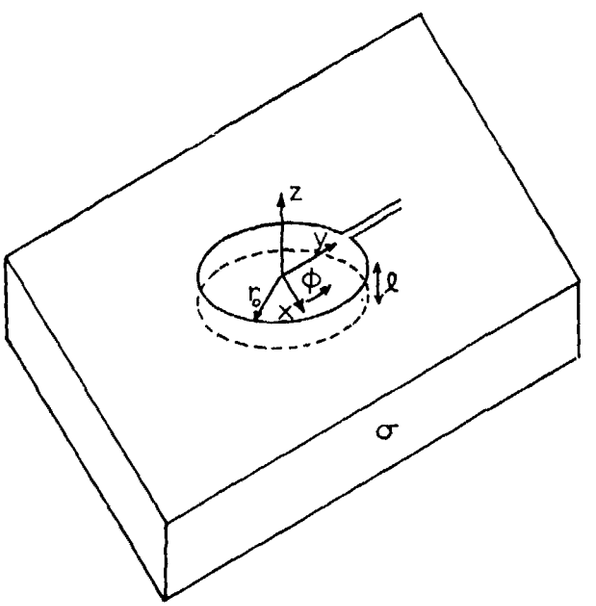

Fig. 1 Geometrical configuration of loop near a conductor.

THEORETICAL ANALYSIS

The basic geometry of the problem is shown in Fig. 1 and consists of a loop radius r_0 oriented parallel to and at a distance ℓ above homogeneous half-space of conductivity σ. Beginning with the basic equation for the vector potential

$$\nabla^2\vec{A} + k^2\vec{A} = -\mu_0 I(t)\frac{\delta(r_0-r)}{r}\,\delta(\ell-z) \qquad (1)$$

and noting the symmetry of the problem, it is seen that the only component of the vector potential present is the circumferential component, A_ϕ, and that A_ϕ is a function of r and z only. Making the usual low-frequency, quasi-static approximation that the $k^2\vec{A}$ term is negligible for z>0, we have:

$$\nabla^2\vec{A} = \frac{\partial^2 A_\phi}{\partial r^2} + \frac{1}{r}\frac{\partial A_\phi}{\partial r} + \frac{\partial^2 A_\phi}{\partial z^2} - \frac{A_\phi}{r^2} = 0 \text{ for } z>0 \qquad (2)$$

and, with $k^2 \doteq -j\omega\mu\sigma$ for z<0:

$$\frac{\partial^2 A_\phi}{\partial r^2} + \frac{1}{r}\frac{\partial A_\phi}{\partial r} + \frac{\partial^2 A_\phi}{\partial z^2} - \frac{A_\phi}{r^2} - j\omega\mu\sigma A_\phi = 0 \qquad (3)$$

for z<0

Solving by the separation of variables technique and using the limiting behavior at $z\to\infty$ and $r\to 0$ yield the following expressions for the solution to Equations (2) and (3).

$$A_{\phi 1}(r,z) = \int_0^\infty B_1 e^{-\alpha z} J_1(\alpha r)\,d\alpha, z>\ell>0 \qquad (4)$$

$$A_{\phi 2}(r,z) = \int_0^\infty [C_2 e^{\alpha z} + B_2 e^{-\alpha z}] J_1(\alpha r)\,d\alpha, \qquad (5)$$

$\ell>z>0$

$$A_{\phi 3}(r,z) = \int_0^\infty C_3 e^{\alpha_1 z} J_1(\alpha r)\,d\alpha \quad z<0 \qquad (6)$$

where α is the separation constant and $\alpha_1^2 = \alpha^2 + j\omega\mu\sigma$.

Since the electric field is proportional to A_ϕ, the boundary conditions for the tangential electric field can be satisfied by equating the values of A_ϕ at the $z=\ell$ plane.

$$\int_0^\infty B_1 e^{-\alpha\ell} J_1(\alpha r)\,d\alpha = \int_0^\infty (C_2 e^{\alpha\ell} + B_2 e^{-\alpha\ell}) J_1(\alpha r)\,d\alpha \qquad (7)$$

Multiplying both sides by the integral operator $\int_0^\infty \{\ldots\} J_1(\alpha' r)\,dr$ and using the Fourier-Bessel identity [3] give an algebraic equation for the unknown coefficients. The radial component of the magnetic field can also be found from the vector potential; $H_r = -\frac{\partial}{\partial z} A_\phi$. H_r is discontinuous at the position of the loop ($r=r_0, z=\ell$) by an amount equal to the surface current density there.

$$\left[-\frac{\partial}{\partial z} A_{\phi 1} + \frac{\partial}{\partial z} A_{\phi 2}\right]_{z=\ell} = \mu I\,\delta(r-r_0) \qquad (8)$$

which yields another equation for the coefficients. The boundary conditions may also be similarly applied at z = 0 where both E_ϕ and H_r are continuous, yielding two more expressions for the constants B_1, C_2, B_2 and C_3. These four equations can then be solved for the constants and used in Equations (4), (5), and (6) to evaluate the vector potential.

Since our principal interest lies in evaluating the vector potential at the location of the loop the most direct route is to evaluate the constant B_1:

$$B_1 = \frac{\mu I r_0 J_1(\alpha r_0)}{2}\left[e^{\alpha\ell} + e^{-\alpha\ell}\frac{(1-\frac{\alpha_1}{\alpha})}{(1+\frac{\alpha_1}{\alpha})}\right] \qquad (9)$$

Thus

$$A_{\phi 1}(r,z) = \frac{\mu I r_0}{2}\int_0^\infty J_1(\alpha r_0) J_1(\alpha r) e^{(-\alpha z - \alpha\ell)} \left[e^{+2\alpha\ell} + \left(\frac{\alpha-\alpha_1}{\alpha+\alpha_1}\right)\right] d\alpha \qquad (10)$$

The two terms in the square brackets represent respectively the vector potential due to the loop itself and that due to the currents induced in the conducting plane. This second term due to the conductive half-space, will produce the change in impedance from the case of the isolated loop to the case of the loop near the plane. This change in vector potential is thus given by this second term.

$$\Delta A_{\phi 1}(r,z) = \frac{\mu I r_0}{2}\int_0^\infty J_1(\alpha r_0) J_1(\alpha r) e^{-\alpha(z+\ell)}\left(\frac{\alpha-\alpha_1}{\alpha+\alpha_1}\right) d\alpha \qquad (11)$$

This change in vector potential can be used to calculate the change in impedance due to the presence of the conductor by integrating the tangential electric field around the position of the loop:

$$\Delta Z = \pi\omega r_0^2 j \int_0^\infty J_1^2(\alpha r_0) e^{-2\alpha\ell}\left(\frac{\alpha-\alpha_1}{\alpha+\alpha_1}\right) d\alpha \qquad (12)$$

The integrand factor $(\alpha-\alpha_1)/(\alpha+\alpha_1)$, essentially a reflection factor, has modulus equal to or less than unity, the extreme value being assumed for $\alpha=0$ and $\alpha=\infty$. The integrand factor $J_1^2(\alpha r_0)$ guarantees that the value of the integral is negligibly affected by values of α greater than about, $10/r_0$. Practical values of r_0 are usually of the order of 10^{-2}m. For such values of r_0 the important range for α is $0\le\alpha\le 10^3 m^{-1}$, while the quantity $\omega\mu_0\sigma$[=2/(skin depth)^2] is, in many practical cases, of the order of 10^7 (e.g., for aluminum at 50 KHz, $\omega\mu_0\sigma = 1.5\times 10^7$). For such cases, $\alpha^2/\omega\mu_0\sigma \le 0.1$, and $(\alpha-\alpha_1)/(\alpha+\alpha_1)$ may be expanded as a power series in $\alpha/\sqrt{\omega\mu_0\sigma}$:

$$\frac{\alpha-\alpha_1}{\alpha+\alpha_1} = -1 + \frac{2}{\sqrt{j}}\frac{\alpha}{\kappa} - \frac{2}{j}\frac{\alpha^2}{\kappa^2} + \ldots = -1 + (1-j)(\alpha\delta) + j(\alpha\delta)^2 + \ldots \qquad (13)$$

where $\delta = \sqrt{2/\omega\mu_0\sigma}$, and $\kappa = \sqrt{\omega\mu_0\sigma}$.

We expect the series above to converge rapidly

provided $\alpha\delta<<1$. As we shall presently show, it is convenient to adopt r_0 as a characteristic length. Since the value of ΔZ is determined almost entirely by values of α for which $\alpha r_0 \leq 10$, we have rapid convergence of the integrated series if $\delta/r_0<<1/10$. Separating $\Delta Z = \Delta R + j\Delta X$ into real and imaginary parts we have:

$$\Delta X = -\mu_0\omega\pi r_0^2\{\int_0^\infty J_1^2(\alpha r_0)e^{-2\alpha\ell}d\alpha - \int_0^\infty \delta J_1^2(\alpha r_0)e^{-2\alpha\ell}\alpha d\alpha\} \quad (14)$$

$$\Delta R = \mu_0\omega\pi r_0^2 \int_0^\infty \delta J_1^2(\alpha r_0)e^{-2\alpha\ell}\alpha d\alpha - \int_0^\infty \delta^2 J_1^2(\alpha r_0)e^{-2\alpha\ell}\alpha^2 d\alpha\} \quad (15)$$

These changes in resistance and reactance can be represented by three integrals:

$$\Delta X = -\pi\omega\mu_0 r_0(I_1(\beta) - (\frac{\delta}{r_0})I_2(\beta)) \quad (16)$$

$$\Delta R = \pi\omega\mu_0 r_0((\frac{\delta}{r_0})I_2(\beta) - (\frac{\delta}{r_0})^2 I_3(\beta)) \quad (17)$$

where $\beta = 2\ell/r_0$ and

$$I_1(\beta) \doteq \int_0^\infty J_1^2(x)e^{-\beta x}dx \quad (18)$$

$$I_2(\beta) \doteq -\frac{d}{d\beta} I_1(\beta) \quad (19)$$

$$I_3(\beta) \doteq \frac{d^2}{d\beta^2} I_1(\beta) \quad (20)$$

$I_1(\beta)$ is just the Laplace transform of $J_1^2(x)$ [4]:

$$I_1(\beta) = \frac{1}{\pi} Q_{1/2}(1+\frac{1}{2}\beta^2) \quad (21)$$

where $Q_{1/2}$ is the Legendre function of the second kind of order 1/2.

$I_2(\beta)$ is therefore given by

$$I_2(\beta) = -\frac{\beta}{\pi} Q'_{1/2}(1+\frac{1}{2}\beta^2) \quad (22)$$

where the prime indicates differentiation with respect to the argument. The required derivative may be found from the recursion relation [5]

$$(x^2-1)Q'_{1/2}(x) = \frac{x}{2} Q_{1/2}(x) - \frac{1}{2}Q_{-1/2}(x) \quad (23)$$

For convenience in evaluation, both $Q_{1/2}$ and $Q_{-1/2}$ may be expressed in terms of complete elliptic integrals [5]:

$$Q_{1/2}(x) = x(\frac{2}{x+1})^{1/2}K[(\frac{2}{x+1})^{1/2}] - [2(x+1)]^{1/2}E[(\frac{2}{x+1})^{1/2}] \quad (24)$$

$$Q_{-1/2}(x) = (\frac{2}{x+1})^{1/2}K[(\frac{2}{x+1})^{1/2}] \quad (25)$$

where K(k) and E(k) are respectively the complete elliptical integrals of the first and second kind of modulus k:

$$K(k) = \int_0^{\pi/2}(1-k^2\sin^2 t)^{-1/2}dt \quad (26)$$

$$E(k) = \int_0^{\pi/2}(1-k^2\sin^2 t)^{1/2}dt \quad (27)$$

Values of K(k) and E(k) may be obtained from standard tables or from readily available computer software.

$I_3(\beta)$ may likewise be reduced to an expression involving K(k) and E(k). However, for most practical cases, the factor $(\delta/r_0)^2$ by which $I_3(\beta)$ is multiplied is so small that the contribution to ΔR from the term proportional to $I_3(\beta)$ is negligible.

RESULTS

To illustrate the changes in impedance as a function of the lift-off distance ℓ and the conductivity σ, calculations were made for a loop of radius r_0 = 1.27 cm (diameter of one inch) at distances ℓ from .05 to 1.5 cm, and for conductivities from 0.1 to 4 times that of aluminum ($\sigma_0 = 3.8\times10^7$ mho/m). These results are shown in Figs. 2 and 3 as a function of ℓ for various constant conductivities. The normalized dimensionless changes in impedance $\Delta X/\omega\mu r_0$ and $\Delta R/\omega\mu r_0$ are chosen as the quantities to be plotted. For all values of conductivity the value of $\Delta X/\omega\mu r_0$ is seen to approach a large negative value as ℓ decreases showing the known decrease in total inductance as the loop approaches the plane. As ℓ becomes large $\Delta X/\omega\mu r_0$ approaches zero as required. Similarly in Fig. 2 $\Delta R/\omega\mu r_0$ is seen to give a large positive contribution for small ℓ and approaches zero as ℓ becomes large.

To illustrate the effects of the conductivity on the changes in impedance for several constant values of lift-off, the results for the same loop are shown in Figs. 4 and 5. The change in reactance $\Delta X/\omega\mu r_0$ is seen to be very nearly independent of conductivity over the range considered. The value of $\Delta R/\omega\mu r_0$, however, is seen to increase for lower values of σ. This resistance term, of course, approaches zero as the conductivity approaches that of a perfect conductor.

Both the variations in resistance and reactance can be combined into the one graph shown in Fig. 6 by plotting ΔX versus ΔR. The solid lines thus show the change in impedance as the lift-off is changed, while the dashed lines show the variation with changing conductivity for constant lift off ℓ.

The limiting values of $\Delta X/\omega\mu r_0$ for large values of σ can be checked by comparing the calculated values with that of the case of a loop above a perfectly conducting plane. Using image theory the mutual inductance between two identical loops located a distance 2ℓ apart can be found to be $M = 2.54\,Nr_0$ [6] where N is a tabulated function of r_0 and ℓ. The

values of M and ΔL at 50 KHz were compared for values of ℓ between 2.5 and 15 cm and quite good agreement was found (within 10^{-4} μH).

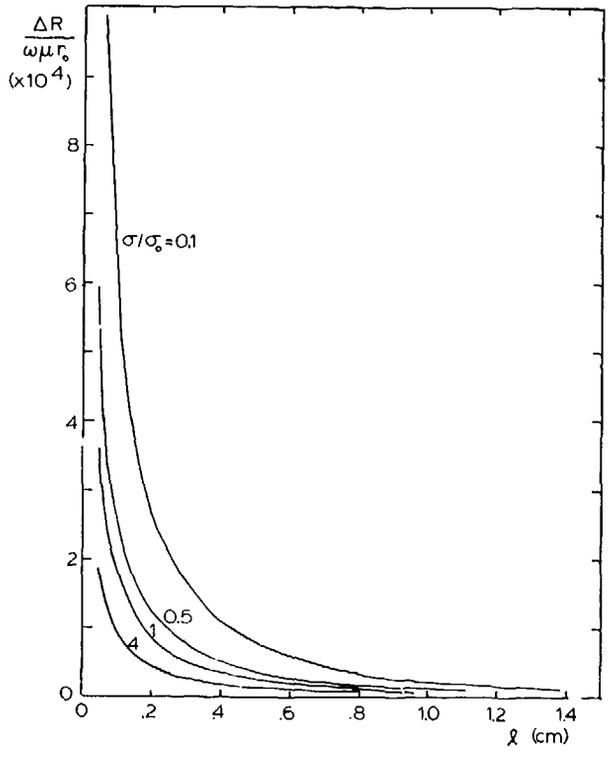

Fig. 2 Change in normalized resistance versus lift-off distance.

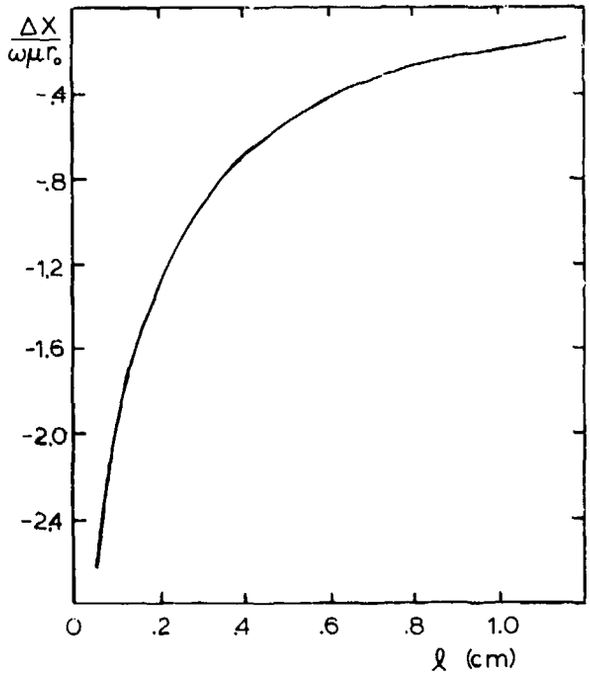

Fig. 3 Change in normalized reactance versus lift-off distance.

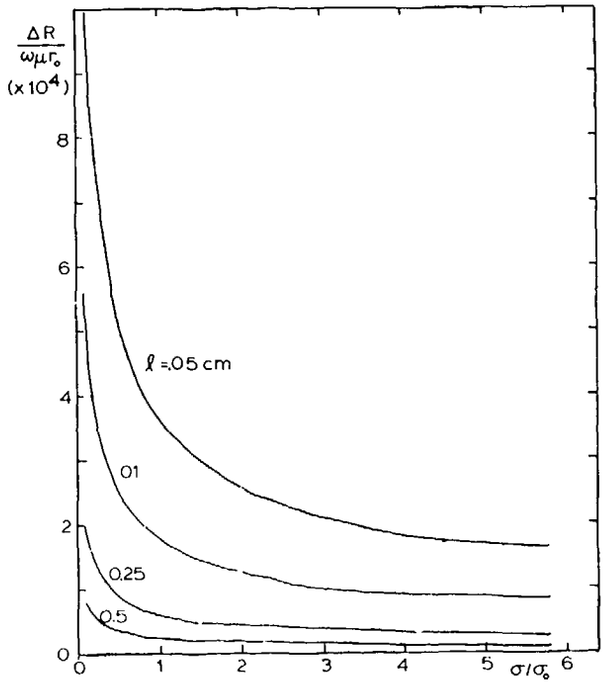

Fig. 4 Change in normalized resistance versus conductivity.

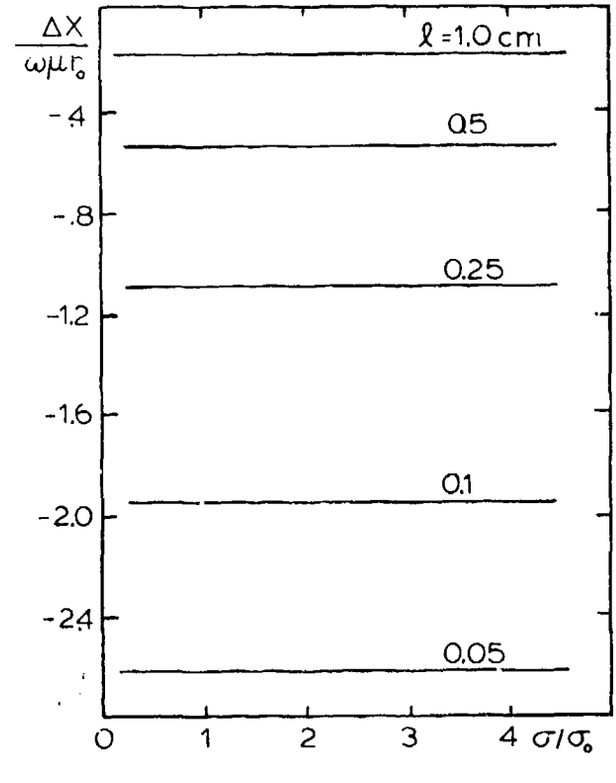

Fig. 5 Change in normalized reactance versus conductivity.

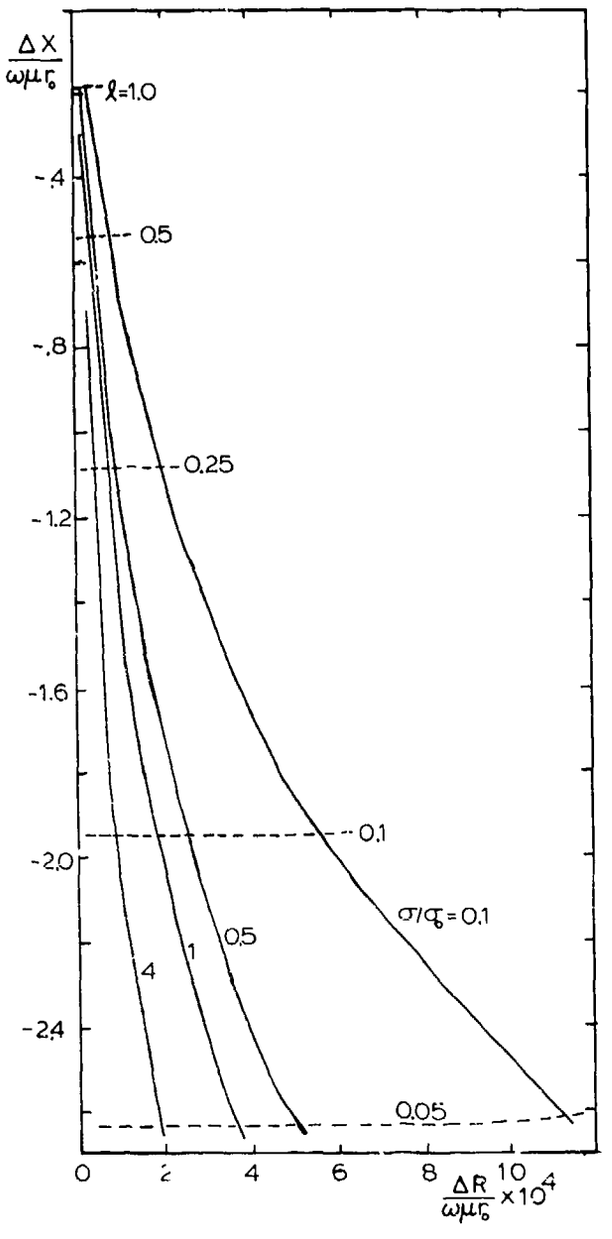

Fig. 6 Change in reactance versus change in resistance.

CONCLUSIONS

For the commonly occurring case where $\delta << 0.1 r_0$, the change in coil inductance is essentially the value that would occur if the substrate were perfectly conductive; ΔL is thus dominated by its dependence on lift-off. The change in resistance is, for constant lift-off, proportional in first order to skin depth (or, for constant frequency, proportional to the square root of substrate conductivity); however, ΔR is also strongly dependent upon lift-off. Second-order changes in ΔL and ΔR, due to small variations in ℓ and σ about nominal values, are well approximated by linear functions of $\Delta\ell$ and $\Delta\sigma$; hence variations in ΔL and ΔR may readily be interpreted in terms of corresponding variations in lift-off and conductivity.

REFERENCES

[1] David H.S. Cheng, "The Reflected Impedance of a Circular Coil in the Proximity of a Semi-Infinite Medium," IEEE Transactions on Instrumentation and Measurement. Vol. 14, No. 3, pp. 107-116, Sept. 1965.

[2] C.V. Dodd and W.E. Deeds, "Analytical Solutions to Eddy-Current Probe-Coil Problems," J. Applied Physics, Vol. 39, No. 6, pp. 2829-2838, 1968.

[3] G. Arfken, "Mathematical Methods for Physicists," 2nd ed., p. 495, Academic Press, N.Y., 1970.

[4] A. Erdelyi et. al., "Tables of Integral Transforms," Vol.1, p. 183, McGraw-Hill, Inc., 1954.

[5] M. Abramowitz and I. Stegun, "Handbook of Mathematical Functions," pp. 334-337, 9th ed., Dover Publications, Inc., N.Y., 1970.

[6] F.E. Terman, "Radio Engineers Handbook," p. 67, McGraw-Hill Book Co., Inc., N.Y., 1943.

ACKNOWLEDGEMENTS

This work was supported in part by the U.S. Air Force Office of Scientific Research through Grant No. 77-3457 and by the Energy Laboratory of the University of Houston through Grant LAP-K-30.

Jim Martin, Chairman (Rockwell Science Center): Thank you. That was an excellent presentation. We have time, I think, for one question. Please remember to identify yourself.

Mr. Lincoln (USC): Did you compare your theory with the case of a single straight wire over a conducting plane by letting the radius of your loop become large and calculating the induction for the loop?

Stuart Long (University of Houston): No, I did not.

Mr. Lincoln: That should also work.

Stuart Long: Would you still have to assume a perfect conductor?

Mr. Lincoln: No, that has already been done.

Stuart Long: Okay, that would be a good test, then.

Jim Martin, Chairman: We will defer the remainder of the presentations until after the break.

Progress in Solving the 3-Dimensional Inversion Problem for Eddy Current NDE

T.G. Kincaid, K. Fong, M.V.K. Chari
General Electric Company
Schenectady, N. Y. 12345

ABSTRACT

The eddy current NDE inversion problem is to determine the parameters of a flaw from the measured eddy current sensor impedance changes. Mathematically, this requires finding the transformation which gives the sensor impedance changes in terms of the flaw parameters, and then inverting this transformation. Finding the transformation is called the forward problem, and finding the inverse of the transformation is equivalent to the inversion problem. The principal difficulty in solving the forward problem is finding solutions to Maxwell's equations in the complex geometries involved. This paper describes a solution to the forward problem which is valid for ellipsoidal shaped void flaws in a non-magnetic conductor, and for flaw dimensions such that the incident field variations are at most linear over the region occupied by the flaw.

INTRODUCTION

The eddy current NDE inversion problem is to determine the parameters of a flaw from the measured eddy current sensor impedance changes. Mathematically, this requires finding the transformation which gives the sensor impedance changes in terms of the flaw parameters, and then inverting this transformation. Finding the transformation is called the forward problem, and finding the inverse is equivalent to the inversion problem.

The principal difficulty in solving the forward problem is finding the solution to Maxwell's equations in the complex geometries involved. The first significant contribution to this problem was the work of Burrows [1], who used the reciprocity theorem and a scattering theory to derive the general form of the transformation between the sensor voltage change and the incident and scattered fields associated with the flaw. In order to get around the difficulties associated with solving Maxwell's equations, Burrows assumed the flaw to be small compared to the spatial variations of the incident field. This is usually not the case, and it eliminates important phase information. The next major advance was made by Dodd et al [2], who recognized that the field incident upon the flaw could be computed by numerical integration techniques, and then Burrows' result could be used to calculate the change in sensor impedance. However, the restriction to flaws which are small compared to the incident field variation remained.

In a previous paper [3] the authors made two advances upon these ideas. First, the incident field was computed by the finite element method (FEM), which is very accurate and can be applied generally. (In fact, the FEM is good enough to solve the forward problem numerically, although this is expensive since the computation must be made for each value of the flaw parameter, and it does not yield the "understanding" of a formula) Second, Burrows' scattering theory was extended to the case of a flaw which is small enough that the incident field varies at most linearly over the flaw dimensions. However, both the FEM and the scattering theory were developed only for two dimensional problems.

In this paper, the scattering theory is extended to three dimensions for the case of an ellipsoidal shaped void flaw in a non-magnetic conductor, with flaw dimensions such that the incident field variations are at most linear over the flaw dimensions.

THREE COMPONENT SCATTERING THEORY

The Scattering Model

In the scattering theory approach to the solution of the forward problem, the change in sensor impedance is found from the incident and scattered fields of the flaw by using the reciprocity theorem, as explained by Auld [4]. For a void flaw in a linear homogeneous, isotropic, conducting medium with free space permittivity and permeability, the change ΔZ in sensor impedance is given by

$$\Delta Z = \frac{1}{I^2} \int_{V_f} \sigma(\bar{E}.\bar{E}') \, dv \qquad (1)$$

where: σ = conductivity of the medium
I = the current at the sensor terminals
$\bar{E}'$ = the electric field without the flaw
$\bar{E}$ = the electric field with the flaw
dv = a differential volume element
V_f = the volume of the flaw

Therefore, to compute the sensor impedance change, it is necessary to compute the electric fields within the boundaries of the flaw both when the flaw is present and when it is not.

The strategy for computing these electric fields is to approximate the incident field in the vicinity of the flaw by its constant plus linearly varying components. The respective scattered

fields are then approximated for an ellipsoidal flaw by the dipole and quadrupole field solutions to the static form of Maxwell's equations. For each component of the incident field, there will be a scattered field solution internal to the flaw and one external to the flaw.

The strengths of these scattered fields are found by matching the boundary conditions for the incident, exterior scattered, and interior scattered fields at the boundary of the ellipsoidal flaw. For a void flaw, the boundary conditions are:

1) the current normal to the flaw boundary is zero i.e. the electric field outside the flaw and normal to the boundary is zero

2) the electric field tangential to the flaw boundary is continuous across the boundary

Note that condition 1) does not require the electric field inside the flaw and normal to the boundary to be zero. This field can terminate on charges on the surface of the flaw.

For the constant and linearly varying components of the incident field, condition 1) will be met respectively by the normal component of the external dipole and quadrupole scattered fields. Condition 2) is met by continuing the incident fields into the flaw to match the tangential components of the incident fields, and by adding internal dipole and quadrupole scattered fields to match the tangential components of the respective external scattered fields.

The Incident Field

The incident field is conveniently described in a cartesian coordinate system with origin at the center of the ellipsoidal flaw. The coordinates x, y, z are aligned with the principal axes of the ellipsoid. The general expression for the incident electric field induced by the eddy current is

$$E = \bar{i}_x E_x + \bar{i}_y E_y + \bar{i}_z E_z \tag{2}$$

where $\bar{i}_x$ is a unit vector in the x-direction, and similarly for $\bar{i}_y$, $\bar{i}_z$. Expanding each of the field components in a Taylor series about the origin gives, to first order

$$\begin{aligned} E_x &= E_1 + A_{11}x + A_{12}y + A_{13}z \\ E_y &= E_2 + A_{21}x + A_{22}y + A_{23}z \\ E_z &= E_3 + A_{31}x + A_{32}y + A_{33}z \end{aligned} \tag{3}$$

This approximation expresses the incident field as the sum of a constant plus a linearly varying field.

The field described by (2) and (3) must have zero divergence since it is induced by an electric current in a conductor. For this to be true, the trace of the matrix of coefficients A_{ij} must be zero. In many cases of practical interest this condition is satisfied because the diagonal terms are individually zero.

The curl of the field described by (2) and (3) will be zero if and only if the matrix of coefficients A_{ij} is symmetric. In general, this will not be true. Thus the incident field cannot be uniquely described as the gradient of a scalar potential. Because of this, the scattering problem is solved here directly in terms of the electric fields rather than potentials.

The Scattered Fields

The scattered fields are most conveniently described in an ellipsoidal coordinate system. The particular form described by Stratton [5] is used here. In this system, the coordinates ξ, η, and ζ are defined by their transformation to cartesian coordinates

$$\begin{aligned} x &= \pm \frac{(\xi + a^2)(\eta + a^2)(\zeta + a^2)}{(b^2 - a^2)(c^2 - a^2)}, \\ y &= \pm \frac{(\xi + b^2)(\eta + b^2)(\zeta + b^2)}{(c^2 - b^2)(a^2 - b^2)}, \\ z &= \pm \frac{(\xi + c^2)(\eta + c^2)(\zeta + c^2)}{(a^2 - c^2)(b^2 - c^2)}. \end{aligned} \tag{4}$$

where $-a^2 < \zeta < -b^2 < \eta < -c^2 < \xi$. The surface ξ = constant is an ellipsoid with principal axes of length a, b, c aligned along the x, y, z axes respectively. The surface η = constant is a hyperboloid of one sheet, and the surface ζ = constant a hyperboloid of two sheets. Since Maxwell's equations are linear in this application, the scattered fields can be determined separately for each of the 12 components of (3), and the results added to give the total scattered field.

The internal and external scattered fields are approximated by solutions to the static form of Maxwell's equations. These solutions can be derived from potentials which are known solutions to Laplace's equations. In ellipsoidal coordinates, the solutions to Laplace's equation are the Lame functions [6].

For the components of the constant incident field, the potentials of the induced internal scattered fields are products of the Lame functions of the 1st kind of degree 1. These are

$$\begin{aligned} F_a(\lambda) &= \sqrt{\lambda + a^2} \\ F_b(\lambda) &= \sqrt{\lambda + b^2} \\ F_c(\lambda) &= \sqrt{\lambda + c^2} \end{aligned} \tag{5}$$

For example, for the $\bar{i}_x E_1$ component of the constant incident field, the potential of the internal scattered field is of the form

$$\psi_{xi} = K_{xi} F_a(\xi) F_a(\eta) F_a(\zeta) \quad . \tag{6}$$

The field derived from this potential is called an "internal dipole" field in this paper. The field is actually constant.

The potentials of the corresponding external scattered fields are products of the Lame functions of the 1st and 2nd kind of degree 1. The Lame functions of the 2nd kind of degree 1 are the of the form

$$G_a(\lambda) = H_a(\lambda) F_a(\lambda) \tag{7}$$

$$\text{where } H_a(\lambda) = \int_\lambda^\infty \frac{ds}{R(s) F_a^2(s)} \tag{8}$$

$$\text{and } R(s) = \sqrt{(s + a^2)(s + b^2)(s + c^2)} \tag{9}$$

with similar expressions for $G_b(\lambda)$ and $G_c(\lambda)$. As an example, the potential of the external scattered field induced by the $\bar{i}_x E_1$ component

$$\psi_{xe} = K_{xe} G_a(\xi) F_z(\eta) F_z(\zeta) \quad . \tag{10}$$

The field derived from this potential is a true dipole field, and is called an "external dipole" field in this paper.

The total electric field solution for a field component $\bar{i}_x E_1$ incident upon an ellipsoidal void is found by matching the boundary conditions 1) and 2) above at the surface of the flaw.

The procedure is as follows. The amplitude of the external dipole field is determined by setting its ξ component equal and opposite to the ξ component of the constant incident field component at the flaw boundary, $\xi = 0$. This satisfies condition 1), i.e. the current normal to the flaw boundary is zero. Next, the constant incident field is continued into the flaw interior to satisfy condition 2) for the constant incident field, i.e. the tangential electric field is continuous across the boundary. Finally, the η and ζ components of the internal dipole field are made equal in amplitude to the η and ζ components of the external dipole field at the flaw boundary, $\xi = 0$. This satisfies condition 2) for the external dipole. The ξ components of the internal fields are terminated by charges on the conducting surface of the flaw. By applying this procedure for each of the 3 cartesian components of the constant part of the incident field, the amplitudes of the induced internal fields can be found. It is these internal fields which are needed for the $\bar{E}'$ term in (1), along with the internal fields induced by the components of the linearly varying part of the incident field.

The total internal fields induced by the constant field components are given in Table 1, along with their special forms for the case of a sphere (a=b=c) and a disc (a=b, c=o) flaw. Note that the total internal field for each component is the sum of two fields, a constant field equal to the incident field, plus an internal dipole field (which is also a constant field).

For the components of the linearly varying incident field, the potentials of the induced internal scattered fields are products of the Lame functions of the first kind of degree 2. Only components of the linearly varying incident field corresponding to the off-diagonal terms in (3) will be considered here, since the diagonal terms are usually zero in practical problems of interest.

For this case, the corresponding Lame functions of the first kind of degree 2 are

$$\begin{aligned} F_{ab}(\lambda) &= \sqrt{(\lambda + a^2)(\lambda + b^2)} \\ F_{bc}(\lambda) &= \sqrt{(\lambda + b^2)(\lambda + c^2)} \\ F_{ca}(\lambda) &= \sqrt{(\lambda + c^2)(\lambda + a^2)} \quad . \end{aligned} \tag{11}$$

For example, for the $\bar{i}_x A_{12} y$ component of the incident field, the potential of the internal scattered field is of the form

$$\psi_{xyi} = K_{xyi} F_{ab}(\xi) F_{ab}(\eta) F_{ab}(\zeta) \quad . \tag{12}$$

Analogous to the case of the dipole scattered field above, it is convenient to call the field derived from this potential an "internal quadrupole" field.

The potentials of the corresponding "external quadrupole" scattered fields are products of the Lame functions of the 2nd kind of degree 1 and degree 2. The Lame functions of the 2nd kind of degree 2 are of the form

$$G_{ab}(\lambda) = H_{ab}(\lambda) F_{ab}(\lambda) \tag{13}$$

$$\text{where } H_{ab}(\lambda) = \int_\lambda^\infty \frac{ds}{R(s) F_{ab}^2(S)} \tag{14}$$

with similar expressions for $G_{bc}(\lambda)$ and $G_{ca}(\lambda)$. As an example, the potential of the external

Table 1 - Internal Scattered Fields for a Constant Incident Field

INCIDENT	INTERNAL		
	Ellipsoid	Sphere	Disc
$\bar{i}_x E_1$	$\bar{i}_x E_1 - \bar{i}_x \frac{1}{2a^2} \frac{H_a(0)}{P_b(0)} E_1$	$\bar{i}_x \frac{3}{2} E_1$	$\bar{i}_x E_1$
$\bar{i}_y E_2$	$\bar{i}_y E_2 - \bar{i}_y \frac{1}{2b^2} \frac{H_b(0)}{P_b(0)} E_2$	$\bar{i}_y \frac{3}{2} E_2$	$\bar{i}_y E_2$
$\bar{i}_z E_3$	$\bar{i}_z E_3 - \bar{i}_z \frac{1}{2c^2} \frac{H_c(0)}{P_c(0)} E_3$	$\bar{i}_z \frac{3}{2} E_3$	$\bar{i}_z \frac{2}{\pi} \frac{a}{c} E_3$

where $P_a(0) = \frac{1}{2a^2} H_a(0) + H'_a(0)$

Table 2 - Internal Scattered Fields for a Linearly Varying Incident Field

INCIDENT	INTERNAL		
	Ellipsoid	Sphere	Disc
$\bar{i}_x A_{12}{}^y$	$\bar{i}_x A_{12}{}^y - \frac{1}{2a^2} \frac{H_{ab}(0)}{P_{ab}(0)} A_{12} \quad (\bar{i}_x y + \bar{i}_y x)$	$\bar{i}_x \frac{4}{3} A_{12}{}^y + \bar{i}_y \frac{1}{3} A_{12}{}^x$	$\bar{i}_x A_{12}{}^y$
$\bar{i}_x A_{13}{}^z$	$\bar{i}_x A_{13}{}^z - \frac{1}{2a^2} \frac{H_{ac}(0)}{P_{ac}(0)} A_{13} \quad (\bar{i}_x z + \bar{i}_z x)$	$\bar{i}_x \frac{4}{3} A_{13}{}^z + \bar{i}_z \frac{1}{3} A_{13}{}^x$	$\bar{i}_x A_{13}{}^z$
$\bar{i}_y A_{21}{}^x$	$\bar{i}_y A_{21}{}^x - \frac{1}{2b^2} \frac{H_{ba}(0)}{P_{ba}(0)} A_{21} \quad (\bar{i}_y x + \bar{i}_x y)$	$i_y \frac{4}{3} A_{21}{}^x + i_y \frac{1}{3} A_{21}{}^y$	$i_y A_{21}{}^x$
$\bar{i}_y A_{23}{}^z$	$\bar{i}_y A_{23}{}^z - \frac{1}{2b^2} \frac{H_{bc}(0)}{P_{bc}(0)} A_{23} \quad (\bar{i}_y z + \bar{i}_z y)$	$\bar{i}_y \frac{4}{3} A_{23}{}^z + \bar{i}_z \frac{1}{3} A_{23}{}^y$	$\bar{i}_y A_{23}{}^z$
$\bar{i}_z A_{31}{}^x$	$\bar{i}_z A_{31}{}^x - \frac{1}{2c^2} \frac{H_{ca}(0)}{P_{ca}(0)} A_{31} \quad (\bar{i}_z x + \bar{i}_x z)$	$\bar{i}_z \frac{4}{3} A_{31}{}^x + \bar{i}_x \frac{1}{3} A_{31}{}^z$	$\frac{4}{3\pi} \frac{a}{c} (\bar{i}_z A_{31}{}^x + \bar{I}_x A_{31}{}^z)$
$\bar{i}_z A_{32}{}^y$	$\bar{i}_z A_{32}{}^y - \frac{1}{2c^2} \frac{H_{cb}(0)}{P_{cb}(0)} A_{32} \quad (\bar{i}_z y + \bar{i}_y z)$	$\bar{i}_z \frac{4}{3} A_{32}{}^y + \bar{i}_y \frac{1}{3} A_{32}{}^z$	$\frac{4}{3\pi} \frac{a}{c} (\bar{i}_z A_{32}{}^y + \bar{i}_y A_{32}{}^x)$

where $P_{ab}(0) = \frac{1}{2} (\frac{1}{a^2} + \frac{1}{b^2}) H_{ab}(0) + H'_{ab}(0)$

quadrupole scattered field induced by the $i_x A_{12} y$ component of the incident field is

$$\psi_{xye} = K_{xye}\, G_{ab}(\xi)\, F_{ab}(\eta)\, F_{ab}(\zeta) \qquad (15)$$

The total electric field solution for a field component $\bar{i}_x A_{12} y$ incident upon an ellipsoidal void is found by matching the boundary conditions in a manner similar to the procedure described above for the constant incident fields and dipole scattered fields.

The total internal fields induced by the linearly varying field components are given in Table 2, along with their special forms for the case of a sphere and a disc flaw. Analogous to the results shown in Table 1, note that the total internal field for each component is the sum of two components, a linearly varying field equal to this incident field, plus an internal quadrupole field (which is the sum of two linearly varying fields).

EXAMPLES

Spherical Flaw

Consider the case of a spherical void flaw of radius a in the volume of a conducting material with conductivity σ. Assume the incident field is only in the x-direction, and that it can be represented in the region of the flaw by the approximation

$$\bar{E} = \bar{i}_x (E_1 + A_{12} y) \qquad (16)$$

where E_1 and A_{12} are complex constants.

The field internal to the flaw is the sum of the responses to the constant and linearly varying fields respectively, as given in Tables 1 and 2.

$$\bar{E}' = \bar{i}_x \frac{3}{2} E_1 + \bar{i}_x \frac{4}{3} A_{12} y + \bar{i}_y \frac{1}{3} A_{12} x \qquad (17)$$

substituting the fields $\bar{E}$ and $\bar{E}'$ into (1) and integrating over the volume of the flaw gives

$$\Delta Z = \frac{\sigma}{I^2} \left(2\pi a^3 E_1^2 + \frac{16}{45} \pi a^5 A_{12}^2\right). \qquad (18)$$

Disc Shaped Flaw

Consider the case of a disc shaped flaw, which is an ellipsoid with a = b and $c \to 0$, in the volume of a conducting material of conductivity σ. The principal axes a, b, c are aligned with the coordinates x, y, z respectively.

Assume first that the incident field is given by (16) above. Then the field internal to the flaw is the sum of the responses to the constant and linearly varying fields respectively, as given in Tables 1 and 2.

$$\bar{E} = \bar{i}_x (E_1 + A_{12} y) \qquad (19)$$

as $c \to 0$, the volume of the flaw goes to zero, and the integral in (1) goes to zero. Therefore,

$$\Delta Z = 0 \qquad (20)$$

which says that a crack cannot be detected by a field which sees only its edge.

Assume now that the incident field is given by

$$\bar{E} = \bar{i}_z (E_3 + A_{31} x). \qquad (21)$$

For this case, the field internal to the flaw is found from Tables 1 and 2 to be

$$\bar{E}' = \bar{i}_z \frac{2}{\pi} \frac{a}{c} E_3 + \left(\frac{4}{3\pi} \frac{a}{c} A_{31}\right)(\bar{i}_z x + \bar{i}_x z). \qquad (22)$$

The corresponding impedance change is found from (1) to be

$$\Delta Z = \frac{\sigma}{I^2} \left(\frac{8}{3} a^3 E_3^2 + \frac{16}{45} a^5 A_{31}^2\right). \qquad (23)$$

Note that ΔZ is independent of the thickness c of the flaw when $c \to 0$.

ACKNOWLEDGEMENT

This work was sponsored by the Center for Advanced NDE operated by the Science Center, Rockwell International, for the Advanced Research Projects Agency and the Air Force Materials Laboratory under Contract F33615-80-C-5004.

References

[1] Burrows, M. L., A Theory of Eddy Current Flaw Detection, University of Michigan Ph.D. Thesis, 1964, University Microfilms, Ann Arbor, Mich.

[2] Dodd, C.V. et al, "Optimizing Defect Detection in Eddy Current Testing", Materials Evaluation, March 1971, pp. 59-63.

[3] Kincaid, T.G. et al, "Two Approaches to Solving the Inversion Problem for Eddy Current NDE", Proceedings of the ARPA/AFML Review of Progress in Quantitative NDE, Rockwell International Report to Air Force Materials Laboratory, 1979.

[4] Auld, B.A., "Quantitative Modeling of Flaw Responses in Eddy Current Testing", Fourth Monthly Report, Electric Power Research Institute Contract No. RPI395-3, Feb. 1979.

[5] Stratton, J.A., Electromagnetic Theory, McGraw Hill, New York, 1941, First Edition.

[6] Whittaker, E.T. and Watson, G.N., Modern Analysis, Cambridge U. Press, 1952, Fourth Edition.

DEVELOPMENT OF EDDY-CURRENT PROBES FOR THE EVALUATION OF MAGNETITE IN THE SUPPORT-PLATE CREVICES OF NUCLEAR STEAM GENERATORS

A. Sagar
Westinghouse Nuclear Technology Division
Pittsburgh, Pennsylvania 15230

ABSTRACT

Eddy current technique has played an important role in the understanding of the corrosion behavior of steam generator components. Until recently, its role has been primarily in the evaluation of the condition of the heat exchanger tubes. Recent developments have led to the use of this technique for detecting corrosion of the carbon steel plates supporting the tubes. The detection and quantification of possible accumulation of corrosion products such as magnetite in the crevices between tubes and supports may often be a desired objective of such inspections since the presence of such deposits is of interest with respect to tube denting and other corrosion phenomena. This paper discusses the difficulty of an unambiguous determination of the presence of magnetite in the tube support crevices and points to the difficulty of obtaining a quantitative estimate for the amount of magnetite which may be present. This paper further discusses the development of new probes which provide improved discrimination between magnetite and a steel support thus providing for a better estimate of the amount of magnetite in tube support crevices.

INTRODUCTION

Eddy current technique has been extensively used for the inservice inspection of nuclear steam generators. The inspections have usually involved the evaluation of the heat exchanger tubes. Recent developments regarding the tube denting phenomena in steam generators have led to an increased interest in the evaluation of the carbon steel support plates and the crevices between tubes and the supports. Although the detection of corrosion of the support plate could be accomplished at some stage by an evaluation of the distortions of the support plate signals, a quantitative estimate of the corrosion of the I.D. of the supports using the standard eddy current inspection data has not been possible. The multi-frequency technique and the use of linear combinations of the multi-frequency data have reduced the ambiguities in the data interpretation and have improved our ability to quantify the depth of tube wall discontinuities in the presence of interfering signals from such sources as support plates, metallic and magnetic deposits on the O.D. of the tubes, etc. However, this technique has not been useful for quantifying the corrosion of the steel supports. An estimate of the I.D. of the support plate holes could be accomplished from the standard eddy current data if one could assume that there are no magnetic or electrically conducting deposits in the crevices. Such an assumption is generally not valid, however, due to the presence of magnetite (one of the products of steel plate corrosion) in the crevices. The varification of its presence can be accomplished by a careful examination of standard eddy current inspection data but the quantification of the amount of magnetite deposits has not been possible from this data.

The detection of magnetic oxides such as magnetite in the absence of other interfering signals such as signals from carbon steel is quite straight forward and has been routinely carried out for years in terms of sludge height determination using the standard eddy current data since the sludge is known to contain magnetic materials. The difficulty of a quantitative evaluation of magnetite build up in the crevices of tube support plates arises because of the interference from the steel support signals which themselves may change upon corrosion of these steel supports. In order to accomplish a quantitative evaluation of magnetite build up and of the I.D. of the tube support, we need sensors which have higher sensitivity for magnetite than for carbon steel (or vice versa).

The conventional probes used for steam generator inspection consist of two circumferential coils within approximately 0.060 inches (1.6 mm)of each other (Fig. 1). The inspection is performed

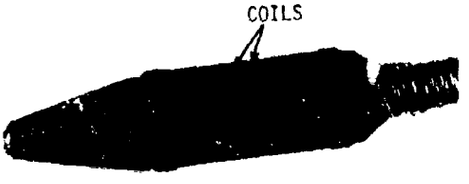

Fig. 1 The conventional eddy current probe used for Steam Generator Inspection consisting of two circumferentially wound coils within 0.060 inches (1.5 mm) of each other.

from the I.D. side of the tubes. The test frequencies used range from about 3 kHz to 500 kHz depending on the objective of the test and the

thickness of heat exchanger tube wall. For the evaluation of the tube support plates and the crevices, the test is performed in the low frequency range (below 10 kHz) in order to minimize the interference from the signals representing discontinuities in the tube wall. The probes can be used in differential or in absolute mode.

This paper discusses the relative sensitivities of the conventional probe (used in normal steam generator inspections) for the magnetite and for the steel supports surrounding the Inconel-600 tubes. It is shown that this probe is quite sensitive to both magnetite and the carbon steel support plate.This results in complicated signals when the two are present simultaneously and makes the job of obtaining a reliable estimate of the I.D. of the steel support or the thickness of the magnetite in the crevice well near impossible. It is further shown that the new probes described in this paper have preferential sensitivity for one (e.g. magnetite) relative to the other (e.g. steel support) for our sample geometry. The work reported here is directed towards designing probes which have large differences in the sensitivities for the two components (magnetite and steel supports) and have 90° phase discrimination between the signals from the two at low enough operating frequencies such that the signals from the tube wall discontinuities would not interfere with the evaluation of the steel support and of the magnetite in the crevice.

EXPERIMENTAL

The geometry of the test specimens used in this work is shown in Fig. 2. The tube alloy was Inconel-600. The O.D. of the tube was 0.875 inches (22.2 mm) and the nominal thickness of the tube wall was 0.050 inches (1.27 mm). The carbon steel support plate sample was 0.75 inches (19 mm) thick and the hole diameter was 1.00 inch (25.4 mm). The magnetite cylinder used was 0.050 inches (1.27 mm) thick a d 0.75 inches (19 mm) long. The density of magnetite was about 93% of the theoretical density. An organic binder was mixed in magnetite powder to fabricate the magnetite samples.

The eddy current instrument used was Model EM3300 (Automation Industries, Inc.). The conventional probe used here was similar to the ones used for standard inspections of steam generators (Fig. 1).

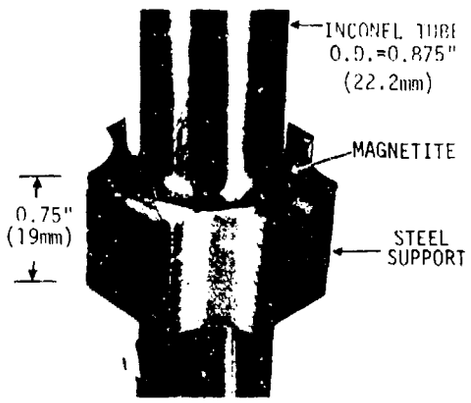

Fig. 2 The crevices between the Inconel-600 tubes and the carbon steel support plates may contain corrosion products such as magnetite.

RESULTS

Figure 3a shows the eddy current signals using the conventional probe of Fig. 1 in the absolute mode at different test frequencies from (1) magnetite cylinder, (2) steel support sample and (3) steel support with magnetite cylinder in the crevice surrounding the Inconel-600 tube. The data shows that the sensitivity of this probe for steel support relative to its sensitivity for magnetite increases slightly with the test frequency. However, the probe sensitivities for our magnetite sample and the steel support sample remain about the same (within 30%) in the frequency range of our work. Because of this somewhat similar sensitivity for the two, the signals marked (3) obtained when the magnetite cylinder is present in the tube support crevice are quite complicated and do not lend themselves to any quantitative evaluation of either the steel support or the magnetite thickness. The addition of magnetite in the crevice results in a counter-clockwise rotation of the steel support signal in addition to the change in its shape. This is most obvious in the low frequency data. The counterclockwise rotation of the signal signifies the presence of high magnetic permeability material in the crevice. It may be noted that at 7 kHz test frequency, there is 90° phase angle separation between the steel support signal and the magnetite signal.

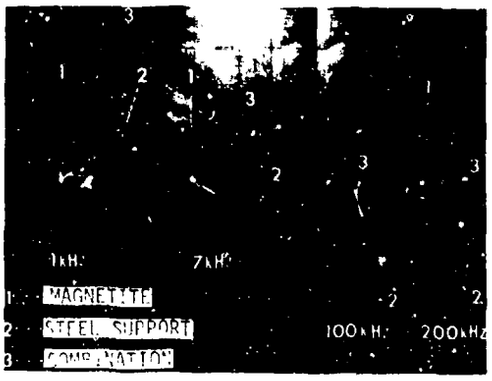

Fig. 3a The eddy current signals using the conventional probe in the absolute mode showing similar sensitivities for magnetite and steel support samples surrounding Inconel-600 tube.

Figure 3b shows the data when the conventional probe is used in the differential mode. Here again, the data shows that the probe has about the same sensitivity for our magnetite as for the steel support sample surrounding the Inconel tube. The meaning of the slope of the signal is not quite so simple here since the separation between the two coils is much smaller than the length of the steel support sample (0.75 inches, 19 mm). If we define the slope of the signal as the slope of the straight line joining the points of maximum amplitude, we note that the angle between the two signals increases with frequency. The counter-clockwise rotation of the steel support signal on the addition of magnetite in the crevice is also apparent in these data. Of course, the 90° phase separation between signals 1 and 2 at 7 kHz noted in the absolute mode data is not obvious here because of the lack of precise definition of signal phase for the differential mode case.

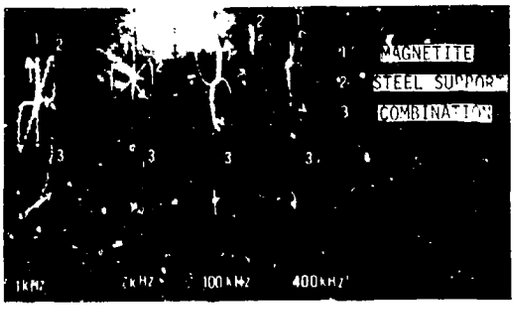

Fig 3b The eddy current signals using the conventional probe in differential mode showing similar sensitivities for magnetite and steel support sample surrounding Inconel-600 tube.

Figure 4a shows the lift-off traces at different test frequencies from magnetite and from carbon steel for a pancake coil of diameter 0.245 ±0.055 inches (6.2 ±1.4 mm). Figure 4b shows similar data for the pancake coil of diameter 0.420±0.035 inches (10.7±0.9mm). The phase angle separation between the magnetite and the carbon steel signals increases with test frequency for both coils as expected(1). For the larger coil, the 90° phase angle separation between the two signals occurs at 150 kHz whereas it occurs at 260 kHz for smaller coil. Of course, the amplitude discrimination between the two signals when they have 90° separation is slightly higher for the smaller coil. At 1 kHz and 10 kHz test frequencies, the magnetite signal is smaller than the carbon steel signal. This is perhaps an indication of lower effective magnetic permeability value for our magnetite sample than for carbon steel.

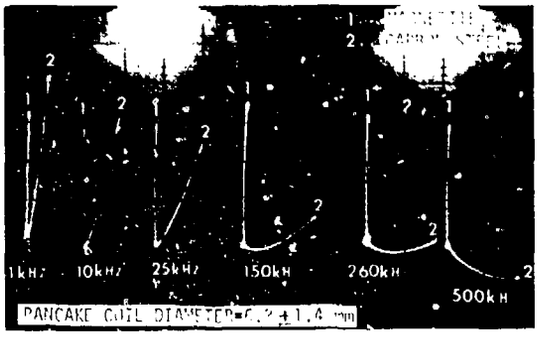

Fig. 4a The lift-off traces for a 0.245 inch (6.2 mm) diameter pancake coil showing that the sensitivity for carbon steel relative to magnetite decreases with the test frequency.

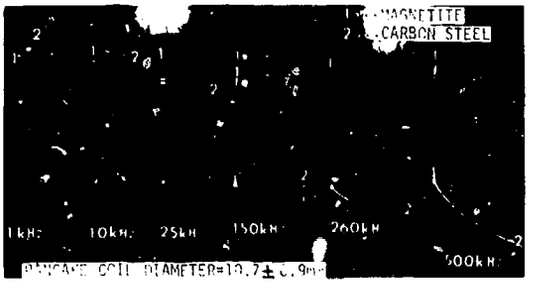

Fig. 4b The lift-off traces for a 0.42 inches (10.7mm) diameter pancake coil showing that the sensitivity for carbon steel relative to magnetite decreases with the test frequency.

Figure 5a shows the signals obtained from the same magnetite and steel support samples surrounding an Inconel-600 tube as in Figs.3a and 3b but using a different probe (also shown in the figure). This probe consists of two circumferential coils wound in opposition and connected in series. It has higher sensitivity for the magnetite sample than for the steel support. This probe has optimum performance near 100 kHz. At this frequency, the phase separation between the two signals is 90° and the ratio of the amplitudes of the signals from magnetite and from steel support is about three. Furthermore, the signal from the combination of magnetite and steel support is about the same as from the magnetite sample alone. The best frequency for 90° phase separation for signals 1 and 2 can be changed by simply changing the spacing between the two coils (Fig. 5b). It may be noted from Fig. 5b that by increasing the coil spacing, the test frequency for the 90° phase separation is lowered from 100 kHz (Fig. 5a) to 16 kHz. However, it may be observed that this results in somewhat similar sensitivities for the two samples (magnetite and steel support) and is therefore not of practical value for a quantitative evaluation of the steel support or of the magnetite in the crevice. Decreasing the spacing between the two coils improves the sensitivity for magnetite as compared to its sensitivity for steel support but it also increases the test frequency for 90° phase discrimination between the two signals.

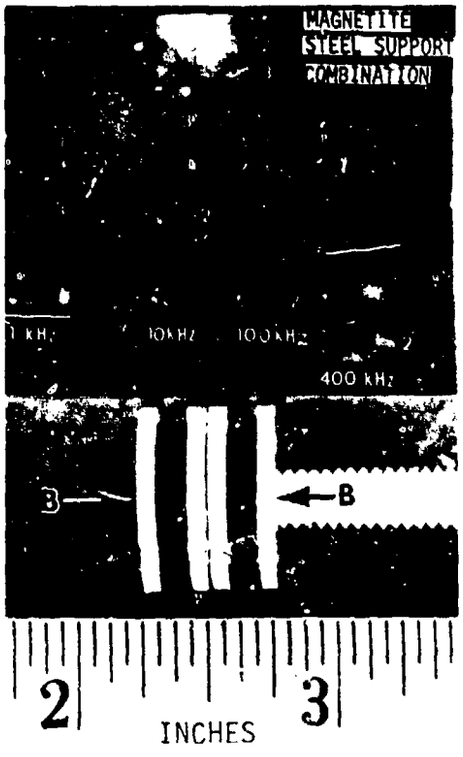

Fig. 5a The eddy current signals using the new probe consisting of two circumferential coils wound in opposition and connected in series, show that the new probe has higher sensitivity for magnetite sample surrounding Inconel-600 tube than for steel support sample surrounding Inconel-600 tube.

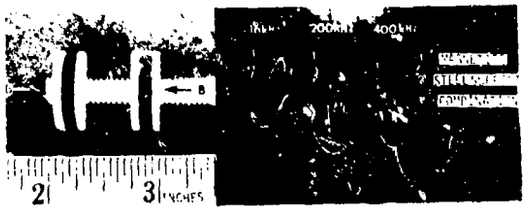

Fig. 5b The eddy current signals from steel support and magnetite samples surrounding Inconel-600 tube obtained by using the modified version of the probe of Fig. 5a. The data shows that the phase separation between the two signals can be changed by simply changing the spacing between the two coils.

Figure 6 shows the signals obtained from the samples using a probe consisting of eight pancake coils in series. The coils were wound on a ferrite piece about 0.25 inch (6.35 mm) thick. The probe has optimum characteristics near 200 kHz. At this frequency there is 90° phase separation between signals 1 and 2 and the ratio of the amplitudes of magnetite signal to steel support signal is about 4. Also the magnetite signal is almost unchanged by the presence of the steel support.

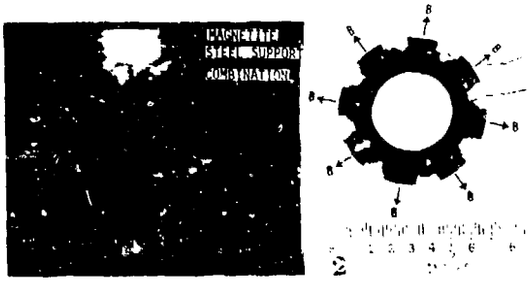

Fig. 6 The eddy current signals from magnetite and steel support surrounding Inconel-600 tube using a probe with eight pancake coils in series. It has optimum performance at 200 kHz.

It may be noted that this probe has somewhat similar characteristics to the probe in Fig. 5a (notice similar shapes of the steel support signals). This is not surprising since the circumferential component of the current resulting from the currents in the pancake coils of this probe has similar features to the current for the circumferential coils of Fig. 5a.

Figure 7 shows the signals using a somewhat similar probe as in Fig. 6 except that the sense of the windings of the alternate pancake coils has been reversed. This probe can be visualized as having eight poles while the probe of Fig. 6 may be considered as having sixteen poles. The test frequency for optimum characteristics of this probe is near 400 kHz. At this frequency, the ratio of the magnetite signal to the steel support signal is about three and the two signals have 90° phase separation. It may be noted that this probe has a large axial component of current which would make it sensitive to the circumferential discontinuities as compared to the performance of the conventional probes with circumferentially wound coils such as Fig. 1 which have poor sensitivity to circumferentially oriented discontinuities. This coil configuration with a radial D.C. magnetic field can also be used for generating higher order tortional mode elastic waves in the tube.

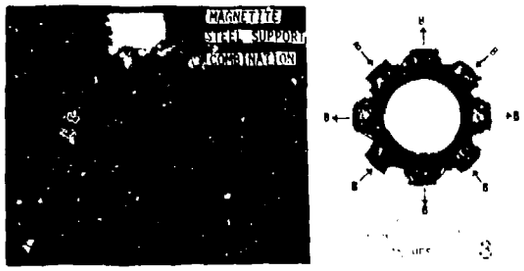

Fig. 7 The eddy current signals from magnetite and steel support surrounding Inconel-600 tubes using eight pancake coils in series but with alternate coils wound in reverse. It has optimum performance at 400 kHz.

Figure 8a shows the results obtained from a long unevenly wound circumferential coil (also shown in the figure). The turn density is gradually increased as we move from the center of the coil to the ends. The coil has higher sensitivity for steel support than for the magnetite sample surrounding the Inconel-600 tube. The sensitivity of the coil to the steel support sample compared to its sensitivity for the magnetite sample increases as the test frequency is increased. This advantage seems to level off around 100 kHz. The ratio of the signal from the steel support sample to the signal from the magnetite sample at 100 kHz is about eight. However, the phase separation between the two signals at this frequency is about 180° instead of 90° which is more the preferred separation. Decreasing the test frequency reduces this phase separation but it also reduces the ratio of the amplitudes of the two signals. At 1 kHz, the phase separation is about 105° but the ratio of the amplitudes of the two signals is only three. This coil has the important characteristic that it produces an unambiguous indication from a steel support with one or more ligaments containing 100% through-the-wall axial slots in its entire 0.75 inch (19 mm) length (Fig. 8b).

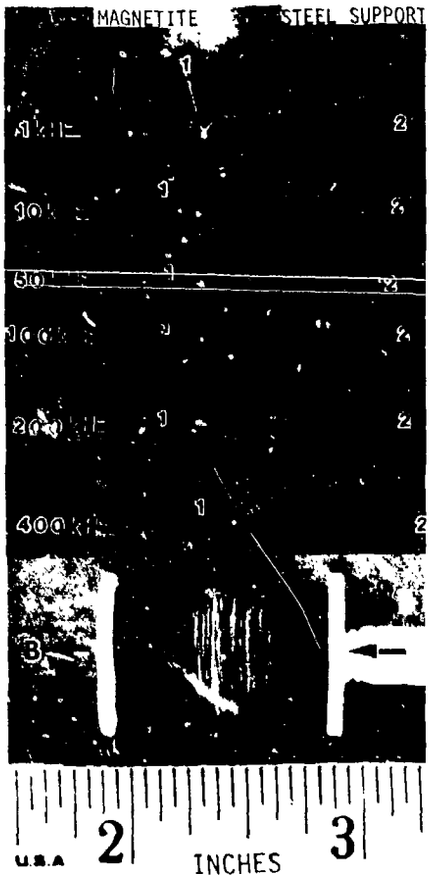

Fig. 8a Eddy current signals from magnetite and steel support surrounding Inconel-600 tube using the long unevenly wound coil. This probe is more sensitive to steel support than to magnetite in crevice.

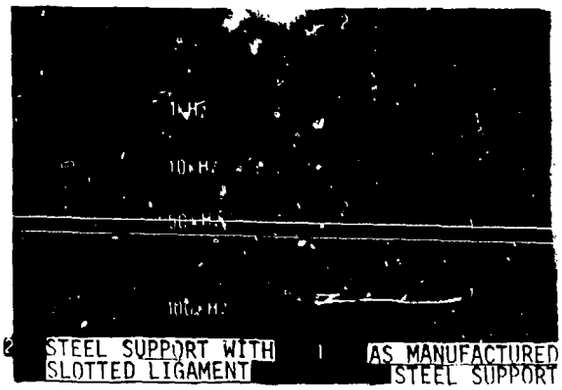

Fig. 8b Eddy current signals from as manufactured steel support surrounding Inconel-600 tube and from a support sample with a 100% through the wall slotted ligament surrounding Inconel-600 tube using the long coil of Fig. 8a. The coil produces unambiguous indication from a steel support with a slotted ligament.

It may be observed that this coil has a straight line response to the steel support surrounding the Inconel-600 tube at 10 kHz test frequency. This was achieved empirically by manipulating the turn density profile along the length of the coil. In fact, one can obtain a straight line response to the steel support at a different frequency by making a judicious choice of coil length and by manipulating the turn density profile along the coil length. The straight line response of this coil to the steel support surrounding the Inconel-600 tube may be compared to the complicated signals obtained by using the conventional coil in absolute mode (Fig. 3a).

DISCUSSION OF RESULTS

The quantitative evaluation of multiple parameters simultaneously present in a specimen can be achieved through multiple tests. The minimum number of tests needed is equal to the number of parameters to be evaluated. In eddy current technique, one of the test variables is the test frequency used since the signals from different test variables often have different frequency dependence. However, the separation of the information about the various simultaneously present test specimen parameters from the multifrequency data is not easy and is often not possible. For example, it has not yet been possible to obtain quantitative information about the steel supports or magnetite in the crevices from multifrequency eddy current data of the type shown in Figs. 3a and 3b. In this study, we are approaching this problem by using different probes which have very different sensitivities for the steel support and for the magnetite. We find that we have here three sets of probes: (1) The conventional probe which has somewhat similar sensitivities for the steel support and for the magnetite sample. (2) Probes which have larger sensitivity for the magnetite sample than for the steel support sample (Figs. 5,6 and 7). The probe shown in Fig. 6 has the best characteristics if the objective is the evaluation of the tube support crevice. (3) The probe which has larger sensitivity for steel support than for the magnetite sample (Fig.8). This probe has the best characteristics if the evaluation of the support plate ligaments is the objective.

A complete understanding of the characteristics of these coils would obviously require computer based solutions(2) of the field problems involved here and is not within the scope of this work. However, an intuitive understanding of the response of coils to magnetite and carbon steel is in order. We will ignore the Inconel tube from this discussion since it is a constant parameter in our tests. The magnetite and carbon steel can be fully defined for this discussion by μ_m, σ_m and μ_s, σ_s the magnetic permeability and electrical conductivity of the respective materials. We will not be too far off if we take $\mu_m \simeq \mu_s$ and $\sigma_m \ll \sigma_s$. We will further assume for this discussion that $\sigma_m \simeq 0$ so that the response of the coils to the magnetite is a measure of μ_m (i.e. eddy current effects can be ignored). The probes discussed in this paper can be classified into two broad catagories, (1) probes with circumferential coils (Figs. 1 and 8) and (2) pancake probes (Figs. 4 to 7). The probe of Fig. 5 has circumferential coils but the field is so arranged that it functions as a pancake probe.

The impedence locus of the test coil caused by the variation in the sample properties is a function of the coil size and geometrical shape(3) For example, the resistance maximum in the conductivity locus of the impedence of cylindrical coils becomes proportionately larger for longer coils which results in the longer coils having proportionately higher sensitivity for higher conductivity samples. Since we can take $\sigma_m \simeq 0$, we are assuming that the magnetite has hardly any effect on the coil resistance. The magnetite only increases the coil reactance. Thus, the sensitivity of a cylindrical coil for carbon steel relative to its sensitivity for magnetite can be increased by increasing the coil length. Increasing the length of the coil would also result in increasing the phase angle separation between the signals from magnetite and carbon steel. The data of Fig. 3a for the short coil and of Fig. 8a for the long coil are consistent with the above qualitative arguments.

The impedence loci of the pancake coils extend less in the resistance direction than even those of the short cylindrical coils. Thus, the sensitivity of a pancake coil for carbon steel relative to its sensitivity for magnetite is smaller than of a short cylindrical coil of similar radius. This is in qualitative agreement with the data of the coil of Figs.4 a,b when compared to the data on the short cylindrical coil (Fig. 3a). Similarly, a decrease in the diameter of the pancake coil means moving the impedence point for carbon steel to a higher location on the conductivity locus since a smaller coil radius gives a lower effective reference number for the same metal. This results in a higher value for the ratio of the magnetite signal to the carbon steel signal for smaller pancake coils and is consistent with our data using pancake coils (Figs. 4a and 4b).

The above discussion helps only in an intuitive understanding of the coil characteristics. It does not attempt to explain the characteristics of coils with complicated shapes (e.g. figs. 6 and 7) nor does it help in the understanding of the complicated signal shapes obtained for carbon steel. A detailed mathematical analysis of the field problem is needed to understand more fully the characteristics of these coils.

The data we have shown here are limited to carbon steel support plate with 1 inch (25.4 mm) diameter hole and a magnetite cylinder of 0.050 inch (1.27 mm) wall in the support plate crevice. We need to obtain data for steel supports of different I.D.'s with the resulting crevices filled with magnetite in order to evaluate these probes more completely. For example, as the support hole I.D. and the thickness of magnetite decreases, the influence of steel support on the coil relative to that of the magnetite would increase which would result in reducing the slope of the signal obtained from the combination of steel support and magnetite for the coils of Fig. 5, 6 and 7. Thus, for a complete characterization of these coils, we need data on signal slope and amplitude as a function of the support plate I.D. and magnetite thickness. However, the data presented here conclusively show that the new probes have much better discrimination between steel supports and magnetite cylinder surrounding the Inconel-600 tubes than the conventional probes.

SUMMARY AND CONCLUSIONS

1. The phase angle separation between signals from steel support and from magnetite surr-

ounding an Inconel-600 tube can be changed by simply changing the coil geometry without changing the test frequency (Figs 5a and 5b).

2. Probes have been designed which have much higher signal phase and amplitude discrimination between steel supports and magnetite cylinders surrounding Inconel-600 tubes than the conventional probes.

3. The long unevenly wound circumferential coil (Fig. 8a) has an unambiguous indication for steel supports with one or more ligaments containing 100% through the wall axial slot

4. More experimental work towards a complete characterization of these probes needs to be carried out.

5. Theoretical work on the coil design is needed in order to determine if the test frequency for optimum characteristics of the coils can be lowered to near 10 kHz.

REFERENCES

(1) H.L. Libby, Introduction to Electromagnetic Nondestrictive Test Methods, Wiley - Interscience, Inc., New York (1971), P.55.

(2) C. V. Dodd, W. E. Deeds, J. W. Luquire and W. G. Spoeri, "Some Eddy-Current Problems and Their Integral Solutions", ORNL-4384, Oak Ridge National Laboratory, April, 1969.

(3) Reference 1, Chapter 2. A very intuitive discussion of coil loci for various coil geometries is given here.

Jim Martin, Chairman (Rockwell Science Center): I think we have time for questions. If not, I have a question.

I am not completely familar with this field. The operation at 10 kilohertz seems to be very important. What is the disadvantage of operating at higher frequencies?

Amrit Sagar (Westinghouse Electric): At high test frequencies, the signals from tube discontinuities such as dents and wall thinning are large and interfere with the evaluation of the support plate condition. At lower test frequencies in the range of 10 KHz, signals from such sources are relatively insignificant and do not interfere with the evaluation of the support plate and crevices.

Bert Auld (Stanford University): I have a question. How do these coils relate to the standard differential and absolute coils in regard to the probe wobble signals? Did you find any differences:

Amrit Sagar: Since we are working at low test frequencies, the probe wobble signals are very small and present no problem. A coil somewhat similar to the long coil was, I guess, tried in the field a couple of years ago. The information I got was that the field people liked its performance since this coil produces very unambiguous signals from the support plates with broken ligaments. In fact, separating the support-plates with broken ligaments from the good support plates becomes a trivial problem. In this presentation, I am not implying that the problem is completely solved. In fact, some of these coils have problems, for example, some of them have optimum performance at high frequencies in which case probe wobble could be a problem.

Thank you.

DETECTION AND CHARACTERIZATION OF DEFECTS BY THE ELECTRIC CURRENT PERTURBATION METHOD

Cecil M. Teller and Gary L. Burkhardt
Southwest Research Institute
San Antonio, Texas 78284

ABSTRACT

The electric current perturbation (ECP) method of nondestructive evaluation is a powerful technique for detection and characterization of very small defects in nonferromagnetic material. It consists of establishing a current flow in the material to be inspected and then measuring current perturbations caused by nonconducting defects such as fatigue cracks. The current perturbation is sensed by a non-contacting magnetometer probe which detects the associated magnetic field perturbation. Recent findings from ECP investigations are reviewed in this paper. First, analytical modeling and experimental results show that single and multiple, closely spaced slots can be characterized from their unique ECP signatures; second, ECP inspection results from tiebolt holes in TF-33 gas turbine engine disks demonstrate the capability to characterize very small (0.305 mm long by 0.137 mm deep), tightly-closed, service-induced fatigue cracks; and third, preliminary results of an ECP experiment on a two layer fastener configuration show that radial slots in fastener holes can be detected in the second layer with the fastener installed.

INTRODUCTION

The nondestructive detection and characterization of (1) tightly-closed, low-cycle fatigue cracks in gas turbine engine components and (2) fatigue cracks emanating from fastener holes in structural elements of aircraft are two of the most pressing problems confronting the Air Force. Nondestructive evaluation (NDE) methods for advanced superalloy and titanium alloy gas turbine engine components are, in fact, pacing the development of retirement-for-cause based on fracture mechanics analyses of crack severity. The size range of interest is 0.254 mm or less surface length, with an aspect ratio of approximately 2 to 1. NDE methods for the detection of interior-layer cracks on critical wing-fastener configurations such as the C-5A wing-splice joint are needed to satisfy both safety-of-flight and repair inspection criteria (2.54 mm and 0.76 mm radial crack length, respectively). It is well documented that fatigue cracks originating at fastener holes are the primary cause of airframe failures (1).

The purpose of this paper is to present results of recent analytical and experimental investigations with the electric current perturbation (ECP) method of nondestructive evaluation which relate to each of these two critical problems. Three areas of research, development and engineering applications are reviewed: (1) analytical and experimental results on surface slots approximating fatigue cracks of both single and multiple closely-spaced configurations; (2) demonstration inspection results on actual service-induced LCF cracks in TF-33 3rd stage, gas turbine engine disks originating in the tiebolt holes of the disks; and (3) preliminary results on interior layer fastener hole cracks approximated by EDM slots in the faying surface of the second layer.

DESCRIPTION OF THE ELECTRIC CURRENT PERTURBATION METHOD

The fundamental principles of the electric current perturbation method are illustrated in Fig. 1. Figure 1A shows an idealized specimen with no defect present in which there exists an unperturbed current density $\vec{J}_0$ and a corresponding magnetic flux density $\vec{B}_0$ immediately above the surface of the specimen. When a defect such as a crack is introduced, the distribution of current density is altered as indicated in Fig. 1B, and the flux density above the surface of the specimen changes from $\vec{B}_0$ to $\vec{B}_0 + \Delta\vec{B}$. The ECP method consists of detecting $\Delta\vec{B}$ with a differential magnetometer probe (Fig. 2) as a function of probe position and relating the resulting signal characteristics to defect geometry.

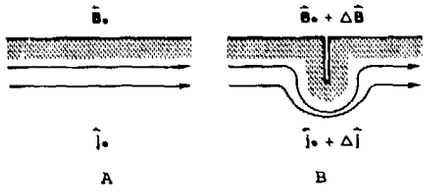

Fig. 1. Principles of the electric current perturbation method

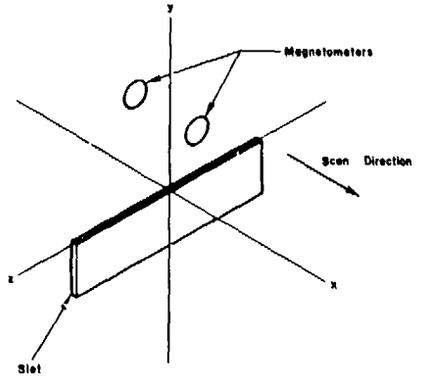

Fig. 2. Schematic of a magnetometer scan

Electric current flow may be introduced by either direct (ohmic) contact with the specimen using a suitable current source or by inducing the current flow in the specimen with an induction coil. A typical laboratory setup for direct injection experiments is shown in the block diagram of Fig. 3. Frequencies in the range of less than 100 Hz to 100 kHz are used depending on the depth of the defect to be detected and the conductivity of the material (skin depth effect).

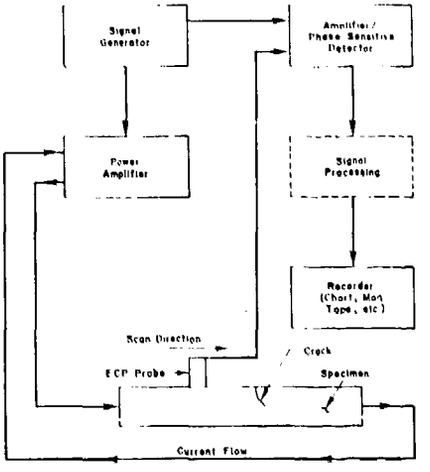

Fig. 3. Block diagram of ECP direct contact experimental apparatus

The signal characteristics for a defect of simple geometry are illustrated in Fig. 4. A small slot was made in the surface of a nickel-base superalloy (Incoloy 901) specimen by air-abrasive machining. This slot was scanned at increments along its length to generate representative signatures. As the scan tracks approach the slot from one end, a sizeable signature is obtained even at a distance of 1.905 mm from the center. At closer scans, the signal builds to a maximum amplitude and then very abruptly changes amplitude, producing an almost null signal at the center of the slot. As the scan passes the center, the signal builds in amplitude again but of opposite polarity and slowly diminishes at further distances away from the slot center.

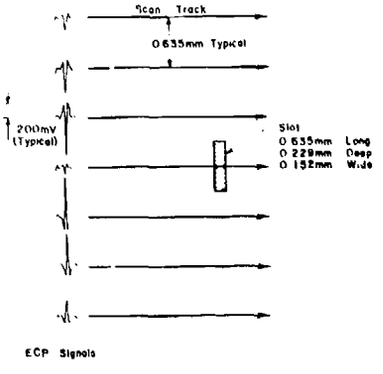

Fig. 4. ECP signatures from a 0.635 mm X 0.229 mm X 0.152 mm slot

Two important signal characteristics are immediately obvious: first, the center of the slot can be located by the null and the polarity reversals on either side. Second, the spacing between maxima in the signal amplitude is related to slot length. In addition, it has been empirically demonstrated that the peak amplitude of the signal is directly proportional to the interfacial area of a slot for small slots.

These characteristics in amplitude, polarity and shape, as well as excellent repeatability, reproducible background from the material and a high signal-to-electronic-noise ratio, are all important in the detection and characterization of defects as discussed in the following sections.

SINGLE VS. MULTIPLE CLOSELY SPACED CRACKS

Of significance to retirement-for-cause (RFC) inspection requirements is the potential of the ECP method to discriminate individual cracks from multiple, closely spaced cracks. Low-cycle fatigue cracks initiate in regions of high strain concentration such as bolt holes in engine disks. In nickel-base superalloy disks, microcracks on the scale of the grain diameter initiate very early in the life of the disk. Most of the lifetime to form a detectable LCF crack, on the order of 0.76 mm length on the surface, consists of the linkup between microcracks. Thus the discrimination between a single, linked-up crack and a row of isolated microcracks, is important to predicting residual lifetime. In particular, the inability to discriminate between single and multiple cracks in coarse-grained materials would cause retirement of the part long before its fatigue life was exhausted.

An approximate analytical model has been developed (2) which gives ECP signal characteristics as a function of defect shape and size for both single and closely spaced slots. A description of the model follows, along with a comparison of theoretical and experimental results for single and closely spaced slots.

Analytical Model - The analytical model for a single slot is based on the following assumptions:

(1) an idealized crack geometry adequately represents the perturbation to current flow and end effects may be ignored.

(2) the unperturbed current density is uniform and constant in time since the skin depth is large compared to slot dimensions.

A geometrical model consistent with these assumptions is shown in Fig. 5. Here, a slot of depth d and infinitesimal width is shown at right angles to the surface. The effect of slot length is ignored and the current perturbation is approximated by a function of x and y only. The resulting two dimensional current density perturbation may then be used to calculate an approximate change in magnetic flux density by integrating over the slot length l. Expressions for the components of the change in flux density caused by the slot were obtained using the method of complex potentials to calculate the current density perturbation (3,4).

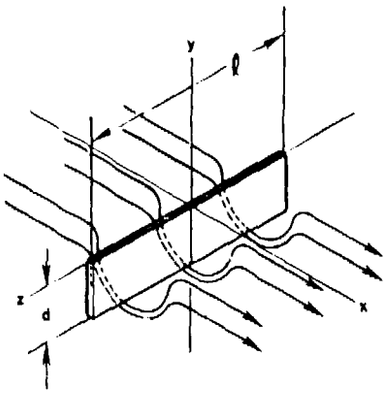

Fig. 5. Geometry for the calculation of electric current perturbation signals

To predict the response of two closely spaced slots, it was further assumed that the solutions to the flux perturbation equations are mathematically uncoupled and obey the law of superposition. Thus, the perturbation in the x-component of the flux for two closely spaced slots is simply the superposition of solutions for the x-component of the change in flux density for each slot. Characteristics of these solutions are most apparent in plots of peak amplitude as a function of position along and beyond the ends of the slots as discussed below.

Comparison Between Theory and Experiment - Two cases were modeled analytically and experimentally:

(1) discrimination of two small cracks of the same size placed end-to-end with a relatively close spacing of less than one crack length from a larger single crack of approximately the same overall length as the two cracks (all cracks having the same aspect ratio).

(2) discrimination of the same two small cracks from a small single crack of the same size and aspect ratio.

In the first case theoretical predictions were calculated using superposition of solutions for two 0.559 mm long by 0.203 mm deep slots with a spacing of 0.381 mm and a single large slot measuring 1.499 mm long and 0.546 mm deep having the same aspect ratio. Theoretical results for these two cases are shown in Fig. 6. Here the distributions of calculated peak signal amplitudes from scans perpendicular to the slot length are plotted versus position along the slot length. The single large slot produces a very large difference in the peak-to-peak amplitude (almost an order of magnitude) compared to the two small slots, and the peak-to-peak spacing for the large slot is significantly greater than that for the two smaller slots. Also, there is a slight inflection in the plot for the closely spaced slots.

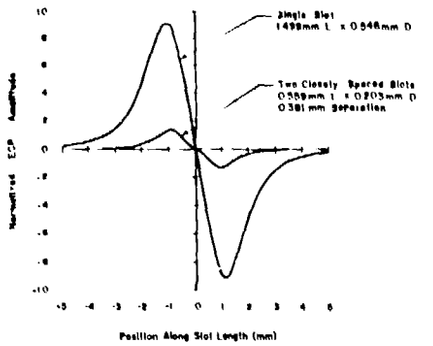

Fig. 6 Theoretical ECP peak signal amplitudes vs. position along slot length for a single 1.499 mm by 0.546 mm slot and two 0.559 mm by 0.203 mm slots separated by 0.381 mm

This first case was approximated experimentally with two small slots 0.610 mm long by 0.203 mm deep, spaced 0.381 mm apart and a single 1.575 mm long by 0.533 mm deep slot. The slots could not be made exactly the same size as in the theoretical calculations due to limitations of the air-abrasive machining process. Figure 7 is a plot of the ECP experimental data with both curves normalized so that the peak amplitude of the double slot signal has the same value as in Fig. 6. Note the excellent agreement of experimental results with the theoretical calculations shown in Fig. 6.

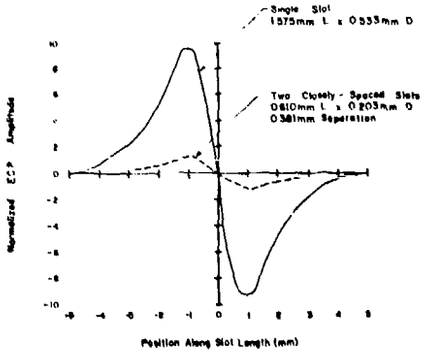

Fig. 7. Experimental ECP peak signal amplitudes vs. position along slot length for a single 1.575 mm by 0.533 mm slot and two 0.610 mm by 0.203 mm slots separated by 0.381 mm

In the second case, discrimination is desired between two closely spaced cracks and a single crack of the same size as one of the closely spaced cracks. Figure 8 shows the theoretical prediction of the peak-to-peak amplitude distributions for this case, utilizing the same 0.559 mm by 0.203 mm slots spaced 0.381 mm apart and a single 0.559 mm by 0.203 mm slot. Again, the signal features can be used to differentiate between the two conditions, i.e. the change in peak-to-peak separation and peak-to-peak amplitude, and again, in the case of the two closely spaced slots, a slight inflection of the curve in the signature region between the upward and downward peaks.

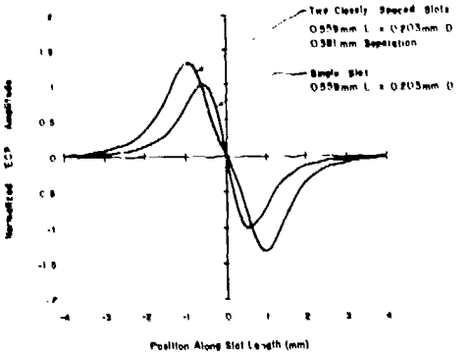

Fig. 8. Theoretical ECP peak signal amplitudes vs. position along slot length for a single 0.559 mm by 0.203 mm slot and two slots of the same size separated by 0.381 mm

This second case was approximated in an experiment which compared ECP signals from a single 0.635 mm by 0.229 mm slot with those from a set of two 0.610 mm by 0.203 mm slots separated by a spacing of 0.381 mm. Figure 9 is a plot of experimental data for these two conditions with both curves normalized so that the peak amplitude of the signal from the single slot has the same value as in Fig. 8. The signal features in the experimental case are similar to those predicted by the theoretical model (Fig. 8) with the exception of the difference in peak-to-peak amplitudes. Also, the experimental peak-to-peak spacing is similar to that predicted by the model and there is a slight inflection in the signal from the closely spaced slots at the center. Some of the differences in the experimental data such as asymmetry of the positive and negative peak amplitudes can be attributed to the fact that the slots, generated by air-abrasive material removal, are somewhat irregular and are slightly different in size than those used in the model predictions. Also, the slots were slightly deeper on one end than on the other as determined from replicas. These data do show, however, that the approximate model predictions agree remarkably well with experimental data obtained from single and closely spaced slots.

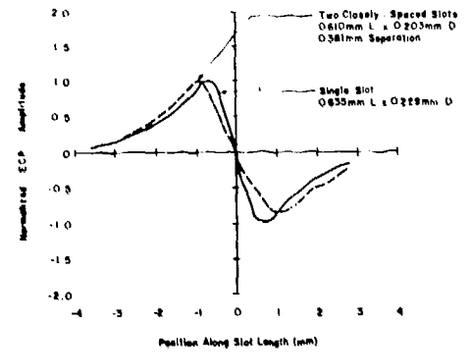

Fig. 9. Experimental ECP peak signal amplitudes vs. position along slot length for a single 0.635 mm by 0.229 mm slot and two 0.610 mm by 0.203 mm slots separated by 0.381 mm

LCF CRACKS IN TF-33 GAS TURBINE ENGINE DISKS

Inspection Procedure - The ECP method was evaluated in a demonstration of its capability to detect and characterize low cycle fatigue (LCF) cracks in tiebolt holes of TF-33, third stage turbine disks fabricated from wrought Incoloy 901 (5). ECP examinations were performed on ten tiebolt holes in each of ten scrap TF-33 disks using circumferential scans at 0.635 mm axial increments.

The scanning apparatus used in the investigation is shown positioned on a TF-33 disk in Fig. 10. An ECP probe employing a non-contacting induction method for establishing current flow in the tiebolt hole was used. The scanning system incorporated a circumferential motor drive with manual axial positioning using a precision lead screw; a shaft angle encoder indicated circumferential probe position on each scan. Data were recorded on a strip-chart recorder.

Fig. 10. ECP scanning system for TF-33 turbine disc tiebolt holes

Typical Crack Signals - Figure 11A shows two typical repeat scans of a single scan track to illustrate the excellent repeatability. Every detail of the crack signal and also of the signal background throughout the entire scan is highly repeatable. These data show that the signal and the background characteristics are precisely related to the hole under inspection and are not due to extraneous influences from electronic noise, probe liftoff variations, etc.

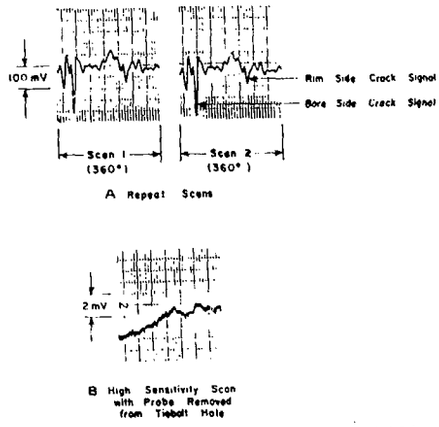

Fig. 11. ECP scans showing repeatability and electronic noise

To illustrate the ECP technique's potential sensitivity to extremely small defects, Fig. 11B shows a trace made with the probe removed from the tiebolt hole and scanned in air; the sensitivity has been increased by a factor of 50 over that shown in the traces in Fig. 11A. Even the background signals in normal scan traces in Figure 11A are far above the electronic background noise. Thus, sensitivity is limited by material characteristics and not by system noise.

Inspection Results - Since the primary objective was to assess capability of the ECP method for detecting and characterizing small cracks, four tiebolt holes were selected which had signatures with a signal-to-noise ratio of approximately two (based on material background noise). These holes were scanned again at 0.318 mm increments between scans to obtain higher resolution. Portions of the four selected tiebolt holes were removed from the disks and examined on the surface using both an optical microscope and a scanning electron microscope (SEM) to determine surface crack geometry. Selected cracks were then sectioned metallurgically and examined with the SEM to determine subsurface geometry. Since the cracks were very tightly closed in both cases, it was necessary to chemically etch the surface to reveal the cracks.

In each specimen, a large number of cracks spaced relatively close together were found, and in most cases they showed a very complex geometry below the surface. Many were at an angle to the surface, while some branched into multiple cracks beneath the surface. In a few cases, subsurface cracks were found with no surface indications. Many subsurface inclusions were also found.

Figure 12 shows a surface photomicrograph of cracks near the top end of one tiebolt hole and ECP signatures obtained at the designated scan track positions. A photomicrograph of the subsurface geometry of crack A is shown in Fig. 13. Note that the ECP scans for the entire circumference of the bolt hole are shown in Fig. 12 and that the region in the photograph comprises only a small segment of the overall ECP signature. Also, since these scans were taken near the top of the hole, a slight gradient is present in the signal near the center of each trace due to an abrupt change in disk thickness in this region.

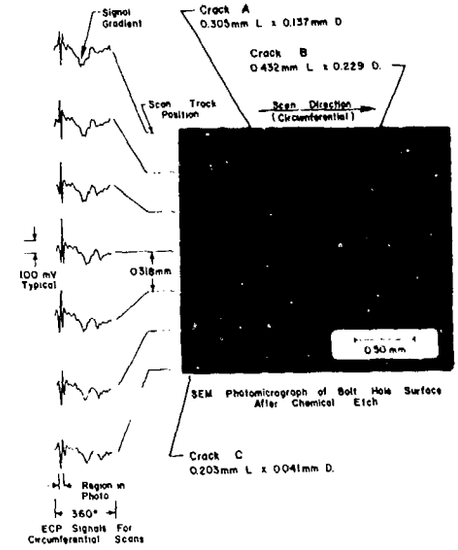

Fig. 12. Correlation of surface photomicrograph and ECP signals for cracks in a tiebolt hole specimen

Fig. 13. Optical photomicrograph of crack A cross-section

As shown in these figures, the crack sizes are very small, yet very pronounced ECP signatures are obtained. Distinct signal features are also evident. For example, as the ECP scans approach crack A from the top, the ECP crack signal is first downward going (negative) and then the signal reverses polarity for successive scan track positions axially along the crack and past the bottom end. A positive polarity is then obtained near the top of crack B. As the scans move over crack B and toward its bottom end, the signal again reverses polarity and also becomes broader in a circumferential direction, probably due to the influence of crack C, the other small cracks shown in the photograph, and additional cracks located further down the hole (not shown).

Because of the complex crack geometries and close spacing of the cracks, interactions exist between the individual ECP signatures. It is therefore difficult at this time to show a precise correlation with crack features since ECP signature characteristics are presently known only for simple crack geometries.

SECOND LAYER FASTENER HOLE CRACK DETECTION

An investigation is presently underway to determine the feasibility of detecting fatigue cracks in the second layer of a two layer structural fastener configuration (fastener installed) using the ECP method. The goal is to detect a slot of approximately 2.54 mm radial length through a full outer layer thickness of 6.35 mm (6). However, this work is not yet complete and only a progress report is given here.

Direct Contact Current Injection Results - Figure 14 is a schematic of a simplified two layer configuration without a hole constructed from aluminum flat plate stock. An electric discharge machine (EDM) rectangular slot measuring 2.794 mm long by 0.889 mm deep was placed in the bottom layer, and several top layer thicknesses were used to study the ECP response as a function of layer thickness. Direct electrical contact was used to establish current flow in the second layer which was separated from the first layer by a 0.076 mm thick nonconducting plastic (Mylar) film. An ECP probe designed specifically for subsurface defect detection was scanned on the surface of the top layer in the direction of current flow.

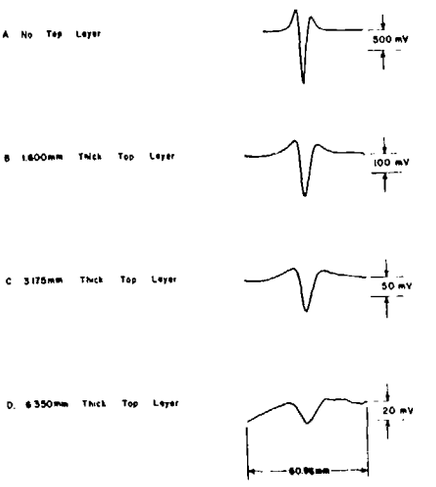

Fig. 15. ECP signals from 2.794 mm by 0.889 mm slot in second layer configuration using direct contact arrangement

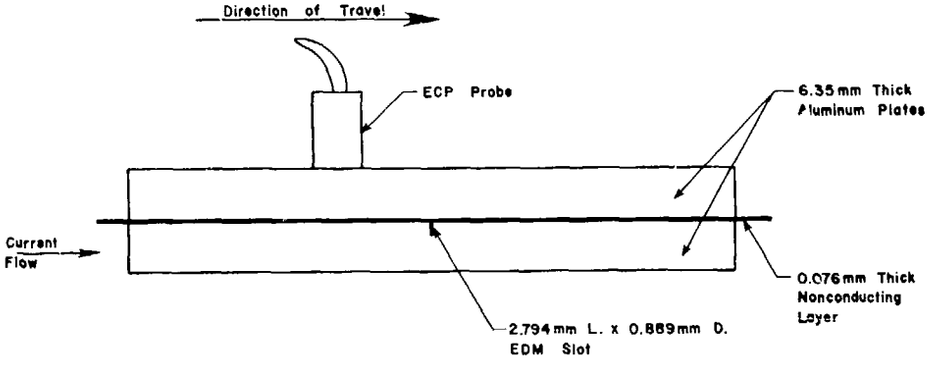

Fig. 14. ECP direct contact configuration for detection of second layer defects

Experimental results shown in Fig. 15 confirm that the slot can be readily detected through a top layer thickness up to 6.35 mm. Moreover, these ECP signals were obtained without the use of any signal processing. As expected, the signal amplitude decreases with increasing top layer thickness, but it is still significantly above background signal gradient level at a 6.35 mm thickness. Although this experiment is greatly simplified in that no hole or fastener was present in the specimen, it illustrates that in this idealized case the electric current method is capable of detecting a defect of the size range of interest in the faying surface of the second layer of the C-5A wing splice joint.

Induced Current Flow - An induction coil was designed which could be placed on the top layer coaxial with a fastener to induce current flow around the fastener hole. A motor driven scanning system was constructed to scan the ECP probe circumferentially around the fastener hole on the top layer. Figure 16 is a schematic of the experimental configuration. Again, a probe designed for subsurface detection was used.

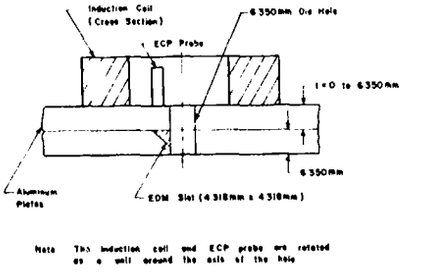

Fig. 16. Induced current configuration for detection of second layer defects

At present experimental data have been obtained only from a 4.318 mm X 4.318 mm triangular slot in the second layer with top layer thicknesses of 1.600 mm and 3.175 mm. The ECP signals are shown in Fig. 17. The excellent signals obtained here provide strong evidence that the desired goal of detecting a 2.54 mm X 2.54 mm triangular slot through a 6.35 mm thick top layer can be achieved.

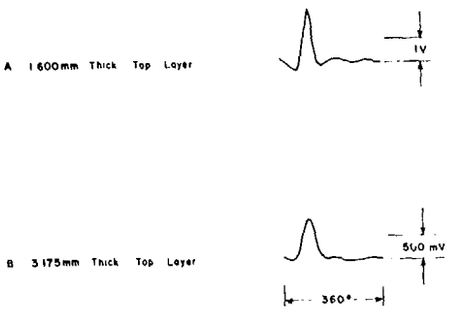

Fig. 17. ECP signals from 4.318 mm by 4.318 mm triangular slot in second layer configuration using induced current arrangement

CONCLUSIONS

Both theoretical and experimental data show that good potential exists to differentiate between small, closely spaced cracks and single cracks although more experimental data, modeling, probe refinements and signal processing will be required to differentiate between cracks with complex subsurface geometries. The potential also exists to determine crack characterization parameters such as depth although again additional data, modeling and signal processing will be required to characterize complex cracks. The ECP method is capable of detecting very small surface entering fatigue cracks as indicated by the relatively isolated crack measuring 0.305 mm long by 0.137 mm deep that was detected in a TF-33 gas turbine engine disk tiebolt hole. Smaller cracks were also detected; however, their signals were complicated by influences from adjacent cracks. Based on extrapolated data obtained with the surface ECP probe, the minimum detectable crack size (using a signal-to-background ratio of approximately two) for disks investigated is approximately 0.254 mm long by 0.076 mm deep.

Applied in the low frequency mode to the second layer crack detection problem, the ECP method has demonstrated good sensitivity to small EDM slots approximating fatigue cracks in the second layer faying surface. The goal of achieving reliable crack detection for safety-of-flight inspection criteria appears to be attainable.

ACKNOWLEDGEMENTS

The authors wish to thank Mr. Tom Doss for assistance with data acquisition and construction of the ECP scanning system; Messers. Ralph Turner and Ron McInnis for performing metallurgical sectioning and photomicroscopy; and Drs. Gerald Leverant and Clifford Wells for assistance with interpretation of metallurgical results. Partial support was provided by the Air Force Wright Aeronautical Laboratories/Materials Laboratory.

REFERENCES

1. 1977 Review of Nondestructive Evaluation (4A,8T) Roadmaps (FY77-FY79), held 19-21 July 1977, Dayton, Ohio, Air Force Materials Laboratory.

2. Beissner, R.E., et al., "Detection and Analysis of Electric Current Perturbation Caused by Defects," ASTM Special Technical Publication on the Proceedings of the Symposium on Eddy Current Characterization of Materials and Structures, National Bureau of Standards, September 1979, in print.

3. Panofsky, W.K.H. and Phillips, M., Classical Electricity and Magnetism, Addison-Wesley, Reading, Massachusetts, 1955.

4. Burns, K.J. and Laurenson, P.J., Analysis and Computation of Electric and Magnetic Field Problems, Pergamon, New York, 1973.

5. Burkhardt, G.L., Teller, C.M., Beissner, R.E., and Barton, J.R., "Demonstration of the Electric Current Perturbation Technique for Fatigue Crack Characterization in TF-33 Turbine Disk Tiebolt Holes," Final Report, Contract Nos. DLA900-79-C-1266 and F41608-79-D-A011-0011, Air Force Materials Laboratory, November 1979.

6. Southwest Research Institute Internal Research Project 15-9221, "An Investigation of Nondestructive Evaluation by the Electric Current Perturbation Technique."

Jim Martin, Chairman (Rockwell Science Center): I think your friends are lucky to have such a clear speaker to represent them.

Are there any questions?

Unidentified Speaker: The original experiment was in steel?

Richard Smith (Southwest Research Institute): The jet engine experiments?

Unidentified Speaker: Yes.

Richard Smith: That was not steel.

Unidentified speaker: Titanium?

Richard Smith: 910.

Al Bahr (SRI): What were the range of the frequencies of the applied currents?

Richard Smith: They ranged from 100 hertz to 10 kilohertz.

Dick Barry (Lockheed Missiles and Space): Did you indicate that this probe is not sensitive to lift off or some of the other problems you had with the other type of eddy current devices?

Richard Smith: No, I did not indicate that. And it would certainly be affected by lift off.

Jim Martin, Chairman: Lets continue.

SURFACE FLAW DETECTION WITH FERROMAGNETIC RESONANCE PROBES

B. A. Auld, F. Muennemann, D. K. Winslow
Edward L. Ginzton Laboratory
Stanford University, Stanford, California 94305

ABSTRACT

Eddy current methods of flaw detection have been in use for many years. Frequencies used in this type of flaw detector normally range from tens of kilohertz to a few megahertz. We report on recent progress using a resonant probe which operates in the gigahertz frequency range, and compare its performance with classical eddy current methods.

INTRODUCTION

Physical Configuration: The probe consists of a single crystal yttrium iron garent (YIG) ellipsoid, less than a millimeter in diameter (Fig. 1). An external magnet lines up the magnetic (and angular) momenta of the electrons in the YIG, which then behaves as a precessing magnetic dipole.[1,2] The crystal is in a wire loop at the end of a semi-rigid coax line, and an RF signal excites the resonant precession. Although uniform precession of all the electrons together is generally the dominant mode, other higher-order modes are possible.[3] These modes are conveniently displayed experimentally on a network analyzer (with Smith Chart display), where each mode appears as a loop on the frequency-scan trace (Fig. 2).

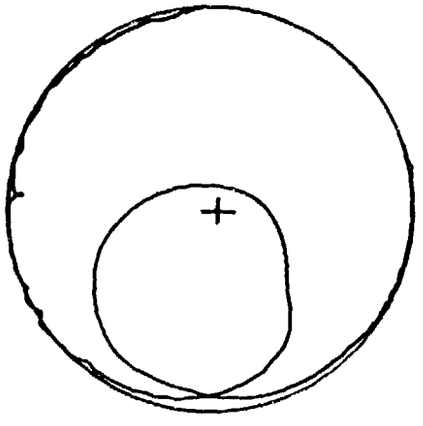

Fig. 2. Display of resonator modes on the Smith Chart. Reflected amplitude is given by the distance of the trace from the center, relative phase by the polar angle. In this display, frequency is swept from about 850 to 950 MHz; the trace advances in phase as frequency increases.

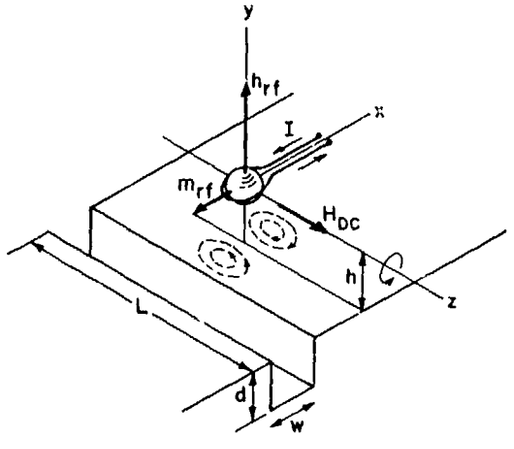

Fig. 1. Probe geometry for flaw detection, showing spherical resonator and coupling loop.

Each mode has a characteristic distribution of magnetization within the YIG, and a characteristic external magnetic field. This oscillating field interacts with the test sample, inducing currents in it, which in turn changes the strength (Q factor) and center frequency of each of the modes. Thus, the analyzer output from a cw input changes as a function of the distance to and conductivity of the test sample. This "wall effect" is well-known in YIG-technology.[4] Experimentally, we measure the impedance of the loop as a function of position on the test surface. We maintain the lift-off between 25 and 50 microns. Because the spatial distribution of the magnetic fields of the higher modes varies even more quickly than the dimension of the YIG, resolution is not strictly limited to the size of the probe. Since different modes can be accessed by changing the frequency of operation, a single probe can have many different "window functions", even though its physical configuration is unchanged. This allows us to discriminate the effect of lift-off from the presence of a flaw, and should ultimately make possible detailed quantitative flaw characterization.

Experimental Set-up: An end-on view of a probe used for flat samples is shown in Fig. 3. The YIG is mounted on a piece of microwave circuit board with a loop etched in it. Wire leads connect the ends of the loop to a semi-rigid coax line. A small SmCo magnet in a nearby brass holder maintains the necessary DC bias field. This is one of the latest generation probes, which has a standardized mechanical mounting for the coax cable, and SMA connector.

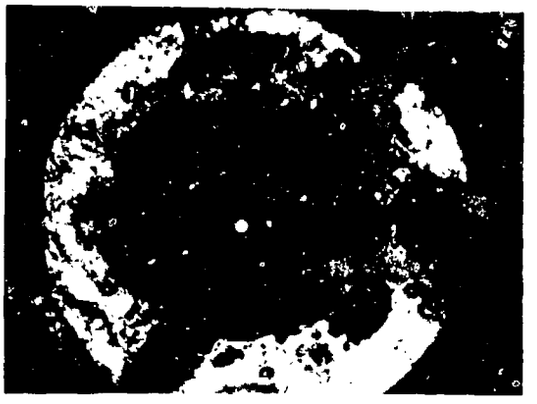

Fig. 3. End-on view of latest generation probe, showing printed-circuit coupling loop. The YIG sphere is visible in the center.

A block diagram for the network analyzer we use is shown in Fig. 4. Since flaw detection requires high-gain differential measurement, as well as compactness and portability, we use a miniaturized analyzer based on a phase discriminator, rather than a commercial network analyzer. The entire device weighs a few pounds, and is small enough to be carried with one hand. For most experiments, positional information as well as probe response is of interest; a mechanized translator with a Linear Voltage Differential Transformer (LVDT) provides this information.

THEORY

Behavior of the Modes: Before attempting to invert the signal from the FMR probe, it is necessary to consider more closely the behavior of the modes. The magnetic bias field is not, in general, exactly parallel to the surface. This is not an experimental requirement, but allowing tilt of the field gives one more parameter for the user to optimize. Since all dimensions of interest are much larger than an electromagnetic wavelength in air (about 30 cm), we use the magnetostatic approximation throughout our calculations. Thus, we write the external field of the probe as a superposition of the fields of the individual modes

$$H = \sum_M \nabla\phi_M \qquad (1)$$

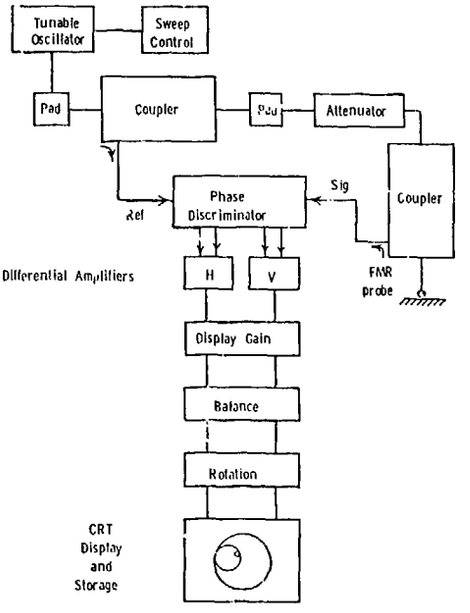

Fig. 4. Block diagram of microwave circuitry for FMR flaw detection.

We model the probe as a system of oscillators coupled to the input line (Fig. 5). Then, the presence of a conducting surface is equivalent to a variable coupling between the modes, which alters the resonant frequency and Q-factor of each of them. From multimode theory,[5] this coupling can be calculated as a surface integral for known magnetic field distributions

$$I_{MN} = \int_{\text{cond.surface}} \left\{ \phi_M \frac{\partial\phi_N}{\partial n} - \phi_N \frac{\partial\phi_M}{\partial n} \right\} dS \qquad (2)$$

The surface of integration depends on the flaw geometry, of course. By identifying each significantly coupled mode, it may be possible to reconstruct the coupling term, and thus obtain the flaw geometry. In present lab set-ups, it is not possible to identify, monitor, and record all modes of interest. For this reason, we develop in the next section some new theoretical concepts based on the general reciprocity relation rather than on the modal analysis approach.

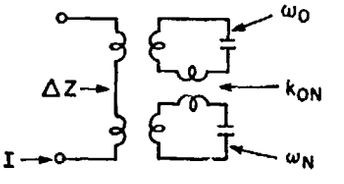

Fig. 5. Circuit model of the FMR system. Each mode is modeled as a resonant element coupled to the wire loop, and the effect of a flaw is modeled as a change in coupling between the resonators.

Electromagnetic Field Interaction With Flawed Conducting Surfaces· The past several years have seen a renewed interest in theoretical research on eddy current probes.[6,7] We will use much of this work as a foundation for our own theory; our ultimate goal is to invert the crack signature to obtain quantitative flaw parameters. The general approach we will follow is applicable to all eddy current measurements, although some features are specialized for the FMR probe. We will outline the method for prediction of the probe output from a given flaw geometry first, and then suggest means of inversion.

Beissner, et al.[8] have shown that solutions for hydrodynamic flow of an incompressible, non-viscous fluid can be applied to electric currents in conductors. Analytic solutions exist for many special cases, and extensive numerical algorithms have been developed for the solution of this equation. The solutions we present here assume a uniform applied field, which is equivalent to a uniform far-field flow. Although this approximation is not in all cases realistic, it makes possible analytic solutions in both two- and three-dimensional geometries. It is clear from Fig. 6 that a probe with a uniform induction near the flaw will not have the null often found in standard probes. The FMR probe operating with the bias field nearly parallel to the surface is, in fact, such a probe.

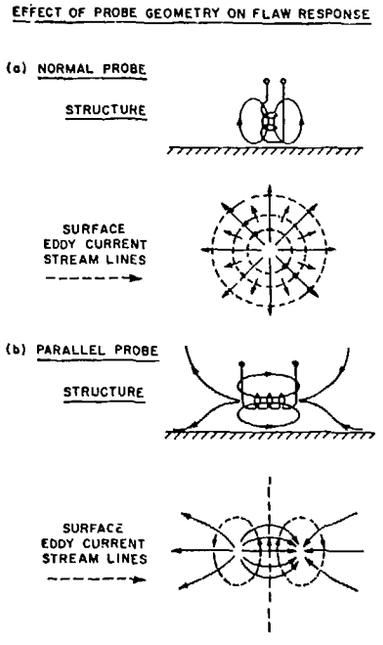

Fig. 6. Patterns of surface eddy currents induced by different probe geometries. (a) Vertical probe (stnadard eddy current) induces currents with a null at the center. (b) Horizontal probe (FMR or modified standard eddy current) induces a uniform current in the vicinity of the probe.

We consider two limits: where the electromagnetic skin depth in the test sample is much smaller and much larger than the flaw dimensions (Fig. 7). The skin depth is given by the formula

$$\delta = \left(\frac{2}{\omega \sigma \mu}\right)^{1/2} \qquad (3)$$

For Al and steel alloys, δ is of order 1 micron at gigahertz frequencies, and 1 mm at kilohertz frequencies. For flaws with dimensions of order 1 mm, we see that low-frequency eddy current methods are often described by the small flaw approximation, and FMR-eddy current behavior is described by the large-flaw approximation. For microcracks, the small a/δ form applies to FMR.

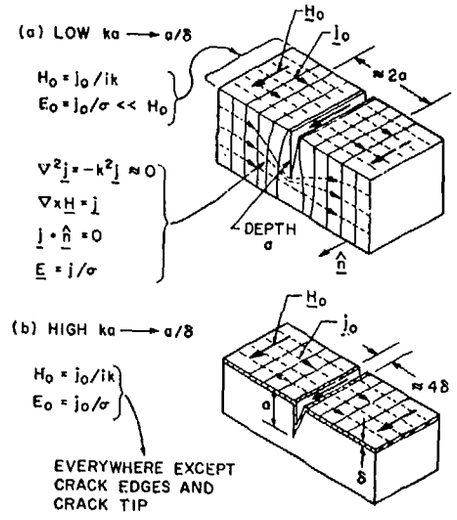

Fig. 7. (a) Three-dimensional view of currents induced when $a \ll \delta$. The flow around the flaw depends almost exclusively on the flaw area, rather than on opening. (b) Same view of currents induced when $a \gg \delta$. The currents cling to the sides of the flaw, and there is strong dependence on the flaw opening.

Small a/δ Approximation: Beissner, et al.[8] have shown that when the flaw depth is much smaller than the skin depth, the electric field obeys the equation

$$\nabla^2 E = 0 \,. \qquad (4)$$

Although this work was done in connection with flux leakage methods, the result is applicable to eddy current as well. In Fig. 8, we illustrate such solutions for a three-dimensional void (analogous to a nonconducting inclusion or a widely opened crack) and a half-penny shaped crack. A feature of small-flaw detection which becomes immediately apparent is that the magnitude of the current disturbance is dependent primarily on the area rather than on the volume of the flaw. For flaw detection and sizing, this implies that crack opening measurements will be extremely difficult to make.

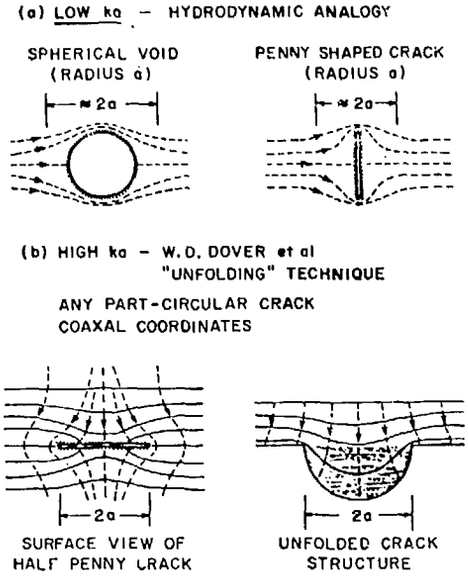

Fig. 8. Analytic solutions for the current flow around flaws in the low and high a/δ approximations, using the hydrodynamic analogy. Again, dependence on the flaw opening in the low a/δ case is minimal.

Large a/δ: For the case where skin depth is much smaller than the flaw dimensions, we can neglect the current normal to the surface.[9] We thus have

$$(\text{two-dim laplacian})\ E = 0 \quad . \tag{5}$$

This is mathematically identical to the problem of a two-dimensional incompressible non-viscous flow on a curved surface. Dover, etal.[9,10] have devised a clever means of unfolding the surface to reduce the problem to a hydrodynamic flow in two dimensions with a boundary. It should be emphasized that this is an entirely analytic solution.

Electromagnetic Fields: To relate the behavior of the currents induced in the sample to the observed impedance of the probe, we consider the fields near the conductor. Throughout this discussion, primed fields are to be taken in the presence of the flaw, while unprimed fields are to be taken for the case of an unflawed conductor. From the reciprocity relation it can be shown that the change of probe impedance produced by a flaw is

$$\Delta Z = \frac{1}{I^2}\int_{S_F} (E\times H' - E'\times H)\, dS \quad . \tag{6}$$

Note that the surface of integration is over any volume containing the flaw; therefore, only changes between the primed and unprimed fields need to be taken into account when evaluating the integral; changes in geometry appear only in the fields.

For the high a/δ case we use the plane of the unflawed conductor as the surface of integration. We then have three regions to integrate over: to the right and left of the flaw, and over the flaw opening. The normal vector to the surface of integration is in the z-direction. H is assumed to lie in the y-z plane. This permits us to write the cross product in the ΔZ formula as

$$(E\times H)\cdot\hat{n} = E_x H_y \quad , \tag{7}$$

from which we are able to write for a two-dimensional crack

$$\Delta Z = \frac{|H|}{I^2}\int_{-\infty}^{\infty} (E'_x - E_x)\, dX \tag{8}$$

where X is normal to the crack line. Further development leads to the formula

$$\Delta Z = \frac{|H|^2}{I^2}\left\{ i\omega\mu_o \frac{a\Delta u}{2} + \frac{1+i}{\sigma}\left(\frac{2a-\Delta u}{\delta}\right) - 0.28 \right\} \tag{9}$$

which directly relates the change in impedance due to the flaw to the crack opening displacement. Here, Δu is the crack opening displacement, a is the depth of the flaw, μ is the frequency of operation, δ is the skin depth, I is the current in the loop, and 0.28 is a geometrical factor.

This simple inversion formula discards much information, since the physical model used does not allow for three-dimensional cracks or nonuniform induction by the probe; it also does not attempt to describe the detailed behavior of the probe as it is scanned over the flaw. Far-reaching conclusions can, however, be drawn from this model, as will be seen.

For the low a/δ case, a similar formula is obtained,

$$\Delta Z = \frac{|H|^2}{I^2}\left\{ \frac{i\pi}{\sigma}\left(\frac{a}{\delta}\right)^2 + i\omega\mu_o \frac{a\Delta u}{2} - (1+i)\frac{\Delta u}{\delta} \right\} \quad . \tag{10}$$

Note that in both formulae, the dependence on crack opening grows linearly with frequency. This implies that to see crack opening, it is necessary to use a high-frequency probe.

The reciprocity relation also leads to a simple three-dimensional inversion solution for a semi-circular surface crack in the low a/δ limit which bears a remarkable resemblance to the low-ka scattering formula for acoustic Rayleigh wave scattering.[11] The formulae for the reflection coefficient/impedance change are

$$\Delta Z = \frac{1}{I^2}\int_{S_F} \Delta\phi\ \underset{\sim}{j}_o \cdot \hat{n}\, dS \qquad \text{(electromag.)} \tag{11e}$$

$$\Delta\Gamma = \frac{i\omega}{4P}\int_{S_F} \Delta u \cdot \underset{\sim}{T} \cdot \hat{n}\, dS \qquad \text{(acoustic)} . \tag{11a}$$

Note that Γ and Z are related by the formula

$$\frac{Z}{Z_o} = \frac{1+\Gamma}{1-\Gamma} \tag{12}$$

Here, Δφ is the electric potential across the flaw, and j is the electric current density. Δu is the crack opening displacement, and T is the acoustic stress. In both formulae, the leading multiplicand accounts for the power input to the probe/transducer. The electric potential across the crack and the crack opening displacement are

given by

$$\Delta\phi = 2j_o \frac{2}{\pi} \frac{1}{\sigma} (a^2 - r^2)^{\frac{1}{2}} \qquad (13e)$$

$$\Delta u = 2T \frac{2}{\pi} \frac{1-\nu}{\mu} (a^2 - r^2)^{\frac{1}{2}} \qquad (13a)$$

where r is the radius of the semicircular crack. An important parameter for stress analysis is the stress intensity factor, given by[11]

$$k_I = 2\sqrt{\frac{a}{\pi}} . \qquad (14)$$

The inversion formulae for the stress intensity factors are

$$\Delta Z \sim k_I^6 \left(\frac{j_o}{I}\right)^2 \qquad (15e)$$

$$\Delta\Gamma \sim k_I^6 \left(\frac{T^2}{P}\right) . \qquad (15a)$$

Again, the formulae are almost identical, except that acoustic stress replaces the current density, and Δu, the crack opening displacement, replaces the potential across the flaw. This result is not surprising when one compares the overall physical configuration of the two probes involved (Fig. 9).

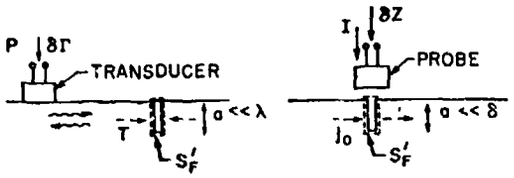

Fig. 9. Comparison of geometries for low ka detection in ultrasonic surface wave detection scheme and for eddy current.

Although this case will only arise for microcracks when using the FMR probe, it provides a useful inversion method for low frequency eddy current testing.

Signal Interpretation: A typical flaw signature is shown in Fig. 10. To obtain this trace, the offset controls are used to center the probe response on the CRT. Gain is then increased, and the probe is mechanically scanned over the sample. Lift-off is 25 - 50 microns, and is maintained as constant as possible. The trace moves back and forth along the lift-off curve due to small variations in the vertical position of the probe relative to the surface. The loop occurs as the probe passes over the flaw.

To generate a "map" of the surface, the display is electronically rotated so that the lift-off curve is as nearly as possible parallel to the horizontal direction. Then the response in the vertical direction (perpendicular to lift-off) is plotted against the LVDT output. The operator monitors lift-off via the horizontal channel. A typical response to a fatigue crack in Aluminum alloy is shown in Fig. 11, together with an optical micrograph of the crack. Note that the probe response matches the photograph in overall features, but is insensitive to surface scratches which clutter the optical picture. Although photography required the crack to be stressed open for visibility, the probe easily detects and maps the flaw even when tightly closed. Computer programs are now in the development phase to provide maps with better lift-off discrimination, close correlation to actual flaw depth, and higher resolution.

Fig. 10. Typical FMR flaw signature. The trace has been rotated so that lift-off response is horizontal (nearly straight portion). The flaw response is a loop. Separation of the vertical channel gives a signal dependent only on the presence of the flaw (lift-off independence).

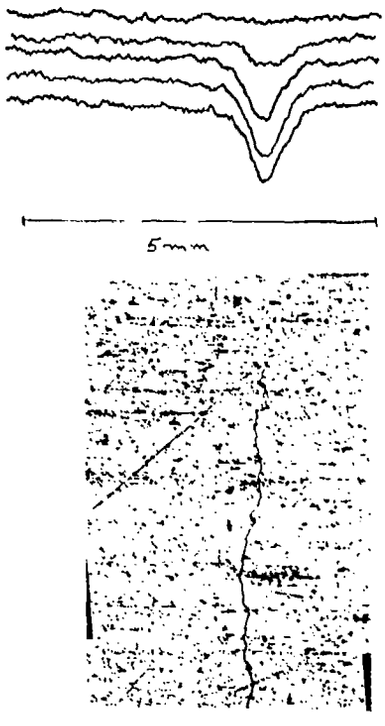

Fig. 11. Comparison of a "map" of the area near the tip of a flaw, generated by plotting flaw response against position, with a photograph of the same flaw. The map is insensitive to scratches, but shows the crack clearly. The flaw was stressed open to make it visible in the photograph.

The actual modal structure of each individual probe depends critically on the strength, orientation,

and uniformity of the magnetic field provided by the external magnet; it is also dependent on the shape of the coupling loop, and its orientation with respect to the crystal structure of the YIG. This large number of variables offers almost unlimited possibilities for the optimization of probes for specific sample geometries.

More information is extracted from the signal by considering the two-dimensional trace, rather than the "separated" flaw signal.[12] At present, this is on an entirely empirical basis; numerical evaluation requires more theoretical development of the probe behavior.

Comparison With Standard Eddy Current Tester: We have compared several aspects of the FMR probe performance with that of a commercial tester. By calibrating the actual impedances of the two probes, we compare sensitivity to tightly closed fatigue cracks and to saw cuts in 6065 Aluminum alloy (Figs. 12(a) and (b)). As expected from Eq. (1), the FMR probe is much more sensitive to opening of a flaw. Whereas the responses of the two probes are almost the same for a fatigue crack, the FMR signals for the saw cut (which is electrically very similar to a widely opened fatigue crack) is more than 20 times as large!

As outlined above, theory predicts that the dependence of the signal on flaw opening varies linearly with frequency (see Eq. (9)). Thus, the FMR probe is much more sensitive to crack opening by virtue of its high frequency of operation. This is especially important in fracture mechanics experiments.

The spatial resolution of the FMR probe is also much higher than that of the standard eddy current probes tested (Fig. 13). A trial with a high-resolution differential probe gives somewhat improved results, although the differential nature of the probe tends to obscure the response; resolution of the device examined was still much less than FMR. The FMR probe is much easier to produce than any low-frequency probe we know of which approaches its resolution.

A situation commonly encountered in NDE is a crack at a corner or edge. Often, special eddy current probes are designed for this type of detection, since the coupling to the sample decreases as one approaches the edge. This effect is also present in the FMR probe. The use of smaller (higher spatial resolution) probes enables us to see an edge crack 1.7 mm by 0.5 mm in a Ti alloy bar (Fig. 14). This crack is particularly interesting because it was not intentionally initiated. The other feature in the map has no optical counterpart in microphotographs of the flawed region; we speculate that it may be a subsurface inclusion related to the initiation of the edge crack.

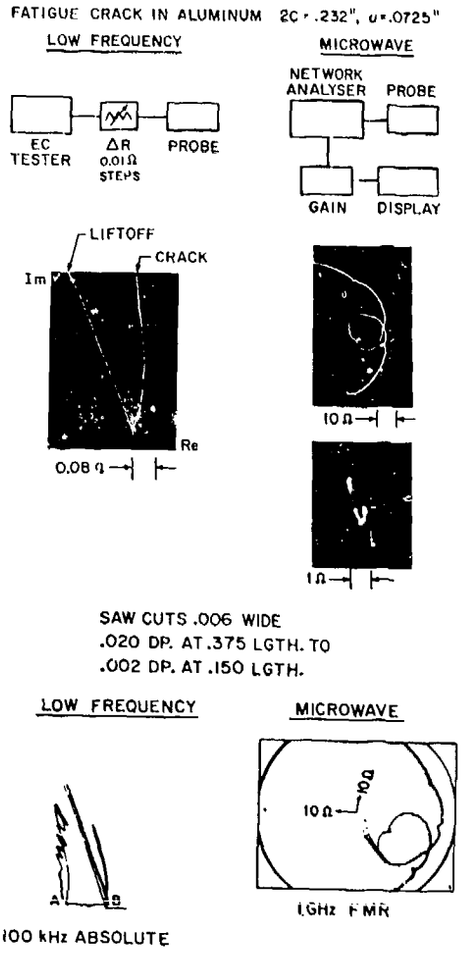

Fig. 12. Low frequency and FMR responses to crack opening. The low frequency signal is almost the same for a fatigue crack and a saw cut, while the FMR signal for the saw cut is 20 times larger!

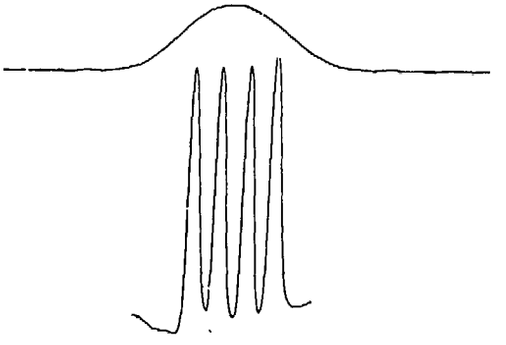

Fig. 13. Spatial resolution of a typical low-frequency probe operating at 1 MHz, and the FMR probe. The sample was an aluminum bar with slots cut 0.02" apart. The low-frequency probe totally fails to resolve the slots.

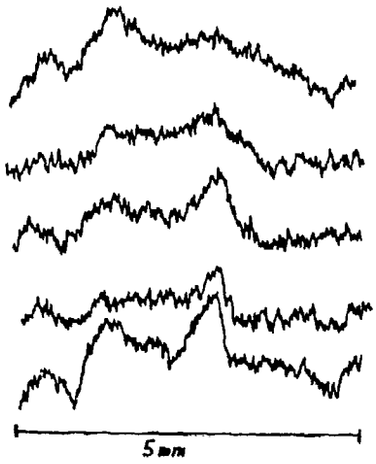

Fig. 14. "Map", generated in the same way as in Fig. 11, of an edge crack in a Ti alloy bar. The flaw, with dimensions 1.7 mm long by 0.5 mm deep as measured by microscope, is clearly visible.

APPLICATIONS

The primary advantages of this type of probe over other NDE methods are:

1) Accessibility to confined areas of complex geometries: Probes can be made smaller than 1 mm in diameter.

2) Probes are sensitive to small flaws, and give quantitative flaw parameters. Spatial resolution is high.

Thus, the primary application is in the testing of complex nonmagnetic parts; these are typically found in aircraft turbine engines. The probe has proven its usefulness as a means of studying fracture mechanics in the laboratory.[12] Yet another potential application[13] would be as a proximity tester. Because the probe is scanned mechanically, its ideal environment is in a computer-controlled robot system, where precision positioning and signal interpretation would be performed by the same computer.

ACKNOWLEDGEMENTS

This work was sponsored by the Center for Advanced NDE operated by the Science Center, Rockwell International, for the Advanced Research Projects Agency and the Air Force Materials Laboratory under Contract No. F33615-80-C-5004. We are grateful to Mike Resch for his help and advice in materials science matters, and to Otto Buck for providing some of the fatigue samples we used to test our apparatus. Dave Walsh of the Stanford Applied Physics department built the probes.

REFERENCES

1. B.A. Auld, "Theoretical Characterization and Comparison of Resonant Probe Microwave Eddy Current Testing with Conventional Low Frequency Eddy Current Methods," in Proceedings of the Symposium on the Eddy Current Characterization of Materials and Structures, G. Birnbaum and G. Free, eds. (ASTM Special Publication) (to be published.

2. B.A. Auld and D.K. Winslow, "Microwave Eddy Current Experiments with Ferromagnetic Resonance Probes." Presented at Symposium on Eddy Current Characterization of Materials and Structures, September 5-7, 1979.

3. L.R. Walker, "Magnetostatic Modes in Ferromagnetic Resonance," Physical Review, Ser. II, vol. 105, no. 2 (1957).

4. L.K. Anderson,"Ferrimagnetic Relaxation Measurements and Microwave Circuit Properites of Ferrite Ellipsoids," Ph.D. Thesis, Stanford University (1962).

5. R. Plumier, "Magnetostatic Modes in a Sphere and Polarization Current Corrections," Physica 28, 423-444 ( ).

6. M.L. Burrows, A Theory of Eddy Current Flaw Detection (University Microfilms, Ann Arbor, Mich. 1964).

7. Kahn, Spal and Feldman, J. Appl. Phys., vol 48, no. 11, p. 4454 (1977).

8. R.E. Beissner, C.M. Teller, F.L. Burkhardt, R.T. Smith, and J.R. Bartor, "Detection and Analysis of Electric Current Perturbation Caused by Defects," in Proceedings of the Symposium on the Eddy Current Characterization of Materials and Structures, G. Birnbaum and G. Free, eds. (ASTM Special Publication) (to be published).

9. W.D. Dover, F.D.W. Charlesworth, K.A. Taylor, R. Collins, and D.H. Michael, "The Use of A.C. Field Measurements to Determine the Shape and Size of a Crack in a Metal," in Proceedings of the Symposium on the Eddy Current Characterization of Materials and Structures, G. Birnbaum and G. Free, eds. (ASTM Special Publication) (to be published).

10. W.D. Dover, F.D.W. Charlesworth, K.A. Taylor, R. Collins, and D.H. Michael, "A.C. Field Measurements: Theory and Practice," in Proceedings of the Symposium on the Eddy Current Characterization of Materials and Structures. G. Birnbaum and G. Free, eds. (ASTM Special Publication) (to be published).

11. B.A. Auld, "General Electromechanical Reciprocity Relations Applied to the Calculation of Elastic Wave Scattering Coefficients," Wave Motion 1 (1979) 3-10 (North Holland Pub. Co.)

12. M.T. Resch, F. Muennemann, B.A. Auld, D.K. Winslow, and J.C. Shyne, "Measurement of Surface Crack Opening Displacements Using Microwave Frequency Eddy Currents," companion paper.

13. M. Perry, private communication.

Jim Martin, Chairman (Science Center): Thank you very much, Frank. Those are pretty results.

Are there any questions?

Frank Muennemann (Stanford University): We'll take theoretical questions.

Amrit Sagar (Westinghouse Electric): Talking about resolution, have you tried current density probes at low frequencies? Because I'm surprised the resolution you show is not very good.

Frank Muennemann: The two-megahertz probe we used was one which was especially designed for GE. It's a differential probe which has two coils very tightly wound. It was designed for high resolution.

Amit Sagar: The other question is: How close to the boundaries can you pick up the cracks?

Frank Muennemann: The crack in the titanium was directly at the edge. It is primarily because we have a small probe that we can see this crack. it is only 1.7 millimeters long; we can detect flaws correctly up to an inch.

Amit Sagar: Supposing we have a cube and the crack is close to the edge of the cube. Can you pick it up?

Frank Muennemann: Yes, we can pick it up.

Unidentified Speaker: You said your nearest scan was 15 millimeters from the edge?

Frank Muennemann: Yes.

Al Bahr (SRI): Do you every let your probe touch the surface as you scan, or does that introduce a lot of noise?

Frank Muennemann: Yes, it does touch the surface during the scan. Actually w use it as a means of calibrating the lift off. When the probe touches the flaw there is a slight deformation since it is set in epoxy. A fairly large signal results. You cannot let the probe actually drag on the surface.

Jim Martin, Chairman: One more question and I would like to move on.

Bill Reynolds (AERE, Harwell): Have you thought of using this probe for examining carbon fibre reinforced plastic?

Frank Muennemann: We thought of it. We do not have any samples at the moment. However, it should be pointed out that this will work best in high conductivity materials.

Bill Reynonds: Low frequency eddy current probes are usable in FRP.

Frank Muennemann: That might be encouraging.

Jim Martin, Chairman: Thank you, Frank.

MEASUREMENT OF SURFACE CRACK OPENING DISPLACEMENTS USING MICROWAVE FREQUENCY EDDY CURRENTS

M.T. Resch, F. Muennemann, B.A. Auld, D. Winslow, and J.C. Shyne
Stanford University
Stanford, California 94305

ABSTRACT

An electromagnetic NDE technique for measuring the crack opening displacement of surface fatigue cracks is described. A ferromagnetic resonance probe utilizing yttrium-iron-garnet was used to induce eddy currents in an aluminum plate. The crack opening displacement of a semi-elliptical fatigue crack evaluated at the surface was measured optically at several values of bending stress on the specimen. A technique is presented which allows the crack depth to be calculated from the measured COD at a given stress. The relative phase and magnitude of input vs. output signal to and from the resonating YIG sphere was recorded during the interaction of the FMR probe eddy currents and the fatigue crack. A method is shown to extract quantitative information from these signals and to correlate this information with the crack opening displacement.

INTRODUCTION

We describe here a new microwave frequency eddy current technique for nondestructive evaluation of the surface crack opening displacement of fatigue cracks. The flaw type treated in this paper consists of a flat, semi-elliptical shaped crack in a 2024 aluminum plate. The procedure is to induce eddy currents to flow in the vicinity of an open fatigue with a ferromagnetic resonance probe, and to measure the changes in the probe's reflection coefficient as the probe is translated across the crack. These measurements are performed at a frequency of approximately one Gegahertz so that the skin depth of the eddy currents will be small relative to the magnitude of the crack opening displacement.

The combined effects of the uniform precession and higher order magnetostatic modes excited in the yttrium-iron-garnet sphere induce eddy currents near the surface of the specimen. The presence of the open crack disrupts these patterns, and couples the crack electronically with the resonance in the YIG sphere. This coupling is seen to change as the sphere is translated across an open surface crack, in a direction along the normal to the crack plane. The change in coupling produces changes in the probe's reflection coefficient. As the probe scans an open crack, the changes in reflection coefficient are recorded on a Smith chart. During a scan, these changes produce a closed figure which is reproducible, and rich in geometric information. The quantified information obtained from this type of scan varies linearly with the optically measured surface crack opening displacement. Additionally, changes in the probe reflection coefficients are seen to give valuable information concerning the crack closure stress of surface fatigue cracks.

MEASUREMENT OF CRACK OPENING

We define the surface crack opening displacement as $\Delta u_z(0,0)$ where subscript z indicates the displacement across the crack faces in the z direction evaluated at $(x,y) = (0,0)$. See Fig. 1. Additionally, we adopt the notation for a = crack depth, and c = crack half-width. The crack resides in a ½ in. thick by 2½ in. wide bar of 2024 aluminum which is loaded in three point bending by an

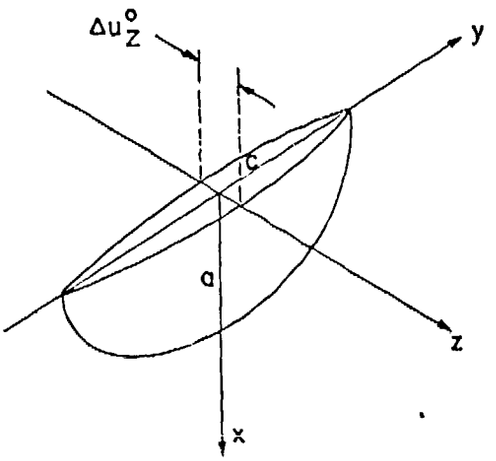

Fig. 1 Crack coordinate system.

MTS System 810 servohydraulic testing machine. In this paper, we will refer to stress σ as the maximum tensile stress evaluated at the surface of the beam at $(x,y,z) = (0,0,0)$.

A ferromagnetic resonance probe with a 30 mil YIG sphere is prepared to measure crack opening in the following manner. The probe is positioned above the aluminum surface with a lift-off, h=25 microns. See Fig. 2. An input signal with a center frequency of approximately one Gigahertz with a sweep range of 100 Megahertz is applied at the terminals of the loop of wire surrounding the YIG sphere. A samarium-cobalt magnet is placed near the sphere to apply a DC bias magnetic field. In Fig. 3, we see the Smith chart response of the probe in this configuration, where the radial distance from the diagram center indicates the magnitude of the reflection coefficient $|r|$, and θ is the phase angle between the incident and reflected signals. The large loop indicates the excitation of the uniform precession which behaves like a magnetic dipole. The smaller loop indicates the excitation of a higher order magnetostatic mode, which may alternatively be modeled as a multipole.

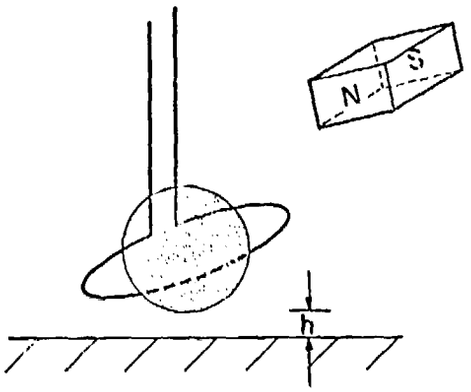

Fig. 2 Ferromagnetic resonance probe near surface.

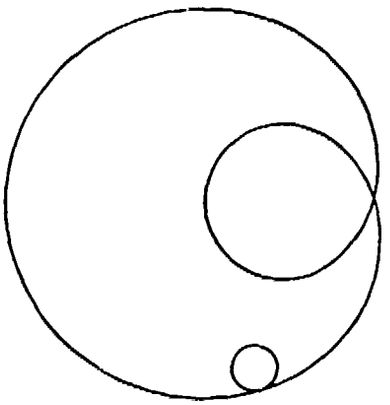

Fig. 3 Smith chart showing uniform precession with higher order resonance.

The electronic modeling of the coupling between these modes is presented in detail in a companion paper by Auld et al [2]. With the probe adjusted so that a higher order resonance is near the frequency of the uniform precession, we adjust the input frequency to the center frequency of the uniform precession. At this fixed frequency we place the probe over an open fatigue crack a distance h from the surface. See Fig. 4. In our tests we set the lift-off, h, to 25 microns. At this value of lift-off the probe is placed approximately 10 mils from the crack. The probe is then translated over the crack at 5 mils/sec until the probe is past the crack by 10 mils. During this translation, the fixed frequency reflection coefficient of the FMR probe is recorded on a x-y recorder. See Fig. 5. This figure shows the features of a crack signature obtained from a scan of an open fatigue crack. The lift off curve is obtained by translating the probe vertically above the crack from the surface to 75 microns above the surface. Then at a near constant value of 25 microns of lift-off, during lateral translation of the probe, the double loop pattern is traced out as the reflection coefficient varies. We have found that the presence of the primary loop corresponds to presence of the fatigue crack, regardless of whether the crack is open or not. The secondary loop has been found to correspond to the amount the crack faces are displaced due to the applied stress. Since the total size of the primary and loops changes somewhat for variations in liftoff, we normalize the crack signature by computing a figure of merit which we call the loop ratio for each value of crack opening. This ratio is simply the amplitude of the secondary loop divided by the amplitude of the primary loop.

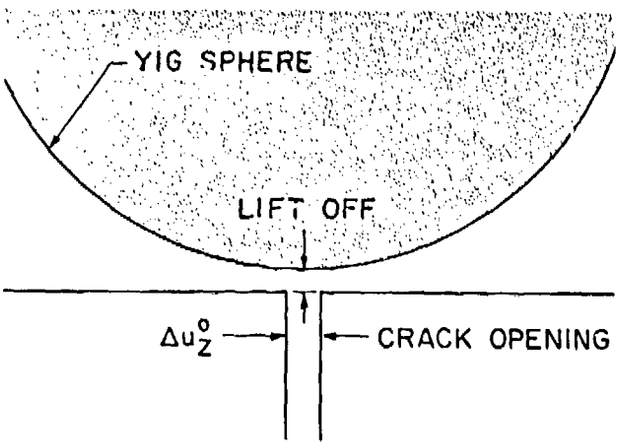

Fig. 4 YIG sphere of FMR probe above open fatigue crack.

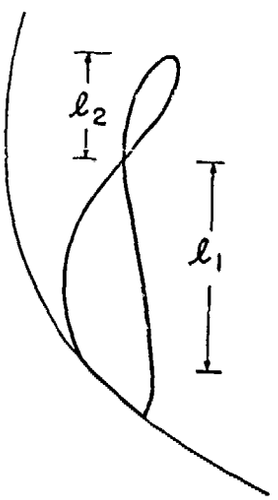

Fig. 5 Crack signature with primary and secondary loops identified.

In Fig. 6 we see the crack signature obtained from a fatigue crack at three different values of bending stress. At zero stress, the crack is completely closed, and we see only the primary loop. At 50 MPa the crack has opened only about 1 micron, and the secondary loop just begins to form. At 150 MPa, the crack has opened 20 microns, and we see here a fully developed secondary loop. On a crack with c=230 mils, we measured the loop ratio at 10 values of bending stress ranging from 0 to 250 MPa (Fig. 7). The loop ratio remains at zero until we reach a stress of 30 MPa. It then jumps

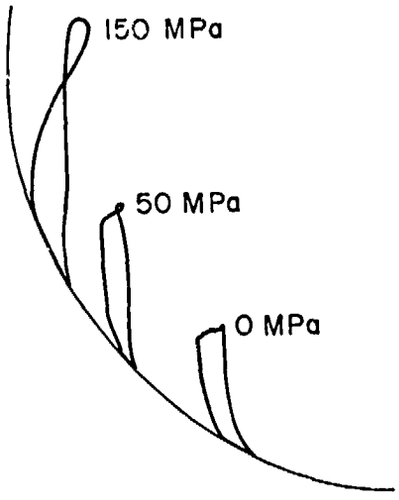

Fig. 6 FMR crack signature at several values of bending stress.

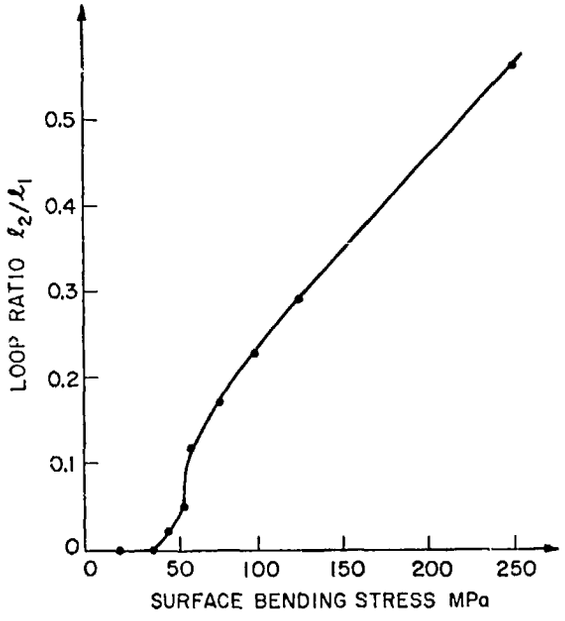

Fig. 7 Loop ratio vs. surface bending stress.

sharply, and above a stress of approximately 75 MPa, the loop ratio increases linearly with increasing bending stress. We measured the crack opening displacement optically at 8 different values of bending stress with an optical microscope, in order to compare the loop ratio with the actual crack opening. See Fig. 8. At 25 MPa, the crack had no visible opening. At 50 MPa we detected approximately 1 micron of opening, and above 50 MPa the crack opening increased linearly with increasing stress. This linear relationship is what we would expect from linear elastic fracture mechanics theory. The delay in linear behavior is caused by

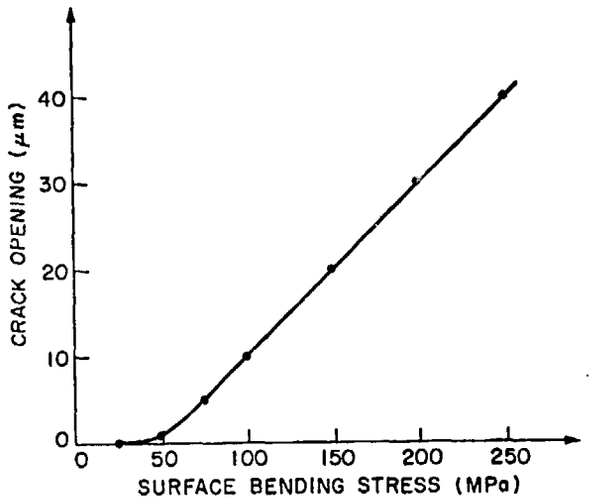

Fig. 8 Optically measured crack opening vs. surface bending stress.

the crack closure phenomenon. Briefly stated, crack closure is caused by compressive residual stresses left in the wake of the plastic zone of the advancing fatigue crack. These residual stresses leave the adjacent crack faces pressed tightly together. The elastic deformation of the crack faces due to externally applied loads must overcome the residual stress displacements before the crack will open completely. Further insight in the crack opening behavior may be obtained by comparing the loop ratio to the optically measured crack opening, as shown in Fig. 9.

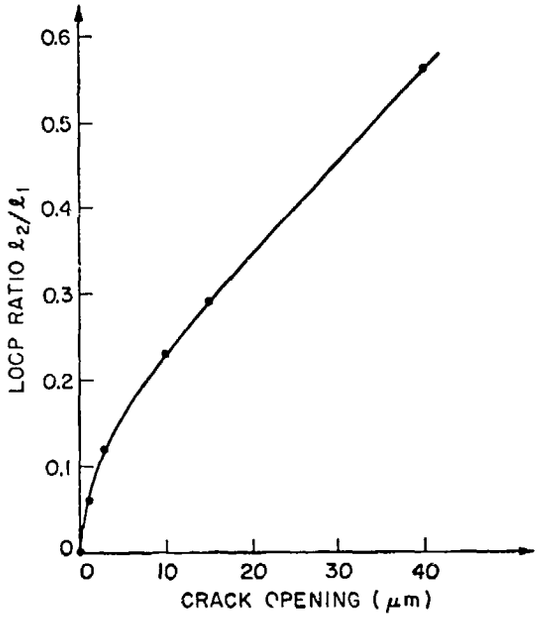

Fig. 9 Loop ratio vs. crack opening.

Here we see that the loop ratio varies in a nonlinear manner with increasing crack opening up to an opening of approximately 10 microns. After the crack opens this amount, the loop ratio varies linearly with increasing crack opening. We believe that the nonlinear behavior of the loop ratio during the initial stages of the crack opening is caused by the crack closure phenomenon. More specifically as increasing bending stress is applied the distribution of residual stress on the adjacent crack faces causes the crack to "peel open," starting at the surface. During this nonlinear opening event, the effective crack length of the fatigue crack changes with changing stress. Here the effective length is defined as the distance below the surface to where the adjacent crack surfaces just begin to touch.

ESTIMATION OF CRACK DEPTH FROM CRACK OPENING

Kobayashi[3] has calculated the normalized crack opening displacement at the origin, $\Delta u_z(0,0)$, of semi-elliptical shaped surface cracks in a finite depth plate under pure bending. In Fig. 10 we show how this result may be replotted to show how the normalized crack opening $\Delta u_z(0,0)/\sigma c \cdot G$, may be plotted as a function of crack depth at constant crack width. Here G is the shear modulus, and $\Delta u_z(0,0)$, σ and c have been defined previously. An estimation of the depth of an arbitrary elliptical crack may be made then by optically measuring the crack half width, applying a known bending stress, and measuring the COD at the crack center. For the sample upon which COD vs. stress measurements were taken for this work, we estimated the crack depth at a = 192 mils.

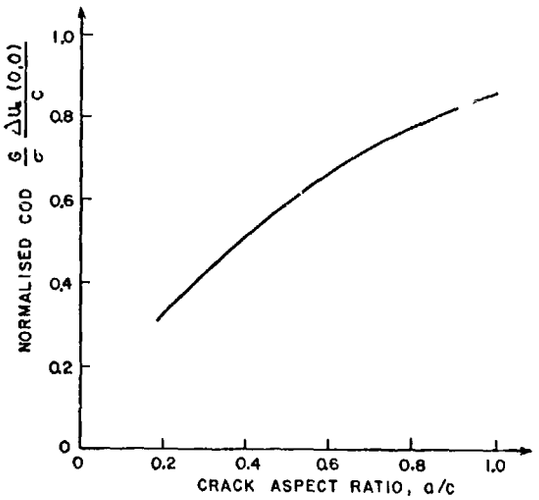

Fig. 10 Normalized crack opening vs. crack aspect ratio at constant value of crack half-width. c = 230 mils, with speciment thickness = 500 mils.

After COD vs. stress measurements were completed on the sample in question, the specimen was cut in half, and polished and etched to reveal that the true crack depth was a = 200 mils. This results in an error of only 4%.

CONCLUSIONS

The electromagnetic NDE technique utilizing microwave frequency eddy currents has been shown to be effective in the detection of a closed surface crack opening displacement of a surface fatigue crack in a body subjected to three point bending. For the probe geometry described in this work, changes in the probe's complex impedance were correlated to the presence of crack opening displacement during translation of the FMR probe over an opened fatigue crack. Additionally, the Smith chart response of the interaction between the probe and a fatigue crack is found to be rich in geometric information, allowing quantization of the probe signal.

REFERENCES

1. L.R. Walker, "Magnetostatic Modes in Ferromagnetic Resonance," Physical Review, Ser. II, Vol. 105, No. 2 (1957).
2. B.A. Auld, F. Muennemann, D.K. Winslow, "Surface Flaw Detection with Ferromagnetic Resonance Probes," companion paper.
3. A.S. Kobayashi, "Crack Opening Displacement in a Surface Flawed Plate Subjected to Tension or Plate Bending," Document No. D-180-19446-1. The Boeing Aerospace Company, March 1976.

SUMMARY DISCUSSION

Jim Martin, Chairman (Rockwell Science Center): Are there any questions?

James Goff (Naval Surface Weapons Center): I suppose this was all done on clean surfaces.

Michael Resch (Stanford University): They were metallurgically prepared.

James Goff: What if some sort of dirt has gotten in the cracks, like some sort of insulating penetrant.

Michael Resch: That won't hurt us, because there is already aluminum oxide film in the open crack that is there. So if there was some dirt in there, I don't think it would effect us at all.

Frederick Vaccaro (The Timken Company): Regarding this question about an oxide in the crack or dirt in the crack: How does the crack opening displacement, then, result in the variation? Are you actually having current transfer through the crack?

Michael Resch: No, it is passing around the crack. What I tried to show is that the change in impedance is really a function of the open volume underneath the probe. There was a term that had the permeability times the crack depth times the opening over two. That is really permeability times the area of the open crack. But it is measured per unit length; for a three-D crack.

Dick Barry (Lockheed Missiles and Space): I hate to keep riding the same horse, but how did you measure the crack depth?

Michael Resch: We cut it in half, polished it, and etched it after we were finished with all of our runs.

Dick Barry: One of the reasons I bring this up is I have done this. The bottom of cracks are not always nice and uniform, and unless you go through a number of different steps in your polishing you may not find the maximum. This may be a region of error you may want to look into. It may be the average you're measuring rather than the absolute maximum depth.

Michael Resch: That't a good point.

Boro Djordjevic (Martin Marietta Laboratories): You listed 25 microns as your lift-off. How critical is it and how producible is it?

Michael Resch: We have performed experiments of comparison showing how the crack signature changes as a function of lift off. And it turns out by normalizing the loop ratio, the L2 over L1, we can keep it near 25 microns. During the test, we can sometimes have variations of 10 to 15 microns difference in height. We found that that changes the loop ratio at a given crack opening depth by less than 20 percent. So to the first order, the loop ratio is relatively insensitive to errors in lift off.

Ross Weglein (Hughes Aircraft Company): Eddy current skin depth is a function of the frequency. If the crack were in fact closed, how close to the surface could it be for you to still show a detectable loop?

Michael Resch: The skin depth at a gigahertz is several microns. We do see a tightly closed crack at that size. The limit is not intuitively obvious to me. However, in general, if the crack is greater than the skin depth, I would predict we would see something.

Ross Weglein: As a function of skin depth?

Michael Resch: Yes.

Jim Martin, Chairman: If there are no more questions, we will proceed.

MICROWAVE EDDY-CURRENT TECHNIQUES FOR QUANTITATIVE NDE

A. J. BAHR
SRI INTERNATIONAL
MENLO PARK, CALIFORNIA 94025

ABSTRACT

The objective of this research program is to develop microwave scattering techniques for obtaining quantitative information about the characteristic dimensions of surface cracks in metals. Work carried out during the past year has emphasized experimental techniques. The use of an IF bridge and a near-field dielectric probe to improve the sensitivity of our 100-GHz eddy-current measurement system is described. The results of measurements made on fatigue cracks in 2024-T3 aluminum using this improved system also are presented. The interpretation of these data to provide information about crack depth is explained in terms of a simple model. Finally, a theoretical approach for modeling the scattering from elliptically shaped cracks is outlined.

INTRODUCTION

In the low-frequency eddy-current testing of metals, currents are caused to flow in a test specimen by placing it in the magnetic field of an induction coil. The flow of currents is affected by the electrical properties and shape of the test specimen, and by the presence of discontinuities and defects. In turn, these currents react on the exciting coil and affect its impedance. Thus, the presence of a defect is determined by monitoring the test coil impedance.

Such eddy-current tests are conducted typically at frequencies of less than 1 MHz, where induction fields predominate and the electromagnetic wavelength is greater than 200 m. However, in quantitative NDE, where it is desired to obtain the defect dimensions from an analysis of the measured data, the use of such low frequencies does not provide the degree of sensitivity to changes in defect dimensions that is necessary for obtaining an accurate determination of these dimensions from an inversion of the eddy-current data. The problem of obtaining sufficient accuracy becomes more difficult as the flaws become smaller.

This problem would be alleviated if higher frequencies were used in eddy-current inspection. Thus, the work reported here addresses the possibility of conducting eddy-current measurements in the microwave-frequency regime (1 GHz to 100 GHz). Previous work[1,2]* using frequencies in the range 10 GHz to 30 GHz has shown that good sensitivity to small cracks can be obtained, and that a clear correlation exists between crack depth and the detected signal.

In using microwave frequencies, the radiation fields associated with the sensors become an important consideration, and the physics involved is best described in terms of fields and waves. For example, a defect should be thought of as producing a change in the scattering of electromagnetic waves from the metal surface. It should also be noted that since microwave frequencies cause currents induced in the test object to flow essentially on the surface (i.e., the skin depth is typically less than 1 μm at 100 GHz), microwave eddy-current techniques for testing of metals are limited to surface inspection, e.g., to detection and characterization of surface-breaking cracks.

Work carried out in the first two years of this program has resulted in a significant improvement in our understanding of microwave eddy-current testing, and of eddy-current testing in general. We have developed a theoretical model for the far-field backscattering from a rectangular slot in a metal plate, and calculations using this model were found to be in good agreement with measurements made at 100 GHz. Given the cross-sectional dimensions of the slot, we were able to estimate slot depths accurately from single-frequency measurements.

Work carried out in the past year has emphasized the improvement of experimental techniques and the measurement of actual fatigue cracks. Recent improvements in our 100-GHz eddy-current measurement system, and the results of measurements carried out using this system, are described in this report. Also, a theoretical method of analyzing the scattering from elliptically shaped cracks is outlined.

MICROWAVE EDDY-CURRENT SYSTEM

The 100-GHz eddy-current system that we have developed was described in last year's annual report.[3] In that system, we realized a microwave bridge using an orthomode coupler for minimizing the backscattered signal produced by an unflawed flat metal plate. An orthomode coupler is a microwave component which transmits a linearly polarized wave traveling in the forward direction (from the source to the probe) and couples out an orthogonally polarized wave traveling in the backward direction (from the probe to the receiver). A crack can be detected by such a system because a crack converts part of the incoming wave to the orthogonally polarized wave, while a perfectly aligned flat plate does not. Background rejection achieved in this way (polarization filtering) does not depend on the distance between the probe and the plate, and thus is analogous to the behavior of the differential probe that is widely used in low-frequency eddy-current testing.

*References are listed at the end of the report.

Unfortunately, no component is perfect, and it proved very difficult to achieve more than 30 dB of rejection using the orthomode coupler augmented by tuning screws. Also, the tuning screws could not be made small enough in terms of a wavelength at 100 GHz, and so the tuning they provided was relatively coarse and difficult to repeat. For these reasons, we decided to modify the system so that the background signal could be cancelled after the signal had been down-converted to 3 kHz, where we expected that the desired amount of background rejection could be obtained more easily. A minor disadvantage of this type of scheme is that the nulling is dependent on the distance between the probe and the metal surface.

A block diagram of the modified measurement system is shown in Fig. 1. In addition to the 3-kHz nulling networks, we also added a circular polarizer. This component provides about 10 dB of backscatter rejection from a flat plate without the need for any fine tuning. Since the circular polarizer combined with a rectangular waveguide functions as a polarization filter like the orthomode coupler, this contribution to backscatter rejection is independent of the probe-to-surface spacing. Use of a circularly polarized wave also is advantageous because the crack signal is independent of crack orientation; however, this experimental convenience entails a 3-dB loss in signal power over that produced by an optimally aligned, linearly polarized incident wave.

We found that the sensitivity of the modified system was about the same as for the old system, but that the adjustments needed to achieve this sensitivity were much easier to carry out and to maintain. The gain of the 3-kHz amplifiers was about the same in both systems. With the improved background rejection in the modified system, we had expected to be able to increase this gain, but we were limited by ground-loop pickup and the finite isolation of the directional coupler. Of course, it should be possible to reduce such stray pickup with further effort.

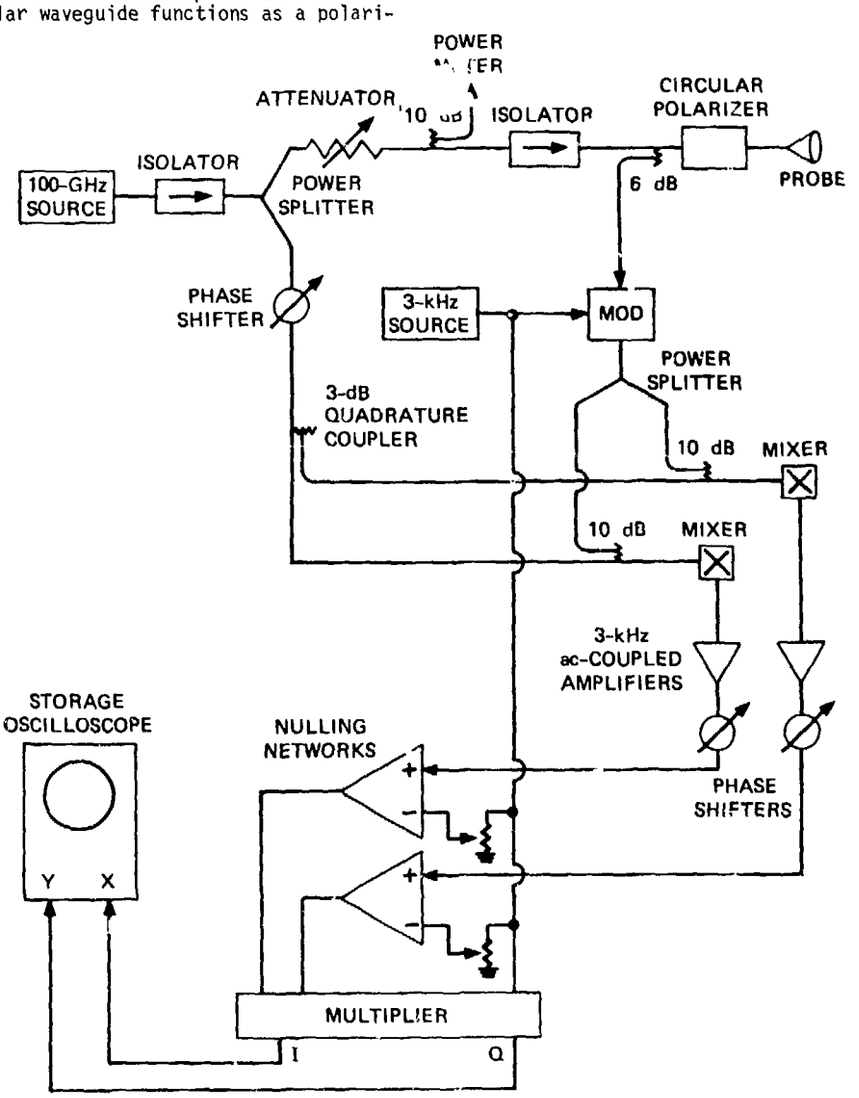

Fig. 1 Microwave Eddy-Current System

The sensitivity of an eddy-current system is also affected by the ability of the probe to convert as large a fraction of its driving current as possible into eddy currents flowing in a region no larger than the flaw being examined. In the system tested last year, the probe used was a microwave lens (polystyrene) having a focal length of 7.6 cm and a focal-spot size of 3 mm. This probe provided nearly plane-wave excitation of the EDM slots, and thus was an important factor in the good agreement obtained between theory and experiment. The spot size of this probe was about optimum for the 2.5- and 1.25-mm-long slots that were examined. However, the scattering patterns for these slots are all broader than the lens pattern; thus, some of the scattered energy is lost, making this probe less efficient than we would like.

One way of obtaining a more efficient probe is to use a near-field probe, such as an open-ended waveguide, and bring it close to the flaw. Such a probe still concentrates its fields in a small region slightly larger than the waveguide cross section, but also captures more of the energy scattered by the flaw. It should be noted, however, that the attendant increase in sensitivity is accompanied by increased difficulty in performing a theoretical analysis of the probe-flaw interaction.

The sensitivity of a near-field probe can be increased further by using dielectric loading to increase the ratio of magnetic field to electric field at the surface of the metal being inspected. One method of dielectric loading is to attach a resonant dielectric sphere to the end of the waveguide. Resonance in the sphere is required so that, by proper positioning of the sphere, we can match the incident wave in the waveguide to the resonant mode in the sphere. An excellent dielectric material for this purpose would be sapphire ($\varepsilon_r \approx 9$). However, we could not easily obtain sapphire spheres of the correct size to be resonant at our system's operating frequency of 100 GHz, and so we did not pursue this approach. However, we believe this approach to be feasible.

Another method of dielectric loading is to couple the air-filled waveguide to a dielectric waveguide. We constructed such a dielectric waveguide out of Delrin ($\varepsilon_r = 3.7$). A good match between the air-filled guide and the dielectric guide was obtained by tapering one end of the dielectric guide to a point. A photograph of the dielectric-waveguide probe is shown in the right-hand side of Fig. 2. The outer diameter of the Delrin probe is 1.1 mm. For comparison, the far-field lens probe is also shown in that figure.

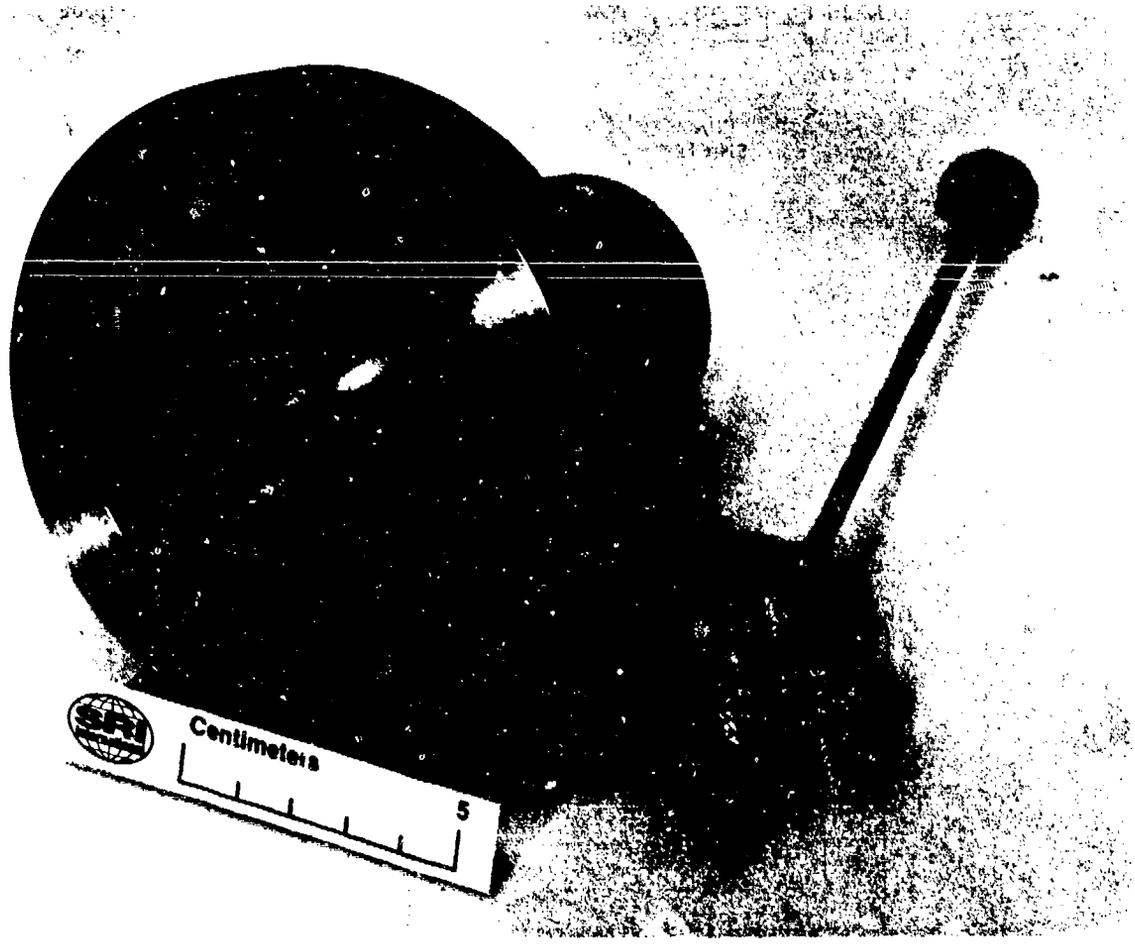

Fig. 2 Microwave Eddy-Current Probes

Figure 3 provides a comparison of the eddy-current responses obtained when the lens probe and open-ended waveguide probe were used to examine the EDM slots studied previously. The two upper photographs were obtained using the far-field lens probe, and the two lower photographs were obtained using the near-field, circular-waveguide probe. The abscissa and ordinate on each photograph are proportional to the real and imaginary parts of the probe reflection coefficient, respectively. Each trace was obtained by mechanically moving the slots through the region illuminated by the probe. The background signal has been suppressed so that no lift-off trace is generated when the plate containing the slots is moved, i.e., the lift-off trace has been reduced to a point. When a slot enters the illuminated area, the spot on the storage-oscilloscope display moves away from its resting point and then returns to that point when the slot leaves the illuminated area. The maximum excursion and angular position of the resulting trace are indicative of the size of the slot.

The eddy-current responses obtained using the lens probe are essentially the same as those obtained previously with the orthomode-coupler scheme. Recall that all the slots are 0.25 mm wide, but vary in length and depth. Slots 1, 2, and 3 are 2.5 mm long, while Slots 4, 5, and 6 are 1.25 mm long. Slots 1 and 4 are 0.25 mm deep, Slots 2 and 5 are 0.5 mm deep, and Slots 3 and 6 are 1.0 mm deep (nominal). Slots 1, 2, and 3 produce responses that are well separated in phase, but the traces produced by Slots 4, 5, and 6 essentially lie on top of one another. These latter traces can be resolved (as was done previously) by tilting the plate to produce an observable lift-off trace. The responses from Slots 1, 2, and 3 have widely different phases because these slots are long enough to support a propagating waveguide mode that can reflect from the bottom of the slot. On the other hand, Slots 4, 5, and 6 support only evanescent modes (at 100 GHz).

The results obtained using the waveguide probe (see the lower photographs in Fig. 3) were somewhat unexpected. Qualitatively, the waveguide probe was indeed found to be more sensitive than the lens probe. The surprising feature of the waveguide eddy-current responses was, however, the asymmetry of the traces; i.e., their open-loop or kidney shape. We believe that this behavior is caused by coupling between two modes in the circular waveguide. The size of our waveguide is such that two modes can propagate: the TE_{11} (dominant mode) and the TM_{01}. The TE_{11} mode is the one eventually detected in the receiver but, in the near field, the slot apparently can couple these two modes and thus change the effective impedance seen by the dominant mode. The electric field in the TM_{01} mode is not symmetrical with respect to a plane containing the waveguide axis, and so the effective impedance depends on which side of this axis the slot is located.

The corresponding eddy-current responses obtained using the dielectric waveguide probe are shown in Fig. 4. These responses are very similar

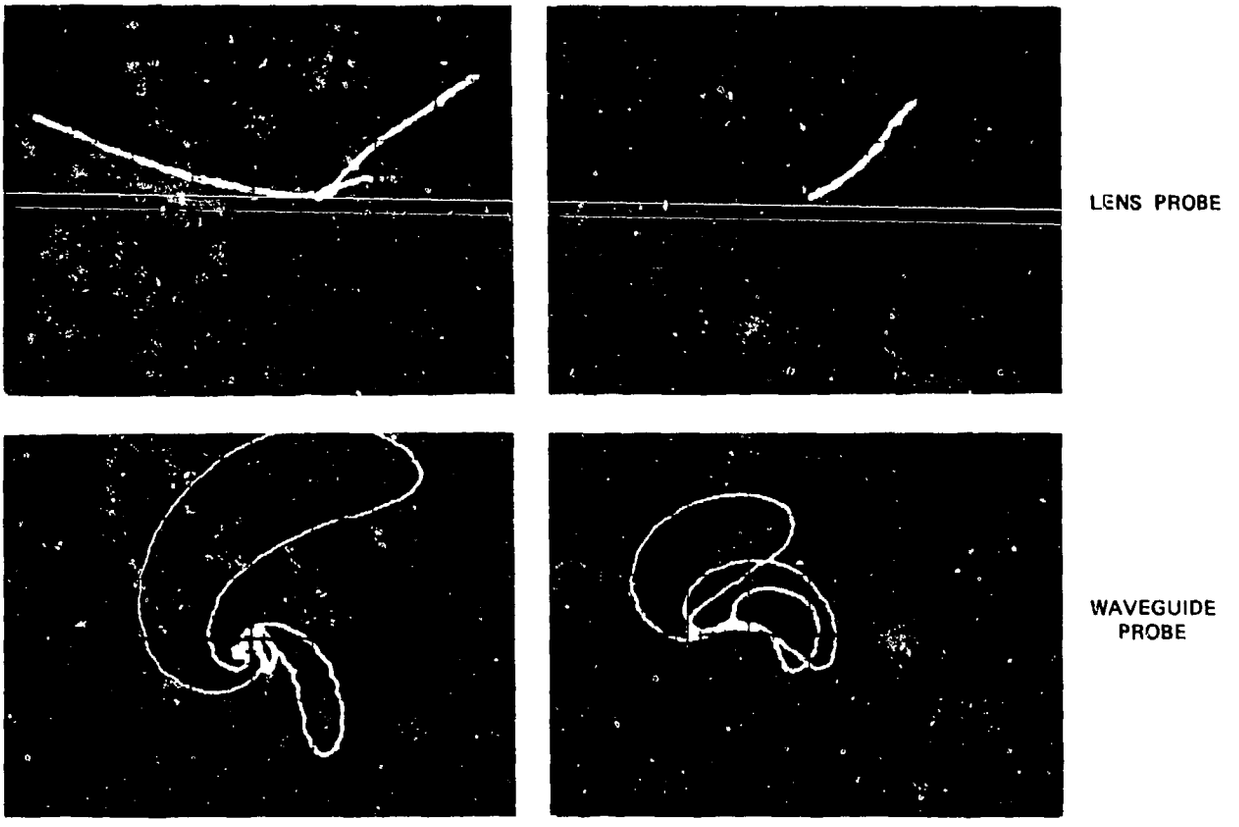

Fig. 3 100-GHz Eddy-Current Responses of EDM Slots in Aluminum

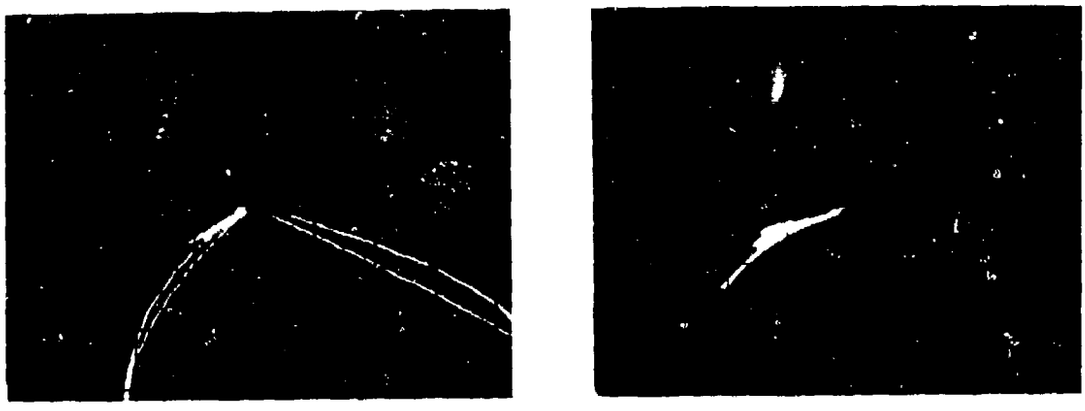

SLOTS 1, 2, and 3 SLOTS 4, 5, and 6

Fig. 4 100-GHz Eddy-Current Responses of EDM Slots in Aluminum (dielectric probe)

to those obtained using the lens probe (the traces obtained in the two cases are obviously rotated with respect to one another, but this difference is due simply to a different choice of phase reference). It is notable that the traces in Fig. 4 show very little of the open-loop shapes exhibited by the response of the open-ended waveguide. We attribute this result to the fact that only one mode can propagate in the dielectric waveguide, and thus there is very little excitation of higher-order waveguide modes by the slot.

MEASUREMENTS ON FATIGUE CRACKS

Three specimens of 2024-T3 aluminum containing fatigue cracks induced by tension-tension cycling were supplied to SRI by Dr. Otto Buck of the Rockwell International Science Center. The lengths of the cracks in the three specimens were measured under a microscope, and these crack lengths are listed in Fig. 5. The eddy-current responses of each of these cracks were obtained using a conventional eddy-current instrument and coil probe. Fig. 5 shows the eddy-current responses obtained at 483 kHz. Note that there is a qualitative correlation between the amplitude of each response and the crack length (and presumably the crack depth). However, the phase of each response seems to depend very little on the crack size. We will see that at microwave frequencies the phase of the eddy-current response can be a strong function of the crack size.

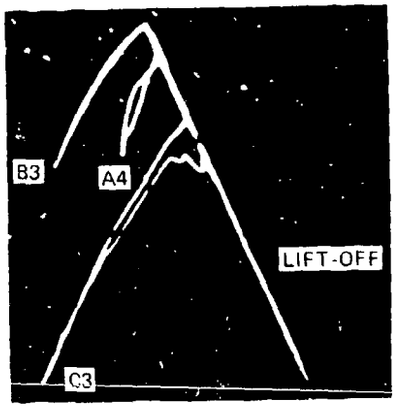

SAMPLE NUMBER	CRACK LENGTH
A4	0.140 in. (3.56 mm)
B3	0.180 in. (4.57 mm)
C3	0.252 in. (6.40 mm)

Fig. 5 Eddy-Current Responses of Cracks in 2024-T3 Aluminum at 483 kHz

The 100-GHz eddy-current responses of these fatigue cracks were obtained by mechanically translating the aluminum samples past the fixed dielectric-waveguide probe. The cracks were relatively tight (the crack opening was on the order of 1 μm), and we found that they could not be detected with our system. Therefore, we built the four-point bending jig shown in Fig. 6. By turning the screw in the jig and bending the aluminum sample, we could control the degree of crack opening in the manner depicted in Fig. 7.

Photographs of the crack opening in sample A4 as a function of the sample's surface displacement produced by bending are shown in Fig. 8. We began to detect the crack with our 100-GHz eddy-current system when the crack opening was about 3 μm, which corresponds to the middle photograph in Fig. 8. The right-hand photograph shows the maximum crack opening that could be obtained under elastic bending (about 6 μm).

The 100-GHz eddy-current response of the crack in sample A4 is shown as a function of relative surface displacement in Fig. 9. The horizontal and vertical axes in these photographs are proportional to the in-phase and quadrature components of the reflection coefficient, respectively. Zero relative displacement refers to the case where the bending is just sufficient to make the crack detectable. We attribute the differences between the responses shown in the eight photographs to the differences in the effective crack depth produced by bending (see Fig. 7).

In order to interpret the responses shown in Fig. 9, further explanation of the experimental procedure is in order. First, the position of the dielectric waveguide was adjusted so that it just touched the surface of the sample where the surface displacement was greatest (close to the position of the crack). Then the sample was moved so that the probe was about 5 cm to one side of the crack and the lift-off signal was nulled out (the resulting point on the X-Y display was moved around for convenience using the offset controls on the storage

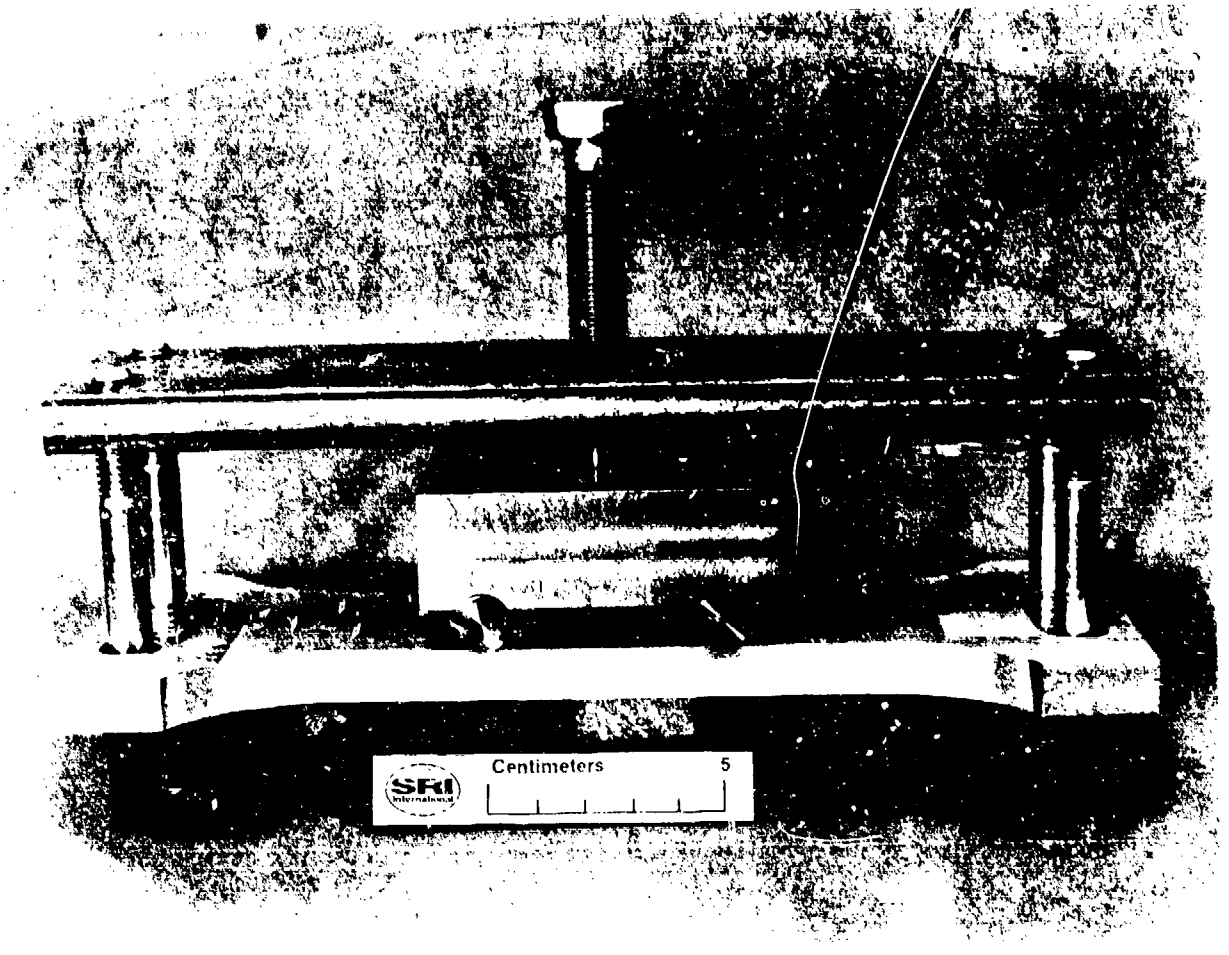

Fig. 6 Aluminum Sample Mounted in Four-Point Bending Jig

oscilloscope). Next, the sample was scanned slowly along a line containing the center of the crack. During this scan, the lift-off signal changes because the distance between the sample surface and the probe changes. This lift-off signal roughly follows a circular path on the oscilloscope, of which only a small part can be seen in the display (the diameter of the lift-off circle depends on the gain of the system). As the probe passes over the crack, the trace departs from its circular path (the amount of the departure from the circular path determines the degree of lift-off discrimination). Finally, as the probe moves past the crack, the response retraces its path, since the sample is bent symmetrically.

The striking feature of the crack signals is not so much the amplitude dependence on effective crack depth, but the phase dependence. For smaller crack depths, the crack-signal trace moves almost directly opposite to the lift-off trace. As the crack depth increases, the angle between the crack trace and the lift-off trace increases, progressing very rapidly through 90^0. This angle opens up to 180^0, and then reverses its direction back toward 0^0. The complete phasor display that would be seen if the entire lift-off circle were visible is illustrated in Fig. 10.

This behavior can be explained in terms of a propagating mode inside the crack. Such a propagating mode can exist in this case because the crack length is greater than half a wavelength. At one frequency, the approximate equivalent circuit for such a mode is a simple short-circuited transmission line shunted at its input by a radiation conductance, G. From our previously developed theory[3] we know that scattering from the crack is proportional to the input impedance of this equivalent network. Therefore, the phase of the crack signal at the metal surface, θ_s, is given by

$$\theta_s = \tan^{-1}[(1/GZ_0)\text{ctn } \beta d] \qquad (1)$$

where Z_0 is the characteristic impedance of the propagating mode and β is its propagation constant. The depth of the crack is d. In the phasor display, θ_s is the angle measured counter-clockwise from the crack phasor to a normal to the lift-off circle, as illustrated in Fig. 10. The variation of θ_s with crack depth calculated from Eq. (1) is shown in Fig. 11 for two values of $1/GZ_0$. The "high-Q" case, $1/GZ_0 = 10$, is more realistic for open cracks according to calculations using the theory developed last year. Qualitatively, the high-Q variation of phase is indeed what was observed during the gathering of data shown in Fig. 9. Furthermore, the calculations also show that the zero crossing of the phase is primarily determined by crack depth, and is

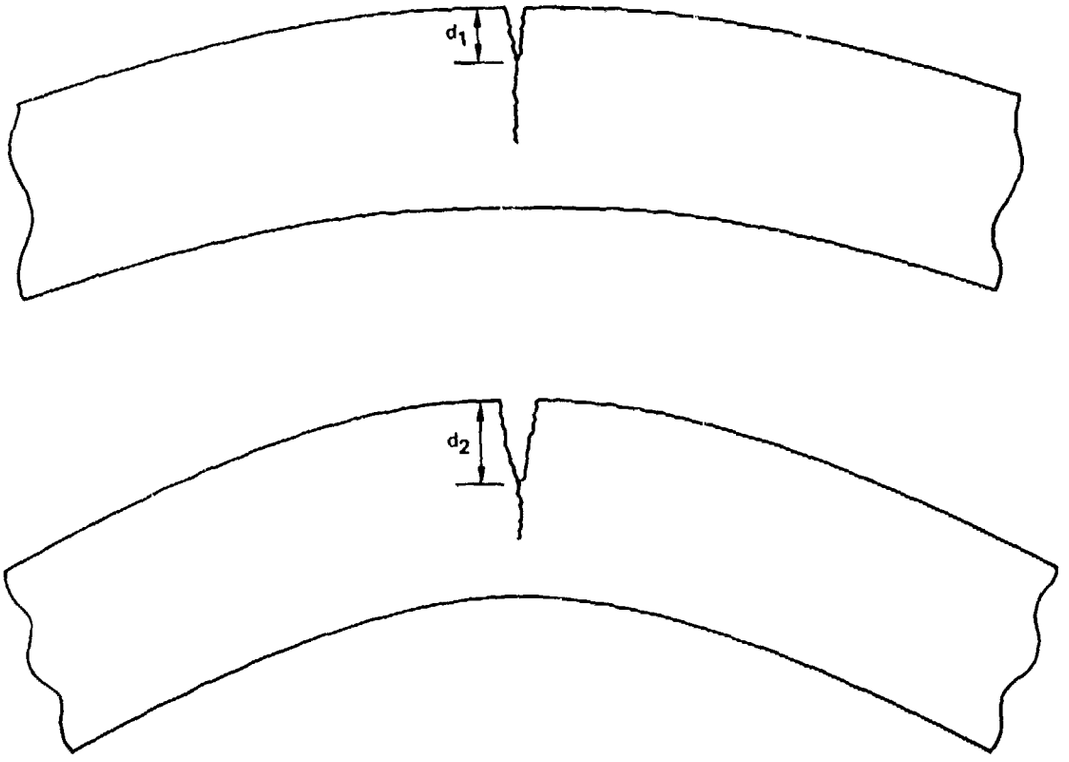

Fig. 7 Illustration of the Variation of Effective Crack Depth with Bending Displacement

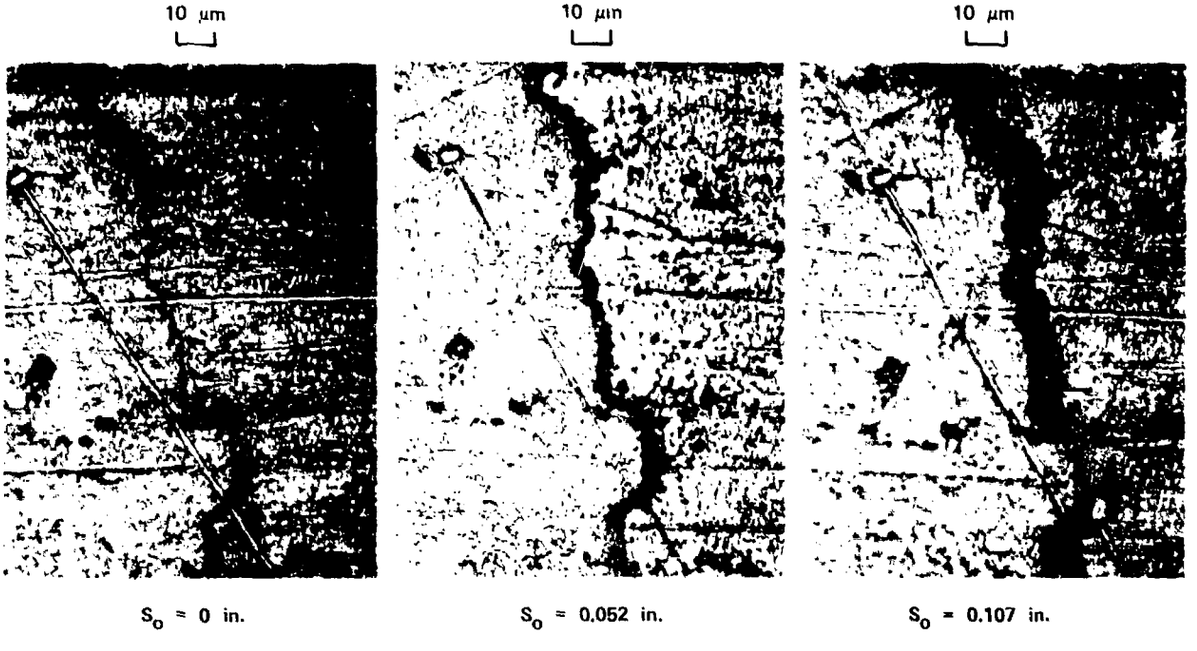

Fig. 8 Crack Opening as a Function of Surface Displacement, S_o

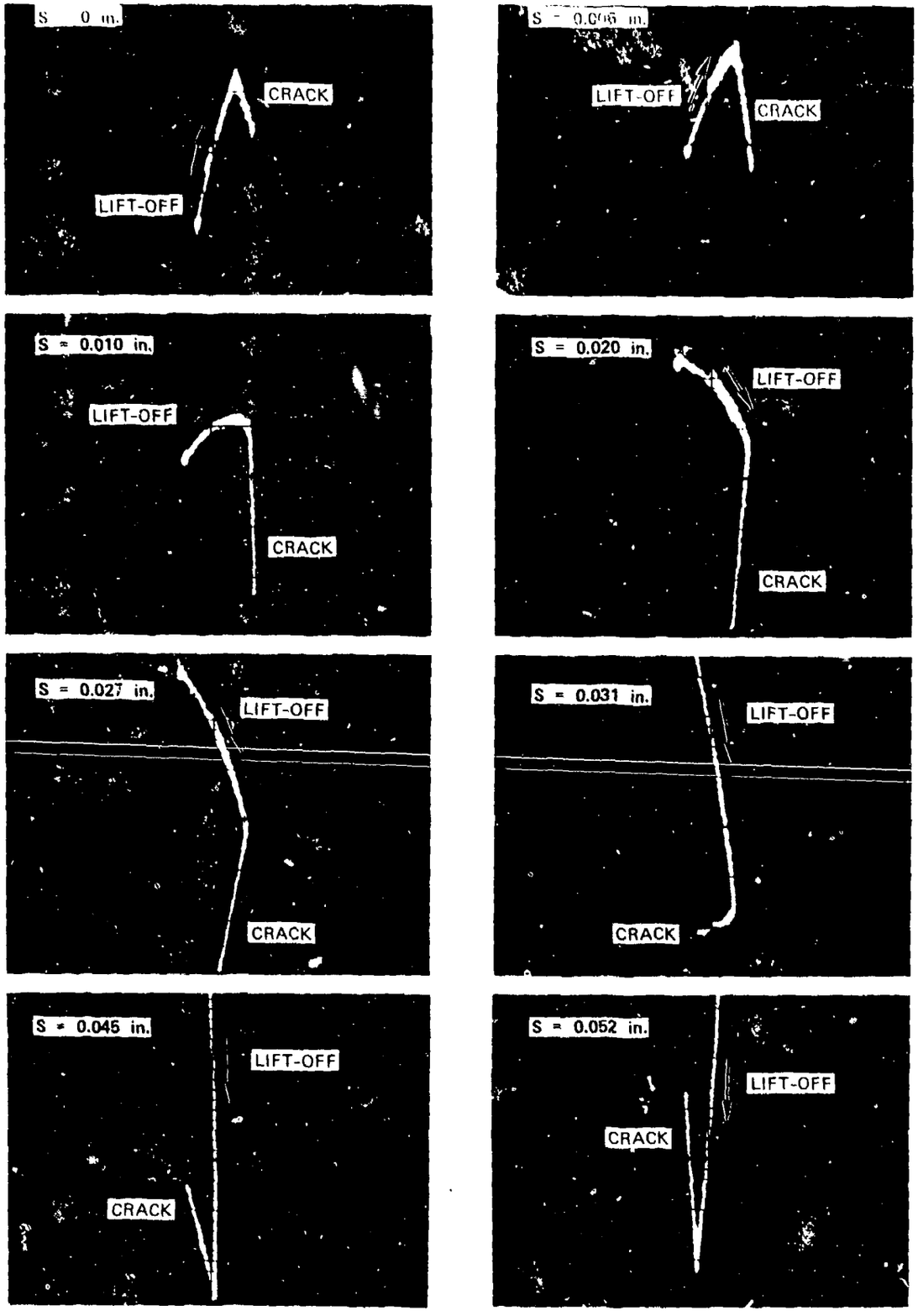

Fig. 9 100-GHz Eddy-Current Response of a Fatigue Crack in Sample A4 as a Function of Relative Surface Displacement, S

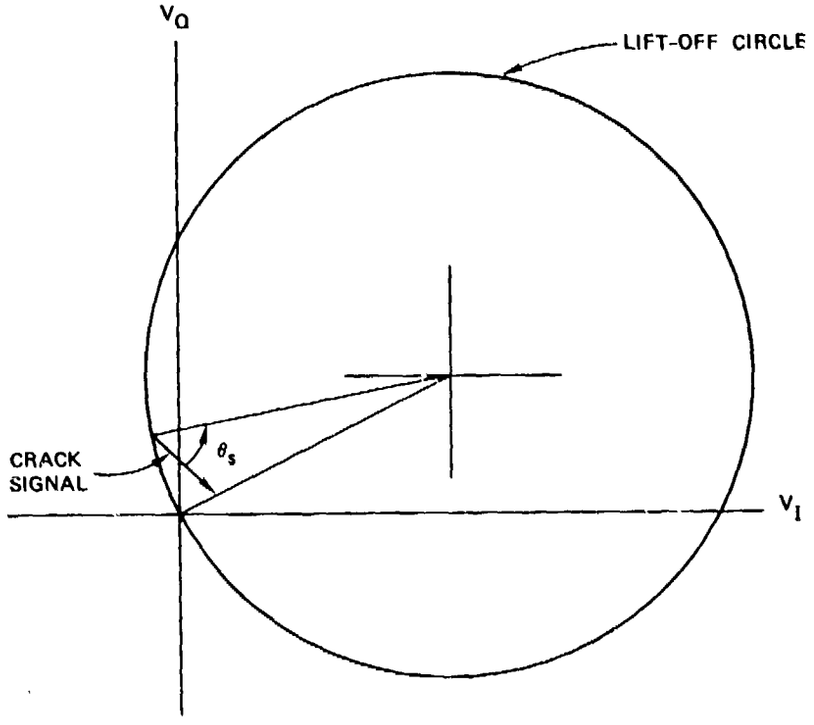

Fig. 10 Phasor Display of 100-GHz Eddy-Current Signal

not a strong function of crack length or opening.

This result suggests that crack depth can be measured accurately with this technique, provided that the crack is sufficiently open to be detectable and have a high Q, and provided that the crack length is larger than one-half wavelength. Rather than bend the specimen, in practice one would vary the frequency (the measurement system would have to be constructed to have sufficient bandwidth) until the crack signal is normal to the lift-off circle. At this point, βd is an odd multiple of $\pi/2$, the ambiguity being resolvable from a knowledge of the crack length. Then, assuming that a crack model is available* to provide an accurate value for β, the depth is determined. An important feature of this technique is that it is self-calibrating, since the phase of the crack signal is measured relative to the lift-off circle.

THEORETICAL SCATTERING FROM AN ELLIPTICAL CRACK

In the theory developed last year we found that the scattering produced by a crack was inversely proportional to a suitably defined crack admittance. This crack admittance is the sum of a radiation admittance and a cavity admittance. If the crack is several times deeper than it is wide, we can assume that the radiation admittance does not depend on the interior geometry of the crack, but only on the geometry of the crack opening. The radiation admittance of a thin rectangular aperture like that shown in Fig. 12(a) has been calculated assuming the electric field in the crack mouth is given by

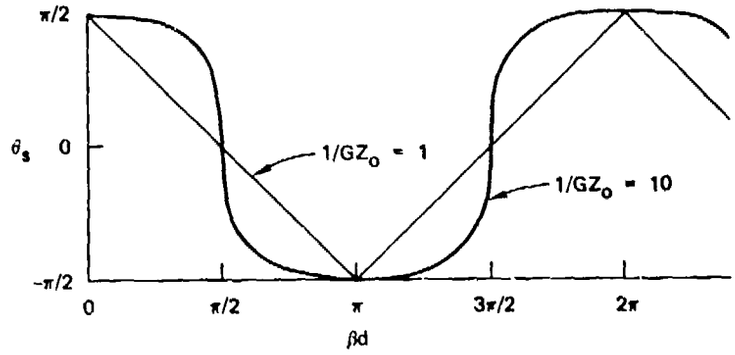

Fig. 11 Crack Signal Phase as a Function of Crack Depth

*The modeling of elliptical cracks is discussed in the next section.

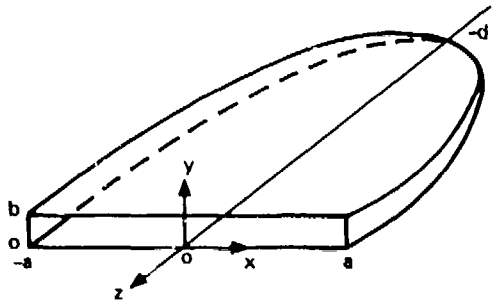

(a) CRACK GEOMETRY

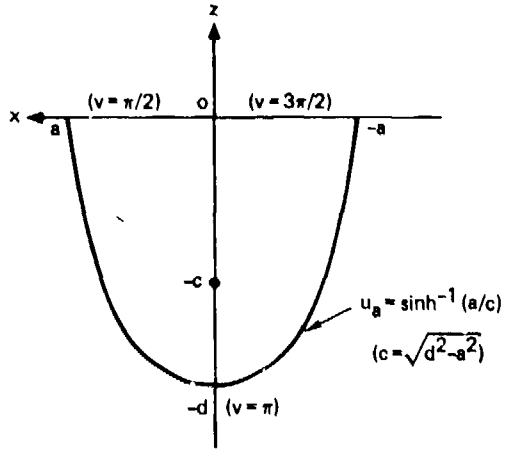

(b) ELLIPTICAL COORDINATES IN Z-X PLANE

Fig. 12 Coordinate Systems for an Elliptical Crack

$$\vec{E}(x,y,0) = \hat{a}_y \frac{1}{b} \sin [k(a-|x|)], \qquad (2)$$

and need not be discussed further. In Eq. (2), k is the free-space wave number and is equal to 2π divided by the free-space wavelength.

Assuming this same aperture field, the cavity admittance is given by

$$Y_c = -\int_{-a}^{a} dx \int_{0}^{b} dy \frac{H_x^c}{b} \sin [k(a-|x|)] \qquad (3)$$

where H_x^c is determined from

$$-j\omega\mu_0 \vec{H}^c = \nabla \times \vec{E}^c . \qquad (4)$$

Here, $\vec{E}^c$ is the interior electric field that is excited by the negative of the assumed aperture electric field. In other words, this interior electric field must satisfy the interior boundary conditions and be equal to the negative of the assumed aperture electric field in the aperture.

In our previous work involving a rectangular crack, the interior electric field was found by expanding the negative of the aperture field in a series of transverse-electric rectangular-waveguide modes. The result of this expansion was

$$Y_c^{rect} = -j \sum_{q \text{ odd}} \left(\frac{8}{\eta_0 kb}\right)\left(\frac{(ka)^2}{(\Gamma_q a)^3}\right) \cdot \cos^2 (ka/2) \operatorname{ctnh} (\Gamma_q d) \qquad (5)$$

where

$$(\Gamma_q a)^2 = (q\pi)^2 - (ka)^2 . \qquad (6)$$

When the interior of the crack assumes an elliptical shape like that shown in Fig. 12(a), we need to find the corresponding solutions of the Helmholtz equation

$$\frac{\partial^2 E_y^c}{\partial x^2} + \frac{\partial^2 E_y^c}{\partial z^2} + k^2 E_y^c = 0 \qquad (7)$$

which satisfy the interior boundary conditions and which can be used to expand the aperture field.

This solution is best obtained by transforming to elliptic cylinder coordinates (ξ,η) where

$$\xi = c \cdot \cosh u , \qquad (8a)$$

$$\eta = \cos v , \qquad (8b)$$

and

$$c = \sqrt{d^2 - a^2} . \qquad (8c)$$

In terms of the rectangular coordinates, (z,x), we can write:

$$z = \xi\eta \qquad (9a)$$

and

$$x = \sqrt{(\xi^2 - c^2)(1-\eta^2)} . \qquad (9b)$$

The coordinates, (u,v), for an elliptical crack are shown in Fig. 12(b). Assuming that the variables are separable in the new coordinate system so that

$$E_y^c(u,v) = U(u) \cdot V(v) , \qquad (10)$$

the Helmholtz equation separates into two equations:

$$\frac{d^2U}{du^2} - \left[h - \left(\frac{c^2k^2}{2}\right)\cosh 2u\right] U = 0 \qquad (11a)$$

and

$$\frac{d^2V}{dv^2} + \left[h - \left(\frac{c^2k^2}{2}\right)\cos 2v\right] V = 0 \qquad (11b)$$

where h is a separation constant. Referring to Fig. 12(b), the boundary condition on the perfectly conducting interior wall is

$$E_y^c(u_a,v) = 0 . \qquad (12)$$

Also, the assumed aperture field will only excite modes that are symmetrical about x = 0. Hence,

$$E_y^c(u,\pi/2) = E_y^c(u,3\pi/2) . \qquad (13)$$

Therefore, E_y^c is even in v with period 2π. This condition determines the separation constant, h.

The solutions to Eq. (11b) are known as Mathieu functions. The even solution with period 2π is designated $ce_{2n+1}(v,q)$, where $q = c^2k^2/4$ and n = 0,1,2,... . Each of these Mathieu functions is associated with a unique separation constant, which is designated as $h = a_{2n+1}$.

The solutions to Eq. (12a) are called modified Mathieu functions. Satisfaction of Eq. (12) requires that both independent solutions to this second-order differential equation for $h = a_{2n+1}$ be used. Therefore, we set

$$U(u) = A_{2n+1}Ce_{2n+1}(u,q) + B_{2n+1}Fey_{2n+1}(u,q) \quad (14)$$

where Ce_{2n+1} and Fey_{2n+1} are modified Mathieu functions of the first and second kinds, respectively. The constants A_{2n+1}, B_{2n+1} are determined by Eq. (12). They are:

$$A_{2n+1} = C_{2n+1}Fey_{2n+1}(u_a,q) \quad (15a)$$

and

$$B_{2n+1} = -C_{2n+1}Ce_{2n+1}(u_a,q) , \quad (15b)$$

with C_{2n+1} an arbitrary constant.

In summary, the solution for the internal electric field is

$$E_y^c(u,v) = \sum_{n=0}^{\infty} C_{2n+1}ce_{2n+1}(v,q)\, Ze_{2n+1}(u,q) \quad (16)$$

where

$$Ze_{2n+1}(u,q) \triangleq Fey_{2n+1}(u_a,q)\, Ce_{2n+1}(u,q) - Ce_{2n+1}(u_a,q)\, Fey_{2n+1}(u,q) . \quad (17)$$

It can be shown that the Ze_{2n+1} are orthogonal over the interval $[0,u_a]$, i.e.,

$$\int_0^{u_a} Ze_{2m+1}\, Ze_{2n+1}\, du = 0 \quad (18)$$

if $m \neq n$. Hence, the constants C_{2n+1} can be determined from the relation

$$C_{2n+1} = \frac{-\int_0^{u_\delta} \frac{1}{b}\sin[k(a-c\cdot\sinh u)]\, Ze_{2n+1}(u,q)\,du}{ce_{2n+1}(\pi/2,q)\int_0^{u_a} Ze_{2n+1}^2(u,q)\,du} . \quad (19)$$

Series expansions for the Mathieu functions $ce_{2n+1}(v,q)$, $Ce_{2n+1}(u,q)$, and $Fey_{2n+1}(u,q)$ can be found in the literature.

The magnetic field in the crack mouth can be obtained from Eq. (4) expressed in elliptic coordinates, that is,

$$-j\omega\mu_0 H_\zeta^c(\zeta,0) = \frac{1}{\zeta}\frac{\partial}{\partial\eta}\left\{-E_y^c(u,v)\right\}_{\eta=0} . \quad (20)$$

From Eq. (9b) we find that

$$dx = \zeta\, du \quad (21)$$

when $\eta = 0$. Hence, substitution of Eqs. (20) and (21) into Eq. (3) gives the result

$$Y_c = (2j/\omega\mu_0)\int_0^{u_a} \sin[k(a-c\cdot\sinh u)] \cdot\left\{\frac{\partial E_y^c(u,v)}{\partial(\cos v)}\right\}_{\cos v=0} du . \quad (22)$$

This integral can be evaluated numerically, but such calculations have not yet been carried out.

SUMMARY AND CONCLUSIONS

Improvements in our 100-GHz eddy-current measurement system have been described, and the results of measurements made on fatigue cracks in 2024-T3 aluminum using this improved system have been presented. It has been shown that the phase of the 100-GHz eddy-current signal is a sensitive measure of crack depth, provided that the crack length is greater than about one-half wavelength. This phase measurement is a self-calibrating technique for determining crack depth. However, this technique requires that the crack be sufficiently open so that the component of crack impedance associated with energy propagating inside the crack is both detectable and larger than the skin-effect component of crack impedance, which is proportional to the surface impedance of the metal. To date, our 100-GHz system has not been sensitive enough to detect the skin-effect component.

In addition to this experimental work, we have also presented the theory necessary to compute the crack impedance associated with energy propagating in an elliptically shaped crack.

Therefore, we conclude that microwave eddy-current techniques can be used to accurately determine the dimensions of surface-breaking cracks in metals. However, more work is needed to improve crack models, system sensitivity, and particulary the practicality and flexibility of the physical implementation.

ACKNOWLEDGMENTS

Several other staff members at SRI made significant contributions to this work: Dr. C. M. Ablow provided the basic mathematical analysis of the elliptical crack, Dr. L. E. Eiselstein designed the four-point bending jig, and Dr. A. C. Phillips designed the 3-kHz nulling network.

This work was sponsored by the Center for Advanced NDE operated by the Rockwell International Science Center under Contract F33615-80-C-5004.

REFERENCES

1 R. J. Hruby and L. Feinstein, "A Novel Nondestructive, Noncontacting Method of Measuring the depth of Thin Slits and Cracks in Metals." The Review of Scientific Instruments, Vol. 41, pp. 679-683 (May 1970).

2 A. Hussain and E. A. Ash, "Microwave Scanning Microscopy for Nondestructive Testing," Proceedings of the 5th European Microwave Conference, Hamburg, Germany, pp. 213-217 (September 1975).

3 A. J. Bahr, "Microwave Eddy-Current Techniques for Quantitative NDE," Proceedings of the DARPA/AFML Review of Progress in Quantitative NDE, La Jolla, California (July 1979).

4 N. W. McLachlan, Theory and Applications of Mathieu Functions, Oxford: Oxford University Press (1951).

SUMMARY DISCUSSION

Jim Martin, Chairman (Rockwell Science Center): Are there any questions?

Dick Elsley (Science Center): What is the skin depth in the aluminum?

Al Bahr (SRI): I don't have an exact number for that.

Jim Martin, Chairman: You said several microns.

Al Bahr: At 1 gigahertz, it's several microns, so at 100 gigahertz the skin depth is one tenth as large.

C.G. Gardner (University of Houston): You said when you change from linear polarization to circular polarization, you become insensitive to the crack orientation. What was the loss of sensitivity you associate with that?

Al Bahr: It's three db because you're lining up the polarization correctly only half of the time, i.e., the polarization is spinning around. So presumably you would be able to detect a particular crack with a smaller crack opening if the polarization were linear and aligned normal to the crack.

I should mention that another thing we are trying to do is to look at resonator probes in an effort to improve our sensitivity. We always need more sensitivity.

Frank Meunnemann (Stanford University): Have you calibrated the actual impedance in ohms?

Al Bahr: No.

Jim Martin, Chairman: If there are no more questions, this concludes today's session.

FEASIBILITY OF NONDESTRUCTIVELY EVALUATING THE M140 RECOIL PISTON HEAD WELD

Roy L. Buckrop
Product Assurance Directorate
U.S. Army Armament Command
Rock Island, Illinois 61299

ABSTRACT

The application of nondestructive testing (NDT) to a weld cracking problem on the M140 Recoil Piston is discussed. Addressed in the presentation is the technique used for screening recoil pistons for crack sensitive weld filler metal and the inspection of piston welds for flaw discontinuities.

INTRODUCTION

Test Date and Place: 15-18 January and 5-8 February 1980, Shop M and L, Rock Island Arsenal.

Object: To establish feasibility of utilizing Nondestructive Testing to identify weld bead alloy and evaluate weld material integrity (soundness) of the M140 Recoil Piston Head Weldment (Fig. 1).

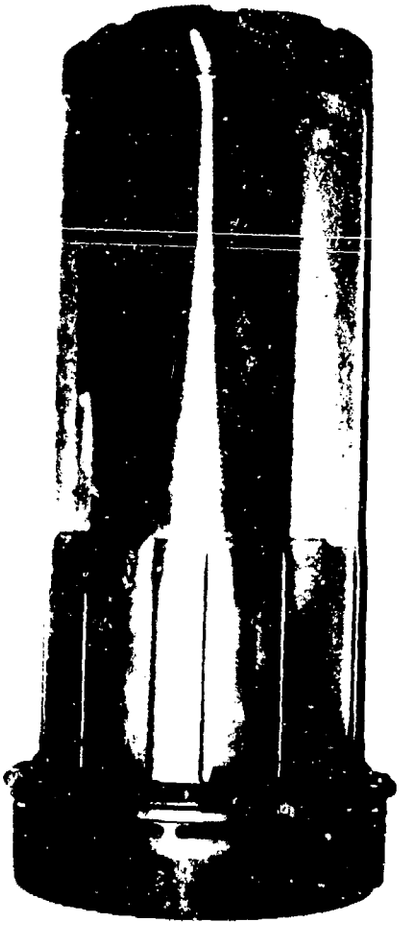

Fig. 1 M140 Recoil Piston Weldment

Scope: During routine machining, longitudinal and transverse surface cracks were observed in the M140 Recoil Piston Head Weld. Test specimens cut from a defective piston also revealed extensive weld root cracking which extended into the weld bead along the weld's longitudinal axis. The cause for both the surface and sub-surface cracking was postulated as resulting from two sources: one being the weld filler material (rod) and the other control of the welding process. This study is concerned with the screening of pistons as to weld filler material (one filler material is suspect of being crack sensitive) and the nondestructive evaluation of M140 Recoil Piston Head Welds for flaw discontinuities.

Approach: There were three NDT (Nondestructive Testing Techniques) considered for this investigation: ultrasonics, magnetic particle, and eddy current.

Test Specimens: Two categories of test specimens were used; type one (Fig. 2) consisted of four fabricated inverted tee ($\perp$) weldments, two heat treated and two as welded. The weld joint for these was a "J" preparation, the same as the piston head. Two were welded with 4130 welding rod, one heat treated and one as welded. The other two were welded with the suspect (crack sensitive) rod L6M (4340), one heat treated and one as welded. The test specimens' weld beads were machined to approximately a 125 finish to accommodate eddy current test probe coupling. These test specimens were used for weld bead alloy evaluations. Type two test specimens (Fig. 3) were used for discontinuity detection and evaluation and consisted of various select sections cut from rough machined defective piston weldments. For the magnetic particle test, .043-inch diameter simulated flaws (holes) were drilled along the longitudinal axis of the weld, starting from the edges and drilling 3/4-inch deep toward the specimen center. The holes were located below the center of the weld face at varying depths of .030 inch, starting at .060 inch. These test specimens were used to evaluate subsurface material discontinuities. The above test specimens were also used for the eddy current discontinuity depth tests. Centered in the specimen weld face, slots approximately .007-inch wide by 1/4-inch long were machined at .025, .050 and .073-inch deep, along the longitudinal axis of the weld (Fig. 3).

Fig. 2 Type One Test Specimens (Fabricated Weld Samples)

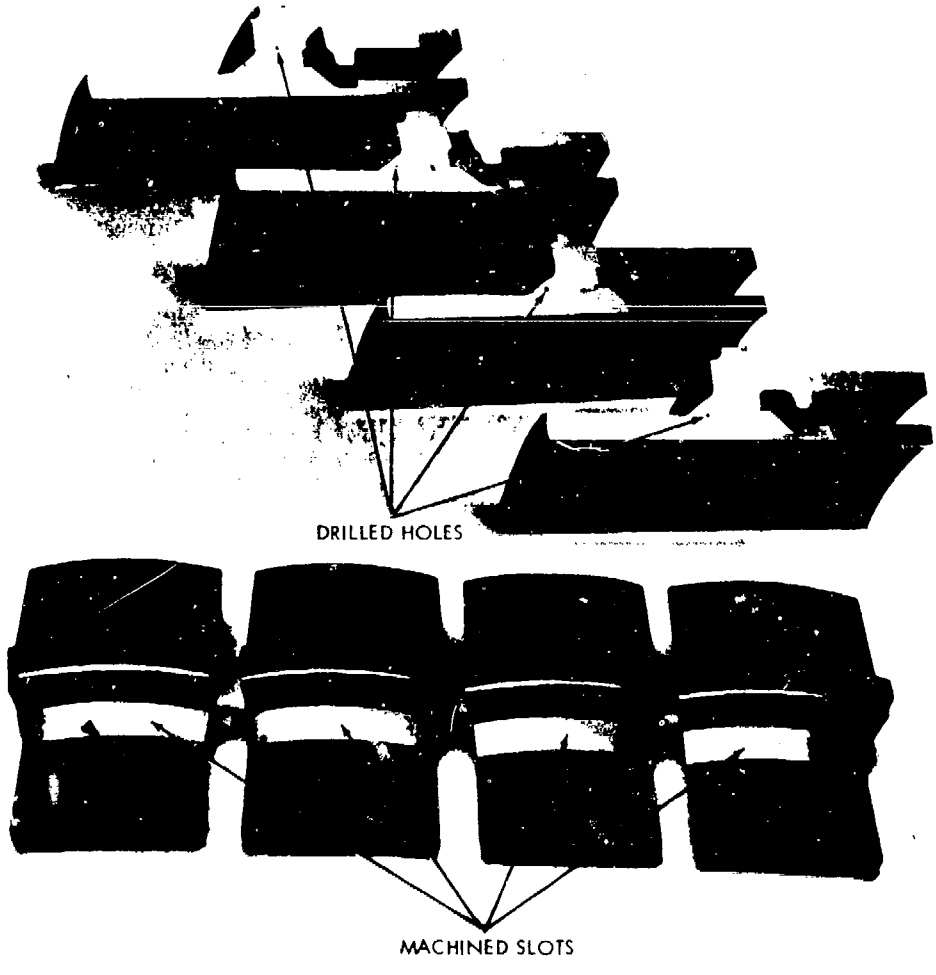

Fig. 3 Type Two Test Specimens (Sections from Defective Pistons)

TEST #1: ULTRASONIC PULSE ECHO

Theory: Angle beam ultrasonic energy transmitted into the outer surface of the weldment, along its longitudinal axis, from the head end, will be reflected from the inner surface of the piston, back into the welded area, allowing for internal inspection of the weld. Discontinuities present in the weld area will reflect a portion of the transmitted sound energy back to the inspection probe. The probe (transducer) will convert the reflection to an electric signal proportional in amplitude to the intensity of the ultrasonic signal. This in turn will be displayed on a cathode ray tube for interpretation.

Equipment: Automation Industries, Inc. Reflectoscope UM 721. One 45° angle beam search unit, 5MHZ.

Procedure: Following instrument warm up and stabilization, a known cracked test specimen (Fig. 4) was coated with oil couplent and a 45° angle beam search unit used to qualitatively scan the defective weld. Signal amplitude was adjusted to full scale for a signal reflection from the corner of a reference block.

Results: Hand scanning produced erratic results and was difficult to control, demonstrating a need for test probe fixturing. Appropriate flaw reference standards would need to be established for discontinuity evaluation.

Conclusion: Due to time limitations, this technique was abandoned. However, it does have enough promise to warrant further development for future application.

Fig. 4 Piston Section Cracked in Production

TEST #2: MAGNETIC PARTICLE

Theory: Ferro-magnetic materials, when exposed to intense and highly concentrated electro magnetic fields, can be made to reveal sub-surface internal discontinuities. Related external leakage fields caused by discontinuities will attract and hold an iron particle media (either dry as powder or in a liquid suspension) revealing their presence and plainer location.

Equipment: Two rectified DC magnetic particle test machines: wet, 5000 amp max capacity with magnetizing coil and dry 1400 amp max capacity with prods.

Procedure: A cursory dry magnetic particle test was performed on a specimen cut from a rough machined defective piston (Fig. 4). The specimen was severely cracked along the weld longitudinal axis, extending from the root nearly through the weld, stopping near the surface. Successful detection of this subsurface crack was followed by a progressive evaluation of fabricated flaws (holes) placed into the edges of test specimens cut from a rough machined defective piston (Fig. 3).

A hole (one) was drilled in from each side of a specimen (two holes per specimen). Starting at .060 inch below the weld surface, the holes were alternately placed at .030-inch increments below the surface down to .270 inch. Both the wet and dry magnetic particle tests were evaluated. The current used was continuous and approximately 3800 ampers for the wet method, which used a coil for magnetization. The specimen was positioned directly on the inner surface of the coil during energizing. For the dry technique, approximately 1400 continuous ampers were used for magnetization, using prods placed at each end of the weld.

Results: Both the wet and dry magnetic tests were able to show sub-surface discontinuity indications on the sectioned test specimen cracked during production welding (Fig. 4). Both methods were also capable of detecting simulated flaws (holes) down to .090 inch below the weld surface (Fig. 4). The dry (powder) method appeared to be somewhat more positive. Further increases in magnetizing force (higher currents) may make it possible to detect discontinuities even deeper below the weld surface. However, for each material there is a practical depth sensitivity limit based on ferric induction characteristics. The degree of sensitivity experienced, however, appeared to result from limited magnetizing force (current) and not necessarily to ferric induction limits of the weld material.

Conclusion: The continuous magnetization method, with both the wet and dry magnetic particle tests, demonstrated the capability of revealing weld material discontinuities approximately one-tenth of an inch below the surface. Discontinuity detection, deeper than one-tenth inch, may be possible with larger magnetizing forces (currents). The dry magnetic particle test demonstrated the strongest sensitivity for the deepest detectable discontinuity (drilled hole).

TEST #3: EDDY CURRENT

Theory: The consideration of eddy current testing for this study is based primarily on its adaptation to metal sorting. However, the response of eddy currents to material discontinuities was used to evaluate the depth of flaw indications located by magnetic particle inspection. The test instrument utilizes a probe coil which is excited by an oscillating electric current. The probe, with its associated field, induces eddy currents in the test part (an electrical conductor) which will reflect changes in material permeability and electrical conductivity according to structure variations. The test signal can be monitored for both amplitude and phase variations.

Equipment: Automation Industries, Inc. Eddy Current Tester, EM 3300 with two probes (Black and Green) both suitable for operation at the selected test frequency of 400 KHZ.

Procedure: The eddy current instrument was allowed to warm up and stabilize prior to testing. An operating frequency of 200 KHZ was set on the frequency counter display with an appropriate probe connected to the instrument. 200 KHZ was used for the weld material evaluation and 400 KHZ for the flaw depth test. The instrument was electrically balanced (nulled). The trace was adjusted to the center of the display and a favorable phase reference angle selected for first quadrant presentation. Two tests were run, one to detect the presence of 4130 or 4340 (L6M) weld material and the other to quantitatively evaluate the depth of surface flaws detected by magnetic particle testing. For the differentiation of weld material, the probe was placed on the machined surface of referenced specimen welds (Fig. 2) and the resulting display trace compared to traces obtained from suspect weld material. For the flaw depth test, the probe was moved (scanned) across suspect flaws. Any surface discontinuity scanned across will produce a blip on the display, projecting out from the basic material trace proportional in amplitude to its perpendicular depth beneath the material surface. Signals obtained from surface flaws are then evaluated by comparing them to signals obtained from referenced slots of known depths (Fig. 3).

Results: The eddy current test was able to distinguish between the 4130 and L6M (4340 alloy) weld material. (See eddy current material response displays in Fig. 5.) The eddy current measurements of surface discontinuity depths by comparison to referenced slots are affected by several factors, such as: Actual cracks will produce deflection signals approximately one-half that of signals produced by referenced slots. Cracks may not cause deflections at the same phase angle as referenced slots. Signals from surface discontinuities will be proportional to their depth as measured perpendicular to the surface, not the dimension of a flaw extending into a material angled away from a perpendicular axis to its surface. Residual magnetism and permeability variations in ferro-magnetic material affect the eddy current response. Because of the above factors, eddy current test techniques for depth evaluations of surface discontinuities must be validated by physical sectioning (destructive tests) or other NDT techniques.

Conclusion: The identification of weld material as to which alloy is present (4130 or L6M) using the eddy current technique is considered feasible. The evaluation of surface discontinuity depths must be approached with caution and each application must be individually validated by either other non-destructive techniques or destructive tests.

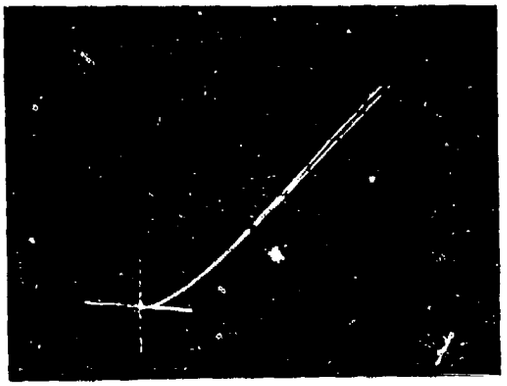

4130 - Upper Trace/L6M - Lower Trace

Instrument Control Settings - EM3300:

freq = 200 KHZ - Pos. 4
R = 456
X = 590
Ø = 132.5
SENS. = 04
VERT. = 1 Volt/Div
HORIZ. = 0.5 Volt/Div

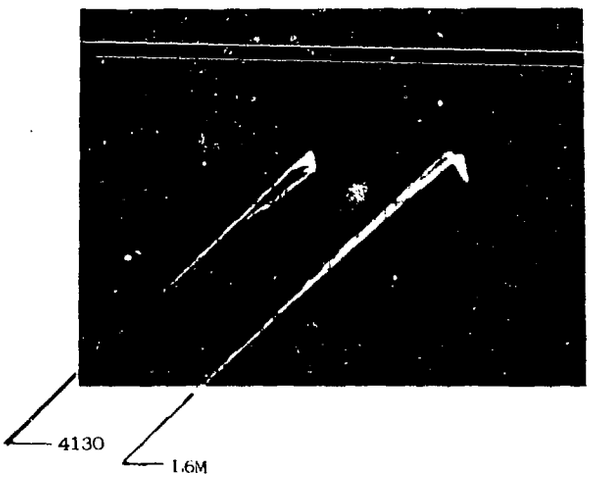

Instrument Control Settings - EM3300:

freq = 200 KHZ - Pos. 4
R = 600
X = 814
Ø = 132.5
SENS. = 09
VERT. = 1 Volt/Div
HORIZ. = 0.5 Volt/Div

Fig. 5 Eddy Current Response-RIA Weld Samples 4130 and L6M

ACKNOWLEDGMENTS

This feasibility study was performed in an atmosphere of emergency, and could not have succeeded without the assistance of Harold Hatch, US Army Materials and Mechanics Research Center, Watertown, MA; Charles Hopper, Ron Paper, Jim Dahms, Tom Behr, and Kim Schluenz, Rock Island Arsenal Quality Assurance, and representatives from Rock Island Arsenal Engineering and Rock Island Arsenal Manufacturing. Mr. Hatch's support and personal commitment was especially appreciated.

WAVEFORM DESIGN FOR MAXIMUM PASS-BAND ENERGY*

Steven R. Doctor, Alan G. Gibbs, R. Parks Gribble
Pacific Northwest Laboratories
Richland, Washington 99352

ABSTRACT

One way to maximize the sensitivity of an ultrasonic inspection is by establishing the pulser output voltage waveform to provide the maximum possible fraction of its energy in the pass-band of the piezoelectric transducer. An analytical study is reported that is backed up with experimental verification. Two pulser constraints are analyzed in this study. The first constraint is to study the common and easily generated waveform shapes for which each waveform has unit energy and compare to the optimum waveform shape with unit energy that is determined analytically. The second constraint is to repeat the first analysis with waveforms having unit amplitude rather than unit energy.

The analysis for the first constraint shows that the numerically intractable problem of summing a very large number of Fourier coefficients can be replaced by a mathematically equivalent evaluation of the pass-band energy which requires only the integration of smooth functions. This alternative formulation also leads to the result that the optimized waveform is the eigenfunction of a particular integral operator corresponding to the largest eigenvalue. The eigenvalue itself gives the maximum attainable pass-band energy. The optimized waveform is compared with sine waves, rectangular waves, trapezoidal waves, triangle waves and exponential spikes for 1/2, 1 and 3/2 cycle durations.

The analysis for the second constraint shows that the unit amplitude is in the form of an inequality which is outside the realm of the classical calculus of variations. An exact characterization of the optimized waveform was not found but numerical integration techniques were employed to determine the pass-band energies for the waveforms considered under the first constraint.

Finally, a breadboard pulser model is constructed and extensive comparisons of the various waveshapes, sensitivity studies, spectral distributions and experimental verification are made for each constraint.

INTRODUCTION

The Manufacturing Technology Program of the U.S. Air Force has undertaken a program to develop a reliable and advanced modular nondestructive testing system that will meet the current and future requirements of USAF Field/Depot NDE activities. As part of this program, a review and evaluation was made of all current technology for improving the performance of ultrasonic inspection equipment. Advances in electronic devices (i.e., high power FET devices) have made it possible to build compact, small, economical and high voltage pulsers capable of generating a variety of waveshapes.

For many years, a controversy has existed over which type of pulser output voltage waveform is the best signal to employ when driving a piezoelectric transducer. The solution to this controversy requires that many UT system parameters need to be evaluated, i.e., sensitivity, resolution, impedance matching, etc. The analysis reported here is for the theoretical optimum waveform design and other selected waveforms which can be generated in the laboratory. The results presented are backed up with laboratory experiments. The details of the analytical analysis are presented first for waveforms which have unit energy, next, the analysis for waveforms which have unit amplitude and finally, the laboratory results are presented.

As a part of the Manufacturing Technology Program of the U.S. Air Force, a survey was made of USAF Field/Depot NDE activities and it was found that the transducer employed in the largest number of inspections was a 5 MHz unit. The following analysis will use a transducer operating at 5 MHz, with a bandwidth of 40%. The 40% bandwidth is chosen because a transducer typical of the ones used by the USAF is available and it has a 41% bandwidth. Therefore, a transducer is available to provide experimental results for comparison with the theoretical results. Beside the data shows that the results would not change significantly for other bandwidths.

MAXIMUM PASS-BAND ENERGY FOR WAVEFORMS WITH UNIT ENERGY

The analysis presented here is in a general form that leads to a closed mathematical solution. Let f(t) denote a function of period T and let f(t) be zero for $\tau < t < T$ and periodic in T, as shown in Figure 1. The energy analysis proceeds by expanding f(t) in a Fourier series and then, either integrating or summing the square of each frequency present to find the total energy (E_T). The fractional energy (E_F) in a particular frequency band can be found by summing or integrating only the frequencies contained in the band (E_B) and dividing by the total energy (E_T).

$$E_F = \frac{E_B}{E_T} = \frac{T \sum_{n \in N} (fn)^2}{\int_0^t f^2(t)dt} \qquad (1)$$

*This work was sponsored by the Manufacturing Technology Division of the Air Force, Wright Aeronautical Laboratories, under Contract F33615-78-C-5032. For further information, contact Battelle Program Manager A.S. Birks (509) 375-2372 or the U.S. Air Force Program Manager R.R. Rowand (513) 255-5407.

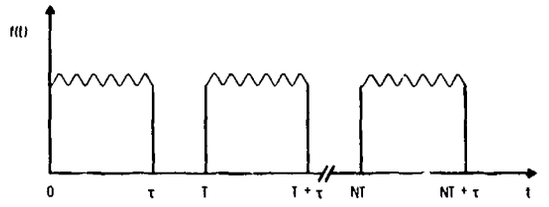

Fig. 1 Definition of the pulser output waveform.

This equation can be manipulated to yield:

$$E_F = \frac{\int_0^1 dx f(x) \int_0^1 dx' f(x') k(x-x')}{\int_0^1 f^2(x) dx} \qquad (2)$$

where $x = t/\tau$, $f(x) = |f(t)|_{t \to x\tau}$ and K is a kernel given by:

$$K(x) = \frac{2}{\pi} \ell\varepsilon_1 \frac{\sin \ell\varepsilon_2 x}{\sin \ell\varepsilon_1} \cos(\pi + \varepsilon_1) \qquad (3)$$

where

$$\varepsilon_1 = \pi/2\ FT \qquad (4)$$

$$\varepsilon_2 = \pi b/200 \qquad (5)$$

Note that K depends on three factors:

ℓ = length of signal in number of half-cycles of the driver frequency

FT = (driver frequency F) x (period T)

b = % bandwidth

This formalism has the advantage that the sum in equation (1) can now be performed in closed form. This formalism has replaced the problem of adding a very large number of $|f_n|^2$ with the easier problem of integrating smooth functions. An additional bonus is that an equation can be obtained for the optimum waveform.

The optimum waveform equation is derived by recognizing that the calculas of variations is applicable to equation (2). This leads to the conclusion that the maximum pass-band energy occurs when f(t) for $0 < t < \tau$ is the eigenfunction of the integral operator K corresponding to the largest eigenvalue. The resulting energy is the size of the eigenvalue. This formalism does not readily lend itself to solutions for various f(t)'s but numerical solutions can be easily obtained. Equation (2) was programmed on the VAX 11-780 computer using available library matrix routines. A Simpson's integration rule was used with good convergence observed on the largest few eigenvalues and eigenfunctions.

The results using numerical integrations are summarized in Table 1. The eigenfunctions for this problem cannot be written in the form of elementary functions. Hence, the optimum function is found numerically, which in this case is fortuitously quite similar to the elementary function sin πx. In reality, the optimum function and sin πx agree only to three figures and round off causes the apparent four figure agreement. For f(t) intervals with an integer multiple (ℓ), of center frequency half cycles, the optimum function is close to sin $\ell\pi x$ but the differences get larger as ℓ increases (see Table 3). In all cases, the differences are genuine, since the true eigenfunction is sin $\ell\pi x$ only in the limit as the bandwidth goes to zero. For all practical purposes, the first four waveshapes provide about the same energy in the 40% bandwidth. It is interesting to note that the exponential was the worst case.

Table 1
Comparison of Different Waveforms with Unit Energy for the Fractional Energy in a 40% Bandwidth

Waveform	Fractional Energy in 40% Bandwidth
Optimum f(x)	19.98%
Sin πx	19.98%
Trapazoid Wave	19.94%
Triangle Wave	19.68%
Square Wave	16.30%
Exponential (e^{-5x})	11.60%

Various trapezoids were evaluated and it was discovered that the symmetrical trapezoids are better than asymmetrical ones. For symmetrical trapezoids of the form shown in Figure 2, the numerical results are listed in Table 2. The limit of the "a" values lead to the square wave for a = 0 and the triangle wave for a = 1/2.

Table 2
Performance of Trapezoidal Waveforms

a Value	Fractional Energy in 40% Bandwidth
0 (rectangle)	16.3%
0.1	18.1%
0.2	19.4%
0.3	19.98%
0.33 (best)	19.94%
0.35	19.94%
0.4	19.87%
0.5 (triangle)	19.68%

Figure 3 shows the plots for four of the waveshapes of interest. This data shows that for other transducers with differing bandwidths, the efficiency for these waveshapes would all vary in about the same proportion, keeping the ordering in Tables 1 and 2 the same. It is also apparent from Fig. 3 why the exponential waveshape has been used extensively. First, the exponential wave is easy to generate and second, the power output remains more nearly constant over a very large frequency band.

Finally, some of the waveforms were examined for ℓ = 2, 3 etc. and these results are contained in Table 3. As ℓ increases, the effect is to

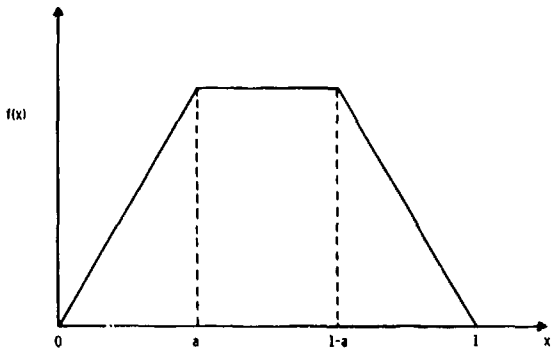

Fig. 2 Trapezoidal waveshapes.

narrow band the power spectrum and concentrate the power into the bandwidth of interest. The only exception was the exponential which provided the maximum power for $\ell = 2$.

MAXIMUM PASS-BAND ENERGY FOR WAVEFORMS WITH UNIT AMPLITUDE

This problem is related to one already solved but with the constraint in amplitude which satisfies:

$$|f(x)| \leq 1 \qquad (6)$$

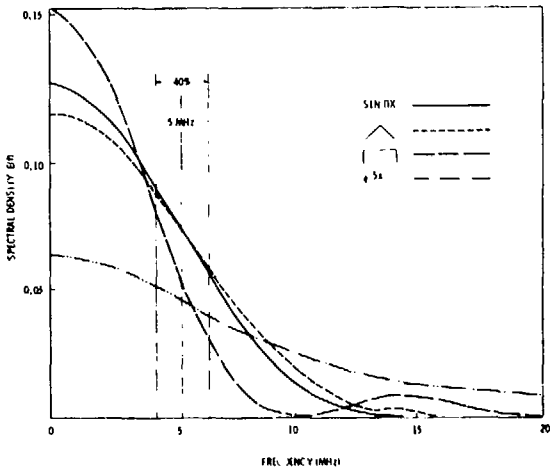

Fig. 3 Power spectral density for a sine wave, triangle wave, square wave and exponential.

Table 3
Fractional Power Supplied by Various Waveshapes for Integer Multiples of Half Cycles of the Center Frequency

	Fractional Energy in 40% Bandwidth for		
ℓ	Optimum f(x)	Sin $\ell\pi x$	$e^{-5t/\ell\tau 1/2}$
1	19.98%	19.98%	11.6%
2	38.67%	38.67%	12.42%
3	55.04%	54.98%	10.85%
4	68.47%	68.18%	8.97%
5	78.81%	77.97%	------

The objective is to determine the actual energy within the 40% bandwidth for various waveforms f(t). Ideally, we would like to find the waveform f(t) which maximizes E_F in equation (2), subject to the constraint of equation (6). However, this constraint is in the form of an inequality and makes this problem fall outside the realm of classical calcules of variations. Methods have been developed in the theory of optimal control for treating problems with inequality constraints but these approaches were not pursued. Instead, a numerical solution was obtained for the waveshapes described in the previous section. There was a change in the time constant for the exponential wave. The previous study used a time constant (5) such that the exponential was reduced essentially to zero in a time of one-half cycle of the center frequency. In the present study, an exponential time constant was selected so that the waveform decayed to one-half its initial amplitude in the same time as one-half cycle of the transducer's center frequency.

The total energy content of each signal can be found by calculating the denominator of equation (2). The integrals can all be performed in closed form and the results are shown in Table 4. Using numerical computer techniques as discussed in the previous section, the fractional energy can be determined. Table 5 contains those results. It is interesting to note that although some of the waveforms are very efficient at getting their available energy into the pass-band (trapezoid, sine and triangle waves), they do not produce maximum pass-band energy. This results from the fact that the total available energy from each waveform is different. Consequently, the waveform which produces the highest pass-band energy appears to be the superior pulse driver waveshape.

Table 4
Total Energy for the Waveforms Shown

Waveform	$E_T = \int_0^1 f^2(x)dx$
Square	a(1.0 for a = 1)
Trapezoid	$1-\frac{4}{3}a$ (5/9 for a = 1/3)
Triangle	1/3
Sin $\ell\pi x$	1/2 (independent of ℓ)
Exponential	$(1-1/4^{\ell})/Ln4^{\ell}$

Figures 4 and 5 contain the power spectral density plots for the waveforms considered. It is apparent from these figures why the square wave is by far the best waveform to be used for maximizing pass-band energy.

TABLE 5

Total Energy E_T, Fractional Energy E_F and Pass-Band Energy E_B for the Waveform Shown

Waveform	E_T	E_F	E_B
Square	1.000	0.1631	0.1631
Trapezoidal (a = 1/3)	0.5555	0.1994	0.1107
Sin πx	0.5000	0.1998	0.09989
Triangle	0.3333	0.1968	0.06568
Exponential	0.7213	0.05582	0.04026

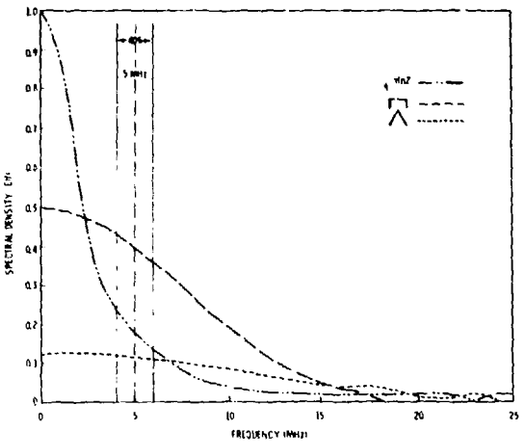

Fig. 4 Power density spectral plot for the square, triangle and exponential waves.

EXPERIMENTAL RESULTS

To verify the results predicted by the two studies reported above, laboratory tests were performed. It is very convenient to generate in the laboratory, waveforms which have the same peak amplitude. However, it is extremely difficult to make the driver output energy equal for the different waveshapes because the piezoelectric transducer is a nonlinear complex load and this creates significant distortions in the driver pulse shape. Consequently, the results reported here will only be for equal driver pulse amplitudes. Furthermore, the two limiting cases in the unit amplitude study are the square wave and the exponential. These two curve shapes were studied in detail.

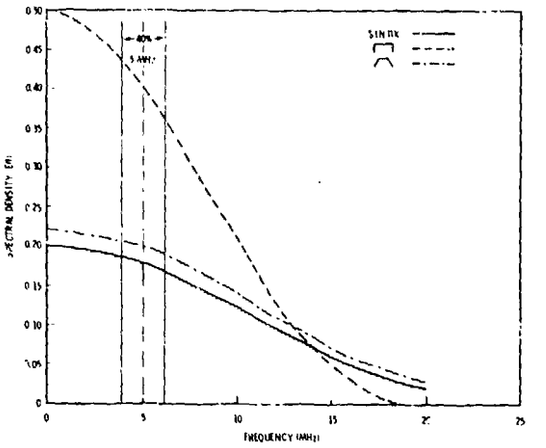

Fig. 5 Power density spectral plot for the square, trapezoidal and sin wave.

The transducer selected is 1/4" x 1/4", designed to operate at 5 MHz, Model No. HMT 7-221. This transducer operated at 4.65 MHz and had a 41% bandwidth as measured with a tone burst method (Ref. 1). A six foot RG-174/u cable was used and an insertion loss of -30 dB was measured and an impedance of Z = 70 ohms ∠ 20° was measured.

The exponential pulse is generated with a Metrotek MP-215 (typical of SCR shock type pulsers) pulser whose output impedance was approximately 10 ohms. The pulse amplitude control is adjusted to 85 V and the damping control is adjusted to provide a pulse whose duration (measured at 50% levels) is set equal to one-half cycle of the center frequency. The exponential has a 20 ns risetime, 120 ns width and an overall duration of 650 ns.

A circuit was developed at Battelle to generate square waves and this circuit provides a control to adjust the width of the square wave. The square wave has an amplitude of 85 V, a risetime of 16 ns and a fall time of 12 ns. The pulser has an output impedance of approximately 13 ohms. The pulser has a width control which was adjusted to give a maximum response from a quartz block submerged in water (a duration of 114 ns).

If we review the theoretical results of the previous section, then there should be a 6 dB difference for the two pulser waveshapes. Comparison of the two pulsers by examining the responses from a quartz block indicated that the return echo amplitude and shape is identical in both cases (see Fig. 6). There are several reasons for the discrepancy (lack of 6 dB difference) between the theoretical and laboratory results. The most important reason is the difference between the exponential waveshape which is generated in the lab and the mathematical exponential wave used for

the calculations as shown in Fig. 6. The mathematical exponential wave has an infinite risetime and decays exponentially from unity. The laboratory exponential wave is rounded and does not start its decline for approximately 30 ns. If, at the 50 ns point, the exponential is projected back to find the peak value, then the exponential would be equivalent to starting its decline from 120 V at time zero. This provides an additional 6 dB of power because of the square relationship of equation (1). The 6 dB of additional power offsets the theoretically predicted 6 dB loss in sensitivity. In general, the shape of a spike pulse will differ considerably for reactive loads from a pure exponential decay. Thus, a spike pulse achieves improved performance by providing more power in the pass-band.

It is important to note that even though there is no sensitivity improvement (i.e., no dB improvement) with the square wave pulser under ideal conditions for the spike pulser, there are several very attractive reasons why it is the best pulser to use. First the square wave pulser does not saturate the front end of the receiver amplifier at the end of the drive pulse because the pulse is driven to and held at 0 V. Consequently, for contact inspection, the near surface resolution is substantially improved. Secondly, the square wave pulser can be easily tuned (via width control) to the operating frequency of the transducer without affecting the voltage amplitude, the waveshape or the output impedance of the pulser. This feature enhances interchangeability of transducers for producing identical UT responses from calibration reflectros and defects.

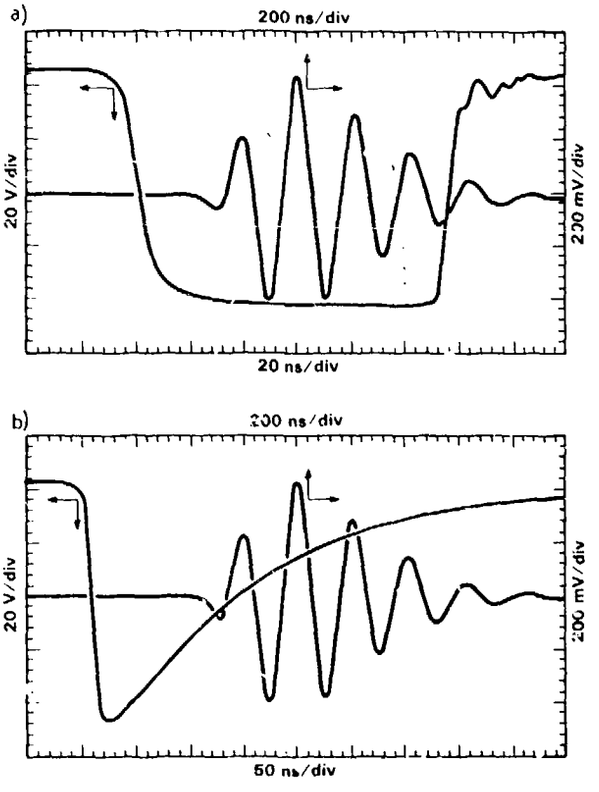

Fig. 6 Pulser output shape and return echo for (a) square wave, and (b) spike (exponential.

CONCLUSIONS

The analytical study using the constraint of unit energy for each waveform, leads to the conclusion that the optimum f(x), sin πx, trapezoid (a = 1/3) and the triangle wave each had essentially the same fraction of energy in the 40% bandwidth. As the number of half-cycles of the transducer center frequency is increased, the fractional energy in the 40% bandwidth increases.

The analytical study using the constraint of unit amplitude for each waveform leads to several conclusions. The first conclusion is that the square wave has the largest total energy E_T, the sin πx wave has the highest efficiency E_F for getting energy in the pass-band but the square wave has the highest pass-band energy E_B. The second conclusion is that the spike pulse exponential wave has 6 dB less energy in the pass-band than the square wave.

Experimental results for the square wave and the exponential wave turned out to be identical. The difference between the mathematical exponential and the experimental exponential pulse results is 6 dB more power in the pass-band, thus, equaling the square wave configuration. The spike pulse waveshape is typical of SCR pulsers and provides the power in the pass-band that allows them to work satisfactorily into a reactive load.

The square wave pulser, on the other hand, possesses several advantages even though in the particular instance studied, no sensitivity improvement is realized. The square wave pulser reduces the need to tailor the waveform and eliminates distortions caused by the exponential decay, thus providing improved near surface resolution and improved UT test reporducibility. Further, the square wave pulser can be optimized to the operating frequency of the transducer by tuning without changing the electrical impedance or other electrical properties of the pulser network. However, the operating and electrical characteristics for the spike pulser change with adjustments to the pulse duration.

ACKNOWLEDGEMENTS

The authors wish to thank Charles A. Ratcliffe for designing the square wave pulser circuit and Paul L. Tomeraasen for building the circuit for testing.

REFERENCES

1. Erickson, K.R., "Tone-Burst Testing of Pulse Echo Transducers," IEEE Transactions on Sonics and Ultrasonics, Vol. SU-26, No. 1, pp. 7-14, January, 1979.

APPLICATIONS OF LASER LIGHT PROBES TO QUANTITATIVE SENSING OF STRESS WAVES

B. Boro Djordjevic
Martin Marietta Laboratories
Baltimore, Maryland 21227

ABSTRACT

The recent development of laser light probes for stress wave measurements has aided our understanding of acoustic emission and ultrasonic signals by allowing quantitative measurements of stress waveforms. This paper reports on applications of the laser interferometer probe for surface detection of stress waves and the laser transmission probe for sensing of stress waves inside transparent materials. Laser light probes were used to characterize ultrasonic and acoustic emission transducers' response in a realistic configuration, with transducers in actual contact with a solid. Laser light probes also were applied in directly detecting acoustic emission due to stress corrosion cracking in 7039 aluminum and crazing of Plexiglass. The results of the laser light probe measurements indicate that conventional piezoelectric transducers, although adequate for many ultrasonic pulse inspection tests, are severely limited as stress pulse sensors for acoustic emission measurements. The acoustic emission signals measured by the laser light probe showed a pulse-like waveform which has not been previously recorded by conventional piezoelectric acoustic emission sensors.

INTRODUCTION

In almost all industrial applications, conventional piezoelectric transducers are used to detect acoustic emission and ultrasonic transients in solid materials. As the demand for accuracy and reproducibility of nondestructive tests and inspection methods increases, the limitations of electromechanical devices such as piezoelectric transducers are becoming more noticeable and must be specified.

Industrial piezoelectric ultrasonic transducers (see Fig. 3) are complex structures of layered active and passive elements, packaged into a small unit which is coupled to the workpiece by a variety of impedance matching fluids. Because of the contact with the test piece, such devices inadvertently mechanically load the contact surface and thus change the test piece behavior. Also, the need for coupling agents between transducer and contact surface introduces the problem of reliable test repeatibility. However, these problems are only secondary to the strong need for industry-wide calibration and standardized comparison of different ultrasonic and acoustic emission transducer units.

To be able to address some of the abovementioned problems, an experimental system was developed that utilizes laser light probes to measure stress waves in solids. The combination of laser probes with digital signal capture and computer data processing enabled accurate evaluation and analysis of the piezoelectric transducers' response. Figure 1 is a schematic representation of a whole test system that allowed ultrasonic or acoustic emission signals to be measured simultaneously by laser probe and piezoelectric sensor.

Two types of laser light probes were used to measure a physically identifiable parameter associated with stress wave propagation. A laser transmission probe sensitive to material density changes was used to measure bulk ultrasonic waves inside transparent test specimens and a laser interferometer probe was used to measure the normal surface displacement produced by propagating ultrasonic waves. The performance of these laser light probes was described in other publications(1,2). However, it is important to note that a laser probe sensor does not alter the stress waves, produce no change in mechanical boundary conditions, and has no intrinsic frequency-response limitations. Thus, the simultaneous use of optical probes and conventional piezoelectric transducers enabled direct signal comparison and critical evaluation of the performance limitations exhibited by piezoelectric sensing devices.

ULTRASONIC TRANSDUCER CALIBRATION AND CHARACTERIZATION

Ultrasonic transducers mounted on the face of a transparent cube test block (such as Plexiglass) were evaluated using a laser transmission probe. By scanning the YZ plane, this arrangement allowed the pointwise measurements of the stress pulse waveform, relative pulse intensity, and arrival time at all test block locations. These measurements were then used to indicate the transducers' beam profile (near field [NF] and far field [FF]) as well as any regions of anomalous nodal lines or high intensities. The three dark photographs in Fig. 2 are indicative of the signals measured at the three different test block locations. The top trace is the signal from the piezoelectric inspection transducer and the bottom trace is due to the signal sensed by the laser transmission probe. Note that the laser probe centered on the block shows the first-signal-arrival-time delay of 1/4 of the total time necessary for the pulse reflection to return to the transmitting transducer. Thus, the centered laser probe sees stress waves twice as often as the surface mounted transducer and

nicely illustrates a phase shift between a transmitted and a reflected ultrasonic stress wave packet. The off-center signal sample by the laser transmission probe is used to demonstrate a spread of the stress wave packet. The signal observed by the laser probe became significant only after a time delay; a few reflections of the ultrasonic pulse allowed significant widening of the original stress wave packet.

Beam intensity assymetry of an ultrasonic inspection transducer is demonstrated by a four-waveform sample taken across the transducer main beam. Transducers with such assymetric beam intensities are not desirable and can be very troublesome when used for ultrasonic inspection. These characteristics sometimes develop only when a transducer is in contact with a solid and cannot be seen with conventional liquid-immersion transducer-beam profile measuring methods.

In general, surface laser interferometer probe measurements agree with transmission probe indications. The transducer and laser interferometer probe signals shown in Fig. 2 are compared in frequency domain. The power spectra of the two sensors simultaneously measuring the same stress wave are similar except for an unavoidable harmonic peak around 3 MHz for the piezoelectric transducers.

ACOUSTIC EMISSION TRANSDUCER CHARACTERIZATION

The response and accuracy of waveform measurements by conventional piezoelectric transducers degrades when complicated waveforms, such as acoustic emissions, are encountered. Figure 3 illustrates the test block arrangement used to evaluate acoustic emission transducers. As reported in other publications, this design (1,2,3) utilizes a glass capillary fracture as a repeatable stress wave pulse. The stress wave signals generated by this arrangement have been analyzed theoretically and confirmed experimentally. For this purpose, the test block was used as a stress signal source and measured by a laser interferometer probe. The response of a typical piezoelectric acoustic emission transducer to the same stimulus is also shown. The difference in the signals observed are more easily explained by a power spectra plot of the signals from the two measurements. The transducer power spectrum peaks at 175 kHz, which was the resonant frequency of the piezoelectric element. Thus, the complexity of the acoustic emission transducer signal output mostly is characteristic of the piezoelectric element and sensor design, thereby masking the true stress waveform signal present in the test block.

ACOUSTIC EMISSION MEASUREMENTS USING LASER INTERFEROMETER PROBES

The laser interferometer probe can be used to sense and characterize stress waves directly. It is especially useful for complex signals such as those encountered in acoustic emissions due to cracking in metals or crazing of polymers.

Acoustic emissions were generated by initiating stress corrosion cracking using dilute sodium chloride solution on a self-loaded, double-cantilever beam specimen made from 7039 aluminum alloy. The observed, fast rise time, pulse-like waveforms suggested that acoustic emission from stress corrosion cracking is due to catastrophic, microscopic fracture events inside the growing crack. It should be noted that these signals have not been observed by conventional acoustic emission methods.

Similar in form, but much slower in time (on the order of milliseconds), are acoustic emissions due to polymer crazing. The crazing of Plexiglass, induced on the surface of a bend-loaded test bar, generated a complex acoustic emission signal lasting a few milliseconds. The complexity of this signal(4) was identified to have been generated by reflections of stress waves at a boundary of the specimen and subsequent constructive or destructive interference of the waves at the location of the laser interferometer probe. The experimental work on polymer crazing is still in progress and should aid our understanding of the dynamics of the failure mechanisms in polymer materials under load.

SUMMARY

By utilizing laser light probes, it is now possible to accurately sense the true ultrasonic signal waveform in solid materials. Therefore, laser probes can be used to critically evaluate piezoelectric transducer response.

In multi-frequency, complex, stress wave signal measurements such as acoustic emissions, laser light probes can measure stress waveforms not observable by piezoelectric devices, which exhibit resonance-like behavior.

ACKNOWLEDGEMENTS

This work was done in part while the author was at the Johns Hopkins University. A special note of appreciation in this regard is due Professor Robert E. Green, Jr This work was supported in part by the U.S. Army Office. Thanks are due in this regard to Dr. George Mayer.

REFERENCES

1. B.B. Djordjevic, R.E. Green, Jr., "High speed digital capture of acoustic emission and ultrasonic transients as detected with optical laser beam probes," Proc. Ultrasonic Int. 79 Conf., Graz, Austria (May 1979) 82-87.
2. R.E. Green, Jr., B.B. Djordjevic, C.H. Palmer, S.E. Fick, "Laser beam detection of ultrasonic and acoustic emission signals for nondestructive testing of materials," Proc. ASM Conf. on Application of Lasers in Materials Processing, Washington, D.C. (April 1979).
3. F.R. Breckenridge, C.E. Tschiegg, M. Greenspan, "Acoustic emission: Some applications of Lamb's problem," J. Acoust. Soc. Am. 57, 626-631 (1975).
4. A. Peterlin, B.B. Djordjevic, J.C. Murphy, R.E. Green, Jr., "Acoustic emission due to Craze formation in polymers," to be published.

ABSTRACT

The recent development of the laser interferometer probe and laser beam transmission probe has allowed quantitative measurements of stress waves in solids. These laser probes were used to evaluate and calibrate ultrasonic inspection transducers and conventional piezoelectric acoustic emission sensors. The laser interferometer probe was used for stress waveform measurements of complex multi frequency acoustic emission signals due to cracking in metals and crazing of polymers. Thus, although adequate for many ultrasonic pulse inspection tests, conventional piezoelectric transducers are severely limited as stress pulse sensors for acoustic emission signals.

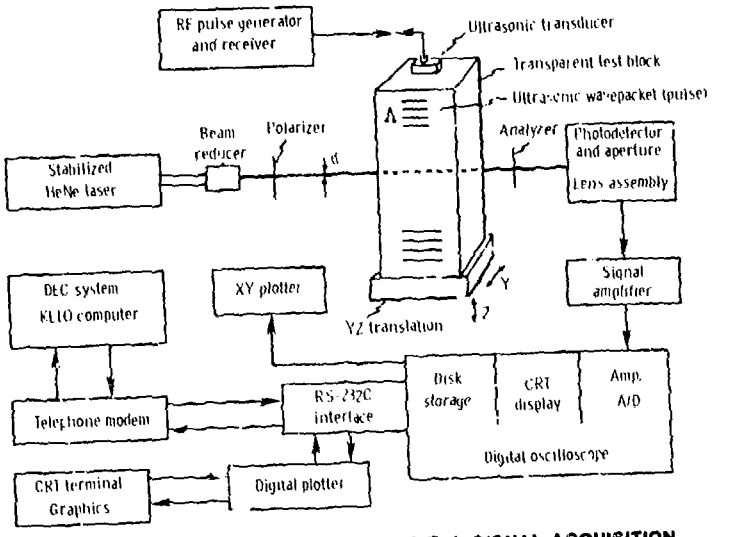

LASER TRANSMISSION PROBE WITH DIGITAL SIGNAL ACQUISITION AND PROCESSING SYSTEM

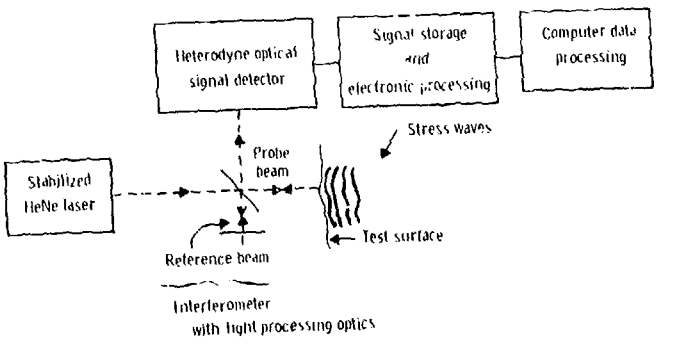

LASER INTERFEROMETER PROBE

FIGURE 1

ULTRASONIC TRANSDUCER CHARACTERIZATION AND CALIBRATION BY LASER LIGHT PROBES

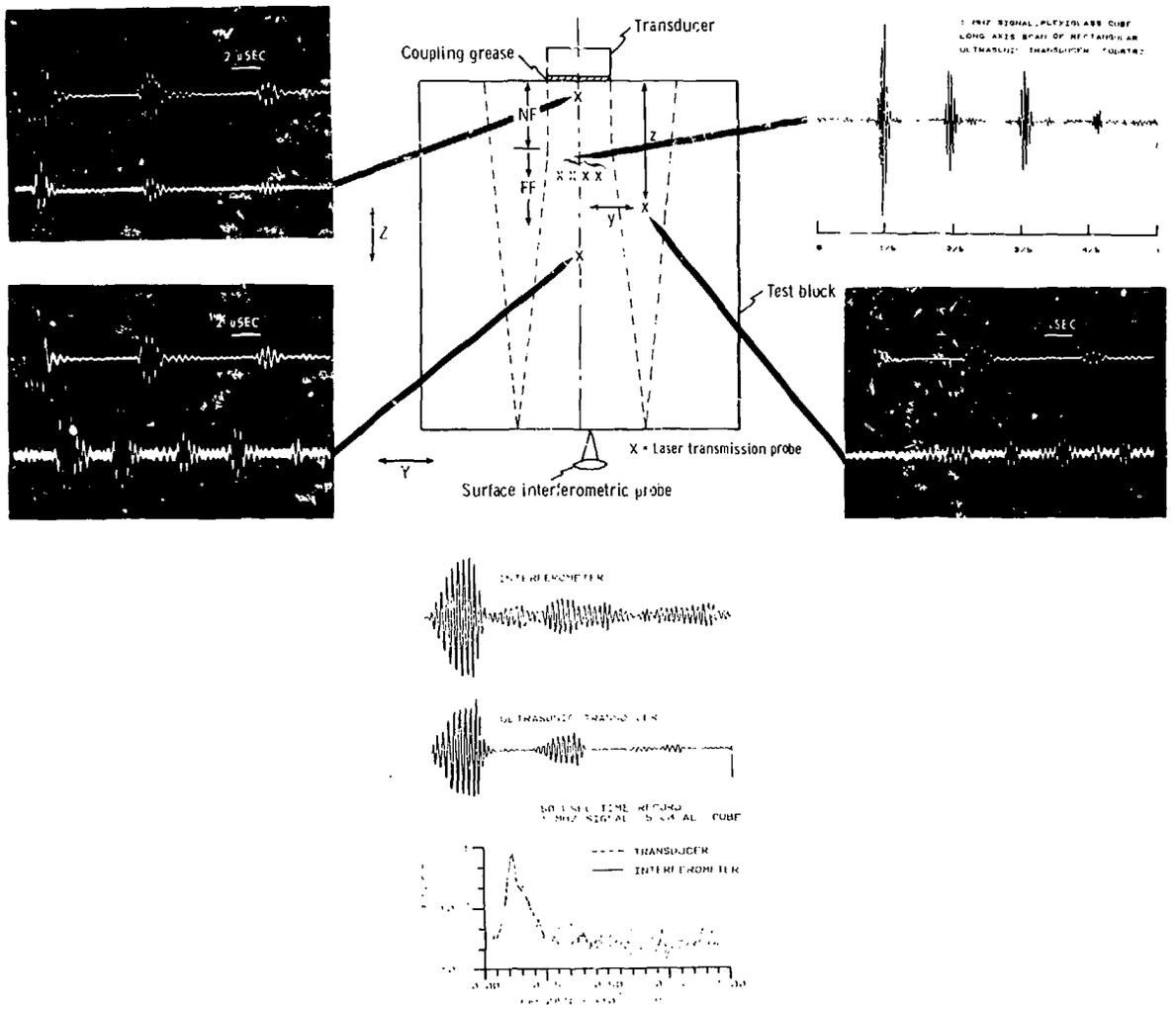

1. Transducer can be evaluated while actually in contact with a solid.
2. Beam profile and ultrasonic stress waveform are measured in bulk and on the surface.
3. The true frequency characteristics of the device are determined.
4. Absolute calibrations can be achieved.

FIGURE 2

ACOUSTIC EMISSION TRANSDUCER CHARACTERIZATION USING LASER INTERFEROMETER PROBE

1. Transducer's response to complex stress waveforms encountered in acoustic emission work can be evaluated.

2. Inadequacies of conventional piezoelectric acoustic emission sensors are demonstrated.

TEST BLOCK

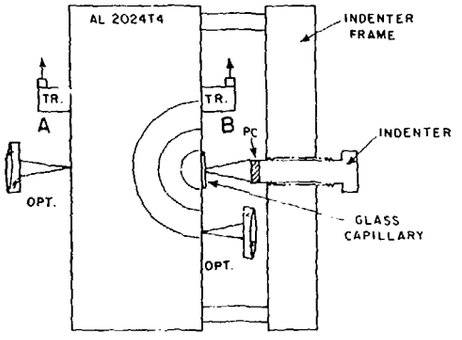

CROSS SECTION OF A PIEZOELECTRIC TRANSDUCER

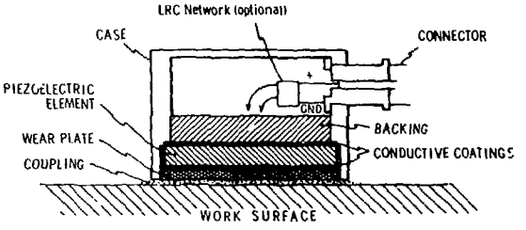

Conclusions:

- THE ACOUSTIC EMISSION TRANSDUCER DOES NOT RESPOND TO STRESS WAVEFORM RESOLVED WITH INTERFEROMETER PROBE.
- ACOUSTIC EMISSION TRANSDUCER SIGNAL OUTPUT IS MOSTLY CHARACTERISTIC OF THE PIEZOELECTRIC ELEMENT AND SENSOR DESIGN.

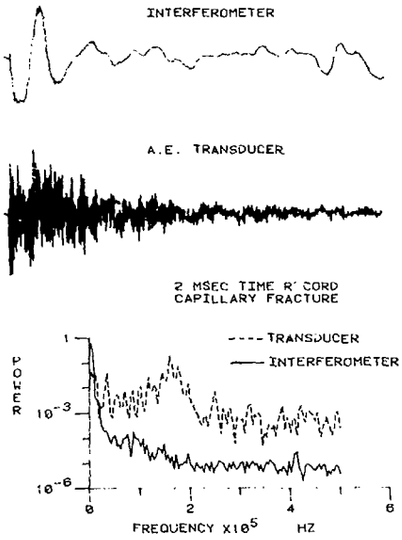

FIGURE 3

ACOUSTIC EMISSION MEASUREMENTS USING LASER INTERFEROMETER PROBES

STRESS CORROSION CRACKING 7039 AL

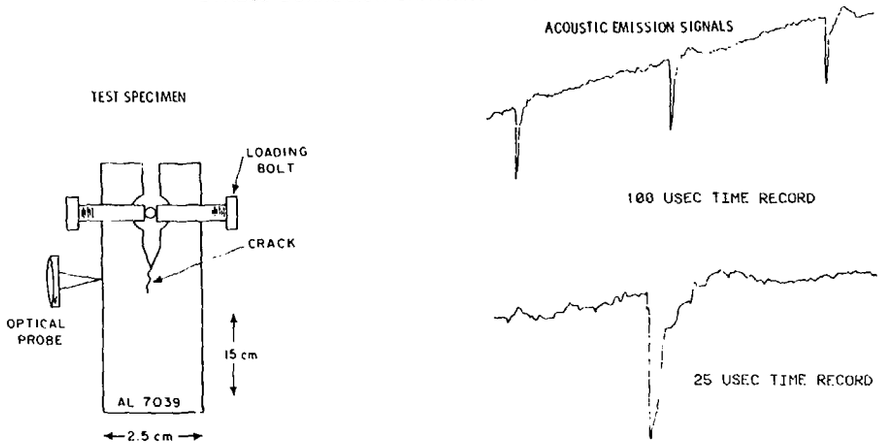

EXPERIMENTAL ARRANGEMENT FOR MEASUREMENTS OF ACOUSTIC EMISSIONS DUE TO CRAZING OF POLYMERS (After Djordjevic, Murphy et. al.)

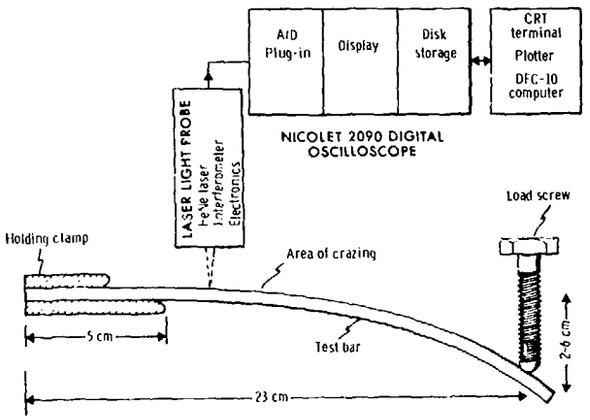

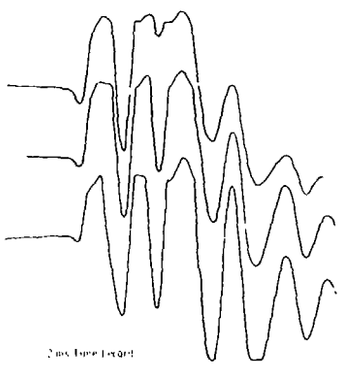

THREE DIFFERENT ACOUSTIC EMISSION EVENTS IN PMMA, MEASURED EXPERIMENTALLY

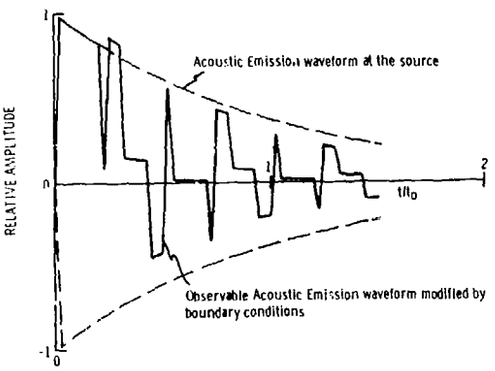

THEORETICAL MODELED EXAMPLE FOR THE OBSERVED WAVEFORM DUE TO SUPERPOSITION OF TWO CONSECUTIVE ACOUSTIC EMISSION BURSTS WITH THE AMPLITUDE RATIO 1:0.8 AND TIME DELAY Δt. (After Petterlin, Djordjevic et. al.)

FIGURE 4

A NOVEL DETECTOR ARRAY FOR INDUSTRIAL X-RAY TOMOGRAPHY*

P. S. Ong and H.T. Huang
University of Houston, EE Department
Houston, TX 77004

ABSTRACT

We are attempting to construct a simple tomographic instrument. The instrument is intended for development and evaluation of a novel x-ray sensitive detector array, which will permit a line resolution of less than 1mm. The system can be constructed as an array of 500 to 1000 detectors suitable for energies in excess of 1 MeV. Each individual detector can be addressed separately and sequentially by means of a scanning light beam. A prototype consisting of 40 elements has been built and its performance evaluated. Details of its construction and the results of its performance will be presented.

INTRODUCTION

Present CAT equipment is designed specifically for medical use, where the object to be examined consists primarily of low atomic number (Z) elements. This is generally not suitable for samples which consist of high Z elements. One of the reasons is that the detector will not be effective for the high energy photons which have to be used to penetrate the sample

The work to be described here deals with a new type detector system which can be constructed as a linear array, and which is suitable for x-ray energies in excess of 1 MeV.

DESCRIPTION OF THE NEW DETECTOR

The first stage of the detector system consists of a linear array of small narrow scintillators, which can be envisioned as a stack of thin (0.5 - 1mm) scintillators (CsI, GBO), each scintillator representing a deparate detector. This is depicted in Fig. 1. The width w can be several times the thickness t. The depth dimension d is chosen so that the scintillator will absorb say 90% of the radiation.

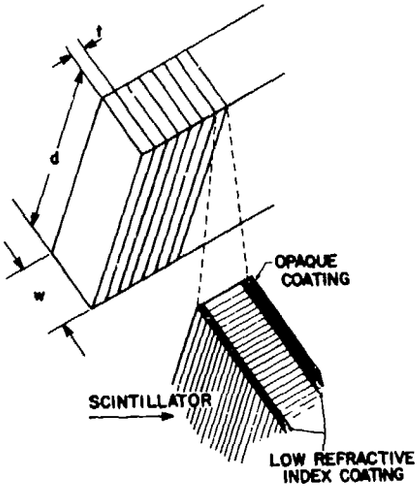

Fig. 1.

The second stage of the x-ray detection system is a converter which uses amorphous selenium to convert light or x-ray photons into electron-hole pairs. For visible light, the quantum conversion efficiency is one electron per photon. It has, therefore, a 10x higher quantum efficiency as compared with the first stage of a photomultiplier. However, the converter does not have internal amplification and requires a low noise, high gain amplifier to further process the signal. The proposed converter can be constructed in such a way that only one such amplifier is required for the whole scintillator array. This is accomplished by use of light activated switches. The principle of operation of the proposed converter will be discussed with reference to Fig. 2.

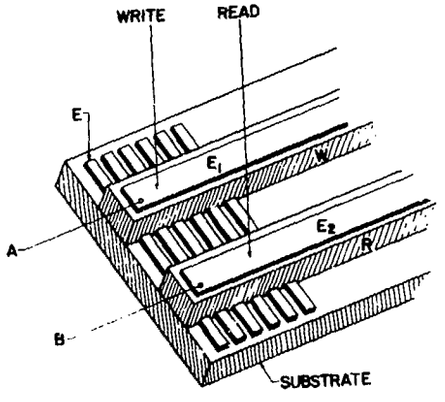

Fig. 2

*Work supported by the Energy Laboratory of the University of Houston.

Basically the converter consists of a substrate onto which are deposited narrow interdigitated electrodes E. Each of the electrodes represents a separate detector. On top of the electrodes are two separate but adjacently located narrow selenium strips, running perpendicular to the electrodes. One of the selenium strips, W, is designed to record (write the photon image) the other, R, to read the recorded image. Both selenium layers have a semi-transparent conductor E_1 and E_2 on the surface. In the dark, each converter element of the device can be represented as two capacitors in series. One of the interdigitated electrodes E serves as the center electrode. All detector elements are connected in parallel by means of the surface electrodes. When, in the absence of light, a voltage is applied across the two surface electrodes, a voltage will develop across each of the selenium layers, which is inversely proportional to its capacitance. Directing a light beam on the R layer effectively short-circuits it, thus the applied voltage is now found across the W layer. This condition is maintained when the light beam is turned off. Photons from the scintillators which are directed to the W layer will generate charge carries which results in a voltage drop in each of the affected interdigited electrodes. This voltage modulation across the detector system can subsequently be read by sequentially illuminating the R surface with a scanning light beam. The output is a video signal. In practice, the scintillator can act as the substrate and the two selenium layers can be deposited on top of each other separated by the interdigited electrodes. Such a geometry is illustrated in Fig. 3.

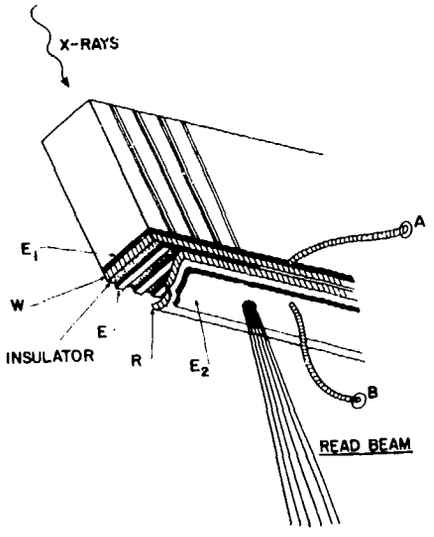

Fig. 3

Another possible geometry is shown in Fig. 4, where separate "Write" selenium layers are located between the stacked scintillators. Here, each scintillator channel is coated on one side with a reflective coating, and on the other side with the three layers E_1, W, and E.

Photons, generated within each channel enters (through E_1) into the active selenium layer as long as the angle of incidence does not exceed the critical angle (ray 1). The reflector on the opposite side of the selenium reflects the light, which otherwise would have escaped, back onto the selenium surface (ray 3). The light (ray 2) which is totally reflected by the scintillator interface, E_1 tends to escape from the surface perpendicular to the selenium surface. Some of this may still be captured by shaping these surfaces as shown in Fig. 4 (ray 4).

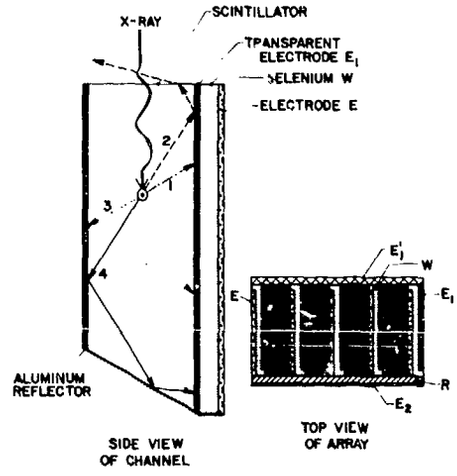

Fig. 4

When the photosensitive W layer is much larger than the thickness of the scintillator, the area of the selenium which receives light due to x-ray photons is quite localized. By subdividing the electrode E_1 in the depth direction of the x-ray is being absorbed. Since the depth distribution of the absorption is closely related to the x-ray energy, the various subelectrodes of the channels exhibit a different energy response. This method is similar to the technique used by Kaplan et al (Nucl. Inst. Mech. 106, 397, 1973) in the split electrode xenon detector.

PULSED ELECTROMAGNETS FOR EMATS

C. M. FORTUNKO*
Fracture and Deformation Division
National Bureau of Standards
Boulder, CO 80303

and

D. MACLAUCHLAN*
New Mexico Engineering Research Institute
University of New Mexico
Albuquerque, NM 87111

ABSTRACT

In many industrial NDE applications pulsed electromagnets may be more desirable than large static electromagnets or permanent magnets for magnetic biasing of electromagnetic acoustic transducers (EMAT's). Since electromagnetic acoustic transduction is confined to one skin depth at the operating frequency of the EMAT, the transduction efficiency can be enhanced by the dynamic concentration of the magnetic flux near the surface. This paper describes a number of physical phenomena associated with EMAT generation under pulsed-magnetic-field bias. In particular, it is observed that for maximum transduction efficiencies the ultrasonic pulse must be retarded relative to the initiation of the current pulse to the electromagnet windings. A second maximum in the transduction efficiency is observed when the pulsed magnet-EMAT system is operated on ferromagnetic steel (1020). The second maximum is associated with magnetostrictive effects. Operation of pulsed magnet-EMAT systems at elevated temperatures (400°C) is demonstrated on aluminum.

INTRODUCTION

The use of a large, pulsed current to generate a biasing field is well suited to EMAT applications, where the ultrasonic system need to be active only for the relatively short period of time when the ultrasonic waves are in the immediate vicinity of the transmitter and receiver transducers. In practice, much of the time between pulses is not used for useful inspection processes because one must wait for the acoustic reverberations to dampen out. During this time, the coil can be switched off, allowing much of the heat generated in the electromagnet by the large current pulse to dissipate. Much higher peak currents can therefore be obtained in a pulsed electromagnet than in a static magnet of the same size. Another advantage of using a pulsed-magnetic bias on the EMAT arises from the fact that the eddy currents induced in the surface of the metal part by pulsed fields act to oppose the applied field and lead to a time dependent flux concentration at the surface. Since the electromagnetic transduction action is confined to a thin surface layer of depth equal to the electromagnetic skin depth at the EMAT-coil-drive frequency, this dynamic concentration of flux can be used to enhance the efficiency of the transducer. Obviously, such enhancement will depend strongly on the geometry of the pulsed electromagnet, the conductivity and permeability of the surface material and the shape of the current pulse to the coil. In this paper a number of practical pulsed-magnet-EMAT configurations are described and the relationship between the ultrasonic transduction efficiency and time development of the pulsed magnetic field is studied experimentally on aluminum and ferromagnetic steel samples. In addition, the operation of a pulsed-magnet-EMAT system is demonstrated at elevated sample temperatures (400°C).

PULSED-MAGNET SYSTEM DESIGN

Pulsed electromagnets, just as static electromagnets, obey the fundamental magnet design rules which relate the magnetomotive force (ampere-turns in the coil), the magnetic flux and the reluctance of the total magnetic circuit. However, when a pulsed electromagnet is operated in the vicinity of a (ferromagnetic) conductor, the reluctance can be expected to be time dependent. Little control can be exercised over the magnetic reluctance of the sample being magnetized by the pulsed electromagnet, but the reluctance of the pulsed coil can be significantly reduced by using a ferromagnetic core constructed of insulated laminations to reduce retardation of the magnetic pulse by eddy current effects.

A simple design formula[1] can be used to relate the magnetic flux density in the air gap (neglecting dynamic effects) to the electrical parameters of the discharge circuit:

$$B = KDS \frac{V_o}{\pi A \omega_o} \qquad (1)$$

where B is the average value of the magnetic field in the air gap beneath the center post, V_o is the discharge voltage of the capacitor bank, N is the number of turns in the coil, A is the effective area of the air gap, and ω_o is the characteristic frequency, $(LC)^{-1/2}$, of the current pulse. The parameters K, S, and D account for the finite reluctance of the magnetic circuit outside the air gap, the uniformity of the magnetic field and the dissipation (damping) rate of the discharge, respectively. For a critically damped circuit, the factor D is 1/e. The factors K and S are less than one and must be determined experimentally. Typical

*Work performed while both authors were with the Albuquerque Development Laboratory, Science Center, Rockwell International Corporation, Albuquerque, NM 87106.

values are 0.25 and 0.50, respectively. It is seen from Eq. (1) that trade-offs can be made by varying the values of the capacitor bank, the number of turns in the coil, N, and the charging voltage, V_o. However, practical design values are established primarily by the voltage and current breakdown characteristics of the capacitor bank and the switch. Although it would be advantageous to generate very short magnetic pulses (large ω_o), to make use of magnetic field enhancement by dynamic effects, practical values for the coil inductance, L, and the energy storage capacitor, C, limit this approach.

Some of the design parameters of two laminated-core electromagnets are summarized in Table 1, below. Both electromagnets used "E-core" transformer grade laminations of 0.5 mm (0.020 in.) thickness and were wound with #14 AWG insulated copper wire. A flux-sensing coil was also attached to the center post of the core. The coil was used in conjunction with a Miller integrator circuit to determine instantaneously the average value of the magnetic flux in the air gap between the center post of the pulsed electromagnet.

Two electronic circuits were used to drive the pulsed electromagnets for various EMAT and sample configurations. The first, shown in Fig. 2, was designed around a commercial "magnet charger" unit in which up to 70,000 μF of capacitance at up to 500 volts could be discharged into a coil. This system was designed for operation on non-ferromagnetic materials where dynamic enhancement of surface fields was not significant and very large peak values of the magnetic field would be needed. Here, a separate transmitter and receiver EMAT were used. For the second case, shown in Fig. 3, the emphasis was placed on achieving faster rise times at the expense of less total energy delivered to the bias-magnet coil. In this case, a special transistor switch discharged a 2,000 μF capacitor at 100 volts into the coil. This circuit was primarily used on ferromagnetic materials, where dynamic enhancement of the fields was predominant, and it utilized a transmit/receive (T/R) switch so that only one EMAT coil needed to be used for both the transmitter and receiver functions. Both of these circuits incorporated a delay circuit to trigger the EMAT transmitter at an adjustable delay

TABLE 1

Physical Dimensions (in mm) of Two Laminated Core Electromagnets Used for Pulsed-Magnet EMAT Studies

Core Dimensions			Center Post	Coil Space		Weight
Length	Depth	Height	Width	Width	Height	(kg)
86	38	57	28	15	41	1.35
66	33	44	22	11.5	30.5	0.54

Figure 1 shows a cross sectional view of one of the electromagnets in Table 1. Although the configuration illustrated in Figure 1 shows the transducer under the center post of the "E-core", this arrangement was not practical when the pulsed magnet was operated on ferromagnetic metal parts. Instead, the preferred location for the EMAT was between the center post of the "E-core" and one of the side posts to take advantage of the strong dynamic effects in ferromagnetic materials.

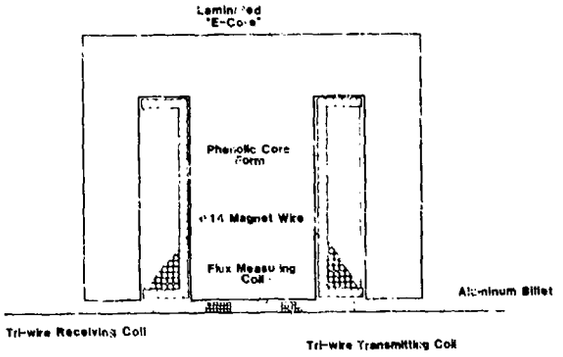

Fig. 1. Cross section of the E-Core electromagnet used in the pulsed-current mode to generate the magnetic field bias for EMAT coils. As a consequence, the magnetic field under the center post of the core is reduced, but the tangential field between the center and side posts of the core is substantially increased.

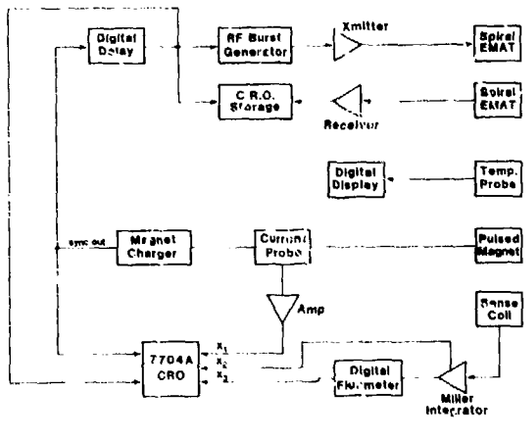

Fig. 2. Block diagram of the pulsed electromagnet-EMAT system. A commercial "magnet charger" supplied the large pulsed current and the ultrasonic transmitter could be triggered at an adjustable time delay after the start of the current pulse.

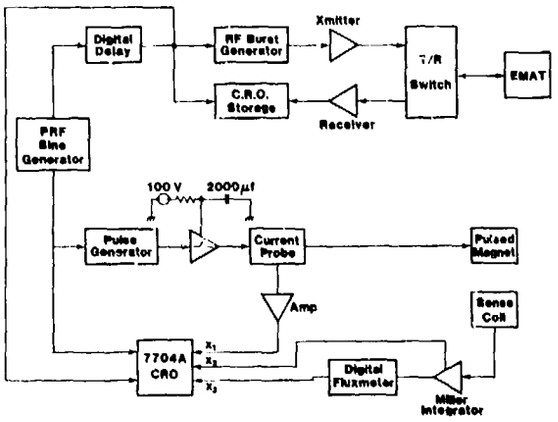

Fig. 3. Block diagram of the pulsed-electromagnet-EMAT system for generating high-rise-time-current pulses.

time after the initiation of the pulsed-magnet current, so that the ultrasonic interrogation of the sample could be carried out while the pulsed magnetic field was at its maximum value.

OPERATION ON ALUMINUM

To demonstrate the excitation and detection of ultrasonic waves in non-ferromagnetic metals (such as aluminum), an EMAT coil was designed to launch bulk longitudinal waves when placed in the tangential magnetic field of pulsed magnet. Figure 4 shows the total experimental configuration in which the aluminum specimen was a half cylinder of 30.5 mm (12 in.) radius and 15.2 cm (6 in.) height. The EMAT-coil configuration is shown in Figure 5 with a copper shield to limit the area over which the coil would induce eddy currents in the aluminum. Hence, the active area of the transducer is the area of exposed coil windings. This EMAT and pulsed electromagnet were used in conjunction with the circuit shown in Figure 2. The choice of a large half cylinder of aluminum was made to enable measurement of the radiation-pattern of any EMAT coil and magnet configuration by plotting the amount of signal received by a piezoelectric-transducer probe positioned at various angular locations on the curved surface of the cylinder. Examples of the measured longitudinal-wave-radiation patterns are shown in Figs. 6 and 7. The beams were generated using the pancake transducer shown in Fig. 5 at 1.8 MHz. Figure 6 shows the angular distribution of the ultrasonic beam for the case in which the short axis of the transducer (9.7 mm) lies in the plane of Fig. 4. Figure 7 shows the angular distribution of the beam when the long axis of the transducer (18.7 mm) lies in the plane of Fig. 4. The beam widths, calculated from a simple antenna model of ± 19° and ± 10° are shown as dashed lines on Figs. 6 and 7. Although there is scatter in the data of Fig. 6, the small width of the aperture radiation pattern observed is in reasonable agreement with theory. Figure 7 appears to show a narrower beam than predicted because of minima at $\theta = \pm 6$ degrees. A beam that is narrower than expected could be interpreted as arising from fringing eddy currents that extend beyond the limits of the wires in the EMAT. The directivity patterns of Fig. 6 and 7 demonstrate that the pulsed-magnet-EMAT system behaves qualitatively as expected from the point of view of a simple antenna model.

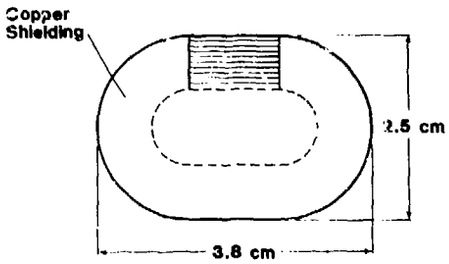

Fig. 5. Spiral pancake EMAT coil with a 0.2 mm copper foil shield to localize the eddy current distribution at the surface of the sample.

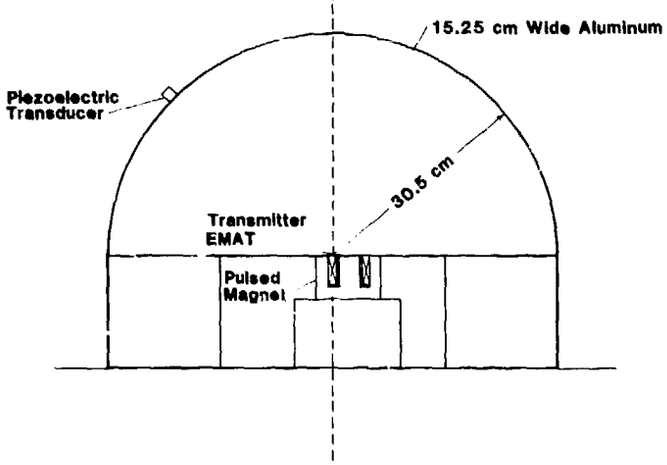

Fig. 4. Experimental configuration for measuring the transduction efficiency and radiation patterns of pulsed-magnet-EMATs on aluminum.

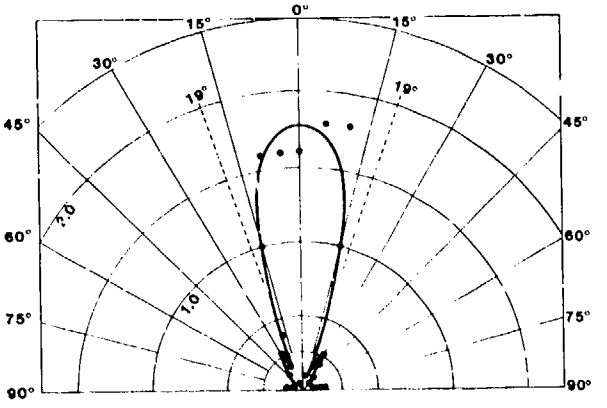

Fig. 6. Radiation pattern observed from the pulsed magnet, longitudinal-wave-generating EMAT shown in Fig. 5 when the long axis of the EMAT laid in the plane of the figure.

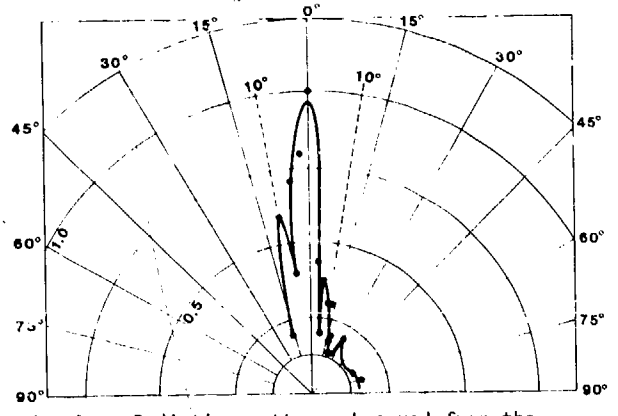

Fig. 7. Radiation pattern observed from the pulsed magnet, longitudinal wave generating EMAT shown in Fig. 5 when the long axis of the EMAT laid in the plane of the figure.

In order to study the dynamics of exciting ultrasonic waves by EMATs under pulsed-magnetic-field bias, the delayed trigger portion of the circuit of Fig. 2 was utilized. The transmitter EMAT was energized with a tone burst of 1.8 MHz after a controlled delay relative to the initiation of the large current pulse in the electromagnet. Thus, the ultrasonic wave was launched at a controlled time in the development of the pulsed magnetic field and a measurement of the ultrasonic signal amplitude could then be used to determine the magnetic field that is actually interacting with the 1.8 MHz eddy currents to excite the ultrasonic wave. Figure 8 shows the configuration of EMAT, pulsed electromagnet and aluminum test specimen used for these experiments. Because of fringing magnetic fields, both longitudinal and shear wave signals were generated. They could be discriminated and treated separately because of their different transit times in pulse-echo experiments. The duration of the magnetic pulses was approximately 10 ms, and the maximum magnetic induction obtained in the air gap under the center post of the core was usually between .8 T and 1.4 T, depending on the electromagnet.

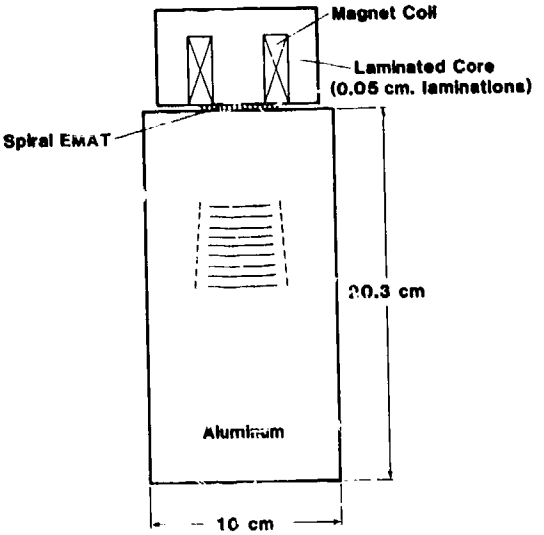

Fig. 8. Experimental arrangement used to excite high amplitude ultrasonic waves in thick aluminum billets.

Figure 9 summarizes the results of the tests performed on the aluminum test samples of 20.3 cm (8 in.) thickness. The amplitudes of the first and second set of reflections are shown, as a function of time delay between the initiation of the current pulse in the coil of the pulsed magnet and the launching of the ultrasonic pulse. The first reflection signal was due to longitudinal waves propagating at approximately 6.3 km/s, while the second reflection contains both a shear wave signal (propagating at approximately 3.1 km/s) and the doubly-reflected longitudinal wave signal.

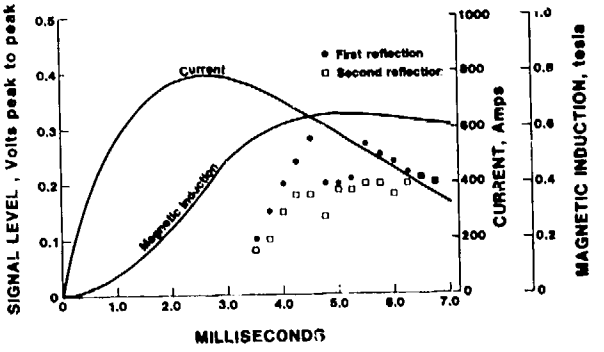

Fig. 9. Development of the magnet induction and the ultrasonic signals in a 20.5 cm (8 in.) aluminum billet in response to the current pulse in the electromagnet coil.

Because of the inhomogeneous nature of the pulsed magnetic fields, it was not possible to excite only the longitudinal wave. The 1- to 2-millisecond delay between the peak magnetic induction in the air-gap and the peak in the ultrasonic reflections from the bottom of the sample can be attributed to the effect of the pulse-induced eddy currents in the aluminum retarding the diffusion of the magnetic field into the skin depth region of the aluminum where the acoustic waves are generated.

This delay cannot be explained in terms of the ultrasonic wave travel time because the round-trip transit time for longitudinal waves in a 20.3 cm (8 in.) billet is only 64.5 microseconds.

As a demonstration of the pulsed-electromagnet-EMAT system's sensitivity to defects in thick-section structures, a 2.5 cm-(1 in.) deep, 0.63 cm-(1/4 in.) diameter, flat-bottom hole was drilled in the bottom of the aluminum billet. The pulse-echo reflection from the bottom surface of the billet in the absence of the hole is shown in Fig. 10a. Figure 10b shows the pulse-echo reflection from the same sample after the flat bottom hole had been introduced. The horizontal scale in both photographs is 10 μs/div. and the vertical scale is 0.1 volts/div. The electronic RMS noise level is approximately 10 mV. The start of the ultrasonic pulse was 3.75 milliseconds after the initiation of the current pulse to the magnet. It can be seen that the reflected signal from the flat bottom hole is approximately ten times the noise level and, hence, can be easily detected. The dynamic effects that cause concentration of the magnetic flux near the surface of the metal part were not observed to be very important in the case of aluminum because of the length of the current pulses to drive the electromagnets. It would be advantageous to use shorter pulses whose duration is approximately the same as that of the ultrasonic signal. However, this cannot be accomplished with laminated iron core electromagnets because the lamination thickness would have to be impractically small.

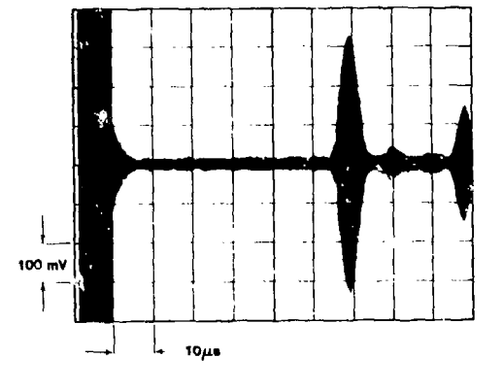

(10a)

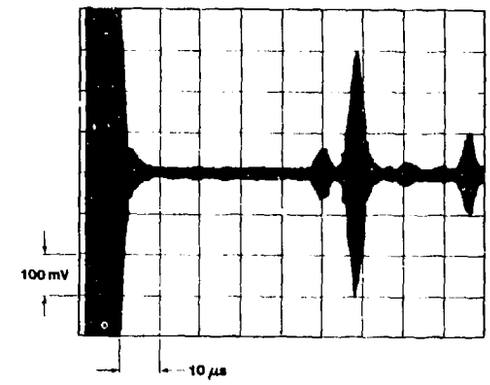

(10b)

Fig. 10. Echo signals observed when the 1.3z kg-pulsed-electromagnet was used to launch and detect ultrasonic pulses in (a) a 20.3 cm (8 in.) long aluminum billet containing no simulated flaws and (b) the same bar with a 2.4 cm (1 in.) deep, 0.63 cm (1/4 in.) diameter, flat-bottom hole drilled into the bottom.

OPERATION ON FERROMAGNETIC STEELS

The high permeability of ferromagnetic samples significantly lowers the reluctance of the magnetic circuit. The lower reluctance of the total magnetic circuit results in a large reduction in the pulsed electromagnet drive level requirements. The high permeability of the sample also enhances the dynamic effects resulting in higher transduction efficiencies. The transduction mechanism can also be enhanced by the magnetostrictive response of the ferromagnetic material.

Previous EMAT studies on iron have shown that there is a large peak in EMAT efficiency when the magnetic bias is tangential to the iron surface at approximately $2.4 \cdot 10^4$ amperes/m.[2] To examine the effect with pulsed EMATs, an experimental arrangement was used in which a meander-coil EMAT (shown in Fig. 11) was placed on a 1.25 cm-(1/2 in.) thick plate of 1020 steel. When driven at 1.8 MHz, the EMAT launches a shear wave beam into the plate at a 35 degree angle relative to the surface normal. An EDM notch 1.25 cm (0.5 in.) long and 0.72 mm (0.03 in.) deep on the opposite side of the plate was positioned to reflect the shear wave back to the EMAT. Because of the reduced drive requirement the circuit of Fig. 3 could be used to energize the coil of the electromagnet.

When the meander coil EMAT was placed in the (nominally) tangential magnetic field between the legs of the E-core electromagnet and triggered at a controlled time after the initiation of the magnet pulse, the results shown in Fig. 12 were obtained. In Fig. 12 the time development of magnetic flux in the gap, the current in the coil, and the amplitude of the 1.8 MHz angle-shear-wave signal reflected from the EDM notch are plotted as a function of

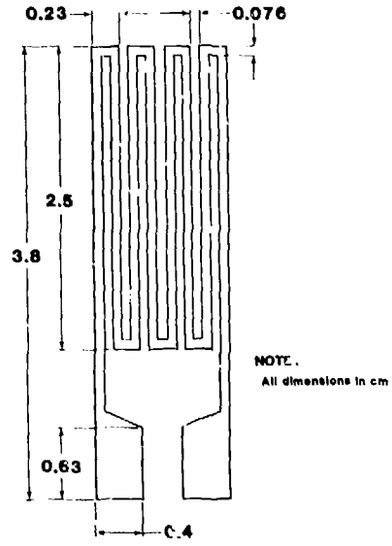

Fig. 11. Meander coil EMAT.

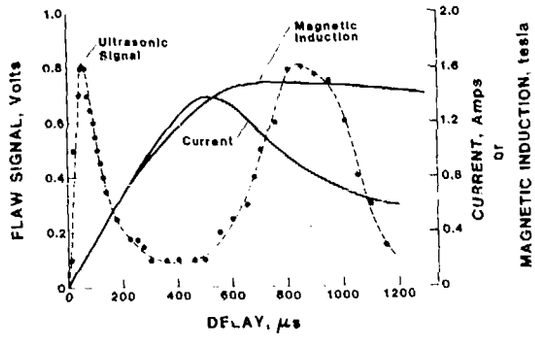

Fig. 12. Time-dependence of the ultrasonic shear wave signal and the magnetic induction under the center of the "E-core" that result from the current pulse shown when applied to a ferromagnetic plate.

time after triggering the pulsed magnet. The most interesting feature of these data is that the amplitude of the ultrasonic flaw signal exhibits a double peak; the first maximum occurs at approximately 50 microseconds, and the second maximum occurs approximately 850 microseconds after the start of the current pulse. The first maximum is caused by magnetostrictive enhancement of the transduction process when the magnetic-field build-up is concentrated near the surface by dynamic effects. This peak was not observed in non-ferromagnetic samples. The second peak in the reflected ultrasonic amplitude is observed when the magnetic field has had sufficient time to distribute itself uniformly throughout the thickness of the plate. Figure 13 compares the reflected ultrasonic signals from the same flaw obtained by biasing the meander coil EMAT by means of the 1.35 kg pulsed electromagnet and a large, 45 kg

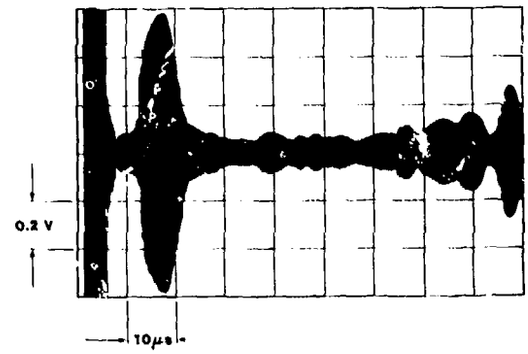

(13a)

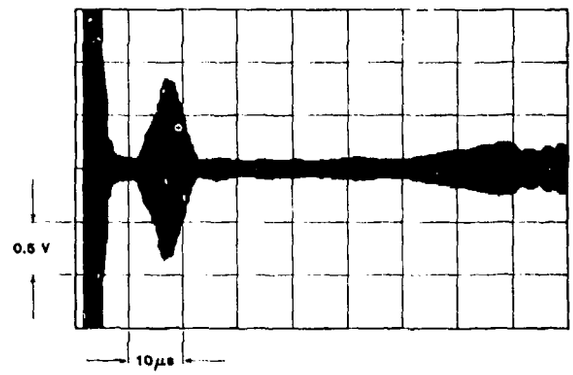

(13b)

Fig. 13. Oscilloscope trace photographs comparing the ultrasonic signals reflected from the same 1.5 mm (0.03 in.) deep EDM notch in 1.25 cm (1/2 in.) thick plate when using a 1.35 kg pulsed electromagnet (top) and a 45 kg static electromagnet (bottom).

static electromagnet when the coil currents were both adjusted to produce the maximum magnetostrictive enhancement. It should be noted that the absolute amplitudes of both signals are the same, as are the signal to noise ratios. The background ultrasonic signals due to excitation of other acoustic plate modes are different because the large static electromagnet produced a very uniform field distribution in the plate while the small pulsed electromagnet had fringing fields that could launch other acoustic beams into the plate.

In summary, high quality ultrasonic pulses were generated with the relatively modest energy input of 2 millijoules in a physically small electromagnet by taking advantage of the dynamic effects that occur in ferromagnetic metals, concentrating the available magnetic flux near the surface. The maximum average magnetic flux density observed in the air gap was 1.4 T. Attainment of higher flux densities would only be possible by completely saturating the core of the pulsed magnet and the metal part. Consequently, the optimum EMAT configuration for operation on ferromagnetic

materials should take advantage of the tangential magnetic field bias and magnetostrictive signal enhancement. This configuration also results in minimum pulsed-electromagnet-drive-current requirement.

OPERATION AT ELEVATED TEMPERATURES

The experimental set-ups of Figures 2 and 8 were used to demonstrate the ability of pulsed-magnet-EMAT systems to operate over aluminum surfaces held at elevated temperatures. The experimental parameters were identical to those used for inspecting aluminum billets at room temperature, except for the setting of the time delay between the initiation of the current pulse to the coil of the pulsed electromagnet and the ultrasonic pulse to the transmitter EMAT. In order to obtain maximum signal levels, a shorter time delay (4 milliseconds vs 4.5 milliseconds) had to be used because of the faster diffusion of the magnetic field into the hot aluminum sample. The sample surface temperature was held at approximately 400°C. Only a 2 dB difference in the signal levels was observed between the room-temperature and elevated-temperature data. The experimental set-up is illustrated in Fig. 14 and an oscilloscope trace of the ultrasonic signals is shown in Fig. 15. The oscilloscope trace of Fig. 15 can be compared directly with the trace of Fig. 10a which shows the room temperature data.

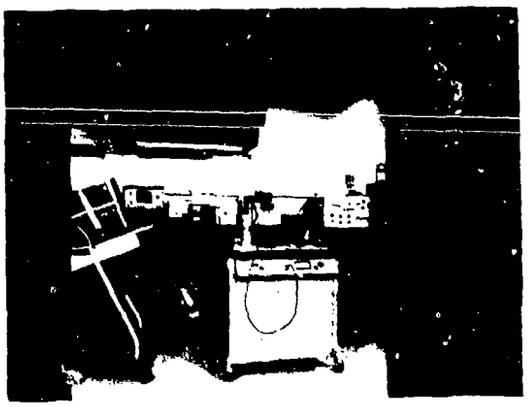

Fig. 14. Experimental set-up used to inspect aluminum billets at elevated temperatures (400°C).

CONCLUSIONS

Compact pulsed electromagnets can replace large static electromagnets in many EMAT systems. In addition to the considerable reduction in bulk, such systems would also require less electrical energy, because the pulsed magnet coil currents need only be switched on when the ultrasonic signals are in the vicinity of a transducer. Considerable reductions in peak coil current requirements can also be realized when pulsed-magnet-EMAT probes are operated on ferromagnetic samples because transduction mechanisms are strongly enhanced by magnetostrictive and dynamic effects. However, for optimum transduction efficiencies, the initation of the ultrasonic signal must be retarded relative to the

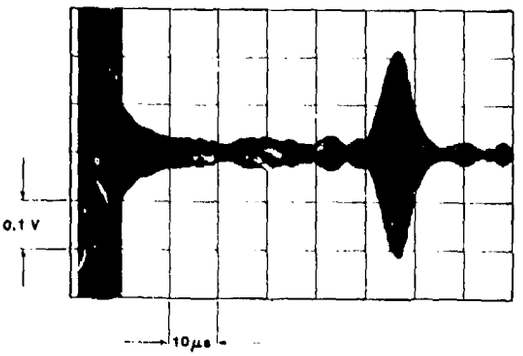

Fig. 15. Echo signals observed when the 1.35 kg pulsed electromagnet was used to launch and detect ultrasonic pulsed in a 20.3 cm (8 in.) aluminum billet held at 400°C.

beginning of the current pulse to the coil of the pulsed electromagnet. Pulsed-magnet-EMAT probes can also be operated at elevated temperatures (400°C). The results point to many prospective applications in the nondestructive evaluation (NDE) of hot metal parts in the steel and aluminum industries.

ACKNOWLEDGMENT

The results reported in this paper were obained while both authors were affiliated with the Albuquerque Development Laboratory, Science Center, Rockwell International Corporation. The authors would like to acknowledge many constructive discussions with Dr. G. A. Alers and other members of the staff of that laboratory. The work was supported by the independent research and development (IR and D) funds.

REFERENCES

1. Heinz Knoepfel, Pulsed High Magnetic Fields, North-Holland Publishing Co., Amsterdam, London, (1970).

2. R. Bruce Thompson, "A Model For The Electromagnetic Generation Of Ultrasonic Guided Waves In Ferromagnetic Metal Polycrystals," IEEE Trans. on Sonics and Ultrasonics SU-25, 7, (1978).

INSPECTION OF WING LAP JOINTS FOR SECOND LAYER CRACKS WITH EMATS

J. F. Martin, P. J. Hodgetts, and R. B. Thompson
Rockwell International Science Center
Thousand Oaks, California 91360

ABSTRACT

The detection of laboratory grown fatigue cracks in the second layer of aircraft wing lap joint fastener holes is demonstrated with EMATs (electromagnetic acoustic transducers). Operating at a 200 kHz central frequency, the EMATs employ acoustic waves in reflection and transmission to measure the presence of both fatigue cracks and loose fasteners. A minicomputer-based data acquisition and analysis system acquires, gates, apodizes and Fourier transforms each received time waveform. The resulting spectra are then compared to the spectra of uncracked holes with tight fasteners to determine the presence of a crack or loose fastener. A method for distinguishing the difference between a crack and a loose fastener is demonstrated. A suggested design for a fieldable instrument capable of the same abilities is presented.

INTRODUCTION

A major problem in aircraft maintenance is the detection of cracks growing from fastener holes in wing lap joints. As shown in Fig. 1, the problem is particularly difficult in the lower half of the joint, where direct measurement is obscured by intervening metallic and sealant layers. The former is opaque to all but low frequency eddy currents, whereas the latter has a variable, and often high, attenuation for ultrasonic waves in the MHz frequency range.

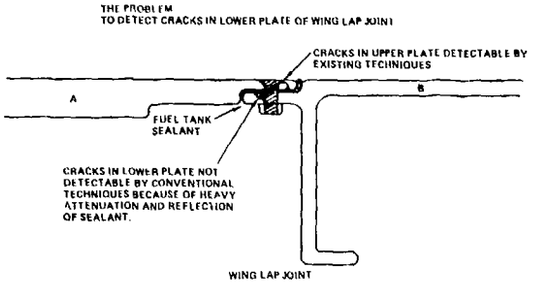

Fig. 1 The problem: to detect cracks in the lower plate of a wing lap joint.

The five-month study described herein followed a previous study (1) which demonstrated the feasibility of using horizontally polarized shear ultrasonic waves to detect saw slots placed in fastener holes in the lower member of the joint. The sample employed was a full scale mockup of the lower member machined out of a single piece of aluminum 24 inches long. As shown in Fig. 2, the waves were injected into the lap joint region by a couplant free EMAT (electromagnetic-acoustic transducer) placed on the exposed portion of the lower half of the joint. The energy propagated around the discontinuities, interrogated the fastener region, and returned to a receiving EMAT probe. An analog-based Fourier transform signal processor analyzed the experimental data. Saw

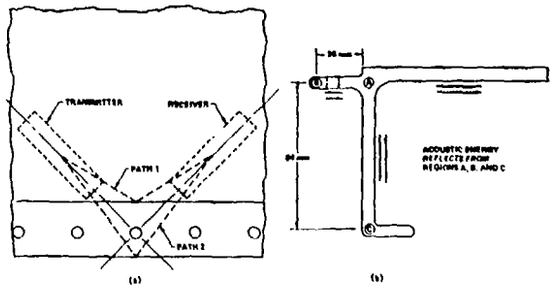

Fig. 2 Placement of EMATs and relevant acoustic beam paths: previous study.

slots originating at the fastener holes were successfully detected and the ultrasonic response quantified in terms of slot length. The primary limitations of that study included a high noise level, the lack of an opportunity to study real fatigue cracks in assembled wing joints, and the lack of an opportunity to explore procedures which could be adapted to changes in part geometry.

The objectives of the present phase were threefold:

1. To achieve refinement of the system developed in Ref. 1, and to establish procedures to distinguish flaw responses from sample-geometry-determined changes in the ultrasonic response.

2. To prepare, and use in experiments, a minimum of three fully assembled wing joint specimens, two of which would contain laboratory grown interior layer corner fatigue cracks.

3. To develop a preliminary configuration design of an EMAT system suitable for field inspection of wing lap joints for such cracks.

For additional information on this or the prior phase, the complete reports are available from the National Technical Information Service. Request parts I and II of AFWAL-TR-80-4081, "Investigation of an EMAT-based system for the detection of bolt hole type cracks."

APPROACH

A. Summary

In order to achieve the above objectives, the following program was conducted. First, the previously used apparatus was modified in several ways to improve the quality and reproducibility of the experimental data. These included changes in probe design, probe positioning hardware, and signal processing techniques.

In order to verify that the new apparatus was functioning properly and represented an improved capability, a series of experiments were performed on the unassembled mock-up sample used in the previous study. The successful results represented a completion of the first half of objective 1.

A set of four, fully assembled samples were then constructed and assembled to evaluate the technique. Two contained 0.030 in. (.076 cm) and 0.100 in. (0.254 cm) corner fatigue cracks in the lower half of the lap joint, grown in a laboratory MTS load-cycling machine under tension-tension fatigue conditions. These two samples lacked the stiffening rib to obtain fabrication savings. A third sample was a section of an actual wing lap joint in which corner EDM notches of the same dimensions had been placed. The fourth was the previously used mock-up, now fully assembled for the first time, which contained saw slots of various lengths.

Experiments were then performed on the assembled samples. The results indicated that the spectral differences between the cracked and uncracked holes were reduced upon assembly to a level which would be difficult to reliably detect. Hence, some recent developments in acoustic theory were applied in order to gain a deeper understanding of the problem. The result of that effort pointed toward some new experiments which proved to be more successful in this problem.

A number of results on the slotted samples and cracked samples are described in detail in Ref. 1. However, the most significant finding is that the 0.100 in (0.254 cm) fatigue crack and radial EDM notches were reliably detected using several different techniques, completing the performance of objective 2. The 0.030 in. (0.076 cm) fatigue crack was also detected, but with lower reliability. Further work is needed for this size of flaw before reduction to practice can be seriously contemplated. In addition, a technique was also defined which allowed the same procedure to be applied to samples of different geometry. This represents a partial attainment of the second half of objective 1. However, some more work is required before a completely unambiguous technique for differentiating flaws from geometrical responses is attained. Finally, going beyond the initial objectives, a technique was found for identifying loose fasteners.

Based on these results, a preliminary configuration design and inspection procedure have been prepared, completing the performance of objective 3. These are reported on briefly in Section IV. In the AFWAL reports mentioned above, a proposed program to reduce this technique to practice, using the cited configuration and procedure, is presented.

B. System Refinement

The system was first refined to improve the quality and reproducibility of the experimental data. Included therein were three major changes. First, the central operating frequency was lowered from 250 kHz to 200 kHz. This placed the operating point further below that point at which higher order modes of the lap joint plate would propagate and produce interfering signals (see Appendix of Ref. 1). It also was designed to place the interference null, used in the previous study for flaw detection and sizing, at the center of the transducer passband rather than at its edge (for the geometry of the original mock-up sample). Second, an improved positioning apparatus was constructed to allow higher quality data to be attained at multiple angles. This was needed for studies aimed at separating flaw from geometric responses. Finally, a digital signal processing system was employed which eliminated the previously observed fluctuations in system outputs, produced a higher signal-to-noise ratio through signal averaging, and allowed much greater flexibility in data analysis.

1. Probes - Four EMATs (electromagnetic-acoustic transducers) were fabricated to generate or receive ultrasonic horizontally polarized shear waves in aluminum, propagating at a grazing angle to the surface. These were implemented as one transmitter and three receivers. Appropriate analog electronic circuits were constructed for the generation of a 5-cycle tone burst and the amplification of the received signal.

2. Probe Positioning - Two new goniometers were constructed, one of plastic and one of brass/aluminum. These were used to accurately and repeatably position the probes with respect to the fastener holes and lap joint. The brass device was designed for more precise control of the angles (±17 mr) and positions (±0.5 mm) of the EMATs. The plastic device was used as a prototype of a hand-held fixture such as might be used in the field.

3. Signal Processing - Using these goniometers, three transmitter-receiver configurations were employed in the program (Fig. 3). The ultrasonic results from each of these varied as a function of angles α, β, and γ. Data was analyzed on a digital signal processing system consisting of a Data General S200 minicomputer-Biomation 8100 combination operating under the control of the Interpretive Signal Processing (ISP) Program. This system was created at the Science Center and is unique in the field of NDE. ISP is a large multitasking program which runs on the S200 under the command of an external terminal. It is tailored for flexible data collection and signal processing applications and capable of over 40 distinct operations including several for graphics. It was designed and developed at the Science Center and is constantly being upgraded for new NDE applications.

C. Fabrication of Samples

Four samples were utilized in experiments reported here and are described in Ref. 1 in detail. A large fraction of the fabrication effort was performed at another division of Rockwell, the North American Aircraft Division

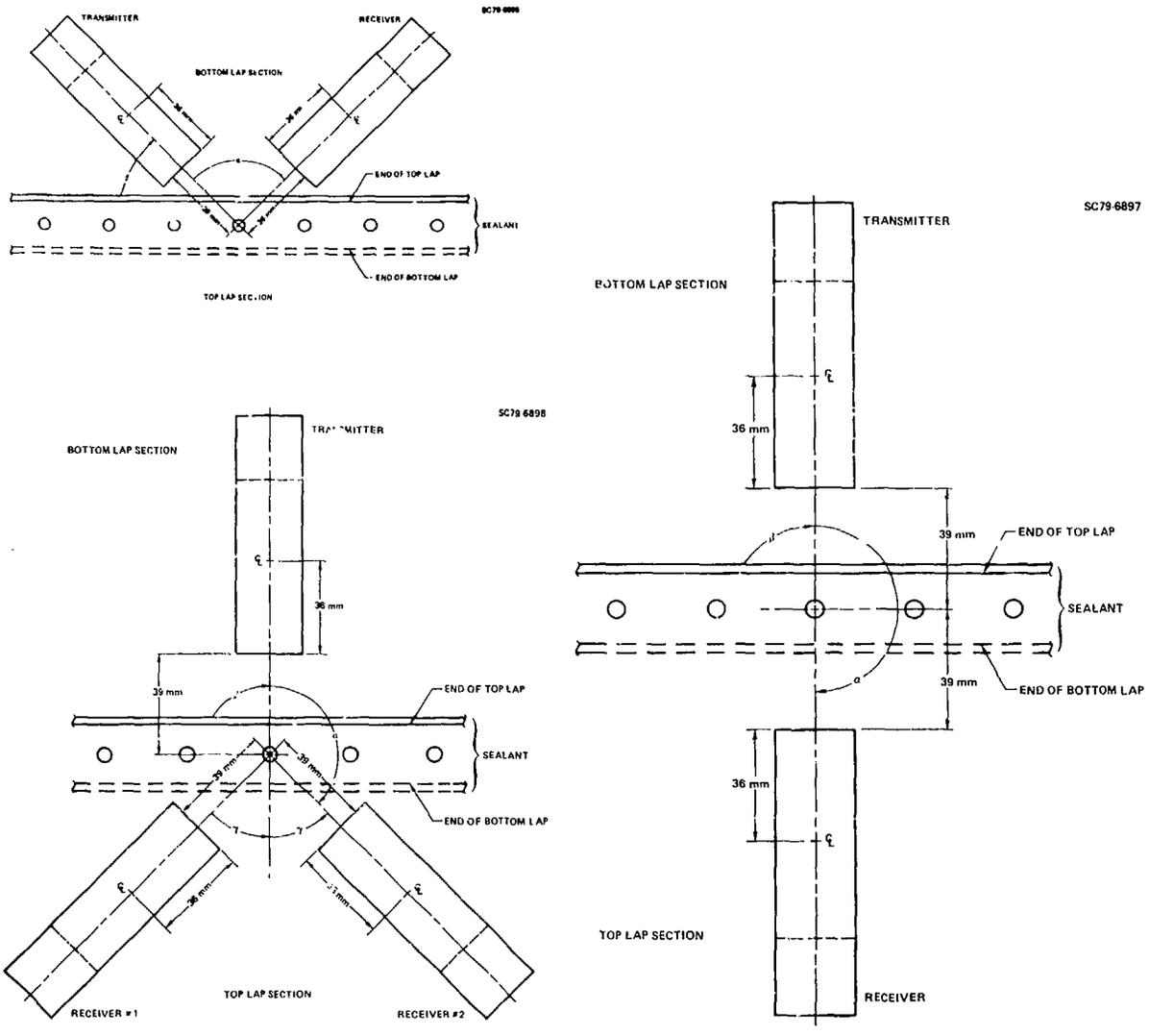

Fig. 3 Sketch of transducer configurations.

(NAAD), for reasons of efficiency and the availability of machine shop time and particular machines needed.

1. Actual Wing Section - This is the actual wing section provided for the previous study in which a saw slot had been introduced at one of the fastener holes (#19). To aid in comparison of EDM notches with fatigue cracks this sample was disassembled and two more flaws were created. These were radial corner EDM notches about 0.010" in width. One was 0.100" long and was placed at a hole in a region at hole #16 in a region of fairly constant geometry. Fig. 4a shows a cross-sectional view of the notch geometry. Furthermore, in reassembling this section, the fastener in hole #4 was omitted and hole #23 was drilled slightly oversize. This was done to provide examples of loose fasteners. The reassembly of this and the other samples was done in a manner very similar to that used for actual wings. This sample, in contrast to the laboratory-created samples, had relatively large geometrical variations in the bond joint dimensions over its length.

2. Wing Section Mock-up - The lower half of this sample was the full geometry aluminum mock-up fabricated for the previous study with five saw slots of various lengths. A mating upper half was constructed and tapered holes were drilled in each half to admit the special fasteners. The actual assembly of this specimen was delayed until after initial studies had been performed on the fatigued samples described next.

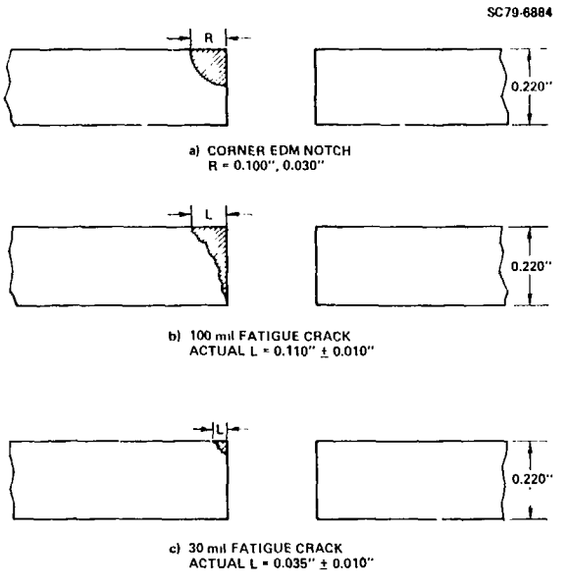

Fig. 4 Cross-sectional views of the radial corner notches and fatigue cracks. a) corner EDM notch, b) 100 mil fatigue crack: estimate, c) 30 mil fatigue crack: estimate

3. Fatigued Samples - This contract required two samples with simulated induced service fatigue cracks at the fastener holes. Consultation with Dr. O. Buck then at the Science Center but now at the Ames Laboratory at Iowa State University yielded a plan for creating such fatigue cracks. The full fabrication of these samples involved over ten separate steps. It took three months and cost approximately $6,000 per sample. In the opinion of the authors of this report, those figures are the minimum which could possibly be expected of any similar future fabrication.

The drawings necessary for fabrication are reproduced in Ref. 1. First, material was obtained for both the upper and lower sections of the joint for each specimen to be fatigued. The lower sections had to be wide enough on each end to provide an area where the MTS load-cycling machines could connect. The first machining steps provided a narrowed region with a pilot hole and an EDM notch which would start a fatigue crack under cycling (the "pre-fatigue shape"). In addition, two spacer pieces of aluminum were constructed for each end of each lower section to provide a fit to the MTS grips. These parts and the section ends were allodyned and bonded together before being drilled to accept the grip bolts. The fatigue cycling was performed over a range of 5 to 50 thousand pounds of tension with a 0.5 Hz cycle rate. Crack initiation required 7600 cycles on one specimen and 11,200 cycles on the other. The cracks could be easily measured under 50,000 pounds of tension. They were allowed to grow long enough that drilling the final taper hole would leave them near the nominal dimensions of 0.030 inch and 0.100 inch (0.076 cm and 0.254 cm). After the correct crack length was reached, the lower sections underwent finish machining, and the upper sections were constructed. The tapered holes were drilled by bolting the upper and lower sections together at each end and drilling them at the same time.

Two methods of confirming the length of the fatigue cracks after final drilling were used. They were etched and viewed under a microscope directly, and then they were treated with a fluorescent penetrant and viewed under a microscope again. Photographs of the cracks are shown in Ref. 1. Figures 4b and 4c show an estimation of the cross-sectional area of these cracks based on the observations made under the microscope.

The absence of the stiffening rib from these samples was motivated by the excessive cost involved and a much greater risk of failing to place a fatigue crack in the desired location. It is justifiable since from the studies in Section IV of Ref. 1 it is known that the rib reflection occurs well after the time window of interest.

D. Initial Experiments

In order to verify that the new apparatus was functioning properly, the results of the previous study on unassembled specimens were successfully repeated. Those results are described in Ref. 1 compared quite favorably to expectations.

However, after assembly of the fatigued specimens a crucial experiment was performed on the sample with the nominal 0.100" fatigue crack. The transducer configuration was that shown in Fig. 3a with $\beta = 45°$. This is the same configuration as that used successfully with the unassembled samples. The results are shown in Fig. 5 with the curves scaled to be of approximately the same peak height for the purpose of comparison. The spectra in Fig. 5 show only a very small systematic difference between hole #9, the hole with a 0.100" fatigue crack, and the other holes. This difference did not appear large enough to serve as a reliable estimate for the presence of a crack, and indicated that this transducer configuration might not be satisfactory

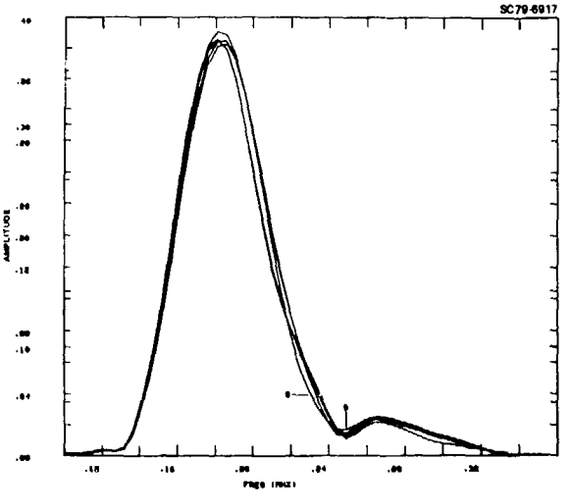

Fig. 5 Initial spectral results for the (assembled) specimen with a 0.100 inch fatigue crack.

for success in the field where only fully assembled wing lap joints are encountered.

The ability to find a fatigue crack of this length in an assembled specimen of uniform geometry is a minimum standard of performance which must be achieved in any transducer configuration. Since the configuration which worked well for the unassembled mock-up did not generalize to the fully assembled structure, an optimization procedure was sought. Ideally, this should be based on an examination of the mechanisms of the interaction of acoustic energy with the fastener hole in much greater detail for this complex geometry. As described in the following section, it was found that some recent developments in acoustic theory (Ref. 2) could be applied to this problem to provide a framework for understanding the dependence of the flaw's reflection coefficient on the angle of the incoming acoustic beam.

E. Development of Analytical Basis for Probe Optimization and Confirming Experiments

1. Theoretical Background

The basic approach used here is the scattering theory work in Ref. 2. It applies to the SH acoustic waves employed in this report. The central concept is an expression for the reflection coefficient for scattering of an acoustic beam from a void in a material. Suppose Γ is the signal propagated between a transmitter and a receiver in the absence of a void. Then, if a void is present, this will change by an amount $\delta\Gamma$ given by

$$\delta\Gamma = \frac{i\omega}{4P} \int_{\substack{\text{void} \\ \text{surface}}} \underline{T_{u'}} \cdot \underline{R_T} \cdot \underline{\hat{n}}\, ds \qquad (1)$$

where the presuperscript refers to the transducer used to generate the elastic fields and the post prime indicates the void is assumed to be present. Thus $\underline{T_{u'}}$ is the material displacement at the surface of the void when it is illuminated by the transmitting transducer driven by a power P, $\underline{n}$ is a unit vector normal to the surface of the void, and $\underline{R_T}$ is the material stress that would be produced at the mathematical location of the void surface if the void was absent and the region was illuminated by an electrical power P applied to the receiving transducer. Similarly, $\underline{R_u}$ which will be used in the following discussion; is the material displacement at the mathematical surface of the void with the void absent, as illuminated by the receiving transducer.

For the case of a crack at a bolt hole Eq. (2) can be simplified and placed in a form containing direct measureables. To do so, it can be noted that, for a crack, the integrations on the left and right. Consequently, Eq. (2) can be simplified into the form

$$\delta\Gamma = \frac{i\omega}{4P} \int_{\substack{\text{surface} \\ (y = +\varepsilon)}} \underline{T_{\Delta u'}} \cdot \underline{R_T} \cdot \hat{n}\, ds, \qquad (2)$$

where ε is small with respect to the radius of the fastener hole and the quantity $\underline{T_{\Delta u'}}$ is defined by

$$T_{\Delta u_y}' \equiv T_{u_y}'(y = +\varepsilon) - T_{u_y}'(y = -\varepsilon) \quad . \qquad (3)$$

$T_{\Delta u_y}'$ can be physically interpreted as the opening of the crack induced by the applied stress field. In order to further simplify Eq. (3), it is desirable to relate $\underline{T_{\Delta u'}}$ to the applied load. This can be done by noting that, when the crack is small with respect to the ultrasonic wavelength, the crack opening is given by

$$T_{\Delta u_y}'(x,z) \propto K(x,z)\, {}^{T}T_{yy}(x=a) \qquad (4)$$

where the factor K can be determined from static elasticity solutions and is a function of crack length. This is known as the quasi-static approximation. Substitution of Eq. (4) into Eq. (1) yields the result

$$\delta\Gamma \propto \frac{i\omega}{4P}\, {}^{T}T_{yy}(x=a)\, {}^{R}T_{yy}(x=a) \int_{\substack{\text{Surface} \\ (y = \varepsilon+)}} dx\,dz\; K(x,z) \qquad (5)$$

Discussion of the remainder of the analytical effort falls beyond the scope of this report but is given in Ref. 1. However, the practical implications of the analysis and the experiments which were performed to confirm it included an increased understanding of acoustic field behavior in the crack region, and the realization that angles of incidence different from the previously studied case of $\beta = 45°$ could yield a better differentiation of the cracked hole.

Armed with this knowledge, two more configurations were employed (Figs. 3b and 3c) to yield useful results; these are reported in the following sections.

RESULTS

The results reported here are extracted from the final report, Ref. 1, since there is space only for the most significant of these results. Three basic experiments are reported below, one for each of the configurations shown in Fig. 3.

A. Transmission Measurements With Two Probes

Figure 3b shows the configuration of transducers employed in this measurement. Acoustic energy was directed at the hole from one side of the lap joint, and received on the other side. In order to be received, the SH waves were forced to travel through the actual wing lap joint. Some of this coupling was no doubt provided by the sealant, and some was provided by the fastener. The spectral plots obtained at each fastener hole position are shown in Fig. 6 for several of the holes in the actual wing sample. At holes #2 (a loose fastener) and #4 (a missing fastener), less than half the acoustic energy was transmitted across the lap joint and the interference notch at 0.21 MHz for the tight fastener holes is not present. Hole #5, directly next to hole #4, also seems to be somewhat affected. Notice that the

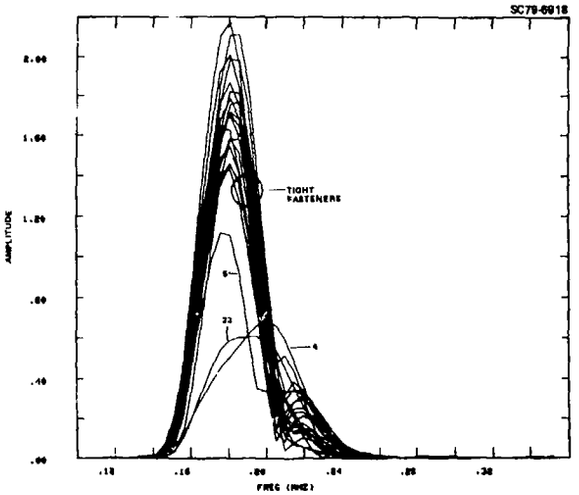

Fig. 6 Amplitude versus frequency for transducer configuration of Fig. 3b - actual wing sample.

effect of a loose fastener in this configuration was much larger than the effect of any notch or slot (included in the tight fastener set) and was not strongly influenced by the geometrical variations in this sample, which were rather large (see Ref. 1). This technique was used on the mockup wing section, where some fasteners were also loosened, with equally good results. Thus it appears that this transducer configuration would be likely to yield a capability for discovering loose fasteners in a large variety of wing lap geometries. Since for a loose fastener the amount of acoustic energy transmitted is strongly damped and the interference notch is eliminated, the signature for a loose fastener should be correspondingly easy to recognize.

B. Three-Probe Measurements

A second set of experiments employed the transducer configuration shown in Fig. 5c. This was motivated by the need to find a configuration which would be less sensitive to the geometry of the wing lap joint than those previously studied. Motivated partly by the theoretical analysis, the signal from one of the two receiver transducers was subtracted from the other and the frequency spectrum of the result found.

It might initially be thought that this difference would vanish for a crack normal to the plate edge by symmetry. However, close examination shows that for shear waves, the two receiver positions are not equivalent since the transducer polarization defines a preferred direction. Moreover, it can be intuitively argued that the degree of this difference is a measure of crack size.

In order to obtain a reproducible spectrum, extreme care was necessary in the alignment of the receiver signals. This is because the difference signal is generally quite small, and it is sensitive to any errors in transducer positioning as well as to the presence of a crack. In general, features in frequency space would not repeat from one data collection to another unless the signal alignment was better than 1% of the period. This tolerance was met using a simple loop feature of ISP to replot the signals from each transducer until the correct mechanical location was secured. Figure 7 exhibits the results for the 0.100 in. fatigue crack. The cracked hole is #9 and displays a significantly different signature from the other non-cracked holes.

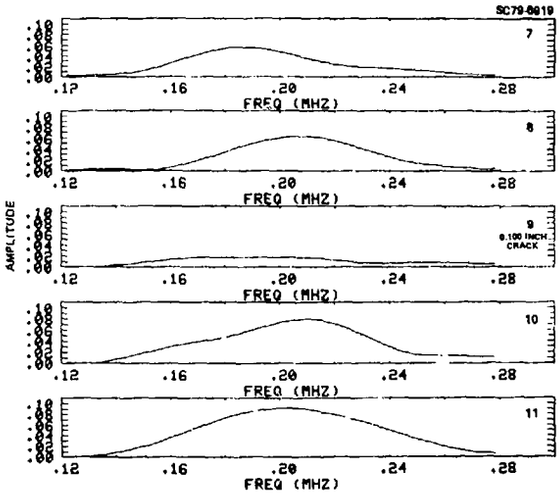

Fig. 7 Amplitude versus frequency for transducer configuration of Fig. 3c - sample with 0.100 inch crack.

The signature appears as a significantly depressed spectrum, as if constructive interference is occurring over the whole frequency range as well as at 200 kHz. A similar result, although not as large, was obtained in the sample with a 0.030 inch crack. Applied to the actual wing section, the phenomenon of a depression or notch at 200 kHz was again correlated with the hole being flawed. However, this technique did not work on the full aluminum mockup with saw slots. This was due to the fact that the fraction of transmitted acoustic energy was three times smaller than in the other samples. The resulting signal to noise ratio was too small and the noise destroyed the capability of this configuration to find the saw slots. The short length of time left in the contract did not permit any investigation of the reasons for the loss of transmission in this sample. Therefore, the efficacy of this method and this transducer configuration must be left as an open question. It is possible that each geometry has its own particular signature for non-cracked holes and that signature would have to be established before cracked holes could be identified. Nevertheless, the success this configuration exhibited with the range of geometrical variation in the first three samples is striking, and it may be the most likely starting point for future investigations.

A final comment is that the configuration 3c is probably sensitive to the quality of the seal at the fastener hole being interrogated. This should be kept in mind when assessing the usefulness of this configuration.

C. Reflection Experiments - Two Probes

The theoretical analysis prompted another set of exploratory experiments, using the configuration of Fig. 5a but varying β, keeping α fixed at 90°. The very encouraging result for the 0.100 in. (0.254 cm) fatigue crack was that, at β = 50°, a difference even in the time waveforms could be observed. Figure 8a shows signals from five different fastener locations for this sample. The plots are over a very narrow time window, centered on a value corresponding roughly to the center of the fastener hold. The cracked hole (#9) is marked with dashes and it stands out nicely from the rest. Figure 8b shows the Fourier transforms of these signals over a 40 μs window centered at 75 μs. Hole #9 does not have as deep an interference notch as the other four fastener locations.

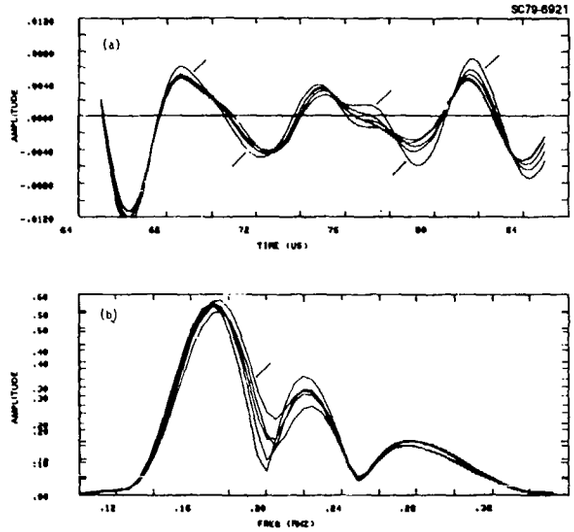

Fig. 8 Fatigue sample with 0.100 in. crack, holes 7 through 11, transducer configuration 5b, β = 50°. (a) Amplitude versus time; (b) amplitude versus frequency for 55 to 95 μs time window.

A straightforward and fieldable method of quantifying this effect is to average the frequency spectra from the nearby uncracked holes in that sample and divide by this average. This operation was performed in the minicomputer on data from both specimens with fatigue cracks. Figure 9 shows the results for the specimen with a 0.100 in. (0.254 cm) crack and Fig. 10 shows the results for the 0.030 in. (0.076 cm) crack. Holes #7, 8, 10, and 11 in each sample are not cracked; thus the statistical sample for this geometry consists of 10 holes, 8 of which are uncracked and serve as a measure of the range of systematic variation or noise.

In each of these figures, the normalization leads to a display which would have a constant value of unity if all holes were identical. The destruction of a null is indicated by a peak in the normalized plot for that hole. For the 0.100 in. fatigue crack sample data shown in Fig. 9 such a large peak occurs at hole #9, which was in fact the cracked hole. Lesser peaks occur

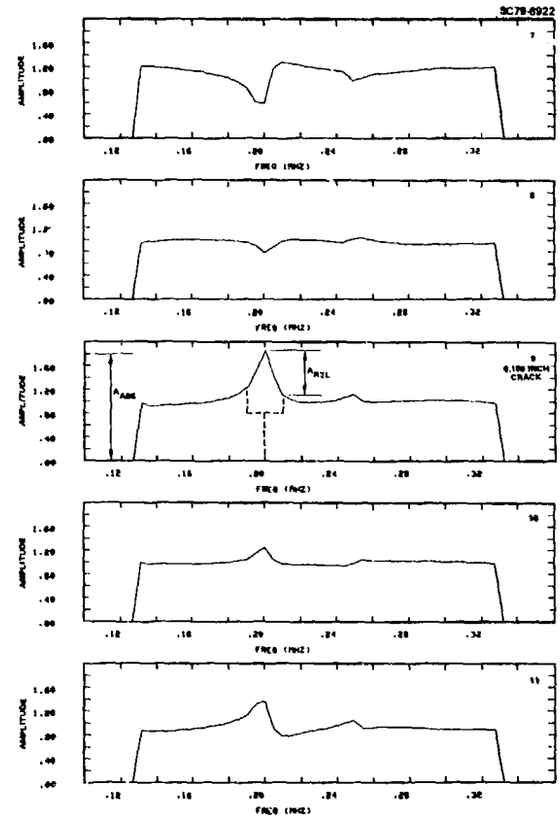

Fig. 9 Fatigued sample with 0.100 in. crack, holes 7 through 11, transducer configuration 5b, β = 50°. Normalized amplitude versus frequency.

in the plots for holes #10 and 11. These presumably are a result of a lack of reproducibility in the sample preparation and/or measurement technique. To a degree, they can be differentiated from true signals by shape criteria, e.g., note the skewing of the peak for hole #11. Beyond this, they represent the sensitivity limit of the system.

Similar results for a 0.030 inch hole are shown in Fig. 10. There again, the cracked hole #9 is indicated by a peak occurring at about 0.2 MHz. The peak is smaller in magnitude, somewhat asymmetric, and is comparable in size to the structure in holes #8 and #11. Again, it appears that it could be distinguished by the size and shape of the peak.

It will also be noted that all of the plots vanish at both low and high frequency. This is an artifact of the signal processing resulting from an automatic zeroing of the ratio when the denominator falls below a minimum level and should be ignored.

Since most of the energy is reflected, this method should be less sensitive to variations in sealant properties or fastener tightness than the transmission method. Variations in these parameters produce large fluctuations in the relatively

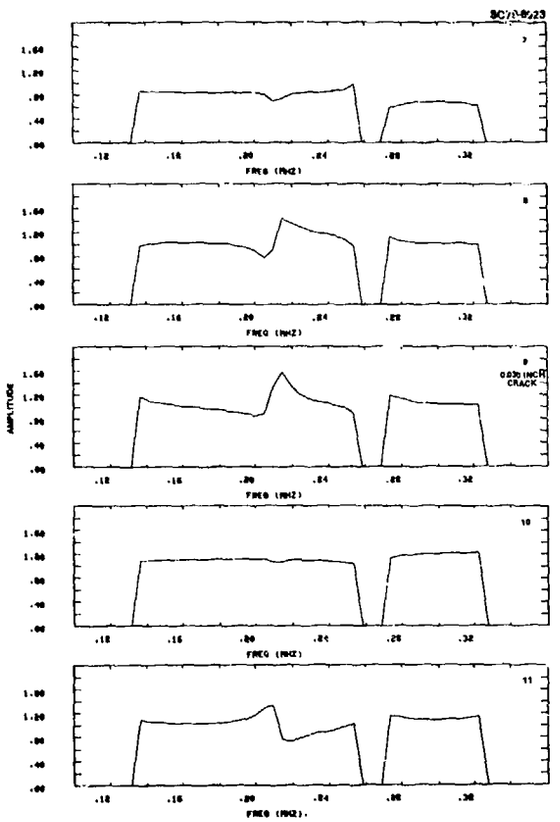

Fig. 10 Fatigued sample with 0.030 in. crack holes 7 through 11, transducer configuration 5b, $\beta = 50°$. Normalized amplitude versus frequency.

small amount of transmitted signal, but produce only small changes in the reflected energy.

These results clearly show that fatigue cracks can be detected by this EMAT technique. The signal from the 0.100 in. hole is well above the noise level set by variations in nominally identical holes and/or measurement error. The signal from the 0.030 in. hole is comparable to the noise but may be enhanced by signal processing based on the shape of the signal peak.

This technique was then applied in turn to the full aluminum mockup and to the actual wing section. The performance was excellent with the full mockup; in fact, it was evident that the size of the peak was definitely correlated with the size of the saw slots. However, in the actual wing section, the results were mixed. In order to further quantify the results from all samples, various size and shape parameters were defined and are plotted versus the length of the crack or slot.

Figure 9 shows how two of these size parameters were defined. A wide window in the spectrum centered on 200 kHz was examined for a peak. Then a narrow window (dashed lines) was established around the peak. A_{abs} was set equal to the absolute amplitude of that peak, and A_{rel} was set equal to the relative amplitude of that peak. In this case, relative amplitude was defined to be the distance the peak fell above the average of the two values of the plot at the edges of the narrow window.

Figure 11 shows a plot of A_{abs} versus crack or slot length for all holes and Fig. 12 shows a plot

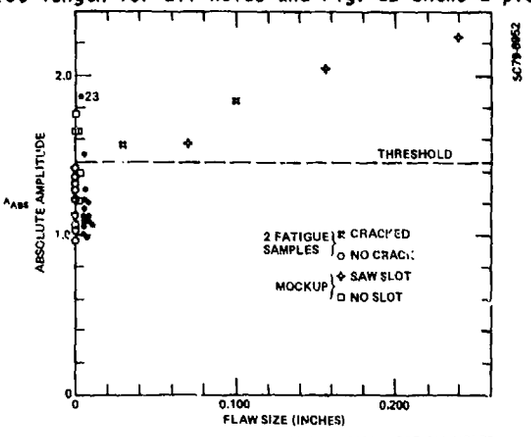

ABSOLUTE AMPLITUDE OF HIGH PEAK NEAR 200 kHz FOR ALL HOLES.

Fig. 11 Absolute amplitude of high peak near 200 kHz for all holes.

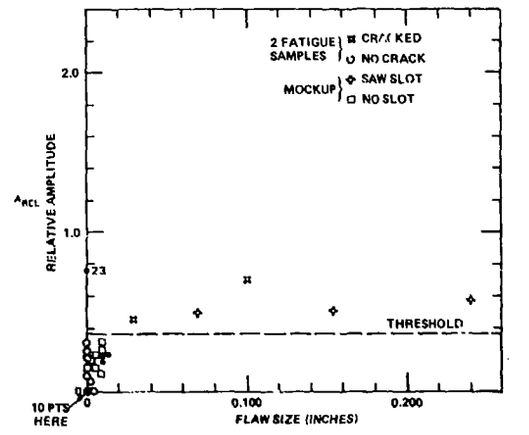

RELATIVE AMPLITUDE OF PEAK NEAR 200 kHz FOR ALL HOLES.

Fig. 12 Relative amplitude of peak near 200 kHz for all holes.

of A_{rel} versus length. Notice that different symbols are used for each of the sample types.

Due to the large number of holes with no crack or slot, many points are clustered near the zero axis of the abscissa. In general, holes with no flaw fell lower on both plots than holes with a flaw. The dashed line in each plot represents a suggested threshold for using that parameter in an accept/reject decision. Clearly, there are fewer false accepts and false rejects in the plot of A_{rel}, but the plot of A_{abs} exhibits a steeper slope as a function of flaw size.

Proceeding with this line of analysis then, one can use both figures to determine the quantitative accept/reject quality. Using Fig. 11, the absolute amplitude of all peaks, the ratio of false rejects to possibles is 0/8 for the two fatigued samples, 3/6 for the mock-up, and 1/13

for the actual wing section. The ratio of false accepts to possibles is 0/2 for the fatigued samples, 0/3 for the mock-up, and 2/3 for the actual wing section for the threshold shown.

Using Fig. 12, relative amplitude of all peaks, the ratio of false rejects to possibles is 0/8 for the fatigued samples, 0/6 for the mockup, and 0/13 for the actual wing sample. The ratio of false accepts to possibles is 0/2 for the fatigued samples, 0/3 for the mockup, and 3/3 for the actual wing section for the threshold shown.

The performance of this technique is thus excellent for the three fixed geometry specimens, but not as good for the actual wing section with different, and varying geometry. However, the Fourier amplitude spectra can be separated out into Real and Imaginary parts. A discussion (Ref. 1) indicates that this could yield a large improvement in the ability to identify flaws in the actual wing section. In addition, the small A_{abs} from the 0.100 in. saw slot in the actual wing section compared to the large response from a very similar flaw in the mockup suggests that the angle β in the transducer configuration should be a function of the geometry of the wing section.

The recommendation emerging from this work for development of a fieldable instrument based on this study included two phases, a detailed instrument design, and prototype construction and testing. Details on those subjects are given in Ref. 1.

CONCLUSION AND RECOMMENDATIONS

In this effort, significant progress has been made in the detection of fatigue cracks under fasteners in the lower half of the C5A wing lap joint. Prior to this study, it had been shown only that the signature of holes with saw slots in an unassembled mock-up could be recognized. In this study the following new results have been obtained.

1. Fatigue cracks at fastener holes can be grown in the laboratory for this geometrical configuration.

2. Fastener holes with the cracks can be found with EMAT-generated acoustic beams, even in an assembled lap joint. This was accomplished in two completely different transducer configurations, with 100% detection capability on the samples with cracks.

3. Limited success was achieved in detecting EDM notches and a saw slot in a wing section with varying geometry.

4. An achievement which was not required by the contract, but which may be significant, is the ability to detect loose fasteners.

Important questions not yet fully resolved concern the detectability of fatigue cracks of 0.030 inch size and the exact procedure for detecting fatigue cracks in other geometries, particularly those with major deviations from the one studied.

The transducers and configurations used in this study appear robust and easily fieldable. The detailed implementation of a crack-finding instrument based on the conceptual design of Section III would require future interaction with knowledgeable field personnel.

ACKNOWLEDGEMENT

This research was sponsored by the Center for Advanced NDE operated by the Rockwell International Science Center for the Defense Advanced Research Projects Agency and the Air Force Wright Aeronautical Laboratories under Contract No. F33615-80-C-5004.

REFERENCES

1. J. F. Martin, P. J. Hodgetts, R. B. Thompson, "Investigation of EMAT Based System for the Detection of Bolt Hole Type Cracks - Part II: Reliability Evaluation and System Definition for Detection of Cracks under Fasteners by EMATs," Air Force Technical Report AFWAL-TR-80-4081, Part II.

2. B. A. Auld, Ginzton Laboratory Report 2808, Stanford University, Palo Alto, CA.

APPLICATION OF EMATs TO IN-PLACE INSPECTION OF RAILROAD RAILS*

H. Maiseri, D. MacLauchlan, and C. Alers**

Albuquerque Development Laboratory
Rockwell International Science Center

ABSTRACT

With the aging of the U.S. railroad system and the increased tonnage being moved, it is more important than ever to monitor the installed railroad track for defects whose growth could lead to track failure and derailments. Current ultrasonic inspection techniques utilize a liquid filled wheel to couple acoustic energy from several piezoelectric transducers into the rail at a variety of angles relative to the head of the rail. This approach limits the speed of inspection to approximately 10 mph, is very sensitive to the surface condition and orientation of the railhead and requires frequent maintenance stops. The feasibility of using EMATs to replace the water filled wheel transducers has been the purpose of this research effort at the Albuquerque Development Laboratory and was sponsored by the Department of Transportation with the cooperation of the Sperry Rail Service Division of Automation Industries, Inc.

INTRODUCTION

Railroad rails are subjected to very high, periodic loads so they usually fail by the growth of flaws under fatigue type conditions. Since the initiating flaws are too small to be reliably detected at the manufacturing facility, they must be found by routine inspections when the rail is in service and after the flaw has had a chance to grow to a detectable size. Thus, inspection cars have been developed that travel along the railroad tracks at 10 to 20 mph looking for cracks and large flaws in each rail. They use both magnetic flux leakage and ultrasonic inspection techniques. The latter method utilizes a rubber wheel filled with water to couple the ultrasonic waves from the piezoelectric transducers into the rail as shown in Fig. 1. By mounting the transducers inside the wheel at an angle relative to the rail head surface, ultrasonic waves can be sent into various parts of the rail. A wave propagating normal to the head detects cracks or separations at the foot of the rail or between the head and web. Waves at an angle of 30 degrees to the head normal are well suited to locating cracks at the bolt holes in the ends of each rail. For flaws in the head of the rail, an ultrasonic wave propagating at 70 degrees to the normal is used.

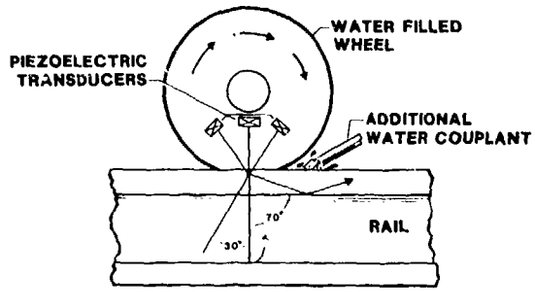

Figure 1. Conventional method of ultrasonic inspection of railroad rails.

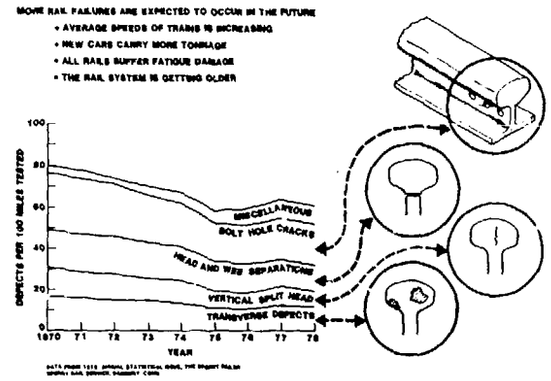

Figure 2. Types of rail flaws and their frequency of occurrence.

Figure 2 shows drawings of the most common rail flaws and displays a graph from which the relative frequency of occurence of each type can be deduced.

Ultrasonics has proven to be a very powerful technique for locating these flaws but the wheel type transducer has proven to be a major source of

* Supported by the Department of Transportation Contract #DOT-Fr-8079.

** All presently at the New Mexico Engineering Research Institute of the University of New Mexico, Albuquerque, New Mexico.

problems in that it has a restricted top speed, it looses coupling when dirt and oil are on the rail surface and small variations in the rail head geometry cause large changes in the direction of the refracted ultrasonic beam inside the rail. In order to overcome or mollify these difficulties, the Department of Transportation awarded the Rockwell Science Center a contract to demonstrate the feasibility of replacing the wheel type transducer with electromagnetic acoustic transducers (EMATs). These devices excite and detect ultrasonic waves in metals by an electromagnetic induction process across an air gap. Hence, they can operate reliably at high speed, over dirty or oily rail heads and are not subject to temperature effects. By using special coil designs, acoustic waves can be launched into the rail at an angle and the transducer can be made light enough to survive the mechanical shocks of moving along an operating railroad system. The program goals of this feasibility demonstration were: (1) to demonstrate operation from the top of the rail head only; (2) to determine how large an air gap could be tolerated between the transducer coil and the rail; (3) to show that angle beam inspection techniques were possible and (4) to establish the sensitivity of an EMAT inspection system to real flaws such as the transverse fracture, the horizontal split head, the vertical split head, the head-web separation, the bolt hole crack and surface shelling.

APPROACH

Figure 3 shows a schematic diagram of an EMAT rail inspection system in which a large electromagnet, suspended from the inspection car, supplies the magnetic field for an array of EMAT coils distributed about the head of the rail. Transducers B launch waves into the rail head propagating along the length of the rail. Transducers A launch waves across the head to locate longitudinal defects in the head. Transducers C launch

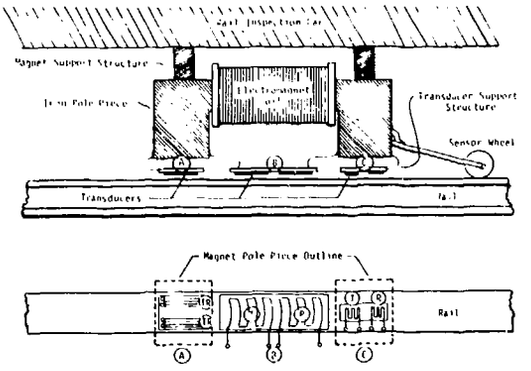

Figure 3. Schematic diagram of a possible EMAT rail inspection system.

waves through the head into the web to locate cracks at the bolt holes and head-web separations. Each of these transducers can be distinguished by its frequency of operation.

The feasibility experiments were also separated according to frequency as shown in Fig. 4. The advantage of the low frequency methods lies in the fact that they are less sensitive to lift off but they suffer from a lower EMAT efficiency. Hence, all three frequency ranges had to be investigated in order to develop trade-off data on lift off and sensitivity.

ENGINEERING TRADE-OFF:

- LOW FREQUENCY EMATs OPERATE WITH LARGE LIFT-OFF
- EMAT EFFICIENCY DROPS AT LOW FREQUENCY

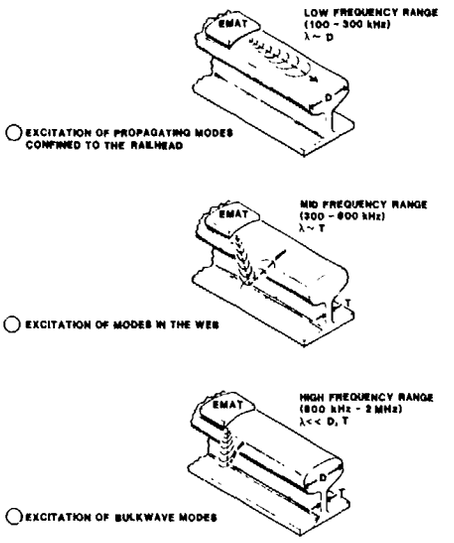

Figure 4. Configuration of EMATs tested in various frequency ranges.

Figure 5 shows a drawing of the oscilloscope trace observed when the low frequency EMAT arrangement was placed on a short length of rail containing transverse defects in the head.

TRANSVERSE DEFECT DETECTION

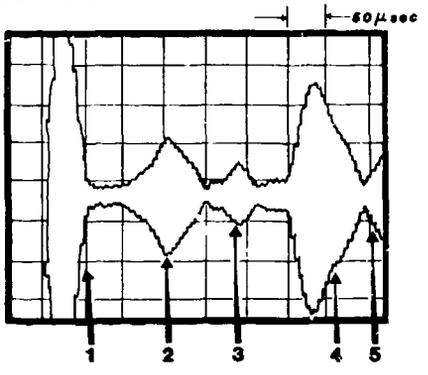

Figure 5. Oscilloscope presentation of echos observed with the low frequency waves on a short section of rail. Echos 1 and 4 are from the ends of the rail and echos 2 and 3 are from a transverse flaw in the rail head. (Frequency 220 KHz, λ=1.4 cm.)

EXPERIMENTAL CONFIGURATION

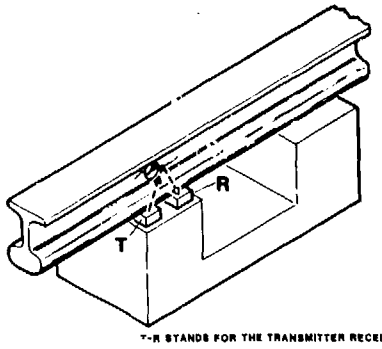

Figure 6. Experimental configuration used to test EMAT detection of bolt hole cracks at mid-frequencies.

At mid-frequencies where a nominally 30 degree acoustic beam is needed to detect cracks at the bolt holes, the experimental configuration shown in Fig. 6 was used. In this case a meander coil type EMAT was used, operated at a frequency such that the ultrasonic energy entered the rail head at an

BOLT HOLE CRACK DETECTION

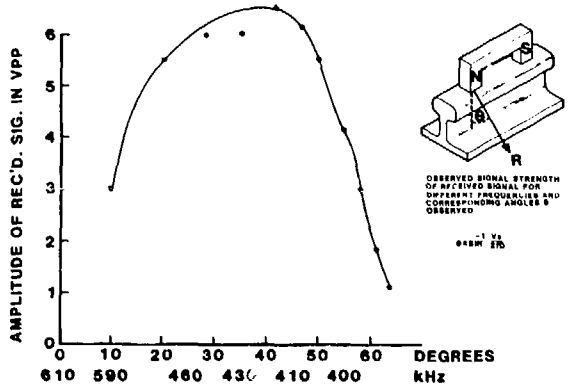

Figure 7. Dependance of EMAT efficiency on frequency and angle of propagation in a rail.

angle to the surface normal. Figure 7 shows how the amplitude of the ultrasonic signal depended upon the angle of propagation and the drive frequency. Figure 8 shows how the oscilloscope display appeared when flawless bolt holes and cracked bolt holes were examined. Because of the uniform circular shape of the flawless hole, there are striking oscillations in the amplitude of the signal reflected from it. A crack in the hole destroys the uniformity and with it the oscillations in the reflected signal strength.

The high frequency EMAT (~2 MHz) designed to launch bulk ultrasonic waves into the rail in a direction perpendicular to the rail head was configured as shown in Fig. 9 to detect defects in the web. In this case, the echo from the base of a flawless rail could be easily detected as shown in the top oscilloscope trace in Fig. 10. If a crack were present in the web such as for the case

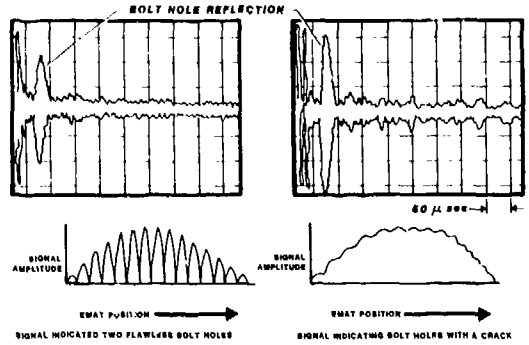

Figure 8. Characteristics of pulse-echo signals observed in the vicinity of flawless bolt holes and cracked bolt holes for EMATs with a spacing between wires of 0.5 cm and operated at 560 KHz.

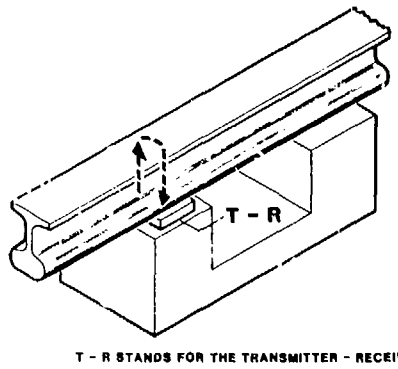

Figure 9. Experimental configuration used to detect flaws in the web of the rail.

of a head-web separation, this base reflection would disappear because the acoustic energy would be dispersed or reflected away by the flaw. This condition is shown in the bottom oscilloscope trace shown in Fig. 10

Throughout the feasibility studies, it was important to measure how each of the EMATs responded to increases in the separation between the EMAT coil and the surface of the rail. Since the low and medium frequency cases utilized meander type EMAT coils their efficiencies decreased rapidly with lift off. The efficiency of a transmitter-receiver pair dropped by a factor of two with a 0.05 inch gap for the low frequency case and a 0.03 inch gap for the mid-frequency case. The high frequency case utilized a spiral coil which has much less inherent sensitivity to lift off than the meander coils. For this type of coil the efficiency fell by a factor of two when the gap reached 0.1 inches.

CONCLUSIONS

The results of the feasibility study showed that EMATs could be designed to inspect railroad rails with ultrasonic beams similar to those used by the wheel type transducers now in use. Studies on rail samples containing actual defects showed

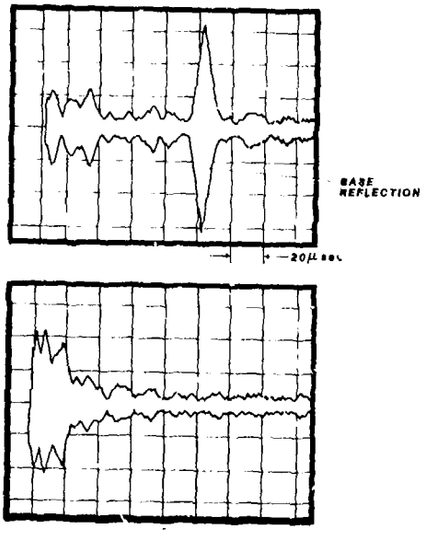

Figure 10. Oscilloscope presentation observed at high frequencies where the ultrasonic waves propagate into the web along the rail head normal direction.

that the EMATs were equal in sensitivity to the piezoelectric transducers because both were limited by the background noise in the metallurgical structure within the rail.

INDUSTRIAL PROBLEMS ENCOUNTERED IN THE EDDY CURRENT INSPECTION OF STEEL

G. V. Jeskey, F. P. Vaccaro
The Timken Company
Canton, OH 44706

ABSTRACT

It is anticipated, that through exposing some of the problems encountered in industrial applications of eddy current technology, technical assistance may be generated through the theoretical community. The specific problem examined involves the development, storage and utilization of calibration masters. Although the use of probes versus coils greatly reduces the number of calibration masters in that probes are not sensitive to overall geometry and mass variations, the eddy current response is influenced by near probe geometry variations. At present, an empirically derived algorithm is relied upon to characterize this phenomenon although it is hoped that an appropriate theoretical model will be developed. In addition to geometry, the non-linear permeability present in ferromagnetics, and the microstructural and compositional variations greatly increase the complexity of constructing such a model.

There are two kinds of talks one encounters at technical conferences such as this one, those which expose and those which solve problems. This presentation will be of the former type and will attempt to elucidate in a more detailed fashion some of the difficulties encountered in the eddy current materials sorting of steel. It is hoped that constructive feedback will be generated from the theoretical community, to the benefit of those of us in industry. The specific problem examined today will involve the influence of steel component curvature on eddy current response.

It might be helpful to review exactly how the influence of component curvature on probe response became a concern and how the problem is being dealt with presently. The important theoretical factors in developing a model descriptive of the phenomenon will be examined.

Most of those present here should be familiar with the basic differences between through coil and probe eddy current inspection techniques. Yet the relative advantages for specific applications are not always appreciated. In Table 1 a detailed comparison is presented for the specific application of heat treatment materials sorting. Both techniques provide excellent sorting capabilities, are available in relatively inexpensive commercial systems and provide inspection speed capacities comparable to many production operations. The coil technique, however, does not focus on the component region of interest whereas the probe can be often located to examine the area of concern. In view of this insensitivity to overall geometry variations, the use of probes, in many applications, substantially reduces mastering requirements.

The most serious limitation in the use of probes involves the strict demands for probe-specimen orientation control, and the dependence of probe response on local component geometry variations. It is with this last point that we are primarily concerned in this presentation, namely the dependence of eddy current response on component curvature.

The populations of eddy current response for four different carburized steel cylinders are shown in Fig. 1. In these data a comparison is being made between properly and improperly heat treated material. In directing our attention to the influence of curvature, it is observed that the eddy current response increases statistically with diameter. This may be interpreted as an increase in the penetration of flux and a corresponding increased interaction with the detection coil in the probe. A similar influence of curvature is observed for a hollow cone (see Fig. 2).

The variation in probe response due to curvature introduces a mastering difficulty tending to decrease the advantage that probes enjoy over through coil techniques. This effect is presently accommodated through a normalization procedure in which empirically derived algorithms adjust the mastering response (see Figs. 3 and 4).

The curves generated from these algorithms are shown in Fig. 5 in relation to the pertinent statistical data. From an engineering standpoint, this approach is satisfactory in establishing sorting limits. However, through the development of a viable theoretical model, increased confidence, predictability, and the suppression of the amounts of statistical data required may be obtained. There are four major

areas requiring consideration in constructing an appropriate theoretical model. They are:

1. The nature and distribution of the probe field.

2. The nature and distribution of the field generated eddy currents.

3. The construction of a mathematical model accommodating the specific boundary conditions as well as the nature and distributions of field and eddy currents.

4. The influences of simplifying approximations on the representative character of the proposed models.

The nature and distribution of the field are dependent upon the specific probe characteristics. These characteristics include coil current, frequency, number of turns, coil area, orientation, and the influence of core material. In addition, the probe may be composed of multiple coils for separating the field generating primary from the detecting secondary, or in a differential arrangement to suppress extraneous noise. The influence of probe characteristics could prove to be one of the most difficult considerations in any theoretical treatment.

The origin, nature and distribution of the eddy currents will be dependent upon the field, the probe-specimen geometry and the electromagnetic properties of the steel specimen. There are few theoretical attempts to explain eddy current phenomena in ferromagnetic, non-linear permeability (μ) materials in contrast to linear, non-ferromagnetic conductors. Analytical solutions have been primarily restricted to assumed linear conditions.

Utilizing the concepts of a linear relationship between the phasor quantities B and H and a representation of hysterisis through complex permeability (in which the B/H characteristic is elliptical through the introduction of a phase lag δh between B and H), D. O'Kelly (1, 2, 3, 4) has calculated the flux distributions and the hysterisis and eddy current losses in steel plates (Fig. 6). The principles applied to the analysis of the fundamental component of B and H were also applied to harmonics providing additional accuracy (2). One other popular approach involves the numerical analyses of network models in which non-linear effects are accounted for in a descretized fashion (5, 6).

For non-linear conditions, many numerical techniques have been utilized with digital computers to obtain solutions. However, most finite element computations have ignored hysteresis effects or employed representation techniques. As one can see, there are several available theoretical approaches to choose from in modeling eddy currents while taking into account non-linear effects.

In the treatments above, it is commonly assumed that the material is homogeneous and isotropic. In actual eddy current inspection of steel, microstructural and compositional variations will greatly influence electromagnetic properties. These effects are especially pronounced when the process involves special compositional treatments such as carburizing, in which a hardened surface layer is created through the impregnation of carbon (Fig. 7). The resulting carbon gradient produces both a compositional effect and will significantly alter the microstructure.

Carbon, both in solution and in precipitated forms, reduces permeability (μ) (Fig. 8) and the saturation induction B_m (Fig. 9) while the coercive force H_c (Fig. 10) and hysteresis loss (Fig. 19) are increased (7). Heat treatment and thermal history have a synergistic influence with composition on the electromagnetic properties. This synergism influences the electromagnetic properties in steels in the same manner as it controls the mechanical properties, namely through regulating microstructure. Many of the variations in magnetic properties are the result of morphological differences and not simply base composition changes. As one might expect, these combined effects are more pronounced at higher carbon levels.

The precise manner in which the electromagnetic properties of steel depend upon composition and microstructure may be classified under four headings:

1. The carbon and alloy content of the primary magnetic phases (i.e. martensite or ferrite).

2. The structure of the primary ferromagnetic phases.

3. The volume percent and distribution of non-ferromagnetic carbides.

4. The volume percent and distribution of retained non-ferromagnetic (paramagnetic) austenite.

The influence of non-magnetic phases has been aptly described in "Metallurgy and Magnetism" by James Stanley (7):

> "Non-ferromagnetic phases or inclusions such as graphite in cast iron or slag in wrought iron have an effect on the magnetic properties similar to that produced by cutting an air gap in a solid magnetic ring." "A similar effect takes place when the gaps are internal which is in reality what happens when a non-magnetic phase or inclusion is present. This is shown in Fig. 43" (Fig. 12) "for the case of steel with different amounts of carbon (the cementite of the pearlite is relatively non-magnetic)."

Although carbon is one of the major modifiers of electromagnetic properties it is by no means the only one. Silicon, aluminum and other alloying elements are known to reduce saturation values and permeability (Fig. 14). The influence of these alloy additions is also very dependent upon the heat treatment.

Composition and microstructure will correspondingly affect electrical conductivity (Fig. 15). Increasing alloy additions, when in solution, will generally decrease conductivity. When microstructural factors become important, the effects become more difficult to predict. Nevertheless, the eddy currents generated will be affected through variations in conductivity.

Extensive efforts have been made at Timken Research to determine the electromagnetic properties of the steels of interest. This effort has included an examination of the influence of composition and heat treatment. Preliminary results may be qualitatively summarized as follows.

In Fig. 16 the B - H characteristic curves for core and case structures are compared. The case displays substantially reduced magnetic properties. This decrease is either the result of high carbon content, high carbide content or the presence of retained austenite. Further exploration of this reduction in properties will be performed in order to understand the individual contributions of the carbon and retained austenite.

The effects of over-tempering are presented in Fig. 17 for core and case respectively. The drastic increase in magnetic properties in the case is attributed to the decomposition of retained austenite into bainite, although the precipitation of carbides and the associated migration of the BCT martensite structure to the equilibrium BCC ferrite structure may also be playing a significant role. In the core, similar increases occur although in view of the originally high properties the improvement with over-tempering is not as dramatic. The increase observed in the core may be attributed to the precipitation of carbides and the corresponding formation of ferrite having characteristically high magnetic properties.

These hysteresis curve effects need to be more fully understood as they depend upon alloy content and heat treatment. The frequency of inspection is also a parameter of great importance in case carburized component inspection in view of the influence that frequency has on depth of penetration.

Once the specific conditions of probe field, material properties and geometry are well defined, the development of a comprehensive mathematical model and the selection of appropriate approximations are all that remain. These two factors were indirectly examined in the previous discussions regarding the available analytical models. Any attempt at combining all of the above considerations in constructing a theoretical model for the effect of curvature on the eddy current response in case carburized steel may prove intractable. Nevertheless, continued research efforts are scheduled at The Timken Company and substantial benefits are anticipated. For those engaged in similar efforts, or who may be able to provide insight into this complex problem, the development of future correspondence would be greatly appreciated by the authors.

REFERENCES

1. D. O'Kelly, "Flux Penetration in a Ferromagnetic Material Including Hysteresis and Eddy Current Effects", J. Phys. D: Appl. Phys., Vol. 5, 1972 page 203, Great Britian

2. D. O'Kelly, "Fundamental and Harmonic Flux Estimation in a Steel Plate with a Sinusoidal Applied Field", J. Phys. D: Appl. Phys., Vol. 10, 1977 page 2107, Great Britian

3. D. O'Kelly, "Hysteresis and Eddy Current Losses in Steel Plates with Non-Linear Magnetisation Characteristics", Proc. IEE, Vol. 119, #11, Nov. 1972 page 1675

4. D. O'Kelly, "Losses in Cylindrical Ferromagnetic Cores Including Hysteresis and Eddy Current Effects", J. Phys. D: Appl. Phys., Vol. 8, 1975 page 568, Great Britian

5. N. A. Demerdash and D. H. Gillott, "A New Approach for Determination of Eddy Current and Flux Penetration in Non-Linear Ferromagnetic Materials" IEEE, Trans. Magn. Vol. MAG 10, #3, Sep. 1974 page 682-685

6. K. Oberretl, "Magnetic Fields Eddy Currents and Losses Taking the Variable Permeability into Account", IEEE, Trans, PAS, Vol. 88, 1979 page 1646-1657

7. J. K. Stanley, "Metallurgy and Magnetism", ASM, 1949, Cleveland, Ohio

TABLE 1

COMPARISON BETWEEN COIL vs PROBE EDDY CURRENT MATERIAL SORTING OF CASE CARBURIZED CYLINDERS

CATEGORY	TECHNIQUE	ADVANTAGES	DISADVANTAGES
SORTING CAPABILITY	COIL	GOOD SORT FOR MANY APPLICATIONS	AMBIGUITIES EXIST FOR SOME HEAT TREAT CONDITIONS
	PROBE	GOOD SORT FOR MANY APPLICATIONS	AMBIGUITIES EXIST FOR SOME HEAT TREAT CONDITIONS
AVAILABILITY AND EXPENSE	COIL	INEXPENSIVE COMMERCIAL SYSTEMS AVAILABLE	
	PROBE	INEXPENSIVE COMMERCIAL SYSTEMS AVAILABLE	
AREA OF EXAMINATION	COIL	WHOLE PART EXAMINED	DOES NOT FOCUS IN AREA OF INTEREST
	PROBE	FOCUSES ON AREA OF INTEREST	RESTRICTED TO EXAMINING ONLY ONE AREA OF PART
PART-PROBE ORIENTATION	COIL	NOT CRITICALLY SENSITIVE TO PART POSITION IN COIL	
	PROBE		LIFT OFF AND PART PROBE MUST BE CONTROLLED OR COMPENSATED FOR

TABLE 1 (CONTINUED)

COMPARISON BETWEEN COIL vs PROBE EDDY CURRENT MATERIAL SORTING OF CASE CARBURIZED CYLINDERS

CATEGORY	TECHNIQUE	ADVANTAGES	DISADVANTAGES
HANDLING AND INSPECTION SPEED	COIL	CONTINUOUS, FAST, SIMPLE, AMENABLE TO MANY HIGH SPEED PRODUCTION LINES	
	PROBE		SOPHISTICATED HANDLING REQUIRED
MULTI MODE/ MULTI FREQUENCY CAPABILITY	COIL		WOULD REQUIRE DISCONTINUOUS OPERATION, RESULTS IN REDUCED SPEED
	PROBE	PRESENTLY EMPLOYED IN AVAILABLE SYSTEMS	
MASTERING AND CALIBRATION	COIL	EASY CALIBRATION WITH REFERENCE MASTER	REQUIRES SEPERATE MASTER FOR EVERY PART...INVENTORY NIGHTMARE
	PROBE	EASY CALIBRATION REDUCES MASTERING INVENTORY SUBSTANTIALLY	MUST ACCOUNT FOR NEAR PROBE GEOMETRY VARIATIONS

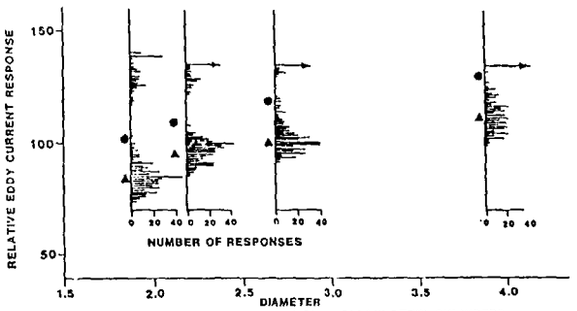

FIG. 1 EDDY CURRENT RESPONSE FOR HOLLOW STEEL CYLINDERS

▲ AVERAGE $(\bar{x})$ ● $\bar{x}+3\sigma$

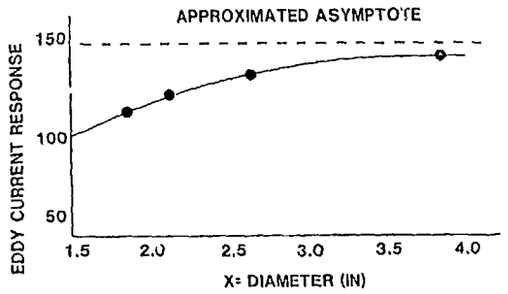

FIG. 4 PLOT OF ALGORITHM, $Y = 135 - 163 \exp(-.87604x)$, EMPIRICALLY DERIVED TO FIT $\bar{x}+3\sigma$ (●)

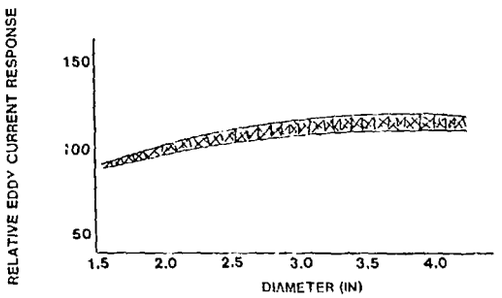

FIG. 2 EDDY CURRENT RESPONSE FOR HOLLOW CONE (REGION OF VARIATION RESULTING FROM ECCENTRICITY IN CARBURIZED CONE CASE DUE TO DISTORTION IN QUENCHING)

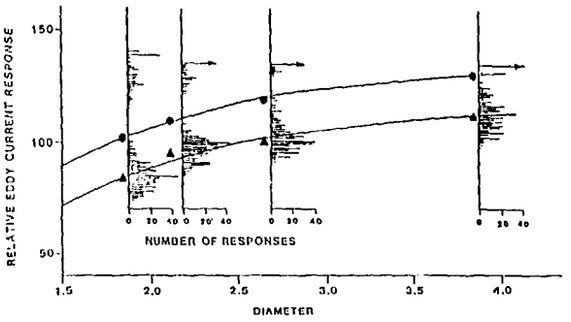

FIG. 5 SUPERIMPOSITION OF CURVES GENERATED FROM ALGORITHMS ON EDDY CURRENT DATA

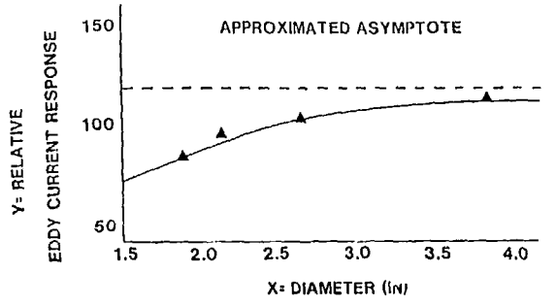

FIG. 3 PLOT OF ALGORITHM, $Y = 117 - 178.6 \exp(-.95729X)$, EMPIRICALLY DERIVED TO FIT $\bar{X}$ (▲)

FIG. 6

IDEALIZED ELLIPTICAL REPRESENTATION OF HYSTERESIS

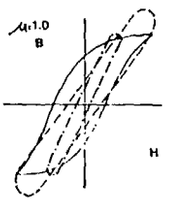

—— TYPICAL B/H CURVE

-·-·- IDEALIZED ELLIPTICAL B/H CURVE ASSUMING SINUSOIDAL FLUX DENSITY B

- - - - - IDEALIZED ELLIPTICAL B/H CURVE ASSUMING SINUSOIDAL MAGNETIZATION FORCE H

(SEE REFS. 1-4)

FIG. 7

COMPOSITIONAL AND MICROSTRUCTURAL EFFECTS IN CARBURIZATION

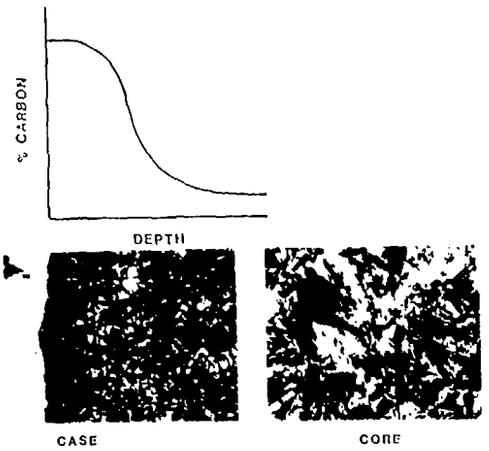

FIG. 10

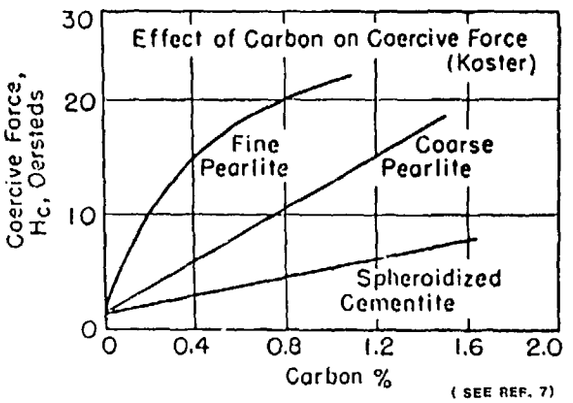

(SEE REF. 7)

FIG. 8

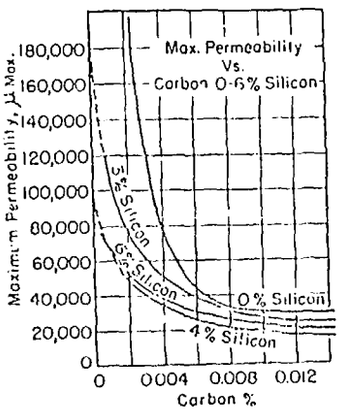

(SEE REF. 7)

FIG. 11

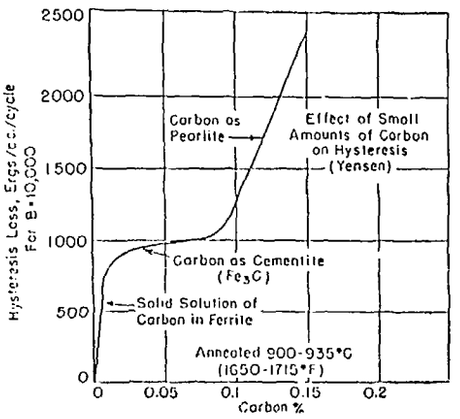

(SEE REF. 7)

FIG. 9

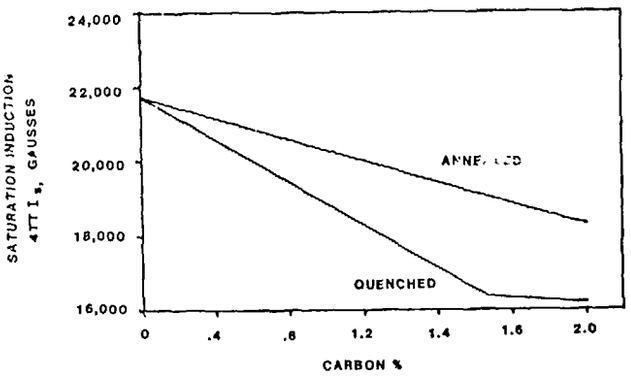

(see ref. 7)

FIG. 12

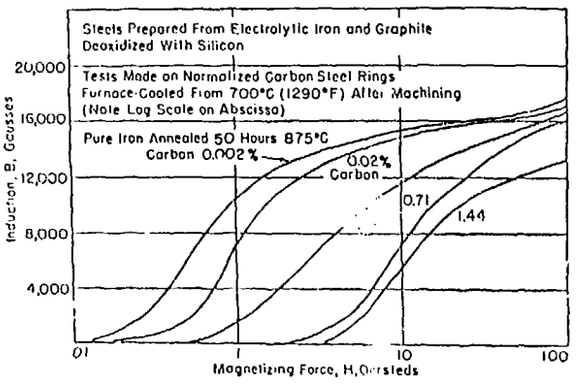

(SEE REF. 7)

FIG. 13

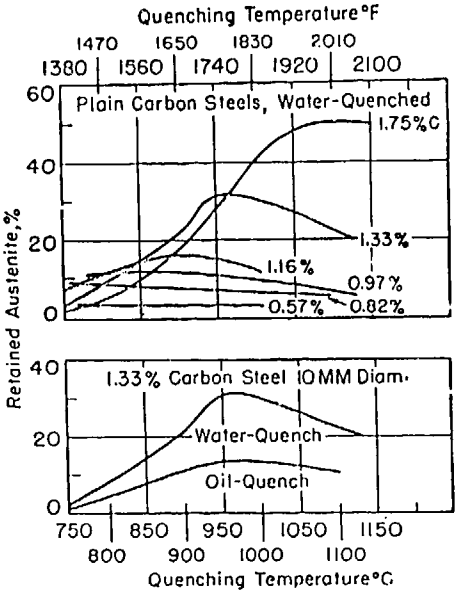

(SEE REF. 7)

FIG. 14

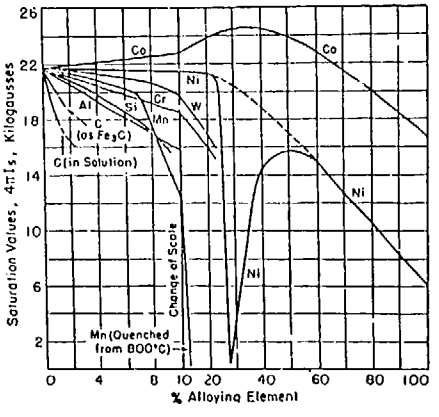

(SEE REF. 7)

FIG. 15

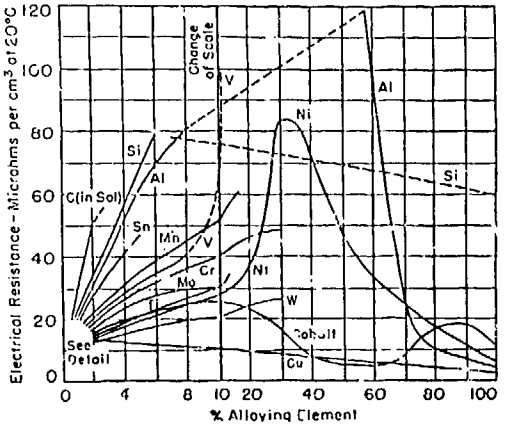

(SEE REF. 7)

FIG. 16

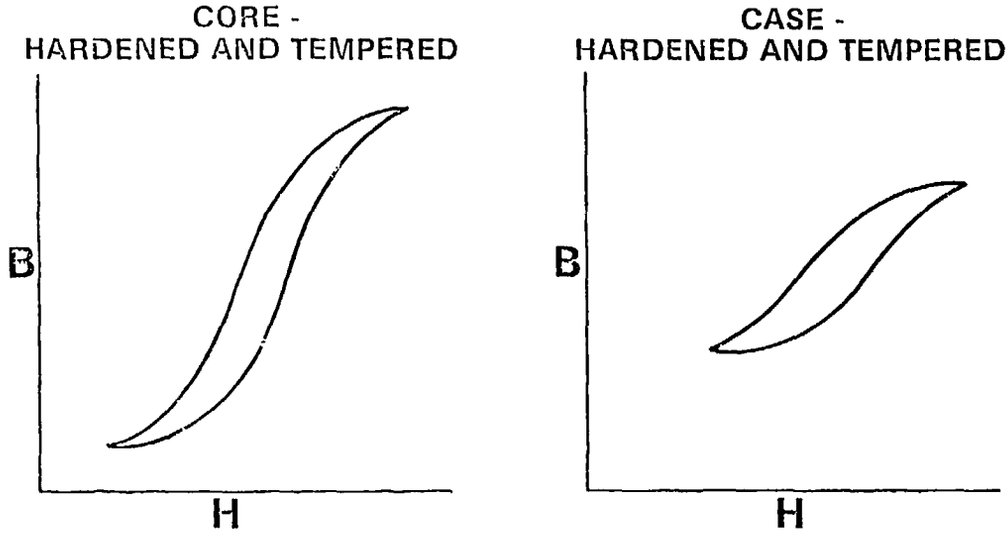
CORE -
HARDENED AND TEMPERED
B
H
CASE -
HARDENED AND TEMPERED
B
H

FIG. 17

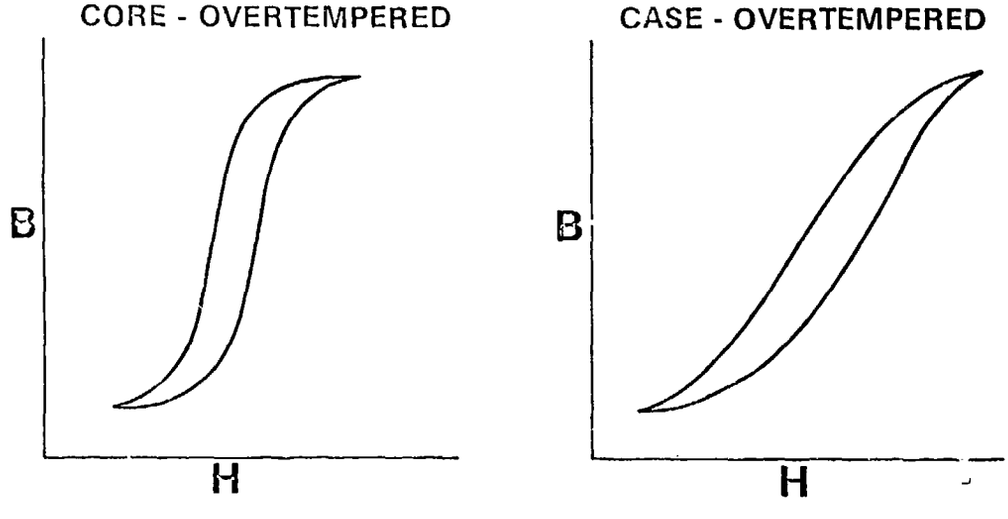
CORE - OVERTEMPERED
B
H
CASE - OVERTEMPERED
B
H

USING CAPACITIVE PROBES IN ELECTROMAGNETIC NONDESTRUCTIVE TESTING

B. A. Auld and M. Riaziat
Edward L. Ginzton Laboratory
Stanford University
Stanford, California 94305

ABSTRACT

In an attempt to expand the scope of electromagnetic testing to include poorly conducting materials, we have tried using a low frequency capacitive probe. This probe has given promising performances in testing materials with resistivities of several hundred ohm-centimeters.

INTRODUCTION

Eddy current flaw detection methods used mainly for the inspection of metal products can be extended to cover materials with poor conductivities. For such materials, however, induced electric "currents" are not well defined, and a more general picture should be used. We define the general flaw detection problem as the detection of an inhomogeneity in a single terminal (or multiterminal) microwave junction.

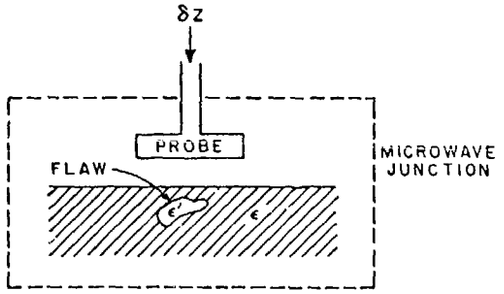

Fig. 1 Microwave junction representation of nondestructive testing.

Looking into the junction, the presence of the inhomogeneity causes an impedance change δZ which can be calculated in terms of the electromagnetic fields (E,H) and material characteristics (ϵ,μ). For nonmagnetic materials and small flaw dimensions it takes the simple form

$$\delta Z = i\omega V_f g(\epsilon,\epsilon')(E^2/I^2) \qquad (1)$$

Here, ϵ and ϵ' are complex permittivities of the host material and the flaw (Ref. 1). V_f is the volume of the flaw, ω is the frequency, and I is the current through the terminal. The function $g(\epsilon,\epsilon')$ is determined by the shape and nature of the flaw. For small spherical inclusions it is given by: $[3\epsilon(\epsilon' - \epsilon)]/\epsilon' + 2\epsilon$, where $\epsilon = \epsilon_0 + (\sigma)/i\omega$ and σ is the conductivity.

Obviously, the ratio E/I plays a crucial role in the sensitivity of our detection system. It can be shown that, in many cases, a capacitive probe will achieve more easily higher ratios of E/I than the conventional inductive coil probes.

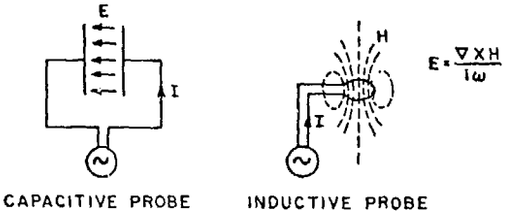

Fig. 2 Electric fields created by capacitive and inductive probes.

For the capacitive probe $E \cong I/i\omega Cd$ or $(E/I) = 1/i\omega Cd$, where C is the capacitance of the probe. For the inductive probe $E \cong V/2\pi R = (i\omega LI)/2\pi R$ or $(E/I) \cong (i\omega L)/2\pi R$, where L is the inductance of the coil. Noting that $C \propto \epsilon(A/d)$, and $L/N \propto \mu RN$,

$$(E/I) \propto 1/i\omega\epsilon A \quad \text{and} \quad (E/I) \propto i\omega\mu N \qquad (2)$$

We conclude that for low frequency flaw detection $(\omega\epsilon A < 1)$ we get higher sensitivities with capacitive probes.

THE DESIGN OF THE PROBE

To detect the changes in the impedance of a probe we make use of a four-arm bridge circuit. The sensitivity of a bridge is proportional to $\delta Z/Z$. We found that δZ is proportional to ω, and $(E/I)^2$. For a capacitive probe $I = i\omega CV$ and $Z = I/i\omega C$. Therefore

$$(\delta Z/Z) \propto \frac{1}{C}(E/V)^2 \qquad (3)$$

This gives us the criteria for the design of our probe: (i) the capacitance of the probe should be as low as possible, and (ii) the ratio of E/V should be as high as possible. Here, V is the voltage applied to the probe. A capacitive probe was designed and built with the geometry shown in Fig. 3.

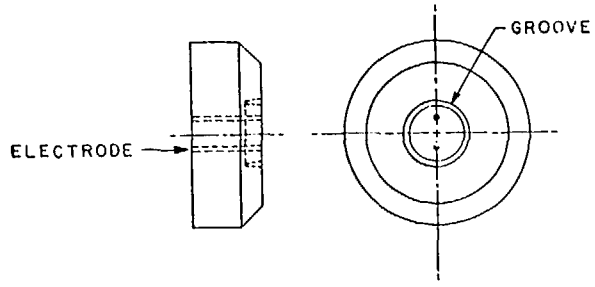

Fig. 3 The geometry of the probe.

We have used a differential probe to minimize lift-off effects. A four-arm bridge (dotted lines) is driven at a frequency of 1.0 MHz. When the impedance of one arm is changed, it gives an output proportional to that change, which is then amplified and detected.

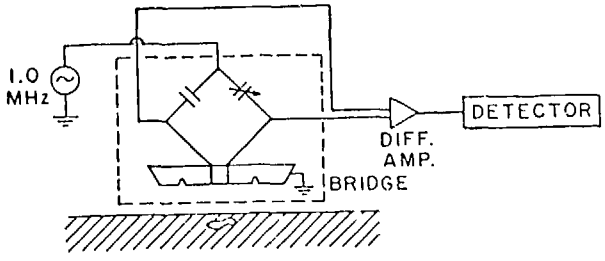

Fig. 4 The circuit diagram.

EXPERIMENTAL RESULTS

In the actual testing we keep the probe fixed and scan the test sample over it. The following graph (Fig. 5) shows the signals obtained from two surface indentations (hemispheres of diameters 250 and 125 microns) in a hot pressed silicon nitride sample ($\rho \cong 700\ \Omega$ cm , $\epsilon \cong 9$ at 1.0 MHz).

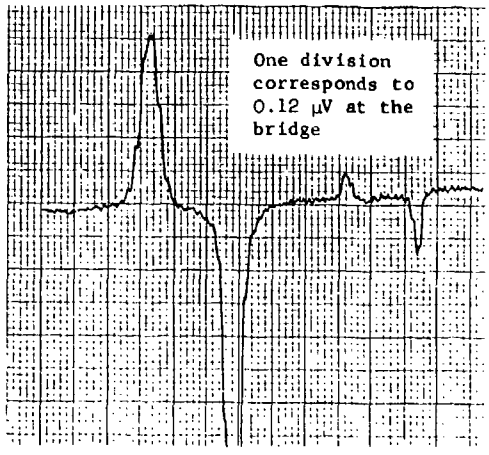

Fig. 5 Signals obtained from indentations in silicon nitride.

PHASE INFORMATION

To be able to predict the phase angle of the signals we pick up, we represent our capacitive probe with the linear circuit model shown in Fig. 6. Here, we represent the material by the combination of R and C(x) and lift-off by C(ℓ) . A flaw in the material modifies the value of C , and to a lesser degree that of R (for dielectrics). We immediately see that for good dielectrics ($R \to \infty$), lift-off and flaw signals will have the same phase. To show the general behavior we have plotted the admittance of the probe in the complex plane and varied the values of R , C(x) , and C(ℓ) from zero to infinity. Note that for high values of R, the phase difference between flaw and lift-off signals become less distinct.

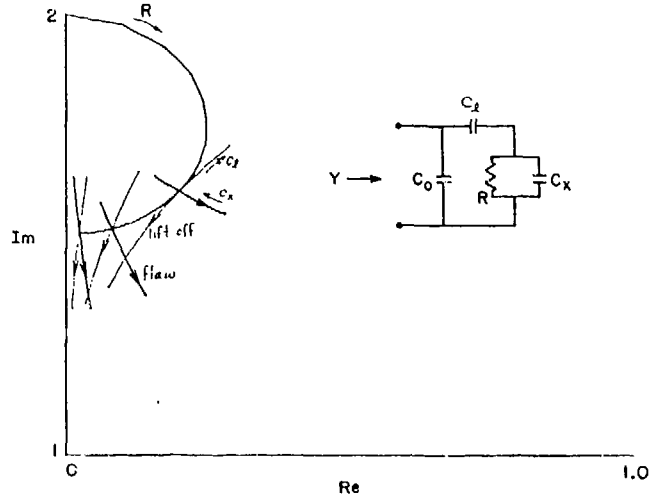

Fig. 6 Phase information from a capacitive probe.

There are similarities between this linear circuit and the one conventionally used for inductive coil probes (Fig. 7). The impedance of this circuit has been plotted in the complex plane for R varying from zero to infinity (Ref. 2). Here, the flaw is represented by a change in R , and the lift-off by a change in the transformer coupling. Signals from the flaw and the lift-off do not have an appreciable phase difference for high-resistivity materials. It should be pointed out also that there is a rapid loss of sensitivity with increasing values of R .

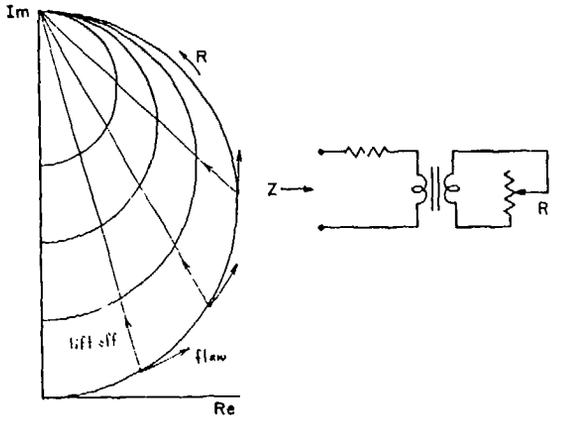

Fig. 7 Phase information from an inductive probe.

APPLICATIONS

Expanding the scope of electromagnetic testing to materials with high resistivities has many potential applications of which we mention a few:

(1) The testing of ceramic structural materials such as silicon carbide and silicon nitride which are used in the aircraft industry.

(2) Monitoring the production of high-resistivity materials when the resistivity is to be kept uniform (electric heating strips).

(3) Testing solid electrolytes such as beta alumina used in electric batteries where the small cracks propagate rapidly under the effect of high currents.

(4) Possibly being able to monitor the production of optical fibers, lens coatings, etc.

REFERENCES

1. B. A. Auld, "Theory of Ferromagnetic Resonance Probes for Surface Cracks in Metals," G.L. Report 2839, Edward L. Ginzton Laboratory, Stanford University, Stanford, California (July 1978).

2. H. L. Libby, Introduction to Electromagnetic Nondestructive Test Methods (John Wiley and Sons, Inc., 1971).

ADVANCED ULTRASONIC NDE EQUIPMENT

A. S. Birks, G. J. Posakony
Battelle Northwest Laboratories
Richland, Washington 99352

ABSTRACT

Procurement specifications for advanced ultrasonic equipment are being established as part of an Air Force Manufacturing Technology Division program to improve the reliability of nondestructive examinations*. A breadboard model of the advanced equipment concepts has been fabricated to demonstrate improvements.

Battelle Northwest Laboratories has established a preliminary specification for the advanced NDE equipment and is current procuring prototype models built by two different manufacturers to this specification. Demonstrations of improvements will be conducted at selected field locations. A procurement specification will be subsequently established and 12 pre-production models of the advanced equipment will be procured to further validate the specification.

The breadboard model demonstrates the concepts and improvements currently incorporated in the equipment. Features include accurate manual and automatic microprocessor adjustments of instrument settings as well as improved circuit and transducer performance.

For further information contact A. S. Birks, Project Manager, Battelle Northwest Laboratories (509) 375-2372 or R. R. Rowand, Program Manager, Air Force Materials Laboratories, Dayton, Ohio (513) 255-5407

*This work is sponsored by the Manufacturing Technology Division of the Air Force Wright Aeronautical Laboratories under Contract No. F33615-78-C-5032.

IN-FLIGHT FATIGUE CRACK MONITORING USING ACOUSTIC EMISSION[a]

P.H. Hutton and J.R. Skorpik
Battelle, Pacific Northwest Laboratory
Richland, Washington 99352

ABSTRACT

The purpose of this effort is to evaluate the use of acoustic emission (AE) methods to detect fatigue crack growth in aircraft structure during operation. A unique AE monitor system installed on an Australian Air Force Macchi 326 aircraft has detected AE which correlates with slow crack growth during operation over the past year and a half.

INTRODUCTION

Much of the application development work on acoustic emission (AE) over the past ten years has been directed toward large, stationary structures such as nuclear reactor systems. There has been relatively limited work concerning application to aircraft.

The program discussed here was initiated in September, 1977. The purpose was to evaluate application of an AE system to monitor fatigue crack growth in the wing structure of a Royal Australian Air Force (RAAF) Macchi MB 326 jet trainer plane.

The wing structure is presently inspected by ultrasonic and magnetic rubber methods. Both methods require some disassembly of the aircraft for application.

DISCUSSION

The Macchi 326 aircraft, shown in Fig. 1, is used by the RAAF as a trainer plane. Fatigue

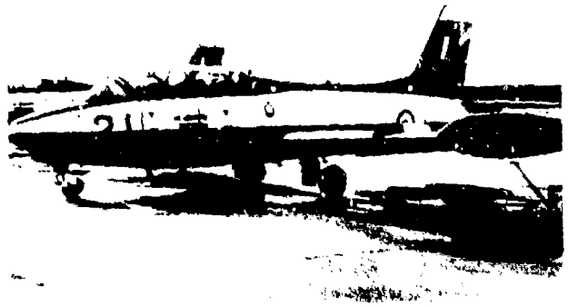

Fig. 1 RAAF Macchi 326 two place jet trainer.

cracks develop in fastener holes in the tension member of the center section of the wing structure (Fig. 2). The material is 4340 steel. The two holes marked "3" and "20" in Fig. 2 are the primary offenders.

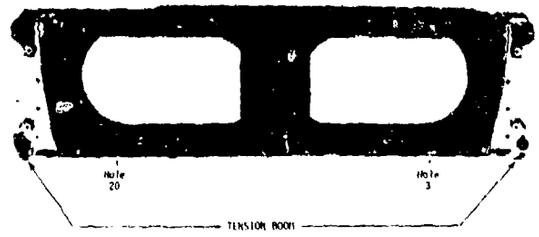

Fig. 2 Wing center section - Macchi 326 aircraft.

Acoustic emission (AE) offers the potential for continuous monitoring of these fatigue cracks to indicate crack growth. The effort discussed in this report is an AE qualification experiment to determine: (a) if meaningful AE data from fatigue crack growth in the fastener holes can be measured during in-flight environment, and (b) if the resulting data can be correlated with crack growth rate or amount of crack growth.

MONITOR SYSTEM DEVELOPMENT

Preliminary system requirements were established through discussion with the Australian Aeronautical Research Laboratory staff, RAAF personnel, and U.S. researchers active in aircraft monitoring programs.

The onboard AE monitoring system developed is shown in Fig. 3. Three functional components installed on the aircraft are: (1) sensors, (2) preamplifiers, and (3) monitor unit. The fourth major piece of hardware is the memory readout unit which is separate from the monitor system mounted on the aircraft. The readout unit has recently been upgraded to a cassette recorder (Fig. 4) for easier input to a computer.

AE data screened by a spatial filter is recorded on a time basis in a nonvolatile solid state digital memory. At the conclusion of a test flight, the memory is removed for interrogation in a separate instrument. After interrogation, the memory is

[a]Work supported by the U.S. Defense Advanced Research Projects Agency and the Australian Department of Defense Aeronautical Research Laboratory.

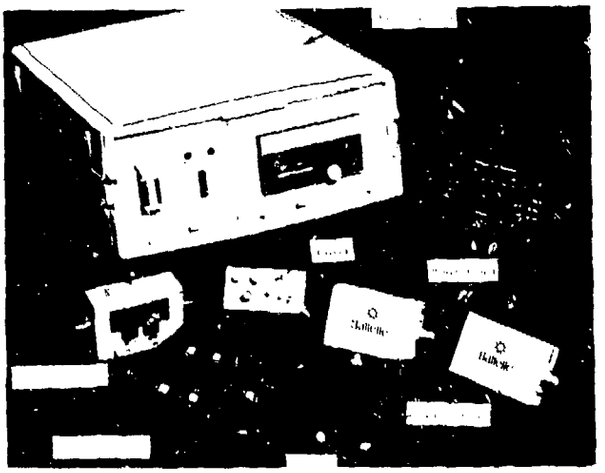

Fig. 3 AE monitor system for Macchi aircraft.

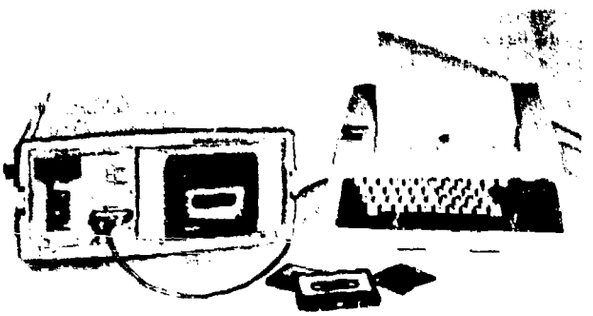

Fig. 4 Cassette memory readout system.

erased and reused. These memories have a large data capacity (more than 66 million counts) and are ideal for continuous monitoring applications.

The system was installed in August, 1978, on a Macchi aircraft at Pearce RAAF Base near Perth, Australia. Inspection during maintenance overhaul established that it had developed fatigue cracking in hole No. 20 in the tension member of the wing structure center section. Figure 5 shows the installed location of the AE sensors on the tension member and the spatial filter accept zone. Pre-amplifiers were mounted on an existing tray in the bottom of the fuselage near the tension member. The AE monitor unit is located in the front cockpit in a console immediately to the right of the pilot's seat (see Fig. 6).

RESULTS

Analysis of AE data relative to growth of the fatigue crack is expected to continue for probably another year. By mutual agreement, the data analysis is being performed by the Australian

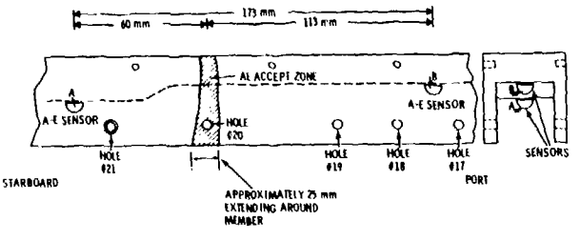

Fig. 5 AE sensor installation - wing center section - tension member.

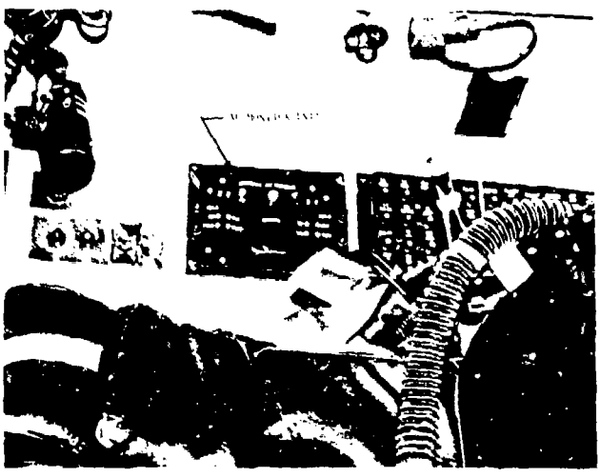

Fig 6 AE monitor unit installed in Macchi aircraft.

Aeronautical Research Laboratory. Results from analysis of data over the past year and a half are highlighted in Fig. 7 and Fig. 8.

FLT. REGIME	VALID AE	TOTAL AE	
	AVERAGE COUNTS/ HR	RANGE OF COUNTS/ ADDRESS	REMARKS
FORMATION	4	0-60	MAINLY 0
CIRCS AND LANDING	8	0-90	SOME 0 GENERALLY<30
AEROBATICS	14	0-200	LOW WITH HIGH BURSTS
LOW FLYING	163	5-250	CONTINUOUSLY HIGH >40

DATA FROM G. MARTIN, AERO RES. LABS MELBOURNE, AUSTRALIA.

Fig. 7 AE versus flight regime - Macchi 326 wing box.

Figure 7 shows that most of the valid AE is generated during low level flying. This is possibly due to increased wing flexure as a result of greater air turbulence. By contrast, high "g" sustained load maneuvers produce relatively little AE. This suggests that the most effective mode for applying AE to detect subcritical fatigue crack growth is continuous monitoring during flight. A proof load approach analagous to the in-flight high "g" sustained load condition may produce little, if any, AE from a subcritical crack.

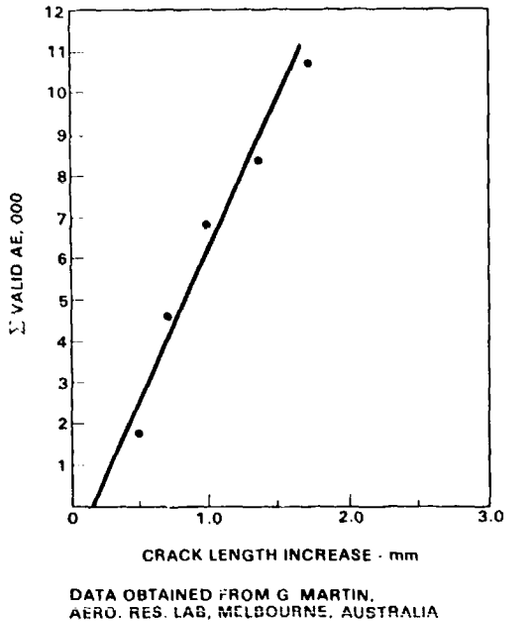

Fig. 8 AE versus crack growth - Macchi 326 aircraft wing box.

Correlation between measured crack growth and valid AE is given in Fig. 8. These results provide very encouraging evidence that the valid AE recorded is directly related to growth of the fatigue crack.

As a further test of the data recorded from the crack area, the accept zone for valid data was shifted to a similar area without any fastener holes. This was done by simply changing the acceptable Δ-time limits. No physical repositioning was involved. Out of 28 flights with a variety of flight regimes monitored in this manner, the valid count was 6--all from the first flight. The remaining 27 flights produced no valid count. The total count (all signals detected regardless of source) remained similar to previous monitoring.

CONCLUSIONS

Conclusions we draw from program results to date are:

1. A compact monitor system can be made to function over an extended period (> one year) under in-flight environmental extremes of temperature, pressure, "g" forces and transient noise signals.
2. AE shows a direct relationship to slow crack growth in the circumstances of this test.
3. Analysis of AE results relative to sustained load versus varying load flight conditions suggests that continuous in-flight AE monitoring would be more effective than proof load monitoring in detecting subcritical cracks. Active subcritical fatigue cracks may not produce AE under sustained load or proof load conditions.
4. The program results justify optimism as to the feasibility of detecting fatigue crack growth in aircraft structure during flight. However, a more positive method of identifying crack growth AE in the presence of noise signals generated near the crack such as fastener fretting is necessary for reliable general application of the capabilities demonstrated. This need is being addressed in a new effort focusing on pattern recognition techniques for signal identification.

ACKNOWLEDGMENTS

The authors wish to recognize the outstanding cooperation, assistance and hospitality provided by Australian ARL and RAAF personnel in the course of this work. Foremost among these are Ian Scott and Gary Martin of ARL and Wing Commander C.E. Bradford and Flight Lieutenant I. Anderson of the RAAF. Base Commander J.W. Hubble, RAAF, graciously extended the use of Pearch Air Base facilities to us during system installation and testing. Also, we wish to credit John Rodgers (at the time, Captain at McClellan Air Force Base, USAF), C.D. Bailey, Lockheed Georgia Co., A.T. Green, Acoustic Emission Technology and S.L. McBride, Royal Military College, Canada, for freely discussing results of their work in AE monitoring aircraft. These discussions were beneficial to this program.

THE ANALYTIC SIGNAL MAGNITUDE FOR IMPROVED ULTRASONIC SIGNATURES

Paul M. Gammell
Jet Propulsion Laboratory
California Institute of Technology
Pasadena, California 91103

ABSTRACT

Conventional pulse-echo ultrasonic receivers rectify the received signal. Because the signature of the reflecting interfaces is modulated by the predominant ultrasonic frequency, interpretation of this signal in terms of the structure of the reflecting interfaces is difficult. Smoothing, as by an R-C filter, ameliorates this effect, giving a less confusing display at the expense of resolution.

The magnitude of the analytic signal, on the other hand, represents the shape of the energy packets arriving from the reflecting interfaces. Since this signature is free of modulation effects, interpretation of the signal in terms of the reflecting interfaces is more straightforward. Furthermore, smoothing is not normally needed.

The analytic signal magnitude can be obtained by several means. The implementation used in this study is particularly suited for digital data processing. The Hilbert Transform of the received signal (the "real part") is obtained with the aid of the Fast Fourier Transform. This produces the quadrature component (the "imaginary part"). The magnitude is calculated from both these components.

In contrast to signal processing techniques involving deconvolution, this technique is surprisingly robust with respect to noise and quantization. Typical signatures obtained with this technique are demonstrated.

INTRODUCTION

The ultrasonic A-mode signal provides the starting point for most ultrasonic systems. Although the A-mode signal is often not displayed, its characteristics, which are affected by the transducer, pulser, and receiver, nevertheless limit the quality of the final display.

Most commercial pulse-echo systems use full-wave rectification as part of the signal processing chain. Since there are only a few peaks in a single reflected pulse, the envelope is poorly defined. It is customary to smooth the signal by an R-C filter. This improves interpretability at the expense of resolution of closely spaced interfaces.

THE ANALYTIC SIGNAL

The analytic signal, which was defined by Gabor in 1947 (1) provides an alternative to rectification. Its magnitude has been shown to be related to the rate of arrival of the energy density (2). The significance of the time-energy concept was the topic of several papers at one of the sessions of the Fall 1980 Acoustical Society of America Meeting (3).

For a more extensive discussion of the analytic signal magnitude and its relations to ultrasonics, the reader is urged to refer to a recent journal paper by the author (4). Basically, the analytic signal is a complex signal whose quadrature components are related by the Hilbert Transform. Generally, the real quadrature component is taken to be the conventional signal, as would be observed on an oscilloscope. (Actually, the conventional signal may be any linear combination of the quadrature components.) One way in which the Hilbert Transform of any function can be obtained is to interchange the sine and cosine terms in the Fourier expansion, replacing cos ωt by sin ωt and sin ωt by -cos ωt (5).

EXPERIMENTAL VERIFICATION

Data were taken to compare this processing scheme with conventional rectification and filtering. A digital data acquisition system was used which digitized the unprocessed (raw r-f) ultrasonic signal. For comparison of the effect of the signal processing schemes, the same digital record that was used for analytic signal magnitude processing was also digitally rectified and smoothed.

The amplified echo was digitized using a Biomation 8100 transient recorder. This instrument was interfaced with a Digital Equipment Corporation LSI-11 microprocessor, which stored the data on diskettes and performed all of the later processing. The plots were produced using the graphics mode of the Diablo Hytype 1641 terminal. All programming was done in LABFORTH (6), which is an RT-11 resident version of FORTH (7,8). This language was chosen because assembly language routines can be written directly in the main program and because it offers the flexibility and immediate accessibility of an interpreter.

The A-scans were produced using a commercial pulser and receiver. The target consisted of a sheet of acrylic plastic, at a range of approximately 10 cm, which was carefully aligned to obtain the maximum specular echo. Because this experiment was concerned with biological applications, a 1 cm section of formalin-fixed hog liver was placed between the transducer and the target to simulate the general type of signal distortion

(attentuation, refraction, and scattering) that is encountered when imaging through biological and other non-uniform media.

The data were digitized to 8-bit resolution at 10 ns intervals for records of 2048 points. A 2048 point real-valued FFT algorithm was used to compute the quadrature component by a Fourier Transform technique. The details of these calculations are explained elsewhere (4).

The results of three types of detection (rectification alone, rectification with smoothing, and computation of the analytic signal amplitude) are compared in Fig. 1, which shows the overlapping echoes from the front and back faces of the lucite. The echoes from the tissue, which would be far to the left of these traces, are not shown. Similar results were obtained when only water was in the path between the transducer and reflector. The results with tissue in the path are shown as they represent a more realistic case which includes distortions induced by the propagation media.

The absolute value of the received signal, which would be the result of the full-wave rectification with little or no smoothing, is shown in Fig. 1a. It is difficult to identify the precise location of the interfaces on this A-mode presentation.

Figure 1b is the result of applying an R-C filter, simulated by digital processing, to Fig. 1a. A time constant of 0.64 μs was used with a transducer center frequency of 2.25 MHz. This choice of a time constant produces a smoothing that represents a typical compromise: it is not quite enough smoothing to give a smooth rising edge to the signal, although it is high enough to produce a long trailing edge, which sacrifices resolution. A longer or shorter time constant would result in improvement of one of these aspects but degradation of the other. Note, incidentally, that smoothing delays the peak by approximately one-half cycle, as compared to Fig. 1a.

The analytic magnitude of the same signal, as shown in Fig. 1c, gives an A-scan that is easier to read than the rectified signal and has better resolution than the rectified and smoothed signal. This signal is much smoother than the signal that is only rectified and yet its peak occurs at approximately the same epoch. The analytic signal magnitude is expected to be the best measure of the time at which the peak occurs. Clearly, the two interfaces are most readily resolved by the analytic signal magnitude.

To answer the question of the suitability of this technique for the complicated echoes, such as arise in biological samples, the echoes from a section of excised injured cat spinal cord were studied. Figure 2 shows the digitized A-mode signal and the calculated analytic signal magnitude of such a specimen. The strong specular echoes are clearly resolved and the fine internal echoes can be seen. Since the processing scheme works for this biological system, it would also be expected to work well with the fine echoes from grain boundaries and other distributed reflections.

CONCLUSIONS

This study clearly demonstrates that the analytic signal magnitude provides better resolution than does either rectification alone or rectification with smoothing. In these experiments, the analytic signal magnitude was calculated by computer processing of sampled data, which demonstrates the utility of the method. Although digital implementation of such processing is currently prohibitively expensive, in a few years, production of a commercial clinical or industrial instrument incorporating this technique may well become commercially viable. Alternative implementations, using analog circuits, have produced equally good results.

The analytic signal magnitude has been successfully used in our laboratory for the production of images of biological specimens that include the soft internal echoes. This technique is expected to be particularly useful in those nondestructive evaluation applications where closely spaced echoes are to be resolved and where signature analysis is to be performed. The signature analysis would be aided by the fact that this signal represents the rate-of-arrival of energy from the specimen and is not affected by the phase characteristics of the transducer.

ACKNOWLEDGEMENTS

The work described in this paper was carried out at the Jet Propulsion Laboratory, California Institute of Technology, jointly sponsored by the National Aeronautics and Space Administration under Contract NAS7-100, and by the National Institutes of Health, Biomedical Research Support Grant Program Division of Research Resources, under BRSG Grant RR07003, through an agreement with the National Aeronautics and Space Administration. The analysis programs and the microprocessor used in this work were originally funded by the NASA Office of Life Sciences. The author is grateful to Richard C. Heyser for his enlightening discussions on the significance of the analytic signal. Thanks are also extended to our medical collaborators at the Georgetown University Medical Center, Washington, D. C., namely C. Kao, M.D. and D. Rigamonti, Ph.D., for the use of the section of injured cat spinal cord which is shown in the last illustration. That scan was taken as part of a NASA Office of Technology Utilization Task.

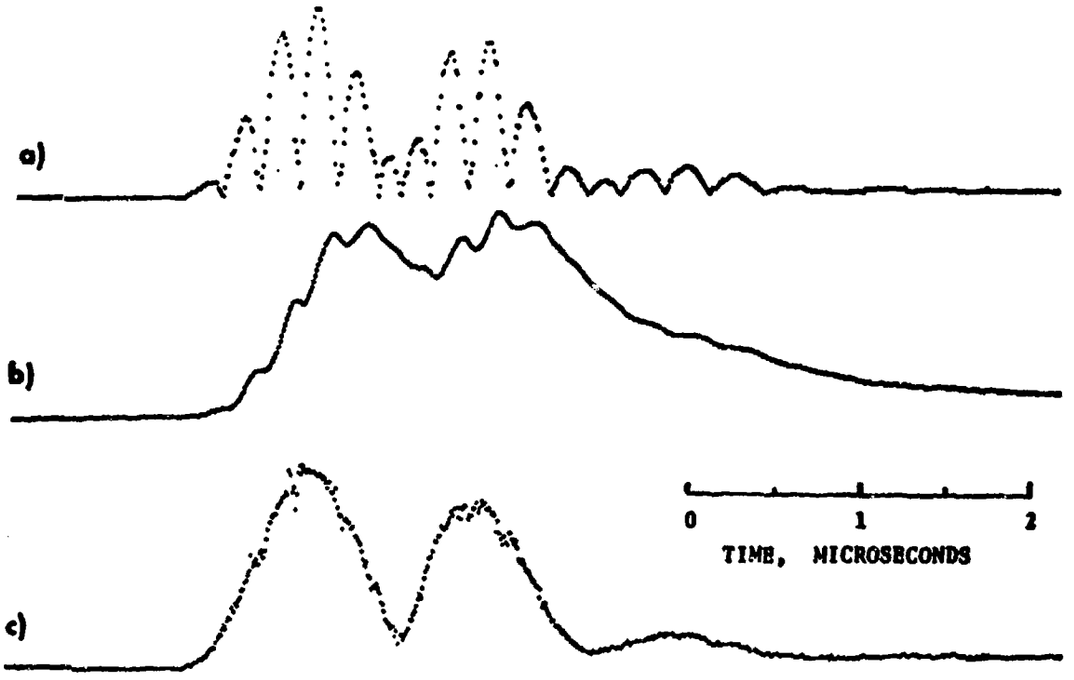

Fig. 1. Processed signatures of a signal from two closely spaced interfaces.

a) rectified

b) smoothed

c) magnitude of the analytic signal

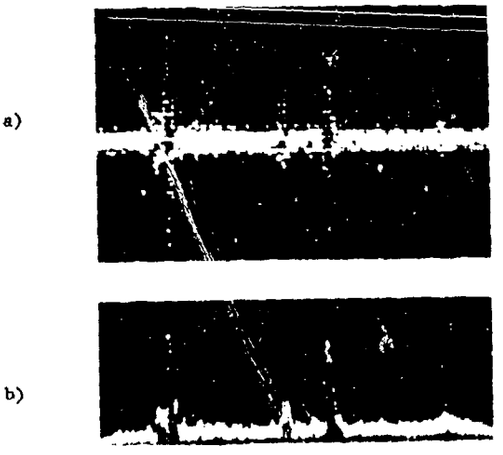

Fig. 2. Ultrasonic pulse-echo signal from an injured section of cat spinal cord.

a) unprocessed signal as digitized

b) result of analytic magnitude processing

The scans are aligned as to timebase.

REFERENCES

(1) Gabor, D., Theory of Communication, J. of the Institute of Electrical Engineers (London), 93 (1946) 429-457.

(2) Heyser, R. C., Determination of Loudspeaker Signal Arrival Times: Part III, J. Audio Eng. Soc., 19 (1971) 902-905.

(3) Heyser, R. C., Chairman, Session X, Architectural Acoustics III: New Discoveries of Time Delay Spectrometry and its Applications to Acoustical Measurements, 100th meeting of the Acoustical Society of America, Los Angeles, California, 17-21 November 1980, J. Acoust. Soc. Am. Suppl. 1, Vol. 68, Fall 1980, (ISSN: 0163 0962), pp. S41-S42.

(4) Gammell, P. M., Improved Ultrasonic Detection Using the Analytic Signal Magnitude, Ultrasonics, 19 (March, 1981), pp. 73-76.

(5) Blake, W. K. and Waterhouse, R. V., The Use of Cross-Spectral Density Measurements in Partially Reverberent Sound Fields, J. of Sound and Vibration, 54 (1977) 589-599.

(6) Laboratory Software Systems, Inc., 3634 Mandeville Canyon Rd., Los Angeles, CA 90049.

(7) Ewing, M. S., The Caltech Forth Manual, Second Edition, Owens Valley Radio Observatory, California Institute of Technology, Pasadena, California 91125 (1978).

(8) Moore, C. H., Forth: A New Way to Program a Mini-computer, Astronomy and Astrophysics Supplement, 15 (1974) 497-511.

FATIGUE CRACK DETECTION AND SIZING IN WELDED STEEL STRUCTURES

I. M. Kilpatrick and J. Cargil
Admiralty Marine Technology Establishment
(Structures)
St. Leonard's Hill
Dunfermline Fife KY11 5PW

ABSTRACT

The paper gives an outline of the non-destructive evaluation (NDE) methods currently being pursued at the Admiralty Marine Technology Establishment, Dunfermline, Scotland.

The methods are being used to locate and characterise fatigue cracks in high yield strength welded steel structures.

The techniques have been applied principally to large fatigue models (5' and 9' diameter) as part of a comprehensive fatigue programme, with back-up work on large T-butt welded "type test" specimens.

Results are presented which illustrate the progress made with each technique in detecting and sizing fatigue cracks in welded structures. An indication of the accuracy and reproducibility is given with particular reference to ultrasonic diffraction and ACPD techniques.

INTRODUCTION

The development of welding, the use of high strength steels, the tendency to increased loading and the need to resist marine environments in naval structures has focussed attention on the significance of defects and their possible extension under cyclic loading.

With the increasing use of fracture mechanics to assess defect tolerance, characterisation of defects, specifically planar defects, by non-destructive evaluation (NDE) has become an integral part of any fracture control plan. Without a knowledge of crack dimensions present in a structure fracture mechanics analyses become of limited value.

The authors are involved in a comprehensive fatigue testing programme incorporating large welded high yield (HY) steel models and intermediate scale "type" tests. NDE forms an important part of this programme. It is aimed at crack detection and sizing with a view to obtaining information on fatigue crack initiation and propagation under appropriate loading conditions.

In this context, the paper outlines NDE methods currently being used (or under consideration) at AMTE Dunfermline, Scotland to characterise surface breaking fatigue cracks in welded HY steel structures. An indication of the types of structure involved is given, the techniques employed described, and results presented to illustrate performance of some of these techniques.

STRUCTURES

Two series of model structures are being investigated.

1. Cylindrical models of about 4 1/2 ft diameter which may be of ring stiffened/unstiffened hourglass or plane stiffened cylinder design.

2. Plane cylinder models of about 9 ft. diameter with multiple ring stiffening.

Figure 1 shows the simplest of the small diameter models, a cylinder with a centrally located bulkhead. The bulkhead to shell joint is a full penetration T-butt weld. A typical small diameter framed hourglass model is illustrated in Fig. 2. The minor cylinders are joined to the major cylinders by 30° and 45° cones resulting in angled butt (knuckle) welds. Frames are attached to the minor cylinders again by full penetration T-butt welds.

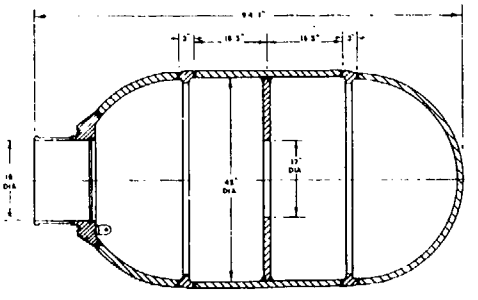

Fig. 1 Model No. S1, general arrangement.

A typical large diameter model is shown in Fig. 3. This contains a range of frame sizes plus a large bulkhead. All welds are full penetration T-butts. The large models weigh somewhere in the region of 40 tons.

All models have dome end closures with an access hatch at one end.

Tension residual stresses induced during welding at the T-butt welds result in a net tension cycle under the externally applied compressive test load. Fatigue cracking under test occurs at both knuckle and T-butt welds. No cracking is experienced at longitudinal or circumferential seam butt welds.

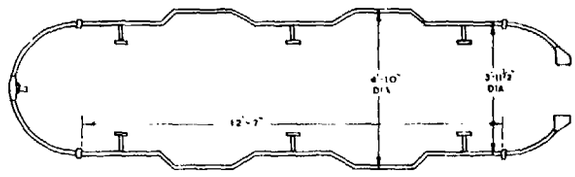

Fig. 2 Framed hourglass, Model - S2.

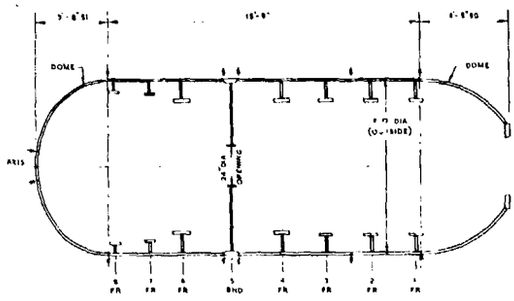

Fig. 3 Model L1.

The principal "type" test specimen used is shown in Fig. 4, i.e., a full penetration T-butt weld. Such a specimen is subjected to fatigue loading under three point bend, see Fig. 5, resulting in fatigue crack initiation at the weld toes and propagation through the plate thickness.

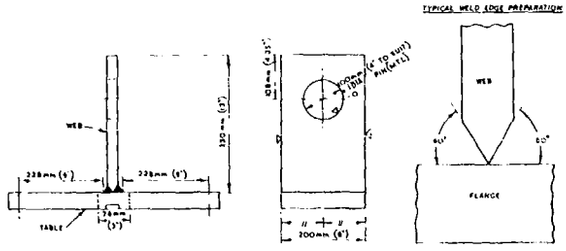

Fig. 4 AMTE - 3 point bend test piece

NDE TECHNIQUES

The techniques being actively employed in detection and sizing of surface breaking fatigue cracks are -

1. Amlec Eddy Current
2. Ultrasonic Diffraction
3. Alternating Current Potential Drop (ACPD)
4. Conventional Pulse-echo ultrasonics

Other techniques at an early stage of investigation include -

5. Acoustic Emission
6. Ultrasonic - mode conversion
7. Fully automated multi-probe ultrasonic scanning unit.

1. Amlec (Eddy Current)

Eddy currents (1) are induced by Amlec and other instruments which can detect the presence of cracks interrupting the eddy currents. This has become a principal method of surveillance.

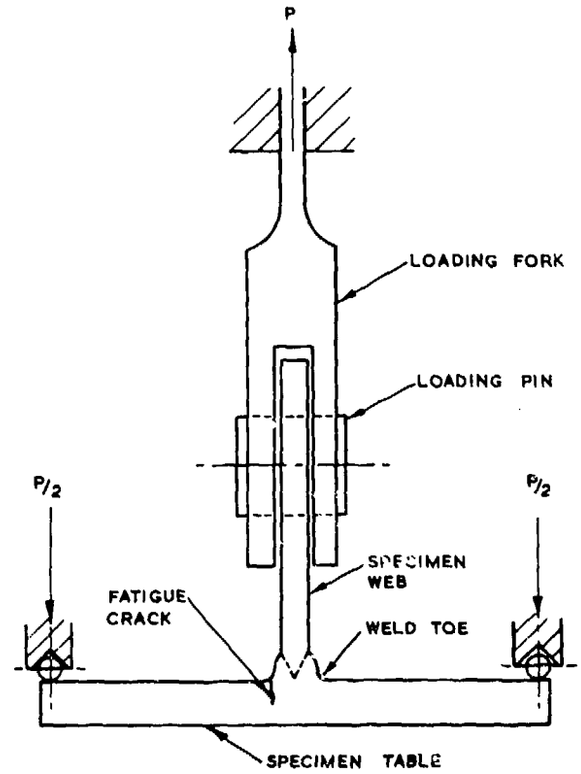

Fig. 5 Loading arrangement for fatigue cycling.

An alternating magnetic field is induced into the material at the position to be inspected and changes in the impedance caused by surface breaking defects can be detected. The instrument is designed to be relatively insensitive to probe position by applying a back-off voltage to the probe. Although changes in the geometry and material which occur at a weld can give rise to changes in Amlec readings, they are usually small enough to be neglected during crack detection.

At AMTE it is used principally as a surface crack detection technique. No reliable relationship between Amlec readings and crack depth are available at present. However, work is in hand to try and quantify results.

2. Ultrasonic Diffraction

This technique is being used at AMTE from both cracked and uncracked surfaces.

When a pulse of ultrasound is projected towards a crack the sound is diffracted (or scattered) at the crack tip. By placing transmitting and receiving transducers on either side of the crack (Fig. 6) and carefully measuring the flight time of such a pulse the crack depth can be calculated from the transducer spacing, velocity, and flight time (2), (3).

Measurement from the Cracked Surface (2) - The position of the crack tip as defined by the flight time lies along an elliptical path the foci of which is the transducer centers. The minimum flight time for a particular transducer spacing occurs when the crack tip is equidistant from each

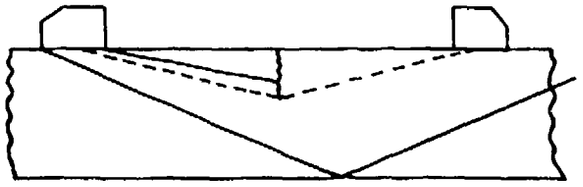

Fig. 6 Ultrasonic diffraction.

transducer. Similarly when the ultrasound is diffracted by two cracks such as may occur when both toes of a T-butt weld are cracked, Fig. 7, the minimum flight time occurs when the entry and exit angles of the ultrasound are the same.

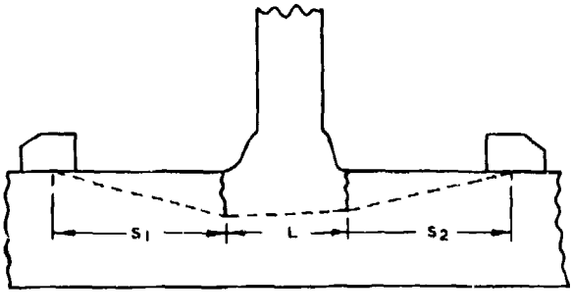

Fig. 7 Ultrasonic Diffraction

For,

$$VT = \sqrt{S_1^2 + d_1^2} + \sqrt{(d_1 - d_2)^2 + L^2} + \sqrt{d_2^2 + S_2^2}$$

Where, V = velocity of sound
T = flight time
S = distance from transducer to cracks on surface
L = distance between cracks
d_1 and d_2 = crack depths

Thus T min. occurs when -

$$\frac{S_1}{d_1} = \frac{S_2}{d_2}$$

Thus, by maintaining a constant transducer spacing and scanning transverse to the cracks to find the position for minimum flight time the depth of both cracks can be measured.

However, this method for both single and double cracks is least accurate for shallow cracks and as the flight time is rather insensitive to lateral movement the position for minimum flight time is difficult to locate in the double crack situation. It is necessary to measure flight times to within 5 nano-seconds in order to measure crack depths of around 5 mm with an accuracy of about 2 mm.

Measurements from the Uncracked Surface (4) - Most of the difficulties in the above method can be resolved by using the technique from the uncracked surface (Fig. 8) at the expense of increasing the amount of signal processing. When using the method from the cracked surface the first signal to reach the receiving transducer is that required

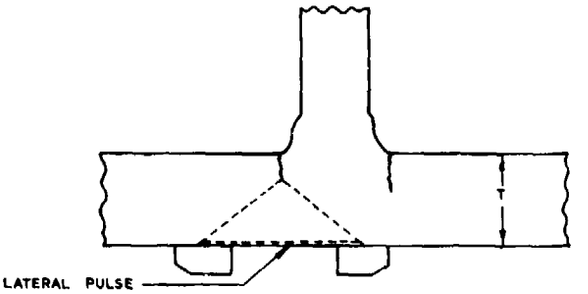

Fig. 8 Ultrasonic diffraction.

for crack depth measurement as the faster longitudinal waves are used and the ultrasound cannot pass through the crack. This is not so when using the method from the uncracked surface; thus it is necessary to carry out some signal processing to extract the required information from the background noise. Figures 9 and 10 are typical records from the diffraction equipment when used from the uncracked surface. The two lines at the top of the records are the lateral pulse which travels directly between the transducers near the plate surface (Fig. 8). The crack depth is given by

$$T\left(1 - \left(\frac{x}{BWE}\right)^{1/2}\right)$$

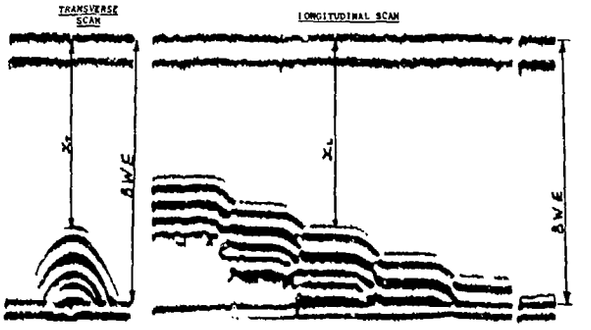

Fig. 9 Ultrasonic diffraction from uncracked surface.

where x is the distance from the lateral pulse to the signal from the crack tip; BWE is the distance from the lateral pulse to the back wall echo and T is the plate thickness. Figure 9 is from a plate with slots of increasing depth and shows a transverse scan where the transducers were scanned at right angles to the crack. Figure 10 is the record from a fatigue crack in a T-butt weld.

3. Alternating Current Potential Drop (ACPD) (5), (6), (7)

Until fairly recently the most widely used PD method for crack sizing was the direct current (DC) technique. This is adequate in small laboratory scale specimens where section sizes are small and consequently current requirements are small. However, its use in large structures is impractical since with the large section sizes involved the resistance is very low necessitating the use of heavy currents to provide a measurable field strength.

Fig. 10 Ultrasonic diffraction from the uncracked surface of a Tee butt weld.

By using alternating current (AC) the current is passed through only a thin surface layer ("skin effect"), and consequently the current necessary to produce a given field strength at the surface is much less than with DC.

ACPD is being used extensively at AMTE both on the large model structures and T-butt 'type' test pieces to size fatigue cracks and also to obtain a continuous reading of crack depth as it increases during a test (i.e., "on-line").

The technique relies on the change in resistance occurring when a crack is introduced into the structure. AC (constant current) is applied to the test area and the PD measured both across the crack and adjacent to it. In Fig. 11, the current path is seen to be restricted to the near surface layers. The PD between the output probes is a measure of the current path, so that the ratio of the PD in the presence of a crack to that in the absence of a crack will allow calculation of the crack length, Fig. 11.

4. Conventional Pulse-echo Ultrasonics

The performance of the pulse-echo technique with regard to sizing of fatigue cracks in T-butt welds is not good. However it is useful in the initial detection of cracks. At AMTE it is used in conjunction with Amlec for datum surveys.

The following techniques are at an early stage of evaluation -

5. Acoustic Emission (8), (9)

Acoustic Emission (AE) analysis is being used in the fatigue model structures to locate "active sites", i.e., as an initiation detection technique.

Trials using up to four transducers are underway in various fatigue models and it is hoped that useful information on defect location will be obtained during 1980/81.

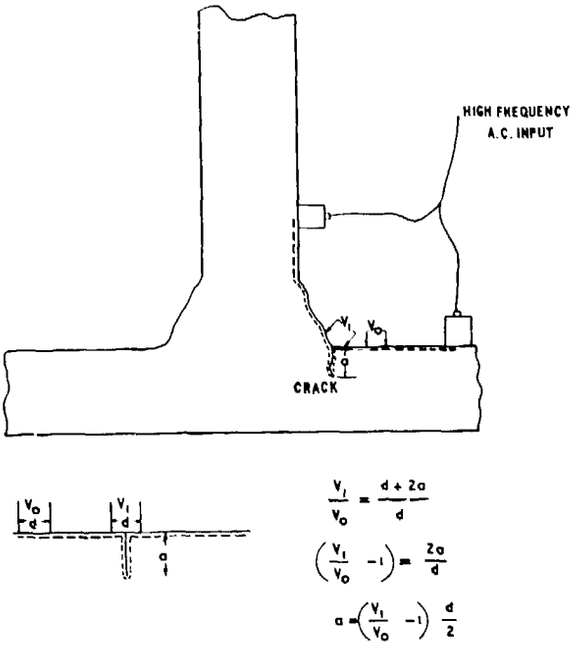

Fig. 11 Arrangement of probe & input points (not to scale).

6. Ultrasonic Mode Conversion Technique (10).

This appears to be a promising technique for fatigue crack sizing. The method was originally used to give depth measurements of thin machined slots (11) by directing compressional waves at the feature and measuring the generated Rayleigh waves, see Fig. 12. The basic technique is a two-probe method which uses the frequency content of mode-converted pulsed ultrasonic waves that are generated when a pulsed wave interacts with a target, for defect characterization. For a surface breaking crack the frequency content of the scattered signals has been found to be related by a $(1/f2)$ relationship to the crack depth (11).

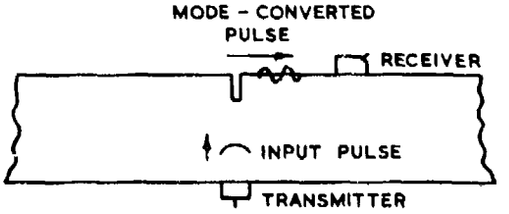

Fig. 12 Compressional - rayleigh, mode conversion technique.

The method has been successfully used to detect and provide the relative sizes of fatigue cracks in an AMTE "T butt" weld (12).

A further test was performed at Dunfermline in early 1980 on one of the AMTE hourglass fatigue models. The results showed that cracks could be detected in such 'real' structural units and that the received signals had structure (13). However,

the system used was a conventional NDT set and there was not sufficient calibration information to perform a complete sizing operation.

An investigation into the development and application of the technique to fatigue crack sizing in "T-butt" weldments is now the subject of an AMTE extramural contract (14).

7. Fully Automated Multi-probe Ultrasonic Scanning Unit

An industrial contract is currently underway to develop a computerised fully automatic ultrasonic multi-probe weld scanner to be used on AMTE fatigue models to locate defects, detect changes in depth, and record the results.

The system has the following specification -

Capability to identify cracks greater than 2 mm deep and to show changes in crack depth greater than 1 mm. The system will be capable of continuously examining one complete weld three metres in diameter.

The system is principally designed to examine T-butt welds in the large fatigue models but will also have the capability of examining longitudinal and circumferential butts.

The ultrasonic head, with two 45° shear wave and one compression wave probe, is held in contact with the outside of the model and scanned transversely across the weld while the model is rotated, thus describing a zig-zag path around the model. The two 45° shear wave probes will be used in the pitch and catch mode on either side of the weld to monitor plate thickness and coupling, while the 90° probe will be looking for lamellar defects. During the remainder of the scan each probe will be recording both flaws and weld profile independently. The output from the ultrasonic probes is stored on floppy discs which can be displayed on a VDU either during the scanning operation or later. The presentation on the VDU will be a "B" scan showing both weld profile and flaws. The system will also have the capability of displaying two such profiles from subsequent tests to look for changes. It will also be possible to compare the output from two floppy discs automatically and get a print-out of the position and amplitude of changes.

RESULTS

Comparative Performance of the Techniques on a Fatigue Model - The majority of the comparative work has been performed on Model S1 (Fig. 1). This model was fatigued to approximately 50,000 cycles until a through crack developed over part of the circumference. Fatigue cracks initiated at the forward and aft weld toes at the bulkhead to cylinder T-butt joint.

Part of the bulkhead to cylinder weld was removed and sectioned for optical measurement of actual crack depths to allow comparison with depth profile estimates made by the five techniques.

The results are shown in Fig. 13a to d. For clarity of presentation only the forward toe crack is considered.

Figure 13 shows the actual crack depth profile over stations 305° to 320°. It may be seen from this figure that the maximum crack depth is about 18 mm.

Figure 13a illustrates the Amlec (eddy current) profile. This of course is, as stated earlier, purely qualitative. However, it does show that the general profile is well represented by Amlec.

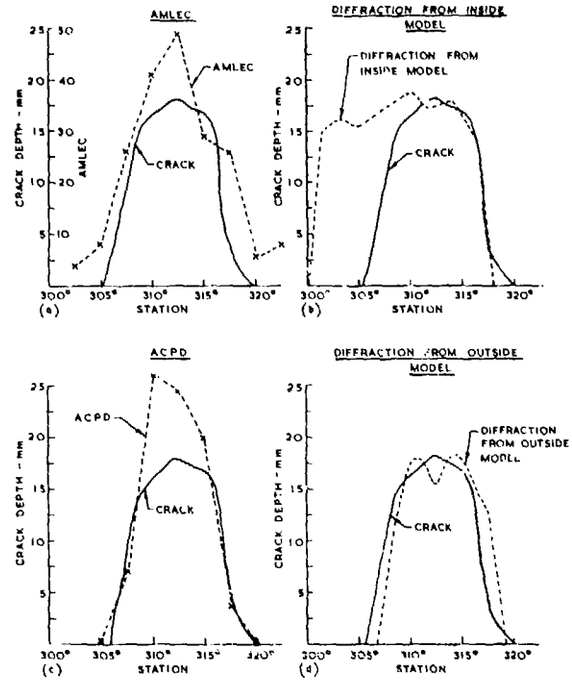

Fig. 13 Comparison of crack depth with various measuring techniques forward TOE of bulkhead weld.

It is also very useful in showing changes in crack depth as the fatigue test proceeds, see Fig. 14. This is a polar diagram of a submerged arc (SA) circumferential angled butt weld in one of our hourglass models showing Amlec readings taken at commencement of test (datum) and after 5,000 and 10,000 cycles. The figure quite clearly shows the progression of the fatigue crack in a qualitative manner. There are several interesting features apparent. It will be seen that the weld was profile dressed (ground) over 180°, the remainder being left in the 'as welded' or unground condition. Additionally it is seen that artificial defects (0.005" wide slits) have been introduced at roughly 90° and 180° in the ground regions. The significant points to note are that crack growth has occurred only in the as welded section even after 10,000 cycles, and that no crack growth has occurred from the artificial defects in the ground section.

The fatigue crack profile predicted by the ultrasonic diffraction technique used from the "crack open" side, i.e., operating from inside the model, is shown in Fig. 13b. This in fact shows the combined for and aft crack profiles as one

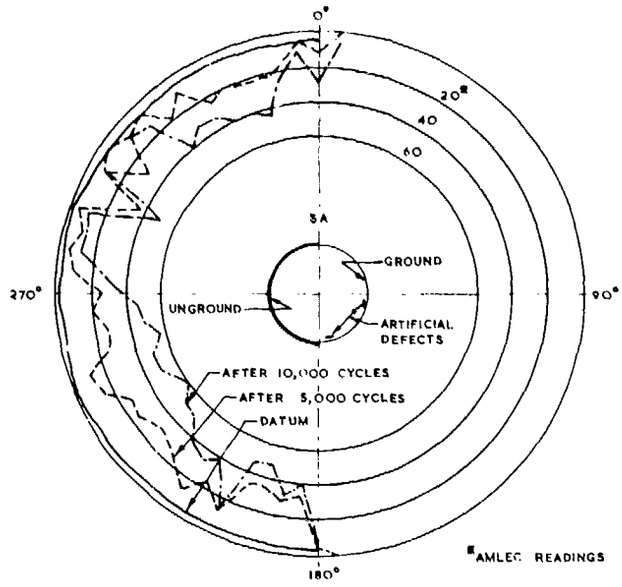

Fig. 14 Hour glass model AMLEC readings.

crack. However, if only the right hand side of the profile is considered (where there is only one crack i.e., the forward toe crack), it is seen that the agreement with the actual measured profile is quite good.

The ACPD estimated fatigue crack profile is shown in Fig. 13c. The agreement here is good except for an over-estimate at the maximum depth. However, since these results were obtained, considerable improvements have been made in the ACPD technique and it now shows a marked improvement in depth estimation (see later).

Figure 13d illustrates the results obtained using the diffraction technique from the "crack closed" side, i.e., operating outside the model. The fatigue crack profile estimate in this case shows very good agreement with the actual profile.

The depth estimate made by the conventional ultrasonic pulse-echo technique was so poor that it was not considered worth illustrating. The method grossly underestimated the crack depth profile and showed that in the T-butt weld situation this technique is of little value.

Tests on T-butt Welds

ACPD - The ACPD technique applied to surface breaking crack depth measurement has been under development for several years. Instruments are now commercially available which claim to be able to measure fatigue cracks to an acceptable accuracy. This, of course, immediately begs the question as to what is "acceptable accuracy."

Since there is little published data on the accuracy and reproducibility of ACPD instruments in sizing surface breaking fatigue cracks, especially in T-butt welds it was decided to conduct a controlled experiment to evaluate the performance of two commercially available instruments.

An "as welded" T-butt was prepared having dimensions shown in Fig. 15. It was subsequently fatigue cracked under 0-tension three point bend loading to give cracks at the weld toes along the full 200 mm width of the specimen. On load PD measurements were taken at 10 mm intervals with each instrument under constant current conditions using input frequencies, input positions and standard output probes as recommeded by the manufacturers. The arrangement of probe and input points was as shown in Fig. 11.

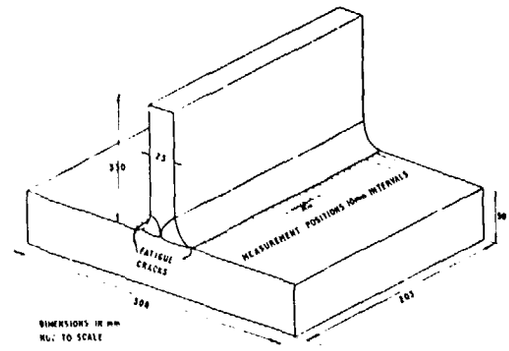

Fig. 15 T-butt weld specimen.

Finally, the actual crack depth profiles were obtain by sectioning and optical microscope measurment at 10 mm intervals corresponding to the instrument measurement position.

Figure 16 shows the results of the accuracy check. Results from both instruments were sufficiently close that only one ACPD profile plot is shown for clarity. It will be seen from this figure that the accuracy of the technique is extremely good, except perhaps towards the edges of the specimen where variation might be expected due to edge effects. These results reflect the improvement in the performance of ACPD achieved since the technique was applied to the early S1 model.

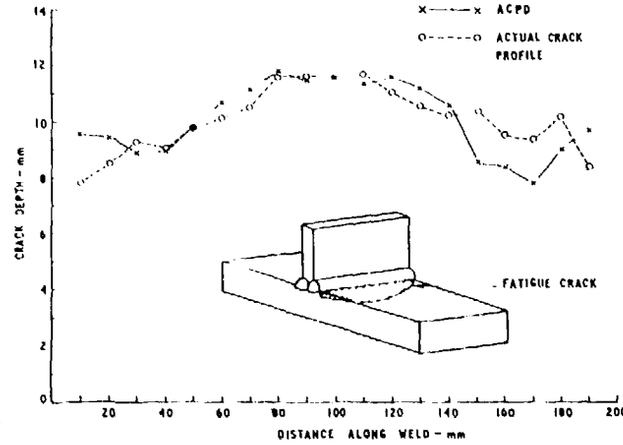

Fig. 16 ACPD estimation of fatigue crack profile in a T-butt weld.

To check on measurement reproducibility three operators obtain ACPD profiles on a T-butt under identical operating conditions. The results are shown in Fig. 17 from which it can be concluded that reproducibility, at lease under favourable laboratory conditions, was of a high degree.

Ultrasonic Diffraction - Preliminary results from a programme designed to investigate the effects of factors such as applied stress, crack closure, environment, weld profile etc., on the results of ACPD and diffraction measurements are given in Fig. 19. Work is at a very early stage, however, Fig. 18 gives some indication of the comparative

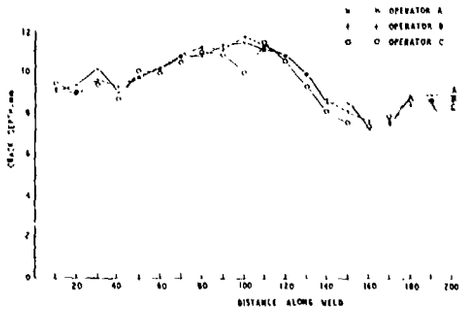

Fig. 17 ACPD estimation of fatigue crack profile in a T-butt weld-reproducibility of results.

performance of ACPD and ultrasonic diffraction of a fatigue cracked T-butt.

The dimensions of the test piece were as in Fig. 15, with the joint in the "as welded" condition. All measurements were performed "on-load." The diffraction measurements were obtained with the transducers on the "crack-closed" side, while the ACPD set-up was again as shown in Fig. 11.

Referring to Fig. 18, over the central 100 mm or so of the crack profile the agreement between between ACPD and ultrasonic diffraction is excellent being for the most part within 1 mm of each other. The agreement of both predicted profiles with the actual profile (obtained by sectioning)

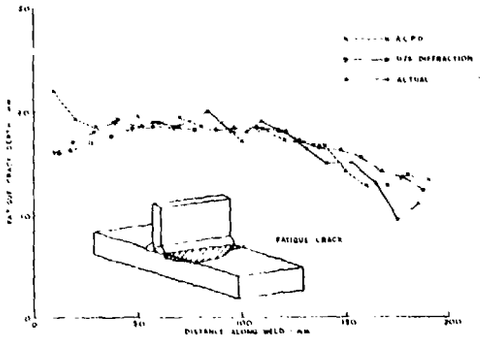

Fig. 18 Comparison of ACPD ultrasonic diffraction and actual fatigue crack profiles in an "AS welded" T-butt.

is again extremely good. In fact an envelope of width just over 1 mm could be drawn to encompass all three results at least over the central 100 mm or so. It is only at the specimen edges where large discrepancies begin to appear due to edge effects. The diffraction results in particular have given a very consistent picture showing a smooth gently bowed crack profile.

Other diffraction work (15) done under contract using a similar T-butt weld containing a fatigue crack of maximum depth about 3 mm has shown that the errors observed between actual and predicted depth were in the region of ± 0.15 mm. It was also found that a crack depth of about 1.5 mm was required before a reasonable precision in percentage terms (10%) was obtained. However, the presence of a crack signal was detectable down to a depth of around 0.5 mm. It should be noted that these results were obtained under very strictly controlled laboratory conditions.

CONCLUDING REMARKS

In this paper an attempt has been made to give a clear indication of the type of NDE work being carried out at AMTE Dunfermline.

The various types of large fatigue model structures being used as vehicles for evaluation of NDE techniques in realistic welded situations have been outlined together with the intermediate scale T-butt weld laboratory "type test."

The NDE techniques being actively pursued and those under consideration for further investigation have been indicated.

The results obtained so far from model and type test have shown that:

1. Ultrasonic diffraction from the "crack closed" side appears to be the most accurate and convenient technique for sizing surface breaking fatigue cracks. The technique used from the crack open side is equally accurate, however, it is less easy to use in the practical model situation. Hence the former is the preferred method.

2. The ACPD technique, used of course from the crack open side, has been shown to be accurate and reproducible in trials on T-butt weld type tests under controlled laboratory conditions.

3. The eddy current Amlec technique has been shown to be adequate for fatigue crack detection and the qualitiative progressing of such cracks in fatigue models.

4. Conventional pulse-echo ultrasonics is inadequate for crack sizing in T-butt weld situations.

5. The ultrasonic mode-conversion technique promises to be a useful method for crack sizing and is being pursued through extramural contract.

6. Acoustic emission is being pursued as a defect location technique in the fatigue models.

7. Encouraging results have been obtained with a multi-probe automated ultrasonic scanning unit for use in fatigue crack detection in models.

8. "On-line" ACPD has been used in model tests to obtain continuous readings of crack depth versus number of cycles. Complete analysis is awaited, however, initial results would indicate that the technique is viable.

FUTURE WORK

Eddy Current - The main requirements here are to quantify results and to automate the technique. Investigations are planned using multi-frequency units (16). Automation would considerably decrease inspection time, however, it may be difficult to attain in complex model structures.

Ultrasonic Diffraction - More practical experience is required in using the technique in complicated model structures. A requirement exists to cope with situations where physical constraints make it impossible to deploy the transducers astride the crack. In this context extramural contract work is underway to investigate the feasibility of operating with the transmitting and receiving transducers on the same side of the crack, other transducer positioning is also being investigated.

In the longer term, it is planned to look at the possibility of incorporating diffraction into the multi-probe scanning unit.

Ultrasonic Mode-Conversion - As indicated earlier extramural contract work is about to commence on the potential of this technique for sizing cracks particularly in the T-butt weld situation. The technique may also prove useful where very small cracks are concerned.

ACPD - To make effective use of ACPD for both point probing and "on-line" crack depth measurement in models and laboratory specimens it is necessary to evaluate parameters which may influence the accuracy and/or reproducibility of results. To this end, intra- and extra- mural work is planned. Several factors require investigation including:

1. Angled, stepped and branching cracks
2. Crack aspect ratio
3. Cracks in both weld metal and parent plate
4. Applied stress effects
5. Crack closure, and debris in cracks
6. Effect of water environment
7. Time dependence

Additionally work is required on several aspects of instrumentation and application particularly with regard to underwater "on-line" work, e.g., watertight pre-amplifiers and switches, optimised screening of input and probe leads, probe design and electrode attachment in difficult geometries etc.

As with diffraction more experience is required on complex model structures.

Acoustic Emission - Work will continue with the development of a reliable defect location system for use in the fatigue models. In addition, laboratory work is planned to investigate the relationships between AE and type of fracture.

ACKNOWLEDGEMENTS

The valuable assistance given by colleagues of the Fatigue and NDT Sections AMTE (Dunfermline) in providing much of the experimental data for the paper is gratefully acknowledged.

REFERENCES

1. Smith, T. P. and Beech, H. G., "The Application and Use of Eddy Currents in Non-Destructive Testing," Brit J. Nondestructive Testing, 18, (5), Sept. 1976.
2. Silk, M. G. and Lidington, B. H., "Defect Sizing Using an Ultrasonic Time Delay Approach," Brit J. Nondestructive Testing. 17, (2), March 1975, 33-36.
3. Mudge, P. J. and Whitaker, J. S., "Depth Measurement of Cracks in Toughness Specimens - Use of an Ultrasonic Time Delay System." Weld Inst. Res. Bull, July 1979, 198-203.
4. Silk, M. G., "Defect Sizing using Ultrasonic Diffraction," Brit J. Non-destructive Testing, Vol. 21, No. 1, Jan. 1979.
5. Ryman, R. J., Mann, D. L. and Blackwell, M. P., "The Use of an ACPD System for Crack Detection and Measurement," Paper presented at British Inst. of Non-destructive Testing, London, Oct. 1979.
6. Dover, W. D., et al, "The Use of AC Field Measurements to Determine the Shape and Size of a Crack in a Metal," Symp. on Eddy Current Characterization of Materials and Structures, NBS Washington D.C., Sept. 1979.
7. Dover, W. D., et al, "AC Field Measurement - Theory and Practice," University College London, 1980 - to be published.
8. ASTM STP 505, 1972.
9. ASTM STP 571, 1977.
10. Bond, L. J., "Methods of Ultrasonic Non-Destructive Testing," Patent Application No. 7923729, 1979.
11. Bond, L. J., "Finite Difference Methods Applied to Ultrasonic Non-Destructive Testing Problems," Proc. ARPA/AFML Review of Progress in Quantitative NDE, July 8-13, 1979, La Jolla, USA.
12. AMTE(S) Dunfermline 1980 - unpublished.
13. AMTE(S) Dunfermline 1980 - unpublished.
14. Bond, L. J., "Investigation of Steel Structures using Ultrasonic Waves," 1980.
15. Silk, M. G., Lidington, B. H. and Hammond, G. C, "The Use of Ultrasonic Diffraction to Detect and Size a Surface Opening Crack Growing From the Opposite Side of the Specimen," AERE, Harwell, Materials Physics Div., Rep. G1490, Oct. 1979.
16. Dukes, R., AMTE(M) Holton Heath, unpublished.

Unidentified Speaker: Your data showing the ground and unground portion of the welds indicate one should draw the logical conclusion that by simply grinding the welds, you eliminate fatigue cracks.

Iain Kilpatrick (Admiralty Marine Technology Establishment): The data was up to 10,000 cycles only. We would expect for these particular vessels a longer fatigue life than 10,000 cycles. We have experienced fatigue cracking in ground welds and in the case shown I would expect the cracks to propagate into the ground section eventually as the number of fatigue cycles is increased.

Unidentified Speaker: At what level of cycles?

Iain Kilpatrick: That depends on lots of things. However, for example, in ground laboratory scale T-butt weld, fatigue tests, it can vary from 3000 or 4000 cycles to as much as 40,000 cycles, and this i one of the difficulties with initiation. We have samples going on for 40,000 cycles before crack initiation, and that is because of the weld and the residual stresses.

Otto Buck (Rockwell Science Center): Grinding puts some residual stresses -

Iain Kilpatrick: We already have some major tensile residual stresses at T-butt welds. We in fact have a very large progra when measuring residual stresses in these particular structures and have been fairly successful in measuring not only the local residual stresses but what we call long-range strain forces, which are the driving forces, rather than the local residual stresses. Local residual stresses are very important in the early stages because they are very high and cause initiation. But the driving stresses are the stresses due to building the actual structure itself, and these long-range restraint forces cause crack propagation. Yes, we appreciate we have got to look at residual stresses.

Richard Elsley (Science Center): What is the nature of the probe that you use for the alternating current potential drop method?

John Cargill (Admiralty Marine Technology Establishment): It has two points which are usually made of tungsten, they are separated by about 10 millimeters and are pushed in to the surface and the potential drop or difference between the points is measured.

Iain Kilpatrick: I think it is true to say we had a lot of difficulty with probe design in the initial stages. Being hand-held was part of the reproducibility problem. We did end up at one stage with a three-legged probe which was fairly stable to apply but in other circumstances was not suitable. But we think we have a fairly good probe design.

John Cargill: Probe design was the stumbling block initially. Obviously the difficulty arose from the massive unwanted pick-up that you can get when pumping something like five amps at eight KHz into a large structure. This can obviously be more than the potential drop due to the crack.

Unidentified Speaker: Do you have any trouble with dirt?

John Cargill: Not in that situation. It can be brushed off with the tungsten points. You can push through the dirt. It is essential to keep the probe points down to a minimum length. The two points of the probe and the test piece are parts of a loop which can cause pick-up of unwanted signals by inductance. Thus it is necessary to keep the area of this loop to a minimum.

TEST BED FOR QUANTITATIVE NDE

R.C. Addison, R.B. Houston, J.F. Martin, R.B. Thompson
Rockwell International Science Center
Thousand Oaks, California 91360

ABSTRACT

The ARPA/AFML Interdisciplinary Program for Quantitative Flaw Definition has demonstrated a number of new techniques for quantitatively sizing flaws, as are reported elsewhere in these proceedings. This paper describes the progress that has been made during the past year on a test bed program to assemble and demonstrate these techniques in a single integrated measurement system that will extend them from the idealized geometries that have been considered thus far to geometries that are a better approximation to those that are found in real parts. The basic system consists of a Data General Eclipse S/200 Minicomputer, a multiaxis microprocessor controller, a Biomation A/D converter, an immersion tank, and a contour following system with six degrees of freedom. The operation of the mechanical system with regard to its accuracy and repeatability will be described. In addition, a review of the conceptual design of the test bed system and experimental results for a number of different flaw geometries will be included.

The Test Bed includes a piezoelectric array transducer and associated electronics. The array system will be used both for the imaging of flaws and the gathering of scattering data to use in other flaw characterization algorithms. The success of this portion of the program depends to a large extent on the availability of a suitable array transducer. Some difficulty has been met in obtaining such a transducer and the system design has been slightly modified as a result. The modified system will be described along with a review of the electronic system and an update on its current status.

The extended data gathering capability of the system has been demonstrated with several diffusion bonded samples containing spherical and spheroidal voids. The noise associated with these signals is chiefly due to the grain scattering and varies in amplitude over a wide range. The effects of this noise on the accuracy of the Inverse Born Approximation has been analyzed and the results will be summarized.

Conceptual Design

The ultrasonic test bed program has been initiated to complement the ARPA/AFML Interdisciplinary Program for Quantitative Flaw Definition. Specifically, we are implementing the variety of new techniques that have arisen for obtaining quantitative data about flaws such as the size, shape, orientation and stress intensity factor. These will be adapted into procedures for identifying flaws in parts of complex geometry such as turbine disks. The results will serve a twofold purpose. First, a new inspection capability will be demonstrated. Second, in cases where the practical constraints of the part geometry degrade the quality of some of the measured flaw parameters, this information can be fed back into the research program to guide that effort.

The Test Bed program is the first step in moving the new NDE techniques from the research laboratory to the production area. It is serving as an effective vehicle for integrating the variety of quantitative techniques into a single coherent system. As the capabilities of the different techniques are explored, it is possible to identify ways of using partial results from each of them that can be combined in a synergistic way to obtain complete information about a flaw.

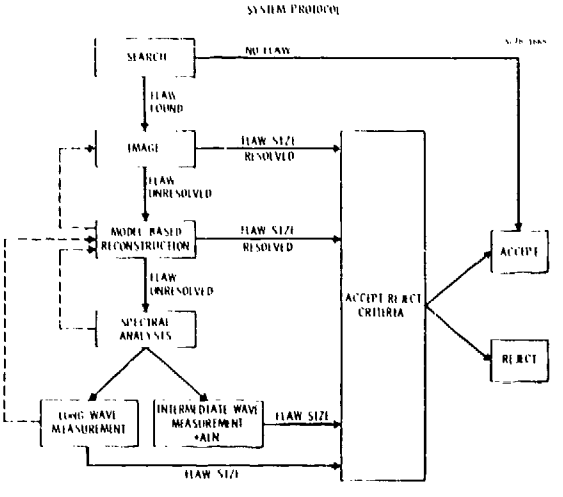

Fig. 1 Ultrasonic test bed system protocol.

The protocol that we had originally suggested is shown in Fig. 1 by the solid lines. This concept entails first searching the part and storing the locations of all regions that possibly contain flaws in the test bed memory. Each of these locations is then inspected in detail to determine the quantitative parameters of the flaw. First an image of the flaw is made, and, if it is resolved, the accept/reject criteria is used to decide if the part is acceptable. If it is unresolved, a map can be made to determine if there are multiple flaws within a small area. Next, appropriate scattering data are obtained so that a model based reconstruction technique can be used to form an

image of the flaw. If the flaw is still unresolved, we will examine the spectral content of the defect signal and determine the approximate ka value of the flaw. For cases where $0.5 < ka < 3$ we will use adaptive learning techniques to extract the flaw parameters. If $ka < 0.5$, we will use long wavelength techniques and determine the stress intensity factor of the flaw.

In addition we have found that in many cases a detailed inspection technique by itself does not give full information about a flaw but provides information that can be used in the interpretation of one of the other techniques. Those situations where additional information can be provided are shown by the dotted lines and the specifics will be given in the sections describing work with those techniques.

System Description

The Test Bed comprises a system that has been assembled through the interconnection of several major subsystems as is shown schematically in Fig. 2. The heart of the system is a minicomputer that is used in a multitasking mode. This unit is used as the central processing unit (CPU) for the system and controls the microprocessor based manipulator control subsystem, the high speed A/D converter used for digitizing r.f. waveforms, and the color graphics display system. In addition there are user terminals which allow the operator to send commands to the CPU and there is a standard disk storage system. The CPU controls the microprocessor by sending it a series of ASCII characters called a data block that specifies how far and how fast the transducer is to be scanned along each axis. The microprocesor then interprets this data block and calculates the distance to be moved along each axis, converts this into stepping motor pulses for the axes involved and sends out the pulses to each axis, appropriately interleaved to provide maximum accuracy in following the contour of the move. The microprocessor also can send response characters to the CPU regarding its position, status, etc.

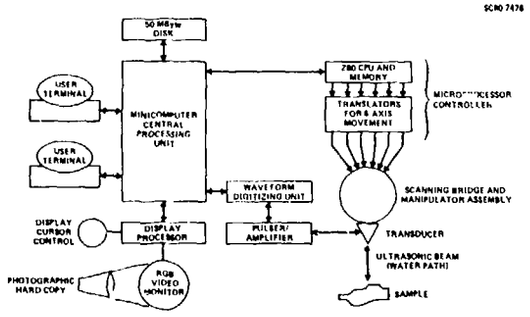

Fig. 2 A computer's eye view of the testbed hardware.

The CPU also controls the display processor using commands that have been created by that unit's manufacturer. The unit basically accepts command and data strings and translates these into arrangements of colored pixels within the 512 × 512 format of the RGB video monitor. The unit can change the corespondence beween the amplitude of the signal and the color of the pixel, can display alphanumerical characters, can display vectors between two points, plus other functions that are useful in displaying graphic data.[1]

To operate these subsystems a body of software has been written that includes four different categories of programs, all of which operate interactively with the user. These categories are listed below:

1) Programs for generating disk files of data blocks which may be interpreted by the microprocessor;

2) Multitasking control programs for managing the manipulator, data acquisition, and storage on disk;

3) Programs for displaying the data in color or black and white via the display processor, and

4) ISP, a signal processing and display program of enormous flexibility.

In category 1) there are two kinds of programs for generating disk files of data blocks. One kind generates a file corresponding to a raster pattern in X & Y which is useful for scanning the transducer over flat parts. The second generates a file of data blocks corresponding to a profile of a complex part shape with rotational symmetry which is useful for scanning over turbine disks. In category 2) there is the multitasking program which manages the manipulator, data acquisition, and storage on disk. It maintains four tasks:

- Task 1 communicates with the operator via the user terminal.
- Task 2 arms the A/D converter, waits for a trigger, collects the digitized waveform and processes it in the designated manner.
- Task 3 reads and interprets response characters from the microprocessor.
- Task 4 stores pertinent data from Task 2 on disk for later access by display programs.

A more detailed description of these tasks has been given in Reference 2. In category 3) there are programs to exercise the display processor. These permit the display of both B-scan and C-scan data using either a black and white, gray scale or one of several types of false color schemes to code the data. Finally, in category 4) there is ISP which is used for implementing the various inversion algorithms. ISP is a large multitasking program which runs on the minicomputer under the control of an external terminal. It has been developed at the Science Center by Richard Elsley and permits a number of signal processing procedures including

1) Waveform acquisition

2) Waveform transformation including: addition, subtraction, Fourier transforming, timeshifting, etc.

3) Feature extraction

4) Display of data.

Because of the flexibility of ISP these operations can be applied in any order necessary for data analysis.

Ultrasonic Array

One of the objectives of the Test Bed program is to utilize an ultrasonic array for imaging and scattering measurements. The electronics for driving this array will have a somewhat different objective than some of the array based systems that are currently available. Our chief purpose will be to obtain a waveform that has as little distortion as possible, whereas for many systems the objective is to obtain an image in as little time as possible. In systems of the latter type one depends on the image enhancement ability of the eye/brain system to filter out the effects of the distortion that results. In the system that is being designed and built for the Test Bed, we would like to be able to display a single frame of an image and be able to recognize the important details of the object under study. In addition the system will be required to collect scattering data that can be used with the various inversion techniques.

The original system was based on a single 240 element array but problems were encountered in obtaining an array containing this many elements and possessing the requisite performance characteristics with regard to both uniformity of response from element to element and bandwidth. In lieu of a single array, the feasibility of the concept will be demonstrated using two 32 element arrays with a variable spacing between them. The system will still operate in both an imaging mode and a scattering mode. The desired specifications of the array have been previously described[2,3] in some detail. The electronics driving the array will be capable of selecting sixteen transmitting and receiving elements independently. The diagram in Fig. 3 shows how the system will work in the reflection mode when it is used for imaging. The beam emanating from the array is scanned and steered so that it will follow a profile. With only a 32 element array this capability will be quite limited, although sector scans, correction for wavefront distortion at curved water/metal interfaces, compound scanning and imaging using the pitch-catch mode will be possible. The second mode, used for obtaining scattering data, is illustrated in Fig. 4. In this case, the separation of the two arrays can be varied by mechanical means from a minimum separation where the outer cases of the two arrays are in contact to a maximum separation where the outermost elements of the two arrays are six inches apart.

The block diagram of the array electronics with the major subsystems labeled is shown in Fig. 5. The basic system operation has been previously described.[3] Recent activity has been directed towards the detailed design of the subsystems between the array and the interface with the exception of the A/D converter and the fast buffer memory which have been completed and were described in Ref. 3. The first item of concern is the hybrid pulser/receiver. The need to apply high voltages to the array elements when transmitting and the need for the low noise amplification prior to sending the received signals into the multiplexer dictate that the pulser/receiver be between the array and the multiplexer. This requirement obliges us to package the pulser/receiver in as compact a form as possible to minimize the length of connecting cables.

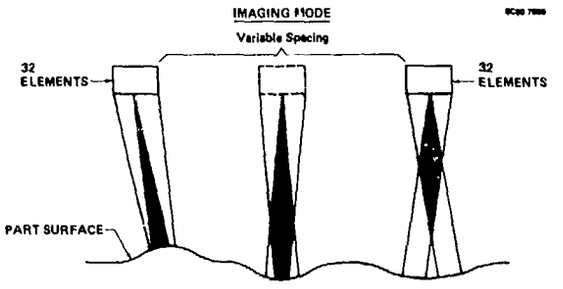

Fig. 3 Two linear arrays used for contour following in the imaging mode.

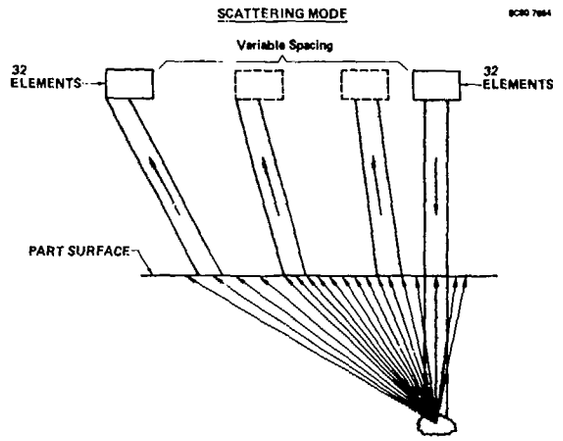

Fig. 4 Two linear arrays used in a pitch-catch mode for obtaining scattering data.

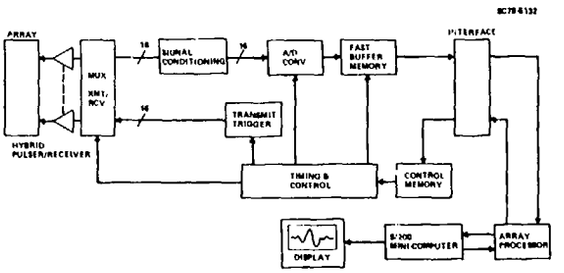

Fig. 5 Ultrasonic array signal processing system.

The pulser circuit is shown in Fig. 6a. The switching element is a SCR which provides repeatable results and operates reliably over a wide range of applied DC voltages providing a mechanism for varying the output amplitude of the transmit

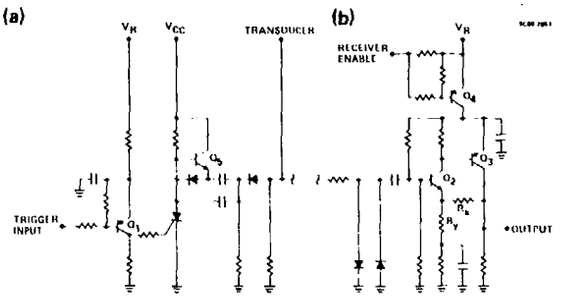

Fig. 6 Hybrid pulser/receiver circuitry.

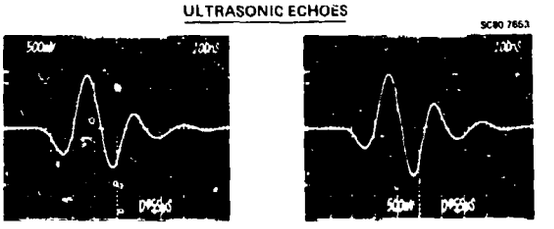

Fig. 7 Comparison of transducer response to excitation by hybrid pulser/receiver and commercial pulser/receiver.

ted pulse by 30 dB. The unit operates at DC voltages of 10V to 300V with a repetition rate of 1 kHz. The pulser has been used to excite a 2.25 MHz commercial transducer and the echo returned from a block of aluminum has been compared with that obtained from a commercial pulser using the same transducer. The results are shown in Fig. 7 where it is readily seen that the transient response of the transducer is essentially the same in both cases.

The receiver circuit shown in Fig. 6b is a two transistor amplifier with a gain of 20, a 3 dB bandpass from 0.7 MHz to 30 MHz and a total power dissipation of only 70 milliwatts. Transistor Q_4 is used to switch the receiver on when it is one of the 16 addressed receivers. It is expected that this will help to reduce the crosstalk from receivers that are not addressed.

We have concluded that the optimum way to minimize the size of the hybrid package is to put two pulser/receiver units in a single package having dimensions of 20 mm × 35 mm × 6 mm. Some engineering evaluation units will be available during the third quarter of this year.

The multiplexer design which was described previously[2,3] consists of three 240:16 multiplexers, two of which are digital units and one which is an analog unit. The entire multiplexer unit has been essentially completed although it has not been tested as a functioning module. The sub units of the multiplexer have been tested for cross talk and have performed satisfactorily. The module will be tested after the hybrids are available.

The purpose of the signal conditioning circuitry is to prepare the signals for the A/D converter. The circuitry is composed of the main amplifier with a gain of 20, a digitally controlled attenuator with a range of 45 dB in 3 dB steps, a clipping circuit to prevent overdriving the A/D, a filter to control the noise bandwidth and suppress feedthrough from the clocking circuits, a dc level shifter and a low impedance buffer amplifier to drive the A/D. All sixteen circuits required for the receiving channels have been fabricated and tested.

Data Acquisition Techniques and Problems

The basic goal of the ultrasonic Test Bed program, as stated previously, is to implement the variety of inversion techniques that have been developed in the Interdisciplinary Program for Quantitative Flaw Definition. To achieve this goal and produce meaningful results, the susceptability of each of the techniques to errors that are likely to be encountered in practical applications must be fully explored. Errors in the calculation of the size, shape, or orientation of a flaw can arise from a variety of different sources. The major sources of error that are known are listed below:

1) Model errors or inherent errors associated with the inversion technique;

2) Contamination of the signal with stochastic noise, either thermally generated or arising from grain scattering;

3) Contamination of the signal with coherent noise such as the low amplitude vestiges of an echo from a strong reflector (i.e., the front surfce of a part) or overlapping of the low amplitude tail of a flaw signal and a strong echo from a reflector beyond the flaw (i.e., the back surface of a part);

4) Band limiting of the flaw signal caused by practical restrictions on the bandwidth of real ultrasonic transducers;

5) Distortion or deviation of the ultrasonic wavefront incident on the flaw from the plane wavefront assumed in the inversion technique;

6) Distortion or deviation of the ultrasonic wavefront producing the echo used in computing the deconvolved signal from the ultrasonic wavefront actually incident on the flaw; and

7) Inadequate spatial window for obtaining data from a flaw leading to errors in the shape or orientation.

The model errors are determined by using theoretical scattering data calculated for a particular flaw as input for the particular inversion technique being investigated. The model selected should not be equivalent to the one from which the (often approximate) inversion technique has been

derived. Instead, it should represent a more accurate solution, such as is obtainable for simple flaw shapes. The resulting estimate of the flaw radius will provide a measure of the accuracy of the model. The investigators who have developed each of the flaw techniques have also considered the validity of the technique using this sort of procedure. It has been repeated in this program to confirm that the technique has been programmed correctly. The next source of error to be considered is that associated with the contamination of the signal with stochastic noise. Since the data taken with the Test Bed system is all digitized and many signals can be averaged together, the thermally generated noise can be reduced to a negligible level and is of no concern. The dominant source of stochastic noise is due to grain scattering. The errors caused by this noise source have been investigated for the Born Inversion technique. The procedure used to calculate these error bars is fully described in the paper entitled "Dependence of the Accuracy of the Born Inversion Upon Noise and Bandwidth" by Elsley and Addison.[4] The paper contains a quantitative treatment of the decrease in accuracy of the Born Inversion technique as the signal to noise ratio decreases. The noise is assumed to arise from grain scattering with an amplitude that increases as the square of the frequency. The essential finding of the paper was that the Born Inversion technique was very robust as far as errors from noise were concerned. Figure 8 shows the variation of the accuracy with S/N ratio for a 400 μm diameter spherical void. The S/N ratio is the ratio of the total power in the signal plus noise to the total power in the noise in a bandwidth from 0 to 10 MHz. Since the noise is non-white it is possible to consider signals in the time domain that have an S/N of less than 0 dB. The error bars denote the 95% confidence limits.

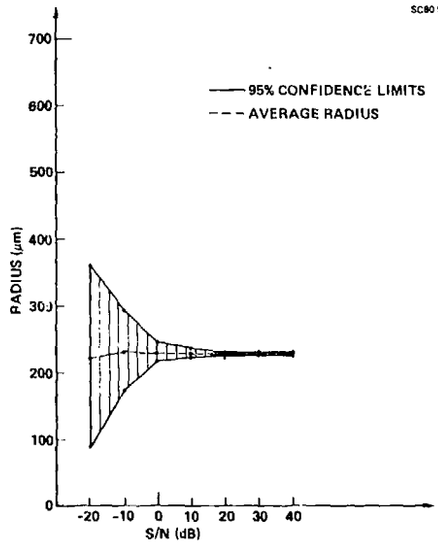

Fig. 8 Born inversion accuracy vs S/N ratio, 400 μm diameter spherical void.

The errors resulting from the contamination of signals with coherent noise are more difficult to analyze in a quantitative manner since the effect of the noise signals vary significantly as the degree of overlap with the desired signal and the amplitude and the phase relationship of the two signals change. A technique for minimizing the effects of these noise signals when they arise from planar interfaces is to acquire two signals, one containing the desired signal plus the contaminating signal and the other containing only the contaminating signal; these two signals are properly aligned temporally and then subtracted.[5] In many practical situations where the degree of overlap of the signals is not too great, this technique produces excellent results.

The bandlimiting of the flaw signal by the ultrasonic transducer can produce significant variations in the estimated radius of the flaw. To understand how the center frequency and bandpass affect the analysis it is essential to understand the characteristics of the magnitude spectrum produced when an elastic wave scatters from an ellipsoidal flaw. Although the details of the spectrum will change as the material properties of the host material and the flaw are varied, certain major features will remain essentially unchanged. As an example, the magnitude spectrum for a spherical void is shown in Fig. 9. There are three features of this curve that will remain the same for all ellipsoidal scatterers. In the low ka region the amplitude of the scattering always increases in proportion to the square of the frequency; the first peak in the curve always occurs at approximately ka = 1; and finally this peak is always followed by many other peaks that are not in general equally spaced nor do their amplitudes have any particular relationship.

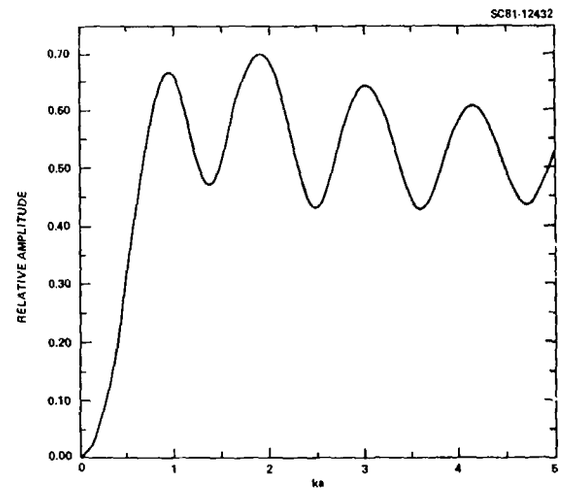

Fig. 9 Magnitude of theoretical scattering spectrum for a spherical void.

The inversion techniques employed for sizing flaws use selected portions of the complex scattering spectrum. The long wavelength technique utilizes the portion of the spectrum where the magnitude is increasing parabolically, while the Inverse Born technique is sensitive to the location of the first peak of the spectrum. The adaptive learning networks use a number of fea-

tures of the scattered waveforms, but for the sizing of flaws, seem to depend on the output of the Inverse Born technique. When these inversion techniques are used, the bandwidth of the transducer must encompass the portion of the scattering spectrum that is essential to its implementation. Therefore, the bandwidth of the transducer for a long wavelength measurement should extend to a low frequency corresponding to ka = 0.5 for the specific flaw and in the case of the Inverse Born technique the transducer bandwidth should encompass the ka range that includes the first peak of the scattering spectrum. In the case of a spherical flaw whose size is known a priori, this requirement imposes a modest burden on the transducer. When the size of the flaw is not approximately known or the flaw has an ellipsoidal shape with a factor of two or more difference in the sizes of the major and minor axes, the bandwidth requirements on the transducer are very severe.

The effects of bandwidth on the accuracy of the Inverse Born Technique have been analyzed in Ref. 4. The findings indicate that if the bandpass of the transducer is below the first peak of the spectrum, there will be an overestimate of the flaw size. If the bandpass of the transducer is above the first peak, the analysis will treat the second peak (or whichever peak is within the bandpass) as if it were the first peak and will estimate the radius accordingly resulting in a serious underestimate of the flaw size. The first type of error involving insufficient high frequency data can be detected by knowing the center frequency of the transducer and the predicted flaw size. The second type of error can be detected by resolving a large flaw using an imaging technique or through an analysis of the scattering spectrum using multiple transducers having different bandpasses to determine the location of the first spectral peak.

There has also been an effort to increase the bandwidth by splicing together the deconvolved responses obtained with two different transducers. The results of this are described in Ref. 4.

When the bandpass of the transducer does encompass the first spectral peak, errors can still occur due to insufficient bandwidth. The nature of these errors can be seen in Fig. 10 where the estimated radius of a flaw is plotted vs the true radius for transducers having different bandwidths. The range of validity extends from 1 on the abscissa to the peak of the curve of interest. Note that the resulting error is an underestimate but can be corrected by using the curves for calibration of the measurement technique.

There are two ways in which distortions of the wavefronts emanating from the transducer can lead to errors in the estimated flaw size. First, the inversion technique assumes that a plane wavefront is incident on the flaw, however, under the best of circumstances this is only an approximation. If the wave has passed through a curved metal/water interface, the wavefront is likely to be spherical or cylindrical. The second source of error arises through the deconvolution process. Recall that prior to using the inversion technique the raw data obtained from the flaw is deconvolved to remove the effects of the transducer. The deconvolution requires a reference signal that is characteristic of the transducer and in principal

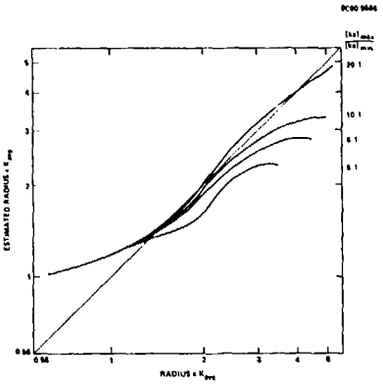

Fig. 10 Estimated flaw size vs true flaw size for several transducer bandwidths.

will only work if the waveform of the reference signal is identical to the waveform incident on the flaw. In practice this is difficult to achieve because the plane reflector used to obtain the reference waveform is generally at a different distance from the front surface of the part than the flaw and hence has experienced different amounts of diffraction, scattering losses and absorbtion. If the metal/water interface is curved, there is also additional focusing of the beam.

The errors caused by these wavefront distortions can be calculated for a specific case but for our current purposes this type of calculation did not seem essential to the primary goal of determining how the inversion techniques work in practical situations. In lieu of a theoretical calculation, an empirical approach has been used to evaluate errors that are encountered with some common geometries. The reference waveform is typically the signal obtained from the normal incidence and reflection of a wave off of a plane water/metal interface. This interface is usually the back face of the specimen being examined and in the cases that have been tried is about 10 to 20 wavelengths further along the path of propagation than the flaw. In a few cases a backface echo from a separate specimen made of the same material has been used as a reference. The signal waveform from the flaw has been obtained both from waves that are incident normally on the front surface of the specimen and from waves that are incident at various angles with the maximum angle corresponding to an internal refraction angle of 60°. In all cases the deconvolution has been computed using the backface echo obtained from the normally incident wave. When flaws having known sizes are examined and the data is analysed using the Inverse Born technique, there is no evidence that there are any errors being generated via the deconvolution that could be attributed to wavefront distortion.

The errors that result from an inadequate spatial window can be considered from two points of view. Some inversion techniques such as the ALN,[6] and POFFIS,[7] require data to be taken via an array of transducers and then combined using a suitable algorithm to produce estimates of the flaw size, shape, and orientation. When the number of elements in this array is reduced or the spacing is allowed to become irregular, the accuracy of the

estimates is decreased. These effects are probably significant although a careful analysis has not yet been made of results obtained with either of these algorithms. The second point of view relates to the Inverse Born technique which requires no fixed array of transducers. For each measurement direction, an independent measurement of the diameter of the flaw along that direction is obtained. If there are only a few directions available, it is only possible to acquire a few measures of the flaw diameter but each of these measures will have the same accuracy. This situation where a better estimate of the flaw size, shape, and orientation is obtained with each additional measurement seems to be preferable to the situation where a minimum of a half dozen or more measurements must be made to obtain any estimate at all and even then the accuracy is degraded.

Analysis of a Flaw

Although the entire array of quantitative inversion techniques are not operational on our system at this time, a sufficient number of them are available to provide an accurate demonstration of how the system will operate. The sample or part is first scanned in a search or mapping mode which provides the locations of tentative flaw sites. The results of such a scan are shown in Fig. 11. Now each of the flaw indications is analyzed in detail to determine its size, shape and orientation. The first step is to provide a high resolution image of the region surrounding the flaw such as that shown in Fig. 12. In this particular case the flaw is too small to be resolved although the image has eliminated the possibility that there are multiple flaws or porosity present. This allows the analysis to continue using a model based reconstruction technique, the Inverse Born technique. Using this technique data is obtained from several different angles. Each angle provides an estimate of the radius of the flaw in that direction. In this case the flaw was below a flat surface and it was possible to interrogate it from 19 different angles. The resulting radius estimates are plotted in Fig. 13 and compared to the known size of the flaw which was a 1200 μm diameter spherical void. Note that all but one of the data points fall very close to a radius of 600 μm and it is clear that the object being examined has a spherical shape. The flaw has now been thoroughly analyzed and it is not necessary to make any long wavelength measurements although this could also be done.

Another flaw type of interest is a surface breaking fatigue crack. It is of interest to be able to measure the depth of such a crack in a quantitative non destructive fashion. Current methods of sizing such cracks in the field only measure the length of the crack at the surface. The depth is inferred by assuming that the crack has a length to depth ratio of 0.5; an assumption that is not strictly valid except for particular loading conditions. The aspect ratio can also be strongly affected by the location of the initiation site in the stress field as well as the material type. An experiment was performed in which a fatigue crack was cyclically stressed until failure of the part occurred. At regular intervals during the fatigue life, the depth of the crack was measured using an ultrasonic technique. This information along with the material param

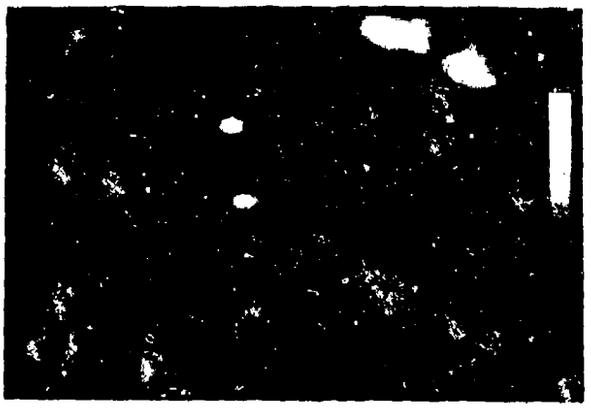

Fig. 11 Focused C-scan of titanium specimen.

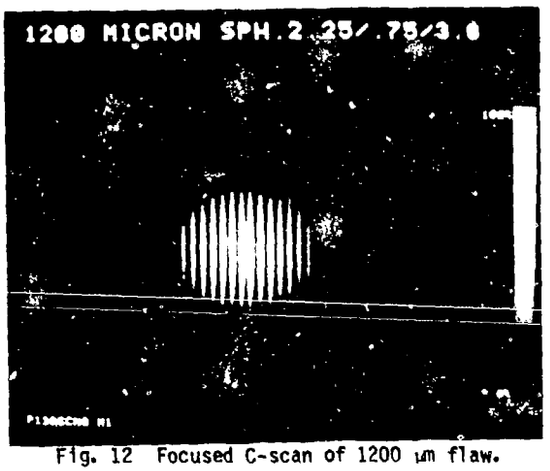

Fig. 12 Focused C-scan of 1200 μm flaw.

eters of the sample were used to predict the number of cycles remaining after each inspection before the crack reached the critical depth leading to failure.

The sample was prepared from 2024 aluminum plate which was fabricated as a "dogbone" sample suitable for cyclic fatigue testing. Initially an EDM starter notch was placed in the sample, which was then fatigued until a fatigue crack had been initiated. The EDM notch was then machined away leaving only the fatigue crack with a length of 0.160" and an estimated depth of 0.045". The thickness of the sample was approximately 1/2" after removal of the EDM notch. The crack was sized using an ultrasonic technique known as the satellite pulse technique.[8] This technique is illustrated in Fig. 14. The ultrasonic beam propagates through the water, refracts at the surface of the aluminum plate and is incident on the crack tip. There is a strong corner reflection from the base of the crack preceeded by a signal that is diffracted from the top of the crack. The depth

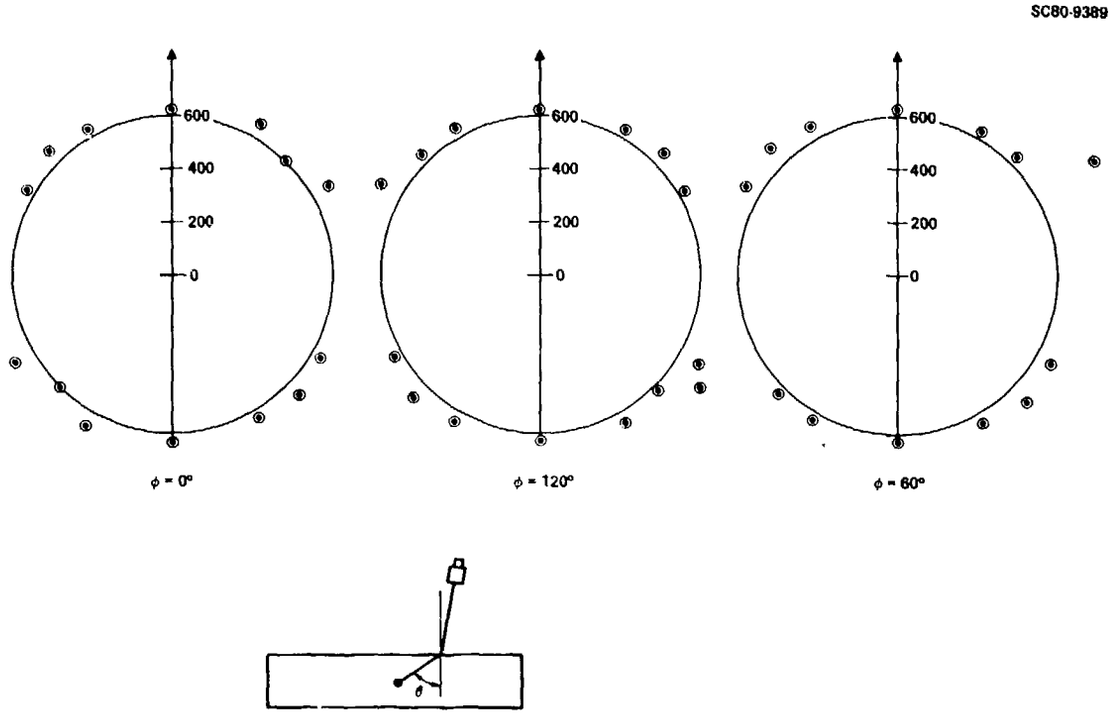

Fig. 13 Born inversion analysis of 1200μm diameter sphere.

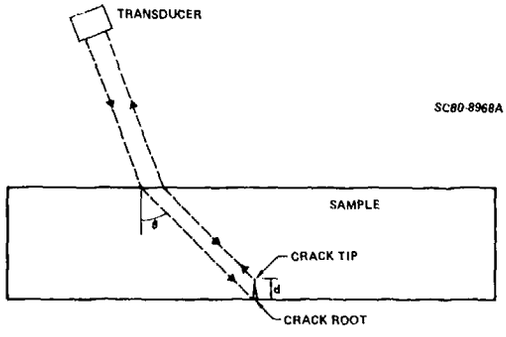

Fig. 14 Schematic of sample geometry and transducer.

of the crack can be determined from the time difference between these two signals.

The sample was subjected to cyclic fatigue stress by mounting it in an MTS machine and sinusoidally varying the stress from 2000 psi to 27,500 psi. During this process the length of the crack was monitored optically and each time that the length of the crack had increased by about .050" the sample was removed from the MTS machine and an ultrasonic measurement of the depth of the crack was made. After each measurement, the crack depth and the material parameters of the sample were used to predict the number of fatigue cycles remaining before the crack would reach its critical depth. After the sample had been stressed to failure, these predictions were compared to the actual number of fatigue cycles that were necessary to fail the sample. The fractional difference in the two values is plotted vs the number of remaining fatigue cycles in Fig. 15. The plotted point used the measured da/dN value for this sample for calculating the number of remaining fatigue samples. The error bars were calculated from the spread that is to be expected in the da/dN vs ΔK data for this material. With the exception of the first observation, all of the error bars span the zero error point. The first observation does not span this point because the measured da/dN value does not lie within the envelope that is assumed to contain the spread in the da/dN values. This is attributed to a lack of measurements on the particular melt of aluminum used for fabricating the test samples. These results are considered to be satisfactory and within the expected bounds of uncertainty. They demonstrate that the number of cycles to failure can be predicted with sufficient accuracy using quantitative ultrasonic techniques for sizing the flaw.

Conclusions

The Test Bed is proving to be a useful system for testing the various inversion techniques that are available. Because a variety of techniques are readily accessible it has proven possible to use pieces of information obtained from several techniques to obtain a more accurate estimate of the size, shape and orientation of a flaw. The system is also serving as an effective means for uncovering aspects of the inversion techniques

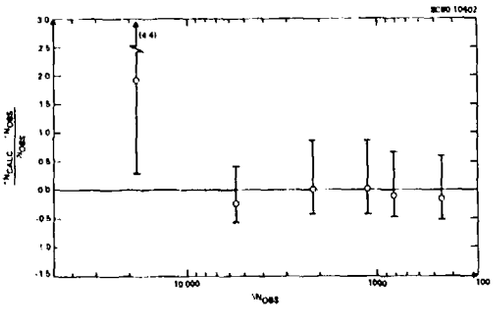

Fig. 15 Fractional error in calculated number of remaining fatigue cycles vs observed number of remaining fatigue cycles.

that need further work or that are impractical. The work on the array system represents a new development in that the received data from each array element can be processed in a very flexible way using the array processor. This sytem promises to provide a unique capability for investigating the utility of electronically scanned arrays for contour following applications as well as for applications requiring the processing of scattering data.

ACKNOWLEDGMENT

This work was supported by the Defense Advanced Projects Agency under Contract No. F33615-78-C-5164.

REFERENCES

1. C.C. Ruokangas and J.F. Martin, "Color Graphics: An Aid to Data Interpretation," Proceedings of the DARPA/AFML Review of Progress in Quantitative NDE, July 1980, LaJolla, California, this volume.

2. R.B. Thompson and R.C. Addison, "Ultrasonic Test Bed for Quantitative NDE,"- Interim Report No. 3, Contract F33615-78-C-5169 Rockwell International Science Center, March, 1980.

3. See Ref. ? as well as R.C. Addison, R.B. Houston, J.F. Martin, and R.B. Thompson, "Test Bed for Quantitative NDE," Proceedings of the ARPA/AF Review of Progress in Quantitative NDE, July 1979, LaJolla, California.

4. R.K. Elsley and R.C. Addison, "Dependence of the Accuracy of the Born Inversion Upon Noise and Bandwidth," Proceedings of the Review of Progress in Quantitative NDE, July 1980, LaJolla, California (this volume).

5. R.K. Elsley, Flow Characterization by Low Frequency Scattering Measurement," Proceedings of the ARPA/AFML Review of Progress in Quantitative NDE, January 1979, LaJolla, California; R.K. Elsley, J.M. Richardson, R.B. Thompson, "Determination of Fracture Mechanics Parameters from Elastic Wave Scattering Measurements at Low Frequencies," Interdisciplinary Program for Quantitative Flaw Definition; Special Report, Fourth Year Effort, October, 1978.

6. M.F. Whalen, P.M. Garafola, L.J. O'Brien, A.N. Micciardi, "Application of Adaptive Learning Networks to Quantitative Flow Definition," Proceedings of the DARPA/AFML Review of Progress in Quantitative NDE, LaJolla, California (this volume).

7. J.K. Cohen and N. Bleistein, "Direct Inversion in Complex Geometries," Ibid.

8. M.G. Silk, B.H. Lidington, "Defect Sizing Using Ultrasonic Time Delay Approach," British J. NDT, 17, 1975, pp. 33-38. M.G. Silk, "Sizing of Cracks by Ultrasonic Means," Research Techniques in Nondestructive Testing, Ed. R.S. Sharpe, Vol. III, 1976, pp. 51-99.

GENERALIZED ULTRASONIC SYSTEM FOR MICROCOMPUTER CONTROLLED DATA COLLECTION

Ronald D. Strong
Los Alamos Scientific Laboratory
Los Alamos, New Mexico 87545

ABSTRACT

A system developed by the NDE Group of the Los Alamos Scientific Laboratory for the automated scanning of objects with an axis of rotation is described. This system is still being expanded to allow greater versatility in the motions. Data which was collected using the system and some typical test objects are also presented and discussed.

INTRODUCTION

In order to provide adequate ultrasonic inspection of parts used or fabricated within the Los Alamos Scientific Laboratory(LASL), it became apparent that a specialized scanning system was necessary to position the transducer relative to the parts and move the parts. Many of the typical parts which are inspected have spherical geometry. Two half shells are usually brazed or welded together to form the sphere. A scanner was designed and fabricated which could scan the surface of a spherical object of virtually any size to a maximum diameter of 225 mm. This scanner is shown in fig. 1. The size variation was partially accommodated through the use of pedestals of different heights. Initially the scanner was continuously driven and the results were plotted using a slaved X-Y recorder. The X- and Y-positions were generated using a sin-cos potentiometer. This caused the recorder to draw a circle as the turntable moved. The radius of this circle was controlled by a potentiometer which was coupled to the worm gear shaft which positions the swing arm. The diameter of the circle is therefore a function of the position of the transducer relative to the equator of the sphere. A relatively simple two angle manipulator, which we had designed and used previously in manual scanners, was mounted on the swing arm to permit aiming of the transducer. The go/nogo output of the flaw gate of the ultrasonic instrument controlled the pen lift mechanism of the recorder.

This scanner worked well. With the availability of microcomputer hardware and software, the equipment was upgraded to allow simple control of the data collection process by the microcomputer. A photosensor was used to indicate the "0" position of the turntable. The amplitude voltage from the gate analog output was fed to an analog-digital converter(ADC). Samples were taken at programmed time increments after the "0" position was passed. The digitized amplitude data were stored in arrays sequentially, so that the location of the datum is representative of part rotation or longitude. Each array represented one complete rotation at a particular latitude. An array length of 1000 words was chosen, which resulted in samples being taken at 0.36° increments.

Fig. 1 Original object scanner.

Many of the inspections are made on equatorial welds in vessels which have a square butt joint configuration at the weld root. The welds frequently are also allowed to have a finite depth of incomplete penetration. This required us to make a quantitive determination of the penetration depth. The measurement of the raw reflection signal did not yield a direct indication of the root height due to saturation of the signal at a notch depth of about 0.5 mm or about 20% of the wall thickness. Greater depths than that do result in the reflection being observed at a greater number of latitudes when the object was scanned. At this point it was decided that it would be advantageous to have the two scanner motions driven under software control using stepper motors.

SYSTEM DESCRIPTION

A duplicate of the original scanner was fabricated with modifications allowing the installation of stepper motors. The scanner is used as part of an integrated system containing a microprocessor for control. Fig. 2 shows the components of the entire system. The scanner is shown in figure 3. Gear reduction drives are utilized to increase the torque output of the motors and to decrease the relative movement of the driven axis to a reasonable value. A 30 to 1 reduction on the vertical axis rotation is used resulting in a incremental movement of 0.12° per step. For the swing arm a 20 to 1 reduction was used which results in a incremental movement of 0.003° per step. The particular motor driver which we are using drives the motors at 100 increments per revolution. The motors operate at 200 steps per revolution but the drive controller outputs two steps per command increment. Both motors are operated within the zero error start/stop speed regime or at about 250 steps per second. Backlash within the scanning motions is reduced or, for our purposes, eliminated by only scanning in one direction. When a particular motion is returned to a starting position, it is moved past the desired start and then repositioned by moving to that position in the same direction as scanning is done. This is a standard method for backlash compensation in numerical control machines.

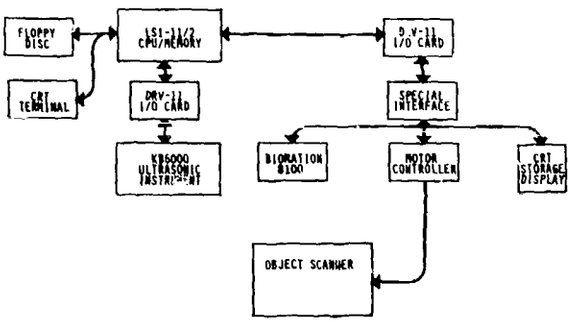

Fig. 2 Block diagram of data collection system.

An additional axis has also been added to the tank portion to allow transverse movement of the transducer assembly. This axis is assembled as a frame so it can be removed when not required. Figure 4 shows the tank with the frame attached. This axis is used when two transducers are required to perform the inspection or experiment. The axis has an incremental movement of 0.03175 mm. per step.

The particular motor controller being used was built by Group M-5 of LASL. It is capable of decoding an instruction from the computer interface to drive one of four motors in a specified direction for a directed number of steps from 1 to 255. Only one axis can be driven at a time, but this is normally not a significant problem. Driver or translator cards built at LASL are also used in the controller. The controller is addressed and coupled to a single interface with a Biomation 8100 transient recorder and a M-5 designed storage display controller.

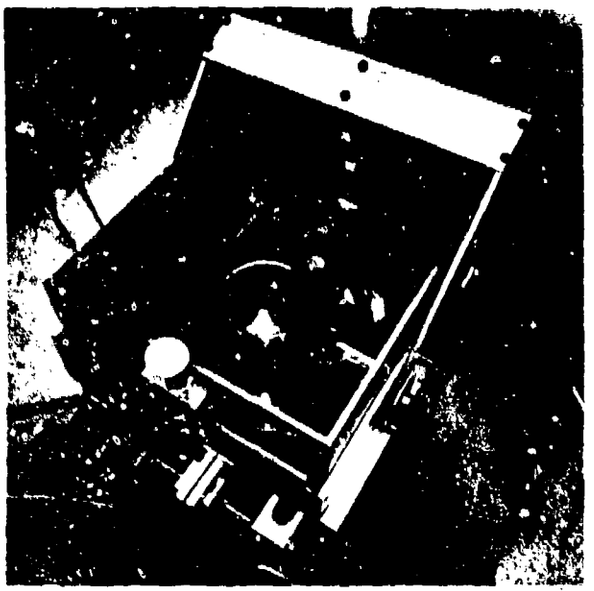

Fig. 3 Scanner driven by stepper motors.

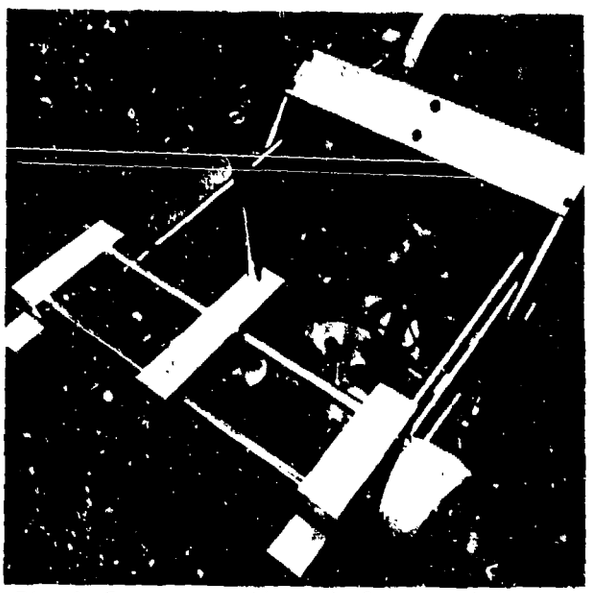

Fig. 4 Transverse motion axis frame mounted on tank assembly.

The microcomputer system that is being utilized is a DEC LSI-11/2 processor with 32k words of memory and the extended and floating point instruction set options. The RT-11 operating system is used. A dual-drive double-density floppy disc unit is used for program and mass storage. DRV-11 parallel interfaces are used to interface with the external devices. FORTRAN is used as the

high level language and the MACRO assembly language is used to program the operation of the peripheral instruments.

DATA COLLECTION EXAMPLES

As stated previously many of the inspections performed using this system are of equitorial welds. The system is set up by adjusting the swing arm frame height until the change or runout in the water path is minimal when the arm is rotated. This positions the arm pivot axis so that it passes through the center of the sphere. Since a shear wave angle beam inspection is desired, the transducer manipulator is adjusted so that the beam is normal to the surface. An offset angle then is turned into the manipulator to give a nominal 45° shear beam angle. A 5.0 Mhz focused broadband transducer(Aerotech Alpha or Panametrics VIP Series) is used. The focusing improves the spatial resolution along the weld length and the material thickness is thin enough that unsymetrical focusing due to the spherical surface does not cause problems. The swing arm is moved so that the beam is out of the weld area, and the scanning process begins. The current program makes twenty rotational scans with the arm being incremented 0.3° per revolution. This is normally sufficient to completely traverse the weld zone on the first bounce. A KBI KB6000 ultrasonic instrument is used. This instrument has a digital output of both gate time and amplitude. At the present time only the amplitude word is used. As the scanning process progresses the data are stored in a two dimensional array. An array of the maximum amplitudes observed at each longitude is also maintained. The maximum amplitude array and a polar plot of any data which exceeds 50% full scale amplitude is displayed on a storage scope along with the current amplitude data. This allows the operator to follow the inspection and to make judgments about the validity of the data. When the scanning is completed, the accumulated data plus some title information is stored on floppy disc for further processing.

The stored data is plotted out using a DEC PDP-11/40 on a Versatec printer/plotter without extensive processing. One output is the maximum amplitude values and a polar plot of all points which are greater than 20% of full scale amplitude. The dot size of the latter plot is varied with the amplitude. These plots are shown in Fig. 5. A second output is an isometric representation of the amplitude data for all scans. This plot is shown in Fig 6. One of the benefits of having the maximum amplitude plot generated by evaluating the data from all scans is that the alignment of the equitorial plane of the test item does not have to be aligned perfectly normal to the rotational axis. Also the notches in the sample or standard do not have to be in perfect alignment, but some tolerance is allowed in their placement.

A second type of evaluation that can be made is studying the refraction and mode conversion of a wave striking a metal disc at varying angles. This geometry is to be used for studying the attenuation in a sample which might contain multiple defects or a zone of modified properties. Fig. 4 shows the basic setup. The longitudinal and shear wave velocities in the disc can be determined.

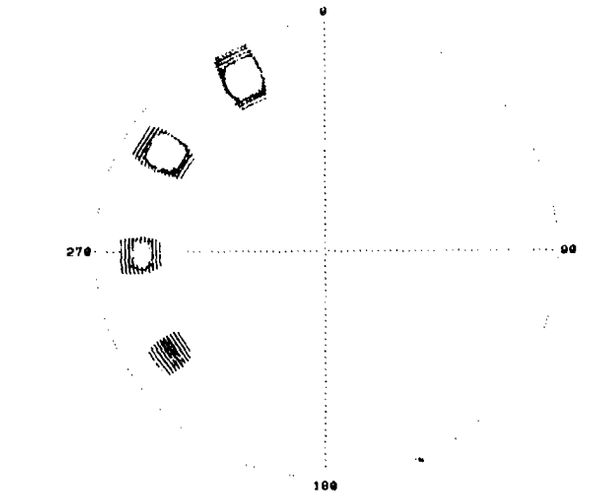

Fig. 5 A graph showing the polar plot and maximum amplitude plot from a standard containing I. D. notches with depths of 5, 10, 20, and 30% of the material thickness.

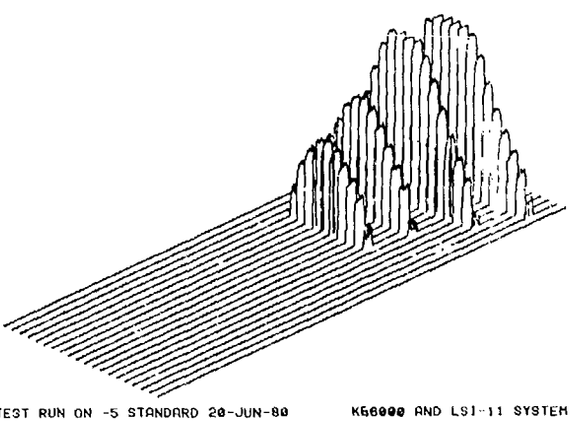

Fig. 6 A graph showing isometric plot representing reflection amplitude for all scans.

Figures 8 through 10 show some of the waveforms obtained from the disc. The wave trains are digitized using a Biomation 8100 transient recorder. The displayed data is the average of the data from 128 pulses. The longitudinal and shear wave velocities that were calculated from the data are 5917 km/sec and 3330 km/sec. This compares with a longitudinal wave velocity of 5907 km/sec measured using pulsed resonant frequency techniques.

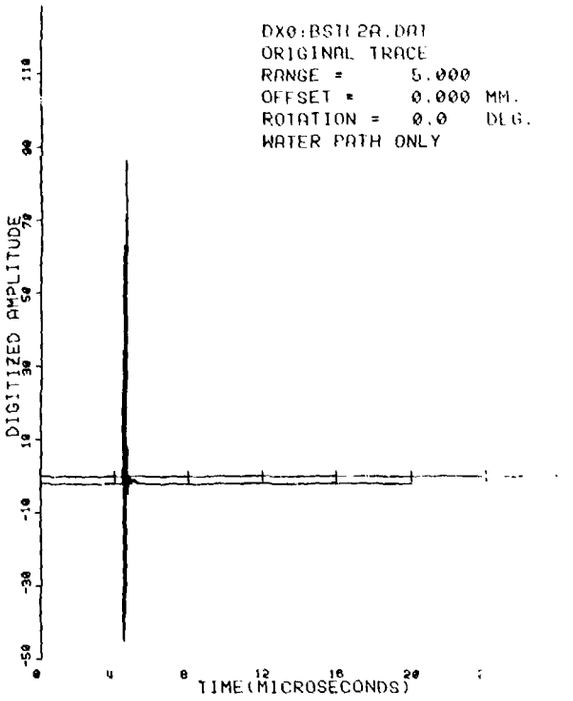

Fig. 7 Wave train obtained without a specimen in the water path.

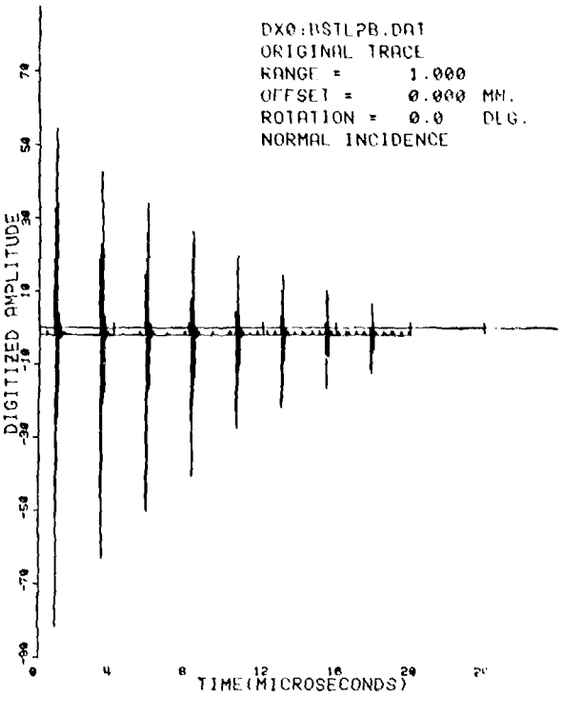

Fig. 8 Wave train obtained with the specimen inserted at normal incidence.

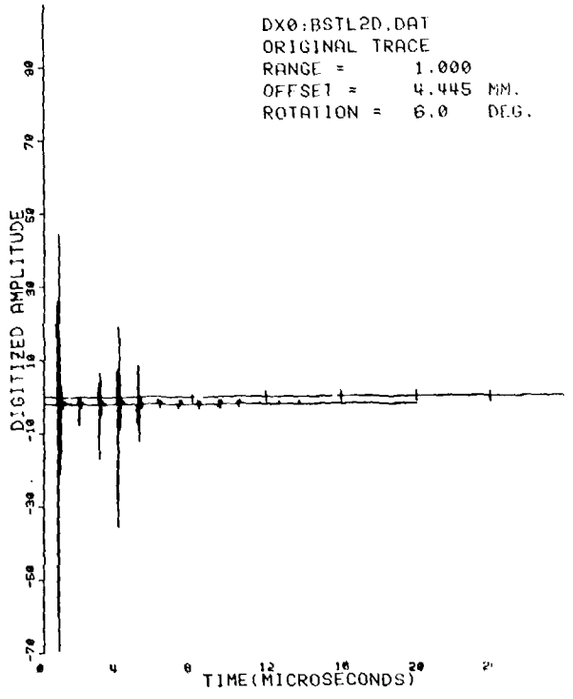

Fig. 9 Wave train obtained with the specimen rotated 6° off normal. The receiving transducer is offset to obtain peak amplitude from the first longitudinal refracted wave.

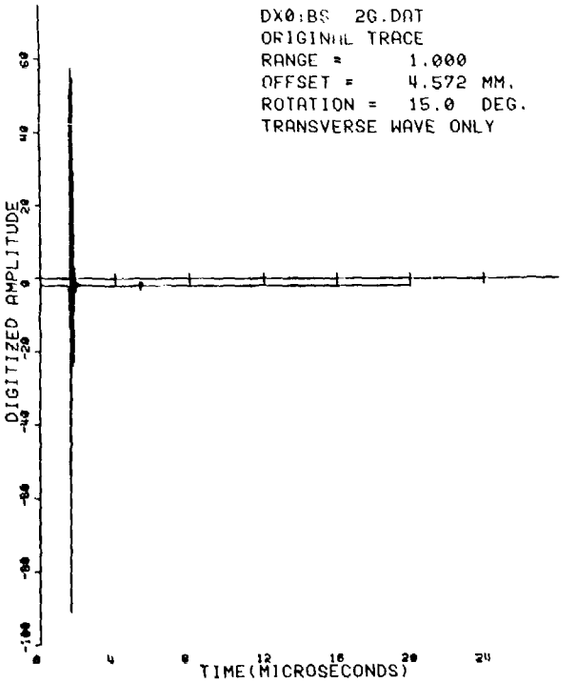

Fig. 10 Wave train obtained with the specimen rotated 15° off normal which is past the longitudinal critical angle. The receiving tranducer is offset to obtain peak amplitude from the refracted shear wave.

SUMMARY

Automatic data collection, processing and display using mini- and microcomputer technology has been used by Group M-5 of the Los Alamos Scientific Laboratory to achieve greater detail in ultrasonic inspections. This was achieved by assembling an automated scanner that although it was specifically tailored to spherical shapes can be utilized to perform the sample and tranducer motions to take data from virtually any sample which must be rotated on an axis during the inspection or experiment. Work on increasing the types of motion that are available is continuing.

ACKNOWLEDGEMENTS

Work performed under the auspices of the U. S. Department of Energy by the Los Alamos Scientific Laboratory of the University of California under contract W-7405-Eng. 36. Reference to a company or product name does not imply approval or recommendation of the product by the University of California or the U. S. Department of Energy to the exclusion of others that may be suitable.

I would like to thank E. J. Vonderheide and R. McFarland of Group SD-5 who performed the fabrication of the scanner and attachments with only the aid of cursory sketches. Also H. W. Johnson who did the photography and graphics reproduction.

SUMMARY DISCUSSION

Tom Moran, Chairman (AFWAL/MLLP): Are there any questions on this paper?

Bob Addison (Rockwell Science Center): On the manipulator you showed in the last slide, what types of precisions and accuracies is your machine achieving?

Ronald Strong (Los Alamos Scientific Laboratory): The worm gear drive is 60 to 1. At 200 steps per revolution the reolution of the manipulator is 0.03 degrees per step. The backlash, when the components are correctly matched, is on the order of that figure also.

Tom Moran, Chairman: Okay. That adjourns the conference for the formal sessions, at least.

Thank you all.

ATTENDEE LIST

REVIEW OF PROGRESS IN QUANTITATIVE NDE

SCRIPPS INSTITUTION OF OCEANOGRAPHY

July 14-18, 1980

J. E. Achenbach (Dr.)
Department of Civil Engineering
Northwestern University
The Technical Institute
Evanston, IL 60201

Marc A. Adams
Jet Propulsion Laboratory
Building 157 Room 418
4800 Oak Grove Drive
Pasadena, CA 91103

Robert C. Addison, Jr. (Dr.)
Rockwell International Science Center
1049 Camino Dos Rios
Thousand Oaks, CA 91360

Laszlo Adler (Dr.)
Welding Institute
Ohio State University
155 West Woodruff Avenue
Columbus, OH 43210

George A. Alers (Dr.)
New Mexico Engineering Research Institute
The University of New Mexico
Building A-6, 2301 Yale SE
Albuquerque, NM 87106

James C. Aller
National Science Foundation
1800 G. Street, N.W.
Washington, D. C. 20550

W. L. Anderson
Electrical Engineering Department
University of Houston
Houston, TX 77004

J. Argento
U. S. Army ANRADCOM, Bldg. 62
Dover, NJ 07801

Bert A. Auld (Dr.)
Edward L. Ginzton Laboratory
Stanford University
Stanford, CA 94305

Sevig Ayter (Dr.)
Edward L. Ginzton Laboratory
Stanford University
Stanford, CA 94305

Alfred J. Bahr (Dr.)
SRI International
333 Ravenswood Avenue
Menlo Park, CA 94025

Clifford C. Bampton
Rockwell International Science Center
1049 Camino Dos Rios
Thousand Oaks, CA 91360

Yoseph Bar-Cohen
AFWAL/MLLP - NDE Branch
Wright-Patterson AFB
OH 45433

Charles S. Barrett
Denver Research Institute
University of Denver
Denver, CO 80208

Richard C. Barry
Palo Alto Research Laboratory
Lockheed Missiles & Space Co., Inc.
P. O. Box 504
Sunnyvale, CA 94056

Narendra K. Batra (Dr.)
Systems Research Laboratories, Inc.,
2800 Indian Ripple Road
Dayton, OH 45440

K. J. Bedell
General Dynamics
P. O. Box 758
Fort Worth, TX 76101

Arden L. Bement, Jr. (Dr.)
Deputy Under Secretary
of Defense for
Research and Engineering
Research & Advanced Technology
Pentagon, Washington, D. C.

Patricia Bennett
Edward L. Ginzton Laboratory
Stanford University
Stanford, CA 94305

Simon Bennett
Edward L. Ginzton Laboratory
Stanford University
Stanford, CA 94305

Harold Berger
Office of NDE
National Bureau of Standards
Washignton, D. C. 20234

Craig Biddle
Pratt & Whitney Aircraft
Box 2691
W. Palm Beach, FL 33402

Albert S. Birks
Battelle Northwest Laboratories
P.O. Box 999
Richland, WA 99352

Donald Birx
Systems Research Laboratory
2800 Indian Ripple Road
Dayton, OH 45440

Norman Bleistein (Dr.)
Denver Applied Analytics
2555 S. Ivanhoe Place
Denver, CO 80222

David B. Bogy (Dr.)
Department of Mechanical Engineering
University of California, Berkeley
Berkeley, CA 94720

John E. Bobbin
Krautkramer-Branson Intl.
250 Long Beach Boulevard
Stratford, CT 06497

Norbert N. Bojarski (Dr.)
16 Pine Valley Lane
Newport Beach, CA 92660

Leonard J. Bond (Dr.)
Department of Electronic and
Electrical Engineering
University College London
Torrington Place
London WCIE 7JE

John Bosko
Rocketdyne Division
Rockwell International
6633 Canogo Avenue
Canoga Park, CA 91304

Robert C. Bray
Edward L. Ginzton Laboratory
Stanford University
Stanford, CA 94305

Richard Brin Department of Civil Engineering
Northwestern University
Evanston, IL 60201

James R. Brink
David Taylor Naval Ship R&D Center
Code 1750.1
Carderock, MD 20084

Alfred L. Broz
Army Materials & Mechanics
Research Center
Arsenal Street
Watertown, MA 02172

Otto Buck (Dr.)
Ames Laboratory
Iowa State University
Ames, IA 50011

Michael J. Buckley (Dr.)
Rockwell International Science Center
1049 Camino Dos Rios
Thousand Oaks, CA 91360

Roy L. Buckrop (Commander)
U.S. Army Armament Materials
Readiness Command
Attn: DRSAR-QAE
Rock Island, IL 61299

Christian P. Burger (Dr.)
Ames Laboratory
Iowa State University
Ames, IA 50011

Lawrence J. Busse
Battelle Northwest Laboratories
P.O. Box 999
Richland, WA 99352

Jean F. Bussiere
Industrial Materials Research
Institute, NRC
1000 de Serigny, Longvevil
Quebec, Canada J4K 5B1

Riley Byrd
Lockheed Missiles & Space Company
Lockheed Palo Alto Research Laboratory
3251 Hanover Street
Palo Alto, CA 94304

Peter Cannon (Dr.)
Rockwell International Science Center
1049 Camino Dos Rios
Thousand Oaks, CA 91360

John M. Cargill
Admiralty Marine Technology Estab.
St. Leonard's Hill, Dunfermline
Fife, Scotland KY115PW

Herbert R. Carleton
State University of New York
Stony Brook, N.Y. 11794

John Carlyle
Naval Air Development henter
Code 6063
Warminster, PA 18974

Roger Chang (Dr.)
Rockwell International Science Center
1049 Camino Dos Rios
Thousand Oaks, CA 91360

Dale E. Chimenti
Materials Laboratory, AFWAL/MLLP
Wright-Patterson AFB, OH 45433

Raymond C. Y. Chin
Lawrence Livermore Laboratory
P. O. Box 808 (L-71)
Livermore, CA 94550

Chou Ching-Hua (Mrs.)
Edward L. Ginzton Laboratory
Stanford University
Stanford, CA 94305

Jack K. Cohen (Dr.)
Denver Applied Analytics
2555 S. Ivanhoe Place
Denver, CO 80222

Frederick Cohen-Tenoudji
Universite Paris VII
Groupe de Physique des Solides
De L-Ecole Normale Superieure
Tour 23-2, Place Jussieu
75221 Paris CEDEX/FRANCE

H. Dale Collins (Dr.)
Battelle Northwest Laboratories
P. O. Box 999
Richland, WA 99352

Bill D. Cook (Dr.)
Cullen College of Engineering
University of Houston-Central Campus
Houston, TX 77004

Thomas Cooper
Materials Laboratory, AFWAL/MLLP
Wright-Patterson AFB, OH 45433

J. Gary Cottingham
Brookhaven National Laboratory
Building 902B
Upton, N.Y. 11973

Robert L. Crane (Dr.)
Materials Laboratory, AFWAL/MLLP
Wright-Patterson AFB OH 5433

T. J. Davis
Battelle Northwest Laboratories
P. O. Box 999
Richland, WA 99852

Vincent A. Del Grosso
Naval Research Laboratory (Code 5831)
Department of the Navy
Washington. D. C. 20375

William S. de Rosset
Ballistic Research Laboratory
ARRADCOM, Attn: DRDAR-BLC
Aberdeen Proving Ground, MD 21005

B. Boro Djordjevic
Martin Marietta Laboratories
1450 South Rolling Road
Baltimore, MD 21227

Steven R. Doctor (Dr.)
Battelle Northwest Laboratories
P. O. Box 999
Richland, WA 99352

James Doherty
Pratt & Whitney Aircraft
Aircraft Road
Middletown, CT 06457

Eytan Domany (Dr.)
Department of Electronics
Weizmann Institute of Science
Rehovot, Israel

Donald G. Eitzen (Dr.)
National Bureau of Standards
Sound A147
Washington, DC 20234

Charles M. Elias
Materials Laboratory, AFWAL/MLLP
Wright-Patterson AFB, OH 45433

Richard K. Elsley (Dr.)
Rockwell International Science Center
1049 Camino Dos Rios
Thousand Oaks, CA 91360

Anthony G. Evans (Dr.)
Dept. of Materials Science &
Mineral Engineering
University of California, Berkeley
Berkeley, CA 94720

William F. Feng
Lawrence Livermore Laboratory
P. O. Box 808
Livermore, CA 94550

J. D. Fenton
Vought Corporation
P.O. Box 225907
Dallas, TX 75265

Kenneth W. Fertig
Rockwell International Science Center
1049 Camino Dos Rios
Thousand Oaks, CA 91360

Ken Fesler
Edward L. Ginzton Laboratory
Stanford University
Stanford, CA 94305

Konan Fong
General Electric Company
Research & Development Center
P.O. Box 43
Schenectady, NY 12301

Christopner M. Fortunko (Dr.)
National Bureau of Standards
325 Broadway
Boulder, CO 80303

Paul M. Gammell
Jet Propulsion Laboratory
Mail Stop 183-901
4800 Oak Grove Drive
Pasadena, CA 91103

C. Gerald Gardner (Dr.)
Electrical Engineering Department
University of Houston
Houston, TX 77004

Michael Gardos
Hughes Aircraft Company
Culver City, CA 90230

W. Gebbardt
Institute for Nondestructive Testing
Saarbrucken, West Germany

Mohan Ghosh
Dept. of Mechanics & Structures
Boetter Hall No. 5705
University of California
Los Angeles, CA 90024

S. W. Gill
General Dynamics/Convair
P.O. Box 80847
San Diego, CA 92138

James F. Goff
Naval Surface Weapons Center
Silver Spring, MD 20910

James E. Green
Effects Technology Inc.
5383 Hollister Avenue
Santa Barbara, CA 93111

Harold Gryting
Southwest Research Institute
6220 Culebra Road
P. O. Drawer 28510
San Antonio, TX 78284

James E. Gubernatis (Dr.)
Los Alamos Scientific Laboratory
T11, MS 457
Los Alamos, NM 87545

Marvin A. Hamstad (Dr.)
Lawrence Livermore Laboratory
P. O. Box 808
Livermore, CA 94550

John A. Harris, Jr.
Pratt & Whitney Aircraft
P.O. Box 2691
West Palm Beach, FL 33402

Stephen D. Hart (Dr.)
Naval Research Laboratory
Code 5831
4555 Overlook Avenue
Washington, DC 20375

G. Hawkins
The Aerospace Corporation
P.O. Box 92957
Los Angeles, CA 90009

Alicia Herrmann
School of Engineering
Stanford University
Stanford, CA 94305

George Herrmann (Dr.)
Division of Applied Mechanics
School of Engineering
Stanford University
St anford, CA 94305

B. P. Hildebrand
Spectron Development Laboratories
3303 Harbor Boulevard
Costa Mesa, CA 92626

Stephen Hopkins
Failure Analysis Associates
Suite 116
750 Welch Roah
Palo Alto, CA 94304

Roger B. Houston
Rockwell International Science Center
1049 Camino Dos Rios
Thousand Oaks, CA 91360

Richard V. Inman
Rockwell International Science Center
1049 Camino Dos Rios
Thousand Oaks, CA 91360

M. H. Jacoby
Lockheed Missiles & Space Company
P. O. Box 504
Sunnyvale, CA 94086

George E. Jahn
Varian Associates
611 Hansen Way
Palo Alto, CA 94303

Suktek Johar (Dr.)
Ontario Research Foundation
Sheridan Park Research Community
Mississauga, Ontario
Canada L5K 1B3

George C. Johnson
Department of Mechanical Engineering
University of California
Berkeley, CA 94720

David H. Kaelble
Rockwell International Science Center
1049 Camino Dos Rios
Thousand Oaks, CA 91360

Frank N. Kelley (Dr.)
Institute of Polymer Science
University of Akron
Akron, OH 44325

Larry Kessler (Dr.)
Sonoscan, Inc.
530 East Green Street
Bensenville, IL 60106

Pramod K. Khandelwal
Detroit Diesel Allison
Division of General Motors Corporation
P. O. Box 894-W-5
Indianapolis, IN 46206

B. Pierre T. Khuri-Yakub (Dr.)
Edward L. Ginzton Laboratory
Stanford University
Stanford, CA 94305

Iain M. Kilpatrick
Admiralty Marine Technology Estab.
St. Leonard's Hill, Dunfermline
Fife, Scotland KY115PW

Richard King
Edward L. Ginzton Laboratory
Stanford University
Stanford, CA 94305

Gordon S. Kino (Dr.)
Edward L. Ginzton Laboratory
Stanford University
Stanford, CA 94305

Timothy E. Kinsella
General Dynamics
Ft. Worth Division
P. O. Box 748
Ft. Worth, TX 76101

Stan Klima
NASA-LeRC Research Center
21000 Brookpark Road
Cleveland, OH 44135

James A. Krumhansl (Dr.)
National Science Foundation
1800 6th Street, NW
Washington, DC 20550

Kenneth M. Lakin (Dr.)
Ames Laboratory
Iowa State University
Ames, IA 50011

Douglas K. Lemon
Battelle NOrthwest Laboratory
P. O. Box 999
Richland, WA 99352

Edward Lenoe
Department of the Army
Materials & Mechanics Research Center
Watertown, MA 02172

Chuk L. Leung (Dr.)
Rockwell International Science Center
1049 Camino Dos Rios
Thousand Oaks, CA 91360

Kenneth Liang
Edward L. Ginzton Laboratory
Stanford University
Stanford, CA 94025

Dean E. Lingenfelter
Lockheed Missiles & Space Co., Inc.
P.O. Box 504
Sunnyvale, CA 94088

Stuart A. Long (Prof.)
Department of Electrical Engineering
University of Houston
Houston, TX 77004

Jim F. Martin (Dr.)
Rockwell International Science Center
1049 Camino Dos Rios
Thousand Oaks, CA 91360

Bruce W. Maxfield (Dr.)
Lawrence Livermore Laboratory
P.O. Box 808
Livermore, CA 94550

Ron McKinney
Cullen College of Engineering
University of Houston - Central Campus
Houston, TX 77004

P. V. McLaughlin, Jr.
Department of Mechanical Engineering
Villanova University
Villanova, PA 19085

David T. Mih
Northrop Corporation
3901 West Broadway Street
Hawthorne, CA 90250

Jovan Moacanin (Dr.)
Jet Propulsion Laboratory
4800 Oak Grove Drive
Pasadena, CA 91103

Thomas J. Moran (Dr.)
Materials Laboratory, AFWAL/MLLP
Wright-Patterson AFB, OH 45433

Roger A. Morris
Group M-5, MS-912
Los Alamos Scientific Laboratory
Los Alamos, NM 87545

Winfred L. Morris (Dr.)
Rockwell International Science Center
1049 Camino Dos Rios
Thousand Oaks, CA 91360

M. William Moyer
Union Carbide Nuclear
P. O. Box Y
Oak Ridge, TN 37830

Joseph A. Morzis, Jr. (Dr.)
Materials Laboratory, AFWAL/MLLP
Wright-Patterson AFB, OH 45433

Anthony N. Mucciardi (Dr.)
Adaptronics, Inc.
Westgate Research Park
1750 Old Meadow Road
McLean, VA 22102

Frank Muennemann
Edward L. Ginzton Laborabory
Stanford University
Stanford, CA 94305

William Munn
Rockwell International
Tulsa Division
P. O. Box 51308
Tulsa, OK 74151

M. K. Murthy
Ontario Research Foundation
Sheridan Park
Mississauga, Ontario
Canada

A. H. Nayfeh
Systems Research Laboratories
2800 Indian Ripple Road
Dayton, OH 45440

Andrew Norris
Department of Civil Engineering
Northwestern University
Evanston, IL 60201

Ron Novak
AiResearch Manufacturing Company
of Arizona
111 South 34 Street
Phoenix, AZ 85010

Louis Odor (Dr.)
Rockwell International Columbus
4300 East 5th Avenue
Columbus, OH 43216

David W. Oliver
General Electric Corporate
Research & Development Center
P. O. Box 8
Schevectady, N. Y. 12301

P. S. Ong
Department of Electrical Engineering
University of Houston
Houston, TX 77024

Jon L. Opsal (Dr.)
Lawrence Livermore Laboratory
P. O. Box 808
Livermore, CA 94550

Derek J. Palmer
Materials Officer
Defence Equipment Staff
British Embassy
Washington, D. C. 20008

G. Pap
U. S. Army ANRADCOM, Building 62
Dover, NJ 07801

William J. Pardee (Dr.)
Rockwell International Science Center
1049 Camino Dos Rios
Thousand Oaks, CA 93160

Neil E. Paton (Dr.)
Rockwell International Science Center
1049 Camino Dos Rios
Thousand Oaks, CA 91360

Malcolm Perry
Rolls Royce Ltd.
P.O. Box 3
Silton, Bristol
England

D. Kent Peterson
Edward L. Ginzton Laboratory
Stanford University
Stanford, CA 94305

John Petru
Air Force NDI Program Office
SA-ALC/MMEI
Kelly Air Force Base, TX 78241

Herbert Popp
Aircraft Engine Group (M-87)
General Electric
Evendale, OH 45215

G. J. Posakony
Battelle Northwest Laboratories
P. O. Box 999
Richland, WA 99352

Ronald Provencher
Naval Sea Systems Command
Code 3232
2531 Jefferson Davis Highway
Arlington, VA 20362

Gerald Quentin (Dr.)
Universite Paris VII
Groupe de Physique des Solides
De L'Ecole Normale Superieure
Tour 23 - 2, Place Jussieu
75221 Paris CEDEX 05/France

Michael T. Resch
Department of Materials Science
Stanford University
Stanford, CA 94305

William N. Reynolds
NDT Centre
AERE Harwell, Oxfordshire
Didcot, Oxon, England

John M. Richardson (Dr.)
Rockwell International Science Center
1049 Camino Dos Rios
Thousand Oaks, CA 91360

M. Rinziat
Edward L. Ginzton Laboratory
Stanford University
Stanford, CA 94305

John Rodgers
Acoustic Emission Technology Corporation
1812 J. Tribute Road
Sacramento, CA 95815

Ron Rogers
Rockwell International Automotive
2135 West Maple
Troy, MI 48098

James H. Rose, Jr. (Dr.)
Ames Laboratory
Iowa State University
Ames, Iowa 50011

Corinne C. Ruokangas
Rockwell International Science Center
1049 Camino Dos Rios
Thousand Oaks, CA 91360

Wolfgang Sachse (Dr.)
Department of Theoretical and
Applied Mechanics
Cornell University
Ithaca, NY 14853

Amrit Sagar
Westinghouse Electric Corporation
Forest Hills Site
Pittsburgh, PA 15230

Kamel Salama (Dr.)
Mechanical Engineering Department
University of Houston
Houston, TX 77004

Wayne F. Savage
Office of Naval Research
Department of the Navy
Code 471
800 North Quincy Street
Arlington, VA 22217

Lester W. Schmerr
Laboratory of Mechanics - 208
Ames Laboratory
Iowa State University
Ames, Iowa 50011

Volker Schmitz
Battelle Northwest Laboratories
P. O. Box 999
Richland, WA 99352

Scott W. Schramm
ITT Research Institute
10 West 35th Street
Chicago, IL 60616

Martin P. Scott
Department of Materials Science
& Engineering
Stanford University
Stanford, CA 94305

Ed Seppi
Varian Associates
611 Hansen Way
Palo Alto, CA 94303

Nisar Shaikh
Applied Mechanics Division
Duranol Building #260
Stanford University
Stanford, CA 94305

Ramesh Shankar
Tetra Tech, Inc.
1911 North Fort Myer Drive
Arlington, VA 22209

Suresh Sharma
Department of Physics
University of Texas, Arlington
P. O. Box 19059
Arlington, TX 76016

John A. Simmons
Metallurgy Division
National Bureau of Standards
Washington, D.C. 20234

Anmol Singh
Southwest Research Institute
6220 Culebra Road
San Antonio, TX 78284

Richard W. Skulski
Rockwell International
Rocky Flats Division
P. O. Box 464
Golden, CO 80401

Ora E. Smith
Rockwell International Science Center
1049 Camino Dos Rios
Thousand Oaks, CA 91360

Richard T. Smith (Dr.)
NTIAC
Southwest Research Institute
Box 28510
San Antonio, TX 78284

Jacques Souquet
Varian Associates
611 Hansen Way
Palo Alto, CA 94303

Frederick E. Stanke
Edward L. Ginzton Laboratory
Stanford University
Stanford, CA 94305

Calvin H. Steinberg
Rockwell International Science Center
1049 Camino Dos Rios
Thousand Oaks, CA 91360

D.E.W. Stone
Structures Department
Royal Aircraft Establishment
Farnborough, Hants
England

W. Ross Stone
IRT Corporation
1446 Vista Claridad
La Jolla, CA 92037

Ronald D. Strong
Los Alamos Scientific Laboratory
P.O. Box 1663
Los Alamos, NM 87545

K. H. Styhr
Aireasearch Casting Company
Division of The Garrett Corporation
2525 West 190th street
Torrance, CA 90509

Robert A. Sulit
COMNAV SURFPAC (N43A)
NAB, Coronado
San Diego, CA 92155

Norman M. Tallan (Dr.)
Materials Laboratory, AFWAL/MS
Wright-Patterson AFB, OH 45433

Frank Taylor
Systems Research Laboratory
2800 Indian Ripple Road
Dayton, OH 45440

Robert L. Thomas (Dr.)
Department of Physics
Wayne State University
Detroit, MI 48202

A. L. Thompson
General Electric - AEG
I-275 & Newman Way
Cincinnati, OH 45215

Donald O. Thompson (Dr.)
Ames Laboratory
Iowa State University
Ames, IA 50011

R. Bruce Thompson (Dr.)
Ames Laboratory
Iowa State University
Ames, IA 50011

Julia Ju-Wen Tien
Edward L. Ginzton Laboratory
Stanford University
Stanford, CA 94305

Bernhard R. Tittmann (Dr.)
Rockwell International Science Center
1049 Camino Dos Rios
Thousand Oaks, CA 91360

Frederick P. Vaccaro
The Timken Company
1835 Dueber Avenue
Canton, OH 44706

Jan Van Den Andel
Westinghouse Canada Inc.
P. O. Box 510
Hamilton, Ontario
Canada, L8N 3K2

W. M. Van Schilfgarde
Edward L. Ginzton Laboratory
Stanford University
Stanford, CA 94305

Marvin C. (Buck) Van Wanderham (Dr.)
Mechanics of Materials & Structures
Pratt & Whitney Aircraft Group
West Palm Beach, FL 33402

Vasundara V. Varadan (Dr.)
Department of Engineering Mechanics
Ohio State University
155 West Woodruff Avenue
Columbus, OH 43210

William M. Visscher
Los Alamos Scientific Laboratory
T-11 MS 457
Los Alamos, NM 87545

James Wadin
Dunagan/Endevco
1717 South State College Boulevard
Anaheim, CA 92806

H. Wadley
National Bureau of Standards
Materials Building 223
Washington, D.C. 20234

Steven G. Wax
Air Force Office of Scientific
Research/NE
Bolling Air Force Base
Washington, D.C. 20332

R. D. Weglein
Missile Systems Group
Hughes Aircraft Company
Canoga Park, CA 91304

David Weinstein, (Dr.)
Edward L. Ginzton Laboratory
Stanford University
Stanford, CA 94305

Clifford H. Wells
Southwest Research Institute
P. O. Box 28410
San Antonio, TX 78284

Michael F. Whalen
Adaptronics, Inc.
1750 Old Meadow Road
McLean, VA 22102

H. K. Wickramasinghe (Dr.)
Department of Electrical Engineering
University College London
Torrington Place
London W.C. 1
England

Alec R. Willis
Sandia National Laboratory
P. O. Box 969
Livermore, CA 94550

Dale W. Wilson
MAE Department
University of Delaware
208 Evans Hall
Newark, DE 19711

D. K. Winslow
Edward L. Ginzton Laboratory
Stanford University
Stanford, CA 94305

William E. Winters
TRW
1 Space Park
Redondo Beach, CA 90278

C. W. Yew
Department of Aerospace Engineering
University of Texas
Austin, TX 78712

*U.S.Government Printing Office: 1981 — 559-006/5018